Konstantinos Kontis
Editor

28th International Symposium on Shock Waves 2

Springer

28th International Symposium on Shock Waves

Konstantinos Kontis (Ed.)

28th International Symposium on Shock Waves

Vol 2

Springer

Editor
Prof. Konstantinos Kontis
The University of Manchester
UK

Co-Editors
Erinc Erdem
Nalleli Gongora-Orozco
Raffaello Mariani
Azam Che Idris
Hossein Zare-Behtash
Daniel Bradford
Mark Quinn
Mohd Rashdan Saad

ISBN 978-3-642-25684-4 e-ISBN 978-3-642-25685-1
DOI 10.1007/978-3-642-25685-1
Springer Heidelberg New York Dordrecht London

Library of Congress Control Number: 2011946107

Printed on acid-free paper

Springer is part of Springer Science+Business Media (www.springer.com)

Preface

The University of Manchester hosted the 28th International Symposium on Shock Waves between 17 and 22 July 2011. The University of Manchester was created by bringing together The Victoria University of Manchester (VUM) and UMIST, two of Britain's most distinguished universities, to create a powerful new force in British Higher Education. Manchester has a long tradition of excellence in Higher Education. UMIST can trace its roots back to 1824 and the formation of the Manchester Mechanics' Institute, whilst The Victoria University of Manchester was founded as Owen's College in 1851.

Among the twenty-six Nobel Prize winners associated with the University are Rutherford, W.L. Bragg, A.V. Hill, P.M.S. Blackett, L. Pauling, R. Robinson and A. Todd. In addition to Rutherford's work on nuclear theory and the splitting of the atom, the University of Manchester led the world in the development of digital computing (with Alan Turing) and radio-astronomy (with Bernard Lovell). Recent outstanding successes include the Millennium Technology award to Prof. Steve Furber in Computer Science and the Nobel Prize for Physics in 2010.

In the field of Fluid Mechanics, Osborne Reynolds, FRS, the first professor of engineering in England, spent his whole professional life at Manchester, during which (among his astonishingly wide-ranging contributions) he shaped the direction of turbulence research for the century which followed. In 1946, Sydney Goldstein was instrumental in establishing the Fluid Motion Laboratory linking mathematical analyses of fluid flows with appropriate experimental work. The Laboratory acquired a supersonic tunnel fitted with liners to provide flow Mach number of 1.96 and 3.0. In the late 1950s the Laboratory had acquired an experimental facility which was to prove highly productive over a number of years. This was the 31ft (9·4m) long, 1ft (0·305m) diameter shock tube, named the Mark II shock tube by the Department, which had been built originally at the Atomic Energy Research Establishment, Harwell.

Manchester is the academic, commercial and financial capital of the UK's largest economic region outside London. It has a population of 2.6 million people and is renowned world-wide as a leading trade centre. The region's universities are a source of world-class research and development, and form a 'Supercampus' which is the largest student campus in Europe. Located nearby are a number of UNESCO

designated World Heritage Sites, all relating to industrialisation. The success of modern Manchester is founded on scientific, industrial and social innovation; for historians, it is one of the world's key sites. Its early modern scientific connections date as far back as the 1600s, but it is from the late 1700s that Manchester establishes itself as a mercantile and industrial capital where sciences thrive. The key figures included John Dalton, the Quaker teacher who became famous for the atomic theory in chemistry; his friend William Henry (Henry's law); and his pupil James Prescott Joule, the brewer who established the mechanical equivalent of heat.

The University of Manchester has recognised the importance of running international conferences as a way of promoting international cooperation in the dissemination of research and building collaborations between scholars across the world. The International Symposia on Shock Waves are the definitive meetings of the scientific community devoted to the study and use of the shock-wave phenomena, of all kinds. Started in 1957, they take place every two years, at places close to centres of activity in the field. After 1971 and 1999 in London, it was an honour for us to host the Symposium again in the United Kingdom.

The call for abstract submission resulted in a total number of 486 abstracts. Each abstract was reviewed by two members of the ISSW28 Scientific Review Committee which consisted of 109 experts in the field of shock wave research. The final programme of the symposium contained 9 plenary lectures and 341 oral and poster contributions. The posters were presented in a dedicated session without overlapping oral presentations. The student papers competing for the International Shock Wave Institute (ISWI) Best Student Paper Award were also presented in dedicated sessions. The mission of ISWI, which was founded in 2005, is to promote international and interdisciplinary collaboration in all areas of shock wave research through the organization of conferences, awards and honours and to facilitate liaison with other organizations with similar interests and activities.

Three hundred and seventy eight participants, of which 82 were students, from 25 countries registered. The nations from which the participants originated were: United Kingdom (57), Japan (55), USA (40), China (34), Germany (30), Russia (30), France (29), India (18), Canada (15), Israel (12), Australia (10), Brazil (8), South Korea (6), The Netherlands (6), South Africa (5), Sweden (4), Singapore (4), Taiwan (4), Chech Republic (3), Nigeria (2), Mexico (2), Norway (2), Austria (1), Belarus (1), and Poland (1). In addition, 34 partners enrolled for the companions programme of ISSW28.

Following the opening ceremony, the symposium was started with the Paul Vieille Lecture, given by Prof. Kazuyoshi Takayama, Tohoku University, Japan, providing an exciting presentation on: ‘Shock Wave Beyond’.

The ISWI Student Award, which was endowed with $1,000 US each, was presented during the ISSW28 Dinner Banquet by Prof. Kazuyoshi Takayama and Prof KPG Reddy, President of the International Shock Wave Institute. The winners are:

- Raffaello Mariani, University of Manchester, United Kingdom for his presentation on: 'Head on Collisions of Compressible Vortex Loops on a Solid Wall' (together with K. Kontis) and
- Randall Paton, University of Witwatersrand, South Africa for his presentation on: 'Imploding Conical Shock Waves' (together with B. Skews)

The scientific programme was complemented by a number of social events. The reception on Monday evening was hosted by Professor Luke Georghiou, Vice-President Research and Innovation of the University of Manchester. On Wednesday, the excursion was to Chatsworth House, Derbyshire. On Thursday, the ISSW28 banquet was held in Runway Visitor Park at Manchester International Airport under the historic Concorde aircraft. British Airways received government approval for the production of the G-BOAC in December 1969. Concorde GBOAC (affectionately known as 'Alpha Charlie') became the second aircraft to join the Concorde fleet when she was delivered to British Airways on 13 February 1976. Two extra excursions for accompanying persons were organised to Quarry Bank Mill on Tuesday 19th July, and the Imperial War Museum North and the Lowry on Thursday 21st July.

During the meeting of the International Advisory Committee of ISSW28, the venue for ISSW29 which will be held in 2013, was selected. Five excellent proposals were presented to the IAC which shows that there is a continuing interest in ISSW. The 29th International Symposium on Shock Waves will be held in Madison, Wisconsin, USA and will be chaired by Professor Riccardo Bonazza of University of Wisconsin-Madison.

ISSW28 could not have been realised without the support of the University of Manchester, and this is gratefully acknowledged. Further, ISSW28 was generously sponsored by the European Office of Aerospace Research and Development (EOARD). The companies Vision Research, Specialised Imaging, Photron High Speed Cameras, CD-Adapco, TSI, LaVision, National Instruments and Photon Lines were the Symposium exhibitors.

On behalf of the Local Organizing Committee of ISSW28, I would like to thank all participants who came to Manchester to support the Symposium with their attendance and oral or poster contributions. I would like to express my gratitude to the members of the International Advisory Committee and Scientific Review Committee for their continuous support during the preparation and running of the conference. I would like to thank those colleagues who served as session chairpersons and who guaranteed an accurate performance of the parallel sessions.

The support of the ConferCare (STARS) team, the University of Manchester Aerospace Research Institute (UMARI), and members of staff of the School of Mechanical, Aerospace and Civil Engineering is also acknowledged. The dedication, enthusiasm and team spirit of my PhD students and post-docs (Aero-Physics Laboratory Group) was the basis of the realisation of ISSW28.

With all the resources and support at our disposal, I am confident that the 2011 International Symposium on Shock Waves in Manchester has made a significant contribution to the international development of our field.

Manchester, July 2011

Professor Konstantinos Kontis
Chairman of the 28th ISSW
Chair in Aerodynamics and Shock Physics
Deputy Director of UMARI

The 28th International Symposium on Shock Waves
Hosted by the University of Manchester
Manchester, UK
18th–22nd July 2011

Chairman

Konstantinos Kontis — University of Manchester

Local Organising Committee

Janet Adnams
Daniel Bradford
Erinc Erdem
Nalleli Gongora-Orozco
Konstantinos Kontis
Brian E. Launder
Raffaello Mariani
Mark Quinn
Alistair Revell
Kate Smith
Sergey Utyuzhnikov
Hossein Zare-Behtash

UK Advisory Committee

Chris Allen
Holger Babinsky
Ken Badcock
David Barton
Neil Bourne
Chris Braithwaite
Stephen Daley
Dimitris Drikakis
David Emerson
Li He
Richard Hillier
Konstantinos Kontis
Lin Li
Hugh McCann
William Proud
Ning Qin
Jason Reese
Brian Richards
Graham Roberts
Neil Sandham
Paul Schuricht
Arthur Smith
John L Stollery
Yong Wang
Phillip Wither

International Advisory Committee

Takashi Abe
Nicholas Apazidis
E. Arunan
Gabi Ben-Dor
Riccardo Bonazza
Martin Brouillette
Keun-Shik Chang
Alina Chertock
Nikita Fomin
Sudhir Gai
Victor Golub
Jagadeesh Gopalan
Yogendra M. Gupta
Abdellah Hadjadj
Klaus Hannemann
Ronald K. Hanson
Koichi Hayashi
Richard Hillier
Yasuyuki Horie
Lazhar Houas
Ozer Igra
In-Seuck Jeung
Zonglin Jiang
Valeriy Kedrinkskiy
Doyle Knight
Konstantinos Kontis
Irina Krassovskaya
Meng-Sing Liou
Frank Lu
Kazuo Maeno
David Mee
Brian Milton
Richard Morgan
Herbert Olivier
Marcello Onofri
William Proud
K. P. J. Reddy
Akihiro Sasoh
Friedrich Seiler
Gary S. Settles
Beric Skews
Kazuyoshi Takayama
Eleuterio Toro
Ji Ming Yang
Zbigniew Walenta
David Zeitoun

Scientific Review Committee

Akihisa Abe
Takashi Abe
Chris Allen
Nicholas Apazidis
Joanna Austin
Holger Babinsky
Ken Badcock
David Barton
Tatiana Bazhenova
Sergey Bobashev
Russell Boyce
Gabi Ben-Dor
Riccardo Bonazza
Chris Braithwaite
Martin Brouillette
Keun-Shik Chang
Alina Chertock
Jeong-Yeol Choi
Dimitris Drikakis
Jean-Paul Dussauge
John Ekaterinaris
David Emerson
Kozo Fujii
Nikita Fomin
Sudhir Gai
Bharath Ganapathisubramani
Domenico Giordano
Victor Golub
Nalleli Gongora-Orozco
Jagadeesh Gopalan
Ali Gulhan
Yogendra Gupta
Jean-François Haas
Abdellah Hadjadj
Klaus Hannemann

Ronald K. Hanson
Koichi Hayashi
Li He
Richard Hillier
Yasuyuki Horie
Hans Hornung
Hamid Hosseini
Lazhar Houas
Dan Igra
Ozer Igra
Kazuhiro Ishii
Katsuhiro Ito
Shigeru Ito
Mikhail Ivanov
In-Seuck Jeung
Zonglin Jiang
Valeriy Kedrinkskiy
Mark Kendall
Herald Kleine
Doyle Knight
Konstantinos Kontis
Wilhelm Kordulla
Irina Krassovskaya
Brian Launder
Qingming Li
Assa Lifshitz
E. Arunan
Meng-Sing Liou
Frank Lu
Kazuo Maeno
Jan Martinez Schramm
Akiko Matsuo
Matthew McGilvray
David Mee
Brian Milton
Toshiharu Mizukaki
Richard Morgan
Christian Mundt
Duncan Murray
Kazuhiro Nakahashi
N Nikiforakis
Herbert Olivier
Marcello Onofri
Eric Petersen
Alexey Podlaskin
William Proud
Ning Qin
A. M. Rajendran
K. P. J. Reddy
Jason Reese
Alistair Revell
Graham Roberts
Paul Roth
Oren Sadot
Tsutomu Saito
Hirotaka Sakaue
Akira Sakurai
Neil Sandham
Selvaraj Saravanan
Akihiro Sasoh
Christof Schulz
Friedrich Seiler
Gary S. Settles
Beric Skews
Julio Srurijes
Johan Steelant
John L Stollery
Mingyu Sun
Kazuyoshi Takayama
Hideyuki Tanno
Evgeny Timofeev
Eleuterio Toro
Nobuyuki Tsuboi
Sergey Utyuzhnikov
Zbigniew Walenta
Shigeya Watanabe
Ji Ming Yang
Vigor Yang
Hossein Zare-Behtash
David Zeitoun
Fan Zhang

Event Coordination

Janet Adnams
Raffaello Mariani
Mark Quinn

External Affairs Liaison

Janet Adnams
Erinc Erdem

Database and IT

Janet Adnams
Mark Quinn

Graphic Design

Nalleli Gongora-Orozco
Student Competition
Alistair Revell
Sergey Utyuzhnikov
Poster Session
Hossein Zare-Behtash
Daniel Bradford

Conference Program

Date	Time	Session	Session Chair	Room
Sunday, 17 July 2011	1600	Registration Opens		Renold Concourse
	1900 - 2100	Welcome Drinks		Renold Concourse
Monday, 18 July 2011	0830 - 0850	Opening Ceremony		Renold C16
	0850 - 0930	Paul Vieille Memorial Lecture: Prof. K. Takayama	Prof. K. Kontis	Renold C16
	0940 - 1040	Hypersonic Flows I	Prof. S. Gai	Renold C2
		Propulsion I	Prof. B. E. Launder	Renold D7
		Shock Wave Propagation and Reflection I	Prof. I. Krassovskaya	Renold C16
		Multiphase Flows I	Prof. S. K. Lele	Renold C9
		Shock Waves in Rarefied Flows I	Prof. A. Sakurai	Renold F14
		Student Competition I	Prof. G. Jagadeesh	Renold E7
	1040 - 1100	Coffee / Tea		Renold Concourse
	1100 - 1220	Hypersonic Flows II	Prof. T. Mizukaki	Renold C2
		Propulsion II	Prof. C. Mundt	Renold D7
		Shock Wave Propagation and Reflection II	Prof. I. Krassovskaya	Renold C16
		Multiphase Flows II	Prof. J. Yang	Renold C9
		Shock Waves in Rarefied Flows II	Prof. A. Sakurai	Renold F14
		Student Competition II	Prof. G. Jagadeesh	Renold E7
	1220 - 1330	Lunch		Barnes Wallis

Date	Time	Session	Session Chair	Room
Monday, 18 July 2011	1330 - 1410	Keynote Lecture 1: Prof. I. Krassovskaya	Prof. K. Takayama	Renold C16
	1420 - 1540	Blast Waves I	Prof. N. Apazidis	Renold F14
		Chemically Reacting Flows I	Prof. C. Needham	Renold D7
		Flow Visualisation I	Prof. H. Kleine	Renold C2
		Shock Wave Propagation and Reflection III	Prof. S. Kobayashi	Renold C16
		Multiphase Flows III	Prof. O. Igra	Renold C9
		Student Competition III	Prof. N. Qin	Renold E7
	1540 - 1600	Coffee / Tea		Renold Concourse
	1600 - 1720	Blast Waves II	Prof. N. Apazidis	Renold F14
		Chemically Reacting Flows II	Prof. C. Park	Renold D7
		Flow Visualisation II	Prof. H. Kleine	Renold C2
		Shock Wave Propagation and Reflection IV	Prof. S. Kobayashi	Renold C16
		Multiphase Flows IV	Prof. O. Igra	Renold C9
		Student Competition IV	Prof. N. Qin	Renold E7
	1900 - 2100	Reception		Sackville Entrance Hall

Date	Time	Session	Session Chair	Room
Tuesday, 19 July 2011	0830 - 0910	Keynote Lecture 2: Prof. Y. M. Gupta	Prof. K. P. J. Reddy	Renold C16
	0920 - 1040	Detonation and Combustion I	Prof. K. Hayashi	Renold C16
		Shock Vortex Interactions I	Prof. F. Seiler	Renold C2
		Shock Boundary Layer Interactions I	Prof. J. Stollery	Renold C9
		Medical - Biological Applications I	Prof. H. Hosseini	Renold D7
		Student Competition V	Prof. L. Houas	Renold E7
	1040 - 1100	Coffee / Tea		Renold Concourse
	1100 - 1220	Detonation and Combustion II	Prof. K. Hayashi	Renold C16
		Shock Vortex Interactions II	Prof. F. Seiler	Renold C2
		Shock Boundary Layer Interactions II	Prof. J. Stollery	Renold C9
		Medical - Biological Applications II	Prof. H. Hosseini	Renold D7
		Student Competition VI	Prof. L. Houas	Renold E7
	1220 - 1330	Lunch		Barnes Wallis
	1330 - 1410	Keynote Lecture 3: Prof. K. Hayashi	Prof. R. Hanson	Renold C16
	1420 - 1540	Detonation and Combustion III	Prof. V. Golub	Renold C16
		Richtmyer-Meshkov I	Prof. R. Bonazza	Renold C9
		Diagnostics I	Prof. G. Settles	Renold D7
		Numerical Methods and Simulations I	Prof. T. Saito	Renold C2
		Student Competition VII	Prof. O. Sadot	Renold E7
	1540 - 1600	Coffee / Tea		Renold Concourse
	1600 - 1720	Facilities I	Prof. D. Buttsworth	Renold C2
		Richtmyer-Meshkov II	Prof. R. Bonazza	Renold C9
		Diagnostics II	Prof. G. Settles	Renold D7
		Shock Wave Phenomena and Applications I	Prof. D. Zeitoun	Renold C16
		Impact and Compaction I	Dr. J. Srulijes	Renold E7

Date	Time	Session	Session Chair	Room
Wednesday, 20 July 2011	0830 - 0910	Keynote Lecture 4: Prof. D. Buttsworth	Prof. H. G. Hornung	Renold C16
	0930 - 1700	Excursion		
Thursday, 21 July 2011	0830 - 0910	Keynote Lecture 5: Dr J. Steelant	Prof. J. L. Stollery	Renold C16
	0920 - 1040	Chemically Reacting Flows III	Prof. C. Park	Renold C2
		Detonation and Combustion IV	Prof. F. Lu	Renold C16
		Hypersonic Flows III	Prof. D. Mee	Renold C9
		Nozzle Flows I	Prof. A. Abe	Renold D7
		Shock Wave Phenomena and Applications II	Prof. M. Brouillette	Renold E7
	1040 - 1100	Coffee / Tea		Renold Concourse
	1100 - 1220	Facilities II	Prof. H. Olivier	Renold E7
		Detonation and Combustion V	Prof. M. Liberman	Renold C16
		Hypersonic Flows IV	Prof. D. Mee	Renold C9
		Nozzle Flows II	Prof. A. Abe	Renold D7
		Numerical Methods and Simulations II	Prof. T. Saito	Renold C2
	1220 - 1330	Lunch		Barnes Wallis
	1330 - 1410	Keynote Lecture 6: Prof. N. Qin	Prof. B. Skews	Renold C16
	1420 - 1540	Detonation and Combustion VI	Prof. M. Liberman	Renold C16
		Diagnostics III	Prof. T. Mizukaki	Renold D7
		Ignition I	Prof. N. Fedorova	Renold E7
		Richtmyer-Meshkov III	Prof. Z. Jiang	Renold C2
		Shock Wave Propagation and Reflection V	Prof. R. Morgan	Renold C9
	1540 - 1600	Coffee / Tea		Renold Concourse
	1600 - 1720	Poster Session	Dr. N. Gongora-Orozco	Renold Concourse
	1830 - 2200	Banquet		

Date	Time	Session	Session Chair	Room
Friday, 22 July 2011	0830 - 0910	Keynote Lecture 7: Prof. S. K. Lele	Prof. E. Timofeev	Renold C16
	0920 - 1040	Special Session on Shock Wave Moderation I	Prof. A. Sasoh	Renold C2
		Detonation and Combustion VII	Prof. A. Hadjadj	Renold C16
		Flow Visualisation III	Dr. H. Sakaue	Renold D7
		Shock Wave Phenomena and Applications III	Prof. Z. Walenta	Renold E7
		Shock Wave Propagation and ReflectionsVI	Prof. M. Brouillette	Renold C9
	1040 - 1100	Coffee / Tea		Renold Concourse
	1100 - 1220	Special Session on Shock Wave Moderation II	Prof. A. Sasoh	Renold C2
		Detonation and Combustion VIII	Prof. A. Hadjadj	Renold C16
		Flow Visualisation IV	Dr. E. Schuelein	Renold D7
		Shock Wave Phenomena and Applications IV	Dr. S. Utyuzhnikov	Renold E7
		Shock Wave Propagation and Reflection VII	Prof. Z. Jiang	Renold C9
	1220 - 1330	Lunch		Barnes Wallis
	1330 - 1410	Keynote Lecture 8: Prof. E. Arunan	Prof. Z. Jiang	Renold C16
	1420 - 1520	Nozzle Flows III	Dr. E. Erdem	Renold D7
		Shock Boundary Layer Interactions III	Dr. H. Zare-Behtash	Renold C16
		Numerical Methods and Simulations III	Prof. K-S. Chang	Renold C2
		Multiphase Flows V	Prof. Z. Walenta	Renold C9
	1540 - 1550	Coffee / Tea		Renold Concourse
	1550 - 1700	Closing Ceremony		Renold C16

Sunday, 17 July 2011

Sunday, 17 July 2011		Renold Concourse
1600 hrs		
Registration Opens		

Sunday, 17 July 2011		Renold Concourse
1900-2100		
Welcome Drinks		

Monday, 18 July 2011

Monday, 18 July 2011		
Opening Ceremony		
0830-0850		
Prof. Konstantinos Kontis, Chairman of ISSW 28		
Prof. Colin Bailey, Dean and Vice-President		
The University of Manchester, Faculty of EPS, School of MACE		Renold C16

Monday, 18 July 2011		
Paul Vieille Memorial Lecture		
0850-0930		
Shock Wave Phenomena and Interactions		
Prof. Kazuyoshi Takayama		
Tohoku University, Japan		
Session Chair:	K. Kontis, University of Manchester UK	Renold C16

Monday, 18 July 2011 AM Session A

Monday, 18 July 2011			
	Hypersonic Flows I		Renold C2
Session Chair:	S. Gai, University of New South Wales, Australia		
Time	0940 hrs	1000 hrs	1020 hrs
Paper number	2431	2453	2744
Paper title	Experimental investigation of mechanical distortions to hypersonic boundary layers	On the stability of pitching motion of re-entry vehicle with the tilted toroidal ballute	Surrogate-based multi-objective aerothermodynamic design optimization of hypersonic spiked bodies
Presenting author	W. Flaherty, University of Illinois, USA	H. Otsu, Ryukoku University, Japan	N. Qin, University of Sheffield, UK

Monday, 18 July 2011			
	Propulsion I		Renold D7
Session Chair:	B. E. Launder, The University of Manchester, UK		
Time	0940 hrs	1000 hrs	1020 hrs
Paper number	2639	2645	2755
Paper title	A computational study of supersonic combustion relevant to air-breathing engines	On thermodynamic cycles for detonation engines	External and internal configurations of the 14-X hypersonic aerospace vehicle
Presenting author	E. Fedina, Swedish Defence Research Agency – FOI, Sweden	F. Lu, University of Texas at Arlington, USA	T. Marcos, Institute for Advanced Studies, Brazil

Monday, 18 July 2011			
	Shock Wave Propagation and Reflection I		Renold C16
Session Chair:	I. Krassovskaya, Ioffe Institute, Russia		
Time	0940 hrs	1000 hrs	1020 hrs
Paper number	2496	2765	2456
Paper title	Shock wave reflection off convex cylindrical surfaces	Determination of the sonic point in unsteady shock reflection using various techniques based on numerical flowfield analysis	Consideration of von Neumann reflection and Mach reflection for strong shock waves
Presenting author	H. Kleine, University of New South Wales, Australia	A. Hakkaki-Fard, McGill University, Canada	S. Kobayashi, Saitama Institute of Technology, Japan

Monday, 18 July 2011			
	Multiphase Flows I		Renold C9
Session Chair:	S. K. Lele, Stanford University, USA		
Time	0940 hrs	1000 hrs	1020 hrs
Paper number	2501	2504	2454
Paper title	Experimental study of scale effects on shock wave interaction with a granular layer	Supercavitation phenomenon during water exit and water entry of a fast slender body	Numerical investigation of processes accompanying energy release in water near the free surface
Presenting author	Y. Sakamura, Toyama Prefectural Technical University, Japan	H-H. Shi, Zhejiang Sci-Tech University, China	N. Petrov, Ioffe Physical Technical Institute RAS, Russia

Monday, 18 July 2011

Shock Waves in Rarefied Flows I Renold F14

Session Chair:	A. Sakurai, Tokyo Denki University, Japan		
Time	0940 hrs	1000 hrs	1020 hrs
Paper number	2441	2480	2514
Paper title	A DSMC-MD investigation of wall effects in a shock tube operating at high Knudsen numbers	Generation of shock wave by temperature change at wall	Numerical simulations of nonequilibrium and diffusive effects in spherical shock waves
Presenting author	U. Bhandarkar, Indian Institute of Technology, India	A. Sakurai, Tokyo Denki University, Japan	V. Riabov, River College, USA

Monday, 18 July 2011

Student Competition I Renold E7

Session Chair:	G. Jagadeesh, India Institute of Science, Banagalore, India			
Time	0940 hrs	1000 hrs	1020 hrs	1040
Paper number	2448	2414	2467	2723
Paper title	Hypersonic flow past spiked bodies	Head on collisions of compressible vortex loops on a solid wall. Effects of wall distance variation	Experimental study on inactivation of marine bacteria using electrodischarge shock waves	Micro-blast waves using detonation transmission tubing
Presenting author	R. Fernandes, Cranfield University, UK	R. Mariani, University of Manchester, UK	N. Tsujii, Kobe University, Japan	O. Isaac, Indian institute of Science, India

Monday, 18 July 2011

Renold Concourse

1040-1100

Coffee / Tea

Monday, 18 July 2011 AM Session B

Monday, 18 July 2011				
	Hypersonic Flows II			Renold C2
Session Chair:	T. Mizukaki, Tokai University, Japan			
Time	1100 hrs	1120 hrs	1140 hrs	1200 hrs
Paper number	2521	2532	2568	2569
Paper title	An investigation of base flow of a circular cylinder at hypersonic speeds	On the numerical solution method of the 2D Oswatitsch equations for hypersonic flow	Modelling the complete operation of a free-piston shock tunnel for a low enthalpy condition	Shock tube experiments on heat transfer at generic re-entry bodies
Presenting author	S. Gai, University of New South Wales, Australia	V. Lorenz, University of the German Federal Forces, Germany	A. Dann, Loughborough University, UK	J. Srulijes, French-German Research Institute of Saint-Louis, France

Monday, 18 July 2011				
	Propulsion II			Renold D7
Session Chair:	C. Mundt, Universität der Bundeswehr München, Germany			
Time	1100 hrs	1120 hrs	1140 hrs	1200 hrs
Paper number	2761	2771	2633	2801
Paper title	Particle-impact ignition measurements in a high-pressure oxygen shock tube	Limiting contractions for starting a Prandtl-Meyer-type scramjet intake with overboard spillage	High Mach number and total pressure flow conditions for scramjet testing	Interaction between combustion and shock wave in supersonic combustor
Presenting author	M. Crofton, The Aerospace Corporation, USA	N. Moradian, McGill University, Canada	D. Gildfind, University of Queensland, Australia	L. Chen, Chinese Academy of Sciences, China

Monday, 18 July 2011

Shock Wave Propagation and Reflection II Renold C16

Session Chair: I. Krassovskaya, Ioffe Institute, Russia

Time	1100 hrs	1120 hrs	1140 hrs	1200 hrs
Paper number	2457	2484	2486	2698
Paper title	Study of shock-wave mitigation through solid obstacles	Guderley reflection for higher Mach numbers in a standard shock tube	Wave processes in transonic airfoil flows	Effect of solution conductivity on shock wave pressure generated by multichannel electrical discharge in water
Presenting author	A. Chaudhuri, CORIA, France	A. Cachucho, Witwatersrand University, South Africa	J. Nies, RWTH Aachen University, Germany	V. Stelmashuk, Institute of Plasma Physics AS CR, Czech Republic

Monday, 18 July 2011

Multiphase Flows II Renold C9

Session Chair: J. Yang, University of Science and Technology of China, China

Time	1100 hrs	1120 hrs	1140 hrs	1200 hrs
Paper number	2515	2528	2584	2601
Paper title	Explosive eruptions of volcanoes: hydrodynamic shock tubes as lab method of simulation	Investigation of bubble collapse and water jet induced by underwater explosion in a rectangular tube	Study of the interaction between a shock wave and a cloud of droplets	Motion of non-spherical particles following shock passage
Presenting author	V. Kedrinskiy, Lavrentyev Institute of Hydrodynamics, Russia	T. Koita, Tohoku University, Japan	A. Chauvin, Aix-Marseille Université, France	D. Murray, DSTL, UK

Monday, 18 July 2011

Shock Waves in Rarefied Flows II Renold F14

Session Chair: A. Sakurai, Tokyo Denki University, Japan

Time	1100 hrs	1120 hrs	1140 hrs	1200 hrs
Paper number	2561	2566	2680	2679
Paper title	Numerical study of hypersonic rarefied flows about leading edges of small bluntness	High-energy molecular beam source using a non-diaphragm type small shock tube	Flow phenomena in microscale shock tubes	Propagating wave in binary gas mixture from boundary of variable temperature and velocity
Presenting author	G. Shoev, Khristianovich Institute of Theoretical and Applied Mechanics, Russia	Y. Yoshimoto, University of Tokyo, Japan	M. Brouillette, Université de Sherbrooke, Canada	K. Yoshimura, Mathematical Science and Information Technology Research Centre, Japan

Monday, 18 July 2011

Student Competition II Renold E7

Session Chair: G. Jagadeesh, India Institute of Science, Banagalore, India

Time	1100 hrs	1120 hrs	1140 hrs	1200 hrs
Paper number	2549	2751	2575	2597
Paper title	Numerical simulation of a shock-accelerated multiphase fluid interface	Supersonic combustion flow visualization at hypersonic flow	Characteristics of shock wave propagating over particulate foam	Triple-shock-wave configurations: comparison of different thermodynamic models for diatomic gases
Presenting author	M. Anderson, Applied Research Associates, USA	T. Marcos, Institute for Advanced Studies, Brazil	M. Liverts, Ben Gurion University, Israel	P. Mostovykh, Baltic State Technical University, Russia

Monday, 18 July 2011

Barnes Wallis

1220-1330

Lunch

Monday, 18 July 2011 PM Session A

Monday, 18 July 2011
Keynote Lecture 1 Renold C16
1330-1410
Reflection and Diffraction of Shock Waves and Shock Wave Configurations
Prof. Irina Krassovskava
Ioffe Institute, Russia

Session Chair: K. Takayama, Tohoku University, Japan

Monday, 18 July 2011

Blast Waves I Renold F14

Session Chair: N. Apazidis, KTH, Sweden

Time	1420 hrs	1440 hrs	1500 hrs	1520 hrs
Paper number	2862	2498	2604	2524
Paper title	Numerical investigation of shock-wave load attenuation by barriers	Numerical analysis of weak-shock attenuation resulting from molecular vibrational relaxation	The influence of water saturation in soil on blast effect	Numerical investigations on muzzle flow under approaching real shooting conditions
Presenting author	S. Berger, Ben-Gurion University, Israel	K. Hatanaka, Muroran Institute of Technology, Japan	I. Kuchuk-Katalan, Plasan Sasa Ltd., Israel	X. Jiang, Nanjing University of Science and Technology, China

Monday, 18 July 2011

Chemically Reacting Flows I Renold D7

Session Chair: C. Needham, Applied Research Associates, USA

Time	1420 hrs	1440 hrs	1500 hrs	1520 hrs
Paper number	2722	2798	2825	2583
Paper title	Prediction of heatshield material performance in an arcjet	Experimental investigation of interaction of shock heated test gases with 7.25µm carbon fibres in a shock tube	A shock-tube with high-repetition time-of-flight mass spectrometry for the study of complex reaction systems	Reactions in H_2+He+CH_4 in strong shock waves: a review
Presenting author	S. McDowell, DSTL, UK	V. Jayaram, Indian Institute of Science, India	M. Fikri, University of Duisburg-Essen, Germany	C. Park, Korea Advanced Institute of Science and Technology, Korea

Monday, 18 July 2011

Flow Visualisation I Renold C2

Session Chair: H. Kleine, University of New South Wales, Australia

Time	1420 hrs	1440 hrs	1500 hrs	1520 hrs
Paper number	2495	2523	2614	2522
Paper title	Time-resolved Mach-Zehnder interferometry of shock waves	Study of normal shock behaviour near second throat	A temperature-cancellation method for motion-capturing PSP system and its application to a hypersonic wind tunnel	Surface pressure measurements on a supercritical airfoil employing pressure-sensitive paint
Presenting author	H. Kleine, University of New South Wales, Australia	A. Pateria, IIT-Madras, India	T. Okabe, University of Electro Communications, Japan	Q. Zhou, China Aerodynamics R&D Centre, China

Monday, 18 July 2011

Shock Wave Propagation and Reflection III Renold C16

Session Chair: S. Kobayashi, Saitama Institute of Technology, Japan

Time	1420 hrs	1440 hrs	1500 hrs	1520 hrs
Paper number	2509	2661	2539	2622
Paper title	Analytical theory for planar shock focusing through perfect gas lens: high compression designs	Area change effects on shock wave propagation	Nonlinear analysis of stability of plane shock waves in media with arbitrary thermodynamic properties	Studies on shock wave attenuation in small tubes
Presenting author	M. Vandenboomgaerde, CEA/DAM, France	J. Dowse, University of the Witwatersrand, South Africa	A. Likhachev, Joint Institute for High Temperatures, Russia	J. Subburaj, Indian Institute of Science, India

Monday, 18 July 2011

Multiphase Flows III Renold C9

Session Chair: O. Igra, Ben Gurion University, Israel

Time	1420 hrs	1440 hrs	1500 hrs	1520 hrs
Paper number	2692	2642	2653	2621
Paper title	The behaviors of a drop in ambient liquid under a sudden impact	Anti-diffusion interface sharpening technique for two-phase compressible flow simulations	Numerical simulation of a transonic gas-droplet two-phase flow over an airfoil with a droplet breakup model	Shocked fluid/fluid and fluid/solid interactions using a conservative level-set method
Presenting author	J. Yang, University of Science and Technology of China, China	K. K. So, Technical University of Munich, Germany	K-S. Chang, Korea Advanced Institute of Science and Technology, Korea	B. Obadia, Cranfield University, UK

Monday, 18 July 2011

Student Competition III Renold E7

Session Chair: N. Qin, University of Sheffield, UK

Time	1420 hrs	1440 hrs	1500 hrs	1520 hrs
Paper number	2605	2466	2606	2677
Paper title	Numerical study on the evolution of the shock-accelerated interface: influence of the interfacial shape	Analytical estimation of microbubble motion exposed to discontinuous pressure change	Imploding conical shock waves	Micro-shock wave assisted bacterial transformation
Presenting author	M. Fan, University of Sciences and Technology of China, China	S. Fukuda, Kobe University, Japan	R. Paton, University of Witwatersrand, South Africa	D. P. Gnanadhas, Indian Institute of Science, India

Monday, 18 July 2011

Renold Concourse

1540-1600

Tea/Coffee

Monday, 18 July 2011 PM Session B

Monday, 18 July 2011				
	Blast Waves II			Renold F14
Session Chair:	N. Apazidis, KTH, Sweden			
Time	1600 hrs	1620 hrs	1640 hrs	1700 hrs
Paper number	2641	2726	2759	2714
Paper title	Blast waves from cylindrical charges	High energy concentration by symmetric shock focusing	A novel experimental system for blast structure interaction research	Blast wave attenuation by dry aqueous foams
Presenting author	C. Knock, Cranfield University, UK	N. Apazidis, KTH, Sweden	O. Ram, Ben Gurion University, Israel	E. del Prete, CEA/DAM France

Monday, 18 July 2011				
	Chemically Reacting Flows II			Renold D7
Session Chair:	C. Park, Korea Advanced Institute of Science and Technology, Korea			
Time	1600 hrs	1620 hrs	1640 hrs	1700 hrs
Paper number	2513	2576	2590	2750
Paper title	Shock tube investigation of molecular oxygen dissociation at temperatures of 4000 to 10800 K	A numeric study of the effects of turbulent flow	Thermo-chemistry modelling in an open source DSMC code	Computations of radiation of high-temperature gases in shock layers
Presenting author	L. Ibraguimova, Lomonosov Moscow State University, Russia	C. Needham, Applied Research Associates, USA	T. Scanlon, University of Strathclyde, UK	M-C. Druguet, Aix-Marseille Université, France

Monday, 18 July 2011

Flow Visualisation II Renold C2

Session Chair: H. Kleine, University of New South Wales, Australia

Time	1600 hrs	1620 hrs	1640 hrs	1700 hrs
Paper number	2724	2701	2716	2732
Paper title	Application of NPLS technique to hypersonic shock-wave and boundary layer interactions	Density field reconstructing in the supersonic wind tunnel using OCT technology	Experimental exploration of an underexpanded supersonic jet	Quantitative measurement and reconstruction of 3D density field by CGBOS (colored grid background oriented Schlieren) technique
Presenting author	M. Li, China Aerodynamics Research and development Center, China	G. Longde, CARDC, China	B. André, Ecole Centrale de Lyon, France	M. Ota, Chiba University, Japan

Monday, 18 July 2011

Shock Wave Propagation and Reflection IV Renold C16

Session Chair: S. Kobayashi, Saitama Institute of Technology, Japan

Time	1600 hrs	1620 hrs	1640 hrs	1700 hrs
Paper number	2555	2577	2684	2551
Paper title	Supersonic patches in steady irregular reflection of weak shock waves	Shear layer evolution in shock wave diffraction	Shock detachment from curved surfaces	Shock and blast wave propagation through a porous barrier
Presenting author	G. Shoev, Khristianovich Institute of Theoretical and Applied Mechanics, Russia	B. Skews, University of Witwatersrand, South Africa	S. Mölder, McGill University, Canada	D. Epstein, ITAM SB RAS, Russia

Monday, 18 July 2011

Multiphase Flows IV Renold C9

Session Chair: O. Igra, Ben Gurion University, Israel

Time	1600 hrs	1620 hrs	1640 hrs	1700 hrs
Paper number	2654	2699	2763	2791
Paper title	Numerical investigation of cavitation bubble dynamics near walls	Application of laser holography and PDPA technology in spray fuel particle field measurement	Dense particle cloud dispersion by a shock wave	Dynamic jet formation from mitigation materials
Presenting author	E. Lauer, TU München, Germany	Z. Long, CARDC, China	M. Kellenberger , Queen's University, Canada	C. Parrish, AWE, UK

Monday, 18 July 2011

Student Competition IV Renold E7

Session Chair: N. Qin, University of Sheffield, UK

Time	1600 hrs	1620 hrs	1640 hrs	1700 hrs
Paper number	2634	2618	2613	2610
Paper title	Free-piston driver optimisation for simulation of high Mach number scramjet flow conditions	Experimental investigations on the effect of dielectric barrier discharge on the hypersonic flow around a flat plate	On the evolution of spherical gas interface accelerated by planar shock wave	Experimental studies on mixing in supersonic ejector
Presenting author	D. Gildfind, University of Queensland, Australia	S. Rengarajan, Indian Institute of Science, India	Z. Zhai, University of Science and Technology of China, China	S. Rao, Indian Institute of Science, India

Monday, 18 July 2011

Sackville Entrance Hall

1900-2100

Reception

Hosted by Prof. Luke Georghiou

Vice-President Research and Innovation, The University of Manchester, UK

Tuesday, 19 July 2011 AM Session A

Tuesday, 19 July 2011
Keynote Lecture 2 Renold C16
0830-0910

Shock Induced Chemical Decomposition in Condensed Energetic Materials: (Molecular Mechanisms)

Prof. Yogendra M. Gupta
Institute for Shock Physics, Washington State University, USA

Session Chair: K. P. J. Reddy, Indian Institute of Science, India

Tuesday, 19 July 2011
Detonation and Combustion I Renold C16

Session Chair: K. Hayashi, Aoyama Gakuin University, Japan

Time	0920 hrs	0940 hrs	1000 hrs	1020 hrs
Paper number	2479	2442	2450	2438
Paper title	Interaction of laser pulse with liquid droplet	Expansion of the detonation products of a TATB based high explosive: Experimental characterization by Photon Doppler Velocimetry and high-speed digital shadowgraphy	Gas detonation simulation in the channel by instant heating of one Its flat end for the case of real chemical reaction	Front structure of detonation and the stability of detonation
Presenting author	K. Volkov, Kingston University, UK	A. Sollier, CEA, France	S. Kulikov, Institute of Problems of chemical Physics RAS, Russia	H-S. Dou, National University of Singapore, Singapore

Tuesday, 19 July 2011

Shock Vortex Interactions I Renold C2

Session Chair: F. Seiler, French-German Research Institute of Saint-Louis, France

Time	0920 hrs	0940 hrs	1000 hrs	1020 hrs
Paper number	2624	2507	2591	2469
Paper title	Complex conservative difference schemes in modeling of instabilities and contact structures	Vortex induced Mach waves in supersonic jets	Numerical investigation of 2D/3D blade-vortex interactions	Shock wave in turbulent flow field
Presenting author	O. Azarova, Institution of Russian Academy of Sciences RAS, Russia	F. Seiler, French-German Research Institute of Saint-Louis, France	E. Yildirim, Imperial College London, UK	M. Tsukamoto, Tokyo Denki University, Japan

Tuesday, 19 July 2011

Shock Boundary Layer Interactions I Renold C9

Session Chair: J. L. Stollery, Cranfield University, UK

Time	0920 hrs	0940 hrs	1000 hrs	1020 hrs
Paper number	2792	2510	2470	2729
Paper title	Boundary layer effects behind incident and reflected shock waves in a shock tube	Flow topology of symmetric crossing shock wave boundary layer interactions	PIV investigation of the 3D instantaneous flow organization behind a micro-ramp in a supersonic boundary layer	Effect of a counterflow plasma jet on aerodynamics characteristic of a blunted cone
Presenting author	R. Hanson, Stanford University, USA	A. Salin, Kingston University, UK	Z. Sun, Delft University of Technology, Netherlands	J. Li, China Aerodynamics Research & Nagoya University, Japan

Tuesday, 19 July 2011

Special Session – Medical / Biological Applications I Renold D7

Session Chair: S. H. R. Hosseini, Kumamoto University, Japan

Time	0920 hrs	0940 hrs	1000 hrs	1020 hrs
Paper number	2845	2849	2846	2627
Paper title	Applications of underwater shock wave research to therapeutic device developments	Focused tandem shock waves in water and their potential application in cancer treatment	High repetitive pulsed streamer discharges in water, their induced shock waves and medical applications	Improved shock wave-assisted bacteria transformation
Presenting author	K. Takayama, Tohoku University, Japan	P. Lukes, Institute of Plasma Physics AS CR, Czech Republic	S. H. R. Hosseini, Kumamoto University, Japan	A. Loske, Universidad Nacional Autonoma de Mexico, Mexico

Tuesday, 19 July 2011

Student Competition V Renold E7

Session Chair: L. Houas**,** IUSTI-CNRS Aix Marseille Université**,** France

Time	0920 hrs	0940 hrs	1000 hrs	1020 hrs
Paper number	2752	2783	2652	2658
Paper title	Supersonic combustion experimental investigation at T2 hypersonic shock tunnel	Model experiment of Munroe jet formation using gelatine driven by a moderate speed impactor	Reflection transition of converging cylindrical shock wave segments	Development of blast-wave mediated vaccine delivery device
Presenting author	D. Pinto, Institute for Advanced Studies, Brazil	K. Suzuki, Nagoya University, Japan	B. Gray, University of Witwatersrand, South Africa	D. P. Gnanadhas, Indian Institute of Science, India

Tuesday, 19 July 2011

Renold Concourse

1040-1100

Coffee / Tea

Tuesday, 19 July 2011 AM Session B

Tuesday, 19 July 2011				
	Detonation and Combustion II			Renold C16
Session Chair:	K. Hayashi, Aoyama Gakuin University, Japan			
Time	1100 hrs	1120 hrs	1140 hrs	1200 hrs
Paper number	2500	2512	2581	2562
Paper title	Flame-acoustic interaction	Effects of vortical and entropic forcing on detonation dynamics	Deflagration-to-detonation transition in highly reactive combustible mixtures	Numerical simulations of afterburning during explosions
Presenting author	V. Golub, Joint Institute for High Temperatures RAS, Russia	F. Lu, University of Texas at Arlington, USA	M. Liberman, Uppsala University/ Moscow State University, Russia	E. Fedina, Swedish Defence Research Agency – FOI, Sweden

Tuesday, 19 July 2011				
	Shock Vortex Interactions II			Renold C2
Session Chair:	F. Seiler, French-German Research Institute of Saint-Louis, France			
Time	1100 hrs	1120 hrs	1140 hrs	1200 hrs
Paper number	2563	2787	2565	2710
Paper title	Post-shock pressure modulation through grid turbulence	Hypersonic interaction of a vortex wake with a bow shock wave	Aerodynamic vibrations caused by vortex ahead of hemisphere in supersonic flow	Bluntness effects in hypersonic flow over slender cones and wedges
Presenting author	A. Sasoh, Nagoya University, Japan	A. Shevchenko, ITAM SB RAS, Russia	T. Kawamura, Tokai University, Japan	S. Karl, Caltech, USA

Tuesday, 19 July 2011				
	Shock Wave Boundary Layer Interactions II			Renold C9
Session Chair:	J. L. Stollery, Cranfield University, UK			
Time	1100 hrs	1120 hrs	1140 hrs	1200 hrs
Paper number	2436	2552	2796	2693
Paper title	Numerical discovery and experimental validation of vortex ring generation by microramp vortex generator	Numerical simulation of conical and spherical shock interaction : hysteresis investigations	Simulation of a practical scramjet inlet using shock-unsteadiness model	Inviscid-viscous interactions of compressible convex corner flows
Presenting author	C. Liu, University of Texas at Arlington, USA	D. Zeitoun, Université de Provence, France	K. Sinha, Indian Institute of Technology Bombay, India	P. H. Chang, ASTRC, Taiwan

Tuesday, 19 July 2011				
	Special Session – Medical / Biological Applications II			Renold D7
Session Chair:	S. H. R. Hosseini, Kumamoto University, Japan			
Time	1100 hrs	1120 hrs	1140 hrs	1200 hrs
Paper number	2847		2669	2731
Paper title	Development of medical and biological applications by shock waves and bubbles		Light syringes based on the laser induced shock wave	Shock wave generation through constructive wave amplification
Presenting author	M. Tamagawa, Kyushu Institute of Technology, Japan		J. Yoh, Seoul National University, Korea	M. Brouillette, Université de Sherbrooke, Canada

Tuesday, 19 July 2011

Student Competition VI Renold E7

Session Chair: L. Houas, IUSTI-CNRS Aix Marseille Université, France

Time	1100 hrs	1120 hrs	1140 hrs	1200 hrs
Paper number	2691	2756	2556	2713
Paper title	Starting characteristics of hypersonic inlets in shock tunnel	Polygonal shock waves: comparison between experiments and geometrical shock dynamics	Numerical simulation of shock wave entry and propagation in a microchannel	Three-dimensional simulation of bow shock instability using discontinuous Galerkin method
Presenting author	Z. Li, University of Science and Technology of China, China	M. Kjellander, KTH Mechanics, Sweden	G. Shoev, Khristianovich Institute of Theoretical and Applied Mechanics, Russia	Y. Sato, Tohoku University, Japan

Tuesday, 19 July 2011

Barnes Wallis

1220-1330

Lunch

Tuesday, 19 July 2011 PM Session A

Tuesday, 19 July 2011

Keynote Lecture 3 Renold C16

1330-1410

How Does Deflagration get Detonated in Gases? Recent Research Progress on DDT

Prof. Koichi Hayashi
Aoyama Gakuin University, Japan

Session Chair: R. Hanson, Stanford University, USA

Tuesday, 19 July 2011

Detonation and Combustion III Renold C16

Session Chair: V. Golub , Joint Institute for High Temperatures RAS, Russia

Time	1420 hrs	1440 hrs	1500 hrs	1520 hrs
Paper number	2527	2537	2595	2720
Paper title	Numerical simulation on detonation formation by shock/flame interaction	Experimental investigation of rupture rate on self-ignition of pressurized hydrogen release	Characterization of soot particles produced from the combustion of hydrocarbon fuels in a shock tube	The effect analysis of flow jam on two-meter direct-connection model
Presenting author	W. Chao, Zhejiang Sci-Tech University, China	V. Golub , Joint Institute for High Temperatures RAS, Russia	E. Petersen, Texas A & M University, USA	L. Xiangdong, China Aerodynamics Research and Development Center, China

Tuesday, 19 July 2011

Richtmyer-Meshkov I Renold C9

Session Chair: R. Bonazza, University of Wisconsin – Madison, USA

Time	1420 hrs	1440 hrs	1500 hrs	1520 hrs
Paper number	2433	2475	2675	2503
Paper title	Effects of initial conditions on mixing in Richtmyer-Meshkov turbulence experiments	Experimental study on a heavy-gas cylinder accelerated by cylindrical converging shock waves	Long time observation of the Richtmyer-Meshkov instability	Richtmyer-Meshkov instability at the interface of gas-oil-water three phases
Presenting author	K. Prestridge, Los Alamos National Laboratory, USA	T. Si, University of Science and Technology of China, China	C. Mariani, IUSTI-CNRS, Aix-Marseille Université, France	H-H. Shi, Zhejiang Sci-Tech University, China

Tuesday, 19 July 2011

Diagnostics I Renold D7

Session Chair: G. Settles, Penn State University, USA

Time	1420 hrs	1440 hrs	1500 hrs	1520 hrs
Paper number	2462	2564	2435	2689
Paper title	Multi-species laser measurements of n-butanol pyrolysis behind reflected shock waves	Quantitative visualization of open-air explosions by using background-oriented Schlieren with natural background.	Cross-wavelet techniques for estimating uncertainty in propagating shocks and detonations	Measurement of vibrational/rotational temperatures of nitrogen behind strong shock wave generated at hypervelocities using CARS method
Presenting author	R. Hanson, Stanford University, USA	T. Mizukaki, Tokai University, Japan	F. Lu, University of Texas at Arlington, USA	H. B. Venigalla, Chiba University, Japan

Tuesday, 19 July 2011

Numerical Methods and Simulations I Renold C2

Session Chair: T. Saito, Muroran Institute of Technology, Japan

Time	1420 hrs	1440 hrs	1500 hrs	1520 hrs
Paper number	2459		2526	2814
Paper title	Antiforce current bearing waves		Effects of turbulent inflow conditions on feedback-loop mechanisms in supersonic cavity flows	Prediction of transition onset location and investigation of its effects on shock bump control on a natural laminar flow aerofoil
Presenting author	M. Hemmati, Arkansas Tech University, USA		W. Li, University of Tokyo, Japan	F. Deng, University of Sheffield, UK

Tuesday, 19 July 2011

Student Competition VII Renold E7

Session Chair: O. Sadot, , Ben Gurion University, Israel

Time	1420 hrs	1440 hrs	1500 hrs	1520 hrs
Paper number	2753	2813	2773	2706
Paper title	OH emission diagnostics applied to study ignition of the supersonic combustion	Benchmarking a new, open-source direct simulation Monte Carlo (DSMC) code for hypersonic flows	Radiative heat transfer measurements in a nonreflected shock tube at low pressures	2D phenomena of shock wave propagation along a non-equilibrium thermal zone formed by surface discharge
Presenting author	R. Vilela, Institute for Advanced Studies, Brazil	A. Ahmad, University of Strathclyde, UK	C. Jacobs, University of Queensland, Australia	E. Koroteeva, Moscow State University, Russia

Tuesday, 19 July 2011

Renold Concourse

1540-1600

Tea/Coffee

Tuesday, 19 July 2011 PM Session B

Tuesday, 19 July 2011				
	Facilities I			Renold C2
Session Chair:	D. Buttsworth, University of Southern Queensland, Australia			
Time	1600 hrs	1620 hrs	1640 hrs	1700 hrs
Paper number	3006	2553	2494	2754
Paper title	Manually operated piston driven mini shock tube	Propagation characteristics of the shock wave in small diameter tubes at atmospheric Initial driven pressure	Numerical study of the shock tunnel flow with a throat plug	Flow characterization of the T3 hypersonic shock tunnel
Presenting author	K. P. J. Reddy, Indian Institute of Science, India	S. Udagawa, Tokyo Metropolitan College of Industrial Technology, Japan	J. K. Lee, Korea Advanced Institute of Science and Technology, Korea	D. Pinto, Institute for Advanced Studies, Brazil

Tuesday, 19 July 2011				
	Richtmyer-Meshkov II			Renold C9
Session Chair:	R. Bonazza, University of Wisconsin – Madison, USA			
Time	1600 hrs	1620 hrs	1640 hrs	1700 hrs
Paper number	2449	2745	2465	2617
Paper title	Numerical investigation of turbulence in re-shocked Richtmyer-Meshkov unstable curtain of dense gas	Experimental characterization of turbulence produced in a shock tube: a preliminary work for the study of the turbulent gaseous mixing induced by the Richtmyer-Meshkov instability	Experimental and numerical investigations of the inclined Air/SF6 interface instability under shock wave	Investigations on a gaseous interface accelerated by a converging shock wave
Presenting author	S. Shankar, Stanford University, USA	S. Jamme, ISAE, France	T. Wang, China Academy of Engineering Physics, China	X. Luo, University of Science and Technology of China, China

Tuesday, 19 July 2011

Diagnostics II Renold D7

Session Chair: G. Settles, Penn State University, USA

Time	1600 hrs	1620 hrs	1640 hrs	1700 hrs
Paper number	2506	2646	2704	2749
Paper title	Extended shock-tunnel operation for free-flight aeroballistics testing	Surface flow visualization of a side-mounted NACA 0012 airfoil in a transonic Ludwieg tube	Photoemission measurements of soot temperature at pyrolysis of ethylene in the shock tube	Modern optical methods for determining the shock Hugoniot of transparent solids
Presenting author	F. Seiler, French-German Research institute of Saint-Louis, France	F. Lu, University of Texas at Arlington, USA	Y. Baranyshyn, Luikov Heat and Mass Transfer Institute, Belarus	G. Settles, Pennsylvania State University, USA

Tuesday, 19 July 2011

Shock Wave Phenomena and Applications I Renold C16

Session Chair: D. Zeitoun, Université de Provence, France

Time	1600 hrs	1620 hrs	1640 hrs	1700 hrs
Paper number	2795	2799	2673	2545
Paper title	Shock dynamics for cylindrical/spherical converging shocks in elastic-plastic solids	Study of the stability of $Na_{0.7}CoO_2$ thermoelectric materials under shock dynamic loading in a shock tube	Hybrid finite element/molecular dynamics simulations of shock-induced particle/wall collisions	Numerical analysis of interaction between moving shock wave and solid particle layer
Presenting author	A. López Ortega, California Institute of Technology, USA	V. Jayaram, Indian Institute of Science, India	M. Micci, Pennsylvania State University, USA	K. Doi, Nagoya University, Japan

Tuesday, 19 July 2011

Impact and Compaction I Renold E7

Session Chair: J. Srulijes, French-German Research Institute of Saint-Louis, France

Time	1600 hrs	1620 hrs	1640 hrs	1700 hrs
Paper number	2588	2728	2602	2502
Paper title	Multiscale modeling and simulation of shock-wave impact failure in hard and soft matter	Tunguska Impact: How far can we move up in our prediction of the past?	High-velocity impact characteristic of CFRP composite at low temperature	Propagation of luminous front at high-speed impact into sand layers
Presenting author	M. O. Steinhauser, Fraunhofer-Institute for High-Speed Dynamics, Ernst-Mach-Institut, Germany	C. Sandaldjian, University of Manchester, UK	A. Shimamoto, Saitama Institute of Technology, Japan	H. Yamamoto, Tohoku University, Japan

Wednesday, 20 July 2011

Wednesday,20 July 2011
Keynote Lecture 4 Renold C16
0830-0910
Super-Orbital Re-Entry in Australia – Laboratory Measurement, Numerical Simulation and Flight Observation
Prof. David Buttsworth
University of Southern Queensland, Australia
Session Chair: H. G. Hornung, Caltech, USA

Wednesday, 20 July 2011

0930-1700
Excursion

Chatsworth House is a stately home in Derbyshire, England that attracts over 300,000 visitors a year. The house has a history ranging from the mid 15th century up to modern day where it featured in the 2005 adaptation of *Pride and Prejudice* and the 2008 film *The Duchess*. The building housed Mary, Queen of Scots during her time in captivity.

The house itself contains a fascinating art collection including countless paintings, four royal thrones, a striking ancient Greek marble foot, and a titanium fan of a Rolls Royce jet engine.

Perhaps the most famous aspect of Chatsworth House is the fantastic gardens. The gardens total over 105 acres in size and contain a 200ft cascading waterfall and a vast hedge maze.

A detailed history about Chatsworth House can be found at the following web address:

http://www.chatsworth.org/files/fom_history.pdf

Thursday, 21 July 2011 AM Session

Thursday, 21 July 2011

Keynote Lecture 5 Renold C16

0830-0910

Pioneering in Hypersonic Transportation: Long Term Perspectives and Technological Challenges

Dr. Johan. Steelant
ESTEC-ESA, The Netherlands

Session Chair: J. L. Stollery, Cranfield University, UK

Thursday, 21 July 2011

Chemically Reacting Flows III Renold C2

Session Chair: C. Park, Korea Advanced Institute of Science and Technology, Korea

Time	0920 hrs	0940 hrs	1000 hrs	1020 hrs
Paper number	2760	2455	2708	2741
Paper title	On the validity of the constant volume assumption in shock tube experiments	Influence of Electronic Excitation on the Transport Properties of Partially Ionized Atomic Gases	Hugoniot of a reactive metal powder mixture	Numerical simulation of thermal-chemical non-equilibrium and radiating hypersonic flow by using hybrid grid
Presenting author	J. Melguizo-Gavilanes, University of Calgary, Canada	V. Istomin, Saint-Petersburg State University, Russia	C. Braithwaite, University of Cambridge, UK	Y. Wang, University of Sheffield, UK

Thursday, 21 July 2011

Detonation and Combustion IV Renold C16

Session Chair: F. Lu, University of Texas at Arlington, USA

Time	0920 hrs	0940 hrs	1000 hrs	1020 hrs
Paper number	2518	2582	2560	2580
Paper title	Initial temperature effect on detonation initiation of JP-8-oxygen mixtures	Hydrogen-oxygen flame acceleration in channels of different widths with no-slip walls and the deflagration-to-detonation transition	Numerical study of gas detonation at the molecular kinetic level	Shock-flame interaction and deflagration-to-detonation transition in hydrogen/oxygen mixtures
Presenting author	C. S. Wen, National Cheng Kung University, Taiwan	M. Liberman, Uppsala University/ Moscow State University, Russia	Y. Bondar, Khristianovich Institute of Theoretical and Applied Mechanics, Russia	A. Kiverin, Joint Institute for High Temperatures, Russia

Thursday, 21 July 2011

Hypersonic Flows III Renold C9

Session Chair: D. Mee, University of Queensland, Australia

Time	0920 hrs	0940 hrs	1000 hrs	1020 hrs
Paper number	2517	2725	2767	2822
Paper title	Numerical studies of hypersonic binary gas-mixture flows near a sphere	On the validation of a hypersonic flow solver using measurements of shock detachment distance	Effect of gas injection on transition in hypervelocity boundary layers	Numerical simulation and experimental validation on shock oscillations of hypersonic vehicle's flowpath
Presenting author	V. Riabov, River College, USA	P. Jacobs, University of Queensland, Australia	J. Jewell, California Institute of Technology, USA	J. Liu, National University of Defence and Technology, China

Thursday, 21 July 2011

Nozzle Flows I Renold D7

Session Chair: A. Abe, Kobe University, Japan

Time	0920 hrs	0940 hrs	1000 hrs
Paper number	2464	2477	2611
Paper title	Experimental investigation of asymmetric and unsteady flow separation in high Mach number planar nozzles	Influence of a normal slot boundary layer suction system onto a shock train	Asymmetric flow separation in de Laval nozzle
Presenting author	E. Shimshi, Ben Gurion University, Israel	A. Weiss, RWTH Aachen University, Germany	V. Golub, Joint Institute for High Temperatures RAS, Russia

Thursday, 21 July 2011

Shock Wave Phenomena and Applications II Renold E7

Session Chair: M. Brouillette, Université de Sherbrooke, Canada

Time	0920 hrs	0940 hrs	1000 hrs	1020 hrs
Paper number	2452	2785	2757	2786
Paper title	Density field measurements of a micro – explosion using BOS	Magnetic configuration effect on the interaction between the weakly ionized flow and the applied magnetic field	Starting flow through planar wedged nozzle: effect of nozzle asymmetry	Features of the impact of a solar wind shock wave on the Earth's bow shock in a strong interplanetary magnetic field
Presenting author	P. Suriyanarayana, CSIR National Aerospace Laboratories, India	M. Kawamura, University of Tokyo, Japan	Y. Shackak, Ben Gurion University, Israel	E. A. Pushkar, Moscow State Industrial University, Russia

Thursday, 21 July 2011

Renold Concourse

1040-1100

Coffee / Tea

Thursday, 21 July 2011 AM Session B

Thursday, 21 July 2011				
	Facilities II			Renold E7
Session Chair:	H. Olivier, RWTH Aachen University, Germany			
Time	1100 hrs	1120 hrs	1140 hrs	1200 hrs
Paper number	2667	2558	2463	2790
Paper title	Modeling of a detonation driven, linear electric generator facility	A new fast acting valve for diaphragmless shock tubes	A second-generation aerosol shock tube and its use in studying ignition delay times of large biodiesel surrogates	Demonstration of some concepts for developing long-test duration shock tunnels
Presenting author	F. Lu, University of Texas at Arlington, USA	H. Olivier, RWTH Aachen University, Germany	R. Hanson, Stanford University, USA	Z. Jiang, Institute of Mechanics at Chinese Academy of Sciences, China

Thursday, 21 July 2011				
	Detonation and Combustion V			Renold C16
Session Chair:	M. Liberman, Uppsala University/ Moscow State University, Russia			
Time	1100 hrs	1120 hrs	1140 hrs	1200 hrs
Paper number	2636	2764		2735
Paper title	Combined effects of a vortex flow and the Shchelkin spiral dimensions on characteristics of deflagration-to-detonation transition	Numerical study of detonation wave propagation in narrow channels		Flame propagation out from wide chamber into narrow channel of subcritical diameter and transition to detonation
Presenting author	K. Asato, Gifu University, Japan	A. Chinnayya, CORIA, France		V. Golub, Joint Institute for High Temperatures RAS, Russia

Thursday, 21 July 2011				
	Hypersonic Flows IV			Renold C9
Session Chair:	D. Mee, University of Queensland, Australia			
Time	1100 hrs	1120 hrs	1140 hrs	1200 hrs
Paper number	2832	2775	2817	2430
Paper title	Application of pressure- and temperature-sensitive paint in a hypersonic double ramp flow	Counterflow injection studies for hypersonic flow fields	Shock tunnel noise measurement with resonantly enhanced focused schlieren deflectometry	Separation length scaling in hypervelocity double-cone air flows
Presenting author	L. Yang, University of Manchester, UK	V. Kulkarni, Indian Institute of Technology, India	N. Parziale, Caltech, USA	A. Swantek, University of Illinois at Urbana-Champaign, USA

Thursday, 21 July 2011				
	Nozzle Flows II			Renold D7
Session Chair:	A. Abe, Kobe University, Japan			
Time	1100 hrs	1120 hrs	1140 hrs	1200 hrs
Paper number	2820	2819	2707	2609
Paper title	Effect of roughness in jets in Mach 5 cross flow	Flow visualization of supersonic free jet utilizing acetone LIF	2D numerical simulation of hydrogen injection into a channel with a cavity	Numerical investigation of over-expanded nozzle flows: Influence of internal shock waves
Presenting author	E. Erdem, University of Manchester, UK	K. Hatanka, Muroran Institute of Technology, Japan	I. Fedorchenko, ITAM SB RAS, Russia	A. Chpoun, LMEE, France

Thursday, 21 July 2011

Numerical Methods and Simulations II Renold C2

Session Chair: T. Saito, Muroran Institute of Technology, Japan

Time	1100 hrs	1120 hrs	1140 hrs	1200 hrs
Paper number	2600	2854	2648	2619
Paper title	Scale-separation for implicit large eddy simulation	An application of adaptive mesh refinement method for modeling of nonstationary hypersonic flows in the atmosphere	Numerical studies of high enthalpy flow over a rearward facing step with rounded corners	On the carbuncle origins from moving and stationary shocks
Presenting author	V. Tritscher, Technical University of Munich, Germany	A. Astanin, Tomsk State University, Russia	S. Gai, University of New South Wales, Australia	K. Kitamura, JAXA, Japan

Thursday, 21 July 2011

Barnes Wallis

1220-1330

Lunch

Thursday, 21 July 2011 PM Session A

Thursday, 21 July 2011

Keynote Lecture 6 Renold C16

1330-1410

Towards Substantial Drag Reduction for Transonic Wings Using Aerodynamic Optimisation with Shock Control through Reduced Wing Sweep

Prof. Ning Qin

University of Sheffield, UK

Session Chair: B. Skews, University of Witwatersrand, South Africa

Thursday, 21 July 2011

Detonation and Combustion VI Renold C16

Session Chair:	M. Liberman, Uppsala University/ Moscow State University, Russia			
Time	1420 hrs	1440 hrs	1500 hrs	1520 hrs
Paper number	2686	2829	2766	2630
Paper title	Fast flame propagation and ignition process of DDT in the boundary layer of H2/O2 mixture	Development of an ethanol/air reduced mechanism and its application to two-phase detonation	Detonation initiation by moving borders	Evolution of autocorrelation in detonation interaction with homogeneous, isotropic turbulence
Presenting author	E. Dzieminska, Aoyama Gakuin University, Japan	A. K. Hayashi, Aoyama Gakuin University, Japan	V. Levin, Institute of Mechanics of the MSU, Russia	F. Lu, University of Texas at Arlington, USA

Thursday, 21 July 2011

Diagnostics III Renold D7

Session Chair: T. Mizukaki, Tokai University, Japan

Time	1420 hrs	1440 hrs	1500 hrs	1520 hrs
Paper number	2789	2824		2592
Paper title	Radiometric temperature analysis of the Hayabusa reentry	Toluene laser-induced fluorescence (LIF) imaging of supersonic flow within a diverging duct		Experimental investigation of aerodynamic interference heat transfer around a protuberance on a flat plate subjected to hypersonic flow
Presenting author	T. Eichmann, University of Queensland, Australia	K. Mohri, University of Duisburg-Essen, Germany		C. Sudhiesh Kumar, Indian Institute of Science, India

Thursday, 21 July 2011

Ignition I Renold E7

Session Chair: N. Fedorova, ITAM SB RAS, Russia

Time	1420 hrs	1440 hrs	1500 hrs	1520 hrs
Paper number	2594	2483	2596	2670
Paper title	Measurement of H_2O_2 broadening parameters near 7.8µm with a shock tube	Laser-based ignition of the preheated supersonic hydrogen-air flow	Shock wave-induced ignition of normal-undecane ($n\text{-}C_{11}H_{24}$) and comparison to other high-molecular-weight n-Alkanes	Ignition of aluminum in air via high power laser ablation
Presenting author	J. Mertens, Trinity College, USA	Y. Tunik, Lomonosov Moscow State University, Russia	E. Petersen, Texas A & M University, USA	C-H Kim., Seoul National University, Korea

Thursday, 21 July 2011

Richtmyer-Meshkov III Renold C2

Session Chair: Z. Jiang, Institute of Mechanics at Chinese Academy of Sciences, China

Time	1420 hrs	1440 hrs	1500 hrs	1520 hrs
Paper number	2794	2736	2548	2696
Paper title	Experiments on the Ricthmyer-Meshkov instability with an imposed, random initial perturbation	Effect of shock Mach number on Richtmyer-Meshkov instability in spherical geometry	Experimental shock-initiated combustion of a spherical density inhomogeneity	Numerical study of shock induced mixing in a cylindrical shell
Presenting author	J. Jacobs, University of Arizona, USA	A. Bhagatwala, Stanford University, USA	R. Bonazza, University of Wisconsin, USA	L. Wang, Institute of Applied Physics and Computational Mathematics, China

Thursday, 21 July 2011

Shock Wave Propagation and Reflection V Renold C9

Session Chair: R. Morgan, University of Queensland, Australia

Time	1420 hrs	1440 hrs	1500 hrs	1520 hrs
Paper number	2578	2659	2497	2616
Paper title	Shock reflection off combined surfaces	Standing shock formation in non-reflected shock tube	Aerodynamic ground effect for transonic projectiles	A simple scheme for calculating distortion of compression wave propagating through a tunnel with slab tracks
Presenting author	B. Skews, University of Witwatersrand, South Africa	R. Morgan, University of Queensland, Australia	H. Kleine, University of New South Wales, Australia	T. Miyachi, Railway Technical Research Institute, Japan

Thursday, 21 July 2011

Renold Concourse

1540-1600

Tea/Coffee

Thursday, 21 July 2011 PM Session B

Thursday, 21 July 2011

1600-1720

Poster Session

Session Chair: N. Gongora-Orozco, The University of Manchester, UK Renold Concourse

Blast Waves

2505	A numerical and experimental study on charge geometries	M. G. Omang	Norwegian Defence Estates Agency	Norway
2572	Pressure propagation and attenuation phenomena of underwater shock wave in visco-elastic fluid	F. Ishiguro	Aichi Institute of Technology	Japan
2632	Structure of the blast wave front	K. Sergey	Institute of Atmospheric Physics, RAS	Russia

Chemical Reacting

2482	Stability of detonative combustion of hydrogen-air supersonic flow in convergent-divergent nozzle	Y. Tunik	SRI for Mechanics of Lomonosov Moscow State University	Russia
2487	Thermal decomposition of 2-bromoethanol: single-pulse shock tube experiments, modelling DFT and TSt calculations	H. Chakravarty	Indian Institute of Science	India
2649	Shock-tube studies on the reactions of o-, m-, and p-xylenes with O(3P) atoms	K. Takahashi	Sophia University	Japan
2650	Shock tube study for pyrolysis and oxidation of ethylene oxide	T. Koike	National Defense Academy Japan	Japan
2538	Influence of static temperature on H_2/Air detonation initiation and evolution	Z. Lin	NUDT	China
2540	Self-ignition of pressurized hydrogen in perforated channels	V. Golub	Joint Institute for High Temperatures, RAS	Russia
2585	Formation of detonation wave of condensation in acetylene	A. Emelianov	Joint Institute for High Temperatures, RAS	Russia

2711	Experimental study of SiC ablations in air plasma freejets	M. Funatsu	Gunma University	Japan
2719	Enhancement of thermal properties for platinum thin film heat transfer gauges with nanofluids	R. Kumar	Indian Institute of Technology Guwahati	India
2485	Hybrid LES/RANS of supersonic compressible mixing layer with droplets evaporation	J. Zhou	National Univ. of Defense Technology	China
2635	Pressure measurement using MEMS based sensors array over a backward facing step in IISc hypersonic shock tunnel	S. N. Ram	Indian Institute of Science	India
2571	Ablation testing of carbon fiber reinforced carbon composite in CO_2 arc plasma flow	T. Ito	Aichi Institute of Technology	Japan
2629	Numerical study of air-He shock tube for hypersonic researches	C-Y. Wen	National Cheng Kung University	Taiwan
2660	Measurement of heat transfer rates around the aerodynamic cavities on a flat plate at hypersonic Mach number.	S. Jobin Philip	Indian Institue Of Science	India
2705	Experimental investigation of the effect of a thermal bump on hypersonic flow	R. Sriram	Indian Institute of Science	India
2776	Simple conjugate heat transfer analysis for hypersonic flows	V. Kulkarni	Indian Institute of Technology Guwahati	India
2623	Oxidation of 3-carene at high temperatures	N. Sharath	Indian Institute of Science	India
2734	Supersonic body streamline in plasma at presence of electric and magnetic fields	S. Ponyaev	Ioffe Physico-Technical Institute, RAS	Russia
2657	Development of blast-wave mediated vaccine delivery device	D. P. Gnanadhas	Indian Institute of Science	India
2694	Development of blast-wave assisted particle delivery system	S. G. Rakesh	Amrita School of Engineering, Amrita Vishwa Vidyapeetham	India
2852	On the effect of a shock wave on a micro-organism	L. Houas	IUSTI-CNRS Aix Marseille Université	France

2432	Simulation of sphere's motion induced by shock waves	O. Igra	Ben Gurion University, Israel	Israel
2828	Experimental investigation of liquid jet into supersonic cross-flow	H. Gu	Institute of Mechanics, C A S,China	China
2481	An Investigation of pressure boundary conditions for the simulation of a micro-nozzle using DSMC method	B. Puranik	Indian Institute of Technology Bombay, India	India
2493	Numerical and experimental studies of fluidic thrust vectoring	L. Li	Muroran Institute of Technology	Japan
2550	Sound generating mechanism in the supersonic mixing layer	Z. Chen	Nanjing University of Science & Technology	China
276	Numerical investigation of nitrogen condensation in nozzles	L Lin	University of Science and Technology of China	China
2533	Integrated LES and NPLS studies of HYLTE nozzle flowfield with supersonic angled injection	Y. Shao	National University of Defence Technology	China
2492	A comparison of higher-order extensions to approximate Riemann solvers	M. Ray	Indian Institute of Technology Bombay	India
2534	Numerical investigation of supersonic combustion using flamelet modeling	Z. Fan	College of Aerospace and Material Engineering	China
2589	The compatible algorithms in radiation hydrodynamics for hohlraum physics simulation	H. Yong	Institute of Applied Physics and Computational Mathematics	China
2644	Development of a numerical approach to deal with fluid-structure interactions in solid propellant rocket motors	J. Devesvre	IUSTI	France
2808	Flow visualisation of scramjet inlet-isolator in Mach 5 using pressure sensitive paint	A. Che Idris	The University of Manchester	UK
2802	Experimental studies of shock diffraction	M. K. Quinn	The University of Manchester	UK
2490	Shock wave diffraction on convex curved walls	A. Muritala	Obafemi Awolowo University ILE-IFE	Nigeria

3007	Unsteady shock wave interactions with 2-D geometries	K. H. Lo	The University of Manchester	UK
2546	Numerical study of stability of con verging shock waves in a hard-sphere fluid	A. Konyukhov	Joint Institute for High Temperatures, RAS	Russia
2625	Influence dispersion and cross flow on structure of shock wave	E. Prozorova	St. Petersburg State University	Russia
2678	Effect of an impinging shockwave on a partially opened door	L. Biamino	IUSTI Aix Marseille University	France
2681	Numerical study on the mechanism of the entrainment of a rectangular solid body by a shock wave	Y. Sakamura	Toyama Prefectural University	Japan
2683	Free standing conical shock	S. Mölder	McGill University	Canada
Shock Vortex Interaction				
2638	Flow establishment around a shock holder in a shock tube	C. Park	Korea Advanced Institute of Science and Technology	Korea
Shock Waves in Rarefied Gases				
2676	Boltzmann-Hermite expansion approach to shock structure problem for binary gas mixture	S. Kuwabara	Nagoya University	Japan
Shock/Boundary Layer				
2655	Shock wave-boundary layer interactions inside the supersonic inlet at on/off design conditions	H. J. Lee	LIG Nex1, Co., Ltd.	Korea
2697	An investigation on the near-wall behaviors of hypersonic inlet flow	J. Yang	University of Science and Technology of China	China
2774	Numerical investigation of three-dimensional shock/boundary-layer interaction in a hypersonic inlet	K. Sinha	Indian Institute of Technology Bombay	India

Thursday, 21 July 2011

1830-2200
Banquet

Guest Speaker: Dr. John Ackroyd
The Invention of the Aeroplane Near Scarborough at the Time of Trafalgar

The ISSW 28 banquet will be held in Runway Visitor Park at Manchester International Airport under the historic **Concorde** aircraft.

British Airways received government approval for the production of the G-BOAC in December 1969. **Concorde G-BOAC** (affectionately known as 'Alpha Charlie') became the second aircraft to join the Concorde fleet when she was delivered to British Airways on 13 February 1976.

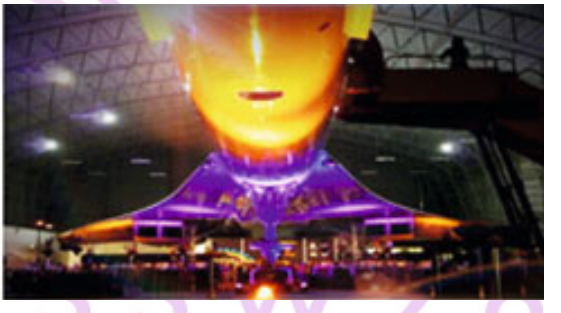

Although G-BOAC was the second **Concorde** to be delivered, she is considered to be the flagship of the fleet as she carries the registration plate BOAC - which were the initials of British Airways' forerunner, British Overseas Airways Corporation, which merged with BEA (British European Airways) to form British Airways.

Concorde Facts

- A specification for the Anglo-French Mach 2.2 airliner was published in October 1962
- Concorde 001 made her maiden flight on 2 March 1969. Concorde 002 took to the air for the first time one month later on 9 April 1969
- Concorde entered commercial service on 21 January 1976. British Airways opened up a London to Bahrain service with G-BOAA and Air France launched a Paris to Rio service via Dakar with F-BVFA
- The airline's second Concorde G-BOAC - which is now in retirement at Manchester Airport's Runway Visitors Park – was delivered one month later on 13 February 1976
- Concorde could accelerate from 0-225 mph in 30 seconds. She could travel faster than the earth rotates.
- More than 2.5 million people travelled on Concorde since she started commercial passenger services in 1976
- The first flight to New York was on 22 November 1977
- On 11 August 1999 two British Airways Concordes flew in a supersonic formation to chase the total eclipse of the sun

Friday, 22 July 2011 AM Session

Friday,22 July 2011
Keynote Lecture 7 Renold C16
0830-0910
Numerical Experiments on Shock-Turbulence Interaction
Prof. S. K. Lele
Stanford University, USA

Session Chair: E. Timofeev, McGill University, Canada

Friday, 22 July 2011

Special Session on Shock Wave Moderation I Renold C2

Session Chair:	A. Sasoh, Nagoya University, Japan			
Time	0920 hrs	0940 hrs	1000 hrs	1020 hrs
Paper number	2478	2730	2816	2838
Paper title	Improvement of supersonic aerodynamic performance using repetitive laser energy depositions	The control of supersonic flow past bodies by upstream energy deposition in toroidal-type regions	Experimental studies on micro-ramps at Mach 5	Effect of dielectric barrier discharge plasma in supersonic flow
Presenting author	A. Sasoh, Nagoya University, Japan	R. Georgievskiy, Institute of Mechanics, Russia	R. Saad, University of Manchester, UK	S. Pal, Indian Institute of Science, India

Friday, 22 July 2011

Detonation and Combustion VII Renold C16

Session Chair: A. Hadjadj, CORIA INSA de Rouen, France

Time	0920 hrs	0940 hrs	1000 hrs	1020 hrs
Paper number	2768	2784	2805	2806
Paper title	Detonation in supersonic flows in channels with obstacles	Application of gas detonation for a needleless device development	Stability of planar ZND detonation waves for three-step chain-branching kinetics	A theoretical approach to one-dimensional detonation instability
Presenting author	I. S. Manuylovich, Institute of Mechanics of the MSU, Russia	V. Golub, Joint Institute for High Temperatures of RAS, Russia	L. Bauwens, University of Calgary, Canada	C. Wang, Institute of Mechanics of Chinese Academy of Sciences, China

Friday, 22 July 2011

Flow Visualisation III Renold D7

Session Chair: H. Sakaue, JAXA, Japan

Time	0920 hrs	0940 hrs	1000 hrs	1020 hrs
Paper number	2434	2615	2530	2703
Paper title	Visualizing the supersonic flow around a microvortex generator	Development of polymer-ceramic pressure-sensitive paint and its application to supersonic flow field	Fine structures of supersonic laminar flow over a backward facing step	The manufacture of high-speed shoot system of adjustable frame
Presenting author	F. Lu, University of Texas at Arlington, USA	T. Hayashi, Tokyo University of Science, Japan	Z. Chen, National University of Defence Technology, China	Y. Furong, CARDC, China

Friday, 22 July 2011

Shock Wave Phenomena and Applications III Renold E7

Session Chair: Z. Walenta, Institute of Fundamental Technology Research, Poland

Time	0920 hrs	0940 hrs	1000 hrs	1020 hrs
Paper number	2888	2804	2812	2468
Paper title	Fracture evaluation using shock-induced borehole waves	Structure of shock waves in dense media	3D MHD description and animation of the process of collision of a solar wind shock with the Earth's bow shock	High-speed opening operation of diaphragmless shock wave generator
Presenting author	H. Fan. Deflt University of Technology, Netherlands	Z. Walenta, Institute of Fundamental Technology Research, Poland	E. A. Pushkar, Moscow State Industrial University, Russia	A. Miyachi, Kobe University, Japan

Friday, 22 July 2011

Shock Wave Propagation and Reflection VI Renold C9

Session Chair: M. Brouillette, Université de Sherbrooke, Canada

Time	0920 hrs	0940 hrs	1000 hrs	1020 hrs
Paper number	2740	2709	2737	~~2685~~
Paper title	On hyperbolic shock wave	Sonic line and stand-off distance on re-entry capsule shapes	Numerical and experimental investigation of the effect of bypass mass flow due to small gaps in a transonic channel flow	~~A study on the unsteady aerodynamics of projectiles in overtaking blast flowfields~~
Presenting author	S. Mölder, McGill University, Canada	H. G. Hornung, Caltech, USA	M. Giglmaier, Technische Universität München, Germany	~~C. Muthukumaran, Indian Institute of Space Science and Technology, India~~

Friday, 22 July 2011

Renold Concourse

1040-1100

Coffee / Tea

Friday, 22 July 2011 AM Session B

Friday, 22 July 2011				
	Special Session on Shock Wave Moderation II			Renold C2
Session Chair:	A. Sasoh, Nagoya University, Japan			
Time	1100 hrs	1120 hrs	1140 hrs	1200 hrs
Paper number	2843	2844	2840	2841
Paper title	Steady energy deposition at Mach 5 for drag reduction	Interaction of a shock wave with a contact discontinuity for local heat release in a flow	Two modes of shock interaction with zone of pulse volume discharges in the channel	Mach 5 bow shock control by a nanosecond pulse surface dielectric barrier discharge
Presenting author	E. Erdem, University of Manchester, UK	V. Zudov, Russian Academy of Sciences, Russia	J. Jin, Lomonsov Moscow State University, Russia	I. Adamovich, Ohio State University, USA

Friday, 22 July 2011				
	Detonation and Combustion VIII			Renold C16
Session Chair:	A. Hadjadj, CORIA INSA de Rouen, France			
Time	1100 hrs	1120 hrs	1140 hrs	1200 hrs
Paper number	2823	2887	2690	2520
Paper title	Experimental and numerical investigation of CH* and OH* chemiluminescence in acetylene combustion behind reflected shock waves	Simulations of non-ideal detonation wave propagation and Its experimental validation	Effect of wave flow structure on combustion at high speeds	Similarity solutions for reactive shock hydrodynamics
Presenting author	M. Bozkurt, University of Duisburg-Essen, Germany	X. Zhang, Chinese Academy of Engineering Physics, China	M. Goldfeld, ITAM SB RAS, Russia	R. Arora, IIT Roorkee, India

Friday, 22 July 2011

Flow Visualisation IV Renold D7

Session Chair: E. Schuelein, DLR, Germany

Time	1100 hrs	1120 hrs	1140 hrs	1200 hrs
Paper number	2663	2777	2738	2909
Paper title	Potential of localized flow heating for wave drag reduction	Quantitative visualization of high speed flow through optical tomography	Application of two sections focusing Schlieren technique on the supersonic combustion wind tunnel	Flow visualization of discontinuities and instabilities in supersonic flow
Presenting author	E. Schuelein, German Aerospace Centre, Germany	G. Hedge, Indian Institute of Science, India	A-M. Xie, China Aerodynamics Research and Development Center, China	Y. Shihe, National University of Defense Technology, China

Friday, 22 July 2011

Shock Wave Phenomena and Applications IV Renold E7

Session Chair: S. Utyuzhnikov, The University of Manchester, UK

Time	1100 hrs	1120 hrs	1140 hrs	1200 hrs
Paper number	2807	2842	2788	2811
Paper title	Structure of the plume emitted during laser ablation of materials	Interaction between laser induced plasma and boundary layer over a flat plate in hypersonic flow	Shock wave boundary layer interaction from reflecting detonations	Laser driven burning and detonation waves in silica-based optical fibers
Presenting author	Z. Walenta, Institute of Fundamental Technological Research, Polish Academy of Sciences, Poland	L.Yang, The University of Manchester, UK	J. Damazo, California Institute of Technology, USA	V. P. Efremov, Joint Institute for High Temperatures RAS, Russia

Friday, 22 July 2011

Shock Wave Propagation and Reflection VII Renold C9

Session Chair: Z. Jiang, Institute of Mechanics at Chinese Academy of Sciences, China

Time	1100 hrs	1120 hrs	1140 hrs	1200 hrs
Paper number	2762	2758	2665	2747
Paper title	Computational study of the interaction of a planar shock wave with a cylinder/sphere: The reflected wave velocity	Experimental and numerical investigation of shock wave interaction with rigid obstacles	Analytical and numerical study of three shock configurations with negative reflection angle	Simulations of reflected shock bifurcation in a square channel
Presenting author	Y. Kivity, Ben-Gurion University, Israel	E. Glazer, Ben-Gurion University, Israel	L. Gvozdeva, Joint Institute for High Temperature RAS, Russia	J. Austin, University of Illinois, USA

Friday, 22 July 2011

Barnes Wallis

1220-1330

Lunch

Friday, 22 July 2011 PM Session A

Friday,22 July 2011

Keynote Lecture 8 Renold C16

1330-1410

Getting Fundamental Molecular Properties from Shock Tubes

Prof. E. Arunan

Indian Institute of Science, Bangalore, India

Session Chair: Z. Jiang, Institute of Mechanics at Chinese Academy of Sciences, China

Friday, 22 July 2011

Nozzle Flows III Renold D7

Session Chair: E. Erdem, University of Manchester, UK

Time	1420 hrs	1440 hrs	1500 hrs	1520 hrs
Paper number	2476	2743	2781	2671
Paper title	Experimental investigation of shock train turbulence	Pseudo-shock system structure in rectangular Laval nozzles with gaps	Thrust shock vector control of an axisymmetric C-D Nozzle via transverse gas injection	Fluid-structure interaction for a flexible overexpanded rocket nozzle using the aeroelastic stability model
Presenting author	A. Grzona, RWTH Aachen University, Germany	T. Gawehn, DLR German Aerospace Center, Germany	V. Zmijanovic, ICARE-CNRS / CNES, France	N. Bekka, Université d'Evry, France

Friday, 22 July 2011

Shock Wave Boundary Layer Interactions III Renold C16

Session Chair: H. Zare-Behtash, University of Manchester, UK

Time	1420 hrs	1440 hrs	1500 hrs	1520 hrs
Paper number	2780	2688	2446	2620
Paper title	A non-linear eddy-viscosity view of shock wave/boundary layer interaction flow simulation	Step configuration influence on structure of supersonic reacting flows in channels with sudden expansion	Shock-wave boundary-layer interaction control on a compression corner using mechanical vortex generators	Transitional shock-wave/boundary-layer interaction behind a roughness element
Presenting author	Y. You, DLR German Aerospace Center, Germany	N. Fedorova, ITAM SB RAS, Russia	C. Manisankar, NAL Bangalore, India	N. de Tullio, University of Southampton, UK

Friday, 22 July 2011

Numerical Methods and Simulations III Renold C2

Session Chair: K-S. Chang, Korea Advanced Institute of Science and Technology, Korea

Time	1420 hrs	1440 hrs	1500 hrs	1520 hrs
Paper number	2815	2770	2460	2499
Paper title	An investigation into solver strategies for the modelling of compressible turbulent flow	Application of a new hybrid explicit-implicit flow solver to 1D unsteady flows with shock waves	Numerical simulation of initial shock- and detonation-wave development in shock-tube configurations	Computations of flow field around an object decelerating from supersonic to subsonic velocity
Presenting author	I. Asproulias, University of Manchester, UK	E. Timofeev, McGill University, Canada	P. Ess, DLR German Aerospace Center, Germany	T. Saito, Muroran Institute of Technology, Japan

Friday, 22 July 2011

Multiphase Flows V Renold C9

Session Chair: Z. Walenta, Institute of Fundamental Technology Research, Poland

Time	1420 hrs	1440 hrs	1500 hrs	1520 hrs
Paper number	2674	2889	2715	2826
Paper title	Time resolved measurements of shock induced cavitation bubbles in various liquids: A novel method of optical measurement	Direct numerical simulations of supersonic interfacial flows	Secondary atomization on two-phase shock wave structure	Interaction of a planar shock wave with a dense field of particles
Presenting author	W. Garen, Hochshule Emden/Leer-University of Applied Sciences, Germany	C. H. Chang, University of California. USA	E. del Prete, CEA DAM, France	J. Wagner, Sandia National Laboratories, USA

Friday, 22 July 2011

Renold Concourse

1540-1550

Coffee / Tea

Friday, 22 July 2011

Renold C16

1550-1700

Closing Ceremony

Guest Speaker: Dr. Sameer Savani, ADS Group LTD
Strategic Overview of UK Aerospace

Sponsors

We wish to thank the following for their contribution to the success of this conference: European Office of Aerospace Research and Development, Air Force Office of Scientific Research, United States Air Force Research Laboratory (www.london.af.mil).

International Shock Wave Institute (ISWI)

ISSW28

28TH INTERNATIONAL SYMPOSIUM ON SHOCK WAVES 2011

Exhibitors

Vision Research

Specialised Imaging

CD-ADAPCO

LAVision

TSI

Photron

Photon Lines

National Instruments

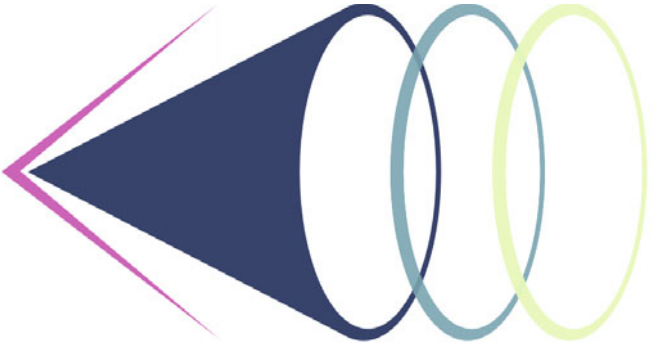

Aero-Physics Laboratory

The University of Manchester
Aero-Physics Laboratory

Contents

Part XII: Multiphase Flow

Part XIII: Nozzle Flow

Part XV: Propulsion

Part XVI: Richtmyer-Meshkov

Part XVII: Shockwave Boundary Layer Interaction

Part XVIII: Shock Propagation and Reflection

Part XIX: Shock Vortex Interaction

Part XX: Shockwave Phenomena and Applications

Part XXI: Special Session Medical and Biological Applications

Part XXII: Special Session Shockwave Moderation

Part XXIII: Student Competition

Part XII
Multiphase Flow

Numerical Investigation of Processes Accompanying Energy Release in Water Near the Free Surface

A. Chernishev, N. Petrov, and A. Schmidt

1 Introduction

The paper is devoted to numerical simulation of processes accompanying underwater explosion near the free surface. In spite of the fact that the problem has been attracting attention of many researchers (see, for example, [1, 2, 3]) challenging problems still remain. The main attention in this paper is paid to compressible and rarefaction wave propagation, to their interaction with each other and with the liquid-gas interface, to deformation of the free surface.

Analysis of these phenomena is important for both progress of theory of heterogeneous media and applications utilizing specific features of underwater explosions. One of goals of this study is development of efficient, convenient, and flexible tool for investigations of such phenomena.

2 A Mathematical Model

Unsteady flow structure induced by a local energy release in water near the free surface is investigated. A developed mathematical model provides description of waves generated by shallow underwater explosion, their propagation and interaction with each other and with the free surface. Various models of inception of cavitation in domains of significant water pressure drop can be incorporated into the proposed model. Governing continuity and momentum conservation equations for considered medium can be written in the following form:

$$\frac{\partial z}{\partial t} + \frac{\partial F_x}{\partial x} + \frac{\partial F_y}{\partial y} = -f \tag{1}$$

A. Chernishev · N. Petrov · A. Schmidt
Computational Physics Laboratory, Ioffe Physical-Technical Institute
of the Russian Academy of Sciences, St. Petersburg, 194021, Russia

$$z = \begin{pmatrix} \rho \\ \rho u \\ \rho v \end{pmatrix}, \; F_x = \begin{pmatrix} \rho u \\ \rho u^2 + p \\ \rho uv \end{pmatrix}, \; F_y = \begin{pmatrix} \rho v \\ \rho uv \\ \rho v^2 + p \end{pmatrix}, \; f = \begin{pmatrix} i\rho u/x \\ i\rho u^2/x + \Sigma_x \\ i\rho uv/x + \Sigma_y \end{pmatrix} \quad (2)$$

Here ρ, p, u, v, Σ are the density, the pressure, the velocity components and the surface tension. Index i denotes flow geometry, $i = 1$ and 0 correspond to axial and plane symmetry, respectively.

In the case of compressible liquid conventional equation of the VOF method [4], which provides determination of interface location, should be rewritten as:

$$\frac{\partial \alpha\rho_l}{\partial t} + \frac{\partial \alpha\rho_l u}{\partial x} + \frac{\partial \alpha\rho_l v}{\partial y} = -i\frac{\alpha\rho_l u}{x} \quad (3)$$

Here ρ_l is the density of liquid, α is the liquid volume fraction.

The surface tension Σ is considered here as a volume force in equation (1):

$$\Sigma = \sigma k \mathbf{n}, \quad \mathbf{n} = \frac{\operatorname{grad} \alpha}{|\operatorname{grad} \alpha|}, \quad k = \operatorname{div}(\operatorname{grad} \alpha) \quad (4)$$

The liquid is assumed to be barotropic medium and obey the Tait equation of state:

$$p = p_a K \left[\left(\frac{\rho}{\rho_a} \right)^{\beta} - 1 \right] + p_a, \quad (5)$$

where $K = 3045$, $\beta = 7.15$, $p_a = 101325$Pa, $\rho_a = 996.5$kg/m^3 in the case of water.

Estimation showed that at pressure jump across the shock wave equal to 1000 MPa, temperature variation in water is about 6 K . At the same time at normal temperature parameters of the Tait equation, K and β, are changed to 1% and 3%, respectively. These estimates justify the applicability of the barotropic equation of state for water. The gas phase is considered to be the ideal perfect one.

Besides, "Stiffened gas" model was also used [5]. This model describes the two phases (liquid and gas) by a single equation of state with parameters depending on properties of the medium. The isotropic relation (for rarefication waves) and Hugoniot relation (for shocks):

$$\frac{p - p_\infty}{\rho} = \text{const} \quad (6)$$

$$\frac{\rho}{\rho_0} = \frac{(N+1)(p+p_\infty) + (N-1)(p_0+p_\infty)}{(N+1)(p_0+p_\infty) + (N-1)(p+p_\infty)} \quad (7)$$

The parameters p_∞, N was determined for water using the Tait equation: $p_\infty = 489.115$MPa, $N = 4.9$. Gas is ideal perfect one: $p_\infty = 0, N = 1.4$.

This model is convenient for solving the Riemann problem at the interface and, consequently, for matching of solutions of the original equations. Validation of this

approach was performed by comparison of data provided by these models for water with those of the International Association for Properties of Water and Steam [6]:

Density, kg/m^3	Pressure, MPa
996.556	0.099
1005.308	20.002
1188.202	700.005

Underwater explosion was simulated by increase of the pressure within a localized domain. Pressure amplitude was determined by released energy.

$$\varepsilon = \varepsilon^{\rho}(\rho) + \varepsilon^{s}(s) = -\int pd\left(\frac{1}{\rho}\right) + \varepsilon^{s}(s) =$$
$$= p_a\left(\frac{1}{\rho_a} - \frac{1}{\rho}\right)(1-K) + \frac{p_a K}{(\beta-1)\rho_a}\left[\left(\frac{\rho}{\rho_a}\right)^{(\beta-1)} - 1\right] + \varepsilon^{s}(s) \qquad (8)$$

Here ε is the internal energy depending on the density and entropy. Comparison of results obtained using the proposed model with the data given in [3] shows the validity of such descriptions of the underwater explosion. Figure 1 shows dependence of pressure jump across the front of the blast wave on the reduced distance for the various parameters of the "explosion" (pressure amplitude and size of the energy release domain).

3 The Numerical Method

The Euler equations is solved by numerical method which is based on high-resolution Godunov-type numerical scheme [7]. This method is explicit, monotonic, and shock-capturing one. It possesses the second order accuracy on the smooth solutions. Convergence of the solution is determined by the CFL condition.

One of the main components of this method is solution of the Riemann problem. Such an approach was proposed by Godunov [8]. Solution of the Riemann problem can be generalized for the Tait equation of state (5) in liquid and for "Stiffened gas" equations (6,7) at interface. This solution was validated using acoustic impedances of the phases.

The liquid volume fraction was used to determine location of the liquid-gas interface. The equation (3) is solved for the liquid phase ($\alpha = 1$) and it is necessary to extend specification of medium parameters in gas region. So the density and the velocity of liquid on the interface were extrapolated into the region where $\alpha \neq 0$. In practice, extrapolation is required only for 2-3 computational cells in the vicinity of the interface. To minimize the region where $0 < \alpha < 1$ Van Leer limiter function

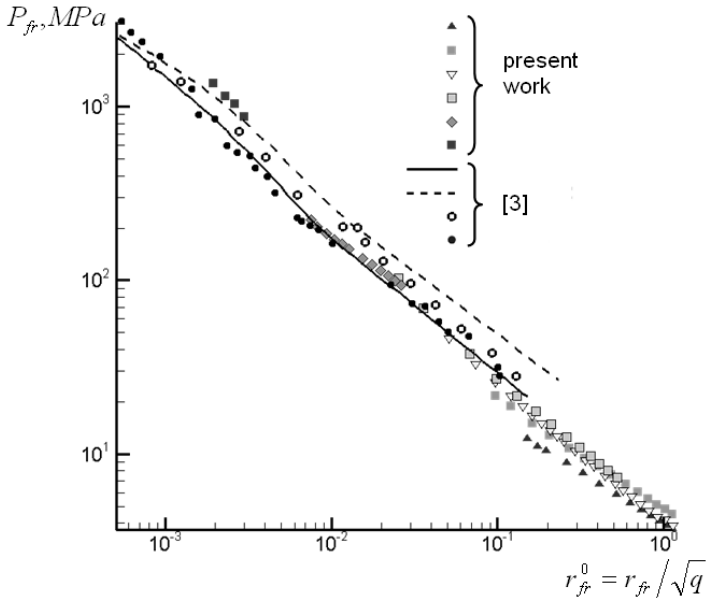

Fig. 1 Comparison of experimental data and calculations of other authors [3]. Dependence of pressure jump across the shock wave on the reduced radius r^0_{fr}. Where r_{fr} is the radius of the cylindrical waves (m), q is released energy per unit length of the cylindrical charge (J/m).

was introduced [9]. This function allows to obtain monotonic solution with steep gradients of hydrodynamic functions.

4 Model Validation

To validate the proposed algorithm local energy release in water near the free surface was considered with parameters corresponding to experimental ones [2]. Results of numerical investigation of underwater explosion of a spherical charge of 10 mg AgN_3 is presented. The center of the charge was located at a distance of 3.3 cm below the free surface. Figure 2 demonstrates photographs of structure of the flow induced by the explosion for 14, 28, and 42 microseconds after the detonation. These Schlieren visualizations are compared with computed distributions of density gradients for the corresponding moments of time. Satisfactory agreement of the predicted and actual flow structure is seen in the figure. It allows concluding that the proposed algorithm provides adequate simulation of the flow structure including such complicated phenomena as propagation of compression and rarefaction waves, their interaction with each other and with the free surface, transmission of pressure pulse into the air. Under experimental conditions, cavitation occurs at the beginning of the rarefaction wave reflected from the free surface.

Propagation and interaction of waves generated by the explosion can be seen in the Figure 3 in more details. Pressure profiles along the vertical axis originated in the center of the explosion.

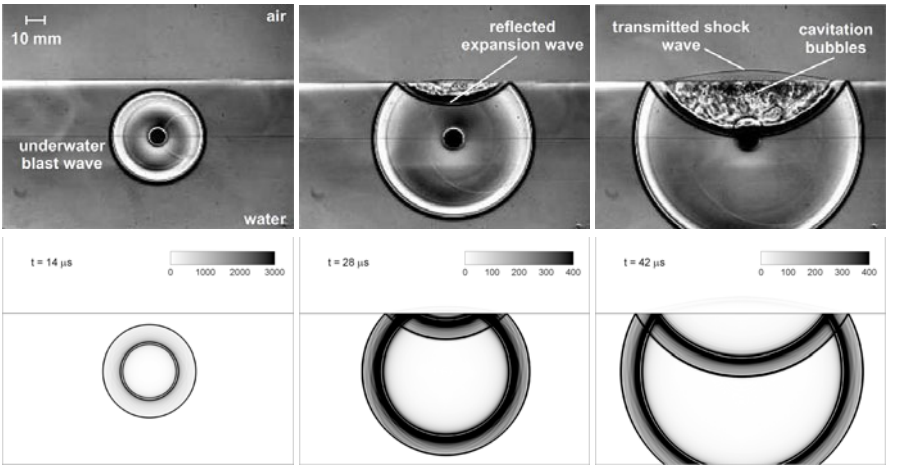

Fig. 2 Comparison of experimental data (Schlieren visualization [2] – the upper part) with predictions of the proposed algorithm (density gradient distributions – the lower part).

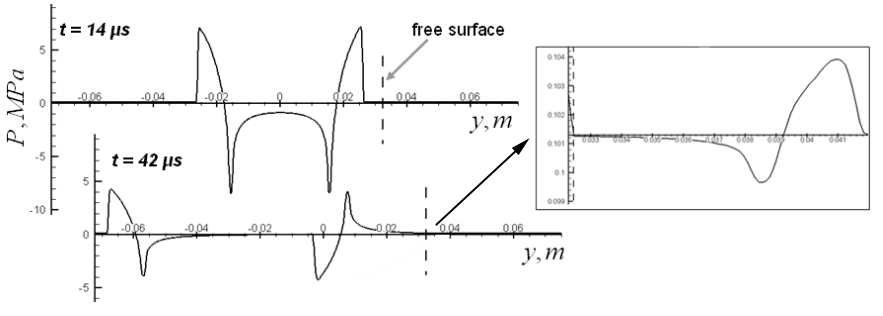

Fig. 3 Pressure profiles along the vertical axis (center of domain). On the right side of the figure is scaled plot.

In Figure 4 flow structure induced by evolution of high pressure gas bubble near the free surface is presented. It is seen that due to multiple refractions of waves between the free surface and the bubble with co-current flows directed upper the liquid velocity in this domain significantly increases which results in free surface deformation. At that the bubble grows and slightly deforms.

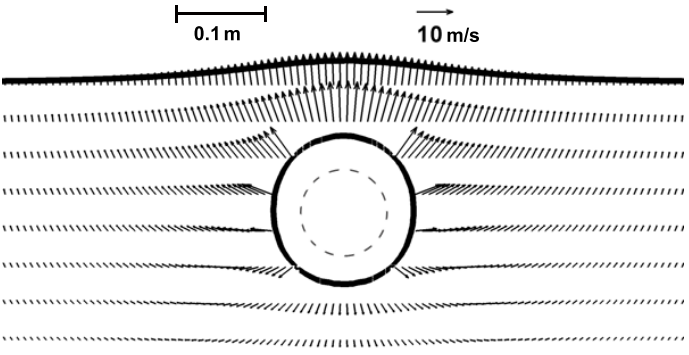

Fig. 4 The velocity of water in 5 ms after "explosion". Initial pressure of bubble was 5 bars.

5 Conclusions

In the present paper an algorithm is proposed that allows to trace the interface between compressible liquid and gas. These method is based on the Riemann problem, that connects the two phases, and on "compressible VOF method" used to determine location of the interface.

Further work is associated with development of the proposed approach, in particular, with detailed description of cavitation and evolution of the bubble produced by explosive detonation.

This study is supported by Government Contract # 02.740.11.0201.

References

1. Pishevar, A.R., Amirifar, A.: An adaptive ALE method for underwater explosion simulations including cavitation. Shock Waves 20, 425–439 (2010)
2. Kleine, H., Tepper, S., Takehara, K., Etoh, T.G., Hiraki, K.: Cavitation induced by low-speed underwater impact. In: Proceedings of 26th Int. Symp. Shock Waves, Göttingen, Germany, vol. 2, pp. 895–900 (2009)
3. Kedrinsky, V.K.: Hydrodynamics of Explosion: Experiment and Models, p. 435. Nauka, Novosibirsk (2000)
4. Hirt, C.W., Amsden, A.A.: An arbitrary lagrangian-eulerian computing method for all speeds. Journal of Computational Physics 14, 227–253 (1974)
5. Harlow, F., Amsden, A.: Fluid dynamics. LANL Monograph LA-4700 (1971)
6. Revised Release on the IAPWS Formulation, for the Thermodynamic Properties of Ordinary Water Substance for General and Scientific Use. The International Association for the Properties of Water and Steam, Doorwerth, The Netherlands (2009)
7. Rodionov, A.V.: Improving the order of approximation of S.K. Godunov's scheme. J. Comp. Mathematics and Mathematical Physics 27, 1853–1860 (1987)
8. Godunov, S.K.: A finite difference method for numerical calculation of discontinuous solutions of the equation of fluid dynamics. Matematicheskii Sbornik 47, 271–306 (1959)
9. Van Leer, B.: Towards the ultimate conservative difference scheme. IV. Journal of Computational Physics 23(3), 276–299 (1977)

Experimental Study of Scale Effects on Shock Wave Interaction with a Granular Layer

Y. Sakamura and T. Onishi

1 Introduction

Shock wave interaction with granular media has attracted great interest due to its relevance to many practical applications such as shock attenuation by granular filters [1] and powder densification and consolidation by shock waves [2]. The primary concern of recent investigations on this phenomenon is the stress enhancement by a granular material placed on a solid wall, instead of expected stress damping. Suzuki and Adachi [3] observed that the propagation of a shock wave over a solid wall covered with a thin dust layer gave rise to a peak in pressure profiles measured under the dust layer. Gelfand *et al.* [4] also verified that when a granular layer covered the end-wall of a vertical shock tube, the pressure measured at the end-wall after head-on collision of a shock wave with the granular layer temporally became larger than that without granular material. In order to understand the fundamental mechanism of the stress enhancement, numerous experimental works ([5]–[12]) have been carried out using vertical shock tubes similar to that used by Gelfand *et al.*

As widely known, the static stress distribution in a container storing a granular material depends on the scale of the container [13]. Analogously, the scale of the shock tube may affect the pressure measured under the granular layers in shock tube experiments such as mentioned above. To the best of our knowledge, however, such scale effects on the shock wave interaction with a granular layer have not been discussed previously. The main purpose of the present study is to examine the scale effects on the shock wave interaction with a granular layer. In the present work, we conducted two sets of experiments by using two vertical shock tubes with different dimensions of the cross section, and then compared their results. In the experiments,

Y. Sakamura
Department of Mechanical Systems Engineering, Toyama Prefectural University,
5180 Kurokawa, Imizu, Toyama 939-0398, Japan

T. Onishi
Rinnai Corporation, Oguchi-cho, Niwa-gun, Aichi 480-0132, Japan

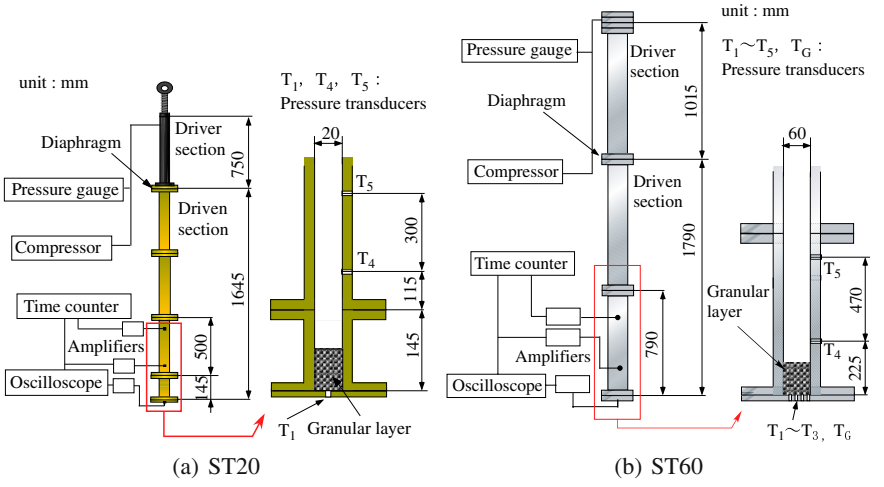

Fig. 1 Experimental setups. **(a)** ST20 with a 20 mm × 20 mm cross section. **(b)** ST60 with a 60 mm × 60 mm cross section

Table 1 Physical properties of the granular particles

Material density (g/cm^3)	Bulk density (g/cm^3)	Average diameter (mm)	S.D. of diameter (mm)
3.5	2.0	0.81	0.07

spherical particles were placed on the end wall of each shock tube and the total and the gas pressures were measured under the shock-loaded granular layer.

2 Experimental Setup and Method

The experimental setups are schematically shown in Fig. 1. Two vertical shock tubes (ST20 with a 20 mm × 20 mm cross section and ST60 with a 60 mm × 60 mm cross section) were used in the present work. Granular layers are modeled as assemblies of spherical particles made of ceramics from Noritake Co. Ltd. The physical properties of the particles are summarized in Table 1.

As shown in Fig. 1, we directly poured the spherical particles on the bottom wall of the shock tube and then made granular layers. The depth of the granular layer (d_L) was set in the range of 10 to 150 mm. Pressure under the granular layers were measured with piezoelectric transducers. In the experiments with ST20, a pressure transducer (Kistler 603B) was mounted at the center of the bottom wall to measure the total pressure (stress). Due to the limitation of the space, it was extremely

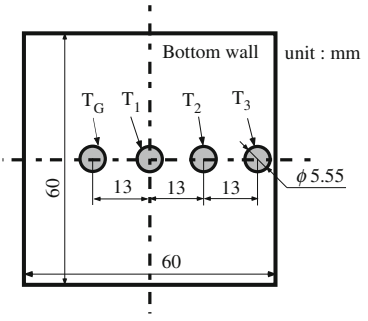

Fig. 2 Locations of pressure transducers installed on the bottom wall of ST60

difficult to mount other transducers on the bottom wall of ST20. Therefore, for measuring the gas pressure, a thin mesh screen was installed between the transducer and the granular layer to prevent a direct contact between them, and another set of experiments was then conducted. In the experiments with ST60, on the other hand, three pressure transducers ($T_1 \sim T_3$) and the other one with a thin mesh screen (T_G) were mounted on the bottom wall as shown in Fig. 2 and the total pressure at different locations and the gas pressure were measured simultaneously. It should be noted here that the gas pressure was found to be distributed almost uniformly over the bottom wall of ST60, so that one transducer (T_G) was enough to measure the gas pressure under the granular layers.

The test sections were initially filed with air at atmospheric pressure and room temperature. The Mach number of the incident planar shock wave was evaluated by measuring the time interval in which the shock wave traveled between two pressure transducers T_4 and T_5 (Kistler 601A) mounted on the side wall of the shock tubes as shown in Fig. 1. In the present study, the Mach number of the incident shock was set to be 1.33 with an accuracy of ± 0.01.

3 Results and Discussion

Figures 3 and 4 show representative pressure traces obtained under the granular layers after the shock impingement. Solid and dotted lines in each figure represent the pressure traces from the experiments using ST20 and ST60, respectively. They were obtained by averaging pressure traces from several shots conducted under the same condition, and the error bars indicate the range of scattering in each series of experiments.

Figure 3 shows averaged total pressure histories recorded at the center of the bottom wall of each shock tube (measured by T_1 transducer) for $d_L = 10$, 30 and 70 mm. It can be seen from Fig. 3 (a) that for the relatively shallow granular layer case ($d_L = 10$ mm), the difference between the two sets of experiments is not so large. However, for deeper cases ($d_L = 30$ and 70 mm), the pressure profiles from ST20 experiments are much different from those from ST60 experiments as shown

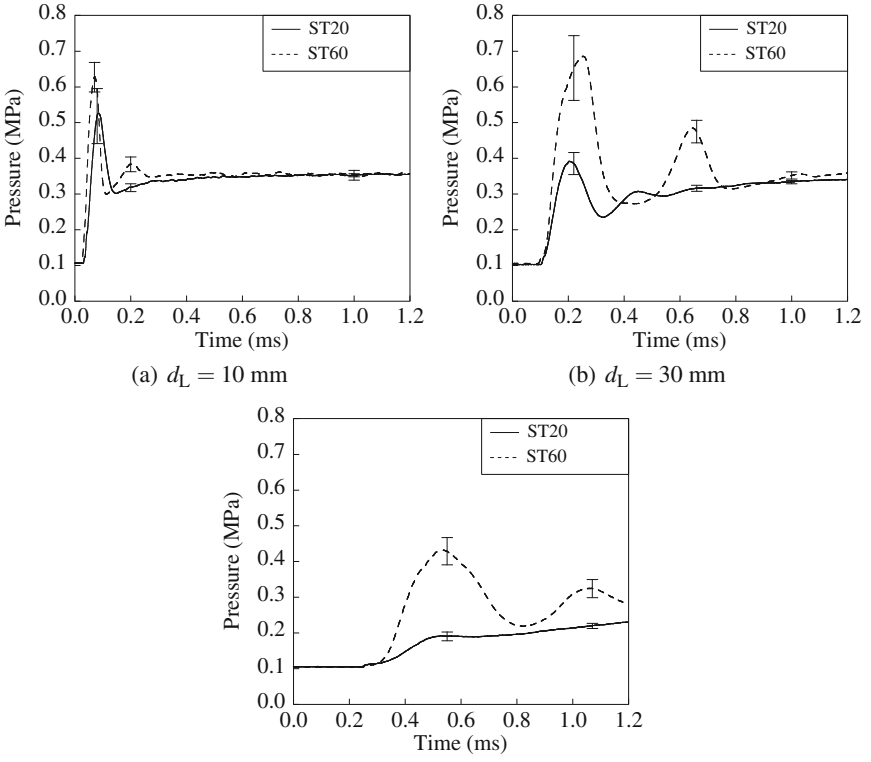

(a) $d_{\mathrm{L}} = 10$ mm (b) $d_{\mathrm{L}} = 30$ mm

(c) $d_{\mathrm{L}} = 70$ mm

Fig. 3 Comparison between total pressure histories obtained from the experiments using ST20 and ST60

in Figs. 3 (b) and (c). It can be also observed that the deeper the granular layer is, the larger the difference in the total pressure profiles is. Thus, the scale effect on the total pressure profile is evident. This may be attributed to the fact that granular media have a marked tendency to redirect vertically applied force toward the sides (the bridging effect), and thus the scale and geometry of the container significantly affects the stress distribution inside the granular media, which is widely acknowledged for static loading situations [14].

On the other hand, it is found from Fig. 4 that the scale of the shock tube also has an effect on the gas pressure although the differences in the gas pressure traces are much smaller than those in the total pressure ones. The result shown in Fig. 4 indicates that the permeability of the granular layer was much reduced for the smaller shock tube (ST20).

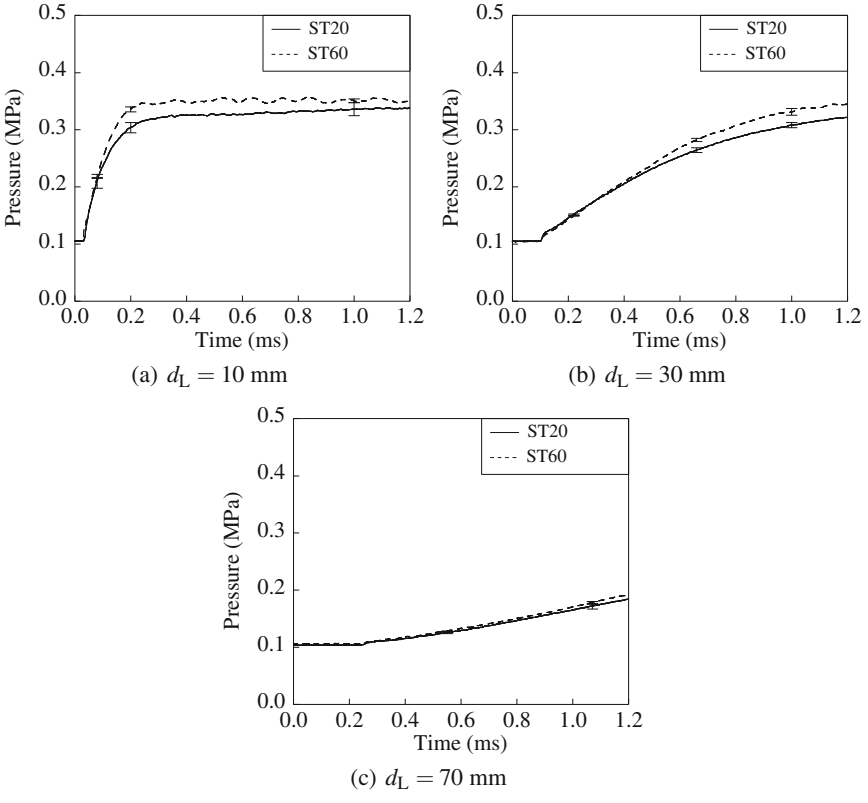

(a) $d_{\mathrm{L}} = 10$ mm (b) $d_{\mathrm{L}} = 30$ mm

(c) $d_{\mathrm{L}} = 70$ mm

Fig. 4 Comparison between gas pressure traces from the experiments using ST20 and ST60

4 Conclusion

In order to study the scale effects on the shock wave interaction with a granular layer, we conducted two sets of experiments using shock tubes with different dimensions of the cross section. The main conclusions derived from the present work are summarized as follows.

1. The scale of the shock tube's cross section has a significant effect on the total pressures under the granular layer, especially for large depth cases.
2. The gas pressure under the granular layer is also affected by the scale of the shock tube although its influence is much smaller than that on the total pressure.

Acknowledgement. The authors would like to express their sincere gratitude to Dr. Tateyuki Suzuki for his encouragement and fruitful suggestions during the course of this study.

References

1. Bakken, J., Slungaard, T., Engebretsen, T., Christensen, S.O.: Attenuation of shock waves by granular filters. Shock Waves 13, 33–40 (2003)
2. Nesterenko, V.F.: Dynamics of Heterogeneous Materials. Springer (2001)
3. Suzuki, T., Adachi, T.: A basic study of the blast waves over a dust deposit. In: The Japan National Committee for Theoretical and Applied Mechanics (ed.) Theoretical and Applied Mechanics, vol. 31, pp. 439–446. Univ. of Tokyo Press, Tokyo (1982)
4. Gelfand, B.E., Medvedev, S.P., Borisov, A.A., Polenov, A.N., Frolov, S.M., Tsyganov, S.A.: Shock loading of stratified dusty systems. Arch. Combust. 9, 153–165 (1989)
5. Sakakita, H., Hayashi, A.K.: Study on pressure profiles in a powder layer using a vertical shock tube. In: Proc. Symp. on Shock Waves, Japan, pp. 655–660 (1992)
6. Ben-Dor, G., Britan, A., Elperin, T., Igra, O., Jiang, J.P.: Experimental investigation of the interaction between weak shock waves and granular layers. Exp. in Fluids 22, 432–443 (1997)
7. Britan, A., Ben-Dor, G., Elperin, T., Igra, O., Jiang, J.P.: Mechanism of compressive stress formation during weak shock wave impact with granular materials. Exp. in Fluids 22, 507–518 (1997)
8. Britan, A., Ben-Dor, G., Elperin, T., Igra, O., Jiang, J.P.: Gas filtration during the impact of weak shock waves on granular layers. Int. J. Multiph. Flow 24, 473–491 (1997)
9. Britan, A., Ben-Dor, G., Levy, A., Igra, O.: Shock wave interaction with granular materials. In: Ball, G.J., et al. (eds.) Proc. 22nd Int. Symp. on Shock Waves, pp. 1375–1380 (2000)
10. Mikami, H., Kaneda, T., Sakamura, Y., Suzuki, T.: Head-on collisions of a planar shock wave with a dust layer. In: Kimura, T. (ed.) Theoretical and Applied Mechanics, vol. 49, pp. 263–270 (2000)
11. Britan, A., Ben-Dor, G., Igra, O., Shapiro, H.: Shock wave attenuation by granular filters. Int. J. Multiph. Flow 27, 634–671 (2001)
12. Britan, A., Levy, A.: Weak shock wave interaction with inert granular media. In: Ben-Dor, G., Igra, O., Elperin, T. (eds.) Handbook of Shock Waves, pp. 597–666. Academic Press, San Diego (2001)
13. Nedderman, R.M.: Statics and Kinematics of Granular Materials. Cambridge University Press (1992)
14. Duran, J.: Sands, Powders, and Grains: An Introduction to the Physics of Granular Materials. Springer (1999)

Supercavitation Phenomenon during Water Exit and Water Entry of a Fast Slender Body

Hong-Hui Shi, Xiao-Ping Zhang, Yan Wu, Hui-Xia Jia, Hao-Lei Zhou, Su-Yun Zhou, Li-Te Zhang, Ruo-Ling Dong, and Chao Wang

1 Introduction

The direct applications of water exit and water entry study are submarine launched ballistic missile and anti-submarine missile [1],[2]. This study is also related to underwater high-speed torpedo which moves in a supercavity and is designed to confront aircraft carrier [3]-[4]. Previous research has suggested that when an underwater body moves close to the free surface, cavitation may become important[5],[6]. However, due to its transient and non-linear nature, water exit is a rather complicated process and many problems remain to be solved.

We have conducted systematic research on water entry problem of a blunt body [7]-[12]. Now, we extend our research activity into water exit problem. Meanwhile, we will also examine the water entry process of a slender body. It is known that the equation of motion for an underwater body is [12]

$$m\frac{dV}{dt} = mg - \frac{1}{2}\rho_w A_0 C_d V^2 \tag{1}$$

where t, g, ρ_w, A_0, m, V, C_d are time, gravity, density of water, the projecting area of the body, body mass, body velocity and the drag coefficient, respectively. The effect of gravity is usually allowed to be ignored. Let

$$\beta = \frac{\rho_w A_0 C_d}{2m} \tag{2}$$

It is easily to get the following equation by integrating Eq. 1,

$$V = \frac{V_0}{\beta V_0 t + 1} \tag{3}$$

Hong-Hui Shi · Xiao-Ping Zhang · Yan Wu · Hui-Xia Jia · Hao-Lei Zhou · Su-Yun Zhou · Li-Te Zhang · Ruo-Ling Dong · Chao Wang
College of Mechanical Engineering and Automation, Zhejiang Sci-Tech University, Hangzhou 310018, China

where V_0 is the initial velocity of the body. Thus we know that the velocity of an underwater body decays with time. This paper's experiments will also confirm this law.

2 Experimental Device and Method

Figure 1 shows the schematic drawing of the experimental devices for conducting water exit/entry experiments. A water tank 2 is located on the support 12. The water tank is made from 5 mm thick stainless plate and the size of $60 \times 60 \times 100$ cm. It also has four observation windows 4 on the four sides, which is made from 5 mm thick plexiglass plate and has the size of 30×80 cm. The testing slender body 9 is a metal nail that is shot into the water tank from its bottom or from its top. An air nail gun 8 fires the slender body. The air compressor 11 provides pneumatic power for the nail gun. The slender body travels through ball valve 5 and connection flange 6 and penetrates through the 10 μm thick tin foil 7 that is fixed by a press ring 18. Then the slender body becomes an underwater body 10 that moves towards the water surface 17. A projectile catcher 3 is designed to catch the body after water exit. A high speed photographic system which consists of camera 13, monitor 14, computer 15 and controller 15 is applied to visualize the flow field. The illumination is provided by light source 1. Before the experiment, the bottom of the water tank

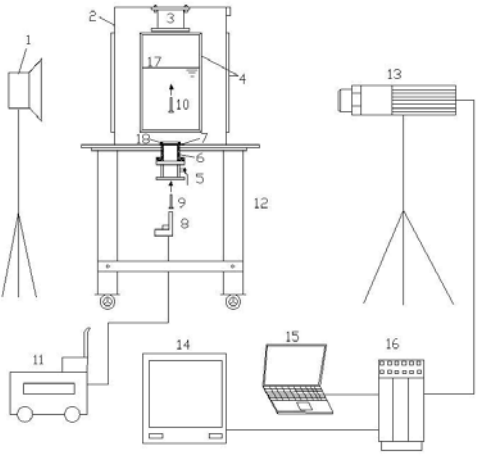

Fig. 1 Schematic of the experimental system for water exit/entry experiments. 1 - Light source, 2 - Water tank, 3 - Projectile catcher, 4 - Observation window, 5 - Ball valve, 6 - Connection flange, 7 - Tin foil, 8 - Air nail gun, 9 - Slender body in air, 10 - Slender body in water, 11 - Air compressor, 12 - Support, 13 - High-speed camera, 14 - Monitor, 15 - Personnel computer, 16 - Controller, 17 - Free surface, 18 - Press ring

is sealed by the tin foil 7 and the ball valve 5 is open. After every experiment, close the ball valve. The geometry of the slender body is given in Fig. 2. It has an apex angle of 84 deg and its total length is about 48 mm.

Fig. 2 Geometry of the slender body

3 Results

Figure 3 shows high-speed photographs of water exit of the slender body. The body appears in the scope of the picture in Fig. 3(1) and its tip starts to exit the water surface in Fig. 1(5). The body has completely left the water surface from Fig. 3(8). The body velocity between Figs. 3(1) and 3(2) is about 43 m/s. The labels S, N and W in the figure mean supercavity, nail and wake respectively. In Figs. 3(4) and 3(7), the label N marks the slender body in water and in air respectively. If comparing the cross-sectional sizes of the slender body in water and air, it is found that the body in Fig. 3(7) is much thinner than that in Fig. 3(4). This means that the underwater slender body has completely surrounded by a supercavity. On the other

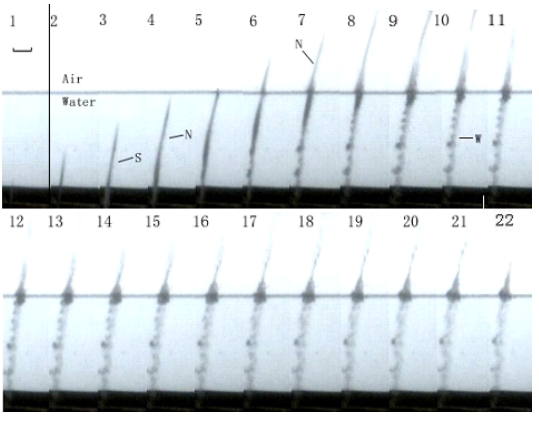

Fig. 3 Sequences of water exit. The water depth is 25 cm. The labels S, N and W mean supercavity, nail and wake. The photograph scale is given in (1) using a horizontal bar, which represents 15 mm. The interframe time is 1 ms.

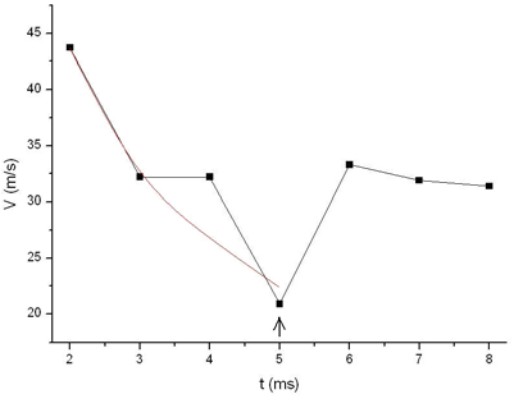

Fig. 4 Variation of slender body velocity with time in water exit. The arrow shows the time when the body starts to exit the free surface. The black square symbols are experimental data.

hand, the well observed wake flow is another evidence of showing the existence of a supercavity because bubbles are stripped from the body tail and play a role of tracing particles in the Karman vortex street. Significant features are that the supercavity is stripped off the body by the free surface (Figs. 3(7)-3(10)) and it merges into an upwards moving splash (Figs. 3(11)-3(14)). The so-called cavitation phenomenon near free surface [5],[6] is not found. This may be attributed to that since the pressure in a supercavity is negative [8], once it meets the open air it will absorb air and surrounding fluid into the cavity. This prevents the supercavity to keep its cavitation characteristic. The velocities of the slender body in Fig. 3 are measured and are given in Fig. 4. The curve in the left of the figure is the correlation curve of the body velocity until water exit, that is

$$V = 69.16t^{-0.6586}, (m/s) \tag{4}$$

where the units of time t and velocity V are ms and m/s respectively. Equation 4 correctly describes that the velocity of underwater body decreases with time, as shown in Eq. 4. In Fig. 4, an arrow at time of 5 ms marks the time when the body stars to exit the water surface. It must be noted that just after water exit, there is a significant velocity increase. From the time of 5 ms to the time of 6 ms, the velocity suddenly increases from 26 m/s to 34 m/s. Experiments at different conditions all show this tendency [13]. The mechanism for this is rapid decrease of the drag coefficient and added mass during the body crossing the free surface from water into open air [1],[2]. The sudden velocity increase will exert extra force and moment to the exiting solid body. Therefore, it is inevitable to consider this effect in designing underwater vehicles.

Figure 5 shows high-speed photographs of water entry of the slender body. The body begins to enter the water between Fig. 5(1) and Fig. 5(2) and the entry velocity is about 53 m/s (see Fig. 6). It is seen that a supercavity is well formed. In

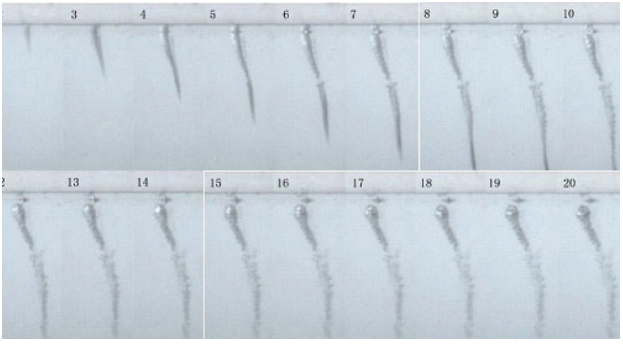

Fig. 5 Sequences of water entry. The interframe time is 1 ms. The height of each picture is 23.16 cm.

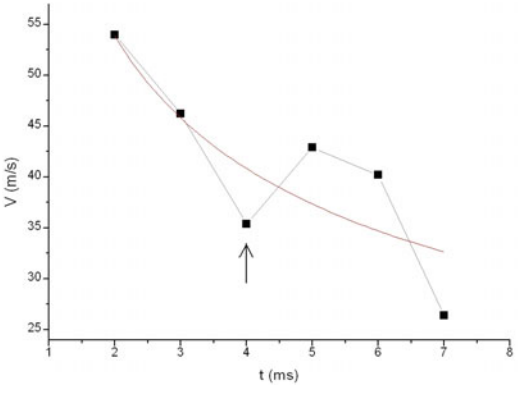

Fig. 6 Variation of slender body velocity with time in water entry. The black square symbols are experimental data. The curve is the correlation curve expressed by Eq. 5.

Figs. 5(4) and 5(5), the supercavity is twisted because the interaction between the slender body and the cavity wall. Because of its long length of a slender body, this kind of interaction often occurs[14]. Then supercavity starts to be broken into two parts (Figs. 5(6)-5(7)). The upper part of supercavity is finally pulled away from the free surface in Figs. 5(10)-5(14). The lower part of supercavity begins cavitation process from Fig. 5(8) to Fig. 5(20). The velocities of the slender body in Fig. 5 are measured and are given in Fig. 6. The curve in the figure is the correlation curve of the body velocity after water entry, that is

$$V = 71.10t^{-0.4003}, (m/s) \tag{5}$$

where the units of time t and velocity V are ms and m/s respectively. Similar to Eq. 4, Eq. 5 also shows the decreasing tendency of the velocity with time. However, it must be understood that Eq. 5 only gives an overall tendency of the velocity variation. From the time of 4 ms in Fig. 6 (marked by an arrow), the slender body starts

to be fully surrounded by a supercavity. Because of the drag reduction effect of a supercavity, the velocity of the slender increases to 46 m/s at 5 ms from 35 m/s at 4 ms.

4 Conclusions

1. In water exit, the supercavity of a slender body stops at free surface. Considering the transient nature of the process, even if cavitation occurs near free surface, the solid body would have already left the water surface. Further research is been undertaken using high-speed underwater blunt body.
2. During exiting water surface, due to rapid decrease of the drag coefficient and other factors, the body velocity will increase suddenly. This will certainly exert extra force and moment to the solid body.
3. In water entry experiment, it is confirmed that a supercavity can be generated around a slender body. However, due to its long length of the body, the body may often impact on the cavity wall, which subsequently causes break-up of the supercavity and deflection of the body trajectory. When the slender body is fully covered by a supercavity, its velocity is increased.

Acknowledgements. This work has been supported by Zhejiang Provincial Natural Science Foundation of China under a Priority Project (Grant No. Z1110123).

References

1. Luo, J.L., Mao, H.Y.: Tactical Missile Technology 4 (2004) (in Chinese)
2. Luo, J.L., He, H.B.: Tactical Missile Technology 3 (2004) (in Chinese)
3. Chen, Y., Lu, C.J.: J. Hydrodynamics Ser. B 20, 2 (2008)
4. Huang, X., Lu, C.J., Li, J.: J. Hydrodynamics Ser. A 24, 6 (2009) (in Chinese)
5. Quan, X.B., Li, Y., Wei, H.P., Lu, H.B., Xin, W.Q., Lu, C.J.: J. Ship Mech. 12, 4 (2008) (in Chinese)
6. Quan, X.B., Wei, H.B., Kong, D.C.: J. Astronautics 29, 6 (2008) (in Chinese)
7. Shi, H.H., Itoh M.: Proc. 7th Int. Symp. on Cavitation, CAV 2009, vol. 142 (2009)
8. Shi, H.H., Kume, M.: Acta Mechanica Sinica 20, 4 (2004)
9. Shi, H.H., Kume, M.: Physics of Fluids 13, 1 (2001)
10. Shi, H.H., Itoh, M., Takami, T.: Trans. ASME, J. of Fluids Engineering 122, 4 (2001)
11. Shi, H.H.: In: Proc. 74th JSME Spring Annual Meeting, vol. 6 (1997)
12. Shi, H.H., Takami, T.: Experiments in Fluids 30 (2001)
13. Shi, H.H., Wu, Y., Zhou, H.L., Zhang, X.P., Zhou, S.Y., Jia, H.X., Zhang, L.T., Wang, C., Dong, R.L.: J. Zhejiang Sci-Tech. University 28, 4 (in Press, 2011) (in Chinese)
14. Jiang, Y.H., An, W.G., An, H.: J. Hydrodynamics Ser. A 23, 5 (2008) (in Chinese)

Explosive Eruptions of Volcanoes: Hydrodynamic Shock Tubes as Lab Method of Simulation

V. Kedrinskiy

1 Introduction

Obviously, it is beyond question that the explosive character of decompression during the volcanic eruption initiates a whole spectrum of phenomena in a pre-compressed magmatic melt containing large amounts of dissolved gases: homogeneous nucleation, bubbly cavitation, gas diffusion, and dynamically increasing viscosity of the melt. It is these processes that determine the eruption character, the magma state dynamics, and the flow structure in decompression waves as a whole. In the same time many aspects of their mechanisms remain unclear. The answers to these questions and, in particular, to the question about the mechanism of the cavitating magma transition to a state of an ash cloud cannot be simple because of extremely complicated and multiple-scale phenomena such as an explosive eruption [1]. In this connection, as it was noted by Gilbert and Sparks [2], laboratory experiments on the dynamics researches of volcanic flows and, in particular, the shock tube methods must become important components of simulation processes together with mathematical models and numerical analysis.

Indeed, the analysis of the pre-eruption hydrodynamic schemes of the St Helens and Kilauea volcanoes has shown that, in terms of structural features, they are similar to hydrodynamic shock tubes (HST) [3], [4]. The ”inversion” variant of the Glass-Heuckroth -scheme [3] turned out to be most close to the real scheme of the pre-eruption state of explosive volcanoes. It includes three basic elements: a high-pressure chamber (analogue of the system consisting of a volcanic chamber and a channel filled by compressed magma), a low-pressure chamber where the gas is under atmospheric pressure (analogue of the free portion of the volcanic conduit and/or a crater bordering with the atmosphere), and a diaphragm (plug) separating these two chambers. Thus, one can consider that pre-eruption schemes of explosive volcanoes have a common gas-dynamic sign.

V. Kedrinskiy
Lavrentyev Institute of Hydrodynamics SB RAS, Lavrentyev prospect 15,
Novosibirsk, 630090, RF

Prof.A. Lacroix (1908) proposed to classify volcanoes on the basis of the intensity of their explosive eruptions: *Hawaiian* - as rarely explosive, *Strombolian* - as moderately explosive, *Plinian/Vulcanian* - as strongly explosive, *Pelean* - as the greatest explosive. It meant that they were classified according to the principal types of behaviour that they exhibited. The magma properties were mainly determined as andesitic or rhyolitic ones.

Fig. 1 From left to right: Vertical and lateral eruptions of the St Helens volcano, successive vertical and lateral eruptions at shallow underwater explosions

An analogue to a similar spectrum of intensity can be found in processes inherent in underwater explosions. It is the field of hydrodynamics of high-velocity unsteady flows initiated by explosive sources of different intensity. The latter depends on the energy release rate, which is insignificant in the case of underwater explosions of wires or gaseous mixtures and reaches a maximum value in the case of explosions of condensed cast and pressed high explosives (HEs). As an example, we can mention directed "eruptions" in the form of jet flux (fountains) on the free surface of a liquid, which are observed during shallow underwater explosions and resembles volcanic eruptions (Fig. 1, [5]).

It should be noted that the mechanics of these phenomena has the same cumulative nature (both for wire and HE explosions) determined only by the interaction of the explosive cavity with the free surface and independent of the energy release rate of the explosive source. For some types of volcanoes of the explosive character from Lacroix's classification, the intensity may also be assumed to exert no significant effect on the mechanisms responsible for the processes inherent in explosive volcanic eruptions. Thus, the community of the mechanisms controlling the eruption process can be considered as the second common sign of processes inherent in examined phenomena.

Finally, the question about the so called M-liquid (a liquid analogue of magma) remains open. In this paper, the experimental results obtained for distilled water will be discussed. This choice is based on one of important common signs (features): the densities of the number of pores per unit volume for a solidified lava sample ($10^{10} - 10^{12} m^{-3}$) and of micro-inhomogeneities in distilled water ($10^{10} - 10^{11} m^{-3}$) have practically close orders.

2 HST-Methods and State Inversion Problem

An analysis of researches in the field of mechanics of liquid destruction under shock-wave loading [6] and data on volcanic eruptions (see, for instance, [2]) suggests that unsteady high-velocity processes initiated by pulsed loading of liquid media can be considered as analogues of natural volcanic processes in terms of both the probable mechanisms of their initiation and the flow state dynamics.

As was mentioned above, the closest example of explosive volcanoes with the pre-eruption state corresponding to the HST-scheme (”inversiion” GH-scheme) is the St. Helens volcano whose powerful eruption was initiated by a huge landslide, which cut off the plug covering the volcano vent, Fig. 2 ([7], [4]).

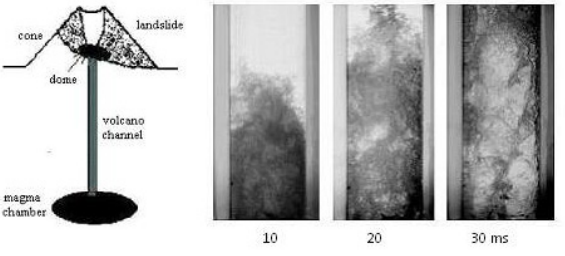

Fig. 2 From left to right: pre-eruption scheme of the St Helens volcano and experimental data on the flow structure simulation in a channel of the inversion GH-scheme.

It is considered ([8], [9]) that the density of cavitation bubbles formed in the magma as a result of explosive decompression is uniform. During cavitation development, the cavitating magma state through a stage of the foam structure is transformed to the gas-droplet state.

However, the experiments (Fig. 2, exposure time1 μs for each frame) shows that this ideal scheme of the transition of the cavitating magma to the state of an ash cloud can be rather far from real processes: the flow can be strongly inhomogeneous and, in particular, have a character of a ”bubbly cluster - slug” regime (see Fig. 2).

Dynamic schemes of the HST (systems initiating a shock wave (SW) in a sample with the free surface) are most interesting for lab applications. An SW propagates within a liquid sample and compresses it, simulating the stage of the hydrostatic state of the compressed magma in a volcanic chamber and channel. Then the SW reflects from the free surface of the sample as a rarefaction (decompression) wave. Propagating over the compressed sample in the opposite direction, it performs the function of a decompression wave.

Figure 3 presents the HST scheme (a) and the scheme of magma state dynamics (b), [8], [9]: volcano chamber, nucleation zone, cavitation zone, foam state, fragmentation zone, and, as result of fragmentation, gas/particles system. In this figure, the diaphragms are indicated by d; and the elements of this scheme are the gas receiver (1), the vacuum channel with a piston p (2), the channel with the liquid

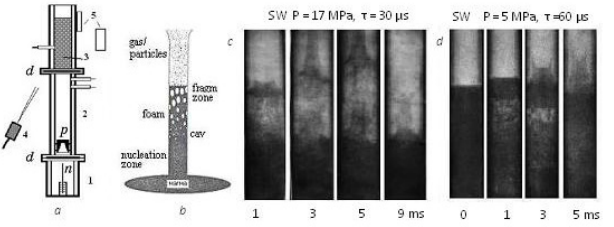

Fig. 3 Dynamic HST-scheme a; Dobran-Woods model of magma desintegration dynamics b and dynamics of intensive cavitation zone development (computer analogue of x-ray negatives) behind the decompression wave front c, d

sample (distilled water) studied (3), the pulse x-ray source (exposure time about 80 ns) (4), and the x-ray receivers (5).

As was noted above, the mechanism of the foam structure destruction or, in other words, "the foam - gas-droplet inversion" is one of unsolved principal problems.

In mid-1990s, however, thanks to the application of the impulse x-ray method, laser scanning, and digital image processing of x-ray negatives, some progress has been achieved in understanding the specific features of the flow structure of a cavitating medium at the late stages of disintegration. According to the data presented in Fig. 3,c the effect of the "foam - gas/droplet system" transition and the eruption of the gas-droplets flow can be realized in the case of sample loading by a strong SW (15 MPa amplitude and 30 μs duration). The intense cavitation development is also observed in the case of loading by a relatively weak SW (5 MPa amplitude and 60 μs duration). In this case, however, the cavitating sample (or at least its part) is also destroyed, but then (see instant $t \approx 5$ ms) it is restored again without eruption (see Fig. 3,d). It is interesting to note that this effect turns out to be close to H.M.Gonnermann's, and M.Manga's idea (Nature, 2003) that the magma deep within volcanoes can be repeatedly torn into fragments and then squeezed together again without an explosive eruption.

The application of the HST- and x-ray methods, Fig. 3, unfortunately gives no idea about the physical mechanism of the transition itself. A new experimental approach makes it possible to considerably restrict the disintegration zone. Recall that $1cm^3$ of a distilled water drop contains about 10^6 micro-inhomogeneities. Hence, water drops of such volume can be considered as the main elements of the flow structure. In this case, it is principally important that the shock wave penetrating into the drop should be ultrashort to result in the cavitation development in small drops. An electromagnetic hydrodynamic shock tube (EM HST) was designed for generation of ultra-short (microsecond duration) shock waves in a liquid.

The experiments, [10], have shown that a dense cavitation zone is formed inside the drop already at the initial stage. During the following inertial development of the cavitation zone to the instant $t \approx 1500\mu$s, the drop takes a cupola shape as a system of small spatial grids. The elements of the liquid grid under further stretching are gradually separated into individual fragments; due to instability, small jets

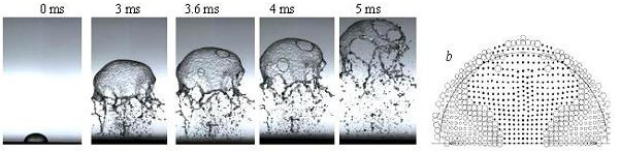

Fig. 4 Transformation of the cavitating drop into a cupola of a grid honeycomb structure and the zone of "cavitative explosion" in the center of the drop (b)

disintegrate into individual drops [10]). As it follows from Fig. 4, the subsequent fracture of the liquid sample is determined by the inversion mechanism, which is related to the dynamically growing zone of disintegration on the "cupola" surface forming the inversion front.

To understand the nature of a rather unbelievable transformation of the liquid drop to the cupola shape, Davydov [11] performed a numerical analysis of the state dynamics of a semispherical drop under ultrashort shock-wave loading within the framework of the IKvanW-model and the model of the "frozen" profile of mass velocities. According to the calculation results, the dynamics of the cavitation zone structure inside the drop confirms that the drop transformation to a cupola shape as a system of grids is a result of a "cavitation explosion" at the drop center: fast growth of bubbles, their coalescence, and inversion of states inside the drop. Figure 4,*b*, for the time $t = 145$ μs presents the distribution of visible (sizes from 0.1 to 2 mm) cavitation bubbles and the coalescence zone (symbols) occupying the central part of the drop.

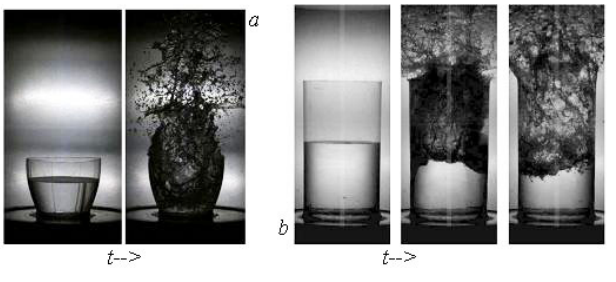

Fig. 5 Two experiments on destruction and eruption of liquid samples under shock-wave loading in the 5kJ of EM HST scheme

The recently created new electro-magnetic HST allows capacity bank to accumulate energy up to 5 kJ (which is approximately equivalent to 1 g of HE). The setup can be used for carrying out more precision experiments for larger-scale samples. First experiments have confirmed the possibility of the 5 kJ EM HST-scheme (Fig 5) to provide loading of samples that will be sufficient for destruction and eruption of a large volume of the examined liquid.

3 Conclusion

The studies have shown that , a number of explosive volcanic systems are close in terms of the structural features of the pre-eruption state to the scheme of the hydrodynamic shock-tube (HST). This fact confirms that the experimental settings for simulating magma behaviour under a decompression wave can be realised within the framework of the HST-scheme. A comparison of characteristic features of state dynamics of distilled water samples under shock-wave loading (studied by the HST-methods) with known existent models of magma behaviour during the eruption shows that high-speed processes in the liquid can be considered as analogues (in terms of some signs) of natural volcanic processes. Thus, one can assume that, independent of the eruption activity, the explosive volcanic processes (at least for some volcanoes from A. Lacroix's classification) are developed according to general gas-dynamic signs and kinetics determining the flow structure.

References

1. Kedrinskiy, V.K.: Gas-dynamic signs of explosive eruptions of volcanoes. Part 1. J. Applied Mech. and Tech. Physics 49(6), 891–898 (2008)
2. Gilbert, J.S., Sparks, R.S.J.: Future research directions on the physics of explosive volcanic eruption. The Physics of Expl. Volc. Erupt. L.: Geolog. Soc. 145, 1–7 (1998)
3. Glass, I.I., Heuckroth, L.E.: Hydrodynamic shock tube. Phys. Fluids 6(4), 543–549 (1963)
4. Kedrinskii, V.K., Makarov, A.I., Stebnovskii, S.V., Takayama, K.: Explosive eruption of volcanoes: some approaches to simulation. Comb., Expl., and SW 41(6), 777–784 (2005)
5. Kedrinskiy, V.K.: Hydrodynamics of Explosions: Experiment an Models, p. 362. Springer, Heidelberg (2005)
6. Kedrinskiy, V.K.: Nonlinear problems of cavitation breakdown of liquids under explosive loading (review). J. Appl. Mech. Tech. Phys. 34(3), 361–377 (1993)
7. Eichelberger, J., Gordeev, E., Koyaguchi, T.A.: Russian - Japanis partnership to understand explosive volcanism, June 22, pp. 1–4 (2006), http://www.uaf.edu/geology/pire/pire.pdf
8. Woods, A.W.: The dynamics of explosive volcanic eruptions. Rev. Geophys. 33(4), 495–530 (1995)
9. Dobran, F.: Non-equilibrium flow in volcanic conduits and application of the eruption of Mt. St. Helens on May 18 1980 and Vesuvius in Ad. 79. J. Volcanol. Geotherm. Res. 49, 285–311 (1992)
10. Kedrinskiy, V.K., Besov, A.S., Gutnik, I.E.: Inversion of two-phase state of liquid at pulse loading. Dokl. RAN 352(4), 477–479 (1997)
11. Davydov, M.N.: Development of cavitation in a drop at shock-wave loading. In: Dynamics of Continue Medium, vol. 117, pp. 17–20. Lavrentyev Institute of hydrodynamics, Novosibirsk (2001)

Investigation of Bubble Collapse and Water Jet Induced by Underwater Explosion in a Rectangular Tube

T. Koita, Y. Zhu, and M. Sun

1 Introduction

The rapid release of energy beneath the surface of water results in movement of the surrounding water, especially on the side of free surface. This can be realized using chemical and nuclear explosions, electric discharge, or pulsed laser focusing. By carefully setting the depth of explosion in a confined tube, a pulsed water jet can be effectively generated at the exit of the tube. The laser-induced liquid jet has been studied in biology and medicine [1]. This water jet is also important in volcanology to investigate explosive volcano eruptions that are driven by expanding gas bubbles [2]. In these applications, the bubble is generated in a confined space as in a pipe or a channel. Shallow and deep underwater explosions have been heavily investigated experimentally and numerically for decades. However the behavior of collapsing bubble and water jet in a confined space have not much been studied so far. The motivation of this study is to investigate the behavior of collapsing bubble and water jet formation in a narrow tube with a rectangular cross-section by underwater explosion. Special attentions are paid on the repeatability, so that the collected data can be used to validate numerical models for these compressibility dominated two-phase flows.

2 Experimental Setup

The rectangular tube is employed as the test section to simulate the bubble expansion and collapse, and the behavior of water jet in closed space. Fig. 1(a) shows the test section. The bottom wall and two side walls are made of stainless steel, and

T. Koita
Department of Aerospace Engineering, Graduate School of Engineering, Tohoku University

Y. Zhu · M. Sun
Center of Interdisciplinary Research, Tohoku University
6-3 Aramaki-Aza-Aoba, Aoba-ku, Sendai, Miyagi, 980-8579, Japan

other two sides are clamped by two optical windows, which are made of transparent plexigalss. The purified water is used in this study and experiment used water with 0.2% surfactant have been reported [3].

The experimental equipment in this study is shown in Fig. 1(b). Underwater explosion is created with high-voltage electric discharge. The driver circuit in high-voltage discharge consists of a high voltage power, a capacitor, a spark trigger and two electrodes (P and N) which are connected with copper wire that of diameter is 0.05mm in water. Capacitor is connected in parallel with voltage power and its capacity C is 0.2μF. The circuit is triggered manually. To investigate the dependence of bubble evolution and water jet on the voltage power V, the geometry of rectangular tube and the explosion depth H in the tube, three voltages, $V = 4.0, 4.5, 5.0$kv, are tested. The corresponding energy Ee[J] are from 1.6J to 2.5J respectively. The geometry of rectangular tube is changed with different tube width W and three patterns of it, W =15, 10, 5mm, are tested. Explosion depth H is varied at every 5mms from 30mm to 5mm with changing amount of test water. The bubble evolution and water jet generation are directly visualized by a high speed video camera at the frame rate of 50 thousands frames per second. The exposure time is 1μsec per frame. The metal halide white lamp with power of 350w is used as a light source. The location and the velocity of flow structures are also obtained by analyzing recorded photos.

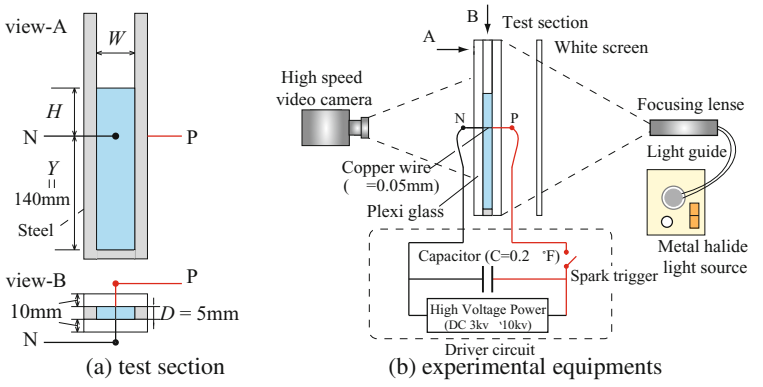

Fig. 1 Test section and experimental setup

3 Results and Discussion

3.1 The Behavior of Bubble Evolution and Water Jet Formation

The experiments are conducted at six depths ($H = 30, 25, 20, 15, 10, 5mm$). From the photos obtained, three typical patterns of the bubble evolution are observed for all voltage power V. Only these observed at $W = 15mm$ are reported in this paper.

Pattern A is observed at the depths of $30mm$, $25mm$ and $20mm$, and pattern B is seen at the depths of $15mm$ and $10mm$. Pattern C is the shallow explosion seen at $H = 5mm$. Three typical photos are shown respectively in Figs. 2(a)-(c).

The bubble is initially cylindrical. When the bubble grows up, the horizontal expansion stops because of the sidewalls but the vertical expansion continues, so that the expansion bubble becomes to be an ellipsoid shape. When the copper wire explodes, a blast wave is generated and propagates in the water. This wave reflects at the water free surface and creates a low pressure region above the expansion bubble in the water. In Fig.2(a) at the time of $0.2ms$, second cavitation is seen at the sidewalls of tube, in the region between the bubble and the free surface because of the low pressure. The cavitation disappears gradually after the expansion wave passes away free surface. In all figures, second cavitations are also observed under the bubble in the water. These cavitation bubbles are formed because of low pressure region in the water generated by expansion waves reflected from the bottom wall.

As seen in Fig. 2(a) for $H = 25mm$, the water above the bubble is accelerated and forms a jet. Two air pockets are generated near sidewalls. The water jet is blunt-shaped at beginning. It is seen that a micro jet is formed inside the bubble from the bottom of the bubble at about $t = 1.0ms$. This inner jet moves upward, and it eventually penetrates the bubble, forming a toroidal bubble. Two air pockets are generated on both sidewalls at late stages. By comparing the location of the base of the pockets at late stages with that of the initial surface height, it is clear that the air pockets move downward. The existence of another downward inner jet in the bubble is seen at $t = 2.0ms$. The bubble is split by the inner jets at late stages. Notice that the air pockets are not connected with the collapsing bubble in this pattern. Fig. 2(b) shows the sequential pictures at $H = 15mm$. The jet formation is very similar to pattern A. The shape of water jet is changed from a blunt shaped jet to a spike-shaped jet at late time. However, the interaction of air pockets near sidewalls with the bubble is different from pattern A. In Fig. 2(b), it is seen that the upward inner jet is not generated so much as that seen in pattern A. The downward inner jet is generated as the air pockets grow because the distance from explosion center to the surface is shorter than the pattern A, so the interaction between air pocket and bubble is intensified. At $t = 2.4ms$, air pocket meets the bubble and the bubble is destroyed by both downward inner jet and air pocket. Pattern C is different from other two patterns. The bubble is formed very near free surface and expands very rapidly. And this bubble meets free surface at early stage before the bubble starts to collapse. The water jet formation is very different from other two patterns. In Fig. 2(c), the water jet is blunt-shaped, and its middle portion spreads toward sidewall. The air pockets and the bubble are connected, so that the bubble is destroyed on the top. When water jet grows, tiny fragments are seen near the top of blunt-shaped water jet, and water jet becomes to spray completely at late stage.

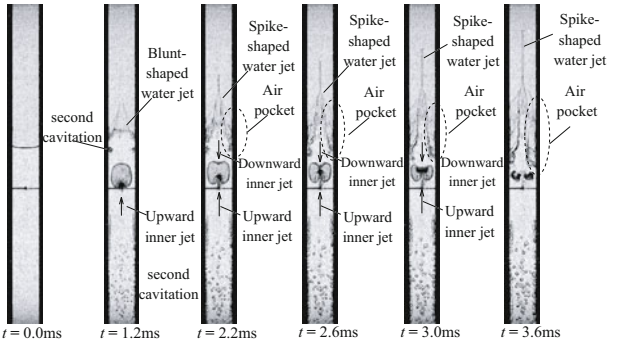

(a)

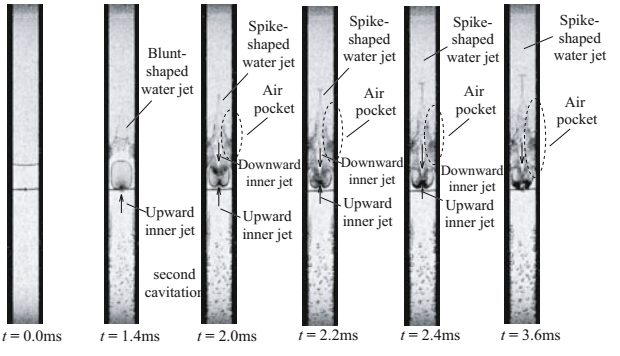

(b)

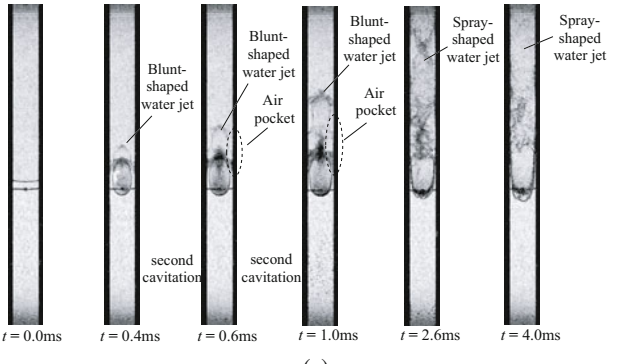

(c)

Fig. 2 Sequential photos of bubble evolution and jet formation in a rectangular tube with a width of 15mm induced by underwater electric discharge located at varied depth (H): (a) $H = 25mm$, (b) $H = 15mm$, (c) $H = 5mm$

3.2 *Location and Velocity of Flow Structures*

The typical flow structures in Figs. 2(a)(b) are sketched in Fig. 3(a). The trajectories of these structures are measured from the photos, and shown respectively in Fig. 3(b) and(c). Their velocities are evaluated from the displacement and the time interval between two frames.

As seen in Fig. 3(b)(c), it is found that after upward inner jet and downward inner jet hit each other, the air pocket starts to rebound. This rebound is clearly seen in Fig. 2(b).

Fig. 4(a)(b) show the velocities of upward and downward inner jet in patterns A and B. It is seen that the upward inner jet is always faster than that of the downward inner jet in pattern A, while the downward inner jet is initially slower, but faster that of the upward inner jet at late stages in pattern B.

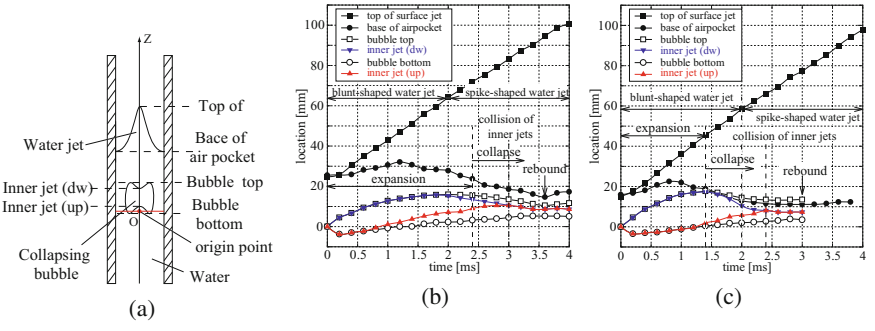

Fig. 3 Trajectory of typical flow characteristics of bubble and jet defined (a), with a width of 15mm for underwater electric discharge located ad varied depth (H): (a) $H = 25mm$, (b) $H = 15mm$

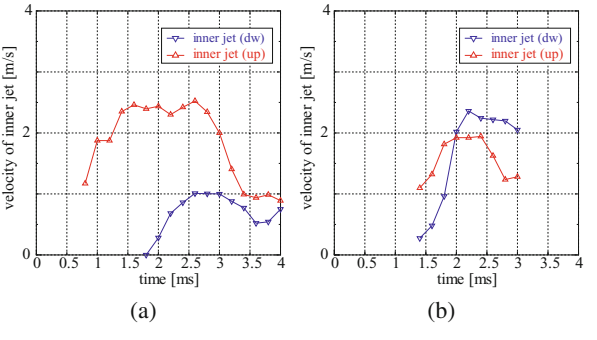

Fig. 4 Comparison of the velocities of the upward and the downward jets inside the bubble at two explosion depths in a tube ($W = 15mm$): (a) $H = 25mm$, (b) $H = 15mm$

The velocities of the top of surface jet for all widths ($W = 15mm, 10mm, 5mm$) at $V = 4.5kv$ are showed respectively at Figs. 5(a)-(c). The water jet is accelerated at the very initial stage, and then gradually converges a nearly constant velocity, except for the case of $H = 5mm$ for all W, where the velocity is still decreasing at late stage. It is seen that the velocity of top of water jet is increased by reducing the explosion depth.

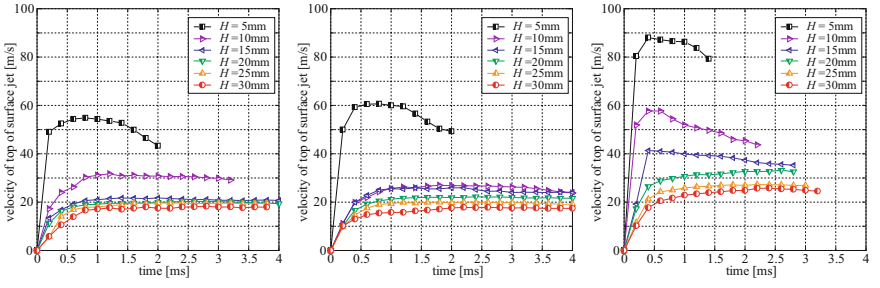

Fig. 5 Effects of tube width on the surface jet velocity at six explosion depths: (a) $W = 15mm$, (b) $W = 10mm$, (c) $W = 5mm$

4 Conclusions

Bubble and water jet induced with underwater explosion with a high voltage electric discharge in a rectangular tube have been investigated. The evolution of bubble varies with explosion depth, and there are three typical patterns for all conditions. The jet velocity generally reduces by the increasing the depths of the discharge, and widening the tube.

References

1. Tominaga, T., Nakagawa, A.: Application of underwater shock wave and laser-induced liquid jet to neurosurgery. Shock Waves 15, 55–67 (2006)
2. Yamamoto, H., Takayama, K., Ishikawa, K.: Model experiment on magma fragmentation in explosive volcanic eruption. Journal of Mineralogical and Petrological Sciences 103(3), 192–203 (2008)
3. Koita, T., Zhu, Y., Sun, M.: The Behavior of Bubble and Water Jet Induced by Underwater Explosion in a Rectangular Tube. In: 49th AIAA Aerospace Sciences Meeting, No:2011-187 (2011)

Numerical Analysis of Interaction between Moving Shock Wave and Solid Particle Layer

K. Doi and Y. Nakamura

1 Introduction

When a shock wave propagates over many small solid particles on a horizontal wall, some particles near the surface of the layer are lifted and dispersed into the shock-induced flow. These dispersed particles is called the dust cloud. This phenomenon is actually seen in galleries of coal mines or in pipelines for neumatic transportation of powder, and mixing dispersed flammable dust particles with high-temprature and high-pressure gas behind the shock wave sometimes causes the dust explosion. And this phenomenon includes some interesting factors, such as the shock structures interacted with the dust layer, interactions between gas and solid particle, and interactions between solid particles.

This phenomenon has been investigated by many researchers. Dawes[1] reproduced the dust cloud by the shock-tube experiment, and examined the characteristics. Gerrard[2] and Fletcher[3] conducted similar shock-tube experiments to examine the initial stage of the dust cloud formation, but the dyanmical mechanism was not able to be shown clearly. Bracht[4] searched for the transitional regime to turbulent flow in the dust cloud by the observation of more time. Suzuki et al.[5] examined the translational and rotational motions of dust particles in detail. On the other hand, Khul et al.[6] conducted the numerical simulation based on the mixture model, and showed appearance of a vortex generated from the interaction between the shock wave and dust layer by baloclinic effect. Jiang[7] and Thevand[8] also conducted the numerical simulation based on the two fluid model. However, they has not shown the dynamic structure of the dust cloud formation clearly.

In the present study, it aims to pay attention at the initial stage of the dust cloud formation process, and to clarify the dynamic mechanism by the numerical simulation. A discrete model is applied to the solid particles whereas a continuum model is applied to the gas in this simulation. As a result, the dynamic status of an individual

K. Doi · Y. Nakamura
Department of Aerospace Engineering, Nagoya University Furo-cho,
Chikusa-ku, Nagoya, 464-8603 Japan

particle that composes the dust cloud can be clearly shown, and the particle-particle interaction can be considered easily in addition.

2 Computational Model

Governing equations for gas phase are as follows.

$$\frac{\partial}{\partial t}(m_f) + \nabla \cdot (m_f \mathbf{u}_f) = 0 \tag{1}$$

$$\frac{\partial}{\partial t}(m_f \mathbf{u}_f) + \nabla \cdot (m_f \mathbf{u}_f \mathbf{u}_f) = -\alpha_f \nabla p + \alpha_f \nabla \cdot \mathbf{T} - \mathbf{F}_i \tag{2}$$

$$\begin{aligned} \frac{\partial}{\partial t}(m_f E_f) + \nabla \cdot (m_f H_f \mathbf{u}_f) \\ = \nabla \cdot (\alpha_f \mathbf{T} \cdot \mathbf{u}_f) - \nabla \cdot (\alpha_f \mathbf{q}) - Q_i \end{aligned} \tag{3}$$

$$p = \rho_f R T_f \tag{4}$$

$\rho_f, p, \mathbf{u}_f, T_f, E_f, H_f$ is gas density, pressure, velocity vector, temperature, total energy, and total entalpy, respectively. α_f is void fraction, and $m_f = \alpha_f \rho_f$. R is gas constant. $\mathbf{T}$ is gas viscous tensor, and $\mathbf{q}$ is gas heat conduction. $\mathbf{F}_i$ and Q_i are interactions of momentum and energy between gas and solid particles.

Governing equations for each solid particle are as follows.

$$\frac{d}{dt}(\mathbf{r}_p) = \mathbf{u}_p \tag{5}$$

$$\frac{d}{dt}(m_p \mathbf{u}_p) = \mathbf{f}_i + \mathbf{f}_c + m_p \mathbf{g} \tag{6}$$

$$\frac{d}{dt}(I_p \omega_p) = \mathbf{M}_i + \mathbf{M}_c \tag{7}$$

$$\frac{d}{dt}(C_p T_p) = q_i + q_c \tag{8}$$

$\mathbf{r}_p, \mathbf{u}_p, \omega_p, T_p$ is position, translational velocity, rotational velocity, and temperature of the particle, respectively. m_p, I_p, C_p is mass, moment of inertia, and heat capacity of the particle, respectively. $\mathbf{f}_i$,$\mathbf{M}_i$, and q_i are interactions of momentum, angular momentum, and energy between gas and each particle. $\mathbf{f}_c$, $\mathbf{M}_c$, and q_c are particle-particle and particle-wall interactions.

The gas-particles interactions, $\mathbf{f}_i$, $\mathbf{M}_i$, and q_i, are assumed to be composed of drag force, $\mathbf{f}_{iD}$, Saffman force, $\mathbf{f}_{iS}$, Magnus force, $\mathbf{f}_{iM}$, macroscopic pressure gradient,

$\mathbf{f}_{iP}$, drag torque $\mathbf{M}_{iD}$, and heat transfer q_{iT}. They are estimated by some results of experimental measurements and numerical simulations for a sphere.

The particle-particle and particle-wall interactions, $\mathbf{f}_c$ and $\mathbf{M}_c$, are estimated by the discrete element model (DEM), where elastic collisions are modeled by springs, dampers, and sliders.

3 Computational Method and Conditions

The governing equations for gas phase are discretised in space by the finite volume method. The solution vectors at the cell-boundary are evaluated by the 3rd order MUSCL method with Van Albada's limiting function, and then the invicid flux is estimated by the approximated Riemann solver. And, spatial gradients of solution vector is estimated by the least square method. On the time integrations, LU-SGS method is used for the gas-phase and the two-stages Runge-Kutta method for solid particles, and they are coupled weakly.

The gas phase is air, and the viscous coefficient is estimated by the Sutherland's equation. The shock wave Mach number is $M_S = 1.44$. The shock-induced flow velocity is $U_O = 211[m/s]$ and the particle Reynolds number is $Re_D = 2100$ in this condition. Each solid particle is a sphere, the diameter is $D = 0.1[mm]$Cthe density is $\rho_p = 980[kg/m^3]$, and the heat capacity is $c_p = 1200[J/kgK]$. As parameters of the DEM, the spring coefficient is $k = 2.05 \times 10^4[N/m]$, the damper coefficient is $c = 7.33 \times 10^{-4}[Ns/m]$Cand the Coulomb's friction coefficient is $\mu = 0.3$, the restitutive coefficient at the collision is $e = 0.7$ and the contacting period is $T_c = 0.5[\mu s]$ in these conditions.

The computational domain is three-dimensional, $0 \leq x \leq 400[mm]$, $0 \leq y \leq 0.3[mm]$, $0 \leq z \leq 100[mm]$. And a trough with depth of $2[mm]$ on the wall of $100 \leq x \leq 400[mm]$ is set to accumurate the solid particles. The conditions of the solid particle layer are shown in Table 1.

Table 1 Conditions of particle size and initial distributions of solid particle layer.

	DL1	DL2	DL3
Basic diameter D [mm]	0.10	0.10	0.10
Contact diameter D_c [mm]	0.10	0.14	0.10
Number of particles N_p	202,000	104,000	101,000
Mean volume fraction $\overline{\alpha_p}$	0.59	0.30	0.29
Particle contact condition	Contact	Contact	Dispersed

4 Results and Discussions

Distribution of solid volume fraction and gas pressure at $t = 0.8[ms]$ in the case of DL1 are shown in Figure 1(a), Figure 1(b), respectively. The shock wave propagated from left to right, the shock is at the position of 290[mm] from a leading edge of the dust layer. The dust cloud is formed behind the shock, where the pressure is disturbed.

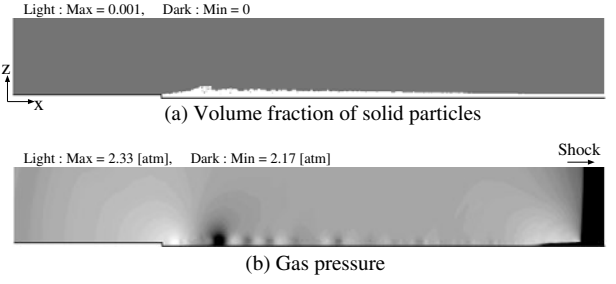

(a) Volume fraction of solid particles

(b) Gas pressure

Fig. 1 Shock wave propagating on the solid particle layer in the case of DL1.

The distributions of solid particles composing the dust cloud at $t = 0.8[ms]$ is shown in Figure 2. The horizontal axis is the distance from the shock, X, and the vertical axis is the height from the surface of the dust layer, h. Comparing the height of computational result with the experimental result, they are almost corresponding. And, it can validate the computational results in this study.

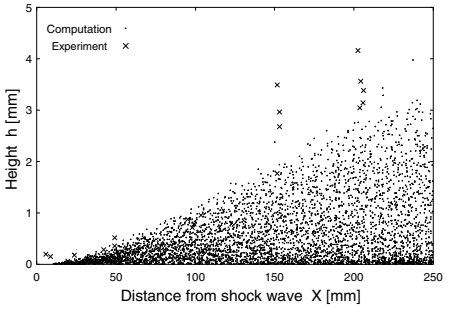

Fig. 2 Distribution of solid particles composing the dust cloud in the case of DL1, The "computation" means the height of each particle in the computational result of this study, the "experiments" means the maximum height of particles in the experimental results conducted by Suzuki et al.[5].

Outer shapes of the dust clouds in each cases of initial solid particle layer, DL1, DL2, and DL3 are shown in Figure 3. And, one in the case of DL1 without Saffman and Magnus forces are also shown in the same figure. It is shown in this figure that the initial condition of the solid particle layer, contacted (DL1,DL2) or dispersed(DL3), is more dependent on the height of the dust cloud than the fluid lift forces. This result means that dust cloud formation is mainly caused by particle-particle direct interactons, that is contacts and collision between solid particles at the initial stage of the dust cloud formation.

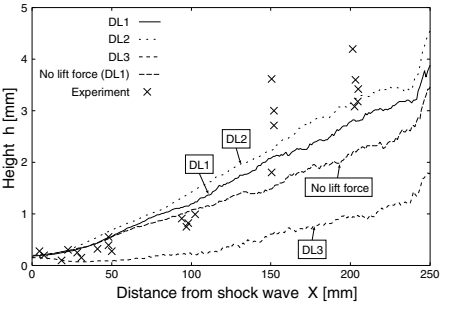

Fig. 3 Outer shapes of dust clouds; effects of initial condition of the solid particle layer and fluid lift force

Pressure distribution where the shock wave interacts with the solid particle layer in the case of DL1 and DL2 are shown in Figure 4. It is shown that the shock wave on the surface of the solid particle layer is curved by the interaction, and it raises the pressure on the surface behind the shock. And, the interaction in the case of DL2, higher void fraction, is stronger than that in the case of DL1, lower void fraction.

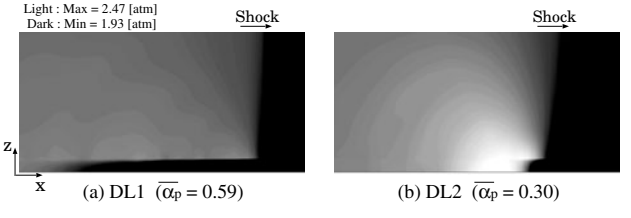

Fig. 4 Gas pressure distributions in shock structures interacting with dust layer; effect of the void fraction of the solid particle layer

Distributions of gas pressure and particle-contacting pressure on the bottom wall of the solid particle layer are shown in Figure 5. The gas pressure in this figure is a difference from that in front of the shock wave, and the particle-contacting pressure is averaged over 1[mm]. Furthermore, both of pressure values are nondimensionalized by the difference between the pressure behind the shock and that in front of the

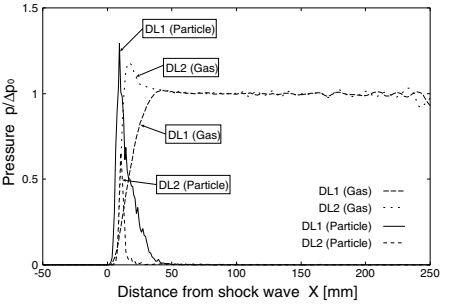

Fig. 5 Gas and solid particles pressure distributions on wall in overpressure behind shock

shock. The curvature of the shock generates the downward flow behind the shock, and then the downward flow pressed the solid particles to the bottom wall and raises the gas pressure in the solid particle layer behind the shock.

5 Conclusion

In the present study, the initial process of forming the dust cloud was numerically simulated to examine its dynamic mechanism. The simulated dust cloud was close to experimental results. It was found by comparing several types of dust layers that the upward velocity of lifted particles was more produced by particle-particle interactions than by fluid lift forces such as the Saffman force and the Magnus force. Moreover, it was confirmed that a relatively strong downward flow was induced just behind the foot of the shock by its curved shape, which promotes the interactions and causes an overpressure on the wall.

References

1. Dawes, J.G.: Safety in Mines Research Establishment, vol. 36, pp. 1–69. Ministry of Fuel and Power, England (1952)
2. Gerrard, J.H.: Brit. J. Appl. Phys. 14, 186–192 (1963)
3. Fletcher, B.: J. Phys. D: Appl. Phys. 9, 197–202 (1976)
4. Bracht, K., Merzkirch, W.: Int. J. Multiphase Flow 5, 301–312 (1979)
5. Suzuki, T., Adachi, T.: JSME Journal B 52, 483, 3742–3746 (1986)
6. Khul, A.L., Ferguson, R.E., Chien, K.Y., Collins, P.: Progress in Astronautics and Aeronautics, vol. 154, pp. 491–515. AIAA, Wash., D.C. (1993)
7. Jiang, J.P.: Ph. D. Dissertation of Ben-Gurion University of the Negev (1996)
8. Thevand, N., Daniel, E.: Shock Wave 11, 279–288 (2002)

Study of the Interaction between a Shock Wave and a Cloud of Droplets

A. Chauvin, G. Jourdan, E. Daniel, L. Houas, and R. Tosello

1 Introduction

The pressure histories obtained when a shock wave propagates into an air-solid particle medium is well known: the overpressure jump decreases, as the shock wave propagates into the mixture and is followed by a pressure build-up corresponding to the velocity relaxation processes. In the present paper, an air-water droplet mixture interacting with a shock wave has been studied and the comportment of the pressure traces was found significantly changed in comparison to the interaction with a air-solid particle mixture. This is attributed to the ability of the droplets to deform and fragment into finer ones. This phenomenon, known as secondary atomisation, widely reviewed by Gelfand[1] and by Guildenbecher[2], affects both the pressure histories and the impulse induced by the shock wave. We have previously studied the influence of the height of cloud of droplets on shock wave propagation [3]. In the present work, we focus our attention on the influence of the droplet diameter on the attenuation of shock wave propagating into the air-water mixture. Moreover, predictions obtained by 1D numerical simulations are compared to the experimental results. The necessity to introduce a secondary atomisation model to fit the experimental behaviour is then underlined.

2 Experimental Set-Up

Experiments were carried out in the T80 shock tube of the IUSTI laboratory, oriented in vertical position. It consists in a 750 mm driver section followed by a 3045 mm driven section which includes a 880 mm plexiglass windows allowing the flow visualisation. A generator of mono-dispersed cloud of droplets was fitted

A. Chauvin · G. Jourdan · E. Daniel · L. Houas
IUSTI-CNRS, Aix-Marseille Université, 5 rue Enrico Fermi, Marseille, 13013, France

R. Tosello
DGA/TN, Avenue de la Tour Royale, Toulon, 83050, France

at the top of the experimental chamber [4], and released downward the air-water mixture characterized by a dispersion of $\sigma = 25\%$ on the mean diameter. The interaction between the cloud of droplets falling downward, and the shock wave propagating upward, was visualized by a high speed direct shadowgraphy system. It includes a Photron FastCam SA1 recording the pictures at an acquisition frequency of 15,000 frames per second with a spatial resolution of 128×864 pixels. For each run, pressure histories were recorded by two and eight PCB pressure transducers (SM113A26 type), located in the driver and the driven sections, respectively. Thus, a map of the pressure evolutions alongside the shock tube and the displacement of the droplet cloud was obtained both qualitatively and quantitatively. The experimental apparatus scheme is presented in Fig. 1 with gauge localisations.

3 Experimental Results

Two drilled grid are used in the cloud generator in order to study the influence of the droplet diameter on two shock wave Mach numbers of $M_{is} = 1.3$ and $M_{is} = 1.5$. The cloud of droplets is characterized by the mean diameter of its droplets, ϕ_d, its height, H_d and its volume fraction, α_d, defined by $\alpha_d = \frac{V_d}{a^2 H_d}$, where V_d is the volume of discharged water . Note that the clouds, composed by droplets of 250 μm and 500 μm in diameter, have a volume fraction of 0.3% and 1%, respectively.

The mean height of the clouds is maintained approximatively constant for the two cases (781 mm $\pm 15\%$), due to the reaction time of the droplet generator. Fig. 1 presents the behaviour of a cloud of 768 mm in height, composed by droplets of 250 μm in diameter, interacting with a $M_{is} = 1.5$ shock wave Mach number. The six lines drawn correspond to the six pressure measurement stations located in the test section. Time in milliseconds indicated at the bottom of the pictures, corresponds to the time elapsed since the shock wave passed at station S_8. From the first picture, showing the two-phase medium before the shock wave impacts it (t_1), the height of the air-water mixture, H_d, and the abscissa of the interaction, X_{int}, are determined. Then, the shock wave propagating in ambient air impacts the water droplet cloud, of higher density. Consequently, a part of the shock wave is transmitted into the air-water mixture whereas an other part is reflected and propagates upstream. The arrow in Fig. 1 indicates the position of the incident (t_1) and transmitted shock wave (t_2 and t_3). As the shock wave penetrates into the two-phase mixture, the droplets are atomised into smaller ones. This phenomenon, known as secondary atomisation, is well observable at t_2. The fragmentation regimes which occurs during this study corresponds to the regime II described by Gelfand [1]. Pilch and Erdman [5] estimated the fragmentation time τ_{frag} required to atomise a droplet into smaller droplets of stable diameter ϕ_f. In Fig. 1, a delay between the observation of the shock wave and the secondary atomisation front is detected. It corresponds to the distance required for a droplet to deform and atomise. From t_2 to t_6, the momentum transfer from the shock wave to the cloud is observable by its displacement. It is one of the attenuation process with the heat transfer and atomisation phenomenon. Fig. 2 presents the pressure histories obtained at four stations (S_8, S_6, S_5 and S_2)

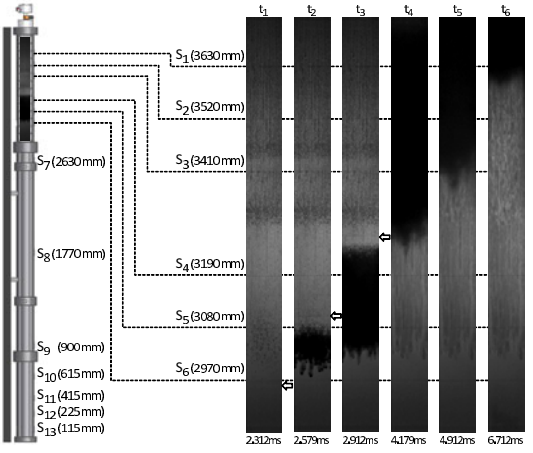

Fig. 1 Sequence of shadowgraph pictures showing the interaction of a planar shock wave of Mach number M_{is}=1.5 moving upwards with a cloud of droplets of 250 μm in diameter and 768 mm in height falling downwards (T80#711), where labels denote exposure timings in milliseconds relative to the shock passage at station S_8

during the interaction of a $M_{is} = 1.3$ shock wave and two water clouds composed by droplets of 250 μm and 500 μm in diameter. They are compared with pressure traces obtained in absence of two-phase mixture. At station S_8, typical pressure histories induced by a shock wave is observed until the arrival of the reflected one by the air-water mixture. We can note that this reflection is smaller than the one coming from a rigid wall and is weaker for the cloud containing the finer droplets (250 μm). The interaction abscissa, X_{int}, of the two clouds composed by 250 μm and 500 μm are respectively of 2873 mm and 2934 mm. Thus, just after the interaction location, station S_6, the pressure increases after the passage of the transmitted shock wave for the two clouds. Finally, the pressure reaches an equilibrium value corresponding to the one induced by the reflected shock wave. As the transmitted shock wave propagates into the water cloud, from stations S_5 to S_2, the frozen pressure jump decays, as observed during the interaction of shock wave with a solid-particle mixture [6]. Nevertheless, in the presence of liquid droplets, this overpressure peak is followed by a rarefaction zone which can be attributed to the capability of droplets to deform and fragment. Therefore, the exchange surface area increases and leads to the augmentation of the transfer between the two media, which will extract energy from the shock wave. As the exchange surface area increases, the flow slows down which causes this rarefaction zone. Afterwards, a pressure build-up occurs, due to the velocity relaxation process. Thus, the droplets are transported to reach the flow velocity which leads to an equilibrium pressure value. Finally, the cloud composed by higher diameter droplets induces a softer pressure evolution than the other cloud, constituted by the 250 μm droplets. It may be linked to the volume fraction three time smaller for the cloud containing the droplets of 250 μm in diameter. The overpressure peak measured just behind the shock wave in presence of a droplet cloud

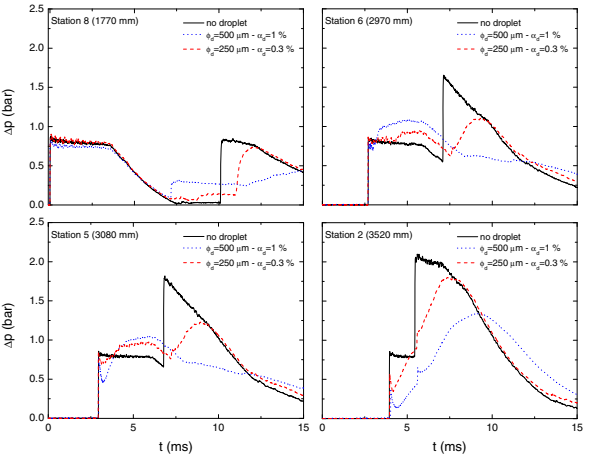

Fig. 2 Comparison of pressure histories obtained with a shock wave of $M_{is} = 1.3$ Mach number, at the stations S_8, S_6, S_5 and S_2, during runs without droplet and with clouds of droplets of 250 μm and 500 μm in diameter with a volume fraction of 0.3% and 1%, respectively

ΔP^{shock} was non-dimensionnalized by the overpressure peak obtained just behind the shock wave without cloud of droplets ΔP_0^{shock} to compare the attenuation capability of the different clouds. The ratio $\frac{\Delta P^{shock}}{\Delta P_0^{shock}}$ versus the position of the shock wave since it encountered the air-water mixture, $X - X_{int}$, non dimentionnalized by the height of the cloud, H_d, is represented in Fig. 3 at each station of measurement X. Note that $\frac{X - X_{int}}{H_d} = 1$ corresponds to the end of the droplet cloud. As we can see from this representation, the overpressure mitigation $(1 - \frac{\Delta P^{shock}}{\Delta P_0^{shock}})$ increases with the shock wave Mach number and the droplet mean diameter.

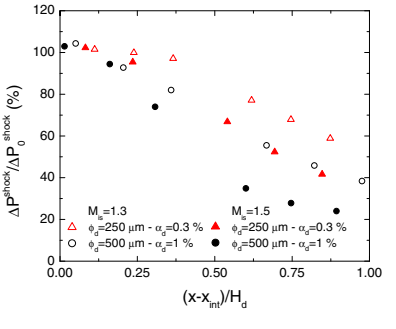

Fig. 3 Attenuation of the overpressure peak behind the transmitted shock front in presence of clouds of droplets for the different cases studied, versus its distance of propagation in the two-phase mixture non-dimensionalized by the height of the cloud. X is the sensor location

Nevertheless, note that the volume fraction is divided by three for the smaller diameter. Therefore, the cloud composed by the 250 μm droplets seems to be more effective to mitigate the shock wave as regards to the volume fractions. Finally, in our experimental conditions, the mitigation of the overpressure peak induced by a shock wave passing through a water cloud can reach up to 80%.

4 Numerical Results

One dimensional unsteady calculations were performed in order to improve the knowledge on the air-water mixture shock wave interaction. Thus, the droplets cloud was approached by a classical two-phase-dilute flows[7], using a Eulerian/Eulerian mathematical model. The drag force, the heat transfer between the air-water mixture and the flow have been taken into account. The droplets are assumed as spherical at uniform temperature. The gas is governed by the Euler equations and the droplet phase by its specific set of partial differential equations [4]. The dispersed phase and the gas phase are coupled by interaction terms. Moreover, a secondary atomisation model of the droplets is introduced. Fig. 4 represents the experimental pressure history obtained at station S_1 for clouds of 500 μm or 250 μm impacted by a M_{is}=1.5 shock wave compared with numerical results. As we can see, if the droplet fragmentation is not taken into account, the computational pressure trace does not fit to the experimental one. This result emphasis the predominant role of the secondary atomisation on the pressure history behaviour. Consequently, we added a source term of droplet production to the equation on the number of droplets per unit volume, which becomes:

$$\frac{\partial n_d}{\partial t} + \frac{\partial (n_d u_d)}{\partial x} = \dot{n_d} \quad with \quad \dot{n_d} = \left(\left(\frac{\phi_d}{\phi_f} \right)^3 - 1 \right) \frac{n_d}{\tau_{frag}} \tag{1}$$

where n_d and u_d are respectively the number and the velocity of the dispersed phase and τ_{frag} is the time, defined in [5], required to reach the final fragmentation of the droplets.

Nevertheless, Fig. 1 shows that the secondary atomisation front is delayed compared to the shock front. Thus, to consider this time, τ, when the flow and the air-water mixture are in unstable conditions, another partial equation is written to delay the initiation of the fragmentation :

$$\frac{\partial \tau}{\partial t} + u_d \frac{\partial \tau}{\partial x} = \dot{\tau} \tag{2}$$

where τ measures the time in order to obtain the total time of breakup, taken from Pilch and Erdman [5], including a delay due to unstable conditions.

Finally the computational results obtained when the secondary atomisation stages of the droplets are considered, give a behaviour closer to the experimental results, as shown in Fig. 4.

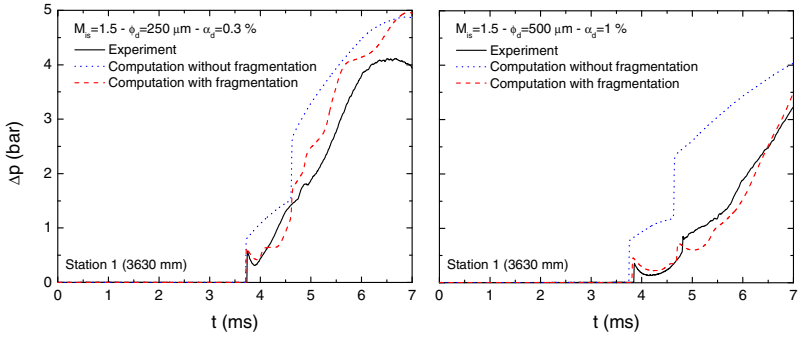

Fig. 4 Experimental pressure histories recorded at the station S_1, for two droplets mean diameter (250 μm and 500 μm) impacted by a $M_{is} = 1.5$ shock wave and compared to the computational pressure trace obtained with and without secondary atomisation model.

5 Conclusion

The present experimental investigation on the influence of the mean diameter of the droplets on the attenuation of shock waves highlighted the major role of the exchange surface. Indeed, the momentum transfer and heat exchange which absorb energy from the shock wave depends on the exchange surface area. The attenuation of the shock wave increases with the Mach number and the droplet diameter studied. Nevertheless, due to our experimental device, the volume fraction was three time higher for the cloud composed by the droplets of $\phi_d = 500\ \mu m$ in diameter. Future study focusing the influence of the volume fraction, maintaining a constant mean diameter are envisaged. It will allow to have a better understanding on the weight of the volume fraction on the shock wave attenuation. Moreover, numerical simulations were carried out and a good agreement with our experimental results is found, particularly, if the fragmentation of droplets is taken into account in the model.

References

1. Gelfand, B.E.: Prog. Energy Comb. 22, 3 (1996)
2. Guildenbecher, D.R., López-Rivera, Sojka, P.E.: Exp. Fluids 46, 3 (2009)
3. Chauvin, A., Zerbib, J., Jourdan, G., Daniel, E., Mariani, C., Houas, L., Biamino, L., Tosello, R., Praguine, D.: Proccedings of the 21th MABS Symposium, Jerusalem (October 2010)
4. Jourdan, G., Biamino, L., Mariani, C., Blanchot, C., Daniel, E., Massoni, J., Houas, L., Tosello, R., Praguine, D.: Shock Waves 20, 4 (2010)
5. Pilch, M., Erdman, C.A.: Int. J. Mult. Flow 13, 6 (1987)
6. Sommerfeld, M.: Experiments in Fluids 3, 4 (1985)
7. Daniel, E., Saurel, R., Larini, M., Loraud, J.-C.: Int. J. Heat and Fluid Flow 4, 3 (1994)

Motion of Non-spherical Particles Following Shock Passage

D. Murray, A. Connolly, and R. Hillier

1 Introduction

A hypersonic vehicle travelling through weather may encounter a wide range of particle environments. The impact of these particles on the vehicle surface may pose a significant erosion hazard to the vehicle's thermal protection system. However, interaction with the flowfield will alter the particle motion, mitigating the erosive impact.

In high altitude weather, a large proportion of ice particles take the form of plate or rod-like hexagonal prisms. Therefore, CFD prediction of ice particle motion requires an accurate description of the effective drag (taking account of the effect of particle rotation) of such geometries. A previous study [1, 2] suggested a correlation based on an averaging process using data from engineering or CFD drag predictions. This study assumed that all random orientations of the particles in a cloud are equally probable. However, this assumption is expected to breakdown following interaction with a shock, imposing a preferred direction on the cloud and increasing the effective particle drag coefficient. To test this assumption a series of shock tube experiments were undertaken to measure the motion and changes in orientation of representative particle geometries.

This study is a continuation of shock tube experiments described in [1] which measured the motion of spherical ballotini (glass) particles. This new study benefits from the availability of a high-speed digital camera; addressing issues of frame alignment previously encountered and eliminating a major source of error.

D. Murray · A. Connolly
Dstl, Portsdown West, Fareham, PO17 6AD

R. Hillier
Imperial College London, South Kensington Campus, London SW7 2AZ

1.1 Ice Habits

According to the classification of Magano and Lee [3] ice particle habits (classes) are grouped by their shape and formation process. Within this classification, there exists a large proportion of habits that may be described as plate or rod-like hexagonal prisms, or as combinations of such shapes. Such habits are typical of high altitude weather clouds (up to approximately $13\,km$) where the major mechanism governing the accumulation of ice is deposition. Ice particles that develop purely via deposition will have a regular crystalline shape and typically range from 10 to $1000\,\mu m$ along their greatest dimension. At lower altitudes the governing mechanism is riming; where a droplet collides with, and leaves water to freeze on, an ice particles surface. In addition, particles may undergo aggregation following collision. Both of these processes may lead to the formation of voids, lowering the bulk density. Where the original shape of an ice particle is still evident, the ice particle is simply described as a lightly or densely rimed snow crystal.

1.2 Drag Correlation

The basis of the correlation described in [1, 2] lies in using engineering methods (such as surface inclination approaches) or CFD prediction to determine the variation of particle drag as a function of incidence. Such drag data is then integrated to arrive at a mean–or effective–drag, averaging over all possible particle orientations and thus accounting for the orientation of each particle in a cloud.

Effective drag values are then normalised by those of a sphere with a diameter equal to the greatest particle dimension, thus the correlation takes the form

$$C_D(S) = f(S)\,C_D(\text{sphere}) \tag{1}$$

where the shape parameter, S, is given by $S = L/D$ and drag coefficient $C_D(\text{sphere})$ is based on the longest dimension: for an oblate or plate-like particle $C_D(\text{sphere})$ is based on diameter D, for a prolate or rod-like particle $C_D(\text{sphere})$ is based on length L. Using this approach, drag correlations have been derived for families of hexagonal prisms and oblate/prolate spheroids with varying S.

2 Experiment

A series of shock tube experiments was undertaken to record the motion of ice particle simulants representative of the shapes found in weather.

The shock tubes internal dimensions are described by a total length of $9225\,mm$, a width of $100\,mm$ and a height of $200\,mm$. The interior of the shock tube was rectilinear, and continuous along its whole length, save for an access port in the roof of the working section. The shock tube was open ended so the driven gas conditions matched the lab ambient.

Nitrogen was used as the driver gas. The ratio of driver pressure to driven pressure was approximately 16.7 resulting in a measured shock velocity of $396 \pm 3\,ms^{-1}$, implying a pressure ratio across the shock of 3.48.

Particles were captured in silhouette (Figure 1); the light source consisted of an array of PAR (Parabolic Aluminised Reflector) lanterns placed directly behind the test section. The resulting uneven background illumination was corrected by constructing a median image, devoid of particles, from each image sequence. This median image was then subtracted from each frame in the sequence.

Images were captured using a digital *Phantom* v7.3 high speed camera. The camera was operated at a resolution of 640×240 pixels and a frame rate of $19047.6\,s^{-1}$ with an exposure time of $1.0\,\mu s$.

Image sequences were initially processed using software provided with the camera before conversion to an *AVI* format for further processing using a bespoke code. The particle translation and orientation was extracted using an approach in which particle objects were identified using a procedure which allocates pixels to labelled sets of contiguously connected regions [4]. Ellipses are then fitted to the perimeter pixels of such regions.

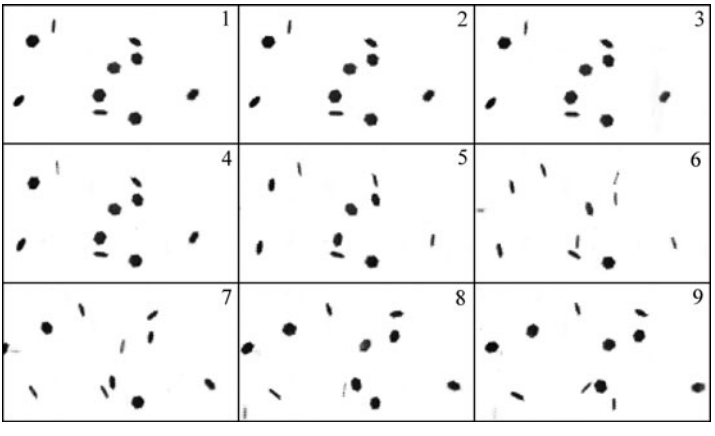

Fig. 1 Frame 1 shows cloud configuration prior to shock passage. Frames 2 and 3 show the configuration during shock passage (from left to right). Subsequent frames show the alignment of the particles with the shock plane (seen edge–on in the images) immediately following shock passage. This is most clearly seen in frame 6.

Particle incidence (in degrees) was calculated by

$$\text{incidence} = \frac{180}{\pi} cos^{-1}\left(sin(\theta)\sqrt{1 - \frac{x_{minor}}{x_{major}}}\right) \tag{2}$$

where θ is the angle between an ellipse's major axis and the horizontal and x refers to the length of the minor and major axes, as depicted in Figure 2.

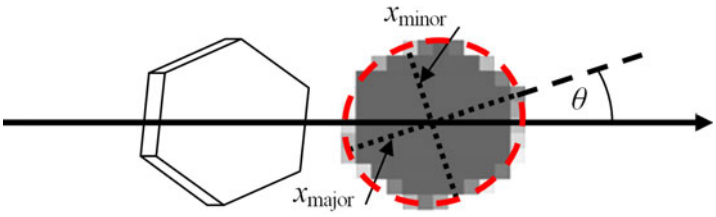

Fig. 2 Extraction of parameters used to describe particle object orientation and to calculate angle of incidence with respect to the shock plane.

2.1 Test Materials

Two products were selected to represent ice particles. Hexagonal plate-like ice particles were simulated by a polyethylene ($\rho \approx 930 \pm 5\, kgm^{-3}$ [5]) glitter, $1.01\, mm$ across and $0.2\, mm$ thick. Rod-like ice particles were simulated by two grades of modeller's flock, 0.7 and $2.0\, mm$ long and $0.1\, mm$ thick rayon fibres ($\rho \approx 1510 \pm 30\, kgm^{-3}$). These materials offered approximately the same density and shape as natural ice particles in weather whilst also meeting the requirements to be of uniform dimension and to be inert and safe to use in the shock tube facility.

2.2 Results

The processed high-speed footage clearly showed the acceleration and rotation of particles following shock passage. Plate-like particles were observed to initially align parallel to the passing shock. This change in orientation was observed to occur at approximately the same rate, occurring over approximately $300\, \mu s$ (depicted in Figure 3). Rod-like particles did not exhibit this behaviour.

Rates of rotation were measured for different particle shapes and were found to range from zero to 2200 revs. per second for plate-like particles (where the variation was due to the pre-shock particle orientation; particles initially in approximate alignment were observed to merely vacillate about zero incidence) and up to 4700 revs. per second for rod-like forms. Figure 4 depicts measurements of particle translation for the plate-like particles. It is evident that those particles that were in alignment with the shock plane prior to passage have the greatest effective drag coefficient. In addition to the measurements, predictions of particle translation were made using the orientation averaged drag correlations included in the *Spiderman* CFD code [1]. Predictions were made using a second-order predictor-corrector integrator with the post shock flow conditions; the change in the conditions about the particle was assumed to be instantaneous. Particle drag was predicted using the correlation of Henderson [6], corrected to account for the particle shape using Equation 1. The result of the prediction for plate-like particles is included in Figure 4; it can be seen that the effective drag is approximately equal to prediction for those particles that were initially normal to the shock plane.

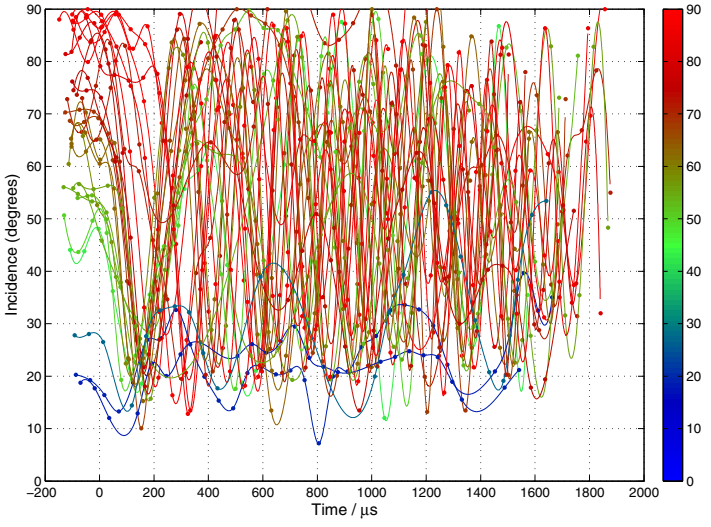

Fig. 3 Changes in particle incidence (with respect to the shock plane) as a function of time from initial shock interaction. Discrete measurements of incidence measured from each frame of high speed footage are fitted with spline curves to clarify the initial shock alignment phase. Data lines are coloured according to the pre-shock particle orientations.

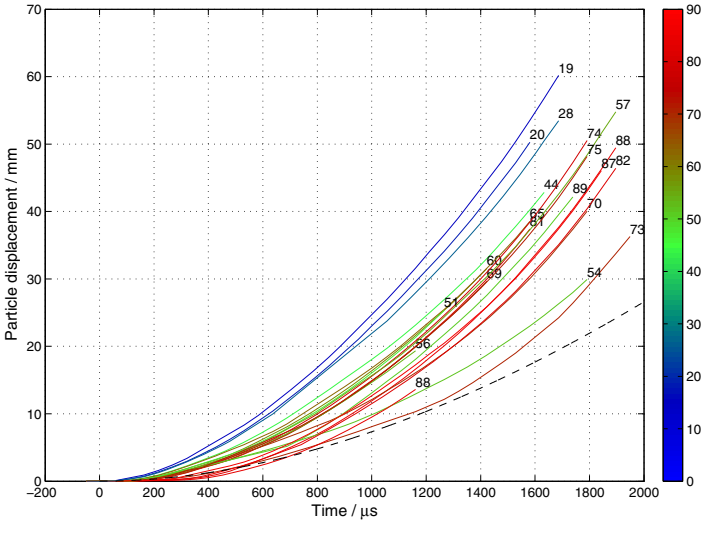

Fig. 4 Horizontal motion of hexagonal plate particles following shock passage. Solid data lines are each coloured (and labelled to the nearest degree) according to the pre-shock particle orientation. Predicted motion is denoted by the dashed black line.

3 Conclusions

A series of shock tube experiments have been conducted to capture the motion of non-spherical particles representative of the shapes found in high altitude weather.

For plate-like particles, it is evident that the effective drag coefficient is a function of initial orientation. This is inconsistent with the assumption of an orientation-averaged drag coefficient. Hence it has been shown that the initial interaction with a shock does have a significant effect on any subsequent translation and should be accounted for in flow predictions.

3.1 Recommendations

In order to model the motion of an arbitrary shaped particle in a flowfield, without resorting to empirical approaches, one can directly solve the Navier-Stokes equations for the flowfield, with the discretized boundary lying on the surface of the particle. The force acting on the particle due to the flow is simply the integral of the pressure over the particle boundary. Approaches to this type of Fully Resolved Simulation (FRS) include the Immersed Boundary Method, the Lattice Boltzmann Method and the Lagrange multiplier/fictitious domain method. However, these methods are algorithmically complicated to solve in three dimensions due to their grid-based nature. In addition, most of the literature on these methods is focussed on incompressible flows.

References

1. Murray, D.P.: A Study of Ice Particle Motion Through a Shock Wave. PhD Thesis, Imperial College London (2010)
2. Love, A.: Determination of the drag coefficient of ice particles behind a hypersonic shock by use of Computational Fluid Dynamics. Dstl Farnborough (2007)
3. Magano, C., Lee, C.V.: Meteorological Classification of Natural Snow Crystals. J. Fac. Sci., Hokkaido Univ. (7), 321–362 (1966)
4. Haralick, R.M., Shapiro, L.G.: Computer and Robot Vision, vol. 1. Addison-Wesley (1992)
5. Bolz, R.E., Tuve, G.L.: Handbook of Tables for Applied Engineering Science, p. 108. CRC Press (1970)
6. Henderson, C.B.: Drag coefficients of spheres in continuum and rarefied flows. AIAA Journal 76 14(6), 707–708 (1976)

Shocked Fluid/Fluid and Fluid/Solid Interactions Using a Conservative Level-Set Method

B. Obadia, P.T. Barton, and D. Drikakis

1 Introduction

Multimaterial problems have always been a challenging topic for research, due to both their complexity, and the range of applications concerned. Several ways of modelling have been developed for such problems during the last decades. From shock impacts between compressible fluids to fluid-structure interaction, with elasto-plastic deformations, several problems may arise. The relevant methods have to take into account the different behaviours that the materials can exhibit, whilst conserving a sharp and accurate interface. In this paper, a new 3D conservative method for interface tracking based on level-set functions is adressed. Each material is treated independently except at the interface where appropriate boundary conditions need to be specified.Solving the Riemann problem at the interface depends on the different set of equations for each component. A new Riemann solver dedicated on solid/fluid interactions has also been derived. Fluid behaviours are governed by the Euler equations, while a recently developed non-linear elasto-plastic model will be used for solids. The sharp interface method is based upon a strict finite volume evaluation of the governing constitutive laws on fixed Cartesian meshes.

2 Interface Tracking Method

The interface tracking method relies on the use of level-set functions to determine the location of material boundaries in space and time; a pre-described isocontour

B. Obadia · D. Drikakis
Cranfield University, School of Engineering, Cranfield, MK43 0AL, UK

P.T. Barton
California Institute of Technology 1200 East California Boulevard,
Pasadena, California, USA

D. Drikakis
Computation-based Science and Technology Research Centre (CaSToRC),
The Cyprus Institute, PO Box 27456, 1645 Nicosia, Cyprus

(usually zero) is chosen to mark the material boundary location. Taking the level-set functions to be signed distances to the interface respective surface enables clear distinction of the material domains. The interface is allowed to evolve through solution of an advection equation for each field with a velocity $\mathbf{V}$ prescribed by the interfacial Riemann solver:

$$\phi_t + \mathbf{V}.\nabla\phi = 0 \tag{1}$$

To ensure the level-set fields satisfy the Eikonal condition $|\nabla\phi| = 1$ the following reinitialisation equation is solved periodically to steady state:

$$\phi_\tau + sgn(\phi).(|\nabla\phi| - 1) = 0 \tag{2}$$

where τ is an artificial time, and sgn(ϕ) denotes the signum function. To avoid spurious movement of the zero contour, as can occur through solution of Eq. (2) with conventional upwind methods, the modified form of Hartmann *et al* [5] is used, which consists in adding a forcing term conserving the zero contour at every iteration.

The level-set functions are used to provide the information required to construct cut cell geometries in order to apply a finite volume discretisation of the governing equations for each material. This includes the cell-wall apertures (it is therefore crucial that the level-set function represents the actual signed distance to the interface), interface plane and volume fraction. For cell-walls single material Riemann solvers are employed to compute the numerical flux functions. For the interface plane in the case of cut (mixed) cells a multi-material Riemann solver is solved between the two potentially dissimilar materials. The volume of each material in a 3D rectangular cell can be assumed to be an arbitrary polyhedron, and the value computed through application of the divergence theorem once the apertures have been determine (see [3]).

It is likely in the course of computation that the volume fraction of a cut cell becomes small such that the time-step is driven to values orders of magnitude smaller than what would otherwise be required to satisfy the CFL condition for regular cells. To overcome this problem, a call merging method is used where cells with a volume fraction less than a predetermined criteria are merged with a neighbouring target cell with volume fraction greater than the criteria. In one-dimension the concept is trivial (Figure 1):

The extension in 3D is done similarly by consideration of the local normal in the small cells to find a neighbouring target cell that ensures the resultant combined cell satisfies the CFL condition computed using regular cell length scales. Following [7] each cell is then updated irrespective of size and the state in target cells adjusted according to the following correction to ensure the final state is equal to that which would have been obtained had the unified cell been discretised explicitly:

$$(\alpha\mathbf{U})^{n+1}_{trg} = ((\alpha\mathbf{U})^{n+1}_{trg})^* + \frac{\alpha^{n+1}_{trg}.\sum^{Nsc}((\alpha\mathbf{U})^{n+1}_{sc})^* - ((\alpha\mathbf{U})^{n+1}_{trg})^*.\sum^{Nsc}\alpha_{sc}}{(\alpha_{trg} + \sum^{Nsc}\alpha_{sc})^{n+1}} \tag{3}$$

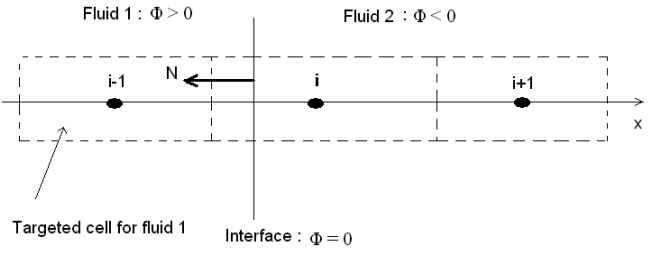

Fig. 1 Mixing procedure in 1D

where *Nsc* is the number of small cells neighboring the target cell, and the asterisk denotes the state of the variables computed individually a time n+1 before the mixing procedure. These newly computed values are then extrapolated into the associated small cells.

3 Constitutive Models

The fluids are modeled using the perfect compressible model (Euler equation), written under conservative form:

$$\frac{\partial}{\partial t}\begin{pmatrix}\rho\\ \rho\mathbf{u}\\ E\end{pmatrix}+\frac{\partial}{\partial x_\eta}\begin{pmatrix}\rho u_\eta\\ \rho\mathbf{u}u_\eta+p\mathbf{e}_\eta\\ (E+p)u_\eta\end{pmatrix}=0 \tag{4}$$

where $\rho, \mathbf{u}, p, E$ are the density, velocity, pressure and total energy, respectively.

For solid materials, the hyperbolic model from [3] (see also [1]) is used, which has the novel property of being expressible in conservative form:

$$\frac{\partial}{\partial t}\begin{pmatrix}\rho\mathbf{u}\\ \rho\mathbf{F}^T\mathbf{e}_1\\ \rho\mathbf{F}^T\mathbf{e}_2\\ \rho\mathbf{F}^T\mathbf{e}_3\\ E\end{pmatrix}+\frac{\partial}{\partial x_\eta}\begin{pmatrix}u_\eta\rho\mathbf{u}-\sigma\mathbf{e}_\eta\\ u_\eta\rho\mathbf{F}^T\mathbf{e}_1-u_1\rho\mathbf{F}\mathbf{e}_\eta\\ u_\eta\rho\mathbf{F}^T\mathbf{e}_2-u_2\rho\mathbf{F}\mathbf{e}_\eta\\ u_\eta\rho\mathbf{F}^T\mathbf{e}_3-u_3\rho\mathbf{F}\mathbf{e}_\eta\\ u_\eta E-\mathbf{e}_\eta^T(\sigma\mathbf{u})\end{pmatrix}=-\mathbf{S}^C-\mathbf{S}^P \tag{5}$$

with:

- The elastic deformation gradient $F_{\alpha\beta}=\frac{\partial x_\alpha}{\partial x_{0\beta}}$ (where $x_\alpha$and $x_{0\beta}$ denote the fixed spatial coordinates and material coordinates of unstressed reference state respectively)
- σ the Cauchy stress tensor, $E=(i+|\mathbf{u}|^2/2)$ the total energy, with i the internal energy and $\mathbf{e}_\eta$ the Cartesian unit vectors.
- $\mathbf{S}^C$ is the vector containing terms associated with compatibility.

- $\mathbf{S}^P$ is the vector associated with limiting elastic deformations in the event of the onset of inelastic flow.

To solve the Riemann problem mentioned earlier in section 2 at the interface, a specific solver has been derived, relying on the use of propagating characteristics in the materials and the known Riemann invariants. Besides, two interfacial conditions expressing a possibly sliding interface are specified to close the system: $\sigma_{11} = -P$, $V_n^{Solid} = V_n^{Fluid}$, σ_{11} being the normal stress in the solid at the interface, and P the pressure of the fluid. The derivation is a bit tedious and won't be described in detail here. It is just reminded that it provides accurate interfacial conditions used to apply our conservative interface tracking method.

4 Numerical Results

4.1 Shocked Fluid/Fluid Interaction

The numerical simulation involving strong fluid/fluid interaction is the impact of a Helium bubble surrounded by air by a shockwave of strength Mach=1.22. Experiments and previous numerical simulations have been carried out on that testcase [6]. Both air and Helium are treated with a Gamma-law gas EOS, with γ=1.4 and γ=1.66 respectively. The computational domain is a rectangle of dimensions (in meters) [0.4; 0.045; 0.045], the bubble is originally centered at [0.22; 0; 0] and has a radius of 0.025 m. The grid used is uniform and is 440x50x50, and the CFL is set to 0.6. The reconstruction scheme used is WENO-3rd, coupled with a 3rd-order Runge-Kutta time integration. The results in Figure 2a show good agreements with both previous 2D numerical and experimental simulations [6]. Figure 2b shows the

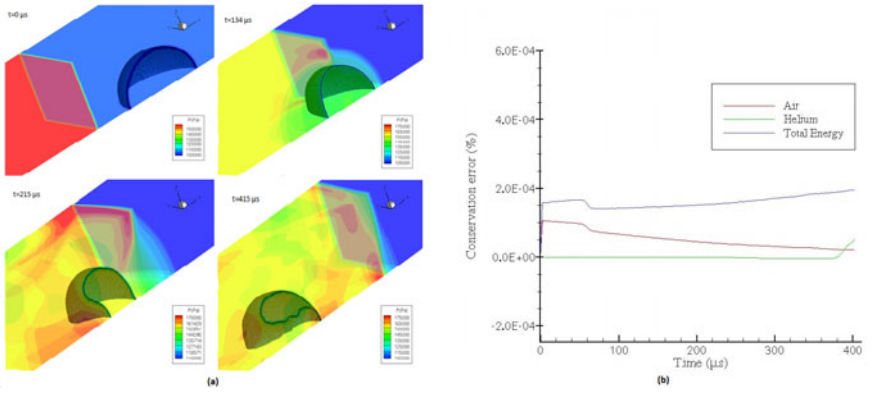

Fig. 2 Helium bubble impacted by an air shock (a) Pressure contours and deformation, (b) Conservation of mass and energy.

quasi-perfect conservation of mass and total energy during the simulation (withdrawing at every time step the mass and energy brought at the inlet), which is below 0.001%.

4.2 Shocked Fluid/Solid Interaction

The numerical simulation selected is a confined can explosion, used by [2]. A reactive gas (PBX-9404) fills a copper can at unstressed state. A layer of fluid is assumed fully reacted and at high pressure (corresponding to the initiation of a detonation; for more information of the burn model, refer to [2]) whilst the remaining fluid is at rest, and totally unreacted. The reaction propagates throughout the fluid, inducing strong load and deformations into the can. At the end of the simulation, the volume of the can has significantly increased, in agreement with [2]. The total length of the can is 24.6 cm, with an outside radius of 14 cm and a thickness of 2 cm. Besides, the corners of the can are given a chamfer of 0.6 cm. The grid is uniform, with Δx=0.2, and the CFL is set to 0.6. The reconstruction scheme used is WENO-3rd, coupled with a 3rd-order Runge-Kutta time integration. Figure 3a shows the deformation of the can along with pressure and stress contours at different stages, while Figure 3b shows the conservation of mass and energy during the simulation. Here again they are very small, not exceeding 0.002%.

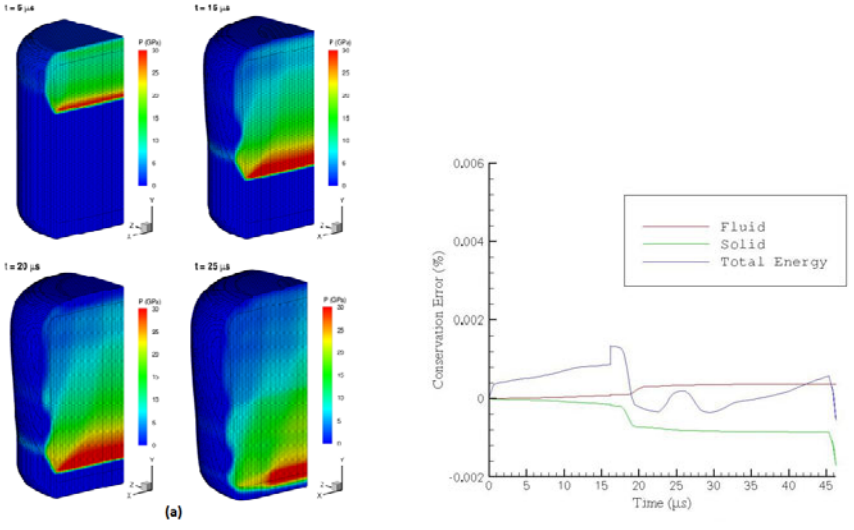

Fig. 3 Confined explosion in a can: (a) Pressure contours and deformation, (b) Conservation of mass and energy.

5 Conclusion

A 3D conservative method has been developed for multiple interaction problem. It has been successfully applied to both fluid/fluid and solid/fluid interactions. The interface remains sharp even in the case of large deformations caused by impacts and strong shocks, while ensuring a nearly perfect conservation of the conservative variables.

References

1. Barton, P.T., Drikakis, D., Romenskii, E.I.: An Eulerian finite-volume scheme for large elastoplastic deformations in solids. Int. J. Num. Meth. Eng. 81
2. Colella, P., Miller, G.H.: A conservative Three-Dimensional Eulerian Method for Coupled Solid-Fluid Shock Capturing. JCP 183 (2002)
3. Godunov, R.S.K., Romenskii, E.I.: Elements of Continuum Mechanics and Conservation Laws. Kluwer Academic/Plenum Publishers (2003)
4. Goldman, R.N.: Area of planar polygons and volume of polyhedra. In: Arvo, J. (ed.) Graphics Gems II: No. 2. Morgan Kaufmann (1994)
5. Hartmann, D., Meinke, M., Schroeder, W.: The constrained reinitialization equation for level set methods. J. Comp. Phys. 229, 1514 (2010)
6. Marquina, A., Mulet, P.: A flux-split algorithm applied to conservative models for multi-component compressible flows. J. Comp. Phys. 185 (2003)
7. Hu, X.Y., Khoo, B.C., Adams, N.A., Huang, F.L.: A conservative interface method for compressible flows. J. Comp. Phys. 219

Anti-diffusion Interface Sharpening Technique for Two-Phase Compressible Flow Simulations

K.K. So, X.Y. Hu, and N.A. Adams

1 Introduction

Shock waves in two-phase compressible flows are a fundamental topic in science and engineering. To better understand instability phenomena that are important for the evolution of such flows, basic configurations such as shock-bubble interactions in two-phase compressible flows are considered to investigate the Richtmyer-Meshkov instability and Rayleigh-Taylor instability. Flows of this type are present in many engineering applications including supersonic mixing and combustion systems and extra-corporeal shock-wave lithotripsy.

Numerical models of two-phase compressible flows play a significant role in the study of the topic as they provide the access to flow regimes and quantities which cannot be studied and obtained analytically and experimentally. The main numerical methods for two-phase compressible flow simulations are the level-set methods [1], the volume-of-fluid (VOF) methods [2], and front-tracking methods [12].

The VOF volume-capturing method possesses the advantage of exact conservation properties, but suffers from numerical diffusion which causes two-fluid interfaces to smear. Specific numerical schemes to suppress or counter-act the numerical diffusion, and to maintain the interface sharpness in the course of simulations are thus desirable for VOF methods. Previous works include the interface compression technique by [9], and the anti-diffusive numerical scheme based on a limited downwind strategy [5].

In this paper, we propose an interface sharpening technique for two-phase compressible flow simulations. The idea is to solve an anti-diffusion equation for counter-acting the numerical diffusion. The technique has been developed and verified for two-phase incompressible flow simulations [10]. It is the objective of this paper to present the key concepts and numerical results of the application of the technique to two-phase compressible flow simulations.

K.K. So · X.Y. Hu · N.A. Adams
Institute of Aerodynamics and Fluid Mechanics, Technische Universität München,
85748 Garching, Germany

2 Governing Equations

We consider the Euler equations assuming a single velocity and pressure equilibrium. The two phases are represented by the volume fractions, where the formulation of the volume-fraction equations of [2] is adopted. The volume-fraction equation formulation has been extensively studied by [6] for simulations with ideal-gas equation of state (EOS) and Mie-Grüneisen EOS, and serves as the governing equations for a computational study for shock-bubble interactions by [7]. With two mass conservation equations, one momentum conservation equation and one energy conservation equation a six-equation model is obtained as follows:

$$\frac{\partial \alpha}{\partial t} + \nabla \cdot \alpha \mathbf{u} = \alpha \frac{\overline{K}_S}{K_S^\alpha} \nabla \cdot \mathbf{u} \quad , \tag{1}$$

$$\frac{\partial \beta}{\partial t} + \nabla \cdot \beta \mathbf{u} = \beta \frac{\overline{K}_S}{K_S^\beta} \nabla \cdot \mathbf{u} \quad , \tag{2}$$

$$\frac{\partial \alpha \rho^\alpha}{\partial t} + \nabla \cdot \alpha \rho^\alpha \mathbf{u} = 0 \quad , \tag{3}$$

$$\frac{\partial \beta \rho^\beta}{\partial t} + \nabla \cdot \beta \rho^\beta \mathbf{u} = 0 \quad . \tag{4}$$

$$\frac{\partial \rho \mathbf{u}}{\partial t} + \nabla \cdot \rho \mathbf{u}\mathbf{u} + \nabla p = 0 \quad , \tag{5}$$

$$\frac{\partial E}{\partial t} + \nabla \cdot (E + p)\mathbf{u} = 0 \quad , \tag{6}$$

where α and β are the volume fractions of the two phases respectively and $\alpha + \beta = 1$, t is the time, $\mathbf{u}$ is the velocity, $\overline{K}_S$ is the mixture bulk modulus, K_S^α and K_S^β are the phase bulk modului, ρ^α and ρ^β are the phase densities, p is the pressure and E is the total energy.

3 Numerical Methods

3.1 Riemann Solver

The HLL Riemann solver [13] is adopted for calculating the numerical flux at cell face, $\mathbf{F}_{HLL}$,

$$\mathbf{F}_{HLL} = \begin{cases} \mathbf{F}_L & \text{if } 0 \le S_L, \\ \frac{S_R \mathbf{F}_L - S_L \mathbf{F}_R + S_L S_R (\mathbf{U}_R - \mathbf{U}_L)}{S_R - S_L} & \text{if } S_L \le 0 \le S_R, \\ \mathbf{F}_R & \text{if } 0 \ge S_R, \end{cases} \quad , \tag{7}$$

where $\mathbf{U}$ is the cell-averaged conserved variable, $\mathbf{F}$ is the cell-average flux, S is the bound of the fastest signal velocity, and the subscripts L and R denote the two sides of the cell face.

3.2 Anti-diffusion Interface Sharpening

The idea of sharpening the two-fluid interface is to provide a correction algorithm which can be applied as post-processing to the volume-fraction field after each time step. For such, an anti-diffusion equation, i.e. a diffusion equation with a positive diffusion coefficient, is solved to counter-act the numerical diffusion

$$\frac{\partial \alpha}{\partial \tau} = -\nabla \cdot (D \nabla \alpha) \quad , \tag{8}$$

where $D > 0$ is an anti-diffusion coefficient and τ is a pseudo time.

A specified discretization scheme is employed to ensure the numerical stability and volume-fraction boundedness in solving the anti-diffusion equation. The solution procedure is described in [10]. First, the limited cell-averaged value of the gradient of α, $\overline{\nabla \alpha}$, is obtained by the regularization based on a minmod limiter. Then, the anti-diffusion flux for α, F_{AD}^{α}, at the cell face between cell P and cell N is obtained by:

$$F_{AD}^{\alpha} = \begin{cases} -|D| \overline{(\nabla \alpha)_P} \cdot \mathbf{S} & \text{if } |\overline{(\nabla \alpha)_P}| \leq |\overline{(\nabla \alpha)_N}| \\ -|D| \overline{(\nabla \alpha)_N} \cdot \mathbf{S} & \text{if } |\overline{(\nabla \alpha)_N}| < |\overline{(\nabla \alpha)_P}| \end{cases} , \tag{9}$$

where $|\overline{(\nabla \alpha)_P}|$ and $|\overline{(\nabla \alpha)_N}|$ are the respective limited cell-averaged value of the gradient in cell P and cell N, $\mathbf{S}$ is the cell surface area vector.

The right-hand-side of eq. (8) is calculated by

$$\overline{\nabla \cdot (-|D| (\nabla \alpha))} = \frac{\sum_{cf} \left(F_{AD}^{\alpha} \right)}{V} \quad , \tag{10}$$

where $\sum_{cf}$ denotes the summation over all cell faces, V is the cell volume.

The volume fraction is advanced in pseudo time by an explicit Euler scheme:

$$\alpha^{AD} = \alpha + \overline{\nabla \cdot (-|D| (\nabla \alpha))} \Delta \tau \quad , \tag{11}$$

with the time step limit on pseudo time, $\Delta \tau$

$$\Delta \tau = \frac{1}{4} \frac{(\Delta x_{min})^2}{|D|} \quad . \tag{12}$$

α^{AD} is the sharpened volume fraction, Δx_{min} is the minimum cell width.

As the anti-diffusion equation is meant to counter-act the numerical diffusion resulted from the volume-fraction transport, the choice of D is based on the numerical

diffusion of the numerical scheme. Hence based on the formulation of the HLL Riemann solver D is chosen to be

$$D = \frac{S_L S_R (\alpha_R - \alpha_L)}{S_R - S_L} \quad . \tag{13}$$

The anti-diffusion equation can be solved repeatedly to attain an even sharper profile. A case- and grid- independent stopping criteria as detailed in [10] is employed to terminate the sharpening iterations.

After each time α is sharpened, all other flow variables in the governing equations are updated according to α^{AD} to ensure the consistency. Typically, only 1-2 sharpening iterations are sufficient in each time step.

4 Numerical Results

For all cases in the section the reconstruction of U_L and U_R is calculated by the van Leer MUSCL scheme. A third-order TVD Runge-Kutta method is employed for time integration. The time step for the governing equations is determined by the CFL requirement with a CFL number of 0.2.

4.1 Shock Tube Problem

The one-dimensional air-helium shock tube case of [4] is considered. The domain is defined as $[0,1]$ and discretized by 200 cells. The initial condition is

$$(\rho, u, p, \gamma) = \begin{cases} (1,0,1,1.4) & \text{if } 0 \leq x < 0.5 \\ (0.125,0,0.1,1.667) & \text{else} \end{cases} , \tag{14}$$

The results with and without the application of the anti-diffusion interface sharpening technique at $t = 0.15$ are shown in Fig. 1. By comparing the two results, one can see that the phase interface is better resolved, as can be seen from the reduced number of transition points in α, with the application of the anti-diffusion interface sharpening technique. The improved interface resolution also transfers to the other variables.

4.2 Shock-Bubble Interaction

The experimental case of a R22 cylinder in air hit by a shock wave at Mach number of 1.22 of [3] is considered. Corresponding to the reference literature, the simulation is treated as two-dimensional and the case set-up of [11] and the fluid parameters of [8] are adopted here. The domain is discretized by a Cartesian grid of

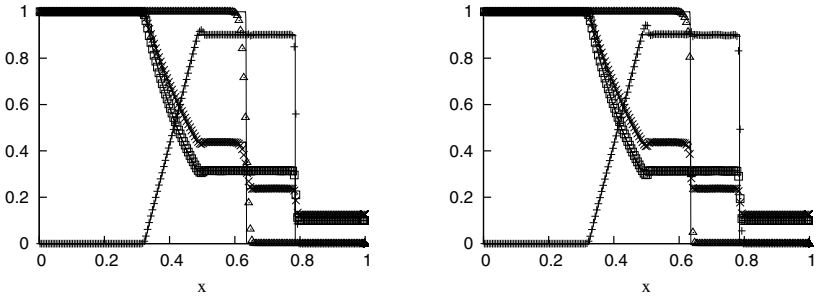

Fig. 1 Variables at $t = 0.15$ of the air-helium shock tube. '$\triangle$' denotes α, '$\times$' denotes ρ, '$+$' denotes $|\mathbf{u}|$, '$\square$' denotes p. Solid lines are the analytical solutions. Left: no interface sharpening; right: with interface sharpening.

$\Delta x/D = \Delta y/D = 0.005$, which is equivalent to a grid of a resolution of 200 cells across the bubble diameter.

The numerical Schlieren images, $|\nabla\rho|$, at $t = 187\mu s,\ 417\mu s$ after the shock impact are shown in Fig. 2. With the application of the interface sharpening technique the two-phase interface is better resolved while the large-scale structures remain consistent with the reference solution where no sharpening was applied, and with the reference literature [8]. More small-scale structures are recovered by the sharpening technique. The interface evolution of the high-resolution simulations computed on a grid of an effective resolution of $\sim$800 cells across the bubble diameter by an adaptive mesh refinement algorithm [8] are recovered by the simulations with interface sharpening on a mesh with about 16 times fewer grid points at the interface.

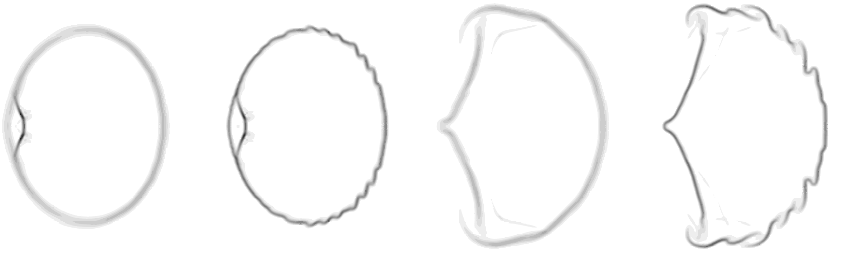

Fig. 2 Numerical Schlieren images, $|\nabla\rho|$, of the air-R22 shock-bubble interaction. From left to right: $t = 187\mu s$ (no interface sharpening), $t = 187\mu s$ (with interface sharpening), $t = 417\mu s$ (no interface sharpening), $t = 417\mu s$ (with interface sharpening).

5 Conclusion

In this paper an interface sharpening technique based on anti-diffusion is presented for two-phase compressible flow simulations. The technique possesses the advantage of being modular and applicable to any underlying VOF discretization schemes. The anti-diffusion flux to counter-act numerical diffusion is based on the anti-diffusion coefficient which is derived from the numerical scheme for the governing equations. The flow variables are updated consistently according to the sharpened volume fraction. Good agreement with experimental observation and simulation results from reference literature shows that more small-scale structures can be recovered by the interface sharpening technique.

References

1. Fedkiw, R.P., Aslam, T., Merriman, B., Osher, S.: A non-oscillatory Eulerian approach to interfaces in multimaterial flows (the ghost fluid method). J. Comput. Phys. 152, 457–494 (1999)
2. Greenough, J.A., Beckner, V., Pember, R.B., Crutchfield, W.Y., Bell, J.B., Colella, P.: An adaptive multifluid interface-capturing method for compressible flow in complex geometries. AIAA Paper 95-1718 (1995)
3. Haas, J.F., Sturtevant, B.: Interaction of weak shock waves with cylindrical and spherical gas inhomogeneities. J. Fluid Mech. 181, 41–76 (1987)
4. Hu, X.Y., Adams, N.A., Iaccarino, G.: On the HLLC Riemann solver for interface interaction in compressible multi-fluid flow. J. Comput. Phys. 228, 6572–6589 (2009)
5. Kokh, S., Lagoutiere, F.: An anti-diffusive numerical scheme for the simulation of interfaces between compressible fluids by means of a five-equation model. J. Comput. Phys. 229, 2773–2809 (2010)
6. Miller, G.H., Puckett, E.G.: A high-order Godunov method for multiple condensed phases. J. Comput. Phys. 128, 134–164 (1996)
7. Niederhaus, J.H.J., Greenough, J.A., Oakley, J.G., Ranjan, D., Anderson, M.H., Bonazza, R.: A computational parameter study for the three-dimensional shock-bubble interaction. J. Fluid Mech. 594, 85–124 (2008)
8. Quirk, J.J., Karni, S.: On the dynamics of a shock-bubble interaction. J. Fluid Mech. 318, 129–163 (1996)
9. Shukla, R.K., Pantano, C., Freund, J.B.: An interface capturing method for the simulation of multi-phase compressible flows. J. Comput. Phys. 229, 7411–7439 (2010)
10. So, K.K., Hu, X.Y., Adams, N.A.: Anti-diffusion method for interface steepening two-phase incompressible flow. J. Comput. Phys. (accepted manuscript)
11. Shankar, S.K., Kawai, S., Lele, S.K.: Numerical simulations of multicomponent shock accelerated flows and mixing using localized artificial diffusivity method. AIAA Paper 2010-352 (2010)
12. Terashima, H., Tryggvason, G.: A front-tracking/ghost-fluid method for fluid interfaces in compressible flows. J. Comput. Phys. 228, 4012–4037 (2009)
13. Toro, E.: Riemann Solvers and Numerical Methods for Fluid Dynamics. Springer (1997)

Numerical Simulation of a Transonic Gas-Droplet Two-Phase Flow over an Airfoil with a Droplet Breakup Model

Geum-Su Yeom and Keun-Shik Chang

1 Introduction

Gas-particle two-phase flows are abundant in the practical engineering problems. A branch of application is involved with the solid particles such as dust cyclone, flight in the hail storm, detonation of the dusty gases in the coal mine and grain storage tank, etc. Another branch of applications happen in the gas-liquid droplet two-phase flows but it is somewhat strange that they have not been much solved in the literature. Examples of this flow are the aviation of a flight vehicle through the cloud, fuel spray combustion and pulse detonation engine. Numerical simulation of the gas flow with the liquid droplets is more difficult than the gas flow with the solid particles. The reason is simple: the liquid droplets are a deformable medium with surface tension, breakup, coalescence, evaporation and condensation. In the present paper, we numerically simulate the transonic flow of air-water droplet mixture over a NACA0012 airfoil: see Fig. 1.

We formulate a two-dimensional compressible two-fluid model. Both the gas and the liquid phases are treated as compressible fluids governed by the stiffened-gas equation of state. We employ the two-fluid model [1] and take account of the droplet breakup by adding the droplet number density equation into the earlier two-fluid model. The viscous drag force, heat transfer and mass transfer between phases are considered. The system of equations is split into two operators by means of the fractional-step method: the hyperbolic operator and the source operator. The former is solved by the second-order accurate WAF-HLL scheme [1] and the source operator by the four-stage Runge-Kutta scheme.

Geum-Su Yeom · Keun-Shik Chang
Department of Mechanical, Aerospace and Systems Engineering,
Korea Advanced Institute of Science and Technology,
Daejeon, 305-701, South Korea

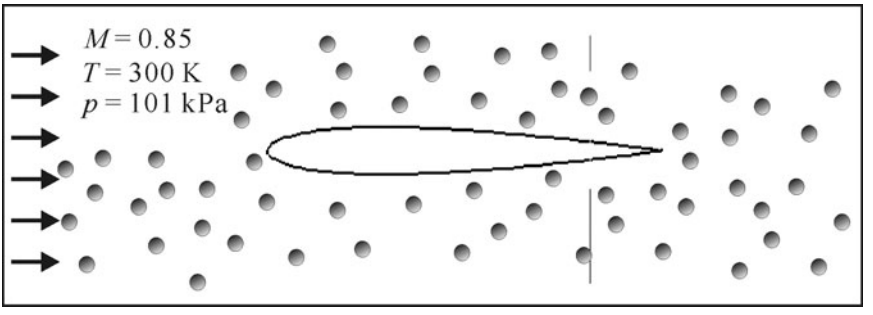

Fig. 1 Gas-droplet flow over a NACA0012 airfoil.

2 Governing Equations

The assumptions made in the present paper are as follows:

- The gas and the droplets are both compressible fluids.
- The gas is perfect.
- The liquid droplet phase conforms to the stiffened-gas equation of state.
- There is no droplet-droplet interaction like collision and coalescence.
- All the droplets are assumed spheres.
- The gravity effect is negligible.

Based on these assumptions, we employ the compressible two-fluid model in the two dimensions [1]. In order to model the droplet fragmentation, we add the following droplet number density equation into the two-fluid model.

$$\frac{\partial N_d}{\partial t} + \frac{\partial u_d N_d}{\partial x} + \frac{\partial v_d N_d}{\partial y} = N_d \frac{(d/d_\infty)^3 - 1}{\Delta \tau_{br}} \tag{1}$$

where d_∞ is the final diameter of droplets after breakup and $\Delta \tau_{br}$ is the breakup time. In the present model, the droplet fragments only when the Weber number of the droplet is greater than the critical Weber number. The critical Weber number is estimated by the empirical correlation by Brodkey [5],

$$We_d^* = \begin{cases} 36\left(\frac{24}{Re_d} + \frac{20.1807}{Re_d^{0.615}} - \frac{16}{Re_d^{2/3}}\right)(1 + 1.077 Oh_d^{1.64}) & for \quad 200 < Re_d < 2000, \\ 5.28(1 + 1.077 Oh_d^{1.64}) & for \quad Re_d \geq 2000, \end{cases} \tag{2}$$

where Oh_d is the Ohnesorge number.

The droplet breakup time is estimated by the correlation of Pilch and Erdman [6]:

$$\frac{\Delta\tau_{br}}{\tau^*} = \begin{cases} 6(We_d - We_d^*)^{-0.25} & for \quad We_d^* \le We_d \le 18, \\ 2.45(We_d - We_d^*)^{0.25} & for \quad 18 \le We_d \le 45, \\ 14.1(We_d - We_d^*)^{-0.25} & for \quad 45 \le We_d \le 351, \\ 0.766(We_d - We_d^*)^{0.25} & for \quad 351 \le We_d \le 2670, \\ 5.5 & for \quad 2670 \le We_d, \end{cases} \tag{3}$$

where $\tau^* = \frac{d}{\Delta V_{dg}}\sqrt{\frac{\rho_d}{\rho_g}}$.

3 Numerical Methods

The two-fluid governing equation system is solved by using the fractional-step method:

$$L_H : \frac{\partial \mathbf{U}}{\partial t} + \frac{\partial \mathbf{F}}{\partial x} + \frac{\partial \mathbf{G}}{\partial y} + \mathbf{H}\frac{\partial \alpha_g}{\partial x} + \mathbf{I}\frac{\partial \alpha_g}{\partial y} = 0, \tag{4}$$

$$L_S : \frac{\partial \mathbf{U}}{\partial t} = \mathbf{S}. \tag{5}$$

The hyperbolic operator, L_H, is discretized using the finite volume method with the numerical flux and the numerical volume fraction at the cell interface [1]. The source operator, L_S, is solved by the conventional fourth-order Runge-Kutta method.

4 Results and Discussion

To validate the present code, gas-only flow is calculated by the two-phase flow code. We calculate NACA0012 airfoil with an angle of attack of 1 degree, for Mach number 0.85 at atmospheric pressure. In the present formulation, the two-phase flow is reduced to the gas-only flow by letting the gas volume fraction take practically a unit, i.e., $(\alpha - 1) = 10^{-8}$. It is necessary to do so because the two-fluid model becomes singular when the void fraction is exactly 1 or 0. We take O-type structured grid (45 x 125) for the airfoil calculation. Fig. 2 compares the present result by the two-phase code with the output of the gas-only Euler code. The agreement is excellent.

Now we investigate the effect of the droplet volume fraction when the droplet diameter is fixed with $d = 100\mu m$. The contours of the gas pressure and the gas phasic Mach number are plotted in Fig. 3 for three droplet volume fractions: 0.01%, 0.1%, and 1%. We observe that the shock waves are relaxed and the flow is finally degraded to subsonic speed as the droplet volume fraction increases. Fig. 4 shows the lift and the drag coefficients dependent on the droplet volume fraction. In this figure, the lift coefficient rapidly decreases with the volume fraction to a minimum at $\alpha_d = 0.1\%$ and slightly re-increases for $\alpha_d > 0.1\%$. The drag coefficient, however, monotonically increases with the droplet volume fraction.

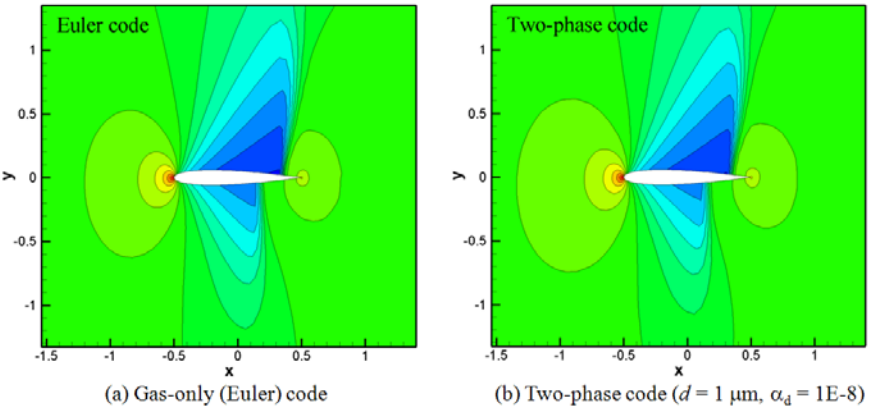

Fig. 2 Transonic gas flow over a NACA0012 airfoil: Left plot is from the Euler code and right is from the present two-phase code (with $d = 1\mu m$ and $\alpha_d = 10^{-8}$).

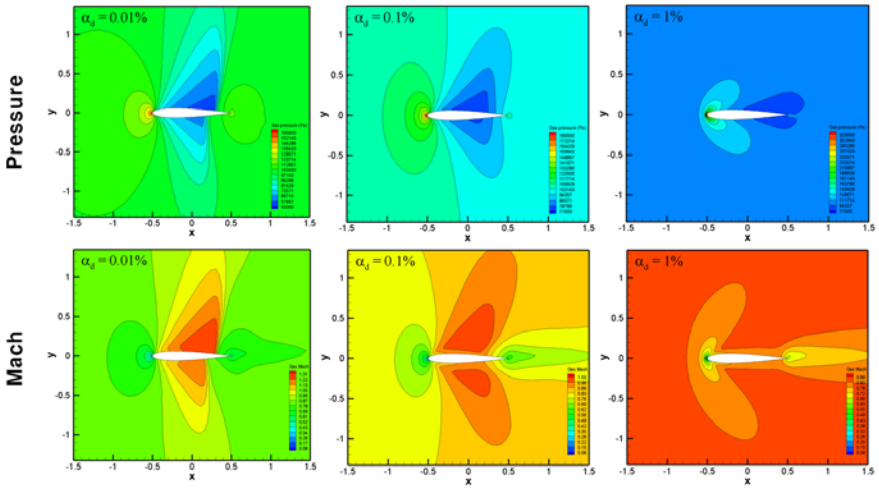

Fig. 3 Contours of gas pressure and gas phasic Mach number for three droplet volume fractions: 0.01%, 0.1% and 1%. The droplet diameter is kept at a constant value, $d = 100\mu m$.

Finally, we investigate the effect of the droplet diameter as the droplet volume fraction is fixed with 0.1%. Fig. 5 shows the contours of gas pressure and gas phasic Mach number for three different droplet diameters: $1\mu m$, $10\mu m$ and $100\mu m$. The shock waves are significantly relaxed and the flow becomes subsonic as the droplet size is reduced. Fig. 6 shows the lift and the drag coefficients dependent on the droplet diameter. In this figure, both the lift and the drag coefficients decrease with the droplet size.

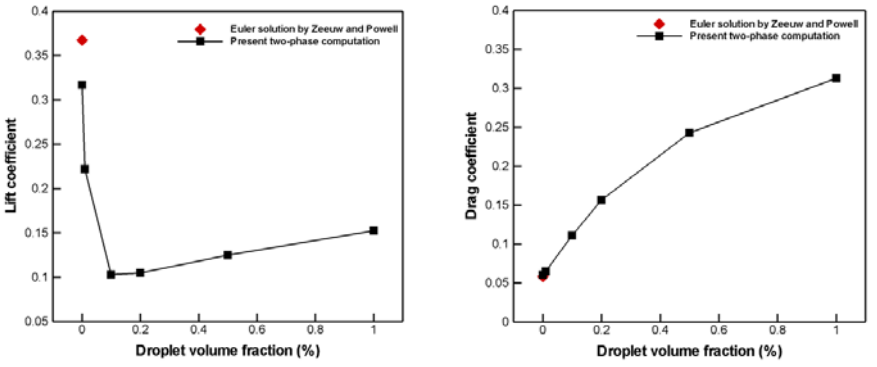

Fig. 4 Lift and drag coefficients vs. droplet volume fraction, for a constant droplet diameter $d = 100\mu m$.

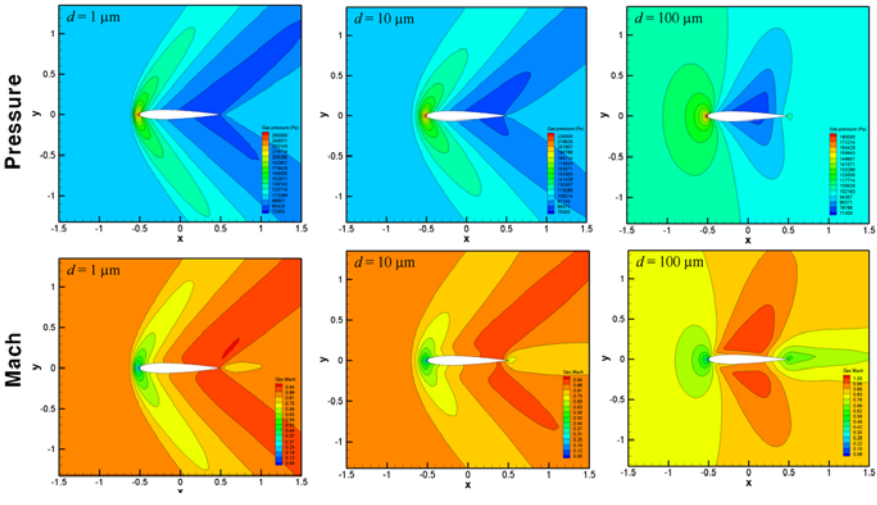

Fig. 5 Contours of gas pressure and gas phasic Mach number for three droplet diameters: $1\mu m$, $10\mu m$ and $100\mu m$. The droplet volume fraction is kept constant at 0.1%.

5 Conclusions

In this paper, we have formulated the two-fluid two-phase model with a droplet fragmentation to simulate aerodynamics of a transonic airfoil in the gas-droplet mixture flow. The present WAF-HLL scheme is very robust and efficient for two-phase flow problems we tested. As the droplet volume fraction and the droplet size increase, the shock waves are much relaxed and the flow becomes subsonic. The flow field,

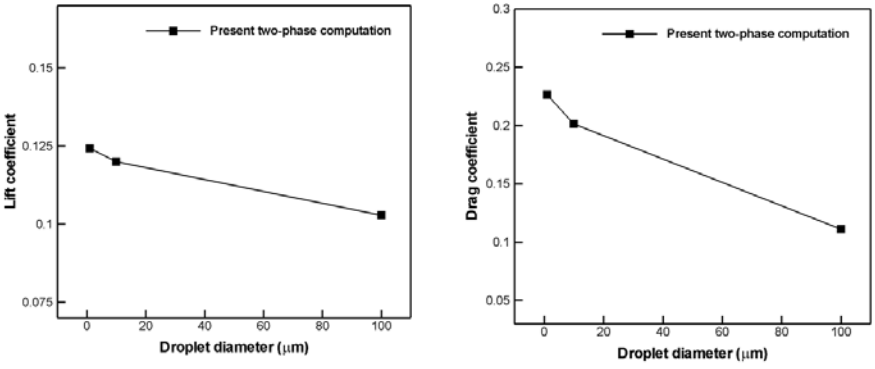

Fig. 6 Lift and drag coefficients vs. droplet diameter. The droplet volume fraction is kept constant at 0.1%.

the lift, and the drag forces are strongly affected by both the droplet volume fraction and the droplet size.

Acknowledgements. This work was supported by the second stage of the Brain Korea 21 Project in 2011.

References

1. Yeom, G.S., Chang, K.S.: Shock Wave Diffraction about a Wedge in a Gas-Microdroplet Mixture. Int. J. Heat Mass Transfer 53, 5073–5088 (2010)
2. Ishii, M., Hibiki, T.: Thermo-Fluid Dynamics of Two-Phase Flow. Springer, New York (2006)
3. Yuen, M.C., Chen, L.W.: Heat transfer measurements of evaporating liquid droplets. Int. J. Heat Mass Transfer 21, 537–542 (1977)
4. Kolev, N.I.: Fragmentation and Coalescence Dynamics in Multiphase Flows. Exp. Therm. Fluid Sci. 6, 211–251 (1993)
5. Brodkey, R.S.: The Phenomena of Fluid Motions. Addison-Wesley, Reading, Mass. (1967)
6. Pilch, M., Erdman, C.A.: Use of Breakup Time Data and Velocity History Data to Predict the Maximum Size of Stable Fragments for Acceleration-Induced Breakup of a Liquid Drop. Int. J. Multiphase Flow 13, 741–757 (1987)

Numerical Investigation of Cavitation Bubble Dynamics Near Walls

E. Lauer, X.Y. Hu, S. Hickel, and N.A. Adams

1 Introduction

The collapse of cavitation bubbles near walls is one of the major reasons for failure of technical devices involving the processing of liquids at large pressure differences. High-speed photography gives a first insight into the bubble dynamics during the collapse [4],[5] and shows two fundamental phenomena during the non-spherical cavitation bubble collapse process: first the development of high-speed jets and second the release of shock-waves upon final bubble collapse. Both, the impact of shock waves and of high-speed jets on a surface can lead to material erosion. A more detailed experimental investigation including a precise determination of peak pressures at the wall and its association with the initial bubble configuration and evolution is beyond current experimental capabilities.

This information can be only obtained from numerical simulations, but the demands on the numerical methods are high. The major challenge for numerical investigations is to accurately reproduce the dynamics of the interface between water and vapor during the entire collapse process including the high-speed dynamics of the late stages, where compressibility of both phases plays a decisive role.

In this paper, we use a model based on the conservative interface-interaction method of Hu et al. [2]. The material interface is accurately resolved by a level-set approach on Cartesian meshes and the interface evolution is computed from a generalized Riemann problem. The effect of condensation and evaporation is taken into account by a non-equilibrium phase-change model.

The objective of this work is to contribute to the clarification of wall-attached cavitation-bubble collapse. Three different configurations of spherical cavitation bubbles are investigated: a detached bubble, a bubble cut by the wall in its lower hemisphere, and one cut by the wall in its upper hemisphere. Depending on the initial wall position, we find a different collapse behavior. We observe wall-normal, as

E. Lauer · X.Y. Hu · S. Hickel · N.A. Adams
Institute of Aerodynamics and Fluid Mechanics, Technische Universität München,
Boltzmannstr. 15, 85748 Garching bei München, Germany

well as wall-parallel jets. In a second step, we focus on the significance of initial bubble asymmetries on the collapse dynamics by considering an initially ellipsoidal vapor bubble attached to a wall. This scenario leads to a significantly different evolution of the topology during the collapse.

2 Numerical Approach

Our numerical approach is based on the conservative interface method of Hu et al. [2]. A sharp interface $\Gamma(t)$, which is tracked with the level-set approach of Fedkiw et al. [1], separates vapor (v) and liquid (li) within the computational domain. We solve the integral form of the Euler equations for both fluids separately on the corresponding subdomains in a conservative way ($m = v, li$).

$$\begin{aligned} V\left(\alpha_m^{n+1}\overline{\mathbf{U}}_m^{n+1} - \alpha_m^n\overline{\mathbf{U}}_m^n\right) = &\int_n^{n+1} dt\ \Delta y\Delta z\left[A_m^{12}(t)\mathbf{F}_m^{12} - A_m^{11}(t)\mathbf{F}_m^{11}\right] \\ &+ \int_n^{n+1} dt\ \Delta x\Delta z\left[A_m^{22}(t)\mathbf{F}_m^{22} - A_m^{21}(t)\mathbf{F}_m^{21}\right] \\ &+ \int_n^{n+1} dt\ \Delta x\Delta y\left[A_m^{32}(t)\mathbf{F}_m^{32} - A_m^{31}(t)\mathbf{F}_m^{31}\right] \\ &+ \int_n^{n+1} dt\ \mathbf{X}_m(\Delta\Gamma(t))\ , \end{aligned} \tag{1}$$

where $\alpha_m\overline{\mathbf{U}}_m$ and $\overline{\mathbf{U}}_m$ are the vector of the conserved quantities in the cut cell and the vector of volume averaged conservative variables respectively. $\mathbf{F}_m^{pq}$ is the average flux across a cell face. The volume fractions α_m and the cell-face apertures A_m^{pq} are reconstructed from the level-set field. The coupling between both fluids is achieved by a conservative interface interaction term $\mathbf{X}_m(\Delta\Gamma(t))$.

The interaction term accounts for the contributions of pressure force and phase change, respectively,

$$\mathbf{X}_m(\Delta\Gamma) = \mathbf{X}_m^p + \mathbf{X}_m^t\ . \tag{2}$$

From the solution of the two-material Riemann problem at the interface, the interface pressure p_I and the interface normal velocity $\mathbf{u}_I$ serve to compute the pressure term $\mathbf{X}_m^p$

$$\mathbf{X}_m^p = \begin{pmatrix} 0 \\ p_I\Delta\Gamma\ (\mathbf{n}_m\cdot\hat{i}) \\ p_I\Delta\Gamma\ (\mathbf{n}_m\cdot\hat{j}) \\ p_I\Delta\Gamma\ (\mathbf{n}_m\cdot\hat{k}) \\ p_I\Delta\Gamma\ (\mathbf{n}_m\cdot\mathbf{u}_I) \end{pmatrix}\ . \tag{3}$$

The mass transfer term $\mathbf{X}_m^t$ is given by

$$\mathbf{X}_v^t = -\mathbf{X}_{li}^t = \begin{pmatrix} \dot{m}\,\Delta\Gamma \\ \dot{m}\,\Delta\Gamma\,(\mathbf{v}\cdot\hat{i}) \\ \dot{m}\,\Delta\Gamma\,(\mathbf{v}\cdot\hat{j}) \\ \dot{m}\,\Delta\Gamma\,(\mathbf{v}\cdot\hat{k}) \\ \dot{m}\,\Delta\Gamma\left(e_v + \frac{1}{2}|\mathbf{v}|^2\right) + p_I\,\Delta q^*\,\Delta\Gamma \end{pmatrix}, \tag{4}$$

where $\mathbf{v}$ is the velocity of the liquid at the interface in case of evaporation and the velocity of the vapor in case of condensation, respectively. $\Delta q^* = \dot{m}/\rho_{li}$ is the phase-change induced velocity and $\dot{m}$ the phase-change rate obtained from [6]

$$\dot{m} = \frac{\lambda}{\sqrt{2\pi R_v}}\left(\frac{p_s(T_{li})}{\sqrt{T_{li}}} - \frac{p_v}{\sqrt{T_v}}\right). \tag{5}$$

Here, R_v is the specific gas constant in the vapor phase, and λ is the accommodation coefficient for evaporation or condensation (assumed to be constant). T_v and T_{li} are the temperatures of vapor and liquid at the phase interface, respectively. p_v is the actual vapor pressure at the interface, and $p_s(T_{li})$ is the equilibrium (saturation) vapor pressure at temperature T_{li}.

For our computations, we use a fifth-order WENO scheme [3] and a third-order TV Runge–Kutta scheme [7] to discretize the Euler equations. Simulations are carried out with the CFL number of 0.6. We always model vapor as ideal gas ($p = R\rho T$ with $\gamma = 1.335, R = 461.5\,\mathrm{J/(kg\ K)}$) and use Tait's equation of state for water ($p = B\,(\rho/\rho_0)^\gamma - B + A$ with $B = 3310\,\mathrm{bar}$, $A = 1\,\mathrm{bar}$, $\rho_0 = 1\,\mathrm{kg/m^3}$ and $\gamma = 7.15$).

3 Spherical Vapor-Bubble Collapse

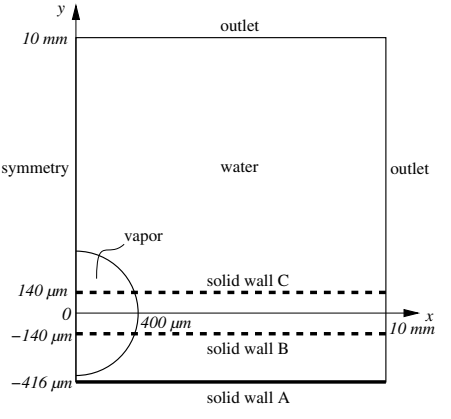

Fig. 1 Sketch of the problem. Three configurations with different wall positions are investigated.

We investigate the collapse of a vapor bubble near a solid wall. As shown in Fig. 1, the initial bubble radius is 400 µm and we consider three different wall positions A, B and C. We take advantage of symmetries and compute only one quarter of the bubble. The grid spacing is equidistant in the bubble region with 100 computational cells over the initial bubble radius. Grid stretching is applied in the far-field. Outlet boundary conditions are imposed at $x, y, z = 10$ mm. Data are mirrored on the (X-Y)- and (Y-Z)-plane for visualization. Both fluids have a common temperature of 293.0 K which is the saturation temperature corresponding to the initial vapor pressure of 0.0234 bar. Initial liquid pressure is 100 bar and the accommodation coefficient is taken as $\lambda = 0.01$.

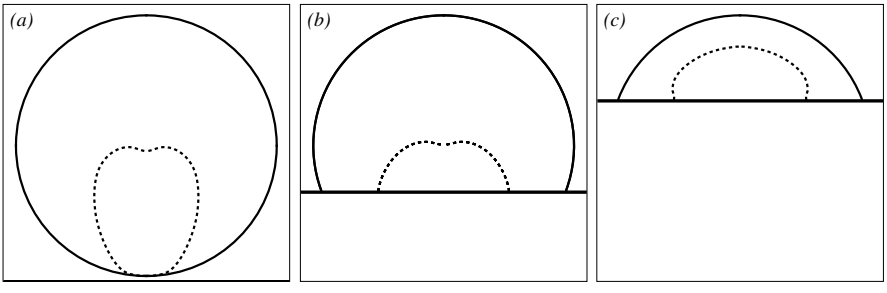

Fig. 2 Initial situation and bubble shape after cavity development for case A, B and C.

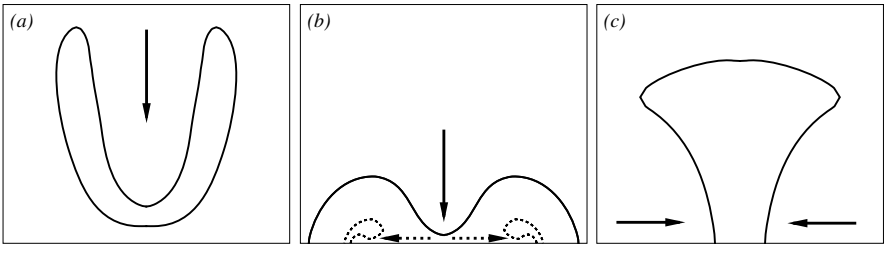

Fig. 3 Liquid jets during vapor bubble collapse near a wall (frame size in µm): (**a**) Wall-normal re-entrant jet for configuration A (296x244), (**b**) primary wall-normal re-entrant jet (*solid line*) and secondary wall-parallel outward pointing jet (*dashed line*) for configuration B (352x292), and (**c**) wall-parallel inward pointing jet for configuration C (128x104). Arrows indicate the jet direction.

For all configurations, the vapor bubble shrinks slowly during the initial period. The rapid stage of the bubble collapse starts with the development of a cavity, followed by the formation of a liquid jet. Two fundamentally different scenarios at the early stages of bubble collapse can be found. For a detached bubble or a bubble cut in the lower hemisphere, the collapse is initiated at the top of the bubble (Fig. 2a,b). A fast liquid re-entrant jet develops and penetrates through the bubble

in wall-normal direction (Fig. 3a,b). For an attached bubble cut in the upper hemisphere, the collapse is initiated between wall and interface (Fig. 2c) and a liquid jet develops radially towards the bubble center (Fig. 3c).

The appearance of a secondary jet can be only observed with configuration B since the wall normal re-entrant jet is deflected at the wall and interacts with the remaining bubble ring (Fig. 3b, dashed lines). This secondary jet is radially symmetric and develops from the symmetry axis outwards in wall-parallel direction. For configuration A no secondary jet develops as the residual bubble ring is not attached to the wall.

Figure 4 gives a three-dimensional visualization of the bubble shape during the stage of the three different liquid jets.

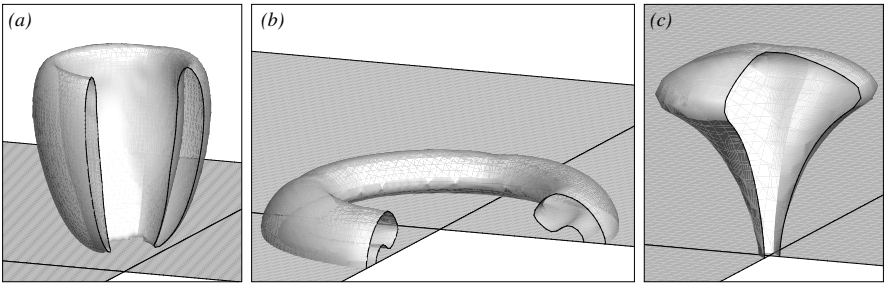

Fig. 4 Cuts through an iso-surface of the zero level-set (interface) showing the shape of the bubble during the stage of the liquid jets.

The first occurrence of extreme pressure magnitudes coincides with jet breakdown. For cases A and B with a wall-normal re-entrant jet, the observed maximum wall pressures are of comparable magnitude of about 100 times the initial pressure. Slightly larger values for the detached bubble can be attributed to a larger jet velocity. Looking at wall-parallel radial jets, one has to distinguish between the outward-pointing secondary jet of configuration B and the inward pointing primary jet of configuration C. In the latter case, the liquid is gradually compressed while being transported towards the symmetry axis, where maximum pressure occurs. The maximum pressure after inward-pointing, wall-parallel jet breakdown is about six times larger than that for a wall-normal jet. For the outward-running, wall-parallel secondary jet of configuration B, extremely low pressure is observed inside the jet as an expansion of the liquid further decreases the pressure of the high-velocity jet. After the jet breaks down, the liquid pressure increases, but remains significantly smaller than for the inward-pointing jet.

During the final stage of the bubble collapse, two different scenarios occur. For cases A and C, the residual vapor bubble is detached after jet breakdown. Thus, the maximum pressure due to final bubble collapse occurs away from the wall. The emitted shock wave impinges on the wall with reduced magnitude, and the wall pressure does not reach the level observed for jet breakdown. The second scenario

can be found for configuration B. After primary and secondary jet breakdown, a residual vapor ring remains at the wall. This ring is surrounded by high pressure which initiates the final collapse radially towards the symmetry axis. Liquid is compressed towards the center region resulting in large pressure with a maximum at the symmetry axis of about 400 times the initial pressure.

4 Ellipsoidal Vapor-Bubble Collapse

The ideal situation of spherical vapor bubbles hardly applies to technical applications, where cavitation bubbles are most likely non-spherical. A moderate increase of geometrical complexity by considering an ellipsoidal vapor bubble near a solid wall allows for an initial estimate on the effect of geometry variations on bubble collapse. As it was found previously that configuration C of a spherical vapor bubble leads to the largest wall pressure, we consider a similar configuration with the ellipsoidal bubble. The equivalent full (non-cut) ellipsoid is rotationally symmetric about the x-axis and has the same volume as the spherical bubble of the previous section. We set the length of the semimajor axis to $a = 3/2\, R_{\text{sphere}} = 600\,\mu\text{m}$, where $R_{\text{sphere}} = 400\,\mu\text{m}$ is the initial radius of the corresponding sphere. The volume is kept constant by choosing $b = \sqrt{2/3}\, R_{\text{sphere}} \approx 326.6\,\mu\text{m}$ as the length of the semiminor axis. We use the initial material states given in §3 and similar grid spacing. Again, only one quarter of the problem is simulated due to sectional symmetry of the setup. For presentation, data are extended to the full domain.

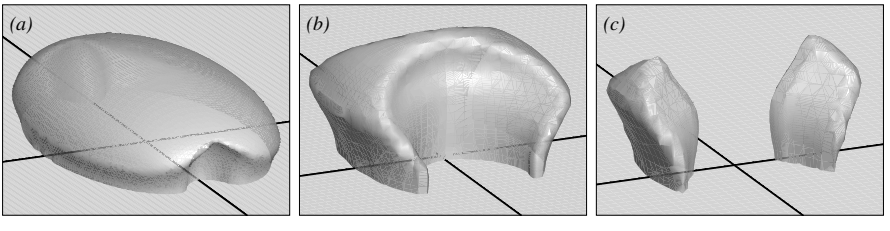

Fig. 5 Bubble shape during the ellipsoidal-bubble collapse.

For the ellipsoidal bubble the contact angle varies along the circumference. Where the contact angle is small, we expect weak expansion and therefore strong acceleration of the interface. As the contact angle is always below 90° the overall behavior resembles that of configuration C. Along the semimajor axis with smallest contact angle, a jet has already developed in Fig. 5(a).

Figure 5(b) shows two different wall-parallel jets. The first jet corresponds to that found already for the spherical bubble. This rotationally symmetric jet leads to a cavity between wall and interface along the circumference of the bubble. The second jet is a consequence of the initial asymmetry. It penetrates into the bubble along the semimajor axis, similarly as a wall-parallel re-entrant jet. It dominates the further bubble collapse as its velocity is larger than that of the first jet.

The axial jet first breaks through the bubble area in the symmetry plane (Fig. 5c) and two bubble fragments are generated. When the axial jet breaks down, the pressure increases rapidly to more than 100 times the initial pressure. The high pressure between the two bubble fragments initiates the collapse of the residual vapor bubble. The maximum wall pressure is reached at final collapse of the remaining bubble parts. With more than 600 times the initial pressure, the wall pressure is of similar magnitude as for the spherical bubble although the collapse mechanisms are significantly different.

5 Conclusions

We have presented simulations with our conservative sharp-interface model for compressible multi-fluid flows with phase-change. Results for the collapse of a spherical vapor bubble close to a solid wall have been discussed for three different bubble–wall configurations. For a detached bubble and a bubble cut by the wall in its lower hemisphere, we found the appearance of the well known wall-normal re-entrant jet. For the latter configuration, also a secondary radial and wall-parallel jet was found. If the bubble is attached, but cut by the wall in its upper hemisphere, the developing jet is wall-parallel and compresses the liquid towards the axis of symmetry. Additional results for the collapse of an ellipsoidal vapor bubble have shown, that the collapse mechanisms is highly dependent on initial asymmetries of the bubble shape.

References

1. Fedkiw, R., Aslam, T., Merriman, B., Osher, S.: A non-oscillatory Eulerian approach to interfaces in multimaterial flows (the ghost fluid method). J. Comp. Phys. 152, 457–492 (1999)
2. Hu, X.Y., Khoo, B.C., Adams, N.A., Huang, F.L.: A conservative interface method for compressible flows. J. Comp. Phys. 219, 553–578 (2006)
3. Jiang, G.S., Shu, C.W.: Efficient implementation of weighted ENO schemes. J. Comp. Phys. 126, 202–228 (1996)
4. Lindau, O., Lauterborn, W.: Cinematographic observation of the collapse and rebound of a laser-produced cavitation bubble near a wall. J. Fluid Mech. 479, 327–348 (2003)
5. Tomita, Y., Shima, A.: Mechanisms of impulsive pressure generation and damage pit formation by bubble collapse. J. Fluid Mech. 169, 535–564 (1986)
6. Schrage, R.W.: A Theoretical Study of Interphase Mass Transfer. Columbia University Press (1953)
7. Shu, C.W., Osher, S.: Efficient implementation of essentially non-oscillatory shock capturing schemes. J. Comp. Phys. 77, 439–471 (1988)

Time Resolved Measurements of Shock Induced Cavitation Bubbles in Various Liquids: A Novel Method of Optical Measurement

S. Koch, W. Garen, F. Hegedüs, W. Neu, and U. Teubner

1 Introduction

Cavitation is a major source of erosion for instance of ship propellers, pumps and water turbines. In such systems low pressure regions (pockets) exist where the water pressure suddenly becomes very low, almost a vacuum. These growing pockets, i.e. the ”cavitation bubbles” propagate to high pressure regions, where they collapse immediately.

Different methods of bubble generation are possible. One of them uses a powerful short laser pulse that is focused into a liquid and there generates an optical breakdown. During the successive plasma recombination, a fast growing nearly spherical bubble arises. When the radius has reached its maximum, the bubble contracts continuously to a minimum and finally it collapses. The onset and the collapse of the bubble are usually combined with shock wave emission (laser generated bubble and shock waves, LGBS). Following Bosset, the initial hydrodynamic bubble energy is redistributed in at least five distinct channels [1]:

1. a new subsequent bubble caused by a partially elastic rebound
2. shockwaves
3. liquid jets (in the vicinity of a solid wall)
4. electromagnetic radiation (for instance sonoluminescence)
5. thermal motion

S. Koch · W. Garen · W. Neu · U. Teubner
Hochschule Emden/Leer, University of Applied Sciences,
Institut für Lasertechnik Ostfriesland, Constantiaplatz 4, 26723 Emden, Germany

F. Hegedüs
Budapest University of Technology and Economics, Departmant of Hydrodynamic Systems,
P.O. Box 91, 1521 Budapest, Hungary

U. Teubner
Carl von Ossietzky Universität Oldenburg, Institute of Physics, 26111 Oldenburg, Germany

The life time of a cavitation bubble depends on the initial energy and usually is of the order of a few microseconds up to several milliseconds. In the case of LGBS in liquids, it is much shorter, i.e. of the order of 10 ns to a few microseconds, respectively. Consequently, although a good temporal resolution would be required in such case, this is not easy to obtain. For investigations on cavitation bubble dynamics, in general high speed cameras with 10^4 - 10^8 frames/s and a large number of time-delayed pictures have been used [2]. Other investigators used a beam-deflection method to detect LGBS. With increasing distances from the plasma these authors were able to obtain information on bubble dimension and wall velocities [3]. Alternatively, the present work reports on a novel and inexpensive optical method to enable a time resolved insight in the formation and the collapse of cavitation bubbles. The method provides also information on the resulting shock waves from the initial state until the end of the rebound process. Under the assumption of a nearly spherical bubble, the method allows the continuous measurement with temporal and spatial resolution of a complete bubble dynamics cycle.

2 Experimental Setup

The present work concentrates on the first two channels of energy redistribution as discussed in section 1. Using a Q-switched Nd:YAG-laser (laser fluence of 0.2 MJ/cm^2, 0.4 MJ/cm^2, 0.6 MJ/cm^2; τ = 6ns) for LGBS (pump) in a cuvette, two different liquids are used: glycerine and distilled water.

An expanded HeNe-laser beam in TEM00 mode (probe) is crossing the cuvette perpendicularly to the pump beam and then is detected by means of a PIN-diode. The cavitation bubble is centered in the middle of probe beam. Due to the smaller refractive index within the bubble with respect to the surrounding liquid, the bubble acts like a negative lens. As a result part of the probe is blocked and thus the temporal evolution of the diode voltage *U(t)* depends on the temporal evolution of the bubble volume *V(t)*. Then, under the assumption of spherical bubble geometry, the radius *r(t)* of the bubble can be calculated. The assumed spherical bubble geometry is verified by a series of CCD images during the measurements. For shocks, normally emitted at the onset and the collapse of the bubble, the experimental arrangement is similar to a Schlieren-apparatus and thus the diode signal yields *dr(t)/dt* and thus provides information on the shock. Consequently this method monitors the complete process from plasma generation, emission of shock waves, bubble growth and bubble collapse as well as the rebound of second and subsequent bubbles. The time resolution only depends on the diode and the electronics.

3 Results and Discussion

As a first result, Fig. 1 shows the evolution of bubbles and shocks by LGBS in glycerine at atmospheric pressure obtained by the novel method discussed in section 2. Initial shock, growth and decrease of the first bubble and its collapse accompanied by a shock wave are well recognized as well as the growth and decrease of the

second bubble (rebound), again accompanied by a shock wave (Fig. 1a). Even more clearly, Fig. 1b shows the signal due to the shock wave generation, obtained by the time derivative of *r(t)*.

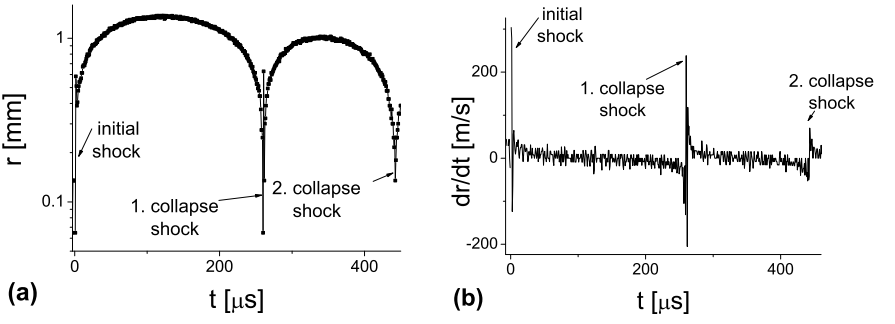

Fig. 1 Shock wave detection by a logarithmic scale of r (a) and v (b)

Fig. 2 displays bubble onset and bubble collapse in more detail and implies an almost spherical bubble structure (see section 1 and 2). However, the onset of the first bubble is difficult to observe because the initial end of the spherical shock and the onset of the first bubble are hardly separable (in Fig. 2 marked as A). In contrast, in the collapse situation a clear changeover from the bubble collapse to the shock is detectible (marked as B).

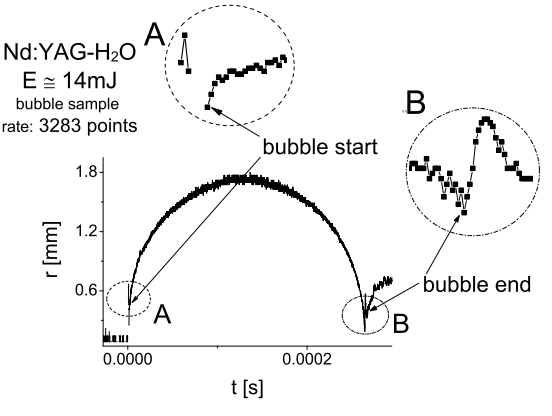

Fig. 2 Fixing of bubble start and bubble end

Single bubble dynamics in glycerine is studied also at different initial temperatures $T_0 = 20°C$, 30°C, 66°C, repectively. For $T_0 = 20°C$ no collapse or shock is visible at the end of the first and further rebound bubbles. For higher temperatures,

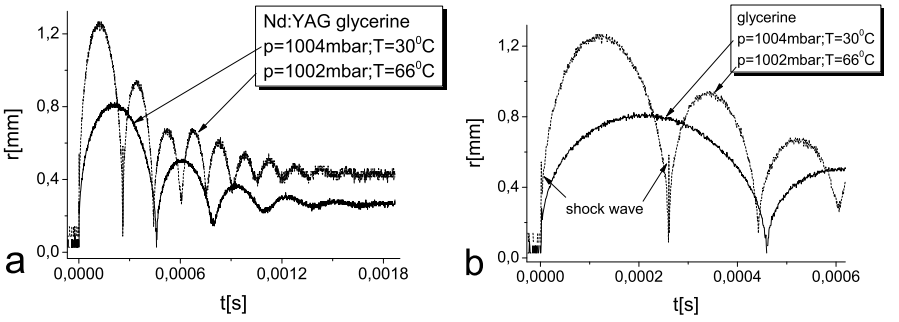

Fig. 3 Bubble life time for different liquid temperatures in glycerine (a) with inset (b)

Fig. 3 shows the bubble dynamics with a moderate time interval between onset and collapse for $T_0 = 30°C$ and a much faster evolution with many rebounds for $T_0 = 66°C$. In even more detail, one can recognize from Fig. 3 that shock waves are generated at $T_0 = 66°C$. In total, collapse time and bubble size significantly increase with temperature.

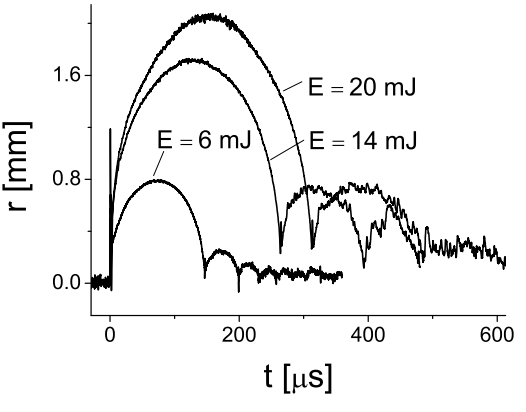

Fig. 4 Bubble life time for different laser energies in distilled water

Further measurements on LGBS are performed with distilled water (Fig. 4). Details of the experiment and theoretical simulations are discussed elsewhere [4].

4 Summary

In conclusion, the presented optical method is a powerful tool to analyze the dynamics of laser driven cavitation bubbles in liquids (LGBS). The main advantage is the high temporal and spatial resolution of bubble dimension from the onset to the collapse. Furthermore, adjacent shocks emitted could be well detected. Presently this method is restricted to spherical bubbles as generated within the present work. However, potentially the method may be extended to other geometries. Further investigations on simultaneous determination of two-dimensional bubble evolution are in progress.

References

1. de Bosset, A., et al.: 58th Int. Astronautical Congress (2007)
2. Brujan, E.A., Vogel, A.: J. Fluid Mech. 558 (2006)
3. Gregorčič, P., et al.: Appl. Phys. A 93 (2008)
4. Hegedüs, F., et al.: To be published

The Behaviors of a Drop in Ambient Liquid under a Sudden Impact

H. Ling, Y. Zhu, R. Xiong, L. Wang, F. Xiao, M. Xu, and J. Yang

1 Introduction

The deformation and breakup of a liquid drop in ambient liquid phase is a common phenomenon in a variety of scientific and engineering applications, such as oil pipeline transport, metallurgy, and certain types of emulsions when they encounter severe disturbances. Therefore it is of great importance to understand the behaviors and mechanisms of the drop under such circumstances.

So far, the understandings on the deformation and breakup of a drop have been established by studies of liquid drop in gas flow. General experimental techniques to study the drop behaviors are shock tube,[1] and continue jet,[2] where the droplet is subjected to a nearly step change of the ambient flow. There are also plenty of numerical studies with varied numerical methods such as front tracking method [3][4], volume of fluid method [5], and moving-particle semi-implicit method [6]. Those works have been reviewed by several authors [7][8]. According to the general understandings, the deformation and breakup of drop can be classified into several distinct regimes, and the phenomenon is governed by a few important non-dimensional parameters, i.e., the Weber number (We) which is the ratio of the disrupting aerodynamic forces to the restorative surface tension forces, the Ohnesorge number (Oh) which is the ratio of drop viscous forces to surface tension, and the density ratio of the drop phase to the ambient phase. *We* is found to be the dominant parameter that determines the breakup regime as long as the *Oh* is sufficiently low. But when *Oh* goes high enough, both *We* and *Oh* have a significant influence on the phenomenon. As a contrast, the effect of density ratio remains unclear due to the technical difficulty of varying this parameter experimentally in a gas-liquid system where the two densities are usually in orders of difference. Some numerical studies have tested the situation of low density ratio[3][4][6][9]. Their results need further experimental data to support though.

H. Ling · Y. Zhu · R. Xiong · L. Wang · F. Xiao · M. Xu · J. Yang
University of Science and Technology of China, Hefei 230027, Anhui, P.R. China

Taking advantage of the close density value of the drop liquid and ambient liquid, this study experimentally investigates the drop behaviors under low density ratio. A drop tower method is designed to impose a sudden impact on the free falling liquid-liquid system. High speed camera is employed to record the configuration and development of the droplet. Results are then further analyzed and discussed.

2 Experiment Method

The principle of current experimental method is described as follow. When a tank filled with ambient liquid and a drop falls on the ground, the ambient liquid is decelerated suddenly by pressure waves generated by the impact. As a result, a relative motion between the drop and ambient liquid is realized and the deformation of the drop begins.

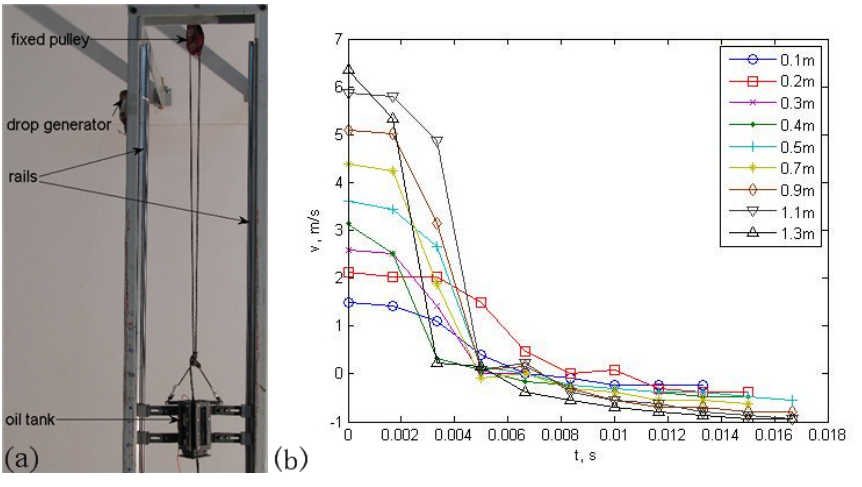

Fig. 1 (a) Drop tower device, (b) Velocity versus time during the deceleration of the tank at different heights

With this principle, a special drop tower system is built as shown in Fig. 1(a), which mainly consists of an tank with interior dimensions of $40 \times 40 \times 190$ *mm* serving as the test section, a fixed pulley for pulling the tank up, two pieces of 2.7 *m* high rails for the guidance of the tank, sands as damping materials, and a record system for visualizing the drop behaviors. The ambient liquid is transparent oil with a density of 810 kg/m^3. The drops come from dyed water which has been mixed with salt or alcohol to change the density ratio roughly from 1.0 to 1.6. Drops are generated by letting the water flow through a capillary tube into the tank in gravity. By controlling the diameter of the tube and the velocity of the flow, drop with different sizes from 2 *mm* to 10 *mm* can be produced and the reproducibility is excellent. The pendent drop method is employed to measure the interfacial tension. The record

system combines a high intensity light source and a high speed camera equipped with a 150 *mm* magnifying lens. The camera has a speed of 60 $frames/second$ with the highest resolution of 6 mega pixels. And the light source set at the back of the tank is intense enough to minimize the exposure time down to 0.1 *ms*.

Current facility provides both a weightless condition and a sufficiently long time for the drop to develop a nearly perfect spherical shape when the tank falls freely. By controlling the falling height, it is convenient to adjust the velocity before the impact. The cease of the ambient liquid over the interface of the drop can be considered instant. As shown in Fig.1(b), the tank stops in less than 10 *ms* which is much shorter than the roughly 100 *ms* drop-developing time observed in experiment. It should also be noticed that, the duration for setting up of an uniform ambient flow in this study is relatively longer than that of shock tube and continue jet method, which will result in a higher critical Weber number [7].

3 Results and Discussions

Under various operational conditions, six distinct modes of drop deformation and breakup are revealed in this study. Typical sequential images of drop development are shown in Fig.2 and Fig.3. Taking the centroid of drop as the reference, the incoming ambient flow moves upward. It is found that several parameters, such as densities of the drop and ambient oil, the interfacial tension, the initial drop diameter as well as the impulse generated by the falling tank, have significant effects on the behaviors of the drop evolution process. However, it is more meaningful to choose a few non-dimensional parameters, such as Weber number and Atwood number (At), to estimate the combined effects of the above factors. Useful parameters for all tested cases are summarized in table.1.

Table 1 Experimental conditions for Fig.2-3. *At* represents the Atwood number, *We* represents the Weber number

Fig	*Dropdimeter* (mm)	*Densityratio* (At)	*Interfacialtension* (mN/m)	*Fallingheight* (m)	*We*
$2(A)$	5.5	1.10(0.05)	7.57	0.1	1574
$2(B)$	5.5	1.10(0.05)	7.57	0.4	7860
$2(C)$	6.6	1.23(0.10)	33.7	0.5	2745
$3(A)$	6.6	1.23(0.10)	33.7	1.1	6851
$3(B)$	5.3	1.42(0.17)	40.3	1.2	5089
$3(C)$	9.1	1.60(0.23)	46.3	1.1	6876

When *We* and *At* are relatively low, the deformed drop tends to restore its initial spherical shape as shown in the three modes of Fig.2. With the increase of *We* and *At*, the drop undergoes a breakup process which produces tiny droplets as shown in Fig.3. Detailed descriptions and relevant discussions on the drop and its behaviors are given below.

3.1 Oscillatory and Bag Modes

When the *We* and *At* are relatively low, the oscillatory and bag modes appear firstly where the deformed drop tends to restore its original spherical shape due to the effect of interfacial tension. In oscillatory mode (Fig.2A), an indentation forms on top of the drop in the first place and then disappears soon, after which the drop displays oscillatory deformation without disintegration. For the first bag mode(Fig.2B), the indentation penetrates deeper. The downward inertia force concentrating along the central column is found to be responsible for the formation of indentation. This indentation develops further into a hollow bag attached to a thick circular rim, where the bottom of the bag is stretched into a thin layer. It is of interest to note that the bag here may persist the thin bottom layer and never breaks into pieces as its counterpart in gas flow. Later on, the effect of interfacial tension becomes dominant along with the dissipation of the initial disturbance, and the drop oscillates and recovers to its solidest shape. The other bag mode (Fig.2C) experiences similar process as the first one in the beginning. But at the final oscillation stage, the drop is prolonged in flow direction and then breaks into two drops of comparable size and a much smaller fragment in between.

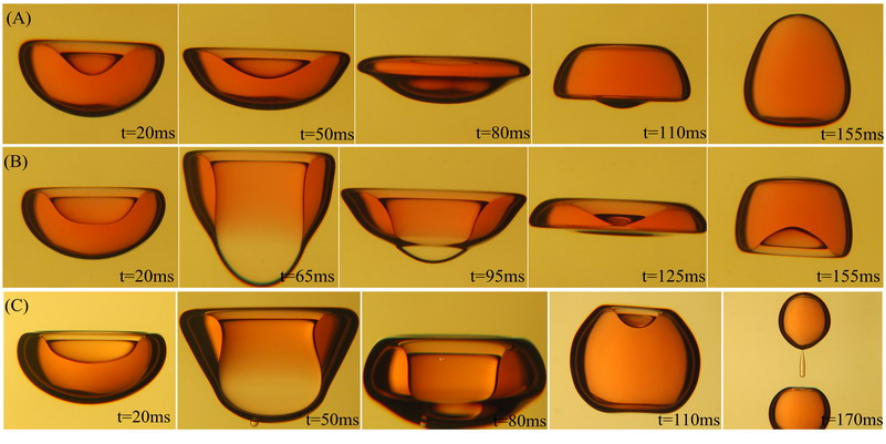

Fig. 2 a typical development of drop behaviors in oscillatory(A), backward-facing bag(B) and forward-facing bag(C) mode

In numerical studies of Han et al.[3] [4], the first bag mode is also referred as the backward-facing bag mode since in later stage an indentation is developed on bottom of the drop whose open end points to the opposite direction of the flow. The second bag mode is therefore referred as forward-facing bag mode as it never presents such an opposite indentation.

3.2 Cap, Bamboo and Mushroom Modes

With the increase of *We* and *At*, the cap, bamboo and mushroom modes are discovered. Similar to the former modes, the drop first develops an indentation and the indentation further extends to a bag with a thin bottom layer. A notable difference in the early stage is that now the vortex in equator becomes stronger and induces a annular jet inside the initially founded indentation. Another important difference appears in the later development of the bag, where thin bottom layer can no more stand the stronger stretching effect and breaks up into pieces due to interfacial tension.

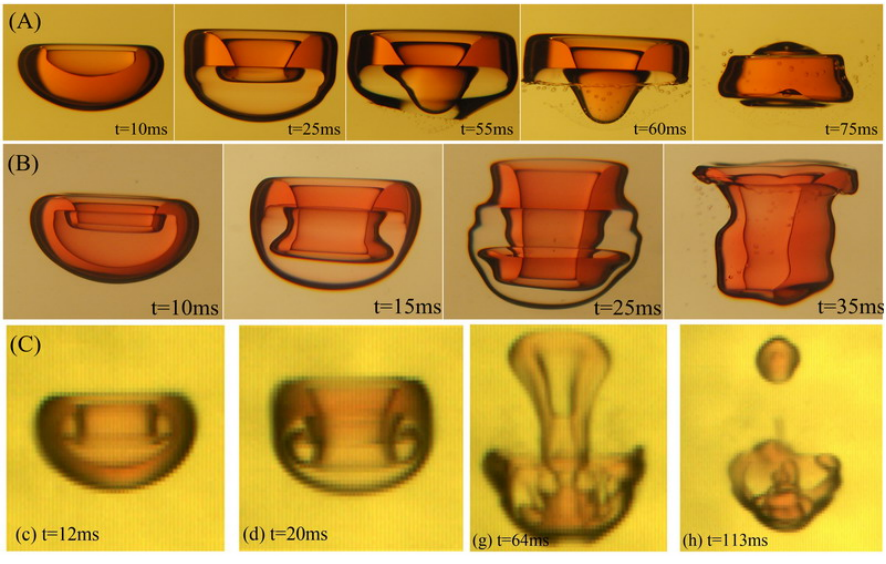

Fig. 3 a typical development of drop behaviors in cap(A), bamboo(B) and mushroom(C) mode, the drop shape at (A)$t = 60$ ms looks like a cap, (B)$t = 35$ ms a bamboo and (C)$t = 64$ ms a mushroom

Among those three modes there are differences as well. Firstly, the developing rate of the annular jet is obviously growing from cap mode to mushroom mode. In the cap mode the annular jet forms after the bag is established, whereas in the bamboo and mushroom mode it has emerged in early development of the indentation. Secondly, the deformation of the inflowing annular jet differs. The jet in cap mode converges when it's growing downwards, and the open head of it finally closes. When the bottom of the bag breaks, this converged jet sticks out to form the so-called 'cap' shape. As for bamboo mode, the jet keeps flipping until the rupture of the bag bottom. After that, it becomes rather stable and tends to close up as well. In mushroom mode, the jet flips continually and prolongs the drop vertically even after the outer bag disappears. It then further breaks into two main pieces accompanied by lots of tiny fragments.

It's also worthy of mention that unstable waves are observed on the thin film of the bag in these three breakup modes. The mechanism of them is still to be understood.

4 Conclusions

The drop tower technique developed in this study is found to be an excellent method to investigate the deformation and breakup process of a spherical liquid drop in ambient liquid subjected to a sudden impact. Six modes, i.e. oscillatory mode, backward-facing bag mode, forward-facing bag mode, cap mode, bamboo mode, and mushroom mode, are experimentally revealed, which in sequence correspond to an increase of deformation rate. The first three modes occur at a relatively low Weber number and Atwood number, and the deformed drop tends to restore its initial spherical shape. The later three are discovered at higher Weber number and Atwood number, where the drop undergoes a notable breakup process. Those results demonstrate complicated competitions between inertia force, vortex effect which acts to distort the drop, and interfacial tension which tends to restore the deformed drop to spherical shape.

References

1. Theofanous, T.G., Li, G.J., Dinh, T.N.: Aerobreakup in Rarefied Supersonic Gas Flows. Journal of Fluids Engineering 126(4), 516 (2004)
2. Zhao, H., et al.: Morphological classification of low viscosity drop bag breakup in a continuous air jet stream. Physics of Fluids 22(11), 103–114 (2010)
3. Han, J., Tryggvason, G.: Secondary breakup of axisymmetric liquid drops. I. Acceleration by a constant body force. Physics of Fluids 11(12), 3650–3667 (1999)
4. Han, J., Tryggvason, G.: Secondary breakup of axisymmetric liquid drops. II. Impulsive acceleration. Physics of Fluids 13(6), 1554–1565 (2001)
5. Igra, D., Ogawa, T., Takayama, K.: A parametric study of water column deformation resulting from shock wave loading. Atomization and Sprays 12(5-6), 577–591 (2002)
6. Duan, R.Q.A., Koshizuka, S., Oka, Y.: Numerical and theoretical investigation of effect of density ratio on the critical Weber number of droplet breakup. Journal of Nuclear Science and Technology 40(7), 501–508 (2003)
7. Gelfand, B.E.: Droplet breakup phenomena in flows with velocity lag. Progress in Energy and Combustion Science 22(3), 201–265 (1996)
8. Guildenbecher, D.R., Lopez-Rivera, C., Sojka, P.E.: Secondary atomization. Experiments in Fluids 46(3), 371–402 (2009)
9. Aalburg, C., van Leer, B., Faeth, G.M.: Deformation and drag properties of round drops subjected to shock-wave disturbances. AIAA Journal 41(12), 2371–2378 (2003)

Application of Laser Holography and PDPA Technology in Spraying Fuel Particle Field Measurement

Zhang Long, Guo Long-de, Zhang Li-hu, and Guan Ping

1 Introduction

For starting and running an engine successfully, the fuel must be mixed with high-speed air rapidly and fully in the combustor. The atomization quality of fuel impacts on the fuel mixture. Therefore study on fuel injection, atomization, diffusion and mixing quality is important, and the measurement of fuel size and spatial distribution is the key to the engine research.

Both PDPA and laser holography can be used to measure aerosol particle field. However PDPA can't be used to deal with the particle field in the experiment wind tunnel where the flow speed is over 1000m/s, the size of atomized particle is in microns, and the running time of wind tunnel is less than hundreds milliseconds. Correspondingly the clear holograms of particle field can be captured by using laser holography instantly, just like the high velocity particles are "freezed". The holograms can provide the distribution, shape, size and other information of fuel particles. At first we measured fuel atomization particle field in this two methods in the circumstance of not having incoming flow. The results of measurement are compared with each other. The result of comparison confirms the reliability of laser holography method. So laser holography method is used to measure the fuel particle field in the wind tunnel experiment.

2 Measurement Theory

2.1 Principle of PDPA

Phase Doppler Particle Analyzer (PDPA) is a modern advanced flow field non-contact measurement method, which obtains the speed of particle by measuring the

Zhang Long · Guo Long-de · Zhang Li-hu · Guan Ping
China Aerodynamics Research and Development Center
Mianyang, China

Doppler frequency shift and gets the size of fuel particle by measuring the phase of scattering light passing through transparent spherical particles. This method can be expressed as the formula.

$$\Phi = F(m)d_p \tag{1}$$

Where Φ is the phase difference, m is the particle refractive index, $F(m)$ is a transfer function which is based on different scattering types, and d_p is the particle diameter. The PDPA system consists of the optic launching system, the optic receiving system, signal processing systems, displacement system, computer and application software. Fig 1 is the schematic of a typical PDPA system.

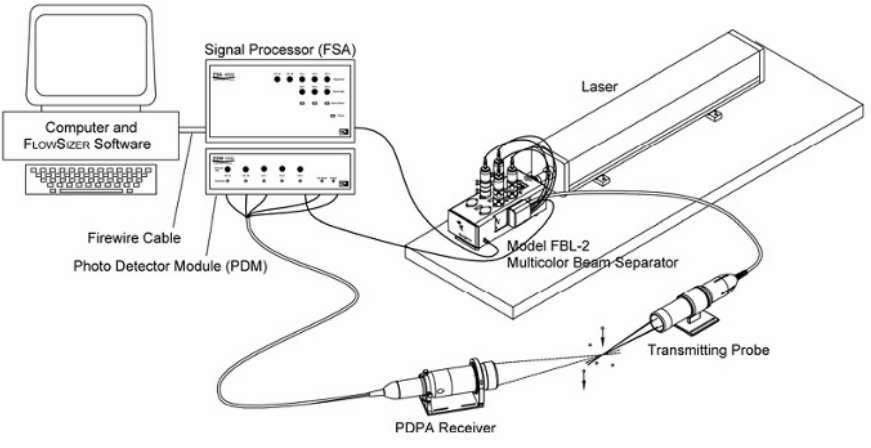

Fig. 1 Schematic of a PDPA system.

2.2 *Principle of Laser Holography*

When a high-coherence pulse laser beam irradiates the particle field, the information can be recorded by the holographic interferogram. During the process of holographic reproduce, images of particle field can be reproduced and recorded layer by layer according to the system field depth and particle far-field conditions. Then the relative size value can be obtained after computer image processing. In accordance with known size of calibrated silk thread or standard particle , the absolute size of atomized particle can be confirmed. With statistical analysis particle density and other parameters can be obtained.

Particle Field Holography measurement system consists of recording, reproduction and data processing parts. The recording system includes pulsed laser, synchronization signal controller, holographic optical system, etc. The reproduction system

consists of a CW laser, the reproduce optical system, a fine-tuning device of stratified reproduction, CCD camera and computers of controlling and recording. Data processing system includes image analysis and processing, verification of particle in focus, particle size analysis and statistical analysis of atomization field. Fig 2 shows the holographic optical recording system (off-axis hologram), and Fig 3 is the holographic reproduction image acquisition system.

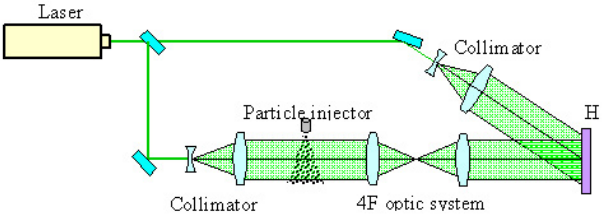

Fig. 2 Schematic of a laser holography system.

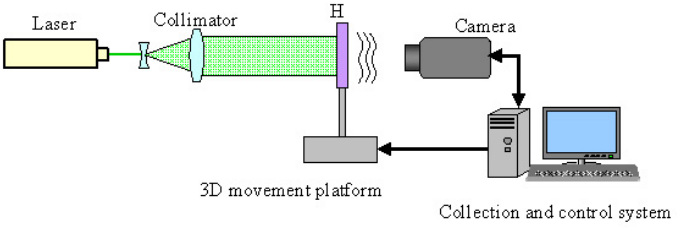

Fig. 3 Schematic of the holographic reproduction system.

3 Comparison Experiment

In the comparison experiment the water is atomized from the injector by the high-pressure gas. The atomization particle field is in the measuring area of PDPA or laser holography device. The main parameters of the test are as follows. The diameter of spray nozzle is 0.5mm. The pressure of gas is 4Mpa.The distance between the nozzle and the center of measuring area is 200mm.The spray liquid is water.

3.1 Measurement Results Based on PDPA

The injection time and the requirement of statistical analysis being considered, the statistical amount of particle measured by PDPA is set as 5000 in this experiment. Fig 4 shows statistical distribution results of particle diameter measured by PDPA. In the diagram the abscissa is the diameter of spray particle (unit um). The vertical

axis is the statistical number of particle. According to the measured result of particle, the smallest particle diameter is about 3um, the biggest particle diameter is 267um (no more than 300um). The highest repetition frequency of particle diameter is 16um,which is about 200.The amount of particles whose diameters are less or equal to 20um is 1321. So the statistical particle diameter D_{32} is 94.91um. After repetitious measurements the D_{32ave}= 95.95um.

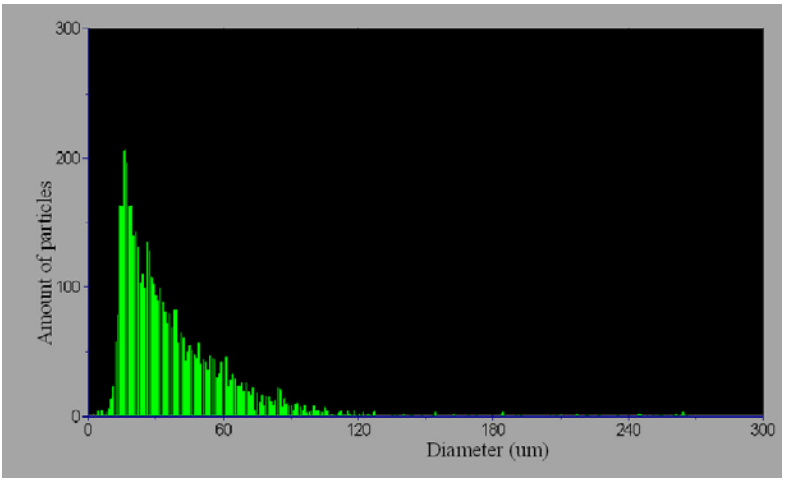

Fig. 4 Distribution of particle diameter measured by PDPA.

3.2 Measurement Results Based on Laser Holography

Fig 5 shows the statistical result based on 125 holographic reproduction images. In the diagram the abscissa is the particle diameter(um). Vertical axis is the particle amount.The volume of statistical area is approximately $2.5 \times 2.5 \times 0.4cm^3$, in which the particle amount is about 4700. As the interval between layered reproduction images along the optical path is defined as 1mm, the information of the particles between the two layers, especially small-size particles, is lost. Consequently the actual amount of particles is more than the statistical amount. Fig 5 shows the statistical distribution of particle diameter. The smallest particle diameter corresponding to the amount peak is 13um and the amount is 1458. There are 680 particles whose diameter are 21um corresponding to the second amount peak. The amount of big size particles shows a downward trend. The total statistical diameter D_{32} is 97.97um which is very close to the measured result based on PDPA.

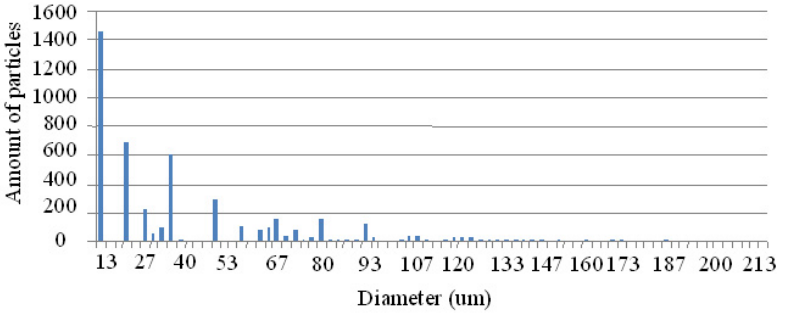

Fig. 5 Distribution of particle diameter measured by laser holography.

4 Experiments in Wind Tunnel

The comparison experiment of two methods on the same nozzle in the same condition indicates that the laser holographic measurement technique is feasible to measure the spray particle field. The error satisfies the requirement of engineering application. In view of the characteristics of two technologies, the laser holography can deal with the transient injection particle field in the shock wave wind tunnel only. Based on this method, the statistical information such as the diffusion of spray fuel and the particle size is easy to be obtained by holographic recording, latter stratification reproduction, digital image processing and identification of spray particles field. Fig 6(a) is a part hologram of the spray particle field acquired in the condition that Mach number is 2, the diameter of the spout is 0.5mm and the injection pressure is 2MPa. In Fig 6(b), the point (0,0) is the position of spout, x direction is corresponded to the flow, y direction is corresponded to the spraying and z is the optic axis. The sampling volume of mesurement area is 2mm×0.75mm×0.1mm.

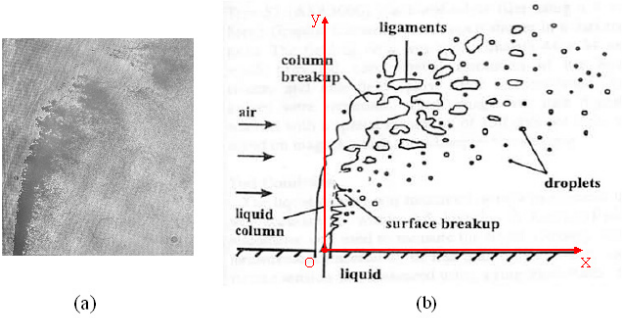

Fig. 6 Part hologram of spray field and schematic of the spray field coordinate.

After layered holographic reproduction of the hologram and spatial reconstructing, the spacial distribution of the spray particles can been obtained. Through statistical calculation, the analysis results show that D_{32} is less than 10 um in two serial samples mostly.

5 Conclusion

PDPA and laser holography are two completely different methods to measure particle field. As a sophisticated commercial instrument, PDPA can accurately measure and give the real-time result about the speed and diameter of particles. The error is generally less than 1um. However, it is a temporal statistical measurement, it requires a stable flow is long enough. The speed of particle is usually less than 500m/s. When laser holography is used to measure the particle size, the flow field can be recorded in an instant. For the laser pulse duration of this system is 150 picosecond, the velocity of particle and the stable duration of flow in wind tunnel test can fulfill the measure demand. Moreover three-dimensional spatial distribution of spray field can be obtained with this method. Although laser holography particle field measurement needs heavy work in data processing, with the development of computer technology, the processing time will significantly be shortened and the method will be more useful and reliable. In short, in the field of particle analysis, PDPA can provide higher precision and relatively simple operation. Laser holography can provide overall information. Especially it can be used in high speed or pulse wind tunnels. So it is more suitable than the PDPA for wind tunnel test.

References

1. Liu, C., Zhao, H.: Liquid fog and laser particle measuring principle. Aerospace Press (1988)
2. Yu, G.X.: Laser holographic technology and its industrial application. Aviation Industry Press (1992)

Secondary Atomization on Two-Phase Shock Wave Structure

E. Del Prete, J.-F. Haas, A. Chauvin, G. Jourdan, L. Houas,
A. Chinnayya, and A. Hadjadj

1 Introduction

The use of sprays in liquid and gas flows covers a wide range of applications [1]. The efficiency of such multiphase systems to mitigate the devastating effects of blast waves which are issued from explosion is well known [2]. Indeed during shock loading, the water mist is subjected to aerodynamic forces from the carrier phase, which leads to a secondary atomization [3] of its individual liquid components. This induces a drastic increase of interfacial surface as well as interphase exchanges. Two-phase shock wave is known to show a long-time self-similarity behavior. The aim of this work is to investigate the transient pressure build-up due to secondary atomization and to confront the results from shock tube experiments with numerical modeling.

An initially spherical droplet can be immersed in a gaseous environment whose velocity is different. The drop is then subjected to aerodynamic forces that can deform it. This distortion is accompanied by surface and/or Rayleigh-Taylor instabilities, which are responsible for the breakup of the droplet into smaller fragments. This process is inferred to as secondary atomization [1, 3].

On the one hand, the inertial forces are responsible for this droplet deformation and distortion. On the other hand, surface tension forces tend to restore the sphericity of the liquid fluid. The Weber number is then defined as the ratio between these inertial and surface tension forces. A greater Weber number reflects a higher propensity to atomization. The liquid viscosity inhibits this deformation as it dissipates the energy which comes from the aerodynamical forces. So to some extent, the tendency to secondary atomization is reduced. The Ohnesorge number represents the ratio

E. Del Prete · J.-F. Haas
CEA, DAM, DIF, F-91297 Arpajon, France

A. Chauvin · G. Jourdan · L. Houas
IUSTI-CNRS, Aix-Marseille Universite, 5 rue Enrico Fermi, F-13013 Marseille, France

A. Chinnayya · A. Hadjadj
CORIA UMR CNRS 6614, Site du Madrillet, F-76801 Saint-Etienne du Rouvray, France

between liquid viscous forces and the surfaces tension forces. A bigger Ohnesorge number will result in lesser atomization.

Secondary atomization comes from the interaction of a droplet and its gaseous environment. Thus it depends on the flow conditions. Different breakup modes can be observed for Newtonian droplets: vibrational, bag, multimode (often called bag-and-stamen), sheet-thinning, and catastrophic. One can refer to Guildenbecher *et al.* [3], Gelfand [1] and Pilch and Erdman [4] for a complete review.

The phenomenology of the secondary atomization of one single droplet under shock impingement can be schematically decomposed into two steps [1]: a deformation stage and the droplet breakup, strictly speaking into a large number of smaller droplets. A time scale τ_1 related to the first deformation step can be defined as in Eq. 1. In the right-hand side of these equalities, the subscript 1 refers to the liquid fluid whereas the subscript 2 refers to the gaseous phase. This time scale represents the ratio between the liquid inertia and the aerodynamical forces after the shock wave passage. This time scale is different from the velocity relaxation time scale between the gas and the drop τ_2 as in Eq. 2.

$$\tau_1 = \left(\frac{\rho_1}{\rho_2}\right)^{1/2} \frac{d}{|u_2 - u_1|} \tag{1}$$

$$\tau_2 = \frac{4}{3C_d}\left(\frac{\rho_1}{\rho_2}\right) \frac{d}{|u_2 - u_1|} \tag{2}$$

The ratio between the two time scale shows that the second one is one order of magnitude greater than the first one, which means that for one droplet, the deformation and atomization stages are very rapid compared to the velocity relaxation time scale.

According to [3, 4], the deformation process is a preliminary to the atomization process and it begins only if the Weber number is greater than a critical Weber number We_c. This critical number, usually around 12 for low viscosity fluids, indicates the limit between inertial and surfaces tension forces. It depends on a lower extent to the Ohnesorge number. Therefore, the secondary atomization is a two-stage process. The first one is a deformation phase where the atomization is almost absent. According to [1], [3] and [5], this deformation stage is completed when the time reaches approximately $2\tau_1$. The second one is the atomization phase. According to [1, 3], this phase is completed for $5\tau_1$.

2 Numerical Modeling

In order to incorporate this phenomenology into an eulerian multiphase model [6], we add an equation for the number of droplets n [7], in which $\dot{n}$ represents the droplet production source term [8]:

$$\frac{\partial n}{\partial t} + \frac{\partial n u_1}{\partial x} = \dot{n} \tag{3}$$

We have added also a new topological equation, which has proved to be necessary. τ is the time during which the droplet is in unstable aerodynamical conditions. It is defined by $\tau = t - t_0$ where t_0 is the first time where the Weber number is greater than We_c. So, τ is defined by Eq. 4.

$$\frac{\partial \tau}{\partial t} + u_1 \frac{\partial \tau}{\partial r} = \dot{\tau} \tag{4}$$

where $\dot{\tau}$ is equal to zero except when the Weber number is superior to We_c. The source term production by secondary atomization is modeled as proposed by [8]. The production term of droplets is explicated in Eq. 5.

$$\dot{n} = \begin{cases} ((d_\infty/d)^3 - 1)\dfrac{n}{\tau_b - \tau_i} \text{ if } \tau \geq \tau_i \\ 0 \text{ else} \end{cases} \tag{5}$$

where $d_\infty = \dfrac{We_c}{\rho_2 |u_1 - u_2|^2 / \sigma}$ is the maximal stable droplet size at the end of the aerobreakup process and σ is the surface tension coefficient. This model has been developed in conjunction with shock tube experiments.

3 Experimental Setup

The interaction of an incident shock wave with a rather dense water spray of 1.3 % volume fraction, with droplet diameter around $d \approx 500\,\mu m$, has been investigated. The experimental setup has consisted of the T80 shock tube of the IUSTI laboratory [9]. The details for the difficulty for synchronisation of all the chain of measurements can be found in [2]. Ten PCB Piezotronics gauges were used for pressure measurements in both high- and low-pressure chambers. Two shock Mach numbers have been considered: 1.3 and 1.5. An illustration of the shock tube configuration is given on Figure 1.

The two gauges placed in the high-pressure (HP) chamber have enabled us to determine the sound speed of the rarefaction waves, and thereby the temperature. The thermodynamical variables of the problem: temperature and pressure could then be completely determined. The gauges C7 and C8 were located outside the water mist. So it was possible to know precisely the velocity of the incident shock wave before interaction with the droplets cloud. The gauges C1 to C6 were in the water mist. They have permitted the visualization of the secondary atomization and its effect on the shock structure.

Figure 2 depicts the results of experiments for a shock of Mach 1.5. The red and dark curves (respectively C8 and C7 gauges) show the behavior of a shock wave in air. The incident shock is followed by an equilibrium state which can be evaluated from the Rankine-Hugoniot relations. This equilibrium is interrupted by

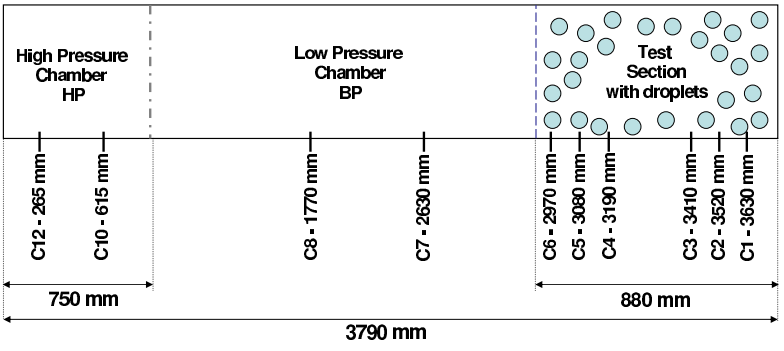

Fig. 1 T80 shock tube configuration and equipment

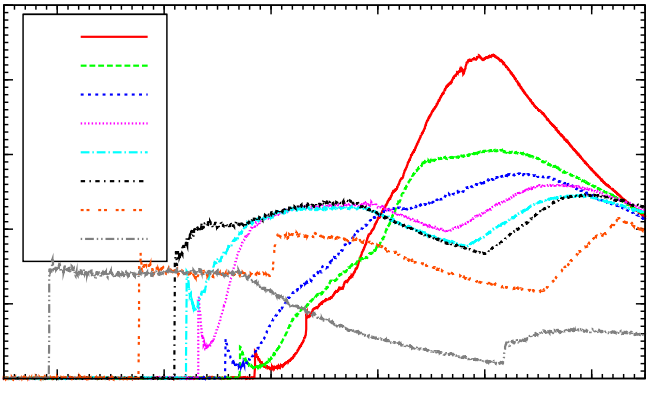

Fig. 2 Experimental results: pressure profiles with a water droplet cloud of 500 μm diameter for Mach number 1.5

the arrival of the rarefaction wave issued from the high-pressure chamber or the reflective shock on the water mist interface.

The gauges C6 to C1 were located within the droplet cloud. They present a particular structure. It can be seen that the presence of the droplets cloud diminishes the strength of the incident shock. The presence of this pressure peak seems to be the signature of the secondary atomization. Indeed, if the latter was absent, a classical two-phase shock structure would be present. We would then have a partially dispersed shock wave, i.e. a shock wave followed by a velocity and temperature relaxation zone. Moreover, this peak tends to diminish in strength as the shock moves away from its initial position. On C6, C5 and C4, a new equilibrium state can be defined at an overpressure of approximately 2.5 bars. It seems that this equilibrium state occurs after the end of the secondary atomization and at the end of the velocity

relaxation process of the newly formed droplets spray. Based on numerical simulation in next section, we will consider the physical mechanism of this evolution.

4 Numerical Results and Discussion

The mesh is composed of 1000 cells. The initial conditions in the shock tube was atmospheric conditions for low pressure chamber and the HP pressure was such that the Mach number of the incident shock wave was 1.5. The experimental determination of the sound speed of the rarefaction wave determines the sound speed and thereby the temperature of the HP chamber. The droplets cloud was defined by its volume fraction, droplets diameter and was present in the section of the shock tube between C6 and C1. Figure 3 depicts the results of the numerical simulation.

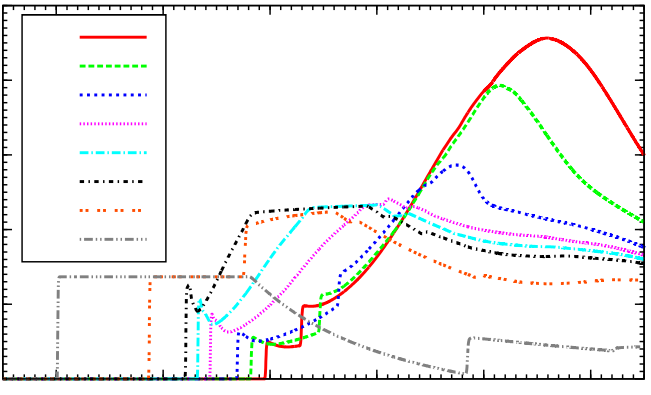

Fig. 3 Numerical results: pressure profiles with a water droplet cloud of 500 μm diameter for Mach number 1.5

It can be seen that the shock wave structure is globally recovered for the different pressure gauges. The C7 and C8 gauges are well reproduced. As in experiments, the presence of the droplets cloud change the shock structure for C1 to C6. It can also be seen that the new mechanical equilibrium present on C6, C5 and C4 on the experimental data is recovered in the simulations by the presence of a pressure plateau. It can be noticed that the level of the plateau is quite the same.

During the first stage of droplet deformation, as the diameter of the droplet is rather high, there is almost no drag. Then the drastic increase of secondary droplet number induces a large increase of momentum exchanges between the phases. The apparent mass of the liquid is ten times greater than that of the gas. So the liquid will strongly slow down the gas. This will generate rarefaction waves which will catch up with the shock wave and will decrease its intensity. Thus the shock wave is followed immediately by rarefaction waves. Then the remainder of the velocity

relaxation process continues. This manifests itself by the pressure build-up to the equilibrium state.

It can also be seen that the peaks of the numerical pressure profiles which are present initially within the spray are not as marked as in the experimental results. It is possible that these discrepancies are due to the choice made to define the secondary atomization model: critical Weber number value, size of the droplets after fragmentation, breakup time. The different coefficients that we have chosen were taken from the phenomenology of the sheet-thinning breakup. As the shock wave penetrates within the droplet cloud, the velocity difference and thereby the Weber and Reynolds numbers decrease. The times scale of the first deformation stage and the second atomization stage vary, as Pilch and Erdman have noted [4], in their compilation of the experimental data available at that time. These constants are to be tested in the model to improve the numerical results compared to the experimental results.

5 Conclusion

The numerical simulation are performed in a similar way using a multiphase compressible approach [6], in which a new sub-model is developed to account for the secondary atomization on a droplets cloud. It seems that the present model is adapted to the treatment of a dense water mist. Some other numerical arrangements and tests have to be conducted to improve the present results. But the present work represents a first step toward a full characterization of the attenuation of blast waves through an aqueous two-phase media [10]. The further developments of this characterization should allow the determination of the importance of the secondary atomization process on the blast wave mitigation by two-phase media.

References

1. Gelfand, B.E.: Prog. Energy Comb. 22, 3 (1996)
2. Jourdan, G., Biamino, L., Mariani, C., Blanchot, C., Daniel, E., Massoni, J., Houas, L., Tosello, R., Praguine, D.: Shock Waves 20, 4 (2010)
3. Guildenbecher, D.R., Lopez-Rivera, C., Sojka, P.E.: Experiments in Fluids 46 (2009)
4. Pilch, M., Erdman, C.A.: International Journal of Multiphase Flow 13, 6 (1987)
5. Hsiang, L.P., Faeth, G.M.: International Journal of Multiphase Flow 18, 5 (1992)
6. Chinnayya, A., Daniel, E., Saurel, R.: Journal of Computational Physics 196 (2004)
7. Saurel, R., Le Métayer, O.: Journal of Fluid Mechanics 431 (2001)
8. Kolev, N.I.: Thermal and Mechanical Interactions, 3rd edn. Springer (2007)
9. Jourdan, G., Houas, L., Schwaederle, L., Layes, G., Carrey, R., Diaz, F.: Shock Waves 13 (2004)
10. Del Prete, E., Domergue, L., Haas, J.-F., Chinnayya, A., Hadjadj, A.: Numerical Modeling and Experimental Investigation of Blast Wave Attenuation by Dry Aqueous Foams. Submitted to ISSW28

Dense Particle Cloud Dispersion by a Shock Wave

M. Kellenberger, C. Johansen, G. Ciccarelli, and F. Zhang

1 Introduction

The study of particle cloud dispersion by a shock wave is important to many applications, including multiphase explosives that comprise a condensed explosive surrounded with packed micrometric reactive metal particles. Detonation of the explosive generates a shock wave which accelerates and compacts the particles. The particles are further accelerated from the reflected rarefaction as the shock wave arrives at the free-surface of the particles, leading to their rapid dispersal into the air. Generally speaking, the shock wave initially propagates through a granular particle bed and much later in time the particle cloud is dispersed and the flow becomes a dilute gas-solid flow. Between these two regimes the flow is characterized by a dense gas-solid flow [1]. Reactive multiphase flow models have been used to simulate the acceleration and dispersion of the particle cloud [2]. The fidelity of the simulations is severely limited by the physical drag models that need to take into account the interactions in the dense gas-solid flow [1]. In order to develop an accurate particle drag model that describes particle acceleration in the dense flow regime, representative experimental data need to be generated. While dispersal experiments have been carried out using a spherical multiphase explosive charge [3], controlled shock wave experiments are necessary to gain understanding of the fundamental physics of the dense supersonic gas-solid flow interactions and quantitative data concerning the particle cloud dispersion. Shock tube experiments have been carried out but typically the particle suspension method influences the shock flow [2] and the particle size is not typical of multiphase explosives. This paper reports on shock tube experiments looking at the acceleration and dispersion of 100 micron-sized aluminum oxide particles. The shock wave propagating into the packed particles provides a low-pressure analogy to multiphase explosive dispersal.

M. Kellenberger · C. Johansen · G. Ciccarelli
Queen's University, Mechanical and Materials Engineering, Kingston, Canada K7L 3N6

F. Zhang
Defense Research and Development Canada-Suffield, Medicine Hat, Canada T1A 8K6

2 Experimental

The shock tube consists of a 1.96 m long, 10 cm diameter driver, a transition section, and a driven section consisting of five 0.6 m long, 7.6 cm square sections as shown in Fig. 1. The transition section is 0.75 m long. A double diaphragm is used to precisely control the driver pressure. Helium is used in the driver and atmospheric air is used in the driven section. Piezoelectric pressure transducers are flush-mounted on the top surface of the driven section, see Fig. 1 for locations. The optical section is equipped with glass windows for flow visualization. A single-pass shadowgraph system is used in connection with a Photron SA5 high-speed video camera to record the shock trajectory and the particle cloud movement. The camera field-of-view covers half the length of the optical section window shown in Fig. 1.

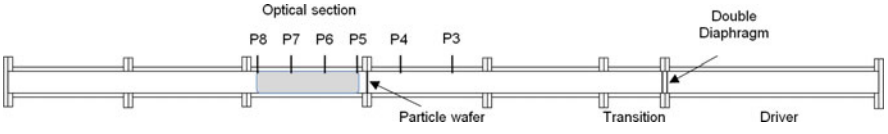

Fig. 1 Schematic of shock tube

The particle wafer is created by compressing 65 g of aluminum oxide powder into a 7.6 cm square cavity machined into a 6.4 mm thick plate that is placed between the flanges between P4 and P5, 1.97 m downstream of the diaphram, as seen in Fig. 1. The particle wafer has a volume fraction of 0.44 and the aluminum oxide powder has a mean particle diameter of 100 μm. A laser based system is used to estimate the local particle cloud density. The 670 nm beam from a 3 mW diode laser is expanded via a series of lenses to roughly 1.5 cm in diameter. The expanded beam enters the channel perpendicularly and is focused onto a 5.1 mm silicone photodiode. The beam passes through a 670 nm filter and a 0.5 mm pinhole in order to minimize the amount of ambient light reaching the photodiode. Calibration of the system was performed in a small acrylic 7.6 cm long, 4.45 cm diameter cylindrical vessel. A known amount of powder was placed on the bottom of the vessel and a high velocity jet of air is used to disperse the powder evenly throughout the vessel. The light attenuation through the particle cloud is recorded in terms of the drop in photodiode voltage output versus the average cloud density (total mass/vessel volume). The calibration was carried out in the range of cloud density of 13.5 kg/m^3 to 60.0 kg/m^3. The calibration provided the following linear relationship between the photodiode voltage drop (ΔV) in mV and the cloud density (ρ_c) in kg/m^3: $\Delta V = -0.0075\rho_c$.

3 Results and Discussion

Reference tests were performed with a solid Delrin plug placed in the same location as the particle wafer. The plug was of the same mass as the particle wafer and was loosely inserted inside the channel. The data from one such experiment with a driver

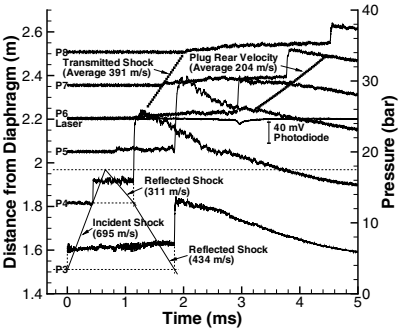

Fig. 2 Results for 11 bar abs. helium driver with solid Delrin plug

pressure of 11 bar absolute is provided in Fig. 2. The incident shock wave reflects off the back of the plug producing a reflected shock wave that propagates back as measured at P4. The loose insertion of the plug resulted in the bypassing of some of the reflected shock gas that results in a shallow pressure gradient in front of the plug. The interaction of the shock wave with the plug produced a transmitted shock wave and a moving plug. The most interesting finding is that there is a well-defined pressure pulse whose shock-like front dictates the motion of the plug back. The peak pressure originates in the reflected shock and decays as it propagates down the channel due to expansion. In this test, the photodiode was located at the same position as P6 and the pressure transducer and photodiode signals both indicate the arrival of the plug at the same time. The photodiode output voltage drop is very small since the time of flight for the plug across the laser beam is on the order of the response time of the photodiode and the plug is thinner than the laser beam.

Results with the particle wafer obtained from two tests performed with a 6.5 bar absolute driver pressure and atmospheric pressure in the driven section is shown in Fig. 3. The camera field-of-view for the test results in Fig. 3a consists of the first half of the window, see Fig. 1. For the results shown in Fig. 3a, the incident shock wave velocity measured from the shock time-of-arrival between P3 and P4 is 581 m/s. The incident shock wave reflects off the particle wafer producing a reflected shock wave that propagates back at an average velocity of 316 m/s. The pressure behind the reflected shock wave measured at P4 remains relatively constant at about 8.5 bar over a period of roughly 0.4 ms, after which time the pressure starts to drop off. Based on the incident shock wave velocity the theoretical reflected shock velocity and pressure that would be produced upon reflection from a solid immobile surface are 333 m/s and 8.4 bar, respectively. The close correspondence between the measured and theoretical reflected shock parameters indicates that the back of the wafer remains largely intact after the reflection and there is very little initial forward movement of the wafer over this time. When the wafer starts to move forward, expansion waves propagate back towards the reflected shock wave dropping the pressure along the way. By the time the reflected shock wave reaches P3 the head of the expansion has

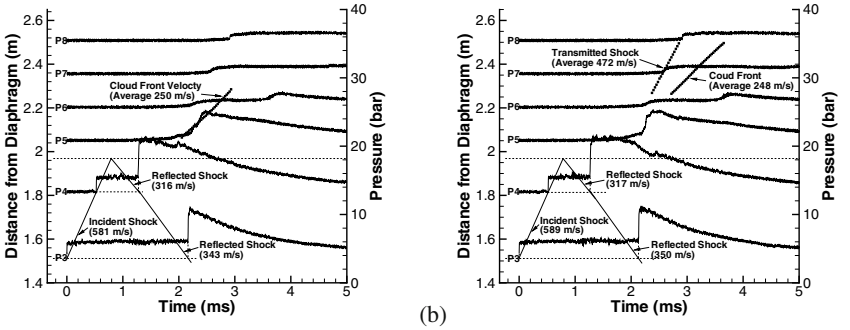

Fig. 3 Results for 6.5 bar abs. driver pressure with the camera field-of-view covering (**a**) the first half of the optical section and (**b**) the second half of the optical section

caught the shock wave and the pressure behind the shock wave drops immediately. The initial slow forward motion of the wafer produces compression waves that move ahead of the wafer. This causes the pressure at transducer P5 to rise slowly. A pressure front forms at P6 that steepens with distance as the compression waves merge. At P8, the compression waves have coalesced to form a shock wave characterized by a steep pressure rise at roughly 3 ms in Fig. 3a.

As long as the back edge of the particle wafer remains intact, it acts like a piston driven by the high pressure produced by the reflection of the incident shock wave. The passage of the rear edge of the wafer therefore passes P5 at 2.2 ms in Fig. 3a when a large pressure rise is recorded. The finite pressure rise-time recorded at P5 indicates that the back of the wafer is no longer a sharp impermeable interface. Instead the wafer becomes porous, i.e., dense particle cloud, with an associated pressure gradient driven flow through it. The pressure pulse propagates forward at a velocity slower than the transmitted shock wave and the magnitude of the pressure pulse dramatically decreases with distance. Also shown in Fig. 3a is the position of the front edge of the particle cloud taken from high-speed video images shown in Fig. 4. The front edge of the cloud moves at a velocity of 250 m/s. From Fig. 3a it is clear that the front edge of the cloud passes the transducer P5 position before the large pressure pulse, which is associated with the passage of the back edge of the particle cloud. More importantly is the fact that the distance between the front edge and back edge (deduced from the pressure pulse) of the cloud increases with propagation distance.

Shown in Fig. 4 is a compilation of high-speed video images taken from the two tests represented by Fig. 3. The initial wafer location is 8.5 cm beyond the right edge of the field-of-view. As the cloud front edge moves forward a weak compression wave forms that eventually is reinforced to form a shock wave by the left edge of the field-of-view, corresponding to the transducer P8 location in Fig. 1. The back edge of the cloud is not viewable because particles are trapped in the slow moving boundary layer flow next to the windows. Particles acquire a static charge during

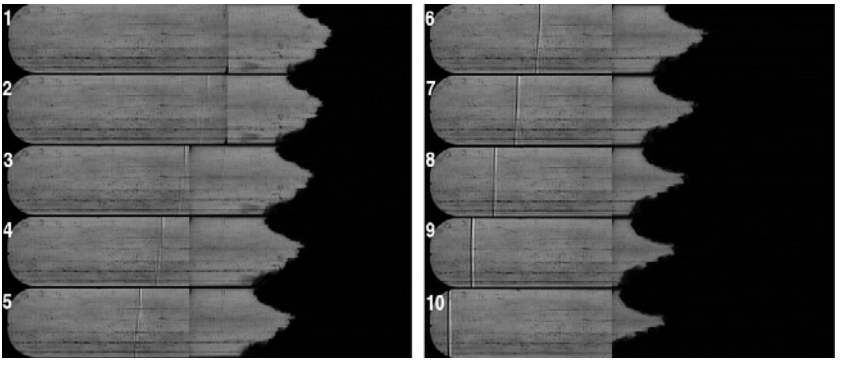

Fig. 4 Compilation of two videos from tests with 6.5 bar abs. helium driver

their motion and adhere to the glass windows. The position of the front edge of the particle cloud and the forming shock wave obtained from the video images from a test where the camera field-of-view covers the second half of the window is plotted in Fig. 3b. The velocity of the transmitted shock wave obtained from the video images is 472 m/s. The transmitted shock wave position obtained from the video agrees very well with the pressure rise recorded at P7 and P8. The video images indicate that the front edge of the cloud propagates at a velocity of 248 m/s. This measured cloud front edge velocity is higher than the theoretical particle velocity of 181 m/s behind the 472 m/s transmitted shock wave.

Results obtained from tests performed with an 11 bar absolute driver pressure and atmospheric pressure in the driven section are shown in Fig. 5. The test results shown in Fig. 5a shows an incident shock velocity of 698 m/s is produced. The reflected shock pressure at P4 is 14 bar, which is lower than the theoretical value of 15.6 bar. The motion of the wafer produces a transmitted shock wave of velocity

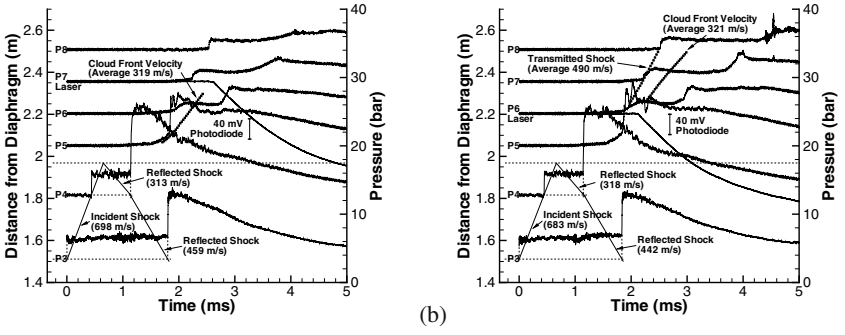

Fig. 5 Results for 11 bar abs. driver pressure with the camera field-of-view covering (**a**) the first half of the optical section and (**b**) the second half of the optical section

507 m/s measured between P7 and P8. On transducers P6 to P8, the transmitted shock wave is followed by a well defined pressure rise associated with the back edge of the particle cloud. As observed in the 6.5 bar driver tests shown in Fig. 3, the pressure rise-time increases as the wafer develops into a dense particle cloud. Based on the video, the velocity of the front of the cloud is 319 m/s, which again is significantly faster than the theoretical particle velocity of 233 m/s behind the 515 m/s transmitted shock wave. Also shown in Fig. 5a is the voltage output obtained by the photodiode located at the axial position coincident with P7. When the front edge of the cloud interrupts the laser there is a drop in the photodiode output voltage. The start of the drop in the photodiode voltage at 2.7 ms agrees well with extrapolation of the trajectory of the front edge of the cloud from the video. There is no recovery in the voltage which is consistent with the video that does not show the back edge of the cloud. The arrival of the back edge of the cloud can be inferred from the arrival of the pressure pulse at P7. In contrast to the shock-like pressure pulse associated with the moving solid Delrin plug in Fig. 2, the pressure structure of the dense multiphase between its front and back edge is fully dissipative. The exact location of the cloud back edge must be after the pressure maximum due to expansion dispersion into rear flow. The data from a test performed under similar conditions with the laser located at P6 is provided in Fig. 5b. In this test the photodiode shows an initial drop at 2.2 ms, consistent with extrapolation of the trajectory of the front edge of the cloud from the video. The arrival of the back edge of the cloud at P6 is again identified after the pressure maximum at 3 ms. The corresponding photodiode voltage at 3 ms is 80 mV, which gives an apparent local cloud density of 10.7 kg/m^3.

4 Conclusions

While the front particles are initially dispersed through the reflected expansion upon the transmission into air, the clear finding here is that the reflected shock generates in the back of the granular bed a pressure pulse that is the driving force to maintain the forward motion of the all the particles. Tests will be conducted with thicker wafers to gain insight into the correlations of the pressure wave structure with the granular bed thickness. The obtained transition phenomena and wave structure will be used to validate the constitutive relations and drag model used in numerical modeling.

References

1. Zhang, F., Frost, D., Thibault, P., Murray, S.: Shock Waves 10, 6 (2001)
2. Rogue, X., Rodriguez, G., Haas, J.F., Saurel, R.: Shock Waves 8, 1 (1998)
3. Frost, D., Zhang, F.: Proc. 19th Military Aspects of Blast and Shock (2006)

Dynamic Jet Formation from Mitigation Materials

C. Parrish and I. Worland

1 Introduction

This work has been carried out to improve the methodology and understanding of mitigating against the effects of large explosive charges. This research specifically focuses on the physical processes involved in the expansion of granular materials. This is an area which has been investigated empirically in the past [1], but still lacks a thorough understanding. Hydrocode calculations are unable to predict the inhomogeneous expansion seen in experiments [2] and thus little confidence can be held in their ability to accurately predict the mitigating mechanisms.

The regime of most interest to AWE is that of a mitigated charge in an enclosed environment where the near field effects are still prominent [3]. Prior experimental work has shown that dynamically fragmented material produces agglomerates with dimensions that are different to that of the original particulate material [4]. It is believed that the formation of these agglomerates, which at later times present themselves as jets, occurs early in the expansion of the mitigant. The use of radiography to image the early time behaviour without shrouding from the detonation products inspired a series of trials to be performed at AWE to support the early results and EDEN (Fluid Gravity Engineering) models. 1D studies in isolation showed a deceleration of a two fluid interface, indicating that Rayleigh Taylor instability [4] is a possible mechanism for formation of the initial fragments. 2D calculations using the EDEN hydrocode, when compared to experimental data suggests that Rayleigh-Taylor instability occurs on too long a timescale and does not lead to the observed jetting structure. Initial analysis of this early phase has also been undertaken by Fluid Gravity Engineering, progressing Grady [5] dynamic fragmentation theories, however, initial observations suggested that a large surface energy would be required to represent the experimental data and it is difficult to imagine such a large surface tension to be present in finer particulates such as sand.

C. Parrish · I. Worland
AWE, Aldermaston, RG7 4PR

Important observations from experiments using embedded metallic particle explosives [6] indicate that the fireball size is not related to the initial metal particle size in experiments where the mass is conserved but the particle sizes differ. Recently published work has focussed on the formation of the initial agglomerates; Frost *etal* performed a series of experiments to investigate the development of surface perturbations on packed beds during explosive events [7]. This work examines the relationship between the number of jets formed and the surface instability, referred to as the particle compaction Reynolds number. This extends the earlier work of Grady and assumes that the ratio of inertial to viscous forces acting on the particles is responsible for the granular bed breakup. This paper will consider this relationship and assess whether the AWE data contributes to this theory.

2 Experimental Evidence

An initial series of nine Rapid Prototype Design (RPD) experiments were performed at AWE in 2008 [2]. Analysis of the data from the initial trials has shown a trend between agglomerate size at break-up for the different mitigants. There is also consistency between the number of early features and late time jets. This paper details the results of four further Dynamic Fragmentation Physics (DFPhys) trials performed in 2010 to investigate system scaling. Previous mitigation trials at AWE have suggested that the mass of the system is key to the overall blast reduction [3] and so understanding if the mechanisms which are responsible for the expansion phenomenon scale with mass is of great interest.

As the previous series confirmed continuity of jet number between early and late times, the radiographic diagnostic was not required for these trials. High speed video (130,000 fps) and blast diagnostics were used to record the expansion. For simplicity of calculation a spherical geometry was used. The experimental shells were 2mm thick plastic spheres with a central spherical component for the explosive and a channel for the detonator as shown in Fig. 1. For reference see Table 1 which lists the four trial configurations.

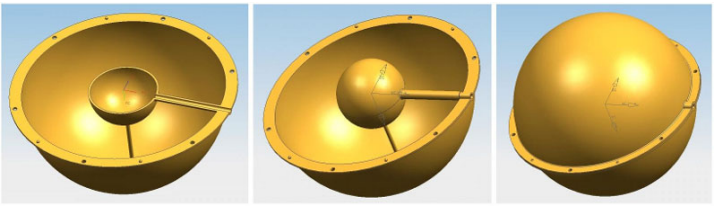

Fig. 1 DFPhys trials mitigated charge setup

Qualitative analysis of the video footage shows visible differences between the three materials as seen in Fig. 2. The two sand trials behaved as the previous RPD video footage, with distinct regular formations becoming visible soon after detonation and continuing to late times. The water displayed similar behaviour with an

Table 1 RPD and DFPhys trial configurations

Trial	Mitigant Type	Charge Mass	Mitigant Mass	Diagnostic
DFP01	Water	100g	1471g	High speed video
DFP02	Dry vermiculite	100g	1283g	High speed video
DFP03	Dry sand	100g	3086g	High speed video
DFP04	Dry sand	250g	3529g	High speed video

apparent higher frequency of structures formed. The dry vermiculite takes much longer to fragment through the shell, presumably due to the snow-plough compression process occurring due to the materials low density granular structure. Once the shell has fragmented the vermiculite expands in a similar way to the sand with more diffuse structures and an apparent fewer number. Solid fragments of the nylon shell are visible ahead of the vermiculite to late times, contrary to the water and sand videos where evidence of the shell disappears very early in the expansion. This suggests the energy available to fragment the shell is reduced by the vermiculite more effectively than the denser mitigants.

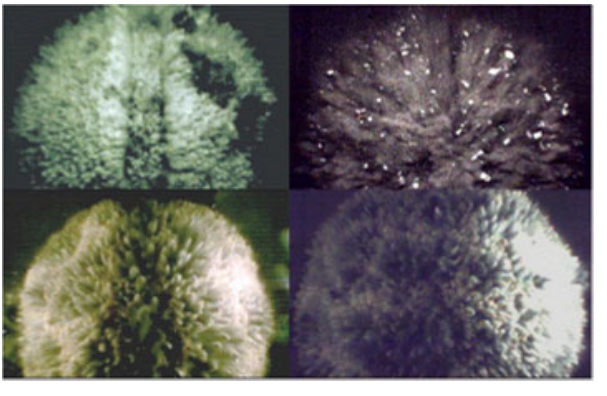

Fig. 2 Video stills from DFPhys Trials Clockwise from top left - DFPhys01 Water, DFPhys02 Vermiculite, DFPhys04 Sand, DFPhys03 Sand

Still frames from the videos were taken at suitable time intervals to provide at least four images showing clear, countable jets per trial. Having obtained the number of jets formed per experiment, the fragment size at breakup was calculated by assuming that all the mass of the experiment forms a single accretion layer as described previously [2]. This analysis, when using the predicted accretion layer density from calculations, also provides a radius of breakup for comparison. Table 2 shows a summary of the results and analysis from the trials, including the previous results from the earlier RPD series for comparison.

Table 2 RPD and DFPhys fragment breakup analysis

Trial	Number of jets/structures	Accretion layer density kg/m^3	Fragment radius r_f mm	Radius of break-up mm
RPD1 Vermiculite	378 ± 30	1130	9.22 ± 0.3	81.5 ± 1.3
RPD2 Sand	342 ± 40	1820	8.92 ± 0.35	75.0 ± 1.5
RPD3 Vermiculite	n/a	n/a	n/a	n/a
RPD4 Sand	365 ± 20	1820	8.72 ± 0.2	75.8 ± 0.8
RPD5 Case	n/a	n/a	n/a	n/a
RPD6 Vermiculite	450 ± 110	1130	8.38 ± 0.6	80.8 ± 3.0
RPD7 Sand	353 ± 40	1630	8.82 ± 0.3	75.4 ± 1.3
RPD8 Vermiculite	240 ± 40	2500	8.88 ± 0.4	62.97 ± 3.0
DFPhys01	729 ± 289	1000	7.84 ± 0.3	96.2 ± 1.8
DFPhys02	181 ± 25	2500	8.78 ± 0.25	53.7 ± 3.2
DFPhys03	546 ± 110	1820	9.05 ± 0.25	96.2 ± 2.0
DFPhys04	708 ± 94	1820	8.68 ± 0.3	105.0 ± 1.3

These results indicate that the trend seen in the earlier RPD experiments is not dependant on mass, as the fragment radii calculated for these trials at accretion layer density are consistent with the previous data, even after varying the system masses. This data supports the theory that the individual particles start life at approximately the same volume, however the assumption that they begin life as cubes or spheres is flawed as the radii representative of shells which would produce such particles are often smaller than the initial radius for compressible materials.

This information also suggests that the cohesion of the particles is a physical function independent of the mass of the system or material type. This implies that the theory set out by Grady [5] and developed recently by Frost *etal* [7] may explain the formation of these jets. Frost *etal* calculated the particle compaction Reynolds number for their trials and displayed it as a function of the number of jets produced for different materials. The particle compaction Reynolds number is defined below (1) where ρ is the density, U is the velocity, L is the mitigant thickness, γ_s is the particle mass density, c_s is the sound speed in the particle phase and d_s is the mean particle diameter.

$$Re = (\rho U L)/(\gamma_s c_s d_s) \tag{1}$$

The Reynolds number was calculated for all the RPD and DFPhys trials and can be seen plotted as a function of jet number in Fig. 3. The data presented here correlates well with the findings of Frost *etal*. There is a positive trend between the two variables with specific materials appearing in discreet groups. This confirms that for specific materials, the balance between the forces tending to fracture, and those tending to infinitely stretch, is proportional to the number of structures produced.

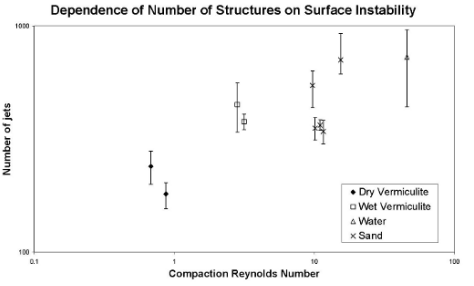

Fig. 3 Dependence of jet number on compaction Reynolds number

3 Calculations

One-dimensional calculations of the four DFPhys trials were performed in EDEN utilising the two-phase model and a cell size no greater than 0.2 mm. The best way to display such calculations is in the form of a density map as in Fig. 4. The greyscale on the plots represents the density of the mitigation, with the shock and detonation products overlaid in red and green. Also plotted is the experiment outer mitigation radius as obtained from the high speed videos, as blue crosses. This outer radius is not expected to represent the position of the accretion layer but either the outer case or detonation products as these can both shroud the accretion layer from view.

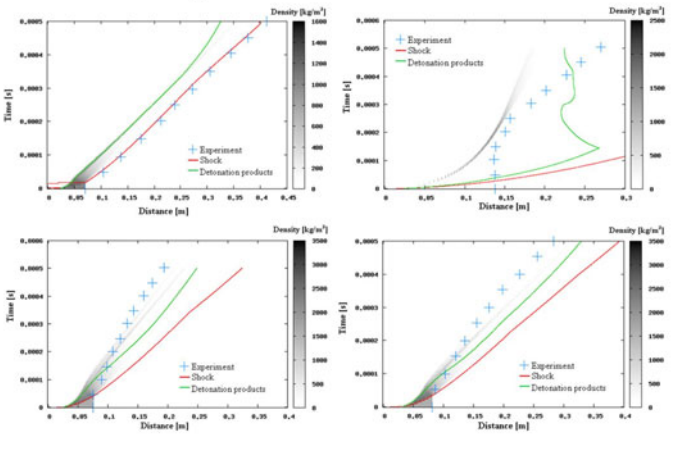

Fig. 4 Density profile maps Clockwise from top left - DFPhys01 Water, DFPhys02 Vermiculite, DFPhys04 Sand, DFPhys03 Sand

It can be seen that the calculation of DFPhys01 is a good representation of the experiment as the outer radius in the videos closely follows the outer spall layer in the simulation with the correct expansion velocity. The agreement is much less close with the remaining trials. The experimental expansion for DFPhys02 was difficult to determine from the videos as the material was so diffuse and the detonation products obscured the mitigant for most of the early stages. As a result the comparison to the 1D simulation shows the experimental velocity to be much higher than the calculated one, although not as fast as the detonation products. It is likely that a combination of the detonation products and the mitigation are observed and that distinguishing between the two as the detonation products become more diffuse is unachievable.

Both DFPhys03 and 04 behave in very similar ways, which is reassuring for both the simulations and the experimental results. In both cases the calculations predict that the sand will expand with a higher velocity than is observed on the experiments. The video images were clear and there was very little shrouding from detonation products at later times. Despite this the observed velocity was still less than that predicted. As the simulation does not represent the formation of jets or structures it could be attributed to the drag force discrepancy between individual particles as calculated in EDEN, or larger clumps of particles as visible in the experiment.

When considering the peak overpressure and impulse for each trial, a comparison has been made between those points where the side-on pressure was measured and those measuring the reflected pressure. The code to experiment comparisons are shown in Fig. 5. It can be seen that the side-on pressure is better represented by the 1D calculation than the reflected pressure. These plots also show that the calculations slightly under predict the peak pressure and over predict the impulse for the reflected pressure measurements. This indicates that the reflected pressure gauges may not be recording the incidence of the mitigating material properly. Additionally, the 1D calculations do not take into account reflections from surrounding objects which may amplify the peak overpressure. Further 2D calculations may improve the peak pressure predictions in this case.

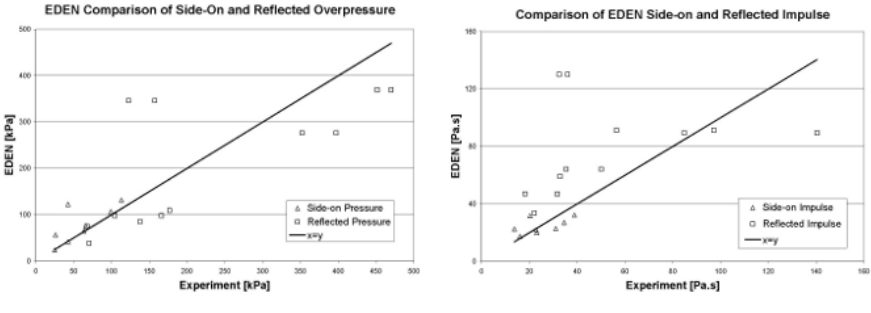

Fig. 5 Comparison of calculation and experiment for blast parameters

4 Conclusions and Discussion

The aim of this work was to investigate the mechanisms responsible for the inhomogeneous expansion of granular materials with the goal of more accurate computational representation. Analysis of the data shows similarities in the structure formation volumes for the different mitigant types, regardless of system masses. This suggests an inherent property of the process rather than the system variables. Comparison of the results to a theory building on the work of Grady [7] suggests that the structures may be the result of the ratio of inertial to viscous forces on the compacted layer of material. While an abundance of inertial forces would represent a situation where the bed fractured dispersedly; a dominance in viscous forces would suggest an infinitely expanding, thinning shell. The ratio of these forces should therefore be proportional to the number of structures formed for a given material irrespective of the system scale; this is evident in the graphical representation of these trials.

Comparison of the experimental velocity data to the EDEN hydrocode highlights the need for accurate equation of state data for the more complex materials. One-dimensional calculations of the incident blast pressure and impulse for the well characterised materials gave good results, suggesting the inhomogeneous expansion does not greatly affect these blast parameters. The data also showed that when considering additional complexities as reflections from boundaries and objects, one dimension is not a sufficient representation.

References

1. Zhang, F., Frost, D.L., et al.: Explosive Dispersal of Solid Particles. Shock Waves 10, 431–443 (2001)
2. Milne, A.M., Parrish, C.E., Worland, I.: Dynamic fragmentation of Blast Mitigants. Shock Waves 20, 41–51 (2010)
3. Parrish, C.E., Worland, I.: Numerical modelling of blast mitigation systems. In: Proceedings of 21st International Symposium on Military Aspects of Blast and Shock, Israel, October 4-8 (2010)
4. Youngs, D.L.: Numerical simulation of mixing by Rayleigh-Taylor and Richtmyer-Meshkov instabilities. Laser Particle Beams 12, 725–750 (1994)
5. Grady, D.E.: Local inertial effects in dynamic fragmentation. J. Appl. Phys. 53, 322–325 (1982)
6. Ritzel, D.V., Ripley, R.C., Murray, S.B., Anderson, J.: Near field blast phenomenology of thermobaric explosions. In: Proceedings of the 26th International Symposium on Shock Waves, Gttingen, vol. 1, pp. 305–310 (2007)
7. Frost, D.L.: Jet Formation During Explosive Particle Dispersal. In: Proceedings of 21st International Symposium on Military Aspects of Blast and Shock (2010)

Interaction of a Planar Shock with a Dense Field of Particles

J. Wagner, S. Beresh, S. Kearney, W. Trott, J. Castaneda, B. Pruett, and M. Baer

1 Introduction

Understanding the particle-particle and shock-particle interactions that occur in dense gas-solid flows is limited by a lack of knowledge of the underlying phenomena. Gas-solid flows are characterized by the particle volume fraction φ_p of the flow [1]. For particle volume fractions less than about 0.1%, flow is considered dilute and the effects of particle collisions are negligible [2]. For packed particles, where the φ_p is greater than about 50%, the flow regime is said to be granular. The dilute and granular regimes have been well studied, but conversely, a substantial knowledge gap exists for dense gas-solid flows, which have intermediate particle volume fractions of about 0.1 to 50%. This regime exists at microsecond time scales during blast-induced dispersal of material when the shocked particles are closely spaced.

Very little experimental data exist for the interaction of a shock wave with a dense gas-solid field of particles, with rare exceptions such as Rogue et al. [3]. Though they provided useful observations of particle trajectories and pressures following the impingement of a shock on a granular bed of particles, much remains unknown regarding the interactions that are involved in the dense gas-solid flow regime. Without data specifically acquired for such flows, simulations of energetic material detonation during the early-time expansion will continue to suffer from limited physical fidelity. To fill the gap in data for shock-particle interactions with initial volume fractions residing between the dilute and granular limits, a multiphase shock tube was recently constructed [4]. The unique facility uses a gravity-fed seeding method to generate a dense, spatially isotropic field of 100-micron diameter particles into which a planar shock is driven. High-speed schlieren imaging and pressure data are used to provide insight into the flow and particle behavior in the dense gas-solid regime.

J. Wagner · S. Beresh · S. Kearney · W. Trott · J. Castaneda · B. Pruett · M. Baer
Sandia National Laboratory, Albuquerque, NM, USA

2 Experimental Program

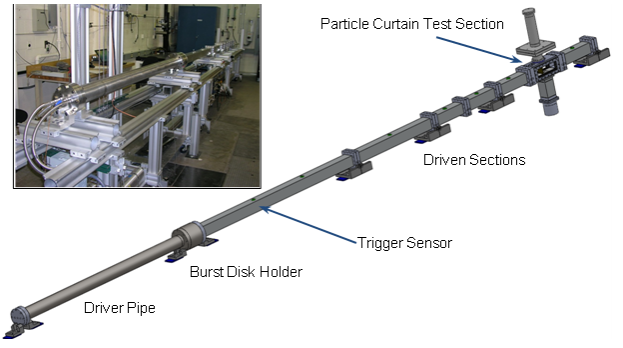

Fig. 1 Schematic and photo of the multiphase shock tube

A schematic of the multiphase shock tube is shown in Fig. 1. The driver section is a 2.1 m long stainless steel pipe with an inner diameter of 88.9 mm and a wall thickness of 12.7 mm, supplied by high-pressure compressed nitrogen. Cruciform scored, nickel alloy burst disks are used as diaphragms. Three disk thicknesses yield shock Mach numbers M_s of 1.66 ± 0.02, 1.92 ± 0.02, and 2.01 ± 0.02. The driven section is 5.2 m long and consists of square aluminum tubing with an inner width of 79 mm. The driven gas is air at an initial temperature of about 300 K and an initial atmospheric pressure of about 84.1 kPa. Pressure measurements have shown that the shock is well planar by the time it reaches the 'particle curtain' test section [5]. The unique aspect of this shock tube is its ability to provide multiphase flows

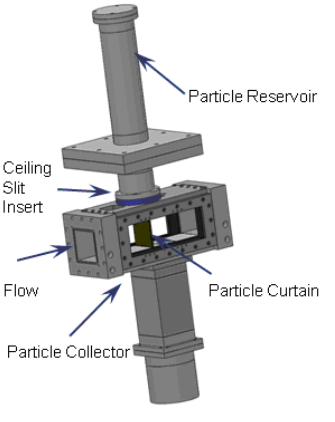

Fig. 2 Particle curtain test section

within the dense gas-solid regime by implementing a gravity fed particle curtain, or particle 'rain,' as shown in Fig. 2. An aluminum chamber having an inner diameter of 76 mm is used to initially store spherical soda lime particles that are sieved to diameters of 100-126 μm. Prior to an experiment, the soda lime particles rest on an initially closed industrial gate valve. During a test, but prior to the rupture of the burst disk, the gate valve opens and the particles flow through a beveled slit in the ceiling insert reaching a nearly constant flow rate in about 100 ms. The particles exit the test section through a similar slit in the floor and then enter a particle collector reservoir, which is emptied after each test. The slit has a 68.6 mm spanwise width, or about 87% of the full span of the test section, with streamwise thickness 3.2 mm. The gravity-fed seeding apparatus shapes the particles into what is termed the particle curtain, which narrows to a streamwise thickness h of about 2.2 mm for the bottom 75% of the test section height. Figure 3 shows a photo of the curtain acquired at an oblique angle with a test section wall removed, demonstrating that the curtain is nearly spatially isotropic. The particle volume fraction can be calculated by measuring the mass flow rate of particles through the ceiling slit and imaging the curtain to determine the velocity of the falling particles [5]. Owing to gravity, the volume fraction varies linearly from about 25% at the ceiling to about 19% at the floor. The particles flow at a velocity of about 1 m/s, which makes them essentially frozen compared to the shock velocities.

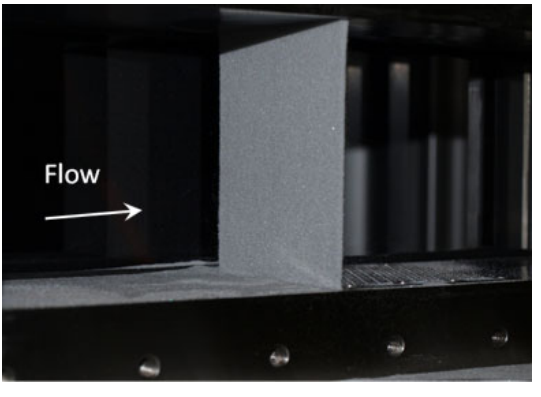

Fig. 3 Photo of the particle curtain acquired with a test section wall removed

A 130 kHz schlieren imaging system is used to study the wave structure and particle motions that occur following the impingement of a planar shock on the particle curtain. In addition, high-speed pressure measurements are made upstream and downstream of the curtain. Details can be found in [5].

3 Results

A high-speed schlieren sequence of a Mach 1.66 interaction acquired with a vertical knife edge, covering a 50 by 25 mm^2 area near the test section center, is shown in Fig. 4. At t = -10μs, the 2.2 mm thick curtain is near the center of the image along with some extraneous particles that have escaped the bulk curtain flow. The incident shock has propagated into the field of view and is about 8 mm upstream of the initial curtain. At t = 5 μs, which follows the impingement of the incident shock, reflected and transmitted shocks are observed. From 5 to 31 μs the transmitted shock travels downstream, appearing to broaden, likely indicating spanwise curvature and/or possibly rippling of the shock. Some shock curvature is to be expected considering that the initial curtain spans 87% of the test section width, with an unattenuated shock allowed to pass along the spanwise edges of the curtain. Pressures acquired from a ceiling sensor 69 mm upstream and a sensor 64 mm downstream of the interaction during the same run as that of Fig. 4 are shown in Fig. 5. The upstream trace shows both the incident (t = -132 μs) and reflected (t = 259 μs) shock pressure increases, while the downstream trace shows the transmitted shock (t = 125 μs). Using the pressure data and one-dimensional unsteady wave theory, the transmitted and reflected shock Mach numbers are calculated to be 1.55, and 1.23, respectively. The flow velocities induced by the transmitted and reflected shocks are 260, and 160 m/s, respectively. The densities compute to 2.1 kg/m^3 in the transmitted flow and 3.0 kg/m^3 in flow induced by the reflected shock. As seen in Fig. 4, in the images from

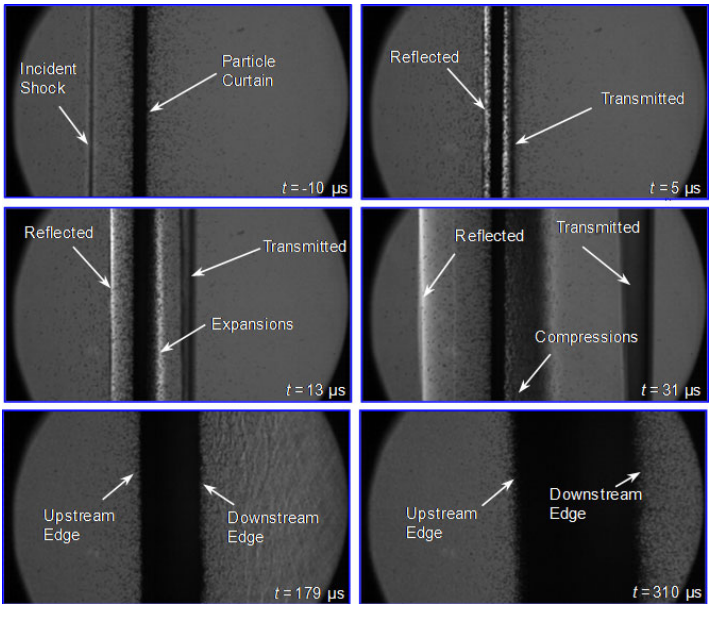

Fig. 4 Schlieren sequence (horizontal gradients) showing a Mach 1.66 interaction

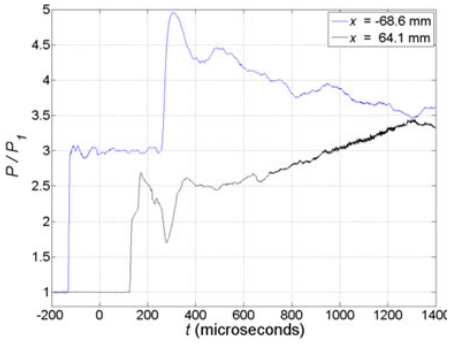

Fig. 5 Ceiling pressures during the interaction of Fig. 4. Origin (x = 0) is the initial curtain upstream edge

31 to 310 μs, the downstream edge of the particle field travels substantially faster than the upstream edge, resulting in a particle field that spreads with time. The difference in flow properties across the streamwise thickness of the curtain leads to a drag difference that in part explains the observed spread.

Expansion and compression waves also play a role in the interaction. In Fig. 4c, pronounced downstream-propagating expansions, similar to those in a detonation, are seen to trail the transmitted shock. Then in Fig. 4d, downstream-propagating compressions follow the expansions as the pressure across the curtain begins to equilibrate. As a result of the expansions and compressions, subsequent to the transmitted shock increase, a downstream pressure trough appears in Fig. 5. Downstream-propagating compressions and upstream-propagating expansions continue throughout the interaction as the pressure equilibrates across the particle field. Similar observations were also made by Rogue et al. [3]. The trajectories of the upstream and downstream edges of the particle fields at three shock Mach numbers for four runs each are shown in Fig 6a and Fig. 6b, respectively. Not surprisingly, both edges travel faster as the incident shock Mach number is increased. Dimensional analysis suggests that the trajectories should exhibit similarity if they are normalized by the

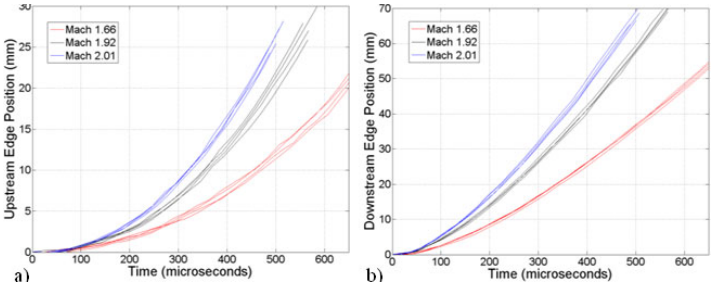

Fig. 6 Trajectories of the particle field edges as determined with high-speed imaging: a) upstream-edge, and b) downstream-edge

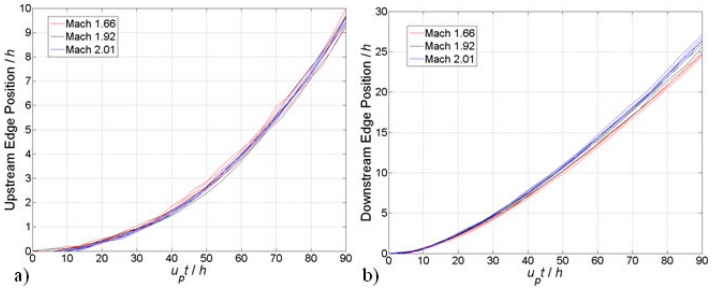

Fig. 7 Normalized particle field edge trajectories: a) upstream-, and b) downstream-edge

incident shock-induced velocity u_p. The resulting normalized trajectories are shown in Fig. 7, where the variables of both axes have also been divided by the initial streamwise thickness of the curtain h. Indeed, Fig. 7 demonstrates that when scaled by the post-shock gas velocity, the particle field trajectories collapse to a single curve. In the downstream edge plot of Fig. 7b, some residual separation between the three Mach numbers at later times, but overall the agreement between trajectories is good.

4 Conclusion

A novel multiphase shock tube at Sandia National Laboratories has been used to study the interaction of a planar shock wave with a gas-solid flow of particles having a volume fraction between the dilute and granular limits. Interactions of planar shock waves on a nearly spatially isotropic curtain of particles were studied. Transmitted and reflected shocks led to a difference in particle drag across the streamwise width of the curtain, which contributed to the spread of the particle field as it propagated downstream. The trajectories of the particle field edges were shown to be similar when normalized by the induced velocity downstream of the incident shock.

References

1. Zhang, F., Frost, D.L., Thibault, P.A., Murray, S.B.: Shock Waves 10 (2001)
2. Rudinger, G.: Fundamentals of gas-particle flow. Elsevier Scientific Publishing (1980)
3. Rogue, X., Rodriguez, G., Haas, J.F., Saurel, R.: Shock Waves 8 (1998)
4. Wagner, J.L., Beresh, S.J., Kearney, S.P., Trott, W.M., Castaneda, J.N., Cooper, M.A., Baer, M.R.: AIAA Paper 2010-4535 (2010)
5. Wagner, J.L., Beresh, S.J., Kearney, S.P., Trott, W.M., Castaneda, J.N., Pruett, B.O., Baer, M.R.: AIAA Paper 2011-188 (2011)

Direct Numerical Simulations of Supersonic Interfacial Flows

C.-H. Chang, X. Deng, and T.G. Theofanous

1 Introduction

Gas-liquid interfaces, when subject to accelerations and/or velocity gradients, are unstable to infinitesimal perturbations—a classical subject that is well understood, mainly via linear theory, but individually for each class of such flows (Rayleigh-Taylor, Kelvin-Helmholtz, and Richtmeyer-Meshkov). Approximate, analytical, weakly non-linear and even non-linear methods exist for some cases, but again only for the rather idealized problems that involve accelerations normal to the interface *or* velocity gradients in flows parallel to the interface. While these inform qualitatively about systems found in practice, absent are understanding and capability to treat superposition of mechanisms in arbitrary flows, as for example those arising in the presence of accelerating, oblique or curved interfaces. More severely, absent are such methods that can accommodate compressible and shock-wave-bearing flows. This is the subject addressed by the numerical work summarized in this paper—the supporting experiments were carried out in a large-scale shock tube, they include Newtonian as well as viscoelastic liquids, and the quantification includes the resulting particle size distributions [1]. The canonical problem is aerobreakup of liquid drops [1], and applications of significant current interest include de-icing of airplane wings, internal-combustion, rocket, and pulse-detonation engines, and dissemination of liquid agents in the atmosphere.

2 The Compressible Sharp Interface Method (CoSIM)

It has been established [2] that the *sine qua non* for our task is a numerical treatment that observes the exact boundary conditions at the interface. An immediate consequence is that the interface must be represented sharply, both dynamically and

C.-H. Chang · X. Deng · T.G. Theofanous
Center for Risk Studies and Safety, University of California at Santa Barbara
6740 Cortona Dr., Goleta, CA 93117, USA

kinematically. This means that the singular surface that marks each elementary portion of the interface must have its own unique velocity that is computed from the balance of forces and kinematics on either side of it. The key to achieving this is an exact Riemann solution that incorporates the capillary force, viscous stress and pressure jump across a curved-interface segment. We use a Level Set function to represent the interface. Rather than the usual approach of convecting it along with the flow field of the neighboring-bulk, at each time step we construct a new Level Set function that is anchored to the interface velocity. The method is fully conservative, and the order of the numerical scheme is further improved by a curved sub-cell representation of the interface.

A high-fidelity treatment also demands that the viscous and conductive fluxes are fully resolved, and we found that even with a highly-efficient code, and with adaptive mesh refinement, the gridding requirements exceeded desirable levels of effort. Thus we have embedded a thin-layer treatment, which was further informed and verified by a conformal-mapping solution of the flow over a solid sphere. The updating of the flow and temperature fields in the vicinity of the interface are computed by exact balances of diffusive fluxes (tangential tresses, heat fluxes) across the interface, while observing equality of temperatures and tangential velocities at the interface. The overall method is summarized by the flow diagram in Figure 1.

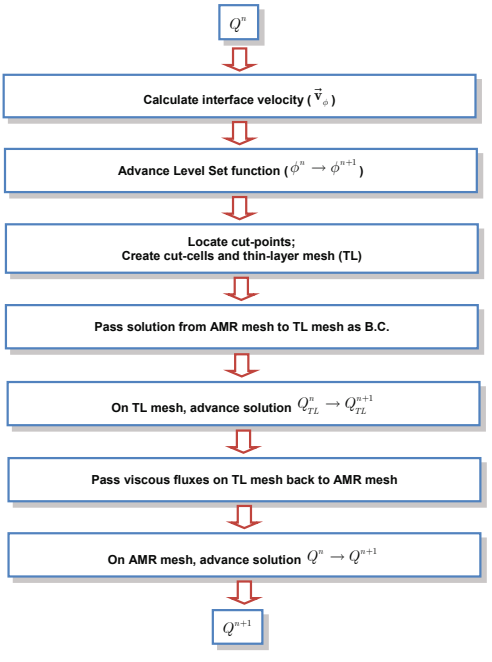

Fig. 1 The MuSiC$^+$ code flow structure.

The above are implemented in an AMR infrastructure with the unstructured cut-cell grid embedded at the lower end of an adaptive hierarchy of nested Cartesian meshes that are tailored to the efficiency of the numerical scheme for this class of problems. All sharp areas, including shocks are subject to refinement, and to release when no further needed. The code has been written in a way that is convenient to parallelize.

3 Sample Simulations

We present three different kinds of simulations to illustrate current capability. The first is an example of deformation and long-wave phenomena on a drop subjected to a relatively weak shock. The second is to address short-wave phenomena that initiate promptly behind strong shocks – these waves are essential to the subsequent evolutions of drop shapes and break up patterns through coupling with the aerodynamics. In both of these cases we present comparisons with experimental data that are first of a kind. The third illustration is for a large scale underwater explosion involving multiple free and rigid interfaces. All calculations are in axisymmetric geometry.

3.1 Long-Wave Phenomena

Here we consider a glycerol drop (1.83 mm in diameter) exposed to a rather weak shock (pressure ratio = 1.51). Interfacial shear is negligible as a direct effect on the drop, but viscous forces are important in controlling separation and thereby in affecting pressure distributions and overall drag. In particular, flow separation creates unbalanced aerodynamics and triggers a sequence of interface movements that lead to a muffin-like shape (Figure 2a) just as seen in the experiment (Figure 2b). The further evolution leads to penetration of the flattened front interface by Rayleigh-Taylor instability, again just as seen in the experiments, and just as predicted by theory that accounts for liquid viscosity [1].

3.2 Short-Wave Phenomena

Next we consider a glycerol drop (1.91 mm in diameter) exposed to a strong shock wave (pressure ratio = 8.15). The key features of the drop response include: a wavy region that begins at an angle of $\sim 30^\circ$, a deep wave at a position of $\sim 45^\circ$, a smooth area over the forward stagnation region, and a flattening at the other end (Figure 3b). They are all found in the numerical simulation (Figure 3a). Independent theory verifies quantitatively that the waves are due to viscous Kelvin-Helmholtz instability. The deep wave is found at the sonic point and derives from known augmentation that is due to compressibility. As the air stream accelerates along the interface to over Mach 2.4, it abruptly separates at about 120° and creates a relatively high-pressure region, which contributes to the flattening of the interface at the rear (Figure 3b).

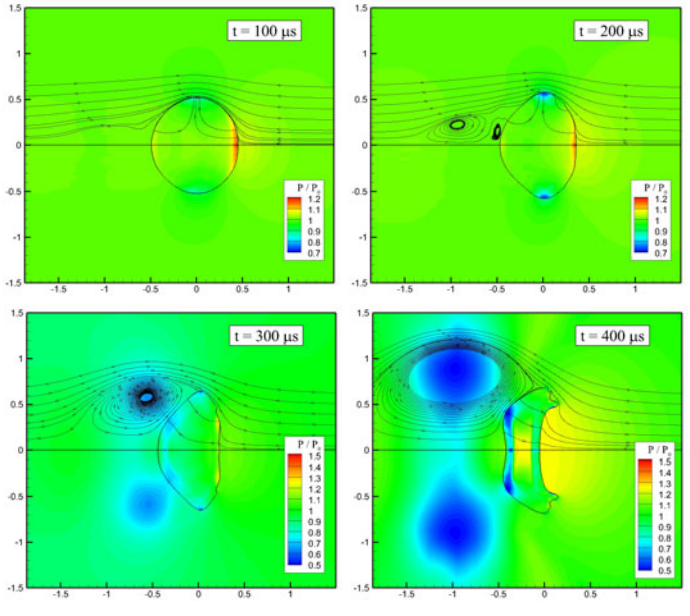

(a)

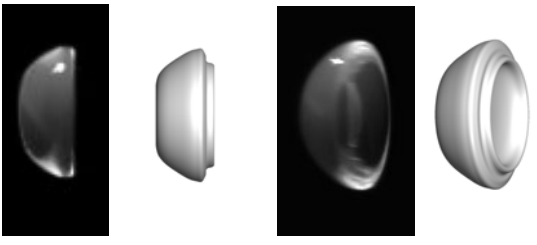

(b)

Fig. 2 Simulation results (a), and comparison with experimental images at 400 μs (b), of a glycerol drop exposed to a shock wave that yields ($Ms = 1.2$, $We = 520$, $Oh = 1.82$ and $Re_g = 1.57 \times 10^4$). The comparison shows straight (left) and oblique (right) views.

3.3 A Large-Scale Underwater Explosion

Last we consider an underwater explosion problem with a target represented by a solid sphere positioned beneath the explosion core (Figure 4, dimensions are in meters). We use two Level Set functions to track the explosion "bubble" and the free interface at the top. The numerical challenge in this type of a problem is the strong shock-interface interactions that occur at the very early stages of the explosion as they involve reflected waves of extremely high pressure ratio. The robust and oscillation-free results demonstrate the effectiveness of the numerical treatment. Moreover the AMR is seen to effectively capture fine details of shock propagation even in very large spatial domains as found in practical applications. In the results shown there is no special treatment of cavitation.

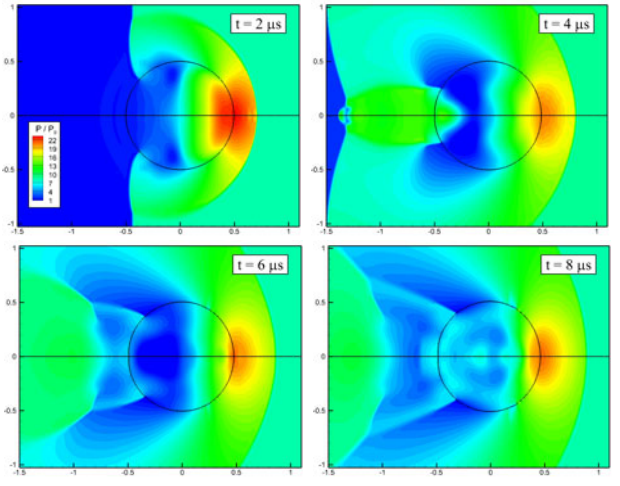

(a)

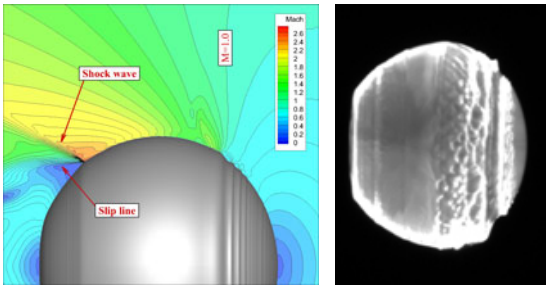

(b)

Fig. 3 Simulation results (a), and comparison with experimental images at 12 μs (b), of a glycerol drop exposed to a shock wave that yields ($Ms = 2.67$, $We = 5.4 \times 10^4$. $Oh = 1.9$ and $Re_g = 1.6 \times 10^5$).

4 Summary

We present a sharp interface method for compressible multiphase flows. Its key ingredients include (a) a Riemann solution that provides the interface velocity in a manner consistent with the exact jump conditions at the interface, and (b) a thin-layer method that resolves the viscous boundary layer at the high degree of accuracy required in simulating unstable interfaces. Our method preserves the conservation laws and satisfies the exact kinematic and dynamic jump conditions across the interface. The accuracy is further improved by using AMR, anchored level set function and curved-interface sub-cell representation. We demonstrate the robustness and accuracy of our method by first-of-a-kind simulations and comparisons with experiments that range from low-speed, R-T-dominated flows, to high speed, K-H-dominated flows. Also, practical utility for large-scale, extremely high-pressure-ratio problems is demonstrated by application to an underwater explosion with multiple interfaces.

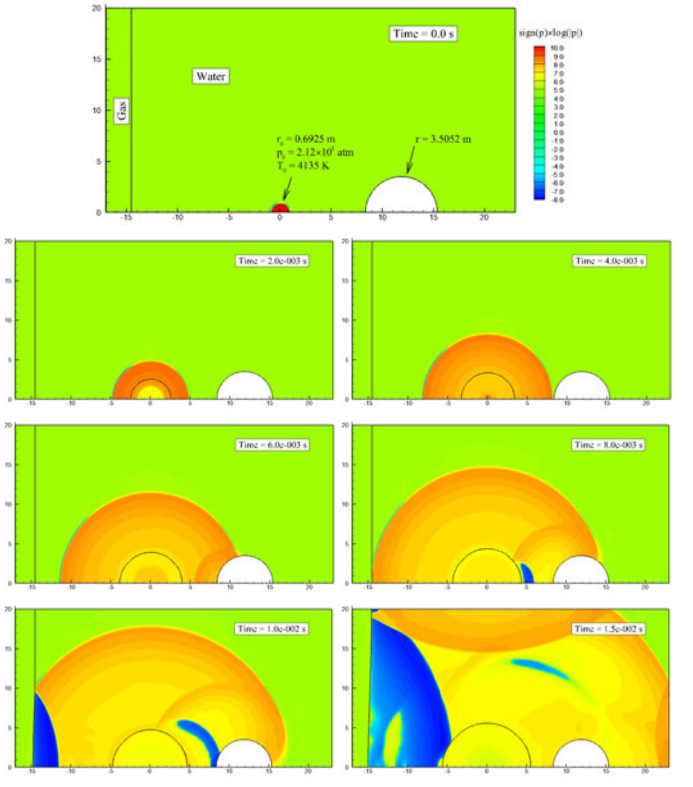

Fig. 4 Initial conditions and time evolution of an underwater explosion above a target.

Nomenclature

$We = \frac{\rho_g u_g^2 d_0}{\sigma}$ Weber number; $Re_g = \frac{\rho_g u_g d_0}{\mu_g}$ Reynolds number;
$Oh = \frac{\mu_l}{(\rho_l \sigma d_0)^{1/2}}$ Ohnesorge number; $M_S = \frac{C_S}{C_g}$ Shock-speed Mach number;

where: d_0 is drop diameter, C_S shock speed, C_g speed of sound in gas upstream the shock, u_g free-stream gas velocity, μ_g/μ_l gas/liquid dynamic viscosity, ρ_g/ρ_l gas/liquid density, σ surface tension coefficient.

References

1. Theofanous, T.G.: Aerobreakup of Newtonian and viscoelastic liquids. Annual Review of Fluid Mechanics 43, 661–690 (2011)
2. Nourgaliev, R.R., Liou, M.-S., Theofanous, T.G.: Numerical prediction of interfacial instabilities, part I: sharp interface method (SIM). Journal of Computational Physics 227(8), 3940–3970 (2008)

Part XIII
Nozzle Flow

Experimental Investigation of Asymmetric and Unsteady Flow Separation in High Mach Number Planar Nozzles

E. Shimshi, G. Ben-Dor, A. Levy, and A. Krothapalli

1 Introduction

Flow separation in convergent divergent (CD) nozzles occurs when the dynamic pressure of the fluid in the boundary layer is not high enough to overcome the rising pressure ratio along the diverging part of the nozzle. This phenomenon has many engineering application aspects such as jet engine performance, noise from jet engines, limitations on the construction of rocket nozzles or thrust vectoring. Therefore it is of interest to understand the physical aspects of the phenomenon. Unlike the inviscid quasi-one-dimensional analysis of nozzle flow, experiments revealed that most often the shock wave that forms inside the nozzle is not a normal one. At low Mach numbers the typical formation is of a slightly convex Mach stem with Mach reflection at its ends often termed "Lambda foot", while at higher Mach numbers an

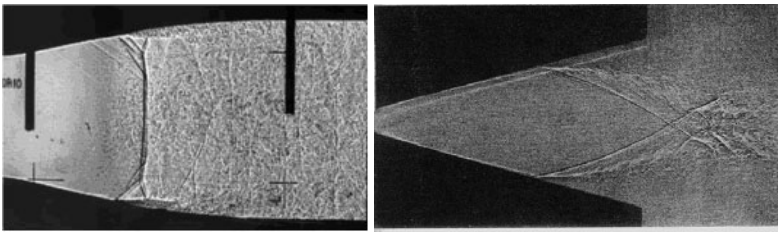

Fig. 1 Flow separation inside a planar nozzle. Mach reflection with a Lambda foot [5] (left); Oblique shock with a regular reflection [1] (right).

E. Shimshi · G. Ben-Dor · A. Levy
Pearlstone Center for Aeronautical Engineering Studies,
Department of Mechanical Engineering, Ben-Gurion University of the Negev,
Beer Sheva, Israel

A. Krothapalli
Department of Mechanical Engineering, A&M University and Florida State University,
Tallahassee, FL 32310, USA

oblique shock is created from opposite sides of the nozzle and reflects at the symmetry plane (Fig. 1). These flow separation structures are most often symmetric when the flow separation occurs close to the nozzle exit plane. When the flow separation occurs away from the nozzle exit, it may become asymmetric or exhibit unsteadiness. Summerfield et al. [1] reported that at low nozzle pressure ratio (*NPR*) the flow separation in a planar nozzle is asymmetric. Arens & Spiegler [2] described stable and unstable flow regions at different Mach numbers and noted that unstable regions also exhibited asymmetric separation. Several investigators studied the occurrence of flow separation inside planar nozzles [3, 4, 5, 6]. It can be deduced that the formation of the shock system starting at the separation point seems to be dictated by the separation Mach number. At low Mach numbers ($M_{sep} < 2.5$), a "Lambda foot" with a Mach reflection is formed, while at higher Mach numbers, an oblique shock with a regular reflection is formed. The type of reflection stays the same regardless of whether the separation is symmetric or asymmetric. In all the cases where the separation was asymmetric with a Lambda foot the flow did not reattach to the wall downstream of the separation point, but rather resulted in "small" and "large" separated regions. In the case of asymmetric oblique separation the flow attached to the wall up to the nozzle exit. The attachment of the flow appears to be related to the Coanda effect where the inability of the jet to entrain ambient fluid due to the proximity to the wall causes it to draw itself closer to the wall until it attaches to it [7]. The type of reflection that occurs depends on the Mach number upstream of the shock system and the pressure ratio across the oblique shock [8]. In order to investigate flow separation in nozzles with varying Mach number ($2.7 > M > 3.7$), a wedge having the same half angle can be inserted into a tapered nozzle at different stream-wise positions. The location of the wedge determines the exit area of the nozzle and thus the fully expanded Mach number. This gives an advantage of allowing a continuous change in area ratio with a single nozzle.

2 Experimental Arrangement

Experimental testing was conducted in the Hot Jet Facility of the Advanced Aero Propulsion Laboratory at Florida State University. The jet from the nozzle exhausts into a fully anechoic chamber and its main use if for studying jet noise. The jet is fed from a 2000 psi (13.8 MPa), 10 m^3 pressure vessel and is regulated by two-stage control valves to achieve long run times and stable pressure conditions. The nozzle used in the experiments was a planar (2D) tapered CD nozzle with an exit-to-throat-height ratio of 8. The throat height was 3.175 mm (1/8"), the divergence half angle was 10°, and the radius of curvature ratio in the converging part was 16 to give a nearly straight sonic line. The diverging part of the nozzle was 65.25 mm long with optical windows enabling a field of view starting from 9 mm downstream of the throat up to 44 mm downstream of the nozzle exit for flow visualization. On the top nozzle plate pressure taps were drilled along and across it. An aluminum block with pressure taps along the centerline could be installed instead of one of the optical windows. This arrangement enabled to measure pressures along the top

wall and the symmetry plane of the nozzle and to verify that the flow was indeed two dimensional by measuring the pressure across the flow. An aluminum wedge with a 10° half angle and a width of 100 mm could be inserted and retracted into the nozzle during the test run. The position of the wedge was controlled by a linear stage connected to a stepper motor. The average pressure along the wall was measured with a pressure transducer connected to a mechanical multiplexer. Far field noise measurements were collected by a B&K model 4939 microphone and recorded at a rate of 44,800 samples/s. The microphone was placed about 1 m upstream from the nozzle exit at 45° off the central axis. Flow visualization was achieved with a straight-line focused shadowgraph system.

3 Experimental Results

The experiments were performed at nozzle pressure ratios (*NPR*) ranging from 5 to 15.5. The location of the tip of the wedge measured from the throat position ranged from 25 to 125 mm. This distance is normalized by the length of the diverging part of the nozzle to give a variation in the location of the wedge tip from $X_W^* = 0.38$ to $X_W^* = 1.92$. At each *NPR* and wedge location the wall pressure on the top plate was measured and a series of images were taken. At several measuring points, the pressure across the nozzle at $X^* = 0.3 (X^* = X/X_{Nozzle})$ was collected to ascertain that the flow was two dimensional.

3.1 Flow Visualization

Shadowgraph images revealed four different flow patterns as shown in the following figures. When the wedge is inserted deep into the nozzle the flow is stable with no flow separation, the wedge tip creates an oblique shock which bounces back and forth between the wedge and the nozzle wall. When the wedge is retracted the flow separation proceeds upstream along the nozzle wall until the separation point is further upstream than the location where the oblique shock from the wedge tip strikes the nozzle wall. The separation shock alternates between the wedge and the jet boundary. (Fig. 2 left). Furthere retraction of the wedge creates substantial instability in the separation location; it is seen as multiple weak shock waves coming from numerous separation points. The smearing of the shock waves as seen in the shadowgraph could also be the result of highly 3D flow effects, but this would be manifested in variation of pressure across the nozzle flow path. Simultaneously with the separation instability a sharp tone can clearly be detected, and its amplitude and frequency increase as the wedge is pulled out (Fig. 2 right). A similar charcteristic tone has been observed in low Mach number nozzles and is termed transonic resonance [9]. Further retraction of the wedge causes the tone to disapear and the flow stabilizes with the separation shock converging at the wedge tip. The oblique shock from the wedge strikes the jet boundary from the separation point causing it to bend outwards and accelerate the flow. For *NPR* greater than 15 this flow pattern remains basically unchanged when the wedge is retracted all the way out of

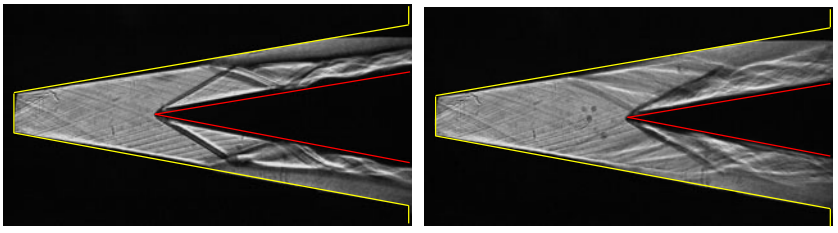

Fig. 2 Shadowgraph image of type I and II flow; Steady symmetric separation (left); Unsteady symmetric separation (right).

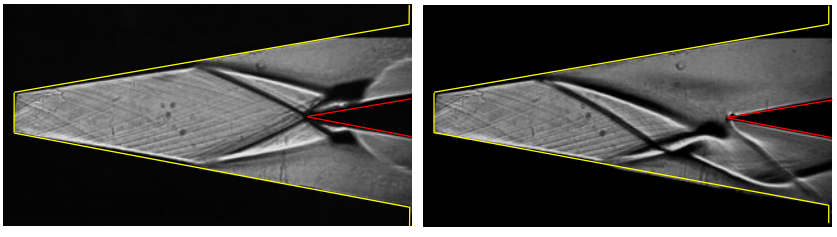

Fig. 3 Shadowgraph image of type III and IV flow; Symmetric separation with reflection at the tip of the wedge (left), Asymmetric separation with flow attaching to the wall (right).

the nozzle (Fig. 3 left). For *NPR* values below 15, further retraction of the wedge causes the flow to separate asymmetrically with the jet attaching to either the top or bottom nozzle walls with reverse flow on the opposite side (Fig. 3 right). In most cases the direction of the asymmetry would remain constant during the same run but may change direction if the alignment of the nozzle was changed between runs. The separation point on the flow reversal side would move upstream while on the flow side it would remain almost unchanged. This flow pattern will remain constant even as the wedge is fully retracted.

3.2 Pressure Measurements

Pressure measurements were taken along the mid section of the top nozzle wall from $X^* = 0.06$ to $X^* = 0.93$. The separation Mach number just upstream of the separation point calculated from the pressure readings ranged from 2.6 to 3.0 according to the *NPR*. Figure 4 shows the static wall pressure for two types of flow patterns normalized by the ambient pressure. In flow type I the pressure increase across the separation point intensifies as *NPR* increases because the separation is at a higher Mach number. The pressure recovery downstream of the separation point is almost linear ending at 80% of the ambient pressure. Once the flow separation becomes unstable (Fig. 4 left), the pressure rise across the separation point is less distinctive, probably due to an averaging effect of the shock motion. When the flow

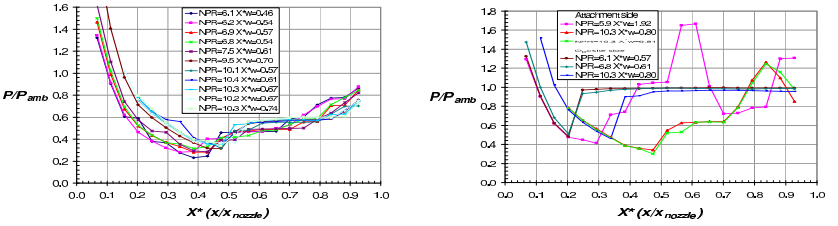

Fig. 4 Normalized pressure measurements along nozzle wall: Type II flow (left), Type IV flow (right).

re-stabilizes the sharp increase in the pressure across the separation point can be seen once again, but the pressure recovery is immediate and remains at a constant value up to the nozzle exit. When the wedge tip is outside of the nozzle ($X_W^* > 1$) the pressure recovery is about 90% of the ambient pressure, while when it is inside the nozzle the pressure is lower and depends on the wedge location. For the case of asymmetric separation, the pressure profile is different for each wall, it increases to about twice the separation pressure along the wall that the flow is attached to and remains constant down to the point the flow reattaches to the wall causing an increase to a pressure above ambient. As the *NPR* increases, the reattachment point moves downstream towards the nozzle exit. On the opposite wall the pressure downstream of the separation point rises immediately to ambient condition and remains constant up to the nozzle exit (Fig. 4 right).

3.3 Sound Measurements

Far field sound measurements with a microphone positioned at 45° to the jet axis were taken at various *NPR*s and wedge locations. In the cases where the flow separation was steady no distinct frequency was found and the noise was broadband in nature. Once the location instability of the separation point was observed a loud high frequency tone was recorded and its FFT showed discreet peaks at 1.7 to 2 kHz with two to three harmonics. Once the flow re-stabilized either with a symmetric or asymmetric separation the sharp tones disappeared. It appears that the noise generation is directly related to the flow instability. In general the basic frequency of the tone ascended as the distance of the wedge tip from the nozzle throat increased. For a constant wedge location, the frequency ascended as the stagnation pressure was increased. Figure 5 shows the relation of the wedge location with the Struhal number $S = fh_{exit}/U_{exit}$ where h_{exit} is the distance between the wedge and the walls of the nozzle, the exit velocity is calculated from $U_{exit} = \dot{m}/\rho_{amb}A_{exit}$. It shows a monotonous increase of Struhal number with wedge location for all stagnation pressures.

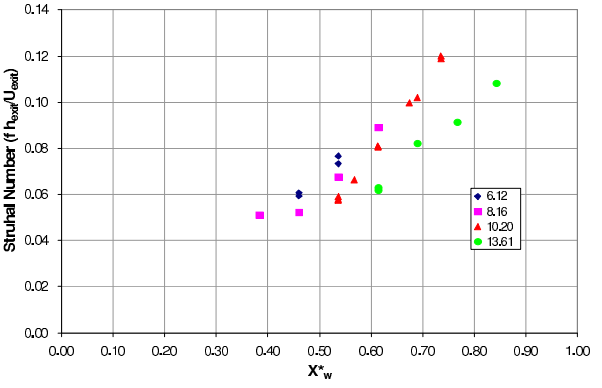

Fig. 5 Variation Struhal number with location of the wedge at different *NPR* conditions.

4 Conclusion

An apparatus for investigating flow separation phenomena inside a planar nozzle with varying area ratio has been devised. Flow visualization revealed four types of flow patterns depending on the *NPR* and the wedge position. Three of the flow types resulted in steady flow either with symmetric or asymmetric flow separations. The forth produced an unstable separation mechanism that was accompanied by a distinct tone. When flow separation became asymmetric the jet attached to the wall and produced a high pressure area. In all cases a regular reflection was produced. The unsteadiness of the separation point location observed in the experiment can be related to a form of transonic resonance.

References

1. Summerfield, M., Foster, C.R., Swan, W.C.: Jet Propulsion 24, 9 (1964)
2. Arens, M., Spiegler, E.: Bulletin of the Research Council of Israel 11C (1962)
3. Hunter, C.A.: Experimental, theoretical, and computational investigation of separated nozzle flows. In: 34th AIAA/ASME/SAE/ASEE Joint Propulsion Conference & Exhibit, July 13-15. AIAA, Cleveland (1998)
4. Papamoschou, D., Zill, A., Johnson, A.: Shock Waves 19, 3 (2008)
5. Bourgoing, A., Reijasse, P.: Shock Waves 14, 4 (2005)
6. Lawrence, R.A., Weynand, E.E.: AIAA Journal 6, 6 (1968)
7. Panitz, T., Wasan, D.T.: AICHE Journal 18, 1 (1972)
8. Shimshi, E., Ben-Dor, G., Levi, A.: Journal of Fluid Mechanics 635, 1 (2009)
9. Zaman, K.B.M.Q., Dahl, M.D., Bencic, T.J., Loh, C.Y.: Journal of Fluid Mechanics 463 (2002)

Experimental Investigation of Shock Train Induced Turbulence

A. Grzona and H. Olivier

1 Introduction

Inside a nozzle with small opening angle the re-compression from supersonic to subsonic flow conditions is conducted by a shock train when the back pressure and the relative thickness of the boundary layer compared to the nozzle height are sufficiently high. A sketch of a typical shock train is depicted in Fig. 1a. Due to the boundary layer effect a series of shocks alternating with expansion zones is formed and the re-compression spans over a certain distance. The shock region is followed by a turbulent mixing region, where the subsonic turbulence layers originating at the foot of the first shock grow together. The turbulent fluctuations homogenise the flow and are accompanied by a rise in static pressure (see Fig. 1d). Caused by shear layers and the associated mixing process, the overall pressure rise in a shock train is lower than for a single normal shock with the same pre-shock conditions. A detailed description of the shock train phenomenon and a comprehensive review of its time-averaged behaviour can be found in [1]. The normal Reynolds stress throughout the shock train on the centre line was measured by [2]. For the cases of a lambda-foot shock train and a x-type shock train a strong intensification of the turbulent fluctuations was observed in the mixing region. The magnitude of the maximum normal Reynolds stress on the centre line strongly depends on the pre-shock Mach number. In the present investigation movable hot-wire probes are used to measure the distribution of the turbulent fluctuations over the complete nozzle height at different positions inside the shock train and the following mixing region. This allows to capture the growth of the turbulence layer. Figure 1b shows a Schlieren image of the flow with the hot-wire probe positioned on the centre line at the beginning of the turbulent mixing layer. Schlieren images with a shorter illumination time show the turbulent structures emerging from the shock/boundary layer interaction (Fig. 1c).

A. Grzona · H. Olivier
Shock Wave Laboratory, RWTH Aachen University
52056 Aachen, Germany

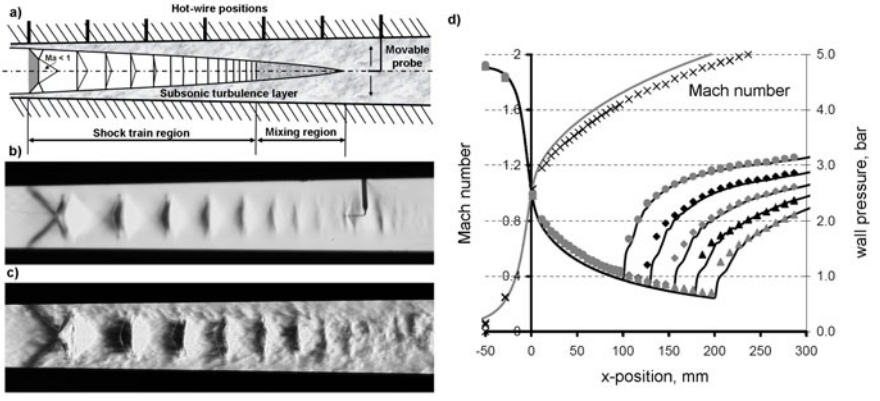

Fig. 1 (a) Principle sketch of a shock train (b, c) Schlieren images with and without hot-wire sensor, $Ma_1 = 1.81$ (d) experimental (symbols) and numerical (lines) wall pressure distributions for different back pressures and free-stream Mach number

2 Experimental Setup

The experiments have been carried out in a continuous cold gas wind tunnel, with a geometry similar to a pilot facility designed for the gas-phase synthesis of nanoparticles presented in [3]. A standard compressor provides a maximum mass flow of 104 g/s with a constant total temperature of $T_{01} = 293\ K$. For the given effective cross section of the first nozzle throat of $A_1^* = 92.8\ mm$, this mass flow results in a maximum total pressure of $p_0 = 4.75\ bar$. The parallel side walls of the test section are made of quartz glass to permit Schlieren visualisation. From the first throat the cross section of the nozzle increases due to a diverging angle between upper and lower walls of $\beta = 1.6°$ over a length of $x = 258\ mm$. Downstream of this position the diverging angle opens to $\beta = 3°$. The shock train position inside the test section can be adjusted by a movable central plug in a conical second nozzle. This allows pre-shock Mach numbers in between $Ma_1 = 1.1$ and 2.1. More details about the wind tunnel, the measurement system and preceding experimental results e.g. the wall pressure distribution along the shock train can be found in [2] and [4]. The velocity and normal Reynolds stress profiles in y-direction are measured at five measurement positions downstream the nozzle throat (see Tab. 1) by a hot-wire sensor operated with a constant voltage anemometer (Model 4-600 CVA, Tao Systems) [5]. Table 1 also gives the distance between the wall and the centre line of the nozzle y_{CL}. Schlieren and shadowgraph images are taken to give an overview of the flow field and the shock train structure.

Table 1 Hot-wire distance S [mm] from the foot of the first shock for different leading shock positions x_1 and pre-shock Mach numbers Ma_1

y_{CL}, mm		Pos. 1 5.82	Pos. 2 6.38	Pos. 3 7.28	Pos. 4 8.33	Pos. 5 9.37
x_1, mm	Ma_1	S, mm				
106	1.62	100				
126	1.68	80				
146	1.74	60	100			
166	1.81		80			
186	1.85		60	100		
206	1.91		40	80	120	160
226	1.93			60	100	
246	1.96				80	
266	2.01				60	

3 Results from Hot-Wire Measurements

A movable hot-wire sensor has been utilized to measure the velocity and normal Reynolds stress distribution in y-direction at five different x-positions for variable pre-shock Mach numbers (see Tab. 1). Each column represents measurements at a fixed sensor position, while the position of the leading shock and therewith the Mach number is changed. Each row represents measurements at a constant Mach number. Due to the hot-wire support the measurement point closest to the wall is at $y = 0.1\ mm$ which corresponds to a y^+ value of about 300. Exemplarily, the results for $Ma_1 = 1.91$ can be found in Fig. 2b. All the other measurements are arranged in a way that a single picture shows the profiles for a constant distance from the foot of the first shock with an increasing pre-shock Mach number (see Fig. 3). The velocity and normal Reynolds stress profiles in the supersonic free stream are depicted in Fig. 2a. They show a slightly increasing boundary layer thickness for increasing Mach numbers and associated boundary layer running length and very low normal Reynolds stresses on the centre line. The velocity fluctuations increase steadily inside the boundary layer which is in qualitative agreement with the results presented in [6]. In Fig. 2b a series of profiles is displayed throughout a shock train and the following mixing layer for a constant pre-shock Mach number of $Ma_1 = 1.91$. While across the supersonic inflow upstream of the first shock high normal Reynolds stresses can only be found close to the wall, the presented results clearly show that with increasing distance from the foot of the first shock the turbulent fluctuations spread towards the centre line. At the position $S = 80\ mm$ downstream of the first shock a significant maximum can be observed at a distance of $y = 4\ mm$ from the wall. Inside the turbulent mixing layer 120 mm downstream of the first shock, the normal Reynolds stress is almost equally distributed over the whole cross section. The latter can also be observed in Fig. 3a for different pre-shock Mach numbers. These results correspond with the observation from Schlieren pictures (turbulence layer growing towards the centre line) and are in qualitative agreement with [7].

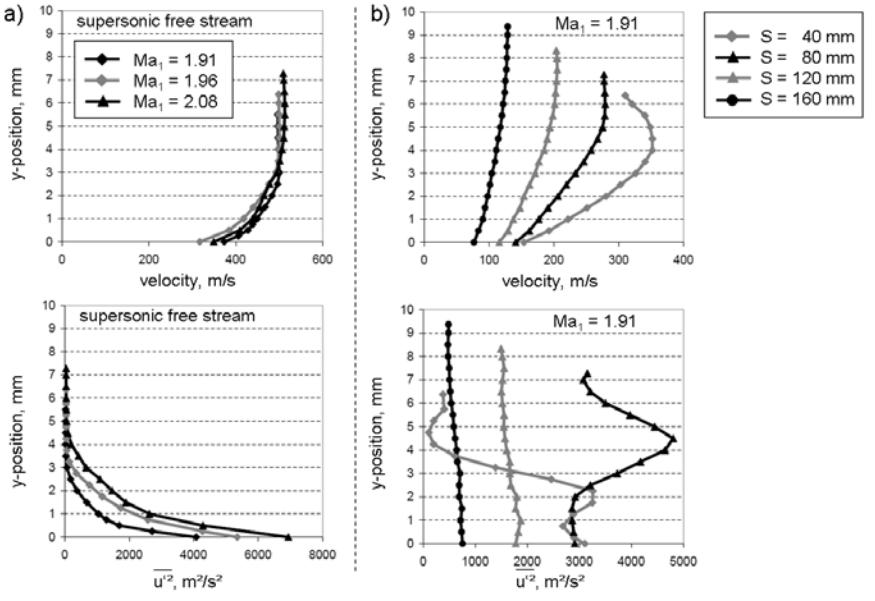

Fig. 2 Velocity and normal Reynolds stress y-profiles in supersonic flow (a) and along a shock train for pre-shock Mach number $Ma_1 = 1.91$ (b)

Figure 3 displays the y-profile of the velocity and the normal Reynolds stress for a constant distance from the foot of the first shock in each case for increasing pre-shock Mach numbers. Due to different shock positions the Reynolds number based on the momentum thickness varies between $Re_\theta = 20,000$ and 30,000. This has no significant effect on the shock train structure [2] and was therefore neglected. The velocity profile inside the shock region is deformed and becomes triangular. This effect is more distinct closer to the foot of the first shock and for higher pre-shock Mach numbers. Therefore, the most deformed velocity profile is found for the shortest distance between shock and sensor (S = 60 mm) at the highest pre-shock Mach number ($Ma_1 = 2.01$). The given normal Reynolds stresses support the observation of a turbulence layer growing towards the centre line and illustrate that the magnitude of the fluctuations increases with increasing pre-shock Mach number. Although a series of profiles have been measured, the presented results are not sufficient to present a comprehensive analysis of the flow field and the dominating factors of influence. This leaves room for further investigations.

4 Numerical Results

Accompanying two-dimensional numerical simulations have been carried out with ANSYS CFX and the Menter SST turbulence model. The utilized mesh has a resolution of 900 x 80 points in x- and y-direction. While the grid spacing in x-direction

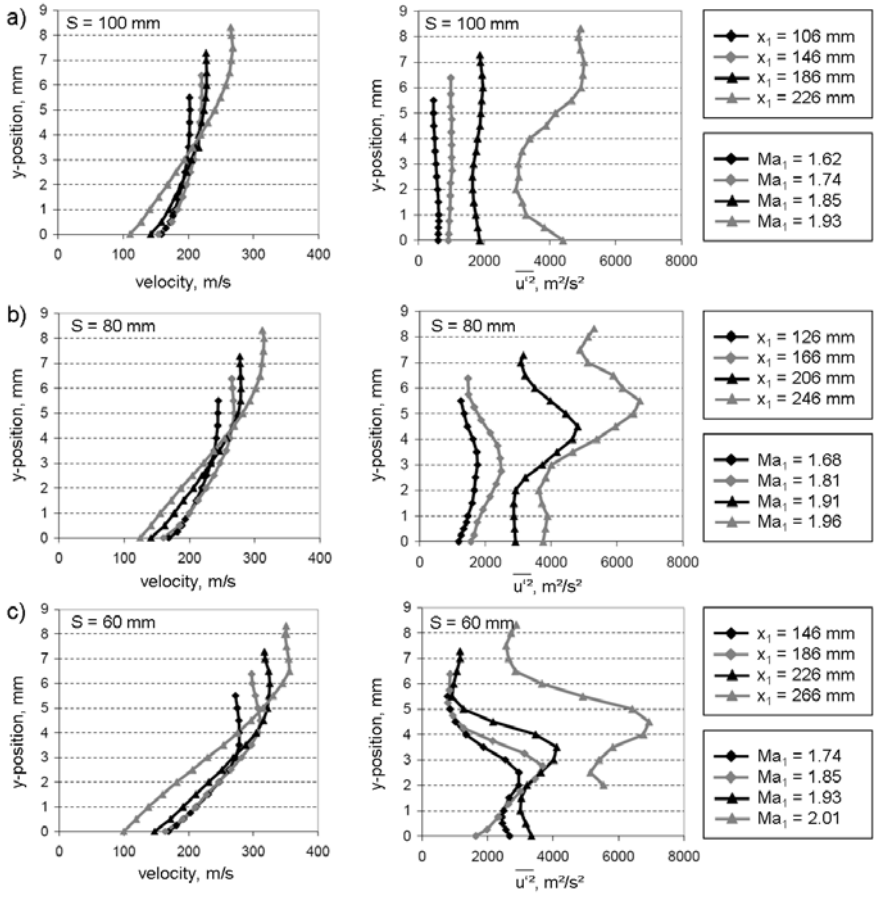

Fig. 3 Velocity and normal Reynolds stress y-profiles for different distances from the foot of the first shock, 100 mm (a), 80 mm (b) and 60 mm (c)

is constant, the spacing in y-direction uses a logarithmic scaling to reach $\Delta y^+ < 1$ for the first cell at the nozzle walls. Wall pressure and Mach number distribution of the simulation fit the experimental data quite well (see Fig. 1d), so that the numerical results can be used to have a qualitative look into the flowfield. A comparison of numerical and experimental results is shown in Fig. 4. The depicted results clearly show that the normal Reynolds stress of the incoming boundary layer is enforced at the foot of the first shock. Downstream, the generated turbulence loses intensity while it spreads towards the centre line. The magnitude of the numerical profiles differ somehow from the measured ones, but qualitatively they are in fair agreement. Especially near the wall deviations of the Reynolds stress profiles occur which may be caused by an inappropriate turbulence modelling.

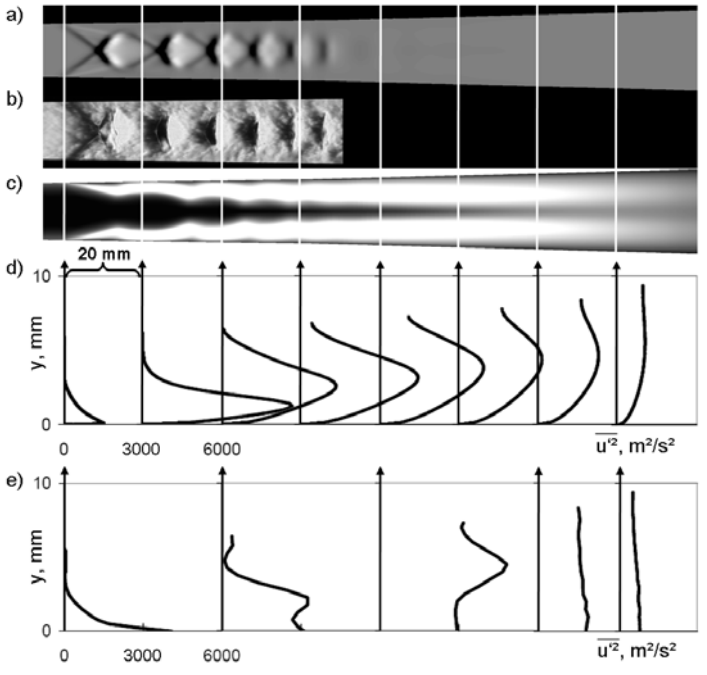

Fig. 4 Numerical (a) and experimental (b) Schlieren image, numerical turbulence contour (c), as well as numerical (d) and experimental (e) normal Reynolds stress profiles for pre-shock Mach number $Ma_1 = 1.91$

References

1. Matsuo, K., et al.: Shock train and pseudo shock phenomena in internal gas flows. Prog. Aerosp. Sci. 35, 33–100 (1999)
2. Grzona, A., Olivier, H.: Shock train generated turbulence inside a nozzle with a small opening angle. Exp. Fluids (2011), doi: 10.1007/s00348-011-1083-5
3. Grzona, A., et al.: Gas-phase synthesis of non-agglomerated nanoparticles by fast gasdynamic heating and cooling. Proc. of ISS 26(2), 857–862 (2007)
4. Weiss, A., et al.: Behaviour of shock trains in a diverging duct. Exp. Fluids 49(2), 355–365 (2010)
5. Comte-Bellot, G., Sarma, G.R.: Constant voltage anemometer practice in supersonic flows. AIAA J. 39(2), 261–270 (2001)
6. Smits, A.J., Dussauge, J.P.: Turbulent shear layers in supersonic flow, 2nd edn., pp. 237–243. Springer (2006)
7. Carroll, B.F., Dutton, J.C.: Turbulence phenomena in a multiple normal shock wave/turbulent boundary layer interaction. AIAA J. 30(1), 43–48 (1992)

Influence of a Normal Slot Boundary Layer Suction System onto a Shock Train

A. Weiss and H. Olivier

1 Introduction

The recompression of supersonic gas flow is a very common flow phenomenon in modern aerodynamics and occurs in a great number of applications for instance supersonic ramjet or scramjet inlets, internal diffusers and supersonic ejectors. Under certain conditions even one or more shocks can appear downstream of the first shock. This series of shocks is a so called shock train. In contrast to other shock systems the supersonic flow is decelerated at first through a shock system and followed by a mixing region as shown in Fig. 1. For the whole interaction region Crocco et al. [1] have coined the term pseudo-shock. The structure and length of the shock train depends very much on the so called confinement level which is the ratio of the boundary layer thickness δ to the half height of the nozzle h. This was investigated very thoroughly by Carroll [2] and Om et al. [3]. In case of a shock train, due to the occurrence of successive shocks the pressure recovery along the shock train extends and greatly deviates form the pressure gradient that would occur at a single normal shock, [4]. However, a short recompression region or at best a single normal shock leads to very high pressure and temperature gradients, which provides interesting opportunities for various gas dynamic applications. In order to reduce the shock train length and thereby increasing the pressure gradient the shock system must be exposed to a higher back pressure. However, under normal conditions this would lead to a relocation of the shock train farther upstream, because the boundary layer can only withstand a certain back pressure level. The ability of the boundary layer to overcome a strong back pressure is limited, because the flow velocity hence impulse drops to zero near the wall. In order to remove the parts of the boundary layer with small impulse a normal suction slot 1.5 mm wide is placed upstream of the shock train, see Fig. 1.

A. Weiss · H. Olivier
Shock Wave Laboratory, RWTH Aachen University, Templergraben 52,
52064 Aachen, Germany

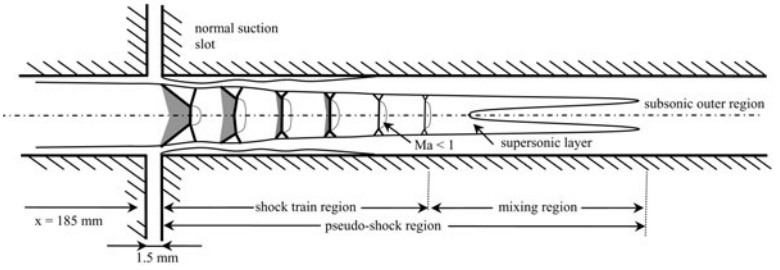

Fig. 1 Schematic sketch of a boundary layer suction system and the shock train

2 Experimental Facility

The experiments presented in this paper have been carried out in a supersonic wind tunnel. A detailed description of this facility can be found in Weiss et al. [5]. For the current measurement two different nozzles have been investigated, whereby the first nozzle exhibits a free stream Mach number upstream of the suction slot of Ma = 1.45 and the second nozzle Ma = 1.65. The distance of the suction slot to the nozzle throat is equal. The back pressure of the shock train inside the primary nozzle can be altered over a wide range. The total pressure p_{01} of the flow can be varied between $p_{01} = 2.0$ bar and 4.75 bar, which in case of Ma = 1.45 leads to a Reynolds number variation upstream of the suction slot between $Re_x = 4.31 \cdot 10^6$ and $Re_x = 9.91 \cdot 10^6$ and in case of Ma = 1.65 of $Re_x = 3.7 \cdot 10^6$ and $8.53 \cdot 10^6$. The primary nozzle can be operated in two configurations, either suction slots are implemented in the upper and lower nozzle wall, whereas the side walls are made from quartz glass, or the suction system extends across all four nozzle walls. The boundary layer upstream of the suction slot has been measured by means of a movable pitot tube. In Table 1 the boundary layer properties are summariesed.

Table 1 Boundary layer properties, x = 182 mm, h half height of the nozzle

Ma = 1.45	h [mm]	δ [mm]	δ/h	Ma = 1.65	h [mm]	δ [mm]	δ/h
upper wall	4.1	2.52	0.62		4.6	2.78	0.60
side wall	7.5	2.25	0.30		7.5	2.11	0.28

3 Transition of a Shock Train into a Curved Shock

Figure 2 depicts five steps how the shock stabilizes at the suction slot as the pressure increases. At first the total pressure ratio p_{02}/p_{01} across the shock train is only 0.6 and the shock train is located downstream of the suction slot. From the edges of the suction slot originate only very weak shocks which are reflected from the nozzle wall father downstream. When the back pressure is increased and the total pressure

ratio reaches 0.63, the primary shock is located at the slot as shown in Fig. 2b. In order to negotiate the steadily increasing back pressure the shock system changes in as much as the shock angle increases. At the primary shock a Mach stem becomes visible near the nozzle axis. Ultimately the shock system concurs in a single curved shock. Downstream of which some weak compressions and expansions prevails. At a certain back pressure level even a strong shock can not provide the pressure increase necessary and the shock suddenly relocates upstream as shown in Fig. 2e. For all measurements the static pressure in the suction cavity is kept equal to the static pressure upstream of the slot, which is therefore lower than the static pressure immediately downstream of the first shock. When suction slots are only installed on the upper and lower nozzle wall the maximum pressure ratio achieved across the first shock did not exceed $p_2/p_1 = 2.08$, which is below the theoretical value of $p_2/p_1 = 3.02$ for a normal shock at Ma = 1.65. Therefore, a 1.5 mm suction slot was implemented on the side walls also and the shock provided a pressure ratio of $p_2/p_1 = 3.01$. In order to study the influence of the Reynolds number onto the stability of the shock the total pressure has been varied between $p_{01} = 2.0$ bar and $p_{01} = 4.75$ bar, whereas the pressure in the suction cavity is kept equal to the pressure upstream of the suction slot. As shown in Fig. 3, across the suction slot a pressure ratio comparable to the normal shock one is obtained for both nozzles. The results show that the back pressure can be increased up to the theoretical maximum if the static pressure and Mach number upstream of the shock as well as the pressure in the suction slot are kept constant. It is found, that if the back pressure increases above the theoretical value of a normal shock the primary shock relocates from the suction slot in upstream direction. Likewise, if the pressure in the suction cavity is higher

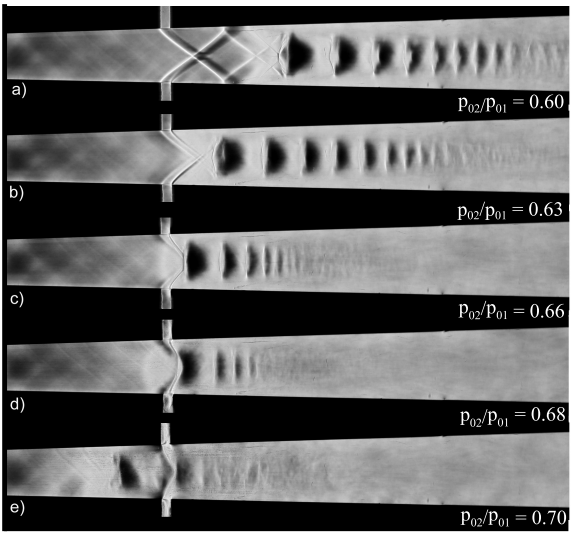

Fig. 2 Behaviour of a shock train at different back pressure ratios, Ma = 1.65

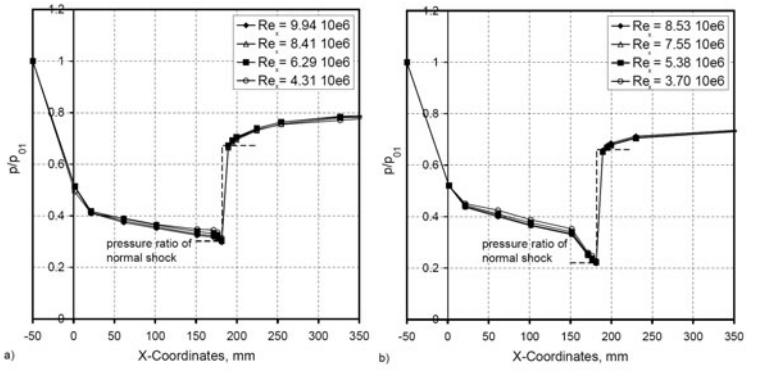

Fig. 3 Normalized wall pressure distribution a) Ma = 1.45, b) Ma = 1.65

than the static pressure upstream of the suction slot the shock becomes unstable and relocates.

4 Simplified Flow Model of the Suction Mechanism

A simplified model of the suction mechanism is sketched in Fig. 4. It can be stated that once the normal shock is established it is located at the upstream edge of the suction slot. As the normal shock enters the boundary layer it becomes very weak near the wall and finally disappears because the local Mach number drops to one, see Fig. 4. Since the static pressure p_1 is constant in the cross section just upstream of the shock and the shock strength varies with the distance from the wall, the pressure downstream of the shock must also vary. Because the shock is very weak or not even exists in the lower part of the boundary layer no significant shock induced compression occurs. Therefore, outside the boundary layer the pressure p_2 is higher than the pressure in the vicinity of the slot p_2'. The vertical pressure gradient downstream of the shock induces a secondary flow towards the suction slot, thereby satisfying the conservation of momentum. For the shock stabilization mechanism the suction mass flow is a significant parameter. Therefore, boundary layer measurements have been carried out in order to determine which part of the incoming boundary layer is removed. As sketched in Fig. 4 a streamline exists inside the boundary layer that determines which part of the flow is removed from the main flow; in the flowing to be called suction streamline. Only the mass flow inbetween the nozzle wall and the suction streamline is removed. As this streamline passes the shock wave it undergoes a significant increase in static pressure, the flow velocity is reduced and a shock induced total pressure loss occurs. Initially the suction streamline is parallel to the nozzle wall and it also does not change its flow direction across the normal shock. Yet due to the pressure gradient downstream of the shock eventually it is turned by 90 deg. This streamline reaches the nozzle wall at the downstream edge of the suction slot, which leads to the formation of a stagnation point. Assuming that

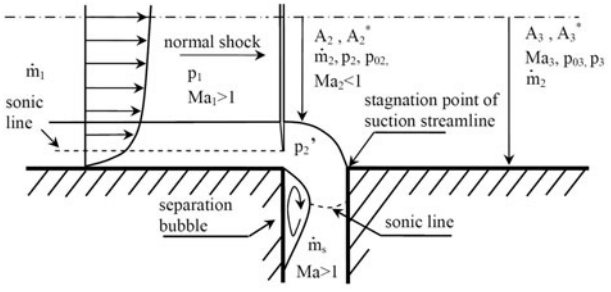

Fig. 4 Sketch of simplified flow model near the suction slot

the suction streamline - once the normal shock is passed - decelerates isentropically towards the stagnation point, the total pressure of the suction streamline must be equal to the static pressure of the flow downstream of the suction slot. This leads to the conclusion, that the mass flow removed from the boundary layer is a function of the total pressure distribution $p_{02}(y)$ across the boundary layer downstream of the normal shock and the static pressure value p_2 downstream of the same shock outside of the boundary layer. In Fig. 5 exemplarily the mass flow distribution over the nozzle cross section and the total pressure distribution immediately downstream of the normal shock are shown. The total pressure values downstream of the normal shock are obtained from the pitot tube measurements. From the measured suction mass flow of 22.9% the thickness of the removed boundary layer can be derived from Fig. 4a, which in this case is $y_s = 0.82$ mm. At this wall distance the local total pressure downstream of the normal shock becomes p_{02} = 3.26 bar. This value is very close to the static pressure measured downstream of the suction slot. Table 2 summarizes the static and total pressure values for all flow cases. One can note that in all cases the agreement of the total pressure $p_{02}(y_s)$and static pressure p_2 is quite

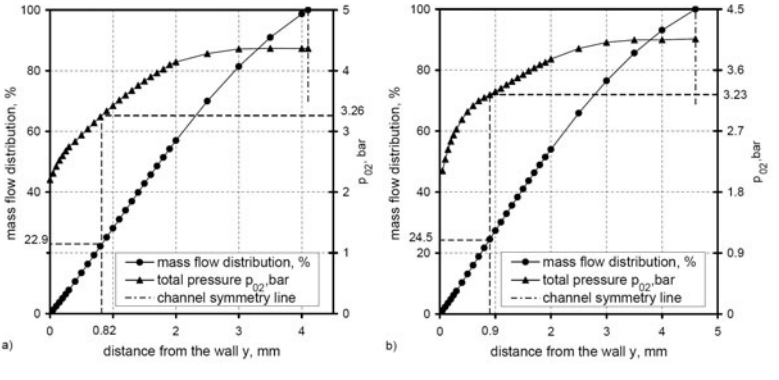

Fig. 5 Mass flow and total pressure distribution p_{01} = 4.75 bar, a) Ma = 1.45 b) Ma = 1.65

Table 2 Boundary layer height removed from main flow, comparison of total and static pressure

Ma = 1.45	p_{01} [bar]	$\dot{m}_s/\dot{m}_1$ [%]	y_s [mm]	p_2 [bar]	$p_{02}(h_s)$ [bar]	devitation [%]
	4.75	-22.9	0.82	3.23	3.26	0.9
	4.0	-21.8	0.76	2.65	2.75	3.8
	3.0	-24.6	0.88	2.05	2.09	1.9
	2.0	-24.7	0.82	1.33	1.38	3.7
Ma = 1.65	p_{01}[bar]	$\dot{m}_s/\dot{m}_1$ [%]	y_s [mm]	p_2 [bar]	$p_{02}(h_s)$ [bar]	devitation[%]
	4.75	-24.2	0.9	3.12	3.23	3.5
	4.0	-26.2	1.0	2.63	2.77	5.3
	3.0	-22.8	0.85	1.94	2.0	3.1
	2.0	-22.8	0.85	1.32	1.37	3.8

good. The remaining error can be attributed to the limited accuracy of the suction mass flow and pitot tube measurements.

The findings of this work can be summarized as follows. Firstly, no active suction needs to be applied to stabilize the shock train. The high pressure downstream of the primay shock of shock train is sufficient to propel the suction mechanism when the pressure inside the suction cavity is equal or smaller than the static pressure upstream of the suction slot. Secondly, due to the pressure gradient towards the suction slot downstream of the normal shock the incoming boundary layer does not need to negotiate a large back pressure, therefore a stable normal shock can establish. Thirdly, in order to obtain a normal shock inside a nozzle with significant boundary layer a certain part of the boundary layer needs to be removed. This part is confined by the suction streamline which exhibits a total pressure $p_{02}(y_s)$ equal to a the static pressure p_2 outside of the boundary layer.

References

1. Crocco, L.: One-dimensional treatment of steady gas dynamics. In: Emmons, H.W. (ed.) Fundamentals of Gas Dynamics, pp. 11–130. Princeton University Press (1958)
2. Carroll, B.F.: Characteristics of multiple shock wave/turbulent boundary-layer interactions in rectangular ducts. Journal of Propulsion and Power 6(2), 186–193 (1990)
3. Om, D., Childs, M.E., Viegas, J.R.: An experimental investigation and numerical prediction of a transonic normal shock/boundary layer interaction. AIAA 23(5), 707–714 (1985)
4. Matsuo, K., Miyazato, Y., Kim, H.D.: Shock train and pseudo-shock phenomena in internal gas flows. Progress in Aerospace Sciences 35, 33–100 (1999)
5. Weiss, A., Grzona, A., Olivier, H.: Behavior of shock trains in a diverging duct. Experiments in Fluids 49(2), 355–366 (2010)

Numerical Investigation of Over-Expanded Nozzle Flows: Influence of Internal Shock Waves

G. Fournier, A. Chpoun, M. Sellam, Ph. Rijasse, and S. Girard

1 Introduction

During ascent in low altitudes, space launchers experience high nozzle exit pressure leading to flow separation in the divergent. Two flow separation regimes have been identified: free shock separation (FFS) and restricted shock separation (RSS) regimes [1]. The transition between these two regimes with potential asymmetry of the flow could lead to high side loads which are of great practical importance. Meanwhile, modern rocket nozzles are optimized for maximum thrust during the entire ascent trajectory. In compliance with the launcher overall dimensions, the divergent part of these nozzles is truncated and the nozzle area-ratio are readjusted to satisfy the exit Mach number. Thus, the resulting nozzle contour (TOC contour) is characterized by a high angle of divergence at the throat compared to an ideal nozzle contour. As a consequence, an internal shock emanating from the nozzle throat region can interact with the shock waves system produced by flow separation at the end of the nozzle. Recently for the first time, the influence of the internal shock wave on the transition between free separation and restricted separation regimes has been questioned [2]. An experimental work has been carried out in the framework of a PhD thesis at ONERA, Meudon, France. This work has had both a theoretical part by analyzing shock waves interferences inside the divergent and an extensive experimental program during which measurements of both stationary and non stationary pressures were obtained.

A preliminary 2D numerical simulation has been also carried out. However, due to three dimensional nature of the experimental flow, the comparison between experimental and numerical computation was not satisfactory enough. After a short validation phase, the present work focuses on three dimensional simulations of

G. Fournier · A. Chpoun · M. Sellam
LMEE, University of Evry, 40 rue du Pelvoux, 91020 Courcouronnes-Evry Cedex, France

Ph. Rijasse · S. Girard
ONERA, 8 rue des vertugadins Meudon, 92190, France

these experiments. For this purpose, the FASTRAN CFD code has been employed. This code has full 3D capability treating both structured and unstructured meshes. It solves averaged Navier-Stokes equations with different turbulence models and numerical schemes. The next sections will provide an overview of the experimental study, the numerical work and the results with emphasis on hysteresis phenomenon that has been observed.

2 Overview of the Experimental Work

The experimental study has been carried out in the S8Ch facility of ONERA research center located at Meudon, France. Figure 2 shows the experimental set-up which consists of a supersonic planar nozzle. The divergent of the nozzle had a profile formed of two straight line segments of a constant angle producing an internal shock. During the course of these experiences, the internal shock intensity was modified by rotating the whole profile around an axis located close to the throat.The flow through the nozzle was established by aspiration of air at atmospheric conditions using vacuum pumps located downstream. The pressure at the nozzle exit section was varied using a second throat located in the diffuser. The nozzle was equipped with pressure transducers of both stationary and un-stationary (Kulite) type. The LDV technic was also employed to investigate the flow velocity profiles at the nozzle exit region. Flows were visualized both inside the nozzle and downstream of the exit section using Schlieren technique.

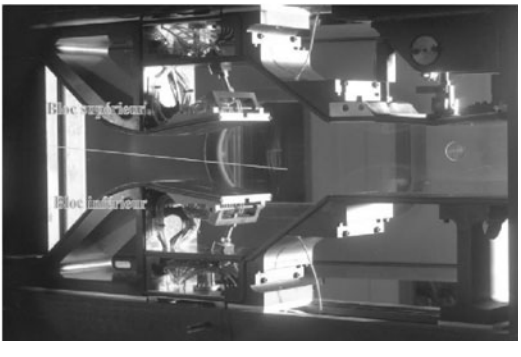

Fig. 1 Experimental set-up.

The main purpose of the experimental work was to investigate the transition of free separation regime to restricted separation regime and to study the influence of internal shock intensity on the whole separation process. As an example of results, Figure 2 shows Schlieren pictures obtained for a wide range of NPR (Nozzle Pressure Ratio). The parameter τ which is the ratio of second throat to the first

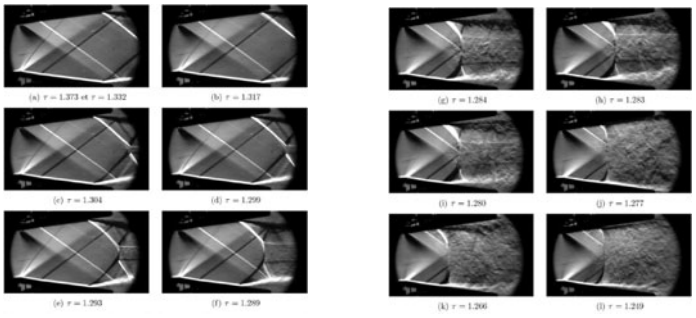

Fig. 2 Schlieren flow visualizations for high (left) and low (right) nozzle pressure ratios.

throat heights, is related to the NPR. These pictures clearly show the two separation regimes: the FSS regime that appears for $\tau \geq 1.280$ and the RSS regime ($\tau < 1.280$).

3 Numerical Work

3.1 CFD Code Description

Numerical study was conducted using a finite volume Reynolds-Averaged-Navier-Stokes (RANS) solver (CFD-FASTRAN) developed by the CFD Research Corporation. This code offers two upwind differencing schemes with a variety of higher order limiters to calculate the convective terms in the transport equations. Both explicit and fully implicit time integration schemes are available for steady and unsteady flow simulations. The code is based on a cell-centered finite volume discretization. Inviscid fluxes may be computed using Roe's flux difference splitting scheme and Van Leer's flux vector splitting. Both schemes are first order spatially accurate. Flux limiters may however be used to rise up the spatial accuracy. For Min-mod and Van Leer limiter the accuracy is 2nd order while for Osher-Chakravarty limiter the accuracy is up to third order. CFD-FASTRAN has five turbulence models ($k-\varepsilon$, $k-\omega$, $k-\omega$, SST-Menter, Spalart-Allmaras and Baldwin Lomax). For this study, the flux vectors are evaluated, at each time step, using Roe's upwind flux difference splitting, with a MINMOD flux limiter in order to achieve a high-order spatial accuracy. The turbulence model used is the one equation algebraic Baldwin-Lomax model. Time-integration is achieved using a fully implicit scheme. Local time stepping is also used to accelerate convergence to steady state. The solutions were allowed to converge until the L2 norm of the density residual dropped at least by four orders of magnitude.

In order to perform 2D CFD simulations of the flow field in the nozzle, finite volume grids are constructed using an algebraic grid generator software CFD-GEOM. Multi-block structured grids are used in this calculation. The computational domain includes the convergent-divergent part of nozzle and the zone downstream. The total number of cells is around 80,000 for the 2D computations and 1,050,000 in 3D.

The refinement of the grids near the wall was such as the first cell-height was about y+=1. The pressure is imposed both at the inlet and the outlet in order to define the Nozzle Pressure Ratio. For the 3D cases, a symmetry condition is applied in the spanwise direction in order to consider only one half of the nozzle in that direction.

3.2 *Validation of the 2D Computations*

Before computing the complex 3D flow in the nozzle, it is necessary to validate the CFD-FASTRAN solver in our case. To do so, 2D simulations for NPR varying from NPR=1.67 to NPR=10 were performed and the converged results were compared to the experimental visualizations from [2]. The comparisons for NPR=3.8 and NPR=2.02 are shown in Figure 3. For both NPR, the numerical results are in fairly good agreement with experiments since the shock structures are very close to each other. Indeed, the shock waves occurring because of the junction of the two segments in the diverging part have the same angle in both approaches and exit shocks happen at the same position and have similar shapes.

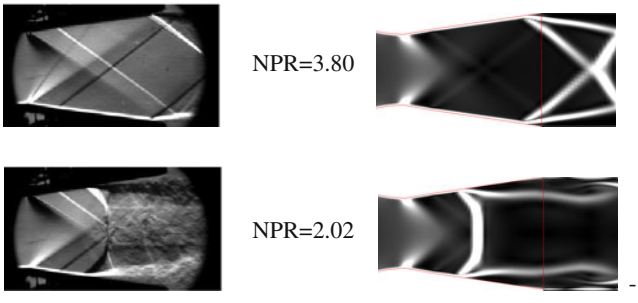

Fig. 3 Comparison of the shock structures obtained by experiments (left) and 2D computations (right) for two NPR. The structures are visualized using Schlieren Technique (experiments) and contours of $|\nabla\rho|$ (computations).

Provided the preceding results, it has then been concluded that the results were close enough from the experiments for the code to be validated in our particular case. It is however noteworthy that due to the highly 3D aspect of the flow, only a qualitative validation is meaningful and that a quantitative agreement, on the pressure distribution for instance, is not expected. As a conclusion, the next section will only provide qualitative observations that can enlighten us on the particular physics involves but no quantitative measurements could be considered as true.

3.3 *Hysteresis Phenomenon*

The flow for several NPR, varying from NPR=1.6 to NPR=10, was independently studied by 2D RANS simulations in order to observe the different flow regimes in

the nozzle. For each case, the flow was initialized with a NPR that was kept constant all along until statistical convergence. It then appears that under a critical NPR, $\mathrm{NPR}_{crit} = 1.9$, the flow in the nozzle becomes asymmetrical with respect to the nozzle axis. This observation is in agreement with experiments since the asymmetry is recovered in Figure 2.(k)-(l) (corresponding to NPR=1.7 and NPR=1.67 respectively), even if the critical NPR is slightly overestimated by RANS simulations with respect to experiments (the flow is still symmetrical in experiments at NPR=1.9).

In order to study if NPR_{crit} as the same value whether the NPR is increasing or decreasing, two additional computations were performed. For the first simulation, the flow was initialized with NPR=2 and the pressure ratio was progressively decreased down to NPR=1.65, the statistical convergence being reached at each step. In the meantime, the initial NPR for the second computation was set to NPR=1.65 and was then increased up to NPR=2. The results at different stages of the simulations are displayed in Figure 4. On the upper part, representing the decreasing NPR simulation, it is clear that the flow is initially symmetrical. Then, for $\mathrm{NPR} \leq 1.90$, the flow becomes more and more asymmetrical when the NPR further decreases. On the contrary, the increasing NPR simulation shows that when the flow is initialized with an asymmetrical regime, one have to increase the NPR much higher than the critical NPR in order to recover a symmetrical flow. The lower part of Figure 4 indeed indicates that the flow is not perfectly symmetrical with respect to the nozzle axis even at NPR=2.0. However, a further increase to NPR=2.1 (not shown here) would lead to a symmetrical flow. To conclude, this part of the study clearly demonstrates that the symmetrical nature of the flow is very dependent on the variation of NPR in the nozzle. This observation is of great industrial interest since the flow asymmetry lasts longer for increasing NPR, which is typically the case during ascent of Spaceship or Rockets.

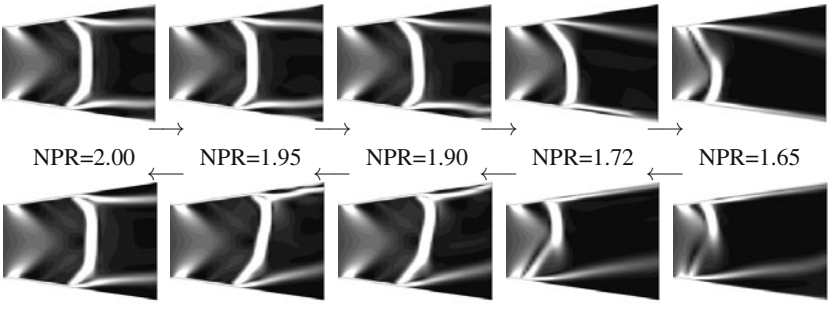

Fig. 4 Comparison of the shock structures obtained by 2D computations for a decreasing (top) and an increasing (bottom) NPR. The structures are visualized using contours of $|\nabla\rho|$.

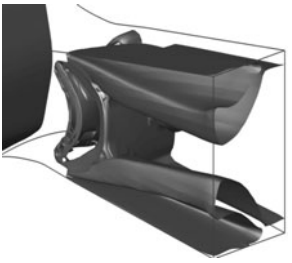

Fig. 5 Shock structures obtained by 3D simulations at NPR=1.90.

A 3D simulation was then conducted for NPR=1.90 in order to study the influence of the transverse direction on NPR_{crit} at which the asymmetry occurs. As shown in Figure 5, the flow is symmetrical at NPR=1.90, unlike for 2D simulations. This observation is consistent with the experimental results since the critical NPR was experimentally found to be around NPR=1.70, meaning that for higher NPR, the flow is still symmetrical. In addition, Figure 5 also emphasizes the highly 3D nature of such a flow.

4 Conclusions

Both an experimental and a numerical study were conducted in order to study the internal shock structures that occurs because of the joint of two flat plates having different angles in the divergent part of a rocket nozzle. It was demonstrated that the flow regimes are really different from one NPR to another. The numerical part of the study shown that an asymmetrical regime occurred under the critical NPR NPR_{crit}, that depends on whether NPR was increasing or decreasing. Finally, 3D simulations were performed and emphasized on the highly 3D aspect of the flow. In a future work, the 3D simulations will be used to study the influence of the inner shock caused by the junction and its interactions with the outlet shock.

References

1. Nave, L., Coffey, G.: Sea Level Side Loads in High-Area-Ratio Rocket Engines. In: AIAA/SAE 9th Propulsion Conference, AIAA-73-1284, Las Vegas, Nevada (November 1973)
2. Girard, S.: Etude des Interférences de Choc dans les tuyères surdétendues à choc interne. Thèse de doctorat de l'Université Pierre et Marie Curie, ONERA-Meudon, septembre 30 (2009)

Asymmetric Flow Separation in de Laval Nozzle

V.V. Golub, S.V. Efremov, and A.S. Saveliev

1 Introduction

Operation conditions of rocket engines at sea-level and at high altitudes are different. The considerable difference in value of pressure of ambient air leads to different regimes of outflow from the nozzle – from the overexpanded regime at ground level to the underexpanded at high altitude. Different regimes of outflow from the nozzle cause considerable changes in flow pattern behind the nozzle outlet cross-section. One of the problems is the presence of shock structure in outgoing jet that causes flow separation from the wall of nozzle. It is known that separation point has no stable position on the nozzle surface, but fluctuates during the time. Boundary layer separation leads to the development of an asymmetric developed unsteady flow separation, and hence to unstable in time side-loads on the nozzle. Although modern rocket nozzles have a high longitudinal strength, they are not designed for side loads of high magnitude. The problem of high side loads was encountered in engine testing Vulcan rocket Ariane-5 [1, 2, 3]. Studies have shown that at the expiration of overexpanded regime two patterns of the jet of a nozzle implement, so-called free (Free Shock Separation, FSS) and restricted (Restricted Shock Separation, RSS) separation, with the side loads appearing in both cases [4].

The asymmetric flow separation can cause considerable side loads on the nozzle due to asymmetric pressure distribution on the nozzle surface. This problem is been investigated from second half of twenty centaury and there are several numerical expressions where the criterion of asymmetric flow separation described in terms of static pressure of jet and ambient pressure [5, 6]. But the conditions of all modern works are almost the same as in real rocket engine. In this experimental work we have tried to investigate the process of overexpanded jet formation and asymmetric flow separation development at relatively low pressure values in ambient air and in "combustion chamber".

V.V. Golub · S.V. Efremov
Joint Institute for High Temperatures RAS, 13/2 Izhorskaya st., Moscow

S.V. Efremov · A.S. Saveliev
Moscow Institute of Physics and Technology, 9 Institutskiy lane,
Dolgoprudny, Moscow reg., Russia

2 Experimental Setup and Diagnostics

2.1 Supersonic Wind Tunnel

The investigations were conducted at atmospheric vacuum supersonic wind tunnel with Mach number M=2. At this setup air from atmosphere goes through the nozzle that forms supersonic jet with M=2 and static pressure p_{st}=0.15 atm. The diameter of outlet nozzle cross-section D=110mm. Approximately first 40 s there is underexpanded regime of submerged jet outflow. Pressure ratio $n=p_{st}/p_a$ is greater than 1, p_a – pressure in working chamber (ambient pressure). Then the fully-expanded regime occurs, when n=1. At this regime the velocity profile is uniform at any point of given jet cross-section as it must be in de Laval nozzle. During the test run n decreases and at $n<1$ the overexpanded regime occurs. At first this regime is characterized by discontinuous surface (in common 3D case) or by pair of oblique shocks (at jet cross-section) that start on nozzle edge. When n reaches some value that is less than 1 this shocks goes into the nozzle causing flow separation from its inner surface as boundary layer becomes unstable with shock presence. This time period was in interest during experiments as it is characterized by considerable unsteadiness and asymmetry in separation point position. Described changes in n and pressures are shown at Fig. 1. Working chamber of wind tunnel was equipped with schlieren and particle image velocimetry (PIV) diagnostics.

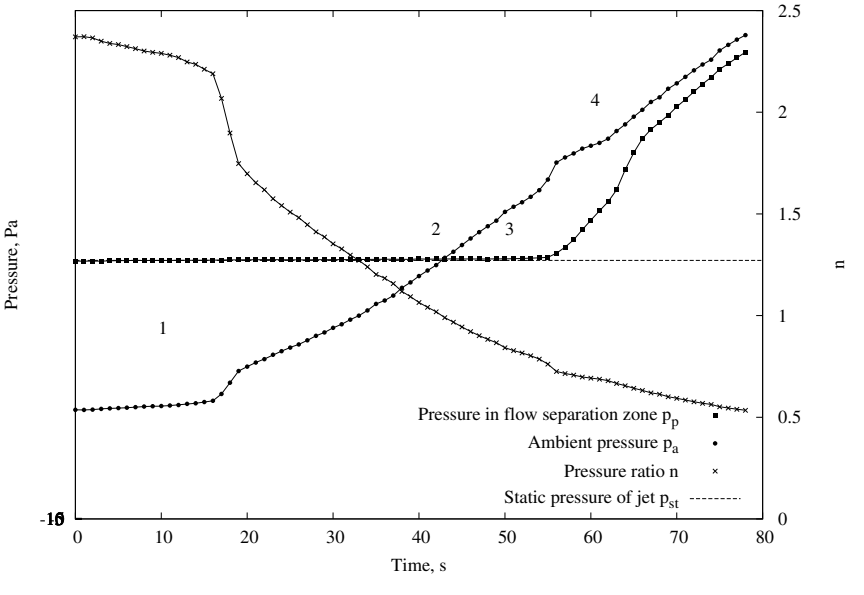

Fig. 1 Pressures and pressure ratio during test run. Atmospheric pressure is 102.5 kPa. 1 – underexpanded regime, 2 – fully expanded, 3 – overexpanded, 4 – overexpanded regime with separation.

2.2 Schlieren and PIV Techniques

The submerged supersonic jet was visualized with digital schlieren imaging by the slit and knife technique, Toepler method. Optical system consists of schlieren device IAB-451 [8], arc xenon lamp XBO 150W/1 as illumination of region to visualize, high speed digital videocamera Photron FASTCAM SA4, that allows registering of frames with speed up to 20000 fps, electronic shutter speed 1/1000000 s, frame resolution of 0.25 MPx. Total videocamera's memory was divided on the ten parts and each part was filled on experimenter's command. The photoregistration process was synchronized with the static pressure in the exit cross section of nozzle and in working chamber (ambient pressure) recording. The experiments have shown that the typical frequency of unsteady formation process of asymmetric flow separation is 1-2 kHz that is one order less than acquisition speed. This circumstance allowed obtaining the detailed dynamics of separation point positions near the upper and down edges of nozzle. Each frame from one series, i.e. that corresponds to the same value of pressure ratio n, was processed by the parallel algorithm, developed on LaVision DaVis 7.2 Command Language.

To show FSS regime of flow separation the PIV was used in experiments. LaVision 2D PIV system was used with CCD-sensor 1600 x 1200 px, with interframe time 0.7 μs and standard Nikon lens with focus length 50 mm. The visible to camera area was 10 x 10 cm^2. The smoke particles with typical diameter <1 μm [7] was used as tracers introduced in flow. The exposition of first image (one shoot gave two separate images because of double frame regime) was synchronized with pressure registration as in a case of schlieren imaging. Each laser (Nd:YAG) pulse had approx 100 mJ at 532 nm wave length and the duration of laser emission was 6 ns.

2.3 Digital Image Processing

As it was mentioned above obtained in experiment schlieren images were digitally processed. The first step is the linear filter Laplas-1 applying, that makes fronts of shocks sharper. Then the image normalization was carried out, i.e. the value in each pixel became the value 0 or 1, and this allowed separate pixels that are on shock fronts. Obtained coordinates of these pixels were approximated by straight line with the root mean square minimization algorithm. Since the equation of inner surface of nozzle is known and the coordinates of pixels is in dependence with real world coordinates inside the working chamber, the intersection of oblique shock and nozzle wall gives the separation point position in relation to nozzle edge at time moment that corresponds to frame exposition time. This algorithm was applied sequentially to each frame of series (i.e. the series of schlieren pictures that were obtained at the same value of pressure ratio n), and then it was applied to each series (usually 10 series were obtained in experiment). As the result the dynamics of difference (Δx) in values of separation points position (top and bottom) during the time of order 100 ms (see Fig. 2). The root mean square $\overline{\Delta x}$ of this quantity is

proportional to the amplitude of side loads. The side loads F_{SL} value was estimated as function of pressure ratio:

$$F_{SL} = \pi \overline{\Delta x} D \cdot (p_p - p_{st}), \tag{1}$$

where p_p – pressure near the nozzle surface in separation region.

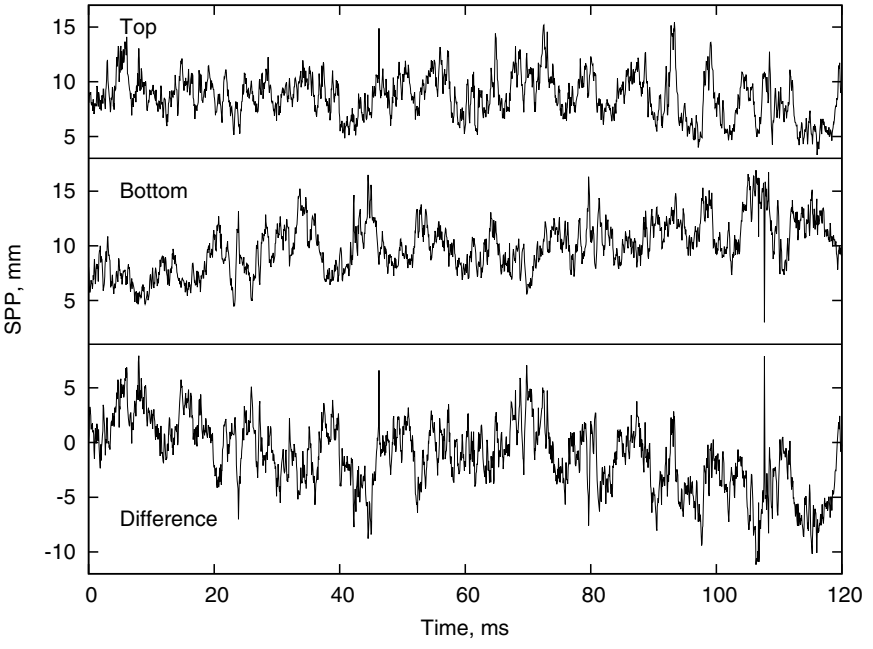

Fig. 2 Top and bottom positions of separation point (SPP) and their difference during the time. Pressure ratio n=0.65

3 Experimental Results

The main results of experiments are in Fig 3. It presents the dependence between relative to thrust side-loads (in %) and pressure ratio. By choosing ylog scale it can be shown that at given experiment conditions the amplitude of side-loads rise significantly by the passing critical value of n_{cr}=0.75. Experiments at n lower than 0.55 are complicated because shocks goes to the opaque nozzle and there is no possibility to obtain the schlieren pictures.

From the sequential images and graphs of separation point position (see Fig. 2) it was found that typical frequency of separation points oscillation is near 1.5 kHz

in n range 0.55-0.75. But this oscillations are modulated by lower frequency with the order of value 0.1 kHz, as it can be seen at Fig. 2.

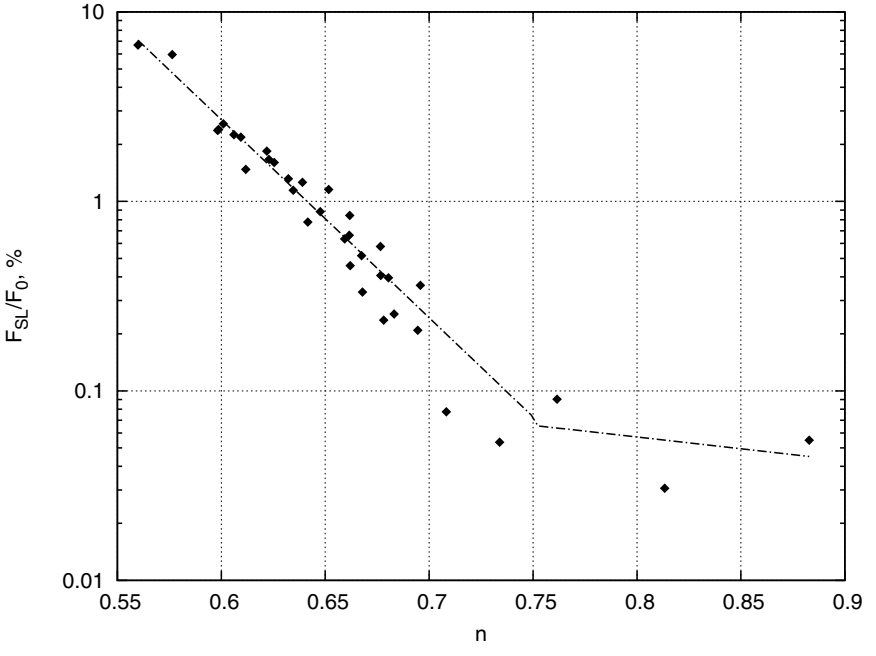

Fig. 3 Relative to thrust value of side-loads at different values of n.

On the Fig. 4 the example of PIV-measurements is presented: the two-dimensional vector field of velocity directions in overexpanded supersonic airjet with flow separation is presented. In this case the pressure ratio is rather low (n=0.65) and there no any recirculation zone is not observed. The same picture is observed in cases on n=0.55-0.75, so under given experimental conditions only FSS is observed.

4 Conclusions

With the digital videoregistration of schlieren pictures, digital pressure recording and with digital processing of acquired images the dependence between the side loads (in relation to nozzle thrust) and pressure ratio was obtained. Critical value of n, when the side-loads rise significantly, was obtained. With the PIV measurements it was shown that only FSS regime can be occurred at given experimental conditions.

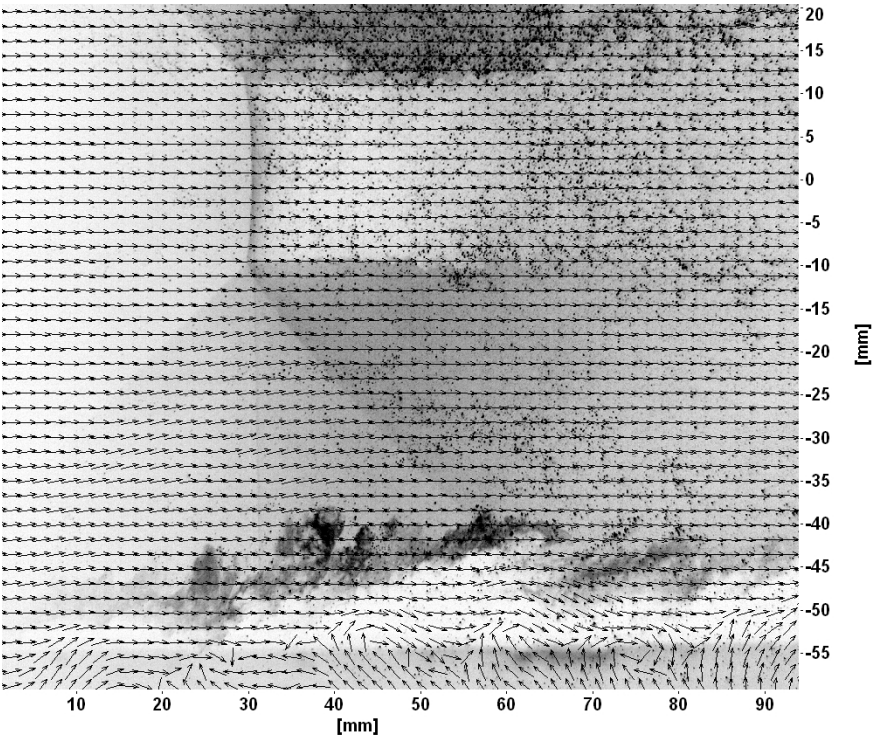

Fig. 4 Velocity vector field in jet behind the nozzle. y = 0 - nozzle axis, x = 0 - nozzle exit section.

References

1. Frey, M., Hagemann, G.: Status of flow separation prediction in rocket nozzles. AIAA Paper 98-3619 (1998)
2. Frey, M., Hagemann, G.: Flow separation and side loads in rocket nozzles. AIAA Paper 99-2815 (1999)
3. Hagemann, G., Frey, M., Koschel, W.: Appearance of restricted shock separation in rocket nozzles. J. Propulsion and Power 18(3), 577–584 (2002)
4. Frey, M., et al.: European cooperation on flow separation control. In: Proc. of 4th International Conference on Launcher Technology "Space Launcher Liquid Propulsion", pp. 1–10 (2002)
5. Summerfield, M., Foster, C., Swan, W.: Flow separation in over-expanded supersonic exhaust nozzles. Jet Propulsion 24(5) (1954)
6. Lawrence, R.A.: Symmetrical and unsymmetrical flow separation in supersonic nozzles. Ph.D. Thesis, Southern Methodist University (1967)
7. Raffel, M., Willert, C.E., Wereley, S.T., Kompenhans, J.: Particle Image Velocimetry. Springer, New York (2007)
8. Vasiliev, L.A.: Schlieren methods. Nauka, Moscow (1968)

2D Numerical Simulation of Jet Injection into a Channel with a Cavity

N. Fedorova and I. Fedorchenko

1 Introduction

Flow configurations with jet/supersonic flow interactions are met in different applications. Among them are supersonic aircraft cooling systems, thrust vector control devices, combustion chambers of hypersonic vehicles (scramjets), etc. From physical standpoint, the resulting flow structure represents complex phenomenon with separated, recompression and jet induced bow shocks, contact discontinuities and recirculating zones included. The jet itself possesses complex underexpanded structure, comprising barrel shocks and Mach disks. Thus, simulation of these types of flows is challenging task for numerical approaches, because accurate prediction of every flow detail has to be provided.

Within several last decades extensive experimental investigations on transverse injections of different gases and liquids into supersonic flows have been carried out. The list of the papers on the topic cited here is far from being complete [1]–[6]. The main investigated characteristic is naturally the mixing rate. High mixing level of the primary and secondary flows is responsible for effective combustion of the fuel in a combustion chamber which is important for scramjet design. Consequently the jet penetration height (depth) is considered to be an important parameter as well, since deeper penetration of fuel provides better mixing. Along with it, a low level of total pressure losses should be ensured. A general representation of the flow structure nearby the jet injection has been reproduced based on the experimental data as shown in [3]. Later it has been verified by numerical investigations.

A brief list of numerical papers devoted to the topic is presented below. 2D RANS-based simulation of slot injection on a flat plate has been performed by [7]. Validation of the numerical results has been made on the basis of experimental data and obtained disagreement has been related to 3D effects. Paper [8] is

N. Fedorova · I. Fedorchenko
Khristianovich Institute of Theoretical and Applied Mechanics SB RAS
Instituskaya St., 4/1 Novosibirsk (Russia)
NSUACI Leningradskaya str., 113 Novosibirsk (Russia)

also performed in 2D approach and investigates mixing characteristics of the flow. Qualitative agreement has been achieved and quantitative discrepancies have been similarly explained by 3D phenomena. Good agreement between computed and measured wall pressure distributions has been attained by [9], and detailed picture of the jet flow has been reconstructed in the frame of 2D setup. 3D numerical simulation of staged transverse sonic injection in Mach 2 flow behind a backward facing step is presented in [10]. The numerical results have predicted the experiments on a good level in area away from the injection locations, though some disagreement in vicinity of the jets has been observed.

It can be concluded that, though 2D simulations of the problem possess understandable simplifications and some inaccuracy, still performance of parametric studies in 2D looks promising due to lower machine time demands that allows carring out multiple computations. In the current paper, a supersonic flow in a channel with an abrupt expansion/cavity interacts with helium/hydrogen jet. Numerical investigation is performed by means of 2D RANS-based approach closed by $\kappa - \omega$ SST model. Previously validation on an air injection through a flat plate slot into Mach 6 flow has been performed by the authors [11] in the frame of experiments [4].

2 Problem Statement, Boundary Conditions and Grid

Two cases are investigated: the case 1 includes a hydrogen jet embedded in a channel with a cavity; the second case represents helium injected in a channel with an abrupt expansion (backward facing step). The computational domains are shown in Fig. 1. The cavity has an inclined aft ramp and the channel has light divergent angle toward the outlet as indicated in Figure. At the inlet section, profiles of all turbulent flow parameters at Mach 2.5 and 2.8 are put taking into account turbulent boundary layer developed at the top and bottom walls. On the walls, non-slip boundary conditions are implemented and temperature of the walls is equal to 300K. At the exit pressure-outlet conditions are used. In the case 1 three different jet pressure values are presented corresponding to three jet to free-stream momentum flux ratio $J = 2.35$; 3.5 and 5, respectively. In the case 2 the jet angle is varied.

The problem has been solved with ANSYS FLUENT 12.0 instrumentation. Density-based solver has been chosen, along with implicit formulation and TVD approach based on the Roe flux splitting scheme for the spatial discretization. The regular quadrilateral grid with towards-to-wall refinement has been constructed, and

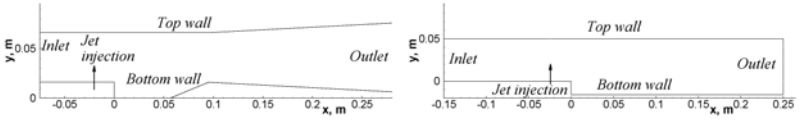

Fig. 1 Computational domains; left: case1; right: case 2.

Table 1 Main parameters of the jet and channel flow

Case No	Parametrs	Channel flow	Jet flow
1	Mass fraction of hydrogen	0	1
	Static pressure, MPa	0.185	2.6; 3.8; 5.5
	Mach number	2.5	1
	Total temperature, K	1800	300
2	Mass fraction of Helium	0	1
	Static pressure, MPa	0.11	1.72
	Mach number	2.8	1.4
	Total temperature, K	2000	293

appropriate resolution of the orifice area is provided. The law of the wall variable y^+ is kept lower then unity everywhere of the domain walls. Convergence study on subsequence of refined grids has been performed and reasonable results have been attained for the grid size of overall node number of about 500 000.

The injectant gases are H_2 (case 1) and He (case 2). Main parameters of the primary and secondary flows are indicated in Table 1.

3 Computations of Hydrogen Injection in Channel (Case 1)

Numerical contours of Mach number for three jet to free-stream momentum flux ratios J are presented in Fig. 2. The jet induced shock (JS) arises in vicinity of the injection, and hits the top wall where a separation appears. Also the recompression shock (RS) behind the injection is observed in the cases of moderate jet mass rate ($J = 2.35$ and 3.5), and it interacts downstream with the shock reflected from the top surface. In vicinity of the aft ramp of the cavity, a compression wave (CW) is generated due to interaction of the mixing layer with the surface. Subsequent shock reflections take place downstream.

It can be seen that with the jet mass rate increase, the size of the separation zones both on the top and bottom walls rises. It is explained by the fact that with jet mass rate increasing, the primary separation zone enlarges. Therefore the primary shock becomes stronger, and it separates the boundary layer at the top of the channel. In return, the top wall separation is intensified as well and produces stronger separation wave. Interacting shocks coming from the bottom and top surfaces in the case of $J = 5$ reflect in irregular way (IR), giving rise to a normal shock in central part of the channel. Examining the flow in vicinity of the jet in the case of $J = 5$ (Fig. 3) allows to observe clearly two jet barrels (JB) and a higher jet penetration into the channel. Accordingly, the separation (S1) ahead of the jet is several times bigger then that for the $J = 3.5$ case. Behind the jet, at moderate mass flow rates the reattachment of the boundary layer takes place, while for $J = 5$ the cavity

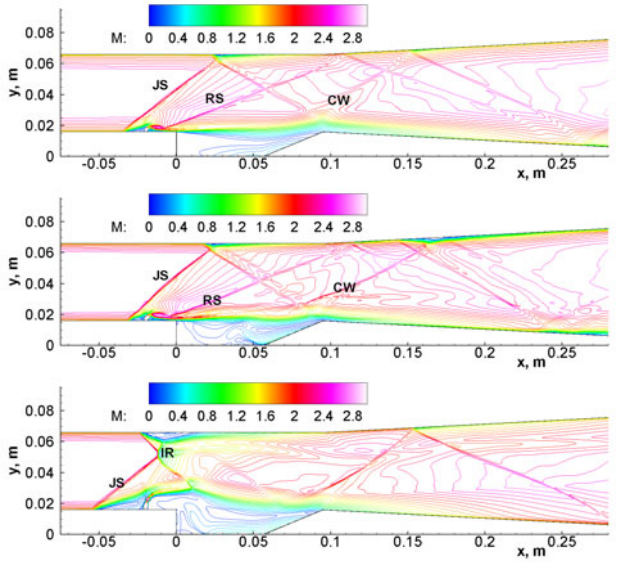

Fig. 2 Mach number contour lines for J top: 2.35, middle: 3.5, bottom: 5.

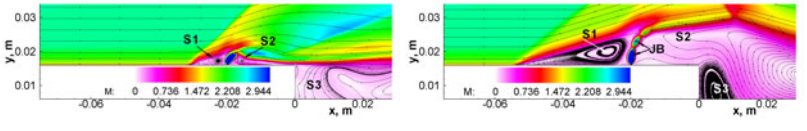

Fig. 3 Mach number fields and stream traces left: $J = 3.5$, right: $J = 5$.

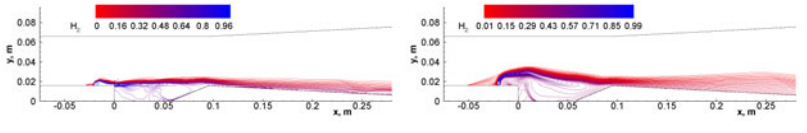

Fig. 4 Mass fraction fields of hydrogen: left: $J = 3.5$, right: $J = 5$.

recirculation zone is merged with the separation zone behind the jet (S2, S3). Therefore, the higher mass flow rate leads to the jet penetration enhancement and wider mixing layer between the gases as shown in Fig. 4 where hydrogen mass fraction fields are depicted.

On the other hand, intensification of the shocks and the Mach reflection generates a zone of high pressure (Fig. 5). I.e., the higher mass flow rates of the jet are, the higher pressure losses occur. Further increase of the J value would lead to the normal shock strengthening and the channel throat chocking.

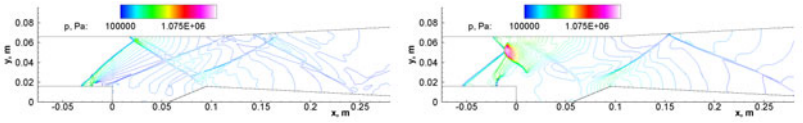

Fig. 5 Pressure fields left: $J = 3.5$, right: $J = 5$.

4 Computations of Helium Injection (Case 2)

We shall consider influence of the jet injection angle on flow in a channel with an abrupt expansion with helium injected into it. The mass flow of the jet is fixed. In Fig. 6 the Mach number fields are depicted for two cases of the jet angles $\alpha = 30^\circ$ and 60°. With the injection angle increasing, the intensity of the jet induced shock (JS) enhances and it produces a larger separation in vicinity of the jet location (S2). In the case of 60° jet angle, the shock JS has higher intensity and when it comes to the top wall, it causes the boundary layer separation S1 (right Fig.6). The top wall separation shock (RS) originates, and the two shocks interact with each other, forming the high pressure zone inside the channel downstream the intersection area. At the top wall, the recompression shock (RW1) is observed which interacts with the recompression wave RW2 generated by the primary recirculation zone behind the step. With the jet angle increase, the size of the recirculation zone behind the jet grows, and, similar to the case 1, combines with the primary recirculation zone behind the step. Further rise of the injection angle up to the transverse one at a fixed mass flow rate leads to the channel chocking, because the shock waves overlap giving rise to the normal shock wave.

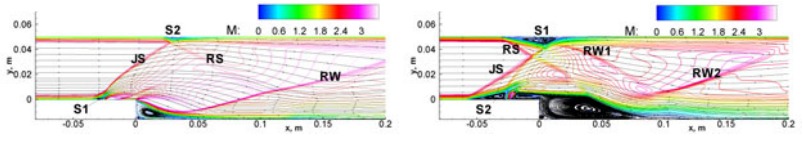

Fig. 6 Mach isolines and streamlines for the helium incjection angles left: $\alpha = 30^\circ$, right: $\alpha = 60^\circ$.

With increasing of the injection angle, the jet penetration into the channel increases, and higher level of mixing is observed at the outlet section along with growth of the mixing layer thickness. It is favorable sign for the mixing of the primary and secondary flows. Meanwhile, the steeper injection accounts for more intensive shock waves inside the channel, which lead to higher pressure losses. The last fact is certainly an undesirable feature for aircraft design.

5 Conclusion

Numerical 2D RANS simulation of helium and hydrohen jet injection into supersonic flows in channels of different geometry is provided under the conditions of high enthalpy aerodynamic facility. Detailed structure of the flow has been obtained and analyzed. It has been shown that increasing of the hydrohen jet mass flow rate leads to the higher jet penetration and better mixing of the primary and injected gases, though higher pressure losses occur. Similar effects are observed with the jet angle growth. Simulation results are aimed on the better understanding of the mixing processes in the combustor chamber of prospective aircrafts.

Acknowledgement. The work has been financially supported by Russian Foundation for Basic Research, grant 09-08-01001-a and by Ministry of Education and Sciences of Russian Federation, AVC Program "Development of Scientific Potentials of Higher School", grant No 2.1.1/11336.

References

1. Hautman, D.J., Rosfjord, T.J.: Transverse Liquid Injection Studies. In: 26th Joint Propulsion Conferenceon. SAE, ASME, and ASEE, AIAA-1990-1965, Orlando, FL, July 16-18 (1990)
2. Schetz, J.A., Billig, F.S.: Penetration of gaseous jets injected into a supersonic stream. J. Spacecraft and Rockets 3(11), 1658–1665 (1966)
3. Spaid, F.W., Zukoski, E.E.: Study of the Interaction of Gaseous Jets from Transverse Slots with Supersonic External Flows. AIAA J. 68 6(2), 205–212 (1968)
4. Sterrett, J.R., Burber, J.B., Alston, D.W., Romeo, D.J.: Experimental investigation of secondary jets from two-dimensional nozzles with various exit Mach numbers for hypersonic control application. NASA TN D-3795 (1967)
5. Ben-Yakar, A., Mungal, M.G., Hanson, R.K.: Time evolution and mixing characteristics of hydrogen and ethylene transverse jets in supersonic crossflows. Phys. Fluids 18, 026101:1–026101-16 (2006)
6. Rothstein, A.D.: A study of the normal injection of hydrogen into a heated supersonic flow using planar laser-induced fluorescence. Los Alamos Report LA-12287-T (1992)
7. Rizzetta, D.P.: Numerical Simulation of Slot Injection into a Turbulent Supersonic Stream. AIAA J. 92 30(10), 2434–2439 (1992)
8. Clark, S.W., Chan, S.C.: Numerical investigation of a transverse jet for supersonic aerodynamic control. AIAA Paper 92-0639 (1992)
9. Erdem, E., Kontis, K.: Numerical and experimental investigation of transverse injection flows. Shock Waves J. 20, 103–118 (2010)
10. Chakraborty, D., Roychowdhury, A.P., Ashok, V., Kumar, P.: Numerical investigation of staged transverse sonic injection in Mach 2 stream in confined environment. Aeronautical J. 107(1078), 719–729 (2003)
11. Fedorov, A.V., Fedorova, N.N., Fedorchenko, I.A.: Numerical simulation of jet injections into supersonic flow. In: Abstracts of XV International Conference on the Methods of Aerophysical Research: Novosibirsk, pp. 85–86 (2010)

Pseudo-shock System Structure in Rectangular Laval Nozzles with Gaps

T. Gawehn, M. Giglmaier, J.F. Quaatz, A. Gülhan, and N.A. Adams

1 Introduction

The acceleration of a fluid in a Laval nozzle to supersonic speed leads to a significant decrease of the static temperature in the flow, and deceleration via a normal shock results in a sudden reheating. Both effects are used within the joint project PAK 75 (Deutsche Forschungsgemeinschaft DFG) for the homogeneous ignition of a precursor and, hence, for the production of gas phase synthesized nanoparticles with narrow size distribution. However, the shock boundary layer interaction at the desired shock position leads to the formation of a so-called pseudo-shock system. Thereby, the heating rate across the shock system is reduced and the homogeneity of the particle growth is negatively affected by the inhomogeneous downstream conditions. Such pseudo-shock systems have been investigated by many research groups and a comprehensive overview is given by [1].

A necessity for many investigations is optical access to the flow. To avoid stresses within the quartz glass side walls, the windows have to be mounted with small gaps of $\Delta z = O(10^{-4})$ m. As it has been shown already in [2], these gaps result in small bypass mass flows which play a significant role in presence of high pressure gradients (e.g. critical cross sections and shocks).

The objective of the current investigation is an experimental analysis on the effect of bypass mass flow on the pseudo-shock system for different gap sizes. Additionally, numerical simulations performed by the Institute of Aerodynamics and Fluid Mechanics are used to verify the observed phenomena.

T. Gawehn · A. Gülhan
Institute of Aerodynamics and Flow Technology, Supersonic and Hypersonic Technology Department, German Aerospace Center (DLR), Linder Höhe, 51147 Cologne, Germany

M. Giglmaier · J.F. Quaatz · N.A. Adams
Lehrstuhl für Aerodynamik und Strömungsmechanik, Technische Universität München
Boltzmannstrasse 15, 85748 Garching, Germany

2 Experimental Tools

The experiments are carried out at a fully automated DLR test rig in Cologne. The test rig allows stagnation pressures p_{01} up to 54 bar, stagnation temperatures T_{01} up to 800 K and mass flow rates $\dot{m}_{01}$ up to 1.5 kg/s. The test conditions are set and controlled by a process control system. The accuracy level of the stagnation conditions is better than $\pm 1\%$ for the stagnation temperature T_0 and $\pm 0.5\%$ for the stagnation pressure p_0.

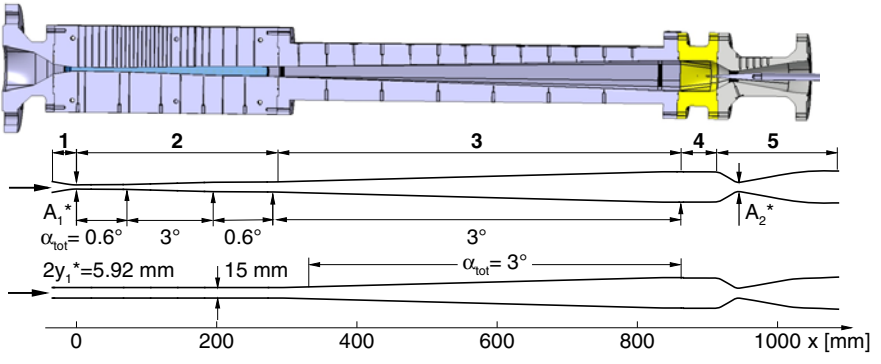

Fig. 1 Geometry of the test rig in Colone

The geometry of the test rig is shown in fig. 1. Within the primary nozzle ① and ②, the flow is accelerated to supersonic flow speed. The location of the shock system within the divergent part ② of the first Laval nozzle is defined by the cross sectional area of the second critical nozzle throat ⑤ and can be controlled by a slender movable cone. For determining the flow conditions, static pressure taps are placed on the top wall of the whole system. The modular primary nozzle can be equipped with optical access on both parallel side walls. Metallic side walls with additional pressure taps for dynamic pressure measurements can be used instead. The downstream conditions of the shock system can be analyzed in the doubly divergent reactor part ③ by means of thermocouples in the flow and pressure taps on the top wall.

In order to analyze the influence of the gap size between the quartz glass side walls and the metal structure of the facility, three different set-ups of the modular primary nozzle are investigated. A sketch of the channel cross section is given in fig. 2. The gap size between the nozzle contour and the side wall can be varied by adding some aluminium sealing. Investigations with approximately 0.0 mm gap (fig. 2a) are performed with metallic side walls without flow visualization. Further tests are performed with quartz glass windows with 0.1 mm (fig. 2b) and 0.2 mm gap width (fig. 2c) . By increasing the gap size to 0.2 mm, the channel half width is increased to 7.6 mm.

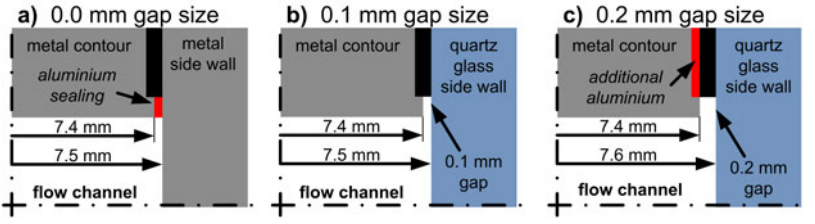

Fig. 2 Cut-view at $x = \text{const.}$ of the analyzed gap configurations

3 Investigation Techniques and Test Procedure

The static wall pressure distribution is recorded with miniature Electronic Pressure Scanners (Esterline ESP-32 HD®) of the PSI System 8400 and Ethernet Intelligent Pressure Scanners (Model 9116 EIPS®). In total, 80 static wall pressures can be recorded simultaneously with an accuracy of better than ± 3.5 mbar. For dynamic pressure measurements five XTL-IA-140M® of Kulite Semiconductor with an accuracy of better than ± 6.8 mbar are used.

Flow visualization is performed with a Z-type schlieren system with spherical mirrors of 150 mm in diameter using an 11 Megapixel monochromatic PROSILICA GE4000 CCD-Kamera and a 50 ns flash lamp. Thereby, the small scale structures of the complex pseudo-shock system can be timely resolved.

For the computation of the flow, the commercial fluid dynamics solver Ansys CFX is used by the Institute of Aerodynamics and Fluid Mechanics. The 3-D time dependent Favre-averaged Navier-Stokes equations for compressible flow are combined with an explicit algebraic Reynolds stress turbulence model (EARSM) to resolve secondary flows such as corner vortices in square cross sections. Further details on the simulation can be found in [3].

The flow is controlled by setting the stagnation conditions (p_{01}, T_{01}) upstream of the primary nozzle and by adjusting the position of the central body in the secondary nozzle throat, i.e. changing the pressure downstream of the primary nozzle. Thereby, different stagnation pressure ratios p_{02}/p_{01} across the pseudo-shock system can be investigated whereas p_{02} indicates the total pressure right upstream of the secondary nozzle, measured at about $x = 900$ mm downstream of the primary nozzle throat A_1^*.

4 Test Results

Effect of Gap Size on the Wall Pressure Distribution

The effect of the gap size on the pseudo-shock system structure has been investigated at different stagnation conditions (p_{01}, T_{01}) and different stagnation pressure ratios p_{02}/p_{01}. Using experiments at $p_{01} = 6.0$ bar and $T_{01} = 300$ K the main effects will be analyzed by means of the recorded static wall pressure distribution.

In fig. 3 experimental data for different gap sizes at stagnation pressure ratios $p_{02}/p_{01} = 0.7$ (3a) and $p_{02}/p_{01} = 0.6$ (3b) are presented together with the numerical simulations at $p_{02}/p_{01} = 0.7$ (3c). Figure 3d shows dynamic pressure measurements for a gap size of 0.1 mm at both stagnation pressure ratios.

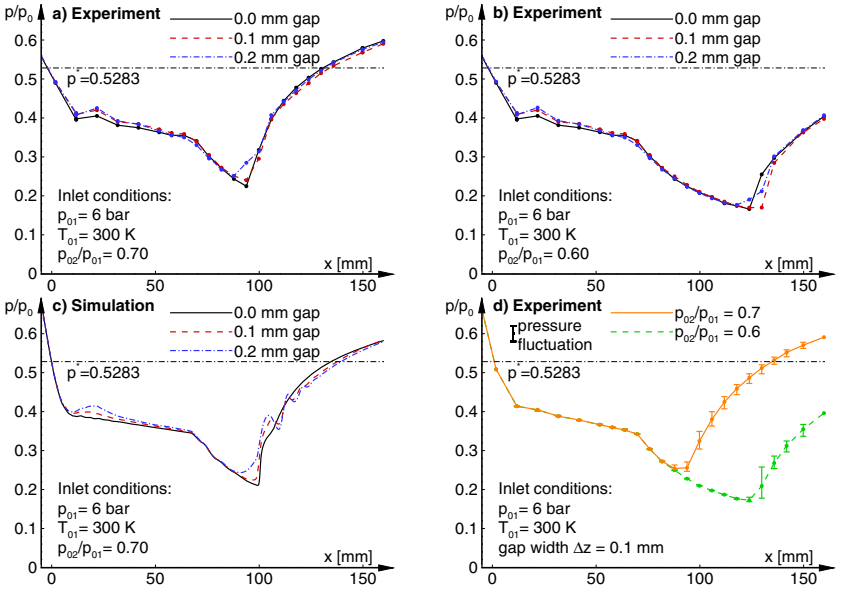

Fig. 3 Pressure distribution along the upper nozzle wall

Each plot in fig. 3a-c shows three curves. The solid black line represents the 0.0 mm gap size, the dashed red line represents the 0.1 mm gap size, and the dash-dotted blue line corresponds to the 0.2 mm gap size. As mentioned before, the gap flow mainly affects the pressure distribution in regions of high pressure gradients. Therefore, downstream of the primary nozzle throat at $x = 0$ mm the static pressure increases with increasing gap size and reaches a local maximum at $x = 22$ mm. The numerical simulations show, that a small bypass mass flow enters the gap shortly upstream of the critical cross section and re-enters into the shear flow of the supersonic part shortly downstream. This leads to a deceleration of the flow and thus to an increase of the static pressure. An obvious difference between the experiments and the simulations is the local maximum of the pressure at $x = 22$ mm. This local peak occurs in the experiment even without noticeable gap and was not reproduced by numerical simulations with exactly 0.0 mm gap size. We assume that the 0.0 mm gap size was not exactly achieved in the experiment.

A significant impact of the gap size on the main flow can be observed at the shock location. The high pressure gradient leads to a reverse flow through the gaps into the supersonic part ahead of the pseudo-shock system. In case of $p_{02}/p_{01} = 0.7$ both, experiment (fig. 3a) and simulation (fig. 3c), show a a static-pressure increase

slightly upstream of the shock. A comparable pre-compression is observed for the stagnation pressure ratio $p_{02}/p_{01} = 0.6$ (fig. 3b). In this test case, the experiment shows a downstream shift of the shock. For proper explanation of this particular behavior, numerical simulations with $p_{02}/p_{01} = 0.6$ are currently in preparation.

Figure 3d shows the time averaged pressure distribution measured by the Kulite®-Sensors for the configuration with 0.1 mm gap size and stagnation pressure ratios of $p_{02}/p_{01} = 0.6$ (green, dashed) and 0.7 (orange, solid). Maxima and minima are indicated by error bars. For both stagnation pressure ratios, the pressure fluctuations in the supersonic part upstream of the pseudo-shock system are negligible. Within the shock system, the high initial fluctuations decay with increasing static pressure. High fluctuations in the pseudo-shock system and the mixing region indicate an axial oscillation of the shock position. This agrees with previous investigations where a streamwise oscillation of the shock system by several millimeters was observed by high speed schlieren visualization [2].

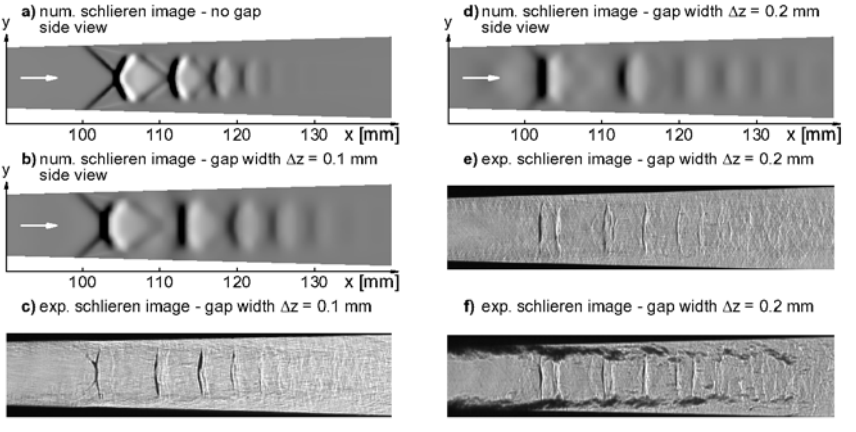

Fig. 4 Numerical and experimental schlieren pictures of the pseudo-shock system

Visual Analysis of the Pseudo-Shock System Structure for Different Gap Sizes

For analysis of the structure of the pseudo-shock system, numerical and experimental schlieren images are used. Unfortunately, an experimental visualization for 0.0 mm gap size has not been achieved, but the numerical schlieren image in fig. 4a shows clearly the series of successive shocks (black) and expansion regions (white). The initial shocks form an x-configuration at the center line followed by a rarefaction region where the flow is re-accelerated until the next re-compression follows. The interaction of these shocks and rarefaction waves with the boundary layer results in its local thickening and, hence, in the formation of a virtual nozzle throat that allows the flow to re-accelerate from subsonic to supersonic conditions.

The numerical and experimental schlieren images for a gap size of 0.1 mm are shown in fig. 4b and fig. 4c. In comparison to the simulation with 0.0 mm gap, the

x-configuration on the center line is now deformed and a Mach disk with a normal shock at the center is observed. The boundary layers at the upper and lower wall remain much thinner and the length of the shock system is increased. The following shock structures are deformed to single normal shocks. A significant difference between the experimental and the numerical schlieren image is the observed and predicted distance between the first and the second shock.

For an assessment of the configuration with 0.2 mm gap a numerical schlieren image is shown in fig. 4d. Again, the compression is indicated in black, expansions are indicated in white. One observes that a strong expansion occurs directly downstream of the first shock. The following shocks show a similar, but much weaker behavior. The corresponding experimental schlieren image is depicted in fig. 4e. The first normal shock (black) is followed by a strong expansion (white). To investigate the origin of this rarefaction another schlieren image is depicted in fig. 4f. Unlike the previous image, this one is created by using a horizontal slit instead of a knife edge. With this technique the boundary layer is clearly visible. One observes that the separated boundary layers form the previously mentioned virtual new nozzle where the subsonic core flow is accelerated again to supersonic conditions.

5 Conclusion

A detailed experimental investigation of the influence of small gaps on a pseudo-shock system has been performed for different gap sizes and pressure ratios p_{02}/p_{01}. Since schlieren images only provide integral information of the total light deflection through the test section, 3-D numerical data was additionally used to investigate 3-D phenomena of the shock system. The combination of experimental and numerical techniques considerably increased the understanding of the underlying mechanisms that cause the change in structure and position of the pseudo-shock system when increasing the gap size.

References

1. Matsuo, K., Miyazato, Y., Kim, H.-D.: Shock train and pseudo-shock phenomena in internal gas flows. Progress in Aerospace Sciences 35, 1 (1999)
2. Gawehn, T., Gülhan, A., Giglmaier, M., Al-Hasan, N.S., Adams, N.A.: Analysis of Pseudo-Shock System Structure and Asymmetry in Laval Nozzles with Parallel Side Walls. In: 19th Interantional Shock Interaction Symposium, Moscow (2010)
3. Giglmaier, M., Quaatz, J.F., Gawehn, T., Gülhan, A., Adams, N.A.: Numerical and experimental investigation of the effect of bypass mass flow due to small gaps in a transonic channel flow. In: 28th International Symposium on Shock Waves, Manchester (2011)

Thrust Shock Vector Control of an Axisymmetric C-D Nozzle via Transverse Gas Injection

V. Zmijanovic, V. Lago, S. Palerm, J. Oswald, M. Sellam, and A. Chpoun

1 Introduction

The flowfield resulting from the transverse gas injection into the supersonic cross-flow is the problematic of many aerospace applications ranging from the scram-jet fuel injection to the reaction jets and fluidic thrust vectoring(FTV). The prominent case of FTV by the use of the secondary injection represents promisingly attractive and effective way of control for small aerospace vehicles. Main advantages of the FTV are light-weightiness, simplicity and potential efficiency of such system comparing to the conventional mechanical TVC and mechanical deflectors. [5] Elimination of heavy and robust actuators and their replacement with only the fast-opening valves leads to the very significant reduction in mass. Fast dynamic response ($\sim$500Hz) to the conventional ($\sim$30Hz) [8] , very small losses in specific impulse and thus thrust are promising efficiency benefits. The CNES "Perseus" project which this study is part of and design concept have aim of incorporating fluidic TVC on the future "micro" launcher. Some of the results from the ongoing investigation are presented in this article.

1.1 Analytical Approach and Description

The secondary injection TVC or Shock Vector Control (SVC) is the type of the fluidic vectoring at which injectant in the divergent portion of the nozzle generates the strong shocks by obstruction of the main flow and thus forces the nozzle exhaust jet to divert. The upstream separation distance is in general determined by the

V. Zmijanovic · V. Lago
C.N.R.S.-ICARE, 1C Av. de la Recherche Scientifique, 45071 Orleans, France

V. Zmijanovic · S. Palerm · J. Oswald
C.N.E.S. Direction des lanceurs, Rond Point de 'Espace -Courcouronnes, 91023 Evry, France

M. Sellam · A. Chpoun
LMEE d'Evry, Universite d'Evry Val d'Essonne, 40 rue du Pelvoux, 91020 Evry, France

flow-regime in the boundary-layer (BL) (laminar or turbulent) and by the penetration height of the injectant. In the basic case Fig.1a, the turbulent BL of the main flow is detached upstream of the injection port due to an adverse pressure gradient with generation of the separation shock. Further downstream, this weaker separation shock is interacting with the strong bow shock which is formed in front of the injection plume as a consequence of the main jet obstruction. This interaction and the shock region between are giving steeper gradient to the main flow deflection [1] while on the inner side between the shock and the wall the recirculation is formed. The structure between the wall, shock region and the injectant plume Fig.1a is characterized by the counter-rotating vortex pair, commonly known as primary upstream vortex (PUV) and smaller counter-rotating secondary upstream vortex (SUV) near the injectant plume. Sonically injected under-expanded gas is expanding in the main flow through the Prandtl-Meyer fan and it is recompressed by the barrel shock formation, with Mach disk at end of this process. Main flow is turning the injectant plume towards the wall and on the downstream side recompression and reattachment occur generating the downstream wake vortex pair (PDV and SDV).

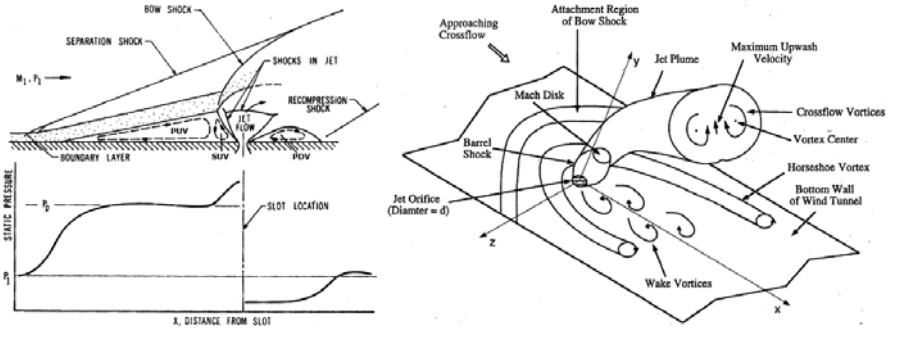

Fig. 1 a)2D flowfield by Spaid et al.[3] b) 3D flow structure by Santigo et al.[2]

The circular injection at the flat plate, on other hand, is characterized with the three-dimensional(3D) flow structure. The simplified scheme Fig.1b presented by Santiago et. al.[2] showed the 3D nature of the bow shock, horseshoe vortex region, 3D barrel shock and Mach disk and counter-rotating vortex pair. The 3D model of transverse injection exhibits effects in downstream-upstream direction as well as in the lateral direction.

The secondary injection into the supersonic convergent-divergent nozzle has increase in complexity due to interactions of the 3D nature of the nozzle jet with transverse secondary injectant. Analytical approach and also analysis of the vectoring possibilities revealed that mass-flow rates, injectant properties, injection port shape and injection angle are the influencing parameters on the effective thrust vectoring. With the industry request for the moderate mass-flow-rate ratios in range of 5% and the same primary and secondary injectant gas a cold flow analysis of the

shock vector control of an axisymmetric C-D nozzle is conducted. The goal is that with keeping the same nozzle-pressure-ratio(NPR) ratio and the second-pressure-ratio(SPR) around unity to optimize secondary injection for the maximum vector side force and the maximal vector deflection angle with minimum loss on the nozzle axial performances. Two identical conical nozzles are designed with injection at $x_j/x_t = 0.7$ and $x_j/x_t = 0.9$, where x_t is x-dimension of the nozzle divergent section and x_j is x-coordiante of the injection port.

2 Experimental Setup

The experiments are performed at the Institute ICARE "FAST" platform using the super/hypersonic wind tunnel EDITH. The wind-tunnel is arranged, equipped and setup by the authors. The EDITH is set as the blow-down type wind tunnel where clean oil-free air is first dried, compressed till 300bars and stored in 320l tank. . The air is supplied with 8mm tube to the pressure-regulator and after regulation through the 12mm diameter tube to the flow-splitter. From there with 6 radial distributed 8mm tubes is injected into the settling chamber of 160mm diameter and exhausted in the test-section through the nozzle. The air is pump out of the section through the system and two primary pumps with a pumping volume of 17 740 m^3/h, giving the ambient pressure of 0,02 bars minimum. The model of the engine is with lower chamber pressure of 3bars exhausting in the depressurized test section of a 0.08bar thus, simulating the conditions for the upper-stages of the launcher. The first experiments are conducted with the 2 same conical type C-D nozzles of designed nozzle pressure ratios $(NPR) = 37,5$, throat radius of $R_th = 9,72mm$ and expansion ratio $A_th/A_e = 0.236$ and the divergent conical half-angle $5.42deg$. The circular $D_j = 6mm$ diameter injection port is normal to the central axis. The secondary air is supplied through the 4 radially distributed tubes into the injectant settling chamber and from there smoothly with 10mm convergent part to the sonic throat. The implemented diagnostics tools were measuring the flow properties; the stagnation pressure and temperature in the main and secondary settling chambers, the ambient pressure and the temperature at the test section. The second nozzle is equipped with a Kulite parietal pressure transducer placed in the line with injection port at $x_j/x_t = 0.35$. Flow visualization is obtained using the Toepler's Z-schlieren configuration at the exit of the nozzle.

To measure forces, two-frame-complex balance is constructed using the HBM force transducers to measure the vertical, axial and lateral forces. All the diagnostic data is recorded using the "NI" SCXI DAQ acquisition cards and the LabView software package. The results are gathered and further treated using the Matlab programs. The experiments are performed keeping the adapted conditions for the nozzle of 3bars stagnation and 0,08bars ambient pressure. The flow was not preheated so the temperature was in constant descent from 260K to 243K. The second pressure was altered from 2 to 3,5bar with 0,5bar step and the test time was between 2 and 3 minutes.

3 Numerical Simulation

Numerical simulations are performed with the CPS (Code pour la Propulsion Spatiale) which is developed by the CNES and Bertin [4]. The CPS is a three dimensional finite volume CFD code designed for the space propulsive flows. The mathematical model is based on the mass-averaged Navier-Stokes equations written for compressible multi-species reacting flows with a fully accounted viscous effects. It is solving on the unstructured 3D computational grid. For the presented study Launder-Jones $k-\varepsilon$ model with realisability viscous-damping function is used with strong coupling of the wall function with the turbulence model. Dry air with gamma(T) and Cp(T) as a 6th degree polynomials is used as the primary and secondary gas and with the same stagnation properties as the experimental setup. Flux vectors are evaluated at each time step using the 2nd order HLLC or Roe's upwind difference splitting. Integration is achieved with fully explicit solver setting time-step control from unsteady for highest time-accuracy to the steady optimized time step with CFL up to 0,3. The 3D computational grid is built on the test nozzle and exterior domain with the 1 million of mapped hexagonal elements. Nozzle domain consists of 600000 hex-elements while the exterior domain has 400000 hex elements.Fig.2a

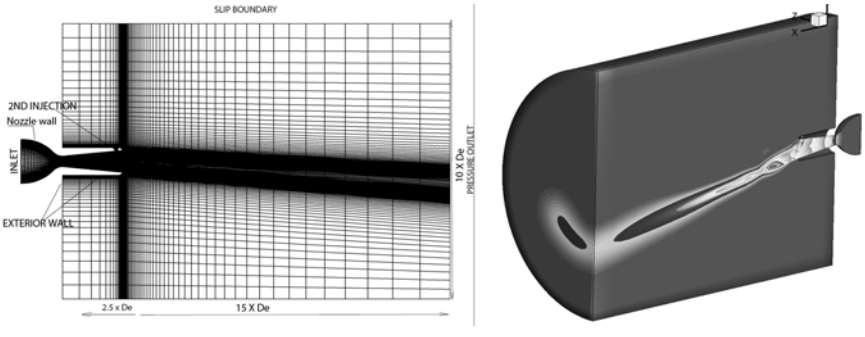

Fig. 2 a)Nozzle C0.9 computational grid b) 3D Mach number plot

Symmetry plane of the divergent section nozzle meshed with quadratic elements has 90 vertices in the normal and 210 vertices in the axial direction with graduation toward the throat and the secondary injection port.Exterior domain is 15 exit diameters in the downstream direction, 2.5 diameters in the upstream direction and 9 exit diameters in the radial direction. Boundary layer consists of 20 cells and 15 transitional cells with growth factor 1,14 and $Y+$ value from 4 to 12.

4 Results

The numerical and experimental data of the two conical nozzles are compared in terms of force-balance measurements, pressures and flowfield schlieren

visualization. The previous analysis and numerical simulations showed that position of the injector closer to the nozzle exit increases TVC efficiency, also reported by Mangin [8] . The experiments and simulation with the preliminary nozzle with injector at $x_j/x_t = 0.7$ revealed the unwanted effects in the produced supersonic crossflow. Fig.3

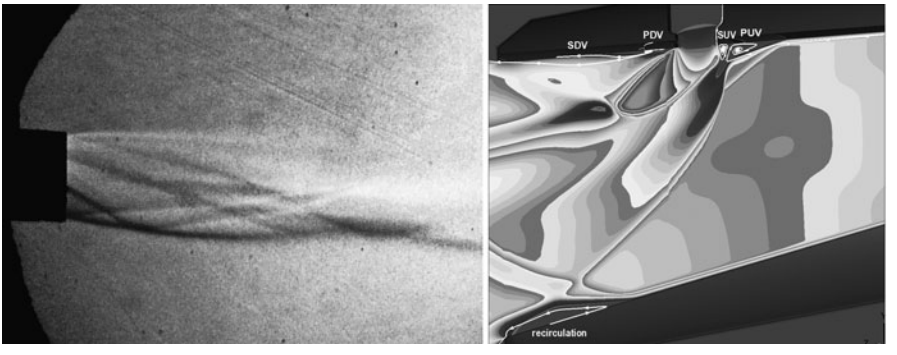

Fig. 3 Nozzle $x_j/x_t = 0.7$ a) schlieren b) 3D numerical flowfield

The leading-frontal surface of the bow-shock wave is reflecting from the opposite wall of the nozzle, separating the BL and generating the recirculation zone, on the end lead to the negative vector side force on the wall. Downstream of the injector, the detached flow reattaches to the wall and with interaction of reflected shock it can lead to instabilities, also reported by Masuya et al.[6]

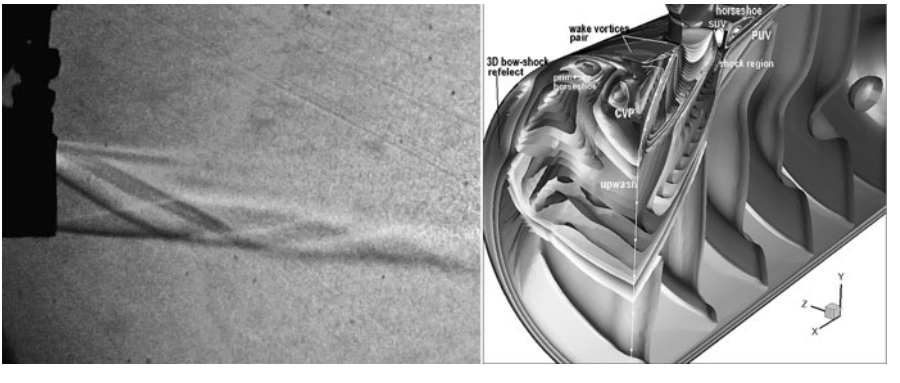

Fig. 4 Nozzle $x_j/x_t = 0.9$ a) schlieren b) 3D numerical flowfield

Injection closer to the nozzle exit $x_j/x_t = 0.9$ eliminates mentioned effects for the adapt-operated nozzle. The additional features of the nozzle flow are influencing vortex and flow structure as depicted on the Fig.4.

Table 1 Experimental and numerical result data of flow-properties and force measurements

SPR	f_m	F_{jy}	F_{wy}	F_v		F_t		δ^o		η
p_c/p_j	$\dot{m}_j/\dot{m}$	[N]	[N]	num	exp	num	exp	num	exp	I_{sj}/I_s
-	(223g/s)	-	-	-		126.38N	126.2N	-		(57.77s)
			case1:	$x_j/x_t = 0.7$						
1	0.081	9.43	-5.86	3.572	4.60	130.31	131.05	1.57^o	2.0^o	0.954
			case2:	$x_j/x_t = 0.9$						
0.667	0.055	6.63	6.04	12.67	12.4	127.76	126.8	5.67^o	5.6^o	0.959
0.833	0.068	8.02	6.92	14.94	15.0	128.39	128.3	6.64^o	6.7^o	0.951
1	0.081	9.88	8.30	18.18	18.4	128.50	127.8	8.05^o	8.2^o	0.942
1.167	0.098	11.47	9.30	20.77	20.5	128.89	127.3	9.15^o	9.2^o	0.927

Lateral spread of the bow shock is restricted with the nozzle wall sides, the reflected side-end interacts with inner region pinching the 3D structures inside. In the conical nozzles usually present weak compression waves may additionally deform the structure. Dimensionless wall pressure distribution Fig.5a gives the variation of the separation upstream and downstream of the injector, and single used parietal sensor matched numerical data. Force measurements presented versus the SPR and mass flow ratios in Table1 showed excellent matching with the numerical results. As the representative value for the TVC efficiency is taken vector deflection angle, as:

$$\delta = \arctan\left(\frac{F_v}{F_t}\right) \tag{1}$$

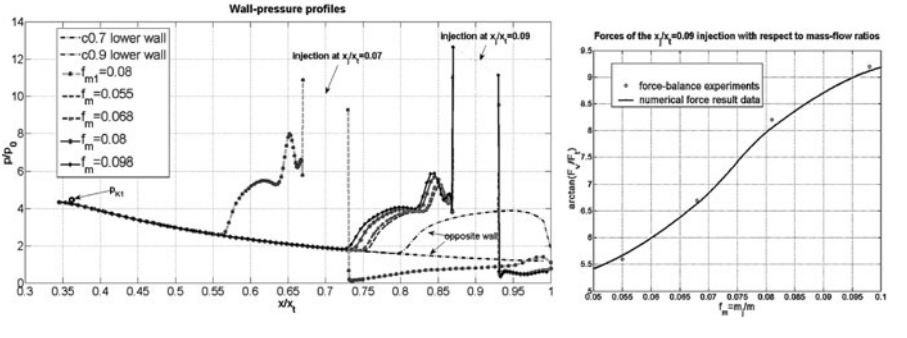

Fig. 5 a) dimensionless wall-pressure distribution b) δ-deflection vector angle vers. f_m

It is presented for adapted nozzle operation with reported I_{sp} ratio, otherwise the δ value is speculative, since decrease of the axial thrust force would increase fictive vectoring efficiency. The side-force value is gradually rising with the increase of SPR - directly proportional to the, mass flow ratio which represents the most influential parameter for side vector force. At the figure 5b which depicts vectoring versus mass-flow ratio, optimal angle is found in the range of SPR=1 delivering the δ of 8.2^o for $m_j/m = 0.08$.

5 Conclusions

Presented study of the thrust SVC for conical axisymmetric nozzles showed that significant vector side force and vector angle is possible to achieve. It has also revealed the influencing parameters and properties which should be investigated in the optimization process. The future steps in the ongoing study will be to experimentally and numerically investigate and optimize thrust SVC possibilities between more injector position, angles and injector shapes of the truncated ideal(TIC) and thrust optimized(TOC) contour nozzles. The investigations are being improved with additional parietal and pressure taps, visualization techniques and higher numerical resolution.

References

1. Neilson, J.H., Gilchrist, A., Lee, C.K.: Side thrust control by secondary gas injection into rocket nozzles. Journal Mechanical Engineering Science 10, 3 (1968)
2. Santigo, J.G., Dutton, J.: Crossflow vortices of a jet injected into a supersonic crossflow. AIAA Journal 35, 5 (1997)
3. Spaid, F.W., Zukoski, E.E.: Study of the interaction of gaseous jets from transverse slots with supersonic external flows. AIAA Journal 6, 2 (1968)
4. Durand, P., Vieille, B., Lambare, H., Vuillermoz, P., Boure, G., Steinfeld, P., Godfroy, F., Guery, J.F.: CPS: A three-dimensional CFD numerical code dedicated to space propulsive flows. AIAA A00-36976 3864 (2000)
5. Wing, D.J., Giuliano, V.J.: Fluidic thrust vectoring of an axisymmetric exhaust nozzle at static conditions. ASME FEDSM97-3228 (1997)
6. Masuya, G., Chinzei, N., Ishii, S.: Secondary gas injection into a supersonic conical nozzle. AIAA Journal 15, 3 (1977)
7. Maarouf, N., Sellam, M., Grignon, M., Chpoun, A.: Thrust vectoring through fluid injection in an axisymmetrical supersonic nozzle. ISSW 26(2), 1141–1147 (2007)
8. Mangin, B., Chpoun, A., Jacquin, L.: Experimental and numerical study of the fluidic thrust vectoring of a two-dimensional supersonic nozzle. AIAA 2006-3666 (2006)

Flow Visualization of Supersonic Free Jet Utilizing Acetone LIF

K. Hatanaka, M. Hirota, T. Saito, Y. Nakamura, Y. Suzuki, and T. Koyaguchi

1 Introduction

A fluid with a certain speed escaping through a hole into an open space forms a jet; and its relevant phenomena are observed in a variety of situations including our daily lives [1]. Scientists and engineers have studied the jet flow for decades since it is related to crucial problems in aerospace engineering [2, 3], natural sciences, and various industries.

The present work investigates unsteady supersonic free jets in compressible gases. It is motivated by the recent attempts to construct new physical modeling of volcanic plumes [4, 5]. Although simple jet flows can be explained well with appropriate basic gasdyamic theories, it becomes increasingly difficult to understand the phenomena when complex factors such as jet-opening geometries, effects of gravity, and mixing of high-temperature erupting gas with ambient atmosphere start to play important roles. The same is true in other areas as well. Once some additional factors or parameters are included in basic problems, the analyses then become complicated, and it becomes difficult to obtain their general solutions. Accordingly, we have to investigate each problem individually with some appropriate means. Difficulties in investigating supersonic flows also arise when the flows are time dependent. It is reported that time-dependent numerical simulations often give solutions with wrong time evolutions even if the flow field at an instance looks reasonable [6]. Therefore, it is necessary to evaluate time-dependent CFD results carefully with experiment data.

K. Hatanaka · M. Hirota · T. Saito
Muroran Institute of Technology 27-1 Mizumoto-cho, Muroran, 050-8585, Japan

Y. Nakamura
Hokkaido University, N13W8 Kita-ku, Sapporo, 060-8628, Japan

Y. Suzuki · T. Koyaguchi
Earthquake Research Institute, The University of Tokyo, 1-1-1, Yayoi, Bunkyo-ku, Tokyo, 113-0032, Japan

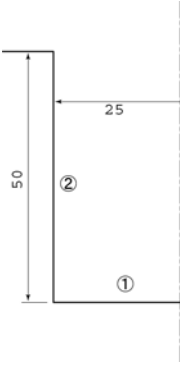

Fig. 1 Geometry of jet nozzle.

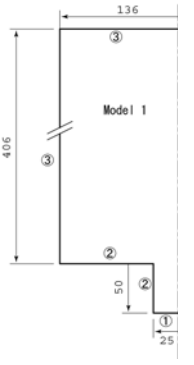

Fig. 2 Whole computational domain.

This paper seeks to establish an accurate means to investigate unsteady supersonic flows, especially free jets. Computational Fluid Dynamics (CFD) is a powerful investigation tools [7]; another is flow-visualization experiments. Besides conventional optical flow visualization techniques, the acetone Planar Laser-Induced Fluorescence (Acetone PLIF) method is applied to visualize the free-jet cross section. Acetone PLIF is widely used for flow visualization because of its high S/N ratio and applicability to quantitative measurement [8]. Although its application has been limited to low-speed flows, it has become to be used for quantitative measurements of supersonic flows [9, 10]. The technique is expected to be useful when CFD results on a cross section of complex flow are to be evaluated with experiments. These two ways of investigating supersonic flows are described below by applying them to supersonic free jet problems.

2 Numerical Investigations

2.1 Numerical Method

Free jet flows are numerically simulated with a two-dimensional axi-symmetric flow solver. This study assumes that gases are inviscid and follow the equation of state for perfect gases. The weighted average flux scheme [11] (WAF) is used to solve the conservation laws of mass, momentum, and energy. The scheme is one of the higher-order extended Godunov schemes with second-order accuracy both in time and space. It is constructed as a finite-volume method using the integral form of the basic equations. The HLLC approximate Riemann solver with a TVD-limiter function is utilized for inter-cell flux evaluation.

A supersonic free jet is numerically simulated for a jet-nozzle geometry, which is equivalent to the nozzle used in the experiment. Figure 1 presents normalized dimensions of the nozzle. Boundary conditions are also indicated in the figure with Figure 1 1 for inflow conditions and 2 for a reflective solid wall. The nozzle is a

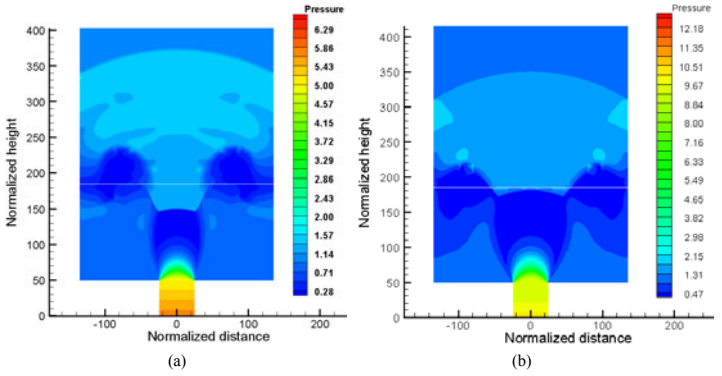

Fig. 3 Pressure distributions.

simple cylindrical tube. Figure 2 presents the whole computational domain for the nozzle. 3 indicates flow out boundary conditions.

2.2 Numerical Results

Numerical results are presented in Fig. 3. Flow variables (pressure, density, and velocity) are given at the bottom of the jet nozzle as boundary conditions. Figure 3a presents the pressure distribution at the normalized time of 200. The pressure at the boundary is 10 times the ambient pressure, and the sonic flow velocity is assigned. With the boundary conditions, the pressure at the nozzle exit is about 5. The jet rapidly expands outside the nozzle and over-expands to a very low pressure until it is compressed by the Mach disc or the barrel shock. The pressure jumps from 0.076 to 1.17 across the Mach disc. The barrel shock, slip line, and reflected shock are clearly seen, and the Mach disc height is approximately two times of the nozzle diameter. The configuration does not change with time since the flow in this region is supersonic. Figure 3b depicts the pressure distribution obtained at the normalized time of 140 for the same geometry as in Fig. 3a but with higher pressure at the bottom boundary. The fixed pressure at the bottom is raised to 20, and the pressure at the nozzle exit becomes about 9.5. Due to higher pressure at the nozzle exit, the jet configuration is larger than in the previous case. The Mach disc height is about 2.6 times of the nozzle diameter, and the pressure increases from 0.135 to 1.3 across the Mach disc.

3 Experiment

3.1 Experimental Setup

A free jet is formed inside an evacuated chamber through a 5-mm diameter hole placed at the test section, which is connected to either ambient atmosphere or a

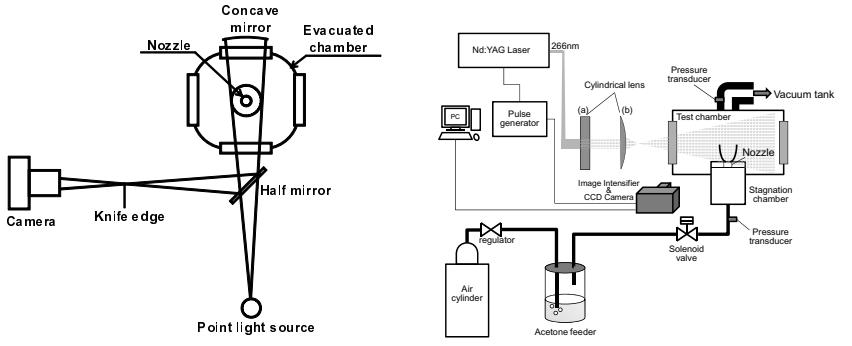

(a) Shlieren method. **(b)** Acetone PLIF method.

Fig. 4 Schematic diagram of the optical systems.

reservoir pressurized with dry air. The flow was visualized by Schlieren and shadowgraph techniques as well as the acetone PLIF method. Visualized flow images are recorded by a high-speed camera (PHOTRON FASTCAM-MAX model 120k) for investigating the time history of the free-jet structure. Still pictures are also taken with a digital camera (NIKON D40X).

Figure 4a presents the optical setup of the Schlieren method. We have adopted the double-pass method with one concave mirror, and the Schlieren images are recorded at 250 fps with a high-speed camera. Figure 4b schematically diagrams the optical system for the acetone PLIF. High-pressure air goes through an acetone feeder before it expands into the low-pressure test chamber. The 4th harmonic (266nm) of a Q-switched Nd:YAG laser is spread by a cylindrical lens to form a sheet and passes through the jet. The laser excites the energy level of acetone molecules from the ground state to higher states. Light is emitted when the molecules in the excited levels fall to their ground state. The cross section of the jet is visualized since the intensity of the emitted light (fluorescence) is a function of the acetone concentration. The fluorescence, however, is weak and an image intensifier is necessary. Observation windows are made of quarts since the laser wave length is ultra violet. Laser pulses are emitted at a rate of 10 Hz and each pulse has duration of 4 – 6 ns. Excited energy levels of acetone molecules are unstable, and their life time is approximately 4 ns. Noting that a typical time scale of gasdynamic phenomena is measured in microseconds to milliseconds, acetone PLIF is considered as a perfect method of taking still images of high-speed flows.

3.2 Experimental Results

The test chamber is evacuated to 10 kPa, and the high pressure at the acetone feeder is measured as 640 kPa before the jet starts.

The distance from the nozzle exit to the Mach disc (L_M) is plotted against time in Fig. 5a. The time is measured from the moment of opening a valve that is

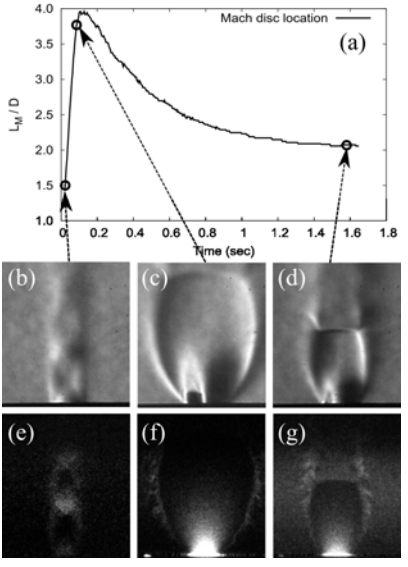

Fig. 5 (a) Mach-disc location with time, (b–d) still images of Schlieren, (e–g) acetone PLIF at different times.

located upstream of the nozzle. The distance L_M is measured in Schlieren images and normalized with the nozzle diameter D. L_M rapidly increases at the beginning, reaches its maximum in 0.2s, and then gradually decreases to a final constant value in about 1.5s. The upstream pressure decreases to 130kPa when L_M is reduced to a constant value. The still images of Schlieren and acetone PLIF methods at different times (20ms, 90ms and 1.6s) are shown in Figs. 5b through g. At the beginning of the jet (0.2s) we can see that the barrel shock structure expands with increasing L_M.

Flow-visualization images obtained by the Schlieren method and acetone PLIF are presented in Fig. 6. Figure 6a is a Schlieren image obtained with the optical system of Fig. 4a. A continuous light source is used, and images were acquired by a digital camera (Nikon D40X) with an exposure time of 8 ms. Images from acetone PLIF are presented in Figs. 6b and c. Ten consecutive images are superimposed in Fig. 6b; Fig. 6c shows a single image. The Schlieren image reflects the integrated information along the light source path regarding the density field including the cylindrical jet. In contrast, the image of Fig. 6b directly reflects the density field in the cross section of the jet. These two images agree qualitatively fairly well. Figure. 6c, however, indicates rather strong flow instability behind the barrel shock, and the flow looks quite turbulent. Details of the jet structure are clearly observed by the acetone PLIF due to the very short durations of the laser pulse and the life times of excited acetone energy levels.

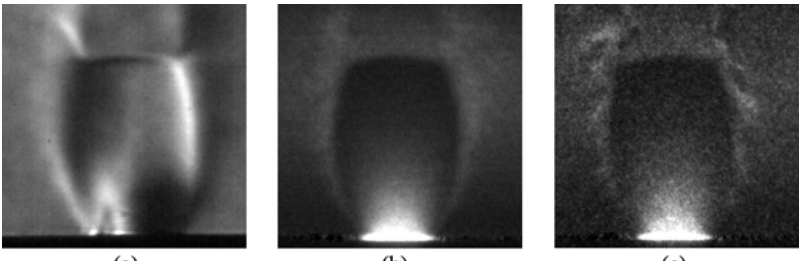

Fig. 6 Flow visualization images: (a) Shlieren method; (b) averaged image of acetone PLIF; (c) single image of acetone PLIF.

4 Conclusions

The structure of an under expanded free jet was analyzed numerically and experimentally. In the numerical investigation, the calculation was performed with a nozzle shape used in the experiment. In the experiment, the flow field was visualized using Schlieren and acetone PLIF methods. We clearly observed both the time history of the jet structure and the eddy structure around the barrel shock. This detailed structure can be observed in PLIF results because instantaneous images are acquired in nanoseconds.

Acknowledgements. This study was supported by the Earthquake Research Institute cooperative research program. This work was also supported by Grants-in-Aid for Scientific Research from the Japan Science and Technology Agency (JST).

References

1. Shakouchi, T.: Series in Computational Methods in Mechanics and Thermal Sciences. Morikita Co. (2006)
2. Nasuti, F., Onofri, M.: Shock Waves 19(3), 229–237 (2009)
3. Stark, R., Wagner, B.: Shock Waves 19(3), 185–191 (2009)
4. Ogden, D.E., Wohletz, K.H., Glatzmaier, G.A., Brodsky, E.E.: Journal of Geophysical Research 113, B02204 (2008)
5. Koyaguchi, T., Suzuki, Y., Kozono, T.: Journal of Geophysical Research 115, B07205 (2010)
6. Saito, T., Takayama, K.: Shock Waves 9(2), 73–79 (1999)
7. Anderson, D.A., Tannehill, J.C., Pletcher, R.H.: Computational Fluid Mechanics and Heat Transfer. Hemisphere Publishing Corporation (1984)
8. Lozano, A., Yip, B., Hanson, R.K.: Experiments in Fluids 13(6), 369–376 (1992)
9. Handa, T., Aoki, T., Masuda, M., Kashitani, M., Yamaguchi, Y.: Journal of the Visualization Society of Japan 26(1), 243–246 (2006)
10. Takahashi, H., Hirota, M., Oso, H., Masuya, G.: Transactions of the Japan Society for Aeronautical and Space Sciences 51(174), 252–258 (2008)
11. Toro, E.F.: Philosophical Transactions: Physical Sciences and Engineering 341(1662), 499–530 (1992)

Effect of Roughness in Jets in Mach 5 Cross Flow

E. Erdem, S. Saravanan, Y. Liu, L. Yang, and K. Kontis

1 Introduction

Transverse jet injection into supersonic/hypersonic cross flow has been encountered in many engineering applications ranging from scramjet combustors and solid rocket motor or liquid engine thrust vector control systems to high speed flying vehicle reaction control jets. These applications all involve complex three dimensional flow patterns comprising separated regions, shock waves, shear layers and wakes in common. Owing to numerous applications and these complicated flow features, transverse injections over different geometries and various forebodies have been received significant amount of interest. Earlier studies were focused on wind tunnel experiments and the utilisation of conventional measurement techniques such as Schlieren/Shadowgraph photography, wall pressure and concentration measurements to better understand the jet interaction and penetration phenomena. These studies aimed to assess the effect of injection pressure ratio, location of injection and state of incoming boundary layer and type of injectant gas on jets in supersonic/hypersonic cross flow. Recent studies of missile/forebody applications involving reaction control jets by several researchers have investigated jet interaction phenomenon on various axisymmetric body configurations at supersonic/hypersonic speeds [1, 2, 3, 4]. Their aim was to investigate control effectiveness of transverse/lateral jets on different missile body configurations.

E. Erdem · L. Yang · K. Kontis
AeroPhysics Lab, School of MACE, University of Manchester, Manchester, M13 9PL, UK

S.Saravanan
Department of Aerospace Engineering , Indian Institute of Science (IISc), Bangalore, 560012, India

Y. Liu
School of Jet Propulsion, Beijing University of Aeronautics and Astronautics, Beijing, 100191, China

In terms of roughness effect on boundary layers, roughness breaks up the laminar sublayer and increases wall shear stress associated with the downward shift of the intercept of velocity profile in semi logarithmic coordinates compared to the smooth case. The fullness of the boundary layer is reduced resulting increased skin friction and surface heat transfer. In high speed flight rough surfaces can also generate shock and expansion waves that interact with boundary layer turbulence compared to low speed counterpart. This interaction is especially prominent at higher Mach numbers where most of the boundary layer is supersonic [5]. A limited number of studies have been performed on the effect of roughness on complex high speed flows; Disimile and Scaggs [6] studied the effects of roughness on Mach 6 compressible turbulent boundary layer characteristics in presence of a 22deg ramp deflection, at three unit Reynolds numbers. The roughness consisted of machined hemispherical protuberances of 0.508mm in radius. It was found that the extent of the separated region for the roughened surface was ten times that for the smooth. Babinsky and Edwards [7] investigated large scale roughness influence on turbulent hypersonic boundary layers approaching compression corners and they found that the shock wave boundary layer interaction was only marginally affected. Recently Prince et al. [8] investigated Mach 8.2 hypersonic turbulent shockwave boundary layer interaction characteristics of a deflected control flap configuration. It was found that surface roughness, of scale 10% of the hinge line boundary layer thickness, significantly increased the extent of the interaction, while increasing the magnitude of the peak pressure on the flap and heat flux only aft of the reattachment region.

Current investigation aims at the investigation of the effect of the roughness on the flowfield due to a transverse sonic air jet over a flat plate at Mach 5 flow.

2 Experimental Setup and Models

All of the experiments are conducted in the High SuperSonic Tunnel (HSST) of the University of Manchester. The tunnel is of the intermediate blowdown (pressure-vacuum) type which uses dry air as working fluid. The details of the facility together with standard instrumentation for stagnation pressure and temperature mesurements as well as high speed schlieren photography setup can be found in Ref. [9]. The layout of the optical setup and the data acquisition architecture with measurement chain is shown in Fig. 1. For the wall pressure measurements in the test section, 1mm tappings are connected to absolute pressure transducers Kulite XTE-190M (0-0.7bar) via flexible tubing and for the jet stagnation pressure, a transducer (Kulite XTE-190M 0-3.5bar) is connected to the 8mm air pipe via T-junction. The model used for this study is a sharp leading edge flat plate with a converging jet hole of 2mm, through which a sonic turbulent jet is injected after regulation. The flat plate is 155mm long, 68mm wide and 5mm thick and shown below in Fig. 1. For the roughness investigation whole flat plate is covered with three different sand papers, P120, P400 and P1000. The sand grain at the leading edge is filed to have a minimal effect on leading edge thickness. The pressure tappings on the surface are punched through the sand paper naturally.

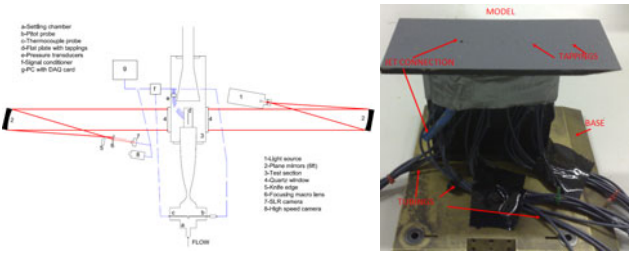

Fig. 1 Left: Schematic setup of Schlieren visualisation with DAQ architecture by Erdem et al. [9]. Right: flat plate model with jet orifice and connections.

3 Results

The experimental freestream and jet conditions are tabulated in Table 1 for all the tests. J is momentum flux ratio of the jet to freestream and expressed as $\gamma_{jet} p_{jet} M_{jet}^2 / \gamma_\infty p_\infty M_\infty^2$.

Table 1 Experimental test conditions.

Test No	Rough Surface	p_0 $(mbar)$	T_0 (^0K)	Re/m $\cdot 10^6 (1/m)$	p_{0jet}/p_∞	Re_{Djet} $\cdot 10^3$	J
1	Smooth	6524	376	13.00	55.8	19.6	1.18
2	Smooth	6489	371	13.22	131.3	46.5	2.78
3	Smooth	6474	369	13.29	248.5	88.5	5.25
4	P1000	6438	378	12.74	55.6	19.5	1.17
5	P1000	6439	375	12.91	131.6	46.7	2.78
6	P1000	6431	364	13.52	248.4	89.7	5.25
7	P400	6442	374	12.97	56.2	19.2	1.19
8	P400	6453	373	13.07	131.0	46.9	2.77
9	P400	6388	366	13.30	251.0	89.2	5.30
10	P120	6398	374	12.88	56.9	19.4	1.20
11	P120	6458	377	12.82	130.6	46.8	2.76
12	P120	6422	375	12.90	249.0	88.4	5.26
Variations		$\pm 0.7\%$	$\pm 1.7\%$	$\pm 3.7\%$	$\pm 2\%$	$\pm 2\%$	$\pm 4\%$

3.1 Schlieren Photography

Long exposure Schlieren photography reveals the prominent flow structures shown below; such as nozzle shock due to pressure difference at the nozzle exit and the vacuumed test section, leading edge shock due to viscous interaction eventually becoming a weak Mach wave at downstream, jet induced strong bow shock due to obstruction caused by the jet, upstream boundary layer diversion and separation shock

due to adverse pressure gradient imposed by the bow shock, Mach disc (a normal shock) due to sudden expansion of the jet and downstream recompression shock to guide the jet flow parallel to flat plate. In general transverse jet penetrates further for higher values of J, curved bow shock moves away from the surface and curved separation region extends in both upstream and downstream directions as deducted from Fig. 2. The three dimensionality of the separation and recompression shocks are superimposed as expected. Mach disc height and the extent of the separation region can be extracted using digital image processing. Separation region is taken as the location where boundary layer starts (visualised as a bright line) to deviate from main flow direction.

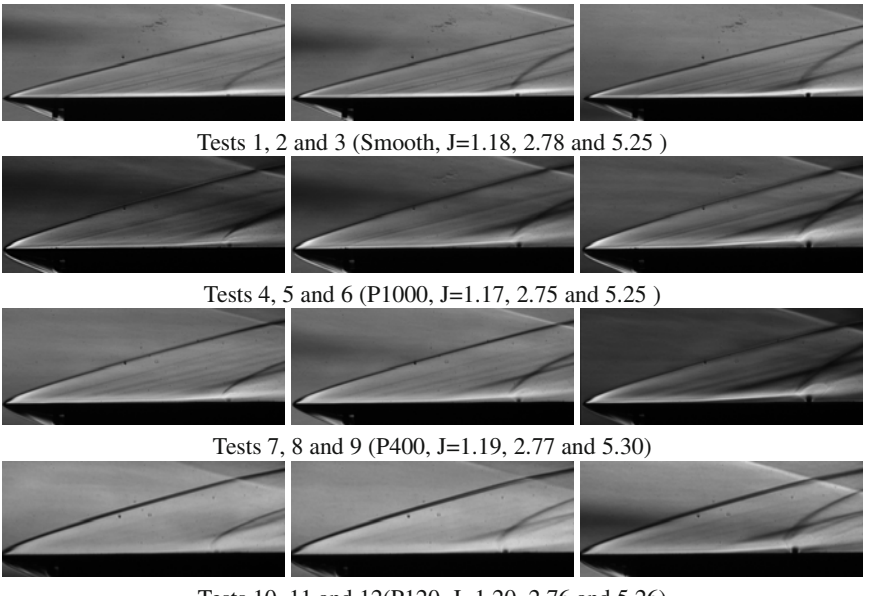

Fig. 2 Schlieren visualisation of flowfield in the presence of the sonic air transverse jet over a flat plate with different roughnesses; tests 1-12.

Mach disc height non-dimensionalised by jet diameter, h/d_{jet}, is plotted against momentum flux ratio, J in Fig. 3 (on the left) for all tests. The trends show that as the momentum flux ratio is increased higher penetration into the main crossing flow is observed as expected. The relation is nonlinear, roughly proportional with root square of J, which is deducted from power law fit applied accurately. This proves that the jet penetration is only dependent on momentum flux ratio, upstream boundary layer thus Reynolds number has no influence. In case of separation length non-dimensionalised by jet diameter, x_{sep}/d_{jet}, against J plot (on the right in Fig. 3), a nonlinear behaviour is observed for both smooth and rough surface with P120

however almost linear pattern is obtained for P1000 and P400. Generally for the extent of the separation region is strongly governed by the state and the shape of the incoming boundary layer (laminar for current test except P120). Roughness weakens the boundary layer, makes it less full and resistant to adverse pressure gradient, thus an increase in separation region is observed for rough surfaces compared to baseline smooth surface. The difference between P1000 and P400 surfaces is not discernible.

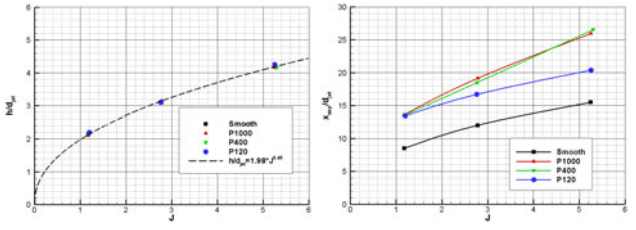

Fig. 3 Left: Mach disc height non-dimensionalised by jet diameter versus momentum flux ratio , right: separation length non-dimensionalised by jet diameter versus momentum flux ratio.

3.2 Surface Pressure Measurements

The data reduction for surface pressure measurements is as follows; $p_0(t)$, $p_{0jet}(t)$, $p_w(t)$ are measured with high sensitivity Kulite©pressure transducers and $p_\infty(t)$ is calculated using isentropic relations from $p_0(t)$, then $p_w(t)/p_\infty(t)$ and $p_{0jet}(t)/p_\infty(t)$ signals are obtained. These signals are integrated and averaged over steady duration of the test run. Following figure shows non-dimensional wall pressure distributions against non dimensional distance, i.e $(x - x_{jet})/d_{jet}$ for different momentum flux ratios and rough surfaces at centreline, z/d_{jet}=5.25 and z/d_{jet}=10.

The wall pressure along the flat plate centreline, starts to increase from the point at which the flow separates, and then there is further rise to a pressure plateau reaching an upstream pressure peak as a general trend. In downstream side of jet there is a significant pressure drop accompanied by the increase due to recompression shock. As the momentum flux ratio is increased separation and reattachment regions expand in size as well as increased upstream pressure peaks and decreased downstream pressure drop. These findings are expected and noted in literature. On the other hand the influence of roughness is heavily felt on the extend of upstream separation region, the magnitude of the pressure peak and the extend of the downstream reattachment region as well as the laterally affected area. The pressure rise becomes almost linear leading to the plateau and does not become apparent until 27.5, 30 and 22.5 jet diameters upstream for tests with P1000, P400 and P120 surfaces respectively with maximum J values. With the roughest surface, P120, the increase in pressure is constant without a plateau until 5

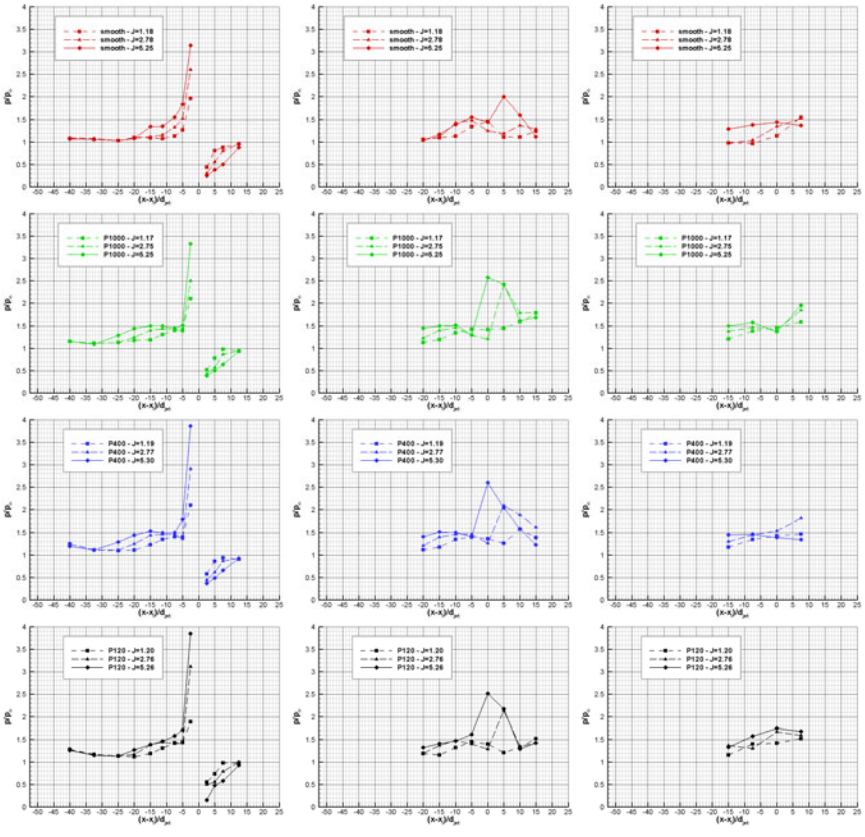

Fig. 4 Non dimensional wall pressure distribution against non dimensional distance at the centreline (left), $z/djet$=5.25 (middle) and $z/djet$=10 (right). 1st row from top: Smooth surface, 2nd row: P1000, 3rd row: P400, 4th row: P120.

jet diameters upstream before the pressure peak. The reason for that might be the transition phenomenon occurring before the jet induced separation. Spanwise pressure distribution is also augmented by roughness with values reaching up to 2.5 times free stream pressure for $z/djet$ of 5.25 and up to 1.8 times free stream pressure for $z/djet$ of 10 respectively which are higher than baseline smooth case.

Following figure compares the sole effect of roughness with different surfaces on non dimensional pressure distribution at the centreline with increasing momentum flux ratio from left to right. Firstly in all these plots the differences between P1000 and P400 is hardly distinguishable as confirmed by Fig. 3 before. Secondly rough surfaces experience longer separation regions and gradual pressure rises followed a plateau except P120. The pressure peak is magnified yet downstream separation region is not significantly altered.

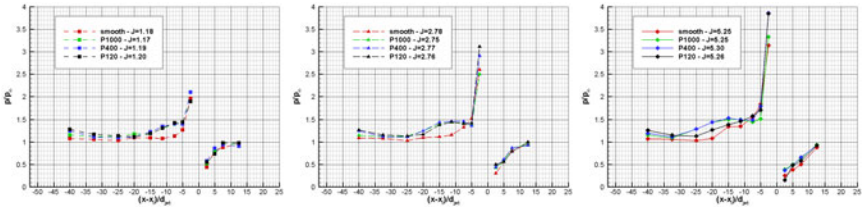

Fig. 5 Non dimensional wall pressure distribution against non dimensional distance for different rough surfaces at the centreline with increasing momentum flux ratio from left to right.

4 Conclusion

Experiments addressing the effect of the roughness on the flowfield due to a transverse sonic air jet over a flat plate at Mach 5 cross flow were carried out. The flat plate is covered with three different sand papers, P1000, P400 and P120, and the results are compared to baseline smooth case in terms of Schlieren images and wall pressure distributions. The main effect of roughness is to dissipate the boundary layer resulting bigger upstream and downstream separation regions as well as bigger spanwise extent of the jet induced region. The magnitudes of pressure peak and distributions are incremented, the effectiveness of jet is increased. P1000 and P400 are found to be favourable surfaces due to their ability to augment pressure distribution without significantly modifying the state of the upstream boundary layer.

References

1. Kumar, D., Stollery, J.L., Smith, A.J.: Hypersonic Jet Control Effectiveness. J. Shock Waves 7, 1–12 (1997)
2. Kontis, K., Stollery, J.L.: Control Effectiveness of a Jet-Slender Body Combination at Hypersonic Speeds. J. of Spacecraft and Rockets 34(6), 762–768 (1997)
3. Seiler, F., Gnemmi, P., Ende, H., Schwenzer, M., Meuer, R.: Jet Interaction at Supersonic Crossflow Conditions. J. of Shock Waves 13(1), 13–23 (2003)
4. Gulhan, A., Schutte, G., Stahl, B.: Experimental Study on Aerothermal Heating Caused by Jet-Hypersonic Crossflow Interaction. J. of Spacecraft and Rockets 45(5), 891–899 (2008)
5. Latin, R.M., Bowersox, R.D.W.: Flow Properties of a Supersonic Turbulent Boundary Layer with Wall Roughness. AIAA J. 38(10), 1804–1821 (2000)
6. Disimile, P.J., Scaggs, N.E.: An investigation into wedge induced turbulent boundary layer separation on a uniformly roughened surface at Mach 6. AIAA 89-2163
7. Babinsky, H., Edwards, J.A.: Large-Scale Roughness Influence on Turbulent Hypersonic Boundary Layers Approaching Compression Corners. J. of Spacecraft and Rockets 34(1), 70–75 (1997)
8. Prince, S.A., Vannahme, M., Stollery, J.L.: Experiments on the hypersonic turbulent shock-wave/boundary-layer interaction and the effects of surface roughness. The Aero Journal, 177–184 (April 2005)
9. Erdem, E., Kontis, K.: Non-Plasma and Plasma Transverse Jets in Hypersonic Cross Flow. AIAA 2009-7347

Part XIV
Numerical Methods

Antiforce Current Bearing Waves

M. Hemmati, W. Childs, H. Shojaei, and D. Waters

1 Introduction

In the case of breakdown waves in a long discharge tube, near the electrode where the potential gradient in the gas is greatest, small quantity of gas is ionized. Analysis of the spectrum of radiation emitted from electric breakdown of a gas reveals no Doppler shift, indicating that the ions have negligible motion. The large difference in mobilities of positive ions and electrons causes establishment of a space charge and consequently a space charge field. The electric field accelerates the free electrons until they aquire enough of energy for collisional ionization of the gas. Since the ionized gas is a conductor and it can not hold internal electric filed, the electric field which has its maximum value at the interface between the ionized gas and the neutral gas has to reduce to a negligible value at the trailing edge of the wave.

Breakdown waves for which the electric field force on electrons causes the average drift velocity of the electrons to be away from the wave front are referred to as antiforce waves. In the case of antiforce waves, the electron fluid pressure is considered to be large enough to provide the driving force and cause the propagation of the wave down the tube with observed velocities. This implies that despite the net electron drift velocity away from the wave front, the electron temperature must be large enough to sustain the wave motion. The wave is composed of two distinct regions. Following the shock front is a thin dynamical region in which the electric field starting from its maximum value at the shock front reduces to a negligible value at the trailing edge of the wave and the electrons slow down to speeds comparable to those of ions and heavy particles. This region will be referred to as the sheath region. Following the sheath region there is a relatively thicker thermal region in which the electron gas cools down by further ionization of the wave. This region will be referred to as the quasi-neutral region.

M. Hemmati · W. Childs · H. Shojaei · D. Waters
Arkansas Tech University, Department of Physical Science, Russellville, AR 72801, USA

2 Model

In our investigation of breakdown waves, we will employ the set of differential equations for the structure and state of the electron gas behind the shock front developed by Fowler et al.[1]. The basic equations for analyzing breakdown waves for the sheath region are the equations of conservation of mass, momentum, and energy coupled with Poisson's equation, and they respectively are

$$\frac{d(nv)}{dx} = n\beta, \tag{1}$$

$$\frac{d}{dx}[mnv(v-V)+nkT_e] = -enE - Kmn(v-V), \tag{2}$$

$$\frac{d}{dx}[mnv(v-V)^2 + nkT_e(5v-2V) + 2envφ - \frac{5nk^2T_e}{mK}\frac{dT_e}{dx}] = \tag{3}$$

$$-3(\frac{m}{M})nkKT_e - (\frac{m}{M})Kmn(v-V)^2, \tag{4}$$

$$\frac{dE}{dx} = \frac{e}{\varepsilon_0}(N_i - n). \tag{5}$$

where n, v, T_e, e and m represent the electron number density, velocity, temperature, charge, and mass, respectively, and M, E, E_0, V, k, K, x, β and ϕ represent the neutral particle mass, electric field within the sheath region, electric field at the wave front, wave velocity, Boltzmann's constant, elastic collision frequency, position within the sheath region, ionization frequency and ionization potential of the gas. The ion number density within the sheath region is represented by N_i.

For breakdown waves moving into a non-ionized medium, the net current ahead of the wave will be zero. This condition, $e(N_iV - nv) = 0$, is known as the zero current condition. Using the zero current condition in Eq.(5) reduces it to

$$\frac{dE}{dx} = \frac{e}{\varepsilon_0}n(\frac{v}{V} - 1). \tag{6}$$

In solving the antiforce case problem, we will use the set of non-dimensional variables and the set of fluid-dynamical equations derived by Hemmati[5]. Hemmati's set of non-dimensional variables are

$$\eta = \frac{E}{E_0}, \nu = (\frac{2e\phi}{\varepsilon_0 E_0^2})n, \psi = \frac{v}{V}, \theta = \frac{T_e k}{2e\phi}, \xi = -\frac{eE_0 x}{mV^2},$$

$$\alpha = \frac{2e\phi}{mV^2}, \kappa = -\frac{mV}{eE_0}K, \mu = \frac{\beta}{K}, \omega = \frac{2m}{M},$$

in which η, ν, ψ, θ, μ and ξ represent the dimensionless net electric field of the applied field plus the space charge field, electron number density, electron velocity, electron gas temperature, ionization rate, and position within the sheath region, while α and κ represent wave parameters.

To apply the set of electron fluid-dynamical equations to antiforce waves, some modifications in the set of electron fluid dynamical equations is required. In the wave, the heavy particles having negligible speed in the laboratory frame, will be moving in the negative x direction with a speed V, therefore, $V < 0$, $E_0 > 0$, and $K_1 > 0$. This leads to both κ and ξ being negative. These dimensionless variables are then substituted into Eqs.[1-4, 6] yielding the set of electron fluid-dynamical equations describing the antiforce waves in non-dimensional form

$$\frac{d}{d\xi}[\nu\psi] = \kappa\mu\nu, \tag{7}$$

$$\frac{d}{d\xi}[\nu\psi(\psi-1)+\alpha\nu\theta] = \nu\eta - \kappa\nu(\psi-1), \tag{8}$$

$$\frac{d}{d\xi}[\nu\psi(\psi-1)^2+\alpha\nu\theta(5\psi-2)+\alpha\nu\psi-\frac{5\alpha^2\nu\theta}{\kappa}\frac{d\theta}{d\xi}] = \tag{9}$$

$$2\nu\eta(\psi-1)-\omega\kappa\nu[3\alpha\theta+(\psi-1)^2], \tag{10}$$

$$\frac{d\eta}{d\xi} = -\frac{\nu}{\alpha}(\psi-1). \tag{11}$$

Considering the ion number density and velocity behind the wave front to be N_i and V_i, in the wave frame eN_iV_i carries a substantial portion of the current; however, in the lab frame, it is almost a zero portion. Therefore, behind the wave front the current is

$$eN_iV_i - env = I_1. \tag{12}$$

Absence of an experimentally observed Doppler shift indicates lack of appreciable ion and neutral particle motion in the laboratory frame. Therefore, considering the ion and neutral particle velocities to be almost equal ($V_i \simeq V$), substituting V for V_i and solving equation [12] for N_i results in

$$N_i = \frac{I_1}{eV} + \frac{n\nu}{V}. \tag{13}$$

Substituting N_i in the Eq. [5] results in

$$\frac{dE}{dx} = \frac{e}{\varepsilon_0}(\frac{I_1}{eV} + \frac{n\nu}{V} - n). \tag{14}$$

Substituting the dimensionless variables for antiforce waves in Eq. [14] reduces it to

$$\frac{d\eta}{d\xi} = \frac{\kappa I_1}{\varepsilon_0 K E_0} - \frac{\nu}{\alpha}(\psi-1). \tag{15}$$

Substituting ι for $\frac{I_1}{\varepsilon_0 K E_0}$ in the above equation reduces the Poisson's equation to

$$\frac{d\eta}{d\xi} = \kappa\iota - \frac{\nu}{\alpha}(\psi - 1). \tag{16}$$

Solving for $\nu(\psi - 1)$ from equation [16] and substituting it in the equation of conservation of energy for antiforce waves, equation [10], gives the final form of the equation of conservation of energy for antiforce waves with a large current in the vicinity of the wave front. Therefore, the final form of the set of electron fluid-dynamical equations describing antiforce current bearing waves, where all quantities, including κ are intrinsically positive, will be

$$\frac{d}{d\xi}[\nu\psi] = \kappa\mu\nu, \tag{17}$$

$$\frac{d}{d\xi}[\nu\psi(\psi - 1) + \alpha\nu\theta] = \nu\eta - \kappa\nu(\psi - 1), \tag{18}$$

$$\frac{d}{d\xi}[\nu\psi(\psi - 1)^2 + \alpha\nu\theta(5\psi - 2) + \alpha\nu\psi - \frac{5\alpha^2\nu\theta}{\kappa}\frac{d\theta}{d\xi} + \alpha\eta^2] = \tag{19}$$

$$2\eta\kappa\iota\alpha - \omega\kappa\nu[3\alpha\theta + (\psi - 1)^2], \tag{20}$$

$$\frac{d\eta}{d\xi} = \kappa\iota - \frac{\nu}{\alpha}(\psi - 1). \tag{21}$$

3 Results and Discussion

In their study of lightning attachment processes in rocket-triggered lightning strokes, for return-stokes, Wang et al.[10] reported a current peak value of about $12kA$ to $21kA$. Also, in his review of characteristics of lightning discharges that transport either positive charge or both negative and positive charges to ground, Rakov [7] reports a return stroke current value of $10kA$.

Determining K from experimental curves [6] gives $K/P = 3 \times 10^8$ for helium and $K/P = 4.8 \times 10^7$ for nitrogen at $273K$. At a temperature of 10^5 , K will be 2.4×10^9 for helium and 9×10^9 for nitrogen and applied fields are usually of the order of $10^5 V/m$. Considering that E_0, K and β in our formulas are scaled with P (the electron gas pressure) and using the values of I_1, ε_0, E_0 and K, one can estimate the value of ι, which is of the order of one.

A trial and error method was utilized to integrate Eqs. [17-21]. For a given wave speed, α, a set of values for wave constant, κ, electron velocity, ψ_1 and electron number density, ν_1 at the wave front were chosen. The values of κ, ψ_1 and ν_1 were repeatedly changed in integrating Eqs. [17-21] until the process lead to a conclusion in agreement with the expected conditions at the end of the dynamical transition region of the wave. For several current values, we were able to integrate the electron fluid-dynamical equations, Eqs. [17-21] for α value as low as 0.01. This value

represents a wave speed of $0.3 \times 10^8 m/s$ and conforms with the lower experimental speed range for return stroke lightning. The successful solutions required the following boundary values

$$\iota = 0.0, \kappa = 1.3, \psi_1 = 0.645, \nu_1 = 0.886$$

$$\iota = 0.5, \kappa = 1.3, \psi_1 = 0.654, \nu_1 = 0.882$$

$$\iota = 1, \kappa = 1.3, \psi_1 = 0.66, \nu_1 = 0.85$$

$$\iota = 2, \kappa = 1.3, \psi_1 = 0.6785, \nu_1 = 0.8435$$

$$\iota = 3.8, \kappa = 1.3, \psi_1 = 0.682, \nu_1 = 0.808$$

$$\iota = 5, \kappa = 1.3, \psi_1 = 0.7, \nu_1 = 0.7696$$

In his review of characteristics of lightning discharges that transport either positive charge or both negative and positive charges to ground, for return stroke lightning (antiforce waves), Rakov[7] reports speeds in the range of $0.3 \times 10^8 m/s$ to $1.7 \times 10^8 m/s$. While, in a study of direct measurement of the time derivative of the electric field of triggered lightning strokes at distances of 10, 14, and $30m$, Uman et al.[9] reported return stroke speeds as low as $0.46 \times 10^8 m/s$.

Figure 1.a represents the electric field, η, as a function of electron velocity, ψ, for dimensionless current values of 0, 0.5, 1, 2, 3.8 and 5 and wave velocity of $3 \times 10^7 m/s$. For all current values, the solutions meet the expected conditions at the end of the sheath region of the wave ($\eta_2 \to 0, \psi_2 \to 1$). Figure 1.b represents the electric field, η, as a function of position, ξ, within the sheath region of the wave. Figure 2.a represents the electron temperature, θ, as a function of position, ξ, within the sheath region for all the above mentioned current values. Figure 2.b represents the electron number density, ν, as a function of position , ξ, within the sheath region of the wave for all the above mentioned current values.

In his fluid model simulations of a 13.56-MHz rf discharge, David Graves[3] reports electron number density values between $5 \times 10^{15}/m^3$ and $2 \times 10^{16}/m^3$. To speed up fluid model for gas discharge calculations, Hagelaar and Kroesen[4], present a technique for the implicit treatment of the electron energy source term, based on linearization with respect to the electron mean energy. In their study, Hagelaar and Kroesen[4] report an average electron number density of $7 \times 10^{15}/m^3$. Our average non-dimensional electron number density of 0.7 represents an electron number density of $7.7 \times 10^{15}/m^3$within the sheath region of the wave.

Applying fluid dynamic techniques to the passage of ionizing wave counter to strong electric fields, for wave speed of $10^7 m/s$, Sanmann and Fowler's[8] electric field peaked at a distance of $0.04m$ behind the wave front and their total sheath thickness was $0.05m$. As our graphs show, for the wave speed of $3 \times 10^7 m/s$, our non-dimensional ξ value of 0.6 represents a sheath thickness of $2.5 \times 10^{-2} m$. Measuring electron density behind shock waves, Fujita et al.[2] report a wave thickness of approximately $5cm$.

For ionizing waves propagating counter to strong electric fields, Sanmann and Fowler[8] reported that the electron temperature increases rapidly away from the

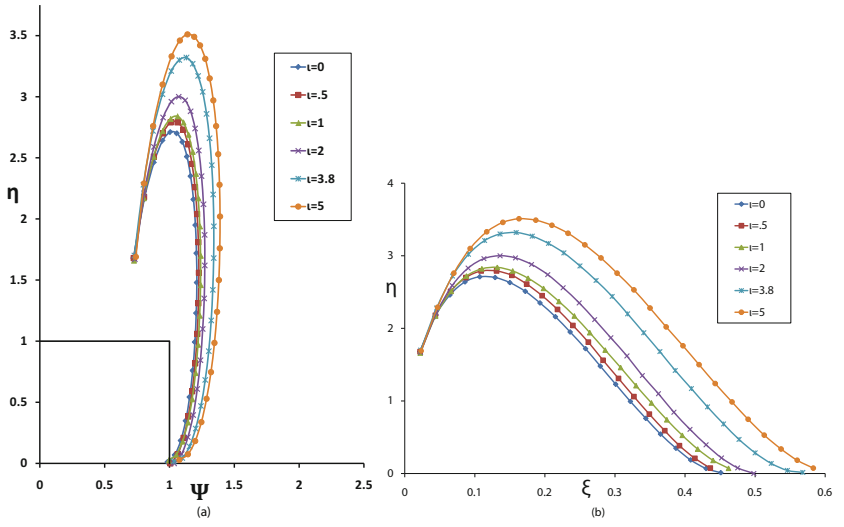

Fig. 1 (a) Electric field as a function of electron velocity within the sheath region of current bearing antiforce waves for current values of 0, 0.5, 1, 2, 3.8, and 5. (b). Electric field as a function of position with the sheath region of current bearing antiforce waves for current values of 0, 0.5, 1, 2, 3.8, and 5.

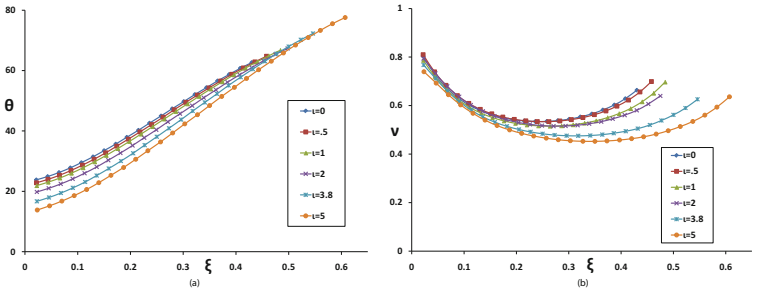

Fig. 2 (a). Electron temperature as a function of position within the sheath region of current bearing antiforce waves for current values of 0, .5, 1, 2, 3.8, and 5. (b)Electron temperature as a function of position within the sheath region of current bearing antiforce waves for current values of 0, .5, 1, 2, 3.8, and 5.

wave front until it reaches a peak value of around $3.17 \times 10^7 K$ at a distance of $5.4 \times 10^{-2} m$ behind the wave front. Our results show that the temperature increases behind the shock front and it reaches its maximum dimensionless value of $\theta = 67$ at the trailing edge of the wave. $\theta = 67$ represents electron gas temperature of $3.88 \times 10^7 K$.

4 Conclusions

For a range of current values behind the shock front, we have been able to integrate our modified set of electron fluid-dynamical equations through the dynamical transition region of the wave. For all current values, our solutions meet the expected conditions at the end of the sheath region of the wave. Our results agree with several other theoretical and experimental results as well. This is a confirmation of the validity of our modified set of equations and also application of fluid model to breakdown waves.

Acknowledgements. The authors would like to express gratitude for the financial support offered by the Arkansas Space Grant Consortium for this research.

References

1. Fowler RG, M Hemmati, RP Scott, and S Parsenajadh: The Physics of Fluids **27**, 6 (1984)
2. Fujita K, Sato S and Abe T.: Journal of Thermodynamics and Heat Transfer **17**,(2003)
3. Graves DB.: J. Appl. Phys. **62**, 1 (1987)
4. Hagelaar GJM and Kroesen GMW: Journal of Computational Physics**159**, (2000)
5. Hemmati M.: Electron shock waves: speed range for antiforce waves. In: *Proceedings of the 22nd International Symposium on Shock Waves*, (Imperial College, London, UK, 1999) pp 995-1000
6. McDaniel, EW: *Collision phenomena in ionized gases*, (Wiley, New York, 1964)
7. Rakov VA.: Positive and bipolar lightning discharges: a review. In: *Proceedings of the 25th International Conference on Lightning Protection*, (2000) pp 103-108
8. Sanmann E and RG Fowler: The Physics of Fluids **18** 11 (1975)
9. Uman MA, VA Rakov, KJ Schnetzer, KJ Rambo, DE Crawford and RJ Fisher: J. Geophys Res. **105** D12 (2000)
10. Wang D, Rakov VA, Uman MA, Takagi N, Watanabe T, Crawford DE, Rambo KJ, Schnetzer GH, Fisher RJ, and Kawasaki ZI: J. Geophys. Res. **104** D2 (1999)

Numerical Simulation of Initial Shock and Detonation Wave Development in Shock-Tube Configurations

P.R. Ess and J.P. Sislian

1 Introduction

The purpose of the present work is to provide insight into the numerical computation of shock- and detonation-waves, with a particular focus on high levels of grid refinement. This addresses the possibility of achieving a grid-independent solution and resolving the zone resulting from the ignition delay in the case of a detonation wave. Both viscous and inviscid flow solutions for shock and detonation waves are compared, and planar flow computations are used to assist with the setup of a two-dimensional flow through a duct, blocked by $1/9$-th of the inflow area by a cube placed on the centre-line of the duct.

2 Governing Equations

The flow is governed by the Navier-Stokes equations for chemically reacting multi-species gas, expressed in terms of density ρ, velocity vector u_i, total energy E, species mass fractions Y_α of species $\alpha = 1..N_s$, pressure p, shear tensor τ_{ij}, diffusion and energy flux vectors $j_{\alpha i}$ and ε_i, respectively, which read

$$\frac{\partial \mathbf{Q}}{\partial t} + \frac{\partial \mathbf{F}}{\partial x_i} + \frac{\partial \mathbf{G}}{\partial x_i} = \mathbf{S}. \tag{1}$$

The vector of conserved variables is defined by $\mathbf{Q} = (\rho, \rho Y_\alpha, \rho u_i, \rho E)$, that of inviscid fluxes and pressure by $\mathbf{F} = (\rho u_i, \rho u_i Y_\alpha, \rho u_i u_j + \delta_{ij} p, \rho u_i E)$, that of viscous fluxes by $\mathbf{G} = (0, j_{i\alpha}, -\tau_{ij}, -u_j \tau_{ij} + \varepsilon_i)$, and the source term accounting for

P.R. Ess
DLR, Institute of Combustion Technology, Pfaffenwaldring 38, 70569
Stuttgart, Germany

J.P. Sislian
UTIAS, 4925 Dufferin Street, Toronto, Ontario, Canada M3H 5T6

chemical reaction by $\mathbf{S} = (0, S_\alpha, 0, 0, 0, 0)$. Diffusion is calculated using Fick's law [1], and the energy flux vector contains heat conduction and enthalpy diffusion. Specific heats, enthalpy and entropy of species are based on polynomials [2] in terms of temperature, and the ideal gas equation is used to relate p, ρ and T. The transport properties viscosity, thermal conductivity and binary diffusion coefficients are calculated following the laws of kinetic gas theory [3]. Further details can be found in Refs. [4, 5].

3 Numerical Method and Validation

The governing equations are solved with an unsteady, implicit, cell-centred, structured multi-block, finite-volume scheme with an accuracy up to third order in time and space. Roe flux-difference splitting in combination with various total-variation diminishing (TVD) limiters, as described by Yee et al. [6], was used to discretize inviscid, and central differences to compute viscous fluxes. For each physical time step, a steady-state problem is solved in a pseudo time domain, employing an implicit lower-upper symmetric Gauss-Seidel (LUSGS) algorithm.

The implementation of the numerical methods used has been validatied against various test cases, such as oscillating shock-induced combustion, detonation waves around blunt bodies, laminar boundary layers and multi-species diffusion [4].

4 Planar Shock Wave Analysis

The numerical representation of a shock wave in pure argon is analysed for a range of shock Mach numbers. In order to achieve a very fine grid spacing, the flow problem is solved in the shock frame, i.e. the shock wave is stationary in the domain. The shock position can be kept fixed, when suitable outflow conditions are applied and properties at the outflow are prescribed corresponding to the inflow conditions. The thermodynamic state at the inflow is given by standard pressure $p = 101325Pa$ and temperature $T = 298.15K$, and the inflow Mach number in a range from $M = 2$ to 6. Mass, momentum and energy conservation equations are employed to compute the corresponding post-shock state, which is used to setup the initial solution of the flow in terms of a shock-tube problem. Starting with the coarse grid, employing a grid spacing of $\Delta x = 1 \times 10^{-5} m$, a solution is computed until convergence is obtained. The solution is then successively transferred onto finer grids, dividing the grid spacing by a factor of two for each finer grid level, until the final grid resolution, based on $\Delta x = 2.44 \times 10^{-9} m$, is reached after 12 levels of refinement. This process is performed for inviscid (only $\mathbf{F}$) and viscous (both $\mathbf{F}$ and $\mathbf{G}$) forms of the governing equations, and the resulting shock profiles for the Mach number three are shown in Fig. 1. While the density profiles for the viscous flow solution converge towards a grid-independent solution, the inviscid flow solution does not and the shock thickness can be directly related to the grid

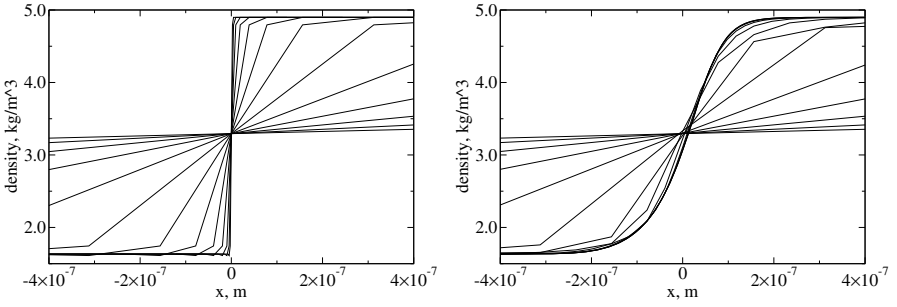

(**a**) inviscid (**b**) viscous

Fig. 1 Density profiles of argon shock wave at Mach number $M = 3$ for grid spacing from $\Delta x/m = 2.44 \times 10^{-9}$ to 10^{-5}.

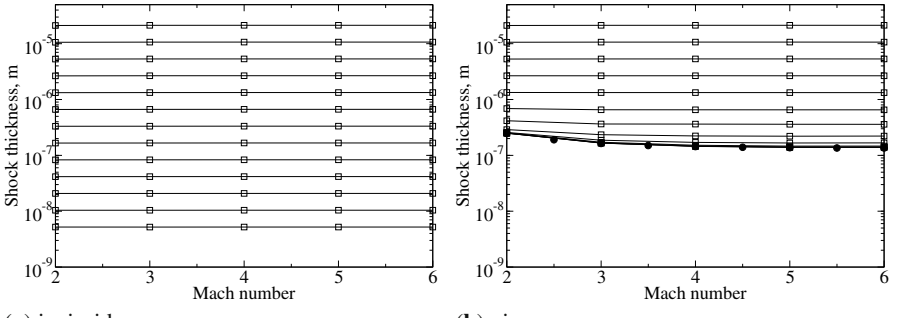

(**a**) inviscid (**b**) viscous

Fig. 2 Thickness of argon shock wave for $M = 2$ to 6. The grid spacing varies from $\Delta x/m = 1 \times 10^{-5}$ (level 0), 5×10^{-6} (1), 2.5×10^{-6} (2), 1.25×10^{-6} (3), 6.25×10^{-7} (4), 3.125×10^{-7} (5), 1.5625×10^{-7} (6), 7.8125×10^{-8} (7), 3.90625×10^{-8} (8), 1.953125×10^{-8} (9), 9.765625×10^{-9} (10), 4.882813×10^{-9} (11), and 2.441406×10^{-9} (12). Symbols "•" represent results from Ref. [7].

spacing employed. This holds over the entire Mach number range investigated, as shown in Fig. 2. In the case of viscous flow, the Mach number dependence of the shock thickness for the converged solution agrees well with that given by Linzer and Hornig [7].

Several important observations can be made. For a coarse grid resolution, the shock thickness in the viscous flow behaves nearly identical to that in the inviscid flow solution. Further, a truly grid-independent solution can only be achieved when employing viscous terms and a sufficiently refined grid. At the same time, the required resolution seems difficult to achieve in any practical size flow problem, even with adaptive grid refinement. The latter would require in excess of 12 refinement levels and a gradual reduction of the refinement towards the original, coarsely resolved, part of the domain. Ultimately, the solution obtained with a sufficiently

refined grid is not the actual shock thickness measured, but somewhat thicker. This is true for moderate shock Mach numbers already [7, 3].

5 Planar Detonation Wave

A planar detonation wave propagating into a gas mixture containing two, one and seven parts in moles of hydrogen, oxygen and argon, respectively, is reproduced numerically. The case corresponds to that studied by Yungster and Radhakrishnan [8] and the same chemical reaction scheme is employed here. The temperature and pressure profiles during the formation and propagation of the detonation wave through the duct are shown in Fig. 3 (a). The detonation velocity obtained is $1602 m/s$, which is very close to that observed by Yungster and Radhakrishnan. Since the post-detonation Mach number is subsonic, the detonation wave must be overdriven, despite the value of the detonation velocity being very close to the computed Chapman Jouguet velocity [8].

When the flow is solved in the detonation frame, i.e. the wave position is fixed in space, a substantial grid refinement can be accomplished, in order to resolve the fine structure of the detonation wave and investigate the impact of viscous terms. However, because the initial shock wave is followed by a reaction zone, this must be resolved as well, and the domain must extend much further than for the argon shock wave analysis. Hence, the grid spacing in the solution shown in Fig. 3 (b) is *only* $\Delta x = 4.88 \times 10^{-7} m$, and uniform in the domain of $0.1m$ lenght, corresponding to over $200k$ cells for a one-dimensional case. Despite the smoother profiles of pressure and temperature shock waves ahead of the reaction zone in the case of viscous flow, the plateau of pressure and temperature and the onset of chemical reaction do not differ. The plateau is due to the ignition delay and, in the present case, $0.175mm$ long. With the post shock velocity of approximately $510 m/s$ this translates to an ignition delay of $0.34 \mu s$.

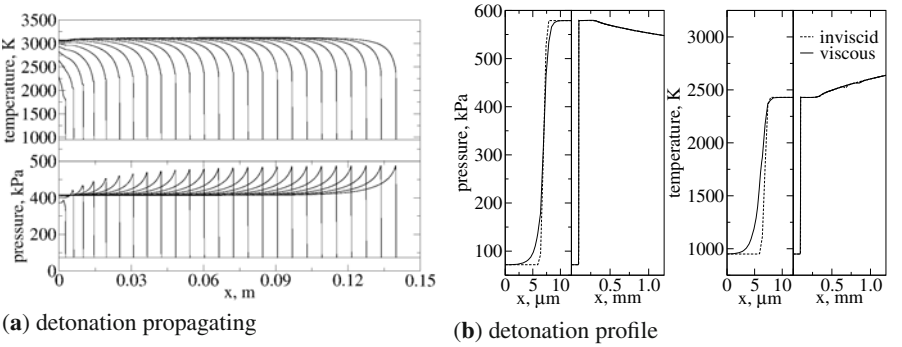

(**a**) detonation propagating

(**b**) detonation profile

Fig. 3 Profiles of detonation wave propagating into a hydrogen-oxygen-argon gas mixture. The case corresponds to that by Yungster and Radhakrishnan [8].

6 Flow in Duct

The flow in the duct presented in the following can be seen in the context of hypersonic propulsion, where the combustion of a premixed flow entering the duct is induced due to a blunt body placed in the duct. This problem has been investigated in the past [5] and a channel blockage ratio of $1/9$ was found to yield an optimum thrust potential for a rod as blunt body. Ambient, initial and final inflow conditions characterised by a flight altitude of $36km$ at a dynamic pressure of $40kPa$ (state 0) are summarised in Tab. 1. The inflow conditions to the duct presume an idealised two-shock inlet, where the flow is deflected by $9.5deg$ twice to achieve a compression of the gas. The chemical reaction of the hydrogen-air gas is represented by the corresponding mechanism of Jachimowski [9].

The initial conditions for the gas in the duct are given by state 1, and two initialisation schemes for the flow through the duct were investigated. In the first, stage A1, air at state 2 is imposed at the inflow boundary until the flow in the duct is uniform, followed by stage A2, where premixed hydrogen-air flow at state 3 is imposed. In the second, stage B1, premixed hydrogen-air flow at state 3 is imposed directly. The leading and trailing waves reach the outflow domain after $51\mu s$ and $71\mu s$ for stage A1, $41\mu s$ and $61\mu s$ for stage A2, and $55\mu s$ and $79\mu s$ for stage B1, respectively. In Fig. 4 the air flow and the direct hydrogen-air flow initialisation are shown. In both cases A1 and B1, nitric oxide forms in the wave system, at slightly lower levels in case B1. In case B1 hydroxyl as well as water forms in the wave system. The chemical reaction is not significant enough to induce detonation.

Planar flow solutions, where the leading wave is just ahead of the cube, were used to initialise the two-dimensional flow computations. In Figs. 5 (a) and (f) the converged solutions of air and hydrogen-air flow are shown. Inbetween, the flow development from state 2 to state 3 is shown. As hydrogen is propagated through the duct, it is ignited as it passes through the shock wave and changes the wave system significantly. A detonation establishes ahead of the cube and the overall flow initialisation process takes longer than in the planar case shown before.

Table 1 Initial and inflow conditions based on flight altitude of $36km$, dynamic pressure of $40kPa$ and idealised two-shock inlet with $9.5deg$ flow deflection angle.

State	p, Pa	T, K	$u, m/s$	Ma	$n_{H2} : n_{O2} : n_{N2}$
0	498.495	239.283	3326.680	10.708	$0 : 1 : 3.76$
1	498.495	239.283	0.000	0.000	$0 : 1 : 3.76$
2	15035.162	813.591	3140.581	5.580	$0 : 1 : 3.76$
3	10681.189	696.264	3125.738	5.070	$2 : 1 : 3.76$

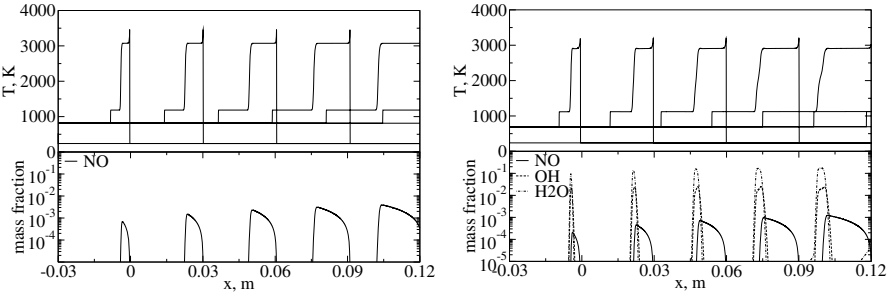

(**a**) air (**b**) hydrogen-air

Fig. 4 Profiles of temperature and selected mass fractions corresponding to flow initialisation of air (a) and hydrogen-air (b) for altitude $H = 36km$ and dynamic pressure $Q = 40kPa$. For pure air, profiles (from left to right) at time $t/\mu s = 10$, 21, 31, 42, and 52 are shown. For hydrogen-air, profiles at $t/\mu s = 11$, 22, 33, 44 and 55 are shown.

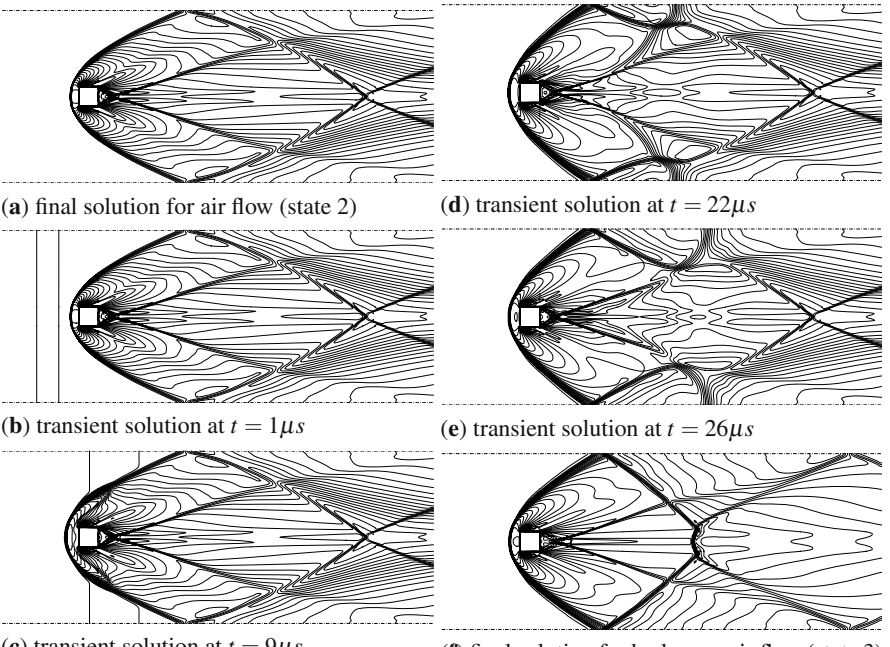

(**a**) final solution for air flow (state 2)

(**b**) transient solution at $t = 1\mu s$

(**c**) transient solution at $t = 9\mu s$

(**d**) transient solution at $t = 22\mu s$

(**e**) transient solution at $t = 26\mu s$

(**f**) final solution for hydrogen-air flow (state 3)

Fig. 5 Temperature iso-lines from $500K$ to $3800K$ at $100K$ increments are shown for converged flow with inflow at state 2 in subfigure (a), and converged flow with inflow at state 3 in subfigure (f). Inbetween flow development during stage A2 is shown in subfigures (b)-(e).

7 Conclusions

The work presented gives insight into numerical requirements and constraints when simulating shock and detonation waves and initial flow development in shock-tube-like flow configurations. It is demonstrated, that grid independent solutions can be obtained for viscous flow calculations only, provided the grid is refined sufficiently. Further, planar detonation waves can be resolved sufficiently to establish the ignition delay and the insensitivity of the grade of resolvement of the preceeding shock wave on the following chemical reaction zone. Finally, the flow development and initialisation process for a duct with a channel blockage of $1/9$ due to a cube placed in the centre-line of the duct has been presented. Despite the inability to reach similar levels of grid refinement in the two-dimensional flow computation, useful information regarding the flow initialisation process could be gained.

References

1. Warnatz, J., Maas, U.: Technische Verbrennung. Springer (1993) (in German)
2. McBride, B.J., Gordon, S., Reno, M.A.: Coefficients for Calculating Thermodynamic and Transport Properties of Individual Species, NASA TM 4513 (1993)
3. Hirschfelder, J.O., Curtiss, C.F., Bird, R.B.: Molecular Theory of Gases and Liquids. John Wiley & Sons (1954)
4. Ess, P.R.: Numerical Simulation of Blunt-Body Generated Detonation Waves in Visous Hypersonic Ducted Flows. PhD Dissertation, Bristol University (2003)
5. Ess, P.R., Sislian, J.P., Allen, C.B.: Journal of Propulsion and Power 21(4) (2005)
6. Yee, H.C., Klopfer, G.H., Montagné, J.-L.: High-Resolution Shock-Capturing Schemes for Inviscid and Viscous Hypersonic Flows 88(1), 31–61 (1990)
7. Linzer, M., Hornig, D.F.: Structure of Shock Fronts in Argon and Nitrogen. Physics of Fluids 6(12), 1661–1668 (1963)
8. Yungster, S., Radhakrishnan, K.: Modeling planar detonation wave propagation using detailed chemistry AIAA-1996-2949 (1996)
9. Jachimowski, C.J.: An Analytical Study of the Hydrogen-Air Reaction Mechanism with Application to Scramjet Combustion. NASA Technical Paper 2791 (1988)

Computations of Flow Field around an Object Decelerating from Supersonic to Subsonic Velocity

T. Saito, K. Hatanaka, H. Yamashita, T. Ogawa, S. Obayashi, and K. Takayama

1 Introduction

A detached shock wave is formed in front of a blunt object moving with supersonic velocities or an object placed in a supersonic flow. The distance from the shock front to the surface of the moving body is called the shock stand-off distance, δ, and is measured along the propagation axis when the object is a solid sphere.

For a fixed Mach number M_0 of a flow or an object, the shock stand-off distance is strongly correlated to the density distribution between the shock front and the stagnation points. Therefore, the shock stand-off distance varies with real gas effects since the density changes with real gas effects in super/hypersonic flows. This naturally suggests a practical means of evaluating the degree of progress of the real gas effect by measuring the shock stand-off distance [1, 2, 3].

Ballistic range is a typical experimental facility for measuring the shock stand-off distance since the thermochemical properties of the incoming flow are precisely known and may even be controllable. However, errors due to model acceleration may affect experimental data. A projectile decelerates with the drag forces caused by pressure and viscosity during its free flight and also often accelerates when exiting from the muzzle as a result of the complex force balance around the projectile. Shock stand-off distance measured at an observation window through certain optical flow visualization techniques reflects such a flight history. Therefore, it is important to consider the non-steadiness of a projectile while interpreting the ballistic-range data.

In this study, numerical calculations were conducted to simulate the time-dependent flow field around a solid sphere decelerating in the transonic velocity range. Simulations for a projectile without deceleration were first conducted, and

T. Saito · K. Hatanaka
Dept. of Aerospace Eng., Muroran Institute of Technology, 27-1 Mizumoto-cho, Muroran 050-8585, Japan

H. Yamashita · T. Ogawa · S. Obayashi · K. Takayama
Institute of Fluid Science, Tohoku University, 2-1-1 Katahira, Aoba-ku, Sendai 981, Japan

the results were compared with experimental data reported by Starr et al. in order to confirm the validity of our numerical calculations. Numerical results including model deceleration were then compared with the experimental data obtained at the Interdisciplinary Shock Wave Laboratory at the Institute of Fluid Science, Tohoku University.

2 Numerical Simulations

2.1 Basic Equations and Numerical Scheme

Basic equations of time-dependent, two-dimensional, axisymmetric flows in the body fixed coordinate system are expressed as follows,

$$\mathbf{U}_t + \mathbf{F}_x + \mathbf{G}_r = \mathbf{H} + \mathbf{I} + \mathbf{F}^{\mathbf{v}}{}_x + \mathbf{G}^{\mathbf{v}}{}_r, \tag{1}$$

where t, x, and r denote, respectively, the time, the space coordinates in the axial and radial directions; the subscripts represent the derivations with the variables. The symbol $\mathbf{U}$ denotes the vector of conserved quantities and its components are the mass and the momentums in the axial and radial directions and the total energy per unit volume. The vectors $\mathbf{F}$ and $\mathbf{G}$ consist of the relevant corresponding flux components, and $\mathbf{H}$ denotes the source terms due to the cylindrical geometry. The terms in the vector $\mathbf{I}$ arises from the accelaration of the grid-system expressed as the sysmol a. Further, $\mathbf{F}^{\mathbf{v}}$ and $\mathbf{G}^{\mathbf{v}}$ are the viscosity and heat conduction terms in x and r directions. The components of each vector are shown as

$$\mathbf{U} = \begin{bmatrix} \rho \\ \rho u \\ \rho v \\ E \end{bmatrix}, \qquad \mathbf{F} = \begin{bmatrix} \rho u \\ \rho u^2 + p \\ \rho uv \\ u(E+p) \end{bmatrix}, \quad \mathbf{G} = \begin{bmatrix} \rho v \\ \rho uv \\ \rho v^2 + p \\ v(E+p) \end{bmatrix}, \tag{2}$$

$$\mathbf{H} = \frac{1}{r} \begin{bmatrix} \rho v \\ \rho uv \\ \rho v^2 \\ v(E+p) \end{bmatrix}, \qquad \mathbf{I} = \begin{bmatrix} 0 \\ \rho a \\ 0 \\ \rho au \end{bmatrix}, \tag{3}$$

$$\mathbf{F}^{\mathbf{v}} = \begin{bmatrix} 0 \\ \tau_{xx} \\ \tau_{xr} \\ \tau_{xx}u - \tau_{xr}v - kT_x \end{bmatrix}, \qquad \mathbf{G}^{\mathbf{v}} = \begin{bmatrix} 0 \\ \tau_{rx} \\ \tau_{rr} \\ \tau_{rx}u - \tau_{rr}v - kT_r \end{bmatrix}, \tag{4}$$

where ρ, p, u, v, k, and T denote the density, pressure, velocity components relative to the body-fitted coordinates in x and r directions, thermal conductivity and temperature, respectively. The total energy per unit volume, E, is expressed using the specific internal energy, ε, as

$$E = \rho\varepsilon + \rho\frac{1}{2}(u^2 + v^2), \tag{5}$$

and the caloric equation of state for ideal gases, $\varepsilon = p/(\gamma - 1)$, with a constant specific heat ratio γ is used for closing the system of equations.

The viscous stress tensor τ_{ij} is expressed with the coefficient of viscosity μ as

$$\tau_{ij} = \mu \left[\left(\frac{\partial u_i}{\partial x_j} + \frac{\partial u_j}{\partial x_i} \right) - \frac{2}{3} \frac{\partial u_k}{\partial x_k} \delta_{ij} \right], \tag{6}$$

where δ_{ij} is the Kronecker's delta, and the summation conventions are used. The coefficient of viscosity μ is assumed to depend only on temperature and is derived from Sutherland's formula [8].

A system of homogeneous equations obtained by neglecting the terms on the right hand side of Eq.(1) represents time-dependent inviscid planar flows and is solved using the WAF method [5, 6]; the WAF numerical scheme is a second-order extension of the Godunov scheme. Further, the HLLC approximate Riemann solver is used for evaluating numerical fluxes in this study. The source terms on the right hand side of the equation are then used to modify the planar inviscid solution into the solution for axisymmetric flow with viscosity and heat conduction. The operator-splitting method proposed by Strang [7] is used for this modification. The fourth-order Runge-Kutta method is used for numerical integration in the operator-splitting method.

A structured numerical grid systm of 1321 $\times$ 501 was generated for covering the computational domain. The diameter of the projectile is 0.03 m, and the upper boundary is 0.3 m from the axis. The computational domain extends 0.27 m in the axial direction both in front of and behind the center of the projectile. Free stream conditions are assigned on the left hand side of the flow domain as boundary conditions, while outflow boundary conditions are used on the right hand side of the domain. Reflective boundary conditions are assigned along the axis of symmetry, projectile surface, and upper edge of the computational domain. A slip or non-slip condition is applied to the projectile surface and upper wall depending on whether the viscous terms are included in the computations or not.

2.2 Numerical Procedure

The steady flow around the projectile is computed first for a fixed-flow velocity, i.e., the initial projectile velocity. And the flow variables of the converged steady solution are used as initial conditions for simulating the unsteady flow field that is caused by the deceleration of the projectile. The unsteady flow is computed by adjusting the flow velocity and the boundary conditions according to the updated projectile speed at each time step. The acceleration and speed are computed from the force acting on the projectile by integrating the equation of motion. In the inviscid computation, the force includes only the pressure component in the flight direction, while in the case of viscous flow, the shear stress acting on the model surface is also considered.

It should be mentioned here that the abovementioned procedure, which starts from a steady flow solution, is an approximation. In this study, the projectiles always accelerate or decelerate during the course of the ballistic range experiments and the flow field at a given moment never becomes equal to the field of the steady flow corresponding to the projectile velocity at that moment. The flow field obtained for a certain decelerated model speed depends on the initial projectile speed at which the initial conditions are set to the corresponding steady flow.

3 Results and Discussion

3.1 Results for the Case of No Projectile Deceleration

The flows around a sphere of 30-mm diameter in steady flight conditions are computed first. Figure 1(Left) shows the converged pressure field around the sphere moving at a constant speed of Mach 1.13.

A detached shock wave is clearly formed ahead of the projectile. Complex pressure-wave interactions behind the sphere and an oblique shock wave originating from the wake region are clearly observed.

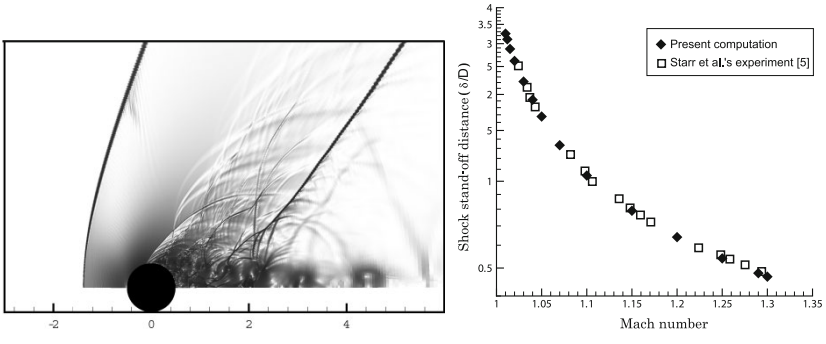

Fig. 1 Left: Pressure distribution around a sphere flying with Ms = 1.13; Distance scale normalized by model diameter, Right:Comparison of the steady numerical solutions

The numerical results of shock stand-off distances normalized by the projectile's diameter are plotted in Fig. 1(Right) for a projectile Mach number ranging between 1.01 and 1.3. The experimental data points obtained by Starr et al.[4] are also plotted in the figure for comparison. The experimental conditions are chosen in such a way that the projectile deceleration is eliminated [4]. In this series of computations, the viscosity and heat conduction are neglected but the numerical results agree quite well with the experimental data.

The good agreement between the inviscid numerical results and the experimental data obtained by Starr et al. indicates that the effect of viscosity and heat conduction

is negligible in this velocity range. This is also observed in Fig. 9 of [9], where the Euler results overlap with the viscous data points.

3.2 Results for the Case of a Decelerating Projectile

Figure 2 compares the shock stand-off distance obtained from the current numerical work with the ballistic range experimental data. Numerical results for the decelerating sphere, obtained using Euler equations, i.e., without a viscous effect, and the experimental data of Starr et al. for steady projectiles are also included in this figure. Three computations with different initial flight Mach numbers were carried out. The initial Mach numbers were 1.25, 1.19, and 1.13, and the shock stand-off distances were measured when these flight Mach numbers became 1.15, 1.09, and 1.04, respectively. These combinations of the initial and final Mach numbers are taken from the ballistic range experiments.

As seen in the figure, the numerical results show slightly larger values for shock stand-off distances as compared to the corresponding experimental data; however, the agreement between the numerical and experimental results is reasonably good. One of the reasons why the numerical results show slightly larger shock stand-off distances may be that the initial conditions in the simulations are set to realize a fully developed steady flow field for the measured muzzle velocities. The projectiles always experience acceleration, either positive or negative, during the course of the ballistic range experiments, and the use of a fully developed steady solution at the muzzle is obviously an approximation. Presently, we do not have sufficient experimental data to further investigate this problem.

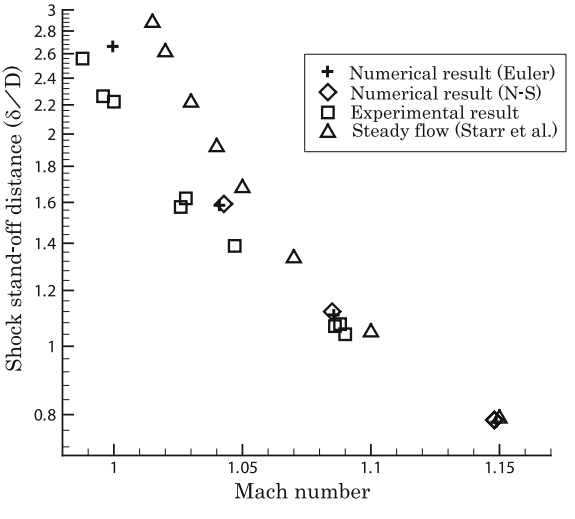

Fig. 2 Comparison of numerical solutions of unsteady flow

It is noticed that the difference between the numerical results with and without the viscosity terms taken into account is very small. The consideration of viscosity terms results in only a fractional difference in the numerical results. This indicates that the viscosity can be neglected in the future for this speed region. A practical merit of this approach is that the computational time is reduced, considering that no fine numerical meshing near the body surface is required.

4 Concluding Remarks

Shock stand-off distances of a solid sphere decelerating in the transonic velocity range are determined via numerical computations using a body-fixed numerical grid system. The numerical results for a steady projectile show good agreement with the experimental data obtained in a previous study, indicating that the reliability of the present computational method is good.

Numerical simulations are carried out by taking the model deceleration into account. The numerical results are in good agreement with the ballistic-range experimental data. The viscous effect is found to be negligible and can be ignored in the present study.

Acknowledgement. Part of the work was carried out under the Collaborative Research Project of the Institute of Fluid Science, Tohoku University.

References

1. Nonaka, S., Mizuno, H., Takayama, K., Park, C.: J. Thermophys. Heat Trans. 14 (2000)
2. Hashimoto, T., Komuro, T., Sato, K., Itoh, K.: Experimental investigation of shock stand-off distance on spheres in hypersonic nozzle flows. In: Proc. 27th International Symposium on Shock Waves, pp. 961–966 (2007)
3. Itoh, K., Komuro, T., Tanno, H., Sato, K., Takahashi, M., Kodera, M., Hashimoto, M.: Flow characterization of high enthalpy shock tunnel based on shock stand-off distance. In: Proc. Japanese Symposium on Shock Waves, Nagoya, Japan, pp. 347–350 (2009) (in Japanese)
4. Starr, R.F., Bailey, A.B., Varner, M.O.: AIAA Journal 14, 537–539 (1976); Proc. 26th International Symposium on Shock Waves, Gttingen, Germany, July 15–20, vol. 2, pp. 1461–1466 (2007)
5. Toro, E.F.: Phil. Trans. Roy. Soc. London, A341, 499–530 (1992)
6. Toro, E.F.: Riemann solvers and numerical methods for fluid dynamics. Springer, Heidelberg (1997)
7. Strang, G.: SIAM J. Numer. Anal. 5(3), 516–517 (1968)
8. Anderson, D.A., Tannenhill, J.C., Pletcher, R.H.: Computational fluid mechanics and heat transfer. Hemisphere Publishing Corporation, New York (1984)
9. Igra, D., Falcovitz, J.: Shock Wave 20, 441–444 (2010)

Effects of Turbulent Inflow Conditions on Feedback-Loop Mechanisms in Supersonic Cavity Flows

W. Li, T. Nonomura, and K. Fujii

1 Introduction

One undesirable problem in open cavity flows is the existence of strong and discrete cavity tones, especially with supersonic incoming flows.[1-4] A sound pressure level of almost 160 dB is observed for a supersonic cavity flow at Mach 2.0.[5] The strong cavity tones possibly result in structural vibrations and fatigue, adverse effects on store separation, and undesirable noise. The mechanism driving the cavity tones need to be clarified. The cavity tones are driven by self-sustained oscillations between the shear-layer instability and acoustic disturbances, which is named a feedback-loop mechanism.[6] Despite the fact that the feedback-loop mechanism itself has been well established and accepted, the dependence of cavity noise on variations of cavity configurations and flow conditions are not well-understood.[7]

The cavity tones are a strong function of the upstream boundary layer, which includes the features of the boundary layer state (turbulent or laminar), boundary layer thickness, and turbulent disturbances. Krishnamurty[8] observed experimentally that laminar upstream boundary layers produce louder cavity tones. Heller et al.[9] reported that there is no evidence of a resonant response when the boundary layer is turbulent at Mach number 3.0; however, a strong resonant peak occurs with higher-amplitude for the laminar cavity. Rossiter[6] emphasizes that the effect of a thickening shear-layer is to decrease the amplitude of pressure fluctuations measured on the cavity walls. Ahuja and Mendosa[7] observed experimentally that all cavity tones can be eliminated by thickening the upstream boundary later for a fixed cavity length. In Rizzetta et al's numerical study[10], a significant attenuation of cavity oscillations is observed with upstream mass-injection, which is attributed to the thickening of the upstream boundary layer. However, there are few data in

W. Li
Dept. of Aeronautics and Astronautics, University of Tokyo, Tokyo, 113-8656, Japan

T. Nonomura · K. Fujii
Institute of Space and Astronautics Science/JAXA, Sagamihara, Kanagawa, 252-5210, Japan

open literatures on the effect of turbulent disturbances. In general, only the velocity profile of turbulent boundary layer is imposed at the inflow boundary conditions in numerical studies of supersonic turbulent cavity flows, while the existence of turbulent disturbances is unexpectedly ignored.[11-14] The inherent existence of turbulent disturbances in the turbulent boundary layer is probably critical to the noise radiation in turbulent cavity flows. Consequently, a correct assessment of turbulent disturbance is needed for the numerical study of turbulent cavity flows.

The aim of this study is to investigate the effects of turbulent disturbances on the self-sustained oscillations in supersonic turbulent cavity flows. Implicit large-eddy simulations of supersonic turbulent flows past a three-dimensional rectangular cavity are conducted with Mach number of 2.0 and Reynolds number of 10^5. Two simulation cases are conducted. In one case, the incoming flows are natural turbulent, while in the other case only turbulent velocity profile is imposed at the inflow condition. The influences of turbulent disturbances both on the flow fields and noise radiation will be discussed.

2 Problem Setting and Numerical Algorithms

Supersonic turbulent flows over a cavity of L/D=2, W/D=0.6 are numerically studied, where L is the length of the cavity, W is the width of the cavity, and D is the depth of the cavity. Details of flow conditions are shown in Table 1. Two simulation cases are conducted. In one case, the incoming flows are in a state of fully developed turbulence, while in the other case only turbulent velocity profile is imposed at inflow condition.The boundary layer thickness (δ_0/D) at the leading edge is set to $0.2D$.

Table 1 Flow Conditions

Cases	M_∞	Re_D	δ_0/D	Upstream boundary layer
Ma2.0-TurBL	2.0	10^5	0.2	Turbulent
Ma2.0-TurBl-pro	2.0	10^5	0.2	Trubulent profile

The governing equations are three-dimensional compressible Navier-Strokes equations in conservative form. Implicit Large Eddy Simulations (ILES) are conducted with a seventh-order weighted compact nonlinear scheme. Details of numerical schemes could be found in our previous works[15,16]. Structural grids are adopted, and the total grid points are about 15 millions. The grid spacing is refined in near-wall regions. The values of $\Delta x+$, $\Delta y+$, $\Delta z+$ at the cavity lips are 5.0, 1.0 and 10.0 respectively. The maximum grid spacing inside the cavity is $0.012D$. No-slip adiabatic wall boundary condition is adopted at all the walls. Zero-gradient pressure condition is employed at outflows, and periodical boundary condition is imposed in

the spanwise direction. Recycling and rescaling technique[17] is used for the generation of a fully developed turbulent inflow condition.

3 Validations

The validations of the numerical codes and problem settings could be found in our previous works.[15,16] The feature of turbulent inflow is validated in the present study. The mean streamwise velocity profile in a semi-logarithmic plot using Van Driest transformation is shown in Fig. 1, which indicates the profile agrees well with theoretical formulations. Velocity fluctuations are plotted in Fig. 2 and compared with direct numerical simulation (Pirozzoli et al, $M = 2.0, Re_\delta = 1.74 \times 10^4$).[18] The comparison shows the ILES results fairly agree with the DNS results. Thus, upstream boundary layer is in a state of fully developed turbulence, which is adoptable for the simulation of supersonic turbulent cavity flow.

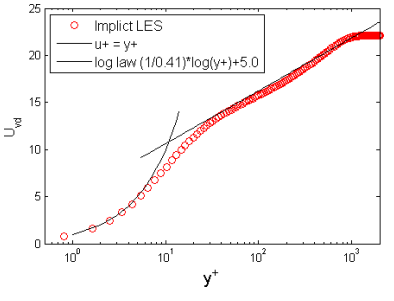

Fig. 1 Mean streamwise velocity profile

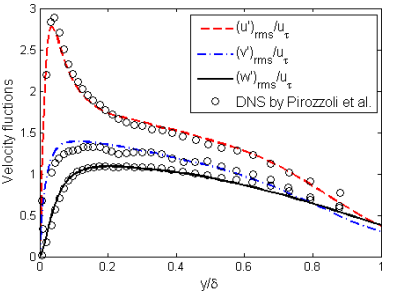

Fig. 2 Velocity fluctuations

4 Results

4.1 Flow Fields

Snapshots of instantaneous flowfields are visualized in Fig. 3. In the Ma2.0-TurBL case, plenty of small-scale vortical structures are observed both in the upstream boundary layer and cavity shear-layer. Three dimensional turbulence dominates the cavity shear-layer. However, in the Ma2.0-TurBL-pro case, the cavity shear-layer has highly two-dimensional vortical structures. These snapshots indicate a good turbulence resolution. Large-scale shear-layer motions present in both cases, which will be discussed later.

The compression wave radiation is indicated in Fig. 4. The significant characteristic in Ma2.0-TurBL-pro case is that Mach waves are radiated from the highly two-dimensional shear-layer and intense compression waves are propagating inside

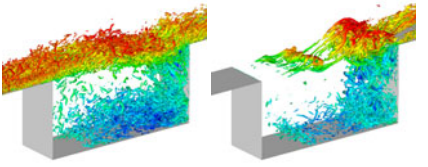

Fig. 3 Isosurface of the second invariant of velocity gradient tensors(Q_{2nd}= 20(a/D)^2) colored with streamwise velocity(-0.5u_∞ <u< u_∞); left: Ma2.0-TurBL, right: Ma2.0-TurBL-pro

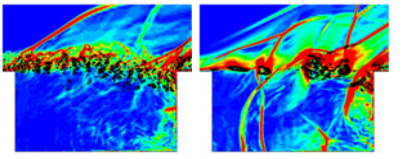

Fig. 4 Compression waves radiation (Background contours represent density gradient,black contour lines represent positive second invariant of velocity gradient tensors; left: Ma2.0-TurBL, right: Ma2.0-TurBL-pro

the cavity. While if the upcoming boundary layer is fully turbulent, no Mach wave and intense compression wave is present in the cavity acoustic fields. Shock waves are observed near the leading-edge and the trailing-edge in these two cases, which are caused by the large shear-layer deformation and explored at supersonic incoming flows.

The profiles of the time-averaged streamwise velocity are plotted in Fig. 5. Differences between these two cases are contributed to different characteristics of shear-layer development. As shown in Fig. 6, the variations of shear-layer vorticity thickness are shown, which are used to measure the shear-layer growth rate. It could be found that the cavity shear-layer in Ma2.0-TurBL-pro case grows slowly in a short distance near the cavity leading edge, and then its growth rate increases and keeps at a linear growth rate until the shear-layer impinging on the trailing edge. The low growth rate near the cavity leading edge is probably due to the transition from laminar to turbulence after the shear-layer separates from the leading edge. While the shear-layer of Ma2.0-TurBL case grows rapidly near the leading edge. The rapid growth rate leads to more fluids inject into the cavity. Consequently, a higher speed of recirculation flow inside the cavity is observed in the Ma2.0-TurBL case, as shown in Fig. 5.

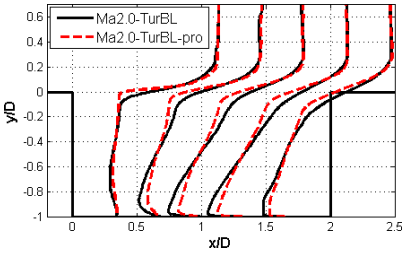

Fig. 5 Mean streamwise velocity profiles

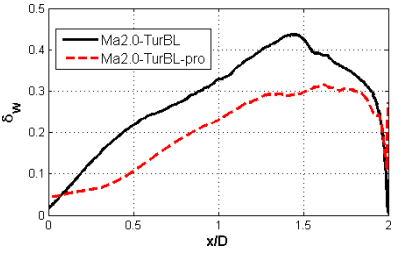

Fig. 6 Variations of shear-layer vorticity thickness

4.2 Noise Radiation

The pressure spectra at the middle of the cavity rear wall are plotted in Fig. 7. The existence of turbulent disturbances in the upstream boundary layer has significant effects on the noise radiation. First, the dominant mode, which has the maximum sound pressure level, is varied to a higher frequency if no turbulent disturbance exits in the upstream boundary layer. The second mode in Ma2.0-TurBL case is the dominant mode, while it is varied to the fourth mode in the Ma2.0-TurBL-pro case. Second, the amplitude of both tone noise and broadband noise becomes stronger in the simulation without turbulent disturbances in the upstream boundary layer. It could be estimated that a 5 dB increasing is observed if turbulent disturbances is absent from the upstream boundary layer. The existence of turbulent disturbances in

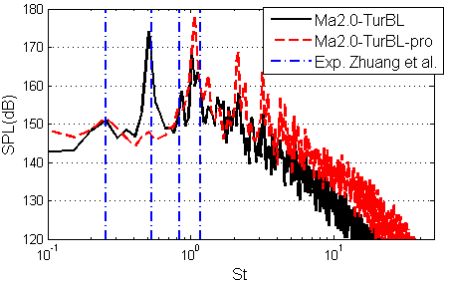

Fig. 7 Pressure spectra at the middle of the cavity rear wall

the upstream boundary layer also has influence on near-field pressure fluctuations (as illustrated in Fig. 8). The distributions of pressure fluctuations are significantly varied, especially in the vicinity region of the cavity shear-layer. In addition, it has higher amplitude of pressure fluctuations near the trailing edge in the Ma2.0-TurBL-pro case than that in the Ma2.0-TurBL case.

The reason for significant impacts on the noise radiation is related to the large-scale vortices in the cavity shear-layer. As demonstrated in our previous work, the successive passage of large-scale vortices over the trailing edge, associated with periodical vorticity productions and pressure oscillations, result in a noise source radiated from the trailing edge. In order to evaluate the feature of large-scale vortices, phase averaging is conducted, which is based on the pressure variations at the middle of the cavity front wall. In Fig. 9, it indicates the size of large-scale vortices in the Ma2.0-TurBL-pro case is smaller than that in Ma2.0-TurBL case. The shear-layer contains more large-scale vortices if their size becomes smaller, which results in a higher frequency of pressure oscillation near the trailing edge. In addition, the large-scale vortices have a feature of strong spanwise vorticity if the upstream boundary layer is absent of turbulent disturbances. These highly two-dimensional vortices are responsible for an strength of the amplitude of cavity tones near the trailing edge.

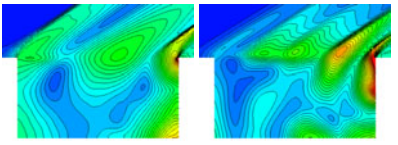

Fig. 8 Contours of pressure fluctuation; left: Ma2.0-TurBL, right: Ma2.0-TurBL-pro

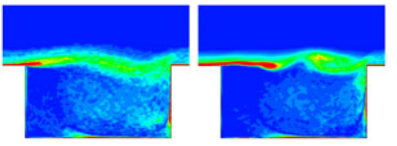

Fig. 9 Vorticity of phase-averaged flow-fields; left: Ma2.0-TurBL, right: Ma2.0-TurBL-pro

5 Conclusion

Implicit large-eddy simulations are conducted for the investigation of the effects of turbulent disturbances on flow fields and noise radiation in the supersonic turbulent cavity flows. First, highly two-dimensional vortical structures are observed in the cavity shear-layer if turbulent disturbances are absent in the upstream boundary layer. A transition exists after the turbulent profiled boundary layer is shed from the leading edge, which results in a slow shear-layer growth rate near the leading edge. A higher speed of recirculation flow is observed in the case with fully turbulent boundary layer. Second, the existence of turbulent disturbances is critical to the noise radiation in the simulation of supersonic turbulent cavity flows. Both the dominant mode and the amplitude of cavity tones are influenced by the existence of turbulent disturbances. The distributions of pressure fluctuations are dramatically varied. The reason for these characteristics variations are assumed to be responsible for the features of large-scale vortices in the cavity shear-layer.

References

1. Rockwell, D., Naudascher, E.: Review: Self-Sustaining Oscillations of Flow Past Cavities. Journal of Fluids Engineering 100(2), 152–165 (1978)
2. Grace, S.M.: An Overview of Computational Aeroacoustic Techniques Applied to Cavity Noise Prediction. AIAA Paper 2001-0510 (January 2001)
3. Colonius, T.: An Overview of Simulation, Modeling, and Active Control of Flow/acoustic Resonance in Open Cavities. AIAA Paper 2001-0076 (January 2001)
4. Lawson, S.J., Barakos, G.N.: Review of numerical simulations for high-speed, turbulent cavity flows. Progress in Aerospace Science (2011), doi:10.1016/j.paerosci, 11.002
5. Zhuang, N., Alvi, F.S., Alkislar, M.B., Shih, C.: Supersonic Cavity Flows and Their Control. AIAA Journal 44(9), 2118–2128 (2006)
6. Rossiter, J.E.: Wind-Tunnel Experiments on the Flowover Rectangular Cavities at Subsonic and Transonic
7. Ahuja, K.K., Mendoza, J.: Effects of Cavity Dimensions, Boundary Layer, and Temperature on Cavity Noise With Emphasis on Benchmark Data To Validate Computational Aeroacoustic Codes, NASA-Contractor-Report-4653 (1995)
8. Krishnamurty, K.: Acoustic Radiation from Two-Dimensional Rectangular Cut-Outs in Aerodynamic Surfaces. NACA TN 3487 (August 1955)

9. Heller, H.H., Holmes, D.G., Covert, E.E.: Flow-induced Pressure Oscillations in Shallow Cavities. Journal of Sound and Vibration 18(4), 545–546 (1971), doi:10.1016/0022-460X(71)90105-2; Speeds, Aeronautical Research Council, Repts. and Memoranda No. 3438, London (October 1964)
10. Rizzetta, D.P., Visbal, M.R.: Large-Eddy Simulation of Supersonic Cavity Flowfields Including Flow Control. AIAA Journal 41(8), 1452–1462 (2003)
11. Tam, C.K.W., Block, P.J.W.: On the Tones and Pressure Oscillations Induced by Flow over Rectangular Cavities. J. Fluid Mech. 89(2), 373–399 (1978)
12. Zhang, X.: Compressible Cavity Flow Oscillation due to Shear-layer Instabilities and Pressure Feedback. AIAA Journal 33(8), 1404–1411 (1995)
13. Nishioka, M., Asai, T., Sakaue, S., Shirai, K.: On the mechanism of supersonic cavity flow oscillations. In: Proceedings of the Fifth World Conference on Experimental Heat Transfer, Fluid Mechanics and Thermodynamics, pp. 153–163 (September 2001)
14. Jeng, Y.N., Paynet, U.J.: Numerical Study of a Supersonic Open Cavity Flow and Pressure Oscillation Control. Journal of Aircraft 32(2), 363–369 (1995)
15. Li, W., Nonomura, T., Oyama, A., Fujii, K.: Numerical Study of Feedback-loop Mechanism of Supersonic Open Cavity Flows. In: AIAA-2010-5112, Chicago (July 2010)
16. Li, W., Nonomura, T., Fujii, K.: Effects of Shear-layer Characteristic on the Feedback-loop Mechanism in Supersonic Open Cavity Flows. In: AIAA 2011-1218, Orlando (January 2011)
17. Urbin, G., Knight, D.: Large-Eddy Simulation of a Supersonic Boundary Layer Using an Unstructured Grid. AIAA Journal 39(7), 1288–1295 (2001)
18. Pirozzoli, S., Bernardini, M., Grasso, F.: Characterization of Coherent Vortical Structures in a Supersonic Turbulent Boundary Layer. Journal of Fluid Mechanics 613, 205–231 (2008)

Scale Separation for Implicit Large Eddy Simulation

X.Y. Hu and N.A. Adams

Introduction

Unlike standard large eddy simulation (LES) (for a review of LES for incompressible and compressible turbulence refer e.g. to [18, 7]), implicit LES (ILES) does not require an explicitly computed sub-grid scale (SGS) closure, but rather employs an inherent, usually nonlinear, regularization mechanism due to the nonlinear truncation error of the convective-flux discretization scheme as implicit SGS model. As finite-volume discretizations imply a top-hat filtered solution, regularized finite-volume reconstruction schemes were among the first ILES approaches, such as the flux-corrected transport (FCT) method [4], the piecewise parabolic method (PPM) [5]. Although ILES is attractive due to its relative simplicity, numerical robustness and easy implementation, it often exhibits inferior performance to explicit LES [8] if the discretization scheme is not constructed properly. Some schemes, such as PPM, FCT, MUSCL [16] and WENO [3] methods, work reasonably well for ILES by being able to recover a Kolmogorov-range for high-Reynolds-number turbulence up to $k_{max}/2$, where k_{max} is the Nyquist wavenumber of the underlying grid [9, 10, 21]. These promising results have led to further efforts on the physically-consistent design of discretization schemes for ILES. Physical consistency implies the correct and resolution-independent reproduction of the subgrid-scale (SGS) energy transfer mechanism of isotropic turbulence. Based on this notion the adaptive local deconvolution method (ALDM) has been developed [1, 11]. Approaches for decreasing excessive model dissipation for the solenoidal velocity field include the low-Mach number switch of [22], and the dilatation switch and shock sensor of [15].

In this work we propose a simple modification of an existing high-order WENO scheme which leads to a physically consistent implicit SGS model while preserving the shock-capturing properties of the underlying WENO scheme. Basis of this ILES scheme is a scale separation built into the nonlinear WENO weights that allows to differentiate between stencils providing contributions from resolved scales and from

X.Y. Hu and N.A. Adams
Institute of Aerodynamics and Fluid Mechanics, Technical Univeristy of Munich

non-resolved scales. It avoids the need for explicit discretization-scheme switches (hybrid schemes) or flow sensors and operates directly on the reconstruction or deconvolution procedure. We point out that physical consistency is recovered for both, the solenoidal and the dilatational components of the velocity field, without requiring an explicit differentiation between these components.

1 Scale-Separation Method

For presentation of the scale-separation method we consider for simplicity a generic one-dimensional convection equation

$$\frac{\partial u}{\partial t} + \frac{\partial f(u)}{\partial x} = 0. \tag{1}$$

By applying a top-hat filter around $x_i = i\Delta x$, where i is an integer and Δx is the support of the filter G_i, i.e., $\overline{u}_i = G_i * u = \int_{x_i-\Delta x/2}^{x_i+\Delta x/2} u(x)dx$, we obtain

$$\frac{\partial \overline{u}_i}{\partial t} + G_i * \frac{\partial f(u)}{\partial x} = \frac{\partial \overline{u}_i}{\partial t} + \frac{1}{\Delta x}\left(f_{i+1/2} - f_{i-1/2}\right) = 0, \tag{2}$$

where $f_{i\pm1/2} = f(u_{i\pm1/2})$ are the unknown exact fluxes at $x_i \pm \Delta x/2$. This is equivalent to taking a volume average over a computational cell as in a finite-volume discretization. Eq. (2) is closed by replacing the exact fluxes by the numerical fluxes $\hat{f}^{k,r}_{i\pm1/2}$ at the cell faces

$$\frac{\partial \overline{u}_i}{\partial t} + \frac{1}{\Delta x}\left(\hat{f}^{k,r}_{i+1/2} - \hat{f}^{k,r}_{i-1/2}\right) = 0\,. \tag{3}$$

A consistent numerical flux is the cell-face value of a polynomial $\hat{f}^{k,r}_i(x)$ reconstructed from neighboring cell averages $\overline{f}_{i-k+r+1}, \ldots \overline{f}_i, \ldots, \overline{f}_{i+r}$, where k is the order of reconstruction. We consider the 6th-order non-dissipative symmetric reconstruction $\hat{f}^{6,3}_i(x)$ and the four admissible upwind- and downwind-biased 3rd-order reconstructions $\hat{f}^{3,r}_i(x)$, $r = 0,1,2,3$, which are dissipative or anti-dissipative. A physically consistent numerical flux is obtained by a proper weighting of these contributions, measured by local smoothness of the solution. In order to decrease the excess dissipation observed for the original WENO schemes the contribution of the higher-order non-dissipative reconstruction should be emphasized for stencils containing resolved scales while dissipative reconstructions should be emphasized for stencils containing non-resolved scales. For this purpose the weighting strategy of the underlying WENO scheme needs to be modified.

We start from a variant of the original WENO scheme [13], the adaptive central-upwind WENO scheme (WENO-CU6) [12]. The adaptation between the higher-order non-dissipative and lower-order dissipative reconstructions requires the smoothness indicators

$$\beta_r^k = \sum_{n=1}^{k-1} \Delta x^{2n-1} \int_{x_i-\Delta x/2}^{x_i+\Delta x/2} \left(\frac{d^n}{dx} \hat{f}_i^{k,r}(x) \right)^2 dx, \tag{4}$$

and a nonlinear weighting

$$\omega_r = \frac{\alpha_r}{\sum_{r=0}^{3} \alpha_r}, \quad \alpha_r = d_r \left(C + \frac{\tau^6}{\beta_r^3 + \varepsilon \Delta x^2} \right), \tag{5}$$

where d_r are linear weights which combine $\hat{f}_i^{3,r}(x)$, $r = 0, 1, 2, 3$ to $\hat{f}_i^{6,3}(x)$. $C \gg 1$ is a positive parameter, $\varepsilon = 10^{-8}$ is a small positive number. Since a Taylor expansion of smoothness indicator yields

$$\beta_r^k = \Delta x^2 \left[f'(x_i) \right]^2 + \mathcal{O}(\Delta x^4), \tag{6}$$

the term $\varepsilon \Delta x^2$ represents the magnitude of smoothness indicator for a solution that can be considered as smooth. $\tau^6 = \beta_3^6 - \beta_{ave}^3$, where $\beta_{ave}^3 = (\beta_0^3 + 4\beta_1^3 + \beta_2^3)/6$ is an average of the lower-order smoothness indicators. Note that it is set $\beta_3^3 = \beta_3^6$ to assure that $\hat{f}_i^{3,3}(x)$ contributes only to the numerical flux of $\hat{f}_i^{6,3}(x)$. Although the WENO-CU6 exhibits much less numerical dissipation than classical WENO schemes, it still is too dissipative for physically consistent ILES [12].

While terms $\tau^6/(\beta_r^3 + \varepsilon \Delta x^2)$ are responsible for the WENO adaptation and give sufficient dissipation for flow discontinuities, the positive parameter C pushes the numerical flux to that of $\hat{f}_i^{6,3}(x)$ when the variation of $\tau^6/(\beta_r^3 + \varepsilon \Delta x^2)$ is relatively small. One could simply increase the value of C so that numerical dissipation is reduced for the resolved scales. However, this will lead to difficulties with the WENO adaptation for flow discontinuities and may result in numerical instability. Such an effect of increasing C can be counterbalanced by steepening the $\tau^6/(\beta_r^3 + \varepsilon \Delta x^2)$ contribution in (5), leading to a stronger separation between resolved and non-resolved scales. For this purpose the following modified weighting, without deteriorating the order of accuracy of the original WENO-CU6 scheme, is introduced

$$\omega_r = \frac{\alpha_r}{\sum_{r=0}^{3} \alpha_r}, \quad \alpha_r = d_r \left(C_q + \frac{\tau^6}{\beta_r^3 + \varepsilon \Delta x^2} \right)^q, \tag{7}$$

where $C_q \gg C$ is a positive modeling parameter and $q > 1$ is an integer. Due to the power function the variation of $\tau^6/(\beta_r^3 + \varepsilon \Delta x^2)$ is strongly magnified. Note that this procedure operates on the reconstruction directly, and does not require a separation of solenoidal or compressional components of the velocity field. In particular, no explicit differentiation between shocks as subgrid scales and turbulent subgrid scales is needed.

2 Numerical Examples

Two test problems are provided to assess the potential of the scale-separation approach for ILES. Parameters are set to $C_q = 1000$ and $q = 4$. The flow is described

by the compressible Navier-Stokes equation with the ideal-gas equation of state. As flows at very large Reynolds number are of interest physical viscosity is set to zero. The equation is solved by the above WENO methodology using an entropy-fix Roe numerical flux function [13, 12].

First we consider the three-dimensional Taylor-Green vortex to examine the capability of the ILES scheme to reproduce transition to turbulence. The evolution of

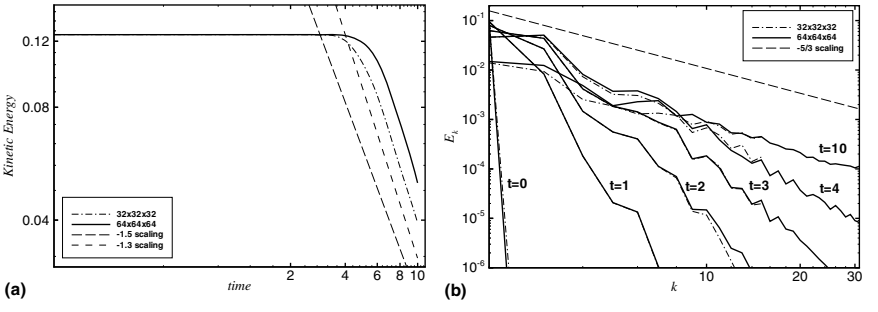

Fig. 1 Taylor-Green Vortex: (a) evolution of kinetic energy; (b) energy spectrum at $t = 0, 1, 2, 3, 4$ and 10. The computations are performed on the periodic domain of $[0,0,0] \times [2\pi, 2\pi, 2\pi]$ on 32^3 and 64^3 grids.

the kinetic energy and the energy spectrum at $t = 0, 1, 2, 4, 10$ are given in Fig. 1. As shown in Fig. 1a, at early stages kinetic energy is merely distributed among the resolved scales (total kinetic energy is constant). At about time $t = 4$ subgrid-scales are produced and kinetic energy begins to decay due to SGS dissipation, and eventually decays as $t^{-1.5}$, which is slightly faster than $t^{-1.2}$ found by [17]. A similar observation has been made for high-resolution ILES [9]. Note also that experimental data indicate a rather large variation of the power-law exponent during different stages of decay, see [20]. As shown in Fig. 1b, the power-law kinetic-energy spectra clearly reflect the infinite-Reynolds-number limit, unlike that obtained by [6] with artificial-fluid LES at the same resolution, showing a pronounced artificial dissipative range. Between $t = 4$ and $t = 10$ turbulence develops, a the kinetic energy builds up a Kolmogorov intertial range, in agreement with the high-resolution LES of [9]. As the above behavior of our ILES scheme also is resolution independent, physical consistency is demonstrated by this test case.

Next we consider a shock density-wave interaction problem [19, 14], which is an one-dimensional generic case to assess shock-capturing and wave-disturbance propagation capabilities of the model at the same time. From the density, velocity and entropy profiles shown in Fig. 2, that the proposed ILES method not only captures the shock wave, but also maintains the amplitudes of density and entropy waves after passing through the shock with comparable or better accuracy than

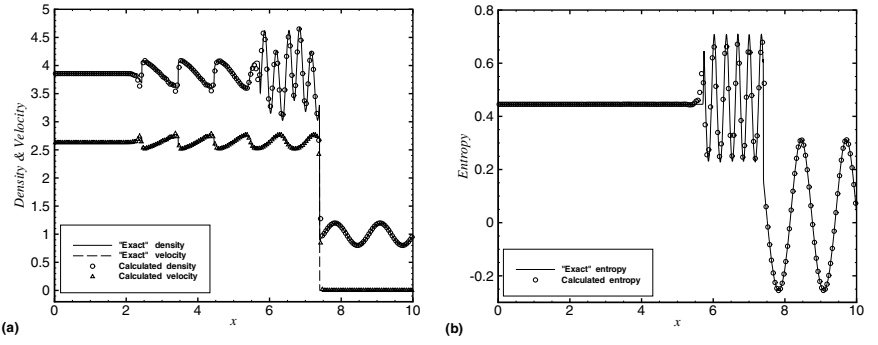

Fig. 2 Shock density-wave interaction problem using a 200 points grid: (a) density and velocity profiles; (b) entropy profile. The "exact" solution is computed by the WENO-CU6 scheme with 3200 grid points.

hybrid schemes [14, 2]. Note also that due to the lack of efficient scale separation the original WENO-CU6 exhibits larger artificial wave dissipation [12].

Concluding Remarks

In this work we have proposed a scale separation approach for ILES. Scale separation is accomplished by a simple modification of the weighting strategy of an existing WENO scheme (WENO-CU6). Basic idea is to counterbalance a stronger bias towards the central high-order non-dissipative stencil by a higher integer power of the smoothness-measure contribution to the weights. This leads to a scale separation of contributions from resolved scales and non-resolved scales. Model parameters are the linear weight bias and the integer power exponent. It was shown that a straight-forward parameter choice is widely effective without further tuning. Numerical examples imply that the scale-separation WENO-CU6 scheme leads to a physically consistent implicit SGS model for incompressible and compressible turbulence, while the shock-capturing capabilities of the original WENO-CU6 scheme are maintained.

References

1. Adams, N.A., Hickel, S., Franz, S.: Implicit subgrid-scale modeling by adaptive deconvolution. J. Comput. Phys. 200(2), 412–431 (2004)
2. Adams, N.A., Shariff, K.: A high-resolution hybrid compact-ENO scheme for shock-turbulence interaction problems. J. Comput. Phys. 127, 27–51 (1996)
3. Balsara, D.S., Shu, C.W.: Monotonicity preserving weighted essentially non-oscillatory schemes with increasingly high order of accuracy. J. Comput. Phys. 160(2), 405–452 (2000)

4. Boris, J.P., Grinstein, F.F., Oran, E.S., Kolbe, R.L.: New insights into large eddy simulation. Fluid Dynamics Research 10(4-6), 199–228 (1992)
5. Colella, P., Woodward, P.R.: The Piecewise Parabolic Method (PPM) for gas-dynamical simulations. J. Comput. Phys. 54(1), 174–201 (1984)
6. Cook, A.W.: Artificial fluid properties for large-eddy simulation of compressible turbulent mixing. Physics of Fluids 19, 055103 (2007)
7. Garnier, E., Adams, N.A., Sagaut, P.: Large Eddy Simulation for Compressible Flows. Springer (2009)
8. Garnier, E., Mossi, M., Sagaut, P., Comte, P., Deville, M.: On the use of shock-capturing schemes for large-eddy simulation. J. Comput. Phys. 153(2), 273–311 (1999)
9. Grinstein, F.F., Fureby, C.: Recent progress on flux-limiting based implicit Large Eddy Simulation. In: European Conference on Computational Fluid Dynamics, ECCOMAS CFD (2006)
10. Grinstein, F.F., Margolin, L.G., Rider, W.: Implicit large eddy simulation: computing turbulent fluid dynamics. Cambridge University Press, Cambridge (2007)
11. Hickel, S., Adams, N.A., Domaradzki, J.A.: An adaptive local deconvolution method for implicit LES. J. Comput. Phys. 213(1), 413–436 (2006)
12. Hu, X.Y., Wang, Q., Adams, N.A.: An adaptive central-upwind weighted essentially non-oscillatory scheme. J. Comput. Phys. 229(23), 8952–8965 (2010)
13. Jiang, G.S., Shu, C.W.: Efficient implementation of weighted ENO schemes. J. Comput. Phys 126, 202–228 (1996)
14. Johnsen, E., Larsson, J., Bhagatwala, A.V., Cabot, W.H., Moin, P., Olson, B.J., Rawat, P.S., Shankar, S.K., Sjögreen, B., Yee, H.C., et al.: Assessment of high-resolution methods for numerical simulations of compressible turbulence with shock waves. J. Comput. Phys. 229(4), 1213–1237 (2010)
15. Kawai, S., Shankar, S.K., Lele, S.K.: Assessment of localized artificial diffusivity scheme for large-eddy simulation of compressible turbulent flows. J. Comput. Phys. 229(5), 1739–1762 (2010)
16. Kim, K.H., Kim, C.: Accurate, efficient and monotonic numerical methods for multi-dimensional compressible flows: Part II: Multi-dimensional limiting process. Journal of Computational Physics 208(2), 570–615 (2005)
17. Lesieur, M., Ossia, S.: 3D isotropic turbulence at very high Reynolds numbers: EDQNM study. Journal of Turbulence 1(7), 1–25 (2000)
18. Sagaut, P.: Large eddy simulation for incompressible flows: an introduction. Springer (2006)
19. Shu, C.W., Osher, S.: Efficient implementation of essentially non-oscillatory shock-capturing schemes, II. J. Comput. Phys. 83(1), 32–78 (1989)
20. Skrbek, L., Stalp, S.R.: On the decay of homogeneous isotropic turbulence. Physics of Fluids 12, 1997 (2000)
21. Thornber, B., Mosedale, A., Drikakis, D.: On the implicit large eddy simulations of homogeneous decaying turbulence. J. Comput. Phys. 226(2), 1902–1929 (2007)
22. Thornber, B., Mosedale, A., Drikakis, D., Youngs, D., Williams, R.J.R.: An improved reconstruction method for compressible flows with low Mach number features. J. Comput. Phys. 227(10), 4873–4894 (2008)

On the Carbuncle Origins from Moving and Stationary Shocks

Keiichi Kitamura and Eiji Shima

1 Introduction

Hypersonic flow computations still suffer from anomalous solutions such as a "carbuncle phenomenon" [1-3]. We still lack an accepted explanation for those anomalies, and we feel there is no single cause, nor is there any single cure. In the present study, we take the viewpoint that the shock anomalies are partly caused by the lack of mathematical expression for internal shock structure by the governing equations, and that they can be examined by numerical experiments. Quirk [1] introduced a benchmark test for numerical schemes on their responses to the captured (fast) moving shock. In this test, the shock took all the possible locations within a cell but instantly passed through them. Roberts [4] chose a more slowly[1] moving shock which took 50 time steps to travel a single cell, and discussed a post-shock numerical noise propagation. Kitamura et al. [3] dealt with a stationary shock located within a cell with an initial shock position parameter ε=0.0, 0.1, ..., 0.9, i.e., the shock was placed at one of 10 possible locations in a cell. Their study discovered that any flux functions including FVS by Van Leer [5] are prone to carbuncles, though some of those methods had been believed to be carbuncle-free accoring to Quirk [1]. In other words, Quirk's test for a moving shock was not enough to examine robustness of a numerical flux for a stationary shock. Moreover, in spite of those findings, the origin of the carbuncle remained a mystery. The present study will pursue its clue by bridging the gap between the works explained above, i.e., by varying the shock propagation speed from 0 of Kitamura et al. to 6 in Quirk's choice and beyond. Following our earlier work, different flux functions by Roe [6], Van Leer [5], Liou ($AUSM^+ - up$ [7]), and Shima and Kitamura (SLAU [8]) will be used since they have different degrees of robustness against the shock.

Keiichi Kitamura · Eiji Shima
JEDI Center, JAXA
3-1-1 Yoshinodai, Chuo, Sagamihara, Kanagawa (Japan)

Keiichi Kitamura
JSPS Research Fellow

[1] The terms "slowly" and "fast" moving shocks are to be redifined later which are different from Robert's definitions[4].

2 Numerical Methods

The two-dimensional Euler equations are solved in this study. The working gas is assumed to be air approximated by the calorically-prefect-gas model with the specific heat ratio $\gamma = 1.4$. The equations are discretized by cell-centered finite-volume method (FVM) with first order both in space and time.

3 Numerical Experiments Setup

3.1 Basic Pre- and Post-shock Relations

The flow across a normal shock wave is adiabatic and then the basic equations called Runkine-Hugoniot relations are derived as follows[9, 10] (Fig. 1a, b):

$$\frac{p_L}{p_R} = 1 + \frac{2\gamma}{\gamma+1}\left(M^2 - 1\right) \tag{1a}$$

$$\frac{\rho_L}{\rho_R} = \left[1 + \frac{\gamma+1}{\gamma-1}\left(\frac{p_L}{p_R}\right)\right] \Big/ \left[\frac{\gamma+1}{\gamma-1} + \left(\frac{p_L}{p_R}\right)\right] \tag{1b}$$

where R and L are pre- (upstream) and post-shock (downstream) states, respectively, in the shock coordinate system (Fig. 1b). M corresponds to upstream Mach number for a stationary shock, or relative upstream Mach number for a moving shock in the shock coordinate, which is regarded as shock strength, $M = (u_s - u_R)/a_R$ (Fig. 1b). Then, velocity normal to the shock is related by continuity equation as

$$u_L = u_s\left[1 - \frac{\rho_R}{\rho_L}\right] + \frac{\rho_R u_R}{\rho_L} \quad \left(since\ \frac{u_s - u_L}{u_s - u_R} = \left(\frac{\rho_L}{\rho_R}\right)^{-1}\right) \tag{2}$$

where u_s is shock propagation velocity and expressed by upstream condition as

$$u_s = M_s a_R, a_R = \sqrt{\gamma p_R/\rho_R} \tag{3}$$

where M_s is the (moving) shock Mach number (If $u_R = 0$, M_s is identical to M) [9]; apparently, $u_s = 0$ for a stationary shock.

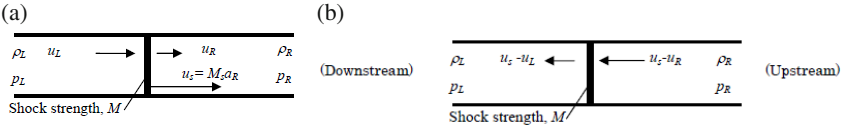

Fig. 1 Schematic of pre- and post-shock relations. (**a**) Laboratory coordinate system, and (**b**) Shock coordinate system

Let us consider wave propagation speed a_L of downstream the shock (Fig. 1) with respect to a_R of upstream sound speed. After some manipulation, the a_L is written as follows:

$$
\begin{aligned}
a_L &= \sqrt{\gamma p_L/\rho_L} = a_R \cdot \sqrt{\left(\frac{p_L}{p_R}\right) \Big/ \left(\frac{\rho_L}{\rho_R}\right)} = a_R \cdot M_{\text{signal}} \\
M_{\text{signal}}(M) &\equiv \sqrt{\frac{1+\frac{2\gamma}{\gamma+1}\left(M^2-1\right)}{\left[1+\frac{\gamma+1}{\gamma-1}\left(1+\frac{2\gamma}{\gamma+1}\left(M^2-1\right)\right)\right] \Big/ \left[\frac{\gamma+1}{\gamma-1}+\left(1+\frac{2\gamma}{\gamma+1}\left(M^2-1\right)\right)\right]}} \\
&\xrightarrow{M\to\infty} \frac{\sqrt{2\gamma(\gamma-1)}M}{\gamma+1} \approx 0.44M\,(\gamma = 1.4)
\end{aligned}
\tag{4}
$$

where M_{signal} is defined as a function of only one parameter, i.e., shock strength M. It is interesting to note that M_{signal} asymptotes to $0.44M$ for $M >> 1$ (Fig. 2). Then, we can compare M_s with M_{signal} (or $0.44M$, instead): if $M_{\text{signal}} < M_s$, the shock moves fast enough to escape from the influence of the left (downstream) region; otherwise, numerical noise in the left region catches up with the moving shock and can disturb it (Fig. 1). We will come back later to this important number.

3.2 Stationary Shock Setup

If a normal shock is placed at a fixed location, the equations (1)-(3) become simpler since $M_s = u_s = 0$. Kitamura et al. [3] varied M from 1.5 to 20 for both 1D and 2D stationary shocks, and discovered that the higher the M was, the more likely the shock anomalies emerged, and that such a sensitivity on M died out for $M \geq 6$. Their additional parameters in numerical setup were shock initial locations, flux functions, and spatial accuracy. The shock initial locations included several possible locations "inside" cells. In this study, however, the shock initial location will be fixed precisely on the cell interface. Thus, the stationary shock ($M_s = 0$) is a special case in which the shock takes only one prescribed location relative to the grid line.

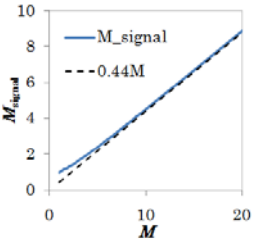

Fig. 2 M_{signal} versus M

3.3 Moving Shock Setup

Quirk [1] proposed a moving shock test with $M = M_s = 6 (u_R = 0)$. In his test, Quirk introduced the grid perturbation parameter ε_g as $1.e-3$ cell size. The perturbation was imposed to the centerline of a 2D duct through which a shock was propagating. The shock can take all the possible locations inside the shocks, but may pass through those locations too quickly to be affected by every state. Roberts [4], on the other hand, chose a more slowly moving shock without grid perturbation ($\varepsilon_g = 0$).

3.4 Present Setup for General Stationary and Moving Shocks

The parameters involved in the present survey are summarized in Table 1. Depending on the magnitudes of M and M_s, flow directions can vary as shown in Fig. 3. The

boundary conditions are such that Riemann invariants are conserved along characteristic curves and either inflow or outflow condition is satisfied according the flow direction. Grid perturbation parameter ε_g is set to $1.e-3$ cell size as default, and 0 and $1.e-6$ as alternatives. Flux functions are chosen from different categories [11] in terms of robustness against shock and other properties: Roe scheme with Harten's entropy fix [Roe (E-fix)] is known to be vulnerable to carbuncle; Van Leer's FVS is almost (but not perfectly) free from such anomalies; AUSM$^+$ – up and SLAU are in the middle. The computations are run for 400 steps with CFL = 0.4. Following Quirk [1], the grid consists of 800×20 cells. The initial shock is placed at the interface between $i = 25$th and 26th cells.

Table 1 Parameters in the present survey

Shock Propagation Speed M_s	0, 0.5, 1, 1.5, 3, 6, 10
Shock Strength M	1.5, 3, 6, 10
Grid Perturbation ε_g	0, 10^{-6}, 10^{-3}
Flux Functions	Roe (E-fix), Van Leer, AUSM$^+$ – up, SLAU

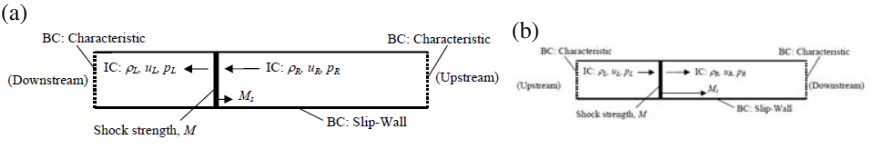

Fig. 3 Typical initial (IC) and boundary (BC) conditions for (**a**) slowly and (**a**) fast moving shock cases (Laboratory coordinate system)

4 Results

Figures 4-6 summarize results for $M = 0, 1.5, 3.0; \varepsilon_g = 1.e-3$, with the following criteria:

◯: Stable.L1-norm of v-velocity residual remained the same order from the beginning.
△: Slight instability, but no carbuncle. L1-norm of v-velocity residual grew over one order.
×: Carbuncle (total break down)

where we used the L1-norm of velocity component v, which is supposed to be zero in a theoretical sense, as a measure of (multi-dimensional) shock instabilities.

The selected results for $M = 6$; $M_s = 0, 1.5, 6$ (corresponds to Quirk [1]), and 10, are shown in Fig. 5-6. Furthermore, histories of the L1-norm of v-velocity residual are compared in Fig. 7 for Roe (E-fix) cases.

The following features are noteworthy from the results.

- Carbuncle tends to appear and grow rapidly for larger M and smaller M_s for Roe (E-fix) and AUSM$^+$ – up.

- Van Leer and SLAU, on the other hand, showed no instability in most cases with a few exceptions (slight instability cases).
- $M_s = 0$ (stationary shock) cases showed different tendencies from the moving shock cases.

Then, the results are categorized into four groups according to M_s and M.

[**Group I (Stationary Shock:**$M_s = 0, M \geq 2$**)**] *Since the shock did not cross any cells, there should be no influence from the grid perturbation. Each flux function has its own comfortable shock location relative to grid lines [3], and* AUSM$^+$ − up*, for instance, showed no instability regardless of shock strength, M.*

[**Group II (Slowly Moving Shock:**$0 < M_s < 0.44M, M \geq 2$**)**] *Since the shock crosses a perturbed grid and since numerical noise from the left (downstream) region (Fig. 3a) can affect the shock itself (as explained in 3.2), the solution is most likely to exhibit carbuncle. In Roe (E-fix), for instance, the solutions are usually carbuncle with a few exceptions of slight instability cases.*

[**Group III (Fast Moving Shock:** $0.44M < M_s, M \geq 2$**)**] *Since the shock crosses a perturbed grid but numerical noise from the left (downstream) region cannot reach the shock itself, the solution is less likely to exhibit carbuncle than Group II. The solutions are mixed with stable, slight instability, and carbuncle cases.*

[**Group IV (Weak shock:** $M < 2$**)**] *The shock strength is not strong enough to provoke carbuncle. The solutions are usually free from such anomalies.*

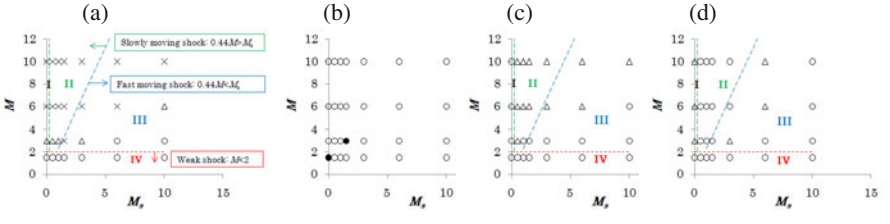

Fig. 4 Moving shock test results ($\varepsilon_g = 1.e-3$): (**a**) Roe (E-fix), (**b**) Van Leer, (**c**) AUSM+-up, and (**d**) SLAU. Open Circle: Stable. L1-norm of v-velocity residual remained the same order from the beginning; Triangle: Slight instability, but no carbuncle. L1-norm of v-velocity residual grew over one order; Cross: Carbuncle; Solid Circle: Shock itself is stable, but v appeared at the boundary

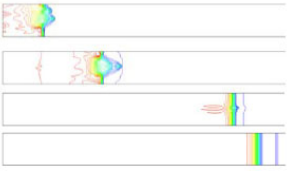

Fig. 5 Moving shock test, from Top to Bottom: M=6; M_s=0, 1.5, 6, and 10 (Roe (E-fix), $\varepsilon_g = 1.e-3$, 400 steps)

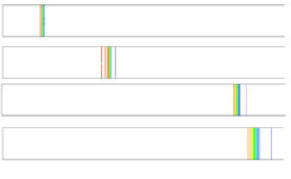

Fig. 6 Moving shock test, from Top to Bottom: M=6; M_s=0, 1.5, 6, and 10 (SLAU, $\varepsilon_g = 1.e-3$, 400 steps)

The robustness against the shock differs from one flux function to another. We point out that Van Leer's FVS is always stable regardless of the Groups.

Finally, Fig. 7 shows the results for $\varepsilon_g = 1.e-6$ and 0 [Roe (E-fix)]. This figure demonstrates that in most cases very small amount of instability v grew and it implies potential carbuncle at a very later stage (i.e., after very long computation). Nevertheless, within the present framework, neither of the results of $\varepsilon_g = 1.e-6$ nor 0 showed a clear sign of carbuncle, and no distinct difference was observed between them. Thus, the grid perturbation ε_g has minor effect on the results as long as it is taken to be small enough, whereas, in Quirk [1], $\varepsilon_g = 1.e-3$ was chosen to be large enough to trigger the carbuncle. Thus, it is confirmed that ε_g is one of the major factors governing the occurrence of carbuncle.

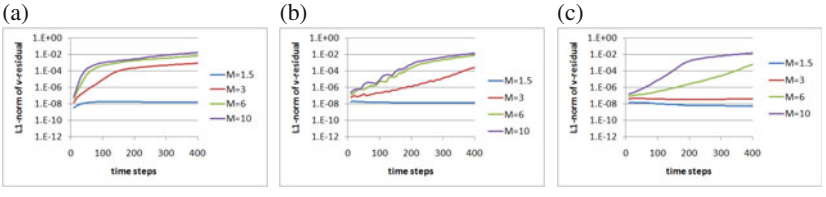

Fig. 7 L1-norm histories of v-velocity residual for moving shock test: M=1.5, 3, 6, and 10 (Roe (E-fix), $\varepsilon_g = 1.e-3$, 400 steps), (**a**) M_s=0.0 (stationary), (**b**) M_s=0.5 (slowly moving), and (**c**) M_s=6 (fast moving)

5 Conclusions

Carbuncle tends to appear and grow rapidly for larger M (shock strength) and smaller M_s (moving shock Mach number). According to M and M_s, the shock waves are categorized into stationary ($M_s = 0$), slowly moving ($0 < M_s < 0.44M$), fast moving ($0.44M < M_s$), and weak ($M < 2$) shocks. These groups turned out to have different (carbuncle) instability origins: The slowly moving shock is the most severe case, since it is affected by both grid perturbation and numerical noise from the left (downstream) region. The fast moving shock cases are less likely to exhibit carbuncle, and the weak shock cases are usually stable. The stationary shocks are either more or less stable than moving ones, depending on the flux functions.

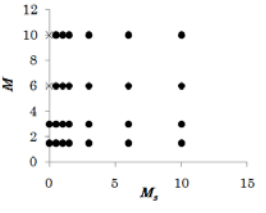

Fig. 8 Moving shock test results (Roe (E-fix), $\varepsilon_g = 1.e-6$ or 0). Cross: Carbuncle (total breakdown); Solid Circle: rapid growth of v, though still very small value

Acknowledgement. We thank Dr. Dan Hori for his cooperation and JSPS for their support.

References

1. Quirk, J.J.: Int. J. for Numer. Methods in Fluids 18, 555–574 (1994)
2. Pandolfi, M., D'Ambrosio, D.: J. Comput. Phys. 166, 271–301 (2001)
3. Kitamura, K., Roe, P., Ismail, F.: AIAA J. 47, 44–53 (2009)
4. Roberts, T.W.: J. Comput. Phys. 90, 141–160 (1990)
5. Van Leer, B.: Lecture Notes in Phys. 170, 507–512 (1982)
6. Roe, P.L.: J. Comput. Phys. 43, 357–372 (1981)
7. Liou, M.S.: J. Comput. Phys. 214, 137–170 (2006)
8. Shima, E., Kitamura, K.: Parameter-Free Simple Low-Dissipation AUSM-Family Scheme for All Speeds. AIAA J.(accepted for Publication), AIAA Paper 2009-136 (2009)
9. Anderson Jr., J.D.: Modern Compressible Flow with Historical Perspective, 3rd edn. McGraw Hill, New York (2003)
10. Van Leer, B.: AE520 Compressible Flow I. In: Fall 2006 Course Pack. University of Michigan (2006)
11. Kitamura, K., Shima, E., Nakamura, Y., Roe, P.L.: AIAA J. 48, 763–776 (2010)

A Numerical Study of High Enthalpy Flow over a Rearward Facing Step with Rounded Corners

N.R. Deepak, S.L. Gai, and A.J. Neely

1 Introduction

The rearward facing step with a sharp corner is a classical configuration for studying separated flows. This configuration is also of practical relevance in a hypersonic vehicle. However, a truly sharp corner is basically a mathematical simplicity [9]. The influence of finite radius at the corner is therefore of significance and is studied here numerically under high enthalpy conditions using state-of-the-art computational fluid dynamics (CFD). The flow conditions are comparable to reentry velocity of 6.7 km/s which corresponds to a total specific enthalpy of $h_o \approx 26$ MJ/kg with a unit Reynolds number 1.82×10^6 per meter and a Mach number $M_\infty \approx 7.6$ with air as the test gas. The geometry consists of an upstream flat-plate of length (L) of 48.4 mm with sharp leading edge. This is followed by a step of height (h) 2 mm and then a downstream flat plate of length (D) of 109.4 mm. Three different radii, $r/h = 1/8$, $r/h = 1/3$ and $r/h = 1/1$ are considered here for the corner radius. The two-dimensional flow-field of interest is modelled using a time-dependent Multi-Block Compressible Navier-Stokes (MB-CNS) solver [6]. Perfect gas calculations were made with air to behave as a single species and real gas calculations were made assuming air to be a mixture of thermally perfect gas with 5 neutral species and adopting Gupta's kinetic scheme for chemical reactions [3]. A multi-block structured grid with 52,000 cells is used. This was arrived at after performing a grid independence study over a sharp corner and modifying the grid topology to suit the curvature for the rounded configurations. Details regarding grid convergence are given in Deepak [1].

N.R. Deepak · S.L. Gai · A.J. Neely
School of Engineering & IT, High Speed Flow Group
University of New South Wales, Australian Defence Force Academy, Canberra 2600, Australia

2 Results and Discussions

In Figure 1, Stanton number (S_t), skin friction (c_f) and pressure (p/p_∞) distributions are shown for a sharp corner for both perfect gas and real gas. Here, the top separation lip is at $s/h = 0$, $s/h = 1$ is the bottom corner of the step and $s/h \geq 1$, is the distance down the plate. The forebody data close to the top corner is shown and very near upstream of the corner, a jump is observed in both the S_t and c_f. This particular behaviour as the corner discontinuity is approached from the upstream is due to the so called Goldstein singularity [2, 8]. In this region, we note that heat flux reduces while skin friction increases for a real gas. The pressure distributions indicate a relatively constant pressure upstream of the corner and, as the corner is approached, there is a steep fall due to expansion. Of particular note is the decrease in pressure on the forebody which begins at $s/h \leq 0.25$ which is the same location at which the skin friction and heat flux start to increase. The favourable pressure gradient allows for this rise in skin friction. Over the face of the step, the Stanton number values gradually reduce and go to zero at the bottom corner and after $s/h \geq 1$ a recovery occurs in the recirculation region which continues at and after reattachment. With respect to the skin friction, it can be seen that it passes from a positive to a negative value at approximately 0.076 step heights. This is the location at which the boundary layer separates and it is not at $s/h = 0$. Downstream from the bottom corner, the skin friction reaches zero once again at s/h = 2.54 when the flow reattaches. This is 1.54 step heights from the step face. The pressure distributions indicate a continuous fall from the top corner, reaching a minimum on the face of the step at $s/h \approx 0.038$ as a result of over expansion at the corner. After $s/h \approx 0.038$, a steep recovery occurs as the flow is recompressed through a lip shock. After $s/h \approx 0.2$, a pressure plateau is seen which is consistent with the constant pressure in the recirculation region. Further increase in pressure is due to the reattachment process. The effect of real gas on S_t, c_f and p/p_∞, seem to be insignificant in the separation and reattachment regions. Based on these results, separation occurs on the face of

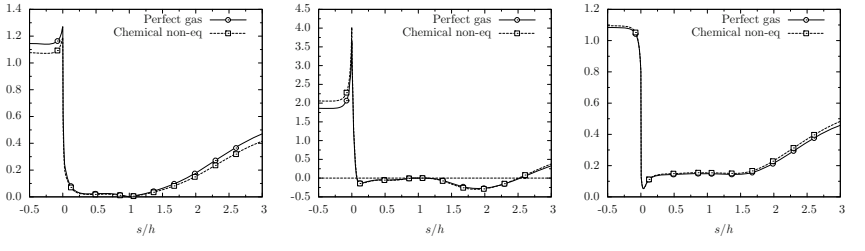

(a) $S_t \times 1000$ (b) $c_f \times 1000$ (c) p/p_∞

Fig. 1 Stanton number, skin friction & pressure distributions for sharp corner between separation and reattachment

the step ($s/h = 0.076$) and reattachment location is at $s/h = 2.54$, which is 1.54 step heights from the bottom corner. The base pressure has a value of $p/p_\infty = 0.146$.

2.1 The Near-Wake with Rounded Corners

The S_t, c_f and p/p_∞ distributions between the regions of separation and reattachment for different corner radii in comparison with those of the sharp corner were investigated. Here, the comparison is restricted to perfect gas as real gas effects were found to be insignificant in the separation/reattachment region as found earlier (Figure 1). In Figure 3, the influence of the corner radius on S_t, c_f and p/p_∞ are compared with those of the sharp corner. The coordinate system used to represent the data here is as follows. The abscissa represent the continuous wetted surface $'s'$, in which $s^* \leq 1$ refers to the normalised forebody distance, $0 \leq s/a \leq 1$, the normalised rounded corner distance and $s/h \geq 1$ the normalised distance downstream of the step. Figure 2 gives a schematic of the coordinate used to present the data. The normalisation of the forebody was obtained using the relation, $s^* = [(x - L_r)/L_r]L/h = [(x - L_r)/L_r]48.4/2$ where, x is the wetted surface coordinate running from the leading edge to the point where the forebody meets the rounded corner and L_r is the wetted distance of the upstream flat plate portion.

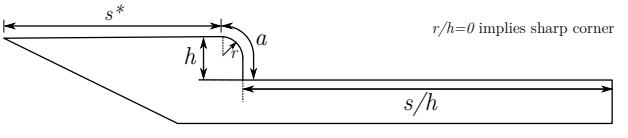

Fig. 2 Schematic representation of coordinate system for rounded corners

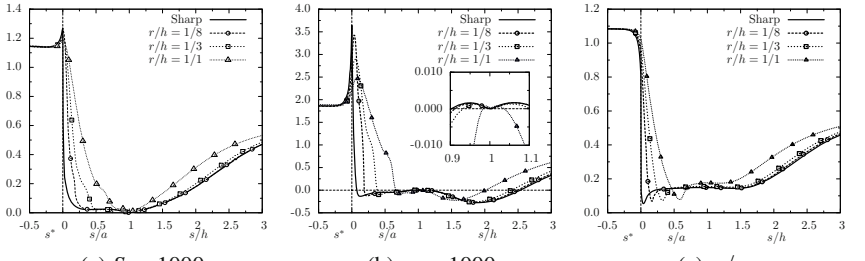

(a) $S_t \times 1000$ (b) $c_f \times 1000$ (c) p/p_∞

Fig. 3 Stanton number, skin friction and pressure distributions for different radii between separation and reattachment

Firstly, considering the heat flux in Figure 3a, over the forebody upstream of the corner, they are all nearly the same. As the corner is approached, jumps in heat flux magnitude can be seen to vary depending on the corner radius, with the maximum occurring for the sharp corner. Note that the locations of the peaks for all the rounded corners occur not exactly at $s^* = 0$ but at $s/a \approx 0.01$ which is the beginning of the curvature of the corner unlike the sharp corner, for which the peak occurs at $s^* = 0$. The Navier-Stokes solution carried out over the Mars path finder configuration [5] for various shoulder radii also showed that heat flux jumps occur at the beginning of the shoulder curvature. The effect of rounding the corner seems to be to reduce the intensity of expansion and spread it over the curved surface. The fall in heat flux is more gradual with the rounded corner and the heat flux for all the corner radii approach zero at the bottom of the step. The higher heat flux with increasing radius implies that the gas entering the recirculation region through the shear layer will be at a higher temperature for a rounded corner than for a sharp corner. Planar laser-induced fluorescence (PLIF) measurements [7] of the temperatures in the base of sharp and rounded shoulder cones showed that they were higher for the latter configuration. This lends some confidence in the higher heat flux noted for the rounded configurations. Downstream, between the bottom corner and the reattachment location ($1 \leq s/h \leq 3$), no great variations in heat flux recovery are noted, except for the fully rounded corner, for which the recovery appears to be more rapid. This is attributed to the smaller recirculation region observed for this configuration. Regarding the skin friction in Figure 3b, over the forebody region, the values are essentially the same. Similar to the heat flux, as the corner is approached, jumps in skin friction are noted and the peak values decrease with increasing radius. However, unlike the heat flux, the locations of these peaks shift slightly with increasing radius. For the fully rounded corner, the peak occurs at $s/a \approx 0.063$. It is also seen that the separation location moves further down with increasing radius. Further, the skin friction goes from negative (separation) to positive before going to zero at the bottom corner and immediately becomes positive before going negative again. These features are thought to be indicative of the presence of secondary vortices. Magnified distributions in this region are shown as inset in Figure 3b. Note that this feature is seen even for a fully rounded configuration. Figure 3c shows variation in pressure with increasing corner radius. As with skin friction, the pressure minima shift downstream with increasing radius. The pressure minima also show decreasing magnitude with increasing radius. It is also interesting to note that while the sharp corner and corner radius $r/h = 1/8$ and $r/h = 1/3$ all show a distinct and large plateau within the recirculation region, the fully rounded corner shows a much smaller plateau with higher pressures indicating a much smaller separated region. The pressure data also show that increasing the corner radius results in increased base pressure. Table 1 shows the normalised separation distances for corners of different radii. We note that the separation region has reduced by 22% from the sharp corner to a fully rounded corner and the base pressure is increased by nearly 97%. Another feature to note is that the reattachment is relatively unchanged for the sharp corner and the two smaller radii while it is substantially influenced by the fully rounded corner.

Table 1 Normalised separation and reattachment distances for the rounded corners

Configuration	Separation s/a	Reattachment s/h	Base pressure p/p_∞
$r/h = 1/8$	0.184	2.5	0.191
$r/h = 1/3$	0.374	2.4	0.220
$r/h = 1/1$	0.664	2.0	0.288

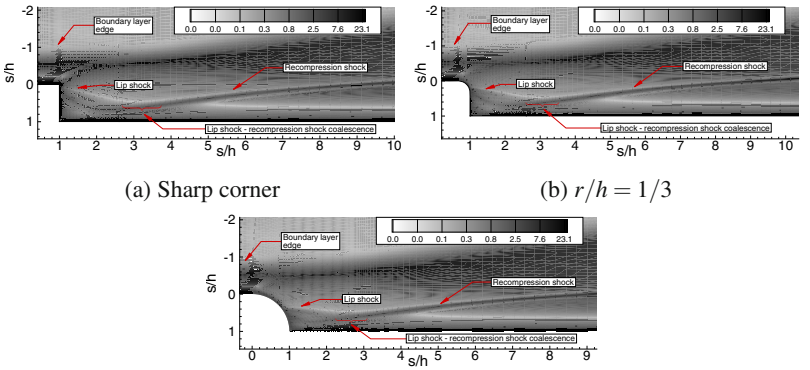

(a) Sharp corner (b) $r/h = 1/3$

(c) Rounded corner ($r/h = 1/1$)

Fig. 4 Magnitudes of density gradient ($|\nabla\rho|$) contours behind the step

In Figure 4, the magnitudes of the density gradients are shown for sharp, slightly rounded ($r/h = 1/3$) and fully rounded corner. The density gradients are calculated using $|\nabla\rho| = \sqrt{\rho_x^2 + \rho_y^2}$. Note that for the rounded corner configurations, the emergence of a weak lip shock emanating from the curved surface is clearly visible close to the location of separation. Further, the lip shock seems to be embedded within the shear layer and seems to coalesce with the recompression shock at about 3 step heights. Compared to that of the sharp corner, the lip shock inclination becomes nearly parallel to the bottom plate as the corner radius increases. This feature of lip shock orientation has been confirmed by previous researchers [4, 7]. It is also seen that with increase in radius, the confluence of lip shock and recompression shock moves closer towards the base.

3 Conclusions

A numerical study of the flow behind a rearward facing step with sharp and rounded corners in a high enthalpy hypersonic flow has been carried out. It was found that in the separated and reattachment region, the real gas effects were not significant.

For the rounded corners, flow separation was seen to occur over the curved surface and it progressed downstream with increase in the corner radius. This is consistent with previous high supersonic and hypersonic Mach number experiments [4, 7]. With increased radius, the strength of expansion decreased and, the pressure minima occurred further down the curved surface. The pressure remained nearly constant within the recirculation region, except for the fully rounded corner where the plateau region was hardly noticeable and the base pressure was much higher. Between the bottom corner and the location of reattachment, heat flux variations among different radii were not significant except for the fully rounded corner. Also, for a fully rounded corner, a much higher heat flux in the separation region was noted. A detailed visualisation of the lip shock structure was made for the rounded corners. The lip shock was seen for all the rounded configurations. The orientation of the lip shock gradually changed with increase in the corner radius and tended to become nearly parallel to the plate for the fully rounded corner. The confluence of the lip shock and the recompression shock was also seen to move closer to the base with increase in corner radius.

References

[1] Deepak, N.R.: Computational Studies of Hypersonic High Enthalpy Separated Flows. PhD thesis, School of Engineering & IT, University of New South Wales, Canberra, Australia (Submitted November 2010)
[2] Goldstein, S.: On laminar boundary-layer flow near a position of separation. Quart. J. Mech. Applied Math. 1, 43–69 (1948)
[3] Gupta, R.N., Yos, J.M., Thompson, R.A., Lee, K.-P.: A review of reaction rates and thermodynamic and transport properties for an 11-species air model for chemical and thermal nonequilibrium calculations to 30 000 k, Technical Report 1232, NASA (1990)
[4] Hama, F.R.: Experimental studies on the lip shock. AIAA Journal 6(2), 212–219 (1968)
[5] Hollis, B.R.: Experimental and Computational Aerothermodynamics of a Mars Entry Vehicle. PhD thesis, Aerospace Engineering, North Carolina State University, Raleigh, North Carolina, USA (1996)
[6] Jacobs, P.A.: Mb-cns: a computer program for the simulation of transient compressible flows. Technical Report 7/98, Department of Mechanical Engineering, University of Queensland, Brisbane (1998)
[7] O' Byrne, S.: Hypersonic Laminar Boundary Layers and Near-Wake Flows. PhD thesis, The Australian National University, Canberra (2002)
[8] Stewartson, K.: On the flow near the trailing edge of a flat plate. Proc. Roy. Soc. A. 306(1486), 275–290 (1968)
[9] Weinbaum, S.: On the singular points in the laminar two-dimensional near wake flow field. Journal of Fluid Mechanics 33(1), 39–63 (1968)

Application of a New Hybrid Explicit-Implicit Flow Solver to 1D Unsteady Flows with Shock Waves

E. Timofeev and F. Norouzi

1 Introduction

Explicit numerical schemes are widely used to simulate essentially unsteady flows with shock waves (e.g., see [1, 2] and numerous references there) because the use of large time steps with implicit schemes is often not possible and necessary due to time accuracy requirements. However, for some flows the time step of explicit time marching becomes severely limited by particular conditions within a relatively small flow area, as compared to the rest of the computational domain where the stability condition admits much higher time steps. The situation can be termed as "temporally-stiff". Out of many examples, we mention the simulations of blast wave propagation when a high pressure/ temperature balloon is used as a blast wave source. When the blast wave propagates away from its origin, a high-temperature (and hence, high speed of sound) spot remains at the explosion center, considerably reducing the allowable time step for the whole simulation. The same effect can be caused by high flow velocities existing just downstream of a sharp corner when a shock wave diffracts over it, or by small computational cells near some small-scale geometrical feature of the problem under study.

Clearly, the simulations of such flows would benefit from a hybrid explicit-implicit method, with smooth switching between the explicit and implicit modes depending upon local flow and grid parameters. The fully explicit mode would be used to obtain time-accurate solution in most areas of the computational domain while gradual transition to the implicit mode in the localized areas, where it is required, would help to overcome unnecessary time step reduction due to temporal stiffness.

In the papers [3, 4, 5], further developing a general hybridization idea proposed in [6], we developed a new hybrid scheme, which is *of the second order both in space and in time for both, explicit and implicit, modes*. This property is important for unsteady computations. The scheme also satisfies the total variation diminishing

E. Timofeev · F. Norouzi
Department of Mechanical Engineering, McGill University, Montreal, Quebec H3A2K6, Canada

(TVD) property to ensure monotone solutions in the presence of discontinuities (e.g. shock waves). TVD limiters are applied to both spatial and temporal gradients of the solution. The time limiters are introduced following the approach proposed in [7]. The Lower-Upper-Symmetric-Gauss-Seidel (LU-SGS) approximate factorization method is used to solve the discretized and linearized governing equations, which allows for easy generalization to unstructured grids (see [6]).

The above developments are limited to scalar linear and non-linear conservation laws. In the present paper we concentrate on the generalization and applications of the proposed scheme to unsteady shocked problems governed by the Euler equations. In Sect. 2 the generalization of our hybrid scheme to the Euler equations is introduced. Section 3 followed by conclusions in Sect. 4 is devoted to its application to two test problems: the moving shock wave problem and the Sod problem.

2 New Hybrid Explicit-Implicit Scheme for the Euler Equations

We consider the one-dimensional Euler equations written in the conservative form $\partial \mathbf{U}/\partial t + \partial \mathbf{F}/\partial x = 0$, where $\mathbf{U}$ is the vector of conservative variables and $\mathbf{F}$ is the flux vector. The general finite-volume Riemann-solver-based discretization can be written as:

$$\mathbf{U}_i^{n+1} = \mathbf{U}_i^n - \frac{\Delta t}{\Delta x_i}\left(\mathbf{F}_{i+1/2} - \mathbf{F}_{i-1/2}\right), \tag{1}$$

where $\mathbf{F}_{i+1/2} = \mathbf{F}(\mathbf{W}_{i+1/2})$ and $\mathbf{W}_{i+1/2}$ is the solution of the Riemann problem at the control volume interface for the left and right values of primitive variables $\mathbf{W}^L_{i+1/2}$ and $\mathbf{W}^R_{i+1/2}$. Our hybridization approach with the hybridization coefficient ω_i ranging from 0 (fully implicit scheme) to 1 (fully explicit scheme) leads, for the Euler equations, to the following left and right face values:

$$\begin{aligned}\mathbf{W}^L_{i+1/2} = \omega_i &\left[\frac{\mathbf{W}_i^n + \mathbf{W}_i^{n+1/2}}{2} + \frac{1}{2}\,(\overline{\nabla \mathbf{W}})_i^n \Delta x_i\right] + \\ &+ (1-\omega_i)\left[\mathbf{W}_i^{n+1} + \frac{1}{2}(\overline{\nabla \mathbf{W}})_i^{n+1}\Delta x_i - \frac{1-\omega_i}{2}(\overline{\Delta_t \mathbf{W}})_i^{n+1}\right],\end{aligned} \tag{2}$$

$$\begin{aligned}\mathbf{W}^R_{i+1/2} = \omega_{i+1} &\left[\frac{\mathbf{W}_{i+1}^n + \mathbf{W}_{i+1}^{n+1/2}}{2} - \frac{1}{2}\,(\overline{\nabla \mathbf{W}})_{i+1}^n \Delta x_{i+1}\right] + \\ &(1-\omega_{i+1})\left[\mathbf{W}_{i+1}^{n+1} - \frac{1}{2}(\overline{\nabla \mathbf{W}})_{i+1}^{n+1}\Delta x_{i+1} - \frac{1-\omega_{i+1}}{2}(\overline{\Delta_t \mathbf{W}})_{i+1}^{n+1}\right],\end{aligned} \tag{3}$$

where the predictor primitive values $\mathbf{W}_i^{n+1/2}$ for the explicit portion of the scheme are calculated from the respective conservative variables obtained from:

$$\mathbf{U}_i^{n+1/2} = \mathbf{U}_i^n - \frac{\omega_i \Delta t}{\Delta x_i}\left(\mathbf{F}(\mathbf{W}^{\text{in}}_{i+1/2}) - \mathbf{F}(\mathbf{W}^{\text{in}}_{i-1/2})\right) \tag{4}$$

with $\mathbf{W}^{\text{in}}_{i\pm1/2} = \mathbf{W}^n_i \pm (\overline{\nabla \mathbf{W}})^n_i(\Delta x_i/2)$. In above equations, $(\overline{\nabla \mathbf{W}})_i$ is the limited spatial gradient of primitive variables in cell i; the *minmod* TVD limiter is used in the computations presented below. The quantity $(\overline{\Delta_t \mathbf{W}})_i$ represents the limited temporal gradient of solution in cell i (see its expression below).

To solve the discretized set of equations, they are linearized with the introduction of iterations, which are performed at each time step until convergence with a prescribed accuracy is achieved. Only the first-order flux is subjected to the linearization. Moreover, the first order flux is approximated by $\mathbf{F}_{i+1/2} = 0.5[\mathbf{F}(\mathbf{U}_i) + \mathbf{F}(\mathbf{U}_{i+1}) - (r_{i+1}\mathbf{U}_{i+1} - r_i\mathbf{U}_i)]$, where r_i is the spectral radius of the Jacobian matrix. The hybridization parameter, which in the nonlinear case is a function of solution, is assumed to be "frozen" when the linearization is performed (i.e. evaluated at the previous iteration). This results in the following linearized equations, with s being the iteration number:

$$-\frac{1-\omega^s_{i-1}}{2}\frac{\Delta t}{\Delta x_i}(\mathbf{A}^s_{i-1} + r^s_{i-1}\mathbf{I})\delta\mathbf{U}^s_{i-1} + \left(1 + \frac{\Delta t(1-\omega^s_i)}{\Delta x_i} r^s_i\right)\delta\mathbf{U}^s_i + \\ + \frac{1-\omega^s_{i+1}}{2}\frac{\Delta t}{\Delta x_i}(\mathbf{A}^s_{i+1} - r^s_{i+1}\mathbf{I})\delta\mathbf{U}^s_{i+1} = -\mathbf{R}^s_i\,, \qquad (5)$$

where

$$\mathbf{R}^s_i = \mathbf{U}^{n+1,s}_i - \mathbf{U}^n_i + \frac{\Delta t}{\Delta x_i}\left(\mathbf{F}^{n+1,s}_{i+1/2} - \mathbf{F}^{n+1,s}_{i-1/2}\right)\,; \qquad (6)$$

$\delta\mathbf{U}_i = \mathbf{U}^{n+1,s+1}_i - \mathbf{U}^{n+1,s}_i$, and $\mathbf{A}$ and $\mathbf{I}$ are the Jacobian and identity matrices. In view of subsequent generalization for unstructured grids, the equations are solved with the forward and backward sweeps of the LU-SGS procedure written as follows:

$$\delta\mathbf{U}^{s,*}_i = -\frac{1}{1 + \frac{\Delta t}{\Delta x_i}(1-\omega^s_i)r^s_i}\left[\mathbf{R}^s_i - \frac{1-\omega^s_{i-1}}{2}\frac{\Delta t}{\Delta x_i}(\mathbf{A}^s_{i-1} + r^s_{i-1}\mathbf{I})\delta\mathbf{U}^{s,*}_{i-1}\right]\,, \qquad (7)$$

$$\delta\mathbf{U}^s_i = \delta\mathbf{U}^{s,*}_i - \frac{1}{1 + \frac{\Delta t}{\Delta x_i}(1-\omega^s_i)r^s_i}\frac{1-\omega^s_{i+1}}{2}\frac{\Delta t}{\Delta x_i}(\mathbf{A}^s_{i+1} - r^s_{i+1}\mathbf{I})\delta\mathbf{U}^s_{i+1}\,. \qquad (8)$$

Inverse linearization can be utilized: $\delta\mathbf{F}^{s,*}_{i-1} = \mathbf{A}^s_{i-1}\delta\mathbf{U}^{s,*}_{i-1}$; $\delta\mathbf{F}^s_{i+1} = \mathbf{A}^s_{i+1}\delta\mathbf{U}^s_{i+1}$. It allows to avoid Jacobian calculations altogether.

The time limiter can be obtained via application of the Harten theorem to the hybrid scheme. It is iterative and can be incorporated into the above general iteration procedure as follows:

$$(\overline{\Delta_t \mathbf{W}})^{n+1,s}_i = \max\left\{0, \min\left\{\frac{2}{\nu^s_i}\cdot\frac{1-\omega^s_i\nu^s_i(2-\omega^s_i\nu^s_i)}{(1-\omega^s_i)^2}(\mathbf{W}^{n+1,s}_i - \mathbf{W}^n_i) + \right.\right. \\ \left.\left. + (\overline{\Delta_t \mathbf{W}})^{n+1,s-1}_{i-1},\ \mathbf{W}^{n+1,s}_i - \mathbf{W}^n_i\right\}\right\} \qquad (9)$$

for non-negative $\mathbf{W}^{n+1,s}_i - \mathbf{W}^n_i$, where $\nu_i = (|u_i| + c_i)\Delta t/\Delta x_i$. For negative $\mathbf{W}^{n+1,s}_i - \mathbf{W}^n_i$, min and max functions in the above expression change places. In the fully implicit mode ($\omega_i = 0$) the limiter reduces to the one proposed by Duraisamy and Baider [7].

3 Computational Examples

3.1 Moving Shock Problem

In this problem, the initial conditions correspond to a shock wave (shock Mach number $M_s = 3$), which is initially at $x_{\text{ini}} = 49.7758$ and then propagates from left to right into the gas ($\gamma = 1.4$) at rest ($\rho_R = 1.0$, $u_R = 0.0$, $p_R = 1.0$) till the time moment $t = 45.0$, when the shock is at $x_{\text{fin}} = 209.5$. The computational grid with 301 nodes in total is uniform with $\Delta x = 1.0$, except for a narrow region, where the grid nodes are linearly ($\Delta x_i = k\Delta x_{i-1}$, where $k = 0.915$) clustered towards its center, so that the ratio of the smallest to the largest (on the uniform mesh) cell size is 85. The narrow region of non-uniform mesh is located on the left from the initial position of the shock, in the uniform post-shock flow. Thus, the shock wave propagates to the right through the uniform mesh only. The non-uniform mesh region is introduced intentionally to create the problem with temporal stiffness: it is obvious that for an explicit scheme the time step is determined by the smallest cell and it is much smaller than the time step dictated by the stability condition applied in the vicinity of the shock.

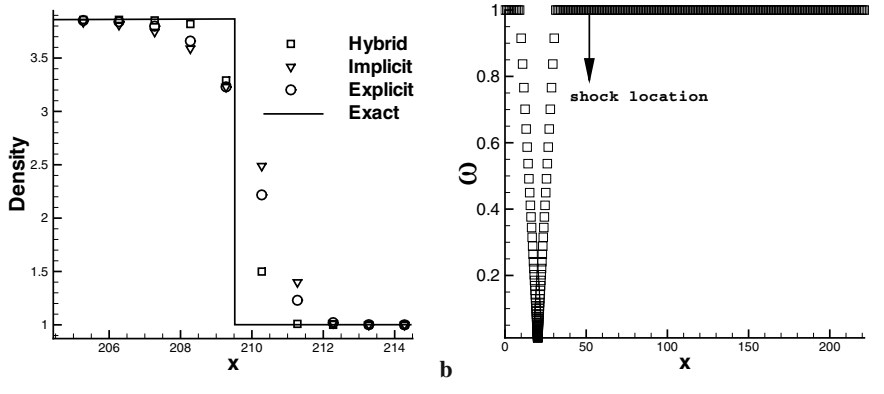

Fig. 1 Plots for the moving shock problem: (**a**) Density profiles in the vicinity of the shock; (**b**) The distribution of the hybridization parameter ω across the computational domain. The initial position of the shock wave propagating to the right is indicated

The problem is calculated with the scheme introduced in Sect. 2 using three modes: the fully explicit one (the hybridization parameter $\omega = 1$ everywhere), which is the well-known MUSCL-Hancock scheme; the fully implicit one ($\omega = 0$) everywhere; and the hybrid one with ω variation shown in Fig. 1b, which indicates that on the uniform mesh the hybrid scheme works in the fully explicit mode and the implicit part is invoked only within the non-uniform mesh region.

For the fully explicit scheme the time step is determined from the CFL stability condition applied to the whole computational domain, with the Courant number chosen to be 0.8. For the fully implicit and hybrid scheme the time step is determined by the stability condition with the same Courant number of 0.8 applied to the uniform mesh region only.

The results are shown in Fig. 1a. It is seen that the hybrid scheme is more accurate than the fully explicit and fully implicit modes. Even though both the fully explicit and the hybrid schemes operate in the fully explicit mode near the shock, the hybrid one is capable of using much higher time steps, which results in lower numerical dissipation and better accuracy. At the same time, due to higher values of time steps the hybrid scheme is 75 times faster than the fully explicit one in terms of CPU time.

3.2 Sod Problem

The classical Sod problem ($\rho_L = 1.0, u_L = 0.0, p_L = 1.0, \rho_R = 0.125, u_R = 0.0, p_R = 0.1$) serves as the second test. The computation proceeds till the time moment $t = 50$. The grid parameters and the CFL number are the same as for the moving shock problem. In this case the initial discontinuity is placed at $x = 74.5$, near the zone of non-uniform mesh (see Fig. 2b), so that the shock wave and the contact discontinuity

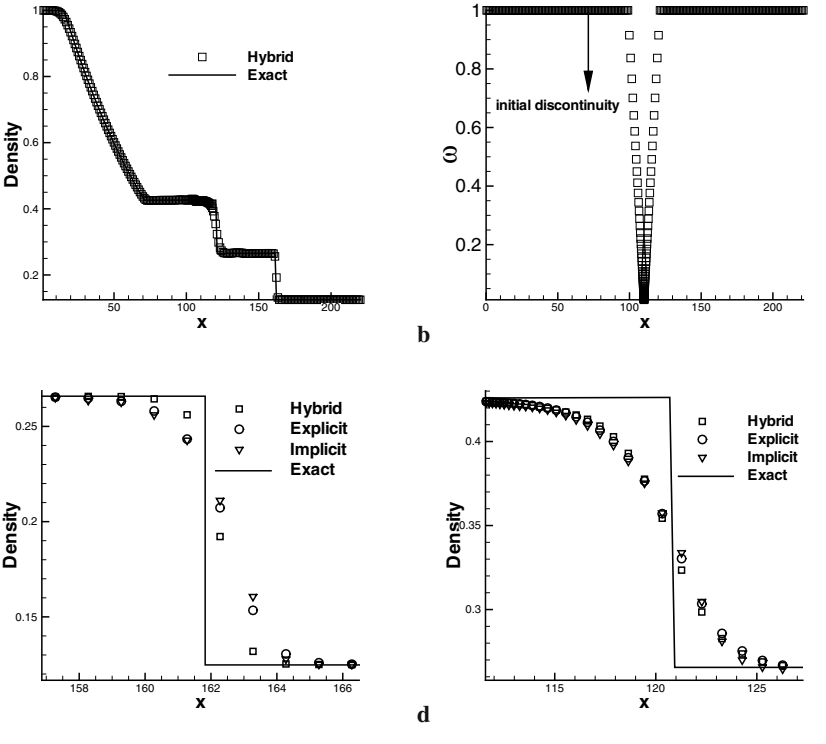

Fig. 2 Plots for the Sod problem: (**a**) Density profile across the computational domain; (**b**) The distribution of the hybridization parameter ω across the computational domain; (**c**) Density profiles in the vicinity of the shock; (**d**) Density profiles in the vicinity of the contact discontinuity

propagate through it in the course of flow development. Nevertheless, as seen in Fig. 2a the hybrid scheme produces an accurate solution without oscillations. As follows from Fig. 2c,d, its solution is again less diffusive than that produced by its fully explicit and fully implicit counterparts.

4 Conclusions

The presented results demonstrate that the application of the hybrid scheme leads to a marked improvement in the numerical solution accuracy as compared to the use of a fully explicit or a fully implicit scheme for unsteady shocked 1D test problems. At the same time, the hybrid scheme is more efficient. Thus, the results are very promising, and the application of the scheme to practical gasdynamics problems is in progress.

Acknowledgments. The present study is supported in part by the NSERC Discovery grant RGPIN/298232-2009 and the FQRNT Team grant PR-126114.

References

1. Toro, E.F.: Riemann solvers and numerical methods for fluid dynamics. A practical introduciton, 2nd edn. Springer, Heidelberg (1999)
2. Toro, E.F. (ed.): Godunov methods: theory and applications. Edited review. Kluwer Academic/Plenum Publishers (2001)
3. Norouzi, F., Timofeev, E.: A hybrid explicit-implicit second order TVD scheme: linear advection equation case. In: Proc. 17th Annual Conf. of CFD Society of Canada, London, Ontario, May 17-19, 6 p (2010)
4. Norouzi, F., Timofeev, E.: A hybrid explicit-implicit second order TVD scheme: the scalar nonlinear equation sase. In: Proc. 18th Annual Conf. of CFD Society of Canada, Montreal, Quebec, April 27-29, 6 p (2011)
5. Norouzi, F., Timofeev, E.: A hybrid, explicit-implicit, second order in space and time TVD scheme for one-dimensional scalar conservation laws. In: 20th AIAA CFD Conference on AIAA Paper, Honolulu, USA, June 27-31 (2011)
6. Menshov, I., Nakamura, Y.: AIAA J. 42(3), 3 (2004)
7. Duraisamy, K., Baeder, J.: SIAM J. on Scien. Comp. 29(6), 2607–2620 (2007)

Prediction of Transition Location and Its Effects on Shock Bump Control on a Natural Laminar Flow Aerofoil

F. Deng, S.C. McIntosh, and N. Qin

1 Introduction

The reduction of overall drag for an aircraft operating at its cruise condition is a prevalent goal for many involved in the aerodynamic design of transonic aircraft. Bringing both financial and environmental benefits, savings on the order of single drag counts are considered to be significant. Many concepts have been trailed in the pursuit of increased lift to drag ratios at transonic cruise. One of them, in terms of novel concepts addressing this issue, is the preservation of natural laminar flow over an increased proportion of the wing area. The laminarisation of a wing reduces overall drag via both a reduction in skin friction drag resulting from decreased mixing across the boundary layer and a reduction in pressure drag resulting from variations in effective aerofoil shape due to reductions in the boundary layer's displacement thickness. Another concept which reduces the wave drag via the reduction of the strength of the near normal shock-waves on the wing upper surface is the application of 2D shock control bumps to the laminar or turbulent wings by Ashill *et al.* [1, 2]. Since Qin *et al.* [3] proposed 3D bumps for shock control, detailed experimental and numerical studies, including bump shape optimisation have been conducted by Wong et al. [4], Ogawa *et al.* [5] and Qin *et al.* [6]. While the λ–shock structure is observed as the key feature for some bump geometries tested [4, 5], e.g. ramp bumps, the optimised 2D and 3D bumps show a "knee-shaped" shock structure for smoothly (continuity of the first derivative) contoured bump designs [6].

In order to explore the combination of the previous two concepts, Computational Fluid Dynamics (CFD) has been utilised to optimise the shape of a shock control bump on a natural laminar aerofoil. Here a popular empirical transition onset criterion by Michel [7] is used to automatically predict the transition onset location. This

F. Deng · S.C. McIntosh · N. Qin
Department of Mechanical Engineering, University of Sheffield, Sheffield, S1 3JD, UK

F. Deng
College of Aerospace Engineering, Nanjing University of Aeronautics and Astronautics, 210016, China

empirical criterion gives fairly good results for many aerofoil flows. Since transition onset location is highly sensitive to the flight condition and the flight environment, the influence of varying transition onset location on the performance and operation of shock control bumps is also investigated

2 Methods

2.1 CFD, Optimisation and Parameterization Method

A compressible flow Reynolds averaged Navier-Stokes solver, MERLIN, is used in this study. This solver, developed at the universities of Sheffield and Cranfield, is an implicit, cell-centred, finite volume scheme employing third order MUSCL spatial discretisation and Osher flux splitting. The Baldwin-Lomax algebraic turbulence model is employed for all simulations.

An efficient global optimisation algorithm proposed by Jones [8], which has the advantage of optimising expensive black-box function such as CFD simulation in the current study, has been utilised to search the design space defined by four design parameters of shock control bump: bump length $bump_{length}$, bump crest location x_{crest}, bump relative crest location $bump_{relative}$, and bump height Δy_h. As shown in Fig. 1.

2.2 Transition Onset Prediction Model

Michel's empirical transition onset criterion [7] is given by:

$$Re_\theta = 2.9 Re_x^{0.4} \tag{1}$$

where Re_θ is the Reynolds number based on the momentum thickness, and$Re_x$is the Reynolds number based on the distance measured from the stagnation point of the boundary layer. After calculating the transition location, the extent of the transition region can be simulated by an intermittency function, which is given by:

$$\gamma_{tr} = 1 - \exp\left[\left(-\frac{Re_{x_{tr}}^{-1.34}}{G_{\gamma_{tr}} \nu^2}\right) U_e^3(x)(x - x_{tr}) \int_{x_{tr}}^{x} \frac{dx}{U_e(x)}\right] \tag{2}$$

where $U_e(x)$ is the boundary-layer edge velocity, $Re_{x_{tr}} = (U_e x/\nu)_{tr}$is the transition Reynolds number, $x_{tr}$is the transition location and $G_{\gamma_{tr}}$is a constant which determines the length of the transitional region. For high Reynolds number the recommended value of $G_{\gamma_{tr}}$is 1200. In order to simulate the transitional aerofoil flow, the turbulent viscosity in MERLIN is multiplied by the intermittency function given in equation (2):

$$\mu_t = \begin{cases} \gamma_{tr}\mu_t' & x > x_{tr} \\ 0 & x \le x_{tr} \end{cases} \tag{3}$$

where μ_t' is the original turbulent viscosity. In practice, a fully turbulent convergent solution is needed before calculating the boundary-layer parameters through the following steps:

Step 1: Calculate the boundary-layer edge velocity through the wall pressure coefficient distribution

$$U_e = U_\infty \sqrt{1 - C_p} \tag{4}$$

Step 2: Calculate the boundary-layer edge through U_e to obtain the kinematic viscosity ν at the boundary-layer edge.

Step 3: Calculate the momentum thickness through an integration of the velocity distribution at the boundary-layer edge

$$\theta(x) \approx \sqrt{\frac{0.45\upsilon}{U_e^6} \int_0^x U_e^5 dx} \tag{5}$$

3 Results

3.1 Validation of Transition Onset Prediction Model

The NACA0012 aerofoil and NLF0416 aerofoil have been chosen to validate and test the transition onset prediction model. The chosen flow conditions for NACA0012 aerofoil are: Ma=0.15, Re=2.9×10^6. The chosen flow conditions for NLF0416 aerofoil are: Ma=0.3, Re=4.0×10^6, $\alpha = 2.03°$. In Table 1 and Table 2, most of the transition onset locations are predicted reasonably close to the experimental values. The primary cause for the discrepancies in Table 1 on the upper surface is possibly due to the laminar separation bubble formed when the angle of attack exceeds about 5° for the NACA0012 aerofoil. Fig. 2 shows the drag results of the transitional simulations in comparison with the experimental data [7] and the fully turbulent computation. In Table 2 for NLF0416 aerofoil, the prediction shows much better agreement with the experimental data and Lee and Jameson's prediction [9] obtained by the e^N-database method.

Table 1 Comparison of transition onset locations of NACA0012 aerofoil

$\alpha(°)$	experiment	present	experiment	present
0	0.45	0.43	0.45	0.43
3	0.20	0.22	0.66	0.66
5	0.085	0.120	0.79	0.79
8	0.024	0.060	0.92	0.95

Table 2 Comparison of transition onset locations of NLF0416 aerofoil

	Upper surface(x/c)	Lower surface(x/c)
experiment[9]	0.35	0.6
Lee[9]	0.348	0.587
present	0.356	0.596

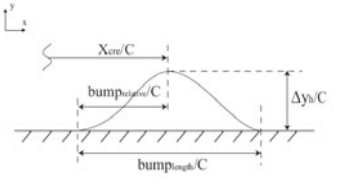

Fig. 1 Illustration of shock control bump parameterization[6]

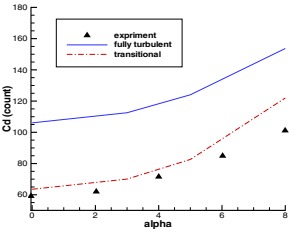

Fig. 2 Comparison of drag coefficients of NACA0012 aerofoil

3.2 Bump Optimisation

In the current study, the natural laminar flow aerofoil RAE5243 investigated by Qin *et al.* [3, 6] is chosen. The chosen flow conditions are: Ma = 0.68, Re = 17 $\times 10^6$, lift coefficient C_L=0.82. The bump optimisation can be treated as a drag minimization problem with constraint: $C_L \geq 0.82$. The predicted transition onset locations on the upper surface and lower surface are 0.396c and 0.564c, respectively. During the shock control bump optimisation process, due to the relative small variation of the aerofoil flow conditions, the transition locations are fixed for simplicity. The parameters of the final optimised bump parameters are: $bump_{length}$=0.3c, x_{crest}=0.665c, $bump_{relative}$=0.7c, Δy_h=0.0075c. Table 3 presents the comparison of total, pressure, and skin friction drag coefficients. The skin friction drag of the optimised bump increases by about one count. However, the reduction of the total drag coefficient is about 35 counts, nearly 30%, which comes from the pressure drag (including wave drag) reduction. In Fig. 3 and Fig. 4, it can be seen clearly that the strong normal shock wave appeared on the upper surface has been smeared out by the optimised shock control bump. The knee-shaped shock structure as discovered by Qin *et al.* [6] before in bump optimisation can be clearly seen in Fig. 4.

Table 3 Comparison of drag coefficients of RAE5243 aerofoils

	Total drag	Pressure drag	Skin drag
without bump	0.01194	0.00890	0.00303
optimised bump	0.00843	0.00527	0.00315

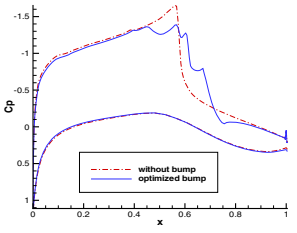

Fig. 3 Comparison of pressure coefficient distributions of RAE5243 aerofoils

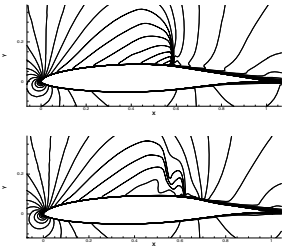

Fig. 4 Comparison of Mach number contours of RAE5243 aerofoils; top: without bump, bottom: optimised bump

3.3 Influence of Varying Transition Onset Locations

Although transition onset location can be predicted by transition models or experiments, there is often uncertainties due to flight condition and environmental change, such as surface contamination, noise, ice formation, and free stream turbulence. As the shock control bump is optimised for a fixed transition location, it is import to find its performance sensitivity to the transition location. In order to test the robustness of the optimised shock control bump, a series of simulations have been carried out by specifying different transition onset locations ($0.10c \sim 0.55c$) on the upper surface. The transition onset location on the lower surface has been kept fixed ($0.564c$) in this study. Fig. 5 shows clearly the benefit of keeping laminar flow on the aerofoil: the longer the laminar flow, the smaller the drag coefficients. By comparing the drag coefficients of the optimised bump with the datum aerofoil, similar trends can be observed with the same difference (or delta), which means the varying transition onset locations actually have little influence on the performance of the optimised bump regarding pressure drag, or wave drag, reduction. The performance of the optimised bump shows little sensitivity to different transition onset locations. However, the pressure distributions shown in Fig. 6 indicate subtle differences on the shock control bump.

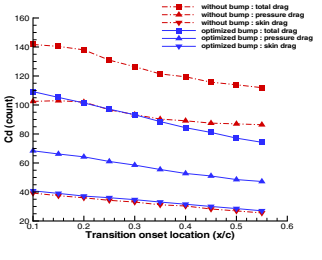

Fig. 5 Drag coefficients of RAE5243 aerofoils with different transition onset locations

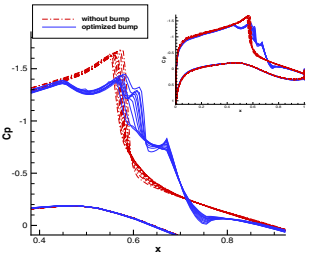

Fig. 6 Pressure coefficient distributions of RAE5243 aerofoils with different transition onset locations

4 Conclusion

This study shows that the transition onset location on aerofoil flow without separation can be reasonably well predicted by a simple empirical criterion based on the Michel's transition model. The optimised shock control bump based on the predicted transition onset location shows similar performance in wave drag reduction, as compared with previous studies assuming fully turbulent boundary layer around the aerofoil. The knee-shaped local shock structure is confirmed for the optimised bump for the transitional flow. Furthermore, the wave drag reduction performance of the shock control bump is shown to be insensitive to the transition location.

References

1. Ashill, P.R., Fulker, J.L., Shires, A.: A novel technique for controlling shock strength of laminar flow aerofoil sections. In: The First European Symposium on Laminar Flow, Hamburg (March 1992)
2. Fulker, J.L., Ashill, P.R., Simmons, M.J.: Study of simulated active control of shock waves on an aerofoil. Defence Research Agency. Technical Report TR93025 (May 1993)
3. Qin, N., Monet, D., Shaw, S.T.: 3D Bumps for Transonic Wing Shock Control and Drag Reduction. In: CEAS Aerospace Aerodynamics Research Conference, Cambridge, UK (2002)
4. Wong, W.S., Qin, N., Sellars, N., Holden, H., Babinsky, H.: A combined experimental and numerical study of flow structures over three-dimensional shock control bumps. Aerospace Science and Technology 12, 436–447 (2008)
5. Ogawa, H., Babinsky, H., Pätzold, M., Lutz, T.: Shock-Wave/Boundary-Layer Interaction Control Using Three-Dimensional Bumps for Transonic Wings. AIAA J. 46(6), 1442–1452 (2008)
6. Qin, N., Wong, W.S., LeMoigne, A.: Three-dimensional contour bumps for transonic wing drag reduction. Proc. IMechE, Part G: J 222(G5), 605–617 (2008)
7. Johanseen, J.: Prediction of Laminar/Turbulent Transition in Airfoil Flows, Risø-R-987(EN), Roskilde, Denmark (1997)
8. Jones, D.R., Schonlau, M., Welch, W.J.: Efficient Global Optimization of Expensive Black-Box Functions. Journal of Global Optimization 13 (1998)
9. Lee, J., Jameson, A.: Natural-Laminar-Flow Airfoil and Wing Design by Adjoint Method and Automatic Transition Prediction. In: AIAA 2009-897, Florida (2009)

An Investigation into Solver Strategies for the Modelling of Compressible Turbulent Flow

I. Asproulias, A.J. Revell, and T.J. Craft

1 Introduction

Sectors of the aerospace and energy industries are amongst those interested in the efficient computational prediction of supersonic flow for both internal and external flow applications; e.g. the internal flow through engines and intake ducts, flow through nozzles, jet thrust vectoring. Shockwaves pose a numerical challenge due to the associated steep gradients in the flow field. Further physical modelling challenges arise from the interactions of these shocks with turbulent boundary layers and separated flow regions; so called Shock Boundary Layer Interactions (SWBLI). The high Reynolds numbers of many such applications mean that industry generally employs Reynolds Averaged Navier-Stokes (RANS) based approaches for turbulence.

General purpose finite volume codes for incompressible flows usually solve the momentum and other transport equations in a segregated fashion, incorporating a pressure-correction scheme to achieve the coupling between velocity and pressure fields, e.g. SIMPLE [9], PISO [5]. Algorithms that are extensions of these solvers for handling compressible flows, described in [3], are referred to as 'pressure-based', and solve for the primary physical variables (ρ, U, e) at each time step or iteration. A second family of solvers, known as density-based solvers, solve instead for ρ, ρU and ρe. These have traditionally been adopted for compressible flows, being regarded as better in resolving shock characteristics since they directly solve for the conserved flow quantities.

This work aims to assess the capability of the different types of compressible solvers available in a popular CFD code to capture the steep-gradient regions and SWBLI effects. The different numerical schemes will first be tested on the inviscid shock tube before being applied to the flow over a compression ramp at 24°.

I. Asproulias · A.J. Revell · T.J. Craft
The School of MACE. The University of Manchester, George Begg Building, Manchester M13 9PL

2 Numerical Setup and Validation

The CFD code OpenFOAM is used for this study. The code includes two pressure-based solvers; *sonicFoam*, which solves the energy equation for total specific energy, e, outside of the pressure-velocity coupling loop and *rhoPisoFoam*, which solves for total specific enthalpy within the pressure-velocity coupling loop (both following the algorithm described in [3]). The code also provides two density-based solvers; *rhoSonicFoam*, in which any of the available convective schemes can be used and it is only for laminar calculations, and *rhoCentralDyMFoam*, which by default uses the Kurganov-Tadmor flux splitting schemes, which are constructed by a user selected Total Variation Diminishing (TVD) scheme. The *rhoCentralDyMFoam* solver can be used for turbulent calculations[1].

The available numerical options were first evaluated for the validation case of the shock tube. A uniform, orthogonal grid of 192 cells and a timestep size $\Delta t = 0.0002s$ was employed; mean and maximum Courant numbers were 0.009 and 0.737, respectively. The limited linear limiter was seen to be the least oscillatory, as shown in Figure 1, and was thus selected for subsequent investigations. A comparison of available solvers is also shown in Figure 1, where *sonicFoam*, *rhoPisoFoam* and *rhoSonicFoam* were used in combination with the limited linear limiter. For the construction of the Kurganov-Tadmor schemes, the van Leer limiter was used. The main conclusions that can be drawn are that the pressure-based solvers are more diffusive in the steep-gradient regions of the solution and fail to predict the correct height of the flat area of the solution in comparison with the density-based. The solver that best resolves the steep gradient regions is *rhoCentralDyMFoam*, which also gives the least oscillatory solution.

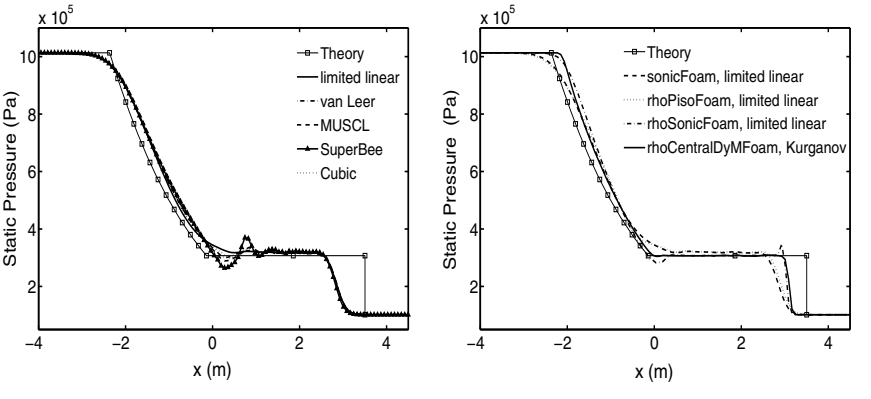

Fig. 1 Comparison of TVD limiters on the left using the pressure-based solver sonicFoam and comparison between the pressure-based and the density-based solvers on the right.

[1] In the case of the *sonicFoam*, *rhoPisoFoam* and *rhoSonicFoam* solvers the user can select among the available convective schemes, and for example the van Leer, SuperBee, limited linear, MUSCL and cubic limiters can be selected for the construction of a TVD scheme.

3 Compression Ramp 24°

The compression ramp is a traditional test case for SWBLI investigations and has been studied extensively; see for example [1, 4, 6, 11]. More recent measurements were made by [2] and [10] for the 24° ramp of [11] at freestream Mach, M_∞=2.9, and Reynolds number based on the momentum thickness $Re_\theta = 2400$; sufficiently small to be accessible for the DNS of [12] at the same flow conditions. These experimental and DNS data were used as the reference for the comparisons between the different RANS solvers in the present study.

The *sonicFoam* solver in combination with the limited linear limiter was used since both two pressure-based solvers have similar performance as shown in Figure 1, while the *rhoCentralDyMFoam* solver was chosen as the density-based solvers. Two turbulence models were used, the low-Reynolds number $k-\varepsilon$ of Launder-Sharma [7] (LS) and the $k-\omega$ SST [8]. For the calculation of the molecular viscosity the Sutherland law was used.

A flat plate boundary layer simulation with 1.5% freestream turbulence intensity was conducted in order to extract suitable inlet profiles for velocity and turbulence. The resultant boundary layer parameters, together with those reported from DNS and measurements, are shown in Table 1. At the wall no slip conditions were applied for the velocity, zero gradient for the pressure and the temperature was fixed at $307K$, as in DNS. At the top boundary zero gradient conditions were applied for all variables. At the outlet, supersonic outflow conditions were applied.

The dimensions of the computational domain is a 2D plane defined by [12], and a grid of up to 155×180 cells was used. In the streamwise direction grid points were clustered at the corner and in the wall normal direction were refined towards the wall; the non-dimensional wall-distance of the nearest node being around $y_w^+ = 0.9$. The timestep size was defined by the maximum Courant number, chosen as 0.2.

Table 1 Inlet conditions for the incoming turbulent boundary layer

	M	Re_θ	θ,mm	δ^*,mm	δ,mm	$C_f x 10^3$	$\rho_\infty, kg/m^3$	U_∞,m/s	T_∞,K	u_τ,m/s
Experiment [10]	2.9	2400	0.43	2.36	6.7	2.17	0.074	604.5	108.1	32.9
DNS [12]	2.9	2300	0.38	2.36	6.4	2.17	0.077	609.1	107.1	34.0
RANS LS	2.93	2390	0.383	1.4	4.7	2.22	0.076	608.9	106.9	33.6
RANS SST	2.92	2380	0.379	1.5	4.0	3.6	0.077	608.6	107.4	43.2

4 Results and Discussion

The deflection of the boundary layer on the inclined wall results in the formation of a shock wave, which imposes an adverse pressure gradient on the boundary layer and causes it to separate. The flow is deflected around the separation bubble and two compression fans arise, one in the separation region and an other one in the reattachment region, forming a λ-shock, which acts to the turbulence. These flow features are presented in Figure 2, where the contour plots of the mean Mach number and normalized Turbulence Kinetic Energy (TKE) are shown. The wall-pressure

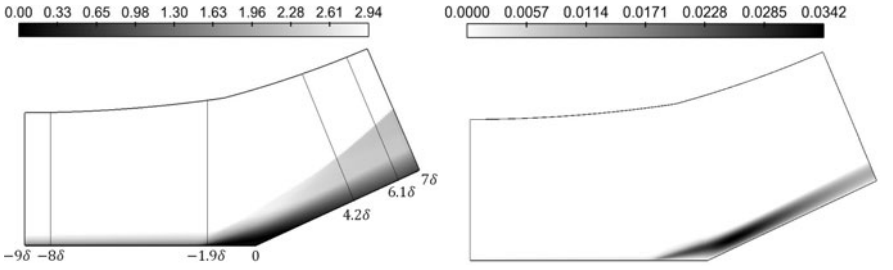

Fig. 2 Contour plots of Mach number on the left and normalized TKE k/U_∞^2 on the right.

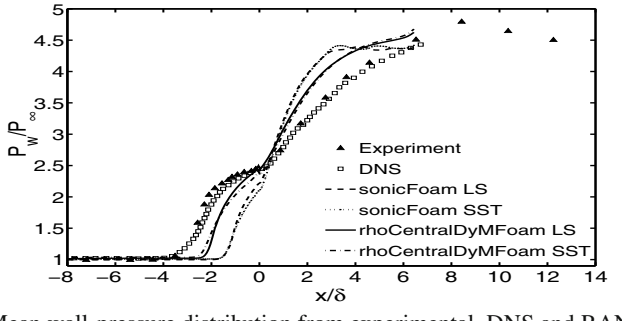

Fig. 3 Mean wall-pressure distribution from experimental, DNS and RANS data.

variation suggests that the pressure-based solver (PBS) predicts a rather later shock wave, and small separation region, while the density-based solver (DBS) provides somewhat better prediction as shown in Figure 3.

Figure 4 displays the profiles of mean velocity, TKE and Reynolds shear stress (uv), normalized with the boundary layer thickness and freestream velocity from the DNS. Each row of the figure corresponds to a different streamwise location $x/\delta = \{-8, -1.9, 4.2, 6.1\}$. At $x/\delta = -8$ both DBS and PBS return similar results, and the LS model predicts a lower peak of TKE than the DNS suggests, whilst the SST approximates it slightly better. At $x/\delta = -1.9$ the boundary layer profiles from DNS and the DBS show that the flow is nearly separated, while for the PBS the boundary layer is still in development stage. Therefore, better comparisons can be made between the DNS and DBS results. Both SST and LS separate later than DNS; the earlier adverse-pressure gradient in the case of the DNS causes a thickening of the boundary layer, introducing a steep-gradient boundary layer and resulting in higher TKE and uv levels in comparison with the RANS models. The SST separates earlier than LS, because of lower levels of uv near the wall upstream the separation point, which lead to lower values of eddy-viscosity and turbulent diffusion near the wall.

The boundary layer from the RANS models at $x/\delta = 4.2$ and 6.1 are in later stages of recovery than the DNS, since they reattach earlier. The DBS provides better mean velocity profile predictions, since the reattachment point is located further downstream than the PBS. TKE and uv are underpredicted by the RANS solvers,

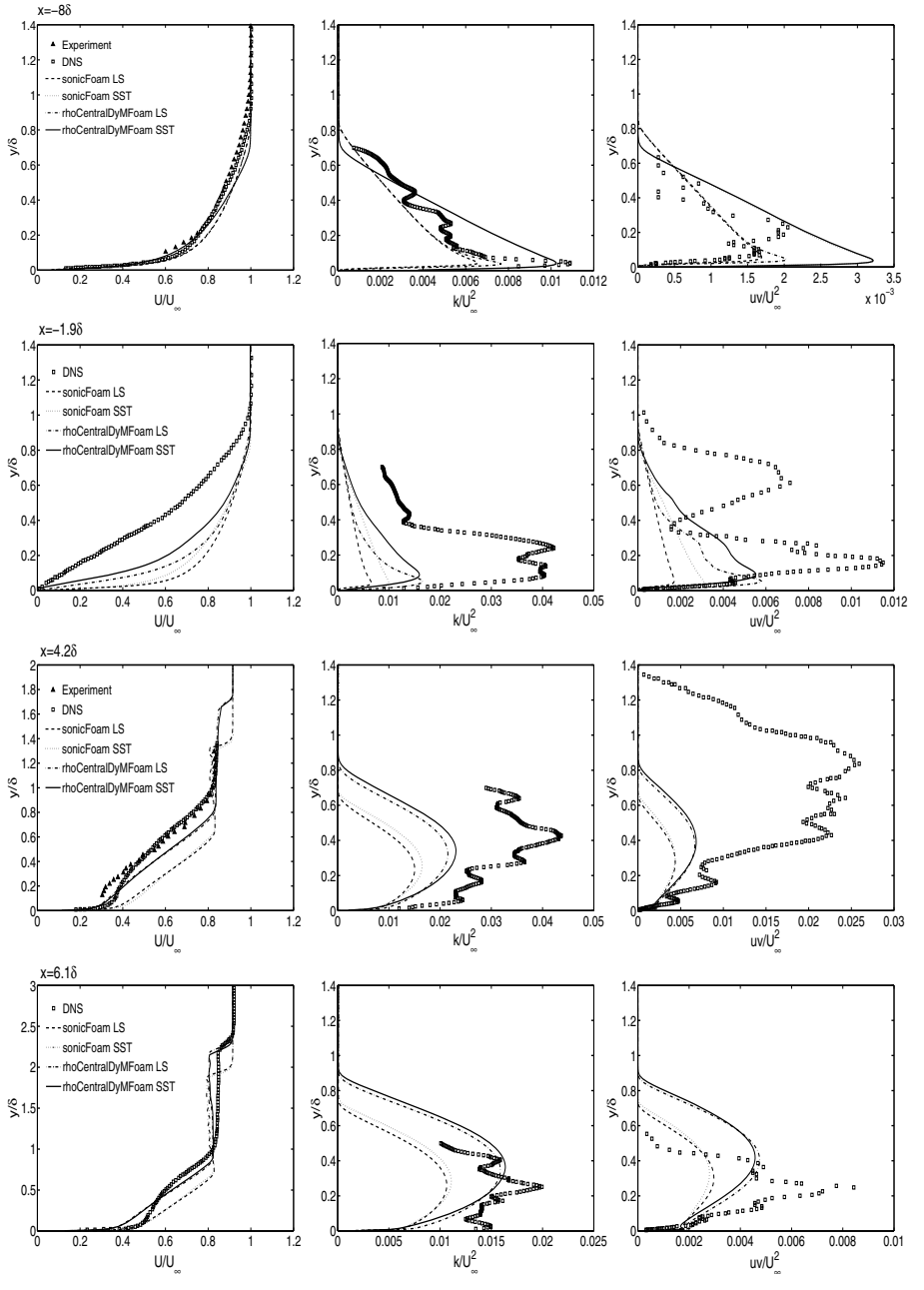

Fig. 4 Comparison of mean velocity (*left*), turbulent kinetic energy (*centre*) and Reynolds shear stress (*right*). Each row corresponds to a different streamwise location (indicated as lines on Fig. 2).

because of the earlier reattachment of flow and the underprediction of the turbulence amplification from the SWBLI, with the DBS giving the more accurate estimations. In the reattachment and recovery region the LS and SST give very similar estimations of the flow quantities. The stronger shock shown in the RANS profiles at $x/\delta = 6.1$ compared to the DNS suggests a more oblique shock in the latter case. The angle of the shock from RANS is $\sim 40^\circ$ from the flat wall, while the shock from DNS is $\sim 37^\circ$. In the case of the PBS the shock is located closer to the inclined wall, while for the DBS the shock location matches better that of the DNS. It should be noted that the TKE and Reynolds shear stress from the DNS data are rather noisy, possibly because of the small length of time over which averaging was done.

5 Conclusion

The density-based solvers are shown to be less diffusive in the steep-gradient regions of the flow than the pressure-based solvers. Additionally, the pressure-based solvers predict a rather later shock in comparison with the density-based solvers and the DNS. The density-based solver gives more accurate predictions for the shock location, the wall-pressure and the separation bubble. The discrepancies between the density-based solver and the DNS can be attributed to the different shock angle and can be linked to the turbulence modelling, since neither of the models used are able to capture the turbulence amplification and Reynolds stress anisotropy enhancement arising from the shock interactions.

References

1. Ardonceau, P.L.: The structure of turbulence in a supersonic shock-wave/boundary-layer interaction. AIAA Journal 22, 1254–1262 (1984)
2. Bookey, P.B., Wyckham, C., Smits, A.J., Martin, M.P.: New Experimental Data of STBLI at DNS/LES Accessible Reynolds Numbers. AIAA Paper 2005-309 (2005)
3. Demirdžić, I., Perić, M., Lilek, Ž.: A colocated finite volume method for predicting flows at all speeds. Int. J. Num. Meth. Fluids 16, 1029–1050 (1993)
4. Dolling, D.S., Murphy, M.T.: Unsteadiness of the Separation Shock Wave Structure in a Supersonic Compression Ramp Flowfield. AIAA Journal 21(12) (1983)
5. Issa, R.I.: Solution of the implicitly discretized fluid flow equations by operator-splitting. J. Comp. Physics 62, 40–65 (1986)
6. Kuntz, D.W., Amatucci, V.A., Addy, A.L.: Turbulent boundary-layer properties downstream of the shockwave/boundary-layer interaction. AIAA Journal 25, 668–675 (1987)
7. Launder, B.E., Sharma, B.I.: Application of the energy dissipation model of turbulence to the calculation of ows near a spinning disk. Letters in Heat and Mass Transfer 1, 131–138 (1974)

8. Menter, F., Esch, T.: Elements of Industrial Heat Transfer Prediction. In: 16th Brazilian Congress of Mechanical Engineering, COBEM (2001)
9. Patankar, S.V., Baliga, B.R.: A new Finite-Difference scheme for parabolic differential equations. Numerical Heat Transfer 1, 27 (1978)
10. Ringuette, M.J., Bookey, P., Wyckham, C., Smits, A.J.: Experimental Study of a Mach 3 Compression Ramp Interaction at $\Re_\theta = 2400$. AIAA Journal 47(2) (2009)
11. Settles, G.S., Bogdonoff, S.M., Vas, I.E.: Incipient separation of a supersonic turbulent-boundary-layer at high-Reynolds-numbers. AIAA Journal 14, 505 (1976)
12. Wu, M., Martin, M.P.: Direct Numerical Simulation of Supersonic Turbulent Boundary Layer over a Compression Ramp. AIAA Journal 45(4), 879–889 (2007)

An Application of Adaptive Mesh Refinement Method for Modeling of Nonstationary Hypersonic Flows in the Atmosphere

A. Astanin and E. Kharik

1 Introduction

Numerical modeling of flows with strong shock waves requires the use of fine meshes for an appropriate resolution. However, using high number of uniform grid cells might be time-consuming and require a large amount of computer resources. One of the way to weaken resources demands is using an adaptive mesh refinement (AMR) technique which tracks gradient of parameters in the cells [1] . A mesh is refined in the area of high gradients of solution, and a coarser grid is used in the case of low gradients.

In the present research, the AMR technique is applied to the study of the Tunguska like meteorite hypersonic impact. This event happened in 1908 in Siberia. Up to now the nature of the Tunguska meteorite is the subject of intensive discussions. The Tunguska impact caused vast destruction of the forest in the area of about 10^2 square km and was accompanied by explosion-like phenomena. The data of the observation were limited by the fallen trees and description of some witnesses. Thus, mathematically the problem on a Tunguska like meteorite study can be considered as a typical inverse problem. In the current paper an AMR-based algorithm was developed for 3D case.

2 Tunguska Meteorite Impact Physical and Mathematical Problem

The following model of the process [2] was used. The meteorite suddenly becomes a gas object at some point of its trajectory. It retains its volume and velocity at the initial time moment.

This assumption has been made on basis of following considerations. There have not been found any solid debris of the Tunguska meteorite despite numerous

A. Astanin · E. Kharik
Tomsk State University, Lenina Ave. 36, Tomsk, 634050, Russia

expeditions to the impact area. The entering of meteorites into a dense atmosphere is accompanied by its progressive destruction because of the hypersonic velocity of meteorite and, hence, the huge pressure. The aerodynamic loads leads to a sharp disintegration of the meteorite into smaller and smaller debris which retain approximately the same total volume [3] . Because the radius of each piece plummets, the heat transfer suddenly increases. As a result, the whole body is converted into vapor and kinetic energy of the meteorite is released into the atmosphere. This process happens almost instantaneously (in comparison to the time of the entire process). It is sometime called the "explosion-in-flight" [4] .

Thus, we arrive at the initial statement of the gas dynamic problem. At the initial time moment a gas in some volume V has the following parameters: $m_g = m_0$, $\rho_g = \rho_0$, $V_g = V_\infty$, $P_g = \rho(h)V_\infty^2$ where m_g, ρ_g, V_g, P_g are the mass, density, velocity and static pressure respectively; m_0,ρ_0,V_∞ are the mass, density and entrance velocity of the meteorite; $\rho(h)$ is the density of the atmosphere gas at height of the "explosion".

In the present research, the parameters of the meteorite are set the following: $m_0 = 216\,t$, $\rho_0 = 10^3\ kg \setminus m^3$ (ice body), the characteristic size of a body is $L = 60\,m$, $V_\infty = 2 \times 10^4\ m \setminus sec$. It is supposed that the meteorite enters the atmosphere at the angle of $\Theta = 45^o$. These data match "average" parameters accepted for Tunguska like meteorite. Under the chosen parameters, the ratio between the internal energy and the kinetic energy of the meteorite is equal to 4×10^{-4}. Grigorian's semi-analytical solution [3] is obtained for an exponential atmosphere $p(z) = \rho_0 \exp(-z/H)$. If $H = 7 \times 10^3\ m$, then it gives the following evaluation of the "explosion" height $h = 2.1 \times 10^4\ m$. The gas in the volume and in the atmosphere is considered as a not viscous gas with the state equation of the ideal gas [5].

The Euler equations for a compressible gas in Cartesian coordinate system (x,y,z,t) are:

$$U_t + E_x + F_y + G_z = Q\,. \tag{1}$$

In (1), $U = (\rho, \rho u_x, \rho u_y, \rho u_z, E)^T$, $E_x = (\rho u_x, \rho u_x^2 + p, \rho u_x u_y, \rho u_x u_z, (E+p)u_x)^T$, $F_y = (\rho u_y, \rho u_x u_y, \rho u_y^2 + p, \rho u_y u_z, (E+p)u_y)^T$, $G_z = (\rho u_z, \rho u_x u_z, \rho u_y u_z, \rho u_z^2 + p, (E+p)u_z)^T$, $Q = (0, \rho g_x, \rho g_y, \rho g_z, \rho \mathbf{g}\cdot\mathbf{u})^T$, ρ is the density; $\mathbf{u} = (u_x, u_y, u_z)^T$ is the velocity; $\mathbf{g} = (g_x, g_y, g_z)^T$ is the gravity vector; p is pressure; $E = \rho(\varepsilon + 0.5\mathbf{u}\cdot\mathbf{u})$ is the total internal energy, $\varepsilon = p/(\rho(k-1))$ is the specific internal energy, k is a adiabatic factor.

3 Essentials of the Numerical Method

The computational domain was oriented along the direction of body entrance. The coordinate system was oriented in space in such a way that the axis X was parallel to the entrance direction and the gravity force vector was in the plane XY. The problem has been solved by using the Godunov's method [6]. It enables to obtain generalized solutions. The algorithm has been tested on model tasks presented in [6].

Adaptive mesh is used in the numerical model. Finer cells are obtained by dividing cubic cell onto 8 equal subcells. Each subcell are possible to divide further and

the maximum of subcell level was 4. The cell fine criterion used in presented work is calculated from the following algorithm:

a) first derivatives are computed for each cell:

$$e_i = \max_{1 \le b \le B} \left(\frac{| \rho_i - \rho_b |}{\Delta x} + \frac{| p_i - p_b |}{\Delta x} \right) . \quad (2)$$

They show places where gas-dynamic features are situated. In (2), ρ_i, p_i - density and pressure of the current cell; ρ_b, p_b - density and pressure of a adjacent cell;Δx - distance between centers of cells; B -number of cells, situated around the current cell;

b) if $e_i \ge 5$, a cell is divided onto 8 subcells;

c) if $e_i \le 1$, a current cell is marked for integration. If this condition is true for all eight subcells in the cell, they will be integrated. The grid reconstruction was done an each odd time step.

Object-oriented programming language C++ has been used for writing the program. OpenMP model has been applied for acceleration of computations on multicore systems (http://openmp.org). Parallelizing application is achieved by adding appropriate controls to a code for compiler. It allows to reduce time of calculations significantly. The supercomputer SKIF-Cyberia installed in Tomsk State University has been used for obtaining the solution. One node containing two processors (Intel Xeon 5150, 2.6 GHz) with two cores has been used for computations. Also computations have been conducted on the computer of the Engineering Design Center of Tomsk State University. One node of it has two processors (Intel Xeon 5650, 2.6 GHz) with six cores.

4 Results

In the present research, the AMR technique is applied to the study of the meteorite hypersonic impact. The size of the computational area has been $2000 \times 1000 \times 1000$ meters. The body has been placed in the point $(500;500;500)$. Incoming boundary conditions have been set in compliance with the altitude. The density has been chosen according to International Standard Atmosphere. It has been approximated as

$$\begin{aligned} \rho(H) &= 1.23\,(1 - H/44300)^{4.256}, \quad H < 11000\,, \\ \rho(H) &= 0.365 \exp(-(H - 11000)/6340), \quad H \ge 11000 \end{aligned} \quad (3)$$

Contour plots of pressure and density logarithm are shown in Fig. 1 in the time $0.05sec$ (plane of section is XY). Logarithms of pressure and density are used for results presentation because of high gradients.

The computational grid for this time is shown in Fig. 2. The figure is turned by 45 degrees clockwise. One can see that fine cells track areas of sharp changes of gas parameters. The total number of cells is 4.8×10^6.

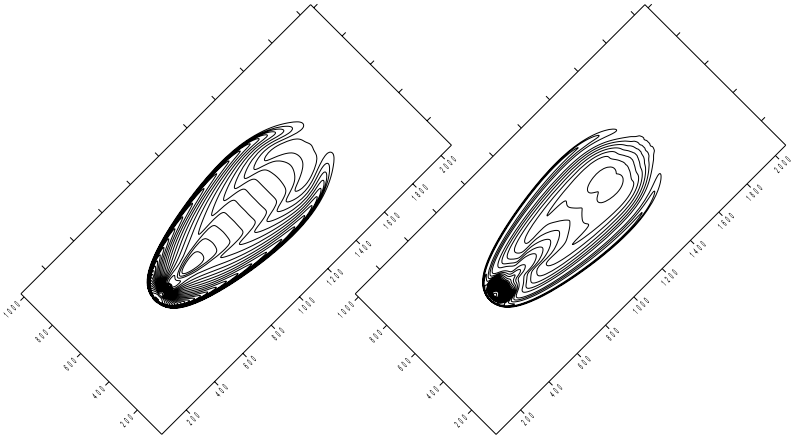

Fig. 1 Contour plots of pressure (left) and density (right) logarithm in the area for time $0.05sec$

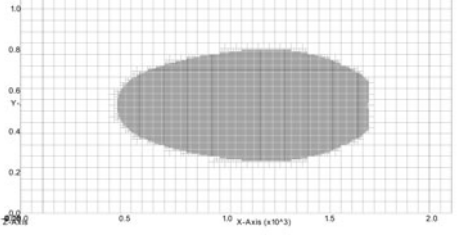

Fig. 2 Computational grid for time $0.05sec$

Contour plots of pressure and density logarithm are shown in Fig. 3 in the time $0.11sec$ (plane of section is XY). The trace has been reached right boundary. The pressure maximum is situated behind shock wave front. The results qualitatively are similar to the ones obtained in [5].

The computational grid for this time is shown in Fig. 4. The figure is turned by 45 degrees clockwise. The total number of cells is 14×10^6.

The distribution of density in the plane of section XY on the distance of 1300 meters is shown in Fig. 5. One can see that density inside the trace is smaller than density of surroundings. The low density trace is generated after the gas object flying with hypersonic speed. This channel could influence on rising of hot gas cloud, which appeared after object deceleration.

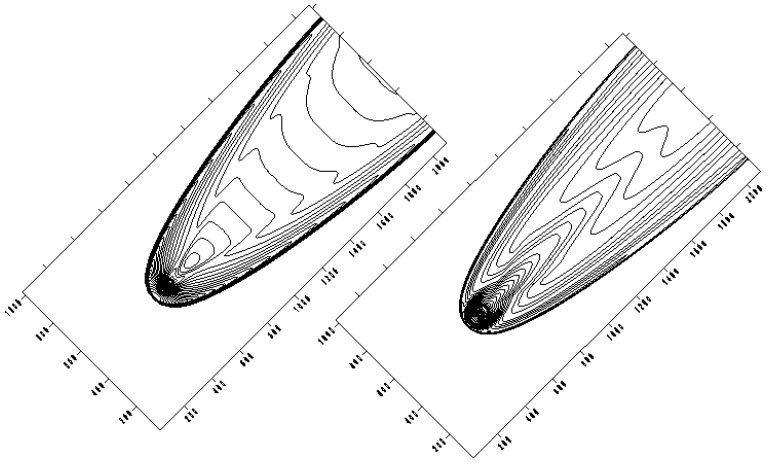

Fig. 3 Contour plots of pressure (left) and density (right) logarithm in the area for time 0.11*sec*

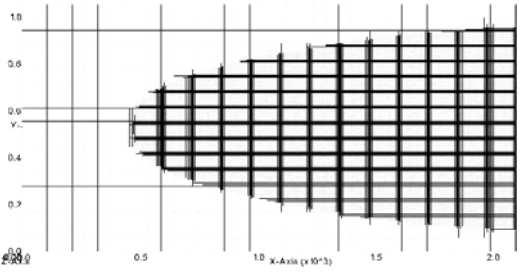

Fig. 4 Computational grid for time 0.11*sec*

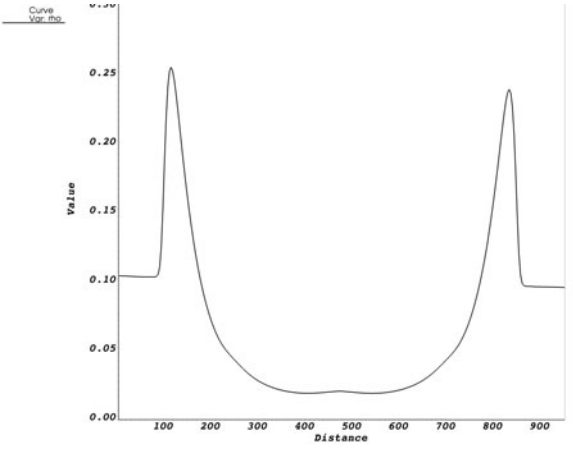

Fig. 5 Density distribution on the distance of 1300 meters in the plane of section *XY*

5 Conclusion

A numerical algorithm to construct 3D adaptive mesh refinement method has been developed. It has been implemented for solving the nonstationary 3D Euler equations for compressible flows with strong moving shock waves. The method can be extended to Navier-Stokes equations without any substantial modification . The developed approach has been applied to the study of hypersonic Tunguska like meteorite impact. The penetration of meteorite into the atmosphere has been modeled first 0.2 seconds after the cosmic body explosion. This consideration can also be related to the general problem of cometary-asteroid hazard.

References

1. Gil'manov, A.N.: Methods of adaptive meshes in gas dynamic problem, p. 247. Publishing Company Fizmatlit, Moscow (2000) (in Russian)
2. Utyuzhnikov, S.V., Konyukhov, A.V., et al.: Gas dynamical model of interaction between a meteorite and the Earth atmosphere. In: 2d IAA Intern. Conference on low-cost planetary missions. Preprints IAA-L-1 - IAA-L-6 (1996)
3. Grigoryan: On motion and destruction of meteors in planetary atmospheres. Cosmic Res. 17(2), 724–740 (1979)
4. Korobeinikov, V.P., Gusev, S.B., et al.: Flight and fracture of the Tunguska cosmic body into the Earth's atmosphere. Computers and Fluids 21, 323–330 (1992)
5. Utyuzhnikov, S.V., Rudenko, D.V.: An adaptive moving mesh method with application to non-stationary hypersonic flows in the atmosphere. Proceedings of the Institution of Mechanical Engineers, Part G: J of Aerospace Engineering 222(5), 661–671 (2008)
6. Godunov, S.K., Zabrodin, A.V., et al.: Numerical solution of multidimentional gas dynamics problems, p. 400. Publishing Company Fizmatlit, Moscow (1976) (in Russian)

Part XV
Propulsion

High Mach Number and Total Pressure Flow Conditions for Scramjet Testing

D.E. Gildfind, R.G. Morgan, M. McGilvray, and P.A. Jacobs

1 Introduction

Scramjet-powered access to space is expected to entail flight between Mach 5 and 15, along a dynamic pressure ascent trajectory of up to 2,000 psf (96 kPa) [1]. Scramjet engines typically need to be tested at sub-scale, even in the largest expansion tube facilities, and in these cases pressure-length (p-L) scaling is applied to maintain similarity for many flight parameters, including Reynolds number and binary reaction rates [2].

Assuming a constant 96 kPa dynamic pressure ascent trajectory, and that density and temperature vary in accordance with the American Standard Atmosphere, flow conditions for Mach 10, 12.5, and 15 flight have been calculated and are detailed in Table 1. Total pressure is calculated using NASA code CEA [3]. Total pressures for full and 1:10 scale models are shown, and it can be seen that these flow conditions are characterised by total pressures of the order of gigapascals.

Table 1 Target flow conditions for 2000 psf (96 kPa) constant dynamic pressure ascent trajectory (consistent with Hunt and Martin [1]).

				1:1 Model		1:10 Model	
Mach [-]	Altitude [km]	V [km/s]	h MJ/kg	p [kPa]	p_0 [GPa]	p [kPa]	p_0 [GPa]
10.0	29.1	3.01	4.76	1.37	0.129	13.7	1.28
12.5	32.1	3.79	7.41	0.876	0.616	8.76	6.01
15.0	34.6	4.61	10.9	0.608	2.55	6.08	24.2

Free-piston driven expansion tubes such as UQ's X2 and X3, which add total enthalpy and total pressure to the test gas through an unsteady expansion, are the only

D.E. Gildfind · R.G. Morgan · P.A. Jacobs
University of Queensland, St. Lucia, QLD, 4067, Australia

M. McGilvray
University of Oxford, Oxford, OX1 2JD, United Kingdom

current facilities which have the potential to achieve these very high total pressures. The smaller of these two facilities, X2, is currently being used as a proof-of-concept facility to develop these new flow conditions. Following successful completion of this initial study, work will transition to the larger and higher performance (in terms of model size and test time) X3 facility.

2 The X2 Expansion Tube with Tuned Driver

X2 is a free-piston driven expansion tube which is primarily used for simulation of hypervelocity flows between 6-10 km/s, although it has also been successfully used to simulate scramjet combustion at Mach 10 [4]. As part of the present study, preliminary attempts to produce a Mach 13 scramjet flow condition indicated the need to develop a new tuned driver for these proposed high total pressure flow conditions. The flow processes associated with shock-processing relatively dense test gases for these conditions take much longer, and the duration of time for which the driver supplies high pressure driver gas must correspondingly increase. Development of the new driver is described in [5].

For these flow conditions X2 was configured with a helium secondary driver. This consists of a tube filled with helium gas, located immediately downstream of the primary diaphragm and separated from the air test gas by a thin mylar diaphragm. The secondary driver is configured to achieve a sound speed increase across the expanded driver gas/driven gas interface. Morgan [6] showed that this sound speed increase produces a stronger shock in the test gas, thereby increasing total pressure, and also provides the acoustic buffer which Paull and Stalker [7] demonstrated is required to prevent the transmission of transverse acoustic noise from the expanded driver gas into the test gas.

The tuned driver condition X2-LWP-2.0mm-0 from [5] was used for flow condition development. A 100 kPa fill pressure was selected for the secondary driver. Driver configuration, and estimated properties of the primary driver gas following primary diaphragm rupture, are summarised in Table 2. Driver gas temperature has been estimated from experimentally measured shock speeds in the driven tube made during the driver commissioning process. For a 100 kPa helium secondary driver fill pressure, this results in a sound speed increase between the expanded primary driver gas and the secondary driver gas by a factor of 1.3, which satisfies the acoustic buffer requirement described by Paull and Stalker [7].

3 Theoretical Calculation of Tube Performance

Initial flow condition development work has been based around the free-piston primary driver and helium secondary driver configuration detailed in Section 2. This effectively limits the flow condition design variables to just the individual fill pressures in the shock and acceleration tubes (with air as the test and acceleration gases for scramjet testing). Based on these two variables, it was considered instructive to examine what range of conditions was theoretically available in X2 using the

new driver. This was achieved by using analytical techniques to predict the test flow properties for a wide range of shock and acceleration tube fill pressures, and mapping contours of test flow Mach number, velocity, and static pressure across this design space.

Table 2 Parameters for X2 tuned driver condition X2-LWP-2.0mm-0.

Compression tube length	4.4 m
Compression tube diameter	0.257 m
Driver tube diameter	0.085 m
Piston mass	10.5 kg
Reservoir fill pressure	6.85 MPa (air)
Compression tube fill pressure	92.8 kPa (80%He/20%Ar)
Primary diaphragm	2.0 mm cold rolled steel
Estimated rupture pressure	23.7 MPa
Estimated driver gas compression ratio	27.8
Estimated driver gas temperature	2,753 K

In order to improve the accuracy of predictions, the NASA equilibrium gas solver, CEA [3] was used to calculate equilibrium gas properties across normal shocks and through unsteady expansions. The calculations account for the possibility of either a reflected shock or unsteady expansion arising following primary shock arrival at the secondary and tertiary diaphragms. However, tube length, Mirels effect, and other secondary wave processes are ignored. This results in no further information about test time, for example.

For a fixed driver configuration, only two of the three parameters - Mach number, velocity, and static pressure - can be matched against the target flow conditions in Table 1. For the present study, Mach number and velocity were considered the most critical flow parameters to match. Three different target flow conditions are described in Table 3.

Table 3 Proposed scramjet flow conditions.

Flow Condition	Driver Condition	Secondary Driver Fill (kPa), He	Shock Tube Fill (kPa), air (unscaled)	Acceleration tube Fill (Pa), air (unscaled)	Shock Tube Fill (kPa), air (scaled)	Acceleration tube Fill (Pa), air (scaled)
x2-scr-m10p0-0	x2-lwp-2p0mm-0	100	345.4	144.1	690.8	288.2
x2-scr-m12p5-0	x2-lwp-2p0mm-0	100	210.1	29.0	420.2	58.0
x2-scr-m15p0-0	x2-lwp-2p0mm-0	100	132.1	6.8	251.0	12.9

4 1-D Analysis with `L1d2`

The 1-D Lagrangian flow solver `L1d2` [8] was used to assess the three flow conditions calculated analytically in the previous section, this time using actual tube

lengths and diaphragm positions. It was found that L1d2 shock speeds in the shock and acceleration tubes exceeded the analytical predictions for each flow condition.

Analytical and L1d2 shock speed estimates matched closely up until the shock tube, whereby the L1d2 prediction suddenly increased. This speed increase was attributed to the reflected shock at the secondary diaphragm. The test gas fill pressure is high for scramjet flow conditions, therefore a reflected shock typically forms when the primary shock reaches the test gas. This reflected shock was accounted for in the analytical calculations. However, the reflected shock continues to propagate upstream until it encounters the interface between the expanded primary driver gas and the shock-processed secondary driver gas, whereupon a compression wave forms which propagates downstream once more. When this compression wave reaches the primary shock, the shock speed increases, and part of the energy of the reflected shock is thus returned to the primary shock. The fill pressures in the shock and acceleration tubes were both scaled upwards by equal amounts to restore the shock speed to target values. The final (scaled) flow conditions are shown in Table 3.

5 Preliminary Experimental and 2-D CFD Results for the Mach 12.5 Condition

A 2D axisymmetric CFD analysis of the entire expansion tube was performed using the transient code Eilmer3 [9] for the Mach 12.5 (scaled) flow condition detailed in Table 3. The driver was modelled as a fixed volume with initial temperature and pressure corresponding to average properties calculated using L1d2 with full piston dynamics. Adjustments were made to these properties until shock speeds in the driven tube were in close agreement. The driver was made sufficiently long to ensure that the unsteady expansion from the driver did not interfere with downstream flow processes during the test time. The model incorporates equilibrium gas properties and the Baldwin-Lomax turbulence model.

Eilmer3 predicted test flow properties at the tube exit are shown in Figure 1 (red curves). It can be seen that there is a period of relatively steady test flow, arriving after the accelerator gas has passed, which is sustained for approximately 60μs. Comparison with Table 1 shows that velocity and Mach number are reasonably closely matched for the Mach 12.5 condition. Static pressure is approximately 10 kPa, which is over 10 times the target static pressure. This indicates the potential for $p-L$ scaling or the use of a nozzle to expand the core flow to a larger diameter. Finally, it can be seen that the predicted total pressure exceeds 2 GPa, demonstrating that this flow condition takes advantage of the unique total pressure capabilities of the expansion tube.

The green curves in Figure 1 show preliminary experimental results for the Mach 12.5 condition in X2. Static pressure on the tube wall adjacent to the exit compare very closely to the Eilmer3 prediction. Further, both traces are approximately steady, indicating that the secondary driver is successfully performing its acoustic buffer function to prevent driver gas noise penetrating the test gas. Pitot pressure midway between the tube centreline and wall compares well with the

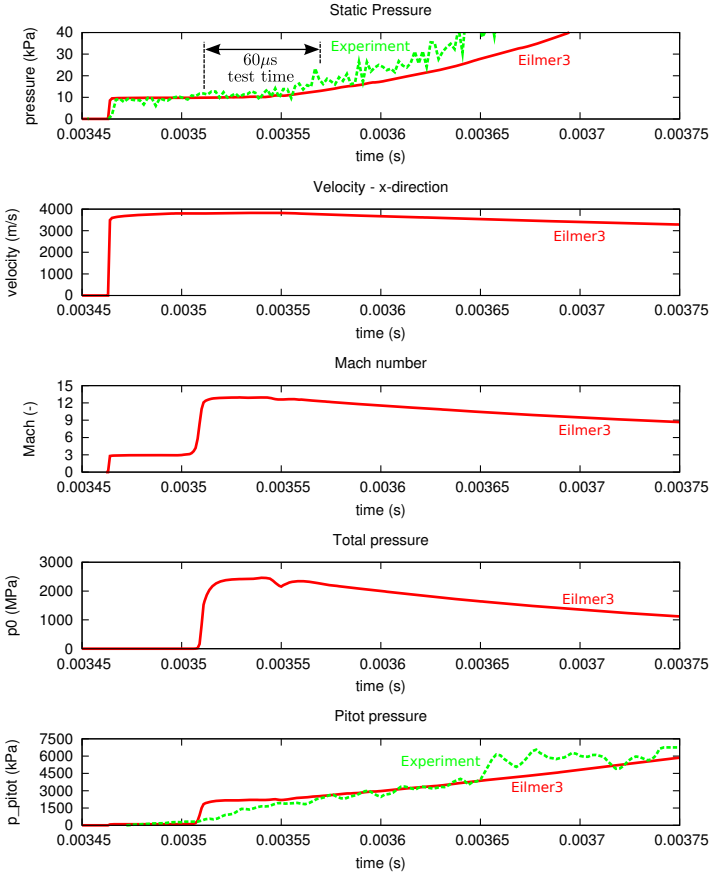

Fig. 1 Flow properties at tube exit for M12.5 flow condition in X2 from Table 3. CFD flow properties (red curves) are recorded 25 mm from tube centreline. Preliminary experimental pressure traces are shown by the dashed green curves. The experimental static pressure trace is measured at tube wall adjacent to exit; Pitot pressure is measured at approximately equivalent location to CFD result.

`Eilmer3` prediction, however the experimental Pitot pressure rise is delayed. This is a characteristic of the sensor arrangement. In order to protect the sensing element, restrictive ports are used to channel flow into the cavity containing the pressure sensor, and these take time to pressurise. This delayed response time can be problematic for measurement of expansion tube flows which typically have very low test times.

Average shock speeds along the tubes were estimated from the time of shock arrival at several sensor locations. These values matched quite closely the shock speeds calculated between corresponding locations in the CFD simulation.

Initial results from these Mach 12.5 experiments indicate that it is certainly viable to produce gigapascal total pressure scramjet flows in an expansion tube.

However, initial testing has also indicated several challenges which must be overcome to achieve these new conditions. These flows are severe, and placing instrumentation in the flow path is difficult in terms of balancing sensitivity with survivability, particularly with Pitot measurements. Further, it is proving difficult to isolate acceleration tube transducers from the severe longitudinal stress waves arising from the rapid deceleration of the piston at diaphragm rupture. For super-orbital conditions these stress waves arrive at the transducers after the test flow; for these scramjet conditions, the shock speeds are slower (especially in the dense air test gas), and these stress waves can cause considerable disruption to transducer responses.

6 Conclusion

This paper details the process used to develop high Mach number scramjet flow conditions for the X2 expansion tube configured with a new tuned free-piston driver. A three stage process based on analytical, 1-D CFD, and 2-D axisymmetric CFD techniques has been used to predict the necessary facility configuration parameters to achieve Mach 10, 12.5, and 15 scramjet flow conditions. Initial experimental results for a Mach 12.5 condition indicate that steady air test flows at gigapascal total pressures can be achieved using an expansion tube.

Acknowledgements. The authors wish to thank: Mr B. Loughrey and Mr F. De Beurs for X2 technical support; The Australian Research Council and The Queensland Smart State Research Facilities Fund 2005 for support and funding.

References

1. Hunt, J.L., Martin, J.G.: Rudiments and Methodology for Design and Analysis of Hypersonic Air-Breathing Vehicles. In: Curran, E.T., Murthy, S.N.B. (eds.) Scramjet Propulsion, vol. 189, pp. 939–978. AIAA (2000)
2. Hornung, H.G.: 28th Lanchester Memorial Lecture - Experimental real-gas hypersonics. Aeronautical Journal (December 1988)
3. Gordon, S., McBride, B.J.: Computer program for calculation of complex chemical equilibrium compositions and applications. Technical Report Reference Publication 1311, NASA (October 1994)
4. McGilvray, M.: The use of expansion tube facilities for scramjet testing. PhD Thesis, Centre for Hypersonics, Department of Mechanical Engineering, University of Queensland (2008)
5. Gildfind, D.E., Morgan, R.G., McGilvray, M., Jacobs, P.A., Stalker, R.J., Eichmann, T.N.: Free-Piston Driver Optimisation for Simulation of High Mach Number Scramjet Flow Conditions. In: 28th International Symposium on Shock Waves, July 17-22, University of Manchester, United Kingdom (accepted, 2011)
6. Morgan, R.G.: Free-Piston Driven Expansion Tubes. Handbook of Shock Waves 1, 603–622 (2001)

7. Paull, A., Stalker, R.J.: Test flow disturbances in an expansion tube. Journal of Fluid Mechanics 245, 493–521 (1992)
8. Jacobs, P.A.: L1d: A computer program for the simulation of transient-flow facilities. Report 1/99, Department of Mechanical Engineering, University of Queensland, Australia (1999)
9. Jacobs, P.A., Gollan, R.J.: The Eilmer3 Code: User Guide and Example Book. Mechanical Engineering Report 2008/07, University of Queensland (2009)

A Computational Study of Supersonic Combustion Relevant to Air–Breathing Engines

Christer Fureby, Ekaterina Fedina, and Jon Tegnér

1 Introduction and Background

The development of high–speed flight and space access vehicles requires the solution of many technical challenges associated with the comparatively small net thrust at supersonic or hypersonic flight speeds. One of the more essential issues is the design of an air–breathing propulsion system capable of operating over the wide range of Mach (Ma) numbers, desired to facilitate the advancement of high–speed flight and space access vehicles. At flight speeds above Ma≈3 turbofan engines fall short since the compressed air through the engine reaches such temperatures that the compressor stage fan blades begin to fail. Instead ramjet engines, in which the profile of the air intake guarantees that the supersonic approach flow is decelerated to a subsonic flow through the combustor, where fuel is injected prior to mixing, self-ignition and combustion, may be used. However, beyond Ma≈5 extreme temperatures and pressure losses occur when decelerating the supersonic airflow to subsonic conditions, making the ramjet unpractical at higher flight speeds. At flight speeds beyond Ma≈5, supersonic combustion ramjets, or scramjets, in which the flow trough the inlet and combustor remain supersonic may be used. Achieving high combustion efficiency under such conditions, with residence time on the order of 1 ms, places extreme demands on the inlet, combustor, fuel–injector as well as on the nozzle design, [1]. The mixing of fuel and air, the self–ignition and the flame stabilization are thus critical processes.

The prohibitive cost of flight–testing, difficulty in reproducing realistic flight conditions in ground facilities, the difficulties in measuring reacting flow quantities at supersonic speeds and the complexity of the aerothermodynamics involved make the use of Computational Fluid Dynamics (CFD) attractive for the analysis and design of high–speed flight vehicles. Conventional Reynolds Averaged Navier Stokes (RANS) models, [2], often provide no more than guidelines to the design

Christer Fureby · Ekaterina Fedina · Jon Tegnér
Defence Security Systems and Technology, Swedish Defence Research Agency – FOI, SE–147 25 Tumba, Stockholm, Sweden

of experiments, and the goal of using numerical simulations to analyze actual flight conditions still remains unreached. Large Eddy Simulation (LES) models, [3, 4], have been proposed as a promising alternative, having the potential to provide both qualitative and quantitative information. The aim of this study is to describe an LES model for high–speed combustion, validate it against experimental data, [5, 6, 7], and use the LES results to describe the underlying physical processes. The goal is to capture the flow physics at a level suitable for analysis, design and optimization of real high–speed flight vehicles, without resolving all of the detail of the flow.

2 LES Model for Supersonic Combustion

The LES model used consists of the balance equations of mass, species mass fractions, momentum and energy, describing advection, diffusion and reactions, [8]. The reactive gaseous mixture is modeled as a linear viscous fluid with Fourier heat conduction and Fickian diffusion, [8]. The viscosity is obtained from Sutherland's law and the thermal conductivity and species diffusivities follow from the viscosity and species (constant) Prandtl and Schmidt numbers, respectively. The mixtures thermal and caloric equations of state are derived under the assumption that each species is a thermally perfect fluid, with tabulated specific heats and formation enthalpies, [8]. The reaction rates are computed from Guldberg–Waage's law of mass action by summation over all participating reactions, with rate constants obtained from modified Arrhenius rate expressions, [10]. The range of scales present in turbulent reacting flows covers about eight orders of magnitude, [4], with the smaller scales being less energetic but important for the chemical kinetics. The LES model employed here is described in more detail in [11], and employs for closure the mixed subgrid flow model, [12], and the Partially Stirred Reactor (PaSR) subgrid turbulence chemistry interaction model, [13]. The LES equations are solved using a fully explicit finite volume scheme, based on the C++ library OpenFoam, [14], utilizing two–stage Runge–Kutta time–integration and monotonicity preserving flux reconstruction algorithms, [15]. The hydrogen (H_2) combustion is modeled by the 5–species 2–step global reaction mechanism of Rogers & Chinitz, [16], and the 8–species and 7–step reduced reaction mechanism of Davidenko et al, [17].

3 Validation and Physics Elucidation

The combustor, [5, 6, 7], consists of a one–sided divergent channel in which a wedge–shaped flameholder is fitted, at the base of which H_2 is injected through a single row of 15 injectors. The combustor has a width of 40 mm, an overall height of 50 mm and a total length of 340 mm, whereas the flameholder is 32 mm long, 6 mm high and located 100 mm downstream of the inlet. Following the work of Oevermann, [2], Fureby, [18] and Genin & Menon, [19], the freestream velocity of the vitiated air is 732 m/s, for a static pressure of 100 kPa and a static temperature of 340 K. The ports for the hydrogen injection system are choked, and the fuel is

assumed to have a velocity of 1200 m/s and static pressure and temperature of 100 kPa and 250 K, respectively.

Two computational configurations are used; the first consist of a narrow domain with three injectors and 6.3 Mcells whereas the second consists of a wide domain with all 15 injectors included and 22.5 Mcells. The grids are topologically similar, and clustered towards the walls, in the wake and around the shear layers. Dirichlet conditions are used for all variables at the inlet and at the H_2–jets at the base of the strut. At the outlet, all variable values are extrapolated from the interior. At the upper, lower, and strut walls, zero Dirichlet conditions are applied to the velocity together with a wall model, [20], whereas zero Neumann conditions are applied to all other variables. All computations are initialized with the state of the incoming air and are continued until the second order statistical moments have converged after about five flow through–times.

Figure 1a shows a perspective view of the combustor with the semi–transparent side–walls and an iso–surface of the vorticity magnitude colored by the temperature, whereas figures 1b and 1c show side views of numerical schlieren images of a non–reacting case with H_2 injection and of a reacting case, respectively. Figure 1a suggests that the reacting flow may be divided into an induction zone, in which turbulence determines the mixing and the progress of combustion, a transitional zone, dominated by coherent structures dynamics, convective mixing and exothermicity, and a turbulent combustion zone dominated by fully developed turbulence, turbulent mixing and lean post combustion. The H_2 jets discharge in the wake of the flameholder, but due to poor convective mixing across the shear layers the cold H_2, the cold air passing trough the combustor and the hot combustion products from downstream do not mix sufficiently until some distance downstream of the wake, where most of the heat release occurs. Unsteady combustion is also observed to take place in the shear layers, shed–off the edges of the flameholder, preventing the flame from blowing out. The vorticity initially consist of spanwise vortices shed off the flameholder but due vortex–stretching, volumetric expansion and interactions with reflected shocks, a less organized vorticity pattern rapidly develops that is dominated by a combination of longitudinal and distorted spanwise vortices. With inert H_2 injection, figure 1b, oblique shocks are formed at the tips of the flameholder that are reflected by the walls before interacting further with the unsteady, partly H_2 filled, wake. Together with the curved expansion fan coming off the base of the flameholder this causes a characteristic shock wave pattern further downstream. At the walls, the boundary layer is affected, at least locally, by the reflected oblique shocks. These local modifications involve thickening of the boundary layer, increased rms–pressure fluctuations, and elevated wall temperatures. With H_2 injection and combustion, figure 1c, the expansion fans at the upper and lower corners of the flameholder essentially vanish, whereas the recompression shocks become weaker as compared to the inert H_2 injection case. With combustion, the recirculation region becomes longer and wider, and serves as a flameholder for the H_2 diffusion flame. Good agreement is obtained between the predicted and experimental shadowgraph images presented in [7].

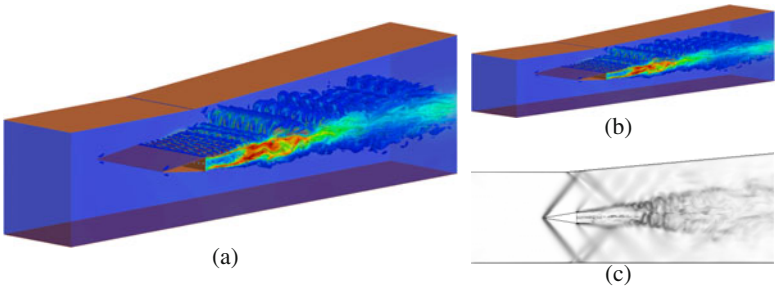

Fig. 1 Flow visualizations in terms of (a) vorticity magnitude colored by temperature and numerical schlieren of (b) non-reacting and (c) reacting case in the wide computational doamin.

In figure 2 we compare predicted and measured time–averaged axial velocity and temperature distributions across the combustor at four cross–sections downstream of the flameholder. Included in this comparison are also earlier LES results using a two–equation flamelet model, [18], with essentially the same laminar flame speed as the 2-step and 7-step reduced mechanisms used in the LES-PaSR simulations. Both the time–averaged axial velocity and temperature show satisfactory agreement with the experimental data for all models investigated, but with the flamelet model performing the least accurate and the 7–step PaSR model performing the most accurate. This suggests that the chemistry by itself is important and that also the resolved turbulence chemistry interactions play a main role in this flow, as can be understood from noticing that the time–scales of the chemistry and the flow are similar. Furthermore, by comparing the 7–step PaSR LES predications in the narrow and wide domains with the experimental data, we find the best overall agreement for the 7–step PaSR LES on the wide domain, in spite of that domain having a coarser grid resolution than the narrow domain. The reason for this is that the spanwise extent of the computational domain must be sufficiently large for spanwise instabilities to develop, and for a sufficient number of longitudinal vortex structures to be maintained in order to support the fully turbulent flow far downstream. In general, all LES presented here tend to underpredict the mean width of the wake at x/h=20.8 and overpredict time–averaged temperatures in the shear layers at x/h=13.0. The agreement between the measured and predicted time–averaged axial velocity profiles at x/h=13.0 is only fair, perhaps due to difficulties in performing accurate measurements in the highly turbulent wake region. Far downstream, at x/h=38.8, only the 7–step PaSR predictions in the narrow and wide domains are able to reproduce the time–averaged temperature, supporting the aforementioned importance of the the chemistry and the resolved turbulence chemistry interactions.

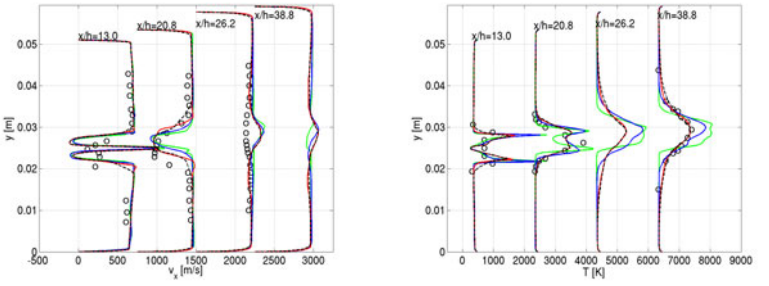

(a) (b)

Fig. 2 Comparison of time averaged (a) axial velocity and (b) temperature profiles across the combustor at four different cross-sections x/h with h being the height of the flameholder. Legend: (○) experimental data, [7], (–) LES using a two–equation flamelet model, [18], (–) LES using a 2–step PaSR model in the narrow domain, (–) LES using a 7–step PaSR model in the narrow domain and (–) LES using a 7–step PaSR model in the wide domain.

4 Summary and Concluding Remarks

In the present work LES has been used to investigate mixing and combustion in a scramjet engine model under realistic operating conditions. Two different LES combustion models have been tested; a flamelet model and a PaSR model, and two different computational domains have been used; a narrow domain with three injectors and a wide domain with 15 injectors. Two different chemical reaction mechanisms have been used together with the LES–PaSR model; a 2–step global mechanism and a 7–step reduced mechanism. Best agreement between experimental data for the time–averaged velocity and temperature is obtained for the 7–step LES PaSR model, with particular good agreement observed in the wide computational domain, due to maintained spanwise development of flow instabilities. The flow physics analysis revealed that most of the heat–release occur downstream of the wake due insufficient mixing across the shear layers. Unsteady (or intermittent) combustion is however observed in the shear layers, thereby essentially preventing the flame from blowing out.

Acknowledgments. The presented work was supported by the Swedish Armed Forces and the Swedish Defense Material Agency and we also acknowledge the DLR Institute of Space Propulsion, Lampoldshausen for providing the experimental data.

References

1. Curran, E., Murthy, S. (eds.): Scramjet Propulsion, ch. 189. AIAA (2000)
2. Oevermann, M.: Aerosp. Sci. Tech. 4, 463 (2000)
3. Ladiende, F. (ed.): Special issue on Scramjet Combustion Technology (2010)
4. Menon, S., Fureby, C.: Computational Combustion. John Wiley & Sons (2010)
5. Oschwald, M., Guerra, R., Waidmann, W.: Int. Symp. on Special topics in Chem. Prop., p. 498 (1993)

6. Waidmann, W., Brummund, U., Nuding, J.: 8th Int. Symp. on Transp. Phenom. in Comb., p. 1473 (1995)
7. Waidmann, W., Alff, F., Brummund, U., Böhm, M., Clauss, W., Oschwald, M.: Space Tech. 15, 421 (1995)
8. Oran, E., Boris, J.: Numerical Simulation of Reactive Flow. Cambridge University Press, Cambridge (2001)
9. Poinsot, T., Veynante, D.: Theoretical and Numerical Combustion. R. T. Edwards, Philadelphia (2001)
10. Levine, R.: Molecular Reaction Dynamics. Cambridge University Press, Cambridge (2005)
11. Berglund, M., Fedina, E., Fureby, C., Tegner, J., Sabel'nikov, V.: AIAA Journal 48, 540 (2010)
12. Bensow, R., Fureby, C.: J. Turb. 8 (2007)
13. Baudoin, E., Nogenmyr, K., Bai, X., Fureby, C.: AIAA 2009-1178 (2009)
14. Weller, H., Tabor, G., Jasak, H., Fureby, C.: Comp. in Physics 12, 629 (1997)
15. Drikakis, D., Hahn, M., Grinstein, F., DeVore, C., Fureby, C., Liefvendahl, M., Youngs, D.: Numerics for ILES: Limiting Algorithms, ch. 4a. Cambridge University Press (2007)
16. Rogers, R., Chinitz, W.: AIAA Journal 21, 586 (1983)
17. Davidenko, D., Gökalp, I., Dufour, E., Marge, P.: 14th AIAA/AHI Space Planes and Hypersonic Systems and Technologies Conference (2006)
18. Berglund, M., Fureby, C.: 31st Int. Symp. on Comb. p. 2491 (2006)
19. Genin, F., Menon, S.: AIAA 2009-0132 (2009)
20. Fureby, C.: Ercoftac Bulletin. Marsh Issue (2007)

On Thermodynamic Cycles for Detonation Engines

R. Vutthivithayarak, E.M. Braun, and F.K. Lu

1 Introduction

Detonation engines are considered to potentially yield better performance than existing turbo-engines in terms of improved thermodynamic efficiency, simplicity of manufacture and operation, and high thrust-to-weight or thrust-to-volume ratio, amongst other advantages. Much effort has been put into the development of pulsed detonation engines (PDEs), including thermodynamic cycle analysis. Thermodynamic analysis of PDEs usually makes use of one-dimensional models, based on the Chapman–Jouguet (CJ) and the Zeldovich–von Neumann–Döring (ZND) theories, although increasingly sophisticated techniques, some involving numerical modeling, have also been developed lately. It is now understood that the Humphrey cycle used to model an isochoric cycle underpredicts the performance of a PDE [1]–[4]. The so-called Fickett–Jacobs (FJ) cycle is based on the CJ model. While an improvement over the Humphrey cycle, its reliance on the CJ model means that it fails to account for the physics espoused by the ZND model [1, 2]. In this paper, a discussion of the Humphrey and FJ cycles is given and the proper ZND cycle is suggested. These cycles are illustrated with a hydrogen/air mixture initially at STP. The use of a generic heat release parameter to construct the ZND cycle is provided.

2 The Humphrey Cycle

Figure 1 shows the three ideal processes under discussion in both the p–v and T–s diagrams. The states portrayed in the plots are the total (or stagnation) states. The initial state of the reactants is (1). The hugoniot running through (1) is shown in Fig. 1 as a dashed line. The post-detonation hugoniot is also shown in the figure by

R. Vutthivithayarak · E.M. Braun · F.K. Lu
Aerodynamics Research Center, Mechanical and Aerospace Engineering Department, University of Texas at Arlington, Arlington, Texas 76019, USA

another dashed line. This hugoniot was obtained using data obtained from the NASA CEA code [5]. The data indicate a dimensionless heat release $\alpha = q\rho_1/p_1 = 27.28$.

Consider first the constant volume, Humphrey cycle [6] which bas been proposed as a surrogate for the PDE cycle perhaps due to its simplicity [2, 3, 7]–[14]. In this process, the working fluid is assumed to be compressed isochorically to state (2H) where $p_{2H} = 0.8$ MPa and $T_{2H} = 2550$ K. The fluid is then expanded isentropically to reach (3H) where $p_{3H} = 0.1$ MPa and $T_{3H} = 1520$ K. The increase in entropy from (1) to (3H) is $\Delta s = 3.08$ kJ/(kg · K). The cycle is closed by a fictitious isobaric process $(3H) \rightarrow (1)$ of heat rejection to the open ambient conditions. A single value of specific heat ratio $\gamma = 1.242$ appears sufficient for such an analysis but with $R = 348$ kJ/(kg · K) and 396 kJ/(kg · K) for the isochoric compression and for the isentropic expansion respectively.

3 The FJ Cycle

The FJ cycle is based on the CJ detonation model. As can be seen in Fig. 1, the cycle consists of a compression process that brings the gas from state (1) to state (2CJ). This process is strictly a nonequilibrium one. However, within the one-dimensional model of the detonation process, this process is identical to Rayleigh heating and thus can be regarded to be a process that is in local thermodynamic equilibrium [15]. Isentropic expansion occurs between (2CJ) and (3CJ) after which the cycle is closed by a fictitious isobaric process to the initial state.

For this study, the detonation process raises the pressure to $p_{2CJ} = 1.5$ MPa and decreases the specific volume to $v_{2CJ} = 0.67$ m^3/kg with the same dimensionless heat release $\alpha = 27.28$ as for the Humphrey cycle. The isentropic expansion from (2CJ) to (3CJ) yields $p_{3CJ} = 0.1$ MPa and $v_{3CJ} = 5.92$ m^3/kg respectively. Finally, a fictitious isobaric process returns both pressure and specific volume to the initial state.

While the calculations of (p_{2CJ}, v_{2CJ}) are straightforward, (T_{2CJ}, s_{2CJ}) are more complicated to determine. The value of the gas constant changes from $(1')$ to (2CJ) as, for example, in computations using Cantera [17]. For simplicity, it was found that a linear variation of R between the value at state $(1')$ and (2CJ) is accurate for modeling the nonequilibrium heat release, which coincided with the equilibrium Rayleigh heat release [16]. The temperature rises from the ZND value of 1545 K to 2920 K and the entropy rises by 3.12 kJ/(kg · K). The gas then expands isentropically from (2CJ) to (3CJ). State (3CJ) is different from state (3H) because the isentropic expansions arise from the different states (2CJ) and (2H) state, respectively. The values of p_{3CJ}, v_{3CJ} and T_{3CJ} are 0.1 MPa, 5.922 m^3/kg and 1562 K respectively.

4 The ZND Cycle

ZND theory captures the physics of a one-dimensional detonation wave. In this theory, the gas is shock compressed to the von Neumann spike, followed by

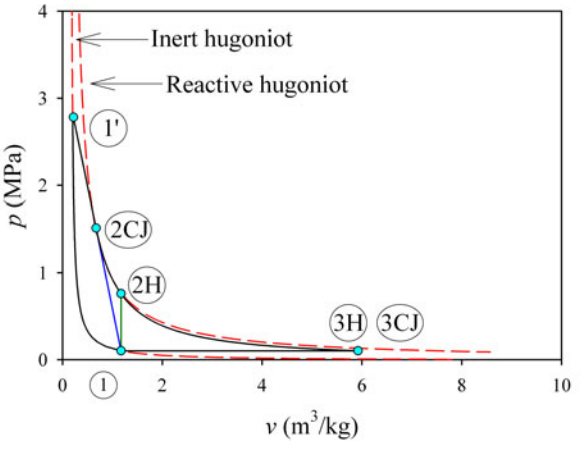

(a) p–v diagram

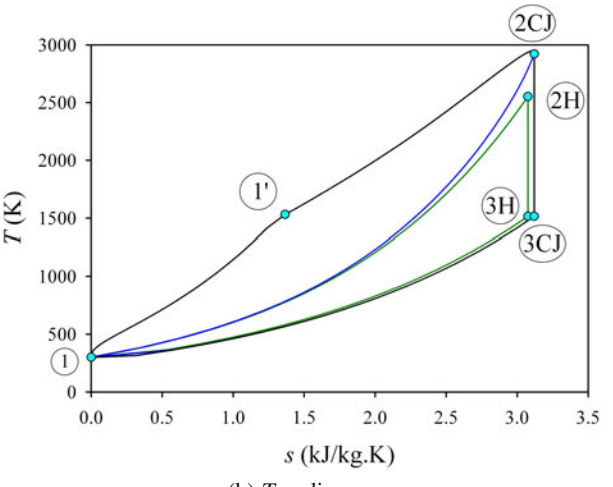

(b) T–s diagram

Fig. 1 Ideal Humphrey ($1 \rightarrow 2H \rightarrow 3H \rightarrow 1$), FJ ($1 \rightarrow 2CJ \rightarrow 3CJ \rightarrow 1$) and ZND ($1 \rightarrow 1' \rightarrow 2CJ \rightarrow 3CJ \rightarrow 1$) cycles for a stoichiometric hydrogen/air mixture initially at STP.

exothermic chemical reactions. The shock compression is assumed to proceed along the inert hugoniot which is equivalent to assuming local thermodynamic equilibrium. The subsequent heat release from exothermic chemical reactions, even though a nonequilibrium process, is identical to that of Rayleigh heating [15] and brings the gas to the CJ state. (In fact, the CJ point is the tangent point from the initial point to the ZND point in the p–v diagram.)

The FJ model fails to account for the physics of a detonation process where shock compression does not increase the pressure directly to the CJ point. Instead, the

shock raises the pressure to the ZND point, commonly called the von Neumann spike. The pressure then decreases to the CJ value due to supersonic Rayleigh heating. It therefore appears that the ZND cycle, also called the PDE cycle in the literature, is the most appropriate one amongst the three cycles evaluated in this paper.

In this example where the stoichiometric hydrogen/air mixture is initially at STP, calculations using Cantera yields the postshock pressure and specific volume as 2.8 MPa and 0.22 m^3/kg respectively. The subsequent CJ value is the same as the FJ cycle reported above. This is followed by the same isentropic expansion as the FJ cycle, followed by a fictitious isobaric process to close the cycle.

For the particular example of a stoichiometric hydrogen/air mixture initially at STP, the shock compression to the ZND point raises the temperature to 1531 K with an entropy increase to 1.366 $kJ/(kg \cdot K)$. The heat addition that brings the gas from the ZND to the CJ point raises the temperature to 2920 K with a further increase of entropy to 3.12 $kJ/(kg \cdot K)$. From Cantera, the gas constant at these two points are 397.6 and 348.22 $kJ/(kg \cdot K)$ respectively. The isentropic expansion to 1 atm lowers the gs temperature to 1515 K. Finally, a fictitious isobaric process closes the cycle.

5 Comparison between the Humphrey, FJ and ZND Cycles

Experimental observations indicate that the detonation front is actually a complex, three-dimensional surface that defies any simplified analytical description. Thus, despite the one-dimensional nature of the ZND model, it is presently acceptable for engineering analysis. In this section, a comparison is provided on the discrepancy in estimating the net work by the Humphrey and FJ cycles when compared to the ZND cycle. The cyclic specific net work produced, the cyclic specific heat input and the efficiency are given by

$$w_{out} = \oint P_t dv \tag{1}$$

$$q_{t,in} = \oint T_t \, ds \tag{2}$$

$$\eta = w_{out}/q_{t,in} \tag{3}$$

In the above, the subscript t is used to indicate that it is the total property that is considered. This distinction may not be required in usual thermodynamic cycle analysis. However, the kinetic energy in the detonation wave is a substantial portion of the total enthalpy that is available for energy conversion. A more detailed first- and second-law analysis exchange is planned. For the present, it can be stated that the ZND cycle accounts for the energy in the shock wave while the Humphrey and FJ cycles do not, these two only accounting for heat addition. The respective data for the stoichiometric oxyhydrogen example are displayed in Table 1. The table shows that there is a large underestimation in performance parameters. These differences will likely affect the entire thermodynamic system. For example, these differences for a power production system will affect the design of the power generator and the

heat exchanger. For a propulsion system, paramount considerations of weight and volume may cause these to be too conservatively estimated.

Table 1 Performance Comparisons

	Humphrey	Fickett Jacobs	Zel'dovich von Neumann Döring
Work (MJ/kg)	0.709	0.834	2.08
Heat (MJ/kg)	1.07	1.3	2.95
Efficiency (%)	66.5	64.3	70

6 Conclusions

An evaluation of the relative merits and shortfalls of three different models for engineering analysis of pulse detonation engines was briefly given. While simple to implement, the constant volume, or Humphrey, cycle does not adequately capture the physics of the detonation phenomenon to provide a realistic estimate of the work. A more sophisticated model to account for the pressure rise in a detonation wave, known as the Fickett–Jacobs model, also underestimates the work. Finally, the Zel'dovich–von Neumann–Döring model appears to be the most appropriate one for use in cycle analysis of pulse detonation engines. While the shock process is a nonequilibrium one, the assumption of local thermodynamic equilibrium makes the cycle analysis tractable. Similarly, the heat release due to exothermic reactions between the ZND and CJ points was found to follow supersonic Rayleigh heating and thus could be modeled as an equilibrium process. Future work includes developing a general cycle analysis for either an airbreathing or a rocket propulsion system based on the approach found in Mattingly [1].

References

1. Mattingly, J.D.: Elements of Propulsion: Gas Turbines and Rockets. AIAA, Reston (2006)
2. Heiser, W.H., Pratt, D.T.: Thermodynamic Cycle Analysis of Pulse Detonation Engines. J. Propul. Power 18(1), 68–76 (2002)
3. Kentfield, J.A.C.: Fundamentals of Idealized Airbreathing Pulse-Detonation Engines. J. Propul. Power 18(1), 77–83 (2002)
4. Wu, Y., Ma, F., Yang, V.: System Performance and Thermodynamic Cycle Analysis of Airbreathing Pulse Detonation Engines. J. Propul. Power 18(4), 556–567 (2003)
5. Gordon, S., McBride, B.J. (1994), Computer Program for Calculation of Complex Chemical Equilibrium Compositions and Applications. I. Analysis. NASA RP-1311, http://cea.grc.nasa.gov/

6. Humphrey, H.A.: An Internal-Combustion Pump, and Other Applications of a New Principle. Proc. Inst. Mech. Eng. 77(1), 1075–1200 (1909)
7. Bussing, T.R.A., Pappas, G.: Pulse Detonation Engine Theory and Concepts. In: Murthy, S.N.B., Curran, E.T. (eds.) Developments in High-Speed Vehicle Propulsion Systems, pp. 421–472. AIAA, Reston (1996)
8. Eidelman, S., Yang, X.: Analysis of the Pulse Detonation Engine Efficiency. AIAA Paper 98–3877 (1998)
9. Hutchins, T.E., Metghalchi, M.: Energy and Exergy Analyses of the Pulse Detonation Engine. J. Eng. Gas Turbines Power 125(4), 1075–1080 (2002)
10. Talley, D.G., Coy, E.B.: Constant Volume Limit of Pulsed Propulsion for a Constant Gamma Ideal Gas. J. Propul. Power 18(2), 400–406 (2002)
11. Harris, P.G., Stowe, R.A., Ripley, R.C., Guzik, S.M.: Pulse Detonation Engine as a Ramjet Replacement. J. Propul. Power 22(2), 462–473 (2006)
12. Wintenberger, E., Shepherd, J.E.: Model for the Performance of Airbreathing Pulse-Detonation Engines. J. Propul. Power 22(3), 593–603 (2006)
13. Bellini, R., Lu, F.K.: Exergy Analysis of a Pulse Detonation Power Device. J. Propul. Power 26(4), 875–878 (2010)
14. Li, J.L., Fan, W., Wang, Y.Q., Qiu, H., Yan, C.J.: Performance Analysis of the Pulse Detonation Rocket Engine Based on Constant Volume Cycle Model. Appl. Thermal Eng. 30(11-12), 1496–1504 (2010)
15. Rao, S.: Effect of Friction on the Zel'dovich–von Neumann–Döring to Chapman–Jouguet Transition. MSAE thesis, Univ Texas Arlington (2010)
16. Vutthivithayarak, R.: Analysis of Pulse Detonation Turbojet Engines. Ph.D. dissertation, Univ Texas Arlington (2011)
17. Goodwin, D.: Cantera: Object-Oriented Software for Reacting Flows (2010), http://code.google.com/p/cantera/

External and Internal Configurations of the 14-X Hypersonic Aerospace Vehicle

F.J. Costa, D. Romanelli Pinto, T.V.C. Marcos, M.A.S. Minucci,
P.G.P. Toro, and E.P. Mergulhão Dias

1 Introduction

Today the access to space is done, only, by multi-stage rocket-powered vehicles, which have flown hypersonically, carrying their own propellant (solid and/or liquid, oxidizer along with fuel) to propel payloads and astronauts to Earth's orbit.

The modern aerospace vehicles utilize multi-stage propulsion system on board, in general not reusable, of combustion chemistry (solid propulsion and / or liquid propulsion), extracting and converting chemical energy into kinetic energy with 97-98% efficiency. Approximately 89% of the weight of the spacecraft at time of launch, is due to the propulsion system be part of the vehicle , with only 1 to 2.5% due to the payload , usually satellites.

A new generation of scientific aerospace vehicles, using advanced hypersonic airbreathing propulsion based on supersonic combustion technology, is in development at several research centers [1]. This new propulsion system (scramjets) is economically and ecologically more attractive than the conventional rocket propulsion.

2 Brazilian 14-X Hypersonic Aerospace Vehicle

The Brazilian 14-X Hypersonic Aerospace Vehicle, designed by Rolim et al. [2], Fig. 1, at the Prof. Henry T. Nagamatsu Laboratory of Aerothermodynamics and Hypersonics, Fig.2, at the Institute for Advanced Studies (IEAv), is part of the continuing effort of the Department of Aerospace Science and Technology (DCTA), to develop a technological demonstrator using: i) "waverider" technology to provide lift to the aerospace vehicle, and ii) "scramjet" technology to provide hypersonic airbreathing propulsion system based on supersonic combustion.

F.J. Costa · D. Romanelli Pinto · T.V.C. Marcos · M.A.S. Minucci · P.G.P. Toro · E.P. Mergulhão Dias
Prof. Henry T. Nagamatsu Laboratory of Aerothermodynamics and Hypersonics
Institute for Advanced Studies
Rodovia dos Tamoios km 5,5 12228-001 São José dos Campos, SP(BR)

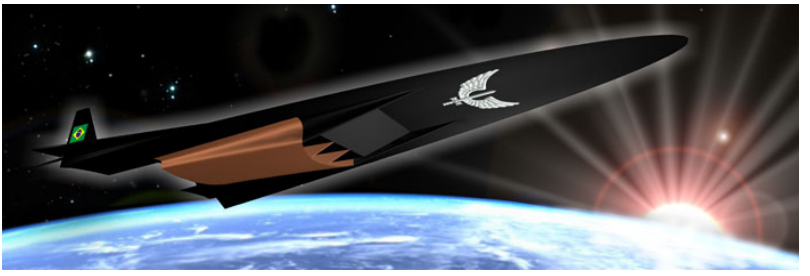

Fig. 1 Brazilian 14-X Hypersonic Aerospace Vehicle.

A waverider vehicle may be defined as a supersonic or a hypersonic vehicle which uses the high pressure zone on its lower surface caused by leading-edge attached shock wave to generate lift surface. Therefore, the attached shock wave in a sharp leading edge isolates the high pressure zone (lower surface) from the low pressure zone (upper surface), which inhibits the flow spillage. In general, the upper surface is aligned with the free stream hypersonic flow. Atmospheric air, precompressed by the leading-edge attached shock wave, which lies between the sharp attached leading edge shock wave and lower vehicle surface may be used in hypersonic airbreathing propulsion system based on ”scramjet” technology.

Hypersonic airbreathing propulsion, that uses supersonic combustion ramjet (scramjet) technology, offers substantial advantages to improve performance of aerospace vehicle that flies at hypersonic speeds through the Earth’s atmosphere, by reducing onboard fuel [4]. Basically, scramjet is a fully integrated airbreathing aeronautical engine that uses the oblique/conical shock waves generated during the hypersonic flight, to promote compression and deceleration of freestream atmospheric air at the inlet of the scramjet. Fuel, at least sonic speed, may be injected into the supersonic airflow just downstream of the inlet. Right after, both oxygen from the atmosphere and on-board fuel are mixing. The combination of the high energies of the fuel and of the oncoming supersonic airflow the combustion at supersonic speed starts. Finally, the divergent exhaust nozzle at the afterbody vehicle accelerates the exhaust gases, creating thrust.

The 14-X Brazilian Hypersonic Aerospace Vehicle project is planned to be accomplished in three phases: project definition, research engine development and atmospheric free flight test using rocket engines as accelerator to the scramjet operation.

3 Brazilian 14-X Hypersonic Aerospace Vehicle External Configuration

The 2,123-m. long Mach number 10 waverider 14-X Hypersonic Aerospace Vehicle, Fig. 2, built from a hypersonic small-disturbance theory for axisymmetric 5.5

degrees semivertex angle conical flow (cone-derived waverider) [5, 6], is designed to flight for the first time, in Brazil, a scramjet-waverider integrated technological demonstrator.

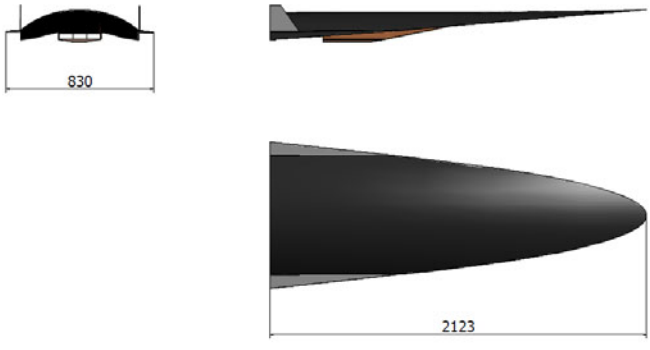

Fig. 2 Schematic view of the Brazilian 14-X Hypersonic Aerospace Vehicle.

The 5.5 degrees waverider compression surface at leading edge is generated 0.945-m. away from of the cone vertex, where the parabolic upper surface is aligned with the free stream hypersonic flow. The 2,123-m. long waverider is defined by the intersection, at the trailing edge, of the 30 degrees azimuthal angle with the conical shock surface attached at the leading edge.

The cross section at axis of symmetry of the 14-X Hypersonic Aerospace Vehicle, Fig. 2, provides the 2-D configuration, Fig. 3, used to analyze the aerodynamics of the hypersonic flow traveling parallel to the free stream flow. The shock wave, from a Mach number 10 hypersonic flow, attached at the 5.5 degrees waverider leading edge along of the lower surface, did not compress the air according to the scramjet inlet condition requirements, so 20 degrees scramjet inlet compression ramp was designed to capture the entire air flow compressed by the 5.5 degrees waverider leading edge and to provide the ideal conditions for the scramjet-powered by hydrogen. Further, a 15 degrees expansion ramp surface, with rounded sides, was added to accommodate a scramjet nozzle and to avoid high vertical flow in the region.

4 Brazilian 14-X Hypersonic Aerospace Vehicle Internal Configuration

The 14-X Hypersonic Aerospace Vehicle will need several subsystems to the atmospheric free flight be operational and, also, to monitor the flight and the scramjet-hydrogen powered at Mach number 10, Fig. 4.

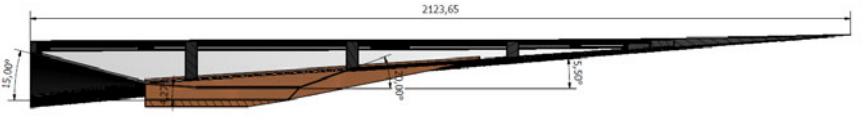

Fig. 3 Schematic view of 2-D waverider scramjet-airframe integrated.

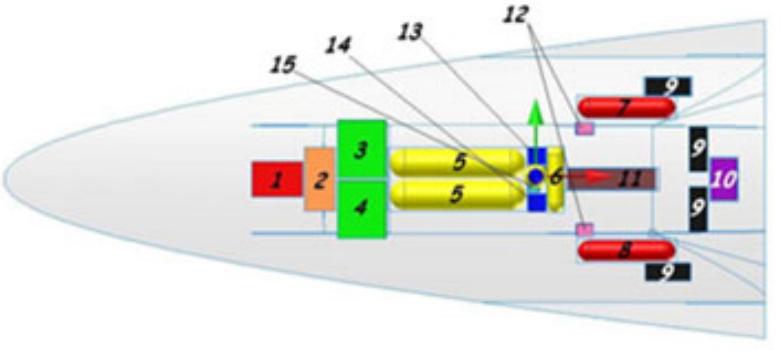

Fig. 4 Schematic internal lay-out of 14-X Hypersonic Aerospace Vehicle.

Where: 1 - Batteries; 2 - Power control unit; 3 - Flight management unit; 4 - Data acquisition system; 5 - Hydrogen tank; 6 - Water tank - cooling system; 7 - Ignition system; 8 - Nitrogen tank for pressurization system; 9 - Actuators; 10 - Control unit actuators; 11 - Pump cooling system; 12 -Solenoid for ignition systems and pressurization; 13 - Telemetry system; 14 - Transponder; 15 - GPS.

Besides basic external configuration and the subsystems needed for the atmospheric free flight of the 14-X Hypersonic Aerospace Vehicle be successful, other design elements are needed as materials, structures, thermal protection system, etc.. This is due to the fact that a hypersonic vehicle powered airbreathing propulsion displays from its concept high degree of integration of their subsystems such as the combustor and the air inlet, aerodynamic heating and structure, and coupling of motion in the longitudinal and lateral axes [7].

The Hypersonic Accelerator Vehicle will accelerate the 14-X Hypersonic Aerospace Vehicle to 30 km altitude reaching a desired speed (of approximately 1,800 m/s, Mach number 10, Fig. 5.

In this condition, the 14-X Hypersonic Aerospace Vehicle will separate of the 2 stage rocket engine of the Hypersonic Accelerator Vehicle. The scramjet will be operational for about 4-5 seconds in upward flight of the 14-X Hypersonic Aerospace Vehicle. After scramjet engine demonstration will be completed, the 14-X

Hypersonic Aerospace Vehicle will follow the ballistic flight. After reaching the apogee, the 14-X Hypersonic Aerospace Vehicle will follow the descending flight to splash into the Atlantic Ocean. Both Hypersonic Accelerator Vehicle and 14-X Hypersonic Vehicle will not be recovered.

Fig. 5 Brazilian 14-X Hypersonic Aerospace Vehicle in ballistic trajectory.

Based on the dynamic pressure at 30 km altitude, the subsystems on-board of the 14-X and the materials available, the internal configuration, Fig. 6, is proposed for further thermal protection system and structural analyses definitions.

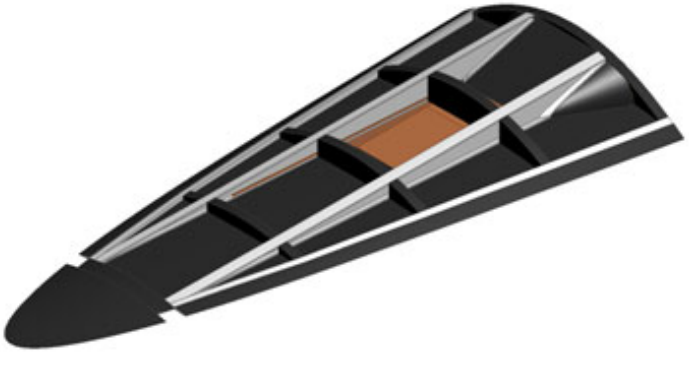

Fig. 6 Internal configuration of the Brazilian 14-X Hypersonic Aerospace Vehicle.

The preliminary Computational Structural Analysis of the 14-X Brazilian Hypersonic Aerospace Vehicle, Fig. 1, using the software ANSYS - Workbench, which is able to obtain structural analysis results to be provide the stringers and ribs wrappers suitable for coating to the flight regime. The ANSYS software simulates loads

faced by the vehicle during the transatmospheric flight hypersonic regime, determining the correct size of the elements to make up the 14-X Hypersonic Aerospace Vehicle.

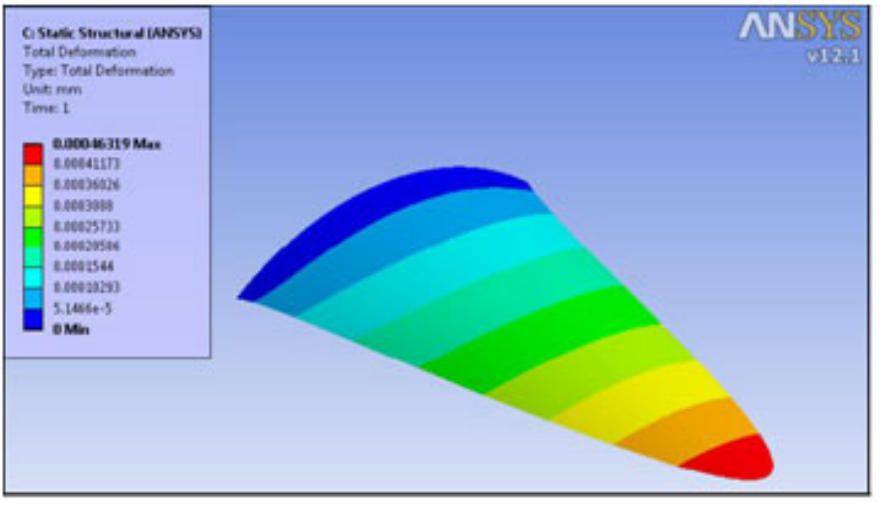

Fig. 7 Aerodynamic load of the 14-X Hypersonic Aerospace Vehicle.

5 Conclusion

The Prof. Henry T. Nagamatsu Laboratory of Aerothermodynamics and Hypersonics, at the Institute for Advanced Studies (IEAv), is developing the 14-X Hypersonic Aerospace Vehicle. External as well internal configuration of pure and scramjet integrated studies are needed for the next step, i. e., to structural analysis of the 14-X Hypersonic Aerospace Vehicle.

References

1. Curran, E.T.: Scramjet Engines: The First Forty Years. Journal of Propulsion and Power 17(6) (November-December 2001)
2. Rolim, T.C., Minucci, M.A.S., Toro, P.G.P., Soviero, P.A.O.: Experimental Results of a Mach 10 Conical-Flow Derived Waverider. In: 16th AIAA/DLR/DGLR International Space Planes and Hypersonic Systems and Technologies Conference, AIAA 2009-7433 (2009)
3. Wang, Y., Zhang, D., Deng, X.: Design of Waverider Configuration with High Lift-Drag Ratio. Journal of Aircraft 44(1), 144–148 (2007)
4. Heiser, W.H., Pratt, D.T., Daley, D.H., Mehta, U.B.: Hypersonic Airbreathing Propulsion. AIAA Education Series, 594 p. AIAA (1994)

5. Rasmussen, M.: Hypersonic Flow. John Wiley and Sons, Inc. (1994)
6. Rasmussen, M.L., He, X.: Analysis of Cone - Derived Waveriders by Hypersonic Small-Disturbance Theory. In: Proceedings of the First International Hypersonic Waverider Symposium, College Park, Maryland, USA, October 17-19 (1990)
7. Ouzts, P., Soloway, D., Moerder, D., Wolpert, D., Benavides, J.: The Role of Guidance, Navigation, and Control in Hypersonic Vehicle Multidisciplinary Design and Optimization. In: Proceedings of the 16th AIAA/DLR/DGLR International Space Planes and Hypersonic Systems and Technologies Conference, AIAA 2009-7329, Bremen, Germany (2009)

Particle-Impact Ignition Measurements in a High-Pressure Oxygen Shock Tube

Mark W. Crofton, Phillip T. Stout, Michael M. Micci, and Eric L. Petersen

1 Introduction

Metal particle contamination is a concern for liquid rocket engines that use enriched O_2 at high pressure. It is believed that under some engine conditions contaminant particle impact could release sufficient kinetic energy to initiate combustion, providing an ignition source for engine components (e.g., turbine blades) impacted by the particles, and subsequently a combustion event that eventually consumes structural materials of the engine. It is important that the combustion properties of these candidate metal particles be studied for their propensity to cause ignition under rocket-like conditions, to reduce the risk of engine failure. Laboratory study of such a mechanism under realistic engine conditions is difficult, and data are lacking. Data that reveal the influence of particle mass, kinetic energy, impacted-surface composition, and environmental conditions on ignition propensity are valuable for launch programs involving oxidizer-rich, staged combustion engines.

Many investigations have been made on the flammability of various materials in oxygen-enriched environments. Of particular relevance is the study of ignition promoted by high-velocity particles [1] and candidate turbopump materials [2], for which flammability rankings have been made. However, none of these investigations was performed under the targeted conditions of the present work, which are relatively extreme with respect to pressure, temperature, and particle velocity.

The combustion of aluminum particles has been extensively studied [3]. Correlations with respect to burn-time dependence on pressure, temperature, particle size and oxygen concentration have been developed. As expected, higher oxygen concentration generally leads to faster particle combustion, however temperature

Mark W. Crofton · Phillip T. Stout
The Aerospace Corporation, El Segundo, CA, USA

Michael M. Micci
Pennsylvania State University, University Park, PA, USA

Eric L. Petersen
Texas A&M University, College Station, TX, USA

and total pressure dependence is much less dramatic. Particle ignition may occur at lower temperatures if the oxide shell is fractured by mechanical stress. Cracking and fragmentation of impacting particles has been studied under various circumstances [4, 5, 6], although not at the extreme temperature-pressure-velocity conditions of the present experiment. Threshold velocities exist, beyond which the complex process of fragmentation can occur.

Extensive fragmentation would not be surprising under the present test conditions, and some evidence exists for this [7]. In addition, deformation, erosion, spallation and other phenomena occur [8]. The kinetic energy of impact will rapidly elevate the temperature at the collision zone, as shown by recent simulations of aluminum particle collisions on a solid nickel target [9], possibly to the melting temperature [10, 11]. Test conditions that span a wide range of pressure, temperature, particle size, and velocity are necessary to learn the importance of the relevant parameters and elucidate the underlying physics and chemistry. Targeted pressure is in the 2000 - 10000 psia (14 - 68 MPa) range, with temperature between 500 and 1300 K, and flow/particle velocity from 200 to 1000 m/s. The desired size range for the aluminum particles is 100 to 2000 μm. These conditions include those relevant to the oxygen-rich liquid rocket engine environment of interest.

The shock-gun apparatus employed herein achieves these somewhat extreme conditions by utilizing a shock wave to compress the oxygen test gas to high temperatures and pressures. Details on the facility are described below, followed by some recent results using aluminum particles that show clear evidence of impact-induced particle ignition.

2 Apparatus

The particle-impact shock tube, described in detail elsewhere [12], consists of driver and driven sections separated by a diaphragm. With its 2-m length, the driven section is much longer than the driver, and its 6.4-mm bore diameter is larger than the 4.8-mm driver bore. Beyond the exit plane of the small bore defining the driven section is an expansion region (see Fig. 1) where a particle-impact target is placed or, alternatively, a cone for measuring oblique shock angle and thereby obtaining flow speed. A Haskel AGT-30/75 booster pump provides helium at about 16,000 psi to the inlet of the driver pump. The latter is driven by a high-torque stepper motor with large gear ratio. The diaphragms used primarily for the tests herein typically burst at about 33,000 psi, but other burst pressures are easily selectable.

Piezoelectric pressure sensors (PCB model 113B23) mounted along the barrels provide shock wave timing information, used to obtain the incident shock wave velocity V_S at the exit plane of the tube. From V_S, oxygen fill pressure and composition, the temperature, gas velocity and pressure behind the incident shock wave are calculated [13]. The P(1) pressure transducer is approximately 80 mm upstream of the target and is the transducer closest to the tube exit plane.

A solid metal target disc is positioned in the expansion region to intercept particles entrained in the gas flow. A cartridge heater (250 W, CCI Thermal), placed inside the target mount assembly, heats the target disc which is screwed onto the

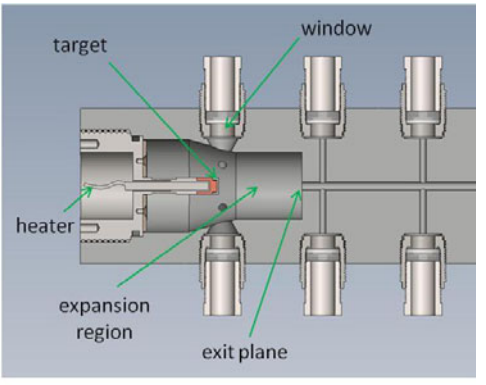

Fig. 1 Detailed schematic for the test section region, showing impingement target, exit plane where the incident shock wave expands, and optical access windows. Windows and their optical access channels to the small center bore were plugged to achieve maximum shock strength.

end. A surface temperature of greater than 400 °C is achievable by this means, however the setpoint for the present measurements was about 80 °C.

Aluminum particles with a broad size distribution were procured from Alfa Aesar and sorted using a shaker system incorporating numerous mesh pans for different size particles. The most common particle group used in the present experiments was 500-600 microns, shown in Fig. 2. The particles have irregular shapes and can be considerably larger in another direction than that of the indicated dimension, due to the sorting mechanics. Particle samples with smaller size were also used.

A high-performance monochrome camera (VRI/V710) with a 105-mm Sigma macro lens was used for flow and particle imaging work. Collimated light from a H55 headlamp bulb provided backlighting for obtaining shadowgraph images; a Schlieren setup was not necessary. For a particle velocity of 750 m/s and a 7.5-mm wide traversal across the viewing region to the target, a 3-frame imaging sequence across the transit requires a 300-KHz frame rate and sub-μs shutter duration. The V710 is just able to meet these specifications. For the current experiments, the camera was operated with a 3.8-μs frame interval and 0.7-μs exposure. An Edmund Optics E-ZOOM6V microscope with a 2048×1536 video camera was used to capture images of target surfaces following particle impingement experiments.

A shock wave is formed upon the rapid bursting of the diaphragm, causing the oxygen to flow at transonic velocities with elevated temperatures and pressures. Achievement of the proper conditions is coupled to the Mach number of the shock wave propagation, which is related to the ratio between diaphragm burst pressure and oxygen fill pressure. The gas flow elevates particles from a small cup machined into the tube wall, and accelerates them to high speed. The pressure at the target is elevated considerably due to the formation of a normal shock just upstream of its surface. This pressure can be obtained by applying normal shock relations for the particular conditions of the experiment [12].

3 Results

Conditions in the target region vary with time; to determine the conditions at the target plane, separate experiments were performed wherein the target was replaced by a cone. The tip of the cone is in the location where the target plane would be, and the resulting conical shock wave attached to the cone during characterization experiments was visualized using the shadowgraphy system. From the angle of the conical shock wave, the local Mach number and hence temperature and pressures can be estimated. Figure 2 illustrates this fact with the output of the P(1) transducer (i.e., the last pressure sensor before the exit plane of the shock-tube barrel) and images of the cone with an attached oblique shock wave. The pressure at the transducer is more than double its initial value at shock wave arrival, from 200 to 900 μs later, due to boundary layer effects in the small-diameter shock tube [12].

A series of test runs was performed with a diaphragm burst pressure of about 32,000 psi with the driven section filled with 150 psi of pure oxygen. The typical pressure at the target when the particles first arrived was on the order of 1990 psi, corresponding to 1070 K, and target impingement velocity for the 500-600 μm particles was on the order of 750 m/s. This set of parameters is called the standard condition in this report. These conditions are based on cone experiments run for the

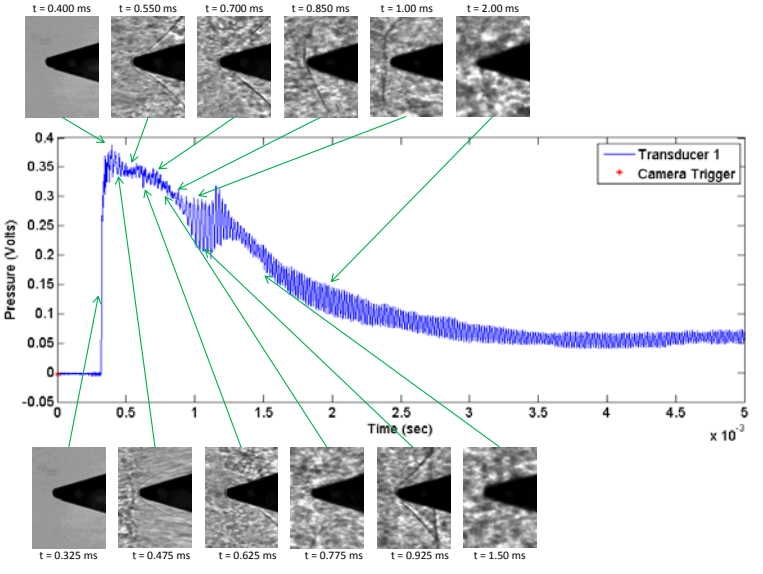

Fig. 2 P(1) pressure transducer raw signal and oblique-shock shadowgraphs for diaphragm burst pressure of 20,800 psi and test gas (air) fill pressure of 152.7 psi. The conical object was positioned where the target would be so that the local Mach number could be discerned from the angle of the conical shock wave. P(1) is the pressure reading closest to the exit plane of the tube barrel.

same experimental condition (32,000 psi driver with 150 psi driven pressure), using the conical shock angle to determine the flow Mach number in front the target. With the target in place, this supersonic flow will go through a normal shock wave, and the pressure and temperature after this normal shock is what is used to estimate the conditions in front of the target. From the schlieren oblique shock images, there is evidence that the jet changes position around the midpoint of the particle arrival times, leading to estimated target pressures and temperatures as high as 3900 psi and 980 K. Figure 3 shows the result of a single test run at the standard condition, using a Monel 400 target disc. It is apparent that the impacts and resulting combustion events had a significant effect on target appearance. The data plotted in the bar chart in Fig. 3 suggest that impacting-particle combustion probability may be influenced by the target composition.

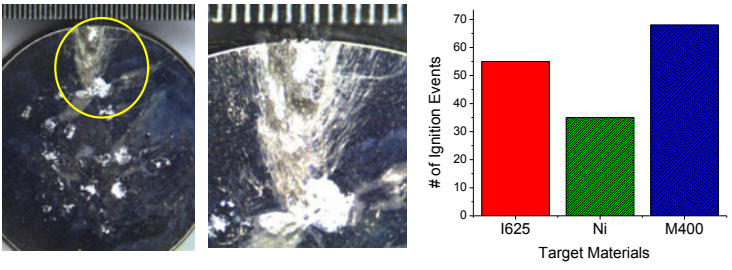

Fig. 3 Photographs of Monel 400 disc after 500-μm aluminum particle impacts under standard conditions. The surface is significantly changed by the impacts and combustion events. Image in the middle is a magnified view of the circled region on the left image. Ruler spacing is 254 m. Right plot: number of ignition events for the standard condition, as a function of the target material.

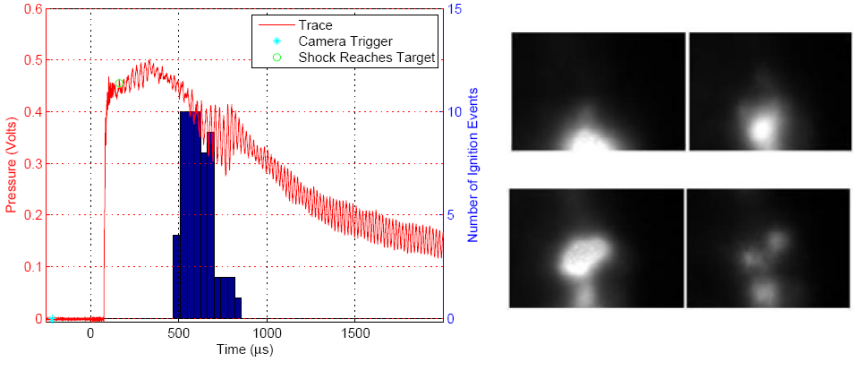

Fig. 4 Left plot: approximate particle arrival distribution as determined by counting ignition events, with signal from the P(1) pressure transducer (closest to tube exit). Right images: series of four frames for the standard test condition (3.7-μs interval).

Particle arrival distributions are very repeatable for a fixed set of shock-tube conditions. Information about the distribution can be obtained from a pressure transducer placed at the target position, as previously done [12], or from the observed rate of particle ignition events as recorded by the camera system. An example of the latter is shown in Fig. 4, where number of observed events during about 30-μs time intervals are plotted. The plot in Fig. 4 suggests that most particles arrived at the target 300 to 700 μs after the incident shock wave arrived. An interesting example of particle combustion dynamics is shown on the right half of Fig. 4.

Acknowledgments. The work was supported under The Aerospace Corporation′s Independent Research and Development Program. The project manager is Dr. Jeff Emdee.

References

1. Benz, F.J., Williams, R.E., Armstrong, D.: Ignition of Metals and Alloys by High-Velocity Particles. In: Benning, M.A. (ed.) Flammability and Sensitivity of Materials in Oxygen-Enriched Atmospheres: Second Volume, ASTM STP 910. American Society for Testing and Materials (1986)
2. Schoenman, L.: Journal of Propulsion and Power 3, 46–55 (1987)
3. Beckstead, M.W.: A Summary of Aluminum Combustion. RTO/VTI Special Course on Internal Aerodynamics in Solid Rocket Propulsion (May 21-23, 2002)
4. Carmona, H.A., Wittel, F.K., Kun, F., Herrmann, H.J.: Phys. Rev. E 77, 051302 (2008)
5. Abraham, F.F., Brodbeck, D., Rafey, R.A., Rudge, W.E.: Physical Review Letters 73, 272–275 (1994)
6. Salman, A.D., Biggs, C.A., Fu, J., Angyal, I., Szabo, M., Hounslow, M.J.: Powder Technology 128, 36–46 (2002)
7. Crofton, M.W., Petersen, E.L.: Particle-Impact Ignition in High Pressure Oxygen: Initial Results. AIAA Paper 2010-7134 (2010)
8. Zukas, J.A.: Impact Dynamics. Wiley (1990)
9. Micci, M.M., Crofton, M.W.: Hybrid Finite Element/Molecular Dynamics Simulations of Shock-Induced Particle/Wall Collisions. In: 28th International Symposium on Shock Waves (July 2011)
10. Hutchins, I.M.: Wear 70, 269–281 (1981)
11. Barradas, S., Guipont, V., Molins, R., Jeandin, M., Arrigoni, M., Boustie, M., Bolis, C., Berthe, L., Ducos, M.: Journal of Thermal Spray Technology 16, 548–556 (2007)
12. Crofton, M.W., Stout, P.T., Albright, T.V., Worshum, M.D., Emdee, J.L., Petersen, E.L.: Development and Characterization of a Particle-Impact Ignition Facility. AIAA Paper 2010-7133 (2010)
13. Gaydon, A.G., Hurle, J.R.: The Shock Tube in Chemical Physics, Reinhold (1963)

Limiting Contractions for Starting Prandtl-Meyer-Type Scramjet Inlets with Overboard Spillage

N. Moradian and E. Timofeev

1 Introduction

The air inlet is a crucial component of hypersonic airbreathing engines, which should decelerate and compress airflow with minimum losses. For efficient engine operation the inlet must be started, i.e., all incoming supersonic flow must be captured and the flow inside the inlet must be predominantly supersonic. Kantrowitz and Donaldson [1, 2] established the classical theory of flow starting in converging ducts. According to the theory, the limiting duct area ratio for spontaneous starting (or self-starting) is based on the flow condition at which a normal shock is positioned exactly at the duct entry and the post-shock subsonic flow isentropically accelerates along the duct to become sonic at the duct exit (i.e., the choked throat is considered). It is assumed that the flow is quasi-one-dimensional and quasi-steady. For exit-to-entry area ratios exceeding the limiting values, which depend on freestream Mach number, the duct (inlet) flow would start on its own, upon the increase of freestream velocity from zero to the required value. As follows from the Kantrowitz theory, limiting contractions for starting lead to low contraction inlets, which do not provide sufficient compression for scramjet operation. Practical, high-contraction inlets do not satisfy the Kantrowitz self-starting condition and would not start spontaneously. This constitutes a well-known inlet starting problem.

The basic inlet starting methods are overspeeding, variable geometry and perforated diffusers. In the overspeeding technique, a supersonic vehicle is accelerated to a Mach number exceeding the Kantrowitz limit for the given area ratio to achieve started flow. Then, it is decelerated to the design point. The usefulness of the technique is limited since it works only for low contraction (high exit-to-entry area ratio) inlets [3]. Another method used to start an inlet is to change its geometry so that to increase the area ratio [3]. In the perforated diffuser technique, the exit flow area is effectively increased by opening holes or slots in the inlet walls to achieve the

N. Moradian · E. Timofeev
Department of Mechanical Engineering, McGill University, Montreal, Quebec H3A2K6, Canada

self-starting condition [4, 5]. The additional mechanical complexity needed to open and close the perforations or change the exit area, represents a certain disadvantage of these techniques.

The overboard spillage is another method to improve startability of inlets. It is probably the simplest one since it does not require any additional mechanisms/arrangements, except properly designed geometry of the inlet itself. The external compression part of the inlet with overboard spillage reduces the flow Mach number in front of the fully enclosed (internal compression) part, which has higher exit-to-entry area ratio than the overall area ratio of the inlet. This effectively brings the inlet above the Kantrowitz limit, resulting in started flow.

Many researchers investigated, both experimentally and numerically, a number of highly integrated scramjet ramp-type inlet concepts in which overboard-spillage-assisted starting plays a role (e.g., [6], [7]). Two-shock inlets and Prandtl-Meyer inlets are two families of ramp-type inlets with a simple, planar (two-dimensional) geometry. Veillard et al. [8] considered a parametric family of two-shock inlets as a whole and determined the designs resulting in the minimum exit-to-entry area ratio A_e/A_i still ensuring self-starting. In other words, they showed how to maximize the overboard spillage effect within the geometrical constraints of the given inlet family. They formulated the strong shock design principle, which stipulates that if the two-shock inlet is designed with *strong* reflected shock, its self-starting characteristics are very close to the ultimate limit, which is achievable in principle for the two-shock inlet family.

In this study, we generalize the startability analysis [8] for the Prandtl-Meyer inlets. When the Prandtl-Meyer compression fan is used to decelerate and compress the incoming flow, the stagnation pressure loss is reduced and the efficiency is increased, which makes the inlets more practical as compared to two-shock inlets. In the next section, the minimum self-starting (Kantrowitz) area ratio is determined for all possible combinations of the parameters defining the inlet family: the freestream Mach number, M_∞, and the flow deflection, δ, across the Prandtl-Meyer compression fan.

2 Theoretical Analysis of Overboard-Spillage-Aided Starting for the Prandtl-Meyer Inlet

The Prandtl-Meyer inlet (Fig. 1a) consists of a compression ramp and a cowl, similarly to two-shock inlets. However, the surface of the ramp is concave rather than straight. Its geometry is defined to produce an isentropic Prandtl-Meyer compression fan centered at the cowl leading edge (instead of an oblique shock wave in the case of a two-shock inlet). In other words, the ramp surface represent a streamline of the centered Prantdl-Meyer compression flow. Across the fan, the flow Mach number is decreased from its freestream value M_∞ to M_2, while the flow is deflected by angle δ. These three parameters are related via

$$\delta = \nu(M_\infty) - \nu(M_2) \,, \tag{1}$$

Where ν is the Prandtl-Meyer angle. Downstream of the concave portion of the ramp, there is a straight section which becomes horizontal (parallel to the internal surface of the cowl) after the ramp trailing edge. The uniform post-compression fan flow is deflected back by angle δ via an oblique shock wave attached to the cowl leading edge. If the oblique shock terminates at the ramp trailing edge (as shown in Fig. 1b), it is said that the inlet is "on-design." The flow Mach number downstream of the oblique shock is M_3.

The family of Prandtl-Meyer inlets can be defined using three parameters: for instance, the freestream Mach number M_∞, the deflection angle δ, and the exit-to-entry area ratio A_e/A_i. Instead of the deflection angle, it is also possible to use Mach number M_2 or the fan angle φ (Fig. 1).

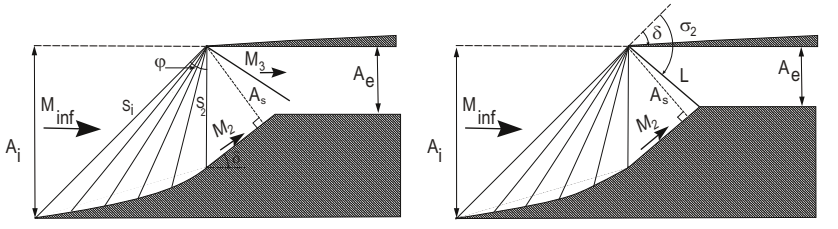

Fig. 1 Schematics of Prandtl-Meyer inlet geometry: (**a**) A general Prandtl-Meyer inlet; (**b**) On-design Prandtl-Meyer inlet

For the subsequent analysis, we denote the areas corresponding to each Mach wave in the compression fan (or in other words, to the lines connecting each point on the Prandtl-Meyer surface with the cowl leading edge) as S (see Fig. 1). In the problem under study it is convenient to normalize it by the area S_i corresponding to the first (upstream) Mach wave where the Mach number is equal to M_∞. From the theory of Prandtl-Meyer flow it can be derived that

$$\frac{S}{S_i} = \frac{f(M)}{f(M_\infty)}, \quad \text{with} \quad f(M) = \left[\frac{\gamma-1}{\gamma+1}(M^2-1)+1\right]^{\frac{\gamma+1}{2(\gamma-1)}}. \tag{2}$$

The startability analysis also requires to establish the external and internal (in other words, fully enclosed) compression sections of the inlet. This is done, similarly to [8], by introducing the normal line drawn from the cowl leading edge to the ramp surface. The respective area is denoted as A_s in Fig. 1. The internal compression section of the inlet is downstream from the normal line while the external compression one is upstream from it. Taking into account that $S_i = A_i/\sin\alpha_i = A_i M_\infty$ and $S_2 = A_s/\sin\alpha_2 = A_s M_2$ (with α being the Mach angle), we get for the area ratio of the external compression section:

$$\frac{A_s}{A_i} = \frac{f(M_2)}{f(M_\infty)}\frac{M_\infty}{M_2}. \tag{3}$$

According to the quasi-1D Kantrowitz theory, the flow in the internal compression section starts spontaneously if its area ratio A_e/A_s is equal or higher than the limiting value $(A_e/A_s)_k$, which is a function of the Mach number M_2. Then the limiting area ratio for self-starting of the overall inlet can be expressed as:

$$\left(\frac{A_e}{A_i}\right)_k = \left(\frac{A_e}{A_s}\right)_k \frac{A_s}{A_i}, \tag{4}$$

where the ratio A_s/A_i is given by Eq. (3). The right hand side of Eq. (4) is a function of M_∞ and δ (via M_2) only. It provides the minimum self-starting area ratio for the given pair (M_∞, δ). Equation (4) is shown graphically in Fig. 2 as an elevated area-ratio surface on the $M_\infty - \delta$ plane; above the surface, the inlet starts spontaneously.

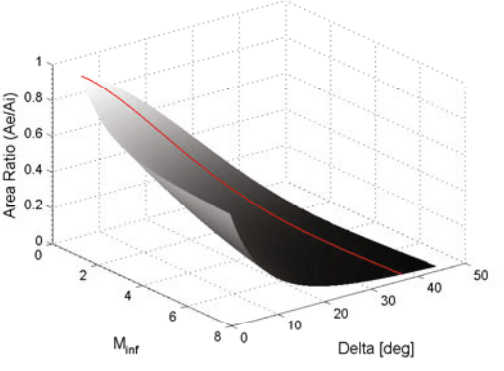

Fig. 2 The Kantrowitz surface (the limiting area ratio for spontaneous starting) for Prandtl-Meyer inlets. The thin line on the surface corresponds to the detachment of the reflected shock from the cowl leading edge

Unlike the Kantrowitz surface for two-shock inlets, which exhibits a minimum, the self-starting surface for the Prandtl-Meyer inlets slopes down monotonically with increasing deflection angle. Therefore, for a given freestream Mach number, the best starting characteristics are achieved at the highest possible deflection angle. However, there are two additional constraints on the deflection angle to be taken into account. First of all, to apply the Kantrowitz theory to the internal compression section, the flow at the cross-section A_s must be uniform. This, in turn, leads to the requirement that the normal line from the cowl leading edge must hit the straight portion of the ramp, with the limiting case being when it comes to the trailing edge of the ramp (so called "normal line design"). Then we arrive at the following constraint on the deflection angle: $(A_e/A_s)_k \leq \cos\delta$. It is seen in Fig. 2 that the maximum deflection angle decreases with decreasing M_∞. Another constraint is related to the fact that at high deflection angles the detachment of the reflected oblique shock from

the cowl edge may occur, thus rendering the flow unstarted due to some spillage near the cowl leading edge. At each Mach number M_2 of the flow downstream of the Prandtl-Meyer compression fan, the maximum possible deflection angle, $\delta_{\max}$, is calculated. The respective line, visible on the elevated surface in Fig. 2, separates the (M_∞, δ) region, where the shock detachment occur, from the region, where the oblique shock remains attached.

To have an on-design inlet, the reflected shock of area L (see Fig. 1b) from the cowl leading edge should be terminated at the trailing edge of the ramp. It is to be noted that there are two on-design solutions: with weak (lower shock angle σ_2) and strong (higher shock angle σ_2) reflected shocks. The on-design constraint on the inlet geometry follows from Fig. 1b:

$$L = \frac{A_e}{\sin(\sigma_2 - \delta)} = \frac{A_s}{\sin\sigma_2} \,. \tag{5}$$

Figure 3a shows the area ratios required for spontaneous inlet starting at free-stream Mach numbers from 1 to 8 (the Kantrowitz lines) for various Prandtl-Meyer inlets. The most important observation from the figure is that the limiting self-starting area ratio for the entire family of Prandtl-Meyer inlets (long dash line) is very close to the Kantrowitz line of the Prandtl-Meyer inlet with the strong reflected shock.

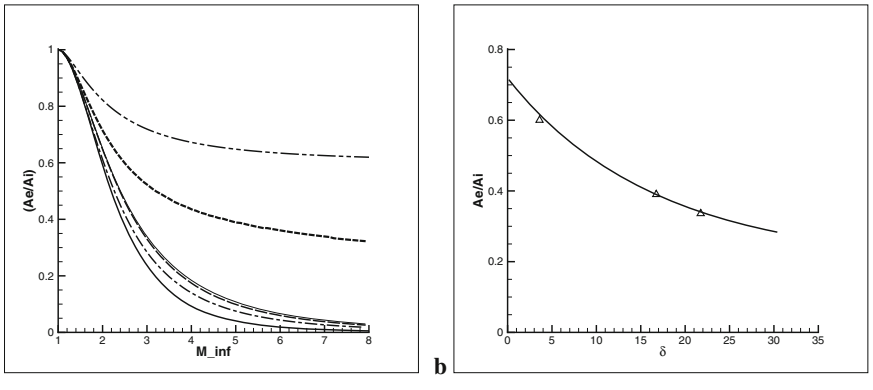

Fig. 3 (**a**) The Kantrowitz (or self-starting) lines for various Prandtl-Meyer inlet designs; from top to bottom: for fully enclosed ducts (the classical Kantrowitz line; dash-double dotted); for Prandtl-Meyer inlets with weak second shock (dash); for Prandtl-Meyer inlets with strong second shock (thin-solid); the line of reflected shock detachment (long dash; projection of the line on the elevated surface (Fig. 2) onto $(A_e/A_i - M_\infty)$ plane); for Prandtl-Meyer inlets with normal-line design (dash-dotted). Isentropic line is also shown at the bottom (thick-solid); (**b**) The comparison of numerical and theoretical limiting area ratios for self-starting at $M_\infty = 3$

3 Numerical Starting Simulations

To verify the derived limiting contractions, numerical simulations using a locally adaptive unstructured finite-volume Euler code [10] are performed. In the course of numerical starting experiments, Prandtl-Meyer inlets are accelerated from zero velocity to the final Mach number with acceleration of $a = 1000g$, which, according to the study by Tahir et al. [9], still does not violate the assumption of quasi-steady flow. It is verified that the difference with the results for $a = 100g$ is insignificant. The grid convergence studies show that three refinement levels are appropriate for the present study. At $M_\infty = 3$, three Prandtl-Meyer inlets with deflection angles of 12.598°, 16.747°, and 21.749° are simulated. Their minimum self-starting area ratios are determined and shown in Fig. 3b. The uncertainty of the numerical results (the difference in the area ratio between the started and unstarted cases) is equal to 0.001. It is clear that the numerical results are very close to the theoretical ones.

4 Conclusion

In the present paper, limiting contractions for starting Prandtl-Meyer-type inlets with overboard spillage alone have been obtained and verified by numerical simulations. It has been found that the limiting self-starting area ratio for the entire family of Prandtl-Meyer inlets is close to the Kantrowitz line of the Prandtl-Meyer inlet with the strong reflected shock. This finding is in agreement with [8], where the same conclusion is made for two-shock inlets. Thus, the strong shock design principle suggested in [8] appears to be rather general. Clearly, the improved startability comes at the expense non-uniform exit flow (usually, inlets are operated with a weak reflected shock rather than a strong one). The degree of non-uniformity and its possible consequences for the combustor flow is the subject of current studies.

Acknowledgments. The present study is supported in part by the NSERC Discovery grant RGPIN/298232-2009 and the FQRNT Team grant PR-126114.

References

1. Kantrowitz, A., Donaldson, C.: Advance Confidential Report L5D20, NACA (1945)
2. Kantrowitz, A.: Technical Note 1225, NACA (1947)
3. Seddon, J., Goldsmith, E.L.: Intake Aerodynamics. AIAA, New York (1985)
4. Evvard, J.C., Blakey, J.W.: NACA, RM E7C26 (1947)
5. Molder, S., Timofeev, E.V., Tahir, R.B.: AIAA Paper 2004-4130 (2004)
6. Koete, J.J., Singh, D.J., Kumar, A., Auslender, A.H.: AIAA JPP 10(6), 841–847 (1994)
7. Smart, M.K., Trexler, C.A.: AIAA JPP 20(2), 288–293 (2004)
8. Veillard, X., Tahir, R., Timofeev, E., Molder, S.: AIAA JPP 24(5), 1042–1049 (2008)
9. Tahir, R.B., Molder, S., Timofeev, E.V.: AIAA Paper 2003-5191 (2003)
10. SolverII, Software Package, Ver. 2.30.2385, RBT Consultants, Toronto, ON (2004)

Interaction between Combustion and Shock Wave in Supersonic Combustor

Lihong Chen, Fei Li, Tian Wan, Zhi Li, and Hongbin Gu

1 Introduction

Interaction between shock wave and combustion is very important for supersonic combustion. For scramjet, isolator is a key element to withstand the high pressure due to combustion and to avoid the unstart of the inlet. Therefore, the flow is very complex in isolator and combustor because of the interaction between combustion and shock wave. Usually, there are two modes of combustion in scramjet: supersonic mode and subsonic mode. Many researches have already shown how to achieve dual-mode scramjet to obtain better engine performance [1] [2] [3].

However, the mechanism of dual-mode combustion is still unclear. In this paper, experimental and numerical investigations were attempted for better understanding of the dual-mode combustion for scramjet applications.

2 Methodology

The experiments were performed in the direct-connected supersonic combustion test facility, of which the inlet vitiated air with high temperatures and high pressures was prepared by burning hydrogen and then supplying oxygen. Fig.1 was the schematic of the facility where the flow direction is from left to right, and Fig.1(a) is a side-view and Fig.1(b) is a topview. It consisted of heater, supersonic nozzle, isolator, combustor and exhaust. The Mach number of the main flow at the inlet of the isolator was Mach 1.8 and 2.5 respectively. The fuel was ethylene, and injected into the main flow upstream of the two cavities as indicated in the figure.

The optical windows were settled at four positions, corresponding to the entrance, the cavity 1, 2, and the exit. Three types of optical measurements: schlieren, TDLAS

Lihong Chen · Fei Li · Tian Wan · Zhi Li · Hongbin Gu
Key Laboratory of High Temperature Gas Dynamics
Institute of Mechanics, Chinese Academy of Sciences
No.15 Beisihuanxi Road, Beijing 100190, China

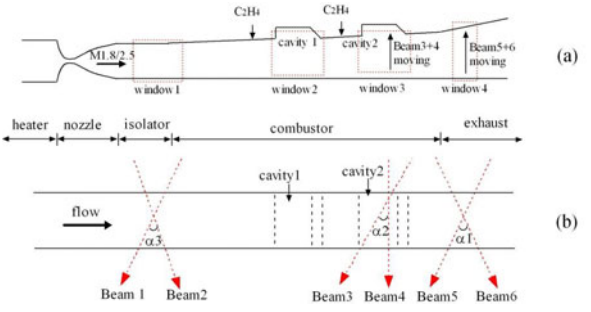

Fig. 1 Direct-connected SCRAMJET test facility.

[4] (Tunable Diode Laser Absorption Spectroscopy) and CH emission were applied in the experiment. The schlieren pictures and CH images were taken by a high-speed camera. As shown in Fig. 1, there are six beams of TDLAS used, to measure the static temperature, the velocity and the H_2O concentration of the combusted gas.

The static pressures along the central line were measured, which gives a pressure distribution along the combustor.

The full unsteady Navier-Stokes equation was solved by using data-parallel line relaxation [5]. Menter's k-ω with a compressibility correction for high Mach number flow was used for the simulation of the turbulence. The convective terms of the governing equations are calculated with a third-order upwind MUSCL-TVD scheme, and the diffusion terms are discretized with a second-order central scheme. The unsteady term is approximated with a second-order scheme, and dual time-step method was used. The reaction mechanism for ethylene is a 10 species, 8 step reduced mechanism [6].

3 Results and Analyses

Based on the experimental and numerical results, three modes of the interaction between combustion and shock wave can be observed. The first is the supersonic mode, which the main flow remains supersonic but the reaction zone is subsonic. The second is the subsonic mode, of which the flow downstream of the shock waves is fully subsonic. The third is the oscillation mode, i.e. the flow pattern changes between subsonic and supersonic with a frequency.

Fig. 2 - 4 shown the typical results for the supersonic mode. Fig. 2 shown the steady results. Fig. 2(a) was the static pressure along the central line of the wall. The isolator was from $x = 0$ to $x = 400$ mm. In the region of $x < 400$ mm, the pressure distribution kept unchanged after combustion, but the pressure of $x > 400$ mm increases due to combustion. The static temperature profile at exit was shown in Fig. 2(b), which was measured by TDLAS scanning. The position $H = 0$ denotes the wall with fuel injections and cavities. As shown in Fig. 2(b), the temperature was not uniform and gives a peak of approximately 1400K at a location closer to the wall

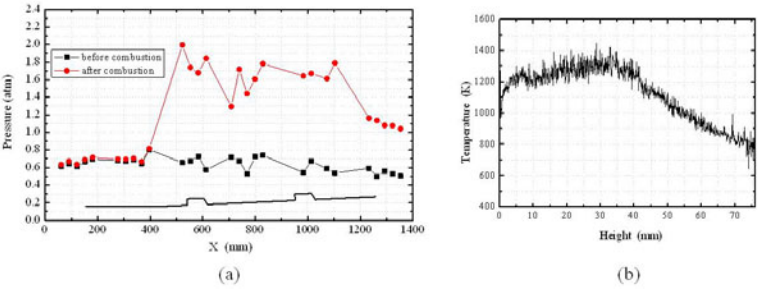

Fig. 2 Typical Profile for supersonic combustion mode; (a): Static pressure distribution along central line; (b): Static temperature at exit.

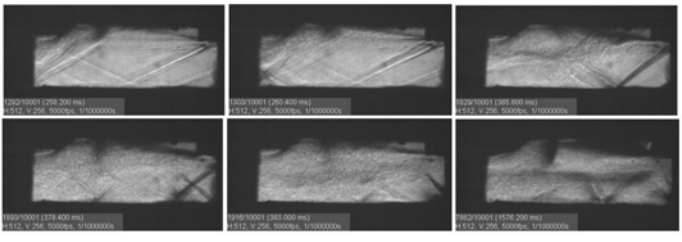

Fig. 3 Schlieren pictures at different moments (from optical window 2).

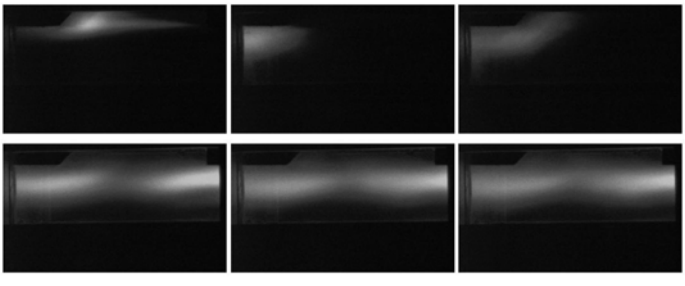

Fig. 4 CH (430nm) emission pictures at different moments (from optical window 2).

with cavities. It implies the combustion occurs only in the vicinity of the wall with fuel injection and cavity.

Fig.3 and Fig.4 demonstrates the establishment of the steady state as a function of time. Fig.3 was the schlieren pictures at different moments. The pictures were taken from optical window 2, as shown in Fig.1. The flow direction is from right to left. The cavity is on the top. The combustion started at the trailing edge of the cavity, as shown in image 1 of Fig.3. Then the main flow was compressed due to the pressure rise inside the cavity. The flow near the cavity then slowed down, which enhances

the fuel/air mixing and reaction. The pressure inside the cavity increased further to push shock waves further upstream. Finally, the shock waves and the combustion approached a balance and a steady state was established. In this supersonic mode, the reaction occurs in a limited region near the cavity and the main flow remained supersonic. This flow change can also be shown in Fig.4 with the results of CH emission at different moments. Since CH is a very active radical, the intensity of the CH emission can be used to indicate the reaction zone. It is clearly shown in Fig.4 that the combustion started from the trailing edge of the cavity, and finally stabilized on the leading edge.

If the reaction is strong enough, the supersonic combustion would not be sustained. Fig.5-7 show the typical results for subsonic combustion mode.

Fig. 5 is the numerical schlieren images of the starting process. The flow direction is from left to right. The first image shows the original shocks generated by the fuel injection and cavity. Then the fuel ignited and caused the high temperature zone inside cavity. This zone expanded and compressed the main flow, causing the expansion wave at the leading edge of the cavity turns to a oblique shock. This shock propagated upstream due to the combustion, and finally, the oblique shock wave moved into the isolator and the downstream flow became subsonic.

Fig.6 is the related experimental schlieren pictures. In first image, there was only the bow shock induced by the fuel injection. After ignition, the pseudo-shock waves were generated. This shock train moved upstream as the combustion continues. Finally, the shock was moved further upstream and no shock wave can be observed in the window, which corresponds to the subsonic combustion mode.

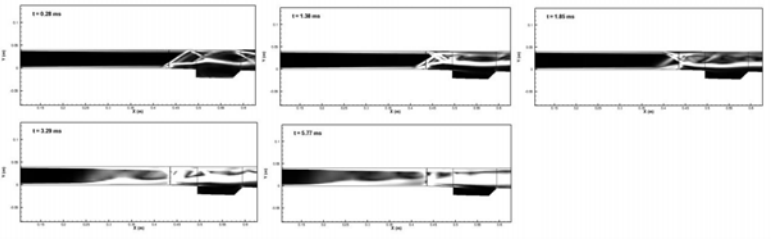

Fig. 5 Numerical schlieren pictures at different moments.

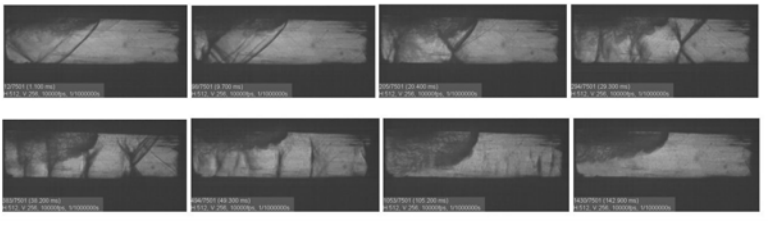

Fig. 6 Schlieren pictures at different moments (from optical window 1).

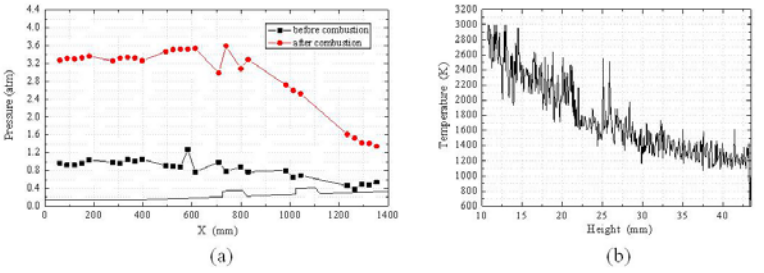

Fig. 7 Typical Profile for subsonic combustion mode; (a): Static pressure distribution along central line; (b): Static temperature at exit.

After the flow reaches a steady state, the pressure distribution of the subsonic mode is completly different from that of the supersonic mode. As shown in Fig.7(a), the pressure is very high in the isolator which indicates the existence of the shock waves. Fig.7(b) gives the static temperature at exit. Compared to the value without combustion, the temperature increases significantly, which indicates a high efficient reaction. Because it was subsonic mode, the static temperature was close to the total temperature, so the temperature was much higher than that of the supersonic mode as shown in Fig.2(b).

Between the above two stable combustion modes, there is an unsteady mode, so called the oscillation mode. In this case, because the combustion was not intensive enough to support the high pressure level, the shock train would oscillate upstream and downstream. The TDLAS results at optical window 1 are shown in Fig.8 and an oscillation at a frequency is obvious. The base line corresponds to the supersonic entrance, which has a lower static temperature, lower H_2O concentration, and higher velocity. In supersonic combustion mode, the reaction does not affect the upstream,

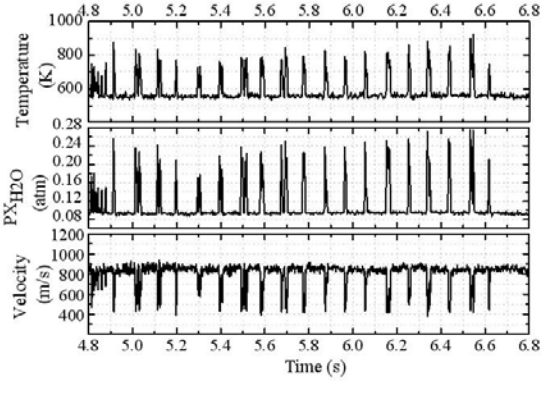

Fig. 8 Parameters by TDLAS (from optical window 1).

so the parameters remained the original supersonic entrance condition. The peaks in Fig.8 are related to the subsonic mode. Because of the movement of the shock, the temperature and H_2O concentration increased but the velocity decreased. Fig.8 also shows that the frequency of such an oscillation was almost a constant, which was about 10Hz.

4 Conclusion

In terms of the experimental and numerical investigations, the following conclusions can be drawn:

(1) The strength competition between combustion and compression is the major factor to determine different modes in scramjet.
(2) When the combustion is strong enough, the main flow is compressed, and the shock wave propagates upstream and generates a subsonic mode.
(3) When the reaction only occurred in a limited region, the flow may be divided into two parts: supersonic main flow with shock trains and subsonic reaction zone.
(4) When the combustion is not strong enough, the oscillation would happen. The flow mode would change between supersonic and subsonic.

The project is supported by the National Natural Science Foundation of China (11002148 and 10772188).

References

1. Eklund, D.R., Baurle, R.A., Gruber, M.R.: Numerical Study of a Scramjet Combustor Fueled by an Aerodynamic Ramp Injector in Dual-Mode Combusion. AIAA Paper 2001-0379
2. Choi, B., Goto, M., Mizushima, H., Masuya, G.: Effects of Heat Addiction and Duct Divergence on Pseudo-shock Waves, ISABE-2007-1235
3. Suguyama, H., Tsujiguchi, Y., Honma, T.: Structure and Oscillation Phenomena of Pseudo-Shock Waves in a Straight Square Duct at Mach 2 and 4, AIAA 2008-2646
4. Yu, X.L., Li, F., Chen, L.H., Chang, X.Y.: Spatial resolved temperature measurement based on absorption spectroscopy using a single tunable diode laser. Acta Mechanica Sinica 26, 147–149 (2010), Technical note
5. Wright, M.J., Bose, D., Candler, G.V.: A Data-Parallel Line Relaxation Method for the Navier-Stokes Equations. AIAA Journal 36(9), 1603–1609 (1998)
6. Mawid, M.A., Sekar, B.: Kinetic Modeling of Ethylene Oxidation in High Speed Reacting Flows. AIAA Paper 1997-3269

Part XVI
Richtmyer-Meshkov

Effects of Initial Conditions on Mixing in Richtmyer-Meshkov Turbulence Experiments

K. Prestridge, S. Balasubramanian, and G. Orlicz

1 Introduction

Often, and especially in canonical turbulence research, the belief is that initial conditions wash-out and the turbulence develops to a universal self-similar state [1, 2]. However, recent numerical work [3, 4] has shown that this hypothesis hold true only for some flows, and that the buoyancy driven (Rayleigh-Taylor) turbulence is dependent upon initial conditions, and a self-similar state has not been measured in experiments. Similarly, R-M flows, driven by a shock wave, have a time-dependent mixing evolution that is also dependent upon initial conditions [5, 6, 7, 8]. In this present study we focus on improving our understanding of the nature of initial conditions on R-M mixing.

For our present experiments, we use the Los Alamos horizontal gas shock tube facility, described in detail in Orlicz *et al.* [9] and pictured in Figure 1. The cross section of the shock tube is 76.2 mm square, to the end of which a test section 45 cm long is adapted allowing us to study the R-M instability and mixing after shock. Each experiment begins with a varicose, heavy gas curtain of SF_6, surrounded by ambient air, that is accelerated by a Mach 1.2 shock. First-shock initial conditions are pictured in Figure 2, which shows a two-dimensional density field imaged 20 mm from the top of the nozzle exit, and the corresponding power spectrum of the density field. The spanwise (y) 1-D power spectrum is obtained by averaging over 5 pixels in the streamwise (x) direction near the center. The primary wavelength, λ, is seen here, with small scale noise overriding the dominant wave mode. The small scale fluctuations caused by random noise present in the laboratory experiments are captured using the power spectrum.

In order to study the effects of varying amplitude and wavelength of the interface on mixing of the two fluids, we change the reshock timing such that different flow morphologies are hit with the reflected shock that comes off a moveable end wall

K. Prestridge · S. Balasubramanian · G. Orlicz
Physics Division, Los Alamos National Laboratory
Los Alamos, New Mexico 87545 USA

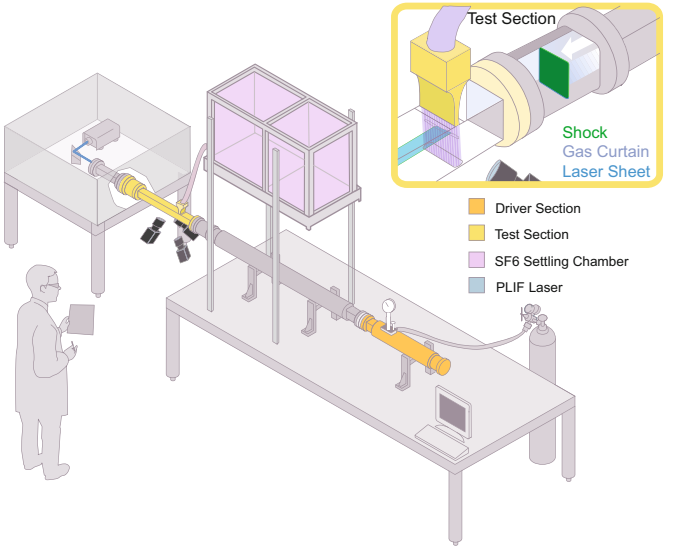

Fig. 1 Horizontal gas shock tube facility.

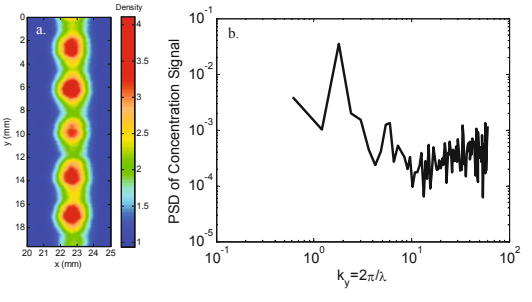

Fig. 2 Initial conditions of the gas curtain. Figure a, on the left, shows the volume fraction of density of the curtain and its spanwise periodicity. Shock moves from left to right when traversing the initial conditions. Figure b, on the right, shows the power spectrum of the initial conditions.

present inside the shock tube. By varying the position of the end wall, we can change the reshock timing. In the following section, we present the experimental measurements of the density field of the shocked (and reshocked) gas curtain using acetone Planar Laser Induced Fluorescence (PLIF). The PLIF images have been calibrated against a known mixture of SF_6 ($\approx 60\%$), air ($\approx 20\%$) and acetone ($\approx 20\%$) at the 20 mm plane, measured using mass spectrometry and a calibration test cell.

2 Experimental Results

After the first shock impacts the stably flowing varicose initial conditions, the R-M instability starts to develop and the flow is allowed to evolve. By varying the end wall position, the time at which the reflected shock hits the evolving interfaces can be varied. Figure 3 shows four different time series of gas curtain experiments, with reshock occuring at time t =90, 170, 280 and 385 μs. The morphologies underneath the white bar in each time series are those that occur after reshock.

In order to understand and quantify the differences in the reshock initial conditions at different times pictured in Fig. 3, we use a metric developed by Ristorcelli *et al.* [10]. The metric, $\kappa\delta$, is based upon δ, the thickness of the interface, and κ the frequency of the interface at a line through the center of mass in the spanwise direction. For a single-mode interface, $\kappa = 2\pi/\lambda$, but for a multi-mode interface, κ can be measured as the number of zero crossings that the density field has over a fixed span. As the value of $\kappa\delta$ increases, the complexity of the interface increases. In the case of the singly-shocked, varicose gas curtain, the value of $\kappa\delta$ over time is shown in Figure 4. At early times, the compression of the gas curtain after first shock causes $\kappa\delta$ to decrease, then as the interface grows in width, the value increases. At approximately 300μs, there is a discontinuity in the value of $\kappa\delta$. This is when the curtain changes from a sinuous shape, as shown in Fig. 3b at 165μs, to a series of mushroom shapes, as shown in Fig. 3d at 315μs. After this discontinuity, $\kappa\delta$ increases slowly,

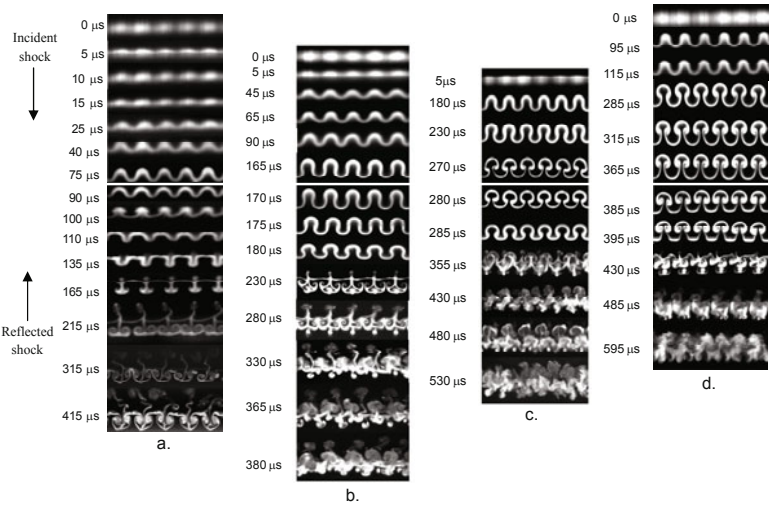

Fig. 3 Four different sets of experiments, each beginning with the varicose gas curtain (top), shocked with a Mach 1.2 shock that travels downward. Each experiment is then reshocked at a different time, as indicated below the white bar crossing the time series. Reshock occurs at time, t= a) 90 μs, b) 170 μs, c) 280 μs, and d) 385 μs. At late times, approximately t≈200 μs after reshock, the large variation in mixing that occurs for each of the four cases is visible.

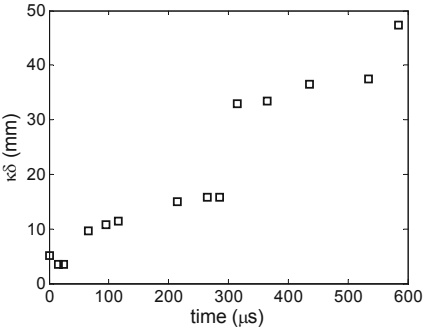

Fig. 4 Measure of $\kappa\delta$ over time for singly-shocked gas curtain. The discontinuity at t=300μs indicates that the flow will mix differently depending upon whether it is reshocked before or after the discontinuity occurs.

until another discontinuity at 600μs. For the four experiments illustrated in Fig. 3, case (a) $t = 90\mu$s, $\kappa\delta = 12$, case (b) $t = 170\mu$s, $\kappa\delta = 15$ and case (c) $t = 280\mu$s, $\kappa\delta = 18$ have low/moderate $\kappa\delta$ values. The increase in $\kappa\delta$ occurs at t≈300μs, hence case (d) at $t = 385\mu$s has a very high value, $\kappa\delta = 35$.

If $\kappa\delta$ is an indicator of the complexity of the interface, it may also be a predictor of mixing after reshock. From Fig. 3, we see visible differences in the density fields at late times, but quantifying these differences will help us understand the impact of the initial conditions on mixing. In order to better quantify the mixing of the fluids after reshock, we look at the power spectral density (PSD) of the instantaneous concentration (density) field.

Figure 5 shows the PSD of the concentration fields 200-210μs after reshock for the four experiments from Fig. 3. The two cases (a) & (b) where reshock occurs with $\kappa\delta \leq 15$, retain a strong peak at low frequency, indicating that the large scale structures in the initial conditions are still present in the flow. For the case (c) where $\kappa\delta = 18$, there is a much smaller magnitude peak at that frequency, and in case (d), where $\kappa\delta = 35$, the spectrum has broadened and lost significant features at the low frequencies. Based on spectral information alone, it looks as if the flow has many smaller scales, and perhaps more significant mixing, for the case where reshock occurs with a high initial value of $\kappa\delta$. In order to get a clearer understanding of the mixing process, we also examined the density-specific volume correlation, or density self-correlation, *b(x)*, [11] where

$$b(x,y) = \overline{\rho'(x,y)\frac{1}{\rho(x,y)}'} \quad \text{and} \quad b(x) = \frac{\int_0^{L_y} b(x,y)dy}{L_y}. \tag{1}$$

As the materials mix, this value should decrease and for homogeneously mixed fluid the value of b tends to zero. Figure 6 shows $b(x)$. At the edges of the mixing region, b tends towards zero because it is a single fluid: air. For the case (b), it is clear that

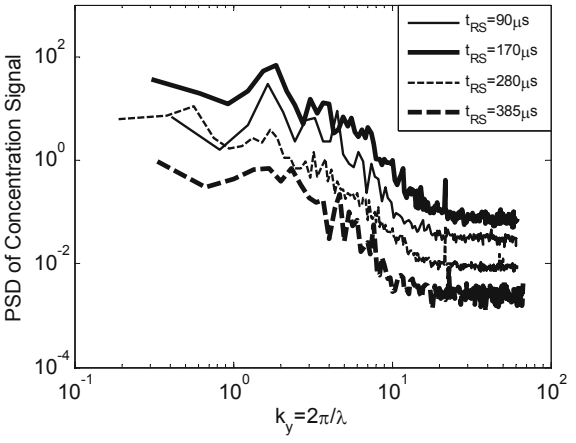

Fig. 5 Power spectra at t=200-210 μs after reshock show that some initial conditions cause the spectrum to become broader with fewer features (t=280 and 385 μs), while some still contain significant low-frequency peaks (t=90 and 170 μs). Increased mixing is indicated when the spectrum broadens and loses features.

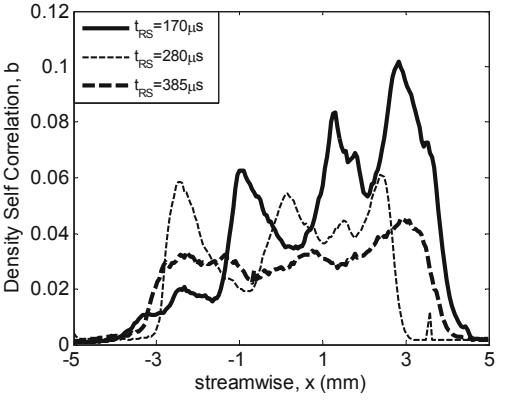

Fig. 6 Density-specific volume correlation through the curtain (streamwise) for three different reshock initial conditions, for structures at t=200-210 μs after reshock. As the value of b decreases and becomes less periodic, it indicates enhanced mixing and the loss of large-scale structure in the mixing region. The flow that is reshocked at 385 μs has lost the imprint of the large-scale structures present at earlier times.

the periodicity and large-scale structures of the flow remain, and the values of b are higher than that for the case (d), where the flow appears to be well-mixed, as indicated by the profile of b.

3 Conclusion

The initial condition dependence of Richtmyer-Meshkov flow was examined by conducting experiments in a shock tube facility using a varicose gas curtain. The evolving interface after first shock (strength Mach 1.2) was reshocked at four different times to understand the nature of amplitude, δ, and wavelength, λ, on R-M mixing. The initial slope of the interface, defined by $\kappa\delta$, was used as a metric for reshocking the developing morphology formed by the incident shock wave. The density fields from these experiments indicate observable differences in the nature and amount of mixing that were quantified by plotting the power spectra of the concentration field and the density self correlation parameter b of late time structure (t$\approx$200μs after reshock). If the flow were fully molecularly mixed, b tends to zero, which is not true for the present set of experiments indicating that the flow might be transitionary to a well mixed turbulent state, also substantiated by the power spectra. However, velocity data are needed to assist with any conclusions about the turbulent nature of the flow. The density field images are not enough, because the flow can appear to be 'mixed,' but the velocity field might not be turbulent, or the turbulence could be decaying. Finally, these metrics, while not comprehensive, provide information about the complexity of the flow and could be used to indicate when a subgrid model might have to be implemented in a simulation.

References

1. Youngs, D.L.: Numerical simulation of turbulent mixing by Rayleigh-Taylor instability. Physica D 12, 32–44 (1984)
2. Oron, D., Arazi, L., Kartoon, D., Rikanati, A., Alon, U., Shvarts, D.: Dimensionality Dependence of the Rayleigh-Taylor and Richtmyer-Meshkov Instability Late Time Scaling Laws. Plasmas of Physics 8, 1362529 (2001)
3. Dimonte, G.: Dependence of turbulent Rayleigh-Taylor instability on initial perturbations. Phys. Rev. E 69, 056305 (2004)
4. Banerjee, A., Andrews, M.J.: 3-D Simulations to Investigate Initial Condition Effects on the Growth of Rayleigh-Taylor Mixing. International Journal of Heat and Mass Transfer 52, 3906–3917 (2009)
5. Miles, A.R., Edwards, M.J., Greenough, J.A.: Effects of initial conditions on compressible mixing in supernova-relevant laboratory experiments. Astrophysics and Space Science 298, 17–24 (2005)
6. Thornber, B., Drikakis, D., Youngs, D.L., Williams, R.J.R.: The influence of initial conditions on turbulent mixing due to Richtmyer-Meshkov instability. J. Fluid Mech. 654, 99–139 (2010)
7. Balakumar, B.J., Orlicz, G.C., Tomkins, C.D., Prestridge, K.P.: Dependence of growth patterns and mixing width on initial conditions in Richtmyer-Meshkov unstable fluid layers. Physica Scripta T132, 014013 (2008)

8. Balasubramanian, S., Prestridge, K.P., Orlicz, G.C., Balakumar, B.J.: Experimental study of initial condition dependence on mixing in Richtmyer-Meshkov instabilities. In: Proceedings of 12th International Workshop on Physics of Compressible Turbulence and Mixing (2011)
9. Orlicz, G.C., Balakumar, B.J., Tomkins, C.D., Prestridge, K.P.: A Mach number study of the Richtmyer-Meshkov instability in a varicose, heavy-gas curtain. Phys. Fluids 21, 064102 (2009)
10. Gowardhan, A.A., Ristorcelli, J.R., Grinstein, F.F.: The Bipolar Behavior of the Richtmyer-Meshkov Instability. Submitted to Phys. Fluids (2011)
11. Besnard, D., Harlow, F.H., Rauenzahn, R.M., Zemach, C.: Turbulence transport equations for variable-density turbulence and their relationship to two-field models. Los Alamos National Laboratory Technical Report LA-12303-MS (1992)

Numerical Investigation of Turbulence in Re-shocked Richtmyer-Meshkov Unstable Curtain of Dense Gas

Santhosh K. Shankar and Sanjiva K. Lele

1 Introduction

When a shock wave impacts an interface between two fluids, the misalignment of the pressure and density gradients results in deposition of baroclinic vorticity on the interface. This leads to the growth of initial perturbations on the interface causing the phenomenon of Richtmyer-Meshkov instability (RMI) [1]. The RMI produces turbulent mixing of the fluids which plays an important role in many physical and technological processes like inertial confinement fusion, supersonic combustion, and impact dynamics of liquids. The RMI is also believed to be the reason for the increased mixing observed in the optical output of supernova 1987A. Understanding this process requires robust numerical algorithms capable of simulating this highly non-linear flow and high quality repeatble experimental data to validate the numerical findings. Experimental limitations (difficulty generating a well characterized initial interface between two fluids, and diagonostic limitations) and shortcomings of numerical algorithms have constrained detailed explorations of the physics of this intability. Recent improvements in experimental methods (like membraneless techniques to generate an interface) have provided reliable data for numerical code validation and simulation of this flow to characterize the turbulent mixing between the fluids. In this work one such configuration of a shock in air impacting a curtain of cylinders of dense gas is chosen for numerical simulation. The results are compared to available experimental data [2] and some turbulence statistics are reported.

2 Numerical Method and Flow Conditions

The problem at hand requires a numerical scheme which is capable of handling multiple species in the flow-field. Many of the previous computational work on RMI

S.K. Shankar · S.K. Lele
Stanford University, Stanford, CA, USA

have made use of upwind biased schemes for species interface capturing. However most upwind biased schemes introduce high numerical dissipation which is not suitable for flows with wide range of scales even if the formal order of accuracy of the scheme is high. These schemes are found to be incapable of resolving the high wavenumber spectrum of the flow-field in either large eddy simulation (LES) or direct numerical simulation (DNS) setting with reasonable computational cost. Many of these calculations [3] have assumed that the species in the flow have the same specific heat ratio which leads to erroneous wave speeds in the flow domain. In an effort to conduct robust simulation of this multi-component compressible flow (with turbulence), a compact central difference scheme (6^{th} order) is used to compute spatial derivatives. The scheme is coupled with the localized artificial diffusivity [4] method to capture discontinuities (shocks and material interfaces) in the flow-field. The $n-$ species are tracked by solving $(n-1)$ mass fraction transport equations along with the equation for total density. Time marching of the governing Navier-Stokes equations is conducted using a fourth order Runge-Kutta scheme. The highlights of this numerical methodology include: 1) capability to handle different specific heat ratios (in general, different thermodynamic properties) of the fluids in the domain, 2) automatic deactivation of the artificial diffusivity method in regions away from strong shocks and density gradients in the flow, hence preserving the high resolution characteristics of the high order compact central difference scheme, 3) lower computational cost and ease of implementation. Details of the scheme and thorough investigation of its performance in various Reynolds number regimes can be found in [4].

The flow is initialized in three regions: a post-shock region of air, an ambient region of air and a curtain of heavy gas in the ambient region. The thermodynamic state of the fluids in the flow domain is shown in Fig. 1. The heavy gas concentration profile in the curtain region is given by the Mikaelian fit indicated in Fig. 2 where the parameters (A,B,β,α,k) are assumed to be gaussian random variables with mean (0.7,0.2,-0.04,0.836,1.745) and standard deviation (5,5,10,0.5,0)% of mean. These are the values reported in the experiment [2] except the std. deviation of k is assumed to be zero, to maintain the periodic boundary condition in the cross-sectional plane. A sample line cut of $\phi_{HeavyGas}$ through the x and z is shown in Fig. 2. Time is initialized to zero when the incident shock meets the interface. A case of reshock is also studied, where the incident shock reflects off the end wall and reimpacts the interface at $\sim 600\mu$s.

The heavy gas is a mixture of SF_6 and acetone. The effect of acetone (used as a tracer species for PLIF visualization purpose) on the flow is found to be non-negligible [5]. In this study we account for the presence of all the three species-air,SF_6 and acetone. Molecular viscosity μ_i of the pure species are computed using the Chapman-Enskog equation (similar model is used for mass diffusivity D_i and thermal conductivity κ_i). The molecular properties of the fluid mixture is calculated using Wilke mixing model (for μ and κ) and the Ramshaw self-consistent effective diffusivity model [6](for D).

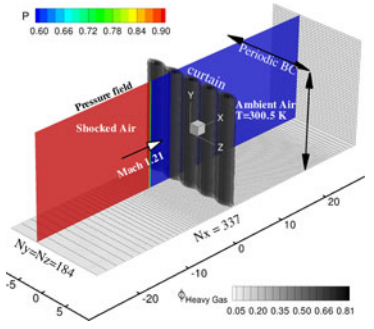

Fig. 1 Initial conditions

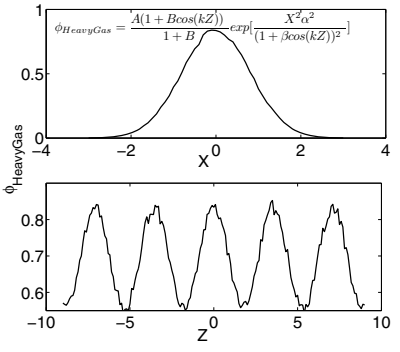

Fig. 2 Mass fraction of heavy gas across curtain

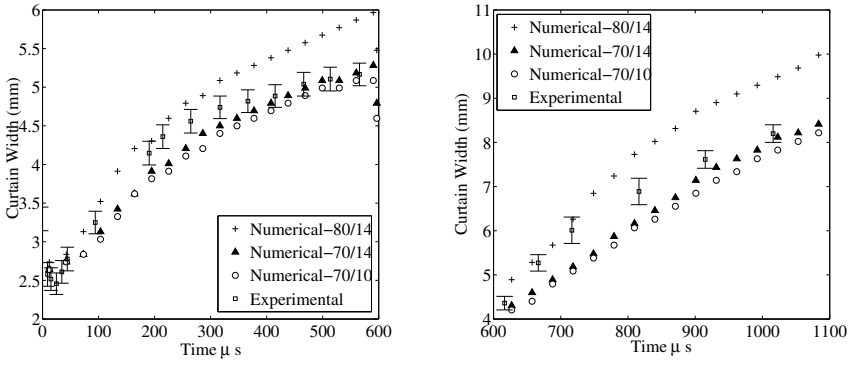

Fig. 3 Temporal evolution of curtain width (**a**) before and (**b**) after reshock

3 Results

Accurate characterization of the absolute concentration levels of the species in the heavy gas mixture at the initial conditions in the experiments is a challenging task and reliable data of the same is not available. Three simulations with different peak concentration levels of the heavy gas mixture are conducted. SF_6 and acetone composing the heavy gas are assumed to be well mixed and have the peak mass fraction values of (0.80,0.14), (0.70,0.14) and (0.70,0.10). Higher concentration levels of the heavy gas mixture cause larger vorticity deposition on the interface following the shock impact, leading to a larger instability growth rate. The measure of the curtain width with time shown along with the experimental data [2] in Fig. 2(a)(before reshock) and Fig. 2(b)(after reshock) exhibits this trend. The numerical simulation corresponding to (0.70,0.14) is seen to be in good agreement with

the experimental data. The following results will correspond to this case. Results are non-dimensionalized by using a reference length scale $l_{ref} = 1mm$ and a reference velocity scale $u_{ref} = a^o_\infty$(upstream sound speed).

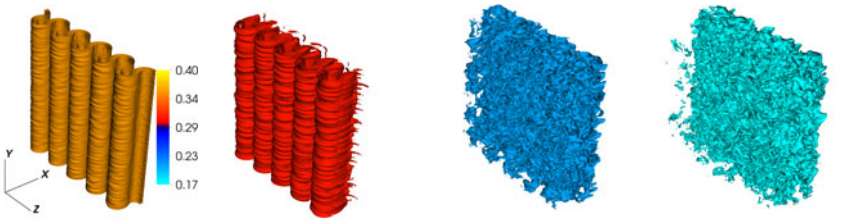

(a) (b) (c) (d)

Fig. 4 Time evolution visualizing iso-surface of $\phi_{HeavyGas}$=45% $\phi^{Max}_{HeavyGas}$ colored by the value at time (**a**) 152 (**b**) 547 (**c**) 943 (**d**) 1247 μs

Temporal evolution of the iso-surface of the heavy gas mass fraction is shown in Fig. 4. Vorticity deposited by the initial shock impact causes counter rotating vortex pairs to be formed which result in the mushroom-like shapes (Fig. 4(a),(b)). Re-shock at 635μs deposits higher energy into the non-linear flow-field causing the large scale structures to break up and causing a chaotic flow-field at late times (Fig. 4(c),(d)).

The fluctuating velocity field is defined as: $u_i\prime(x,y,z,t) = u_i(x,y,z,t) - \langle u_i\rangle(x,t)$ where the average velocity field is the velocity averaged over the cross section: $\langle u_i\rangle(x,t) = \int_{-Ly/2}^{Ly/2}\int_{-Lz/2}^{Lz/2} u_i(x,y,z,t)dydz$. A measure of the turbulent kinetic energy given by TKE$= \langle u\prime_i u\prime_i\rangle$ is plotted in Fig. 5. Following the initial shock impact the TKE in the domain shows a slow decay and a double peak structure after re-shock followed by a rapid decay. The fluctuating velocity field is characterized by the histogram at t$\sim 715\mu$s plotted along with the experimental data [2] in Fig. 6. While the span-wise component of velocity shows good agreement with the experimental data, the stream-wise component is seen to have a double-peak structure. This is perhaps due to the fact that the velocity measured in the experiments only records the velocity of the seeded heavy gas and the component of velocity of the surrounding air is ignored while the numerical result takes into account the velocity field in the entire domain (including air and heavy gas). The spectra of TKE and variance of the scalar mass fraction of the heavy gas measured as the sum of two dimensional spectras computed over the stream-wise extent of the curtain are shown in Fig. 7(a) and (b). The spectra show a -5/3 slope for more than half a decade. The large scale structures persistant at the initial times, characterized by the multiple peaks in the spectra, are seen to transition into smaller scale chaotic motion at late times. Also the amplification in TKE following reshock (domain integral of the spectra) is evident from the overall increase in the magnitude of the spectra.

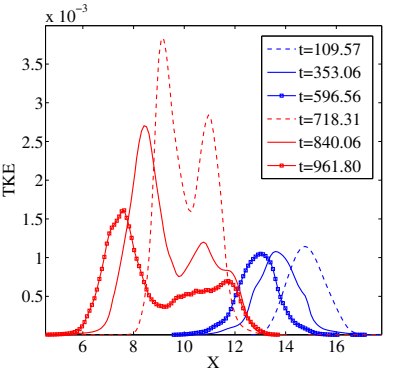

Fig. 5 Evolution of turbulent KE before (blue) and after (red) re-shock

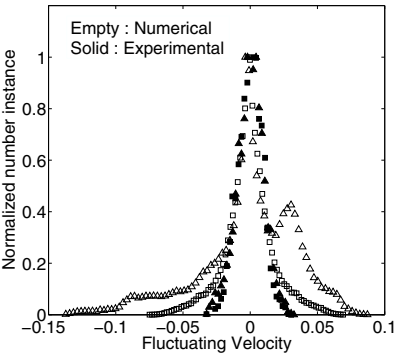

Fig. 6 Histogram of flucuating streamwise (△) and spanwise (□) velocity at t=715μs

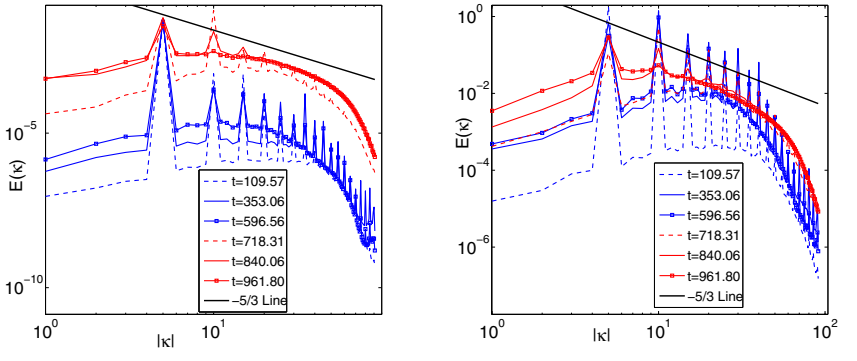

(a) (b)

Fig. 7 Spectra of (**a**) Turbulent KE and (**b**) Scalar Variance at different times before (blue) and after (red) reshock

4 Conclusions

Impulsive acceleration of a dense gas curtain in air is investigated by carrying out 3-d multi-species compressible Navier Stokes simulation of the flow. The growth of the primary instability is seen to be sensitive to the initial concentration profile of the species present in the flow requiring accurate characterization of the initial flow conditions. The reshock destroys the ordered velocity field present in the flow leading to a transition to turbulent flow causing enhanced mixing of the species present in the flow. Statistics of the fluctuating velocity field from the numerical simulations are compared to experimental measurements. Furthur investigation of the flow-field will be carried out through higher resolution calculations and reshock at different times. Other configurations like interaction of a planar shock with a

planar interface between two material, a spherical shock with a spherical interface between two material are problems being currently investigated.

Acknowledgments. The work is supported by DOE-SciDAC grant DE-FC02-06-ER25787. The code used is based on the extension of the code FDL3DI provided by Dr.M.R.Visbal. We acknowledge very helpful collaborations and discussions on the role of initial conditions and effect of tracer species with Dr. Prestridge.K. and Dr.Balakumar.B.J (experimental data) and team at Los Alamos National Lab. Computer time was provided by Argonne Leadership Computing Facility through the INCITE award.

References

1. Brouillette, M.: Annu., Rev. Fluid Mech. 34 (2002)
2. Balakumar, B.J.: Physics of Fluids 20 (2008)
3. Hill, D.J., Pantano, C., Pullin, D.I.: J. of Fluid Mech. 557 (2006)
4. Kawai, S., Shankar, S.K., Lele, S.K.: J. of Comput. Physics 229(5) (2010)
5. Shankar, S.K., Kawai, S., Lele, S.K.: Physics of Fluids 23(5) (2011)
6. Ramshaw, J.D.: J. of Non-equilibrium Thermodynamics 15 (1990)

Experimental and Numerical Investigations of the Inclined Air/SF_6 Interface Instability under Shock Wave

T. Wang, J.H. Liu, J.S. Bai, P. Lit, and K. Liu

1 Introduction

When the material interface separating two different fluids is accelerated by shock wave, a hydrodynamic instability happens, which is well known as the Richtmyer-Meshkov instability (RMI) [1,2]. The physical mechanism for the occurrence of RMI is the deposition of baroclinic vorticity produced by the misalignment of the pressure gradient of the shock wave and the local density gradient at the interface (i.e. $\nabla\rho\times\nabla p\neq 0$). Another type of instability is called the Kelvin-Helmholts instability (KHI) [3], which is because of the presence of tangential velocity jump at the interface. At late times of the RMI developing, because of the larger velocity difference at both sides of the spike and at the tip of the bubble, the KHI also starts to develop. The RMI is of importance in a wide range from man-made applications to natural phenomena such as inertial confinement fusion (ICF) and astrophysics. The KHI also has a prominent significance in plasma flow, radioactively driven molecular clouds [4], etc. So they have gained much attention for many years.

Various experiments [5-8] have been designed to study the interface instability. The apparatus of shock tube [7-9] is a kind of more attractive and useful experimental equipments. With the help of modern computers, numerical simulations have become a very useful and powerful method to investigate the interface instability [10-12]. It allows us to examine the data in detail far beyond the capability of the experimental apparatus. In this paper, we presented a parallel algorithm and code MVFT (multi-viscous-fluid and turbulence) of large-eddy simulation, which is based on the piecewise parabolic method (PPM) [13] and volume of fluid (VOF) [14], to simulate the multi-viscous hydrodynamic problems.

T. Wang · J.H. Liu · J.S. Bai · P. Li · K. Liu
Institute of Fluid Physics, China Academy of Engineering Physics, Mianyang 621900, China

And the code MVFT is used to simulate detailedly two shock tube experiments of shock-accelerated inclined Air/SF_6 interface instability, which are conducted in the National Key Laboratory of Shock Wave and Detonation Physics (LSD)'s horizontal shock tube apparatus. The numerical simulations have reproduced the developing process of interface, the complex waves structure. Good agreements between simulations and experiments have been achieved.

2 Experimental and Numerical Methods

2.1 Experimental Method

The experiments are conducted in LSD's horizontal shock tube apparatus of 5 m long and 5 cm×5 cm square cross-section. The flow visualization is done by a high-speed Schlieren photogray, and the time interval of two consecutive frames is 100 μs. The initial inclined interface between air and SF_6 is separated by the nitrocellulose membrane (approximately 1 μm thickness), which has an angle of 60 degree between its normal direction and the propagating direction of shock wave. The Mach numbers of incident shock wave are 1.23 and 1.41 in experiments. When the shock wave passes through the interface the nitrocellulose membrane has been broken up. A schematic of the shock tube apparatus and the computational model are shown in Fig. 1.

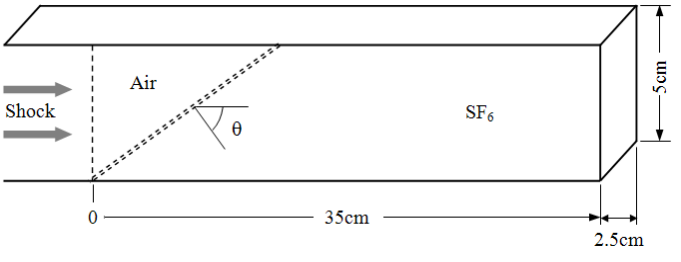

Fig. 1 Schematic of shock tube apparatus and computational model

2.2 Numerical Method

The governing equations of LES are filtered multi compressible N-S equations considering the viscosity and heat conduction. After Favre filtering, dropping the nonlinear terms, and assuming the subgrid-scale (SGS) turbulence behavior to be analogous to molecular dissipative mechanism, the filtered equations are obtained as follows in tensor notation:

$$\begin{cases} \dfrac{\partial \overline{\rho}}{\partial t}+\dfrac{\partial \overline{\rho}\widetilde{u}_j}{\partial x_j}=0 \\ \dfrac{\partial \overline{\rho}\widetilde{u}_i}{\partial t}+\dfrac{\partial \overline{\rho}\widetilde{u}_j\widetilde{u}_i}{\partial x_j}=-\dfrac{\partial \overline{p}}{\partial x_i}+\dfrac{\partial\left(\overline{\sigma}_{ij}+\tau_{ij}\right)}{\partial x_j} \\ \dfrac{\partial \overline{\rho}\overline{E}}{\partial t}+\dfrac{\partial\left(\overline{\rho}\widetilde{u}_j\overline{E}+\overline{p}\widetilde{u}_j\right)}{\partial x_j}=-\dfrac{\partial\left(\overline{q}_j+Q_j\right)}{\partial x_j}+\dfrac{\partial\left(\widetilde{u}_i\left(\overline{\sigma}_{ij}+\tau_{ij}\right)\right)}{\partial x_j} \\ \dfrac{\partial \overline{Y}^{(s)}}{\partial t}+\widetilde{u}_j\dfrac{\partial \overline{Y}^{(s)}}{\partial x_j}=\dfrac{\partial}{\partial x_j}\left(\widetilde{D}\dfrac{\partial \overline{Y}^{(s)}}{\partial x_j}\right) \quad s=1,2,\cdots,N-1 \end{cases} \tag{1}$$

Here, i and j represent the directions of x, y, z respectively; $\overline{\rho}, \widetilde{u}_k\left(k=i,j\right), \overline{p}, \overline{E}$ are the resolved-scale density, velocity, pressure and total energy per unit mass; N is of the kinds of fluids; $\overline{Y}^{(s)}$ is the volume fraction of the s^{th} fluid and satisfies $\sum_1^N \overline{Y}^{(s)}=1$; $\widetilde{D}$ is the diffusion coefficient and set to $\widetilde{D}=\nu/Sc$, ν is the kinematic viscosity of fluid and Sc is the Schmidt number. $\overline{\sigma}_{ij}$ is the deviatoric Newtonian stress tensor:

$$\overline{\sigma}_{ij}=\mu_{lam}\left(\frac{\partial \widetilde{u}_i}{\partial x_j}+\frac{\partial \widetilde{u}_j}{\partial x_i}-\frac{2}{3}\delta_{ij}\left(\frac{\partial \widetilde{u}_k}{\partial x_k}\right)\right) \tag{2}$$

μ_{lam} is the dynamic viscosity. $\tau_{ij}=\overline{\rho}\left(\widetilde{u_iu_j}-\widetilde{u}_i\widetilde{u}_j\right)$ is the SGS stress tensor and is calculated by the SGS model, which will be described in follows. $\overline{q}_j$ and Q_j are the resolved and SGS heat transport flux respectively, $\overline{q}_j=-\lambda_{lam}\partial\overline{T}/\partial x_j$, $Q_j=-\lambda_{SGS}\partial\overline{T}/\partial x_j$, $\overline{T}$ is the temperature, λ_{lam} and λ_{SGS} are the resolved and SGS heat conduction coefficient, $\lambda_{lam}=\mu_{lam}c_p/Pr_{lam}$, $\lambda_{SGS}=\mu_{SGS}c_p/Pr_{SGS}$, c_p is constant pressure specific heat, μ_{SGS} is the SGS turbulent viscosity, Pr is the Prandtl number. The equation of state (EOS) is the ideal gas state form.

The physical process, as described by eqs. (1), is decomposed into three sub-processes, i.e. the calculation of inviscid flux, viscous flux and heat flux by operator splitting technique. The PPM for multi-fluids is used to calculate the inviscid flux. The three-dimensional inviscid problem can be simplified into multi one-dimensional ones by using the dimension splitting technique, the two-step Lagrange-Remapping algorithm is applied to solving the one-dimensional equations in each direction respectively. Then the viscous flux and heat flux are calculated based on the computation of inviscid flux by using second-order spatial center difference and two-step Runge-Kutta time marching. The detailed derivations of numerical algorithm are referred in references [15, 16].

The SGS stress is calculated by Vreman SGS model [17], which is proposed by Vreman A W in the year of 2004. It is as follows:

$$\mu_{SGS}=c\rho\sqrt{\frac{B_\beta}{\alpha_{ij}\alpha_{ij}}} \tag{3}$$

where

$$\alpha_{ij} = \partial_i \tilde{u}_j = \frac{\partial \tilde{u}_j}{\partial x_i}$$
$$\beta_{ij} = \Delta_m^2 \alpha_{mi} \alpha_{mj} \tag{4}$$
$$B_\beta = \beta_{11}\beta_{22} - \beta_{12}^2 + \beta_{11}\beta_{33} - \beta_{13}^2 + \beta_{22}\beta_{33} - \beta_{23}^2$$

The model constant c is related to the Smagorinsky SGS model's constant C_S by $c \approx 2.5C_S^2$, C_S is determined to be 0.17 for isotropic turbulent flow by Lilly [18]. The symbol α represents the (3×3) matrix of derivatives of the filtered velocity $\tilde{u}$. If $\alpha_{ij}\alpha_{ij}$ equals zero, μ_{SGS} is consistently defined as zero. This model is essentially not more complicated than the Smagorinsky model, but is constructed in such a way that its dissipation is relatively small in transitional and near-wall regions, and it is found to be more accurate than the Smagorinsky model and as good as the dynamic model [17].

3 Results and Discussion

The two shock tube experiments are numerically simulated by the code MVFT. The width of shock tube in transverse direction (z direction) is 2.5 cm when simulating, the computational domain is [-5 cm, 35 cm]×[0 cm, 5 cm]×[0 cm, 2.5 cm]∈(x, y, z) and is divided into 32 sub-zones (using 16×2×1 CPUs) with total 800×100×50 grids for parallel calculation, the initial properties of air and SF_6 are listed in Table 1.

Table 1 Initial properties of air and SF_6

Gas	ρ (kg/m^3)	p (Pa)	V (m/s)	γ	μ_{lam} (Pa·s)
SF_6	5.34	1.0×10^5	0.0	1.09	1.4746×10^{-5}
Air	1.12	1.0×10^5	0.0	1.40	1.8526×10^{-5}

Fig. 2 shows the comparisons of experimental and simulated images of the interface and waves structure at the Mach number 1.23 (left column: experiments, right column: simulations, the dark, vertical band is the membrane support.), it reveals clearly the propagation of shock wave, the shape and position of shock front, its refraction at the interface and reflection at the upper and lower wall of shock tube, and the interface configuration, good agreements have been achieved between simulations and experiments. In addition to the occurrence of RMI at the interface, because the initial interface has an angle to the propagating direction of incident shock wave, the presence of tangential velocity difference at the interface also results in KHI, the small vortex structures appear at the interface (see Fig. 2(c)) and grow larger gradually for merging the surrounding smaller ones (see Fig. 2(c)-(g)). When the incident shock wave interacts with the initial inclined Air/SF_6 interface, the shock wave is refracted at the interface (see Fig. 2(a)). The propagating speed of shock wave in air is faster than in SF_6, so the refracted wave is also inclined, and the interface behind the refracted wave is deflected. The refracted wave is reflected at

the lower wall of shock tube, mach reflection occurs (see Fig. 2(b)), which is named as the 1st mach reflection. The refracted wave (OI), reflected wave (OR) and mach stem (OT) are all curved shock and intersect at a point which is called triple point (O), they are displayed in Fig. 3, the reflected wave, mach stem and triple point are all called the 1st ones. It can be seen that the waves structure is very complex around the triple point. If the angle of refracted wave to the lower wall of shock tube is less than a critical value θ_{cr}, the regular reflection [19] will happen, which is that the refracted wave and reflected wave intersect at a point located on the wall and move along the wall with the point, and has been verified in our other simulations. The 1st reflected wave interacts with the interface again, and the interface reflects an inward rarefaction wave. The 1st triple point moves obliquely-upwardly, and the 1st mach stem grows longer gradually. While the 1st reflected wave arrives at the upper wall of shock tube, the 2nd mach reflection happens again (see Fig. 2(e)), the 2nd reflected wave and mach stem are both weaker curved shock wave, and intersect the 1st reflected wave at the 2nd triple point, the 1st and 2nd triple points coincide presently (see Fig. 2(e)). When the 1st reflected wave has been reflected completely, the 1st

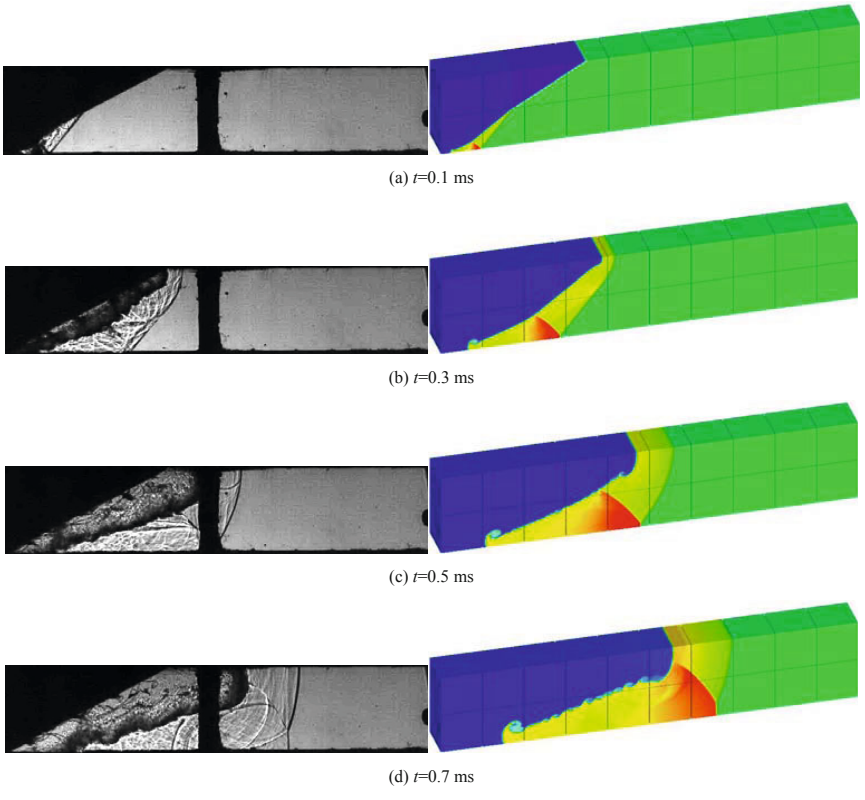

(a) t=0.1 ms

(b) t=0.3 ms

(c) t=0.5 ms

(d) t=0.7 ms

Fig. 2 Comparisons of experimental and simulated images of interface and waves structure (Ma=1.23, left column: experiments, right column: simulations)

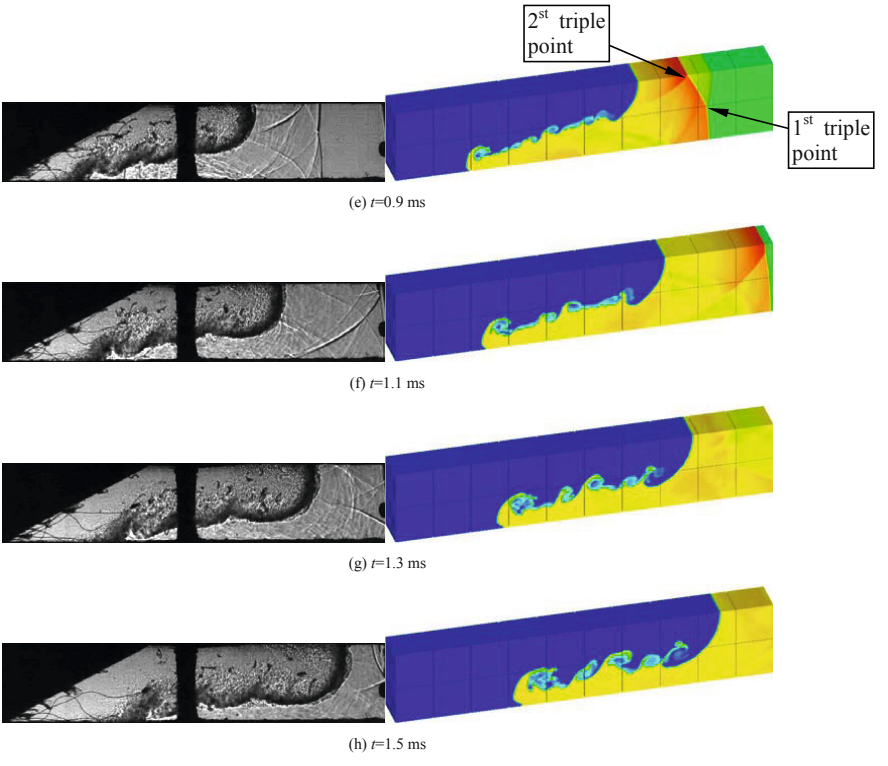

Fig. 2 (*Continued*)

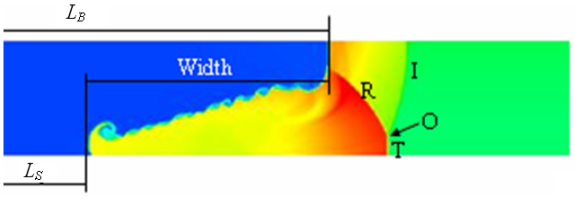

Fig. 3 Schematic of the refracted wave, reflected wave, mach stem, triple point, width of TMZ, displacements of bubble and spike

triple point has disappeared, the 2nd triple point changes to the 3rd one at which the 1st mach stem, 2nd mach stem and reflected wave intersect (see Fig. 2(f)). It also has been display that the 3rd mach reflection happens, and the 3rd and 4th triple points coincide in simulations, which are just beyond the observing test window.

The schematic of TMZ width, the displacements of bubble L_B and spike L_S are also given in Fig. 3. Fig. 4 shows the time history of TMZ width at the Mach number 1.23 (line: simulated results, symbol: experimental results). By the

comparison, the simulated width is very good agreement with the experimental one. In the beginning, because of the compression of incident shock wave, the width of TMZ decreases. When the incident shock wave has passed through the interface at about 0.2 ms, the shock compression vanishes, the width of TMZ starts to increase. Fig. 5 shows the time history of displacements of bubble and spike at the Mach number 1.23 (line: simulated results, symbol: experimental results), the simulated and experimental data also agree very well.

Fig. 6 displays the comparisons of experimental and simulated images of the interface and waves structure at the Mach number 1.41 (left column: experiments, right column: simulations, the dark, vertical band is the membrane support), the propagation of shock wave, the shape and position of shock front, its refraction at the interface and reflection at the upper and lower wall of shock tube, and the interface configuration are revealed clearly as well, good agreements have been achieved. The developing laws of interface and waves are similar to the ones at the Mach number 1.23, just because of the larger strength of incident shock wave, more energy is injected into the TMZ, therefore the interface and waves develop faster. Fig. 7 shows the time history of TMZ width at the Mach number 1.41 (line: simulated results, symbol: experimental results), the simulated data agrees well with the experimental ones except after about 1.0 ms when the largest error is about 5%. The interface is compressed more severely before the incident shock wave passes through it, and the interface evolves more quickly after the shock has passed through the interface completely, the width of TMZ also increases faster. Fig. 8 shows the time history of displacements of bubble and spike at the Mach number 1.41 (line: simulated results, symbol: experimental results), it reveals that they also agree well.

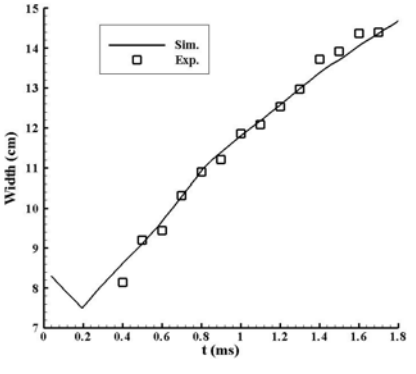

Fig. 4 Width of the TMZ vs. time (*Ma*= 1.23, line: simulated results, symbol: experimental results)

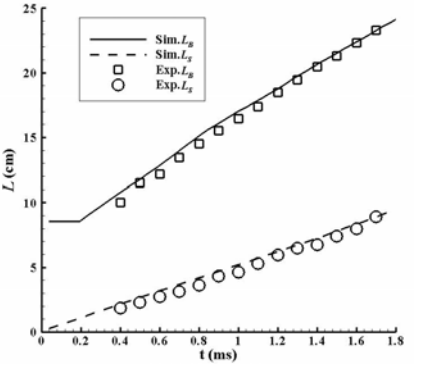

Fig. 5 Displacements of bubble and spike vs. time (*Ma*=1.23, line: simulated results, symbol: experimental results)

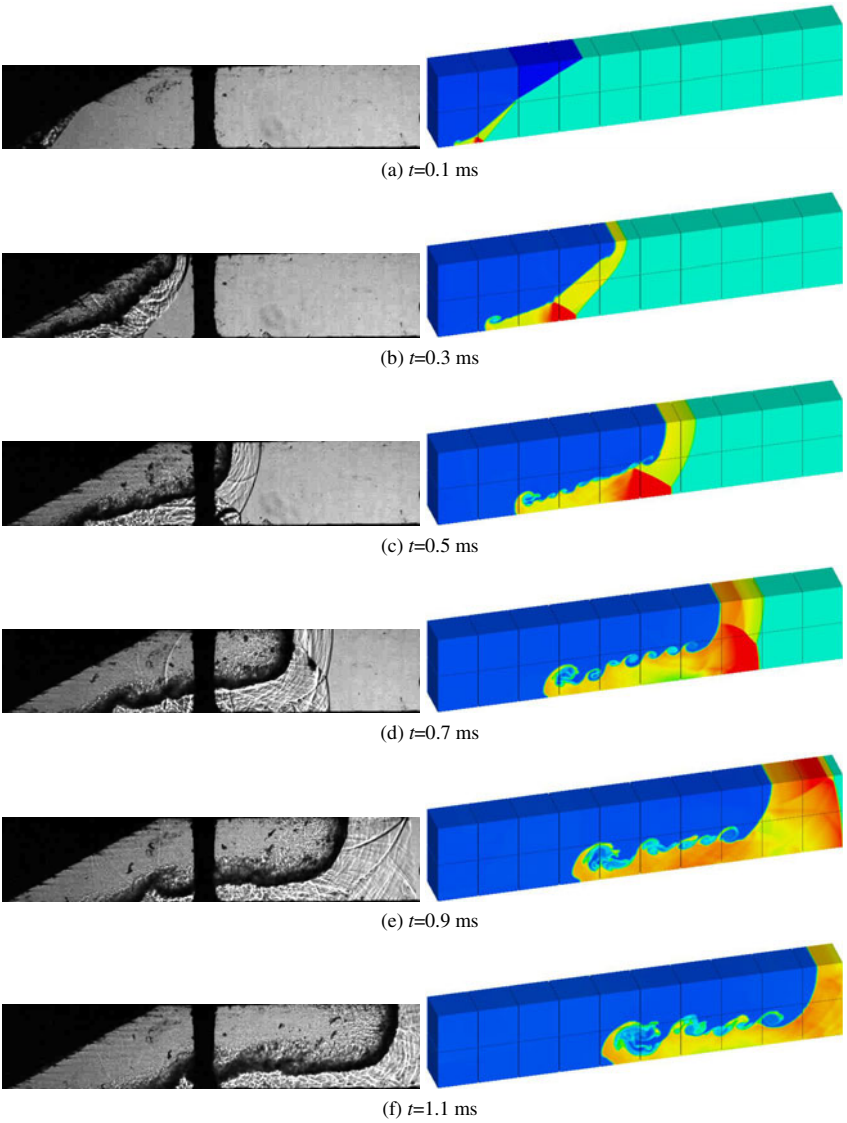

Fig. 6 Comparisons of experimental and simulated images of interface and waves structure (*Ma*=1.41, left column: experiments, right column: simulations)

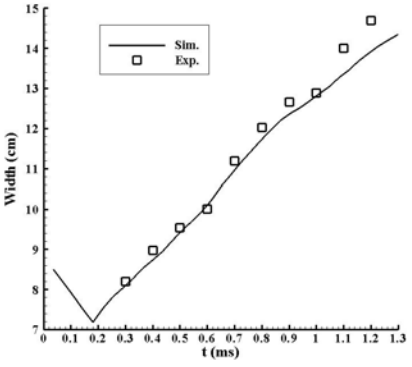

Fig. 7 Width of the TMZ vs. time (*Ma*= 1.41, line: simulated results, symbol: experimental results)

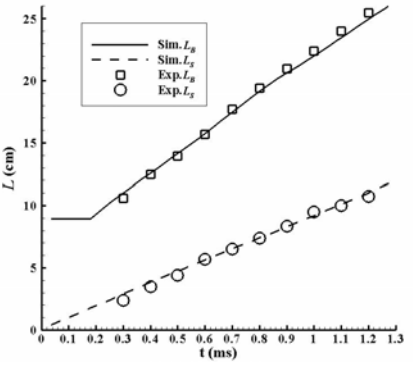

Fig. 8 Displacements of bubble and spike vs. time (*Ma*=1.41, line: simulated results, symbol: experimental results)

3 Conclusion

In this paper, two shock tube experiments of shock-accelerated inclined Air/SF_6 interface with different Mach numbers 1.23 and 1.41 are presented, and have been numerically simulated by our parallel code MVFT of LES. The developing process of interface and complex waves structures, e.g. the propagation, refraction, reflection of shock wave, mach stem and triple point in flows are reproduced and revealed by simulations. The interaction and combination of RMI and KHI lead to the turbulent mixing. The simulated evolving images are well consistent with the experimental ones, including the interface configuration, shape and position of shock fronts. The simulated width of TMZ, the displacements of bubble and spike also agree well with the experimental ones. The multiple mach reflections at the lower and upper walls of shock tube result in the alternate appearance of single triple point and double triple points. When the incident shock wave has a larger Mach number, more energy will be injected into the TMZ and the perturbed interface will develop faster.

References

[1] Richtmyer, R.D.: Communications on Pure and Applied Mathematics 13(2) (1960)
[2] Meshkov, E.E.: Soviet Fluid Dynamics 4(5) (1969)
[3] Chandrasekhar, S.: Hydrodynamic and Hydromagnetic Stability, p. 480. Oxford University Press (1961)
[4] Committee on High Energy Density Plasma Physics, Plasma Science Committee, Board on Physics and Astronomy, Division on Engineering and Physical Science. Frontiers in High Energy Density Physics. The National Academies Press (2001)
[5] Dimonte, G., Schneider, M.B.: Physical Review E 54(4) (1996)

[6] Jacobs, J.W., Sheeley, J.M.: Physics of Fluids 8(2) (1996)
[7] Houas, L., Jourdan, G., Schwaederlé, L., et al.: Shock Waves 12(5) (2003)
[8] Hosseini, S.H.R., Takayama, K.: Physics of Fluids 17(8) (2005)
[9] Holder, D.A., Barton, C.J.: Shock tube Richtmyer-Meshkov experiments: inverse chevron and half height. In: Dalziel, S.B. (ed.) 9th IWPCTM, p. 365. Cambridge University Press (2004)
[10] Mügler, C., Gauthier, S.: Physics of Fluids 12(7) (2000)
[11] Cohen, R.H., Dannevik, W.P., Dimits, A.M., et al.: Physics of Fluids 14(10) (2002)
[12] Bates, K.R., Nikiforakis, N., Holder, D.: Physics of Fluids 19(3) (2007)
[13] Colella, P., Woodward, P.R.: Journal of Computational Physics 54 (1984)
[14] Hirt, C.W., Nichols, B.D.: Journal of Computational Physics 9(1) (1981)
[15] Wang, T., Bai, J.S., Li, P., et al.: Science in China Series G 53(5) (2010)
[16] Bai, J.S., Liu, J.H., Wang, T., et al.: Physical Review E 81(5) (2010)
[17] Vreman, A.W.: Physics of Fluids 16(10) (2004)
[18] Lilly, D.K.: In: Goldstine, H.H. (ed.) Proceedings of IBM Scientific Computing Symposium on Environmental Sciences, Yorktown Heights, New York, p. 195 (1967)
[19] Wang, J.H.: Two-Dimensional Nonsteady Flow and Shock Waves, p. 74. Science Press (1994) (in Chinese)

Experimental Study on a Heavy-Gas Cylinder Accelerated by Cylindrical Converging Shock Waves

Ting Si, Zhigang Zhai, Xisheng Luo, and Jiming Yang

1 Introduction

When an initially perturbed interface separating two fluids with different properties is impulsively accelerated by a shock wave, the flow field will exhibit complex fluid dynamic phenomena due to the misalignment of the density and pressure gradients. It is often referred to as the Richtmyer-Meshkov (RM) instability [1, 2] and has been investigated within the past several decades due to its extensive physical applications such as inertial confinement fusion (ICF) [3], turbulent mixing in scram jet [4] and collapse in supernova [5]. Specifically, in most applications the shock waves maintain two-dimensional (e.g. cylindrical) or three-dimensional (e.g. spherical) converging shapes. Taking the ICF experiments, the thermonuclear fuel is contained in a small spherical solid capsule in advance and illuminated evenly by a number of well-designed laser beams. Simultaneously a spherical converging shock wave is generated and traverses the capsule. In the process even a tiny imperfection of the capsule surface can induce the RM instability and may destroy the fusion reaction [3]. It is therefore of fundamental interest and practical significance to explore the fluid dynamics of the flows in the interaction of interfaces with a converging shock wave.

The generation of converging shock waves in laboratory situations is a prerequisite in study of the RM instability experiments with respect to such shock waves. Perry and Kantrowitz [6] reported the design of a horizontal annular coaxial shock tube for the first time and visualized a cylindrical converging shock wave. Takayama et al. [7] established a horizontal converging shock tube and observed cylindrical shock waves with mode three or four instability generated by the struts supporting the inner core. Subsequently, a vertical coaxial diaphragmless shock tube was constructed [8] and later modified to produce a uniform cylindrical converging shock wave [9]. Besides the annular coaxial shock tube systems, recently Dimotakis and

Ting Si · Zhigang Zhai · Xisheng Luo · Jiming Yang
Department of Modern Mechanics, University of Science and Technology of China, Hefei, 230026, P.R. China

Samtaney [10] reported a gas lens technique in a two-dimensional wedge geometry to generate cylindrical shock waves and Hosseini and Takayama [11] designed an aspheric lens-shaped transparent test section to produce spherical shock waves by explosion of silver azide pellets.

Although attempts have been made for generating converging shock waves, most previous experimental works were conducted by studying the interaction of interfaces with a planar shock wave. Experimental study of the RM instability induced by converging shock waves is still limited [12]. The reason probably lies in the difficulty of the initial interface formation and the observation of flows [10, 12]. Recently, a simple but effective technique of generating the cylindrical converging shock waves based on shock dynamics theory was proposed by Zhai et al. in our laboratory [13]. A curved wall profile is designed in the shock tube test section and is capable of changing the incident planar shock waves directly into perfectly cylindrical ones. Experimental studies as well as further numerical and theoretical analyses have been performed to assess the influence of several parameters including the shock tube height, the converging angle and the incident planar shock Mach number on the wall profile and the resulting converging shock waves. The good agreement among them is achieved and verifies the method. Furthermore, the test section seems convenient for setting different types of interface and applying various diagnostic techniques for flow visualization. These include interfaces such as soap film bubbles, nitrocellulosic membranes, gas cylinders [14, 15] and gas curtains [16] and diagnostic techniques such as schlieren, shadowgraphy and laser sheet methods [14, 15, 16]. The present work is intended to investigate the interaction of the cylindrical shock waves with a heavy-gas (SF_6) cylinder in shock tube experiments. The originality lies in not only the cylindrical converging shock waves, but also the imaging method utilizing a high-power continuous laser (532 nm) combined with a high-speed video camera to capture the evolution of flow structures during a single test shot. The sequences of images based on the Mie scattering of the glycol droplets seeded in the gas cylinder obtained in a single run clearly show the development of the gas cylinder accelerated by converging shock waves.

2 Experimental Methods

The experiments were conducted in our 95 mm$\times$ 95 mm square cross section shock tube, whose total length is 9 m with a driver section of 2 m and a driven section of 7 m. Nitrogen was used as the driver gas and air as the driven gas. A planar shock wave with the Mach number M_0=1.2 was generated by the rupture of a polypropylene diaphragm initially separating the nitrogen and the driven air. For this investigation, the test section was fabricated with a well-designed wall profile based on the shock dynamics theory [13]. The gas cylinder flowing vertically through the test section was created in a careful procedure. In order to observe the development of the gas cylinder, planar imaging diagnostics were adopted. In particular, a continuous laser-sheet imaging method was developed to capture the evolution of the gas cylinder in a single run. The experimental and diagnostic details are documented below.

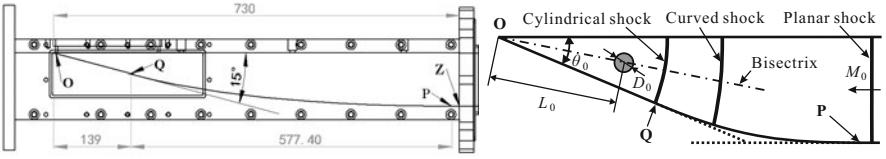

Fig. 1 Drawing of the test section (left) and schematic of initial conditions (right).

Fig. 1 presents the drawing of the test section which is designed by the shock dynamics theory and schematic of the initial conditions. The lower curved wall manufactured accurately by the linear cutting technique can be divided into three parts: the oblique line (from end point O to point Q) for focusing the cylindrical shock wave, the horizontal line (from point P to point Z) for connecting the shock tube and the middle curved line (from point Q to point P) for transferring the planar shock wave into the cylindrical one. In this study, the known parameters are chosen as the incident planar Mach number M_0=1.2, the converging angle θ_0=15^0, the test section height h=95 mm and length l=730 mm. Then the Mach number of Q can be calculated as M_Q=1.29, and the length of $\overline{OQ}$ is R_Q=143.87 mm.

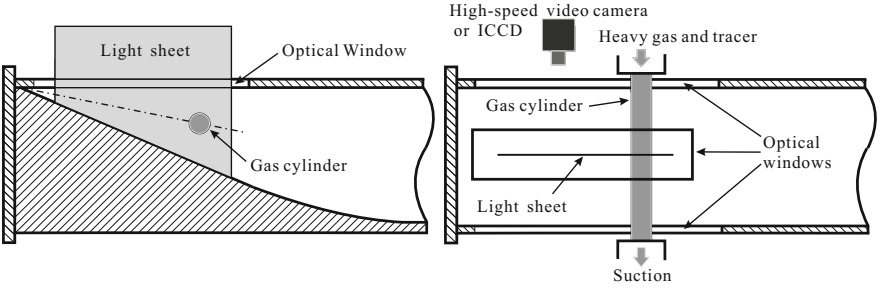

Fig. 2 Schematic of top view (left) and side view (right) of the test section.

Fig. 2 presents the detailed schematic of the test section showing the planar imaging diagnostics such as Mie scattering. The heavy-gas (SF_6) cylinder flows under gravity into the test section through a single, round nozzle of diameter D_0=5 mm mounted along the bisectrix of the converging angle on the top wall and is sucked mildly through a plenum on the bottom wall by a vacuum pump. The distance from the gas cylinder axis to the center of the curvature (i.e. the end point O in Fig. 1) is L_0=181.55 mm (Note that here L_0 is a little longer than R_Q, which means that the gas cylinder is not positioned within the converging section. That's why the evolution of the gas cylinder shown in Fig. 4 is asymmetric. More experiments will be performed and presented elsewhere.). Optical windows are located in top, bottom and side walls of the test section. The light sheet with thickness of less than 1 mm illuminates the flow through the center of the optical window horizontally. In our early

experiments, the flow was illuminated by a 1 Hz pulsed Nd:YAG laser operating at 532 nm and the scattering light of glycol droplets mixed with the heavy gas was captured by a 1024x1024 intensified charge coupled device (ICCD) (DH734i-18F-03). The triggering of the laser and ICCD was controlled by the pressure transducers and the timings after shock impact were controlled by a four channel delay generator (DG645). It is noting that the facility is analogical to the PLIF widely used in the previous works [14, 15, 16]. In such situations, however, numerous experiments must be performed to obtain the evolution process and the same initial conditions must be confirmed prior to each run again and again. In order to avoid the imperfect repeatability of the experiment, a continuous laser-sheet imaging method utilizing a high-power continuous laser (SDL-532-15000T, 15 W, 532 nm) combined with a high-speed video camera (FASTCAM SA5) is introduced in our current experiments. In particular, the evolution of flow structures can be captured during a single test shot. The success of this method lies in finding the equilibrium between the shutter speed of the camera and the brightness of the resulting images.

3 Results and Discussion

The shape of the shock waves moving in the converging part without any interfaces has been proven to be of cylindrical shapes experimentally and numerically [13]. Thus the detailed validation is neglected here and we mainly focus on the RM instability characteristics of the gas cylinder.

As mentioned above, our experiments were carried out using different planar imaging diagnostics. In the early stage, Mie scattering was implemented using the pulsed Nd:YAG laser and ICCD. In each test run the incident Mach number was checked according to the pressure transducer signals and the generation of the gas cylinder was operated carefully. Fig. 3 presents an example of the distorted interfaces captured by this Mie scattering system. It is shown that the gas cylinder is distorted and the change with time of the interface can be observed. However, it is a heavy work to obtain quantitative results and moreover, the precision is suspectable owing to the imperfect repeatability of the experiment. In the current stage, the continuous laser-sheet imaging method is utilized and the evolution of the gas cylinder can be observed in a single test run. Fig. 4 gives the evolution of the gas cylinder when the shock wave propagates towards and reflects from the end point. The time interval between two consecutive frames is 50 μs and the shutter of the camera is settled 1/153,000 s to ensure that the images with no superposition are visible.

As the shock passes by, the gas cylinder develops a crescent shape and then forms a vortex pair due to the vorticity that is initially deposited on the boundary of the gas cylinder (frames 1 to 11). The interface in bottom position of the frames (named bottom interface hereinafter) forms an arch and the boundary of the top interface is spreading, which is different from that accelerated by a planar wave in the previous studies [14, 15]. About 600 μs after the shock passage, the interface stops moving and is further compressed due to the reflected shock from the end point (frame 12). Then the bottom interface grows with a round shape, while the top interface

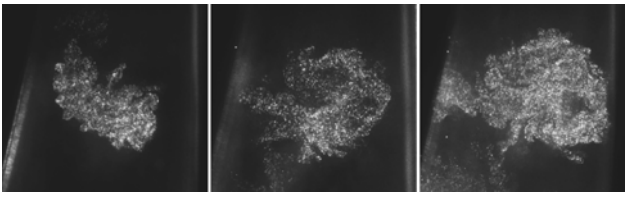

Fig. 3 Images of the distorted interface captured one per run by Mie scattering at different times with time interval of 1,000 μs and 200 μs, respectively.

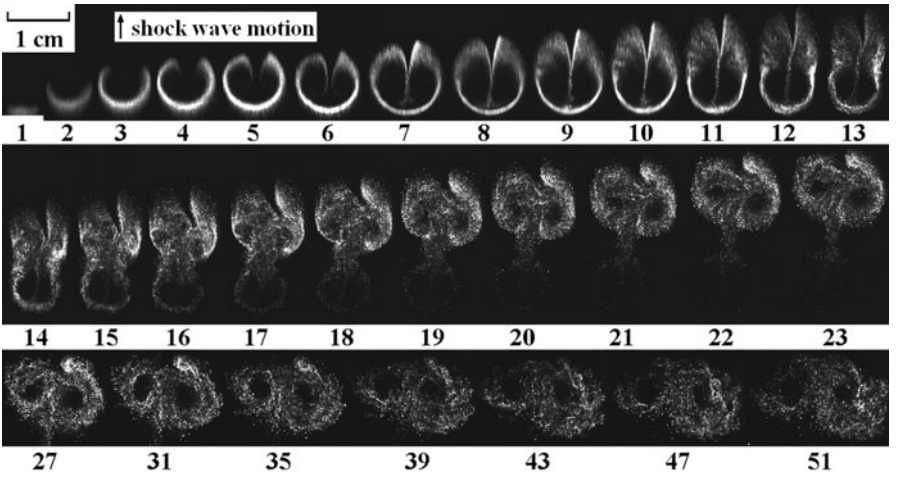

Fig. 4 The evolution of the heavy-gas cylinder. The frame rate is 20,000 fps and the shutter is 1/153,000 s.

develops into another vortex pair because of the formation of additional vorticity (frames 13 to 20). The results indicate that the vortical direction of the second vortex pair is opposite to that of the original one. At late times, the bottom interface diffuses and the second vortex pair develops due to its induced velocity and small scale disturbances are amplified (frames 21 to 51).

Although the evolving interfaces are asymmetric because of the nonuniform initial conditions (i.e. L_0 is longer than R_Q), the results obtained by the continuous laser-sheet imaging method still show the complete evolution process of the gas cylinder, which provides the possibility for further precious measurements and will be helpful for numerical validation and theoretical modeling.

4 Conclusion

The interaction of a heavy-gas (SF_6) cylinder with cylindrical converging shock waves was investigated experimentally in our well-designed shock tube. The flow

features were obtained by the Mie scattering. The ICCD combined with the 1 Hz pulsed laser captured the images only one per run, while the high-speed video camera combined with a high-power continuous laser was able to capture the evolution process in a single run. The RM instability characteristics of the gas cylinder accelerated by converging shock waves were presented. More improved experiments and corresponding quantitative analysis will be performed in the future.

Thanks to the support of the National Natural Science Foundation of China Project No. 10972214 and NSAF10776031 and the Fundamental Research Funds for the Central Universities.

References

1. Richtmyer, R.D.: Taylor instability in shock acceleration of compressible fluids. Commun. Pure Appl. Math. 13, 297–319 (1960)
2. Meshkov, E.E.: Instability of the interface of two gases accelerated by a shock wave. Transl. of Izv. Acad. Sci. USSR Fluid Dyn. 4, 151–157 (1969)
3. Lindl, J.D., McCrory, R.L., Campball, E.M.: Progress toward ignition and burn propagation in inertial confinement fusion. Phys. Today 45(9), 32–50 (1992)
4. Yang, J., Kubota, T., Zukoski, E.E.: Applications of shock-induced mixing to supersonic combustion. AIAA J. 35(31), 854–862 (1993)
5. Arnett, W.D., Bahcall, J.N., Kirshner, R.P., Woosley, S.E.: Supernova 1987A. Annu. Rev. Astron. Astrophys. 27, 629–700 (1989)
6. Perry, R.W., Kantrowitz, A.: The production and stability of converging shock waves. J. Appl. Phys. 22, 878–886 (1951)
7. Takayama, K., Kleine, H., Gronig, H.: An experimental investigation of the stability of converging cylindrical shock waves in air. Exps. Fluids 5, 315–322 (1987)
8. Watanabe, M., Onodera, O., Takayama, K.: Shock wave focusing in a vertical annular shock tube. In: Brun, R., Dumitrescu, L.Z. (eds.) Shock Waves at Marseille IV, pp. 99–104. Springer (1995)
9. Hosseini, S.H.R., Onodera, O., Takayama, K.: Characteristics of an annular vertical diaphragmless shock tube. Shock Waves 10, 151–158 (2000)
10. Dimotakis, P.E., Samtaney, R.: Planar shock cylindrical focusing by a perfect-gas lens. Phys. Fluids 18, 031705 (2005)
11. Hosseini, S.H.R., Takayama, K.: Implosion of a spherical shock wave reflected from a spherical wall. J. Fluid Mech. 530, 223–239 (2005)
12. Hosseini, S.H.R., Takayama, K.: Experimental study of Richtmyer-Meshkov instability induced by cylindrical shock waves. Phys. Fluids 17, 084101 (2005)
13. Zhai, Z.G., Liu, C.L., Qin, F.H., Yang, J.M., Luo, X.S.: Generation of cylindrical converging shock waves based on shock dynamics theory. Phys. Fluids 22, 041701 (2010)
14. Jacobs, J.W.: The dynamics of shock accelerated light and heavy gas cylinders. Phys. Fluids A 5, 2239–2247 (1993)
15. Tomkins, C.D., Kumar, S., Orlicz, G.C., Prestridge, K.P.: An experimental investigation of mixing mechanisms in shock-accelerated flow. J. Fluid Mech. 611, 131–150 (2008)
16. Orlicz, G.C., Balakumar, B.J., Tomkins, C.D., Prestridge, K.P.: A Mach number study of the Richtmyer-Meshkov instability in a varicose, heavy-gas curtain. Phys. Fluids 21, 064102 (2009)

Richtmyer-Meshkov Instability at the Interface of Gas-Oil-Water Three Matters

Hong-Hui Shi, Kai Du, Li-Te Zhang, Ruo-Ling Dong, Hui-Xia Jia, and Chao Wang

1 Introduction

Richtmyer-Meshkov (RM) instability occurs when a shock wave passes an interface that separates two media with different densities [1, 2]. Its research is of importance in inertial controlled fusion (ICF), shock-flame interaction in Scramjet engines, detonation wave generation and propagation in pulsed detonation engines, volcanic eruption, vapor explosion of nuclear fuel in nuclear power plants, etc. RM instability also appears in supernova explosion in astronomy and it has often been used in modeling the formation of fixed stars. On the other hand, since turbulent mixing becomes dominant in the later stage of RM instability, its study is theoretically meaningful in understanding turbulence problems [3]-[6]. The first theoretical model of RM instability was given by Richtmyer in 1960 [1]. He proposed an impulse model considering fluid compressibility. The first experiment of RM instability was done by Meshkov in 1969 [2]. Later, Benjamin and Fritz [7] conducted experiments of RM instability on a shocked interface between liquids having a density ratio of 10. In 1972, Myer and Blewett [8] simulated RM instability using Lagrange method and their results are qualitatively in agreement with that of Meshkov's experiment. Recent investigations have shown that the early stage of the instability is compressible and nearly linear and its later stage is nearly incompressible and nonlinear. In fluid mechanics, RM instability is a typical and difficult problem whereas innovation in experimental techniques is necessary in research deeply into RM instability phenomenon. Due to the great density difference between a gas and a liquid, it is convenient to visualize a gas-liquid interface in RM instability [9]-[12]. Based on these work, we put a layer of silicon oil on the water column. Thus, the oil layer is bounded by a gas-oil interface and an oil-water interface. Therefore, when a shock wave passes through the layer, RM instabilities with the Atwood number $A_t = 1$ and $A_t = 0$ all occur simultaneously. This means that an interface with a wide range of

Hong-Hui Shi · Kai Du · Li-Te Zhang · Ruo-Ling Dong · Hui-Xia Jia · Chao Wang
College of Mechanical Engineering and Automation, Zhejiang Sci-Tech University, Hangzhou 310018, China

Atwood number from 1 to 0 has been constructed and the experimental capability of the facility has been extended. The definition of the Atwood number is

$$A = \frac{\rho_2 - \rho_1}{\rho_2 + \rho_1} \tag{1}$$

where ρ_1 and ρ_2 are the fluids densities at two sides of the interface respectively. This paper's results have not been seen in open literatures.

2 Experimental Facility and Method

The experimental system is given schematically in Fig. 1, in which the main part is a vertical rectangular shock tube with inner dimension of 35 mm. The shock tube are mainly composed of (a) on the top, a 500 mm long high pressure section 3 filling with nitrogen or helium gas from high pressure tank 1; (b) in the middle, a 750 mm long low pressure section 6 at atmosphere; (c) in the lower part, a 200 mm long discharging section 11 that is open to a water container 13. The low pressure chamber 6 consists of two parts: the upper part of 500 mm long stainless section and the lower part of test section which has two side windows for observation. A light source 17 and a high-speed camera 16 are put on each side of the test section. The camera is FASTCAM-super10KC, PHOTRON Co. Ltd., Japan. The pictures taken by the camera are stored in a personnel computer 15. In experiments, the high pressure and the low pressure sections are separated by an aluminium diaphragm. The low pressure and the discharging sections are separated by a tin foil of 10 μm thickness. At the bottom of the water column, a 1 cm thick and 33 mm length square Teflon plate is placed to make sure the lower water surface keep plane shape in motion. The plate mass is 24 g. Water 8 is first filled into the low pressure section and then a layer of dyed silicon oil 7 is put on it. When the nitrogen or helium gas pressure in the high pressure section reaches the rupture pressure, a shock wave forms and moves downwards. When the shock wave impacts on the liquid column and accelerates it, the RM instability occurs. The initial curvature of the interfaces prior to shock arrival is due to the surface tension effect between the liquid and the solid wall of the shock tube. The wall effects (boundary layers) may influence the fluids behavior nearby the wall but will not affect the RM instability nature at the central area of the interface. Figure 2(a) shows the constructed testing fluid interface. The thickness of silicon oil layer can be adjusted according to requirements. The downward moving shock wave first accelerates the air/silicon oil interface and then it accelerates the silicon oil/water interface. Because silicon oil itself is transparent, this makes that the interface between silicon oil and water be difficult to be distinguishable. Therefore, we dye the oil chemically. Thus the interface of gas-oil-water three phases is clearly constructed. When the interface becomes unstable, the spike height h_s and bubble depth h_b are shown in Fig. 2(b). Zhuo [13] and Zhang [14] have provided their definitions and measurement methods about h_s and h_b. Combining their methods, this paper proposes a new measurement method, that is, the bubble depth is $h_b(2)=h_b(1)+\Delta h_b\text{-}v\Delta t$, where $h_b(2)$ is bubble depth at a later time (2) and $h_b(1)$ is

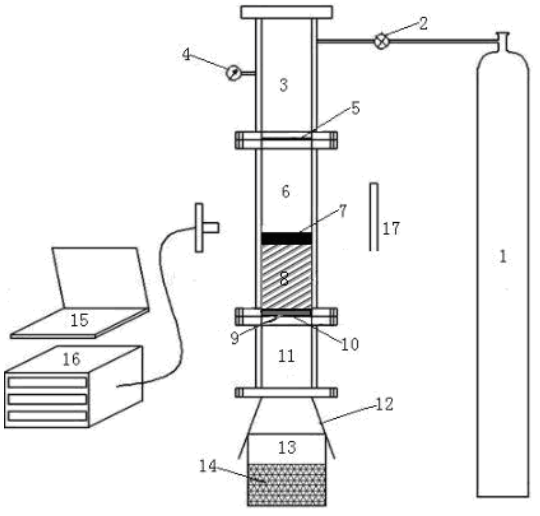

Fig. 1 Schematic of the experimental system. (1) High pressure tank; (2) Valve; (3) High pressure chamber; (4) Pressure meter; (5) Aluminium diaphragm; (4) Low pressure chamber; (7) Silicon oil; (8) Water column; (9) Teflon plate; (10) Tin foil; (11) Discharging chamber; (12) Cover; (13) Water container; (14) Sponge; (15) Computer; (16) High-speed camera; (17) Light source

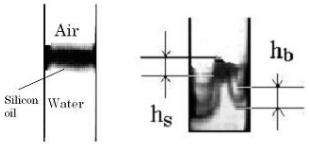

Fig. 2 The testing fluid interface and the definition of h_s and h_b

bubble depth at a previous time (1), Δt interval between time (1) and (2), Δh_b displacement of bubble bottom during Δt, v interface velocity. When the framing rate is 1000 fps, Δt = 1 ms. The spike height is $h_s(2)=h_s(1)+\Delta h_s - v\Delta t$, where $h_s(2)$ is spike height at time (2), $h_s(1)$ spike height at time (1), Δh_s displacement of spike tip during Δt (from time (1) to time (2)), interface velocity, v interval between time (1) and (2).

3 Results and Analysis

Figure 3 gives high-speed photographs of RM instability at the interface of air-silicon oil-water three matters when nitrogen gas is the driving gas and the shock Mach number is 1.20. It is seen that the interface experiences different stages such as small disturbance, interface deformation, formation of spike and bubble.

In Figs. 3(1)-(9), the interface starts to be accelerated by the shock wave and gradually becomes narrower after compression. From Fig. 3(10), air-silicon oil interface begins to be twisted but silicon oil-water interface still remains relatively flat. From Fig. 3(19), the oil-water interface also starts to deform, on which bubble structure appears prior to that on the air-oil interface, as shown in Fig. 3(26). Bubble on the air-oil interface first appears in Fig. 3(30). The annexing phenomenon among bubbles with different wavelengths has not been found. The reasons for this are that (1) bubble number on the same interface are little and there are actually two bubbles. The distance between the bubbles is sufficiently large; (2) the velocities of the two bubbles are quite close so that it will not happen that large bubble becomes larger and small bubble becomes smaller [10, 13]. Spike structure only appears on the air-oil interface (see Fig. 3(43)) and is belong to single module. Experimental results at different Mach numbers all confirm the single module spike structure. In Figs. 3(26)-(27), $h_b(L)$ and $h_b(R)$ represent bubble depths on the left and right sides of the oil-water interface respectively. In Fig. 3(30), h_b^* represents bubble depth at the air-oil interface. In Fig. 3(34), h_s represents spike height at the air-oil interface. Because it is difficult to distinguish outline at the top portion of the oil-water interface, spike height there will not be measured and accounted. The relationships of above parameters variation with time are given in Figs. 4(a)-(c) respectively. Figure 4(a) show that at the oil-water interface (when Atwood number approaches 0), bubble depth varies with time linearly. Figure 4(b) show that at the air-oil interface (when Atwood number approaches 1), relationship between bubble depth and time is a squared one. These results are different from that of Alon et al. [5] who consider that $h_b \propto t^{0.4}$ fits any Atwood number. However, they are basically in agreement with that of Zhang's experiment [11, 14], i.e., $h_b \propto t^2$, in which Zhang

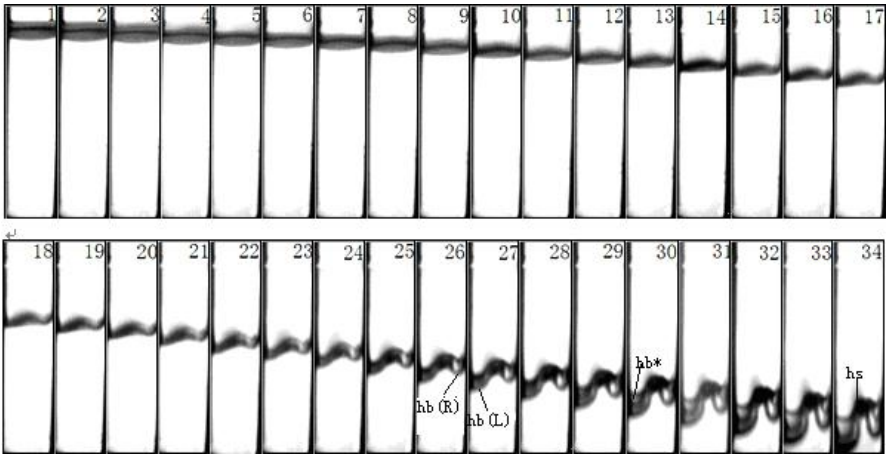

Fig. 3 RM instability at the interface of air-silicon oil-water three matters. Nitrogen gas as driving gas, shock Mach number $M = 1.20$, interframe time $\Delta t = 1$ms, height of water column 145 mm, thickness of silicon oil 9-10mm

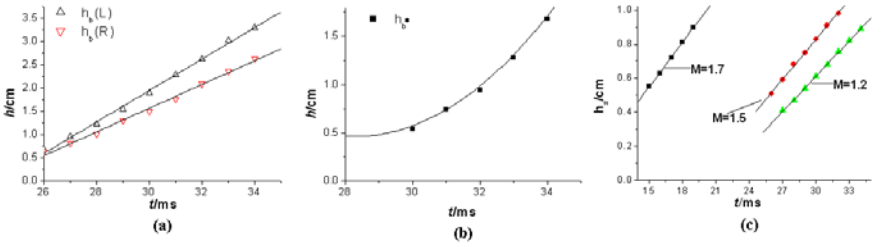

Fig. 4 Relationships of spike height, bubble depth and time. RM instability at the interface of air-silicon oil-water three matters driven by nitrogen gas. (a) Bubble depth at silicon oil-water interface, M = 1.20, (b) Bubble depth at air-silicon oil interface, M = 1.20, (c) Spike height at air-silicon oil interface at different Mach numbers

tested air-water and air-alcohol interfaces where Atwood numbers are close to 1. We also find that formation of bubble at the upper interface is slower than that at the lower interface. Therefore, if the shock Mach number is increased, there may be no bubble formation on the upper interface because the interface is accelerated to move too fast to allow bubble forming. In accordance with [3], $h_i=\alpha_i A_t g t^2=2\alpha_i A_t Z$, where A_t is Atwood number, Z interface position at time t, α a constant, i representing b or s which denotes bubble or spike respectively. Obviously, this formula is not suitable for the case of $A_t \to 0$ such as a silicon oil-water interface because the result of $h_i \to 0$ is impossible in actual situations. This demonstrates one of the advantages of our experiment to explore this result. For the air-silicon oil interface of $A_t \to 1$, the experimental data show that $\alpha_s/\alpha_b \approx 0.53$ that is much smaller than $\alpha_s/\alpha_b=3$ in [3]. It is seen from Fig. 4(c) that spike heights at different Mach number all grow with time linearly, i.e., $h_s \propto t$. Greater the Mach number is, much faster the growing velocity. This is in agreement with [5] and [14]. Figure 5 gives high-speed photographs of RM instability at the interface of air-silicon oil-water three matters when helium gas is the driving gas and the shock Mach number is 2.25. It is seen that although the interface evolution process driven by helium gas is similar to that driven by nitrogen gas, there are some differences, e.g., smooth single module spike can not been seen on the air-oil interface but many short thin thorns appear (see the black square frame in Fig. 5(22)). The definitions of $h_b(L)$, $h_b(R)$ and h_b^* in Fig. 5 are same as those previously stated. Figures 6(a) and (b) gives the measured data. Obviously, under the experimental conditions, bubble depth at the oil-gas interface is proportional to squared time. It is expected that as shock Mach number is increased the curves will be more like as quadratic curves. It has been found that in cases of M = 1.51 and 1.85 driven by helium gas, bubble depth at the oil-water interface is proportional to first order of time. At the air-oil interface, the results show that bubble depth grows with quadratic time.

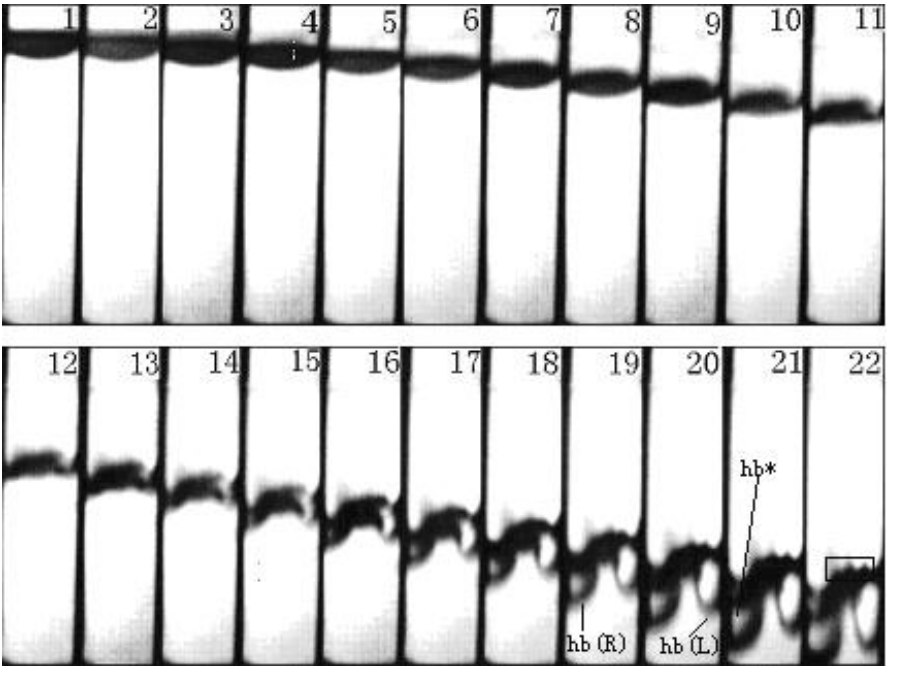

Fig. 5 RM instability at the interface of air-silicon oil-water three matters. Helium gas as driving gas, shock Mach number $M = 2.25$, interframe time $\Delta t = 1$ms, height of water column 145 mm, thickness of silicon oil 9-10mm

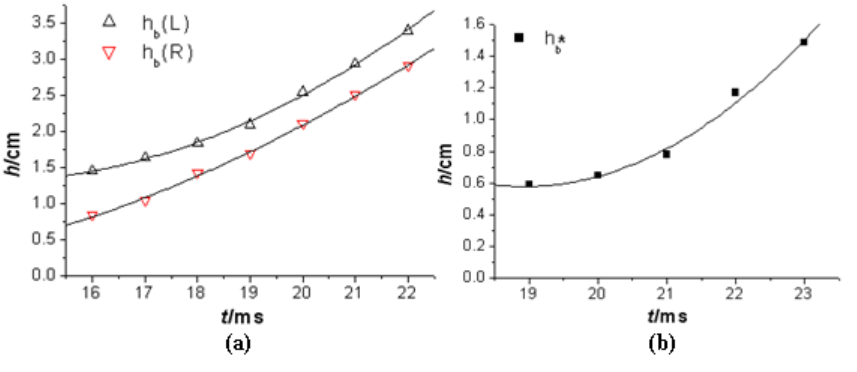

Fig. 6 RM instability at the interface of air-silicon oil-water three matters driven by helium gas. (a) Silicon oil-water interface, M = 2.25. Relationships of bubble depth and time. (b) Air-silicon oil interface, M = 2.25.

4 Conclusions

Silicon oil is a kind of high viscosity fluid. The high viscosity resists surface deformation and this makes turbulent mixing at the later stage of RM instability not occur or be delayed. This paper's work confirms the effect of fluid viscosity on transient RM instability which was reported by Shi and Kishimoto [15]. It is also known that the interface with small Atwood number is easier to develop in comparison with the large Atwood number interface. RM instabilities driven by nitrogen and helium gases are somewhat different. Change in shock Mach number does not change the general tendency of the instability but changes speed of the upper interface development. The thickness of silicon oil layer is also an important factor of affecting RM instability. When 4 5 mm thick oil layer presents, the layer separates from water and breaks up after instability begins. When $A_t \rightarrow 0$,$h_b \propto t$; when $A_t \rightarrow 1$, $h_b \propto t^2$ and $h_s \propto t$. This conclusion is in agreement with those in [14, 15]. However, this paper's experiment indicates that when using helium gas as driving gas, the first half of the conclusion is true only when the Mach number is not large

Acknowledgements. This work was supported by the National Natural Science Foundation of China with grant no. 10802077 and 10672144.

References

1. Richtmyer, R.D.: Commun. Pure Appl. Math. 13 (1960)
2. Meshkov, E.E.: Fluid Dynamics 4 (1969)
3. Zhou, Y.: Phys. Fluids 13, 2 (2001)
4. Ramshaw, J.D.: Phys. Rev. E 58 (1998)
5. Alon, U., Hecht, J., Ofer, D., Shvarts, D.: Phys. Rev. Lett. 74 (1995)
6. Zhang, Q., Sohn, S.-I.: Phys. Rev. Lett. 212 (1996)
7. Benjamin, R.F., Fritz, J.N.: Phys. Fluids 30 (1987)
8. Meyer, K.A., Blewett, P.J.: Phys. Fluids 15 (1972)
9. Shi, H.H., Zhuo, Q.W.: Chinese Journal of Theoretical and Applied Mechanics 39 (2007)
10. Zhuo, Q.W., Shi, H.H.: J. Exp. Fluid Mech. 21 (2007)
11. Shi, H.H., Zhang, G., Du, K., Jia, H.X.: Journal of Hydrodynamics Ser. B 21(2009)
12. Shi, H.H., Zhuo, Q.W.: Shock Wave Induced Instability at a Rectangular Gas/Liquid Interface. In: Shock Waves, pp. 1211–1216. Springer (2009)
13. Zhuo, Q.W.: Experimental Study of Richtmyer-Meshkov Instability at a Gas/Liquid Interface in a Shock Tube. Masters Thesis, Institute of Mechanics, Chinese Academy of Sciences (2006)
14. Zhang, G.: Experimental Research on the Linear and Non-linear Fluid Dynamic Processes in Richtmyer-Meshkov Instability at a Gas/Liquid Interface. Masters Thesis, Zhejiang Sci-Tech University, China (2009)
15. Shi, H.H., Kishimoto, M.: Explosion and Shock Waves 23 (2003)

Experimental Shock-Initiated Combustion of a Spherical Density Inhomogeneity

N. Haehn, C. Weber, J. Oakley, M. Anderson, D. Rothamer,
D. Ranjan, and R. Bonazza

1 Introduction

A planar shock wave that impulsively accelerates a spherical density inhomogeneity baroclinically deposits vorticity and enhances the mixing between the two fluids resulting in a complex, turbulent flow field. This is known as the classical shock-bubble interaction (SBI) and has been a topic of study for several decades [1,2,3,4,5,6,7,8,9,10,11,12], and closely related the Richtmyer-Meshkov instability (RMI) [13,14]. While the classical SBI problem concerns a reactively neutral bubble, the present experimental study is the first of its kind in which a spherical bubble filled with a stoichiometric mixture of H_2 and O_2 diluted with Xe is accelerated by a planar shock wave ($1.35 < M < 2.85$) in ambient N_2, and will be referred to as reactive shock-bubble interaction (RSBI).

The first SBI experiments were performed by Rudinger and Somers [15]. Haas and Sturtevant utilized shadowgraph diagnostics to visualize the bubble morphology and complex shock patterns that develop during SBI [1]. High speed shadowgraph diagnostics were first implemented by Layes et al. [8,10,9] and were used to generate time histories of the bubble morphology resulting in less temporal variation inherent to most experiments.

Ranjan et al. utilized a retractable injector which released the bubble into a state of free-fall (or free-rise) and resulted in more spherical initial conditions while removing the influence of the stationary injector on the evolving flow field [2,4]. These experiments also used planar Mie scatter diagnostics which provided a 2D cross-section (as opposed to the integrated nature of the shadowgraph diagnostics)

N. Haehn · C. Weber · J. Oakley · M. Anderson · D. Rothamer · R. Bonazza
University of Wisconsin - Madison
Madison, WI 53706

D. Ranjan
Texas A&M University
College Station, TX 77843

which offered better resolution of small scale structures and internal vortex ring geometry. Haehn et al. performed experiments with reshock, where the incident shock wave reflects off the tube end-wall and reaccelerates the bubble, which had, at the time of reshock, developed into a vortex ring [5, 12].

A lot of work has been performed on deflagration to detonation transitions of reactive flows [16, 17]. This class of problems has special significance in astrophysical flows, and as such, are often studied numerically [18, 19]. The experiments of Liu et al. [17] studied the detonation ignition and diffraction within a layered shock tube with undiluted mixtures of H_2 and O_2. This situation has since been the topic of several numerical studies [20, 21] because of the complex interaction between detonations, shocks, reacted and unreacted regions and numerous shock diffractions/reflections.

For the present RSBI experiments, we would like to determine if it is possible to use the hydrodynamic phenomena of shock-focussing to initiate the chemical reactions within the isolated reactive mixture. If so, how and when does this reaction initiate and then how does the reaction front progress? Are the two processes (hydrodynamics and chemical reactions) highly coupled? What are the time scales associated with each process?

2 Experimental Description

The RSBI experiments are performed at the Wisconsin Shock Tube Laboratory (WiSTL) in a 9 m-long vertical shock tube with a square (25.4×25.4 cm^2) cross-section. A schematic of the last 2 m of the shock tube is shown in Fig. 1. A soap bubble containing a mixture of gases is prepared on a pneumatically-retracted injector and released into free-fall approximately 250 ms prior to the arrival of the incident shock wave.

A small quantity of the reactive gas mixture is prepared ahead of time (56% Xe, 29% H_2, 15% O_2, resulting in a mixture density and experimental Atwood number of 3.28 kg/m^3 and 0.48, respectively). Xenon was chosen for the diluent because it is chemically inert and has a larger density than Ar (leading to a stronger shock-focussing effect), even though more data is available in the literature for Ar as a diluent. For the present study, the higher density of Xe is crucial for maintaining a large Atwood number, and the converging lens geometry.

The initial bubble free-fall and shock arrival are captured on two front-lit, high speed, CCD cameras (Redlake MotionPro X4-Plus) at 250 fps, oriented perpendicular to one another as seen in Fig. 1. This orientation allows the capture of the precise time, location and size of the bubble prior to the first shock acceleration. It also serves to ensure that the free-falling bubble has not veered from the imaging plane. A series of pressure transducers along the length of the shock tube measure the wave speed and control the external triggering of the time-sensitive diagnostics.

The post-shock bubble morphology is imaged using planar Mie scattering diagnostics. A double-pulsed Nd:Yag laser (15 ns pulses at $\lambda_{\text{Laser}} = 532$ nm) illuminates the midplane of the bubble. The Mie scattered signal is reflected off the atomized

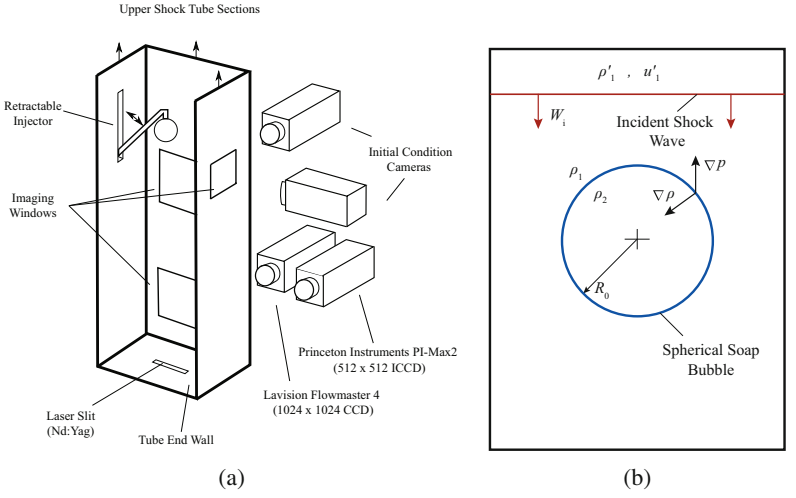

Fig. 1 Schematic of the experimental setup showing: a) The bottom 2 m of the shock tube. Two initial condition cameras capture the free-fall and shock acceleration of the bubble with perpendicular orientations. Two additional cameras are used to image the post-shock bubble morphology and combustion. b) The initial condition for the free-falling spherical bubble with a planar shock wave incident from above.

soap film and imaged with a dual frame, 1024 × 1024 CCD camera (Lavision Flowmaster 4) with a band-pass filter centered on 532 nm. Two post-shock Mie scatter images are recorded per experiment at times $t_{M,1}$ and $t_{M,2}$, measured from when the shock wave first contacts the apex of the bubble. Subscript 'M' is used to denote a Mie scatter image.

As a chemical intermediate of the combustion process, the OH radical (OH^*) is used to image the ignition and flame propagation separate from the hydrodynamic bubble morphology. The chemiluminescence signal from the OH* is recorded at a resolution of 512 × 512 on a dual-frame ICCD camera (Princeton Instruments PI-MAX 2). The camera is fitted with a UV lens (50 mm, $f/1.2$) along with a long-pass ($\lambda > 275$ nm), short-pass ($\lambda < 325$ nm) and a color glass (UG11) filter. These exposures range from 3-1,000 μs, with two exposures recorded per experiment at times $t_{C,1}$ and $t_{C,2}$, which are again measured from the contact of the shock wave with the bubble apex. In this case, the subscript 'C' denotes a chemiluminescence image. The exposures durations of each image are labeled as $\Delta t_{C,1}$ and $\Delta t_{C,2}$, respectively.

3 Analysis

Figure 2 shows composite images for three different Mach numbers where the chemiluminescence images in yellow and red (corresponding to the first and

second exposures, respectively) have been over-layed upon the planar Mie scatter images shown in grayscale. In Figs. 2a and b, the combustion is seen to begin at a single location and to proceed throughout the duration of both exposures. As the reaction front propagates outward in the spanwise direction away from the ignition location, the vortex ring also translates downwards. A dramatic change occurs in the chemiluminescence images between Figs. 2b,c. Instead of a triangular shaped signal, which suggests a prolonged combustion phase with slower reaction front propagation speeds, a much faster combustion occurs, resulting in an oblate signal.

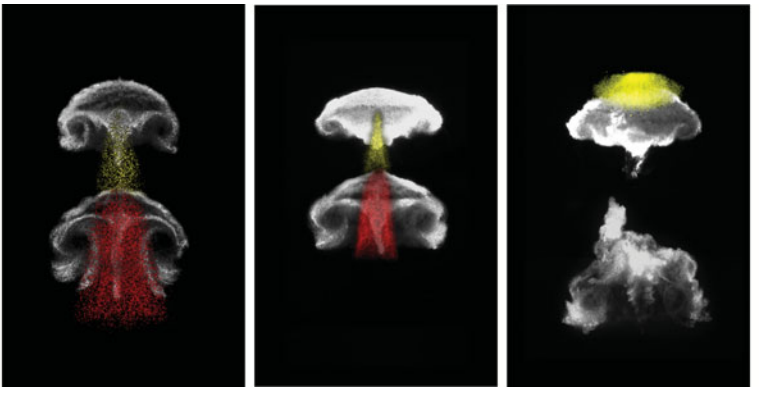

Fig. 2 Composite images showing the development of a shock-accelerated bubble filled with a reactive mixture (55% Xe, 30% H_2, 15% O_2). Each image consists of two chemiluminescence exposures in yellow and red overlayed upon two planar Mie scatter images in grayscale. For clarity, the signal levels have been adjusted and do not reflect the intensity of the chemiluminescence signal. In each image, the incident shock wave travels downward. The corresponding Mach number (in N_2) and image times are: (a) $M = 1.65$, $\tau_{M,1} = 3.6$, $\tau_{M,2} = 6.6$, $\tau_{C,1} = 3.6$, $\tau_{C,2} = 6.6$, $\Delta\tau_{C,1} = 3.0$, $\Delta\tau_{C,2} = 3.0$ (b) $M = 2.07$, $\tau_{M,1} = 1.90$, $\tau_{M,2} = 3.75$, $\tau_{C,1} = 1.90$, $\tau_{C,2} = 3.75$, $\Delta\tau_{C,1} = 1.85$, $\Delta\tau_{C,2} = 1.85$, and (c) $M = 2.85$, $\tau_{M,1} = 1.7$, $\tau_{M,2} = 3.7$, $\tau_{C,1} = 1.3$, $\tau_{C,2} = 2.3$, $\Delta\tau_{C,1} = 0.6$, $\Delta\tau_{C,2} = 0.6$

Summaries of the post-shock conditions and time scales are given in Table 1. The post-shock bubble temperature, T_B, and pressure, P_B are calculated from 1D gas dynamics for a slab geometry. The temperature and pressure were then used in a model developed by Tonello et al. [21] to obtain estimates of induction times, $\tau_{i,m}$, which are also shown in the Table 1. The hydrodynamic time scale, τ, is defined as the 'cloud-crushing' time of the bubble, $\tau = D_o/W_i$, where D_o is the initial bubble diameter, and W_i is the speed of the incident shock wave. Induction time estimates are also obtained from the experiments, measured from time $t^* = 1$, where $t^* = t/\tau$. Finally, using the hydrodynamic time scale and the experimentally measured induction time, a Damköhler number can be defined for this flow as $Da = \tau/\tau_{i,e}$, also summarized in Table 1. In these RSBI experiments, the temperature and pressure behind the transmitted shock wave will increase above these slab calculated values since the curvature of the transmitted shock wave is increased.

Table 1 Parameter overview for the reacting bubbles.

M	T_B (K)	P_B (atm)	$\tau_{i,m}$ (μs)	τ (μs)	$\tau_{i,e}$ (μs)	Da
1.35	401	2.25	∞	85	300	0.28
1.70	506	3.79	∞	68	270	0.25
2.07	690	6.63	∞	56	72	0.78
2.85	1155	13.96	11	40	5	8

For lower Mach numbers ($M = 1.35, 1.70, 2.07$), the 1D gas dynamics calculations for a slab geometry suggest the temperatures and pressures behind the transmitted shock wave should not be sufficient to initiate the reaction of the mixture without the benefit of shock-focussing (at least within a time scale relevant to the hydrodynamics of SBI), as is evidenced by the infinite induction times, $\tau_{i,m}$, shown in Table 1. The shock-focussing effect minimizes the induction time within a localized region, and therefore, the reaction is expected to initiate at this point.

For the high Mach number case, $M = 2.85$, the model predicts an induction time of 11 μs. This time scale is now comparable to, and even shorter than, the hydrodynamic time scale associated with the SBI. These values are also summarized in Table 1. This suggests that ignition could occur before the peak shock focussing has occurred, and could occur just upstream of the bubble nadir. Indeed, the experimental results suggest that, in the majority of instances, some amount of convergence occurs before ignition begins. The ignition appears to begin at a small region centered in the span-wise direction and located approximately 1/4 of a diameter upstream of the original bubble nadir.

4 Conclusion

A series of RSBI experiments have been carried out where shock-initiated combustion was observed as a result of the shock focussing effect. The time scales associated with the competing physics (hydrodynamics and chemical reactions) were shown to play an important role in the reaction ignition and propagation. For lower incident Mach numbers ($M < 2.07$), the hydrodynamic times scales are shorter than the chemical reaction time scales. This relationship inverts for the higher Mach number ($M = 2.85$), with a transition occurring just above $M = 2.07$.

References

1. Haas, J.F., Sturtevant, B.: Interaction of weak shock waves with cylindrical and spherical gas inhomogeneities. Journal of Fluid Mechanics 181, 41–76 (1987)
2. Ranjan, D., Niederhaus, J., Motl, B., Anderson, M., Oakley, J., Bonazza, R.: Experimental investigation of primary and secondary features in high-mach-number shock-bubble interaction. Physical Review Letters 98, 024502 (2007)

3. Ranjan, D., Oakley, J., Bonazza, R.: Shock-bubble interactions. Annual Review of Fluid Mechanics 43(1), 117–140 (2011)
4. Ranjan, D., Niederhaus, J., Oakley, J., Anderson, M., Bonazza, R., Greenough, J.: Shock-bubble interactions: Features of divergent shock-refraction geometry observed in experiments and simulations. Physics of Fluids 20, 036101 (2008)
5. Haehn, N., Ranjan, D., Weber, C., Oakley, J., Anderson, M., Bonazza, R.: Experimental investigation of a twice-shocked spherical density inhomogeneity. Physica Scripta T142 (2010)
6. Niederhaus, J.H., Greenough, J.A., Oakley, J.G., Ranjan, D., Anderson, M.H., Bonazza, R.: A computational parameter study for the three-dimensional shock–bubble interaction. Journal of Fluid Mechanics 594, 85–124 (2008)
7. Layes, G., Jourdan, G., Houas, L.: Distortion of a spherical gaseous interface accelerated by a plane shock wave. Physical Review Letters 91(17), 174502 (2003)
8. Layes, G., Jourdan, G., Houas, L.: Experimental investiagtion of the shock wave interaction with a spherical gas inhomogeneity. Physics of Fluids 17, 028103 (2005)
9. Layes, G., Jourdan, G., Houas, L.: Experimental study on a plane shock wave accelerating a gas bubble. Physics of Fluids 21, 074102 (2009)
10. Layes, G., LeMetayer, O.: Quantitative numerical and experimental studies of the shock accelerated heterogeneous bubbles motion. Physics of Fluids 19, 042105 (2007)
11. Samtaney, R., Zabusky, N.J.: Circulation deposition on shock-accelerated planar and curved density-stratified interfaces: Models and scaling laws. Journal of Fluid Mechanics 269, 45–78 (1994)
12. Haehn, N., Weber, C., Oakley, J., Anderson, M., Ranjan, D., Bonazza, R.: Experimental investigation of a twice-shocked spherical gas inhomogeneity with particle image velocimetry. Shock Waves, 1–7 (2011)
13. Richtmyer, R.D.: Taylor instability in shock acceleration of compressible fluids. Physica D: Nonlinear Phenomena 12, 1–3 (1984)
14. Meshkov, E.E.: Instability of a shock wave accelerated interface between two gases. NASA Technical Translation 13, 1–14 (1970)
15. Rudinger, G., Somers, L.M.: Behavior of small regions of different gases carried in accelerated gas flows. Journal of Fluid Mechanics 7, 161–176 (1960)
16. Gamezo, V., Khokhlov, A., Oran, E.: Deflagrations and detonations in thermonuclear supernovae. Physical Review Letters 92(21), 1–4 (2004)
17. Liu, J., Liou, J., Sichel, M., Kauffman, C.: Diffraction and transmission of a detonation into a bounding explosive layer. In: Twenty-first Symposium (International) on Combustion, pp. 1639–1647 (1986)
18. Gamezo, V., Khokhlov, A., Oran, E.: Thermonuclear supernovae: Simulations of the deflagration stage and their implications. Science 299, 77–81 (2003)
19. Oran, E., Gamezo, V.: Origins of the deflagration-to-detonation transition in gas-phase combustion. Combustion and Flame 148, 4–47 (2007)
20. Sichel, M., Tonello, N.A., Oran, E.S., Jones, D.A.: A two–step kinetics model for numerical simulation of explosions and detonations in H2–O2 mixtures. Proc. R. Soc. Lond. A 458, 49–82 (2002)
21. Tonello, N.A., Sichel, M., Oran, E.S.: Numerical simulations of the diffraction of planar detonations in H2-O2 mixtures. In: Symposium (International) on Combustion, vol. 26(2), pp. 3033–3039 (1996)

Investigations on a Gaseous Interface Accelerated by a Converging Shock Wave

Xiansheng Wang, Ting Si, Zhigang Zhai, Minghu Wang,
Jiming Yang, and Xisheng Luo

1 Introduction

The shock-accelerated inhomogeneous flows have been widely investigated for the fundamental interests and diverse applications in a broad range of spatial, temporal and energy scales, such as the supernova explosions, supersonic combustions and inertial confinement fusion (ICF) implosions. The particularly simple configuration, the shock-bubble interaction [1], has been considered as a basic configuration to study the flows. With respect to the development of the density-stratified interface impulsively accelerated by a shock wave, analogies may be drawn to the study of the Richtmyer-Meshkov (RM) instability [2, 3].

Most previous investigations were conducted on a simple but effective model including a gaseous bubble subjected to a planar shock wave which was first studied by Markstein [4] and Rudinger and Somers [5] about fifty years ago. Due to the difficulties in forming the inhomogeneity, Haas and Sturtevant [6] used a soap film to separate two gases and experimentally observed the shock refraction and interface deformation. Recently, more detailed mechanisms of the planar shock wave interacting with the spherical and cylindrical inhomogeneity have been experimentally studied in the shock tube [7-10] and numerically modeled [11, 12] in two and three dimensions with the results showing a good agreement with the experiments. The planar shock wave provides a simple configuration to study the shock-bubble interaction. However, in many cases, such as ICF, it is more suitable to employ the curved shock wave whose intensity varies with propagation, for example, the cylindrical shock waves generated in an annual coaxial vertical diaphragmless shock tube [13]. The flowfield becomes complex when the curved shock wave is involved. To authors' knowledge, experiments about the interaction of a curved shock wave with the inhomogeneity are still lacking.

Xiansheng Wang · Ting Si · Zhigang Zhai · Minghu Wang · Jiming Yang · Xisheng Luo
Department of Modern Mechanics, University of Science and Technology of China,
Hefei, 230026, P.R. China

The present paper discussed the interaction of a converging cylindrical shock wave with a cylindrical sulfur hexafluoride (SF_6) bubble. A technique based on the shock dynamics theory [14] was applied to design the shock tube test-section and made it available to produce the curved shock wave. The experimental results were acquired during a single run with assistants of the planar Mie-scattering imaging and high-speed photography. The corresponding numerical simulation was performed by means of a two-dimensional solver VAS2D [15]. The results showed a good agreement with the experiments. Furthermore, the numerical results were analyzed by a wavelet transform. A quantitative feature of the regular vortical structure in the flowfield was revealed in the wavelet results.

2 Experimental and Numerical Methods

The present experiments have been conducted at a 70×40 mm^2 rectangular shock tube consisting of a driver section (1.7 m) and a driven section (2.5 m). A schematic of the experimental setup is depicted in Fig. 1. The cylindrical shock wave is generated after passing through the curved wall segment $\widehat{PQ}$ which is designed under the condition of an incident shock wave Mach number $M_i = 1.2$, a converging angle $\theta_c = 15^\circ$ and a height of curving wall $h = 70$ mm. When the incident shock wave enters the linear segment $\widehat{QO}$ of 107.5 mm in length, it deforms from a planar shape to a cylindrical shape [14] and the corresponding Mach number changes from M_i = 1.2 at point P to M_Q = 1.29 at point Q. The total length of the wall $\widehat{ZPQO}$ is 565 mm in horizontal direction.

In order to form the inhomogeneity, a hole on top of the shock tube is first wetted with soap liquid prior to the experiment, so that it provides an approach for SF_6 to flow slowly through a pipe with one end inserted in the hole to form a cylindrical soap interface. When the interface is formed in the test section, the pipe is pulled out and the hole is sealed by a screw. Due to the gravity effect, the center of the interface curvature is under the end of the curved wall corresponding to point O in Fig. 1. The length of $\overline{DO}$ as shown in Fig. 1 is selected as the characteristic length D_0 and it is nearly 90 mm in the current experiment. As impacted by the shock wave, the soap film shatters into particles whose size depend on the strength of the shock wave. The size of atomized soap droplets after impaction of the shock wave is estimated using the model proposed by Cohen [16]. When the incident shock wave gets close to the interface, the Mach number increases to around 1.3 and the corresponding droplet size is on the order of 20 μm. The atomized particles are illuminated by the laser sheet which is produced by a continuous laser (SDL-532-15000T, 15 w, 532 nm) and shaped through a lens-system. The 105×15 mm^2 optical window on the top wall permits the laser sheet to illuminate the slice and a pair of 270×70 mm^2 optical windows on the side wall provide the approach to visualize the flow field.

Images have been captured during a single run by a high-speed video camera (Photron FASTCAM SA5). In present experiments, the camera works at a frame rate of 50000 frames per second (fps). The size of images is 960×392 pixel^2 with a spatial resolution up to 0.08 mm/pixel. The entire event lasts about 1200 μs.

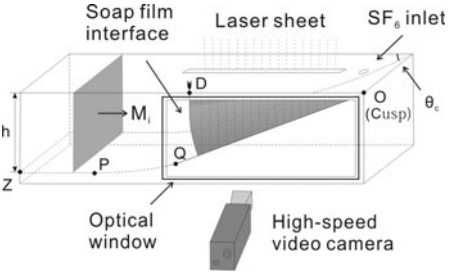

Fig. 1 Schematic view of the experimental configuration.

In order to compare with the experimental results, a numerical method VAS2D (2-Dimensional Vectorized Adaptive Solver) is applied and it is validated in simulating compressible flows [15]. The initial condition corresponds to the experiments with an initial temperature 298 K and pressure 1.01 bar. The technique of adaptive unstructured mesh refinement (AMR) is applied to the solution to enhance the space resolution. The maximum size of the adaptive grid is 0.5 mm, while the minimum size is 0.25 mm.

3 Flow Visualization

Various sets of experiments have been carried out. Although the repeatability of the experiment (especially the initial interface shape) is imperfect, the results in the same run are in good order and comparable. The evolution of the flow field is shown in Fig. 2, which involves two processes: one is the interaction of the incident converging shock wave with the initial bubble, the other is the interaction of the reshock reflected from the end of the curving wall with the deformed bubble. The initial geometry of the interface (see Fig. 2(o1)) was captured by a camera (NIKON D50) at the side of test section prior to the interaction.

Fig. 2 shows that the deformation of the interface agreed qualitatively with the numerical results. A smoothing technique was imposed on the numerical density results. The initial stage in Fig. 2(a) was captured at $t = 400$ μs measured from the first impact of the converging shock wave. The interface was compressed and distorted into an oblique profile shape as shown in Fig. 2(b). This can be illustrated by an important detail that the initial geometry of the bubble caused by the gravity leads to an impact beginning from the bottom to the top of the interface during a very short time interval. The variation in velocity among different elements of the bubble surface was so slight that the oblique profile didn't deform sharply until $t = 680$ μs after the first impact. An example of the deformed interface after the reshock was shown in Fig. 2(c). The top of the interface was first confronted with the reshock and became deformed in reverse direction. The post-reshock particles stopped moving from left to right and then moved back because of the reshock. The motion of particles indicated the deformation of the interface. Consequently, a

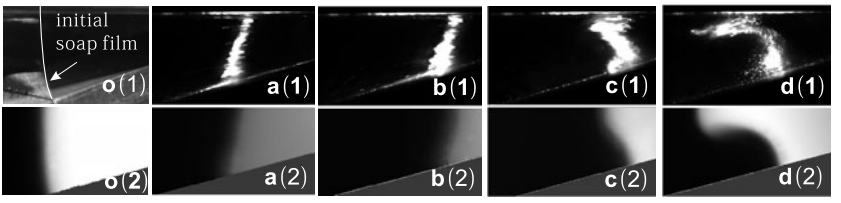

Fig. 2 Comparison of the experimental and numerical initial geometry (o) and deformations of the cylindrical bubble interacting with the incident shock wave (a,b) and the reshock (c,d). The numerical results correspond to the density field.

deformation reversal occurred as a result of the varied velocity on different elements of the interface.

An obvious feature of the flow was the vortical structure mainly caused by the baroclinic mechanism of the misalignment of local density and pressure gradients, as shown in Fig. 2(d). Baroclinic vorticity accumulated on the interface and intensify the vortical structure.

4 Wavelet Analysis

In order to study the evolution of the vortical structure strengthened by the reshock, a two-dimensional wavelet analysis was performed on the numerical vorticity filed under the impact of the reshock. A detailed description to construct the wavelet transform has been described by Farge [17]. The standard procedure includes 1) selecting a mother wavelet function which satisfies the admissibility condition, namely an integral function having zero mean; 2) generating a sequence of the daughter wavelet by translating, rotating, dilating the mother wavelet; 3) filtering the known field by the daughter wavelets; 4) analyzing the filtered result.

In the current study, an isotropic real-valued mexican hat wavelet is selected as the mother wavelet. By translating and dilating the mother wavelet $\psi(\mathbf{r}), \mathbf{r} \in \mathbb{R}^2$, we generate a family of wavelets $\psi_{l,\mathbf{r}'}(\mathbf{r})$:

$$\psi(\mathbf{r}) = (2-|\mathbf{r}|^2)e^{-|\mathbf{r}|^2/2}, \tag{1}$$

$$\psi_{l,\mathbf{r}'}(\mathbf{r}) = l^{-1}\psi(\frac{\mathbf{r}-\mathbf{r}'}{l}), \tag{2}$$

$$\tilde{f}(l,\mathbf{r}') = \int_D f(\mathbf{r})\psi^*_{l,\mathbf{r}'}(\mathbf{r})dS. \tag{3}$$

where l represents the dilation parameter and the scale of daughter wavelet, $\mathbf{r}'$ represents the translation parameter and location of the daughter wavelet, $\psi^*_{l,\mathbf{r}'}(\mathbf{r})$ denotes the complex conjugate of $\psi_{l,\mathbf{r}'}(\mathbf{r})$ from Eq. (2), $f(\mathbf{r})$ denotes the known scalar field.

The application of the wavelet transform used in the term 'wavelet filter' is performed on the two-dimensional vorticity field at the period of the reshock interacting with the interface. The operation is equivalent to the convolution of the scalar filed with the dilated mother wavelet. When a wavelet-like structure, such as vortex, appears in the vorticity field, the wavelet filter transforms the scalar field to an image plane, calculated from Eq. (3), with a positive peak value. The peak represents the most similarity between the scalar field and the daughter wavelet, the scale and location of the daughter wavelet correspond to that of the vortical structure [18]. The scale l and the distances between the structure's location and the field's boundary *px*, *py* are shown in Fig. 3.

The results in Fig. 3(a) shows the mexican hat wavelet transforms to the vorticity field. When the reshock passing through the center of the shocked bubble, the wavelet result appears a peak at the corresponding wavelet scale $l/D_0 = 0.37$. The location of the vortical structure is shown in Fig. 3(b). Until the arrival of the reshock, the vortex moves relatively faster downstream. Later, the reshock changes the direction of the structure's motion and the location of the structure can be identified by searching the peak from wavelet transform results.

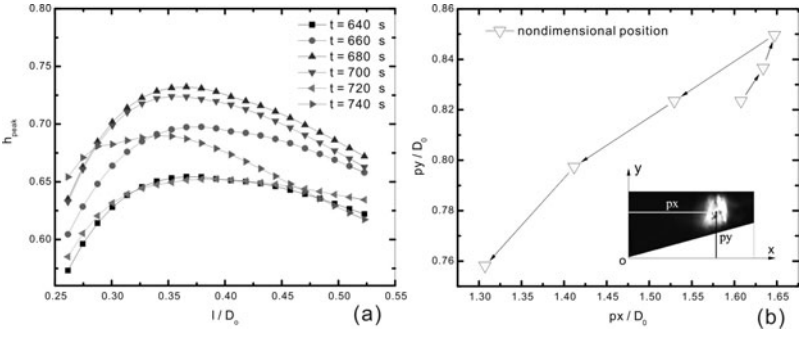

Fig. 3 Mexican hat wavelet transform of the vorticity field in the numerical simulation. (a) The peak value h_{peak} corresponding to the maximum of the transform calculated from Eq. (3) versus the wavelet scale l, (b) Location of the vortical structure. The characteristic length was selected as the initial size of the bubble D_0.

5 Conclusion

The results of the converging shock-bubble interaction were acquired by the high-speed photography and planar Mie-scattering imaging. The numerical simulation and wavelet analysis on the cylindrical bubble configuration were also presented. The reshock in the flowfield results in a reversal of the interface that is impacted by the incident shock wave, and evolves the flowfiled into an intensified vortical structure. The corresponding numerical results show a qualitative agreement with the experiments. Results from the wavelet transform reveal that the reshock changes the direction of the vortical structure's movement and increases its velocity magnitude.

Overall, the converging shock wave was introduced in the study of shock-bubble interaction and an attempt was made to analyze the result by wavelet transform which laid the first stone for the further work.

This research was carried out with the support of the National Natural Science Foundation of China under Grants 10972214, NSAF 10776031 and the Fundamental Research Funds for the Central Universities.

References

1. Ranjan, D., Oakley, J.: Shock-Bubble Interactions. Annu. Rev. Fluid Mech. 43, 117–140 (2011)
2. Richtmyer, R.D.: Taylor instability in shock acceleration of compressible fluids. Commun. Pure Appl. Math. 13, 297–319 (1960)
3. Meshkov, E.: Instability of the interface of two gases accelerated by a shock wave. Fluid Dyn. 4, 101–104 (1969)
4. Markstein, G.H.: A shock tube study of the flame front-pressure wave interaction. In: 6th International Symposium on Combustion, Reinhold, New York, pp. 387–398 (1957)
5. Rudinger, G., Somers, L.M.: Behavior of small regions of different gases carried in accelerated gas flows. J. Fluid Mech. 7, 161 (1960)
6. Haas, J.F., Sturtevant, B.: Interaction of weak shock waves with cylindrical and spherical inhomogeneities. J. Fluid Mech. 181, 41 (1987)
7. Layes, G., Jourdan, G., Houas, L.: Distortion of a Spherical Gaseous Interface Accelerated by a Plane Shock Wave. Phys. Rev. Lett. 91, 17 (2003)
8. Ranjan, D., Anderson, M., Oakley, J., Bonazza, R.: Experimental investigation of a strongly shocked gas bubble. Phys. Rev. Lett. 94, 184507 (2005)
9. Ranjan, D., Niederhaus, J., Motl, B., et al.: Experimental investigation of primary and secondary features in high-Mach-number shock-bubble interaction. Phys. Rev. Lett. 98, 024502 (2007)
10. Tomkins, C., Kumar, S., Orlicz, G., et al.: An experimental investigation of mixing mechanisms in shock-accelerated flow. J. Fluid Mech. 611, 131–150 (2008)
11. Santhosh, K.S., Soshi, K., Sanjiva, K.: Two-dimensional viscous flow simulation of a shock accelerated heavy gas cylinder. Phys. Fluids 23, 024102 (2011)
12. Niederhaus, J.H.J., Greenough, J.A., Oakley, J.G., et al.: A computational parameter study for the three-dimensional shock-bubble interaction. J. Fluid Mech. 594, 85–124 (2008)
13. Hosseini, S.H.R., Takayama, K.: Experimental study of Richtmyer-Meshkov instability induced by cylindrical shock waves. Phys. Fluids 17, 084101 (2005)
14. Zhai, Z.G., Liu, C.L., Qin, F.H., et al.: Generation of cylindrical converging shock waves based on shock dynamics theory. Phys. Fluids 22, 041701 (2010)
15. Sun, M., Takayama, K.: Conservative smoothing on an adaptive quadrilateral grid. J. Comp. Phys. 150, 143–180 (1999)
16. Cohen, R.D.: Shattering of a liquid drop due to impact. Proc. R. Soc. Lond. A 435, 483–503 (1991)
17. Farge, M.: Wavelet transforms and their applications to turbulence. Annu. Rev. Fluid Mech. 24, 395 (1992)
18. Rightley, P.M., Vorobieff, P., Martin, R., et al.: Experimental observations of the mixing transition in a shock-accelerated gas curtain. Phys. Fluids 11(1), 186–200 (1999)

Long Time Observation of the Richtmyer-Meshkov Instability

C. Mariani, L. Biamino, G. Jourdan, L. Houas,
M. Vandenboomgaerde, and D. Souffland

1 Introduction

Richtmyer-Meshkov (RM) instability occurs when a interface separating two fluids of different density is impulsively accelerated in the direction of its normal. It is one of the most fundamental fluid instabilities and is of importance to the fields of astrophysics and inertial confinement fusion. RM instability experiments are normally carried out in shock tubes, where the generation of a sharp, well-controlled interface between gases is difficult, so there is a dispersion in terms of experimental results. The experiments presented here were conducted in a horizontal shock tube where the materialization of the initial interface was achieved by a thin nitrocellulosic membrane (0.5 μm thick) deposited on a stereolithographed grid support, computer-aided designed and constructed with chosen shape and dimensions. As diagnostic, we used laser sheet flow visualization to yield time-motion image sequences of the linear and the non-linear developments of the instability. In previous investigation [1], we have already shown that residual pieces from the membrane constituting the initial interface tend to delay the interpenetration in the light-to-heavy gas configuration and specifically during the linear stage of the interface evolution. In order to reduce these effects in the present experiments, we have increased the strength of the shock wave (Mach$\sim$1.5). We have also extended the test section from 0.46 m to 1.5 m which allows the instability to grow further and thus to observe the whole non-linear phase until the transition to turbulence. The present paper summarizes the results obtained during this study undertaken for air/SF_6 and air/He gas combinations (positive and negative Atwood numbers, respectively) in 2D and 3D geometries.

C. Mariani · L. Biamino · G. Jourdan · L. Houas
IUSTI-CNRS, Aix-Marseille Université, 5 rue Enrico Fermi, Marseille, 13013, France

M. Vandenboomgaerde · D. Souffland
CEA/DAM, DIF, Arpajon, 91297, France

2 Experimental Set-Up

The experimental investigation was realized in an horizontal shock tube which square cross section is of 20 cm$\times$20 cm. An extension of the experimental chamber has been built so that the installation is 1m longer than in its precedent configuration. This was made to delay the return of the shock that is reflected on the end wall of the experimental chamber. Four piezoelectric dynamic pressure gauges allow to measure the velocity of the pressure discontinuities (incident, transmitted and reflected shocks) and one of them is used to trig the visualization device and the measurement acquisition. A laser sheet passing trough the end wall of the experimental chamber gives a 2D-longitudinal observation of the flow and an acquisition is realized with an high speed digital camera at a frame frequency of 10kHz. The initial perturbated interface is artificially created and stabilized by a nitrocellulosic film lightly stuck on a CAD grid. By this way, perfect sinusoidal interfaces in 2D or 3D can be produced to generate the Richtmyer Meshkov instability. One of the two gases need to be seeded to reveal the position of the interface; incense smoke is blown into the low pressure section of the tube while the test gas (He or SF_6) is filling the windowed compartement on the other side of the grid.

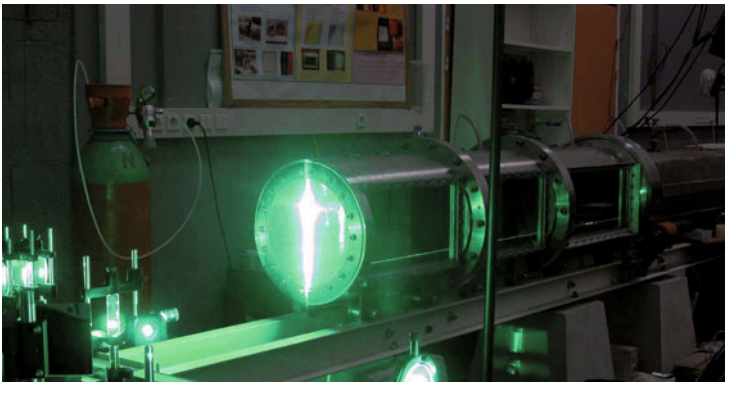

Fig. 1 View of the test section, extended from 0.46 m to 1.5 m.

3 Results and Discussion

3.1 Remarks on the Initial Conditions

The sizes of the initial perturbations are chosen to follow the development of the RM instability from the linear stage until the highly non linear one; this implies that the wave length λ_0 of the initial sinusoids is much greater than their amplitude η_0 or $\frac{\eta_0}{\lambda_0} \ll 1$. In order to have close time evolutions of the sinusoid amplitude in 2D and 3D configurations, the wave lengths in 3D were chosen according to a known correlation [2] $\lambda_{eff} = \lambda_{2D} = \frac{\lambda_{x-3D} \cdot \lambda_{y-3D}}{\sqrt{\lambda_{x-3D}^2 + \lambda_{y-3D}^2}}$ and if $\lambda_{x-3D} = \lambda_{y-3D} = \lambda_{3D}$ then $\lambda_{2D} = \frac{\lambda_{3D}}{\sqrt{2}}$.

3.2 *Long Time Observation of the RM Instability*

Figure 2 shows the development of the Richtmyer-Meshkov Instability when the shock passes through a 3D sinusoidal interface from a light gas (seeded air) to a heavier one (SF_6). Concerning the experiments in this configuration, we notice that after a long time the perturbations are no more sinusoidal. Spike and bubble shapes appear but they are different in the 2D geometry and in the 3D one. In 2D, due to a shorter wave length, the bubble structures thicken until they quickly touch each other; this makes more difficult the measurement of the spike positions especially on the latest frames. In 3D, the spike and bubble structures are more like pyramid

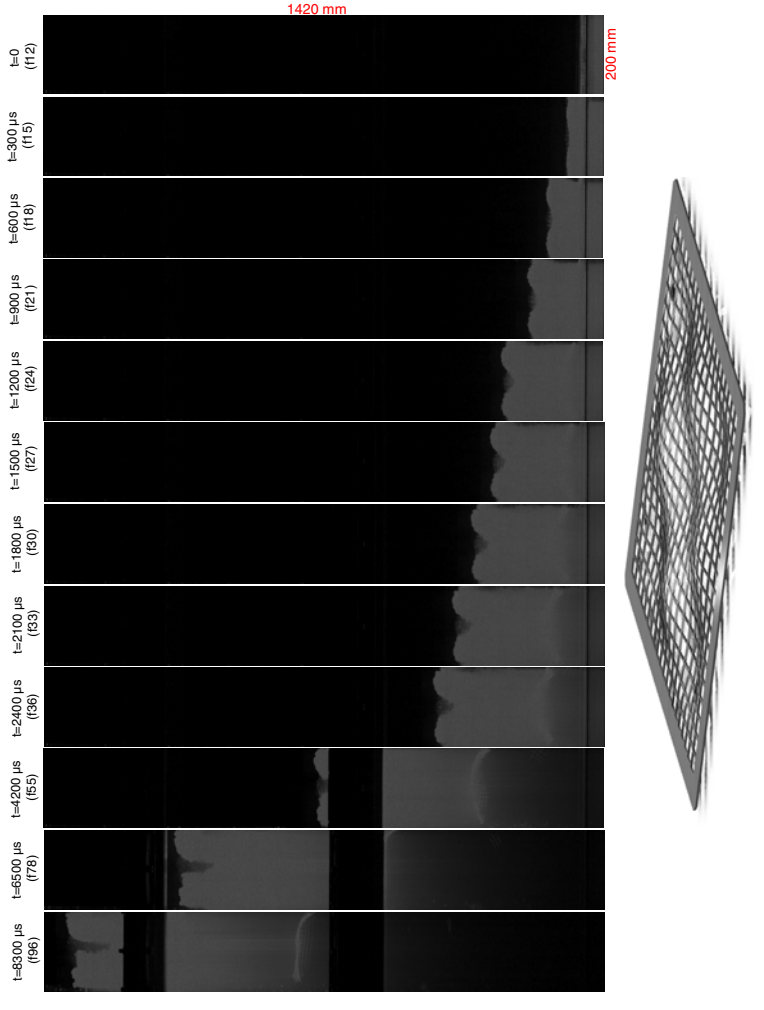

Fig. 2 Laser sheet frames of an air/SF_6 3D-interface (λ_0=11.317 cm and η_0=0.306 cm) accelerated by a strong shock wave (M_{isw}=1.44)

and bubble structures due to the geometry. Later, slots and crenelate shapes appear due to the thickening of the sinusoids. A work on Fourier serie decomposition of the interface profile is in progress in order to measure the deformation of the initial sinusoids according to time.

In the heavy/light gas configuration (air/He interfaces), the extension of the test section allows to observe the RM instability three times longer. The frames show the known reversal phase and the one of linear growth (see Fig. 3). It reveals the weakly non linear stage of development of the RM instability and the apparition of bubble

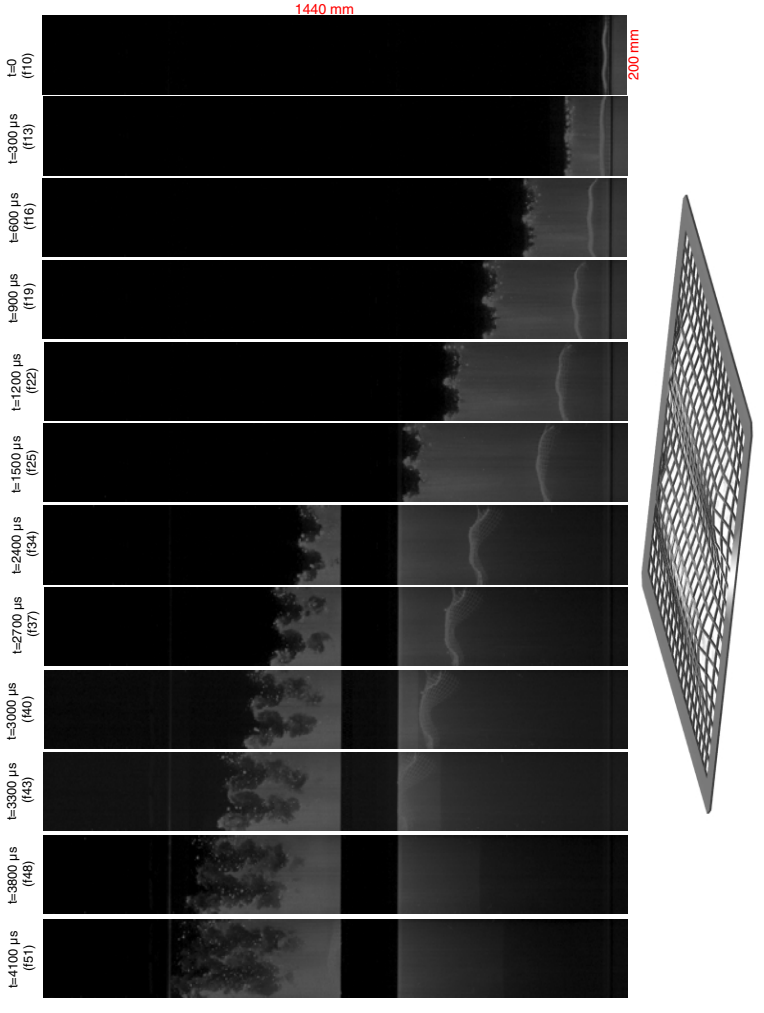

Fig. 3 Laser sheet frames of an air/He 2D-interface (λ_0=8 cm and η_0=0.306 cm) accelerated by a strong shock wave (M_{isw}=1.44)

and spike shapes in 2D geometry and bubble and pyramids in 3D. Figure 3 shows an air/He experiment with initial sinusoids in 2D geometry.

3.3 Time Evolution of the Sinusoids Amplitude

The amplitude of the perturbations is measured by taking half the difference of positions of the opposite extrema of the interface. Figure 4 represents the time evolution of this amplitude for all the runs in each gas configuration. The significant result which is revealed by this figure is the good superimposition of the evolutions in 2D and 3D for same initial amplitude and same incident shock wave; four times, the graphs are comparable in pairs. This validates the use of the correlation between the wavelengths in 2D and 3D that must be respected when one wants to obtain similar chronologies of growth in amplitude. In the case of air /SF_6, interfaces strongly perturbated and accelerated by a strong shock, the growth in the 2D geometry is slower than in the 3D one. This is due to the faster thickening of the perturbations in 2D which makes the spikes more and more thin so that their length seems to grow slower.

In figure 5, the time evolution of the amplitude is represented in a dimensionless coordinate system in order to compare all the results together and also with two known models. The first observation is the good superimposition of the evolutions at least on the beginnings (except for the above case in air/SF_6 configuration). A second relevant point is the improvement of the results concerning the linear phase of growth in the ligth/heavy configuration. Indeed in our previous work, the growth rate in this configuration was 30 % lower than the one predicted by Richtmyer. In these experiments, the growth rate is less than 10 % lower; that is the consequence of a better destruction of the residual pieces of nitrocellulosic membrane by stronger shock waves. The last interesting point is the good agreement with the non linear model for the two gas configurations [3]. Notice that the model of Vandenboomgaerde is non-dimensionalized by the compressible linear growth rate.

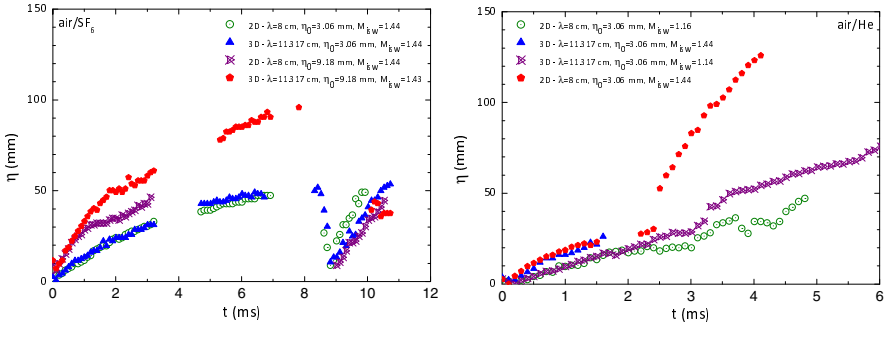

Fig. 4 Time evolutions of the amplitude for different perturbated air /SF_6 (on the left) and air /He (on the right) interfaces accelerated by shock waves of different intensities.

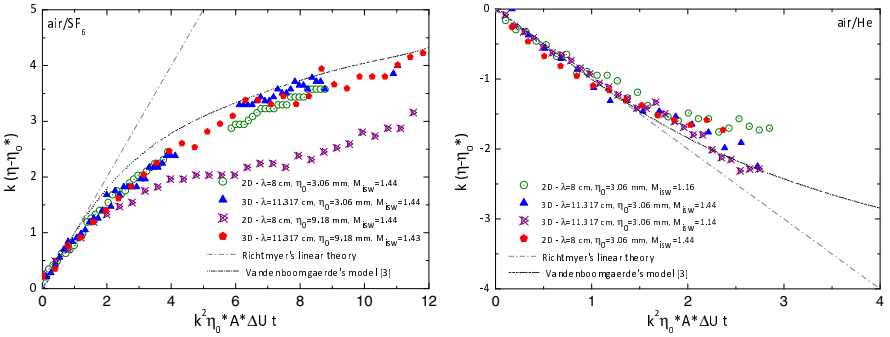

Fig. 5 Dimensionless time evolutions of the amplitude for different perturbated air /SF_6 (on the left) and air /He (on the right) interfaces accelerated by shock waves of different intensities.

4 Conclusion

The Richtmyer Meshkov instability has been studied with perfect sinusoidal interfaces which sizes were chosen to follow the different phases of growth in amplitude of the initial defaults. The non linear phase was longer observed due to the extension of the test section of the tube. The comparison of the time evolution of the amplitude in experiments and in theories (linear or non linear) are in well agreement in both light/heavy and heavy/light cases. A real difference in the evolution of shapes appeared especially after a long time depending on whether the geometry is 2D or 3D.

References

1. Mariani, C., Vandenboomgaerde, M., Jourdan, G., Souffland, D., Houas, L.: Phys. Rev. Lett. 100, 254503 (2008)
2. Yosef-Hai, A., Sadot, O., Kartoon, D., Oron, D., Levin, L.A., Sarid, E., Elbaz, Y., Ben-Dor, G., Shvarts, D.: Laser and Particle Beams 21, 363 (2003)
3. Vandenboomgaerde, M., Boudesocque, C., Griffond, J., Boulet, M.: Proc. of 10th IWPCTM, France, pp. 383–386 (2006)

Numerical Study of Shock Induced Mixing in a Cylindrical Shell

Lili Wang, Yihong Hang, and Shudao Zhang

1 Introduction

The Richtmyer-Meshkov instability (RMI) develops when a shock wave traverses a density interface separating two gases. The miss-alignment of the pressure gradient across the shock and the local density gradient at the contact during shock passage leads to vorticity production at the interface. Subsequently the flow driven by the deposited vorticity leads to interfacial instability growth and eventually to turbulence mixing. RMI is important in many areas of physics, from geophysical and astrophysical problems to industrial applications. In particular, attention has recently focused on RMI and RM mixing in the converging geometry such as that occurs in an imploding inertial confinement fusion (ICF) capsule. When a stratified cylindrical shell with initial perturbations is driven by a convergent shock wave, the effect of convergence tends to enhance the perturbation growth compared with that in a planar geometry. The convergent incident shock wave reflects at the cylinder center and the succedent reflected shock waves move to and fro within the whole region. Besides, the Rayleigh-Taylor instability (RTI) also occurs whenever the light fluid accelerates the heavy one during the evolution. All these factors make the mixing procedure in a stratified cylindrical shell driven by shock wave much complex than that in the planar geometry. Although many models have been proposed to predict the instability growth in the linear, weakly nonlinear, and turbulent regimes, each of these models has limitations and a restricted domain of applicability. For this complex mixing process with strongly nonlinear transition stage, the direct numerical simulation with high resolution is the common way to study its evolution. In this paper a hybrid scheme combined with the finite-difference and the weighted essentially non-oscillatory (WENO) method, combined with high order strong-stability preserving Runge-Kutta scheme for the time integration, is used to simulate the mixing due to the interfacial instability in a stratified cylindrical shell driven by convergent shock wave. Growth and mixing properties of the turbulent mixing zone

Lili Wang · Yihong Hang · Shudao Zhang
Institute of Applied Physics and Computational Mathematics, Beijing, 100094, P.R. China

(TMZ) have been investigated using the simulation results. And the effect of initial perturbation on the mixing has been discussed.

2 Equations of Motion

We use the N-species Navier-Stokes equations to simulate the motion as follows

$$\frac{\partial \rho}{\partial t} + \frac{\partial \rho u_i}{\partial x_i} = 0 \tag{1}$$

$$\frac{\partial \rho u_i}{\partial t} + \frac{\partial (\rho u_i u_j + p\delta_{ij})}{\partial x_j} = \frac{\partial d_{ij}}{\partial x_j} \tag{2}$$

$$\frac{\partial E}{\partial t} + \frac{\partial (E+p)u_j}{\partial x_j} = \frac{\partial d_{ij} u_i}{\partial x_j} \tag{3}$$

$$\frac{\partial \rho \varphi_m}{\partial t} + \frac{\partial \rho \varphi_m}{\partial x_j} = 0, \text{ for } m = 1, N-1 \tag{4}$$

where repeated indices denote summation and φ_m denotes the m-th species mass fraction. Pressure is determined from the ideal equation of state for a mixture of gases,

$$P = \frac{\rho RT}{\bar{m}} \tag{5}$$

where R denotes the ideal gas constant, while $\bar{m}$ denotes the mean molecular weight which is given by

$$\frac{1}{\bar{m}} = \sum_{i=1}^{N} \frac{\varphi_i}{m_i} \tag{6}$$

m_i is the molecular weight of the i-th species of the mixture.

The Newtonian stress tensor d_{ij} of the mixture is expressed as

$$d_{ij} = \mu \left[\left(\frac{\partial u_i}{\partial x_j} + \frac{\partial u_j}{\partial x_i} \right) - \frac{2}{3} \frac{\partial u_k}{\partial x_k} \delta_{ij} \right] \tag{7}$$

where the shear viscosity μ is calculated as follows

$$\mu = \frac{\sum_{i=1}^{N} \mu_i \varphi_i m_i^{-1/2}}{\sum_{i=1}^{N} \mu_i m_i^{-1/2}} \tag{8}$$

3 Numerical Method

For the turbulent mixing we examined in this paper, simulation demands two mutually exclusive numerical approaches. On one hand, the presence of shocks, whose

length scale is of the order of the mean free path, implies that the numerical method must be of a shock-capturing type. On the other hand, turbulence is better simulated when the numerical method is non-dissipative. Since all shock-capturing methods are dissipative, two mutually orthogonal numerical requirements arise. To address this difficulty, we used the TCD-WENO hybrid method proposed by Hill and Pullin[1] to approximate the derivatives in the advection terms, in conjunction with a third-order strong-stability preserving Runge-Kutta scheme for the time integration. The fluxes of the viscous and diffusion transport terms are computed using explicit center-difference operator.

The WENO method is a successful shock-capturing scheme with high order precision. But its up-winding strategy makes it too dissipative for the smooth turbulent regions. In the TCD-WENO hybrid method, the tuned centre-difference scheme with low numerical dissipation and good wave-dispersion properties is adopted in the regions away from shocks and material interfaces, while the WENO scheme[4] based on the characteristic decomposition is used around discontinuities(shocks and material interfaces) .We utilized a discontinuity detection criterion to switch the two different schemes suggested by Ref.[2]. In the tuned centre-difference scheme, the skew-symmetric form is employed to improve the numerical stability. For details the reader is referred to Ref. [2, 3].

4 Numerical Results

The calculation model is shown schematically in figure 1. The shell is driven by a convergent incident shock wave. There are three materials and two material interfaces within the calculation region. The main parameters we used are as follows:

$$\rho_{in} = 1.0 \tag{9}$$

$$\rho_{shell} = 10.0 \tag{10}$$

$$\rho_{out} = 1.0 \tag{11}$$

$$P_0 = 80000.0 \tag{12}$$

$$Ma = 1.5 \tag{13}$$

For the simulations in this paper, broadband random perturbations have been set on the initial outer interface. Figure 2 shows the evolution of the mixing zone in a typical case. During the interval corresponding to fig. 2(1) and fig. 2(3), the shell is compressed by the incident shock wave. RMI occurs and both the shell's and the inner material's densities increased. Then the shell begins to slow down and then rebound when the shock wave reaches the center and reflects outwards, and mixing grows due to both RMI and RTI. We can see mixing near both the outer interface and the inner interface in fig. 2(5). If the shell is thin enough or the mixing has undergone enough time, the shell may be shredded.

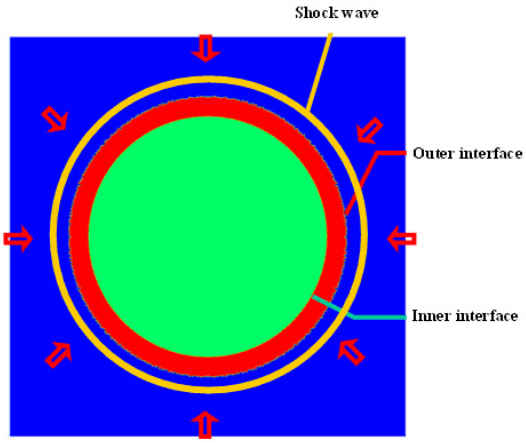

Fig. 1 Schematic showing the calculation model.

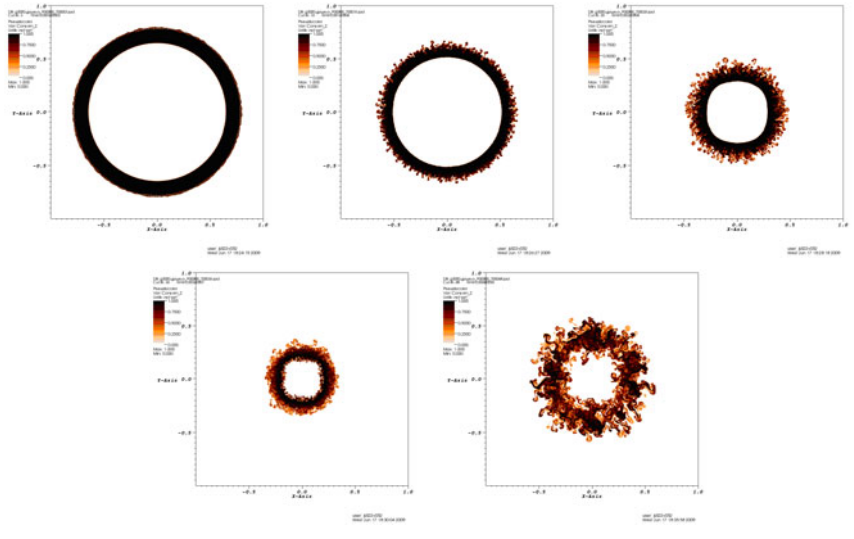

Fig. 2 Evolution of the mixing zone.

In order to investigate the effect of initial perturbation, various initial spectra were considered in our calculations including the flat distribution and the Gauss distribution. Random phases were assigned to each mode in every simulation case. And the averaged perturbation amplitudes of all cases are the same.

case 1: flat spectrum within [0,200]
case 2: flat spectrum within [100 , 300]
case 3: flat spectrum within [200, 400]
case 4: flat spectrum within [300,500]
case 5: flat spectrum within [0,400]
case 6: flat spectrum within [200,600]
case 7: flat spectrum within [400,800]
case 8: Gauss spectrum within [400, 800], half-width: 100
case 9: Gauss spectrum within [400, 800], half-width: 50

Figure 3 shows the mixing zone's width near the outer interface with time. We can see that the mixing zone's growth is quite sensitive to the initial perturbation scale. There is no apparent approach to a self-similar regime independent of the initial conditions. And the mixing zone grows more slowly with smaller scale perturbations.

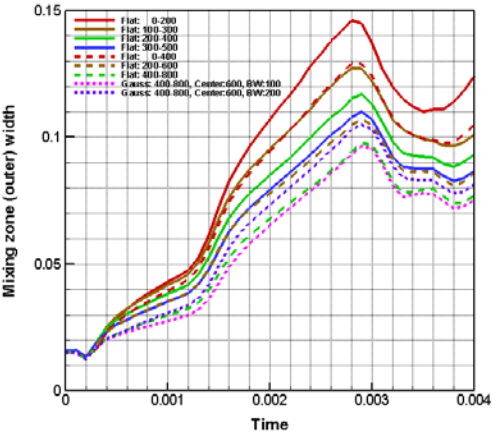

Fig. 3 Width of the mixing zones vs time.

For better understanding of the mixing evolution, we used some statistical quantities of the mixing zone as follows. The reader is referred to Ref. [5]for details. Figure 4 shows the mixing fraction within the mixing zone, which indicates the atomic mixing degree. For this measure, values near unity correspond to complete mixing, while values near zero correspond to little atomic mixing. In fig. 4, the mixing fractions approach an asymptotic value in range [0.6, 0.8] at late time in all cases. It means that as refer to the atomic mixing degree, the imprint of initial perturbation tends to be lost at late time, although it affects the mixing zone's width obviously.

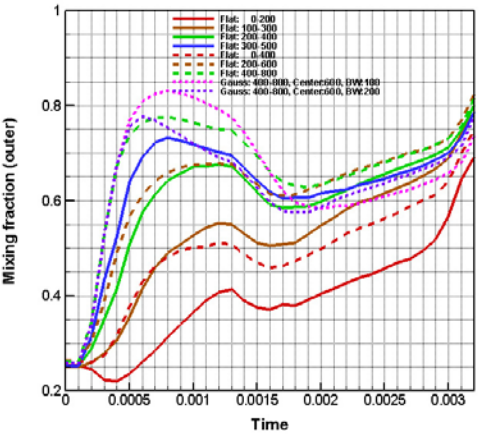

Fig. 4 Mixing fraction within the mixing zone

5 Conclusions

In this paper the mixing process in a stratified cylindrical shell driven by a convergent shock wave is numerically studied by using a hybrid method combined with the weighted essentially non-oscillatory shock-capturing method and the tuned center difference scheme. We investigate the mixing according to the mixing zone width and the mixing fraction. It was found that the mixing zone's growth is quite sensitive to the initial perturbation scale, while the atomic mixing degree tends to be independent of the initial perturbation at late time.

References

1. Hill, D.J., Pullin, D.I.: Hybrid Tuned Center-Difference-WENO Method for Large Eddy Simulations in the Presence of Strong Shocks. J. Comp. Phys. 194, 435–450 (2004)
2. Pantano, C., Deiterding, R., Hill, D.J., Pullin, D.I.: A Low-Numerical Dissipation Patch-Based Adaptive Mesh Renement Method for Large-Eddy Simulation of Compressible Flows. J. Comp. Phys. 221, 63–87 (2004)
3. Hill, D.J., Pantano, C., Pullin, D.I.: Large-Eddy Simulation and Multiscale Modelling of A Richtmyer-Meshkov Instability with Reshock. Journal of Fluid Mechanics 557, 29–61 (2006)
4. Jiang, G.S., Shu, C.W.: Efficient Implementation of Weighted ENO Schemes. J. Comp. Phys. 126, 202–228 (1996)
5. Latini, M., Schilling, O., Don, W.S.: Effects of WENO Flux Reconstruction Order and Spatial Resolution on Reshocked Two-Dimensional Richtmyer-Meshkov Instability. J. Comp. Phys. 221, 805–836 (2007)
6. Latini, M., Schilling, O., Don, W.S.: High-Resolution Simulations and Modeling of Reshocked Single-Mode Richtmyer-Meshkov Instability: Comparison to Experimental Data and to Amplitude Growth Model Predictions. Phys. Fluids 19, 024104 (2007)

Effect of Shock Mach Number on Richtmyer-Meshkov Instability in Spherical Geometry

Ankit Bhagatwala and Sanjiva K. Lele

1 Introduction

Lombardini et al. [1] have recently carried out Richtmyer-Meshkov instability (RMI) simulations in cylindrical geometry. RMI for a spherical axisymmetric flow was investigated by Dutta et al. [2]. We consider a more general initial interface perturbation, with a spherical egg-carton profile similar to the one used in planar RMI simulations [3, 4]. An interesting feature of this profile is that the perturbation wavelength is nearly constant over the spherical shell spanned by the material interface. The fluids considered in this study are air outside and SF_6 inside. The shock is launched from the air (lighter) side of the interface. As the flow evolves, a series of reflected and transmitted shocks are generated, which via baroclinic deposition of vorticity and its subsequent transport serve to mix the two fluids in a turbulent mixing zone.

2 Methodology and Simulation Parameters

Euler equations for a perfect gas in Cartesian coordinates are solved. Due to the strong nature of the shocks, shock-capturing is needed and provided through artificial viscosity following Cook [5], but with a modified coefficient for bulk viscosity as described in Bhagatwala & Lele [6]. The non-dimensional Euler equations are as follows

$$\frac{\partial Q}{\partial t} + \frac{\partial F_j}{\partial x_j} = 0 \tag{1}$$

where $Q = (\rho, \rho u_i, \rho e_t, \rho Y)$ and $F_j = (\rho u_j, \rho u_i u_j + p\delta_{ij}, (\rho e_t + p)u_j, \rho Y u_j + J_j)$

Following Cook [5], the following artificial terms are employed.

$$\mu_h = C_\mu \overline{\rho |\nabla^4 S|} \Delta^6 \qquad \beta_h = C_\beta \overline{\rho |\nabla^4 S|} \Delta^6 \qquad \kappa_h = C_\kappa \overline{\frac{\rho c}{T} |\nabla^4 e|} \Delta^5 \tag{2}$$

Ankit Bhagatwala · Sanjiva K. Lele
Department of Aeronautics and Astronautics, 496 Lomita Mall, Stanford, CA 94305

$$D_i = C_D \overline{c_s |\nabla^4 Y_i|} \Delta^4 + C_Y \overline{c_s \{[Y_i - 1]H(Y_i - 1) - Y_i[1 - H(Y_i)]\}} \Delta \tag{3}$$

where Δ is the grid spacing, $S = \sqrt{\mathbf{S} : \mathbf{S}}$ is the magnitude of the symmetric strain rate tensor, $C_\mu = 0.002$, $C_\kappa = 0.01$, $C_D = 1.0$ and $C_Y = 100$.The effective gamma formulation is used for computing the ratio of specific heats as follows

$$\gamma_{eff} = \frac{C_{p,eff}}{C_{v,eff}} = \frac{Y_1 C_{p1} + Y_2 C_{p2}}{Y_1 C_{v1} + Y_2 C_{v2}} = \frac{\frac{Y_1 \gamma_1}{\gamma_1 - 1} + \varepsilon \frac{Y_2 \gamma_2}{\gamma_2 - 1}}{\frac{Y_1}{\gamma_1 - 1} + \varepsilon \frac{Y_2}{\gamma_2 - 1}} \tag{4}$$

where $\varepsilon = M_1/M_2$ is the ratio of gas constants or molecular weights.

The grid is uniform Cartesian with a resolution of 128^3. Only an octant of the sphere is represented and appropriate symmetry boundary conditions are used. A compact finite difference scheme described in Lui [7] is used. A low dissipation and dispersion RK4 method described in Hu *et. al.* [8] is used for time stepping.

The interface perturbation profile is given by $h_0 = A_0 \cos(32\theta)\cos((32\sin\theta)\phi)$ to obtain an egg carton shaped disturbance. Three simulations with initial shock Mach numbers M_I of 1.2, 1.8 and 3.0 have been carried out. Figure 1 shows density slices as the flow evolves for a Mach 1.8 initial shock. We study the evolution of the mixing layer width, vorticity and turbulent kinetic energy. Table 1 lists parameters for the initial perturbation to the interface and quantities useful for scaling the computed results.

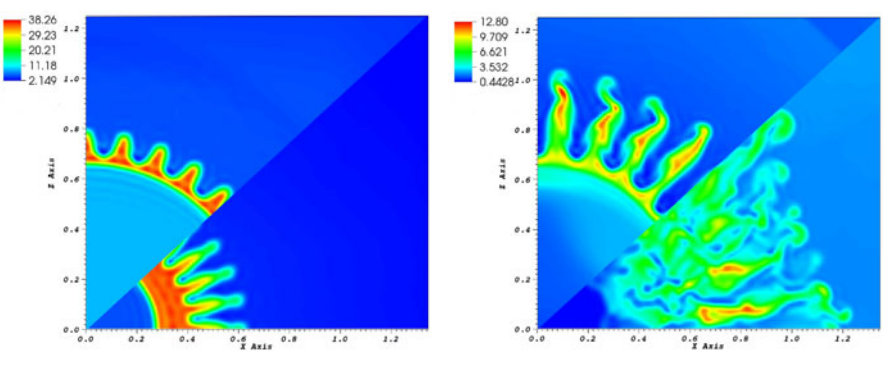

Fig. 1 Evolution of spherical RMI for $M_I = 1.8$. Slices of density, $\rho/\rho_{air}^{unshocked}$ (a) Converging $t/t_s = 0.4$, $t/t_s = 0.8$, (b) Post-reshock regimes. $t/t_s = 2.4$, $t/t_s = 3.1$ Only half of the computed octant is shown.

3 Results

The mixing layer width is defined as $h = \int_{s=0}^{s=R_{max}} \langle Y \rangle (1 - \langle Y \rangle) ds$ where angled brackets $\langle . \rangle$ indicate a tangential average as a function of radius. Figure 2 compares mixing layer widths for the same initial perturbation, only the incident shock Mach number is varied. For all temporal profiles, time has been normalized with time taken for the shock to reach the origin so that the time of first shock and reshock are

Table 1 Initial conditions. Initial radius of shock,R_{s0}, Initial radius of interface, R_0, Initial pertrubation amplitude A_0, Initial wavelength of perturbation, λ_0, Initial wavenumber of perturbation, k_0, Atwood number, $At = (\rho_2 - \rho_1)/(\rho_2 + \rho_1)$, Shock Mach number, $M_s = \dot{R}_s/c_0$, Velocity impulse to interface due to shock, $\Delta v/c_0 = 2(M_s^2 - 1)/(\gamma + 1)M_s$. c_0 is the speed of sound in air, t_s is the time taken for the shock to reach the origin.

R_{s0}/R_0	A_0/R_0	k_0R_0	A_0/λ_0	At	M_s	$\Delta v/\dot{R_{s0}}$	$t_s\dot{R_{s0}}/R_{s0}$
1.03	0.01	33	0.03	0.67	1.2	0.32	3.8
1.03	0.01	33	0.03	0.67	1.8	0.61	3.7
1.03	0.01	33	0.03	0.67	3.0	0.74	4.0

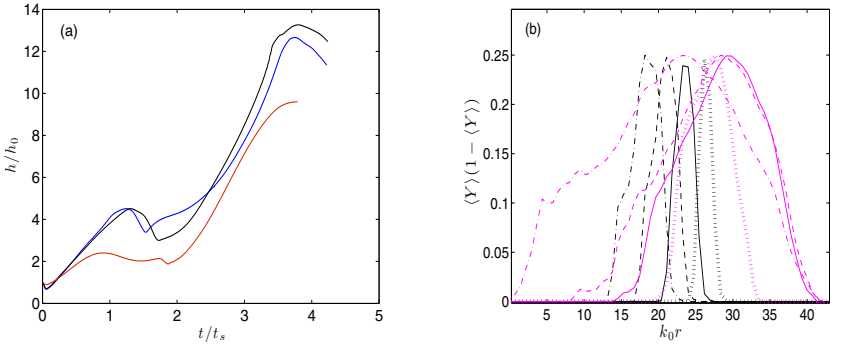

(a) (b)

Fig. 2 (a) Comparison of mixing layer width. $M_I = 1.2$ (red), $M_I = 1.8$ (black), $M_I = 3.0$ (blue). Width normalized by initial perturbation amplitude. (b) Profiles of $\langle Y\rangle(1 - \langle Y\rangle)$ for $M_I = 1.8$ case, Converging (black) and post-reshock (magenta) phases. For line style labels, please refer to figure 4. Y is the mass fraction of Air

similar for all cases. Note that they cannot be identical, as in the planar case, because shock speed is a nonlinear function of time for a spherically converging shock. We also plot spatial profiles of $\langle Y\rangle(1 - \langle Y\rangle)$ for the $M_I = 1.8$ case which corroborates the trend observed in the temporal profiles.

The h profile has a shape similar to that observed in the planar case, with a slight initial drop as the incident shock compresses the perturbation, then a rise as the interface perturbation to grow into spikes and bubbles under the action of baroclinically deposited vorticity. The compression due to the reshock causes another drop in h, followed by a rise as the mixing layer grows in size and becomes turbulent. The Mach number dependence is quite evident. In the linear growth phase, the profiles line up at early times, except for the lowest Mach number, which flattens out earlier. After reshock, peaks of the turbulent mixing layer widths occur at different

times with the chosen time normalization. The shock speed based scaling of time therefore does not apply to the post reshock phase of the mixing layer growth. It is not clear that simple scaling parameters exist for this highly nonlinear process. The slope of the h/h_0 curve when evaluated against the scaled time is similar. This is an indication that the scale used in the plot captures an important dependence. Simulations at other Atwood numbers and interface perturbations are needed to judge if this is a robust scaling.

Figure 3 shows the evolution of domain integrated vorticity variance i.e enstrophy and perturbation kinetic energy, which eventually becomes turbulent kinetic energy (TKE) as the flow becomes turbulent. For ease of nomenclature, both are referred to as TKE in this paper. Similar to the planar case, it shows a double peak structure. The first rise and decay corresponds to the linear growth phase, while the second corresponds to the post-reshock turbulent mixing layer growth and eventual decay. Enstrophy is normalized by a time scale based on the initial velocity impulse to the interface by the incident shock, while TKE is normalized by shock speed. The vorticity profiles collapse quite well during the linear phase, but diverge at late times, when the flow is nonlinear and turbulent. The TKE profiles do not show as good a collapse, but the chosen normalization yields the best comparison between different cases.

To study the spatial nature of the vorticity field as it evolves over time, we plot it during the converging and reshocked phases of the shock in figure 4. The baroclinic vorticity deposited by the initial shock passage is amplified by the post-shock compression. The plot for the post-reshock flow shows the turbulent phase of RMI. The growth of the turbulent mixing layer can be clearly seen in the radial profiles.

Figure 5 plots tangentially averaged radial profiles of TKE for the converging and post-reshock phases. During the converging phase, we observe two peaks, one corresponding to the evolving mixing zone where the material interface is and the other at the shock location due to shock corrugation. The peak at the shock grows as the shock gets stronger as it propagates inwards, whereas the peak at the interface

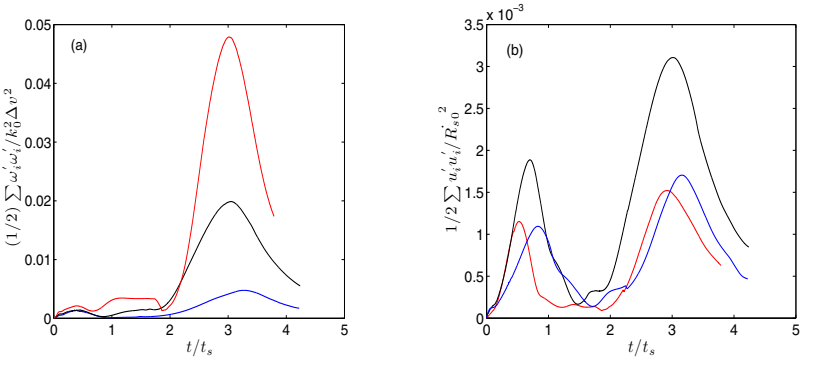

Fig. 3 Comparison of Enstrophy and TKE. $M_I = 1.2$ (red), $M_I = 1.8$ (black), $M_I = 3.0$ (blue). (a) Enstrophy (b) TKE.

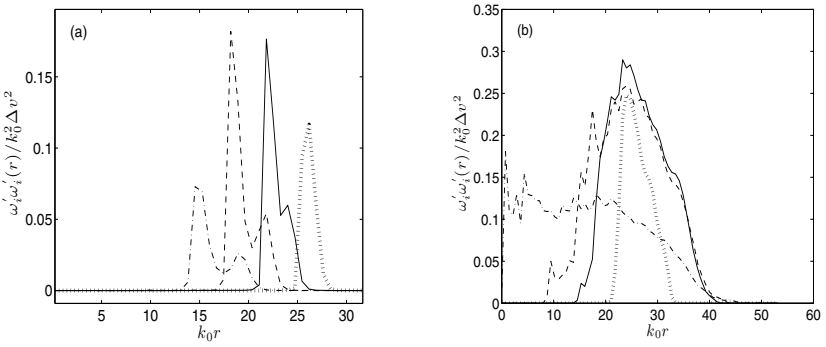

Fig. 4 Radial profiles of vorticity for shock with $M_I = 1.8$ (a) Converging, $t/t_s = 0.2$ (dotted), $t/t_s = 0.36$ (solid), $t/t_s = 0.52$ (dashed), $t/t_s = 0.68$ (dash-dotted). (b) Post-reshock regimes, $t/t_s = 2.23$ (dotted), $t/t_s = 2.88$ (solid), $t/t_s = 3.1$ (dashed), $t/t_s = 3.74$ (dash-dotted).

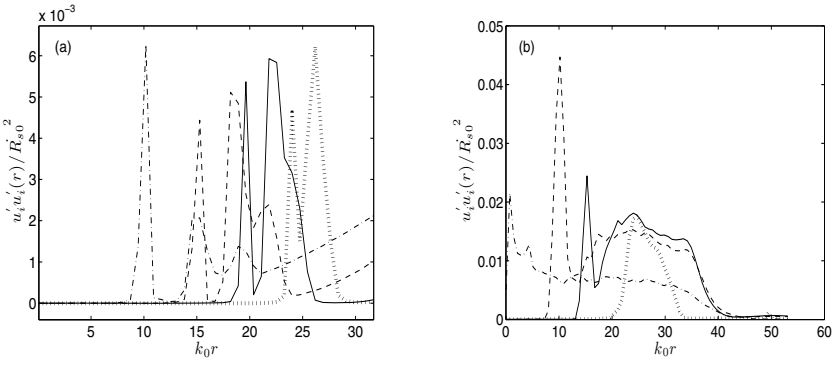

Fig. 5 Radial profiles of TKE for shock with $M_I = 1.8$ (a) Converging (b) Post-reshock regimes. For legend, please refer to figure 4

decays as there is no fresh energy deposition and numerical viscosity damps the fluctuations. Similar to vorticity profiles earlier, growth of the turbulent mixing layer can be seen in the TKE profiles for the post-reshock flow as well.

4 Conclusion

Exploratory simulations of the Richtmyer-Meshkov instability for an Air-SF_6 interface in spherical geometry have been carried out with three-dimensional 'egg-carton' type interface perturbation. Parametric variation with respect to initial shock Mach number has been studied. Effect of shock Mach number on growth rates of the mixing layer, vorticity and turbulent kinetic energy have been studied. Through tangentially averaged radial profiles of vorticity and TKE, the growth of the mixing

zone through the various phases of linear growth, transition to turbulence and decay have been studied. Attempt was made to scale the data in different regimes. Additional simulations with larger set of parametric variation and simulations at higher resolution are required to establish whether the approximate scaling behavior observed here is more generally valid.

Acknowledgement. We would like to acknowledge financial support from the DOE-SciDAC project grant # DE-FC02-06-ER25787. Computer resources were provided by the Argonne Leadership Computing Facility through the INCITE award.

References

1. Lombardini, M., Deiterding, R., Pullin, D.I.: Quality and Reliability of Large-Eddy Simulations, pp. 283–294 (2008)
2. Dutta, S., Glimm, J., Grove, J.W., Sharp, D.H., Zhang, Y.: Mathematics and Computers in Simulation 65, 417 (2004)
3. Vetter, M., Sturtevant, B.: Shock Waves 4, 247 (1995)
4. Hill, D.J., Pantano, C., Pullin, D.I.J.: Fluid Mech. 557, 29 (2006)
5. Cook, A.W.: Phys. Fluids 19, 055103 (2007)
6. Bhagatwala, A., Lele, S.K.: J. Comput. Phys. 228, 4965 (2009)
7. Lui, C.: PhD thesis, Stanford University, Stanford (2004)
8. Hu, F.Q., Hussaini, M.Y., Manthey, J.L.: J. Comput. Phys. 124, 177 (1996)

Experimental Characterization of Turbulence Produced in a Shock Tube: A Preliminary Work for the Study of the Turbulent Gaseous Mixing Induced by the Richtmyer-Meshkov Instability

G. Bouzgarrou, Y. Bury, S. Jamme, J.-F. Haas, D. Counilh, and J.-B. Cazalbou

1 Introduction

The Richtmyer-Meshkov Instability (RMI) occurs in several physical and technological processes such as supernova explosion, supersonic combustion, detonics or inertial confinement fusion. This instability develops when interfacial perturbations, between two fluids of different densities, grow because of a shock wave induced impulsive acceleration. The basic mechanism for the initial growth of perturbations on the interface is the baroclinic generation of vorticity which results from the misalignment of the pressure and density gradients when the shock crosses the interface. Early time linear and following nonlinear growth of the RMI have been, and are still widely investigated, either theoretically, numerically and experimentally [1]. Nevertheless, experimental investigation of the Turbulent Mixing Zone (TMZ) induced by a rapidly growing RMI is still nowadays poorly documented, even if we can mention for instance the work of Leinov et al. [2] who characterized the growth of the MZ with time following the passage of the re-shock (with an emphasis on the influence of the initial amplitude of the MZ and the reshock strength), and the study of Poggi et al. [3] in which the production of turbulence by the TMZ has been investigated in a vertical shock tube using two-components Laser Doppler Velocimetry (LDV).

The main objective of the present work is to provide a detailed characterization of our shock tube in order to discriminate the turbulence level produced by the mixing of the two gases in the TMZ, through baroclinic effects, from the background turbulence level of the experimental set-up. We thus investigated several configurations without the mixing zone (pure air).

G. Bouzgarrou · Y. Bury · S. Jamme · J.-B. Cazalbou
Université de Toulouse, ISAE, 10 Avenue Edouard Belin, F-31055 Toulouse, France

J.-F. Haas · D. Counilh
CEA, DAM, DIF, F-91297 Arpajon, France

2 Experimental Set-Up

The experimental apparatus used in this study consists of a 5 m long, 130 mm square cross section vertical shock tube that was initially operated at CEA [4] before being transferred to the Institut Supérieur de l'Aéronautique et de l'Espace (ISAE) in Toulouse in 2009. For studies involving RMI and the resulting turbulent mixing, a shock wave (Mach number 1.2) travels upward and crosses an air/sulphurhexafluoride (SF6) interface, which sets the Atwood number at 0.699. Both gases are initially separated by a thin nitrocellulosic membrane (0.5 μm thick) trapped between two grids, the upper one imposing a two-dimensional initial perturbation of wavelength equal to 1.8 mm. According to RMI models, a perturbation with this wavelength induces a fully developed turbulence in a short time compared to the transient time of the shock in the observation chamber.

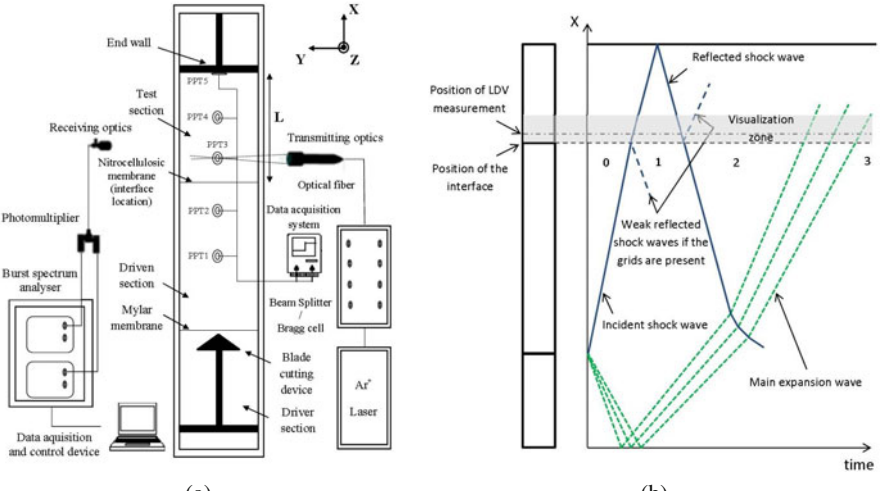

(a) (b)

Fig. 1 Description of the experimental apparatus (a) and (X-t) diagram of an homogeneous shot (b).

A schematic of the experimental set-up is shown in Figure 1. The length of the test section has been fixed to L=250 mm. The incident Mach 1.2 shock wave is generated by impacting a Mylar diaphragm, initially separating the driven and the driver sections of the shock tube, using a blade cutting device. The pressure ratio between both chambers is fixed to 2.7 before the diaphragm disruption. One has to notice that this value differs from the 2.38 value given by the non viscous theory. This is attributed to dissipative effects in the shock tube.

Mean and fluctuating X and Y-velocities, hereafter denoted U and V, and respectively corresponding to the vertical and first-lateral velocities, are measured inside the shock tube using two-components LDV. The two measurement volumes, of approximative dimensions $\Delta X = 46$ μm, $\Delta Y = 46$ μm, $\Delta Z = 850$ μm, are located

at the center of the test section of the tube, 43 mm above the position of the nitrocellulosic membrane. The fluid is seeded with 1 μm-diameter olive oil spherical particles. In the region of interest, located between the incident and the reflected shock waves, data rates above 500 kHz (resp. 250 kHz) were obtained for the U velocity (resp. V velocity). Pressure histories of the flow in the shock tube are obtained using five piezoelectric pressure transducers. The acquisition frequency was fixed to 2.5 MHz. For each shot, the incident Mach number is determined via the two pressure transducers PPT1 and PPT2 respectively located 315 and 115 mm below the interface. In the test section, three additional pressure transducers PPT3, PPT4 and PPT5 are mounted respectively at 43, 213 and 250 mm above the interface. The LDV measurements were triggered on the PPT2 pressure signal. This allows to achieve phase-averaged statistics based on the crossing instant of the incident shock in the measurement volume.

Time-resolved Schlieren visualizations are simultaneously operated. Videos of the travelling shock wave and the resulting series of compression/expansion waves inside the test section are recorded thanks to a high-speed Phantom V12 camera. The data rate of the image recording is fixed to 27000 images per second.

3 Turbulence Characterization

Before considering air/SF6 mixing, the background turbulence level of the shock-tube is evaluated by considering several test configurations with pure air :

- Conf1: experiments with a clean test section (no grid and no nitrocellulosic membrane inside the shock tube);
- Conf2: experiments with two grids at the interface location (bottom wire mesh with a wire spacing of 1 mm, upper wire mesh with a wire spacing of 1.8 mm), without nitrocellulosic membrane, in order to quantify the influence of the grids on the turbulence levels compared with Conf1;
- Conf3: experiments similar to Conf2 with the addition of the nitrocellulosic membrane trapped between the two grids, in order to quantify the effect of the fragments generated by the crossing of the shock across the membrane on the turbulence production.

For each configuration, 40 shots were conducted and the mean and fluctuating, phase-averaged, U and V velocities were computed. Time discretization into consecutive time windows was fixed to 10 μs around the incident and reflected shocks and to 30 μs elsewhere. Those time steps were determined as a compromise between sufficiently high number of samples per time step (imposing a minimum temporal width), and the time-filtering effect induced by too large time steps. Convergence of the first and second order statistics was demonstrated to be obtained for samples numbers above 150 in each time window. Figure 2 reveals that this was achieved in most of the region of interest located between the incident and reflected shocks, occuring at $t = 0$ μs and $t = 1150$ μs respectively, except for Conf3 where large membrane fragments temporarily cross the LDV measurement volumes, cutting the Doppler signals between $t = 260$ μs and $t = 560$ μs.

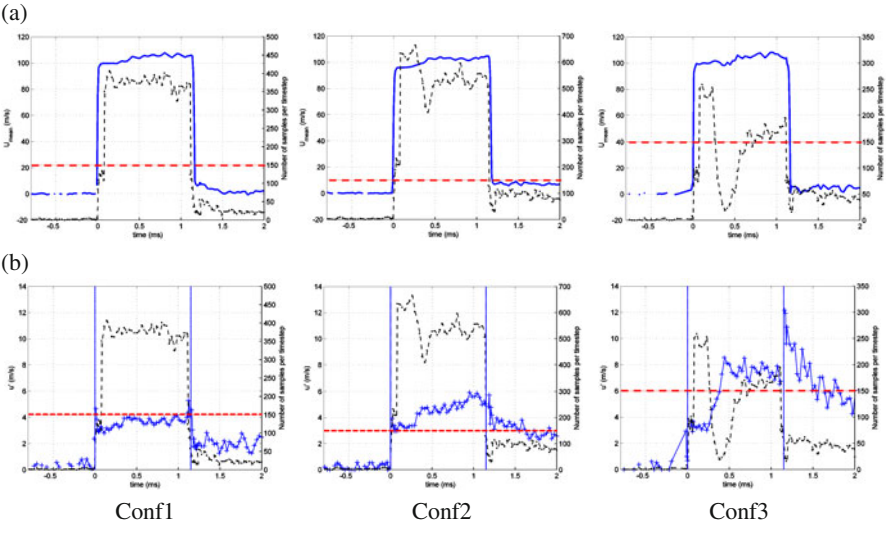

Fig. 2 Evolution of the vertical mean velocity $\bar{U}$ (a) and fluctuating velocity $\sqrt{\overline{u'^2}}$ (b) (blue continuous line, left vertical axis). Number of samples used for the calculation of the statistics on each time step of the discretized velocity signal (black dashed line, right vertical axis). The red horizontal line corresponds to the number of samples necessary to get convergence.

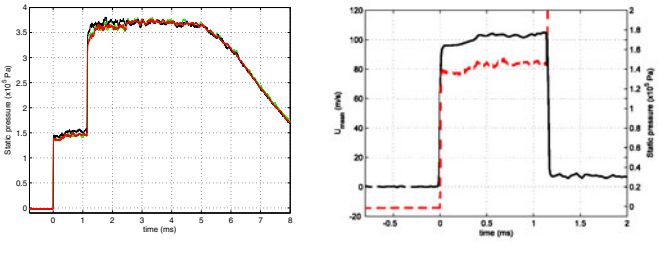

Fig. 3 Static pressure signals PPT3 (X=43 mm above the interface) for the 3 configurations over the whole history of the phenomenon (a); Concurrent evolutions of the mean vertical velocity (black continuous line) and PPT3 static pressure (red dashed line), zoom around the velocity plateau between the incident and reflected shock waves (b).

Figure 2 (a) depicts time evolutions of the phase-averaged U velocity for the three previously described test configurations. Corresponding PPT3 pressure signals are illustrated on Figure 3. Figure 4 shows the simultaneously acquired Schlieren images. Interestingly enough, those images reveal a complex acoustic field in the wake of the incident shock wave, comprising series of compression/expansion non planar waves. Those waves are induced by the travelling of the shock wave over slight parietal defaults, in the form of steps a few tens of micron deep, at the junction of

the different modules constituting the tube. This results in a non uniform velocity plateau between the incident and reflected shock waves. For the three test configurations, this plateau displays a first velocity level around 100 m/s, between $t = 0$ μs and $t = 250$ μs, followed by a second velocity level around 107 m/s, corresponding to the expected velocity behind the M=1.2 incident shock wave. The second part of the plateau is also characterized by oscillations whose periods are in good agreement with both the PPT3 pressure signals and the tracks of the previously evoked series of compression/expansion waves clearly observable on the Schlieren images.

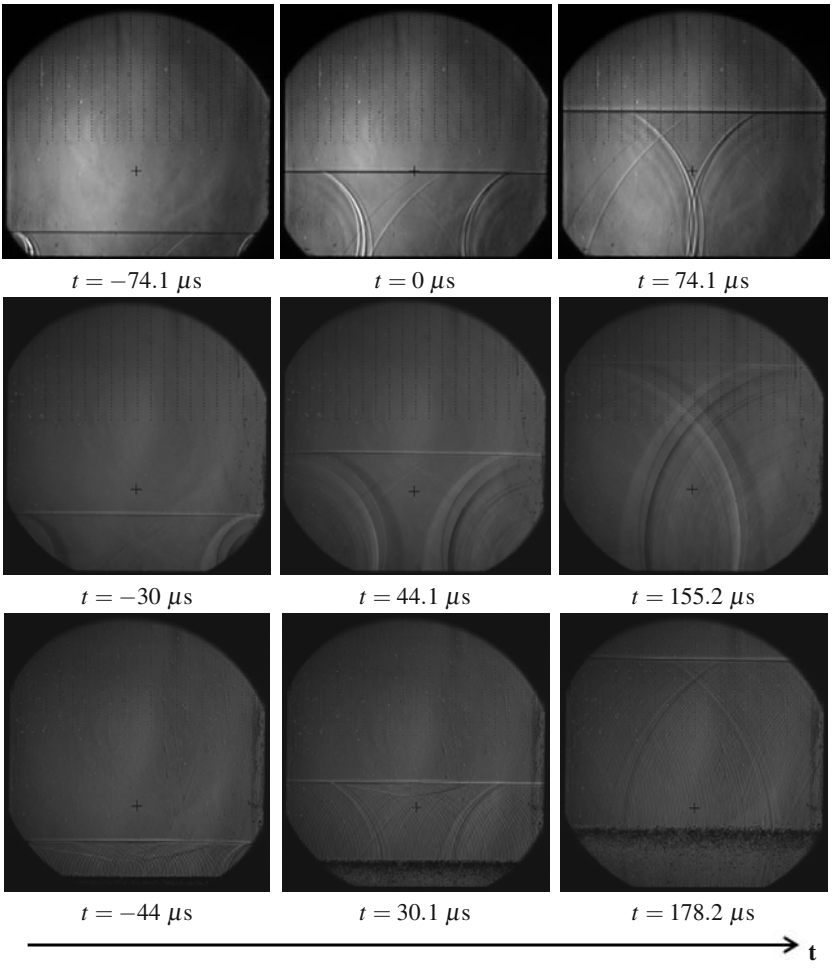

Fig. 4 Schlieren images of the perturbations generated by the shock wave in pure air, Conf1 (up), Conf2 (middle), Conf3 (down). The black cross on the images indicates the location of the measurement volume for LDV. The origin of time on the figure corresponds to the passage of the incident shock wave on the measurement volume.

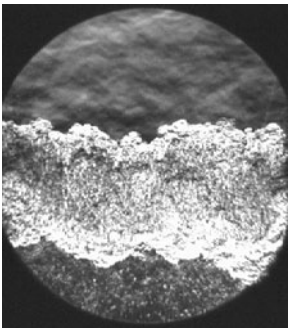

Fig. 5 Schlieren visualization of the TMZ 3 ms after the shock passage across the initial interface.

Figure 2 (b) displays the phase-averaged U-velocity fluctuations for the three test configurations. The previously evoked level shift of the plateau located between the incident and the reflected shock waves still remains on the U and V velocity fluctuations time evolutions. For sake of conciseness, only the U fluctuating component will be analysed. Superimposition of the three curves (not shown) reveals that the first level is perfectly similar for the three configurations, in terms of duration as well as turbulence level, close to 3.2%. However, and while for Conf1 the second level depicts turbulence intensities around 3.7%, this value rises up to 4.9% for Conf2 (2 grids without nitrocellulosic membrane), and over 7.5% for Conf3 (nitrocellulosic membrane trapped between the 2 grids). It can thus be concluded that the grids increase the turbulent intensity up to 1.5%. The membrane fragments induce a further increase of 2.6%. This is of prime interest for the precise characterization of the air/SF6 mixing through the RMI and baroclinic torques induced turbulence production, illustrated on Figure 5.

Acknowledgments. This work is supported by CEA, DAM, DIF under grant number 09-37-C-SACO.

References

1. Brouillette, M.: The Richtmyer-Meshkov instability. Annu. Rev. Fluid Mech. 34, 445–468 (2002)
2. Leinov, E., Malamudi, G., Elbaz, Y., Levin, L., Ben-Dor, G., Shvarts, D., Sadot, O.: Experimental and numerical investigation of the Richtmyer-Meshkov instability under re-shock conditions. J. Fluid Mech. 626, 449–475 (2009)
3. Poggi, F., Thorembey, M.H., Rodriguez, G.: Velocity measurements in turbulent gaseous mixtures induced by Richtmyer-Meshkov instability. Phys. Fluids 10, 2698–2700 (1998)
4. Haas, J.F., Counilh, D., Perez, A., Montlaurent, P., Houas, L., Mariani, C., Jourdan, G., Schwaederlé, L.: Schwaederlé L.: Laser Doppler measurements and visualization of shock induced turbulent mixing zones. In: Turbulent Mixing and Beyond Workshop, Trieste, Italy (2007)

Experiments on the Richtmyer-Meshkov Instability with an Imposed, Random Initial Perturbation

J. Jacobs, V. Krivets, V. Tsiklashvili, and O. Likhatchev

1 Experimental Set-Up

Membraneless Richtmyer-Meshkov instability experiments have previously been carried out in a vertical shock tube using a single-mode two- and three-dimensional initial perturbations [1], [2]. The present study utilizes the apparatus and experimental techniques of these previous investigations modified to allow the generation of a random three-dimensional initial perturbation.

A 5 m long vertical shock tube with a 10.2 cm diameter round driver, and a 8.9 cm square test section is used for this study. The light gas (air) enters the tube at the top of the driven section immediately below the diaphragm, and the heavy gas (SF_6) enters at the bottom of the test section. The gases exit the shock tube through a series of small holes in the test section walls, leaving behind a flat, diffuse interface. In the previous studies the initial perturbation was generated by periodically oscillating the square shock tube, laterally, to produce a nearly single-mode two-dimensional standing wave. More recently [3] we have found that we can produce similar single mode three-dimensional standing waves by oscillating the gas column within the shock tube vertically using the periodic motion of a piston mounted at the bottom of the test section. The work presented here is a continuation of that work in which the frequency of this motion is increased producing a more random, short wavelength pattern.

The initial perturbation for this study is created using two reinforced loudspeakers mounted in the shock tube wall, one near the bottom of the test section and the other near top of the driven section. The two speakers are oscillated out of phase from one another producing the vertical oscillation of the gas column within the shock tube. This motion generates Faraday waves on the interface which result in a small random three-dimensional perturbation imposed on the otherwise flat interface.

J. Jacobs · V. Krivets · V. Tsiklashvili · O. Likhatchev
University of Arizona, Department of Aerospace and Mechanical Engineering, Tucson AZ 85721 USA

A weak shock wave ($1.1 \leq M \leq 1.2$) is generated in the shock tube by puncturing a polypropylene diaphragm. The flow is visualized utilizing planar laser Mie scattering movies. The light gas is seeded with incense smoke and illuminated by the second harmonic of a pulsed Nd:YLF laser operated at 6 kHz and positioned at the lower end of the shock tube. The the laser's output is passed through circular and cylindrical lenses and reflected upward through a window in the shock tube end wall producing a light sheet that illuminates a thin cross section of the interface. The resulting Mie scattered image is captured using three high-speed CMOS video cameras positioned to cover the full visualization zone.

2 Results

Figure 1 is three dimensional view of a typical initial perturbation. In this case the perturbation has been made visible by the addition of a dense water droplet fog to the heavy gas which is then illuminated using a strobe light source. As can be seen in this image the perturbation has a complex, random form but with a dominant wavelength present.

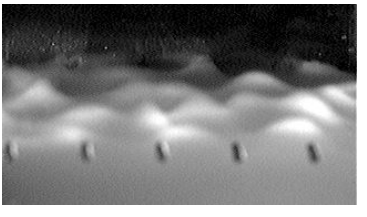

Fig. 1 Three-dimensional view of the form of the initial perturbation.

Figure 2 shows a sequence of Mie scattering images taken from a typical experiment. In this sequence one can observe the initial perturbation prior to shock interaction followed by the development of the instability following interaction by the incident shock wave and including reshock. Early in the development the instability retains an imprint of the initial perturbation. However, with time turbulence develops in what appears to be a self-similar fashion, with length scales increasing with time. Following reshock, extremely small scales are generated accompanied by the accelerated growth of the mixing zone.

Figure 3 is a plot of mixing layer width versus time for 16 experiments showing the instability growth following initial shock interaction and then following reshock. As can be observed in this plot, the mixing layer width initially shows power law growth $h = Ct^{\theta}$ with growth exponent $\theta < 1$. After reshock, however, the growth rate is constant. Evident in this plot is a small amount of scatter produced by small inconsistencies in the initial perturbation. Note that the amplitude and dominant wavelength of the perturbation is reasonably reproducible. However, there are variations in the random nature of the initial perturbation which are difficult to control.

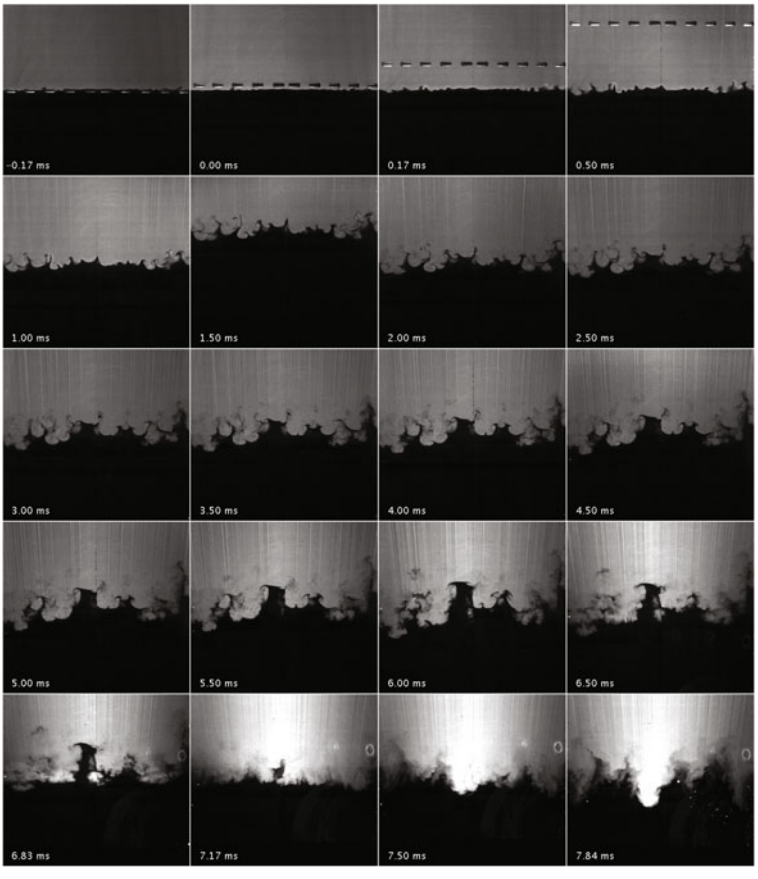

Fig. 2 Image sequence taken from a typical experiment using the Mie scattering diagnostic.

Nevertheless, in examining the growth curves of individual experiments, two growth behaviors can be observed and these are illustrated in figures 4. The plot on the right shows a very rapid initial growth followed by much slower growth later on, while the plot on the left shows a much more consistent growth rate for the entire experiment.

In order to investigate the value of growth exponent log-log plots of averaged values of the data from figures 4 are shown in figures 5. Note that if growth of the form $h = Ct^{\theta}$ is expected then the slopes of lines fitted to the curves of figures 5 should yield the growth exponent θ. It can be observed that both sets of data show two distinct linear regions (in these log-log plots) indicating two values of growth exponent. In the early portions of both plots a growth exponent of $\theta \approx 0.5$ is achieved. However, at later times a much more variable growth constant is observed with θ lying in the range $0.3 < \theta < 0.4$.

Following reshock much more consistent growth is observed as can be seen in figure 6. In this case both sets of experiments show identical values of growth rate

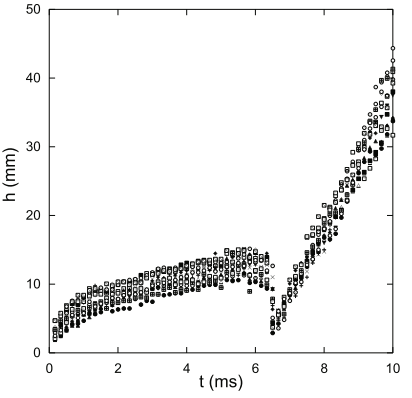

Fig. 3 Plot of mixing layer half width for 16 experiments.

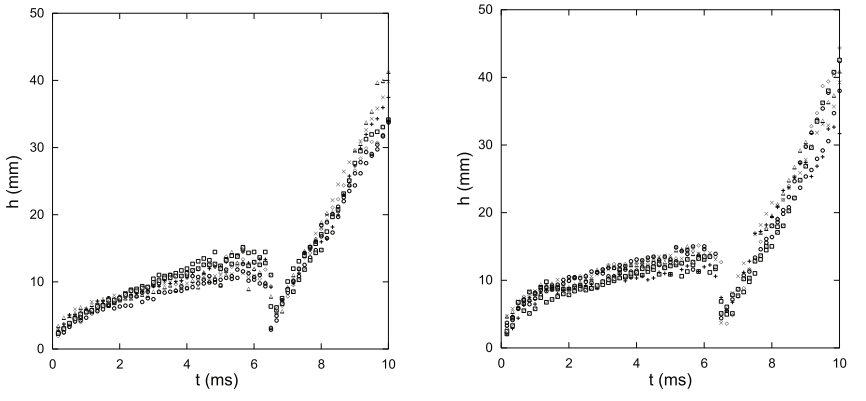

Fig. 4 The data of figure 3 separated into two groups showing different growth behaviors.

of $dh/dt = 9.26\,\mathrm{m/s}$. In order to provide comparison with previous reshock experimental results a dimensionless version of the reshock growth rate is plotted in figure 7. Note that following the suggestion of Mikaelian [4], Leinov et al. [5] have proposed that since $dh/dt \propto A\Delta U$, where ΔU is the reshock impulse, one can define a dimensionless reshock growth rate as $C = \frac{2}{A\Delta U}\frac{dh}{dt}$. Note that using this definition Mikaelian has indicated that $C = 4\alpha$, where α is the Rayleigh-Taylor growth constant. Thus figure 7 is a plot of C versus ΔU for the current experiments along with those of Leinov et al. showing relatively good agreement with the previous work. However, it is noteworthy that the present experiments have noticeably smaller values of growth rate that could be attributed to the fact that the experiments of Leinov et al used a membrane to initial separate the two gases. Since the presence of membrane fragments could be expected to produce greater mixing upon reshock, our experiments could be viewed as exhibiting a better correspondence to a membrane free situation. Also shown on figure 7 are two lines indicating the range of C values

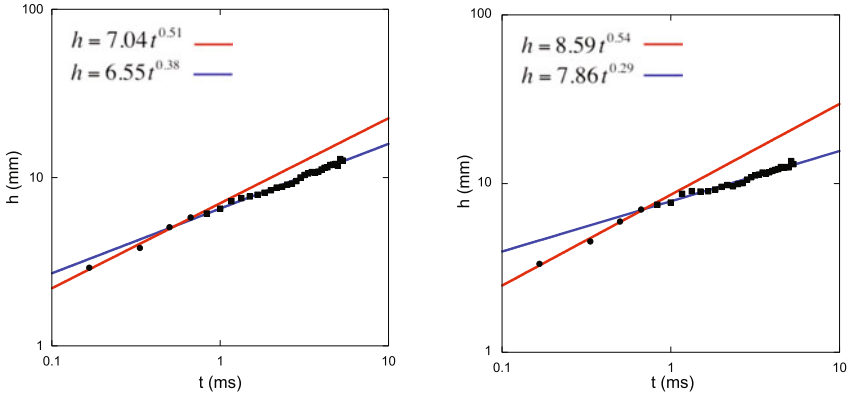

Fig. 5 Log-log plot of mixing layer half width for the two sets of experiments of figure 4.

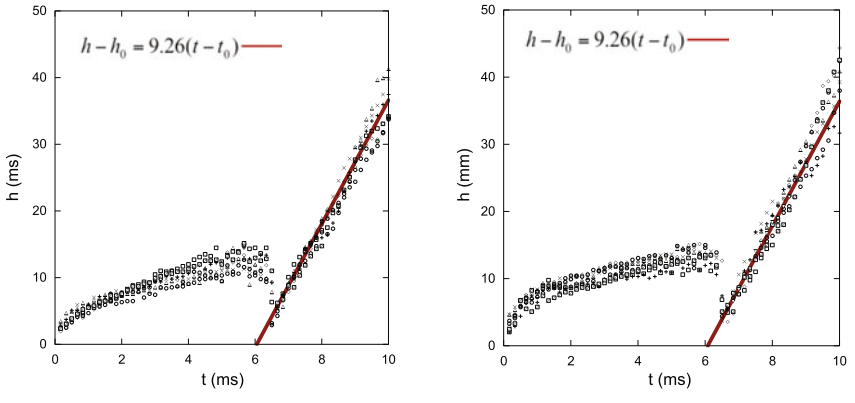

Fig. 6 Plot of mixing layer half width for the two sets of experiments showing identical growth rates following reshock.

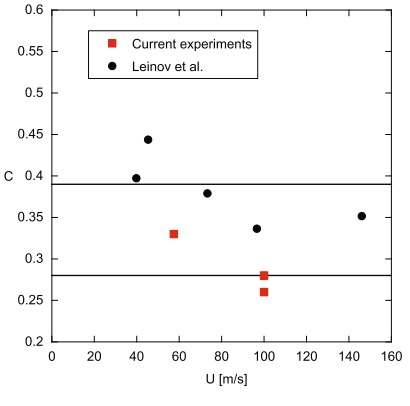

Fig. 7 Comparison of measured dimensionless reshock growth rates from this study to those measured by Leinov et al.

expected from Mikaelian's model using the range of expected α values found in previous Rayleigh-Taylor instability experiments having the same Atwood number as that used here.

3 Conclusions

The Richtmyer-Meshkov instability initiated with an imposed random perturbation has been investigated in shock tube experiments. Measurements of the mixing layer width following initial shock interaction show a power law growth similar to that observed in previous experiments and simulations. However, two different growth behaviors are observed. Both behaviors show growth constants θ approximately equalling one half, initially. However at late times a range of growth constants is observed with $0.3 < \theta < 0.4$. Following reshock much greater consistency is achieved with the measured growth rate in good agreement with previous studies. The only difference observed is that in the present experiments that do not use membranes to initially separate the two gases, the measured reshock growth rate is noticeably smaller that that measured in the previous experiments that do employ membranes.

This research was supported by Lawrence Livermore National Laboratory and by the DOE National Nuclear Security Administration under its Stewardship Science Academic Alliances program.

References

1. Collins, B.D., Jacobs, J.W.: PLIF Flow visualization and measurements of the Richtmyer-Meshkov instability of an air/SF_6 interface. J. Fluid Mech. 464, 113–136 (2002)
2. Jacobs, J.W., Krivets, V.V.: Experiments on the late-time development of single-mode Richtmyer-Meshkov instability. Phys. Fluids. 17, 034105 (2005)
3. Long, C.C., Krivets, V.V., Jacobs, J.W.: Shock tube experiments and numerical simulation of the single-mode, three-dimensional Richtmyer-Meshkov instability. Phys. Fluids. 21, 114104 (2009)
4. Mikaelian, K.O.: Turbulent mixing generated by Rayleigh-Taylor and Richtmyer-Meshkov instabilities. Physica D 36, 343–357 (1989)
5. Leinov, E., Malamud, G., Elbaz, Y., Levin, L.A., Ben-Dor, G., Shvarts, D., Sadot, O.: Experimental and numerical investigation of the Richtmyer-Meshkov instability under reshock conditions. J. Fluid Mech. 626, 449–475 (2009)

Part XVII
Shockwave Boundary Layer Interaction

Numerical Discovery and Experimental Validation of Vortex Ring Generation by Microramp Vortex Generator

Qin Li, Ping Lu, Chaoqun Liu, Adam Pierce, and Frank Lu

1 Introduction

Micro vortex generators are a new kind of passive flow control instruments for shock-boundary layer interaction problems. In contrary to the conventional vortex generator, they have heights approximately 20-40% (more or less) of the boundary layer. Among them, Mircoramp vortex generators (MVG) are given special interest by engineers because of their structural robustness. The mechanism of the flow control was thought that a pair of streamwise vortex is generated by MVG and remains in the boundary layer for relatively long distance; the down-wash effect by the streamwise vortices will bring about momentum exchange, which makes the boundary layer less liable to separation. During such process, a specific phenomenon called as momentum deficit will happen [1], i.e., a cylindrical region consisted of low speed flows will be formed after the MVG. It was pointed out by Li and Liu [2] that the origin of deficit comes from the shedding of boundary layer over MVG.

Numerical simulations have been made on MVG for comparative study and further design purposes. Ghosh, Choi and Edwards [3] made detailed computations under the experimental conditions given by Babinsky by using RANS, hybrid RANS/LES and immersed boundary (IB) techniques. Lee et al [4, 5] also made computations on the micro VGs problems by using Monotone Integrated Large Eddy Simulations (MILES). Basic flow structures like momentum deficit and streamwise vortices were reproduced in the computation. Further studies were also conducted on the improvement of the control effect.

It is definitely needed to find physics of MVG for design engineers. RANS, DES, RANS/DES, RANS/LES, etc are good engineering tools, but may not be able to reveal the mechanism and get deep understanding of MVG. We need high order DNS/LES. A powerful tool is the integration of high order LES and experiment. An implicit large eddy simulation was conducted on the MVG controlled flow at

Qin Li · Ping Lu · Chaoqun Liu · Adam Pierce · Frank Lu
University of Texas at Arlington, 701 S. Nedderman Drive, Arlington, TX 76019, USA

Mach number 2.5. Flows of MVGs are studied with back edge declining angle (see Figure 1(left)).The geometries for the cases are shown in Figure 1(right). The details about the geometric objects, grid generation, computational domain, etc, are introduced in our previous paper [3, 6] and will not be repeated here. Through the computation, a new phenomenon called as vortex rings was first discovered, i.e., a train of vortex rings will be generated continuously within the boundary of the momentum deficit. The mechanism for the vortex rings was analyzed and found that, the existence of the high shear layer and inflection surface generated by the momentum deficit will cause the corresponding Kelvin-Helmholtz instability, which develops into a series of vortex rings. An experiment was designed to validate the discovery. The snapshot of the laser sheet at the center plane demonstrated the vortex structures after MVG and confirmed the discovery by our LES.

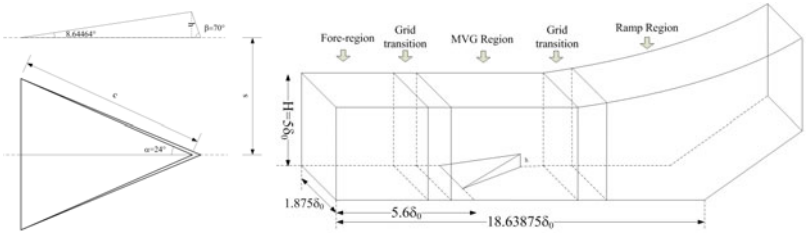

Fig. 1 Left: the sketch of MVG at $b = 70°$, right: the schematic of the half grid system.

2 Numerical Method

In this paper, we investigate vortex ring generation by microramp vortex generator at $M = 2.5$ and $Re_\theta = 5760$. A kind of large eddy simulation method is used by solving the unfiltered form of the Navier-Stokes equations with the 5^{th} order Bandwidth-optimized WENO scheme [7], which is generally referred to the so-called implicitly implemented LES [8]. Without explicitly using the subgrid scale (SGS) model as the explicit LES, the implicitly implemented LES uses the intrinsic dissipation of the numerical method to dissipate the turbulent energy accumulated at the unresolved scales with high wave numbers.

The adiabatic, zero-gradient of pressure and non-slipping conditions is adopted at the wall. To enforce the free stream condition, fixed value boundary condition with the free parameters is used on the upper boundary. The boundary conditions at the front and back boundary surface in the spanwise direction are treated as the mirror-symmetry condition, which is under the consideration that the problem is about the flow around MVG arrays and only one MVG is simulated. The outflow boundary conditions are specified as a kind of characteristic-based condition, which can handle the outgoing flow without reflection [3].

The inflow conditions are generated using the following steps:

1. A turbulent mean profile is obtained from previous DNS simulation result [9] for the streamwise velocity (w-velocity) and the distribution is scaled using the local displacement thickness and free stream velocity. The basic transfer is based on the assumption that the same distribution exists between the relations of $U/U_e \sim y/\delta^*$. And the averaged streamwise velocity of MVG case can be got by interpolation (3^{rd} spline interpolation).
2. The pressure is uniform at inlet and is the same as the free stream value. The temperature profile is obtained using Walz's equation for the adiabatic wall: first the adiabatic wall temperature is determined using: $T_w = T_e\left[1 + r(\gamma-1)/2M_e^2\right]$, where the subscript e means the edge of the boundary layer and r is the recovery factor with value 0.9; next the temperature profile is obtained by Walz's equation: $T/T_e = T_w/T_e - r(\gamma-1)/2M_e^2\,(U/U_e)^2$.
3. The fluctuation components of the velocity are separated from the velocity at every instantaneous data file (total 20000 files). And such fluctuations are rescaled in the same way. Because $\overline{T}/T_e = T_w/T_e - r(\gamma-1)/2M_e^2\left(\overline{U}/U_e\right)^2$, considering the non-dimensional form and ignore the T_e and U_e, we get $\mathrm{d}\overline{T} = -r(\gamma-1)\,M_e^2\,U\mathrm{d}\overline{U}$, or $\Delta T = -r(\gamma-1)\,M_e^2\,U\Delta U$. Density fluctuation is determined by $\Delta\rho/\overline{\rho} = -\Delta T/\overline{T}$.
4. Finally, the transformed parameters are $u = U + \Delta u$, $v = V + \Delta v$, $w = \Delta w$, $\rho = \overline{\rho} + \Delta\rho$, $p = \rho T/\left(\gamma M^2\right)$ and $T = \overline{T} + \Delta T$.

3 Inflection Surface, K-H Instability and Vortex Ring Generation by MVG

3.1 Inflection Surface in 3-D Flow Behind MVG

In order to explore the mechanism of the vortex ring generation, the distributions of averaged streamwise-velocity are given in Figure 2(left) along the normal grid lines at the center plane. The streamwise positions of the lines are $L_{from\,apex}/h \approx 3.3, 6.7, 10$ and 11, where $L_{from\,apex}$ is the streamwise distance measured from the apex of MVG. The dip of the lines corresponds to the momentum deficit. From the results, it can be seen clearly that there are at least two high shear layers in the central plane, one is located at the upper edge of the dip and the other is located at the lower edge. Within the shear layer, there is at least one inflection point. In order to demonstrate the existence of the inflection points, the second order derivative $\partial^2 w/\partial y^2$ (w is the stremwise velocity and y is the normal direction) is calculated along the lines, and the result of the line at $L_{from\,apex}/h \approx 6.7$ is plotted in Figure 2(center and right) as an example. The existence and correspondence of the inflection points at the upper and lower shear layers is illustrated by two dashed lines intersecting the distribution of the streamwise velocity and its second order derivative.

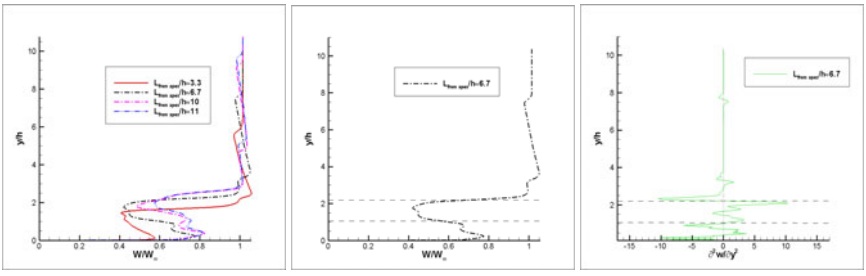

Fig. 2 Left:Averaged streamwise velocity at different sections. Inflection points (surface for 3-D). Center: averaged stremwise velocity at $L_{from\ apex}/h \approx 6.7$, right: $\partial^2 u/\partial y^2 = 0$.

3.2 Vortex Ring Generation

Based on the above analyses, it can be concluded that the existence of the inflection points (surface in 3-D) in the shear layer causes the flow instability and generates vortex rollers by K-H instability in a cylindrical coordinate system. Therefore, the mechanism of the vortex ring generation should be K-H instability. The lost of the stability of the shear layer will result in the roll-up of the vortex, which appears in ring-like structure in a 3-D view (Figure 3). In Figure 3(b), λ_2 is certain eigenvalue of the stress tensor, and its iso-surface is usually used to describe the vortex surface. The intensity of the upper shear layer appears to be stronger than that of the lower shear layer (Figure 3). In Figure 4, another qualitative checking about the shear layer and K-H instability is made by using the instantaneous flow field. In the figure, the background at the central plane and the spanwise plane is colored by the value of the streamwise velocity, so that the green regions in two planes represent the momentum deficit. In the central plane, the pressure contours are superimposed on the background cloud-map. The figure shows that, the blue circle structures, which indicate the core of the ring like vortices cut by the plane, are located on the boundary of the deficit circle. Such positions are exactly the same place where the high shear layer exists. In Figure 5, we give the instantaneous numerical schlieren picture at the central plane. From the figure, we can see many vortex rings appear in the circular

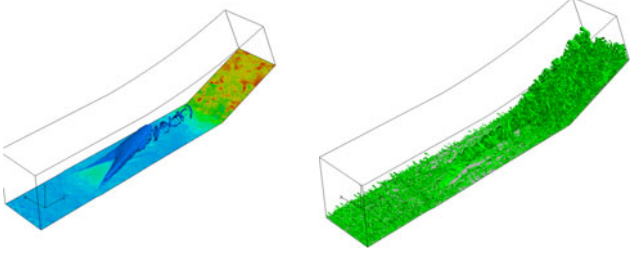

Fig. 3 Vortex ring generation by MVG due to K-H instability. Left: iso-surface of pressure, right: iso-surface of λ_2.

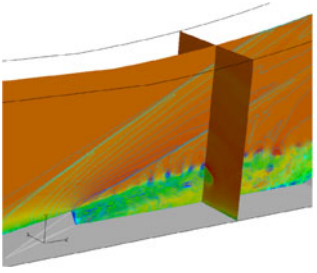

Fig. 4 The instantaneous pressure and streamwise velocity contour on different cross sections.

shapes. After being told the prediction of the vortex rings, the same experimentalists in UT Arlington tried some techniques to validate the discovery. They used techniques of the particle image velocimetry (PIV) and the acetone vapor screen visualization to track the movement of the flow, and specifically the flash of a laser sheet is used to provide the light exposure at the time level of micro seconds. In Figure 6, a typical image at the center plane is presented taken by using PIV and the acetone vapor (Lu et al [10]). It is clearly demonstrated that a chain of vortex rings exist in the flow field after the MVG! And these structures qualitatively resemble that in Figures 5-6.

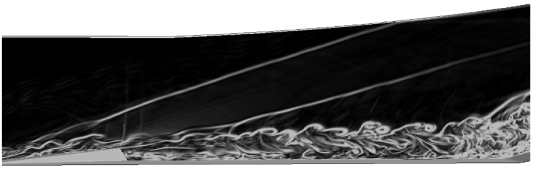

Fig. 5 The numerical shilieren at the center plane.

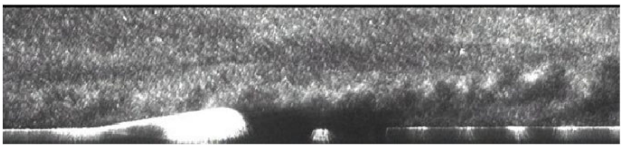

Fig. 6 The laser-sheet flash image at the center plane. Upper: using PIV, lower: using the acetone vapor.

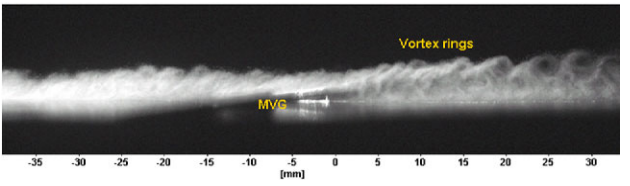

4 Conclusion

Base on numerical results, the inflection points (surface in 3-D) inside the deficit area are found. The mechanism for the vortex rings was analyzed and found that, the existence of the high shear layer and inflection surface generated by the momentum deficit will cause the corresponding Kelvin-Helmholtz instability, which develops into a series of vortex rings. Kelvin-Helmholtz type instability is caused by the momentum deficit. Vortex rings are generated by K-H type instability after MVG. The experiment work demonstrated that a chain of vortex rings exist in the flow field after the MVG, and these structures qualitatively resemble that in numerical simulation.

References

1. Babinsky, H., Li, Y., Ford, C.W.P.: Microramp Control of Supersonic Oblique Shock-Wave/Boundary-Layer Interactions. AIAA J. 47(3), 668–675 (2009)
2. Li, Q., Liu, C.: LES for Supersonic Ramp Control Flow Using MVG at $M = 2.5$ and $Re_\theta = 1440$. AIAA Paper 592 (2010)
3. Ghosh, S., Choi, J., Edwards, J.R.: Numerical Simulations of the Effects of Micro Vortex Generators Using Immersed Boundary Methods. AIAA J. 48(1) (2010)
4. Lee, S., Loth, E.: Supersonic Boundary Layer Interactions with Various Micro-Vortex Generator Geometries. AIAA Paper 3712 (2009)
5. Lee, S., Loth, E.: Microramps Upstream of an Oblique-Shock/Boundary-Layer Interaction. AIAA J. 48(1) (2010)
6. Li, Q., Liu, C.: Numerical Investigations on the Effects of the Declining Angle of the Trailing-Edge of MVG. AIAA Paper 714 (2010)
7. Wu, M., Martin, M.P.: Direct Numerical Simulation of Supersonic Turbulent Boundary Layer over a Compression Ramp. AIAA J. 45(4), 879–889 (1996)
8. Grinstein, F.F., Margolin, L.G., Rider, W.J.: Implicit Large Eddy Simulation. Cambridge university press (2007)
9. Liu, C., Chen, L.: Study of Mechanism of Ring-Like Vortex Formation in Late Flow Transition. AIAA Paper 1456 (2010)
10. Lu, F., Pierce, A., Shih, Y.: Experimental Study of Near Wake of Micro Vortex Generators in Supersonic Flow. AIAA Paper 4623 (2010)

Shock-Wave Boundary-Layer Interaction Control on a Compression Corner Using Mechanical Vortex Generators

C. Manisankar, S.B.Verma, and C. Raju

1 Introduction

Shock-wave boundary-layer interactions (SWBLI) are prevalent in many supersonic applications, e.g., over deflected flaps, fore-body ramp corners, on leading edges where the bow shock from the vehicle nose interferes, along axial compression corners inside air-inlets, shock reflection and crossing-shock interactions in the inlets etc. The adverse pressure gradient across the interaction shock can cause separation of the incoming boundary-layer leading to increased aerodynamic drag, heat transfer and unsteady pressure loads. Much of the early work over forward-facing steps [1], un-swept compression ramp flows [2-4] and in interactions induced by blunt fins [5], circular cylinders and sharp fins at angle of attack [6] was focused on understanding the dynamic/unsteady behavior of these interactions. It has been observed that the flow in these interactions in unsteady if the pressure ratio across the oblique shock is such that the mass of the fluid reversed at the reattachment point does not balance the scavenged fluid from the separated region [7-8]. As a result, the separated region "breathes" and during one half of pulse, mass is injected into it while during the other half it is ejected out resulting into an unsteady mass exchange.

Recently, studies have been carried out to diminish the detrimental effects of SWBLI using flow control [9]. The most popular of these techniques have been the use of vortex generating devices such as micro-ramps, vane-type VG fixed at an angle to the main flow or the use of micro air-jets at an appropriate distance upstream of the region of interaction [10-14]. These devices generate either co-rotating or counter-rotating vortices depending upon their design and angular positions with respect to the main flow direction. Significant modifications in the overall interaction have been reported with control. The spanwise spacing between the VG devices also seems to be an important parameter in controlling the flow interaction. However, in

C. Manisankar · S.B.Verma · C. Raju
CSIR-National Aerospace Laboratories, Experimental Aerodynamics Division, Bangalore, 560017, India

order to reduce wave-drag penalties, it is suggested [10-11] that the height of VGs should be below the sonic line of the boundary-layer. Such studies are relevant to air-inlets so as to increase mass-flow ingestion resulting in enhanced inlet operability and therefore, improve overall engine performance.

The present paper reports an exploratory study conducted to control the amplitude of shock unsteadiness associated with the SWBLI on a 24° compression corner using mechanical VG devices in the form of single-row delta ramps. The primary focus of the study is to investigate the phenomena of SWBLI with emphasis on the effect of VG devices on the overall flowfield characteristics. The interaction is studied using color schlieren, Kulite pressure sensors, oil-flow and pressure-sensitive paint (PSP).

2 Experimental Set Up and Procedure

2.1 Wind Tunnel Facility and Model Details

Tests were conducted in 0.457m x 0.3m blow-down tri-sonic wind-tunnel at National Aerospace Laboratories (NAL). The compression corner model was mounted on a sting along the tunnel centerline in order to (i) avoid effects of noise levels from turbulent boundary-layer present on wind-tunnel wall and to facilitate PSP measurements. The test Mach number was 2.05±0.02 while the stagnation pressure and temperature was 30psia±1% and 298K±0.4%, respectively. This gives a unit Reynolds number of 25.257 x 10^6 $m^{-}1$. The wall temperature was approximately adiabatic. The compression ramp model used for the present investigation is mounted on a sting along the tunnel centerline to (a) avoid effects of noise levels from turbulent boundary-layer normally present on wind tunnel walls and, (b) to facilitate PSP measurements. The flat plate of the model is 28cms long with a span of 11cms, Fig. 1 (a). The ramp plate angle was set at 24 degrees. No side-fences were used in order to facilitate schlieren imaging. A boundary-layer trip, made of 60 grit carborundum particles spanning 4mm in length and placed at 17mm from the leading edge was used to ensure sufficiently thick (turbulent) boundary-layer so

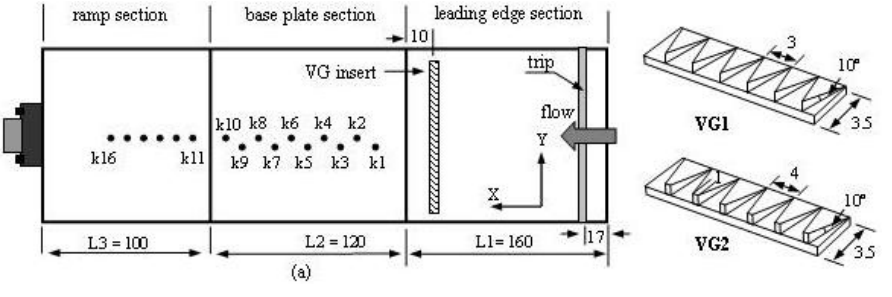

Fig. 1 Schematic showing (a) the compression model details with the sensor locations and, (b) the micro-ramp configurations used in the present study. All dimensions are in mm

as to ensure that the VGs are embedded in them. The boundary-layer thickness δ is 1.53mm at the VG location resulting in h/δ= 0.65. Figure 1 (b) shows the two VG configurations tested. The VG insert is located 130mm upstream of the corner, Fig. 1 (b). With respect to the interaction location (located 20mm upstream of corner; δ= 4mm), this corresponds to 27.5δ.

2.2 Data Acquisition System and Analysis

Simultaneous wall pressure measurements along the centerline were made using fast piezo-resistive transducers (Kulite models XT-140M and XCQ-093). Nine such transducers were mounted upstream of the corner with a pitch of 5.5mm while six of them were mounted on the ramp surface with a pitch of 5mm. The transducer data was acquired using truly simultaneous data acquisition card NI4495 DC series at a sampling frequency of 50kHz. Later on FFT analysis was carried out using bin size of 4096 points and averaged over 200 samples. Tests were also carried out using a sol-gel based binary pressure sensitive paint (PSP) in order to study the overall surface pressure field with and without VGs. Color schlieren was used to study the flowfield interaction using Palflash 501 with spark duration of 750ns and pulse energy of 6 Joules.

3 Results and Discussions

3.1 Flow Visualization

Figures 2 show the spark color schlieren images for the test cases without and with flow control. For the test case with trip and no VG (Fig. 2 (a)), flow-field upstream of the interaction is clean. A weak wave visible upstream of the interaction is due to the insert fabricated for the clean case with no VG and does not seem to introduce perturbation in the boundary-layer. The interaction region is characterized by a λ-shock pattern consisting of separation and reattachment shocks that merge to form the interaction point (marked with a dashed circle) above the ramp section. Introduction of VG devices are seen to generate flow perturbations - compression wave (inclined at 30° to the main flow and is the Mach angle for M=2 flow) and expansion wave - locally. Relative to the no VG case, with VG1, it is observed that the angle of the separation shock decreases

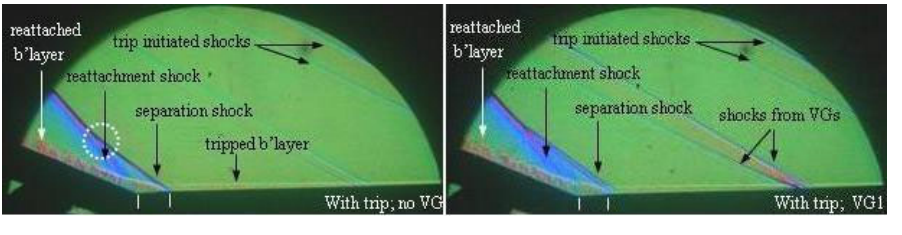

Fig. 2 Color schlieren images of the flow over a 24° compression ramp at M_∞ =2.0

(from 39° to 36°) along with a downstream shift in the interaction point (Fig. 2 (b)) while with VG2, the interaction point shifts upstream.

A comparison between the surface oil pictures of the interaction region indicates significant modifications in the surface flow separation pattern without and with control. A well-defined separation line seen for the case of no control (Fig.3 (a)) is replaced by a corrugated separation line (Fig. 3 (b))and is caused by the presence of streamwise counter-rotating vortex pairs (CVP) [14]. Upstream of the interaction, traces of CVPs are clearly indicated by streamwise accumulation of oil pigment, Fig. 3 (b). The corrugated separation line is formed as a result of the interaction between the streamwise CRVs and the reverse flow in the separated region (separation bubble), as shown in Fig. 3 (c). As a result in the region of the upwash (low shear), the reverse flow is able to penetrate into the main flow while in the region of the downwash (high shear), the main flow is able to penetrate into the region of reverse flow. A well-defined reattachment line for no control case is also completely replaced by a striation pattern (beginning from ramp corner itself) with each striation originating exactly in line with the location of each crest of the corrugated separation line. The origin of these striations is, therefore, different from those originating due to Goertler vortices in reattaching boundary-layers. The streamwise vortices generated by the VG devices, therefore, dramatically modify the overall flow structure development in the entire interaction region.

3.2 Streamwise Mean Pressure Distribution

Figure 4 shows the distribution of streamwise mean pressure and its corresponding *rms* value for the test cases without control and with VG devices. It is seen that in the region of separation, VG1 results in a higher wall pressure before the pressure plateau, Fig. 4 (a). When VG2 is used, the pressure plateau seems to get modified and shows wall pressures in this region much higher relative to other test cases. This behavior is advantageous as this means a reduction in strength of the reattachment

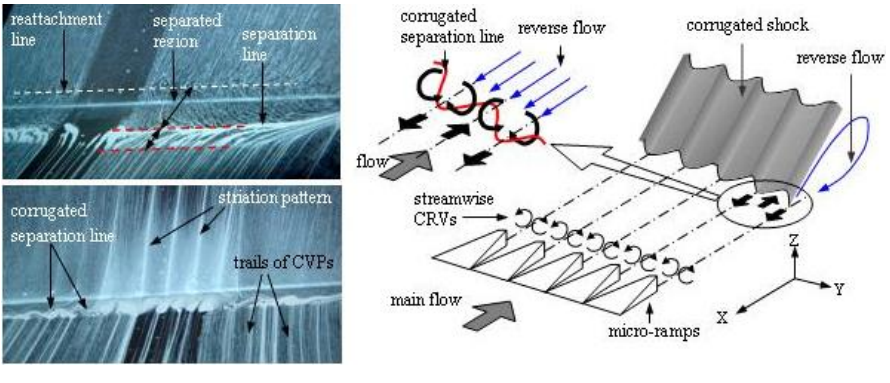

Fig. 3 Surface oil flow picture showing the flow pattern in the region of separation for (a) no VG and, (b) with VG2; 24deg, (c) schematic of the surface flow pattern development

shock and hence, pressure loads. The corresponding *rms* distributions show a significant reduction (50%) for VG1 in the region of separation, Fig. 4 (b). VG2, however, shows an increase in this value.

Figure 5 shows the comparison of spectra of wall pressure fluctuations in the region of separation for all test cases. Relative to the reference case, the amplitude of pressure fluctuations in the separation location (1), with VG2, is seen to increase in the entire range, Fig. 5 (a). With VG1, on the other hand, a considerable drop in energy levels in compliance with rms values is observed. These high-amplitude low-frequency fluctuations attribute to the back- and forth unsteady motion of the separation shock over this sensor location. Further downstream (2) and inside the separation bubble, the energy levels relative to the separation location drop considerably (which corresponds to the character of the flow structures inside the separation bubble), Fig. 5 (b). Relative to the reference case (with control), the spectra shows a considerable decrease in the amplitude of pressure fluctuations with VG2 showing the lowest amplitude followed by VG1.

3.3 Pressure Sensitive Paint (PSP) Measurements

The intensity based PSP measurements were conducted in the solid-wall test section of the tunnel with the optical access provided by the modified sidewall-mounted

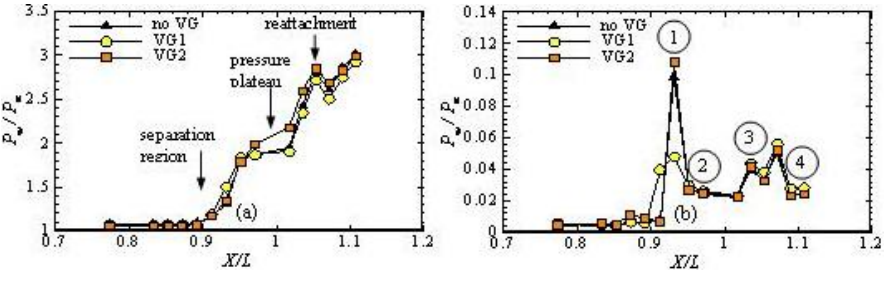

Fig. 4 Streamwise distribution of (a) mean wall pressure and, (b) the corresponding *rms* values for SWBLI at $\theta = 24^\circ$ and $M_\infty = 2.0$; h/$\delta = 0.65$

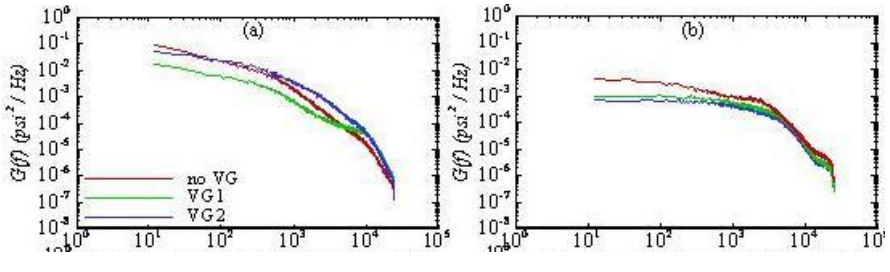

Fig. 5 Comparison of the real-time wall pressure signal spectra for the 24o compression corner, $M_\infty = 2.0$ at (a) separation location (b) inside the separation bubble

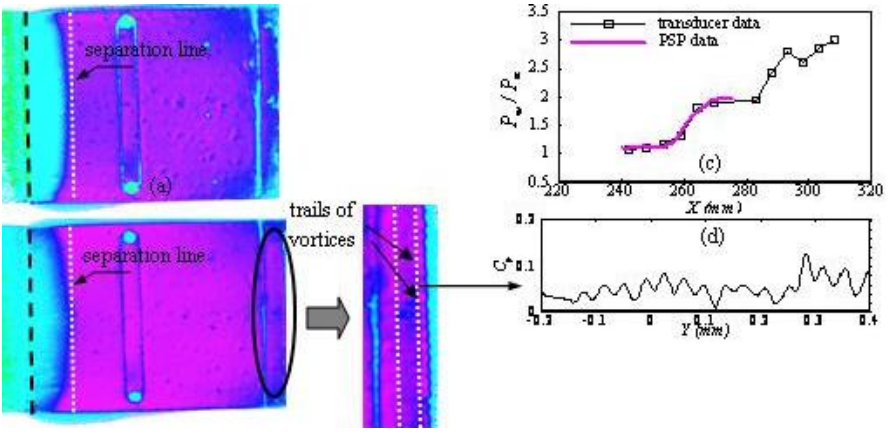

Fig. 6 Quantitative PSP pressure maps of surface pressure (C_p) for (a) no VG, (b) with VG2 for h/δ=0.65 and, (c) comparison of the streamwise mean pressure distribution for no VG case from PSP and transducer measurements and (d)-(e) spanwise sinusoidal pattern of C_p variation at two axial locations for VG2 showing trails of streamwise vortices.

Schlieren window (for details see ref. 15). The indigenous NAL-G8 pyrene based binary PSP is excited at 330 nm using a xenon flash lamp and the PSP emissions detected using two 12-bit CCD cameras. The intensity images are converted to pressure maps based on a-priori-calibration using OMS processing software. Figure 6 (a)-(b) shows the quantitative PSP pressure maps for no control and with VG2. These pressure maps are obtained using an appropriate spatial filter (10 pixelx10 pixel Gaussian filter) to smoothen the PSP data [15]. The comparison between the pressure port data and PSP for no VG case, Fig. 6 (c), is generally good and the agreement in P/P_∞ is within $\pm$0.03 to 0.05 for most data. The region of the separation on the base plate can be seen very clearly. Further for test case of VG2, trails of vortices immediately downstream of the VG insert are also seen, Fig. 6 (b), the C_p plot of which is shown in Fig. 6 (d). This sinusoidal pattern of wall pressure seen in the spanwise direction indicates that the VG configurations successfully generate streamwise vortices that help modify the separation characteristics in the intermittent region of separation, observed earlier. Further downstream, however, these vortex trails could not be captured.

4 Conclusions

An experimental study was conducted to control the amplitude of separation shock unsteadiness on a 24° compression ramp using mechanical vortex generators in a Mach 2.0 flow. Flow control devices in the form of a single-row delta ramps were placed far upstream (27.5δ) of the interaction region. Upstream of the interaction, traces of counter-rotating vortex pairs are clearly indicated by streamwise accumulation of oil pigment. These structures on interaction with the reverse flow in the

separation bubble, replace a well-defined separation line (with no control case) by a corrugated separation line. The reattachment line, however, shows no signs of corrugation. But downstream of flow reattachment on the ramp, a well-defined reattachment line is replaced by a striation pattern (with control) with each striation originating exactly in line with the location of each crest of the corrugated separation line. PSP measurements show a spanwise sinusoidal pattern of wall pressure variation indicating generation of streamwise vortices from these control devices. The mean pressure distribution in the interaction region also gets modified and the maximum rms value, in the intermittent region of separation, shows a significant reduction (50%) in its value for VG1. Further investigations will be carried out for VG location at 12.5δ with respect to the interaction location (i.e., $h/\delta = 0.26$).

References

1. Kistler, A.L.: Fluctuating Wall Pressure Under Separated Supersonic Flow. Journal of Acoustical Society of America 36, 543–550 (1964)
2. Dolling, D.S., Murphy, M.T.: Unsteadiness of the Separation Shock Wave Structure in a Supersonic Compression Ramp Flowfield. AIAA Journal 21(12), 1628–1634 (1983)
3. Muck, K.C., Andreopoulos, J., Dussuage, J.P.: Unsteady Nature of Shock-Wave/Boundary- Layer Interactions. AIAA Journal 26(2), 179–187 (1988)
4. Verma, S.B.: Experimental Study of Flow Unsteadiness in a Mach 9 Compression Ramp Interaction Using a Laser Schlieren System. Measurement Science and Technology Journal 14, 989–997 (2003)
5. Dolling, D.S., Bogdonoff, S.M.: An Experimental Investigation of the Unsteady Behavior of Blunt Fin-Induced Shock Wave Turbulent Boundary Layer Interaction, AIAA Paper 81-1287
6. Dolling, D.S., Brusniak, L.: Separation Shock Motion in Fin, Cylinder, and Compression Ramp-Induced Turbulent Interactions. AIAA Journal 27(6), 734–742 (1989)
7. Maull, D.J.: Hypersonic Flow over Axially Symmetric Spiked Bodies. Journal of Fluid Mechanics 4, 584–592 (1960)
8. Charwat, A.F., Dewey, C.F., Roos, J.N., Hitz, J.A.: Investigation of Separated Flows, Part II; Flow in Cavity and Heat Transfer. Journal of Aeronautical Sciences 28(7), 513–527 (1961)
9. Dolling, D.S.: Fifty Years of Shock-Wave/Boundary-Layer Interaction Research: What Next? AIAA Journal 39(8), 1517–1531
10. McCormick, StateD.C.: Shock-Boundary layer interaction control with low-profile vortex generators (SBVGs) and passive cavity. AIAA Paper 92-0064
11. Babinsky, H.: Makinson, and Morgan: Micro-vortex Generator Flow Control for Supersonic Engine Inlets. AIAA Paper 2007-0521, 0521 (2007)
12. Szwabe, R.: Shock Wave Induced Separation Control by Streamwise Vortices. Journal of Thermal Sciences 14(3), 249–253 (2005)
13. Blinde, P.L., Humble, R.A., Oudheusden, B.W., Scarano, F.: Effects of Micro-Ramps on a Shock Wave/Turbulent Boundary Layer Interactio. Shock Waves 19, 507–520 (2009)
14. Bur, R., Coponet, D., Carpels, Y.: Separation Control by Vortex Generators Devices in a Transonic Channel Flow. Shock Waves (2009)
15. Raju, C., Vishwanath, P.R.: Pressure-Sensitive Paint Measurements in a Blowdown Wind Tunnel. Journal of Aircraft 42(4) (July-August 2005)

PIV Investigation of the 3D Instantaneous Flow Organization behind a Micro-ramp in a Supersonic Boundary Layer

Z. Sun, F.F.J. Schrijer, F. Scarano, and B.W. van Oudheusden

1 Introduction

Shock wave boundary layer interaction (SWBLI) is a flow phenomenon that is critical for many high speed applications, such as supersonic inlets and propulsion-wing or -fuselage interactions. Much effort has been devoted to investigate the mechanism of SWBLI, its turbulent nature and the role of large-scale fluctuations[1]. Different types of flow control techniques have been proposed to alleviate the adverse effects introduced by SWBLI, such as flow separation and fluctuating pressure loads. Micro-ramp vortex generators are considered to be a preferred type of passive boundary layer control technique, due to a limited increase in drag compared to conventional larger vortex generators that emerge outside the boundary layer, while still being effective in reducing flow separation.

Using the geometry that follows the optimization study performed by Anderson et al[2], the working principle of a micro-ramp has been investigated through both experimental and numerical approaches. A mean flow description by Babinsky et al[3] depicts the streamwise counter rotating vortex pair and other secondary vortices in streamwise direction. Using these observations a general working mechanism of the micro-ramp was deduced: the boundary layer is energized by the high momentum fluid in the free stream entrained by the downwash caused by the streamwise primary vortex pair. This results in a fuller boundary layer profile, which is more capable of enduring the adverse pressure gradient induced by incident shock waves or compression ramps. However, due to the strong three-dimensionality of the flow past the micro-ramp, the instantaneous flow structure is rather different from the one obtained in the mean sense. Blinde et al[4] identified several vortex pairs developing downstream of a micro-ramp array through stereo-PIV in two planes parallel to the surface at different heights. These vortex pairs were suggested to be cross sections of legs of hairpin vortices similar to those that naturally occur

Z. Sun · F.F.J. Schrijer · F. Scarano · B.W. van Oudheusden
Faculty of Aerospace Engineering, Delft University of Technology
Kluyverweg 1, 2629 HS, Delft (The Netherlands)

in a turbulent boundary layer. Based on their observations Blinde et al formulated a conceptual model of a train of hairpin vortices developing downstream of each micro-ramp. An LES simulation of the flow past a single micro-ramp performed by Li et al[5] visualized a series of vortex elements behind the trailing edge. The structure of these vortices only partly confirms the model obtained from Blind et al's experiment. In fact the legs of the vortices in the computations of Li et al do not appear to align with the wall like hairpins proposed by Blinde. Instead, they rather appear to have a ring shape belonging to a plane slightly inclined to the wall normal direction. In their paper, Li et al concluded that the vortices are connected also on the bottom side therefore featuring full rings. The structure of the upper part of the wake has also been confirmed by a recent experimental research performed by Lu et al[6] using laser sheet visualization. The visualizations revealed a pronounced Kelvin-Helmholtz instability developing downstream of micro-ramps. According to the explanation by Lu et al, the KH instability structures develop as a secondary instability of the streamwise vortex pair, which is more stable in the region near the micro-ramp and breaks down downstream. This latter description is in contrast with the previous two where no mention is made of the interaction between the streamwise vortices and the hairpin- or ring-shaped rollers formed at the wake interface.

Since the results from experimental and numerical approaches partially agree on the appearance of the intermittent vortices and their relation with the streamwise vortices, the present experimental research aims at visualizing the controversial vortices and identifying their origin. Tomographic-PIV (Elsinga et al[7]) is chosen for the reason that it offers the capability of detecting instantaneous patterns in a complex three-dimensional flow.

2 Experimental Arrangement

Experiments were carried out in the blow-down supersonic wind tunnel ST15 of Delft University of Technology. The wind tunnel was operated at Mach 2.0 (free stream velocity U_{ref}=532 m/s), with a stagnation pressure of P_0=3.2 bar. The boundary layer developing along the tunnel bottom wall was selected for the micro-ramp investigation. After developing for approximately 1.0 m past the throat section of the nozzle, the boundary layer reaches a thickness of 4.8 mm.

The investigated micro-ramp height is 4 mm, the geometry follows that proposed in the study of Anderson et al[2] resulting in a chord length of 27.4 mm and a spanwise width of 24.4 mm. Tomo-PIV measurements were carried out within two volumes starting 35 mm downstream of the micro-ramp of $25\times15\times6$ mm^3 size. The layout of the two measurement volumes is schematically depicted in figure 1.

The flow was seeded by DEHS droplets with a diameter of approximately 1 μm. The tracers were injected into the flow through a seeding device placed upstream of the settling chamber. According to the study of Ragni et al[8] the DEHS particle tracers have a relaxation time of approximately 2 μs, which enable accurate tracking of flow structures down to 1 mm. The seeded flow was illuminated by a Spectra-Physics Quanta Ray PIV-400 double pulse Nd:Yag laser at a wavelength of 532 nm.

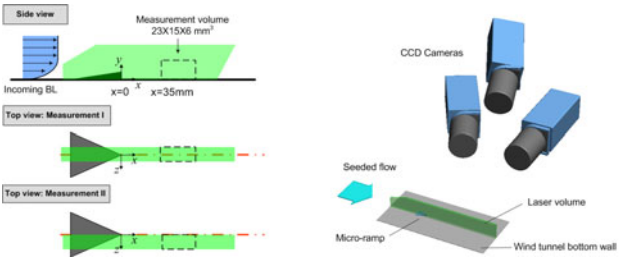

Fig. 1 left: arrangements of the two measurement volumes; right: camera positions with respect to laser volume and micro-ramp.

Each pulse has energy of 400 mJ and duration of 6 ns. A laser probe was inserted from the side wall downstream of the test section, through which the laser beam was shaped into a volume of 6 mm thickness.

Three PCO Sensicam QE CCD cameras with a sensor of 1376×1040 pixels were equipped with Nikon 105 mm objectives (see figure 1) set at numerical aperture of $f_{\#}$=11, 11 and 9 respectively and the Scheimpflug principle was applied. Two cameras were viewing from upstream to take the benefit of the forward light scattering of the particles. The laser pulse separation time was selected at 0.6 μs and image pairs were recorded at a rate of 5 Hz. A digital image resolution of 43.7 pixel/mm was achieved with a particle displacement of 14 pixels in the free stream. 400 images were recorded for each volume to achieve data convergence.

3 Results and Anlysis

3.1 Mean Flow Characteristics

Previous studies on micro-ramp flow reveal that a streamwise counter rotating vortex pair symmetric to the center plane (z=0) dominates the mean flow field. Contour plots of u-component shown in figure 2 are extracted to represent the mean flow structure. One of the pairing vortices can be observed through the vectors overlaid

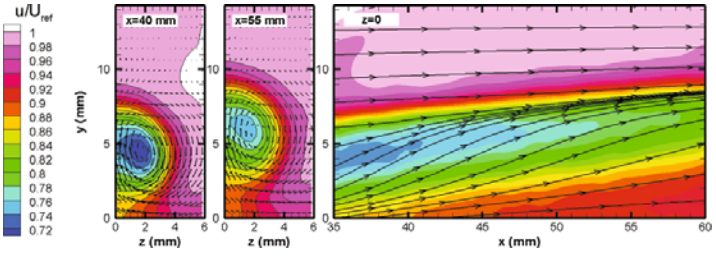

Fig. 2 Selected contour plots of the mean flow field from Measurement II.

on the $y-z$ plane contours. An additional proof of the vortices is provided by the streamline pattern in the center plane, which is the footprint of the central upwash induced by the vortices.

Another significant phenomenon revealed through figure 2 is the wake region of low streamwise momentum that encompasses the streamwise vortices. Assuming the flow axisymmetric, the wake is expected to obtain a smooth circular shape. Along its streamwise movement, the wake is lifted and also expands. A shear layer following the wake configuration is located at the edge, where the streamwise velocity is reduced from U_{ref} to approximately $0.8U_{ref}$ near the core region at this distance behind the micro-ramp element.

3.2 Turbulent Characteristics

The distributions of the two fluctuation components, $\langle u' \rangle$ and $\langle v' \rangle$, in the center plane ($z = 0$) shown in the left part of figure 3 reveal a similar shear layer structure with higher fluctuations at the center and lower fluctuations at both edges.

Profiles of the turbulent components and averaged streamwise velocity at $x = 40$ mm are shown in the right part of figure 3. From the streamwise velocity profile, the wake is composed of the upper and lower shear layers, within which $\langle u' \rangle$ and $\langle v' \rangle$ exhibit considerable increase and the maxima are reached in the upper shear layer. The positions of turbulent maxima do not exactly coincide for the two components. Also, $\langle v' \rangle$ is larger than $\langle u' \rangle$ in the center region of the wake, which suggests anisotropy of the turbulent fluctuations.

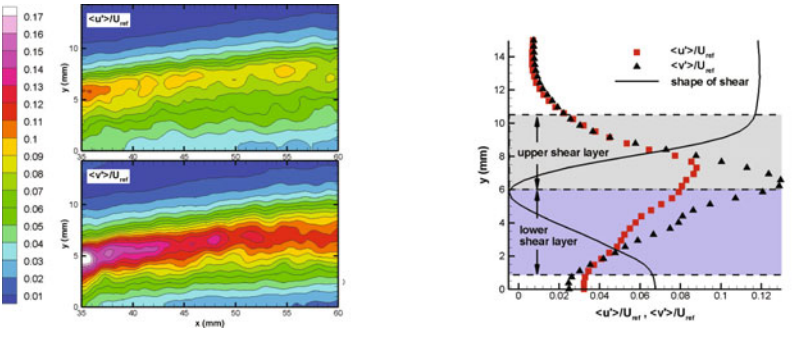

Fig. 3 Fluctuation velocity distributions, left: contour plots of $\langle u' \rangle$ (up) and $\langle v' \rangle$ (down) at center plane; right: fluctuation and averaged streamwise velocity profiles at $x = 40$ mm of the center plane.

3.3 Cross-Sectional Representations

To assist the interpretation of the instantaneous flow structure, figure 4 shows three cross-sectional contours of u-component, two in $y-z$ plane at $x = 42$ mm and

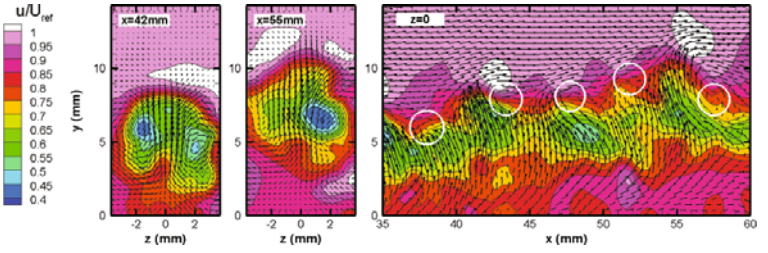

Fig. 4 Selected contour plots of the instantaneous flow field from Measurement I.

55mm and the third in $x-y$ plane at $z=0$, extracted from an instantaneous three-dimensional flow field from Measurement I.

The dominating streamwise vortex pair is revealed in the $y-z$ planes. Its appearance is not as symmetric to the center plane as observed from the mean flow field, suggesting an instantaneous meandering behavior. Also, the wake exhibits a modulated edge, whereas it is a smooth and axisymmetric in the mean flow.

The wavy velocity interface of the wake edge visualized in the $x-y$ plane can be understood as the imprint of a Kelvin-Helmholtz instability of the shear layer. After subtracting a constant value from the vector field, the KH vortices are visualized, which are indicated by the white circles in the contour plot. Due to their clockwise rotational direction these vortices induce local regions of increased and decreased velocity on the upper and lower sides of the vortices, respectively. It may be noted that the areas with high streamwise velocity on top of the wake in the $y-z$ contours are intersections of such high speed regions.

3.4 Volumetric Representations

The instantaneous three-dimensional structure, as obtained from the Tomo-PIV measurements, is characterized by means of velocity and vorticity iso-surfaces, as shown in figure 5. These volumetric renderings relate to the same flow realization as the cross-sectional flow fields in figure 4. Two values of the u-component are displayed: high speed in pink ($1.02U_{ref}$) and low speed in green ($0.8U_{ref}$), which correspond to high and low speed regions induced by the KH vortices. Both regions are separate in space and exhibit a typical intermittency similar to the one observed in KH instability.

The vorticity representations reveal both the primary streamwise vortex pair and the KH vortices simultaneously. The streamwise vortices are visualized through ω_x in different colors, because of their opposite rotational directions. The intermittent KH vortices are presented though ω_z, which explains why only the top part of the KH vortices is visualized, while an arc shape can be expected for the KH vortices which follow the shape of the instantaneous shear layer in $y-z$ cross section.

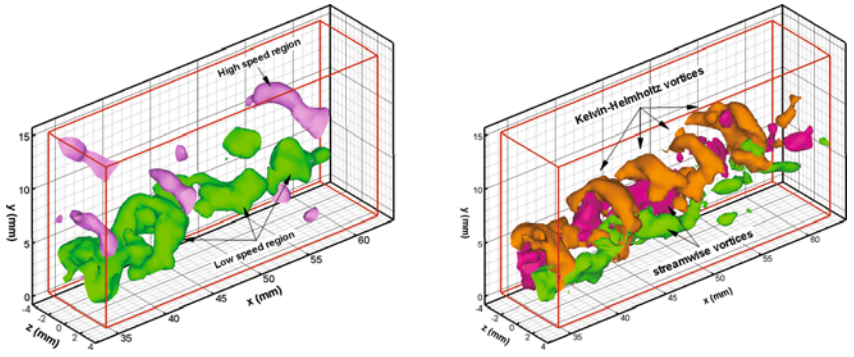

Fig. 5 Volumetric representation, left: iso-surfaces of u-component; right: iso-surfaces of vorticity.

4 Conclusions and a Conceptual Model

An experimental study has been carried out to investigate the instantaneous organization of the three-dimensional micro-ramp flow using Tomo-PIV. As a result, a few conclusions can be drawn.

The streamwsie vortex pair and the arc-shaped Kelvin-Helmholtz vortices exist simultaneously in the wake of the micro-ramp, thus a two-type vortex flow model (illustrated in figure 6) can be summarized. These two categories of vortices are generated out of different mechanisms, the streamwise vortex pair is produced by the chamfered side edges of micro-ramp, while the arc-shaped vortices are caused by the KH instability at the interfacial shear layer between the wake and free stream. The streamwise vortex pair makes the major contribution to the control effectiveness, however, the impact of the KH vortices towards SWBLI requires further investigation.

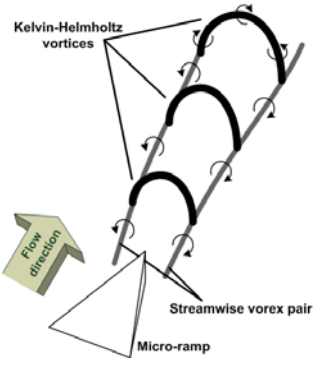

Fig. 6 A conceptual model of the instantaneous vorticity structure.

References

1. Dolling, D.S.: Fifty years of shock-wave/boundary-layer interaction research: What next? AIAA J. 39(3), 1517–1531 (2001)
2. Anderson, B.H., Tinapple, J., Surber, L.: Optimal control of shock wave turbulent boundary layer interactions using micro-array actuation. AIAA Paper 2006–3197 (2006)
3. Babinsky, H., Li, Y., Pitt Ford, C.W.: Microramp control of supersonic oblique shock-wave/boundary-layer interactions. AIAA J. 47(3), 668–675 (2009)
4. Blinde, P.L., Humble, R.A., van Oudheusden, B.W., Scarano, F.: Effects of micro-ramps on a shock wave/turbulent boundary layer interaction. Shock Waves J. 19(1), 507–520 (2009)
5. Li, Q., Liu, C.: LES for supersonic ramp control flow using MVG at $M = 2.5$ and $Re_\theta = 1440$. AIAA Paper 2010–592 (2010)
6. Lu, F.K., Pierce, A.J., Shih, Y.: Experimental study of near wake of micro vortex generators in supersonic flow. AIAA Paper 2010–4623 (2010)
7. Elsinga, G.E., Scarano, F., Wieneke, B., van Oudheusden, B.W.: Tomographic particle image velocimetry. Exps. Fluid 41(6), 933–947 (2006)
8. Ragni, D., Schrijer, F., van Oudheusden, B.W., Scarano, F.: Particle tracer response across shocks measured by PIV. Exps. Fluid 50(1), 53–64 (2011)

Flow Topology of Symmetric Crossing Shock Wave Boundary Layer Interactions

A. Salin, Y.F. Yao, S.H. Lo, and A.A. Zheltovodov

1 Introduction

Three-dimensional crossing-shock-wave and turbulent boundary-layer interactions can generate intense wall heat flux rates, high pressure levels, and large-scale flow separations on high-speed vehicle surfaces. To reproduce such complex flow physics, simple configurations, such as single-sharp fin and double-sharp fin mounted on a flat plate, were adopted in previous investigations. Review papers by Knight *et al.* [1] and Zheltovodov [2] provided summary of current state-of-the-art of research advancements in this field. Recently, Yao *et al.* [3] carried out numerical simulation of symmetric double fin configurations of $7^o \times 7^o$, $11^o \times 11^o$, and $15^o \times 15^o$ wedge angles. Results of surface static pressure distributions were found in good agreement with wind tunnel experiments [4] and other numerical simulations [5] but heat flux coefficient distribution differed from experimental data at the $15^o \times 15^o$ case. In this work, an additional configuration of $19^o \times 19^o$ case is introduced to investigate flow topology due to increased shock-viscous interaction strength. The predicted flow field will be compared qualitatively with available experiments [6, 7] and other relevant numerical studies [7, 8].

2 Flow Problem and Numerical Methods

Figure 1 depicts top-view of two symmetrical chamfered sharp double fins (DF) of $15^o \times 15^o$ and $19^o \times 19^o$ wedge angles with 192 mm in length, and 100 mm in height. The throat distance (B) is 32 mm for both cases, whereas the inlet widths

A. Salin · Y.F. Yao · S.H. Lo
School of Aerospace and Aircraft Engineering, Kingston University London, Roehampton Vale, Friars Avenue, London SW15 3DW (UK)

A.A. Zheltovodov
Khristianovich Institute of Theoretical and Applied Mechanics, SB RAS, Novosibirsk 630090 (Russia)

(A) are 79.2 mm for $15^o \times 15^o$ case and 83.2 mm for $19^o \times 19^o$ case, respectively. Same as Thivet *et al.* [5], a computational domain height of 80 mm (not shown) is used, based on the fact that no significant vertical gradients were observed between y = 70-90 mm. For each configuration, four cross sections are chosen accordingly to shock flow structures depicted by the pressure gradient magnitude (Fig. 1), such that results of both cases can be compared consistently.

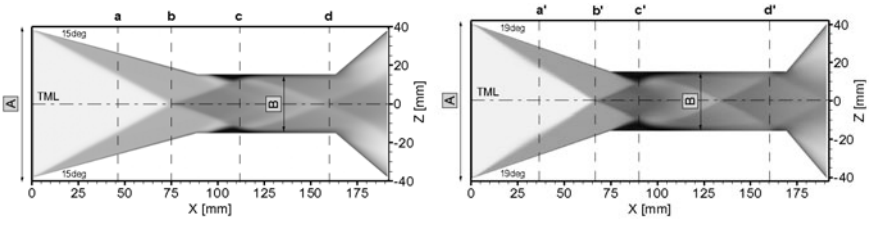

Fig. 1 Contours of pressure gradient magnitude for double-fin configuration, Left: $15^o \times 15^o$ case, Right: $19^o \times 19^o$ case.

The computation applies an unstructured 3-D compressible Reynolds-averaged Navier-Stokes (RANS) solver using second-order finite-volume method. An upwind scheme with the min-mod limiter is used for shock-capturing and the viscous terms are evaluated by central scheme. Grid refinement and turbulence model influence were carefully studied in a previous research [3] and results presented hereby are those from the shear stress transport (SST) k-ω model due to its enhanced capabilities in capturing flow separations. Due to the inherent symmetry of the crossing shock wave interaction presented, only half of a model has been used for computation. Further details can be seen in a reference paper [3].

3 Results and Discussions

For clarity, the following nomenclature is adopted; i.e. 'S' and 'R' stand for separation (convergence) and reattachment (divergence) lines, whereas singular points are identified with 'C' (saddle), 'N' (node), and 'F' (focus), respectively. Symmetric counterparts' features have the superscript ^{1} and arrows give local flow directions. Figure 2 shows the flow topology on the bottom wall for both $15^o \times 15^o$ and $19^o \times 19^o$ DF configurations. At the channel entrance, the flow is determined by the interaction of swept shock waves that are generated by the sharp fins with a developing supersonic turbulent boundary layer on the flat plate. Due to the strong primary inviscid shocks, the boundary layer separates along the lines S_1 and S_1^1, and reattaches to the lines R_1 and R_1^1, forming a pair of counter-rotating vortices. The incoming bifurcated shock structures merge in a large vortical region on the centreline, becoming distorted slightly but broadly maintaining the typical λ-shaped shock structure. It was found that the primary separation lines S_1 and S_1^1 intersect

the centreline at the node point N_0 in a vicinity of observed fluidic throat in experiment between these lines located downstream the central saddle C_0 (see, e.g. [4, 5]). Additional flow features, not observed in the experiment in this case, are two saddle points C_1 and C_1^1 located symmetrically near the throat mean line. The resulting diamond-shaped flow pattern qualitatively agrees with those reported by previous investigations [5, 9]. A large-scale flow separation region bounded by two side separation lines S_3 and S_3^1 is also observed just behind N_1, which is found to be compressed slightly (in width) compared to that observed in the experiments. So far no RANS-based investigation is able to accurately predict the unsteady intermitted behaviors of the flow observed in the experiments and this causes the noted differences in the topology of surface flow pattern. Also, using half a domain in the study will prevent any possible shock movements that may occur for strong crossing shock interactions, and this might be detrimental to capture the inherent flow physics correctly. For a strong interaction case with the fin angles of $19^o \times 19^o$, flow topology shows some interesting features in the vicinity of the interaction region, similar to those previously observed at Mach 5 test case with $23^o \times 23^o$ wedge angle [6, 7, 8, 10]. The reversed flow penetrates from the node N_1 up to the central saddle point C_0 located in the middle of the cross separation line S_0 which is limited by two symmetric nodes N_0 and N_0^1 at its ends (Fig. 2 (right)). Interaction of the secondary flows directed to the central separated zone ceases, forming two additional symmetric saddle points C_1 and C_1^1. Interestingly, an additional C_2-N_2 combination is also observed downstream at x = 74-80 mm approximately. The focus F_1 together with its counterpart F_1^1, captured on each side of the fin shoulder, blocks almost half a channel passage suggesting that, for stronger interactions, the channel width should increase to avoid any flow blockage phenomenon. The interaction of the reflected shock waves and the expansion waves originating from the fin shoulder, compresses the secondary separation lines S_3 and S_3^1 towards the centreline until they penetrate downstream close to R_3 and R_4. Note that the well-known topological rule of thumb

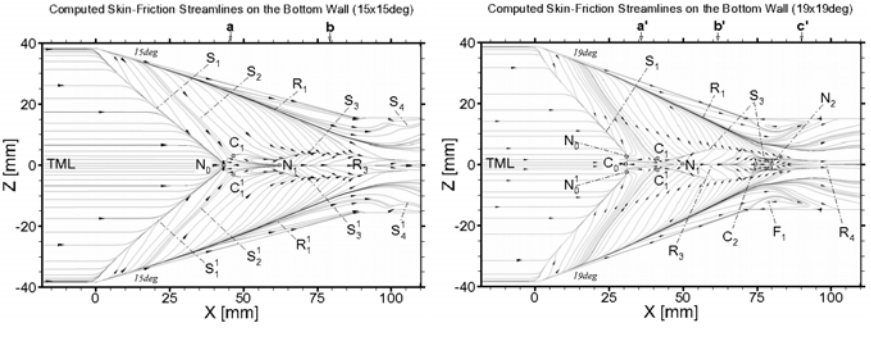

Fig. 2 Flow topology at the bottom wall with interaction region details of $15^o \times 15^o$ case (left) and $19^o \times 19^o$ case (right).

requiring equality of node and saddle points is satisfied for both configurations. It is worth to point out that, despite the Mach 5 $23^o \times 23^o$ interaction examined in reference papers [6, 7, 8, 10] is stronger than the present Mach 3.92 $19^o \times 19^o$ case, the dominant surface oil-film flow features are generally similar, except for a lack of the distinct secondary separation and reattachment lines arising in the first case close with the lines R_1 and R_1^1 in the secondary flows directed to the symmetry plane. As was demonstrated by Zheltovodov for the interaction generated by a single fin [2], the secondary separation disappears at the Mach 3.92 for the wedge angles approximately $19^o - 25^o$ and reappears again in the conically-supersonic turbulent cross flow at the angles higher than 25^o.

Figure 3 depicts streamlines on the symmetry plane normal to the bottom wall. In the following flow topology interpretation, lowercase letters are used to identify critical points and only the $19^o \times 19^o$ DF case is analyzed. The streamlines exhibits the presence of two half-saddle points c_0 and c_1 and an unstable focus/node n_1. According to Schmisseur and Gaitonde [8] this feature is similar to the owl-face type flow pattern described by Perry and Chong [11]. An additional stable focus point f_2 observed downstream suggests a U-shaped like separated flow pattern [11]. As displayed by the 3-D streamline B in Fig. 3, the fluid particle moves away from the symmetry plane as it flows around the body, as observed by Visbal [12] on the structure of laminar juncture flows. Due to the strong adverse pressure gradient encountered immediately downstream the crossed shock-wave location, the flow lifts up without reattaching throughout the domain, as indicated by the boundary layer vortex interaction (BLVI) shear layer observed by Gaitonde and Shang [9]. The superimposed static temperature contours on the symmetry plane, suggest that higher temperature values are confined within the separation region, nearby two node/focus points. Figure 3 also suggests that surface heat migrates from two focus points until the BLVI shear layer is reached. Details of this heat migration mechanism will be investigated later. Within the separation region and at one layer above the BLVI, the flow has been expanded twice ($n_1 < X < f_2$ and $X > f_2$). Two high energy jets are observed and they are formed locally within the BLVI, constituting part of the entertainment flow which energizes the flow downstream, while a previous study by Gaitonde and Shang [9] only captured one high energy jet flow.

In order to understand the 3-D kinematic flow structure of the double fin configuration, limiting streamlines are shown on the fin side walls (Fig. 4). Note that only half a height is presented, beyond that flow features are observed to change insignificantly. It shows that the agreement between experimental and numerical oil-flow visualizations on the fin side walls is fairly good. A large separation region is detected between the separation line S_5 and the reattachment line R_5, caused by the interaction of the reflected shock wave impinging onto the fin surface, and the expansion fan resulting from the fin shoulder. Limiting streamlines prove the existence of the node N_5 and saddle point C_3 observed in the experiments [4] and previous calculations [13]. However, an extra node N_4 above the saddle point C_3 is captured for the $15^o \times 15^o$ DF case. This discrepancy with the experiments might be due to the definition of the top boundary as a free-slip wall condition, which tends to obstruct streamlines to be lifted up, as observed in the experiment surface oil flow

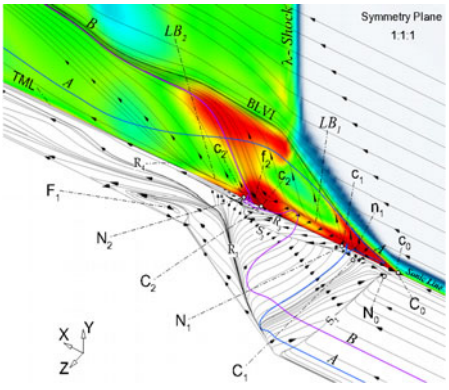

Fig. 3 Isometric view of surface streamlines near the interaction region of the bottom and the symmetry planes of $19^o \times 19^o$ case. 3-D streamlines - A (blue line), B (violet line).

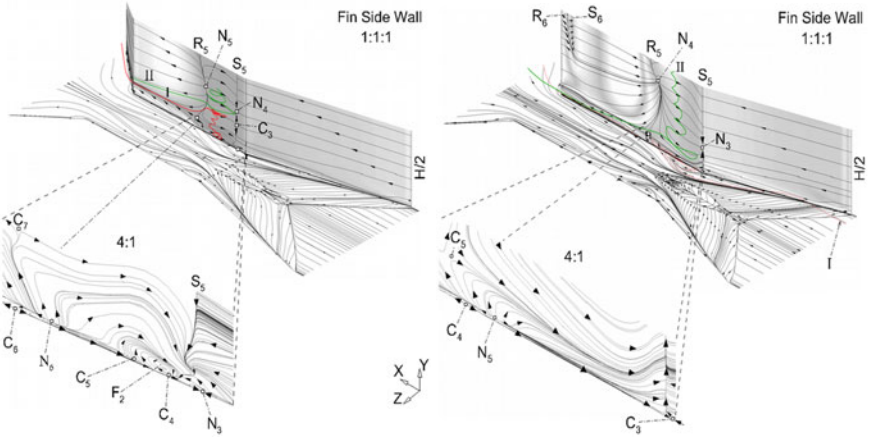

Fig. 4 Details of flow topology in the interaction region on the fin side walls downstream of the fin shoulders: the $15^o \times 15^o$ case (left) and the $19^o \times 19^o$ case (right).

patterns [4, 13]. Figure 4 also shows an enlarged view of the fin side walls, where computations reveal the existence of six additional singular points near the bottom wall; i.e. three saddle points C_4, C_5 and C_6, two nodes N_3 and N_6, and one focus F_2. Such flow features are not yet observed in the experiment, and this might be due to either numerical modeling, or possibly poor local measurement quality. On the other hand, the saddle point C_7 and focus F_2 are well captured in accordance with the experiments. Two selected 3-D streamlines suggest that the flow tends to be lifted up from the foci (I, red line) and meet the 'descending' vortex (II, green line) at about four boundary layer heights. After this point both streamlines continue downstream as part of the side entrainment flow.

As the interaction strength increases, the stable focus is observed to vanish upstream towards the bottom wall. The streamline I (red line) is now 'enclosed' primarily on the bottom wall, where the focus F_1 exists (Fig. 1). In the meantime, as indicated by the streamline II (green line), a side wall vortex firstly descends until almost one boundary layer height and then lifts up again due to the upward flow along the separation line S_5. Note that two further separating and reattaching streamlines S_6 and R_6 appear downstream. The location and the shape of these lines are consistent with the reflected shock wave patterns within the channel, further confirmed by the superimposed density gradient vectors.

4 Conclusion

Flow topology of two symmetric crossing shock waves interacting with a turbulent boundary layer at Mach 3.92 has been numerically examined using RANS approach with the SST k-ω turbulence model. For $15^o \times 15^o$ double-fin case, computed flow topology is in good agreement with the experimental visualization, with new kinematic flow structures observed on the fin side walls. For $19^o \times 19^o$ double-fin case, computation exhibits additional features, including stable U-shaped like flow structure downstream the interaction. As the interaction strength increases, the foci on the fin side wall tends to move upstream towards the bottom wall, then vanishes eventually. Higher surface temperature has been concentrated around two foci structures in symmetry plane. Further in-depth investigation is desirable to explore the method to reduce surface heating.

References

1. Knight, D., Yan, H., Panaras, A.G., Zheltovodov, A.A.: Advances in CFD prediction of shock wave turbulent boundary layer interactions. Progress in Aerospace Sciences 39(2-3), 121–184 (2003)
2. Zheltovodov, A.A.: Some advances in research of shock wave turbulent boundary layer interactions, AIAA-2006-0496 (2006)
3. Yao, Y.F., Salin, A., Lo, S.H.: Numerical analysis of wall properties in cross shock wave and boundary layer interactions, AIAA-2011-0860 (2011)
4. Zheltovodov, A.A., Maksimov, A.I., Shevchenko, A.M.: Topology of three-dimensional separation under the conditions of symmetric interaction of crossing shocks and expansion waves with turbulent boundary layer. Thermophysics and Aeromechanics 5(3), 293–312 (1998)
5. Thivet, F., Knight, D.D., Zheltovodov, A.A.: Analysis of observed and computed crossing-shock-wave/turbulent-boundary-layer interactions. Aerospace Science and Technology 6(1), 3–17 (2002)
6. Schülein, E., Zheltovodov, A.A.: Development of experimental methods for the hypersonic flows studies in Ludwieg tube. In: Proc. International Conference on the Methods of Aerophysical Research, Novosibirsk, Russia, pt. 1, pp. 191–199 (1998)

7. Zheltovodov, A.A., Maksimov, A.I., Schülein, E., Gaitonde, D.V., Schmisseur, J.D.: Verification of crossing-shock-wave/boundary layer interaction computations with the k-ε turbulence model. In: Proc. International Conference on the Methods of Aerophysical Research, Novosibirsk, Russia, pt. 1, pp. 231–241 (2000)
8. Schmisseur, J.D., Gaitonde, D.V.: Numerical investigation of new topologies in strong crossing shock-wave/turbulent boundary-layer interactions. AIAA J. 39(19), 1742–1749 (2001)
9. Gaitonde, D., Shang, J.S.: Structure of a turbulent double-fin interaction at Mach 4. AIAA Journal 33(12), 2250–2258 (1995)
10. Panaras, A.G.: Calculations of flows characterized by extensive crossflow separation. AIAA Journal 42(12), 2474–2481 (2004)
11. Perry, A.E., Chong, M.S.: A description of Eddying Motions and Flow Patterns using Critical-Point Concept. Annual Review of Fluid Mechanics 19, 129–155 (1987)
12. Visbal, M.R.: Structure of Laminar Juncture Flows. AIAA 29(8), 1273–1282 (1991)
13. Zheltovodov, A.A., Maksimov, A.I., Gaitonde, D., Visbal, M.R., Shang, J.S.: Experimental and numerical study of symmetric interaction of and asymmetric crossing-shocks and expansion-waves with a turbulent boundary layer. Thermophysics and Aeromechanics 7(2), 155–171 (2000)

Numerical Simulation of Conical and Spherical Shock Interaction: Hysteresis Investigations

J.D. Parisse, J. Giordano, and D.E. Zeitoun

1 Introduction

In the literature, we can find lot of analytical or numerical studies about shock wave interaction. However, in the major part of this work, the two dimensional assumption is used [1]-[4]. Although we know that in real flight conditions the interaction is at least axisymmetrical or three dimensional, we have also chosen to deal with axisymmetrical interaction. Indeed, the comprehension of the axisymmetrical phenomena is needed before taken into account a more realistic three dimensional case. Thus, in the present paper, we have numerically studied the interaction between a shock generated by a conical ring and a shock generated by a sphere (respectively called the conical and spherical shock). A schematic description of the study case is given by the figure 1. The inlet conditions are: $M = 4.96$, $T = 77\ K$ and $P = 1700\ Pa$. The preliminary results on this topic have been presented in [5] and [6].

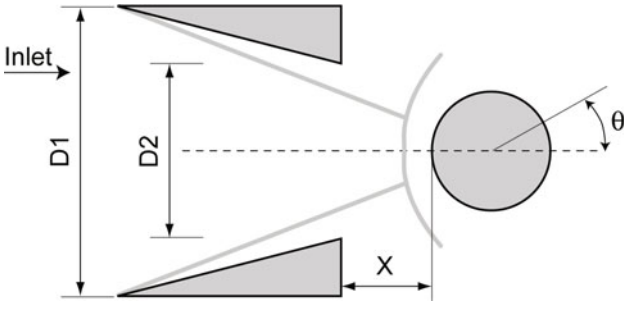

Fig. 1 Schematic description

In a first section of this paper, the numerical code used for the simulations will be presented. Then, several geometry cases will be studied and for the most interesting

J.D. Parisse · J. Giordano · D.E. Zeitoun
Aix Marseille Université, IUSTI/UMR CNRS 6595, Technopôle de Château Gombert, 5 rue Enrico Fermi, 13013 Marseille, France.

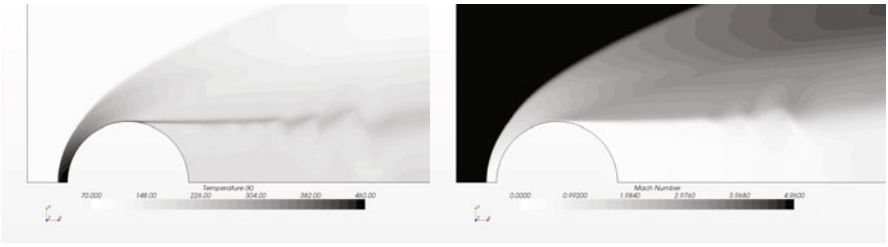

Fig. 2 Preliminary results for a sphere alone

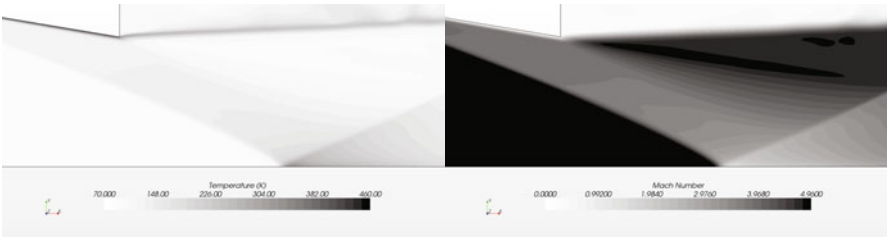

Fig. 3 Preliminary results for a the conical ring alone alone

one hysteresis phenomena will be investigated. Eventually, we will conclude and give some perspectives of this work.

2 Numerical Method

To solve the laminar Navier-Stokes equations in the axisymetric case, the commercial code STARCCM+, from CD-ADAPCO is used. STARCCM+ has ben chosen for his versatility, his accuracy and to be used in 3D in a future work. These capabilities are demonstrated in Figures 2 and 3 which show that the code is able to capture strong discontinuity as sock waves. Moreover, this code is able to describe fine structures like boundary layers, slipping lines and after body wake.Besides, this code is efficient to deal with moving mesh and, as consequence here, allows us to characterize hysteresis phenomena.

For the calculations the mesh used is a seven block one of 100×100 of Q_4 cells, the minimum cell size is 10^{-5} m. As a first step, we have chosen to used the the steady solver with AUFS Riemann solver, the CFL coefficient use for the implicit solver is equal to 3.0. All the solid part of the calculation domain are supposed to be adiabatic wall.

3 Results

Taking into account our previous work [5] and [6] the sphere diameter has been set to 15 mm and the X distance range from 12.5 mm to 17.5 mm. To investigate hysteresis

phenomena calculation have been for X varying from 12.5 *mm* to 17.5 *mm* and back to 12.5 *mm*.

Figure 4 and 5 respectively show the Mach number and Temperature iso-values at different positions for the forward and backward motion. As it has already been demonstrated, [5] and [6], this two figures show that the shock wave

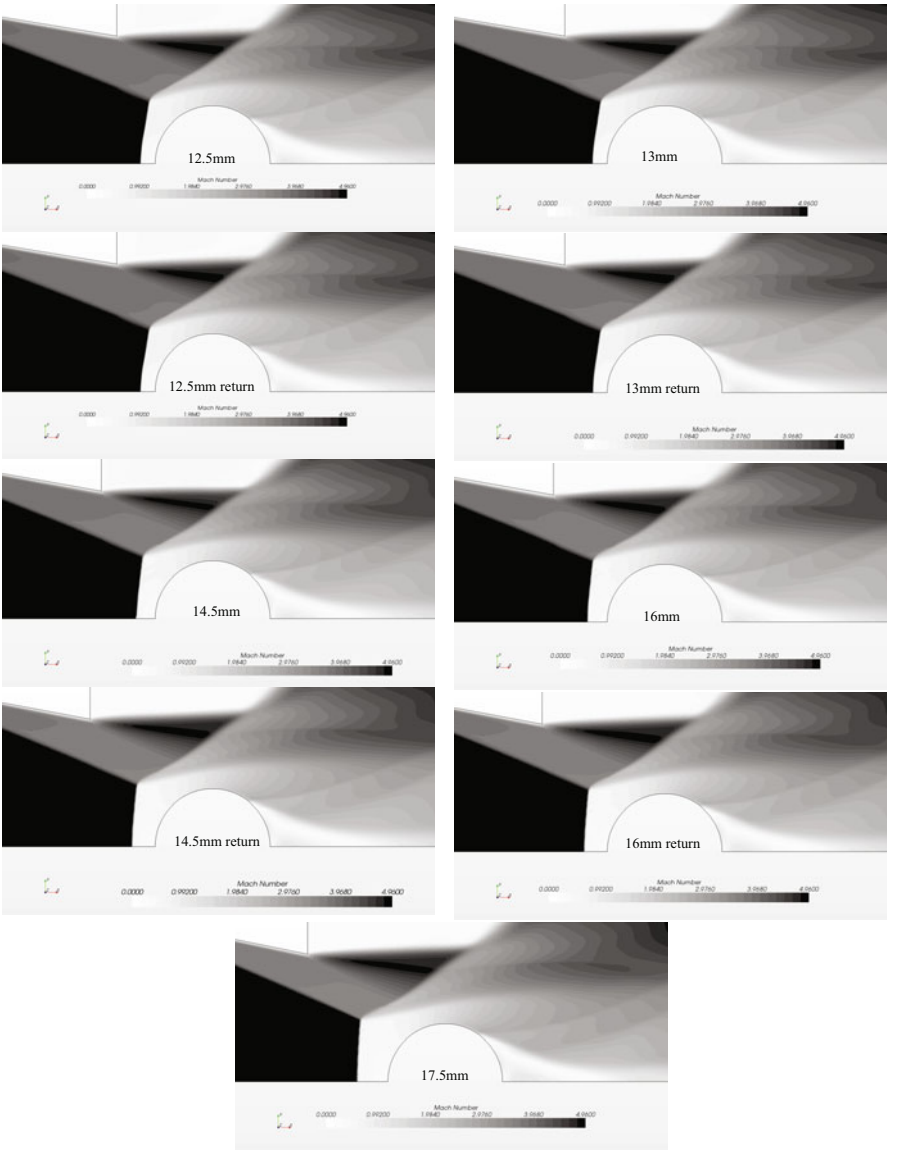

Fig. 4 Mach number isovalue for different positions for the forward and backward motion

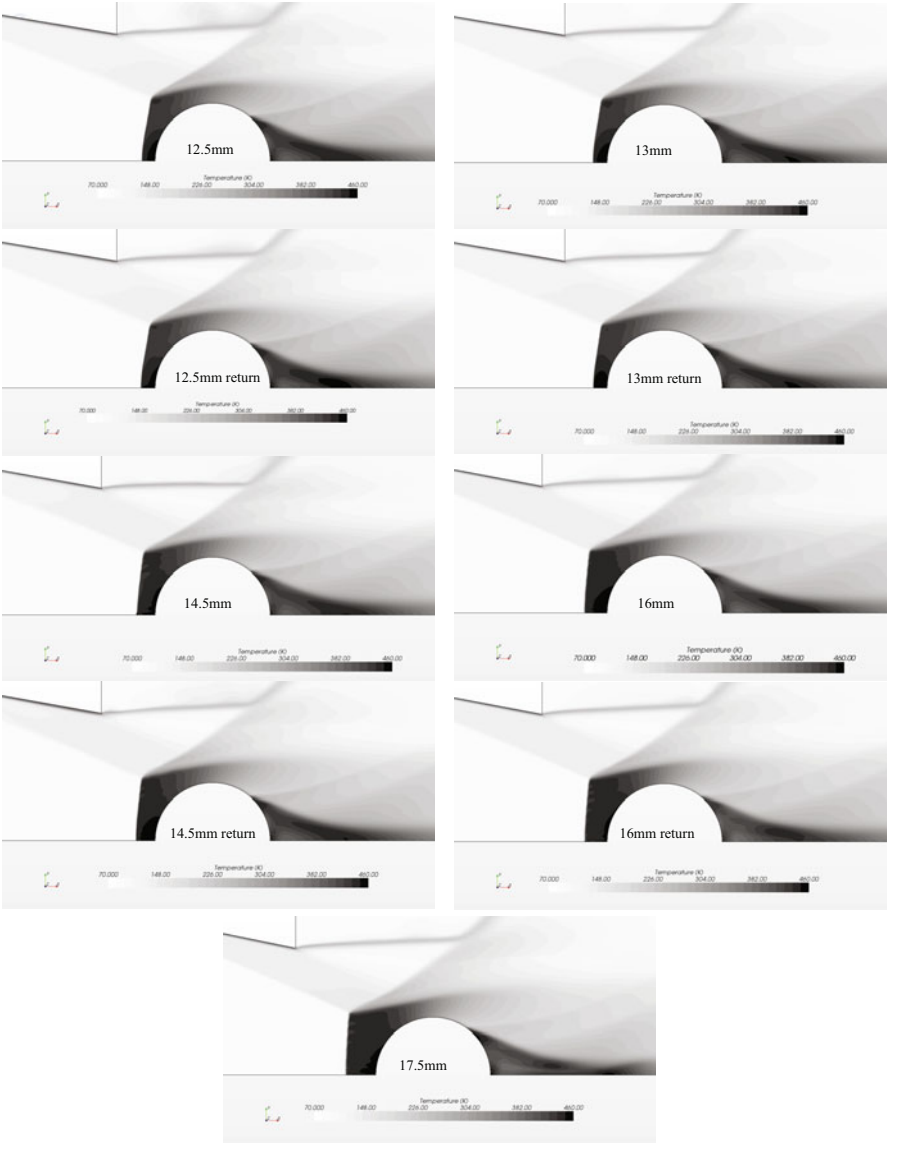

Fig. 5 Temperature isovalue for different positions for the forward and backward motion

becomes straighter as the increasing of X. This shock wave modification leads to an increasing of the average temperature over the sphere surface without any notable modification of the maximum temperature. For this sphere diameter the shock interaction looks like a Mach inverse one: the slipping line diverges from the symmetry axis.

With the taken into account of the sphere motion, we are able to consider hysteresis phenomena. Thus, we have found that the shape and the position of the shock wave are slightly modified. We can seen that the shock is straighter on the way back and that the stand off distance is greater when the sphere is on its return path. The shock is also more stable on the way back. For the temperature, there is a decreasing in the second case but the variations are quite small. The slipping line is not really affected by this hysteresis, this logical as its location is due to the sphere size.

So, there is an hysteresis for that kind of shock wave interaction. It is important to notice that the differences between the two cases are much more important for the biggest value of the X distance.

4 Conclusion and Perspectives

This works has shown the capability of STARCCM+ to deal with shock wave interaction for quite high Mach number value. Moreover, it has mainly demonstrated that there is hysteresis phenomena for this conical-spherical shock wave interaction. Nevertheless, we have to get a closer look to stability problem. To deal with this problem some explicit unsteady calculations will be done and some investigation about the turbulence will be carried out using the Spalart-Allamaras model [7] with the Catris and Aupoix's correction [8] to take into account compressibility effects.

A more detailed description of the heat exchange between the fluid and the solid boundary of the fluid domain must be done. The adiabatic wall assumption is to rough to have a fine understanding of these interactions. To do so, will use STARCCM+ capabilities to solve heat transfer equation in solid and to couple it with the fluid.

References

1. Ben-Dor, G.: Hysteresis phenomena in steady shock wave reflection ISSW 22, London UK (1999)
2. Edney, B.: Anomalous heat transfer and pressure distribution on blunt bodies at hypersonic speeds in presence of impinging shocks. Aeronautical Research Institute of Sweden, Report 115 (1968)
3. Bertrand, F.: Etude du flux thermique genere par interaction d'ondes de chocs sur les mats d'injection d'un statoreacteur combustion supersonique, France (1997)
4. Grasso, F., Purpura, C., Chanetz, B., Dlery, J.: Type III and type IV shock/shock interferences: theoretical and experimental aspects. Aerospace Science and Technology 7(2), 93–106 (2003)
5. Parisse, J.D., Chpoun, A., Giordano, J., Burtschell, Y., Zeitoun, D.: Numerical investigation of conical shock and spherical shock interaction. ISSW 25, Bangalore, India (2005)

6. Parisse, J.D., Giordano, J., Ducarme, G., Burtschell, Y., Zeitoun, D.: Conical and spherical shock interactions: Numerical investigations. ISIS 18, Rouen, France (2008)
7. Spalart, P.R., Allmaras, S.R.: A One-Equation Turbulence Model for Aerodynamic Flows. In: 30th Aerospace Sciences Meeting & Exhibit, Reno N.V., AIAA paper 92-0439, January 6-9 (1992)
8. Catris, S., Aupoix, B.: Density Corrections for Turbulence Models. Aerospace Science and Technology 4, 1–11 (2000)

Transitional Shock-Wave / Boundary Layer Interaction behind a Roughness Element

Nicola De Tullio and Neil D. Sandham

1 Introduction

Interactions of shock-waves with boundary layers are a common feature in high-speed flight. Depending on the nature of the incoming boundary layer such interactions may lead to large unsteady thermal and pressure loads which may reduce the aerodynamic performance and the structural integrity of hypersonic vehicles. Despite numerous investigations our current knowledge of the fundamental physical mechanisms involved in unsteady shock-wave/boundary-layer interactions (SBLI) is far from complete and a number of aerospace applications would benefit from a deeper understanding of the subject. Most of the research efforts in this field have been directed to the analysis of shock-waves interacting with nominally two-dimensional turbulent boundary layers [1]. Flows over high-speed vehicles and, in particular, inside the intakes of their air-breathing propulsion systems are very complex and include interactions of shock-waves with three-dimensional transitional boundary layers. The transition process is very sensitive to flow conditions and geometric parameters. Experiments have shown that small roughness elements, less than a millimetre in height, can lead to early breakdown to turbulence even in a quiet environment [2]. In high-speed flows, transitional boundary layers can also be affected by the interaction with shock-waves through mechanisms which are largely unknown. A detailed study of three-dimensional transitional SBLI will help understand how shock-waves affect the transition process at high-speeds. The limited number of studies available in the literature on transitional SBLI show that for strong interactions (in the convective instability regime) small-amplitude disturbances experience strong amplification across the separation bubble due to the instability of the separated shear layer [3]. In addition, transitional interactions induce higher levels of unsteadiness and stronger thermal loads than in the fully turbulent case [4, 5].

Nicola De Tullio · Neil D. Sandham
School of Engineering Sciences, University of Southampton, Southampton SO17 1BJ, UK

The present work focuses on the interaction of a weak oblique shock-wave with the transitional boundary layer developing behind an isolated sharp-edged roughness element, complementing the previous work of [6]. The investigation is conducted by performing direct numerical simulations (DNS) of the transition process with and without SBLI, so that the effects of the shock interaction can be clearly seen by comparing the two resulting flow fields.

2 Methodology

The present study focuses on DNS of the compressible Navier-Stokes equations. The calculations were carried out using a parallel, multi-block code which uses a fourth-order central spatial differencing scheme. Time integration is based on a third-order compact Runge-Kutta method. An entropy splitting approach by Sandham *et al.* [7] is used to split the inviscid flux derivatives into conservative and non-conservative parts, thereby improving the stability of the non-dissipative central scheme. Periodic boundary conditions are applied in the spanwise direction, while the walls are considered no-slip and isothermal, with a temperature equal to the laminar adiabatic wall temperature. The reflection of waves from the domain external boundaries is minimised by using integrated characteristic conditions for the top and outflow boundaries. The inflow is initialised with the compressible laminar similarity solution and a pressure extrapolation boundary condition is then applied, whereby in the subsonic region of the boundary layer the inflow conservative variables are calculated by extrapolating the pressure from the domain using a first order approximation.The code was made parallel using the *MPI* library.

The impinging shock-wave was captured using the method of Yee *et al.* [8] coupled with the Ducros sensor [9]. The presence of a sharp-edged roughness element induces small spatial grid-to-grid-point oscillations in the density field due to an inherent discontinuity in the derivatives at the roughness edges. The computational grid was substantially refined near the roughness element and the residual spurious oscillations were treated using a sixth order filter by Visbal and Gaitonde [10]. The filter is applied at each time step and the conservative variables array ($\mathbf{U} = \{\rho, \rho u, \rho v, \rho w, \rho E\}^T$) is updated as follows

$$\mathbf{U} = \mathbf{U} - \sigma \left(\mathbf{U} - \mathbf{U}_{filtered} \right), \tag{1}$$

where $\sigma = 0.05$ so that only 5% of the filtered field was used.

The transition process is initiated by forcing a small broadband acoustic disturbance in the free-stream upstream of the roughness element. The forcing takes the following form

$$\rho(\mathbf{x}, t) = A \exp\left(-\tilde{r}^2\right) \sum_{m=1}^{M} \sum_{n=1}^{N} \cos\left(\beta_m z + \phi_m\right) \sin\left(\omega_n t + \phi_n\right), \tag{2}$$

where M and N are the total number of spanwise wavenumbers and frequencies respectively. The coordinate $\tilde{r}$ is defined as $\tilde{r}^2 = \left[(x-x_f)^2 + (y-y_f)^2\right]/L_f$, where L_f determines the radius of the forcing region and x_f and y_f its centre. Random phases ϕ are introduced to avoid spurious high amplitude peaks in the forcing signal which might trigger nonlinearities. The signal contains $N = 18$ non-dimensional frequencies in the range $0.06 - 0.4$ with steps of 0.02. Here the non-dimensional frequencies are expressed using the Strouhal number, defined in terms of the roughness height h^* and the reference velocity U^*_∞ as $St = f^* h^*/U^*_\infty$, where f^* is the dimensional frequency. The forcing contains $M = 25$ spanwise modulations. The amplitude $A = 6 \times 10^{-5}$ was selected to introduce disturbances in the linear regime. Note that here asterisks denote dimensional quantities.

3 Results

As already mentioned the present study focuses on the analysis of DNS data from two numerical simulations of transition induced by roughness with and without SBLI at Mach 2.5 and $Re_{\delta^*_{in}} = 3300$. The flow configuration and computational grid are shown in Table 1 and are the same for the two simulations analysed. The same table also reports the grid resolution in the turbulent boundary layer and information about the sample used to compute statistical data in the two cases. As can be noticed the interaction studied is relatively weak but still strong enough to trigger separation. Stronger interactions would induce big separation bubbles making the simulations both prohibitively expensive and difficult to compare with the case of no interaction. The grid spacings expressed in wall units are taken inside the turbulent wedge at $x/\delta^*_{in} \approx 240$. The spanwise grid spacing is expressed as an interval and increases from the roughness centerline to the sides of the turbulent wedge (due to the grid stretching applied). The grid resolution is typical of fully resolved DNS studies [11] for both cases, although the grid requirements increase in the shock interaction case.

Figure 1 shows instantaneous contours of the temperature field on the roughness centerline plane for the two cases analysed. The main features of the transition process can be inferred. The roughness induces a pair of counter-rotating streamwise vortices (not shown) which lift up low velocity fluid from the wall at the centerline, thereby creating a region of high shear detached from the wall. The small acoustic

Table 1 Simulation parameters, grid resolution and sampling information.

Wedge angle, degrees	0.0	1.93
$L_x \times L_y \times L_z/\delta^*_{in}$	$250\times20\times60$	$250\times20\times60$
$N_x \times N_y \times N_z$	$1989\times222\times547$	$1989\times222\times547$
Grid resolution, Δx^+, Δy^+_{min}, Δz^+	6.3, 0.73, [2.6, 7.6]	7.5, 0.9, [3.1, 9.3]
Observation period, $T_s U_\infty/\delta^*_{in}$	1200	1600
Sampling frequency, $f_s \delta^*_{in}/U_\infty$	0.1	0.1
Time step, $\Delta t U_\infty/\delta^*_{in}$	0.02	0.02

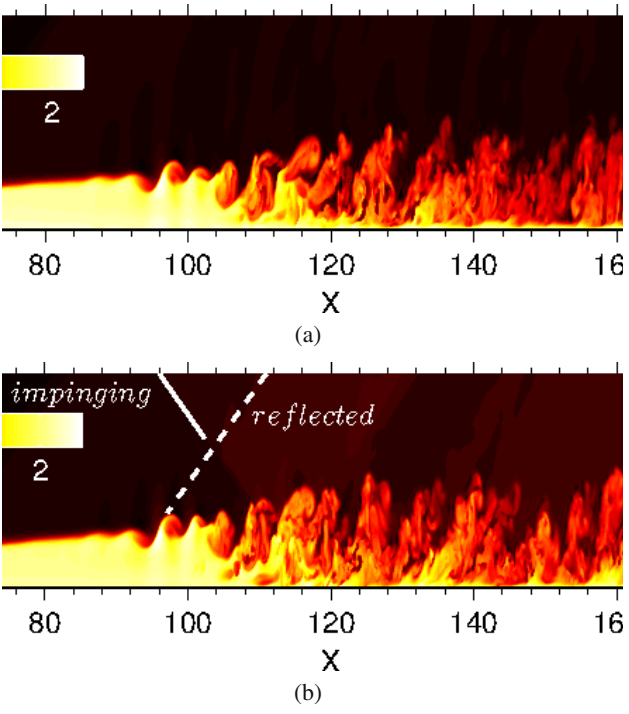

Fig. 1 Instantaneous contours of the temperature field. The white lines show the shock system and the balck lines indicate regions of separated flow.

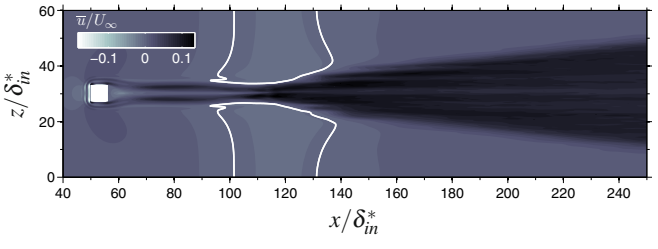

Fig. 2 Contours of time averaged streamwise velocity very close to the wall ($y/\delta^*_{in} = 0.03$). The white line shows the time-averaged separation bubble.

disturbances enter the shear layer and grow exponentially (initially) leading to the breakdown of the shear layer, which then quickly drives the transition of the entire boundary layer. The oblique shock is set to impinge at $x_{imp}/\delta^*_{in} = 118$ in a region of three-dimensional transitional flow. The initial growth of disturbances in the shear

layer is not affected by the interaction. The shock system, highlighted by the two white lines in the figure, is weak and does not separate the transitional/turbulent region of the boundary layer. On the other hand, a relatively large separation bubble is formed in the laminar region, as can be seen in figure 2, which shows time-averaged streamwise velocity contours near the wall. The white contour line shows the time-averaged separation bubble. The length L_{sep} of the bubble ranges from about 30 inflow displacement thicknesses at the sides of the domain to about 40 close to the transitional region. The figure also shows the foot-prints of a pair of co-rotating horseshoe vortices immediately upstream of the roughness element and the big streamwise vortices downstream of it. The latter seem to influence the boundary layer up to the end of the computational domain.

Figure 3 gives the skin friction at two different locations along the span, namely $z/\delta^*_{in} = 30$ (centerline) and $z/\delta^*_{in} = 36$. At the centerline the skin friction suddenly rises and overshoots the turbulent value, as expected for a transitional boundary layer. The shock displaces the skin friction peak slightly upstream and, more notably, increases the skin friction in the turbulent region downstream. At $z/\delta^*_{in} = 36$ transition happens significantly earlier in the case with shock impingement, suggesting an important effect of the interaction on the lateral spreading of turbulence. Comparing the skin friction at the two spanwise positions one can notice that the modifications induced by the roughness in the turbulent region of the boundary layer are not negligible.

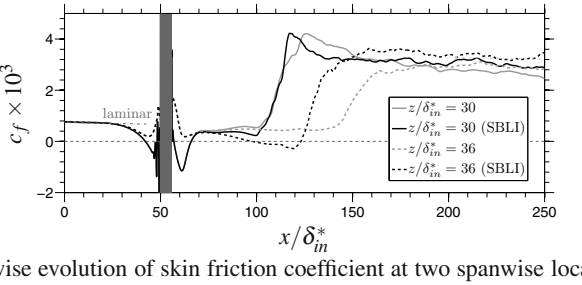

Fig. 3 Streamwise evolution of skin friction coefficient at two spanwise locations. The grey shaded area indicates the position of the roughness.

The lateral spreading of the turbulent wedge developing behind the roughness element is compared in figure 4, where the distribution of turbulent kinetic energy at $y = 1.0$ is plotted for the two cases. The effect of the impinging shock is to induce a region of high turbulent energy. In particular, the streamwise normal stress (not shown) accounts for the most energy. The region of amplified turbulent intensity is located at the sides of the turbulent wedge right after the shear-layer breakdown. Turbulence spreading is fast in these regions so that the wedge thickens rapidly. Further downstream the turbulence seems to recover the same spreading rate of the case without interaction.

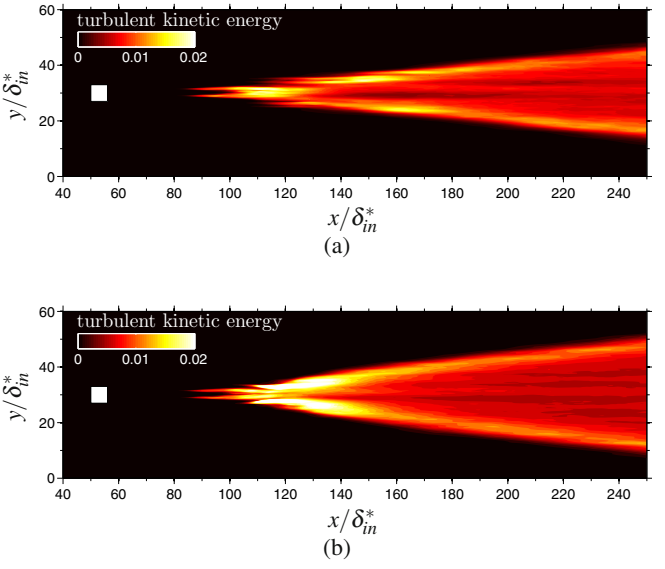

Fig. 4 Contours of turbulent kinetic energy at $y/\delta^*_{in} = 1.0$

4 Conclusion

The modifications induced by transitional SBLI in the roughness-induced transition process were studied by direct numerical simulations. Despite the relatively weak transitional interaction considered, the results show a big influence of the shock on the transition process and on the state of the turbulent boundary layer downstream of the interaction. The shock was found to enhance the lateral spreading of turbulence locally leading to a thicker turbulent wedge.

Acknowledgements. The work was performed within the Long-Term Advanced Propulsion Concepts and Technologies project investigating high-speed air breathing propulsion. LAPCAT II, coordinated by ESA-ESTEC, is supported by the EU within the 7th Framework Programme, Collaborative Project: Small or Medium- Scale Focused Research Project, Theme 7: TRANSPORT, contract no.: ACP7-GA-2008-211485. Further information on LAPCAT II can be found on `http://www.esa.int/techresources/lapcat`.

References

1. Dolling, D.S.: Fifty Years of Shock-Wave/Boundary-Layer Interaction Research: What Next? AIAA J 39(8), 1517–1531 (2001)
2. Schneider, S.P.: Effects of Roughness on Hypersonic Boundary-Layer Transition. J. Spacecraft and Rockets 45(2), 193–209 (2008)

3. Yao, Y., Krishnan, L., Sandham, N.D., Roberts, G.T.: The Effect of Mach Number on Unstable Disturbances in Shock/Boundary-Layer Interactions. Phys. Fluids 19, 054104 (2007)
4. Benay, R., Chanetz, B., Mangin, B., Vandomme, L., Perraud, J.: Shock Wave/Transitional Boundary-Layer Interactions in Hypersonic Flow. AIAA J. 44(6), 1243–1254 (2006)
5. Murphree, Z.R., Jagodzinski, J., Hood, E.S., Clemens, N.T., Dolling, D.S.: Experimental Studies of Transitional Boundary Layer Shock Wave Interactions. AIAA paper 2006-326 (2006)
6. Redford, A.J., Sandham, N.D., Roberts, G.T.: Compressibility Effects on Boundary-Layer Transition Induced by an Isolated Roughness Element. AIAA J. 48(12), 2818–2830 (2010)
7. Sandham, N.D., Li, Q., Yee, H.: Entropy Splitting for High-Order Numerical Simulation of Compressible Turbulence. J. Comput. Phys. 178, 307–322 (2002)
8. Yee, H.C., Sandham, N.D., Djomehri, M.J.: Low-Dissipative High-Order Shock-Capturing Methods using Characteristic-Based Filters. J. Comput. Phys. 150, 199–238 (1999)
9. Ducros, F., Ferrand, V., Nicoud, F., Weber, C., Darrac, D., Gacherieu, C., Poinsot, T.: Large-Eddy Simulation of the Shock/Turbulence Interaction. J. Comput. Phys. 152, 517–549 (1999)
10. Visbal, M.R., Gaitonde, D.V.: On the Use of High-Order Finite Difference Schemes on Curvilinear and Deforming Meshes. J. Comput. Phys. 181, 155–185 (2002)
11. Pirozzoli, S., Grasso, F., Gatski, T.B.: Direct Numerical Simulation and Analysis of a Spatially Evolving Supersonic Turbulent Boundary Layer at $M = 2.25$. Phys. Fluids 16(3), 530–545 (2004)

Step Configuration Influence on Structure of Supersonic Reacting Flows in Channels with Sudden Expansion

N.N. Fedorova, Yu.V. Zakharova, and M.A. Goldfeld

1 Introduction

The study of supersonic turbulent flows in the channels with sudden expansion (step/cavities) is actual task since this configuration is used for ignition and flame stabilization. Supersonic combustion is studied for many years in order to support the future hypersonic flights. It well known that it is rather difficult to get the ignition and stable combustion at supersonic speeds [1]. The flow in the supersonic combustion chamber js charachterized by a short residence time which is only a few milliseconds of magnitude. A simple geometry to generate a flameholding region in supersonic flow is a backward facing step (BFS). Flows around BFS configuration were studied for decades and many papers were published regarding fundamental flow properties [2] as well as the scramjet combustion chamber utilization [3]. The effect of step configuration (”boattailing”) on the structure of compressible base flows was investigated in a numerous papers since Hama’s work [4]. Nevertheless, the question is little studied as far as supersonic chemically reacting flows in channels are concerned.

The main purpose of the present paper is to investigate the influence of the step configuration on the structure of supersonic reactive and non–reactive flows in the channel under adiabatic and cold wall conditions. The joint numerical and experimental study was carried out for the three step configurations, namely, a baseline 90° BFS configuration, BFS with a preliminary compression and with a preliminary expansion. It was shown that the change of step configuration affected significantly the size of the recirculation zone. Essential effect of the temperature factor on the vortex structure and the temperature level behind a step is revealed. Computations

N.N. Fedorova
Novosibirsk State University of Architecture and Civil Engineering (Sibstrin), Leningradskaya, 113, Novosibirsk, 630008

Yu.V. Zakharova · M.A. Goldfeld
Khristianovich Institute of Theoretical and Applied Mechanics SB RAS, Instituskaya, 4/1, Novosibirsk, 630090, Russia

of the premixed stoichiometric air and hydrogen mixture were performed to understand the influence of the step geometry on the ignition processes.

2 Experimental Setup and Equipments

Experimental investigations were carried out in the hot–shot aerodynamic wind tunnel IT–302M of ITAM SB RAS. This wind tunnel is a short–duration facility, in which an arc electric–discharge heater is used. The duration of the operation regime is up to 200 msec. The first pre–chamber of the wind tunnel can be used as a high–enthalpy gas source to perform the experiments in the connected–pipe mode. In this mode, tests with a combustion chamber could be performed with incoming Mach number from 2 to 3 and high total temperatures.

The experimental model of 50×100 mm rectangular cross–section was connected to the nozzle block through isolator being 200 mm length. The backward–facing step was located at the entrance of the measuring section. The three configurations of BFS were experimentally investigated (Figure 1), namely, the baseline rectangular BFS (1), the step with a preliminary compression ramp of 8° (2) and the step with a preliminary expansion of 8° (3). The values of geometrical parameters used in this study were as follows: $h_1 = 16$ mm, $h_2 = 22$ mm and $h_3 = 10$ mm.

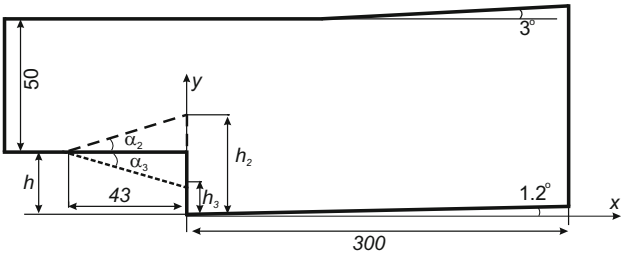

Fig. 1 Three configurations of backward–facing step

The top and bottom walls of model were equipped with the gages for measurements of static pressure and heat fluxes. Experimental runs were performed at incoming Mach number $M_\infty = 2.8$. Parameters of flows under investigation for the three configurations are shown in Table 1. Due to a short run duration, the walls of the experimental model remained cold ($T_w = 300$ K) during the operation regime.

3 Method of Computations

The simulation of 2D flows were carried out with ANSYS CFD 12.0 (Fluent) instrumentation on the basis of the Reynolds averaged Navier Stokes equation and Wilcox $k - \omega$ turbulence model. The density based solver was chosen together with AUSM scheme of the third order of approximation. The simplified computational domain

Table 1 Experimental flow conditions.

Configuration #	P_0, bar	T_0, K	P_∞, bar	T_∞, K	T_{ad}, K
1	35	1721	1.12	643	1672
2	30	1813	0.98	677	1713
3	41	1974	1.3	690	1856

was used where the nozzle part and isolator was replaced by a plane channel of the equivalent length x_0. At the entrance of the computation domain which was 100 mm upstream of the BFS, the profiles of gas–dynamic and turbulence parameters were set up. As the experimental measurements at $M_\infty = 2.8$ have shown, the boundary layer thickness at the entrance of test section was about 10 mm. The same thickness was achieved in the boundary layer computations at $x_0 = 0.8$ m. At the outlet section, "soft" extrapolated conditions were used for all gas–dynamic parameters. At the channel walls, the no–slip velocity and temperature conditions of two types were specified, namely, the adiabatic and constant temperature conditions.

For the hydrogen combustion modelling, a detailed kinetics scheme [5] with 38 reactions of 8 species was implemented. Previous computations [6] have demonstrated the ability of this kinetics scheme to describe the ignition delay time in a wide range of flow temperatures.

4 Results and Discussions

First, the computations were carried out for the baseline configuration 1 under the conditions presented in Table 1. In Figure 2 (left), the computed static pressure contours are shown. The characteristic flow structure can be seen, which includes the expansion fan (EF), formed on the external corner of the step, recirculation zone (RZ) behind the face wall and the tail shock (TS) formed in the region of mixing layer reattachment. An additional expansion fan is originated in the corner on the top wall and further falls on the bottom surface resulting in significant pressure decreasing. In Figure 3 (left) the experimental (symbol) and computed (lines) pressure distributions are shown for this configuration. Computations were performed under adiabatic and cold wall ($T_w = 300$ K) temperature conditions. Variation of wall temperature did not lead to essential change of the pressure level downstream the reattachment, but resulted in the change of the base pressure level and the separation zone length (Figure 3, left). In the case of the cold wall, the level of base pressure was lower and separation length shorter than those for the adiabatic wall.

Next, the results for the configuration # 2 are presented. The shock wave formed at the ramp before BFS (Figure 2, left) extended downstream reflecting from channel walls and essentially reconstructing the flow structure. Repeatedly reflected shock wave was united with the tail shock wave that resulted in the formation of the massive separation zone on the top wall. Pressure distributions along the bottom wall

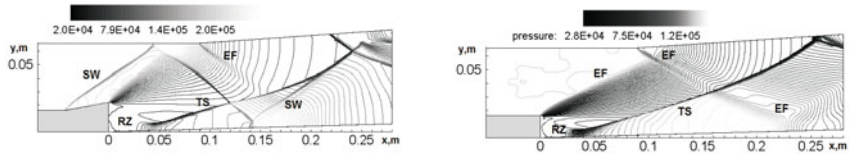

Fig. 2 Computed static pressure contours (left) and static pressure distribution along the bottom wall (right) for the baseline configuration 1

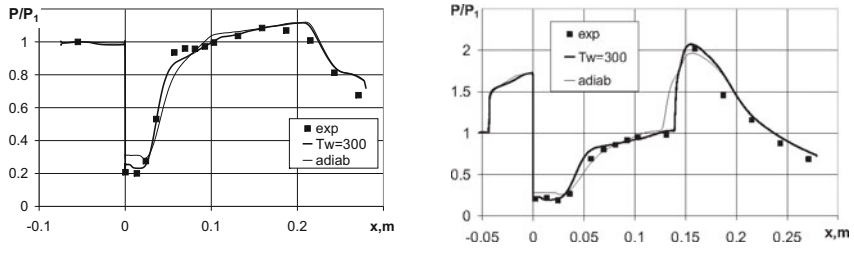

Fig. 3 Computed static pressure contours (left) and static pressure distribution along the bottom wall (right) for the baseline configuration 2

(Figure 3, right) show that in a case of adiabatic wall, the boundary layer separation takes place at $x \approx 0.13$.

The calculated static pressure distribution on the bottom wall for the configuration 3 is presented in Figure 4. Comparison of Figures 4 and 3 shows that the preliminary expansion results in some increase of the base pressure. Similar to the previous configurations, wall temperature influences on the separation zone extent and the base pressure level. Base pressure for adiabatic wall conditions is higher than that for the cold wall.

As a next step, the computations of the premixed air and hydrogen mixture flow in the channel with BFS were performed under the similar conditions. It was supposed that at the entrance of the computational domain, the pre–mixed hydrogen–air mixture was supplied with hydrogen mass fraction equal to 0.028. First, the flow for the baseline configuration 1 was computed under the cold wall conditions, namely, $T_w = 300$ K. As Table 1 shows, for this case the stagnation temperature was lower

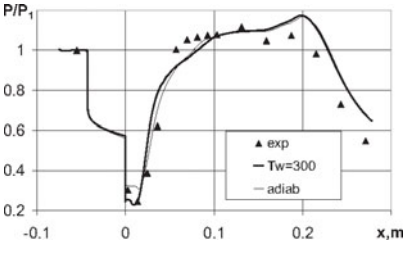

Fig. 4 Static pressure distribution along the bottom wall for the configuration 3

then that for the two others configurations. Due to this fact, at the cold wall condition the ignition $T_w = 300$ K did not occur in the flow. But when flows under higher temperature conditions ($T_w = 800$ K or adiabatic) are simulated, the mixture ignited. The ignition zone could be identified by the non–zero H_20 values in Figure 5 where H_2O mass concentrations is presented computed under $T_w = 800$ K (left) and adiabatic (right) wall temperature conditions. Figure 5 shows that for a for $T_w = 800$ K case, the ignition took place in the region of the reattachment of the mixing layer and then spreaded downstream, but a flame front did not penetrate into the recirculation region after BFS. For adiabatic conditions, the flame front shifted upstream and occupied the recirculation zone entirely.

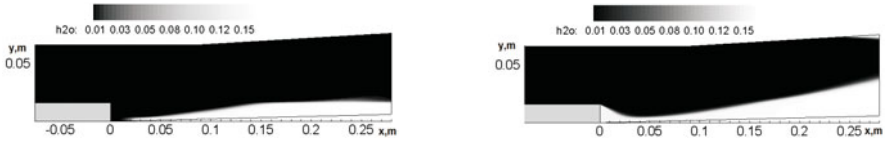

Fig. 5 Mass fraction of H_2O for the configuration 1 computed under $T_w = 800$ K (left) and adiabatic (right) temperature conditions

Figure 6 demonstrates the results of the reactive flow simulations for the configurations 2 and 3. The cold wall temperature conditions were applied in these computations, but the additional shock as well as rather high stagnation temperature assisted the ignition of the flow. The ignition first took place in the separation zones organized on the top and bottom walls and further spreads upstream. The two ignition zones merged, and and intensive combustion occured in the whole channel width.

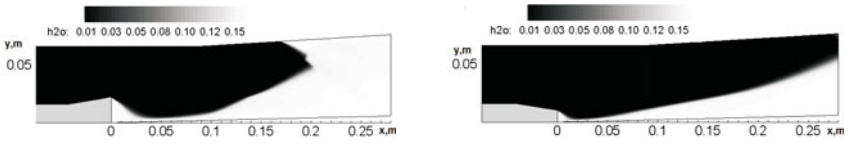

Fig. 6 Computed H_2O mass fraction field for the configuration 2 (left) and 3 (right)

The flow over configuration 3 is characterized by additional expansion that makes the main recirculation zone shorter. Due to high stagnation temperature, mixture ignites near the bottom wall just downstream the reattachment of the mixing layer. The flame spreads upstream and occupies the entire base region. But no ignition takes place in the vicinity of the top wall. Since the flame shape follows the tail shock, the burning in the whole channel may be possible further downstream outside of the computational domain.

5 Conclusion

Experimental and CFD results are presented for 2D flows in a channel with backward facing step of the three various configurations. Good agreement between experimental and simulated results was achieved. Essential influence of the temperature factor on the base pressure level and the separation length was revealed. Numerical simulations were conducted to predict the ignition of the premixed air and hydrogen mixture in flows under the conditions which are typical for the experimental facility. It was shown that depending on the incoming flow parameters and channel geometry, various scenario of ignition can be realized. When the cold wall condition was considered, the ignition shifted downstream the recirculation zone or did not occur at all.

Acknowledgements. This work was supported financially by Russian Foundation for Basic Research grants # 09–08–01001 and # 10–08–00465.

References

1. Curran, E.T., Heiser, W.H., Pratt, D.T.: Fluid Phenomena in Scramjet Combustion System. Annual Review of Fluid Mechanics 28, 323–360 (1996)
2. Scherberg, M.G., Smith, H.E.: AIAA Journ. 5(1), 51–56 (1967)
3. Uenishi, K., Rogers, R.C., Northam, G.B.: J. Propulsion 5(2), 158–164 (1989)
4. Hama, F.R.: Experimental investigation of wedge base pressure and lip shock. TR 32-1033, Jet Propulsion Lab (1966)
5. Tien, J.H., Stalker, R.J.: Combustion and Flame 130, 329–348 (2002)
6. Bedarev, I.A., Fedorov, A.V.: Combustion, Explosion, and Shock Waves 42(1), 19–26 (2006)

Inviscid-Viscous Interactions of Compressible Convex Corner Flows

K.M. Chung and P.H. Chang

1 Introduction

Variable camber concept, such as deflection of flaps or ailerons in cruise, could play a role in performance optimization for current- and future-generation aircrafts. Within the operational flight envelopes, it would change the flowfield and consequently modify aerodynamic characteristics[1]. A study by Szodruch and Hilibig[2] also indicated that variable camber can be employed to improve the transonic maneuvering characteristics of a fighter aircraft. Furthermore, Parndtl-Meyer expansion is well known in supersonic flows. However, the subsonic expansion or transonic expansion flows around a sharp convex corner are less studied. At lower Mach number, the flow is expanded and recompressed around a sharp corner. With increasing Mach number or convex-corner angle, the boundary layer is subject to a rapid acceleration and the flow switches to transonic expansion flow. Noted that Chung[3] proposed a similarity parameter to characterize the flowfield, in which the transition of subsonic and transonic expansion flows is observed at $M^2\eta$=6.14. Shock-induced boundary layer separation is also another concern for application of variable camber concept.

The focus of the present work is to adopt another similarity parameter to scale the characteristics of compressible convex-corner flows, including transition of subsonic and transonic expansion flows and peak pressure fluctuations. The phenomenon of shock excursion is also addressed.

2 Experimental Apparatus and Measurement Techniques

The experiments were performed in the blowdown transonic wind tunnel located at the Aerospace Science and Technology Research Center (ASTRC) at the National

K.M. Chung · P.H. Chang
Aerospace Science and Technology Research Center (ASTRC),
National Cheng Kung University, Taiwan, ROC
Institute of Aerospace and Astronautics,
National Cheng Kung University, Taiwan, ROC

Cheng Kung University (NCKU), Taiwan. The test section is 600 mm 600 mm and 1500 mm in length. The operating Mach number ranges from 0.2 to 1.4, and the simulated Reynolds number is up to 20 millions per meter. Major component of the facility consists of compressors, air dryers, a cooling water system, air storage tanks, and the tunnel. The volume of three storage tanks is 180 m^3 at 5.15 MPa. The dew point of high-pressure air through the dryers is maintained at -40°C under normal operation conditions. The freestream Mach numbers are 0.34, 0.64, 0.70, 0.83 and 0.89 ± 0.01. All tests were conducted at stagnation pressure of 172 ± 0.5 kPa and at stagnation temperature of room temperature.

The test model includes a flat plate, an instrumentation plate and a single-foot support. Chung[4] provide full details of the model geometry and coordinate system.The sharp convex corner angles are 5°, 10°, 13°, 15°, 17° and 20°. The instrumentation plates had 19 transducers taps available along its centerline at centre-to-centre spacing of 6 mm. To prevent cross flow from the underside of the plate, the side fences were installed.

The mean and fluctuating wall pressures were measured using flush-mounted Kulite pressure transducers (XCS-093-25A). The outside diameter is 2.36 mm, and the sensing element is 0.97 mm in diameter. The natural frequency is 200 kHz as quoted by manufacturer. All of the pressure transducers were powered by a Topward Electronic System (TES-6102) power supply at 15.0 V. The output of each of the transducers was amplified by an external amplifier (Ecreon Model E713), in which the roll-off frequency is about 140 kHz, to improve the signal-to-noise ratio. The sampling rate is 200 ksamples/s (or 5 μs).

The NEFF 620 System and the NI-PXI recorders were used as the data acquisition systems. The test conditions of wind tunnel were recorded by the NEFF system, whereas the NI-PXI recorders were used to measure the surface pressure. All input channels were triggered simultaneously using an input channel as the trigger source. During a typical run, each data record possesses 131,072 data points for statistical analysis. The data were divided into 32 blocks. The basic statistical properties of data (mean, fluctuating, etc) were calculated.

3 Surface Pressure Distributions

Transonic flow is inherently nonlinear. Such a complex phenomena could not be described by simple linear relationships. However, a similarity parameter β (= $M^2\eta/\sqrt{1-M^2}$) was used in the present study to correlate the experimental data. The similarity parameter comes from Prandlt-Glauer role [C_p=$C_{p,0}/\sqrt{1-M^2}$ [5]]. In addition, most early studies about transonic expansion corners have been investigated by hodograph method, which adopts conformal mapping[6]. The Cartesian coordinate system could be transformed into hodograph without losing physical meanings.

The surface pressure normalized by stagnation pressure and is plotted against β, as shown in Fig. 1. Although there is a gap between the lower Mach number and higher one, the experimental data was correlated reasonably well. For $\beta<8$, the pressure distribution shows a typical case of subsonic expansion flow and then the

flows expand to supersonic speed at higher β. It should be noted that the minimum surface pressure increases when $\beta > 10$ at M=0.70. This is due to the upstream movement of shock wave. At higher Mach number, the flow switches to supersonic completely. Furthermore, it is obvious that the minimum surface pressure may be roughly grouped into two regimes. Each of them was regressed by a straight line as shown in Fig. 2. The minimum surface pressure decreases linearly asincreases. Then, in the region of $\beta > 20$, the minimum surface pressure tends to approach an asymptotic value.

The ratio of surface pressure and stagnation pressure corresponds to local Mach number. Fig. 3 shows the distribution of the peak Mach number for all test cases. Again, β is adopted as the flow similarity parameter. The higher slope of peak Mach number with β is observed at lower Mach number region. It implies that flow expansion near a sharp corner is sensitive to β at lower freestream Mach number and convex-corner angle. It is also observed that the peak Mach number increases with β except for the case at M=0.7 and near $10 < \beta < 15$. A early study by Liu and Squire[7] indicated that the critical peak Mach number $M_{p,cr}$ at transonic flow regime is about

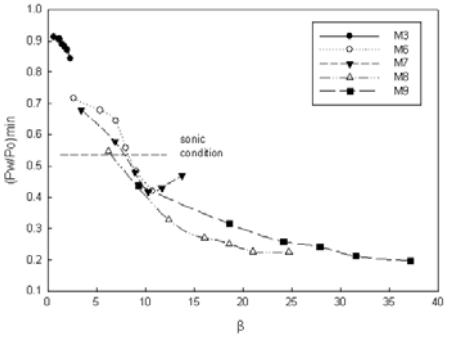

Fig. 1 Mean surface-pressure distributions

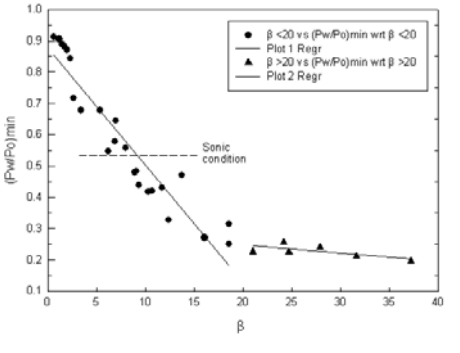

Fig. 2 Mean surface-pressure distributions with linear regression

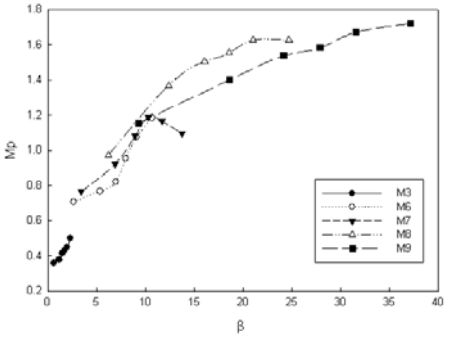

Fig. 3 Peak Mach number distributions

1.3, which corresponds to shock-induced boundary layer separation. As shown in Fig. 4, the peak Mach number with β could be regressed by two straight lines. For $\beta > 20$, the slope of peak Mach number become plainer. However, it is not clear that the peak Mach number distribution approach a asymptotic value at $\beta > 20$.

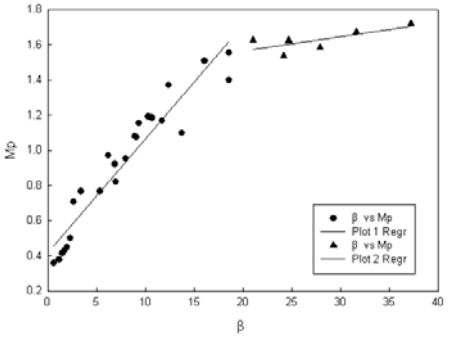

Fig. 4 Peak Mach number distributions with linear regression

4 Shock Motion Frequency

The compressible flow around a sharp corner could be accelerated to supersonic, and usually contains shock wave generated near the corner. Undergoing the shock formation, the local pressure increases and might induce boundary layer separation. Fig. 5 (M = 0.89, $\eta = 17^\circ$) shows the successive downstream three pressure signals, which clearly indicates low frequency shock oscillation. However, it should be noted that the frequencies, which the last two pressure signals have do not stand for the principal frequency of the shock motion. In fact, that is the background noise of

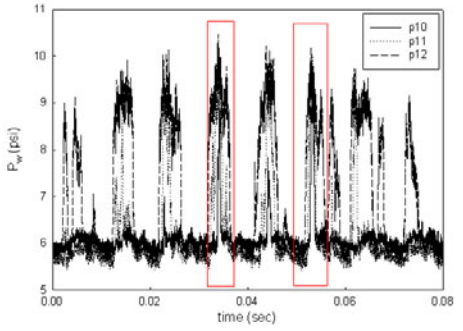

Fig. 5 Wall pressure signal measured in downstream of corner

the wind tunnel. On the other hand, only the first pressure signal can be regard as the shock induces pressure rise. Furthermore, the pressure rise is less than that of a normal shock and this might correspond to a λ-shock. Furthermore, there are two pressure peaks within 0.01 second. Brusniak and Dolling [8] concern with the bandwidth of the shock-foot-associated low frequency component is a few hundred Hz to several kHz. Although this study is focused on the corner flow, it has frequency bandwidth in common with ramp flow.

When the shock strength increases, it would induce boundary layer separation (SIBLS). Many earlier investigations have showed that the separation onset and its pressure rise can be influenced by the incoming boundary layer shape parameter which represents the fullness of the boundary layer, the Reynolds number and the effect of the downstream flow organization [9][10]. However, when it comes to transonic corner flow, the effect of downstream flow organization may be a dominator. The reason is that when the flow was accelerated to supersonic flow, the incoming boundary layer shape parameter will be damped. In other words, it could be expected that the downstream flow is more important to the transonic convex-corner flows.

5 Conclusion

A similarity parameter β was used to correlate the experimental data of compressible convex-corner flows. The surface pressure ratios, the peak Mach number and the minimum surface pressure coefficients are plotted against β. For $\beta > 20$, the surface pressure rations and peak Mach number tend to approach an asymptotic value. This might correspond to free interactions proposed by Chapman et al. [11], in which the region of flow are free from direct influence of downstream geometry. The separation bubbles can be predicted by only the Mach number just upstream of the shock wave. The shock induced by compressible convex-corner flows is a type of oblique shock, and the order of shock excursion is the same order as Dolling's work.

References

1. Bolonkin, A., Gilyard, G.B.: Estimated Benefits of Variable-Geometry Wing Camber Control for Transport Aircraft. NASA TM-1999-206586, Dryden Flight Research Center, Edwards, California (1999)
2. Szodruch, J., Hilbig, R.: Variable Wing Camber for Transport Aircraft. J. of Fluid Mechanics 187, 467–486 (1988)
3. Chung, K.: Transition of Subsonic and Transonic Expansion-Corner Flows. J. of AIAA 37(6), 1079–1082 (2000)
4. Chung, K.: Investigation on Transonic Convex-Corner FLows. J. of AIAA 39(6), 1014–1018 (2002)
5. Anderson Jr., J.D.: Fundamentals of Aerodynamics. McGraw-Hill. McGraw-Hill, New York (1997)
6. Verhoff, A., Stookesberry, D., Michal, T.: Hodograph Solution for Compressible Flow Past a Corner and Comparison with Euler Numerical Predictions. AIAA Paper91-1547 (June 1991)
7. Liu, X., Squire, L.: An Investigation of Shock/Boundary Layer Interactions on Curved Surfaces at Transonic Speeds. J. of Fluid Mech. 187, 467–486 (1987)
8. Brusniak, L., Dolling, D.S.: Physics of Unsteady Blunt-Fin-Induced Shock Wave/Turbulent Boundary Layer Interactions. J. of Fluid Mech. 273, 375–409 (1994)
9. Kim, H., Matsuo, K., Setoguchi, T.: Investigation on Onset of Shock-Induced Separation. J. of Shock Wave 6, 275–286 (1996)
10. Dussauge, J., Piponniau, S.: Shock/Boundary-Layer Interactions: Possible Sources of Unsteadiness. J. of Fluids and Structures 24, 1166–1175 (2008)
11. Chapman, D.R., Kuehn, D.M., Larson, H.K.: Investigation of Separated Flows in Supersoinc and Subsnoic Stream with Emphasis on the Effect of Transition. NACA TN 3869 (1957)

Effect of a Counterflow Plasma Jet on Aerodynamics Characteristic of a Blunted Cone

Xue-jun Zeng, Jie Li, Cheng Cao, and Hai-feng Shu

1 Introduction

The characteristic of aircraft drag is one of main qualifications to judge the performance of an aircraft. Aircraft drag reduction is a very actual and important problem. One percent drag decrease lets, approximately, to 10 percent increase aircraft payload or increase long-range. Many reports[1-7] were made on this subject presenting multifarious new technique for drag reduction. Hereinto, it is a novel approach for reducing aerodynamic drag by employing plasma.

An attractive plasma aerodynamic augmentation device is a counterflow plasma jet. In reference 1-2, tests in wind tunnels and experiments with numerical calculation were carried out with the same cone-cylinder model to research the influence of plasma injection from model surface towards external flow on aerodynamic drag. Injecting gas from cone nose into oncoming flow realized at the same Mach number M_j=3.65, same stagnation pressure P_{0j}=1.54 atm and three hard different stagnation temperature T_0=600, 2000, and 6000K. The external flow was at P_0=12atm, T_0=290K and M_∞=4. The investigations showed that the plasma injection can be used to reduce drag at supersonic Mach number. The drag reduction may be reached to 2 times and more.

The aim of this work is to investigate the influence of jet pressure ratio on the value of drag reduction employing counterflow plasma jet. Experiments were carried out on Φ1m Hypersonic Wind Tunnel utilizing a blunted cone with a plasma generator and a strain gauge annular balance inside it. Mach number of free stream is 7 and jet pressure ration 1000, 1809, 3000, 5013, 10449 and angle of attack 0°, 3°, 5°, 8°, 10°. The investigation showed that the forehead bow shock of the model expanded and axial force reduced obviously with counterflow plasma jet. Furthermore, the degree of the reduced augmented with the increase of jet pressure ratio.

Xue-jun Zeng · Jie Li · Cheng Cao · Hai-feng Shu
Hypervelocity Aerodynamics Institute, China Aerodynamics Research and Development Center, Mianyang Sichuan, 621000, China

However, the axial force reduction achieved on with some certain appropriate jet pressure ratios if the thrust of the plasma generator was considered.

2 Test Facility and Equipment

The experiments were carried out on Φ1m Hypersonic Wind Tunnel, which is an intermittent type blow-down conventional hypersonic wind tunnel equipping Laval nozzle. Diameter of the nozzle exit is 1m and Mach numbers 3, 4, 5, 6, 7, 8.

The counterflow plasma jet was generated by a plasmatron, which has the similar configuration with the subminiature solid propellant rocket engine and its nozzle shoots out through the forehead center of the model. The plasma generator is composed of long-tailed nozzle, combustion chamber, solid fuel and igniter body. The operating principles and steps of the plasmatron are that: first provide a certain volts d.c. on the igniter electrode, then the amorce is enkindled by the electronic ignition tube, at last the solid fuel begin to combust. In this way, the plasma gas with high temperature and high pressure will generate in the combustion chamber and plasma jet is exhausted from model nose through the nozzle.

The test model was a blunted cone which half-angle is 8°. Diameter of the ball as the forebody is 30mm. A stain gauge tubular three-component balance was utilized to measure the aerodynamic force of the cone model. The precision of each component is less than 3%. The model was mounted in the wind section by means of a strut and its forebody could be seen through the test section optical glass. A special broach penetrated through the forehead of blunted cone was necessary to accommodate the nozzle of the plasma generator and to inject the plasma jet. Fig.1 shows the configuration of the blunted cone, plasma generator, tubular balance and the strut. The plasma generator was attached to the strut through the lumen of the tubular balance that did not affect the measured value of the force to the blunted cone. The strain gauge registered forces acting only on the blunted cone. The forces acting on the plasma generator (including the jet reaction force), were compensated by the strut response that was not measured by the balance.

Experiments were performed at Mach number M_∞=7, jet pressure ratio 1000, 1809, 3000, 5013, 10449 (by changing stagnation pressure of free stream and total pressure of plasma jet), and angle of attack α=0°, 3°, 5°, 8°, 10°, and stagnation temperature of free stream T_0=650K and total temperature of plasma jet T_{0j}= 2000K.

The axial force coefficient is

$$C_A = \frac{A}{q_\infty S_M} \tag{1}$$

The normal force coefficient is

$$C_A = \frac{N}{q_\infty S_M} \tag{2}$$

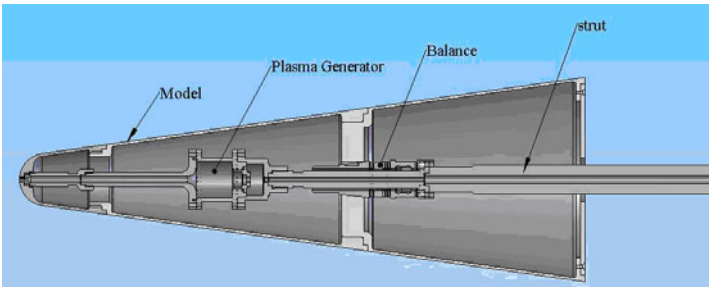

Fig. 1 The configuration of model

The effect of the plasma jet is

$$dC_A = \frac{C_{Ajeton} - C_{Ajetoff}}{C_{Ajetoff}} \tag{3}$$

$$dC_N = \frac{C_{Njeton} - C_{Njetoff}}{C_{Njetoff}} \tag{4}$$

3 Experiments Results and Analysis

Fig.2 shows typical schlieren pictures of the flow filed that angle of attack is 0°. Fig.2a corresponds to an ordinary shock wave configuration without counterflow plasma jet. Bow shock presses close to the forehead of the blunted cone.

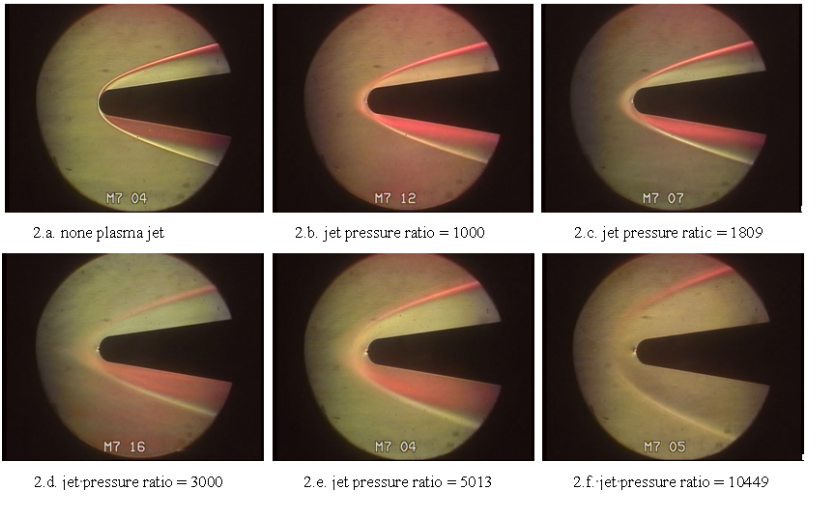

Fig. 2 Schlieren pictures at different jet pressure ratio, $\alpha = 0°$

At the duration of the counterflow plasma jet injecting from model nose through the nozzle, the flow picture near the model changed significantly at all jet pressure ratios. From the video-filming recorded by a color schlieren-meter, you can watch the decomposition of the original bow shock wave and the formation the plasma ball in front of the model and forming a quite new shock wave configuration. The distance between the forehead of blunted cone and the bow shock wave augments comparing with none plasma jet. And the aggrandizement of separate distance is along with jet pressure ratio.

Fig.3 shows the curve of time dependence of axial force. After the flow field of wind tunnel building, the blunted cone model receives stress only from free stream. At the instant of counterflow plasma jet exhaust from the forehead of the cone through the nozzle, the cone was forced by external flow and counterflow plasma jet together, the axial force decreased significantly. When plasma generator quenched, it restituted to the ordinary state.

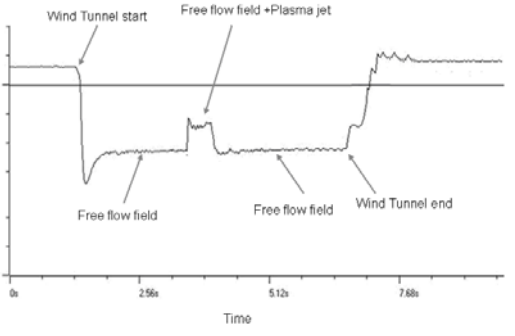

Fig. 3 $\alpha = 0^\circ$, Dependence of axial force on time

Fig.4 plots the model axial force coefficient dependences on angle of attack at different jet pressure ratio at prior to and with the plasma injection. Fig.4a corresponds to the case that without considering to the thrust of plasma generator. Comparatively, the force of the model cone includes free stream and thrust of the plasma injection in Fig.4b. Fig.4 plots the model normal force coefficient dependences on angle of attack at different jet pressure ratio.

In Fig.4a, the axial force of blunter cone only was produced by free stream without considering thrust of plasma generator. Axial force coefficient decreases significantly with the synergistic effect of counterflow and external flow. Furthermore, the degree of the reduction augments with the increase of jet pressure ratio. At zero angle of attack, axial force coefficient decreases about 50% when jet pressure ratio is 10449, decrease about 40% when jet pressure ratio is 3000, and decrease about 22% when jet pressure ratio is 1000.

However, if the plasma generator is integrated with the blunted cone, axial force coefficient (in Fig.4b) could be calculated from the axial force of cone measured by

the balance and the thrust of the plasma generator. At this rate, axial force coefficient increase about 50% when jet pressure ratio is 10449, without obvious change when jet pressure ratio is 5000, decrease 13%, 11% and 12% when jet pressure ratio is 3000, 1809, 1000 respectively.

As jet pressure ratio is bigger, normal force coefficient reduces obviously. But along with the jet pressure ratio diminishing, normal force coefficient decreases first and increases afterward.

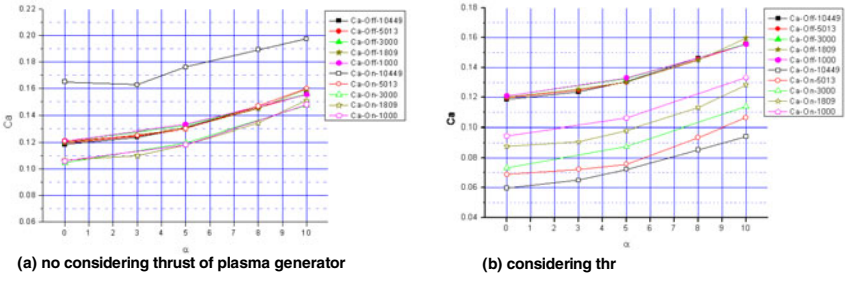

Fig. 4 Dependence of axial force coefficient on angle of attack at different jet pressure ratios

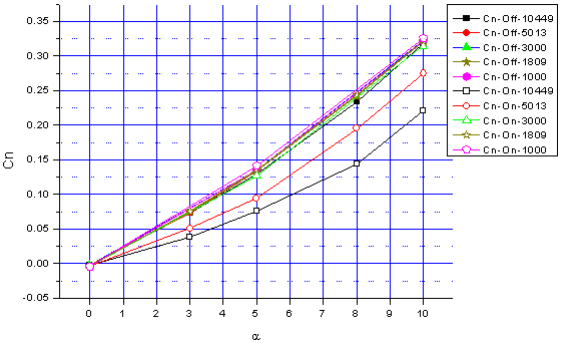

Fig. 5 Dependence of normal force coefficient on angle of attack at different jet pressure ratios

4 Conclusion

With a counterflow plasma jet injecting from a blunted cone nose through the nozzle, the flow picture near the model changed significantly at all jet pressure ratios. The distance between the forehead of blunted cone and the bow shock wave augments comparing with none plasma jet. And the aggrandizement of separate distance is along with jet pressure ratio.

Axial force decreases significantly with the synergistic effect of counterflow and external flow. Furthermore, the degree of the reduction augments with the increase of jet pressure ratio. However, axial force reduction achieved on with some certain appropriate jet pressure ratios if the thrust of the plasma generator was considered.

Summarily, it is demonstrated that the possibility of reducing aerodynamic drag by employing a counterflow plasma jet. The value of drag reduction depends on jet pressure ratio.

References

1. Ganiev, Y.C., Gordeev, V.P., et al.: Theoretical and Experiment Study of the Possibility of Reducing Aerodynamic Drag by Employing Plasma Injection. AIAA 99-0603
2. Babichev, J., Krasilnokov, A., et al.: Effect of Plasma Jet Characteristics on Supersonic Cone-Cylinder Drag. AIAA 99-4881
3. Malmuth, N.D., Fomin, V.M., et al.: Influence of a Counterflow Plasma Jet on Supersonic Blunt Body Pressures. AIAA 99-4883
4. Kremeyer, K., Newell, A., et al.: The Effect of Fore-Shock Heating in the Plasma Drag-Reduction. AIAA 2000-2700
5. Soloviev, V., Krivsov, V., et al.: Simulation of Supersonic body drag reduction produced by Forebody Filamentary Plasmas. AIAA 2001-2727
6. Menart, J., Shang, J., et al.: Total Drag and Lift Measurements in a Much 5 flow Affected by a Plasma Discharge and a Magnetic Field. AIAA 2005-947
7. Wilkerson, J.T., Van Wie, D.M.: Numerical Assessment of Heterogeneous Plasma Discharge Effects on Supersonic Forebody Drag. AIAA 2003-526

A Non-linear Eddy-Viscosity View of Shock Wave/Boundary Layer Interaction Flow Simulation

Y. You and D. Liang

1 Introduction

Shock wave/boundary-layer interaction (SWBLI) is a common but important flow phenomenon, within various engineering design areas such as engine inlets, compressors and turbines. In past decades, researchers have made great efforts towards better understanding and modeling of SWBLI flows. The reviews by Knight and Degrez[1], Zheltovodov[2], Dolling[3] examine the capability of Reynolds-averaged Navier-Stokes (RANS) turbulence models in the prediction of SWBLI. The common conclusion is that most RANS models based on the linear formulation of the Boussinesq assumption are difficult to accurately predict details of flow separation, i.e. the distributions of pressure loads, heat transfer and skin friction. In consequence, a lot of efforts are put in deriving non-linear RANS turbulence models, either in an explicit algebraic form or through transport equations for the Reynolds stress components. The ongoing research emphasis is to get a physically reliable understanding of SWBLI and to reach a point where a unique non-linear formulation could be used for the modeling of Reynolds stress in a large range of flow configurations.

The objective of this paper is firstly to make some analyses of the SWBLI phenomenon and then couple a non-linear formulation obtained from the experimental result[4] with the eddy-viscosity gained in a conventional algebraic turbulence model to construct a mathematically simple non-linear eddy-viscosity turbulence model. Afterwards, two cases of SWBLI are chosen for model assessment. Comparisons with experimental surface pressure and profile measurements for turbulent quantities are performed to study the model's capability in predicting detailed flow phenomenon. These test cases contain fundamentally essential characteristics of the SWBLI flows so that the verified model could be extensively used in other separation cases.

Y. You · D. Liang
College of Energy and Power Engineering, Nanjing University of Aeronautics and Astronautics, 29 YuDao St. 210016 Nanjing (China)

2 A Non-linear Eddy-Viscosity View of SWBLI

In order to have a deeper insight of the turbulence characteristics of SWBLI, an intensive experimental study was undertaken by Delery[4] in 1983. Figure 1 shows the measured developing history of the dissipative layer by plotting the square root of the maximum shear stress coefficient C_τ against the equilibrium shape parameter $J = 1 - 1/H$. H refers to the boundary layer shape factor given by δ^*/θ.

According to Delery's analysis, the straight line in Figure 1 specifies a function G based on the maximum stress, which is constant for all equilibrium incompressible boundary layer flows and equal to the flat plate value 6.55. The experimental points fall below the equilibrium locus at the beginning of the interaction, indicating that, there exists a departure from equilibrium characterized by a lag of the shear stress. Then, as a consequence of the continuous increase of $\sqrt{C_\tau}$, whereas J passes through a maximum and then diminishes, the corresponding curves bend and cross the equilibrium locus. Thereafter, the points are above the equilibrium locus and reach a new situation of maximum departure from equilibrium. Downstream of this station, the flows relax towards a new equilibrium state.

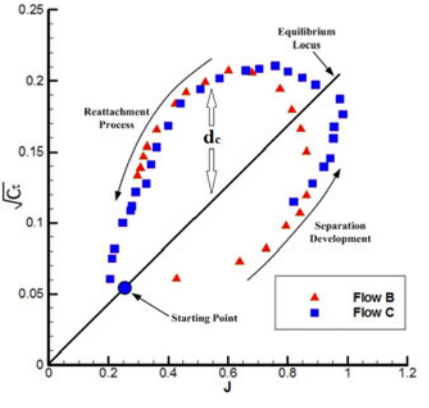

Fig. 1 Evolution of the maximum shear stress with the equilibrium shape parameter (Delery[4]).

The out of equilibrium property shown in Figure 1 can be illustrated in the view of eddy-viscosity development,

$$C_\tau = \sqrt{\frac{2\tau_{max}}{\rho_e \bar{u_e}^2}} \tag{1}$$

$$\tau_{max} = [(\mu_l + \mu_t)S]_{max} \tag{2}$$

where S is the strain rate. According to the classical turbulence boundary theory of inner and outer eddy-viscosity distributions, μ_t gets its peak value and keeps

constant during most of the outer region. In addition, Delery's experimental results present a good similarity of the velocity profile in separated zones, which indicates that the maximum value of strain rate (simplified as normal velocity gradient in two-dimensional flows) is constant in separated flows. Thus,

$$\tau_{max} = [\mu_l + (\mu_t)_{max}]S_{max} \tag{3}$$

As laminar viscosity is relatively small when compared to the maximum value of eddy-vicosity, it can be concluded that $(\mu_t)_{max}$ has the same distribution as τ_{max} in the separated zone, by substituting $S_{max} = const.$ into Equation 3. In other words, the eddy-viscosity should be lowered in the separated part and then enlarged during reattachment and relaxation processes. This is a useful indication for the non-linear eddy-viscosity construction in SWBLI zone. A new mathematic simple algebraic correction is developed as follows,

$$(\mu_t)_{max}^{nonequilibrium} = (\mu_t)_{max}^{equilibrium}(\frac{d_c + k_c J}{k_c J})^2 \tag{4}$$

where nonequilibrium refers boundary layer behaviors during the separation process which is out of equilibrium. And d_c denotes the departure of $\sqrt{C_\tau}$ between equilibrium locus and the experiment data, as shown in Figure 1. k_c is the slope of the equilibrium locus[6] that equals to 0.215877. The variable d_c is then modeled as,

$$d_c = \frac{J-0.2}{J_c-0.2}(0.1471 - 1.0763J_c + 2.9097J_c^2 - 4.0602J_c^3 + 2.0457J_c^4), \frac{dJ_c}{d\xi} > 0 \tag{5}$$

$$d_c = \frac{J-0.2}{J_c-0.2}(-0.2834 + 2.3152J_c - 5.0307J_c^2 + 4.6480J_c^3 - 1.6843J_c^4), \frac{dJ_c}{d\xi} < 0 \tag{6}$$

Please note that these correlations only be available when $J > 0.2$, where J_c is the non-dimensional shape parameter.

$$J_c = 0.2 + 0.8 \times \frac{J-0.2}{J_{max}-0.2} \tag{7}$$

J_c helps d_c of separation flows with different intensities converge to the universal formula of Equation 5 and 6. Corresponding to different developing trends of $\sqrt{C_\tau}$ in the separation and reattachment regions, the formula of d_c is grouped into two branches. In the numerical process, the selection of Equation 5 or 6 is determined by the streamwise gradient of J_c, $\frac{dJ_c}{d\xi}$.

In summary, an algebraic simple non-linear eddy-viscosity correction is proposed in this section, see Equation 4. This modification concentrates on the non-linear adjustment of the maximum eddy-viscosity. We take the simplest turbulence model, Baldwin-Lomax model [5], as our baseline model in this paper. The improved BL (IBL) model is validated for two separated flows in the following section.

3 Results and Discussion

3.1 *Delerys Transonic Bump*

Delery's Case C is selected as the first validation case of the new model, since the present nonlinear eddy-viscosity model is originated from this experiment.The resulting wall pressure distribution is shown in Figure 2 (left). The pressure distribution of the IBL model agrees well with the experimental data. The agreement is even better than that of the $v^2 - f$ model, which is a two-equation model incorporated some near-wall turbulence anisotropy as well as non-local pressure-strain effects[7]. Moreover, in all the previous RANS modeling study of this case, a known issue is that the wall pressures after the shock, particularly within the separation region, are higher than that in the experiment. Only with an additional 3-5% increase of the back pressure at the outflow plane can derive the shock to the appropriate position. This back-pressure enhancement was usually viewed as the effect of the blockage' arising from boundary layers on the side walls of the wind tunnel since the real flow is three dimensional [7] [8]. However, the IBL model achieves the correct shock position and the pressure plateau without any enlargement of the back pressure. The back pressure shown in Figure 2 (left) is set up to be 60500 Pa, almost the same as the experiment data.

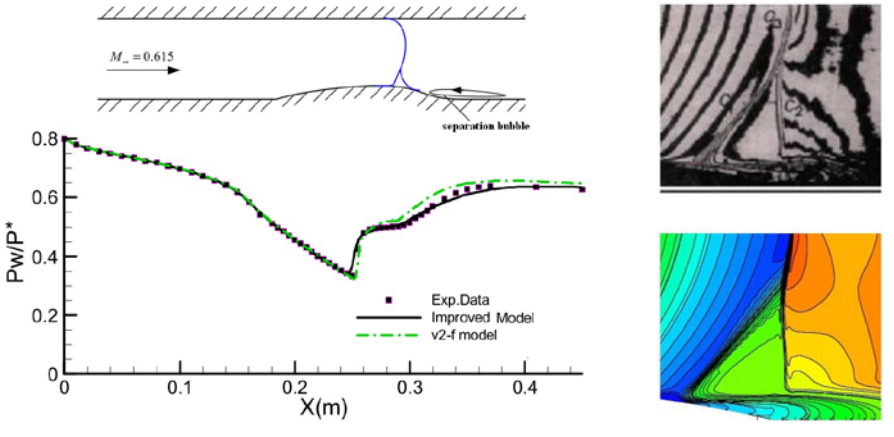

Fig. 2 Delery's Case C transonic bump flow. left: pressure predictions by different turbulence models, upper right: experimental interferogram; lower right: density isolines.

The two figures on the right side of Figure 2 are the comparison of shock patterns between the numerical result of IBL model and the experimental interferogram. The calculated density isolines distribute properly according to the test result. The large lambda shock is accurately captured by the IBL model in the correct position. The recirculation bubble size also agrees well the the experimental observation. All these

results above indicate that the proposed non-linear model has a good performance in simulating this Delery'C flow.

3.2 *Axisymmetric Transonic Bump Flow, Case 8611*

A transonic flow with embedded shock waves is selected as the second test case and its flow sketch is shown in Figure 3. This flow was identified as Case 8611 in the 1980 AFSOR-HTTM-Stanford Conference [9]. Test conditions are a freestream Mach number of 0.875 and unit Reynolds number of $13.1 \times 10^6/m$. Figure 3 shows the comparison of the pressure coefficients along the surface of the axisymmetric bump and the shear stress values at several different slices of the flowfield. Several other models feature in the comparisons, and are designated as follows: IBL, Improved BL model, the nonlinear eddy-viscosity model proposed in this paper; JK, Johnson and King's half-equation model [9]; SST, Menter's Shear Stress model [10]; and the standard linear $k-\varepsilon$ model. The linear $k-\varepsilon$ model predicts a delay of the shock position and therefore underpredicts the size of the flow separation. The improved BL model, JK model and the SST model return a considerably more pronounced pressure-plateau region. The IBL model proposed in this paper provides the best overall performance.

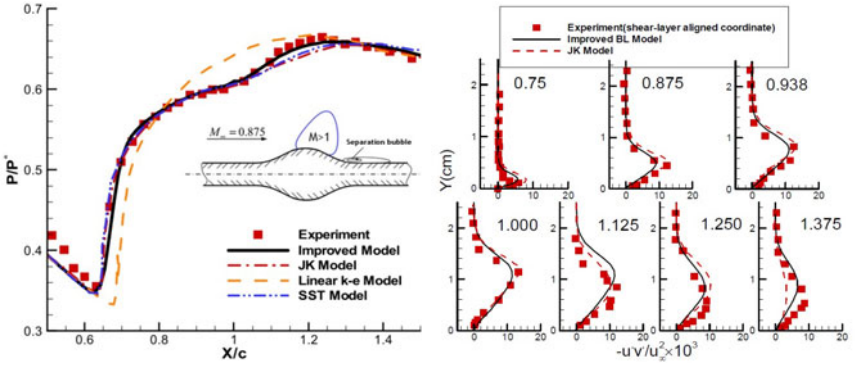

Fig. 3 Comparison of wall pressure and shear stress distributions; left: wall pressure, right: shear stress.

As for shear-stress profiles, after the transform suggested by Johnson [11], in the region of strong interactions (x/c=0.75-1.125), JK model seems to simulated a slightly better peak value of the Reynolds shear stress. However, at the reattachment region (x/c=1.25, 1.375), the IBL model has a better prediction. Anyway, the IBL model has a very similar global performance as the JK model, which is originated from the 8611 case. All these results show that the IBL model can be used for the prediction of transonic shock/boundary layer interaction.

4 Conclusions

A study of turbulence modeling of shock wave/boundary layer interaction flows is presented. Analysis of Delerys transonic bump experiment data shows that the eddy viscosity should be lowered in the separation part and then enlarged during reattachment and relaxation processes. The nonlinear correlation obtained from the experiment data is applied into the Balwin-Lomax model according to this idea.

The new non-linear model's predictions of two transonic SWBLI flows are compared with experimental data and with other RANS models. While the current model is still mathematically simple algebraic turbulence model, it yields acceptable results and provides improvements over some other models in predictions of surface pressure and shear-stress profiles.

Acknowledgement. The work is supported by the Chinese National Nature Science Foundation No 51006051.

References

1. Knight, D., Degrez, G.: ShockWave Boundary Layer Interactions in High Mach Number Flows - A Critical Survey of Current CFD Preiction Capabilities. AGARD AR-319 (1998)
2. Zheltovodov, A.: Shock Waves / Turbulent Boundary Layer Interactions - Fundamental Studies and Applications. AIAA Paper 1996-1977 (1996)
3. Dolling, D.S.: Fifty Years of Shock-Wave/Boundary Layer Interaction Research:What Next. AIAA J. 39(2), 1517–1531 (2001)
4. Delery, J.M.: Experimental Investigation of Turbulence Properties in Transonic Shock/Boundary-Layer Interactions. AIAA J. 21(2), 180–185 (1983)
5. Baldwin, B.S., Lomax, H.: Thin Layer Approximation and Algebraic Model for Separated Turbulent Flows. AIAA Paper 1978-0257 (1978)
6. East, L.F., Sawyer, W.G.: An Investigation of the Structure of Equilibrium Turbulent Boundary Layers. AGARD CP-271 (1979)
7. Lien, F.S., Kalitzin, G.: Computations of Transonic Flow with the v2-f Turbulence Model. International Journal of Heat and Fluid Flow 22, 53–61 (2001)
8. Goldberg, U., Palaniswamy, S.: The k-e-fu Turbulence Closure Model. Computer Methods in Applied Mechanics and Engineering 179, 139–149 (1999)
9. Johnson, D.A., King, L.S.: A Mathematically Simple Turbulence Closure Model for Attached and Separated Turbulent Boundary Layers. AIAA J. 23, 1684–1692 (1985)
10. Menter, F.R.: Two Equation Eddy Viscosity Turbulence Models for Engineering Applications. AIAA J. 32(8), 1598–1605 (1994)
11. Johnson, D.A.: Transonic Separation Flow Predictions with an Eddy-Viscosity / Reynolds-Stress Closure Model. AIAA J. 25(2), 252–259 (1987)

Boundary Layer Effects behind Incident and Reflected Shock Waves in a Shock Tube

S. Li, W. Ren, D.F. Davidson, and R.K. Hanson

1 Introduction

In ideal shock tube experiments, flow properties behind the incident and reflected shock waves do not vary with distance or time, and can be calculated using the standard normal shock equations and the known incident shock speed. However, nonideal effects result in flow nonuniformity behind the incident shock wave, leading in turn to nonuniformity behind the reflected shock. It has been observed that behind the reflected shock, pressure typically increases gradually with time (positive dP_5/dt) [1-3]. Such deviations of pressure (and concomitantly the temperature) from ideal values cause errors in chemical kinetic studies of rate coefficients and ignition delay times [2, 3]. Thus it is worthwhile to analyze nonideal shock tube effects and determine their impact on flow conditions, with a goal of improving experimental methods and gasdynamic models that will lead to more accurate experiments.

One of the most important nonideal effects is sidewall boundary layer formation. Among previous studies of boundary layer formation behind incident shocks, Mirels' method [4, 5] is most widely adopted. In Mirels' model, it is assumed that the boundary layer formed behind the incident shock is equivalent to a 1D distribution of mass sink that generates pressure waves and perturbs the core flow. As a result of boundary layer growth, the incident shock speed attenuates along the tube. The perturbation at a specific point in the region between the incident shock front and the contact surface can be found by summing the perturbation of pressure pulses that arrive at that point along characteristic lines from both upstream and downstream on an $x-t$ diagram [4]. It is assumed that the perturbation to the main flow is small, so that the perturbation can be superimposed linearly on the main flow [4, 5].

Most shock tube kinetics studies are carried out between the reflected shock and the shock tube end wall. Since the gas between the reflected shock front and the end wall is substantially brought to rest, it is assumed that no further waves are generated

S. Li · W. Ren · D.F. Davidson · R.K. Hanson
Mechanical Engineering Department, Stanford University, Stanford, CA 94305, USA

in this region, and the flow conditions can be determined using the wave-diagram techniques by Rudinger [6]. Using this boundary layer model, the spatial and temporal variations of pressure and temperature behind the incident and reflected shock waves were calculated and compared with recent experimental data. In Mirels' theory, the boundary layer is assumed to be either totally laminar or totally turbulent. In the real case, a laminar boundary layer exists before transition into a turbulent boundary layer. In this work, a transition Reynolds number [7] was used to determine where the transition takes place, and the effects of boundary layer transition on property time-histories were analyzed.

2 Flow Nonuniformity behind the Incident Shock

For flow behind the incident shock, the wall boundary layer acts as a mass sink to the inviscid flow [5]. By averaging mass fluxes over the shock tube cross section at different locations, the equivalent one dimensional (1D) volumetric mass source can be used for flow perturbation calculations. Based on Mirels' small perturbation assumption [4], flow properties in region 2 can be inferred by superimposing boundary layer perturbations to the value predicted by ideal shock-jump equations.

In Mirels' turbulent boundary layer theory, the Blasius wall friction relation was used [4]. However, simulations using this relation predict a shock attenuation rate different from our experimental results. The method introduced by Petersen and Hanson [8] was thus implemented to incorporate different wall friction relations into Mirels' model, leading to better agreement with experimental results.

The method of characteristics was used to analyze the spatial and temporal influences of the boundary layer formation on specific points in the core flow. The $x-t$ diagram used for the method of characteristics analysis is shown in Figure 1. (Note that the incident shock propagates from right to left in this coordinate system.) To simplify the calculation, the shock trace and all the characteristic lines on the $x-t$ diagram were assumed to be straight. The overall boundary layer perturbation at a specific point in region 2 can be obtained by summing all the perturbations along the characteristic lines that intersect at that point. Details of Mirels' boundary layer model and the method of characteristics can be found in [4].

In practice, the incident shock speed is typically measured using pressure transducers mounted at multiple axial locations. In order to compare with experimental results, an initial Mach number was specified that leads to the observed shock strength at the test location [6]. For our experimental conditions, the laminar portion of the boundary layer is usually very short and hence it has been assumed in sections 2 and 3 of the paper that the boundary layer is totally turbulent to simplify the calculations.

Using Mirels' model, simulations were carried out to compare with pressure and temperature measurements [9] in the $14cm$ diameter Kinetic Shock Tube (KST) [10] at Stanford University. Calculated flow property results right behind the incident shock, for one specific condition with $M_s = 2.1$ and an attenuation rate of $1.1\%/m$, can be found in Figure 2. The model predicts that temperature and pressure behind

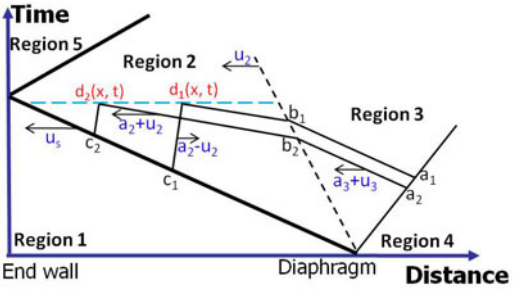

Fig. 1 $x-t$ diagram for shock tube flow; incident shock propagates from right to left

the incident shock decrease as the shock moves toward the end wall with a corresponding decrease in shock strength. As the incident shock travels down the tube, the boundary layer behind the shock grows and the mass sink effects of the layer become more significant, causing the incident shock to slow down.

A snapshot of the property distributions between the shock front and the contact surface, at the time when the shock arrives at the test location (69 cm from the end wall), is shown in Figure 3. Properties are normalized with the respective value right behind the shock (with the subscript *s*). Figure 3 shows that the pressure, temperature and density all decay in value from the contact surface to the incident shock front. Compare two points at the same time but different locations on the $x-t$ diagram (d_1 and d_2 in Figure 1). The boundary layer located within the end points of left and right running characteristic lines in region 2 affects the point we are interested in (boundary layer spatially between b_1 c_1 for point d_1, and between b_2 c_2 for point d_2). For a location closer to the shock front (d_2), the length of the boundary layer affecting that point is longer than that for a location closer to the contact

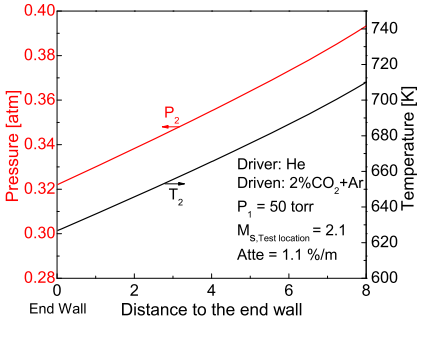

Fig. 2 Pressure and temperature behind the incident shock as a function of shock position

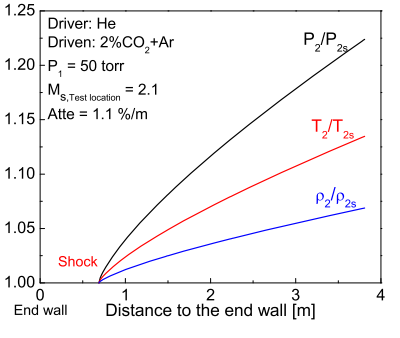

Fig. 3 Snapshot of property distributions in region 2

surface (d_1). Hence the property values at a point closer to the shock front are lower than those at a point closer to the contact surface.

3 Flow Conditions behind the Reflected Shock

Rudinger's method [6] was used to calculate time- and space-varying flow variables in region 5, for the same experimental conditions considered in the previous section. For shocks of moderate strength (M_s around 2), the gas velocity in region 5 and the entropy changes along characteristic lines may be neglected [6]. The flow immediately behind the reflected shock is determined by the upstream conditions (region 2, calculated using Mirels' boundary layer model) and the inferred reflected shock strength, while the flow conditions at other region 5 locations are related to the points behind the reflected shock through characteristic lines.

Temperatures and pressures immediately behind the reflected shock, as the reflected shock propagates from left to right, are shown in Figure 4. The model predicts that both pressure and temperature behind the shock front increase as the shock moves away from the end wall. Because the flow field ahead of the reflected shock is nonuniform, the increase of properties behind the reflected shock does not necessarily indicate that the reflected shock strength increases. Calculations and experiments show that the reflected shock attenuates.

Shown in Figure 5 is a snapshot of the pressure, temperature and density distributions in region 5, when the reflected shock meets the contact surface at $x = 1.2m$. It is evident that pressure, temperature and density are greater further from the end wall. It is thus possible that a combustible mixture could first achieve ignition at a location far from the end wall, instead of closest to the wall as normally be expected.

The simulated pressure time history at the test location 69 cm from the end wall shows that pressure increases continuously with time behind both the incident and reflected shocks, assuming the incident boundary layer is totally turbulent. This result differs from experimental observations. In our experiments, it is often observed

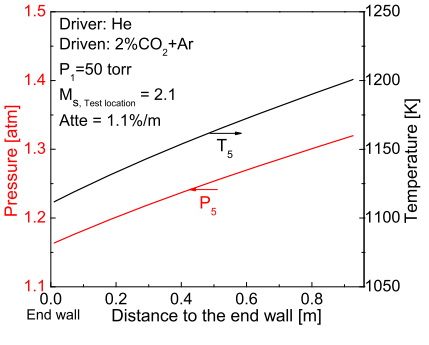

Fig. 4 Pressure and temperature immediately behind the reflected shock as a function of shock position

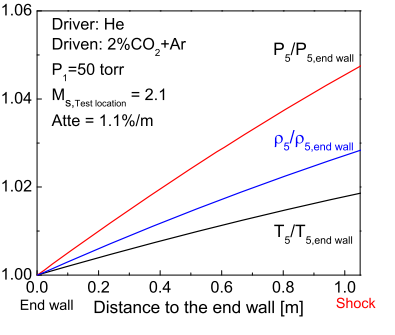

Fig. 5 Snapshot of region 5 property distributions at $t = 2.6ms$ after shock reflection

that the pressure in region 2 drops very slightly before it increases with time, and the pressure in region 5 typically stays at a near constant level for a short time before a subsequent increase in pressure (positive dP_5/dt) is observed (see Figure 6a). The experimental pressure time history can be found in Figure 6a. It is suspected that laminar to turbulent boundary layer transition, neglected in the previous sections, might explain this type of pressure time history.

4 Boundary Layer Transition

In order to add boundary layer transition effects to the original Mirels' model, a transition Reynolds number was defined as $Re_t = (U_s - u_2)(\rho_2/\rho_1 - 1)^2 l_t/\nu_2$ [7]. Ignoring the transition region length, Mirels' laminar and turbulent boundary layer model can be used ahead of and behind the transition point respectively. In this study (M_s around 2.0), Re_t values ranging from 0 (total turbulent boundary layer) to 1×10^6 were tried in an effort to achieve a good comparison with experiment.

A simulated pressure trace considering boundary layer transition is shown in Figure 6 (a), with the corresponding experimental data. It can be seen that pressure behind the incident shock drops slightly before increasing as time increases. This can be explained by the existence of a short laminar boundary layer segment ahead of the turbulent boundary layer. For a total laminar or turbulent layer, at a fixed location for increasing time, the perturbation at this location becomes weaker (see Figure 1), and the pressure increases. For the case with transition, and before the transition point arrives at the test location, as time increases there is an increasing portion of the turbulent layer that influences the test location. The turbulent layer is thicker and has larger mass sink effects than the laminar layer, and the increase of this turbulent portion causes the pressure to drop. After the transition point passes the test location, the pressure will start to rise for the same reasons as in the total

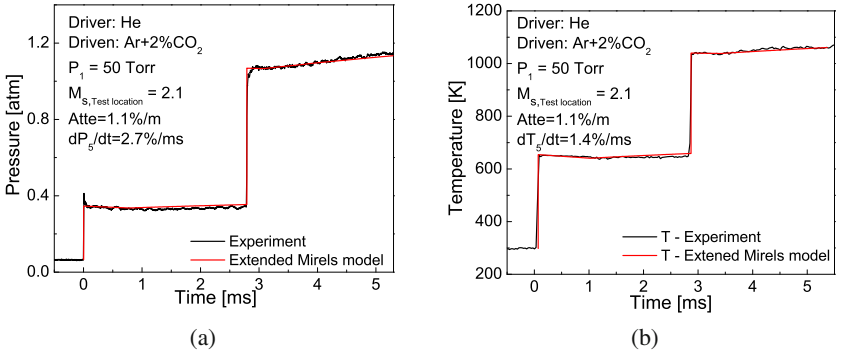

Fig. 6 Measured and simulated pressure (a) and temperature (b) time histories at a fixed location 69 cm from the end wall. The simulations using extended Mirels' model with Spalding-Chi turbulent wall friction relations [8] and a transition Reynolds number of 8×10^5

turbulent boundary layer case. The corresponding temperature measurement of the same shock, using CO_2 absorption near 2.7 μm [9], is shown in figure 6 (b) and compared with the simulated results using our extended Mirels' model. By choosing proper boundary layer wall friction relations and laminar to turbulent transition Reynolds number, simulations are in close agreement with the measured P and T time-histories. The success of this model, in capturing the temperature and pressure time histories, supports use of this boundary layer model in further study of nonideal effects in shock tubes.

5 Concluding Remarks

Mirels' boundary layer theory was extended using Rudinger's method to study shock tube flow variations behind the incident and reflected shock waves in a shock tube. The simulations predict that properties behind the incident shock increase from the shock front to the contact surface. This nonuniformity leads in turn to an increase of property values from the shock tube end wall to the reflected shock wave. Boundary layer transition effects were studied based on a chosen transition Reynolds number. By including boundary layer transition, simulated pressure and temperature at a fixed location behind the incident shock drop very slightly before increasing with time; and behind the reflected shock, pressure and temperature also drop very slightly for a short period, before increasing gradually. These simulations are in good agreement with experiments.

Acknowledgments. This research was supported by the Air Force Office of Scientific Research and the U.S. Department of Energy.

References

1. Petersen, E.L., Hanson, R.K.: Shock Waves 10, 405–420 (2001)
2. Lam, K.Y., Hong, Z., Davidson, D.F., Hanson, R.K.: Proc. Combust. Inst. 1, 251–258 (2010)
3. Hong, Z., Pang, G.A., et al.: Shock Waves 19, 113–124 (2009)
4. Mirels, H.: NACA TN 4021 (1957)
5. Mirels, H.: Boundary layer growth effects in shock tubes. In: Stollery, J.L., Gaydon, A.G., Owen, P.R. (eds.) Shock Tube Research. Proceedings of the Eighth International Shock Tube Symposium, vol. 6, pp. 1–30. Chapman and Hall (1957)
6. Rudinger, G.: Phys. Fluids 4(12), 1463–1473 (1961)
7. Hartunian, R.A., Russo, A.L., Marrone, P.V.: J. Aerospace Sci. 27(12), 587–596 (1960)
8. Petersen, E.L., Hanson, R.K.: AIAA Journal 41(7), 1314–1322 (2003)
9. Ren, W., Jeffries, J.B., Hanson, R.K.: Meas. Sci. Technol. 21, 105603 (2010)
10. Oehlschlaeger, M.A., Davidson, D.F., Hanson, R.K.: J. Phys. Chem. A 108(19), 4247–4253 (2004)

Simulation of a Practical Scramjet Inlet Using Shock-Unsteadiness Model

Amjad Ali Pasha, C. Vadivelan, and Krishnendu Sinha

1 Introduction

The main function of a scramjet inlet is to capture air flow from the incoming hypersonic stream, compress it through a series of shocks or compression waves, and provide uniform flow to the combustor. There should be maximum mass capture along with a minimum stagnation pressure loss in the inlet.

The shock waves in the inlet duct interact with the boundary layer on the walls and can result in flow separation due to strong adverse pressure gradient across the shock wave. The shock/boundary-layer interaction often results in a complex flow pattern, comprising of additional shocks, expansion waves, shear layer and separation bubble. The separation bubbles are highly viscous, and hence increase the stagnation pressure loss. Peak values of pressure, skin friction and heat transfer rates are found at reattachment point. Also, the separation bubble acts as a blockage to the flow inside the inlet duct and can result in inlet unstart. It is therefore important to predict the shock/boundary-layer interactions in a scramjet inlet, including the size of the recirculation region, accurately.

Reynolds-averaged Navier-Stokes methods are commonly used in simulation of practical configurations of engineering interest. However, their accuracy is often limited in shock dominated flows, where conventional turbulence models developed for low-speed flows do not predict the underlying physics correctly. Several modifications have been proposed in literature [1], namely, compressibility correction, realizability constraint, rapid-distortion correction and length-scale correction. Their performance vary from one test case to another.

The flowfield in a shock/boundary-layer interaction is inherently unsteady. Sinha *et al.* [2] found that unsteady shock interaction with incoming turbulence fluctuations dampens the amplification of turbulent kinetic energy. A correction was added to standard one- and two-equation turbulence models to account for this damping

Amjad Ali Pasha · C. Vadivelan · Krishnendu Sinha
Department of Aerospace Engineering, Indian Institute of Technology Bombay, Mumbai-400076, India

effect. The resulting model predictions were found to match DNS data of turbulent kinetic energy amplification across a shock. The shock unsteadiness modification when applied to canonical compression corner [3] and oblique shock impingement flows [4] improved the prediction of flow separation point, and the resulting pressure and skin friction distribution.

In a practical inlet configuration, presence of geometric variations add to the overall complexity of the flowfield. In the absence of experimental data, CFD is often relied upon to predict and improve the performance of scramjet inlets. It is therefore essential to perform detailed CFD simulations of the flowfield inside an inlet duct. The focus of the current work is to study the reflection of the cowl shock and to predict the resulting separation bubble size accurately using the shock-unsteadiness model.

2 Simulation Methodology

We solve two-dimensional Reynolds-averaged Navier-Stokes (RANS) equations. The Spalart-Allmaras (SA) turbulence model with shock-unsteadiness correction [3] is used in the simulations. In-house code [5] based on finite-volume formulation of the governing equations and a modified low-dissipation form of the Steger-Warming flux splitting approach is used. The discretization method is second-order accurate in space. The implicit Data Parallel Line Relaxation method is used to integrate the equations in time and reach a steady-state solution. The code has been validated for several supersonic and hypersonic flow applications [3, 4].

A scramjet inlet of the mixed-compression type is shown in Fig. 1. The geometry consists of two forebody ramps of 10.5° and 21° respectively, followed by three expansion corners, each of 7°, leading to the inlet duct. The forebody shocks and expansion fans are shown in the figure.

The cowl is bent by 6° and results in formation of oblique shocks from the cowl tip and hinge location. The shock/boundary-layer interaction due to the impingement of the cowl and hinge shocks on the opposite wall is marked in the figure.

Freestream conditions of M_∞ = 6.5, temperature = 219.3 K and pressure = 2.16 kPa correspond to an altitude of 26 km. Isothermal (T_w = 300 K), no-slip and

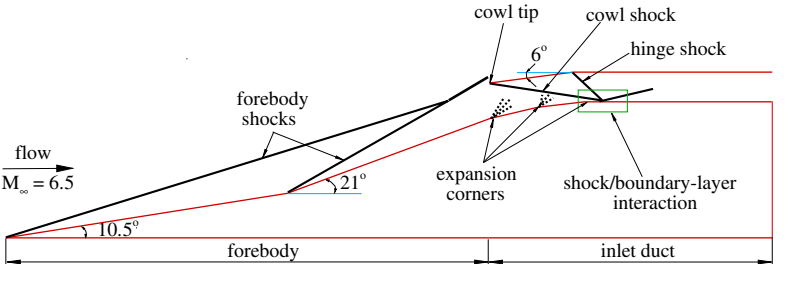

Fig. 1 Geometric configuration with flow schematic for the scramjet inlet.

zero pressure gradient boundary conditions are assigned at solid boundaries. An extrapolation condition is specified at the exit of the inlet duct. Freestream and wall conditions for turbulence model are calculated from the formulations used in Ref. [3].

Based on a separate grid refinement study, a 337×190 mesh is used for the simulation. A wall-normal spacing of 1×10^{-6} m corresponds to about 0.35 wall units on the forebody and less than 1.7 wall units in the inlet duct. CFL numbers up to 1000 are used in the simulation and it takes 40-cpu hours to obtain a steady state solution.

The computed shock-structure inside the inlet duct is shown in Fig. 2a in terms of the normalized mean dilatation contours. The shock structure is similar to that obtained in the interaction of an incident oblique shock with a flat plate boundary layer, shown in Fig. 2b. The incident shock, separation shock, induced shock, transmitted shock and reflected shock follow the same pattern in the two flows. The differences are the additional shock generated by the hinge and the reflection of the induced shock from the top wall. These are not present in the isolated shock impingement case shown in Fig. 2b.

The impingement of an incident oblique shock on a turbulent boundary layer developed on a flat-plate is studied experimentally in Ref. [7]. Measurements are taken in the shock/boundary-layer interaction region for 14° shock generator at Mach 5. The variation of surface pressure in the interaction region is plotted in Fig. 3 where the initial pressure rise at $x \approx -38$ mm represents the separation location. It is apparent that the standard SA model predicts a delayed separation ($x \approx -20$ mm) as compared to the experiment. The shock-unsteadiness correction reduces the turbulent eddy viscosity at the separation shock and thus enhances flow separation.

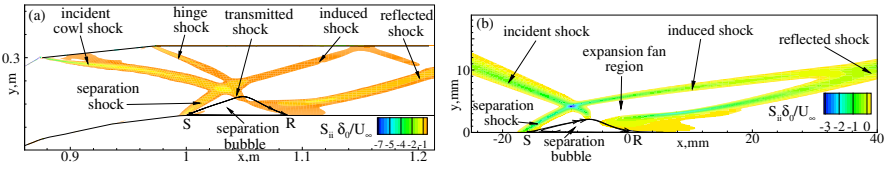

Fig. 2 Normalized dilatation contours identifying shock regions in (a) the inlet duct and (b) oblique shock/boundary-layer interaction with deflection angle of 14° at Mach 5.

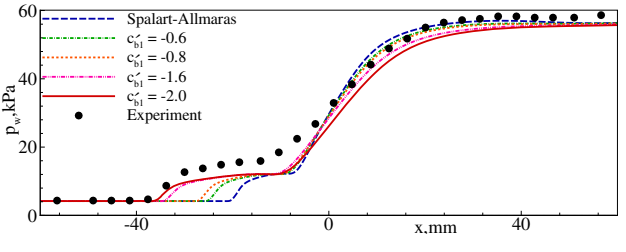

Fig. 3 Computed wall pressure using standard SA model [6] and shock-unsteadiness modified SA model [3] with deflection angle of 14° and $M_\infty = 5$, compared with experiments [7].

Solutions computed using different values of the shock-unsteadiness parameter c'_{b_1} are also plotted in Fig. 3. A higher magnitude of c'_{b_1} yields a larger separation, and c'_{b_1} = -2.0 is found to match the experimental separation location closely. This value of the shock-unsteadiness parameter is found to match the separation location for a range of shock strengths and therefore it is used in the study of cowl shock impingement.

3 Flowfield and Wall Data

Figure 4 shows the flowfield in the inlet duct in terms of computed pressure contours. The cowl shock and hinge shock impinge on the turbulent boundary layer on the vehicle wall and form a recirculation region. A separation shock is formed at the separation point and a shear layer develops over the separation bubble. Intersection of the separation and incident shocks generate the induced and transmitted shock waves. The flow turns over the separation bubble to generate an expansion fan. The compression waves generated by flow reattachment coalesce to form the reflected shock. There are multiple reflections of shocks and expansion waves in the duct.

The surface pressure and skin-friction coefficient along the inlet bottom wall is shown in Fig. 5. The wall pressure drops across the two expansion corners at x = 0.86 m and x = 0.94 m. The expansion fan at the third expansion corner is cancelled by the separation shock. Pressure rises at flow separation, remains approximately constant

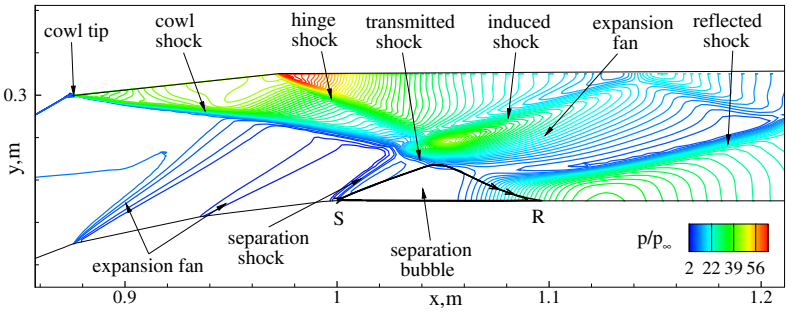

Fig. 4 Distribution of computed pressure, normalized by freestream pressure, inside the inlet duct.

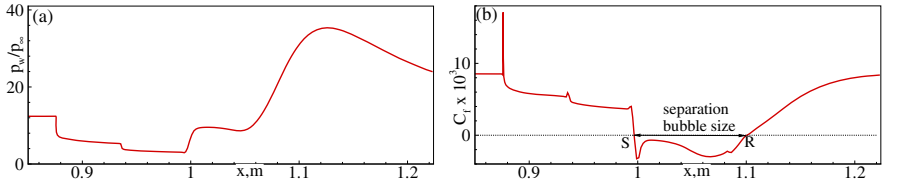

Fig. 5 Computed (a) normalized wall pressure and (b) skin-friction coefficient on the inlet duct bottom wall.

along the separation bubble and rises to peak values in the reattachment region. The skin friction data shows a large negative region between the separation (S) and reattachment (R) points. The separation bubble is 104 mm long in the streamwise direction and extends to about one third of the duct height.

The computed separation bubble size is compared with available experimental data to ascertain the accuracy of the results. In the absence of experimental data for the current geometry, the data reported by Schulein [7] is used for validation. Specifically, the size of the separation bubble predicted in the inlet duct is compared with those reported in the oblique shock impingement experiments. The variations due to differences in the inflow conditions are accounted for three cases reported in Ref. [7], which correspond to shock generator angles of 14°, 10° and 6° placed in a Mach 5 flow. By comparison, the flow conditions at the entrance of the inlet duct correspond to a Mach number of 3.4, density of 0.089 kg/m^3 and temperature of 382.2 K. These are the inviscid conditions downstream of the forebody ramp shock.

The extent of flow separation in a shock/boundary-layer interaction mainly depends on the shock strength and the Reynolds number of the flow. A stronger incident shock wave results in a larger separation bubble and vice versa. On the other hand, a higher Reynolds number results in a higher level of turbulence. This in turn leads to a fuller boundary layer profile, thus resulting in delay of flow separation. Also, the separation bubble size is found to scale with the boundary layer thickness upstream of the interaction. These parameters are listed for the current configuration and for the three test cases of Schulein [7] in Table 1.

Deflection of a Mach 3.4 flow by the cowl shock results in a pressure rise of 11.34. A comparison of the inviscid pressure rise values places the shock/boundary-layer interaction in the inlet duct between the experimental test cases 1 and 2. The recirculation bubble in the inlet duct is however much larger than those reported in the experiments. This is because of a thicker boundary layer than that in the experimental cases. On normalizing the separation bubble size with the incoming boundary layer thickness, the simulation results compare well with the experimental data. From above analysis, $\Delta s/\delta_0 = 4.58$ for the inlet duct lies in between the experimental test cases 1 and 2.

Table 1 Comparison of flow parameters between the scramjet inlet configuration and oblique shock impingement cases [7].

Parameters	Inlet	Oblique shock impingement		
		case-1	case-2	case-3
Free stream Mach number, M_∞	3.4	5	5	5
Deflection angle, θ°	15	14	10	6
Inviscid incident shock strength, p_2/p_1	11.34	13.62	7.63	3.76
Unit Reynolds number, $Re_{1\infty} \times 10^7$, m^{-1}	0.74	3.7	3.7	3.7
Upstream boundary layer thickness, δ_0, mm	22.7	4.66	4.66	4.66
Separation bubble size, Δs, mm	104	34	12	-
Normalized separation bubble size, $\Delta s/\delta_0$	4.58	7.30	2.58	-

4 Conclusions

Reynolds-averaged Navier-Stokes simulations are performed for a practical scramjet inlet geometry at Mach 6.5 and the focus is the shock/boundary-layer interaction generated by cowl shock impingement on the opposite wall. The flow is similar to the canonical oblique shock/boundary-layer interaction. The geometry of the inlet generates additional shocks and expansion waves and adds to the complexity to the flowfield. The shock-unsteadiness modified Spalart-Allmaras model is used in the simulations and the model parameter is calibrated against experimental data for canonical oblique shock/boundary-layer interactions. The simulations predict a large separation bubble inside duct and its size is validated against available experimental data for canonical flow configurations.

Acknowledgment. The authors thank Indian Space Research Organization (ISRO) for supporting this research under the RESPOND programme.

References

1. Roy, C.J., Blottner, F.G.: Review and Assessment of Turbulent Models for Hypersonic Flows. Progress in Aerospace Sciences 42(7-8), 469–530 (2006)
2. Sinha, K., Mahesh, K., Candler, G.V.: Modeling Shock Unsteadiness in Shock/Turbulence Interaction. Physics of Fluids 15(8), 2290–2297 (2003)
3. Sinha, K., Mahesh, K., Candler, G.V.: Modeling the Effect of Shock-Unsteadiness in Shock/Turbulent Boundary-Layer Interactions. AIAA Journal 43(3), 586–594 (2005)
4. Pasha, A.A., Sinha, K.: Shock-Unsteadiness Model Applied to Oblique Shock-Wave/Turbulent Boundary-Layer Interaction. International Journal of Computational Fluid Dynamics 22(8), 569–582 (2008)
5. Sinha, K., Candler, G.V.: Convergence Improvement of Two-Equation Turbulence Model Calculations. AIAA Paper, 98-2649 (June 1998)
6. Spalart, P.R., Allmaras, S.R.: A One-equation Turbulence Model for Aerodynamic Flows. AIAA Paper, AIAA-92-0439, Reno, NV (January 1992)
7. Schulein, E.: Optical Skin Friction Measurements in Short-duration Facilities. AIAA Journal 44(8), 1732–1742 (2006)

Part XVIII
Shock Propagation and Reflection

Consideration of von Neumann Reflection and Mach Reflection for Strong Shock Waves

S. Kobayashi and T. Adachi

1 Introduction

Oblique shock reflection phenomena have been long considered to preserve self-similarity. However, the authors' investigation of von Neumann reflection [1] was a turning point that cast doubt on self-similarity. The von Neumann reflection is a new type of oblique reflection first referred to by Colella and Henderson [2]. This reflection is geometrically characteristic in that a Mach stem is tangentially connected with an incident shock at a triple point. Furthermore, its reflected wave is very weak and a slipstream is barely optically observable (Fig. 1 (a)), and stands in contrast to ordinary Mach reflection (Fig. 1 (b)). This reflection takes place when the incident shock Mach number M_i and/or the reflecting wedge angle θ_w are small. According to Colella and Henderson [2], von Neumann reflection exhibits the von Neumann paradox. For weak shock waves, Kobayashi et al. [1, 3] found that, as the incident shock proceeds, the wave angles vary along a trivial solution curve of von Neumann's three-shock theory, while the triple point moves along a straight line passing through the wedge apex as if self-similarity holds. Further investigations [4] revealed experimentally that oblique shock reflection in a shock tube is generally non-self-similar, even though the triple-point trajectory is linear. This non-self-similarity is a new idea requring reconsideration of the von Neumann paradox.

In the early period of the investigation, the transition criterion between Mach and von Neumann reflection was a point of issue [5, 6]. It is quite reasonable to consider that there might be some criterion that discriminates the two reflections, just as in the case for regular and Mach reflections. The classical idea of transition is based on the pseudo-steadiness of shock-reflection phenomena, i.e., the reflection configuration is determined by three dimensionless parameters, M_i, θ_w, and the specific heat ratio κ. However, according to Kobayashi et al. [1, 3], the von Neumann reflection is neither pseudo-steady nor self-similar, and thus the transition criterion had to be

S. Kobayashi · T. Adachi
Department of Mechanical Engineering,
Saitama Institute of Technology, Fusaiji, 369-0293 Saitama Institute of Technology (Japan)

reconsidered. A conspicuous case is the dynamic transition [7, 8, 9] that occurs when θ_w is slightly below the transition wedge angle, in which regular reflection becomes Mach reflection during propagation. This dynamic transition suggests that Mach reflection might not be observed because it does not become well-developed when the wedge length is short. This phenomenon explains the von Neumann paradox of the first kind in which regular reflection persists for an incidence angle where it is theoretically impossible.

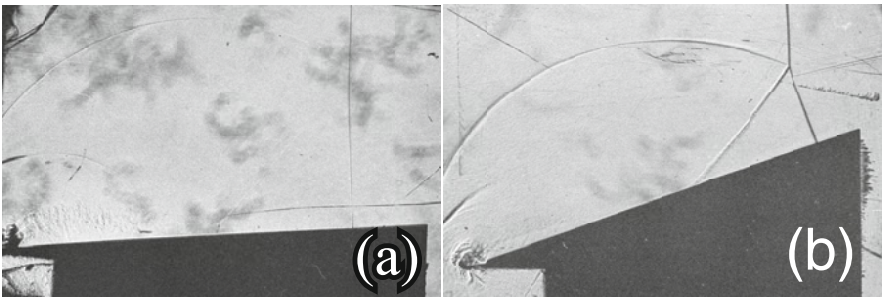

Fig. 1 Shock reflection configuration for $M_i = 1.915$. (a) $\theta_w = 5.93°$, $x = 67.5$mm. (b) $\theta_w = 19.33°$, $x = 61.3$mm.

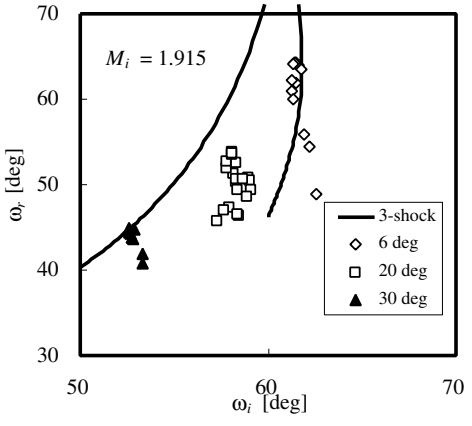

Fig. 2 Relation between angles of incidence and reflection ($M_i = 1.915$).

According to the authors' investigation of strong Mach reflection [10], the wave angles do not agree with the three-shock theory in an early stage of reflection (the von Neumann paradox), but they approach the theory as the incident wave propagates, and the paradox is resolved in the end (see Fig. 2 for $\theta_w = 29.12°$; angles in the legend are rounded). For a smaller wedge angle, $\theta_w = 19.33°$, the wave angles

approach the theory but the paradox is not resolved. For $\theta_w = 5.93^\circ$, von Neumann reflection occurs. In this case, the wave angles are not constant and, except for an early stage of reflection where the error due to wave thickness is large, they vary almost along a trivial solution branch of the three-shock theory toward an asymptotic state where the reflected wave is a sound wave (Fig. 2). However, for intermediate incidence angles, the three-shock theory gives a large reflection angle and it seems difficult to attain such a value. The authors had a question: What would happen when the reflecting wedge angle θ_w lies in between these angles? It seems that the theoretical value is far greater under these conditions and is difficult to attain. In the present study, we carried out a series of experiments using reflecting wedge angles between the Mach and von Neumann reflections and investigated the behavior of the various wave angles.

2 Experiment

2.1 Apparatus

A conventional shock tube at the authors' institute was used; details are given in Kobayashi et al. [3]. To generate a strong shock wave, the driver gas was *He* at high pressure and the driven gas was air at room temperature and atmospheric pressure. The incident shock Mach number M_i was 1.915 ± 0.005, meaning that only data for $1.910 < M_i < 1.920$ were utilized. The reflecting wedge angle θ_w was 14.90°.

2.2 Measurement

The triple-point coordinate (x, y) and the angle ω_{ir} made by the incident and reflected shocks at the triple point were measured directly from photographic negatives enlarged by a factor of fifty using a profile projector (V-12, Nikon, Inc.). The triple-point location was first measured in the coordinate system (ξ, η), where ξ is the abscissa along the wedge surface, and η is the ordinate perpendicular to it, with the wedge apex taken as the origin O (Fig. 3).

3 Results

3.1 Mach Stem Near the Triple Point

Figure 4 presents visualized wave configurations around the triple point for various reflecting wedge angles. One of the characteristics of von Neumann reflection is that the Mach stem is tangentially connected with the incident shock, as seen in Fig. 4 (a) for $\theta_w = 5.93^\circ$. Figure 4 (c) depicts a typical Mach reflection, in which the incident shock and the Mach stem make a corner ($\theta_w = 29.12^\circ$). For an intermediate angle $\theta_w = 14.90^\circ$, the Mach stem is curved near the triple point, but makes a small angle with the incident shock. This means that the reflection is not von Neumann

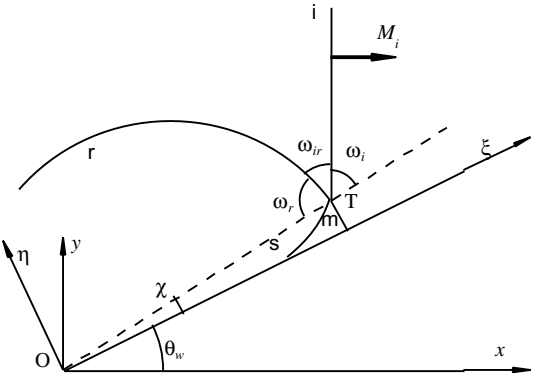

Fig. 3 Coordinate system and nomenclature.

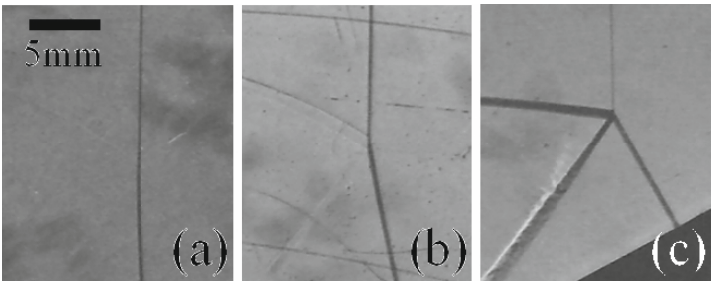

Fig. 4 Enlargement near the triple point for $M_i = 1.915$. (a) $\theta_w = 5.93°$, $x = 59.65$mm. (b) $\theta_w = 14.90°$, $x = 60.21$mm. (c) $\theta_w = 29.12°$, $x = 56.42$mm.

type. The reflection configuration in Fig. 4 (b) has been considered to be a Mach reflection, but the Mach stem near the triple point is obviously different from that in Fig. 4 (c).

3.2 Triple-Point Trajectory

Figure 5 plots the location of triple point over the model wedge for $\theta_w = 14.90°$, and good linearity is evident. The slope of the least-squares approximation line is 29.76°, which corresponds to $\chi + \theta_w$. The error in the incidence angle ω_i due to wave thickness is as large as 5° near the wedge apex (0mm $< x <$ 10mm). Self-similarity is not ensured by the linearity of the triple-point trajectory alone, as discussed in the next section.

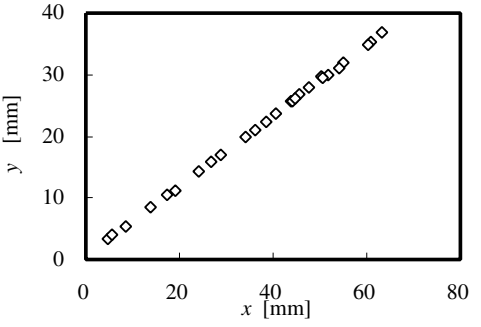

Fig. 5 Location of the triple point ($M_i = 1.915$, $\theta_w = 14.90°$).

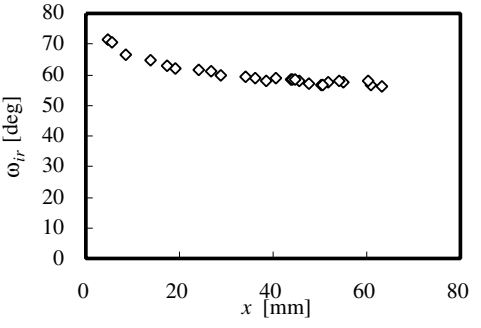

Fig. 6 Variation of the wave angle ($M_i = 1.915$, $\theta_w = 14.90°$).

3.3 Variation of Wave Angle

Figure 6 presents the variation of the angle ω_{ir} made by the incident and reflected shocks for $\theta_w = 14.90°$. In the early stage of reflection, the rate of change is large, but it diminishes as the incident wave proceeds. There seems to be some asymptotic value. The angle ω_{ir} is independent of a reference line such as the triple-point trajectory, and thus Fig. 6 proves non-self-similarity.

3.4 Relation between Angles of Incidence and Reflection

The experiment data for $\theta_w = 10.03°$ and $\theta_w = 14.90°$ are added to Fig. 2 and appear in Fig. 7. Due to wave thickness, the error in ω_i and ω_r near the wedge apex is very large. These are circled in Fig. 7. Except for these data, for $\theta_w = 14.90°$, the reflection angle increases but the discrepancy with the three-shock theory is still large (the three-shock theory gives $\omega_r = 75.20°$ for $\omega_i = 60.24°$). How such a discrepancy is supported physically is a point of issue. Kobayashi et al. [10]

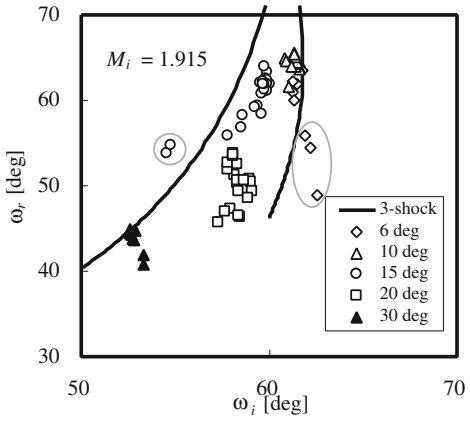

Fig. 7 Relation between angles of incidence and reflection.

indicated that it could be explained by supposing a small quantity of slipstream divergence δ.

4 Conclusion

We conducted a series of strong-shock reflection experiments for various wedge angles. For all cases, the wave angles vary as the incident shock proceeds, and thus the reflection configuration is not self-similar. For large wedge angles, the wave angles approach the three-shock theory, and the paradox is resolved in the end. For small wedge angles, the wave angles vary almost along the trivial solution curve of the three-shock theory. For intermediate wedge angles, although the wave angles seem to approach some asymptotic values, the paradox is not resolved. In the case of intermediate wedge angles, the Mach stem is curved near the triple point but the reflection is not von Neumann type. Our results suggest that a reflection whose Mach stem is curved near the triple point should be discriminated from Mach reflection.

References

1. Kobayashi, S., Adachi, T., Satoh, M., Suzuki, T.: On the Formation Mechanism of von Neumann Reflection. In: Proc. Int. Shock Wave Symp., vol. 21, pp. 881–885 (1997)
2. Colella, P., Henderson, L.F.: The von Neumann Paradox for the Diffraction of Weak Shock Waves. J. Fluid. Mech. 213, 71–94 (1990)
3. Kobayashi, S., Adachi, T., Suzuki, T.: Non-self-similar Behavior of the von Neumann Reflection. Phys. Fluids 12(7), 1869–1877 (2000)
4. Kobayashi, S., Adachi, T., Suzuki, T.: Non-self-similar Characteristics of Weak Mach Reflection: the von Neumann Paradox. Fluid. Dyn. Res. 35, 275–286 (2004)

5. Sasoh, A., Takayama, K., Saito, T.: A Weak Shock Reflection over Wedges. Shock Waves 2(4), 277–281 (1992)
6. Sasoh, A., Takayama, K.: Characterization of Disturbance Propagation in Weak Shock-wave Reflection. J. Fluid. Mech. 277, 331–345 (1994)
7. Itabashi, S., Henderson, L.F., Crutchfield, W.Y., Takayama, K.: Effetcs of Viscous and Thermal Dissipation on the Eruption of Mach Reflection on Rigid Steel Ramps. In: Proc. Int. Shock Wave Symp., vol. 21, pp. 887–891 (1997)
8. Kobayashi, S., Adachi, T.: Unsteady Behavior in the Transition Phenomenon of Shock Reflection Nagare. J. Japan Society Fluid. Mechanics 18, 387–390 (1999) (in Japanese)
9. Kobayashi, S., Adachi, T., Suzuki, T.: On the Unsteady Transition Phenomenon of Weak Shock Waves. Theoret. Appl. Mech. 49, 271–278 (2000)
10. Kobayashi, S., Adachi, T., Suzuki, T.: The von Neumann Paradox for Strong Shock Waves. In: Proc. Int. Shock Wave Symp., vol. 27, pp. 1539–1542 (2007)

Study of Shock-Wave Mitigation through Solid Obstacles

A. Chaudhuri, A. Hadjadj, O. Sadot, and G. Ben-Dor

1 Introduction

The physical understanding and modeling of shock mitigation are important for the development of an effective barrier arrangement related to disaster management. While it is not currently feasible to simulate and analyze full configurations in detail, sufficient progress has been made to analyze the dynamics of simpler building block flows that provide useful insights into the underlying dynamics of these complex flows. Also, apart form the experimental study, numerical simulation has become quintessential tool for prediction of complex physics in solid/fluid interaction problems. Several authors dealt with experimental or numerical approaches in order to study the unsteady shock wave interaction with multiple obstacles, such as cylinders, spheres and triangular prisms [1, 2, 3, 4]. According to the recent findings of [5], the influence of different geometrical shapes on shock-wave attenuation is negligible for higher open passage. However, this finding requires a systematic study of the effects of different parameters for lower values of the open passage. In our previous works [6, 7], excellent agreement between experimental and numerical results is obtained for the case of shock-wave interaction with single cylinder and triangular prism. These validations prove the reliability of the computational techniques used for the present study. It is being observed that after the passage of the shock through the obstacle matrix, eddies of different length scales are generated, but the later stage of shock-vortex, shocklet-vortexlet interaction are different for inviscid and viscous computations [8]. We carried out several preliminary test cases with cylinder matrix configuration to investigate i) the effect of the variation of the open passage (or porosity). The open passage is defined as $\varepsilon = 1 - \sum_{i=1}^{N_c} (D_i/L_y)$ and the porosity is given by $\varphi = \mathscr{V}_v/\mathscr{V}_t$, where N_c is the number of cylinder in a column, D_i's are the diameters of the cylinders, $\mathscr{V}_t$ is the total volume and $\mathscr{V}_v$ is the void volume. ii) the number of cylinders in a column of obstacles,

A. Chaudhuri · A. Hadjadj
INSA of Rouen, CORIA UMR 6614 CNRS, 76801 Saint-Etienne du Rouvray, France

O. Sadot · G. Ben-Dor
Ben-Gurion University of the Negev, Dept. Mech. Eng., Beer Sheva, Israel

iii) the relaxation length between two consecutive columns, iv) the number of columns. The usual trend of pressure attenuation and speed of the transmitted shocks are found by the simulations (for a given obstacles arrangement at lower ε (or φ), the pressure attenuation as well as the speed of the reflected shock are higher, while the speed of the transmitted shock is lower). It has also been found that, the reduction of the speed of the transmitted shock can become significant with the increase of the number of cylinders in a column of obstacles for lower ε. Similar results of shock attenuation have been reported by Suzuki *et al.* [9], for higher porosity cases, by varying the diameter of the cylinder. It is important to note that, although this fact appears to be contradictory with the usual effects of variation of porosity, the effects of transverse waves are evidently important in the cases of more cylinders. It can be concluded that the evolution of transverse waves produces drag effects on the speed of the axial shock front. At low open passage ($\varepsilon \leq 0.25$), we compared the three different 6×4 matrix configurations with the variation of the relaxation length λ_x (distance between two consecutive columns). Although the reduction in speed of the transmitted shock is found to be insignificant for these cases, the pressure attenuation shows the following trend; $\lambda_x = 0.7D < \lambda_x = 2.4D < \lambda_x = 4.1D$. This obviously reflects the importance between the interaction of the moving shock and the transverse waves in terms of pressure attenuation.

The present paper focuses on the geometrical aspects of the matrix like barrier with lower open passage for shock mitigation. The paper is organized as follows. In section 2, brief descriptions of the numerical solver as well as the flow configuration are given. Results for various geometrical configurations are presented and discussed in section 3. Finally, conclusions are drawn in section 4 along with recommendations for future investigations in this area.

2 Numerical Method and Problem Setup

An in-house compressible Navier-stokes flow solver equipped with a fifth-order WENO scheme and an immersed boundary method [10] is used to simulate the interaction of shock waves with rigid obstacles. The ghost fluid based direct forcing methodology is adopted for this purpose. We carried out 2D viscous computations for all the cases presented in this paper. Detailed description of the applied methodology is presented in our previous work [6]. Series of different benchmark problems are solved to validate the developed solver. Based on our previous experience, the simulations are carried out on an uniform mesh using $\Delta x \approx 60\,\mu$m to ensure grid independent solution.

A rectangular domain of size 400 mm$\times$46.7 mm is taken as computational domain. The width of the computational domain, L_y, is similar to the experimental shock-tube dimension reported in [9]. The leading point of the first column of the 4×4 obstacle matrix is located at 160.6 mm. The relaxation length λ_x is taken as 10 mm. Transient flow-field data are recorded for downstream (70 mm) and upstream (300 mm) probes for analysis of the physics of the complex flow. We have also recorded the centerline density field to track the speed of the reflected and

transmitted shock waves. In order to avoid shock-boundary layer interactions, top and bottom boundaries are treated as symmetry planes. Computations are stopped before the reflected and transmitted waves reach the domain boundaries (left/right). At time $t = 0$, the position of the shock is considered at the leading edge of the first column of the obstacles. The initial flow discontinuities for the shocked gas (left state, subscripted as "2") and the stagnant gas (right state, subscripted as "1") are specified using the Rankine-Hugoniot relation. Seven test cases of 4×4 matrix configuration are formulated with various obstacle geometries and arrangements while keeping $\varepsilon = 0.25$. The first four cases are having non-staggered arrangement of obstacles (C_1 : square prism , C_2: cylinder C_3: triangular prism C_4: reverse triangular prism) and rest of the cases are arranged in a staggered manner (C_{1S} : staggered square prism , C_{2S}: staggered cylinder, C_{4S}: staggered reverse triangular prism). In order to keep a constant ε, the diameters of the cylinders, the dimension of bases of the triangular prisms (wedge angle 30°*degrees*) and the dimensions of box prisms are taken as 8.8 mm.

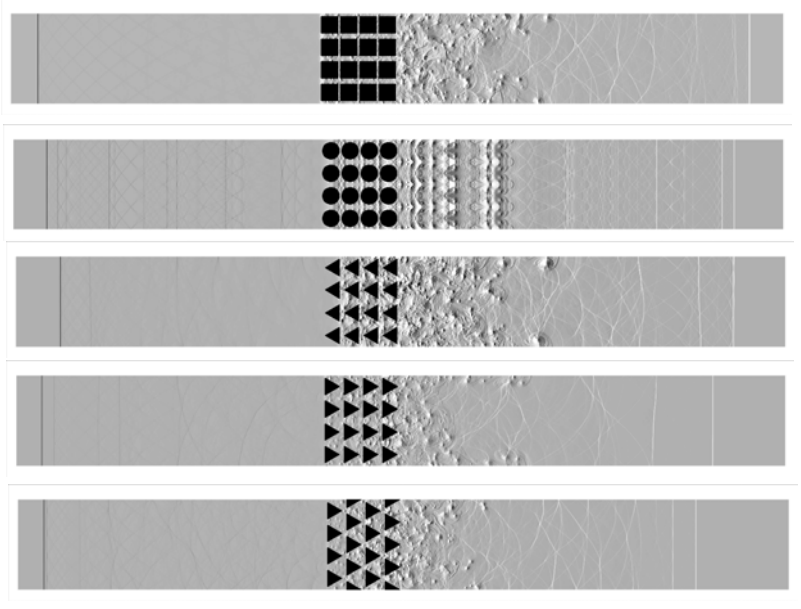

Fig. 1 Numerical schlieren for different test cases (C_1, C_2, C_3, C_4 and C_{4S}, from top to bottom).

3 Results and Discussion

Numerical schlieren pictures at time $t = 500\,\mu$s are shown in Fig. 1. A careful examination of the locations of the transmitted shock fronts of these figures reveals that the staggered arrangement of the obstacles are advantageous in terms of reduction of the shock speed traversing through the obstacle matrix.

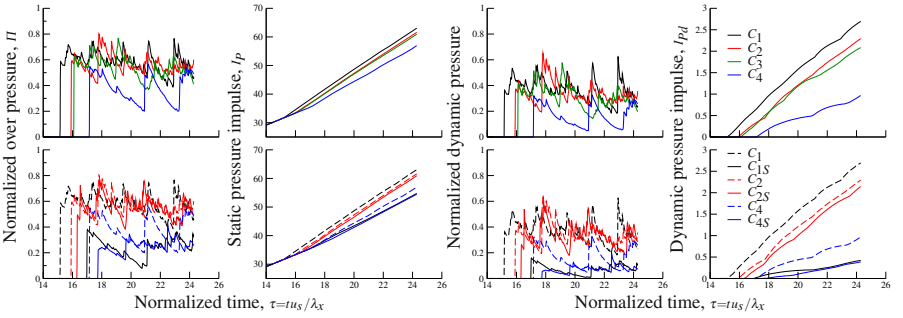

Fig. 2 Pressure evolution at downstream probe, dynamic pressure p_d is normalized by p_{d2}. The normalized over-pressure is given by $\Pi = (p - p_1)/(p_2 - p_1)$. Static and dynamic pressure impulses are defined as $I_P = \int_{t_0}^{t_f} p\,dt$ and $I_{Pd} = \int_{t_0}^{t_f} \frac{1}{2}\rho \mathbf{u}^2\,dt$, respectively.

The downstream signals are important in terms of pressure attenuation for different barrier arrangements. Fig. 2 shows both static and dynamic pressure impulses, along with the corresponding normalized signals. It appears that case C_4 is the most favorable among the non-staggered arrangements of matrices. The initial peak pressure as well as the impulses are least for C_4 when compared with C_1 to C_3. The effect of non-staggered arrangement is visible in the bottom plots of Fig. 2. Also, one can observe that the first peak pressures as well as the impulses for the cases C_{1S}, C_{2S} and C_{4S} substantially get reduced when compared to their corresponding non-staggered counterpart C_1, C_2 and C_4, respectively. The level of pressure attenuation appears closely similar for cases C_{1S} and C_{4S}. As mentioned before, the centerline transient data are utilized to retrieve the relevant speeds of the principal shock waves. Fig. 3 shows the variation of the reflected (x_R) and transmitted (x_T) shock fronts in time. After an initial nonlinear evolution, the reflected shock moves at a constant velocity as shown in this figure. This is true for the evolution of transmitted shock as well. However, due to the presence of multiple transverse wave interactions just downstream of the shock front, the tracked shock front appears little wiggly sometimes. We presented the linear fit of the tracked locations for transmitted wave in Fig. 3. Table. 1 summarizes the extracted properties for all test cases.

It can be seen, from table 1, that u_T/a_1 is least for case C_{4S} and it reduces from 1.4 to 1.11. The lowest normalized velocity of the reflected shock u_R/a_1 for case C_3 also corroborates the observed upstream pressure signals (figure not shown). The calculated pressure impulses during the relevant time duration also reflect the suitability of staggered reverse triangular prism agreement as a most effective barrier configuration among the considered cases.

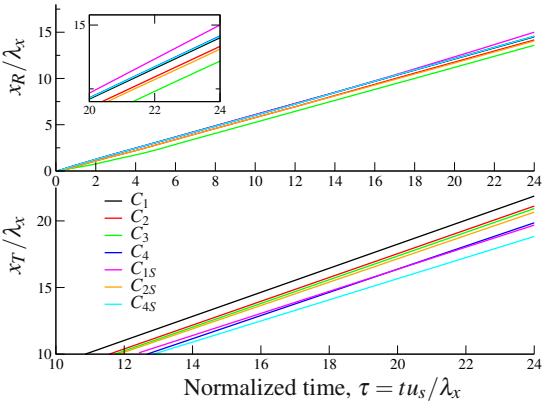

Fig. 3 Evolution of reflected and transmitted shock fronts.

Table 1 Comparison of different parameters for all test cases. The mean pressure, $\bar{p} = \frac{1}{\Delta T}\int_{t_0}^{t_f} p\,dt$, is integrated over a time interval $\Delta T = (t_f - t_0)$, where t_0 is the time when the shock arrived at the probe location, and t_f is a given final time taken as 500 μs.

Case	C_1	C_2	C_3	C_4	C_{1S}	C_{2S}	C_{4S}
φ	0.32	0.46	0.70	0.70	0.32	0.46	0.70
u_R/a_1	0.84	0.83	**0.82**	0.85	**0.87**	0.83	0.85
u_T/a_1	1.26	1.25	1.25	1.22	1.16	1.23	**1.11**
$\Delta T \approx 0.2$ s							
I_P (N s m^{-2})	63.06	61.60	60.95	**56.95**	**54.75**	60.92	**54.48**
I_{Pd} (N s m^{-2})	2.69	2.29	2.08	**0.97**	**0.42**	2.14	**0.39**
$\overline{p}/p_2$	0.78	0.77	0.76	0.67	**0.60**	0.76	**0.60**

4 Conclusions

In this paper, we report a numerical study of shock wave interaction with matrix of different geometrical obstacles for $\varepsilon = 0.25$ with $M_s = 1.4$ and $Re \approx 1.1 \times 10^5$. The computations highlight the essential flow features of the complex shock/obstacle interactions. The analysis of the downstream pressure signal reveals the behavior of the principal shock waves in relation with the overall attenuation of the barrier configurations. Based on the present investigation, the following conclusions are drawn i) there exists an influence of the geometry at low opening passage of the barrier configuration, ii) among the non-staggered formulations, reverse triangular prism matrix arrangement (C_4) shows $\approx 13\%$ of reduction in the speed of the transmitted shock with $\approx 30\%$ of pressure attenuation. Subsequently, this arrangement produces least impulses compared to other non-staggered arrangements, iii) staggered arrangements of obstacles favor overall performance towards shock wave mitigation, iv) among all the reported test cases, the reverse triangular prism, with

staggered arrangement (C_{4S}), is the most effective in terms of shock attenuation. We observed $\approx 21\%$ reduction in speed of the transmitted shock and $\approx 40\%$ pressure attenuation for this arrangement. Although, the overall performance of staggered box prism arrangement (C_{1S}) is comparable to C_{4S}, it can be realized that the porosity of the latter case is maximum. This additionally makes the performance of C_{4S} as superior over C_{1S}. Further investigations will concern the effectiveness of barrier configurations having combinations of geometrical shapes/arrangements, as well as the extension of the above findings to higher M_s.

References

1. Skews, B.W., Draxl, M.A., Felthun, L., Seitz, M.W.: Shock wave trapping. Shock Waves 8, 23–28 (1998)
2. Sasoh, A., Matsuoka, K., Nakashio, K., Timofeev, E., Takayama, K., Voinovich, P., Saito, T., Hirano, S., Ono, S., Makino, Y.: Attenuation of weak shock waves along pseudo-perforated walls. Shock Waves 8, 149–159 (1998)
3. Ball, G.J., East, R.A.: Shock and blast attenuation by aqueous foam barriers: influences of barrier geometry. Shock Waves 9, 37–47 (1999)
4. Britan, A., Karpov, A.V., Vasiev, E.I., Igra, O., Ben-Dor, G., Shapiro, E.: Experimental and numerical study of shock wave interaction with perforated plates. J. of Fluids Engineering 126, 399–409 (2004)
5. Berger, S., Sadot, O., Ben-Dor, G.: Experimental investigation on the shock-wave load attenuation by geometrical means. Shock Waves 20(1), 29–40 (2010)
6. Chaudhuri, A., Hadjadj, A., Chinnayya, A.: On the use of immersed boundary methods for shock/obstacle interactions. J. Comput. Phys. 230, 1731–1748 (2011)
7. Sadot, O., Glazer, E., Ben-Dor, G., Britan, A., Chaudhuri, A., Hadjadj, A.: Study on the shock-cylinder interaction. In: 19th Int. Shock Interaction Symp., Moscow (2010)
8. Chaudhuri, A., Hadjadj, A., Sadot, O., Ben-Dor, G.: Numerical study of moving shock waves interacting with array of cylinders. In: 19th Int. Shock Interaction Symp., Moscow (2010)
9. Suzuki, K., Himeki, H., Watanuki, T., Abe, T.: Experimental studies on characteristics of shock wave propagation through cylinder array. The Institute of Space and Astronautical Science Report No. 676 (March 2000)
10. Peskin, C.S.: Flow patterns around heart valves: a digital computer method for solving the equations of motion, PhD thesis. Albert Einstein Coll. Med. Univ. Microfilms 378, 30–72 (1972)

Guderley Reflection for Higher Mach Numbers in a Standard Shock Tube

André Cachucho and Beric Skews

1 Introduction

To resolve the von Neumann paradox, Guderley (1947) proposed a four-wave structure, consisting of an expansion fan in addition to the three shock wave configuration [1]. Despite intensive experimental work at the time, no evidence of this expansion fan was observed, therefore dismissing Guderley's proposal. Experimental work conducted by Skews and Ashworth [2] with the use of a large-scale shock tube showed experimentally for the first time that Guderley's proposal was, in fact, correct.

It is known that the size of the supersonic region behind the triple point is proportional to the length of the Mach stem [3]. Hence, a large-scale shock tube was thus necessary to produce weak Mach reflections with Mach stem lengths of approximately 0.8 m. The large scale Mach reflections allowed the four-wave structure consisting of the expansion wave emanating from the triple point to be observed. This rare shock wave reflection was consequently named the Guderley reflection (GR). Further experimental work by Skews et al. [4] yielded improved evidence that there were at least two supersonic patches along the Mach stem, shown in Fig. 1(a). This validated the numerical results of Tesdall et al. [3] which showed a sequence of supersonic patches along the Mach stem, shown in Fig. 1(b).

The observation in Fig. 1(a) required the use of a specially constructed shock tube (large-scale, height of 1.10 m), but the present study finds a novel and practical method to observe the GR using a standard shock tube (small-scale, height of 0.45 m).

André Cachucho · Beric Skews
School of Mechanical, Industrial and Aeronautical Engineering, University of the Witwatersrand, PO WITS, Johannesburg, 2050, South Africa.

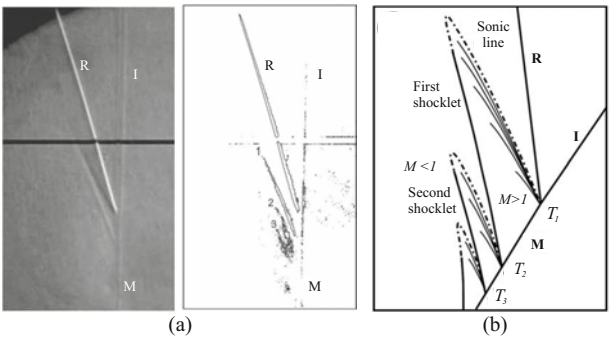

Fig. 1 Comparison between sequence of supersonic patches observed: (a) experimentally in Skews et al. [4], and (b) numerically in Tesdall et al. [3].

2 Apparatus

Experiments were conducted using a standard shock tube facility combined with a variety of optical components to capture both single and multi-frame images of the GR.

2.1 Experimental Facilities

The shock tube layout (Fig. 2) consists of a cylindrical cross-sectional driver and a variable diverging section connected onto a 4.0 m expansion chamber (rectangular cross-sectional of 0.45 m $\times$ 0.10 m). Three ramp angles (10°, 15°, and 20°) were interchanged in the diverging section, and the expansion chamber length could also be shortened by removing the first 2.0 m expansion section. Tests were conducted for nominal driver pressures of 1.4, 3.4, 7.0, and 13.0 bar and the incident shock Mach numbers were estimated by the time taken for the shock reflection to travel between the two pressure transducers positioned at A in Fig. 2. For an ambient pressure of 0.83 bar and an average temperature of 20°C, the Mach numbers were measured approximately as 1.10, 1.20, 1.30 and 1.40 respectively. Actual Mach numbers of the shock reflection in the viewing port were determined from the multi-exposure imaging. Note that the triple point of the reflection did not passing by the viewing port for a number of test conditions.

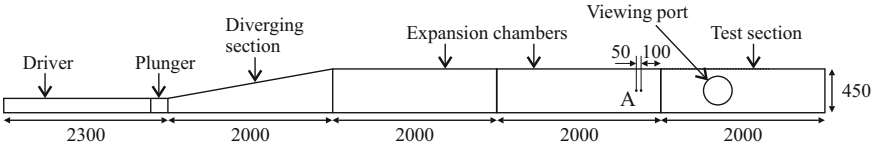

Fig. 2 The shock tube. Dimensions in mm.

2.2 Photography

A general Z-layout schlieren system was used to capture the GR. Single-frame images were captured using a 1.9 μs xenon flash lamp and a Nikon D40X digital camera of 10.0 million pixels. All images were captured at least twice to ensure the repeatability of the results. The sensitivity of the system was continuously adjusted during testing which resulted in the varying illumination of the images.

The most resolved images of the GR were obtained for a knife edge positioned parallel to the reflected wave. A multi-frame camera (Cooke Corporation) was used to obtain superimposed images of the propagating shock reflection, but due to the lower pixel resolution no clear evidence of the expansion waves were detected. The application of the oblique shock equations to the superimposed images allowed quantitative data of the wave velocities to be obtained.

3 Principle of Experiment

Previously experiments required a large-scale shock tube to produce Mach stem lengths in the order of 1.0 m [2, 4]. However, a new technique is found whereby longer Mach stem lengths can be attained by the successive reflections of Mach reflection off the ceiling and floor of a standard shock tube. Fig. 3 shows the overall trajectory path of the triple point of the developed shock reflection at different time intervals t_i. The cylindrical wave at t_0 in the diverging section strikes the roof of the facility resulting in the desired reflection pattern at t_1. The shock reflection then propagates downstream where it undergoes three triple point reflections, off the floor and the ceiling of the shock tube, before being observed at t_5. After each triple point reflection the orientation of the wave configuration changes, where it is seen that the Mach stem before the triple point reflection transforms into the incident wave for the new shock reflection. A detailed analysis of the wave strengths as a result of the triple point reflection is presented in Section 5.

This paper determines that the Mach stem attached to the shock reflection is not the apparent Mach stem length observed at each time interval, but rather the overall vertical distance traveled by the triple point from where the reflection was created. We denote the latter as the virtual Mach stem length (l_{vms}).

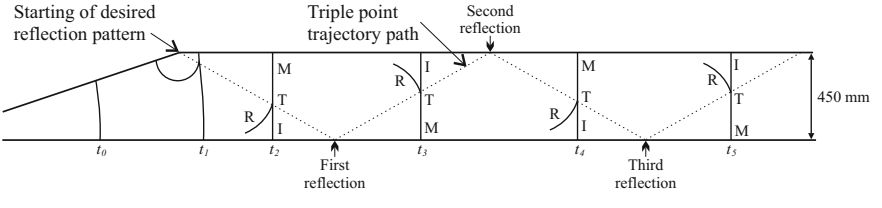

Fig. 3 Progression of developed shock reflection downstream for different time steps t_i showing the overall trajectory path of the triple point in a standard shock tube, and the change in shock wave orientation after each triple point reflection.

4 Numerical Set-Up

Two-dimensional simulations of the propagating weak Mach reflection were performed using the Fluent package on the commercially available Ansys 12. The simulations were built on a density explicit solver and an inviscid model, where an adaptive mesh scheme based on pressure gradients refined the moving shock waves in the flow field. The computational work was mainly used to predict the propagation path of the triple point downstream, and was not capable of resolving the flow features in the vicinity of the triple point.

5 Results and Discussion

5.1 Shock Wave Amplification Due to Triple Point Reflections

Fig. 4 shows the dynamics of a shock reflection produced for a 15° ramp angle and a test section Mach number of $M_{ts} = 1.30$. The successive triple point reflections off the floor and ceiling of the shock tube resulted in the amplification in strength of the incident wave and Mach stem by approximately 3% and the reflected wave by 0.2% after each reflection. This is an important characteritic of the experiment, as the strength of the shock reflection is maintained, allowing stronger shock reflections in the order of M = 1.40 to be studied. It is seen that a final incident wave and Mach stem strength of around 1.30 was obtained at the end of the shock tube. A very weak reflected wave of Mach 1.003 was also produced. Note that the triple point

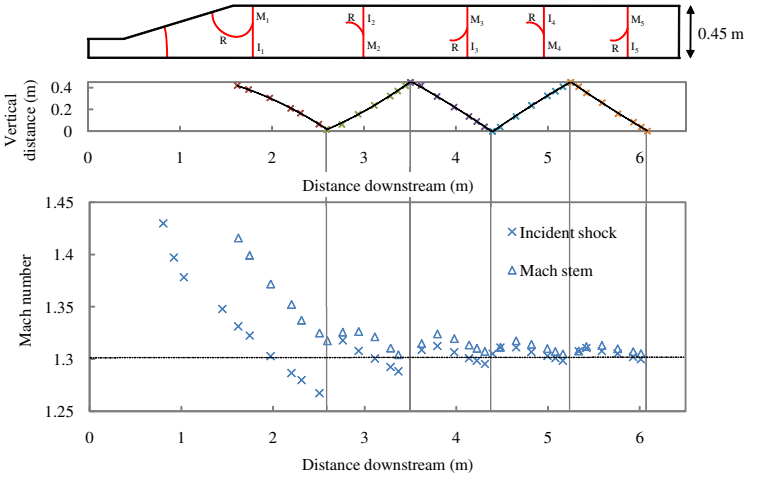

Fig. 4 Dynamics of the shock reflection in the shock tube for a 15° ramp angle, $M = 1.30$, 4.0 m expansion chamber. First image illustrates the change in orientation of the shock reflection downstream, second image illustrates the trajectory path of triple point, and the third image plots the incident wave and Mach stem wave strength versus the downstream shock tube length.

traverses five heights of the shock tube, developing a virtual Mach stem length (l_{vms}) of 2.25 m.

5.2 The Expansion Wave

A number of tests showed evidence of the expansion wave of the GR as shown in Fig. 5. The orientation of the shock reflection pattern in the images consist of the undisturbed flow on the right and the incident shock at the top. The dark vertical and horizontal lines are cotton threads mounted across the window, separated by 50 mm, to give a scale to the images. Note all the images have been scaled and cropped to show only the region behind the triple point.

All the images presented in Fig. 5 show a black fan-shaped region immediately behind the reflected wave. This region emanates from the triple point and is referred to as the expansion wave as originally predicted by Guderley [1]. It is shown that the GR occurs for various conditions, where in some cases more clearly defined flow features are observed which could be attributed to the sensitivity of the schlieren system. A number of tests were not captured as the triple point trajectory path did not pass by the viewing port. Despite the very sensitive schlieren system, no evidence was found of a slipstream when changing the knife edge orientation.

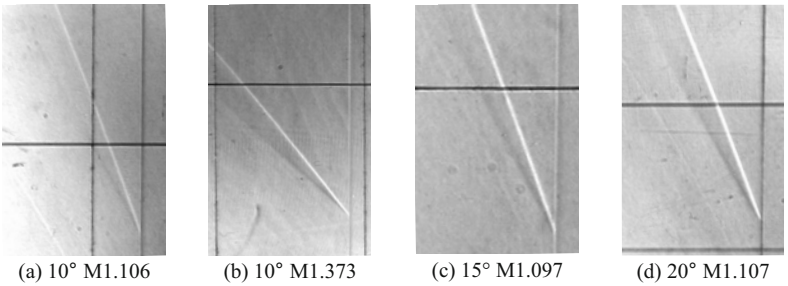

(a) 10° M1.106 (b) 10° M1.373 (c) 15° M1.097 (d) 20° M1.107

Shock reflections for 4.0 m expansion chamber

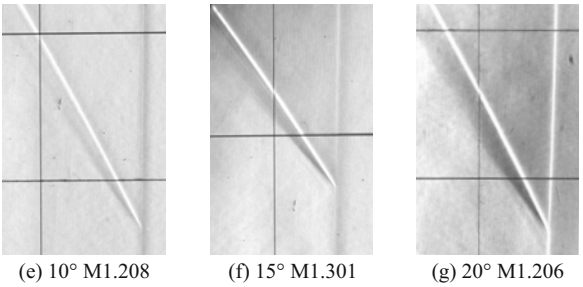

(e) 10° M1.208 (f) 15° M1.301 (g) 20° M1.206

Shock reflections for 2.0 m expansion chamber

Fig. 5 Summary of the images showing evidence of the fourth wave of the GR for both the 2.0 m and 4.0 m expansion chambers. The black fan-shaped region immediately behind the reflected wave represents the expansion wave. All images are the same scale.

5.3 *Evidence of First Shocklet*

Fig. 6 shows the images captured with an expansion fan and a clearly defined terminating shock as predicted in [3] and observed in [2, 4]. The reflection patterns observed in Fig. 6 are similar to those seen in [4], except that a second expansion wave and shocklet were not resolved. When analysing Fig. 6(b) for the 4.0 m expansion chamber it is seen that the expansion wave and shocklet are more than double the length when compared to the images in Fig. 6(a). This is expected as the shock reflection shown in Fig. 6(b) traveled nearly double the downstream distance compared to Fig. 6(a) resulting the flow features behind the triple point to be enlarged. It was determined that the size of the supersonic region was directly proportional to the size of the virtual Mach stem length. The supersonic patch size was found to vary between 2.3% to 4.8% of the virtual Mach stem length which is comparable to the 2% obtained experimentally in [4].

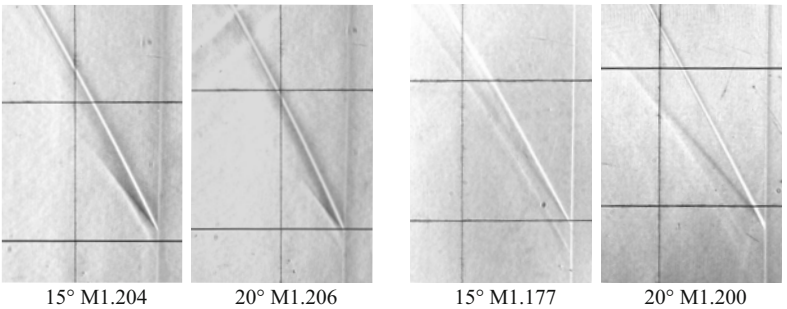

Fig. 6 Comparison between the shocklets produced by the 15° and 20° ramp angles for 2.0 m & 4.0 m expansion chambers. Larger expansion waves were observed for the 4.0 m expansion chamber tests shown in (b) due to the larger virtual Mach stem lengths.

An oblique shock analysis under the assumption of plane waves was conducted on superimposed images for the 15° ramp angle for $M \approx 1.20$. It was shown that the reflected wave was very weak with the flow Mach number ahead of it being approximately 1.02 with a reference frame fixed to the primary triple point. It was determined that the flow behind the Mach stem was approximately 1.02, which being supersonic confirms that the reflections observed for the 15° ramp angle and $M \approx 1.20$ are in fact GR.

6 Conclusions

The high-resolution experiments with the use of a very sensitive schlieren system showed evidence of the fourth wave in the GR, confirming that the GR can be produced in a standard shock tube. The overall vertical distance travelled by the triple

point during the successive reflections in the shock tube was determined to be the length of the Mach stem attached to the Mach reflection. This provides a new technique in which shock reflections can be studied. The majority of the images captured only the expansion wave behind the reflected wave, whilst a few images provided evidence of the shocklet terminating the expansion wave. Interestingly the shocklet was mostly observed for incident Mach numbers of around 1.20 for the 15° and 20° ramp angles. The multiple supersonic patches as predicted by the computations of Tesdall et. al [3] were not resolved.

References

1. Guderley, K.G.: Considerations on the structure of mixed subsonic-supersonic flow patterns, Wright Field. Report F-TR-2168-ND, 144–149 (1947)
2. Skews, B.W., Ashworth, J.T.: The physical nature of weak shock wave reflection. Journal of Fluid Mechanics 542, 105–114 (2005)
3. Tesdall, A.M., Hunter, J.K.: Self-similar solutions for weak shock reflection. SIAM J. Appl. Math. 63, 42–61 (2002)
4. Skews, B.W., Li, G., Paton, R.: Experiments on Guderley Mach reflection. Shock Waves 19, 95–102 (2009)

Wave Processes in Transonic Airfoil Flows

V. Hermes, J. Nies, I. Klioutchnikov, and H. Olivier

1 Introduction

Upstream moving pressure waves are observed in transonic flows over airfoils already for decades. They can be generated actively by flap or airfoil oscillations [6]. But, they are also naturally present in airfoil flows [1, 4]. Upstream moving pressure waves can lead to flow instabilities by forcing shock and stagnation point oscillations. Furthermore, it is expected that they affect the laminar-turbulent transition [5]. Hence, the phenomenon is of great engineering interest.

The goal of the presented experimental and numerical investigation is the reduction of the pressure wave amplitude by passive means like serrated trailing edges. For this, reference experiments are performed without serrated trailing edge with a symmetric, generic airfoil model with blunt trailing edge. The trailing edge bluntness generates pressure waves of a specific frequency ($Sr_d \approx 0.2$) via wake fluctuations. Here Sr_d is a non-dimensional frequency scaled with the inflow velocity u_∞ and the trailing edge thickness d. First, the base flow is assessed and analysed in detail. The inflow conditions are systematically varied. Preliminary results of the flow over generic airfoil model with serrated blunt trailing edges are also presented.

2 Experimental and Numerical Methods

The used test facility is a modified shock tube allowing transonic Mach numbers ($0.6 < Ma_\infty < 0.85$) and relatively high Reynolds numbers based on chord-length ($1 \cdot 10^6 < Re_c < 4 \cdot 10^7$) [1]. The main disadvantage, which is typical for all impulse test facilities, is the relative short testing time of 5 - 10 ms. Nevertheless the testing time is sufficient to establish the flow and perform reliable measurements during the quasi-stationary flow period. To reduce the influence of the channel walls a relatively

V. Hermes · J. Nies · I. Klioutchnikov · H. Olivier
Shock Wave Laboratory, RWTH Aachen University, Templergraben 55, 52062 Aachen, Germany

thin airfoil model with 8.8 mm thickness is used. The generic airfoil model has a chord length of 80 mm and a variable trailing edge to modify its thickness.

Several measurement techniques are applied simultaneously. The free stream Mach number is deduced from Pitot and static pressure transducers, which are mounted upstream of the airfoil model. To perform pressure measurements four miniature Kulite pressure transducers are mounted flush to the upper model surface inbetween $x/c = 0.386$ and $x/c = 0.611$. The natural frequency of the pressure transducer configuration is 150 kHz. Furthermore, a Schlieren/shadowgraph system using a high speed Shimadzu-HV1 camera is used to obtain highly time-resolved visualisation of the flow. The laminar-turbulent transition is detected by infrared thermography.

The numerical simulations are performed using a solver, which was developed at the RWTH Aachen University based on a finite-difference WENO method of high order accuracy in space and time and shock capturing capability. The inviscid fluxes are approximated using a ninth order WENO scheme formulation according to [2]. The viscous fluxes are discretised using central difference operators of tenth order accuracy. The time integration is explicit and performed with a third order, low-storage Runge-Kutta-TVD-Scheme. The numerical method is described in detail in [3].

3 Flow over Straight Blunt Trailing Edges

Figure 1 (right) shows an experimental Schlieren picture of the instantaneous airfoil flow over the generic model. The trailing edge thickness is $d = 4$ mm and the inflow conditions are $Ma_\infty = 0.71$ and $Re_c = 1 \cdot 10^6$. Distinct, upstream moving pressure waves are observed on both airfoil sides. Furthermore, the pressure waves on the upper airfoil side are shifted by the half of the wavelength compared to the lower airfoil side. The pressure waves are generated near the trailing edge due to wake fluctuations. An ordered vortex street is observed in the wake forcing a

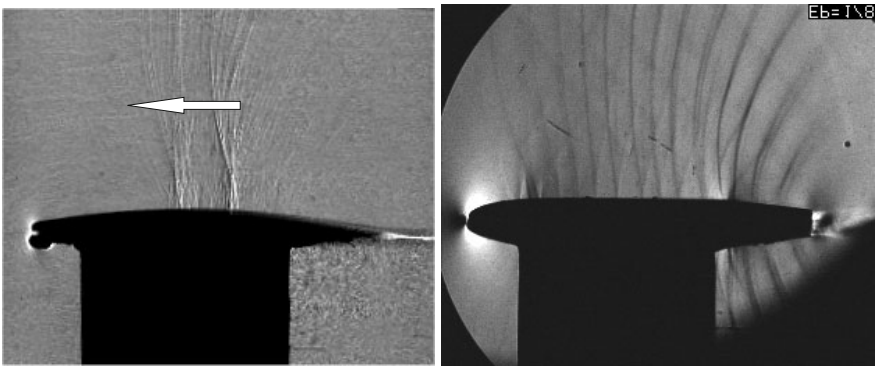

Fig. 1 Schlieren visualisation of the flow over two different airfoil models at transonic speed.

sinusoidal wake oscillation. The frequency of the pressure wave corresponds well to the typical frequency of vortex streets behind blunt bodies of $Sr_d \approx 0.2 - 0.3$. While propagating upstream, the pressure waves become apparently weaker and disappear near the leading edge. A three-dimensional numerical simulation of the flow under the same condition has been performed using a grid of 1280x128x128 grid points in wall-tangential, wall-normal and spanwise direction, respectively. It is found that the pressure wave fronts are two-dimensional (figure 2 a)). Furthermore, a laminar-turbulent transition is observed at $x/c \approx 0.3$ that corresponds well to experimental findings. There the transition is found to take place between $x/c = 0.25$ and $x/c = 0.33$ using infrared thermography. In figure 2 b) an instantaneous configuration of vortices inside the boundary layer is depicted. The turbulent boundary layer vortices interact at the trailing edge with the vortex street. Nevertheless, the vortices in the wake stay predominantly two-dimensional. Hence, the generation of the pressure waves and their propagation is mostly two-dimensional and the phenomenon can be sufficiently well described using two-dimensional numerical simulations. In figure 3 the flow visualisation and the powerspectra of the normalised pressure measurements (normalised with p_∞) obtained experimentally and numerically (2D-simulation) are compared for the same flow conditions. The qualitative agreement between experimental and numerical Schlieren is excellent. Even the reflection on the wind tunnel walls are captured well in the numerical simulation. The qualitative comparison of the powerspectra is good as well. The amplitude of the pressure waves (peak for $Sr_d = 0.2 - 0.3$) is about $p'/p_\infty = 0.005$. Besides the upstream moving pressure waves ($Sr_d = 0.2 - 0.3$), strong pressure fluctuations are detected for low frequencies ($Sr_d \approx 0.04$). This frequency range corresponds to natural wind tunnel frequencies and to a natural airfoil flow instability frequency (compare with i.e. [1]).

The Reynolds number is varied in the experiment between $Re_c \approx 5 \cdot 10^5$ and $Re_c \approx 3 \cdot 10^6$. The absolute pressure amplitude increases nearly linear with increasing Reynolds number. Therefore, the upstream propagating pressure waves are

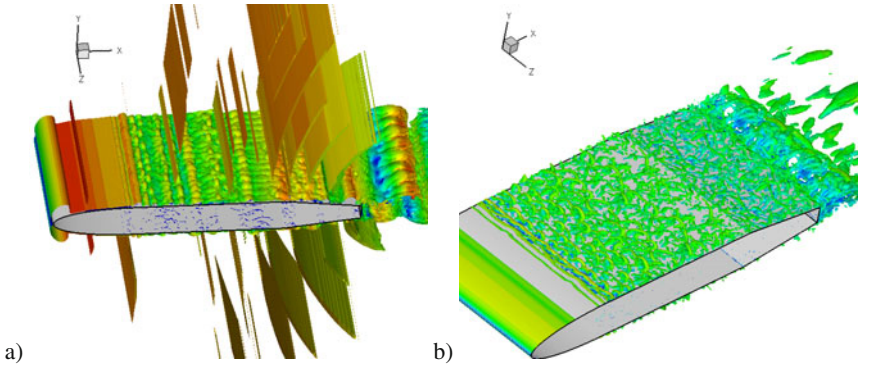

Fig. 2 a) Isosurface of $|grad(\rho)|$ and b) visualisation of instantaneous vortex formation for $Ma_\infty = 0.71$, $Re_c = 1 \cdot 10^6$ and $d = 4$ mm

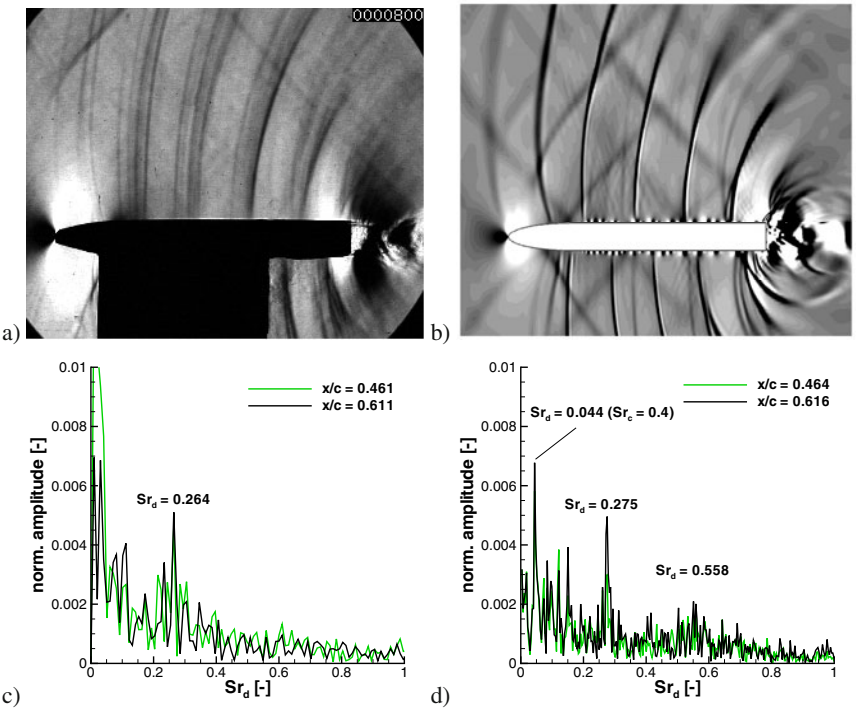

Fig. 3 Schlieren visualisation of the instantaneous flow field from a) Experiment and b) 2D-Simulation. Powerspectra: c) Experiment and d) 2D-simulation. Flow over generic model with $Ma_\infty \approx 0.65$, $Re_c \approx 1 \cdot 10^6$ and $d = 8.8$ mm.

easier to visualise and to measure in experiments at higher Re_c. But the pressure amplitude normalised with the 'ambient' pressure p_∞ are nearly independent on Reynolds number. Thus, it can be concluded that the Reynolds number Re_c has no major influence on the observed phenomenon in the assessed range.

The Mach number is varied in the experiment between $Ma_\infty = 0.65$ and $Ma_\infty = 0.8$. The numerical simulations are performed for three different Mach numbers in the same range. It is found that the Strouhal number determined by the fluctuating wall pressure is nearly constant with Mach number Ma_∞ (fig. 4 a)). The damping of the pressure wave amplitude is strongly dependent on Mach number. In figure 4 b) the standard deviation of the pressure fluctuations is depicted for two different inflow Mach numbers. The pressure wave amplitude at the trailing edge is nearly constant. While propagating upstream the pressure waves are decaying more rapidly with higher Mach number before a plateau is reached. By analysing the distribution of the pressure amplitude over frequency for two different positions, it is found that the low frequency pressure waves are nearly undamped. Whereas the amplitude of the pressure waves in the frequency range $Sr_d = 0.2 - 0.3$ is strongly decaying

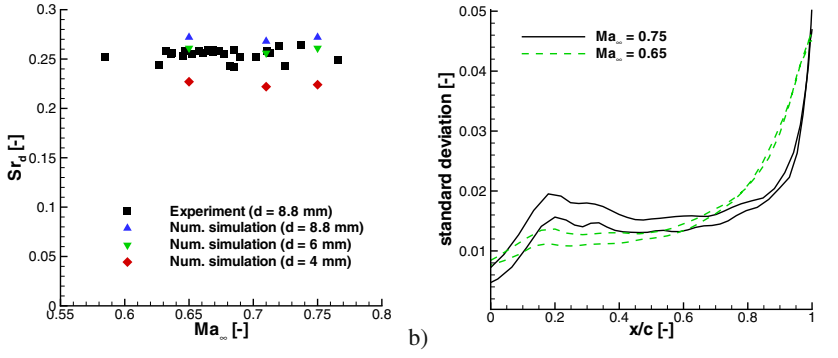

Fig. 4 a) Strouhal number Sr_d for different inflow Mach numbers Ma_∞ and trailing edge thicknesses d. b) Numerically obtained standard deviation of the pressure fluctuations for $Ma_\infty = 0.65$ and $Ma_\infty = 0.75$ and constant $Re_c = 10^6$ and $d = 8.8$ mm

with propagation distance from the trailing edge. Thus, for low Mach numbers the upstream moving pressure waves are better detectable in the pressure history plots.

Trailing edges with two different thicknesses $d_1 = 4$ mm and $d_2 = 8.8$ mm are investigated experimentally and numerically. Whereas, the upstream moving pressure waves are visuable for both trailing edges using Schlieren, the result of the pressure transducer signal is meaningfull only for d_2 for the whole Mach number range. With the small trailing edge bluntness d_1 the upstream moving pressure signal is only detectable for low Mach numbers $Ma < 0.7$. Furthermore, numerical results indicate a weak dependence of the pressure wave Strouhal number Sr on the trailing edge thickness d (s. fig. 4 a)) that is observed in the experiment as well.

4 Flow over Serrated Blunt Trailing Edges

In figure 5 a) a Schlieren picture of the instantaneous flow field over the sketched model with $Ma_\infty = 0.66$, $Re_c = 2 \cdot 10^6$ and $d = 8.8$ mm is depicted. The upstream moving pressure waves are not detectable here. The distinct peak observed in the powerspectrum of the reference case (fig. 3 c)) in the frequency range of $Sr_d \approx 0.25 - 0.27$ cannot be found for the serrated trailing edge. It is rather observed that the powerspectrum becomes more 'noisy' for Strouhal numbers smaller than $Sr_d = 0.3$ (s. fig. 5 b)). First results of the 3D zonal numerical simulation of the serrated trailing edge flow show that instead of the spanwise oriented vortex street fully three-dimensional oriented vortices are present in the wake (fig. 5 d)). Thus, the wake fluctuation are less ordered. These findings will be further analysed by a combined experimental and numerical approach to clarify the main cause of the reduction of the pressure wave amplitude.

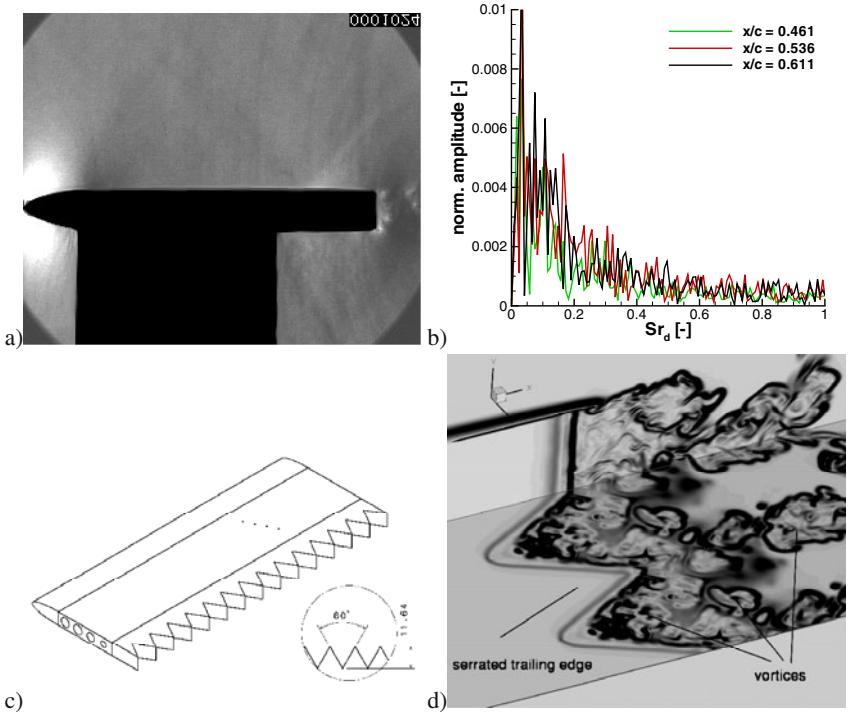

Fig. 5 Experimentally obtained a) instantaneous Schlieren visualisation and b) powerspectrum of the flow field over the sketched model with $Ma_\infty = 0.66$, $Re_c = 2 \cdot 10^6$ and $d = 8.8$ mm. c) Sketch of the generic airfoil model with a serrated trailing edge. d) Visualisation of vortices using $|grad(\rho)|$ in the wake of the serrated trailing edge.

References

1. Alshabu, A., Olivier, H.: Unsteady wave phenomena on a supercritical airfoil. AIAA J. 46(8), 2066–2073 (2008)
2. Balsara, D., Shu, C.W.: Monotonicity preserving WENO schemes with increasingly high order of accuracy. J. Comp. Phys. 160(2), 405–452 (2000)
3. Klioutchnikov, I., Ballmann, J.: DNS of transitional transsonic flow about a supercritical BAC3-11 airfoil using high-order shock capturing schemes. In: DLES VI. ERCOFTAC Series, vol. 10, pp. 737–744. Springer (2006)
4. Lee, B.H.K., Murty, H.: Role of Kutta waves on oscillatory shock motion on an airfoil. AIAA J. 32(4), 789–796 (1994)
5. Seiler, F., Srulijes, J.: Vortices and pressure waves at trailing edges. In: Proc. of 16th Intern. Cong. on High Speed Photography and Photonics, Strasbourg, France (1984)
6. Tijdemann, H.: Investigation of the transonic flow around oscillating airfoils, NLR TR-77090 (1977)

Shock Wave Reflection Off Convex Cylindrical Surfaces

H. Kleine and B. Skews

1 Introduction

In spite of considerable research effort in past decades, the reflection of shock waves off convex cylindrical surfaces still poses a number of unanswered questions. For a given shock Mach number M_S, the reflection pattern changes from regular to irregular at a certain wall angle Θ_W. If one determines this transition angle by visual inspection of the reflection pattern and defines it as the location of the first occurrence of a visible Mach stem, one typically arrives at wall angle values lower than the one found in the pseudo-steady case for a straight wedge at the same Mach number [1]. This would indicate that the regular reflection pattern is maintained longer on the cylindrical surface compared to the straight wedge case. Numerical simulations, on the other hand, suggest that the transition occurs at the same wall angle as for the straight wedge. If this were the case, the transition would be governed by the local wall angle and would not be influenced by the preceding history of the reflection. Furthermore, the delayed transition observed experimentally would then have to be explained as a consequence of insufficient spatial resolution of the optical records used to classify the type of reflection: If the Mach stem is too small to be optically resolved, the reflection pattern will remain to appear regular beyond the transition angle predicted by the theory for straight walls.

The situation is further complicated if one considers the location at which the flow behind the reflected shock becomes subsonic relative to the reflection point so that perturbations created by the reflecting shock catch up with the reflection point. For a straight wedge, such a 'catch-up' condition is known to be an indicator of the

H. Kleine
School of Engineering and IT, University of New South Wales/Australian Defence Force Academy, Canberra, ACT, Australia

B. Skews
School of Mechanical, Industrial, and Aeronautical Engineering, University of the Witwatersrand, Johannesburg 2050, South Africa

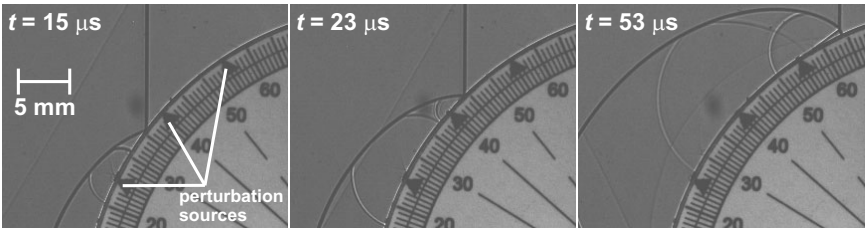

Fig. 1 Three frames of a time-resolved visualization of a shock ($M_S = 1.22$) reflecting off a 60 mm diameter cylinder with perturbations on the surface; time t is counted from the instant the wave hits the cylinder; the first perturbation at 25° generates a forward- and a backward-facing wave, while the second perturbation at 40° only produces a backward-facing wave which indicates that the flow has become subsonic with respect to the reflection point. The angles indicated in this front-lit shadowgraph visualization are the polar angles Θ_p of the cylinder with $\Theta_W = 90° - \Theta_p$. A Mach stem only becomes visible at later times (see third frame)

onset of irregular reflection, as formulated in the so-called sonic criterion [2]. Tests with a new experimental technique based on the tracking of deliberately introduced small perturbations in the flow [3] have revealed that the 'catch-up' occurs at wall angles Θ_W that are larger than the transition wall angle for this Mach number on a straight wedge (Fig. 1). Therefore an area of flow behind a shock reflecting off a convex circular surface becomes subsonic relative to the reflection point much earlier than one would expect from predictions based on the sonic criterion on plane walls or from results based on the first visual appearance of a Mach stem. If this 'catch-up' were the mechanism responsible for the transition, the reflection may already become irregular at wall angles larger than the one for straight walls.

Two other points of contention in this shock reflection configuration are whether the radius of the cylinder and the initial angle (in the case of partial cylindrical models) influence the transition point. Experiments reported in the literature [1] appear to confirm such an influence. Our results so far [4] suggest that the aforementioned catch-up angle is, indeed, a function of radius while the initial angle has no influence, provided it is larger than the catch-up angle. The tests described in the following were conducted to clarify these two aspects of shock reflection off a cylindrical surface, namely the role of cylinder radius and initial angle. Both aspects are directly linked to the aforementioned quest for a transition criterion for shock reflection off curved surfaces.

2 Experimental Setup

As the shock Mach number M_S is expected to be an important factor so that the shot-to-shot repeatability of the shock tube may become crucial, tests are conducted with two cylindrical models mounted on top and bottom floor of the shock tube, respectively, so that both models are subjected to the same shock wave. The models

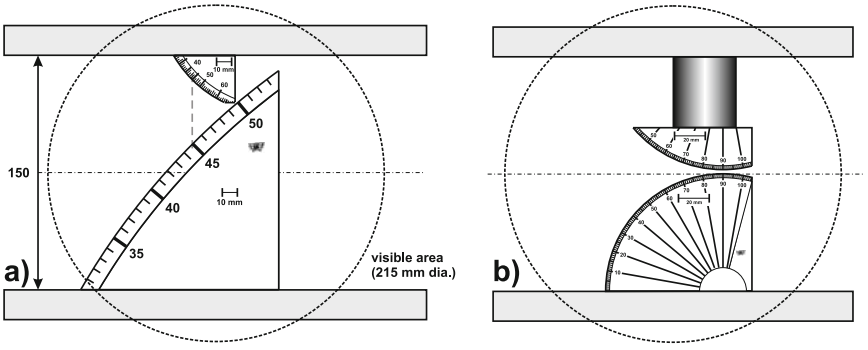

Fig. 2 Test configurations: (a) cylinder models of different radius (75 mm and 450 mm) (b) cylinder models (75 mm radius) with different initial angles

have either identical radii but different initial angles or identical initial angles but different radii. The investigated configurations are schematically summarized in Fig. 2. Time-resolved flow visualization with a high-speed video camera (Shimadzu HPV-1) is the key diagnostic tool for the tests. All models are equipped with a degree scale that is imaged simultaneously with the flow field by adequate front lighting. The camera is typically run at its maximum frame rate of 10^6 frames per second (fps). The relatively moderate resolution of the camera (312×260 pixel) necessitates high image magnification, which in turn means that the models have to be brought as close together as possible, as shown in Fig. 2b. The used conventional shock tube with a cross section of 150 mm (height) $\times$ 75 mm (width) is operated at ambient pressure in the test section for shock Mach numbers up to $M_S \approx 1.4$ and at subatmospheric initial test gas pressures for higher shock Mach numbers. The nominal Mach numbers investigated here were $M_S = 1.23, 1.34$ and 1.49.

3 Results

3.1 Models with Different Radii

Data from the literature [1] as well as our previous results [4] indicate that the transition point moves to smaller wall angles if the cylinder radius is increased. These results also show that at identical wall angles on cylinders with significantly different radii (radius ratio ≥ 6), the complete shock profiles are not self-similar, which indicates Reynolds number effects and thus a possible influence of cylinder radius on the transition process. The tests described in this section were conducted to clarify the extent of the aforementioned Reynolds number effects. The dimensions of the shock tube allow one to use two models with a scale factor of six, one with a radius of 75 mm and the other with 450 mm. The models are arranged in the test section in such a way that the shock passes the wall angle $\Theta_W = 45.2° \pm 0.1°$ simultaneously on both models, but the time-resolved recording also allows one to

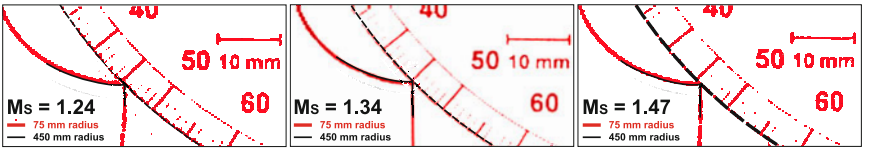

Fig. 3 Shock shapes for cylinders with different radii (75 mm and 450 mm) for three different shock Mach numbers

compare the patterns at other wall angles in the range $35° \leq \Theta_W \leq 53°$. In the shock reflection process with these two models, the Mach number is identical while the Reynolds numbers differ by a factor of six and thus by almost one order of magnitude. Scale factors higher than six, which would require a second model with a radius significantly smaller than 75 mm, are impractical for the given test section size and the possible spatial and temporal resolution of the visualization system.

Figure 3 summarizes the results obtained for three different Mach numbers for wall angles close to $\Theta_W = 45.2°$. For these images, the shock contour on the smaller model on the top of the test section is magnified six times and superimposed on the shock pattern obtained for the larger model on the shock tube floor. As the initial angles of both models are identical, the influence of the corner signal on the shape of the reflected shock is also identical so that the complete patterns can be compared. While the results indicate that the reflected shock on the larger model is always slightly shallower compared to the one seen on the smaller cylinder, which confirms the observation made in [4], the differences are less significant than previously assumed. On the basis of these observations, the Reynolds number influence can therefore be considered to be minimal unless the differences exceed one order of magnitude. Time-resolved visualizations with at least the same frame rate (10^6 fps) and twice the current spatial resolution or exactly synchronized single high-resolution images would be needed to fully quantify the effect of cylinder radius on shock shape and possibly on the transition point.

3.2 Models with Different Initial Angle

Shock tubes can only accommodate partial cylinder models once the cylinder radius exceeds the height of the shock tube test section. As long as it is above the value associated with the catch-up of signals from the wall, the initial wall angle of the partial model should have no influence on the subsequent reflection process other than generating a different corner signal from the model's front edge, which subsequently changes the shape of the reflected shock downstream of the reflection point [4]. On the other hand, if the transition were governed by the same processes as on a straight wall or if it were, indeed, delayed to even smaller wall angles as suggested by the experimental records, one could expect that the initial wall angle would only influence the onset of irregular reflection if it were below the wall angle associated with the transition. The initial angles of the partial models used here were chosen to fall below at least one of the angles expected to be relevant for transition,

as indicated in Fig. 4. The partial models were placed directly opposite to a half-cylinder of the same radius. If the initial angle of a partial model influenced the transition, it was expected that this influence would become directly obvious in the form of an asymmetry of the shock reflection patterns.

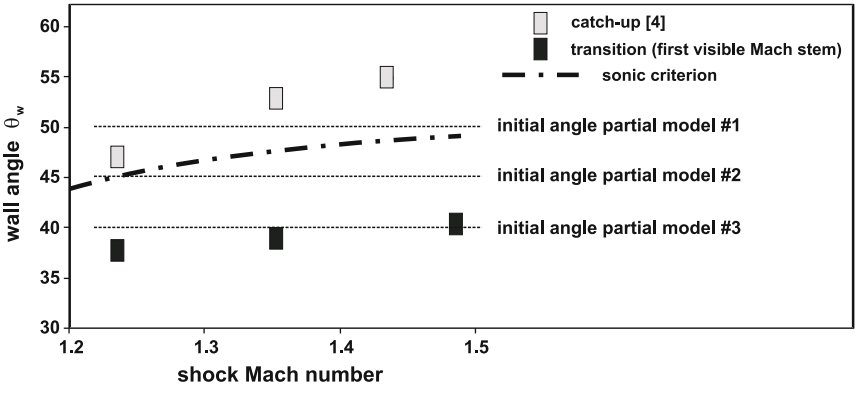

Fig. 4 Initial wall angles Θ_W of the partial models compared to the wall angles at which perturbations from the surface of the cylinder are seen to catch up with the reflection point (from [4]) and to the wall angles at which a Mach stem becomes visible for the first time (these tests).

A set of representative results obtained with these models is given in Fig. 5. The influence of the initial angle is most obvious for the reflected shock, which is affected by the earlier corner signal. In the case of the partial model with the lowest initial wall angle of $\Theta_{W\,in\,3} = 40°$, the expected asymmetry of the reflection pattern is clearly obvious for all three investigated shock Mach numbers. The Mach stem on the partial model is smaller and its foot is at a visibly lower wall angle than that of its counterpart on the half-cylinder, which indicates that the transition process on the partial model "missed" the initial stages and was hence delayed. The first visible Mach stem appears about two degrees later than on the half-model. These results clearly indicate that the transition process has started before the Mach stem becomes visible.

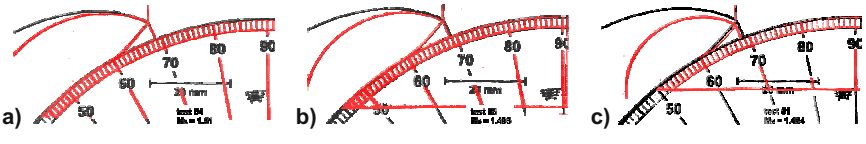

Fig. 5 Superimposed shock patterns of the half model (black) and the partial model (red) for $M_S = 1.49$ (a) initial angle $\Theta_{W\,in\,1} = 50°$ (b) initial angle $\Theta_{W\,in\,2} = 45°$ (c) initial angle $\Theta_{W\,in\,3} = 40°$

For the second partial model with $\Theta_{Win2} = 45°$, the asymmetry is only obvious in the case of the highest shock Mach number $M_S = 1.49$ (Fig. 5b). A minute difference can be detected for the medium shock Mach number of $M_S = 1.34$, while the patterns for $M_S = 1.23$ are indistinguishable within the given image resolution. The initial angle of the largest partial model, $\Theta_{Win1} = 50°$, while below the catch-up values for $M_S = 1.34$ and 1.49 and hence in a regime where the flow behind the reflected shock is already subsonic with respect to the reflection point, does not lead to asymmetries that can be measured with the available resolution. The time-resolved records indicate, however, a systematic difference in the onset of the irregular reflection – for all three shock Mach numbers, the Mach stem appears consistently about one degree later on the partial model than on the half model. Similarly to the tests described in the previous section, visualizations with considerably higher spatial resolution will be needed to fully clarify this aspect.

4 Summary

The analysis of the obtained records is, at the time of writing this paper, not completed, but based on the results gathered so far, one can draw the following conclusions:

- the radius of the cylinder influences the shock pattern, but this influence appears to be minute unless one compares cylinders that differ in size by more than an order of magnitude.
- tests with the partial models have clearly shown that the transition process has started before the Mach stem becomes visible; the transition delay reported in the literature may therefore simply be caused by the difficulties to detect a minute Mach stem.
- it could not clearly be shown whether the transition process already starts once the flow becomes subsonic with respect to the reflection point, as it was not possible to detect asymmetries in the shock patterns that were large enough to be properly resolved; the time-resolved records indicated, however, that the first appearance of a visible Mach stem is delayed by about one degree if the partial model has an initial angle lower than the catch-up value found in [4], which could suggest that an initial phase of the transition has already commenced.

References

1. Ben-Dor, G.: Shock Wave Reflection Phenomena. Springer (2007)
2. Hornung, H.G., Oertel, H., Sandeman, R.J.: J. Fluid Mech. 90 (1979)
3. Skews, B.W., Kleine, H.: Exp. Fluids 46, 1 (2009)
4. Skews, B.W., Kleine, H.: J. Fluid Mech. 654 (2010)

Aerodynamic Ground Effect for Transonic Projectiles

H. Kleine, J. Young, B. Oakes, K. Hiraki, H. Kusano, and Y. Inatani

1 Introduction

The aerodynamic characteristics of an object flying in close proximity to a solid surface are altered by the presence of this boundary. This phenomenon, known as aerodynamic ground effect, has been thoroughly investigated in the subsonic flow regime [1], but to the best of the authors' knowledge, high-speed applications of this effect with objects flying at transonic speeds have only been briefly considered on a theoretical basis [2]. Furthermore, most of the ground effect literature concentrates on lift-generating objects such as wings and/or aircraft where the presence of the ground alters an existing but inherently asymmetric pressure distribution. A non-lifting body – a projectile – is arguably a simpler case as the ground effect would immediately become obvious through an asymmetry in the originally symmetric pressure distribution. This was clearly shown in an earlier study on projectiles at medium supersonic speeds ($M = 2.4$). In this case, the pressure distribution around the projectile remained unaffected by the presence of the ground until the reflected bow shock impinged on the projectile. From this point onward, the pressure distribution was drastically changed and led to a non-negligible lift force, an associated pitching moment and a change of the drag (the latter influence was primarily due to a change of base pressure). As soon as the reflected shock did no longer impinge

H. Kleine · J. Young · B. Oakes
School of Engineering and IT, University of New South Wales/Australian Defence Force Academy, Canberra, ACT, Australia

K. Hiraki
Department of Mechanical and Control Engineering, Kyushu Institute of Technology, Kitakyushu, Fukuoka, Japan

H. Kusano
Shimadzu Corporation, Tokyo 101-8448, Japan

Y. Inatani
Japanese Space Exploration Agency, ISAS, Sagamihara 229-8510, Japan

on the projectile or the near wake, the pressure distribution was not affected and the aerodynamic ground effect became negligible and eventually non-existent. For the investigated projectile at $M = 2.4$ this occurred for clearances $h/d > 1$, where h is the clearance between the projectile and the ground and d is the projectile diameter. Experiments and numerical simulations established the trends for lift, drag and aerodynamic moment [3].

The situation is expected to be different in the transonic case, when the projectile moves with a Mach number slightly larger than unity. Using the same approach as for the previously discussed supersonic case, it was the aim of this investigation to identify and possibly quantify these differences.

2 Methods of Investigation

2.1 Ballistic Trials

In the ballistic tests, a projectile was fired from a rifle to fly at a small distance over a flat plate which was typically positioned at a distance of 25 m. A set of two pressure transducers recorded the pressure signature of the projectiles immediately upstream of the plate in order to determine the projectile speed and to trigger the visualization system, which was a standard schlieren setup with a powerful flash (Metz Mecablitz CT45) and a high-speed camera (Shimadzu HPV-1) on the light source and camera side, respectively. A second strong flash light was used for front lighting, so that one could determine the spin rate of the projectile and also identify surface irregularities as possible sources of occasionally observed asymmetries in the flow pattern around the projectile. These tests required a high degree of accuracy and repeatability from shot to shot, and apart from choosing an adequate high-precision rifle with appropriate visor for accurate aiming, the choice of the projectile was of crucial importance. The requirements were that the projectile be stable in the desired speed range (between Mach 1.05 and 1.2) and that it be of similar secant ogive design as the ones used in the supersonic tests. As it was not possible to source commercially available ammunition that met these requirements, it was decided to use reloadable cartridges and adjust the amount of propellant in order to achieve the required projectile velocity. The chosen projectile was a Nosler 50gn S.H.O.T., which through *a priori* calculations and independent testing was shown to be sufficiently stable when flying at transonic Mach numbers [4].

2.2 Wind Tunnel Tests

Two 7.5:1 scale models of the selected Nosler projectile, each instrumented with 16 pressure tappings, were used in the wind tunnel experiments. A bracket that allowed the projectiles to be rotated and indexed every 15° was also manufactured. From previous ground effect experiments it is known that in wind tunnel tests the flow field and thus the pressure distribution are influenced by the boundary layer developing along the test section walls. To overcome this problem, the symmetry

or mirror method was used, in which the effect of the wall is simulated by placing a second identical model below the original model, at a distance $2h$, where h is the distance between the projectile and the solid surface [5]. The holder for the models had four possible mounting points which allowed one to test three different model separations, corresponding to $h/d = 0.5, 0.75$ and 1. The wind tunnel tests were conducted at the transonic wind tunnel facility of the Institute of Space and Astronautical Science (ISAS) of the Japan Aerospace Exploration Agency (JAXA) in Sagamihara, Japan. The tunnel has a test section of 600 mm $\times$ 600 mm and was run at Mach number $M = 1.1$.

2.3 Computational Fluid Dynamics

The flow around the bullet at $M = 1.1$ was simulated with the commercial solver Fluent 13.0. The flow was solved as two-dimensional axisymmetric for the free flight condition ($h/d = \infty$) and three-dimensional for the $h/d = 0.5$ case. In the latter, the wall was simulated both with wall and symmetry boundary conditions, and negligible differences were found between these two approaches. A density-based solver with second-order upstream spatial discretisations was used, with the Spalart-Allmaras turbulence model. The mesh was adapted based on density gradients to refine the solution around the shocks, resulting in final mesh sizes of 52,000 cells for the 2D axisymetric case and 8.25 million cells for the 3D case.

3 Results

Figure 1 is a sequence of schlieren images showing how the bow shock around a Mach 1.13 Nosler projectile changes as it encounters a straight wall at a clearance of $h/d = 0.46$. At this clearance, the bow shock does not reflect but curves forward to meet the wall at a right angle. During the initial interaction process, neither the shock shape on the freestream side nor the stand-off distance are visibly affected by the interaction with the wall. A generally similar behavior is observed further downstream of the edge of the flat plate (Fig. 2a). The images give a clear indication of an established asymmetry in the flow, caused by the presence of the solid wall.

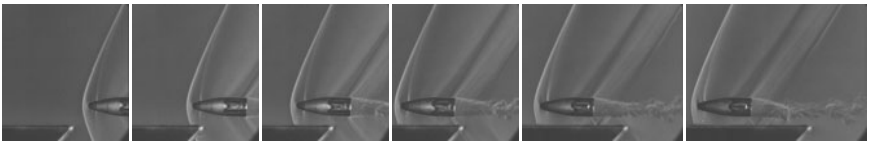

Fig. 1 Initial interaction of the bow shock with the ground plate for a projectile flying with Mach number $M = 1.13, h/d = 0.46$; sequence taken with 500,000 fps, time between shown frames: 20μs; the small discontinuities visible downstream of the nose of the Nosler projectile are caused by a small surface step generated by the leaden tip of the projectile – these perturbations change size and location as the projectile rotates, because the tip has no straight border (adapted from [4])

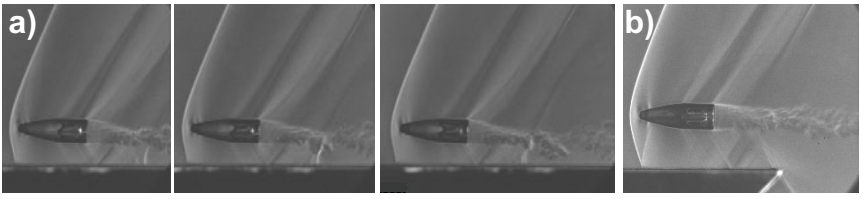

Fig. 2 a) three frames from a time-resolved visualization of the Mach 1.1 flight of a Nosler projectile over a wall at $h/d = 0.9$; sequence taken with 500,000 frames per second (fps), time between shown frames: 20μs; b) $M = 1.08, h/d = 1.59$ (adapted from [4])

Whether or not a reflected shock forms, depends for the given projectile and the given nominal Mach number of $M = 1.1$ primarily on the clearance h between the projectile and the ground. Other ballistic tests show that at this Mach number, one can expect a reflected shock for clearances $h/d > 1.5$, see Fig. 2b.

The physical reason for the observed shock reflection behavior is the presence of a large subsonic zone behind the bow shock. The numerical simulation indicates that for the given projectile at $M = 1.1$, this zone can extend as much as $1.8d$ from the projectile surface (Fig. 3). If the bow shock encounters a solid wall while its post-shock flow is still subsonic, no reflected shock can be formed and the shock itself has to change its curvature to allow its post-shock flow close to the shock impingement point on the wall to move parallel to the wall.

Results of the wind tunnel tests are shown in Fig. 4. There is good agreement in terms of shock shape and stand-off distance between the single model test and the ballistic trial without a wall ($h/d = \infty$). In the double-model configuration that represents the $h/d = 0.5$ case, however, both shock shape and stand-off distance are considerably different from the flow field observed in the ballistic tests: the shock has become steeper and the stand-off distance has increased, which resembles the flow field one would expect for this projectile flying at a lower Mach number. The steady-state numerical simulation of this configuration reproduces the flow field seen in the wind tunnel tests.

A numerical simulation of the transient initial wave impingement process observed in Fig. 1 indicates a multi-step adjustment process with different inherent time scales. The wave impingement and the subsequent change of shock shape lead to a growth of the subsonic zone, both downstream in the area between the projectile

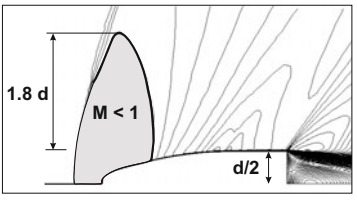

Fig. 3 Subsonic zone behind the bow shock of the Nosler projectile flying at $M = 1.1$ for $h/d = \infty$ (results of numerical simulation)

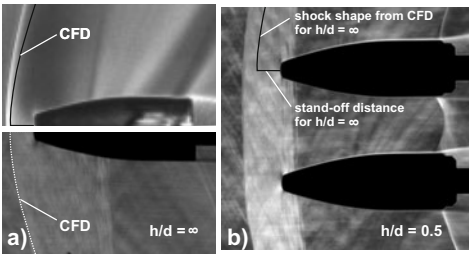

Fig. 4 a) flow field around the Nosler projectile model at $M = 1.1$ for $h/d = \infty$; ballistic trial (top) and wind tunnel test (bottom); b) wind tunnel test at $M = 1.1$ for $h/d = 0.5$; in both parts of the figure, the superimposed curve is the shock shape obtained from numerical simulation

and the wall, and in vertical direction towards the free stream. The downstream growth occurs in parallel with the adjustment of the bow shock shape to avoid a reflection from the wall, while the growth of the subsonic zone in vertical direction is at least one order of magnitude slower. As a consequence of this adjustment process, the shock stand-off distance gradually increases and the leading shock front steepens until eventually the configuration observed in the wind tunnel tests is reached. The simulations indicate that this process requires several tens of projectile lengths to be completed whereas the initial shock shape adjustment next to the wall is finished within less than five projectile lengths, as also seen from the ballistic records. As the field of view of the schlieren system used in the ballistic trials was limited to about 150 mm, it can be assumed that the shock configuration seen in the wind tunnel tests and the simulation will only be reached outside of the field of view currently available. A future test series with visualizations conducted over a considerably wider field of view is planned to verify the findings of the wind tunnel tests and the numerical simulation.

In the tests with the supersonic projectile ([3], [5]) the reflected bow shock provided a clear demarcation line between parts of the flow influenced by the presence of the ground and those not affected. In the transonic case where no reflected shock is formed, this boundary has disappeared, and one has to assume that the entire projectile "feels"the vicinity of the ground. This is also seen in the pressure distribution along the length of the projectile (Fig.5). The reference test (Fig.5a) is a single projectile that corresponds to the free flight case. Measured pressure coefficients are compared with the numerical prediction from the simulation. With the exception of a single outlier which is attributed to a possibly faulty pressure tube connection the agreement is seen to be excellent.

The pressure data indicate that the presence of the ground (Fig.5b) leads to an overall change of the pressure levels compared to the free flight case and to the expected asymmetry between the pressure on the ground-facing side and the freestream-facing side, which will result in an overall vertical force. The single-point pressure measurements are, with one or two exceptions, in excellent agreement with the simulation results. From these measurements it is obvious that the pressure on the freestream-facing side is only mildly modified by the presence of the ground.

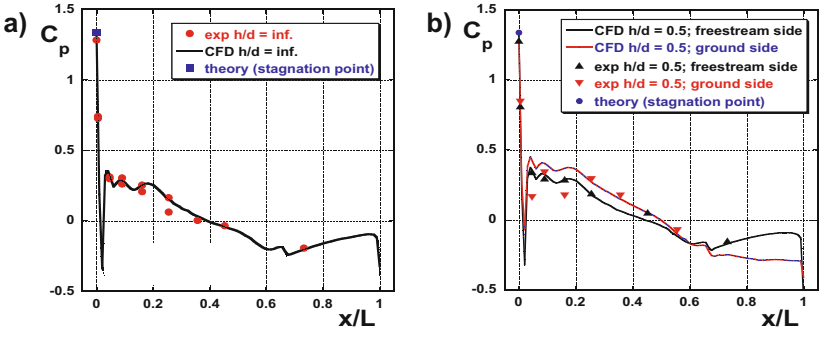

Fig. 5 Pressure distribution along the centreline of the Nosler projectile model at $M = 1.1$ a) for $h/d = \infty$; b) for $h/d = 0.5$

The limited amount of measured pressure data is not sufficient to determine the sign of the resulting force with confidence and a large degree of certainty, but it is obvious that the differences are not as pronounced as in the supersonic case. Further measurements of aerodynamic forces and moments as well as CFD are required to confirm the trend the initial results indicate.

4 Summary

The aerodynamic ground effect of projectiles flying in close vicinity to a straight solid surface was investigated numerically and experimentally through a number of ballistic trials and corresponding wind tunnel tests with scale models. All data obtained so far indicate that in contrast to the similar scenario with supersonic projectiles, the presence of the ground led to a growth of the subsonic zone behind the bow shock, which in turn changed shape and position of the shock. This bow shock was seen, over a range of clearances, to bend forward or to straighten and move away from the projectile, in each case avoiding the establishment of a reflected shock. Pressure measurements indicated that the ground led, as expected, to an asymmetry in the pressure distribution and thus to a vertical force that is not present in free flight. Based on the limited amount of quantitative data obtained so far, the effect of this asymmetry is, however, relatively minor.

References

1. Halloram, M., O'Meara, S.: Win. In: Ground Effect Craft Review. DSTO Report, Aeronautical and Maritime Research Laboratory (1999)
2. Rozhdestvensky, K.V.: Aerodynamics of a Lifting System in Extreme Ground Effect. Springer (2010)
3. Doig, G., Barber, T., Leonardi, E., Neely, A., Kleine, H.: AIAA J. 48, 12 (2010)
4. Kleine, H., Hiraki, K., Oakes, B., Young, J., Kusano, H., Iritani, Y.: Projectiles in transonic ground effect. In: Sato, E. (ed.) Proc. 29th Int. Cong. High-Speed Imaging & Photonics (2011), paper C05
5. Doig, G., Barber, T., Leonardi, E., Neely, A., Kleine, H.: Shock Waves 18 (2007)

Analytical Theory for Planar Shock Focusing through Perfect Gas Lens: High Compression Designs

M. Vandenboomgaerde and C. Aymard

1 Introduction

As it can be used to efficiently concentrate energy through high compressions [1], the collapse of imploding shock waves is of great interest. The stability and the modeling of these waves are still subject to studies. Furthermore, when a shock wave crosses an interface between two materials, this interface becomes unstable and the Richtmyer-Meshkov (RM) instability develops [2, 3]. In spherical geometry, experiments about this instability are scarce. As a consequence, there is a strong need of experiments about spherically imploding shock waves.

Planar shock waves are most easily generated in conventional (straight section) shock tubes [4, 5]. Some attempts have been carried out to generate convergent shock waves and RM instabilities in these shock tubes. Conical or wedge test sections were mounted on these tubes, but the waves remain roughly planar. In 2006, Dimotakis and Samtaney [6] proposed an elegant method in order to convert a planar shock wave into a cylindrical two-dimensional (2D) one. This is done as the shock wave passes a shaped interface between two gases. The shape and the impedance mismatch at the interface build a transmitted circular shock wave. This interface leans on a wedge which guides the shock wave towards the focus line. The shape of the lens is found to closely match an ellipse or a hyperbola. In 2010, we revisited this gas lens theory and generalized it [7]. The spherical three-dimensional (3D) geometry was considered and we established that the cross-section of the lens, viewed in a plane of symmetry, is exactly an ellipse or an hyperbola. A simple formula was derived for its eccentricity.

In this paper, we focus on the design of high compression experiments using a gas lens. These experiments would give data in order to study the stability of high Mach number 3D shock waves and to benchmark numerical simulations. We will characterize the compression by the Mach number, M_t, of the imploding shock wave.

M. Vandenboomgaerde · C. Aymard
CEA, DAM, DIF
F-91297 Arpajon (France)

In Sec. II, we validate our theory and study the time evolution of M_t when the Mach number, M_i, of the incident shock wave equals 1.15. Theoretical and numerical results are presented. In Sec. III, higher values of M_i are used in order to reach higher values of M_t. This leads to a disruption of the sphericity of the implosion as a shock-shock[8] appears on the main shock. We discuss this disruption and present a way to avoid this problem.

2 The Gas Lens Technique

2.1 Principle

We intend to create a circular (cylindrical or spherical) shock wave by morphing the refracted wave of a planar shock wave through a shaped gas interface, $\mathscr{C}$. The mismatch between the velocities, W_i and W_t, of the incident and the refracted waves, and the shape of the interface can build a circular transmitted wave. A circular refracted wave imposes the following set of geometrical equations, if $W_i > W_t$ (fast-slow (f-s) configuration) (see Fig. 1-a):

$$\begin{cases} r(0) - t\,W_t = r(\theta) \\ r(0) - t\,W_i = r(\theta)\,cos\,\theta \end{cases}, \tag{1}$$

where θ, r and t are the angle and the radius of the curve which describes $\mathscr{C}$ in the polar coordinate system, and the time ($t = 0$ is the time of the shock wave-interface contact), respectively. The Eqs.(1) lead to the following expression for $\mathscr{C}$: $r(\theta) = r(0)\,\frac{1-e}{1-e\,cos\,\theta}$, where $e = W_t/W_i$. It can be verified that this formula also holds in the slow-fast (s-f) configuration (see Fig. 1-b). It has been verified in Ref.[7] that such a shape of the interface is an arc of ellipse or hyperbola with the eccentricity, e. It has also been shown that the pressure field behind the transmitted shock wave is uniform. As the shock is circular and the pressure field uniform, the flow is purely radial and the shock wave should remain circular during its collapse.

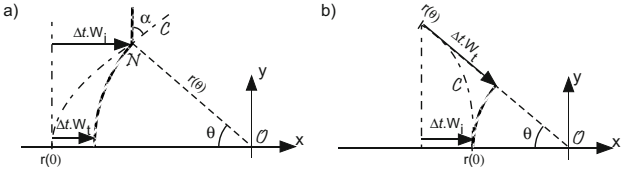

Fig. 1 Sketches of circular transmitted waves. The dash-dotted line and curve represent the incident shock wave (s.w.) and the interface $\mathscr{C}$ at $t = 0$, respectively. The hatched curves represent the transmitted s.w.(a) and (b): f-s and s-f configurations.

2.2 Domain of Validity

The wedge of the lens guides the shock wave during its collapse. The fact that the wedge intersects the interface imposes that the half aperture, θ_w, of the wedge has a maximum value, θ_m, which is given by: $cos(\theta_m) = \min(e, 1/e)$. Some other limits can further restrict θ_w: the here-above modeling is derived on the assumptions of the regularity of the waves and unperturbed pressure field behind the shock. The transition from regular to irregular shock-interface interaction is determined by the value of the angle, $\alpha(\theta)$, between the incident shock wave and the interface. Extensive literature about this transition and various criteria can be found to estimate critical values of α. Here, we will mainly consider the sonic criterion, *i.e.* the critical angle for the flow to remain sonic behind the wave, and the precursor criterion, *i.e.* the critical angle for a precursor wave to appear and link the incident shock wave and the refracted one. Since the shape of the interface is a conic, the two angles, α and θ, are related by $sin(\alpha - \theta) \,/\, sin(\alpha) = \pm e$. A critical value for α leads to a new value θ_m which can be more restrictive than the one given above.

The assumption of an uniform pressure field behind the shock wave is expected to be fulfilled as the wave quickly moves away from the interface and the potential perturbations that it could emit.

2.3 Numerical Validation

In order to test the accuracy of our theory, we have computed several gas lenses for the fast-slow and the slow-fast configurations in 2D and 3D. The simulations were run by the multi-material Arbitrary Lagrangian Eulerian (ALE) package of the Hesione code [9]. Computations are run in cylindrical (2D) as well as in axy-symmetrical (3D) geometry. An incident shock wave in Air with a low Mach number, $M_i = 1.15$, is considered and the pressure of Air at rest is $P_0 = 1\,atm$. SF_6 and He are used as second gases for the f-s and the s-f configurations, respectively. These parameters give respective eccentricities equal to $e = 0.42$ and $e = 2.75$. The height of the shock tube is taken equal to $0.08\,m$ and $\theta_w = 30^\circ$ for the convergent section. The Figs. 2-a,d present the morphing of the transmitted shock waves into circular ones. The Figs. 2-b,e show the fully formed waves as they travel down the wedge. It can be verified that no deviation from the circular arc with center $\mathscr{O}$, which is used for reference, is noticeable. The Figs. 2-c,f present the trajectories of the shock waves. Their velocities are found nearly constant and equal to the velocity of the planar case during about 2/3 of the implosion. In a second stage, the waves accelerate and the trajectories are in very good agreement with the Guderley's strong shock model [10].

The theoretical study of spherically imploding shock waves is commonly based on the Whitham's geometrical approximation [8]. The following equation between M_t, and the area, A, of the shock wave can be derived:

$$\frac{M_t\, dM_t}{M_t^2 - 1}\lambda(M_t) + \frac{dA}{A} = 0, \tag{2}$$

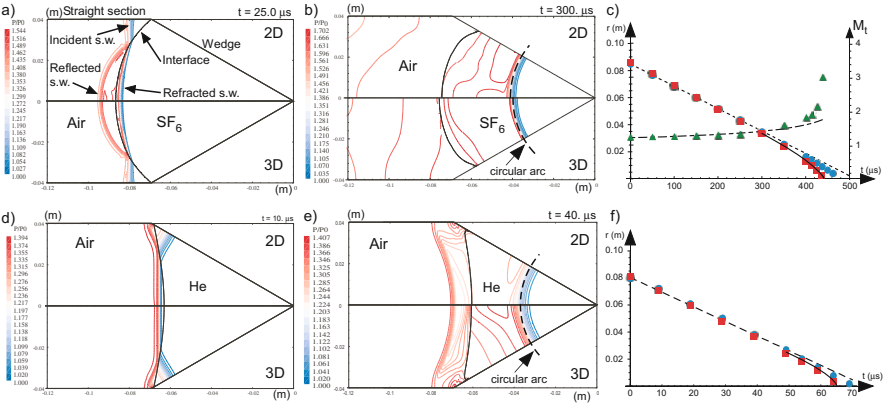

Fig. 2 Upper and downer figures present f-s and s-f configurations. (a),(d) Morphing of the transmitted shock wave. (b),(e) Circular shock wave. (c) Trajectory and Mach number of the shock wave. (f) Trajectory of the shock wave. Squares and circles represent the 3D and 2D geometry, respectively. The dashed and full lines are calculated from the planar case and the Guderley's model.

where $\lambda(M) = (1 + \frac{2}{\gamma+1}\frac{1-\mu^2}{\mu})(1 + 2\mu + \frac{1}{M^2})$, with $\mu^2 = ((\gamma-1)M^2+2)/(2\gamma M^2 - \gamma + 1)$. The strength of the shock wave, as it implodes, can be studied through M_t. This Mach number can be estimated in two ways. Firstly, Eq.(2) can be used with an estimate of $A(t)$. Secondly, M_t can be computed from the pressure jump across the shock wave in the simulations. Hereafter, as the constant velocities of the shock waves allow to easily estimate $A(t)$, we will consider the first stage of the implosion. The Fig. 2-c presents the comparison between the theoretical and computed M_t, in the 3D case. It can be verified that the theory and the simulations are in good agreement. This agreement and the fact that the transmitted shock waves are circular in s-f as well as in f-s configurations, and in 2D or 3D geometry, validate our design of gas lenses.

3 Strong Shock Wave Designs

As shown in Fig. 2-c, values of M_t about 3 are reached; they corresponds to a compression ratio equal to 9.35. The study of higher compression would require measurements in the last few micro-seconds of the implosion, which would be extremely difficult experimentally. In order to increase the compression, we have naturally increased the value of M_i. We have taken $M_i = 1.5$, keeping $\theta_w = 30°$ for the Air/SF_6 configuration. The following numerical results underline the fact that the reflected shock wave cannot expand freely as supposed in the theory (see Fig. 3-a).

The wave bounces back on the straight section of the shock tube and crosses the interface which increases the RM instability. At $M_i = 1.5$, these two phenomena concur in the disruption of the refracted shock wave. Firstly, the twice-reflected shock

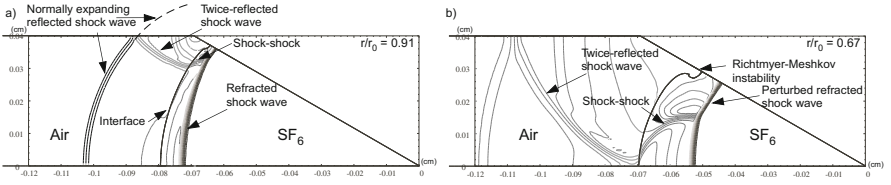

Fig. 3 Pressure field of the Air/SF_6 case for $M_i = 1.5$ at $r/r_0 = 0.91$ and $r/r_0 = 0.67$, respectively.

wave is strong enough to generate a shock-shock on the refracted shock. Secondly, the RM instability is enhanced and becomes able to interact with the refracted wave (see Fig. 3-b). As a result, the refracted shock wave is no more circular. Furthermore, the shock-shock travels towards the axis where it rebounds. At that time, the pressure sharply increases on the axis which can even reverse the curvature of the imploding shock wave. The effect of the rebound of the shock-shock can be tracked through the local M_t on the axis. The Fig. 4-a presents this value of M_t versus r/r_0, where r now represents the location of the shock wave and r_0 its initial radius, respectively. The jump pressure due to the shock-shock can be clearly identified at $r/r_0 \approx 0.4$ for the Air/SF_6, $\theta_w = 30°$ case.

A lower value of θ_w will reduce the strength of the reflected shock wave: as the geometry tends to the planar one, the twice reflection tends to disappear. A numerical simulation with $\theta_w = 15°$ was run. The overpressure is lessened (see Fig. 4-a) but the sphericity of the transmitted wave is nevertheless disrupted. In order to further lessen the twice-reflected wave effect, the density ratio across the interface must also be reduced. This induces three effects: the reflected Mach number is lessened, the difference between the velocities of the interface and the transmitted wave is increased, and the growth rate of the RM instability is decreased. In order to check this statement, we have run an Air/CO_2, with $M_i = 1.5$ and $\theta_w = 15°$. The density ratio is now equal to 1.54 against 5.04 in the Air/SF_6 case. As expected, the Fig. 4-b shows a spherical unperturbed transmitted shock wave. This is further confirmed by the computation of M_t on the axis which is nearly unaffected by the shock-shock

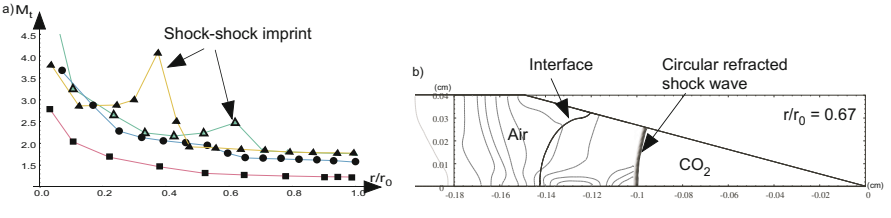

Fig. 4 (a) Mach number of the transmitted shock wave versus its location. Squares, full and empty triangles, and circles represent Air/SF_6, ($\theta_w = 30°, M_i = 1.15$), ($\theta_w = 30°, M_i = 1.5$), ($\theta_w = 15°, M_i = 1.5$) and Air/CO_2, ($\theta_w = 15°, M_i = 1.5$) cases, respectively. (b) Pressure field of the Air/CO_2, ($\theta_w = 15°, M_i = 1.5$) case at $r/r_0 = 0.67$

(see Fig. 4-a). Near the collapse time, M_t easily reaches the value of 4 which corresponds to a compression ratio of 18.

4 Conclusion

We have established that an interface between two gases can focus a planar shock wave into a spherical one if the shape of the interface is a conic with an eccentricity equal to W_t/W_i. This has been validated by numerical simulations. As the incident shock wave Mach number increases, the assumption of uniform pressure behind the imploding shock wave is no more fulfilled. As a result, a shock-shock disrupts the sphericity of the shock wave. In order to address this issue, the aperture of the convergent section and the density ratio between the two gases must be reduced. In these conditions, the shock-shock effect becomes negligible and high compressions can be easily reached before the final collapse of the shock wave.

References

1. Lindl, J.D., McCrory, R.L., Campbell, E.M.: Progress towards ignition and burn propagation in inertial confinement fusion. Phys. Today 45(9), 32 (1992)
2. Richtmyer, R.D.: Taylor instability in shock acceleration of compressible fluids. Commun. Pure Appl. Math. 13, 297 (1960)
3. Meshkov, E.E.: Interface of two gases accelerated by a shock wave. Fluid Dyn. 4, 101 (1969)
4. Long, C.C., Krivets, V.V., Greenough, J.A., Jacobs, J.W.: Shock tube experiments and numerical simulation of the single-mode, three-dimensional Richtmyer-Meshkov instability. Phys. Fluids 21, 114104 (2009)
5. Mariani, C., Vandenboomgaerde, M., Jourdan, G., Souffland, D., Houas, L.: Investigation of the Richtmyer-Meshkov instability with stereolithographed interfaces. Phys. Rev. Lett. 100, 254503 (2008)
6. Dimotakis, P.E., Samtaney, R.: Planar shock cylindrical focusing by a perfect-gas lens. Phys. Fluids 18, 031705 (2006)
7. Vandenboomgaerde, M., Aymard, C.: Analytical theory for planar shock focusing through perfect gas lens and shock tube experiments designs. Phys. Fluids 23, 016101 (2011)
8. Whitham, G.B.: Linear and nonlinear waves. Wiley Interscience, New York (1974)
9. Eder, D., Bonneau, F., Vierne, J., et al.: Simulation of shrapnel to aid in the design of NIF/LMJ target diagnostic configurations. In: Proc. Inertial Fusion Science and Applications, IFSA 2003, pp. 572–575. Elsevier (2004)
10. Guderley, G.: Starke kugelige und zylindrische Verdichtungsstöβe in der Nähe des Kugelmittelpunkter bzw. der Zilinderachse. Luftfahrforsch 19, 302 (1942)

Nonlinear Analysis of Stability of Plane Shock Waves in Media with Arbitrary Thermodynamic Properties

A. Konyukhov, A. Likhachev, V. Fortov, and S. Anisimov

1 Introduction

S. D'yakov was the first who considered the problem of the shock wave (SW) stability in media with arbitrary thermodynamic properties [1]. He developed the linear theory of the plane SW stability on a basis of the normal mode analysis and obtained simple quantitative criteria for different types of the shock behavior: $-1 < L < L_0$ (absolute stability), $L_0 < L < 1 + 2M$ (neutral stability), $L < -1$ or $L > 1 + 2M$ (instability). The notations are the same as in [1], correct expression for the lower boundary of the neutral stability region L_0 was given by V. Kontorovich in [2]. The same results were obtained in works [3-5] differing from [1] in the features of the linearized formulation and/or used mathematical technique. More recently (see, e.g., review [6]), it was found that the Hugoniot fragments meeting to the instability conditions lie within the region of the SW ambiguous representation. The solution choice in such regions is of great interest, the more so the feasibility of the unstable SW with an unlimited growth of the amplitude of the front perturbations raises justified doubts [6]. It is also problematic the spontaneous sound emission by the front of the neutrally stable SW predicted by the linear theory. The attempts of the theoretical analysis of the neutrally stable SW behavior in certain nonlinear formulations [6-7] gave sufficiently presumable and discrepant results. Besides, the neutral stable or unstable SW (at least, in the form predicted by the linear theory) are not yet observed in experiments. It is clear that the problem considered goes beyond the linear theory and must be solved in the framework of as far as possible complete nonlinear formulation. In the paper presented we briefly review results of our systematic nonlinear analysis of the plane SW stability problem. Due to space restrictions some details of problem formulations and solutions we are obliged to omit, but they may

A. Konyukhov · A. Likhachev · V. Fortov
Joint Institute for High Temperatures, RAS, Izhorskaya str., 13 b. 2, Moscow, 125412 Russia

S. Anisimov
Landau Institute for Theoretical Physics, RAS, Akademika Semenova av., 1-A, Chernogolovka, Moscow region, 142432 Russia

be found in our works [8-10] The emphasis is placed on the origin of the cellular shock front structure arising if the SW has ambiguous representation caused by the fulfilment of the instability condition $L > 1 + 2M$ (this phenomenon has been first found in [10]).

2 Neutral Stability of Shock Waves

The approach elaborated in [9] allows determining the SW neutral stability region from the analysis of the equation of state (EOS) (pre-shock pressure is used as parameter). This approach has been applied for the analysis of the EOS of some real media and to define the initial conditions for simulation. The numerical modeling of the neutrally stable shock behavior in media with real (van der Waals gas and magnesium) and model [5] equations of state has been performed. The problem has been solved in inviscid and viscous models in two- and three-dimensional formulations (for details see [9]). In all versions of calculations, the spontaneous sound emission by the neutrally stable shock wave was not observed. As result of forced emission the characteristic lattice of downstream acoustic waves is formed with time. The angles acoustic waves make with undisturbed shock front coincide with the predictions of the linear theory (Figure 1a), but their intensity decreases. The damping of acoustic perturbations behind the neutrally stable shock wave is much slower than that for absolutely stable shocks (Figure 1b, inviscid model). Dissipative processes accelerate the damping of the post-shock flow perturbations. Besides, the data obtained have confirmed found theoretically "angle rule" [9]: the angle between the acoustic and entropy-vortex waves in the triple configuration on the neutrally stable SW front is smaller than 90^o; if the SW is absolutely stable, this angle is greater than 90^o. This rule is useful to detect the neutrally stable SW in experiments.

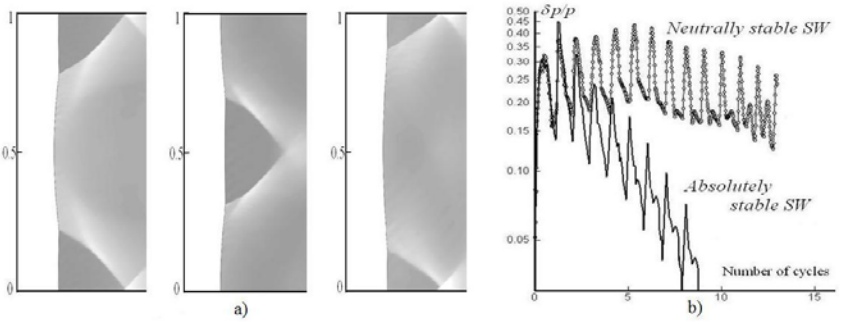

Fig. 1 The neutrally stable shock behavior in the van der Waals gas: the change of the lattice of the acoustic waves in time (a), and the damping of perturbations in neutrally and absolutely stable shock waves (b).

3 Shock Ambiguous Representation

The shock instability condition $L < -1$ means the presence of a bend (in the limiting case, kink) on the Hugoniot curve at a negative sign of the derivative $(\partial p/\partial V)_H$ and is satisfied in real substances near a first order phase transition or at the transition from an elastic state to a plastic one. It directly follows from this condition that the Mach number in the flow behind the SW (in the reference frame tied to the front) is greater than unity and, hence, one of the conditions of the SW evolutionarity is violated. Moreover, the derivative $(\partial^2 p/\partial V^2)_S$ at the beginning of the Hugoniot curve section with $L < -1$ is negative; i.e., compression SW corresponding to this region cannot exist. Such SW appearing naturally or created artificially must instantaneously decay. It is more difficult to predict the SW behavior in the ambiguous representation region expanding beyond the section $L < -1$ towards higher pressures, where the choice between the primary SW and the splitting wave configuration is independent of the thermodynamic constraints. To study the shock behavior in the region of its ambiguous representation caused by the fulfillment of the condition $L < -1$ the one- and two-dimensional computations in inviscid and viscous models have been carried out (for details see [8,10]). The results obtained are presented in Figure 2. In the case of the smooth Hugoniot (Figure 2a) the primary shock splits into the incomplete (interval 1-2) or complete (interval 2-4) composite compression wave. The former consists of shock wave corresponding to the point 1 and adjacent isentropic (”nonbreaking”) compression wave. The latter involves in addition the second (closing) SW moving in the same direction as the first (opening) shock but with a higher velocity. Approaching the ambiguity region boundary 4, the velocities of opening and closed shocks are equalized and only the primary SW can exist beyond this region. It has been first found that the closed shock may be neutrally stable [8]. For the kinked Hugoniot (2b) the fragment with negative $(\partial^2 p/\partial V^2)_S$ contracts into a point. In this case only the complete composite compression wave occurs within the ambiguity region 1-4, but instead isentropic compression wave the section of the uniform flow occurs between shocks (so-called ”two-wave” structure).

Although the shock instability condition $L > 1 + 2M$ is not limited by basic thermodynamic constraints, its fulfillment in real media has not yet been found. Nevertheless, the analysis of the shock behavior in the corresponding ambiguity region is of undoubted fundamental interest as a part of the problem of the plane shock wave stability and can be valuable to identify this phenomenon in future experiments. To study the shock behavior caused by the condition $L > 1 + 2M$ fulfillment the one-, two- and three-dimensional computations have been carried out using modification [10] of the model equation of state [5]. The theoretical analysis of the intersections of the Hugoniot under consideration with the secondary Hugoniot curves and isentropes has been carried out. Its results are shown in Figure 3a. The region of the ambiguous SW representation DG overlaps the section EF in which the instability condition $L > 1 + 2M$ is fulfilled. In addition to the primary SW, the following wave configurations are possible within the region DG: $\overleftarrow{S}\,T\,\overrightarrow{S}$ in section DE, $\overleftarrow{S}\,T\,\overrightarrow{S}$ or $\overleftarrow{S}\,T\,\overrightarrow{R}$ in section EF, and $\overleftarrow{S}\,T\,\overrightarrow{R}$ in section FG, where S is the shock wave, T is the

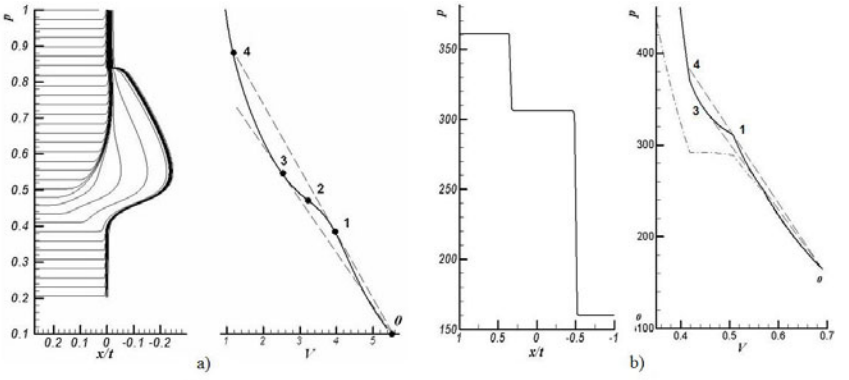

Fig. 2 The analysis of the SW behavior on the basis of the model EOS [5] (a) (left panel: splitting diagram in terms of pressure versus scaling variable x/t; right panel: the smooth Hugoniot fragment) and the deuterium EOS [11] (b) (left panel: the two-wave structure occurrence; right panel: the kinked Hugoniot). The intervals of the stability (0-1), negative $(\partial^2 p/\partial V^2)_S$ (1-2), condition $L < -1$ fulfillment (1-3), neutral stability (upper point 3), and ambiguous shock representation (1-4) are indicated.

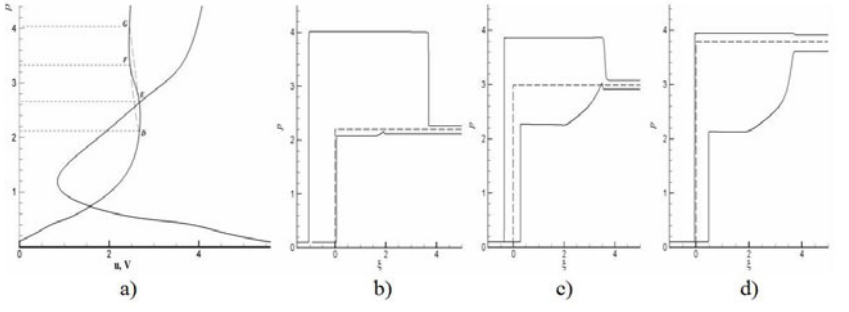

Fig. 3 The Hugoniot curve (a) and results of the one-dimensional simulation with perturbation of the parameters behind the shock wave (b-d). The dashed lines correspond to the primary shock wave. The deviation of the solid lines from the dashed line characterizes the perturbation type and intensity.

contact discontinuity, R is the rarefaction wave, an arrow indicates the direction of the motion of the wave with respect to the contact discontinuity. The results of the one-dimensional simulation of the behavior of the SW disturbed by weak compression or rarefaction wave are shown in Figure 3(b-d). As is seen from pictures, the primary shock belonging to the region DF may split or remain unchanged depending on the position within this region and the disturbance type. The last circumstance is important to understand results of the multidimensional modeling demonstrating the shock front undamped oscillations with the formation of the unsteady cellular

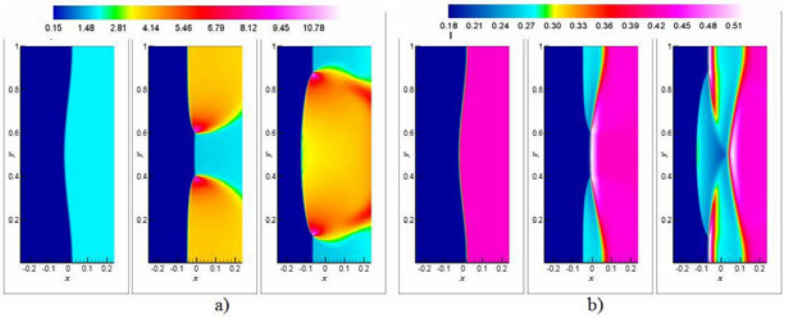

Fig. 4 The initial stage of the two-dimensional solution (viscous model) with periodic perturbation of the shock front in terms of pressure (a) and density (b).

structure. The initial stage of the process is shown in Figure 4. The primary SW corresponds to the Hugoniot point situated in the section DE with theoretical possibility of its preservation or splitting on two oppositely directed shocks. At the initial instant of time the SW surface has been periodically disturbed (the formulation details see in [10]). The SW distortion leads to post-shock pressure perturbation: rarefaction and compression regions appear behind respectively convex and concave (with respect to the shock wave propagation direction) sections of the SW front. In accordance with the one-dimensional results, the SW remains in the initial state in the convex segment and splits into two oppositely directed shocks ($\overleftarrow{S}\,T\,\overrightarrow{S}$ configuration) in the concave one (Figure 4, middle panels). Pressure between these shocks is much greater than its value behind the primary SW and corresponds to the Hugoniot section FG. Triple-shock configurations are formed on every semi-period. The nodal points on neighboring semi-periods move towards to each other. The pressure between shocks near the nodal point increases to values going beyond the upper bound of the ambiguity region DG. Since the shock $\overrightarrow{S}$ is diverging, the rarefaction wave propagating to the shock $\overleftarrow{S}$ is formed. As follows from the one-dimensional analysis the interaction of $\overleftarrow{S}$ with rarefaction wave leads to its break-up into configuration $\overleftarrow{S}\,T\,\overrightarrow{R}$. The intensity of shock in this configuration approaches the intensity of the primary SW, and its front becomes practically flat. It is attended with occurrence of specific "disks" of elevated density seen in right panel of Figure 4b. After intersection of the nodal points the region of elevated pressure arises and the process continues as if semi-periods reverse roles. After few cycles the solution gains periodic character as shown in Figure 5. Thus the shock behavior observed is explained by the switching of the shock parameters between the wave configurations found in one-dimensional computations. The switching is induced by the transverse waves which propagate along the shock front from the post-shock side.

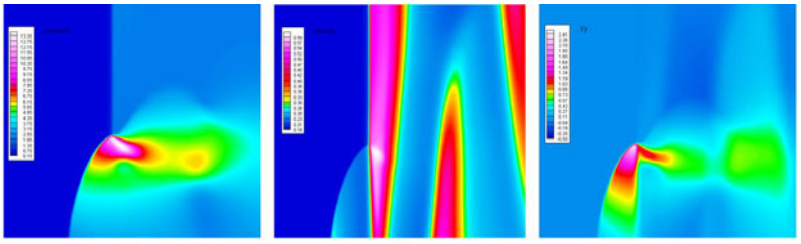

Fig. 5 The instant of the shock periodic regime in terms of pressure (a), density (b), and transverse velocity (c).

4 Conclusion

The nonlinear analysis conducted showed that the predictions of linear theory [1,2] do not fulfilled completely (for unstable shocks) or partially (for neutrally stable shocks). When the shock wave belongs to the ambiguous representation region, it splits or has cellular structure. The origin of the latter is revealed and described. The spontaneous sound emission from the neutrally stable shock wave is not observed. If the emission is forced, acoustic waves downstream the shock front are slowly damped.

References

1. D'yakov, S.P.: Shock wave stability. Zh. Eksp. Teor. Fiz. 27(3), 288–295 (1954)
2. Kontorovich, V.M.: On shock wave stability. Zh. Eksp. Teor. Fiz. 33(6), 1525–1526 (1957)
3. Erpenbeck, J.J.: Stability of Step Shocks. Phys. Fluids 5(10), 1181–1187 (1962)
4. Swan, G.W., Fowles, G.R.: Shock wave stability. Phys. Fluids 18, 28–35 (1975)
5. Ni, A.L., Sugak, S.G., Fortov, V.E.: Quasi one-dimensional analysis and numerical modeling of stationary shock wave stability in media with arbitrary equation of state. Teplofiz. Vys. Temp. 24(3), 564–569 (1986)
6. Kuznetsov, N.M.: Stability of shock waves. Usp. Phys. Nauk. 159(3), 493–527 (1989)
7. Egorushkin, S.A.: Nonlinear instability of a spontaneously radiating shock wave. Izv. AN SSSR, Ser. Mekh. Zhidk. Gasa (3), 110–118 (1983)
8. Konyukhov, A.V., Likhachev, A.P., Fortov, V.E., et al.: Numerical modeling of shock-wave instability in thermodynamically nonideal media. JETP 98(4), 811–819 (2004)
9. Konyukhov, A.V., Likhachev, A.P., Fortov, V.E., et al.: On neutral stability of a shock wave in real media. JETP Letters 90(1), 18–24 (2009)
10. Konyukhov, A.V., Likhachev, A.P., Fortov, V.E., et al.: Stability and ambiguous representation of shock wave discontinuity in thermodynamically nonideal media. JETP Letters 90(1), 25–31 (2009)
11. SESAME Report on the Los Alamos Equation-of-State Library, Report LANL-83-4 (1983)

Shock and Blast Wave Propagation through a Porous Barrier

D.B. Epstein and A.N. Kudryavtsev

1 Introduction

It is well known that a shock wave can be attenuated when propagating through a porous barrier. Better understanding of this phenomenon is of significant importance in practical applications, e. g. in problems of industrial safety. As a result, the interaction of shock waves with a porous barrier has been studied in many papers. In particular, in [1, 2] a theoretical model, which assumes that a discontinuity breakdown happens at the moment when the propagating shock wave hits the barrier, has been developed. In accordance with this model the flow at large times is self-similar and the intensities of reflected and transmitted shock waves can be determined provided that some model is adopted for the flow through the barrier itself (typically it is considered as a steady subsonic flow).

In recent years, this problem has been investigated repeatedly both numerically and experimentally. In the experiments [3] a shock wave interacts with a regular system of cylinders installed inside a shock tube of rectangular section. Shock wave reflection from a rigid wall covered by a porous material is investigated in [4] and transmission of a shock wave through a perforated wall is considered in [5]. B. Skews has studied oblique interaction of a shock wave with a perforated plate [6] and reviewed results of experimental investigations of the problem in [7]. The numerical investigation [8] deals with the pressure amplification experienced behind a rigid, porous barrier exposed to a shock wave. Recently shock wave attenuation over obstacles of different geometrical shapes has been studied in [9].

In the present paper we investigate numerically the interaction of shock and blast waves with a porous barrier which is modelled by system of regularly spaced cylinders and spheres. The shock or blast wave intensity as well as the barrier porosity and thickness are varied and results of this parametric study are presented and discussed.

D.B. Epstein · A.N. Kudryavtsev
Khristianovich Institute of Theoretical and Applied Mechanics, Institutskaya St. 4/1, Novosibirsk, 630090, Russia

2 Governing Equations and Numerical Method

The problem under investigation is simulated by solving numerically 2D and 3D Euler equation for the perfect gas with the ratio of specific heats $\gamma = 1.4$. An unstructured, finite-volume flow solver, which utilizes triangular (in 2D) or tetrahedral (in 3D) grid cells as control volumes, is employed. The solver is based on a shock-capturing TVD scheme with the second-order MUSCL reconstruction of cell-face variables from cell-averaged values. The *minmod* limiter is used to avoid numerical oscillations. Numerical fluxes through cell boundaries are calculated with the HLLE approximate Riemann solver. Time integration is performed using the second-order Runge-Kutta method. The numerical code is parallelized using the MPI library.

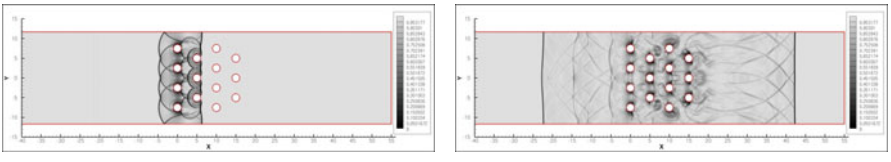

Fig. 1 Numerical schlieren pictures of shock wave ($M_s = 1.4$) interaction with a cylindrical array mounted in a plane channel.

Numerical simulation of the interaction between a shock wave propagating with the Mach number $M_s = 1.4$ and an array of 14 cylinders mounted inside a plane channel has been performed in order to validate the code. The computations were performed exactly at the same geometrical arrangement and flow parameters as in the experiments [3].

Numerical schlieren pictures of Fig. 1 shows the flow images at two time moments: when the incident shock wave has just passed the second column of cylinders (left) and when multiple shock waves generated during the interaction have merged and formed the transmitted and reflected shock waves (right). In the last picture a complex structure of weak shock waves, contact surfaces and vortices in the space between the transmitted and reflected shocks is also clearly visible. Comparison of pressure time histories in several points with experimental measurements reveals reasonable agreement of the data.

3 Interaction of Shock Wave with a Porous Barrier

Detailed numerical simulations of the interaction between the incident shock wave and a cylinder array, which model a porous barrier, have been performed. Unlike the previous test case, the barrier is assumed to be infinite in the vertical direction so that the periodic boundary conditions can be imposed on the top and bottom boundaries of the computational domain. The cylinders are arranged in several columns and the centres of three neighbouring cylinders form an equilateral triangle.

The major parameters of this study are the ratio of the distance between the centres of cylinders H and the cylinder radius R and the Mach number of the incident

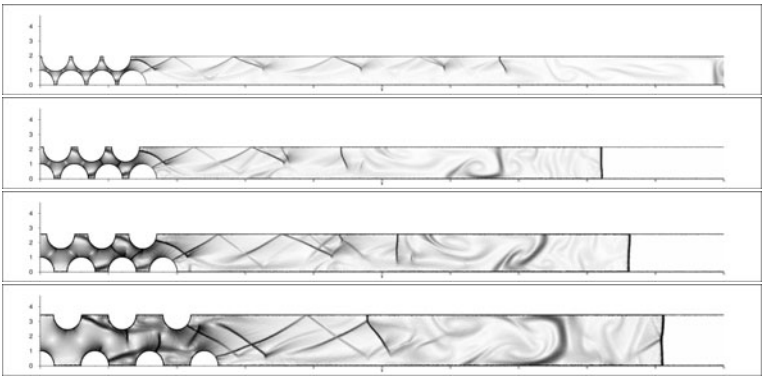

Fig. 2 Numerical schlieren pictures of $M_s = 4.0$ shock wave transmission through a cylindrical array at $H/R = 2.25, 2.5, 3.0, 4.0$.

shock wave M_s. Both the parameters have been varied in rather a wide range. The Mach number is varied from 1.2 to 6 by increments of 0.4, while the distance between the cylinders was taken equal 2.1, 2.25, 2.5, 3.0 and 4.0 radii.

Fig.2 shows typical numerical schlieren pictures obtained at $M_s = 4.0$ and $H/R = 2.25, 2.5, 3.0, 4.0$ for the barrier composed of 7 columns. There is a complex flow structure consisting of multiple secondary shock waves and vortical wakes behind the barrier, however the transmitted shock waves recovers a plane shape at the distance of a few barrier thicknesses.

Computations have also been performed for 3D interaction of a shock wave with a system of spheres. The spheres are arranged in a body-centred cubic lattice. The length of cube edge H is 3.0, 4.0 and 5.0 of R and the barrier is also composed of 7 layers. The Mach number of incident shock is varied from 2.0 to 4.0 by increments of 0.5.

A typical flow images obtained is shown in Fig.3 where density isosurfaces are displayed for the 3D interaction at $H/R = 5.0$, $M_s = 3.0$.

The pressure rise Δp behind the transmitted shock wave has been determined as the maximum pressure jump over a region between the barrier (stepping few radii downstream) and the transmitted shock wave. These results are shown in Fig.4 as function of the incident shock Mach number at some fixed distances between the bodies for the 2D (left) and 3D (right) configurations. As can be seen, Δp monotonically increases when the Mach number grows. For the 2D case, with increasing distance up to 4 radii, the pressure behind the transmitted shock wave almost coincides with that behind the incident shock wave. This means that the attenuating effect of the barrier is hardly noticeable at large barrier porosities. Surprisingly, for the 3D case the attenuating effect vanishes at the same distance between spheres $H/R = 4.0$ as in the case of cylinders. For a large distance $H/R = 5.0$ even small shock wave amplification has been observed.

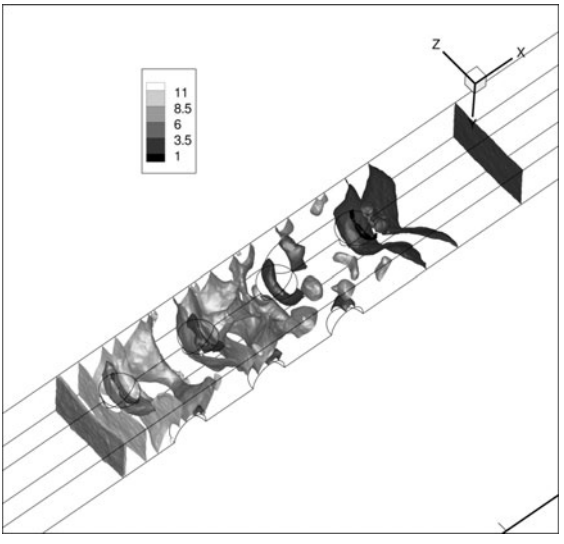

Fig. 3 Density isosurfaces for 3D interaction of shock wave and array of spheres at $H/R = 5.0$, $M_s = 3.0$

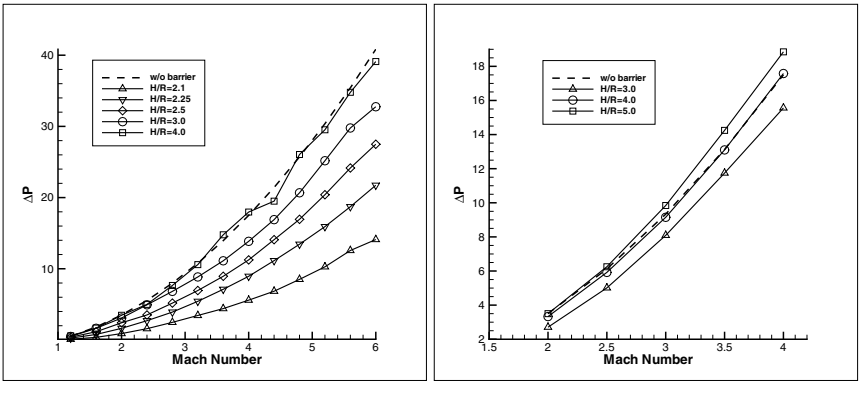

Fig. 4 Pressure rise in transmitted shock wave as function of M in 2D (left) and 3D (right) cases.

4 Interaction of Blast Wave with a Porous Barrier

The problem of a blast wave propagating from a localized explosion and interacting with the barrier has also been considered. The major differences with the previous case are the cylindrical (in 2D) rather than plane shape of the incident wave and a non-uniform flow behind the wave. As earlier, the porous barrier is modelled by an array of the cylinders.

The computational domain, in this case, has the following configuration. The bottom and left boundaries are solid walls where the reflection boundary conditions are imposed. On the right and the top boundaries the extrapolation conditions are used. The initial flowfield is a quiescent gas. The localized explosion is modelled by a significant pressure and temperature rise in several cells in the left lower corner of the domain. The pressure rise there Δp can be calculated from the given energy deposition as $\Delta p = (\gamma - 1)E/V$ where V is the total volume of the cells in which the pressure was risen.

As a result of the pressure rise, a blast wave propagates from this place, and very soon its shape becomes cylindrical (numerical simulations for the cylindrical blast wave have been performed as a first step to more realistic spherical blast wave case).

The flow evolution for the energy deposition $E/\gamma p_0 R^2 = 1000$ (where p_0 is the quiescent gas pressure) is shown in Fig. 5. As can be seen in the Fig. 5 (middle and right), after passing through the barrier, shock wave propagation along the X axis is delayed with respect to the wave moving along the Y axis.

Fig. 6 shows the pressure distributions along the X and Y axes for different distances between the cylinders at the moment when the waves reach points located at the distance $L = 35R$ from the place of explosion. As seen in the figure, the closer the cylinders to each other, the lower pressure behind the transmitted wave. Namely, the pressure rise Δp is 0.8, 1.0, and 1.12 for $H/R = 3$, 4, and 5, respectively while it is equal to 1.14 with no barrier.

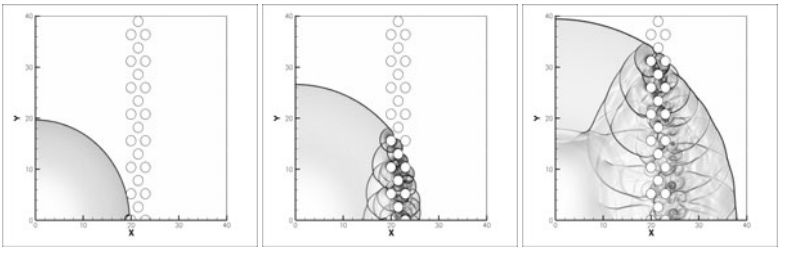

Fig. 5 Blast wave interaction with a cylinder array. $H/R = 3$, $E/\gamma p_0 R^2 = 1000$

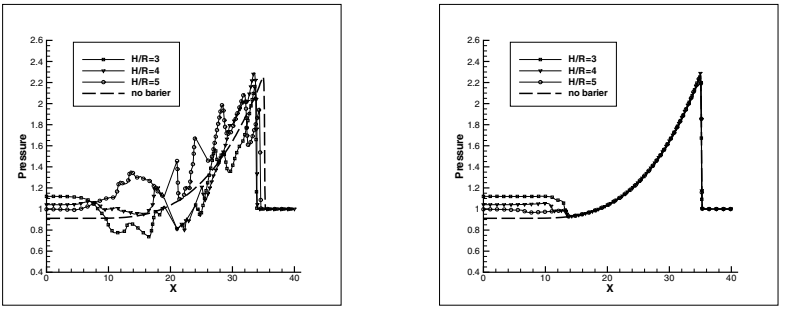

Fig. 6 Pressure distribution along X (left) and Y (right) axis.

5 Conclusions

Numerical simulations of interaction of plane shock wave with porous barrier modelled by an array of cylinders or spheres has been performed. Influence of the shock wave Mach number and the distance between cylinders has been investigated. It has been shown that pressure behind the transmitted shock wave is reduced by barrier provided that $H/R < 4$. The interaction of blast wave with the porous barrier has also been numerically investigated to study the effect of the cylindrical shape of the blast wave and non-uniformity of the flow behind it. The influence of the distance between cylinders has been studied. It has been observed that in all cases simulated the pressure behind the blast wave is lower than without barrier. The decrease in the distance between cylinders leads to attenuation of the transmitted shock wave.

Acknowledgements. The present study was supported by Russian Academy of Sciences under the Program "Fundamental Problems of Mechanics of Interactions in Technological and Natural Systems, Materials and Media".

References

1. Grin, V.T., Kraiko, A.N., Miller, L.G.: Decay of a shock wave at a perforated baffle. Fluid Dyn. 22(3), 372–378 (1981)
2. Kraiko, A.F., Miller, L.G., Shirkovskii, I.A.: Gas Flow in a Porous Medium with Porosity Discontinuity Surfaces. J. Appl. Mech. Techn. Phys. 23(1), 111–118 (1982)
3. Suzuki, K., Himeki, H., Watanuki, T., Abe, T.: Experimental Studies on Characteristics of Shock Wave Propagation through Cylinder Array. Inst. Space Astronaut. Sci. Rep., No. 676 (2000)
4. Gubaidullin, A.A., Britan, A., Dudko, D.N.: Air Shock Interactions with an Obstacle Covered by Porous Material. Shock Waves 13(1), 41–48 (2003)
5. Britan, A., Karpov, A.V., Vasilev, E.I., Igra, O., Ben-Dor, G., Shapiro, E.: Experimental and Numerical Study of Shock Wave Interaction With Perforated Plates. J. Fluids Eng. 126(3), 399–409 (2004)
6. Skews, B.: Shock Wave Interaction with Porous Plates. Exp. Fluids 39(5), 875–884 (2005)
7. Skews, B.: Experimental Studies of Shock Wave Interactions with Porous Media. In: Shock Wave Science and Technology Reference Library, pt. III, pp. 271–295 (2007)
8. Naiman, H., Knight, D.D.: The Effect of Porosity on Shock Interaction with a Rigid Porous Barrier. Shock Waves 16(4-5), 321–337 (2007)
9. Sadot, O., Ben-Dor, G., Hadjadj, A.: Experimental and Numerical Investigations of Shock Wave Attenuation over Obstacles. In: Book of Proceedings of ISSW-27, p. 327 (2009)

Supersonic Patches in Steady Irregular Reflection of Weak Shock Waves

M. Ivanov, G. Shoev, D. Khotyanovsky, Y. Bondar, and A. Kudryavtsev

1 Introduction

Guderley theoretical model [1, 2] for weak shock wave reflection is a well-known way to overcome the von Neumann paradox within the gas dynamic framework. Recent Euler calculations [3] confirmed conceptual issues of Guderley theory for steady shock reflection. An expansion fan and a local supersonic patch were found behind the triple point. A numerical simulation based on the shock fitting technique was used in that study. Ivanov et al. [4], however, did not reveal any supersonic patches in Euler computations based on both the shock-fitting and shock-capturing techniques. Tesdall et al. [5] discovered a sequence of supersonic patches and triple points along the Mach stem for unsteady shock reflection. The results of numerical simulation showed a sequence of triple points and tiny supersonic patches behind the leading triple point. Another interesting result was also obtained in [6] within the framework of depth-averaged two-dimensional inviscid shallow water flow model. The nested-block grid refinement technique was used in those studies to achieve high resolution of the computational mesh. A supercritical patch was discovered. Thus, at the present time, the question about the supersonic patch structure is still open.

Another way to overcome the von Neumann paradox is to take into account the effects of viscosity [7, 8]. According to Sternberg model [7], instead of the triple point, there must be a transition zone in a viscous flow, where the Rankine-Hugoniot (R-H) relations cannot be applied. Recent viscous computations [9] at low Reynolds numbers confirmed the validity of this viscous model and did not reveal any supersonic patches. Moreover, similarity of the flow fields at different Reynolds numbers was found in the vicinity of shock intersection. However, it is still unclear whether the viscous flow structure at $Re_w \to \infty$ can continuously transform into the flow pattern predicted by the inviscid Guderley model. This question became curious, since

M. Ivanov · G. Shoev · D. Khotyanovsky · Y. Bondar · A. Kudryavtsev
Khristianovich Institute of Theoretical and Applied Mechanics,
Institutskaya str. 4/1, Novosibirsk, 630090, Russia

the size of the supersonic patch obtained in inviscid computations is commensurable in order of magnitude with the shock wave thickness at moderate Reynolds numbers $Re_w = 10^4 - 10^6$. The computations at extremely high Reynolds $Re_w = 10^9$ numbers are required to completely clarify the behavior of the viscous solution.

2 Problem Formulation and Numerical Methods

In this study we investigate irregular reflection (Fig. 1) of weak shock waves in a steady supersonic flow with a Mach number M_∞ between two symmetrical wedges with identical angles θ_w. The reflection of the incident shock (IS) occurs on the plane of symmetry half-way between the wedges. A reflected shock wave, RS, and a Mach stem, MS, are formed at the intersection triple point. The trailing edge of the wedge generates an expansion fan that is refracted on the RS and then interacts with the slip surface (or mixing layer in viscous case). The computations are conducted with the Euler, Navier-Stokes (NS) equations and the direct simulation Monte Carlo (DSMC) method [10]. The Euler/NS code is a time explicit shock capturing code based on 5^{th} order WENO reconstruction of convective fluxes and central 4^{th} order approximation of dissipation terms. The 2^{nd} order Runge-Kutta scheme was used for time iteration. The NS computations were run in a rectangular computational domain (see Fig. 1). The left boundary of the computational domain is a supersonic inflow, the right boundary is a supersonic outflow. At the lower boundary of the domain, symmetrical boundary conditions were used. The upper boundary was placed at $y = g$ corresponding to the vertical position of the trailing edge of the wedge. The boundary conditions on the upper boundary were specified using a special procedure to maintain flow conditions at the horizontal line $y = g$. Supersonic free stream conditions were specified along the segment 1-2 (see Fig. 1). The segment 2-3 corresponds to a smooth variation of the flow parameters inside the shock. Along the line segment 3-4 the flow parameters corresponding to R-H conditions behind the incident shock were imposed. Along the segment 4-5 the inviscid wall boundary conditions were used. The power-law dependence of the dynamic

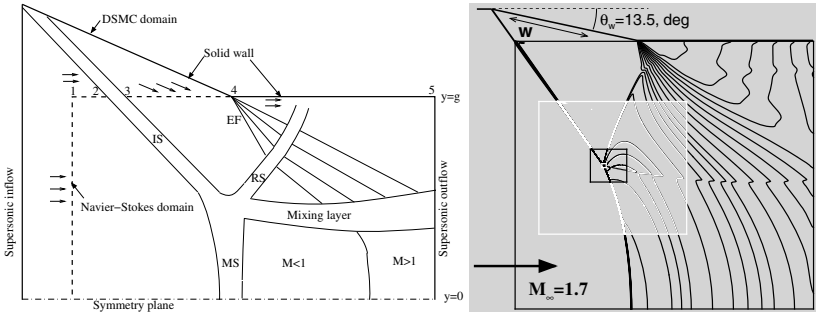

Fig. 1 Structure of Mach reflection and schematic of computational domains (left). Euler computations on the nested-block grids (right).

viscosity coefficient μ on temperature T with the exponent $\omega = 0.81$ was used in the NS computations.

The DSMC computations were performed by the SMILE software system [11]. The DSMC computational domain is shown in Fig. 1. Specular reflection condition was used at the lower boundary (the symmetry plane), the wedge surface (to avoid the viscosity effects on the wall) and the part of the upper boundary ($y = g$). The variable hard sphere model (VHS) was used in the DSMC computations with the VHS parameter chosen to provide the same dependence of viscosity on temperature as in NS computations.

The NS and DSMC computations were performed at various Reynolds/Knudsen numbers with full resolution of the internal structure of shock waves. To eliminate possible DSMC and NS cross-validation issues, a monatomic gas, argon, with $\gamma = 5/3$ was considered.

Numerical simulations in the entire domain become computationally expensive as the grid resolution increases. Therefore, we also used the nested-block grid refinement technique [6], which has the following features. The computational domain size is reduced, but the number of grid nodes remains constant. The nested-block domains are shown in Fig. 1. Then, the numerical solution obtained in the entire computational domain is interpolated to the sub-domain. After that, the computations are continued in the sub-domain. This procedure was repeated until necessary grid resolution was achieved.

3 Results of Numerical Simulations

The results of DSMC and NS computations are shown in figure 2. As can be seen these two numerical results are very close to each other (Fig. 2a, 2b). The results of the computations are also illustrated by diagram (θ, P) (Fig. 2c). Point A is located directly on the symmetry plane, where the Mach stem in the limit with $y \to 0$ is a normal shock. At this point, the angle of flow deflection equals zero, and the point in the plane (θ, P) lies on the intersection of the polar of the incident shock with the P axis. By moving upward along the Mach stem (from point A to point B), we obtain points with lower pressures and higher deflection angles, which is associated with curving of the Mach stem. The point where the computed results start to deviate from the theoretical polar is denoted as point B. Point C corresponds to the maximum angle of flow deflection along the both shocks considered. At point D, the numerical values arrive on the reflected shock polar and follow this polar from point D to point E. Above point E, the reflected shock starts interacting with the expansion fan and the points go away from the reflected shock polar. The deviation of the flow parameters from the shock polars between point B and point D effectively means that the R-H relations are not valid within the viscous triple-shock zone, which supports the conclusions of analysis [7]. Figure 2d shows a zoomed-in area of the plane (θ, P), where curve corresponding to the Guderley solution [1, 2] is clearly visible. The numerical results in Fig. 2c, however, do not coincide with this solution.

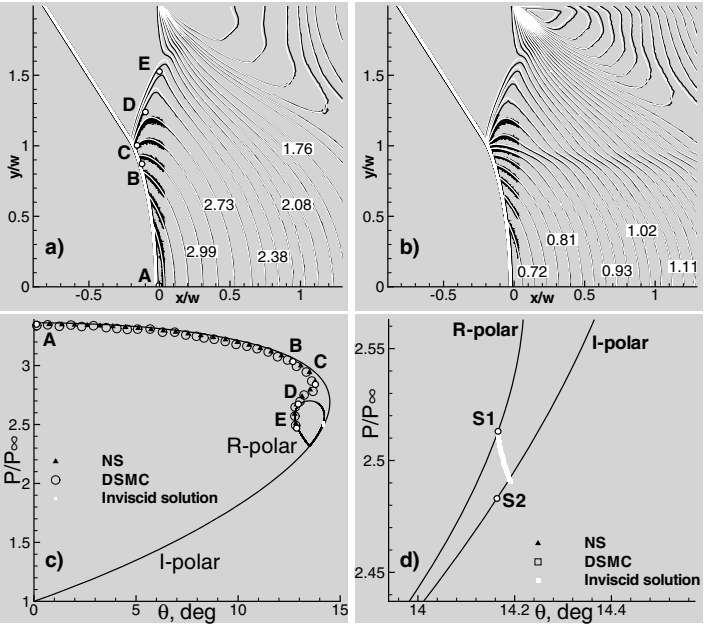

Fig. 2 Results of NS and DSMC computations at $M_\infty = 1.7$, $\gamma = 5/3$, $\theta_w = 13.5$, $Re_w = 2123$, $Kn = 0.001$. The white and black isolines (in a-b figures) show the results of NS and DSMC computations, respectively. a) Pressure. b) Mach number. c) Plane (θ, P). d) Guderley solution in the plane (θ, P). S1 and S2 are sonic points on shock polars of reflected and incident waves.

The results of NS computation obtained by the nested-block grid refinement technique are presented in Fig. 3. This computational method allows considering flow fields in a large range of Reynolds numbers. Numerical simulations predict subsonic flow fields in the vicinity of shock intersections at $Re_w < 8 \cdot 10^8$. At the same time flow fields near the shock intersection are distinct from each other. It is possible to distinguish two main types of a flow near shock intersection. First one is a smooth transition zone between Mach stem and reflected shock without any patches, like in Fig. 3a and 3b. Second one is the flow with sub- or super- sonic patches, like in Fig. 3e, 3f and 4a. It is worth to note that there is transition regime between first and second type. The flow patterns of transition regime are shown in Fig. 3c and 3d. The results of the computations are also illustrated by diagram (θ, P) in Fig. 3g. Numerical data become closer to curve, corresponding to expansion fan centered at the triple point, as the Reynolds number increases.

Figure 4 shows comparison between Euler computation and NS computation at $Re_w = 1.6 \cdot 10^9$. Both computations predict supersonic patches behind shock intersection, but structure and size of these patches are different. Comparison of numerical data in plane (θ, P) is given in Fig. 4c. It is clearly seen that numerical data of both computations are close to Guderley solution.

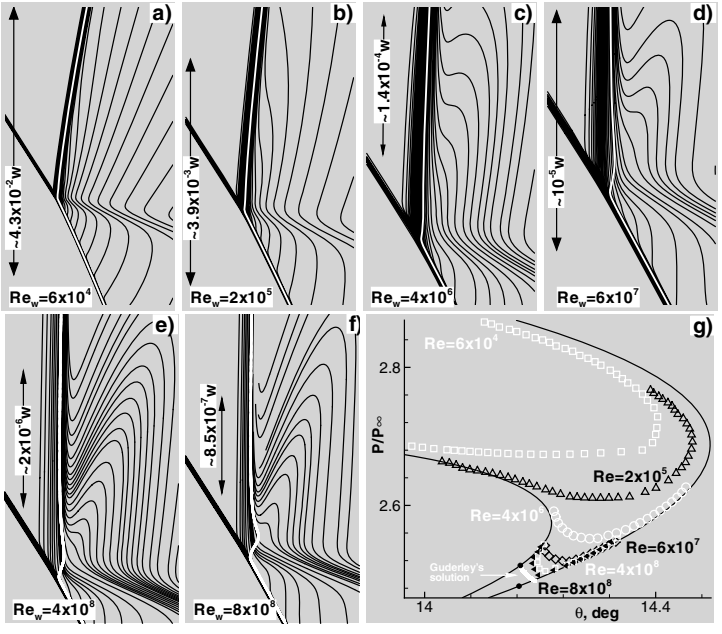

Fig. 3 Results of NS computations at $M_\infty = 1.7$, $\gamma = 5/3$, $\theta_w = 13.5$ and different Reynolds numbers. a)-f) Density contours. The white isolines show sonic lines. g) plane (θ, P).

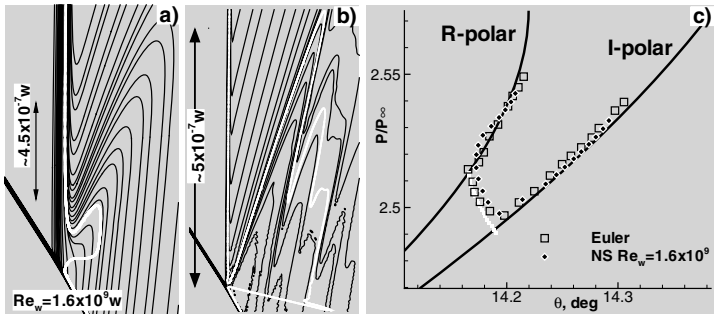

Fig. 4 Results of NS (a) and Euler (b) computations at $M_\infty = 1.7$, $\gamma = 5/3$, $\theta_w = 13.5$. a)-b) Pressure contours. The white isolines show sonic lines. c) plane (θ, P).

4 Conclusions

A steady flow around symmetric wedges with Mach number $M_\infty = 1.7$ was numerically studied under von Neumann paradox conditions.

Euler computations based on shock-capturing technique predict supersonic patches in the vicinity of the triple point, which confirm conceptual issues of Guderley model.

In the range of Reynolds numbers $Re_w = 10^3 - 10^9$ results of NS computations did not reveal evidence of supersonic patches. Instead of a supersonic patches, in viscous flow there is a smooth three shock transition zone, where R-H relations are not valid.

The first indication of supersonic patch formation near the triple point can only be observed at $Re_w > 10^9$. It seems that the viscous solution can ultimately converge to the inviscid pattern as the viscosity tends to zero, but the effects of viscosity are essential in the vicinity of the triple point at finite Reynolds numbers.

This work was supported by the Russian Foundation for Basic Research (grant No. 10-08-01203-a), Government contract N16.740.11.0303, Board of the Russian Academy of Sciences (Fundamental Research Program 11), Russian-Taiwanese joint project SB RAS - NSC 2010 "Numerical Study of Rarefaction Effects and Thermochemical Nonequilibrium Problems on Hypersonic Flow around Space Vehicles". The computations were performed at the Siberian Supercomputer Center, Novosibirsk, and at the Joint Supercomputer Center, Moscow.

References

1. Guderley, K.: Considerations on the Structure of mixed subsonic supersonic flow patterns, HQ Air Materiel Command, Wright Field, Dayton, Ohio. Technical Report F-TR-2168-ND (1947)
2. Guderley, K.G.: The theory of transonic flow. Translated from the German by J.R. Moszynski, p. 344. Pergamon Press, Oxford (1962)
3. Vasilev, E., Olhovskiy, M.: The complex structure of super sonic patches in the steady Mach reflection of the weak shock waves. In: Abstracts of the 26th International Symposium on Shock Waves, p. 322 (2009)
4. Ivanov, M., Paciorri, R., Bonfiglioli, A.: Numerical simulations of von Neumann reflections. In: AIAA 40th Fluid Dynamics Conference and Exhibit, Chicago, Illinois, June 28 - July 1, vol. 4859 (2010)
5. Tesdall, A.M., Sanders, R., Keyfitz, B.L.: Self-similar solutions for the triple point paradox in gasdynamics. SIAM J. Appl. Math. 68, 1360–1377 (2008)
6. Defina, A., Viero, D.P., Susin, F.M.: Numerical simulation of the Vasilev reflection. Shock Waves 18, 235–242 (2008)
7. Sternberg, J.: Triple-Shock-Wave Intersections. Physics of Fluids 2(2), 179–206 (1959)
8. Sakurai, A.: On the problem of weak Mach reflection. Phys. Soc. Japan 19, 1440–1450 (1964)
9. Ivanov, M., Bondar, Y., Khotyanovsky, D., Kudryavtsev, A., Shoev, G.: Viscosity Effects on Weak Irregular Reflection of Shock Waves in Steady Flow. Progress in Aerospace Sciences 46, 89–105 (2010)
10. Bird, G.: Molecular gas dynamics and the direct simulation of gas flows. Oxford Press (1994)
11. Ivanov, M., Markelov, G., Gimelshein, S.: Statistical Simulation of Reactive Rarefied Flows: Numerical Approach and Applications. AIAA Paper 98-2669 (1998)

Shear Layer Evolution in Shock Wave Diffraction

B.W. Skews, C. Law, A.O. Muritala, and S. Bode

1 Introduction

All previous studies on shock wave diffraction in shock tubes have spatial and temporal limitations due to the size of the test sections. These limitations result from either the reflection of the expansion wave, generated at the corner, from the top wall and/or of the reflection of the incident diffracted shock from the bottom wall of the test section passing back through the region of interest. This has limited the study of the evolution of the shear layer and its associated vortex which forms a relatively small region of the flow behind the shock and yet is a region of significant interest. A special shock tube is used in the current tests which allows evolution of the flow to be examined at a scale about an order of magnitude larger than in previously published results, with shear layer lengths of up to 250 mm being achieved. Tests were conducted at Mach numbers from 1.4 to 1.6 with wall angles of 10, 20, 30 and 90°.

2 Apparatus

The basic facility consists of a simple rectangular shock tube 100 mm wide and 450 mm high with a 2 m long driver and a 6 m driven section. It opens up into a 2 m long test section of the same width and 1100 mm height thereby enabling large scale diffraction experiments to be carried out compared to most conventional tubes with test sections about one fifth this size. Because it is impractical to have windows spanning the full height of the test section, two pairs of 310 mm diameter windows are mounted in a rotating frame allowing most of the test section to be covered in turn. Figure 1 shows the arrangement. Two pressure transducers positioned just upstream of the entrance to the test section are used to determine the transit time of the incident shock wave, and hence its Mach number.

B.W. Skews · C. Law · A.O. Muritala · S. Bode
Flow Research Unit, School of Mechanical, Industrial, and Aeronautical Engineering, University of the Witwatersrand, Johannesburg, PO WITS 2050, South Africa

The test pieces were bolted onto a universal mounting frame and the surfaces following the corner were fitted with transducer ports down their length, of about 400 mm. As it has been shown [1] that the greatest variability in flow patterns occur for small wall angles, models were made with 10, 20, 30 and 90° corners.

Imaging was done with a conventional Z-configuration schlieren system, with a $2\mu s$ duration xenon flash light source. A series of thin threads were accurately positioned 50 mm apart across the windows in a grid fashion for scaling and distortion tests.

Fig. 1 Experimental layout showing the 1.1 m high test section with rotatable window frame connected to the 450 mm high shock tube driven section

3 Results

3.1 10° Corner

Previous research [1] has indicated that no visible separation occurs at this wall angle. This is confirmed in the current tests. However, the larger scale allows a more detailed view of the corner flow. Figure 2 clearly shows the expansion at the corner with the shock and contact surface further downstream. What is particularly noticeable is the distinct thickening of the boundary layer, particularly in the second image. It is important to note that this occurs between the corner and the contact surface. The contact surface separates the gas that has passed over the corner from that which has been engulfed by the shock wave only after it passed over the corner. This thickening of the boundary layer may eventually lead to a more clearly defined separation at much later times, as is shown for the 20° case discussed below.

3.2 20° Corner

This wall angle is particularly interesting being midway between the case of no evident separation and distinct separation found for a 30° corner. For a low Mach

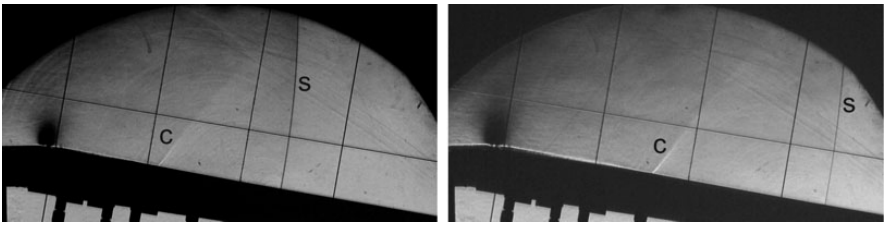

Fig. 2 Diffraction of a Mach 1.51 incident shock over a 10° corner, showing the shock and contact surface positions

number of 1.3, as shown in Fig. 3, there is no separation at early times but a short while later (middle frame) the flow downstream of the corner thickens with clear indication of instability and possible separation. At later times as shown in the last frame not only is there clear evidence of separation but the boundary layer upstream of the corner also appears turbulent. This possible upstream influence on the downstream flow has not been considered before.

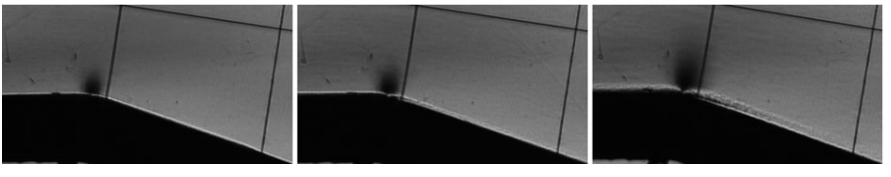

Fig. 3 Shear layer development in diffraction of a Mach 1.3 incident shock over a 20° corner. Images at 430, 630 and 930μs after shock arrival at the corner.

For a higher Mach number the situation becomes more complex because of the generation of transonic flow over the corner, resulting from the expansion of the flow. Figure 4 shows this development. The initial stage, shown in the first frame, indicates growing, and somewhat regular, instabilities developing on the boundary layer with it growing all the way from the contact surface upstream to the corner. This increases and by the fourth and fifth frames there is clear evidence of the expected transonic lambda shock developing with its downstream leg terminating above the wall, thus confirming distinct separation of the flow. The downstream flow becomes increasingly turbulent and by the last frame this turbulence extends to the upstream boundary layer before the corner as well. The early tests [1] were unable to determine whether there was a shear layer or not for this wall angle and Mach number because of the small scale of the experiments.

3.3 30° Corner

Figure 5 displays a series of images of the evolution of the shear layer and separated region for a Mach 1.5 incident shock. These images show similar features to those

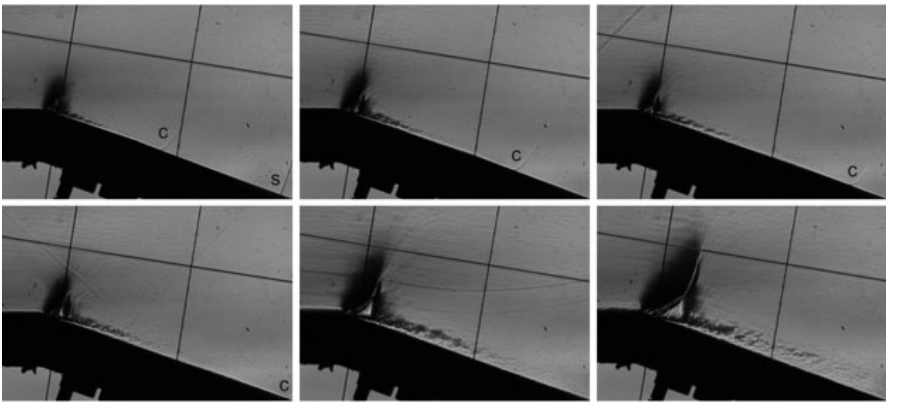

Fig. 4 Shear layer development in diffraction of a Mach 1.51 incident shock over a 20° corner. Images at 220, 330, 410, 470, 630, and 940μs

of previous tests taken at earlier times but now show details not distinguished before. In the first three frames the shock is still visible and the shear layer terminates in a distinct vortex. Transonic lambda shocklets appear on the upper surface of the shear layer as expected for this Mach number. However, in contrast to the impression obtained from smaller scale tests there is now distinct evidence of shear layer broadening and instability with some evidence of structure and turbulence development underneath. In the second row of images the main vortex breaks down into a turbulent patch although there are signs of some of the smaller vortices generated from the initial instability remaining.The wavelet system above the shear layer is more complex and structured and has been affected by the breaking up of the shear layer into vortices. This occurrence enhances the development of a strong turbulent flow around the shear layer. It may be that the shear layer break up is not two dimensional and that it develops some structure in the transverse direction. This will clearly influence the development and position of the lambda shocks and explain the much more complex appearance of a multiplicity of shocklets that are visible. The pattern of shocklets moves down with the shear layer as shown in the last row of images but appear to become successively weaker with time. The angle that the shear layer makes with the downstream wall also increases with time becoming almost parallel to the upstream surface. The turbulent patches become more homogeneous and the remaining small vortex structure disappears in the last frame. It is also apparent in the last frame that the upstream boundary layer has become turbulent.

3.4 90° Corner

The 90° corner diffraction case has become somewhat of a standard test case, particularly for an incident wave Mach number of about 1.5. Takayama and Inoue [2] reported on it as a benchmark test for numerical simulations. Many of these showed Kelvin-Helmholz instability developing on the shear layer even at short times,

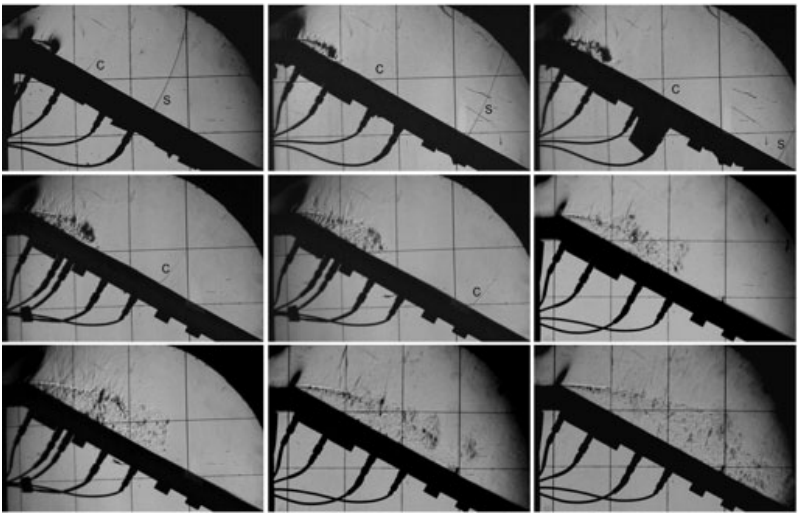

Fig. 5 Shear layer development in diffraction of a Mach 1.5 incident shock over a 30° corner.

although no experiments did. This issue has been explored in more detail by Sun and Takayama [3] who showed that by increasing the numerical dissipation through viscous laminar and turbulent models that experimental results with no vortex breakdown could be simulated.

The first frame of Fig. 6 is a typical result similar to that obtained many times in typical laboratory scale shock tubes with the incident shock having traveled some 200 mm from the corner. At a time about three times longer the second frame shows distinct development of Kelvin-Helmholtz instability with three distinct small vortices becoming evident with a clear S-shaped flow feature between the second and third, typical of this flow.

As the flow develops further the shear layer extends and the main vortex enlarges. The recompression shock between the main vortex and the wall is evident in all subsequent images but appears to become weaker as the vortex core moves away from the wall. The main vortex develops a set of spiral arms similar to that noted for galaxies and there is strong evidence of transition to turbulence throughout the flow, part due to the break up of the shear layer and part due to the propagation of the turbulence initially generated under the shear layer and which remains close to the wall.

It is evident that a more detailed examination of such flows is required since they indicate that small scale tests are unable to capture the full complexity of the evolving flow. It indicates that although there is no length scale associated with the geometry the process is not self similar in time due to the effects of viscous dissipation. It would be expected at even longer times than those achieved with this large facility, that the features will eventually decay fully.

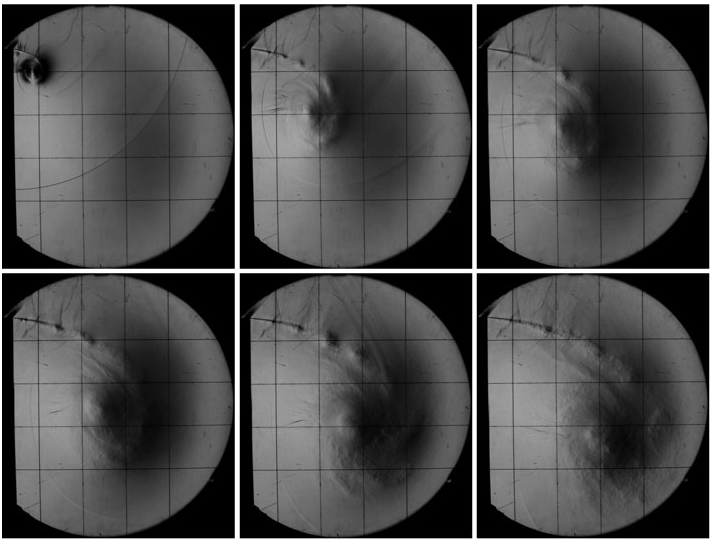

Fig. 6 Shear layer development in diffraction of a Mach 1.5 incident shock over a 90° corner.

4 Conclusion

A series of large scale experiments have been conducted over a limited range of Mach numbers, of the diffraction of a shock wave over a sharp corner between two plane surfaces. It is shown that the separation patterns of the shear layer and the evolution of the flow is somewhat different to that obtained in small scale tests, primarily due to the development of flow instabilities, boundary layer effects, and transition to turbulence. It thus is clear that any numerical simulation of these phenomena to replicate realistic scales of the phenomena need to take account of these effects as well as upstream flow within the boundary layer.

References

1. Skews, B.W.: J. Fluid Mech. 29, 705–719 (1967)
2. Takayama, K., Inoue, O.: Shock Waves 1, 301–312 (1991)
3. Sun, M., Takayama, K.: Shock Waves 13, 25–32 (2003)

Shock Reflection Off Combined Surfaces

Beric Skews and Anneke Blitterswijk

1 Introduction

A mismatch has been shown to exist between the shock wave reflection behaviour on a circular arc and that on a plane wall at the same angle of incidence [1]. For reflection off a plane wall, this change in reflection pattern from regular to Mach reflection occurs at a wall angle where the flow behind the reflection point is just sonic in a frame of reference fixed in the reflection point. This transition condition is labeled the sonic criterion [2]. Experiments confirm this (except for some minor effects due to boundary layer growth). Data for convex cylindrical surfaces has shown that the visible eruption of a Mach stem, which is taken to be evidence of the point of transition, occurs at smaller wall angles than for plane walls [3]. On the other hand, recent tests [1] using perturbations generated by shock passage over a very small step in the wall have shown that the sonic catchup occurs at wall angles not only larger than those found for the visible eruption but also larger than the angles associated with sonic catch-up for the plane wall case. Due to the relatively low resolution of the time-resolved imaging system used, the accuracy of identifying the angle of sonic catchup could be questioned in the same way as identifying the visible eruption of the Mach stem could be resolution dependent. The stem could be erupting earlier if beyond the imaging resolution and the catch up could be occurring later bringing them both closer to the plane wall case. Due to this limitation time resolved tests were then conducted on a 45° plane wall preceded by a 75mm circular arc and the change in reflection angle measured in order to confirm that the reflection was different for the same incidence angle on the two different surfaces [1], this technique not being dependent on using perturbations. The existence of a significant transition length was confirmed in the reflection pattern adjusting from the curved wall to an eventual pseudo-stationary pattern on the plane wall. The results were still limited due to imaging resolution issues so a new set of tests have

Beric Skews · Anneke Blitterswijk
Flow Research Unit, School of Mechanical, Industrial, and Aeronautical Engineering, University of the Witwatersrand, Johannesburg, PO WITS 2050, South Africa

been undertaken using high resolution single shot tests over a range of wall angles and a range of combined surfaces. An additional test was conducted with a circular surface on both ends of a plane wall to explore how information from each of the joints influence the reflected shock.

2 Apparatus

Experiments were conducted in a simple shock tube at a Mach number of 1.346 ± 0.005. Test section dimensions are 180 mm high and 76 mm wide. Three test pieces consisting of circular sections of 30, 50, and 75 mm radius, followed by a plane wall section were made from aluminium and were polished to a near-mirror finish. An adjustable mount was used to set wall angles and these were measured using a digital inclinometer to better than 0.1°. Additional tests were conducted on a 57 mm long plane wall model with 30 mm radius circular sections on either end. Flow visualization was done using standard shadowgraph and schlieren systems. Single-shot recording was with a Fujifilm Finepix S3 Pro digital camera at a resolution of 3030x2036x48b. The viewing area of the test section had a square wire grid fitted on the outside of the test section door, with dimensions of 25 mm x 25 mm.

3 Results

3.1 Transition Lengths

Multiple tests were undertaken with the test pieces at a variety of wall angles and with the point of reflection at increasing positions along the plane section of each test piece for each angle. The images were used to determine the angle of the reflected wave and the corresponding position of the shock. Only regular reflection cases were recorded. Once Mach reflection was observed no further images were taken higher up the wall.

Figure 1 shows enlarged images of tests on the 44° wall. von Neumann theory does not permit regular reflection at this angle but the previous studies showed regular reflection to exist on the circular section at the same angle. The situation is complicated by the known boundary layer effects resulting in the persistence of regular reflection but this wall angle is sufficiently far from the detachment condition (47.19°) that a Mach stem could be expected to erupt. Smith [4] showed that for a Mach number of 1.363 the persistence exists for about 1° so a similar difference would be applicable for the current Mach number of 1.346. Three-shock theory gives a triple point trajectory angle of 1.744° so Mach reflection should become visible. Nevertheless in the current work comparisons will be made with reflected shock angles as a better indicator of a flow approaching transition conditions.

The first two images, and the corresponding enlargements below them, clearly show regular reflection. The third image appears to show a regular reflection but the enlargement indicates the possibility of the existence of a shear layer although no Mach stem is evident. Both a very small Mach stem and a shear layer are detectable in the final frame.

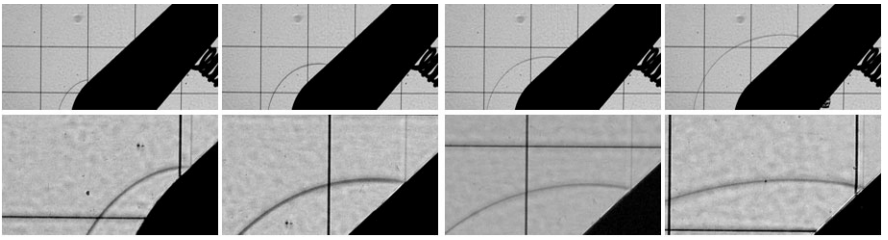

Fig. 1 Shock wave propagation up a plane wall at 44°, with enlargements of the reflection area

Typical results for the reflected shock angle at different positions along the plane section for the 50 mm radius leading surface test piece is given in Figs. 2. The reflection angle was measured along the plane section where regular reflection persisted. Clear trends are evident. The figures indicate that the reflection angle generally increases along the plane wall section of the test piece until it reaches an asymptote. Estimates of this asymptotic level are shown as solid horizontal arrows and will be discussed further later. The leveling out of the reflection angles illustrates the position along the length of the plane section where the flow becomes pseudosteady. Propagation further up the wall would then be the same as that along a wedge. The influence of the circular inlet thus reduces and eventually becomes insignificant. The vertical arrow in the 45° wall angle case is for a test where a Mach reflection became visible in the image. It is notable that this is significantly higher than where the reflection angle tends to become independent of wall angle. This implies that transition and eruption of a Mach stem occurs earlier but cannot be seen because of

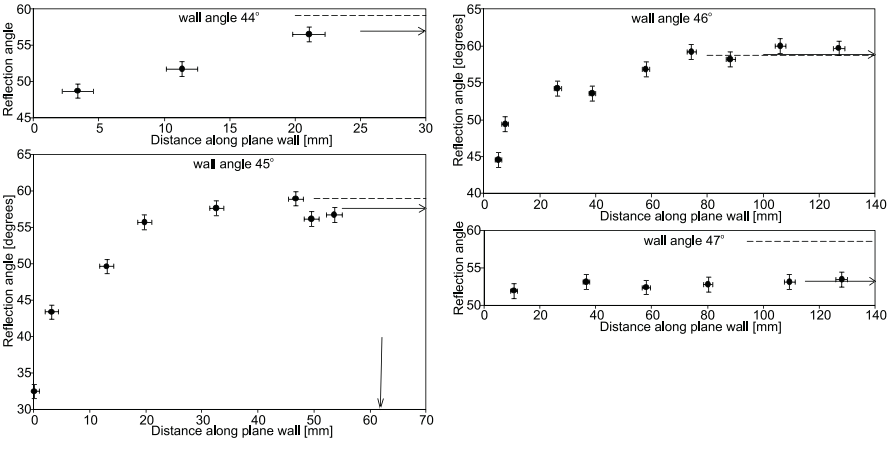

Fig. 2 Typical results for the 50 mm radius leading surface test piece. The horizontal arrow is the estimated asymptotic vale of the data, the dashed line is from two- and three-shock theory, as appropriate, and the vertical arrow is where a Mach reflection is visible

the imaging resolution. The theoretical reflection angle was determined using three-shock and two-shock theory as appropriate for the Mach number and wall angle, and is indicated on each image as a dashed line.

Whilst it is not simple to accurately identify the asymptotic level that the reflection angle reaches, in most cases this may be estimated to within ± 1 degree. These estimates are given in Fig. 3 where they are compared with the two- and three-shock theories. The results are what would be expected for reflection off a plane wedge without a curved leading surface since pseudosteady flow has been achieved.

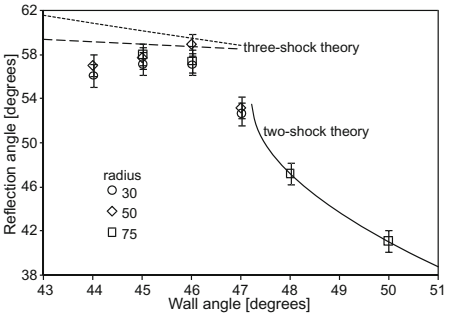

Fig. 3 Reflection angle asymptotes. Lower and upper three-shock theory curves are for angles relative to the surface and relative to the triple point trajectory respectively

For large wall angles the experiments lie on the regular reflection curve except for the 47° case which lies close to the regular reflection curve. Theoretical transition (detachment criterion) is at 47.2° for a Mach number of 1.346 so Mach reflection is predicted. However, it is well known that regular reflection persists beyond detachment and this result is simply evidence of that.

For the smaller wall angles (44, 45 and 46°) the reflection angle approaches the theoretical three-shock curve as the reflection approaches transition. It should be noted that since reflection angle measurements for the experiments are made relative to the wall and not to the triple point trajectory comparisons need to be made on the same basis; thus the lower of the two theoretical curves shown in Fig. 3 is the relevant one. The results indicate that the reflection is Mach reflection even though in many cases no Mach stem or shear layer is actually visible. All the above results are totally consistent with those of Smith [4] for a similar Mach number of 1.363 (inverse pressure ratio of 0.50) with actual transition occurring about 1° lower in wall angle than detachment and the difference between measurement and the three-shock theory becoming greater as the wall angle decreases. From the current data and extrapolating from the regular and Mach reflection cases it would appear that the pseudosteady transition is occurring at a wall angle of about 46.7°.

It is even more difficult from the given data to estimate at what distance along the plate the asymptotic level is reached. Rough estimates are plotted in Fig. 4. Also shown, as a vertical dashed line, is the transition angle inferred from the data of Fig. 3 and the length where Mach reflection is visible in terms of the appearance of

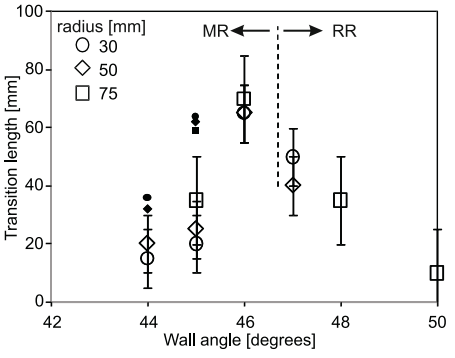

Fig. 4 Estimated transition lengths. The dashed line is the estimated experimental transition angle between regular and Mach reflection as determined from Fig. 3. Filled symbols are for the positions where a Mach reflection becomes visible in the images

a Mach stem and/or shear layer. It is notable that these lie further along the surface thus again indicating that embryonic Mach reflection occurs well before it becomes visible in the image. In view of the limited accuracy associated with the estimation of transition length it is not possible to correlate whether the upstream radius has an influence. This figure supplies very interesting indications. For Mach reflection the transition length increases as the wall angle increases toward the transition condition indicating that it could be quite significant near transition. On the other hand, in the regular reflection regime the transition length steadily reduces as the wall angle increases and may well become zero at increasing angles. More refined measurements are called for.

3.2 Propagation of Curvature Information

It is clear from the above that for surfaces with different curvatures joined together it takes some time for the flow to adjust to new boundary conditions. The mechanism whereby this occurs is for information from the one surface to communicate to the reflected wave through acoustic signals so that it can adjust to the new boundary. In order to demonstrate this a test piece was constructed consisting of a 57 mm plane section with a 30 mm circular arc on either side. Tests were conducted at the same Mach number as those described above with the plane section at a wall angle of 60°.

In order to track how information is propagated perturbation sources are positioned on the surface so as to generate very weak, nearly sonic, waves, as described in [5]. Perturbation sources were placed at the points where the circular sections joined to the plane section of the test piece. Two 18 mm wide pieces of $45\mu m$ thick adhesive tape were attached transversely on the test piece. This resulted in two further perturbation sources; one 18 mm further up the plane section and one 18 mm further down the plane section from the second circular section. Single-shot high resolution schlieren images were obtained as the incident waves moves along the test piece. The

perturbation wave moving up the plate toward the reflection point is called a P wave and the wave moving toward the start of the plane section is called a Q wave. Where these waves meet the reflected wave defines the point where the reflected wave is informed of the conditions at the perturbation source point on the wall.

A typical result is given on the left in Fig. 5. The white dots are where the P wave from the lower change of slope and the Q wave from the upper change intersect the reflected wave. A series of such images are overlaid on the right image. Within the accuracy of measurement the trajectories of these intersection points appear to be straight up until they meet. The important point to note is that in the triangular area between the trajectories and the surface of the test piece the reflected shock remains straight. This is because it has no knowledge of the existence of the two circular sections. During this phase the curvature of the reflected shock on either side of the straight section is determined by the combined surface contour on either side.

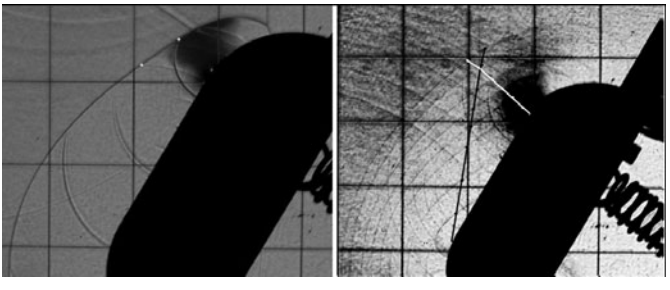

Fig. 5 Determination of the trajectories of how information from the changes in slope reach the reflected wave. The right image overlays a number of tests. The black line is for the P wave and the white line for the Q wave. The reflected wave remains plane between these lines until they meet

4 Conclusion

When a plane shock wave propagates over a surface made up of multiple sections of differing shapes and slopes it takes a finite time for the reflected wave profile to adjust to the new boundary conditions. In flows near transition conditions between regular and Mach reflection the adjustment time appears to increase as the transition conditions are approached.

References

1. Skews, B.W., Kleine, H.: J. Fluid Mech. 654, 195–205 (2010)
2. Hornung, H.G., Oertel, H., Sandeman, R.J.: J. Fluid Mech. 90, 541–560 (1979)
3. Ben-Dor, G.: Shock wave reflection phenomena. Springer (2007)
4. Smith, L.G.: Photographic investigation of the reflection of plane shocks in air. Tech. rept., Off. Sci. Res. Dev. OSRD Rep. 6271 (1945)
5. Skews, B.W., Kleine, H.: Experiments in Fluids 46, 65–76 (2009)

A Simple Scheme for Calculating Distortion of Compression Wave Propagating through a Tunnel with Slab Tracks

T. Miyachi, S. Ozawa, T. Fukuda, M. Iida, and T. Arai

1 Introduction

A high-speed train entering a tunnel generates a compression wave that propagates through toward its exit. When the compression wave reaches the tunnel exit, a pressure pulse ("micro-pressure wave" [1, 2]) is radiated from the exit portal, and it causes an environmental problem. The magnitude of the micro-pressure wave is approximately proportional to the maximum pressure gradient $\partial p/\partial t_{\max}$ (p: acoustic pressure, t: time) of the compression wave arriving at the tunnel exit [1].

This paper is concerned with the distortion of the compression wave in a concrete slab-track tunnel of the Japanese Shinkansen without ballast. In the slab track tunnel, the whole of the boundary wall, such as a tunnel wall and a track surface, is smooth. The nonlinear effect that tends to steepen the compression wavefront surpasses the attenuation effects that tend to spreads it out in the slab-track tunnel. Many studies have been made on the distortion of the compression wave, for example [2, 3, 4, 5]. Numerical simulations have been usually conducted for these studies, although the calculations require a great amount of time and memory. For reducing them, a coordinate system fixed to the compression wave has been used in 1D CFD (Computational Fluid Dynamics) [4].

In the present study, a simple scheme for calculating the distortion of the compression wave in the concrete slab-track tunnel is proposed. The accuracy of the proposed scheme is verified by comparison of the calculation results by this method with those by 1D CFD.

T. Miyachi · T. Fukuda · M. Iida
Railway Technical Research Institute, 2-8-38 Hikaricho, Kokubunji, Tokyo, Japan

S. Ozawa
Tokyo University of Technology, 1404-1 Katakura, Hachioji, Tokyo, Japan

T. Arai
Osaka Prefecture University, 1-1 Gakuencho, Nakaku, Sakai, Osaka, Japan

2 Governing Equation

We derive a simple scheme for calculating the distortion of the compression wave propagating through a concrete slab-track tunnel from the following equations of 1D CFD [4]

$$\frac{\partial}{\partial t}\begin{bmatrix}\rho\\ \rho u\\ e\end{bmatrix}+\frac{\partial}{\partial x}\begin{bmatrix}\rho u\\ p+\rho u^2\\ (e+p)u\end{bmatrix}+\begin{bmatrix}0\\ f\\ q\end{bmatrix}=0, \tag{1}$$

$$f=\frac{4\tau}{d_H}, \tag{2}$$

where, t: time, x: axial coordinate fixed on the ground, p: acoustic pressure, u: air velocity, e: total energy per unit volume, ρ: density, f: frictional term, q: heat transfer term, τ: sheer stress at wall, d_H: hydraulic diameter of the tunnel. Air at any observation point in the tunnel is at rest before the compression wave arrives there. Combining three equations of Eq. (1) yields the following equations along the characteristic lines $dx/dt = u+c,\ u,\ u-c$ (c: speed of sound), respectively:

$$\frac{D_+p}{Dt}+\rho c\frac{D_+u}{Dt}=-[c-(\gamma-1)u]f-(\gamma-1)q,\quad \frac{D_+}{Dt}=\frac{\partial}{\partial t}+(u+c)\frac{\partial}{\partial x}, \tag{3}$$

$$\frac{Dp}{Dt}-c^2\frac{D\rho}{Dt}=-(\gamma-1)(q-uf),\quad \frac{D}{Dt}=\frac{\partial}{\partial t}+u\frac{\partial}{\partial x}, \tag{4}$$

$$\frac{D_-p}{Dt}-\rho c\frac{D_-u}{Dt}=[c+(\gamma-1)u]f-(\gamma-1)q,\quad \frac{D_-}{Dt}=\frac{\partial}{\partial t}+(u-c)\frac{\partial}{\partial x}. \tag{5}$$

Equation (3) describes the distortion of the compression wave (the forward traveling wave) propagating through the tunnel. Fluctuations of pressure, density and velocity of the air in the tunnel excited by the compression wave are small relative to their undisturbed values, p_0, ρ_0 and c_0, respectively. The friction term and the heat transfer term are very small relative to the acoustic pressure gradient of the compression wave. Additionally, along the characteristic lines u and $u-c$ the friction term and the heat transfer term affect in small length as long as the compression wave relative to the length of the tunnel. Accordingly, we use Eq. (3) directly and approximate Eqs. (4) and (5) as follows, respectively:

$$\frac{dp}{d\rho}\approx c^2=\frac{\gamma(p_0+p)}{\rho}, \tag{6}$$

$$dp\approx\rho c\,du. \tag{7}$$

Integrating Eq. (7) and neglecting the second order perturbations, we have

$$p \approx \rho_0 c_0 u. \tag{8}$$

Substituting Eqs. (6) and (8) into Eq. (3) and neglecting the second order perturbations except for the nonlinear term and the third order perturbation for the nonlinear term, we have

$$\frac{\partial p}{\partial t} + \left(c_0 + \frac{\gamma+1}{2} \frac{p}{\rho_0 c_0} \right) \frac{\partial p}{\partial x} = -\frac{1}{2} \left[c_0 \frac{4\tau}{d_H} + (\gamma-1) q \right]. \tag{9}$$

Furthermore, dividing Eq. (9) by $c_0 + (\gamma+1)\, p/2\rho_0 c_0$, and neglecting the third order perturbation for the nonlinear term again, and performing the coordinate transformation $x' = x$, $t' = t - x/c_0$, we obtain the following space evolution equation:

$$\frac{\partial p}{\partial x} = \frac{\gamma+1}{2} \frac{p}{\rho_0 c_0^3} \frac{\partial p}{\partial t} - \frac{1}{2} \left[\frac{4\tau}{d_H} + (\gamma-1) \frac{q}{c_0} \right], \tag{10}$$

where x' and t' are rewritten again as x and t respectively. In the present study, we propose a simple simulation scheme based on Eq. (10) for calculating the distortion of the compression wave in the concrete slab-track tunnel. Hereafter, this scheme is called a "simple scheme". The simple scheme is suitable for predicting the micro-pressure wave for the following reasons:

(a) The calculation using the proposed scheme is very fast because its CFL condition is relaxed to $O(M)$ $(M = u/c)$, namely calculation time is reduced to about $1/100$, from that of the CFD based on Eq. (1),

(b) The space evolution equation such as Eq. (10) is useful because we can obtain time series data of the compression waveforms directly and they are suitable for comparing the calculated results with those of the field measurements or model experiments.

3 Numerical Simulations

We verify the accuracy of the simulation scheme based on Eq. (10). Tables 1 and 2 show the parameters used for numerical simulations of the compression wave propagating through a typical Shinkansen tunnel with slab-tracks. The grid interval of CFD and that of Simple 1 in Table 2 are equal. The Chakravarthy's TVD scheme [6] is employed for both of the numerical simulations.

The following models [7, 8] are employed as the friction term and the heat transfer term with isothermal wall assumption,

$$\frac{4\tau}{d_H} = \frac{\lambda}{2d_H}\left(\frac{p^2}{\rho_0 c_0^2}\right) + \varepsilon\frac{4\sqrt{\nu}}{\sqrt{\pi}c_0 d_H}\int_0^t \frac{\partial p}{\partial t}(t-\phi)\frac{\exp\left[-B4\nu\phi/d_H^2\right]}{\sqrt{\phi}}d\phi, \quad (11)$$

$$B^* = 0.135Re^{\log_{10}\left(\frac{14.3}{Re^{0.05}}\right)}, \quad (12)$$

$$q = \frac{4C_p(T-T_0)}{(p/\rho_0 c_0)d_H Pr^{\frac{2}{3}}}\tau, \quad (13)$$

where λ: pipe friction factor, ε: unsteady friction factor [9], Re: Reynolds number $(Re = ((p/\rho_0 c_0)d_H)/\nu)$, ν: kinematic viscosity, C_p: specific heat at constant pressure, T: temperature, Pr: Prandtl number. Using Eqs. (6), (10), (13) and the equation of state of ideal gas, we have

Table 1 Parameters of concrete slab-track tunnel.

Main tunnel	Cross-sectional area (m^2)	63.4
	Hydraulic diameter (m)	8.0
Side branch Type 1	Cross-sectional area (m^2)	7.1
	Length (m)	2.0
Side branch Type 2	Cross-sectional area (m^2)	7.1
	Length (m)	5.0

Table 2 Parameters for calculation.

	CFD	Simple 1	Simple 2
Grid interval	Δx =0.8 m	Δt =2.35×10^{-3} s	Δt =1.0×10^{-3} s
Integration interval	Δt =1.5×10^{-4} s	Δx =4 m	Δx =2 m
Courant Number	approx. 0.1		
Pipe friction factor	0.04		
Unsteady friction factor i	8		
Speed of sound c_0	340 m/s		

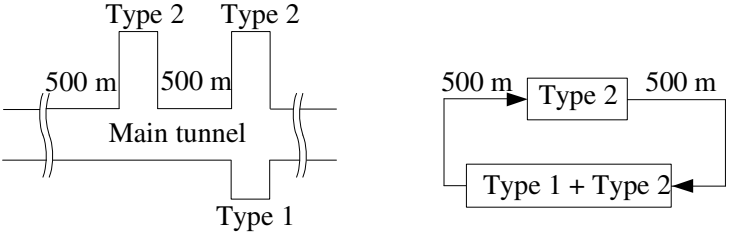

Fig. 1 Arrangement of short side branches for numerical simulations.

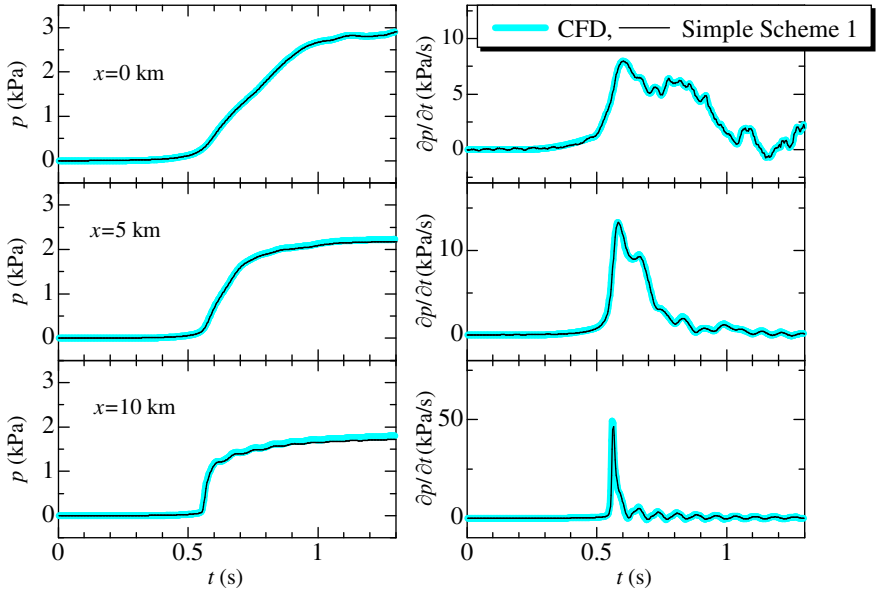

Fig. 2 Comparison of compression waveforms: Case1.

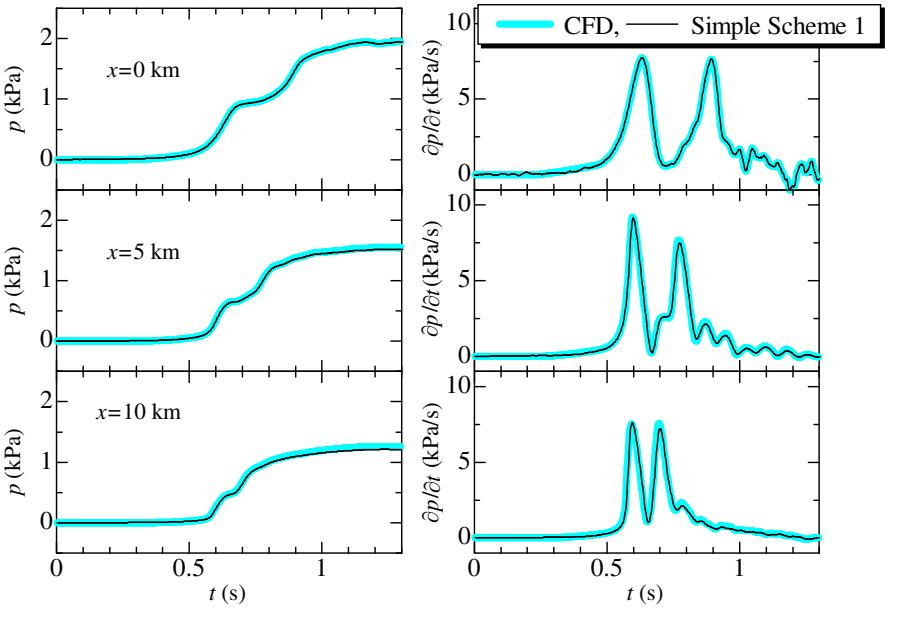

Fig. 3 Comparison of compression waveforms: Case2.

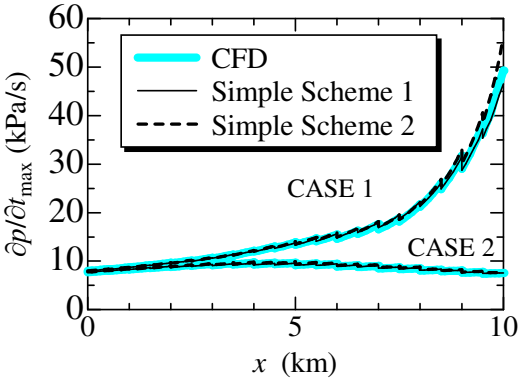

Fig. 4 Comparison of the maximum values of the pressure gradients.

$$\frac{\partial p}{\partial x} = \frac{\gamma+1}{2}\frac{p}{\rho_0 c_0^3}\frac{\partial p}{\partial t} - \frac{1}{2}\left(1+\frac{\gamma-1}{Pr^{\frac{2}{3}}}\right)\frac{4\tau}{d_H}. \tag{14}$$

We assume that the short side branches are arranged at regular intervals of 0.5 km for simulating a typical Japanese Shinkansen tunnel as shown in Fig. 1. The effects of these branches are calculated using one-dimensional acoustic analysis [2, 4].

Figures 2 and 3 show comparisons between the compression waveforms calculated by the 1D CFD and those by the simple scheme. Figure 4 shows the maximum pressure gradients of the compression waves. In two cases, case 1 and case 2, the initial waveforms of Figs. 2 to 4 at the tunnel entrance $(x = 0)$ are measured data by different actual Shinkansen trains. Discontinuities of the lines in Fig. 4 show the effects of the short side branches arranged at regular intervals. Figures 2 to 4 show that the calculated results using the proposed scheme agree well with those by the 1D CFD. Additionally, the calculation time by it is approximately 1/100 as long as that by the 1D CFD.

4 Conclusion

A simple scheme for calculating the distortion of the compression wave propagating through the concrete slab-track tunnel of the Japanese Shinkansen is proposed. This scheme is composed of a single equation derived from three conservation equations of compressible fluids (mass, momentum and energy) considering the effects of wall friction and heat transfer. The calculated results using the proposed scheme agree well with those by the 1D CFD based on the three conservation equations. Besides, remarkable reduction of computing time is obtained. The proposed simple scheme is practical and useful for the estimation of the micro-pressure wave.

References

1. Yamamoto, A.: Micro-pressure wave Radiated from Tunnel Exit. Preprint of Spring Meeting of Physical Society of Japan (1977) (in Japanese)
2. Ozawa, S.: Studies of Micro-Pressure Wave Radiated from a Tunnel Exit. Railway Technical Research Report, Japanese National Railways, 1121 (1979) (in Japanese)
3. Ozawa, S., Maeda, T., Matsumura, T., Nakatani, K., Uchida, K.: Distortion of compression wave during propagation along Shinkansen tunnel. In: 8th International Symposium on Aerodynamics and Ventilation of Vehicle Tunnels, pp. 211–226, BHR Group (1994)
4. Fukuda, T., Ozawa, S., Iida, M., Takasaki, T., Wakabayashi, Y.: Distortion of compression wave propagating through very long tunnel with slab-trucks. JSME International Journal B 49(4), 1156–1164 (2006)
5. Aoki, T., Nakao, S., Matsuo, K., Kashimura, H., Yasunobu, T.: Attenuation and distortion of compression and shock waves propagating along high-speed railway tunnels. In: 21st International Symposium on Shock Waves, p. 1140 (1997)
6. Chakravarthy, S.R., Osher, S.: A new class of high accuracy TVD schemes for hyperbolic conservation laws. AIAA Paper, 49-0363 (1985)
7. Vardy, A., Brown, J.: Transient, turbulent, smooth pipe friction. Journal of Hydraulic Research 33, 4 (1995)
8. Hartunian, R.A., Russo, A.L., Marrone, P.V.: Boundary-Layer Transition and Heat Transfer in Shock Tubes. Journal of the Aerospace Sciences 27, 8 (1960)
9. Vardy, A., Brown, J.: An overview of wave propagation in tunnels. In: TRANSAERO - A European Initiative on Transient Aerodynamics for Railway System Optimisation. Notes on Numerical Fluid Mechanics, vol. 79, pp. 249–266. Springer (2002)

Studies on Shock Wave Attenuation in Small Tubes

S. Janardhanraj and G. Jagadeesh

1 Introduction

Shock waves are formed when there is a sudden release of energy in limited space resulting in a supersonic displacement of the gas. Shock tubes are one of the easiest ways to generate good repeatable shock waves in ground-based test facilities with a good control over its parameters. A classical shock tube consists of a driver section(filled with high pressure gas) and a driven section(filled with low pressure gas) separated by a metal diaphragm. The rupture of the metal diaphragm generates a shock wave in the driven section of the shock tube. This mechanism of shock generation has been used for many decades and has been well investigated[1]. For classical aerodynamics studies, shock tubes of circular, rectangular or square cross-section and length scales of the order 50-100 mm are usually used. But the applications of shock wave assisted techniques in new areas like industry and medicine has led to reduction in the diameter of shock tubes and requires the understanding of shock tube flow at different length scales. The Ideal shock tube theory is based on assumptions like inviscid adiabatic flow, instantaneous diaphragm rupture and ignores aspects like diameter of the tube, surface roughness, boundary layer effects, heat and mass transfer effects, non-uniformity in driver section (Eg: combustion driven shock tube), possibilities of combustion at the contact surface and chemical kinetic effects. These effects which are ignored at macro-scales play a very important role when the diameter of the shock tubes are reduced and give rise to very interesting gasdynamic phenomena.

Various research teams around the world have presented numerical and experimental studies for shock wave transmissions and propagation in small channels [2],[3]. But there is lack of experimental data in diaphragm-type shock tubes of diameters less than 10mm which is mainly attributed to difficulties in choosing diaphragms and also difficulties in makes measurements at these length scales. The

S. Janardhanraj · G. Jagadeesh
Laboratory for Hypersonic and Shock wave Research, Department of Aerospace Engineering
Indian Institute of Science, Bangalore - 560012, India

numerical studies also do not give any final word on the flow physics in small-scale shock tubes. In this study, we focus on investigating the effects of important parameters like P_4/P_1 and T_4/T_1 as a function of diameter of the shock tube(the subscript 4 refers to the initial conditions int he driver section and subscript 1 refers to the initial conditions in the driven section). The internal diameters of the shock tube that are studied for the variation of P_4/P_1 are 50 mm and 6 mm while it is 100 mm and 6 mm for variation of T_4/T_1.

2 Experimental Studies

Experiments are first carried out to investigate the effect of the ratio P_4/P_1 in some of the existing facilities like CST3(50 mm diaphragm-type shock tube) and DST(50 mm diaphragmless shock tube). The details of the shock tubes are presented in the table 1. DST is a facility that uses a fast acting pneumatic cylinder instead of a metal diaphragm to generate shock waves in the driven section[4]. But since the speed of the pneumatic cylinder cannot match the metal diaphragm rupture, it can be used to study the effect of diaphragm opening time on shock wave attenuation. Air is used as driver and driven gas in all the cases. Static pressure measurements are made by flush mounting PCB piezoelectric pressure transducers to the inner wall of the shock tubes. Figures 1(a) and 1(b) show the typical pressure signals obtained from the pressure transducers for CST3 and DST respectively for $P_4/P_1 = 15$.

A new small-scale diaphram-type shock tube of internal diameter 6 mm has been built as shown in the figure 2. Different grades of paper have been used as diaphragms to obtain different pressure ratios of P_4/P_1. Air is used as driver and driven gas while few experiments have been performed for helium as driver gas. Figure 3(a) shows the plot between $LogP_{41}$ and shock Mach number (M_S).

Table 1 Details of the various shock tubes and the measured quantities

	CST3	DST	Small-scale shock tube
Internal diameter	50 mm	50 mm	6 mm
Type	Diaphragm-type	Diaphragmless	Diaphragm-type
Driven tube length	5 m	6.024 m	70 mm
Sensor locations (from diaphragm station)	sensor1 - 3.78 m sensor2 - 4.46 m sensor3 - 4.94 m	sensor1 - 3.944 m sensor2 - 5.954 m	sensor1 - 48 mm sensor2 - 58 mm
M_S (Experiment)	1.71	1.57	2.06
Diaphragm opening time	390 μs	4.85 ms	*to be calculated*
Shock intensity at sensor locations	2.067	2.5	3.24

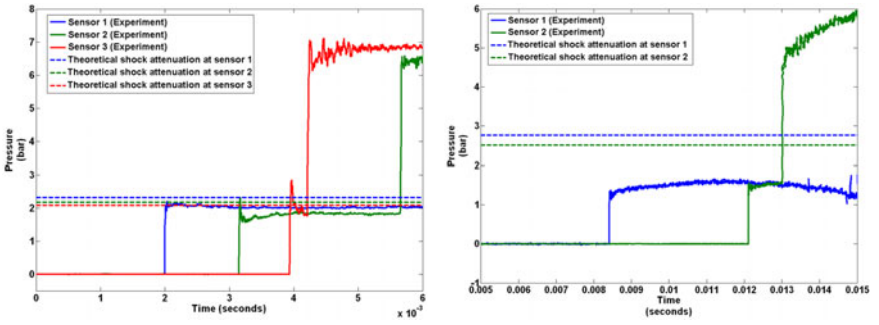

(a) CST3 (50 mm diaphragm-type shock tube) (b) DST (50 mm diaphragmless shock tube)

Fig. 1 Static pressure signals obtained for $P_4/P_1 = 15$

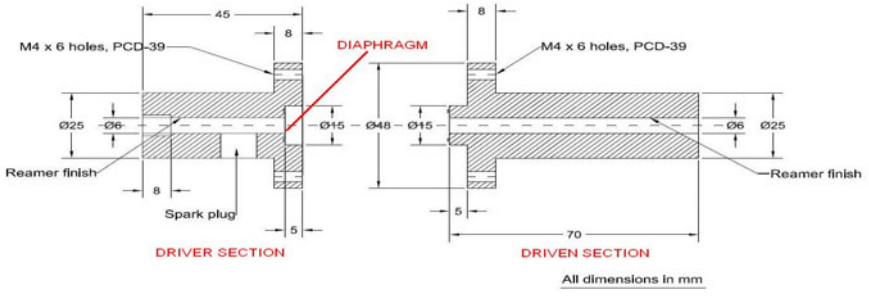

Fig. 2 Schematic diagram of the 6 mm diaphragm-type shock tube

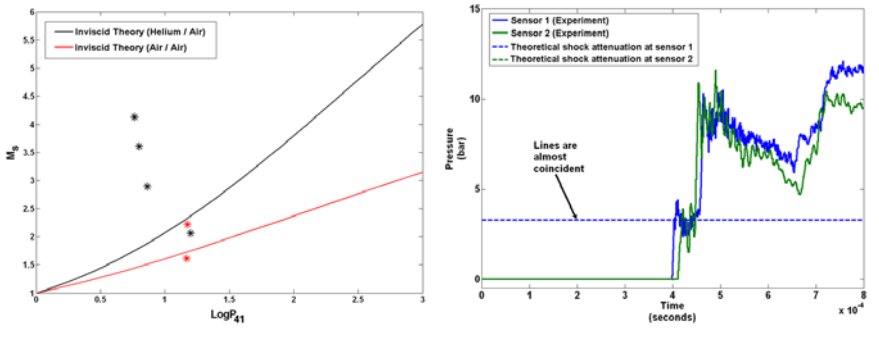

(a) Plot of $LogP_{41}$ vs M_S (b) Static pressure signals for $P_4/P_1 = 15$

Fig. 3 Experimental results for the small-scale shock tube (6 mm diaphragm-type shock tube)

Figure 3(b) shows the pressure signals obtained from the pressure transducers. Schlieren images are also obtained from the open end of the small-scale shock tube for P_4/P_1 of 15 shown in figure 4. A high-speed camera (Vision Research,USA, Phantom 7.1 operated at 40,000 frames per second and 256 x 128 pixel resolution) has been used to carry out the visualization studies.

The ratio T_4/T_1 is changed in the shock tube by performing H_2-O_2 combustion in the driver section. A simultaneously in situ generated H_2-O_2 mixture is used in the driver section of the small-scale diameter shock tube. The mixture is generated by using a H_2-O_2 generator which is connected to the small-scale shock tube through a non-return valve to prevent explosion of the generator during ignition. The mixture is ignited using a spark plug mounted near the diaphragm. The experimental setup is shown in the figure 5. The numerical code developed by Joarder [5] is modified to get an idea of the pressure and temperature in the driver section of the small-scale shock tube. The initial pressure in the driver section is 0.85 bar(gauge) and the H_2-O_2 fill pressure is 0.45 bar(gauge). From the code, the P_4 and T_4 are 15 bar and 900 K respectively. Therefore, experiments are carried out in the small-scale combustion driven shock tube for the same initial conditions and pressure signals are obtained at the end of the shock tube shown in the figure 6. Experiments are still underway in the 100 mm internal diameter combustion driven shock tube.

3 Numerical Studies

A 1-D numerical code has been written on the formulations of Mirshekari [2]. The code is run for the inviscid case first for conditions of $P_4/P_1 = 15$ and compared to the experimental signals obtained for the 50 mm diaphragm-type shock tube shown in the figure 7. The simulations for the viscous case and comparison with the signals obtained from the 6 mm shock tube is still underway.

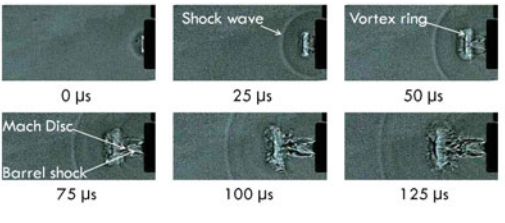

Fig. 4 Schlieren photographs at the open end of the 6 mm shock tube

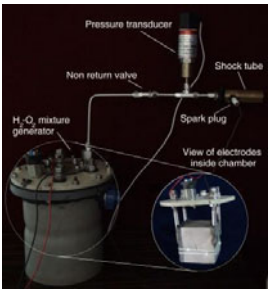

Fig. 5 Photograph of the setup used for 6mm combustion driven shock tube

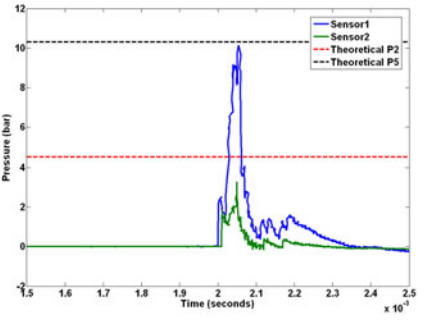

Fig. 6 Pressure signal obtained from the end of the 6 mm combustion driven shock tube

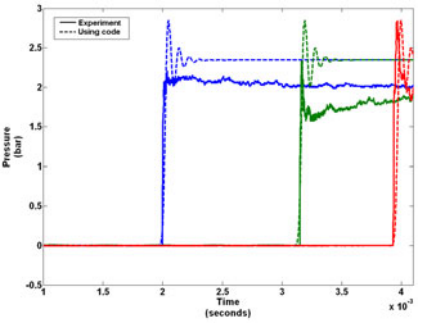

Fig. 7 Comparison of the pressure signal obtained through experiment and 1-D code for the 50mm shock tube

4 Results and Discussion

The empirical relations for attenuation of shock wave intensity (P_2/P_1) and opening time of diaphragm have been given by [6] and [7] respectively.

$$\pi^* = \pi_i^* . e^{\left(-\frac{Ax}{r}\right)} \tag{1}$$

where $\pi^* = \left(\frac{P_2}{P_1} - 1\right)$, $A = 0.0024$, x = distance along the tube, r = hydraulic radius and the subscript 'i' refers to the unattenuated shock intensity.

$$t_{op} = K\sqrt{\frac{\rho b \tau_1}{P_4}} \tag{2}$$

where $K = 0.93$, ρ = density of material, τ_1 = length of petal base and b is the thickness of diaphragm.

The theoretical values of shock wave intensity and diaphragm opening time have been calculated using the above relations and presented in table 1. The dotted line in figures 1(a), 1(b) and 3(b) indicates the theoretically calculated attenuation at the sensor locations using empirical relation aforementioned. It can be seen that the theoretical values of shock wave intensity are closer to the experimental values for the 50 mm diaphragm type and the 6 mm diaphragm type but not in the case of the 50 mm diaphragmless type. This is due to the larger value of t_{op} for the 50 mm diaphragmless shock tube. The attenuation of shock in the case of the 6 mm shock tube is lesser compared to the larger diameter shock tubes. Also, the experimentally obtained shock Mach number is higher in the case of 6 mm shock tube and the trend followed by the experiments in the calibration plot (Figure 3(a)) is completely different from the inviscid theory. The schlieren images obtained from the open end of the 6 mm shock tube shows flow features that are typical of the macro-scale open ended shock tube flows as indicated in the figure 4. The presence of an initial shock wave, vortex ring, Mach disc and barrel shock show the formation and propagation of a shock wave in the 6 mm shock tube. Using the values P_4=15 bar and T_4 = 900

K from the modified Joarder's code, the inviscid theory gives values of $P_2 = 4.5$ bar, $P_5 = 10.3$ bar and $M_S = 2.167$. The dotted lines indicate these values of P_2 and P_5 in the figure 6 (subscript 2 indicates the region behind incident shock and subscript 5 indicates the region behind the reflected shock). It can be seen that the P_5 is close to the theoretical value for one of the pressure sensors. The experimentally obtained shock Mach number is 2.16 which is close to the theoretical value. From figure 7, it can be seen that the pressure signals are not matching for the first two sensors but for the third sensor the experimental value is close to the numerical value. But the pressure jumps at the various sensor locations are the same instants of time which shows that the shock Mach number is the same for the experiment and the signal obtained from the code.

5 Conclusions

Experiments have been performed in the small-scale shock tube of diameter 6 mm to investigate the effect of P_4/P_1 on shock wave attenuation. The shock Mach number obtained experimentally is higher than the theoretical value for the 6 mm shock tube. But the value of experimentally obtained shock intensity is close to the value given by the empirical relation. Schlieren images have been obtained from the open end of the 6 mm diaphragm-type shock tube which shows that a shock is formed in the tube and propagates through it. A novel in situ generated H_2-O_2 combustion driven small-scale shock tube has been designed, fabricated and initial experiments have been performed to investigate the effect of T_4/T_1 on shock wave attenuation. A numerical code has been developed on basis of Mirshekaris 1D model and initial attempts have been made to complement the experiments performed.

References

1. Gaydon, A.G., Hurle, I.R.: The Shock tube in High-Temperature Chemical Physics. Chapman and Hall Ltd., London (1963)
2. Mirshekari, G., Brouillette, M.: One-Dimensional model for microscale shock tube flow. Shock Waves J. 19, 25–38 (2009)
3. Giordano, J., Parisse, J.D., Biamino, L., Devesvre, J., Perrier, P.: Experimental and numerical study of weak shock wave transmissions through minitubes. Phys. Fluids 22, 061703 (2010)
4. Hariharan, M.S., Janardhanraj, S., Saravanan, S., Jagadeesh, G.: Diaphragmless shock wave generators for industrial applications of shock waves. Shock Waves J. (2010), Online First
5. Joarder, R.: Demonstration of supersonic combustion in a combustion driven shock tunnel. Dissertation, Indian Institute of Science, Bangalore, India (2009)
6. Bradley, J.N.: Shock waves in Chemistry and Physics. Chapman and Hall Ltd., London (1963)
7. Rothkopf, E.M., Low, W.: Diaphragm opening process in shock tubes. Phys. Fluids 17, 1169–1173 (1974)

Standing Shock Formation in a Non-reflected Shock Tube

R.G. Morgan, U.A. Sheikh, and D.E. Gildfind

1 Introduction

The study of thermo-chemical relaxation processes in shock tubes requires flow with sufficient residence time to allow the relaxation process to complete. In the context of hypersonic reentry, the length scales of interest are determined by the size of the flight vehicles, which in general are too large to be reproduced in the laboratory. For non-equilibrium binary kinetic processes, density-length scaling (where the product of density with a characteristic length scale is conserved) may be used to reproduce flight conditions. However, for situations where equilibrium is reached, any change to the overall pressure level will change the chemical composition, and similarity with flight will not occur, Morgan [1]. Therefore to study the radiation from regions of equilibrium flow, test gas at the same pressure as exists in flight must be used. Because the conditions at equilibrium are not path dependent, provided the appropriate pressure and temperature are reached, it is possible to study the radiation from an equilibrium region by creating just a small section of the flow field.

In order to achieve this, it is necessary to reproduce the region of non-equilibrium flow that precedes the equilibrium zone. The physical extent of this section is highly condition dependent, reducing with simulated altitude, but may extend up to 100's of mm for upper atmosphere flight. In studies relating to reentry vehicles of the order of 5 m diameter near peak heating, length scales of several mm will usually suffice. Blunt bodies in non reflected shock tubes represent a possible mechanism for doing this, but their shock stand-off distances scale between 0.1 to 0.35 of the body radii (axi-symmetric shapes), effectively limiting the useful length scale to less than approximately 0.175 times the test section diameter.

An alternative to using a large blunt body is offered by configuring the shock tube to create a standing shock wave in the test section, without using a model, as shown in Figure 1. In this configuration, a standing shock is created in the test section by installing an extra section of tube downstream of the inspection station. If

R.G. Morgan · U.A. Sheikh · D.E. Gildfind
University of Queensland, St. Lucia, QLD, 4067, Australia

the density of the downstream tube is correctly set, a shock will form at the interface between the two gases which is stationary in a laboratory reference frame, and will stay there until the test gas is used up, or other wave processes intervene. The full width of the test section and axial extent of the slug of processed gas is available for viewing, not just the small region contained between the bow shock and the model placed in the exit flow. Instrumentation mounted on the side of the tube can then make detailed radiation measurements transverse to the flow direction. This paper presents preliminary results from testing this configuration in the X2 expansion tube, operated as a non-reflected shock tube. The pressure ratio required between the driven tube and the downstream deceleration tube to create a stationary shock is only weakly Mach number dependent at high speeds. For perfect gas air, a pressure ratio of 25 will create a standing shock, but for highly reacting flows the increased shock density ratio leads to a required pressure ratio of the order of 200 to 300.

2 Apparatus

The region where the standing shock is created is shown in Figure 1, and the overall facility layout is shown in Figure 2, where the region of heated test gas behind the standing shock is identified as region 8.

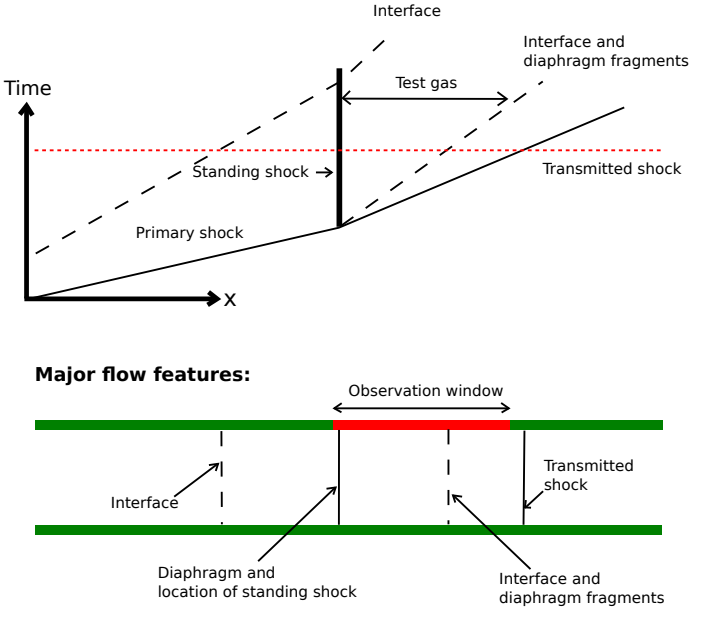

Fig. 1 Formation of standing shock. The location of flow features shown at the bottom of the figure correspond to the time indicated by the red dotted line.

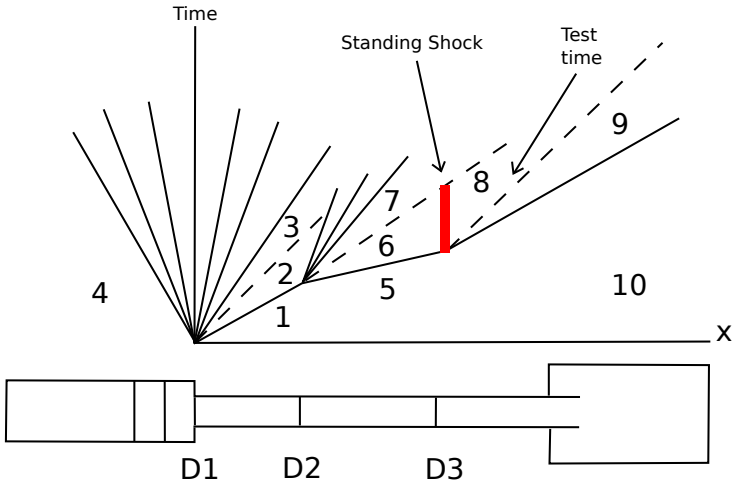

Fig. 2 *x-t* diagram for standing shock.

The driver conditions from Gildfind et al. [2] were used to drive a shock heated driver through helium initially at 45 kPa (region 1, Figure 2) at a speed of 4450 m/s. The shock tube was filled with air at a pressure of 200 Pa (region 5, Figure 2), and an incident shock speed of 6800 m/s resulted. The dump tank and acceleration tube section were filled with air at 45 kPa (region 10 in Figure 2). The proposed flow conditions were predicted using an equilibrium chemistry 1D analysis. For the initial 'proof of concept' study, no transparent section was fitted to the tube to observe the standing shock, and correct operation could only be deduced from observations of the pressure sensors, and the subsequent *x-t* diagrams. The primary shock speed agreed well with the analytical predictions, and CFD, and was measured at 6800 m/s. The standing shock could not be seen in the pressure traces, but the relative trajectories of the incident and transmitted shocks were seen from Figure 3 to closely match equivalent values computed using the 1D equilibrium CFD code `L1D2` code, Jacobs [3].

In Figure 3, the 'standing' shock is seen to be propagating slowly downstream at about 200 m/s, and there is a lag of approximately 30 μs between the extrapolated arrival of the incident shock, and the initiation of the transmitted shock at the tertiary diaphragm location. These computations were run assuming instantaneous diaphragm rupture, to give a 'best case' analysis of the flow conditions. The discrepancy is attributed to diaphragm opening delay. The CFD was rerun with an inertial diaphragm rupture model, whereby the diaphragm mass was removed over a characteristic timescale (Potter [4]). The results of this simulation are shown in Figure 4, and give very close agreement with the experimental data.

The reverse shock starts out as a fully reflected wave, and decays to a standing shock in about 25 μs. The length of the slug of processed test gas is approximately 50 mm at the termination of the test flow. This calculation is inviscid, and

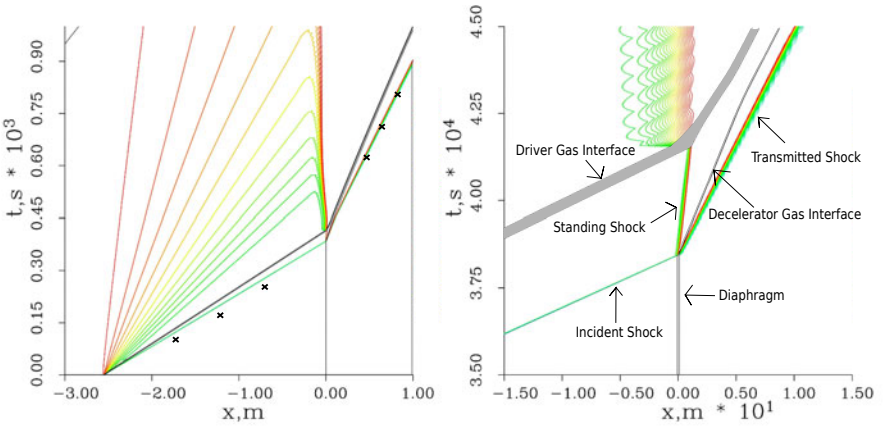

Fig. 3 *x-t* diagram from CFD with experimental shock arrival marked ×.

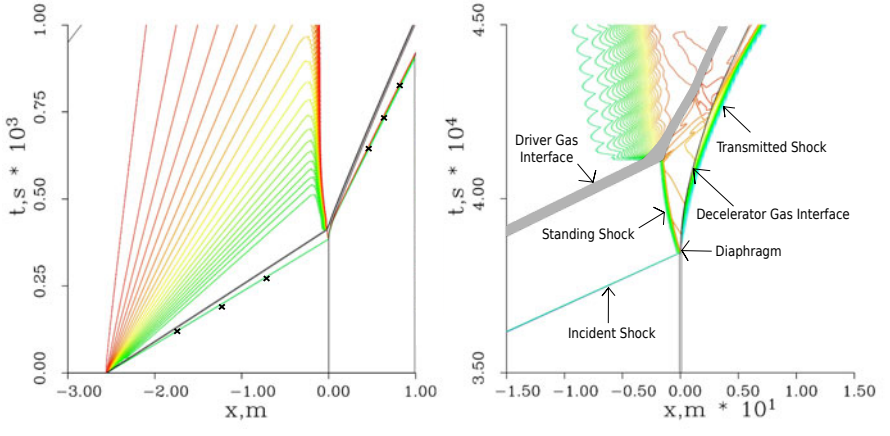

Fig. 4 CFD with inertial diaphragm rupture model removed over 100 μs.

unconfirmed by any direct experimental measurements or observations taken in the actual shock heated region. However, the quality of the data and the good agreement with analysis justifies the continuation of the program to construct a transparent test section, and to proceed with high speed visualisation and spectrometric measurements.

The presence of a diaphragm adjacent to the region of interest is of concern, because of the possibility of contamination of the test gas with vapourised or solid diaphragm fragments, and because diaphragm curvature may preclude 1D shock formation. The bulging of the tertiary diaphragm would be expected to be of the order of a centimetre or two, so with the slug of pre-shock processed gas being of the order of 200 mm, it is possible that a planar shock might not form within

the available flow. This needs to be investigated by further experimentation and visualisation.

A possible way to overcome this issue is to set up a counter flow shock tube, as shown in Figure 5. This configuration has an upstream facing shock tube mounted near the tunnel exit, which fires a reverse shock back through the quiescent test gas just before the incident shock arrives. If the conditions are matched appropriately, when the two shocks collide, a standing upstream propagating shock will form at the point of intersection, and the reverse shock will reflect back downstream. The flow conditions behind the standing shock will be identical with the former configuration presented above, but now there will be no diaphragms in the vicinity of the test gas. Practical difficulties anticipated would be the precise and repeatable timing of the two shocks so that the standing shock forms in the instrumented test section, and the extra experimental uncertainties introduced by two colliding shocks. However, it would form a very clean environment in which to study radiation, and provide a very useful test bed for the study of shock-shock interactions and CFD validation.

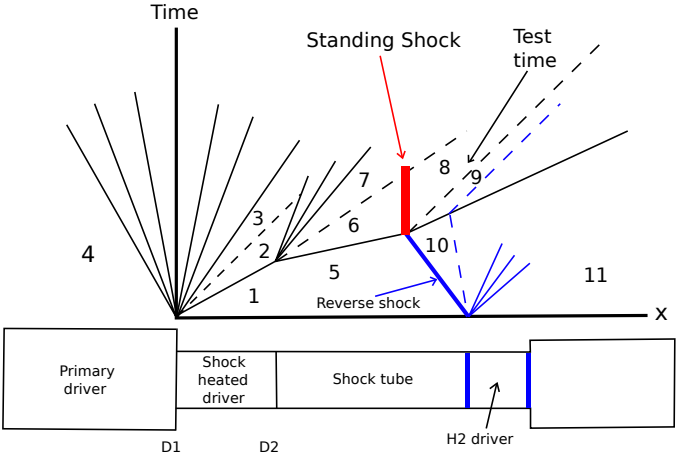

Fig. 5 Standing shock formation using counter flow shock tube.

This technique is analogous to the counter flow facilities that were used from the 60's whereby projectiles were launched upstream into the nozzles of hypersonic shock tubes (Seiff, [5]), but without the difficulty of launching and controlling free flying bodies.

3 Conclusions

Pilot tests have been performed on a shock tube to create a standing shock for the study of radiation in shock layers, by the addition of a 'deceleration' tube at the exit of a shock tube. Preliminary results at an enthalpy of 43 MJ/kg indicate that a stable

standing shock can be formed, and can give a much larger slug of shock heated gas than can be obtained in the same facility by using a stationary blunt body in the test section. The current configuration does not permit observation of the standing shock directly, but its location is inferred from CFD which gives a very good match to the measured shock propagation paths. Follow on experiments are planned with a transparent and heavily instrumented test section to observe the standing shock directly, and to make spectrometric measurements of the radiation from the shock layer. Because the shock layer is fixed in space and time, it is expected that more accurate spatial resolution can be obtained than is possible in either a non reflected shock tube with a moving shock, or behind a bow shock on a laboratory fixed model. The difference between this configuration and using a reflected shock tube at the same total enthalpy, is that test conditions are created in a steady flow situation. The stagnation region created in a reflected shock tube is 'no-flow', and will suffer from a continuous reduction in total temperature from radiative cooling in highly coupled flows.

The presence of a 'tertiary' diaphragm between the test gas and the decelerator gas in the current configuration can potentially contaminate the test gas and perturb the flow field. A new operating mode using a reverse propagating 'counter flow' shock wave is proposed which would create a standing shock without the associated diaphragm. This technique would be valuable for the study of radiation flows, and the study of shock-shock interactions in general.

Acknowledgements. The authors wish to thank: Mr B. Loughrey and Mr F. De Beurs for X2 technical support; The Australian Research Council and The Queensland Smart State Research Facilities Fund 2005 for support and funding.

References

1. Morgan, R.G., Gnoffo, P., McIntyre, T., Sheikh, U.: Simulation of Radiating Flows in Impulsive Facilities. In: Proceedings of the 49th AIAA Aerospace Sciences Meeting including the New Horizons Forum and Aerospace Exposition, Orlando, Florida. AIAA-2011-250, January 4-7 (2011)
2. Gildfind, D.E., Morgan, R.G., McGilvray, M., Jacobs, P.A.: High Mach number and total pressure flow conditions for scramjet testing. In: Proceedings of the 28th International Symposium on Shock Waves, Manchester, July 17-22 (accepted, 2011)
3. Jacobs, P.A.: Lld: A computer program for the simulation of transient-flow facilities. Report 1/99, Department of Mechanical Engineering, University of Queensland, Australia (1999)
4. Potter, D., Eichmann, T., Brandis, A., Morgan, R., McIntyre, T.: Simulation of radiating CO2-N2 shock layer experiments at hyperbolic entry conditions. In: Proceedings of the 40th Thermophysics Conference, Seattle, Washington, AIAA-2008-3933, June 23-26 (2008)
5. Seiff, A.: Ames Hypervelocity Free-Flight Research. Astronautics and Aerospace Engineering 1(11), 16–23 (1963)

Area Change Effects on Shock Wave Propagation

J.N. Dowse and B.W. Skews

1 Introduction

When a planar shock wave propagating down a channel encounters a decrease in cross-sectional area, not only is the shock strengthened but the shock shape and post-shock flow are disturbed. The current research investigates how various area reduction profiles affect the shock strength and shape, as well as the uniformity of the post-shock flow for planar shocks. Bird [1] and Russell [2] investigated experimentally the effects of wall shaping and strengthening by convergence respectively using strong incident shock waves; however the current study looks at relatively low Mach numbers of $1 < M < 2$. By optimising the wall shape an area reduction can be used to increase the strength of a shock significantly without compromising on the quality of the post-shock flow, which is of particular importance in the design of experimental shock tube testing. More importantly, by analysing different profiles using numerical studies, the technique could then potentially be generalized to examine to what extent a shock shape may be purposefully manipulated to a required profile by suitable wall shaping. In order to provide a comprehensive study of the topic, numerical, analytical and experimental analyses are conducted. A comparison of computational fluid dynamic (CFD) simulations and Milton's corrected ray-shock theory [3] is examined in detail.

2 Review of Shock Wave Strengthening by Area Reduction

When a shock wave travelling down a channel encounters a small change in area, the strength of the incident shock changes continuously and during the transition reflected disturbance waves and contact surfaces are also generated. Chester [4, 5] analysed this problem and assumed that if the area of the channel changes by a

J.N. Dowse · B.W. Skews
Flow Research Unit, The School of Mechanical, Industrial and Aeronautical Engineering, The University of the Witwatersrand Johannesburg, Wits 2050, South Africa

small fraction of itself, the disturbances produced in the flow behind the shock are regarded as negligible thus enabling the equations of motion to be linearised. The approximate solution derived by Chester was also derived by Chisnell [6] using steady state theory, and Whitham [7] using a simpler linearised characteristics approach. The derived relation is a one-dimensional differential solution that relates the average shock strength to the cross-sectional area of a channel, and is referred to as the CCW relation. It is described as an approximate solution because the CCW relation neglects the effects of reflected disturbances from the subsequent flow and Russell [2] suggests it is only valid within a region of monotonically changing area. So, when considering a large change in area, the CCW relation can only provide an approximation because any disturbances on the shock front caused by reflected shock waves are no longer negligible [8].

Whitham later developed an approximate theory that uses analytical methods to predict the shape and strength of a moving shock in two-dimensions [9]. The theory is based on a grid of progressive shock front positions and orthogonal 'rays' that are used as coordinates. Whitham's theory is particularly successful at predicting the shock's motion at high Mach numbers, as well as predicting the triple-point locus, but is regarded as unreliable at lower Mach numbers where the effect of weak reflected and re-reflected waves are no longer negligible. Milton's [3] modified version of the ray-shock theory introduces a correction term that accounts for the disturbed Mach reflection case. The correction term was evaluated using "strong" shock equations for the shock front, but the range of agreement with experimental data is vastly improved over the unmodified ray-shock theory.

Bird [1] showed experimentally that the degree of reinforcement of a converging shock wave is critically dependent upon the wall shape; where the gain in shock strength continues to increase with the number of incremental steps taken to reduce the area. He showed that by optimising the transition region for the area reduction, the gain in shock strength rose significantly and approached theoretical maximum values. Theoretical maxima were based on the ideal case of an infinite number of vanishingly small area changes. Bird conducted his research using very strong initial shock waves where his initial shock Mach numbers ranged between 6.4 to 7.3. Later, Russell [2] investigated shock wave strengthening by area convergence and compared his results with the CCW relationship. Russell analysed an area convergence from a 17 inch shock tube to a 1 inch tube with a 10° convergence half-angle with initial shock speeds of between Mach 2.0 and 6.0. He showed that shock exit speeds agreed to within 5% of predicted non-steady theory for a real-gas based on the CCW relation. Russell also investigated how the strengthened shock decays once it has passed through the area change. Once the shock has left the convergence, weak reflected waves attenuate it to an asymptotic solution which is typically reached after a distance of four to six convergence lengths. He suggested that for half-angles under 30° two-dimensional effects are of limited importance when considering shock decay.

3 Numerical Computation of Planar Shock Waves through Area Reductions

Numerical simulations carried out involved an unsteady two-dimensional analysis of a planar shock wave propagating through a channel with a variable area reduction. By varying the Mach number and wall shape the change in shock strength, shock shape and post-shock flow were analysed. The curve defining the boundary wall profile consists of two intersecting parabolic curves as shown in Figure 1. The point of intersection between the two parabolic curves or the 'point of inflection' was varied by moving it to 25%, 50% and 75% of the total profile length. Shifting the point of inflection provides different cases for variable rates of shock compression and expansion as the shock progresses through the area change. Based on the maximum length of the experimental facilities available, the profile lengths chosen were 130mm, 195mm and 260mm. Similarly, the total channel inlet height was fixed at 120mm. The range of area reductions chosen for investigation include 40%, 60%, 80%, 90% and 95%. Finally, the analysis was conducted for shock waves with initial Mach numbers of 1.2, 1.4, 1.6 and 1.8.

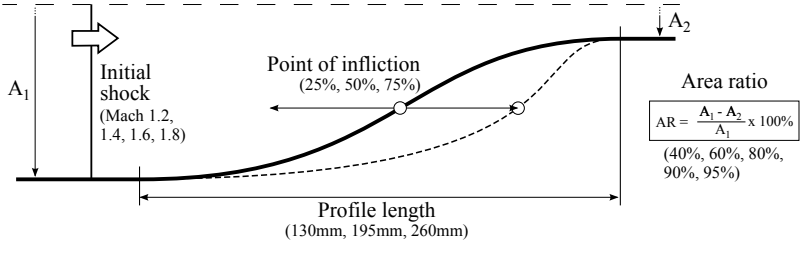

Fig. 1 Illustration of parameters used to define a double-sided parabolic area reduction

Numerical simulations were carried out in ANSYS FLUENT 12.0 using an inviscid, second order, implicit, density-based solver. The domain consisted of a half profile reduction with a symmetry boundary condition enforced on the upper plane; a pressure inlet located 50mm upstream of the profile start and a pressure outlet 200mm downstream of the profile end. The flow was modelled using a third order MUSCL scheme with Roe-Flux Difference Splitting scheme where the domain was meshed using the least-squares, cell-based spatial discretisation technique. The mesh was adaptively refined up to five times in regions where pressure and Mach number gradients exceed 10% of the local normalized value. Initial simulations were run with a minimum cell size of 1mm and 0.5mm, but reduced to 0.2mm to adequately capture shock curvature and possible shear layer development. Quadrilateral, triangular and tri-quad meshes were compared and a mapped quadrilateral mesh was chosen due to its superior computational efficiency whilst producing similar results. Pressure data for the average pressure ratio across the transmitted shock were extracted when the shock reached a distance of between 0.4 and 0.8 convergence lengths downstream from the exit of the area reduction. At this position the

shock in all numerical cases proved to be planar in shape. Theoretical curves were calculated by integrating Milton's modified $A = f(M)$ relation and evaluating the integral using initial area and final area conditions for various initial shock Mach numbers.

4 Discussion

Figure 2 shows a comparison of Milton's modified ray-shock theory and calculated transmitted Mach numbers for a given percentage in area reduction and profile length at various Mach numbers. The filled data points indicate that the reflection pattern transitioned to a simple Mach reflection, whilst the open points indicate that only a strong compression wave behind the incident shock was observed. Figure 3 shows a comparison between the development of Mach 1.8 planar shock wave propagating through a 260mm (a,b,c,d) and 130mm (e,f,g) parabolic profile respectively. The flow features are labelled as follows: m - Mach stem; i - incident shock; r - reflected shock; s - shear layer; T - triple point.

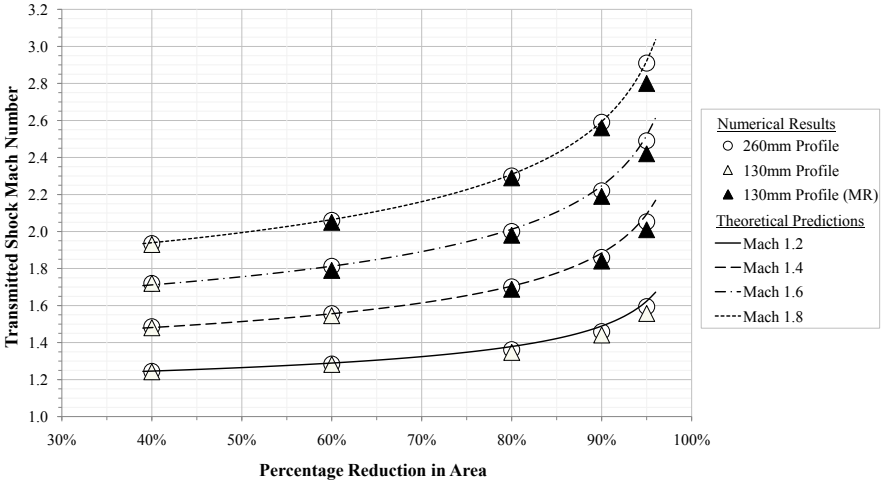

Fig. 2 Comparison between numerical results for 130mm, 260mm parabolic profiles and theoretical predictions from Milton's modified $A = f(M)$ relation for Mach 1.2, 1.4, 1.6 and 1.8

At smaller area reductions of 40 and 60%, the theoretical prediction for the transmitted Mach number agrees well with results from simulations for all tested Mach numbers. The difference in results between 130 and 260mm profiles in this region is also negligible. This indicates that any reflections and re-reflections produced from the profile are relatively weak compared to the strength of the incident shock and later transmitted shock. In the larger area reductions of 80, 90 and 95% results from the shorter 130mm profile start to deviate from those obtained for the 260mm profile

as well as the theoretical prediction. The difference in transmitted Mach number between theoretical and the 130mm profile is quite significant at Mach 1.8 where the difference is Mach 0.98. The difference in results between the 130mm and 260mm profiles for 95% area reduction continues to increase as the incident shock strength increases. This shows that losses associated with the formation of Mach reflection and its interaction with the incident shock negatively affects the performance of the area reduction. This means that the performance of the area reduction is dependant not only on the rate at which the area decreases, but also on the incident Mach number. Simulations conducted for the point of inflection located at 25% and 75% of the profile's length for an 80% area reduction and 130mm profile showed only 0.5% difference in shock strength. Given the possibility of numerical noise propagating through the system, it is reasonable to conclude that changing the profile by moving the point of inflection does not improve the efficiency of the design. Bird [1] showed that he was able to obtain a maximum rise of 130% in Mach number for an 80% area reduction and $M = 7.0$ incident shock. For this case, Bird calculated that the theoretical maximum gain in Mach number is 150%. In comparison, results for an 80% area reduction and 260mm parabolic profile varied from 112% ($M = 1.4$) to 128% ($M = 1.8$) where all approached to within 1% of their respective theoretical maxima.

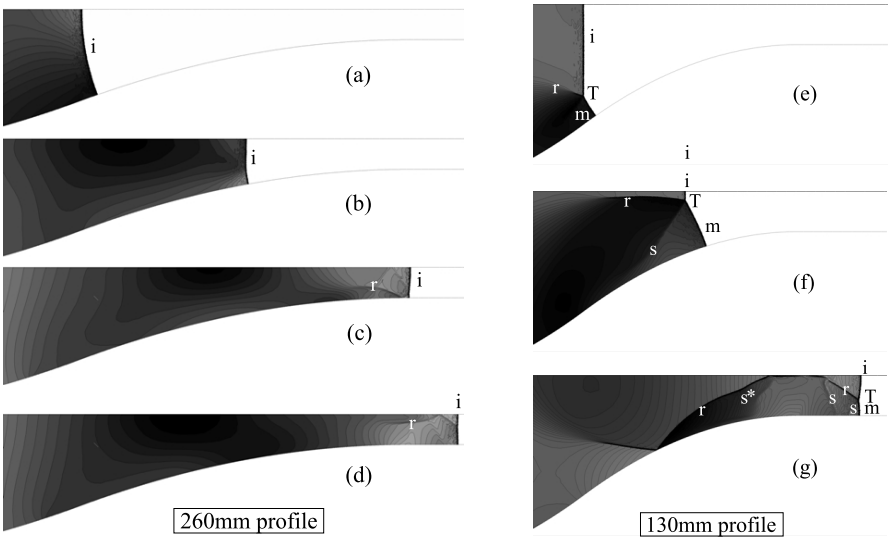

Fig. 3 Development of Mach 1.8 planar shock wave propagating through a 260mm (a,b,c,d) and 130mm (e,f,g) parabolic profile respectively

In Figure 3(a) a strong compression wave is seen developing behind the curved incident shock but this does not result in Mach reflection at (b). Instead, due to the gradual slope of the compression the shock and flow are able to adjust adequately.

Besides the relatively weak reflections that arise from the reflection of the original compression, the flow is quite uniform by position (d) and the shock is almost planar. In contrast, the shock propagating through the 130mm profile has transitioned to Mach reflection at position (e). At position (g) the re-reflected shock is distorted as it moves through different flow regions thereby bowing the shock further. In later time steps (not shown), the reflected shear layers are shown to break down and form large Kelvin-Helmholtz instabilities, the formation of which is doubtful considering the exaggeration of such features for the solution to the Euler equations. Overall, it is clear that formation of a strong Mach reflection increases the level of entropy in the system thereby affecting the quality of the post-shock flow.

5 Conclusions

Results showed that Milton's modified ray-shock theory accurately predicts transmitted Mach numbers for lower area reductions of 40 and 60% for relatively weak incident shock waves. At high area reductions, theoretical predictions do not agree with numerical results because the Mach reflection developed is of significant strength relative to the transmitted shock to affect it. Overall, the performance of the area reduction is dependant not only on the rate at which the area decreases but also on the incident Mach number. Adjusting the profile for variable rates of compression does not produce any difference in the transmitted shock strength as shown in results by changing the profile by moving its point of inflection.

References

1. Bird, G.A.: The effect of wall shape on the degree of reinforcement of a shock wave moving into a converging channel. J. Fluid Mech. 5(01), 60–66 (1959)
2. Russell, D.A.: Shock-wave strengthening by area convergence. J. Fluid Mech. 27(2), 305–314 (1967)
3. Milton, B.E.: Mach reflection using Ray-Shock theory. AIAA Journal 13, 1531–1533 (1975)
4. Chester, W.: The Propagation Of Shock Waves in a Channel of Non-Uniform Width. The Quart. J. Mech. App. Math. 6(4), 440–452 (1953)
5. Chester, W.: CXLV. The quasi-cylindrical shock tube. Phil. Mag., Series 7 45(371), 1293–1301 (1954)
6. Chisnell, R.F.: The motion of a shock wave in a channel, with applications to cylindrical and spherical shock waves. J. Fluid Mech. 2(03), 286–298 (1957)
7. Whitham, G.B.: On the propagation of shock waves through regions of non-uniform area or flow. J. Fluid Mech. 4(04), 337–360 (1958)
8. Ben-Dor, G., Igra, O., Elperin, T., Lifshitz, A.: Shock Wave Interaction and Propagation. Handbook of Shock Waves, vol. 2. Academic Press (2001)
9. Whitham, G.B.: A new approach to problems of shock dynamics - Part I: Two-dimensional problems. J. Fluid Mech. 2(02), 145–171 (1957)

Analytical and Numerical Study of Three Shock Configurations with Negative Reflection Angle

L.G. Gvozdeva, V.L. Borsch, and S.A. Gavrenkov

1 Introduction

The three-shock configuration is quite typical for the aircraft internal and external aerodynamics. For example, it appears at supersonic steady free-stream conditions in intakes (Fig. 1, *left*) and unsteady shock wave reflection from 2D wedges (Fig. 1, *right*). In the latter case the resulting flow is experimentally proven to be pseudo-stationary, and the triple point trajectory makes the constant angle χ with respect to the 2D wedge surface.

The triple shock configuration is perfectly predictable using the three-shock theory [1], the free-stream Mach number and the specific heats ratio being given, and the triple point location being specified. This means that one can compute the configuration as a part of the corresponding well-posed boundary-valued problem using some proper numerical approach. The results obtained are known to agree well with the theory [1] for strong shock waves in some close vicinity of the triple point A dashed round in Fig. 1.

Numerous known numerical computations for the three-shock configuration performed at $\gamma = 1.66$ and 1.4 are similar to those shown in Fig 2, *a* and in all the current textbooks. The computations manifest that the reflection angle $\omega_2 > 0$ with respect to the free-stream direction at any admissible Mach number. The configuration with $\omega_2 > 0$ is experimentally confirmed to exist at flow conditions when internal degrees of freedom are not excited and the effective specific heats ratio $\gamma \gtrsim 1.4$. For flow conditions when physical and chemical phenomena behind the incoming and/or reflected shock waves take place the three-shock configuration with negative reflection angle (Fig. 1, *b*) is experimentally shown to exist in pseudo-stationary flow over 2D wedges and is known as double Mach reflection (DMR) with

L.G. Gvozdeva · S.A. Gavrenkov
Joint Institute for High Temperature of RAS Izhorskaya st., 13/19, Moscow, 127412, Russia
e-mail: gvozdevalg@mail.ru, gavrenkov@gmail.com

V.L. Borsch
Faculty of Mechanics and Mathematics, Dnepropetrovsk National University Gagarin av., 72, Dnepropetrovsk, 46010, Ukraine
e-mail: bvl@dsu.dp.ua

negative reflection angle. Since the above flow conditions lead to decreasing the effective specific heats ratio it was hypothesized in [2] that at supersonic steady flow conditions similar to that shown in Fig. 2, *b* there emerge a transition to some unknown flow regimes.

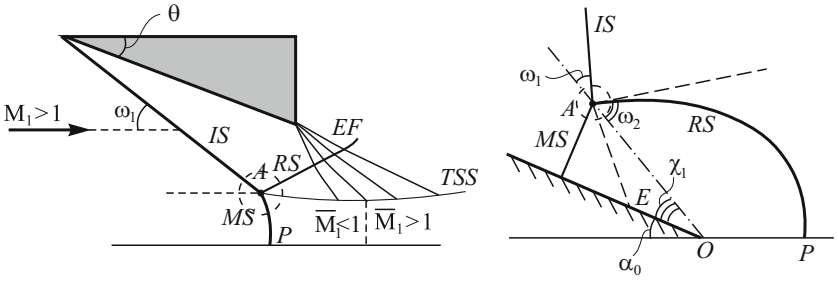

Fig. 1 Schematic illustrations of Mach reflection with $\omega_2 > 0$, left: stationary flow, right: pseudo-stationary flow

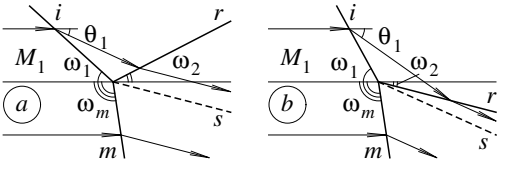

Fig. 2 Schematic illustrations of three-shock configurations: (**a**) $\omega_2 > 0$, (**b**) $\omega_2 < 0$

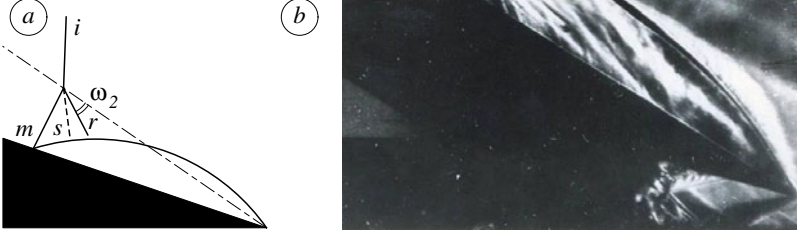

Fig. 3 DMR over the wedge ($\omega_2 < 0$): (**a**) schematic illustration of DMR; (**b**) schlieren image of DMR in carbon dioxide at $M_1 = 5.18$, $p_\infty = 20\ torr$, $\alpha_0 = 32^\circ$ [3]

One of possible logical chains leading to putting forward the above hypothesis is as follows. Self-similar DMR with $\omega_2 < 0$ is known to exist in a pseudo-stationary flow [3], and both experimental [4, 5, 6] and numerical [7] studies revealed intensive wall-jetting very similar by its nature to the flow choking in intakes. Such flows are pseudo-stationary since the leading front of the shock wave configuration runs away from the 2D wedge sharp leading edge faster than the wall jet moves, and the former is not influenced by the latter. It is in agreement with [8]. In 2D case at stationary flow conditions the negative reflection angle immediately leads to the flow choking, but contrary to self-similar solutions the resulting flows are conjectured to be transient since the flow choking is a time-dependent phenomena influencing the subsonic region upstream. But it is the point what sort of transition develops.

The underlying idea of the current study is to implement a preliminary testing the conjecture [2]. it is obvious that the verification of it should be carried out numerically. The study is organized in two parts. In the first part an analytical study is performed, whereas in the second part numerical testing the conjecture is performed.

2 Analytical Study of the Problem

Analytical study was performed using the exact 2D gas dynamics known as shock polar based approach to prove: 1) that stationary three-shock configurations (Mach reflections) with $\omega_2 < 0$ (Fig. 2, *b*) are theoretically admissible; 2) to evaluate conditions at which searching for such configurations is promising. Results obtained are briefly presented in Fig. 4. They prove that: 1) reflection angle is always positive for $\gamma \geqslant 1.4$ and the Mach numbers M even as large as it is physically possible; 2) negative reflection angle configurations are possible at low values of the specific heats ratio γ and high Mach numbers M.

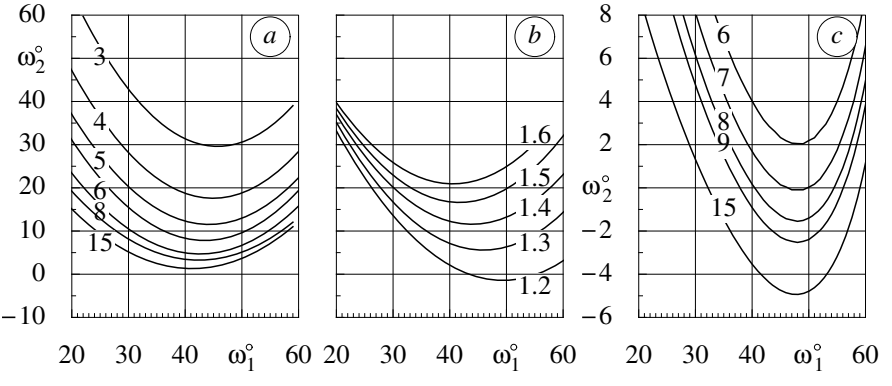

Fig. 4 The angle of reflection ω_2 vs the angle of incidence ω_1 for steady Mach reflection: (**a**) $\gamma = 1.4$, $M = 3 - 15$; (**b**) $M = 5$, $\gamma = 1.2 - 1.6$; (**c**) $\gamma = 1.3$, $M = 6 - 15$

3 Numerical Study of the Problem

Two approaches are used in the current numerical study of shock wave reflections.

The *first approach* is fully based on the self-similar formulation of the time-dependent Euler equations. The governing equations are explicitly integrated in time-asymptotic manner to obtain stationary solutions provided they do exist. Numerical fluxes at the intercells of structured grids are computed using various 1D Riemann solvers, spatial second order being achieved by using MUSCL extrapolation.

The problem of DMR ($\omega_2 < 0$) over the 2D wedge (Fig. 3) has been studied using the above approach. All the solutions obtained turned out to be converged, that is they are all of pseudo-stationary type. The agreement with the three-shock theory is satisfactory, the condition $\omega_2 < 0$ being necessary for the DMR. The influence of γ on the flow pattern turned out to be direct and is clearly seen from Fig. 5. As γ decreases the wall-jetting increases, and eventually approaches the Mach shock wave and destroys it from within. It should be noted that the phenomenon was not reported in [7], and very similar results were obtained numerically in [10].

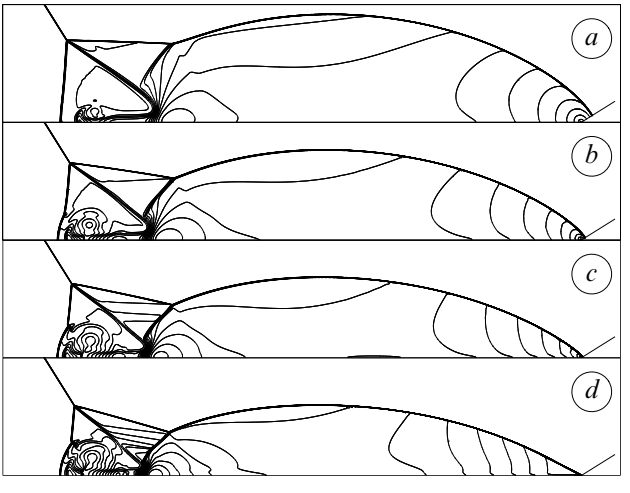

Fig. 5 Numerical isopicnics of DMR [3] (see Fig. 3), numerical flux [9] + *minmod*, the number of nodes along the wedge surface ∼1000, ω_r $(< 0\ or\ > 0)$ and wall-jetting are clearly seen to be dependent on γ: (**a**) 1.40; (**b**) 1.30; (**c**) 1.25; (**d**) 1.20

The *second approach* is fully based on the Navier-Stokes time-dependent governing equations for turbulent 2D flows closed with the Spalart-Allmaras model implemented in the STAR-CCM+ code.

The problem considered using this approach is the shock wave reflection from the plane of symmetry shown in Fig. 1, a. During the preliminary runs of the STAR-CCM+ code the agreement with the known experimental test cases proved to be

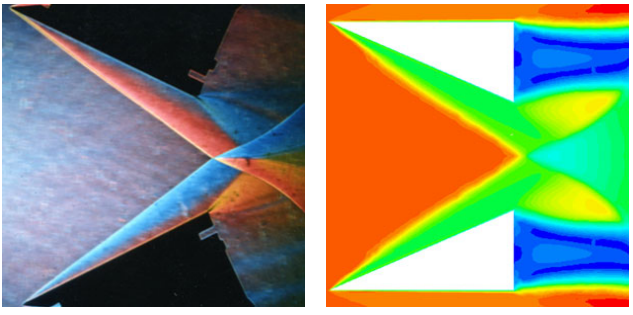

Fig. 6 Regular reflection in air at $M_1 = 5$, $\theta_i = 25°$, left: schlieren image, right: numerical isopicnics (STAR-CCM+)

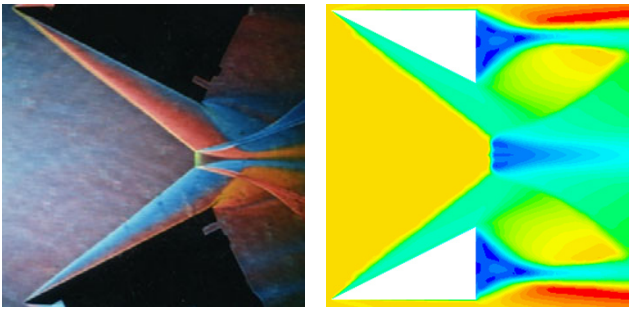

Fig. 7 Mach reflection in air at $M_1 = 5$, $\theta_i = 27°$, left: schlieren image, right: numerical isopicnics (STAR-CCM+)

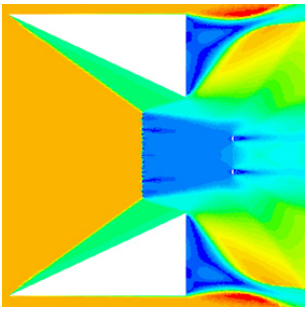

Fig. 8 Numerical isopicnics (STAR-CCM+) for Mach reflection at $M_1 = 5$, $\theta_i = 27°$, in air (two small wedges placed in subsonic region lead to the increase of the Mach stem height essentially)

perfect (Figs. 6 and 7). Mach reflection is known to be very sensitive to the flow conditions downstream the shock wave intersection. Introducing in this region two very small 2D wedges imitates the influence of some disturbances and leads to the increase of the Mach stem height (Fig. 8). Currently 2D time-dependent shock wave reflections at different incoming flow conditions leading to $\omega_2 < 0$ are studied.

4 Conclusions

There are theoretically admissible two distinct three-shock configurations depending on the free-stream Mach number, the incidence angle ω_1, and the gas specific heats ratio, with $\omega_2 > 0$ and $\omega_2 < 0$. In pseudo-steady case the condition $\omega_2 < 0$ leads to DMR with negative reflection angle. In 2D case the resulting flow is still unknown, but it has been conjectured that there should appear a transient flow with detached single shock wave, and it is probable that the transition is eventually followed by some oscillations. In any case a preliminary conclusion has been put forward that configurations appearing in this case can not be steady. Currently computations for 2D case are in progress to test preliminary conclusions.

References

1. Courant, R., Friedrichs, K.O.: Supersonic Flows and Shock Waves. Intersicence, NY (1948)
2. Gvozdeva, L.G.: Conditions of Instability of Three Shock Configuration in Steady Flows. In: ISIS, vol.19, Moscow (2010)
3. Gvozdeva, L.G., Predvoditeleva, O.A.: Experimental Investigation of Mach Reflection of Shock Waves with Velocities of 1000-3000 m/s in Carbon Dioxide Gas. Nitrogen and Air. Sov. Phys. Dokl. 8(10), 694–697 (1965)
4. Bazhenova, T.V., Gvozdeva, L.G., Lobastov, Y.S., Naboko, I.M., Nemkov, R.G., Predvoditeleva, O.A.: Shock Waves in Real Gases, Nauka, Moscow (1968) (in Russian); Engl. transl. NASA TTF-585, Washington, D.C. (October 1969)
5. Bazhenova, T.V., Gvozdeva, L.G.: Unsteady Intersection of Shock Wave, Nauka, Moscow (1977) (in Russian)
6. Bazhenova, T.V., Gvozdeva, L.G., Nettleton, M.A.: Unsteady intera-tions of shock waves. Progr. Aerosp. Sci. 21(4), 250–322 (1984)
7. Henderson, L.F., Vasilev, E.I., Ben-Dor, G., Elperin, T.: The Wall-Jetting Effect in Mach Reflection: Theoretical Consideration and Numerical Investigation. J. Fluid Mech. 479, 259–286 (2003)
8. Barenblatt, G.I.: Scaling Phenomena in Fluid mechanics. CUP, Cambridge (1994)
9. van Leer, B.: Flux-Vector Splitting for the Euler Equations. Lect. Notes Phys. 170, 507–512 (1981)
10. Semenov, A.N., Berezkina, M.K., Krasovskaya, I.V.: Classification of Shock Wave Reflections from a Wedge. Part 2. Tech. Phys. 54(4), 497–503 (2009)

Shock Detachment from Curved Surfaces

S. Mölder, E. Timofeev, and G. Emanuel

1 Introduction

Attached-to-detached-shock transition analysis is of particular interest because the transition introduces radical changes in the flowfield and abrupt changes in flow characteristics. Section 2 of this paper discusses the possible causes of shock detachment from a sharp curved wedge. The concepts of *local and global choking* are introduced as causes for shock detachment from a sharp curved leading edge. Then the analytical conditions are shown under which the above causes are produced. Section 3 is a CFD confirmation showing flow field computations of attachment/detachment with the unstructured adaptive finite-volume Euler code `SolverII` [4] at the analytically predicted conditions. Two items are introduced here to aid the subsequent development of discussion, theory and computation.

The Unit Ring-Wedge (URW) is an annular ring with a sharp leading edge that is everywhere at unit radius from the axis of symmetry ($y = 1$). The outer surface of the ring turns the flow outward by δ_o and the inner surface turns the flow towards the axis by δ_i, at the leading edge. The surface curvature, D_2, in any meridian (flow) plane is zero, positive (when the flow turns away from the axis) and negative (when the flow turns toward the axis). The shock has an acute angle on the outside and an obtuse angle on the inside; giving a positive/negative flow deflection on the outside/inside. Shock curvature in the meridian plane is S_a, defined as positive when the shock is concave towards the oncoming flow. In the transverse plane the shock curvature, at the leading edge, is $S_b = -\cos\theta/y$, which, for the URW becomes simply $-cos\theta$. All radii of curvature $R_a = -1/S_a$, $R_b = -1/S_b$ and $r_2 = -1/D_2$ are normalized with respect to the unit ring-wedge radius $y = 1$. The URW provides the normalizing dimension and a convenient geometry for the study of doubly curved

S. Mölder · E. Timofeev
Department of Mechanical Engineering, McGill University, Montreal,
Quebec H3A2K6, Canada

G. Emanuel
Department of Mechanical and Aerospace Engineering,
University of Texas at Arlington, Arlington, Texas 76019-0018, USA

shock waves and surfaces in axial flow. The term *axial* is synonymous with axisymmetric and what is often called two-dimensional is referred to as *planar*; the latter being a limiting case of the former when $y \to \infty$.

Curved shock theory (CST) relates flow gradients on the up and downstream sides of a doubly curved shock wave. Two major results of CST, applicable to shock detachment formulations, are the algebraic expressions for pressure gradient and streamline curvature behind a curved shock in terms of the shock's curvatures:

$$P_2 = a_1 S_a + a_2 S_b \; ; \qquad D_2 = b_1 S_a + b_2 S_b \; , \tag{1}$$

where S_a and S_b are the shock's curvatures and their coefficients are all functions of shock angle and freestream Mach number [1, 2, 3].

2 Shock Detachment from a Sharp Leading Edge

The oblique shock equations readily show that a shock, attached to the leading edge of a wedge, is incapable of turning the free stream flow into being parallel with the wedge surface beyond a certain maximum wedge angle. This can be referred to as *detachment by excessive flow turning* – $\delta_{\max}$ *criterion*. The appearance of another type of detachment – *detachment by excessive back-pressure* – is more likely in internal flows where it is easier to apply a back-pressure through downstream flow choking. Two types of excessive pressure choking are possible and here referred to as *global choking* and *local choking*.

Shock detachment by global choking appears in internal flow when the mass outflow is restricted to such an extent that it is less than that passed into the inlet by an attached shock at the entrance. The excess flow must be spilled overboard and this is made possible by the shock detaching and moving upstream to allow a gap for flow spillage. **Shock detachment by local choking** appears, near the leading edge, when the sonic surface is not able to pass all the mass flow entering the portion of the shock between the leading edge and the sonic line behind the shock. As with detachment due to global choking, the shock detaches, opening a gap between the leading edge and the shock for excessive flow spillage. In distinction to global choking, the conditions for detachment due to local choking depend on the geometric details of the leading edge surface. It is the purpose of this paper to examine the conditions necessary for detachment by local choking using both analysis and CFD.

An approximate analytical method, based on CST, is developed below for predicting the conditions necessary for shock detachment by local choking in axial flow. The major premise is that a sonic line cannot exist on a surface if the flow area on that surface is contracting, this principle is the same that applies to steady flow in a converging/diverging passage where the sonic surface can exist only at the throat. For any wedge geometry (angle and curvature) we attempt to find the wedge length required to choke the flow. The starting point is the curved shock equations (1). Using $S_b = -\cos\theta$ for the URW and eliminating S_a from Eqn. (1) gives,

$$P_2 = (a_1/b_1)D_2 + \cos\theta(a_1 b_2 - a_2 b_1)/b_1 \ . \tag{2}$$

This expression gives the normalized pressure gradient at the URW leading edge (both top and bottom) in terms of the leading edge curvature, D_2, and the Mach number and shock angle which are the only parameters contained in the a and b coefficients. The first term on the r.h.s. is the contribution to pressure gradient due to the stream-wise curvature of the surface, D_2, and the second term, which vanishes for planar flow, is the contribution of lateral surface curvature. For the isentropic flow behind the shock the Mach number gradient can be written in terms of the pressure gradient. This enables the Mach number gradient to be expressed in terms of the normalized pressure gradient, $\mathrm{d}M_2^2/\mathrm{d}s = -[2+(\gamma-1)M_2^2]M_2^2 P_2$, where s is the distance along the wedge (streamline) in the flow direction. Using P_2 from above and making the approximation that the post-shock Mach number gradient equals the average gradient to the sonic surface, $\mathrm{d}M_2^2/\mathrm{d}s = (1-M_2^2)/L^*$, where L^* is the distance from the leading edge to the sonic point on the wedge, gives,

$$L^* = \frac{\frac{b_1}{a_1}(M_2^2-1)}{[2+(\gamma-1)M_2^2][D_2 - (b_1\frac{a_2}{a_1} - b_2)j\cos\theta]} \ , \tag{3}$$

where $j = 0/1$ for planar/axial flow. The post-shock Mach number, M_2, is expressed in terms of M_1 and θ, so that the independent parameters that make up the right-hand side of this expression are the freestream Mach number, M_1 , the shock angle, θ, and the wedge curvature, D_2. The shock angle can be traded for the wedge angle, δ, by the (M,θ,δ)-relation for oblique shocks so that the right side becomes an expression containing the freestream Mach number, M_1, and wedge geometry as specified by (δ, D_2, L^*). Equation (3) implies that shock detachment is promoted by a decrease in freestream Mach number and an increase in value of any one of the geometric parameters. It gives the relationship between the variables at incipient detachment; the inference being that the shock will detach at the sonic wedge angle when L^* is zero and at the maximum deflection angle when L^* becomes very large. So that, if the surface length in the flow direction at any intermediate wedge angle, is more than L^*, the shock will detach at this intermediate wedge angle. Figure 1 is a plot of Eqn. (3) for L^* against M_1 with the wedge angle as parameter for $D_2 = 0$, i.e an URW as described above with straight conically convergent inner surface. The various values of δ on the abscissa, where $L^* = 0$, are the $\delta_{\max}$ values, indicating that, for $\delta_{\max}$, local choking occurs right at the leading edge, effectively requiring a very short duct length to cause detachment. An examination of this figure shows that moving to a smaller duct convergence angle increases the length of duct, L^*, required to produce local choking and hence detachment at that angle. At Mach numbers below 2.5 the colour bands for δ are almost vertical so that the effect of local choking on shifting shock detachment away from $\delta_{\max}$ is small.

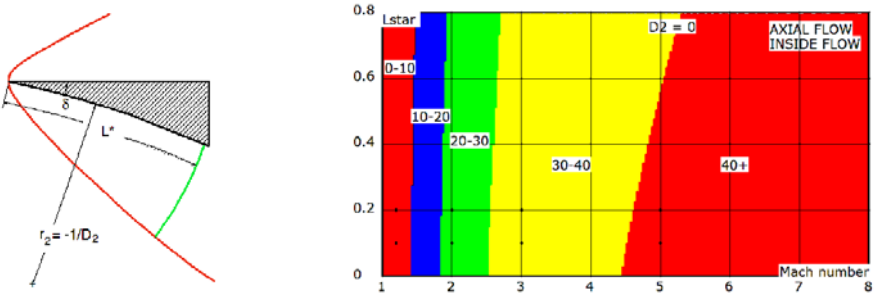

Fig. 1 Distance from leading edge to sonic line L^* vs. Mach number M_1 and wedge angle δ

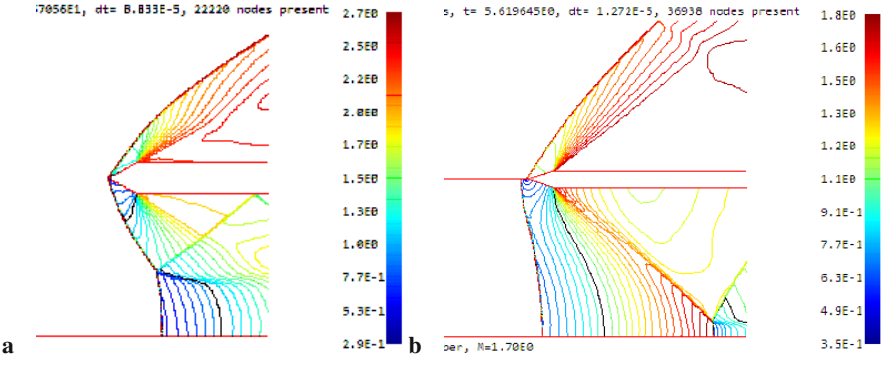

Fig. 2 Mach contours on URWs (the sonic line is shown in black): (**a**) the freestream Mach number $M_1 = 2.7$, the upper (outer) and lower (inner) wedge angles are both 30°; (**b**) $M_1 = 1.7$, the wedge angles are both 16°; an infinitely thin tube has been inserted, extending forward from the leading edge into the free stream. Its purpose is to isolate the outer and inner flow calculations so that surface curvature effects appear separately on each side without spillage effects from detached flows on either side affecting the flow on the other side

3 Computational Examples

Figure 2 illustrates the difference between global and local flow choking in an axial converging duct. For the case shown in Fig. 2a, the maximum deflection angle is 31.7406° and the sonic shock deflection is 31.64294° so that on a plane wedge the shocks would both be attached. Flow is supersonic on the outer wedge surface and the shock is attached. On the lower wedge the flow is subsonic and the shock is very close to detaching. This is an example of shock detachment by local choking where the sonic surface, appearing as a black line from the shoulder to the shock, is not able to pass the flow entering through the shock in front of it. Although there is a Mach disk at the centre line, the global (inside) flow is not choked and the choked flow is confined to the leading edge without being affected by downstream conditions – hence the term 'local choking'. Shock detachment is caused by the curved shape of the inside surface at the leading edge. For the case shown in Fig. 2b, the maximum

deflection and sonic shock angles are 17.01194° and 16.63108°. In this case the outer shock is attached whereas the inner shock is detached from the leading edge. All of the inner flow is choked at the sonic surface and the shock has assumed a steady shape and position in front of the URW.

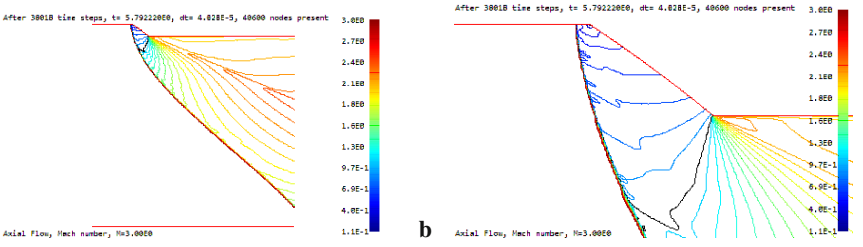

Fig. 3 Constant Mach number contours for a Mach number of 3 over an URW with a wedge angle of 33.5°. The axial wedge surface at the top is curved towards the flow with a radius of curvature of 1. The distance from the axis of symmetry at the bottom to the top of this figure is also 1. Image (**b**), where detachment is clearly visible, is an enlarged view of the subsonic region of the flowfield depicted in the contour plot (**a**)

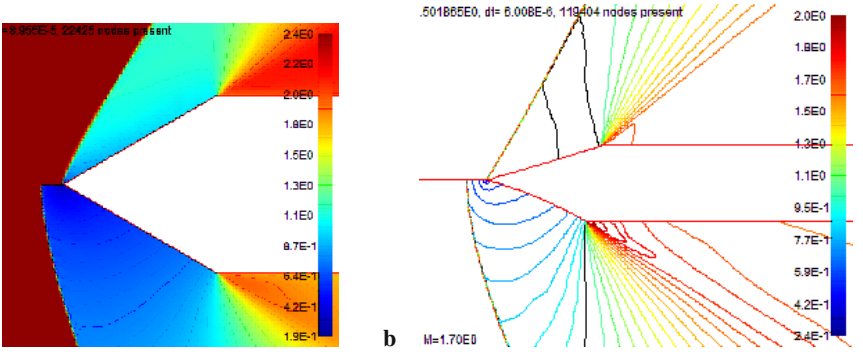

Fig. 4 (**a**) Mach number shading over the leading edge of a URW with outer/inner deflection angles ±30° in a Mach 3 freestream flow. An infinitely thin splitter tube is inserted, in the computational domain, projecting upstream from the leading edge, to keep the effects of the upper and lower curvatures from interacting. The *streamwise* curvature for both surfaces is zero, $D_2 = 0$. For the upper/outer surface the *lateral* curvature is $-\cos 30° = -0.8660$ and for the lower/inner surface it is $-\cos 150 = 0.8660$ with curvature radii 1.1547 and −1.1547 respectively; (**b**) Constant Mach number lines for planar flow at Mach 1.7, where the outer and inner wedge angles are ±16.5°

For the Mach number of the case shown in Fig. 3 the flow deflection angle for sonic flow is 34.00835° and for maximum deflection it is 34.07344° so that, on a plane wedge, the shock remains attached. The doubly curved leading edge supports a detached shock with subsonic flow between the shock and the surface and a sonic

line from the corner to the shock. The result is in agreement with the CST predictions of Eqn. (3). This is an example of shock detachment occurring due to local flow choking as induced by wedge curvatures in both streamwise and transverse directions. In the case shown in Fig. 4a the negative and positive curvatures cause expansive and compressive flows on the upper and lower surfaces as specified by the second term of Eqn. (2). Expansive flow on the top is supersonic whereas compressive flow on the bottom is subsonic. The bottom flow chokes at the corner causing detachment of the lower shock. This is an illustration of shock detachment as caused by lateral surface curvature through the action of local choking. At the Mach number of Fig. 4b the sonic and maximum deflection angles are 16.6311° and 17.0119°, so that, on plane wedges the shocks would remain attached. In fact the upper wedge is plane and the shock is attached with a sonic line shown between the plane surface and the shock, indicating just-supersonic flow. The bottom wedge is curved towards the flow in the streamwise direction ($D_2 = -1$) so that, according to the first term in Eqn. (2), the flow is compressive. The thin black line shows where the *flow chokes locally by streamwise surface curvature, eventually causing shock detachment*.

4 Conclusions

Detachment by *global choking* is a flow area effect that occurs in the starting and unstarting of air intakes. It is due to the global mismatch of mass flow passing through the shock and the sonic surface downstream. If it occurs in a duct, it preempts *local choking*, which is due to the same mismatch but now at the leading edge. It has been shown that shock detachment can occur from a sharp leading edge that is curved either along or transverse to the freestream direction by *local* choking of the post-shock flow. Detachment by local choking is attributed uniquely to the shape of the leading edge and the freestream Mach number and occurs when the convergent flow is not globally choked. Both local and global choking can cause shock detachment from a sharp wedge whose angle is smaller than the maximum flow deflection angle as well as smaller than the angle for sonic down-shock flow. Mach number driven hysteresis is possible for both global and local choking. If the mechanism for RR→MR transition has the same underlying cause as shock detachment from a curved wedge then the occurrence of transition depends on the curvature of the reflecting surface and hysteresis-induced flow duality becomes a possibility.

Acknowledgments. The present study is supported in part by the NSERC Discovery grant RGPIN/298232-2009 and the FQRNT Team grant PR-126114.

References

1. Darden, C.M.: NASA TM 85782 (1984)
2. Emanuel, G., Liu, M.-S.: Phys. Fluids 31(12), 3625–3633 (1988)
3. Mölder, S.: CASI Transactions 4(2), 73–80 (1971)
4. SolverII, Software Package, Ver. 2.30.2385, RBT Consultants, Toronto, ON (2004)

Effect of Solution Conductivity on Shock Wave Pressure Generated by Multichannel Electrical Discharge in Water

V. Stelmashuk, P. Lukes, and P. Hoffer

1 Introduction

Starting from the mid-1980s and up to now, experimental studies of the extracorporeal shock wave lithotripsy (ESWL) applications are performed in different fields of medical sciences, such as the treatment of kidney stone disease, neurosurgery, assisted drug delivery, the treatment of cerebral embolism, orthopedics and in the veterinary medicine. A generator of focused shock waves based on a high current spark discharge in water was developed in the Institute of Plasma Physics AS CR (IPP) [1, 2]. Hospitals in the Czech and Slovak Republic are equipped by such generators produced by the company MEDIPO, Brno. Number of patients undergo a course of medical treatment by these devices every year.

A new apparatus for shock waves generation using cylindrical electrode was developed in IPP [3, 4] (Fig.1). An experimental setup of the arrangement is schematically shown in Fig. 1. A tank containing conducting and non-conducting liquids is separated by acoustically transparent partition. Conductive part, which is filled with highly conducting saline solution (with the conductivity in the order of tens mS/cm), consists of a metallic cylindrical high-voltage electrode covered by a thin porous ceramic layer (composite anode) placed along the axis of the outer metallic parabolic reector (cathode). The pulsed high voltage applied to the composite electrode is provided by a pulse power supply that consists of a 0.8 μF capacitor charged up to 30 kV and a triggered spark gap. The focal point of the reflector is situated in the second part of the generator, which is filled by a tap water.

Design of the composite electrode allows simultaneous generation of a large number of filamentary discharge channels in water, which are distributed almost homogeneously along the whole surface of the electrode at a moderated applied voltage (20-30 kV) [5]. Every discharge channel creates a semi-spherical pressure wave, and by superposition of all of the waves a cylindrical pressure wave propagating from the anode is formed. The primary cylindrical pressure wave is focused by a reflector and it is transformed into a strong shock wave near the focus [3, 4].

V. Stelmashuk · P. Lukes · P. Hoffer
Institute of Plasma Physics AS CR, Za Slovankou 1782/3 182 00 Prague 8 Czech Republic

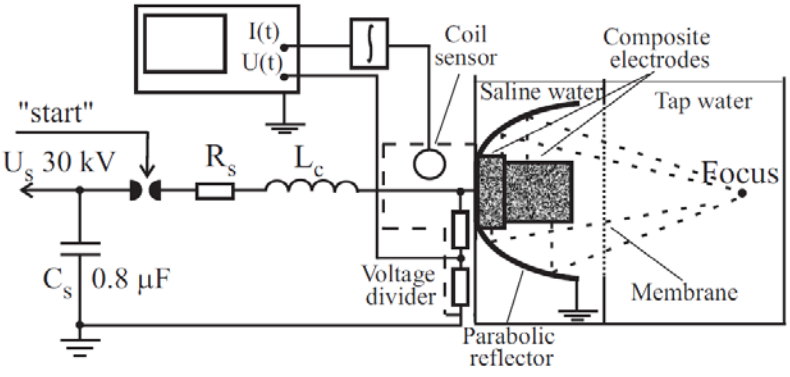

Fig. 1 Experimental setup

A special sensor assembly (Fig. 1) was constructed for measuring high voltage and current directly on the electrode. It is designed to withstand high voltage breakdown and is compatible with high voltage (HV) cable RG58A utilised in our laboratory. An induction coil sensor based on Faradays law followed by a passive integrator is a suitable solution for current pulse measurements. Three windings of the coil were made of RG174 coax cable with shield interruption for the screening against the electric field. The coil is mounted in the middle of the 25 cm long copper tube with a diameter of 10 cm and is followed by the passive integrator [6]. This sensor system was calibrated using Pierson probe.

The temporal waveforms of the focused shock waves were measured by polyvinilidene fluoride (PVDF) shock gauges model S25TCB, produced by a French company PIEZOTECH S.A. and Muller-Platte Needle Probe produced by Mueller Instruments. Both sensors are based on the same principle of the generation of electric signal on piezo element under changing pressure.

2 Experimental Results

The measurements of shock waves generated by the discharge on composite electrode were performed in our laboratory. The results of these measurements by PVDF sensors at different water conductivity can be seen in Figure 2. Measurements were made along the major axis of the reflector at different distance from the focus. As well as the well-known pressure distributions in the focus region, this plot illustrates the fact that the shock wave amplitude has non-linear dependence on water conductivity. The focus profile reveals maximum shock wave amplitude at water conductivity 18 mS/cm ÷ 19mS/cm. Further increase of conductivity from 18 mS/cm up to 36.5 mS/cm leads to the decrease of the shock wave pressure. The lower curve in Fig.2 shows that the shock wave generated at 15 mS/cm possesses minimum acoustical energy, in comparison with other measurements.

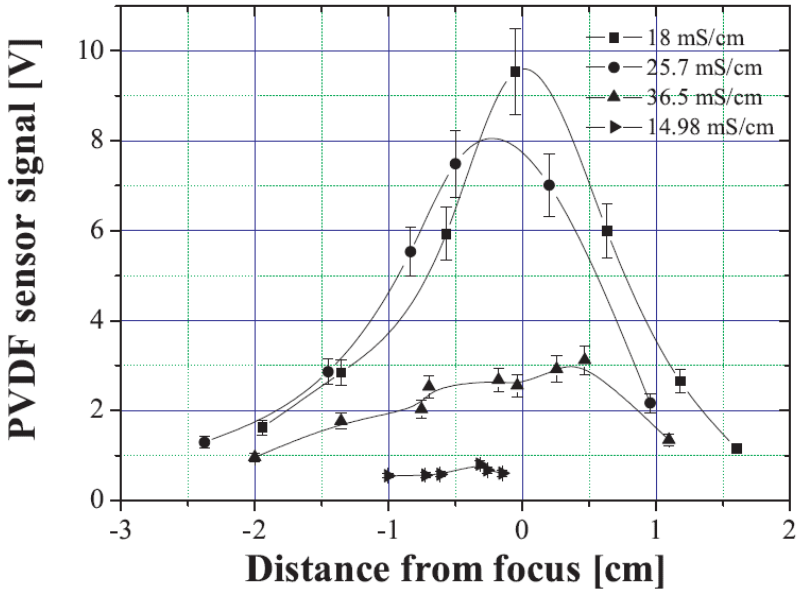

Fig. 2 The effect of solution conductivity on the energy injected to the discharge.

In an attempt to understand the effect of water conductivity on acoustical energy of shock wave, the voltage-current measurements of the electrical discharge on composite electrode were performed. The obtained voltage-current temporal waveforms vary at different water conductivities. As an example, voltage and current traces at 15 mS/cm and 39 mS/cm are presented in Fig.3. It should be noted that negative part of current trace grows with water conductivity. This fact points to the increase of the impedance mismatch between power source and electrode-reflector system. As a result, the part of the energy delivered to the electrode from the source reflects back. This reflections increase with the increase of water conductivity.

The instantaneous power delivered to the discharge is given by multiplication of instantaneous current by instantaneous voltage. The time integral of power gives the total energy injected into the discharge. Performing calculations by using the data obtained from our experiments, we received the plot presented in Fig.4. One can conclude from Fig.4, the increase of water conductivity leads to the monotonic decrease of electric energy delivered to the electrode-reflector system. Approximately 25 % of electrical energy delivered to the discharge is spent on the acoustical energy of streamers expansion [7]. Therefore, the acoustical energy of the shock wave in the focus must decrease with water conductivity. This is clearly visible for water conductivities 18 mS/cm ÷ 39 mS/cm, as shown in Fig.3.

The Fig. 3 contains the focus profile with anomaly low pressure amplitudes. In spite of the fact that the maximum electrical energy injected to the discharge was at water conductivity 15 mS/cm, the acoustical energy is minimal. We think that the

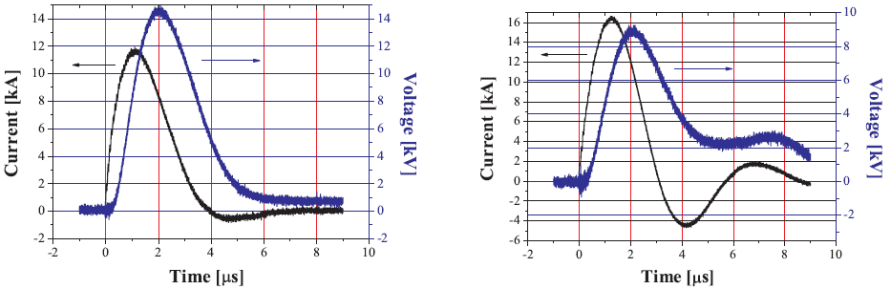

Fig. 3 Voltage-current temporal waveforms measured for water conductivity, left: 16.0 mS/cm, right: 39.0 mS/cm.

explanation of this contradiction is to be found in the characteristics of the streamer expansion. As noted by Joshi at all [8] in their comprehensive review, exchange of energy and momentum between the streamers and surrounding liquid is a complex process determined by the plasma composition, streamer conductivity and self-consistent electric field updates. From this review we want to highlight three major factors determining streamer expansion: the dependence of streamer growth on the rate of field ionisation which has an exponential dependence on the local electric field; the filamentary brunching of streamers and the generation of shock waves non-perpendicular to the electrode surface; the streamer expansion in the radial direction.

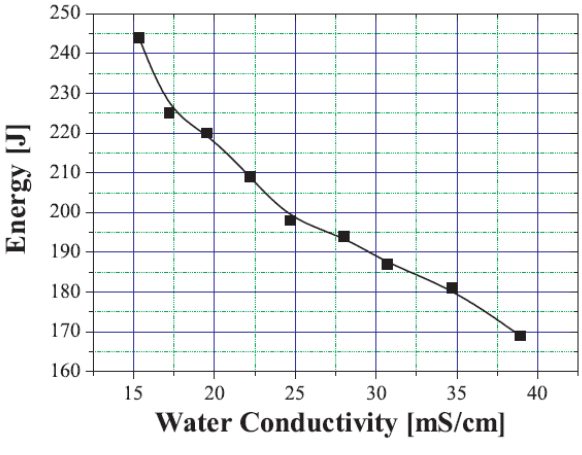

Fig. 4 The effect of solution conductivity on the energy injected to the discharge.

We can only suppose that in accordance with Joshi at all [8], these processes can be advanced or expelled, depending on water conductivity during discharge on composite electrode. Precise measurements of streamer speed and observation of

their shape are not possible in the experimental setup available. Special apparatus to be utilised for such studies is being constructed at present.

3 Conclusion

The amplitudes of shock wave in the focus region were measured at different water conductivities. The combined effects of electrical energy injected to the discharge and characteristics of the streamer propagation result in non linear character of the dependence of amplitude of focused shock wave versus water conductivity. The water conductivity affects the impedance of the electrode-reflector system thereby influences the energy delivered to the discharge. Unusually low energy of shock wave generated at water conductivity 15 mS/cm can be explained by the characteristics of the growth speed of the streamer and its specific shape.

Acknowledgement. This work was supported by the Czech Science Foundation under the contract No. 202/09/1151.

References

1. Kolacek, K., Babicky, V., Preinhaelter, J., Sunka, P., Benes, J.: Pressure distribution measurements at the shock wave focus in water by schlieren photography. J. Phys. D 21(3), 463–469 (1988)
2. Sunka, P., Babicky, V., Clupek, M., Stuka, C.: New Discharge Circuit for Efficient Shock Wave Generation. In: Brun, R., Dumitrescu, Z. (eds.) Shock Waves, Marseille III, pp. 455–458. Springer, Berlin (1995)
3. Sunka, P., Stelmashuk, V., Babicky, V., Clupek, M., Benes, J., Pouckova, P., Kaspar, J., Bodnar, M.: IEEE Trans. on Plasma Sci. 34(4), 1382–1385 (2006)
4. Stelmashuk, V., Sunka, P.: Mutual interaction of two shock waves with a different time delay. J. Phys. D 56(2), B396–B400 (2006)
5. Lukes, P., Clupek, M., Babicky, V., Sunka, P.: Pulsed electrical discharge in water generated using porous-ceramic-coated electrodes. IEEE Trans. on Plasma Sci. 36(4), 1146–1147 (2008)
6. van Deursen, A.P.J., Stelmashuk, V.: Integrator test report, ILDAS-WP3-021, Netherlands (2008)
7. Naugolnykh, K.A., Roy, N.A.: Electric Discharge in water, Moscow, Nauka, pp. 46–72 (1971)
8. Josh, R.P., Kolb, J.F., Xiao, S., Schoenbach, K.H.: Aspects of Plasma in Water: Streamer Physics and Applications. Plasma Process. Polym. 11(6), 763–777 (2009)

Sonic Line and Stand–Off Distance on Re–entry Capsule Shapes

Hans G. Hornung, Jan Martinez Schramm, and Klaus Hannemann

1 Introduction

In hypersonic flow over a sphere, the shock wave stand–off distance is related to the density ratio by

$$\Delta/r = 0.78\,\rho_\infty/\overline{\rho},$$

where Δ is the stand–off distance, r is the sphere radius, ρ_∞ is the free–stream density and $\overline{\rho}$ is the average density along the stagnation streamline, see *e. g.*, Hornung [1]. For a sharp cone of a given angle, the stand–off distance increases linearly with $\rho_\infty/\overline{\rho}$ from a critical onset point and is scaled by the base radius R of the cone, see *e. g.*, Leyva [2]. For a spherically blunted cone, one may therefore expect a transition to occur between sphere behavior and sharp cone behavior. This would be undesirable for stability and heat–flux reasons. A possibly more benign shape is an oblate ellipsoid, as suggested by Brown [5]. We study features of such flows on the basis of perfect–gas computations. Since the density ratio is very sensitive to reaction rate in flows with vibrational and chemical relaxation, these phenomena are very important in entry of vehicles into atmospheres such as that of Mars. The computations are therefore extended to include the effects of reacting CO_2 flows.

2 Theoretical Considerations

The sketches of Fig. 1 illustrate the features of the flows of interest here. When the angle of a sharp cone in a steady supersonic flow is increased, there comes a point at which a sonic line appears at the surface of the cone. As the angle is increased further, the sonic line moves toward the shock wave, and reaches it at the point of shock detachment. Further increase of the cone angle causes the shock to detach

Hans G. Hornung
GALCIT, Caltech, 1200 E. California Blvd, Pasadena, CA91125, USA

Jan Martinez Schramm · Klaus Hannemann
DLR–AS/RF, 37073 Göttingen, Bunsenstr. 10, Germany

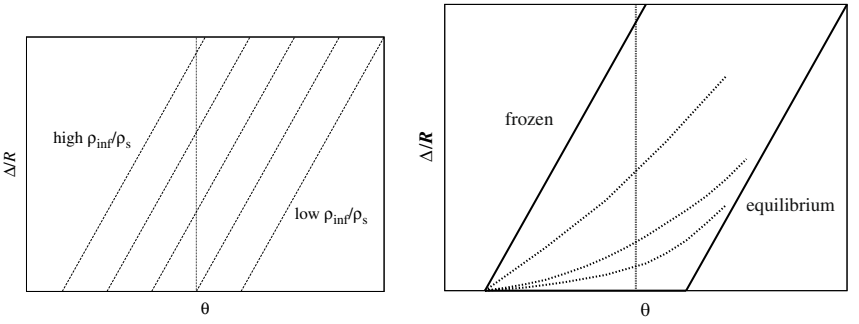

Fig. 1 Sketches of the behavior of the shock standoff distance on a sharp cone. Left: frozen flow. Right: reacting flow. On the left, if, in a flow with a particular density ratio (particular γ), the shock angle is increased, there comes a point where the angle reaches the detachment angle, *i. e.*, the point where the oblique line for that γ intersects the θ axis. Further increase in θ causes Δ/R to increase along the oblique line. For a cone of a particular angle, a change of density ratio causes Δ/R to follow the vertical line. On the right, for reacting flow, changing the density ratio from very large to very small causes the curves to change from the straight oblique line for frozen flow to the straight oblique line for equilibrium flow. For intermediate values of the density ratio all the curves emanate from the frozen detachment point, see Leyva [2]. For a fixed angle, changing the density ratio therefore causes the stand-off distance to behave differently in reacting flow.

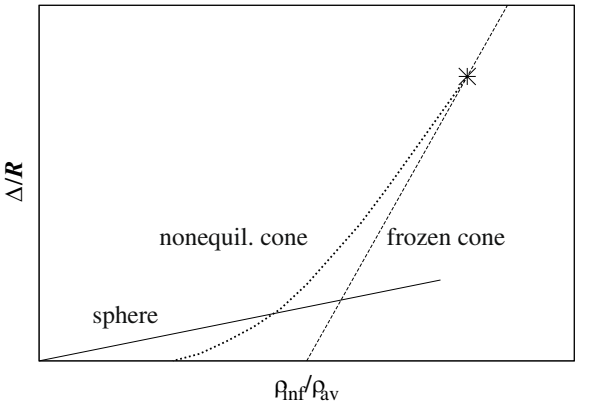

Fig. 2 Sketch of expected behavior of the stand–off distance on a spherically blunted cone of a particular angle with density ratio. The consequence of the features described in the sketches of Fig. 1 is that the stand-off distance at small density ratios follows the line for the sphere in both frozen and reacting flow. However the transition to the sharp cone behavior is different. In the frozen case, the transition occurs fairly abruptly at the point where the sharp–cone line intersects the sphere line. In reacting flow the transition is more gradual, because the sharp–cone line leaves the density ratio axis at a smaller detachment angle.

by a distance which increases linearly with further shock angle increase. This is illustrated in the left part of Fig. 1 corresponding to perfect–gas or frozen flow. For decreasing values of ρ_∞/ρ_s the detachment angle increases.

The situation is different for reacting flow. This is illustrated by the sketch on the right of Fig. 1. Here the detachment angle for frozen flow is significantly smaller than that for equilibrium flow. In each of these limits, Δ/R increases linearly with further increase of cone angle. However, at intermediate values of the density ratio, where nonequilibrium effects apply, all the curves for different density ratios emanate from the frozen detachment point. This was shown by the extensive experiments and computations of Leyva [2].

The difference between the behaviors of the sharp–cone detachment process in perfect–gas and in reacting flows as illustrated by the sketches of Fig. 1 now permits us to construct an expected behavior of the detachment process on a spherically blunted cone. This is illustrated in the sketch of Fig. 2.

In the following we aim to test these theoretical considerations by performing numerical computations of the relevant flows. In addition, we test the feasibility of using an oblate ellipsoid to avoid the relatively sudden transition from sphere behavior to sharp cone behavior that is typical of the spherically blunted cone.

3 Computational Method

The perfect gas computations were made with the Euler code formulation within the computational system Amrita written by Quirk [3]. A kappa-MUSCL scheme was used with HLLE reconstruction and a coarse Cartesian 400×500 grid with adaptive mesh refinement of one level by a factor of 3. The body was inserted by a level set.

The reacting flow computations were performed with the hybrid structured–unstructured grid DLR-Navier-Stokes solver TAU which has been validated for a wide range of steady and unsteady sub- trans- and hypersonic flow cases, see Schwamborn et al. [4]. For the present investigation an AUSMDV flux vector splitting scheme is used with HLLE gradient reconstruction. The gas is considered to be a reacting mixture of thermally perfect gases. Equilibrium properties are calculated from partition functions or look–up tables. Modified Arrhenius reactions model the forward reactions and the vibrational equilibrium and rate equations use the Landau–Teller and Millikan–White models. While TAU is designed for viscous flow with heat and species diffusion, inviscid, non-conducting flow is assumed for the present calculations.

4 Results of Computations

The results of Euler computations of flows over blunted cones shown in Figs. 3 and 4 nicely confirm the behavior expected from the sketch of Fig. 2. A brief discussion of the behavior of the sonic line on blunted cones may also be found in [6].

Brown [5] showed that an oblate ellipsoid is a better reentry shape than the blunted cone, or, for that matter, the Apollo shape. The latter two suffer from the

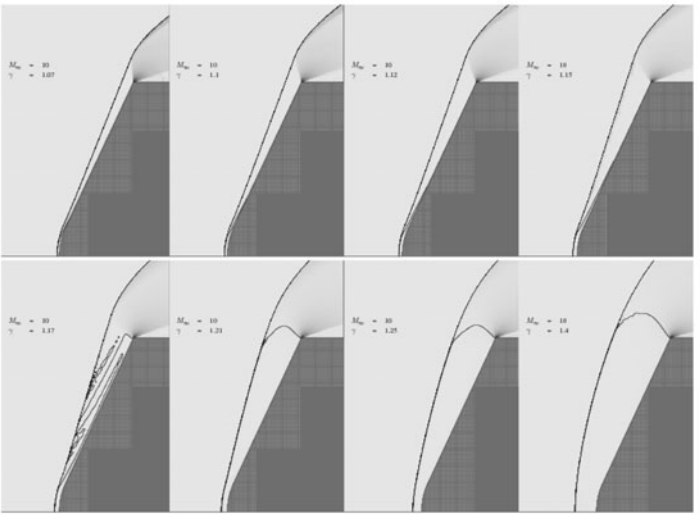

Fig. 3 Euler computations of perfect–gas flow over a spherically blunted 65° cone with different specific heat ratios ranging from 1.07 to 1.4. Note how the sonic line terminates at the junction of the sphere and cone for γ close to 1 (or small ρ_∞/ρ_s, top half of figure) so that the stand–off distance follows the sphere behavior, until the density ratio reaches a value at which even the sharp cone would exhibit a detached shock.

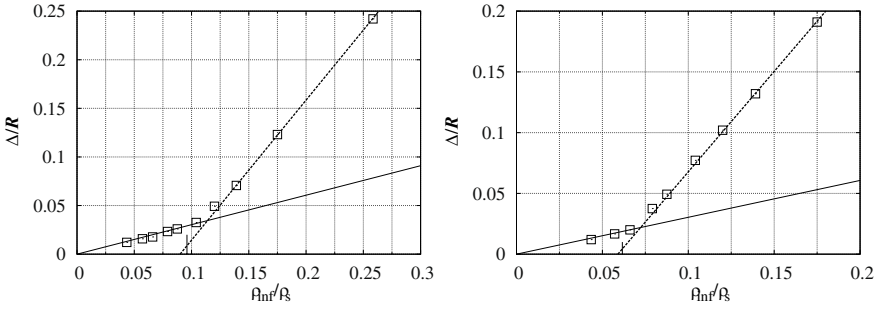

Fig. 4 Left: Results of computation of frozen flow over a 65° spherically blunted cone, showing that the behavior is indeed as discussed in the sketches. The short vertical line indicates the theoretical detachment value of the density ratio. Right: Same as left, but for a 70° cone.

fact that the heat flux at the high–curvature shoulder is high, which is avoided by the smooth change of curvature of the ellipsoid. In gases where a very high density ratio occurs across a normal shock wave, the blunted cone exhibits the undesirable abrupt change from sphere to sharp–cone behavior discussed in the previous section. To show that the ellipsoid also avoids this difficulty, we present ellipsoid computations in Fig. 5. Also, Fig 6 (left) shows the stand–off density ratio graph, in which a very smooth transition away from the sphere–behavior is exhibited.

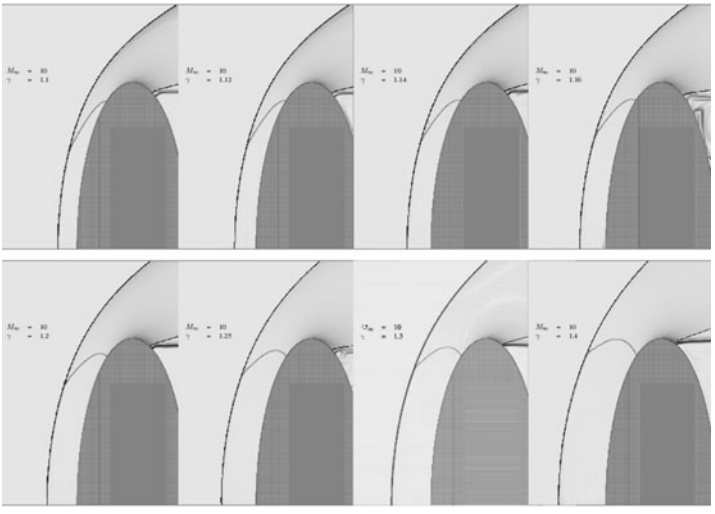

Fig. 5 Euler computations of perfect–gas flow over a 3:1 oblate ellipsoid with different specific heat ratios. For this body the sonic line moves smoothly from the sphere behavior for γ close to 1 to the situation in which it terminates on the body shoulder as γ increases. Accordingly, the stand–off distance also increases smoothly, see Fig. 6.

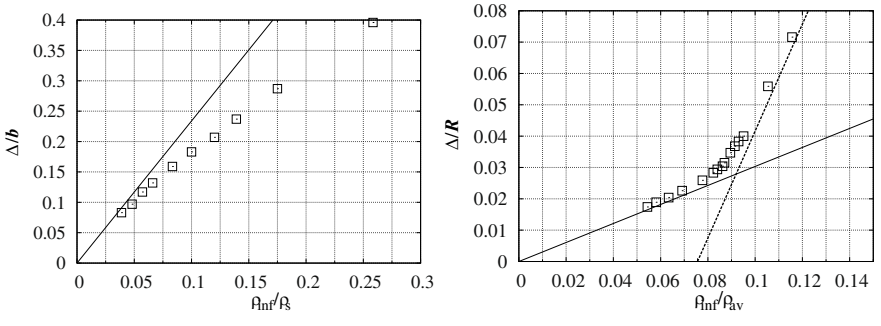

Fig. 6 LEFT: Results of computation of perfect–gas flow over a 3:1 oblate ellipsoid, showing that the stand–off distance increases smoothly away from the straight line for the sphere as the density ratio is increased. RIGHT: Results of computations of reacting CO_2 flow over a spherically blunted 68° cone, showing that the stand–off distance follows sphere behavior at small density ratios and departs to the cone behavior earlier and less abruptly than the perfect gas line, just like the curve labeled "nonequil. cone" in the sketch of Fig. 2.

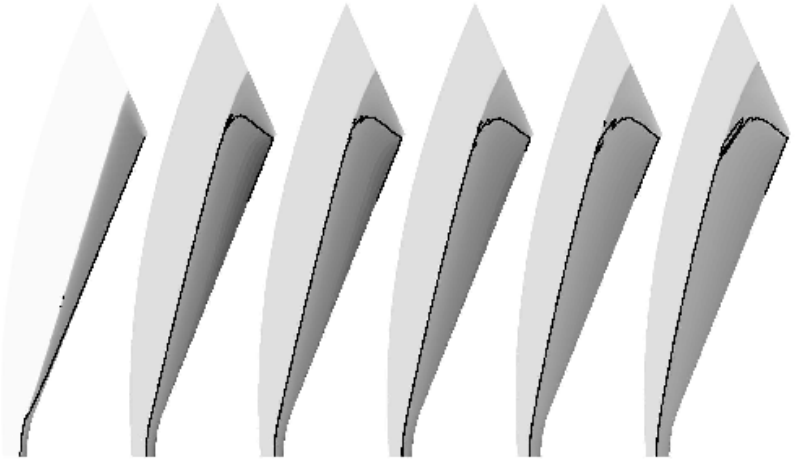

Fig. 7 Reacting CO_2 flow over a spherically blunted 68° cone. Left to right, increasing $\rho_\infty/\overline{\rho}$. The leftmost case exhibits sphere behavior, while the sonic line terminates at the cone shoulder in the other cases.

5 Conclusions

Theoretical arguments about the behavior of the stand–off distance on various reentry shapes lead to the expectation that changing the density ratio leads to a dramatic change of behavior in the case of the spherically blunted cone. A difference in this transition between perfect–gas and reacting CO_2 flow is predicted. Computation of perfect–gas and reacting CO_2 flows confirm these arguments nicely. Choosing an oblate ellipsoid as first suggested by Brown [5] avoids the dramatic change that occurs on the spherically blunted cone and should also be desirable from the point of view of heat flux distribution.

References

1. Hornung, H.G.: Nonequilibrium dissociating flow over spheres and circular cylinders. J. Fluid Mech. 64, 725–736 (1972)
2. Leyva, I.A.: Shock detachment from a cone in reacting flow. In: Ball, G.J., Hillier, R., Roberts, G.T. (eds.) Proceedings of the 22nd International Symposium on Shock Waves, Southampton University Media (2000)
3. Quirk, J.J.: Amrita–A computational facility (for CFD modelling) VKI 29th CFD Lecture Series (1998), ISSN 0377-8312, http://www.amrita-ebook.org

4. Schwamborn, D., Gerhold, T., Heinrich, R.: The DLR TAU Code: Recent Applications in Research and Industry. In: Proceedings of the European Conference on Computational Fluid Dynamics ECCOMAS CFD (2006), http://tau.dlr.de
5. Brown, J.L.: The Effect of Forebody Geometry on Turbulent Heating and Thermal Protections System Sizing for Future Mars Mission Concepts. In: 4th Interplanetary Planetary Probe Workshop (IPPW4), Pasadena, CA (June 2006)
6. Krasil'nikov, A.V., Nikulin, A.N., Kholodov, A.S.: Some features of flow over spherically blunted cones of large vertex angles. Izvestiya Akademii Nauk SSSR, Mekhanika Zhidkosti i Gaza (2), 179–181 (1975)

Numerical and Experimental Investigation of the Effect of Bypass Mass Flow Due to Small Gaps in a Transonic Channel Flow

M. Giglmaier, J.F. Quaatz, T. Gawehn, A. Gülhan, and N.A. Adams

1 Introduction

Within the joint project PAK 75 (Deutsche Forschungsgesellschaft DFG), a novel process for the production of gas phase synthesized particles is developed. The key features of the process are shock induced precursor combustion, homogeneous particle growth at constant thermodynamic conditions and gas dynamic nozzle quenching within a double choked Laval nozzle system (fig. 1) [1] [2].

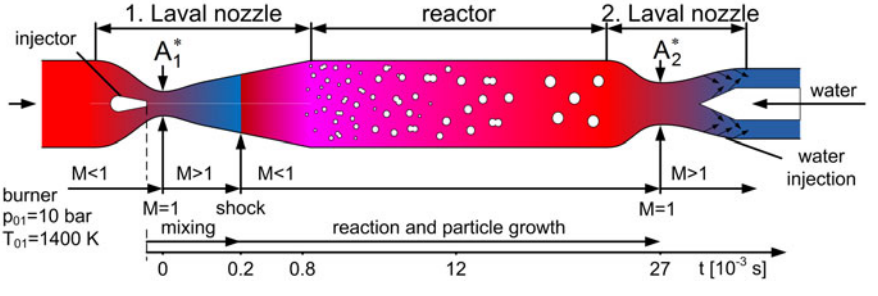

Fig. 1 Schematic of the new process of gasdynamically induced particle production

In order to guarantee a homogeneous mixture of the precursor with the carrier gas, a certain mixing length is needed. For this purpose, a low static temperature is necessary to suppress a pre-reaction of the precursor. This is achieved by accelerating the flow to supersonic speed. The required mixing length results in the

M. Giglmaier · J.F. Quaatz · N.A. Adams
Lehrstuhl für Aerodynamik und Strömungsmechanik, Technische Universität München
Boltzmannstrasse 15, 85748 Garching, Germany

T. Gawehn · A. Gülhan
Institute of Aerodynamics and Flow Technology, Supersonic and Hypersonic Technology Department, German Aerospace Center (DLR), Linder Höhe, 51147 Cologne, Germany

development of the boundary layers that reach a maximum thickness of 15% of the channel height at the desired shock position. The shock boundary layer interaction within the channel leads to the formation of a series of oblique shocks and rarefaction waves, a so-called pseudo-shock system. Thereby, the heating rate across the shock system is decreased, recirculation zones are formed and inhomogeneous flow conditions downstream the shock system reduce the homogeneity of the particle growth. Previous investigations within the project already improved the understanding of the dominating effects on the shock structure [3], shock asymmetry and unsteady behaviour [4], active and passive shock stabilisation and the turbulent flow characteristics shortly downstream of the shock system [5]. Pseudo-shock systems are investigated by other groups as well, a detailed review of the topic is given by [6]. Various measurement and visualisation techniques (e.g. Schlieren visualisation, LDV, PIV, LIF) require optical access to the flow. Commonly, quartz glass windows are mounted on the side walls of the test section. However, to avoid strong stresses within the glass, these windows should not be flush mounted to the facility. Thus, small gaps of $\Delta z = O(10^{-4})\ m$ can occur between the glass side walls and the metal contour. During our previous investigations we observed that these gaps result in a small bypass mass flow. Especially at high pressure gradients (e.g. shocks and critical cross sections), this mass flow results in a significant drift of the measurements. The focus of the present study is a detailed numerical analysis of the flow within the gaps and its feedback on the transonic main flow within the slender nozzle.

2 Experimental and Numerical Set-Up

To investigate occurrence and shape, as well as the dominating mechanisms of pseudo-shock systems for a certain range of operating conditions and nozzle geometries, a test rig with optical access is build up at the DLR in Cologne.

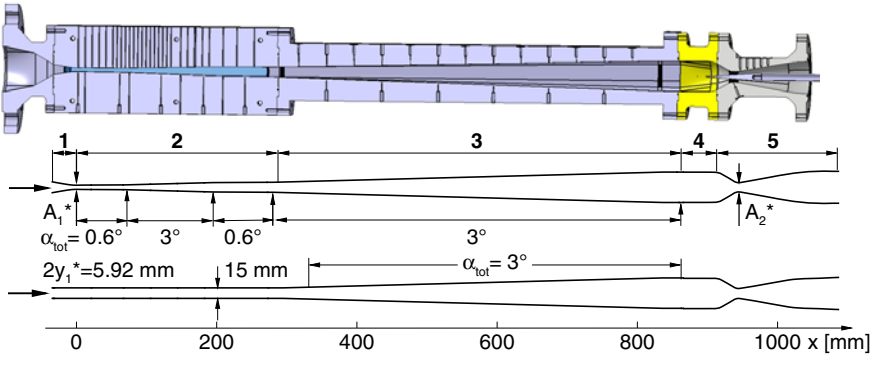

Fig. 2 Geometry of the test rig in Cologne

Similar to the previously described particle reactor, the test rig consists of a double choked Laval nozzle system (fig. 2). The primary nozzle (1, 2) is equipped with parallel quartz glass side walls in order to perform Schlieren imaging. To record the wall pressure distribution, the upper and lower contour inliners are equipped with 28 pressure sensors. The flow is further decelerated in the double divergent reactor part (3, 4). A slender movable cone within the second Laval nozzle (5) defines the area of the second critical cross section. For constant adiabatic mass flow, the ratio of the critical cross sections A_1^*/A_2^* is proportional to the inverse ratio of the stagnation pressure. The reduction of the stagnation pressure is caused by shock-losses and by friction. However, shock-losses can be reduced by decreasing the area of the second critical cross section. As a result, the pseudo-shock system moves upstream and re-establishes at a lower pre-shock Mach number. The influence of different nozzle shapes is investigated by two interchangeable contour inliners (fig. 3a) within the first Laval nozzle. The gap flow is analysed for three experimental set-ups. Reference data is obtained with approximately zero gap width by using flush mounted metal side walls. Two gap sizes of 0.1 mm and 0.2 mm are investigated with quartz glass side walls mounted on both sides of the nozzle (fig. 3b).

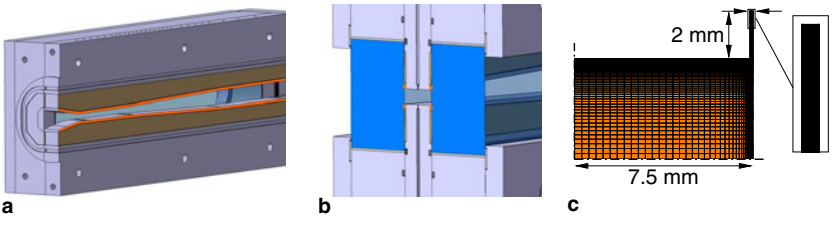

Fig. 3 a) Primary nozzle with contour inliners b) cut view through x=0 c) mesh at x=0

For the computation of the flow, the commercial pressure-based solver Ansys CFX is used. The governing equations are the 3-D time dependent Favre-averaged Navier-Stokes equations for compressible flow. By applying an explicit algebraic Reynolds stress turbulence model (EARSM) the occurrence of secondary flow, such as corner vortices in the square cross section of the reactor, is resolved. The computational effort is significantly reduced by assuming symmetry boundary conditions in order to model only one quarter of the flow field. Furthermore, the second Laval nozzle is not considered but a suitable boundary condition is used instead. Grid studies showed that $4.1 \cdot 10^6$ finite volumes (hexahedrons) provide sufficient resolution to resolve even delicate 3-D flow details arising within the channel with zero gap width. The boundary layers are resolved by at least 20 finite volumes in wall-normal direction, resulting in a dimensionless wall distance of $y^+ \leq 1$. For the computation of the gap flow, two additional grids are employed. The cross sections of the gaps along the primary nozzle (fig. 2, 1 and 2) are 2 mm x 0.1 mm and 2 mm x 0.2 mm. The 0.1 mm gap is discretised with $1.7 \cdot 10^5$ additional finite volumes, the 0.2 mm

gap with additional $2.9 \cdot 10^6$ finite volumes. A planar cut of the mesh at the critical cross section is shown in fig. 3c.

3 Experimental and Numerical Results

In the present study, a numerical analysis of the main effects of the gap flow is performed by investigating one characteristic operating point in detail.

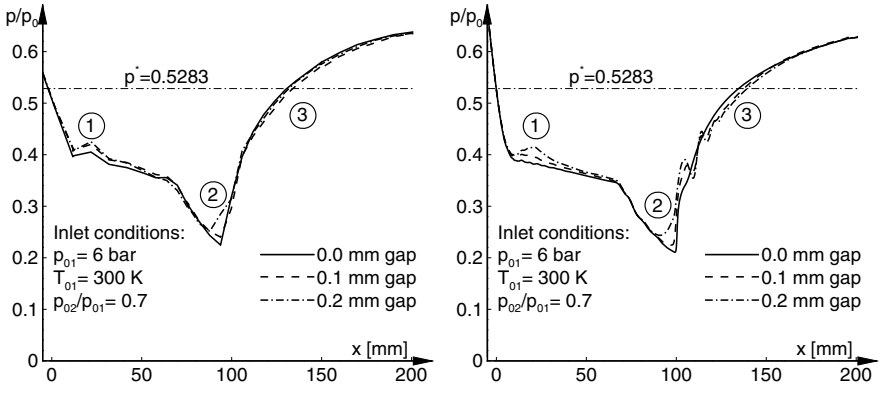

Fig. 4 Experimental (left) and numerical (right) pressure distribution along the upper nozzle wall

Figure 4 shows the experimental (left) and numerical (right) dimensionless pressure distributions along the upper wall of the primary nozzle. The critical cross section is located at $x = 0$ *mm*, the inlet conditions are $p_{01} = 6$ *bar*, $T_{01} = 300$ *K*, and a total pressure ratio of $p_{01}/p_{02} = 0.70$ is applied. Discrete measurement points are connected by line segments. The solid line represents the pressure distribution for the flow without gaps, the dashed line and the dash-dotted line indicate the pressure distributions corresponding to a gap width of 0.1 mm and 0.2 mm. The experiment shows three reproducible differences between the flow with approximately zero gap and the flows with gaps:

① The pressure directly downstream of the critical cross section increases due to the gap flow and shows a local peak at $x = 22$ *mm*.
② The pressure significantly increases ahead of the pseudo-shock system.
③ The pressure in the region of the pseudo-shock system in the case of the gap flow is slightly decreased.

One difference between the numerical results and the measurements is that the simulation without gap does not produce a local pressure peak at $x = 22$ *mm*. Since the overall tendency is clearly reproduced as soon as the gap flow is taken into account we assume that even for this configuration the experiment was not perfectly sealed. An obvious reason for the occurrence of the pressure peak can be found by

investigating the flow through the gap. Figure 5 shows the Mach number distribution together with representative streamlines on a cut plane through the middle of the gap. Since the maximum mass flow density is reached at $M = 1$, the flow is forced to enter the gap in the subsonic region slightly upstream of the critical cross section. It re-enters into the shear flow of the supersonic part downstream of the critical cross section, where mass addition leads to a deceleration of the flow and to an increase of the pressure. This mechanism is comparable to heat addition or to a reduction of the cross section in supersonic flows.

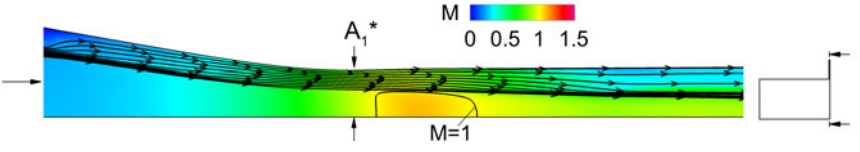

Fig. 5 Mach number distribution at a slice through the gap. Streamlines indicate the flow direction.

A significant impact of the bypass flow on the main flow can be seen by investigating the structure of the pseudo-shock system. Figure 6a) shows a simulation of the flow without gaps. The yellow iso-surface of Mach number $M = 1$ shows the supersonic flow while recirculation zones are indicated in blue (iso-surface $u = -0.01\ m/s$). One observes oblique shocks originating from all side walls at the same x-position. Recirculation zones shift the pseudo-shock system towards the centre of the channel. Figure 6b) shows the influence of the gap flow onto the shock system. In this case, the high positive pressure gradient across the shock leads to a massive reverse flow through the gaps. Therefore, the first oblique shocks are induced by a predominant corner separation and the entire pseudo-shock system is deformed. In particular, these shocks are responsible for the pre-compression observed at position ②.

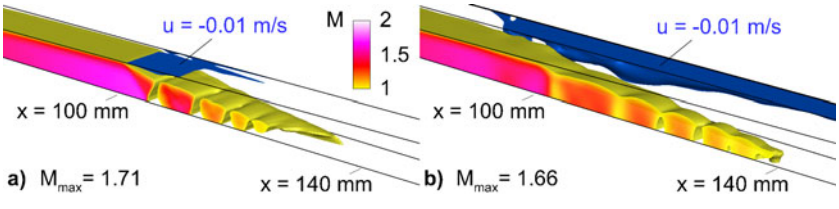

Fig. 6 Comparison of the shock system without and with gap, the yellow iso-surface with M=1 covers the supersonic flow, the blue iso-surface with u=-0.01 m/s covers the recirculation zones

This effect becomes more obvious by comparing the flow at different x-positions. The left slice in fig. 7 depicts the Mach number distribution at $x = 90\ mm$. The bypass mass flow from the gap re-enters the main flow and causes an oblique shock

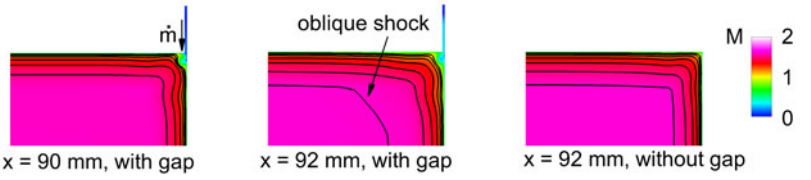

Fig. 7 Mach number distribution at different x-positions for the flow with and without gap

that can be seen at the second slice with $x = 92\ mm$. In contrast, the third slice with the same x-position for the flow without gap shows a homogeneous core flow.

Another effect of the bypass flow is that the supersonic part of the shock system remains much closer to the side walls due to the suppressed separation of the entire boundary layer. This explains the numerically predicted pressure oscillations between ② and ③, which can not be resolved by the measurement. Furthermore, the displacement thickness of the corner separation increases the velocity of the core flow. Consequently, the static pressure in the pseudo-shock system and the following mixing zone (position ③) is decreased.

4 Conclusions

Our numerical investigations demonstrated that small experimental uncertainties of the facility (gap width) may result in significantly altered flow physics. For a comparison of experimental and numerical results a detailed specification of all possible uncertainties seems inevitable in case of sensitive transonic flows. Heat deformation, potential gaps and surface roughness are the predominant effects.

References

1. Grzona, A., et al.: Gas-Phase Synthesis of Non-Agglomerated Nanoparticles by Fast Gasdynamic Heating and Cooling. Shock Waves 11, 4 (2009)
2. Giglmaier, M., Al-Hasan, N.S., Adams, N.A.: 3-D Simulation of the Production of Gas-phase synthesized Non-aggregated Spherical Nano-particles in Continuous Gasdynamic Flow Particle-Laden Flows. In: Proceedings of 7th International Conference on Multiphase Flow - ICMF 2010, VID00264 (2010)
3. Gawehn, T., Gülhan, A., Al-Hasan, N.S., Schnerr, G.H.: Experimental and Numerical Analysis of the Structure of Pseudo-Shock Systems in Laval Nozzles with Parallel Side Walls. Shock Waves 20, 4 (2010)
4. Gawehn, T., Gülhan, A., Giglmaier, M., Al-Hasan, N.S., Adams, N.A.: Analysis of Pseudo-Shock System Structure and Asymmetry in Laval Nozzles with Parallel Side Walls. In: 19th Interantional Shock Interaction Symposium, Moscow (2010)
5. Grzona, A., Olivier, H.: Shock train generated turbulence inside a nozzle with a small opening angle. Experiments in Fluids (2011)
6. Matsuo, K., Miyazato, Y., Kim, H.-D.: Shock train and pseudo-shock phenomena in internal gas flows. Progress in Aerospace Sciences 35, 1 (1999)

Flow behind a Concave Hyperbolic Shock

S. Mölder, E. Timofeev, and G. Emanuel

1 Introduction

In the design of supersonic airplane and air intake shapes, for specific performance, it is useful to begin with a known shock wave shape and flow-field and deduce the required wall shapes – design methods referred to as "wave rider" or "wave trapper". Questions then arise as to the nature and existence of flow behind a given shock shape. The left lobe of a hyperbola of revolution shape is proposed as a particular example of a doubly curved, concave axisymmetric shock surface. It offers an analytically simple surface for the study of pressure gradient and flow curvature effects on shock detachment and reflection where the cumulative effects of both shock curvatures are present. Such shock shapes are physically plausible for internal, converging flow and Mach disk shapes. In this paper the concave, hyperbolically shaped shock in both planar and axial flow is investigated analytically with oblique shock theory as well as curved shock theory to discover any tendency towards the formation of a shock wave in the flow immediately behind the hyperbolic shock. If such a shock appears, and impinges on the back of the shock, then there would have to be a kink in the originally posed smooth shock and a Mach interaction would ensue. The onset of Mach interaction, at the sonic point is shown to depend on the freestream Mach number and the ratio of shock curvatures. Critical roles are attributed to both the subsonic patch of flow behind the strong portion of the shock and the orientation of the sonic surface at the shock. There is much experimental evidence of the existence of strong concave shock waves in the studies of Mach reflection where such shocks constitute the Mach stem. No experimental or CFD examples of continuously curved concave shocks that span both the weak and strong shock range have been found; probably because the enclosing ducts have to have very special shapes. Such surface shapes (both planar and axial) are suggested here.

S. Mölder · E. Timofeev
Department of Mechanical Engineering, McGill University, Montreal,
Quebec H3A2K6, Canada

G. Emanuel
Department of Mechanical and Aerospace Engineering,
University of Texas at Arlington, Arlington, Texas 76019-0018, USA

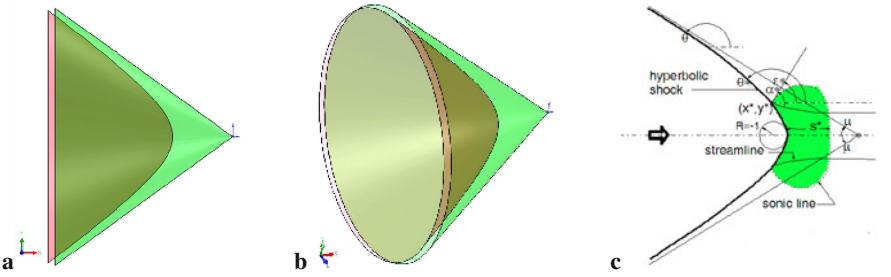

Fig. 1 Hyperbolic shock and subsonic patch

2 Geometry of the Concave Hyperbolic Shock

In Fig. 1a,b, the hyperbolic shock is shown as a purple surface. Its enveloping Mach cone is in green. In Cartesian coordinates the equation of a hyperbola of revolution, that has two lobes lying on the positive and negative x-axis, is,

$$x^2/a^2 - y^2/b^2 = 1\ . \tag{1}$$

The left lobe, which presents a concave surface to the left, towards the oncoming flow, has a shape that can be found from, $x = -a\sqrt{1+y^2/b^2}$. Setting $a = M_1^2 - 1$ and $b = \sqrt{M_1^2 - 1}$ makes the far-out branches of the hyperbola asymptotic to the freestream Mach waves and the radius of curvature of the hyperbola at the horizontal axis equal -1 (see Fig. 1c). Each freestream Mach number, M_1, thus has a unique shock shape with the common radius of curvature -1 at the axis and with its extremities asymptotic to the Mach waves. Such a shock shape, for Mach 1.7, is shown in Fig. 1c, located inside its Mach cone asymptote. Keeping the radius of curvature constant with Mach number is for convenience; it sets the problem's scale and facilitates comparison between shocks for various Mach numbers on the same plot. For any one Mach number the hyperbolic shock contains all possible shock angles for that Mach number, from normal shock to Mach wave. The slope of the hyperbolic shock, at any point (x,y) on the hyperbola is, from Eq. (1), $\mathrm{d}y/\mathrm{d}x = \tan\theta = n(x/y)$, where $n = b^2/a^2 = 1/(M_1^2 - 1) = \tan^2\mu$ and θ is the shock angle (obtuse in second quadrant), so that the left-lobe shock curvature is,

$$S_a = \frac{\mathrm{d}^2y/\mathrm{d}x^2}{\left[1+\left(\mathrm{d}y/\mathrm{d}x\right)^2\right]^{3/2}} = \frac{n[1-n(x^2/y^2)]}{y[1+n^2(x^2/y^2)]^{3/2}} = \frac{\tan^2\mu - \tan^2\theta}{y(1+\tan^2\theta)^{3/2}}\ . \tag{2}$$

This formulation for S_a matches our definition of shock curvature in the flow plane[1] $S_a = d\theta/d\sigma$. Flow-plane shock curvature, S_a, is defined to be positive when the

[1] The *flow plane* is the plane surface that contains the smallest angle between the downshock flow vector and the shock surface; it also contains the upstream flow vector.

shock is concave towards the oncoming flow. The curvature in the flow-normal plane, S_b, and the *ratio of shock curvatures*, S_a/S_b, for obtuse shocks, at any value of shock angle, are,

$$S_b = -\cos\theta/y\,, \qquad \mathscr{R} = \frac{S_a}{S_b} = (1+n)\sin^2\theta - n\,. \tag{3}$$

On the shock surface, $\mathscr{R}$ varies from 0 to 1 as θ varies from μ to $\pi/2$. The shock intercepts the x-axis at $x=-a$ and $y=0$ so that the shock angle there is $\pi/2$ and the ratio of curvatures is 1. The solution for x and y with the shock angle appearing as parameter is $x = a\tan\theta/\sqrt{\tan^2\theta - n}$ and $y = 1/\sqrt{\tan^2\theta - n}$. The (x,y)-location of any significant shock angle, such as the angle for sonic post-shock flow, can then be determined directly using these equations. Positive square roots are taken in both cases resulting in a positive y and a negative x value for the upper-left branch of the hyperbola. The above has shown that, given a Mach number, a hyperbolic shock shape can be calculated and, given any shock angle, locates a point on the shock where the shock's surface curvatures are determinable. All of this applies to planar shocks as well as axial ones. For planar shocks $S_b = 0$ so that $\mathscr{R} \to \infty$.

3 Flow Properties and Streamlines behind a Curved Shock

We now establish relations for flow properties behind the hyperbolic shock. The properties fall into two categories: the 'zeroth order' properties such as pressure, Mach number and the flow deflection angle; these requiring as inputs the ratio of specific heats, the shock angle and the freestream Mach number. The second category, the 'first order' properties, such as pressure gradient, streamline curvature and vorticity, require the previous three inputs plus the shock curvature(s). The zeroth order quantities are obtained from the algebraic Rankine-Hugoniot equations and the first order quantities require the use of the Euler equations. Curved shock theory (CST) for planar flow is derived in [1, 4, 7, 8]. Application of CST to axial flow and shocks with compound curvature is found in [5]. The streamline curvature, D_2, pressure gradient, P_2, [5], and vorticity, Γ_2, [2], behind the hyperbolic shock, are found from the curved shock equations,

$$P_2 = \frac{[BC]}{[AB]}S_a + \frac{B_2G'}{[AB]}S_b;\; D_2 = \frac{[CA]}{[AB]}S_a - \frac{A_2G'}{[AB]}S_b;\; \Gamma_2 = \frac{\rho_2}{\rho_1}\left(1-\frac{\rho_1}{\rho_2}\right)^2\cos\theta\cdot S_a\,, \tag{4}$$

where the coefficients multiplying S_a and S_b are all functions of the freestream Mach number and the shock angle. These equations are general to any doubly curved, axial shock surface. For a given Mach number, the shock geometry, including the shock curvatures are calculated, at selected points, using Eqs. (1) to (3). Oblique shock theory gives the slope, $\tan\delta_2$, of the post-shock streamlines at any point on the shock. The *curved shock theory* equations (4) are then used to find the streamline curvature, D_2, at the selected points, (x_s, y_s), along the shock and the streamline

shape is calculated from a Taylor series approximation $y = y_s + (x - x_s)\tan\delta_2 + 0.5(x - x_s)^2 D_2$, where (x_s, y_s) is the starting point of the streamline, on the shock.

4 Orientation of Sonic Line behind the Shock

The angle α^*, between the sonic line and the streamline is, from Eq. (6.1.1) in [3] and curved shock theory, $\tan\alpha^* = -(\mathrm{d}M/\mathrm{d}s)^*/(\mathrm{d}M/\mathrm{d}n)^* = P_2^*/(D_2^* - \Gamma_2^*)$, where the asterisk indicates that all quantities have been evaluated at the sonic condition. Hayes and Probstein [3] present a formula for α^* for acute shocks in *planar* flow,

$$\tan\alpha^* = \frac{\tan^3(\theta^* - \delta^*)[3(\gamma+1)\tan^2(\theta^* - \delta^*) + 5 - \gamma]}{[1 - \tan^2(\theta^* - \delta^*)][(\gamma+1)\tan^2(\theta^* - \delta^*) + 2]} \,. \tag{5}$$

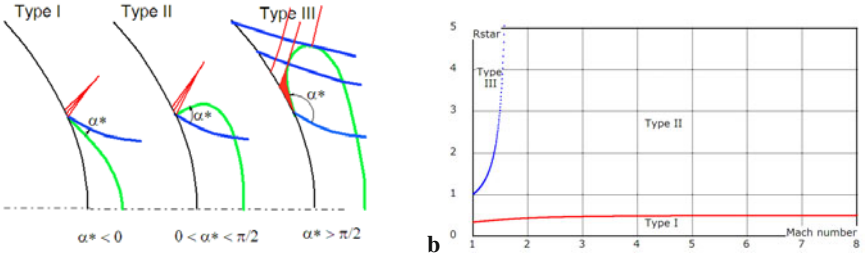

Fig. 2 (**a**) Illustration of the flow types at the sonic point, depending on the orientation of the sonic line; (**b**) Diagram showing the three types of sonic flow in the shock curvature ratio vs. Mach number space

One of three types of flow can exist at the sonic point on the shock, depending on the orientation of the sonic line, α^*: Type I for $\alpha^* < 0$, Type II for $0 < \alpha^* < \pi/2$, and Type III for $\alpha^* > \pi/2$. Figure 2a illustrates the three types where shocks are black, streamlines are blue, sonic lines are green and the $C+$ characteristics are red. Flow is left-to-right. These three types determine the existence and nature of the flow at the sonic point. For Type I, supersonic flow, leaving the shock just outboard of the sonic point continues supersonically. Hayes and Probstein have shown that Type I flow does not exist for planar flow. For Types II and III the supersonic flow outboard of the sonic point has to cross the sonic line to become subsonic and then to accelerate to sonic at its second crossing of the sonic line. Types II and III are further distinguished by the fact that, for Type III, the $C+$ characteristics, reflecting from the supersonic downstream side of the shock near the sonic line become incident on the sonic line and are thus intercepted and blocked from coalescing to form a reflected shock. This occurs in the area shaded red on the Type III sketch. Thus Type III flow may have a continuous incident shock whereas Types I and II are likely to develop a reflected shock and Mach reflections. This will become more evident when considering the orientation of reflected characteristics and the sonic

line. For planar flow, the angle that the sonic line makes with the streamline is shown in Fig. 3a. Type III flow exists between Mach 1 and 1.7. Above Mach 1.7 only Type I or II flow is possible. This means that, in planar flow, a continuous shock can be expected only below Mach 1.7 and above that a Mach reflection will occur. Type I flow is not possible for planar flow since the curve never becomes negative. Shock curvature does not affect these results since the flow has planar symmetry.

The picture is more complicated when the shocks are axial (axisymmetric) with curvatures S_a and S_b, and curvature ratio $\mathscr{R}^* = S_a^*/S_b^*$ at the sonic point. In this case the curved shock theory equation (5), for the sonic line orientation, α^*, takes the form $\tan\alpha^* = (k_1\mathscr{R}^* + k_2)/(k_3\mathscr{R}^* + k_4)$, where asterisks denote values at the sonic point. The coefficients k_1-k_4 are all functions of the specific heat ratio and the freestream Mach number only. The shock curvature ratio plays an important role in determining the character of flow behind a doubly curved shock.

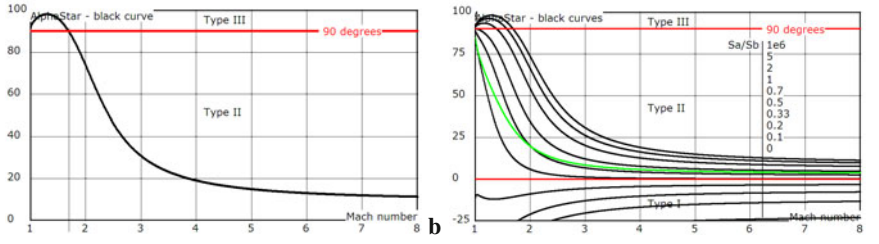

Fig. 3 (**a**) Angle between streamline and sonic line for planar flow; (**b**) Angle between streamline and sonic line vs. Mach number and shock curvature ratio

In Fig. 3b, α^* (`AlphaStar`), the angle from the streamline to the sonic line, is plotted against the freestream Mach number, with the shock curvature ratio, $\mathscr{R}^* = S_a/S_b$, at the sonic point, as parameter. The two red, horizontal lines, at zero degrees and 90 degrees, separate the regions for the three types of flow. The top-most curve, for $S_a/S_b = 1e6$ (i.e. 10^6) is effectively for planar flow as was presented in Fig. 3a. The bottom curve, for $S_a/S_b = 0$, is for conical flow. Type I flow, generally above Mach 2, appears for curvature ratios below 0.5. For a curvature ratio of 0.5, above Mach 3, α^* is approximately zero, indicating that the sonic line and streamline are collinear. This, in turn, means that the isobaric (Thomas) point is at the sonic point and that pressures in the supersonic/subsonic regions on either side of the streamline are increasing/decreasing. Type II flow is possible for curvature ratios between 0.5 and 10^6 for all Mach numbers. Type III ($\alpha^* > 90°$) flow is possible for curvature ratios above 1 and Mach numbers between 1 and 1.7. Only for these conditions can a smoothly curving incident shock wave be expected for the whole range of shock angles from μ to $\pi/2$. The above conclusions apply to concave shocks of any shape – not only hyperbolic. For planar, concave, hyperbolic shocks the top-most curve applies, showing that both Types II and III flow are possible and that we can expect a single shock, without a reflected shock, at Mach numbers below 1.7. This lower limit to Mach reflection of 1.7 is only for planar incident shocks. For axial shocks the

lower limit depends on the ratio of shock curvatures at the sonic point. For example, for a ratio of 2 the lower limit is about Mach 1.4 and for a ratio of 1 there is no lower limit – implying that Mach reflection will appear for all Mach numbers as long as the ratio of shock curvatures is below 1. The green curve is for concave, *hyperbolic* shocks, showing that only Type II shocks are possible and we should not expect a complete *hyperbolic* axial shock at any Mach number. At the same time it does not mean that complete axial shocks (Type II) do not exist. If they do, they would have to have a ratio of shock curvatures at the sonic point higher than that provided by the present type of axial, *hyperbolic* shock. Figure 2b shows where the three types of sonic flow exist in the shock curvature ratio (`Rstar`) vs. Mach number space.

5 Conclusions

Analytical results are presented for flow behind concave shocks. The existence of a reflected shock and hence the non-existence of a continuous smooth shock depends on the orientation of the sonic surface at the back of the shock. In turn, sonic surface orientation depends on the upstream Mach number and the ratio of shock curvatures at the sonic point. For planar shocks, a single, continuously curved shock is possible only below Mach 1.7. At higher Mach numbers Mach reflection will result in planar flow. For shocks with positive curvature ratio, $\mathscr{R}^*$, this Mach number limit is reduced until for $\mathscr{R}^* < 1$, no continuous concave shock is possible for any Mach number. A hyperbolic shock will revert to Mach reflection. The analytical results show that the shock curvature ratio plays an important role in determining the character of flow behind a doubly curved shock. It is a determining factor, beyond shock polar intersections, as to what type of shock reflection can take place at any freestream Mach numbers.

Acknowledgments. The present study is supported in part by the NSERC Discovery grant RGPIN/298232-2009 and the FQRNT Team grant PR-126114.

References

1. Gerber, N., Bartos, J.M.: Tables for determining flow variable gradients behind curved shock waves, U.S.A. Ballistics Research Laboratories, Rep. 1086 (1960)
2. Hayes, W.D.: J. of Fluid Mech. 2, 595–600 (1957)
3. Hayes, W.D., Probstein, R.F.: Hypersonic Flow Theory. Academic Press (1966)
4. Lin, C.C., Rubinov, S.I.: J. of Math. and Phys. XXVII(2), 105–129 (1948)
5. Mölder, S.: CASI Transactions 4(2), 73–80 (1971)
6. Rusanov, V.V.: Ann. Rev. Fl. Mech. 8, 377–404 (1976)
7. Thomas, T.Y.: J. Math. and Phys. 26, 62–68 (1947)
8. Truesdell, C.: J. Aero. Sci. 19, 826–828 (1952)

Simulations of Reflected Shock Bifurcation in a Square Channel

A. Khokhlov, J.M. Austin, C. Bacon, B. Clifford, A. Knisely, and S. Aithal

1 Introduction

Reflected shock interaction with an incoming boundary layer produces a complex, unsteady, three-dimensional flow field. Shock bifurcation, formation of recirculation bubbles, and turbulent jets are all observed and have been extensively studied experimentally ([1, 2, 3, 4, 5, 6]). The details of the reflection are known to depend on the inflow conditions, including the boundary layer behind the incident shock, and the wall boundary conditions. Reflected shock tube experiments have been conducted in shock tubes with both circular and rectangular cross-sections. There is experimental and numerical evidence that the bifurcated structure is substantially more complex near the corners of a rectangular tube as compared to the bifurcated structure on the centerline of a rectangular tube or in a round tube ([7, 8]). In this study, we present and analyze results of three-dimensional Navier-Stokes direct numerical simulations (DNS) of shock reflection in a square channel for three different incident shock Mach numbers. Key features of the present simulations are very high resolution inside the boundary layer and temperature-dependent material and transport properties. We compare and contrast our results as a function of the incident shock Mach number with the existing theoretical model of Mark [1]. The simulations reveal additional flow features in the recirculation and corner regions that are not captured by the model.

2 Results

Simulations were performed using the high-speed combustion and detonation code (HSCD) which includes the multi-species equation of state and viscous terms for

A. Khokhlov · B. Clifford
The University of Chicago, Chicago IL, USA

J.M. Austin · A. Knisely
University of Illinois, Urbana IL, USA

C. Bacon · S. Aithal
Argonne National Laboratory, Chicago IL, USA

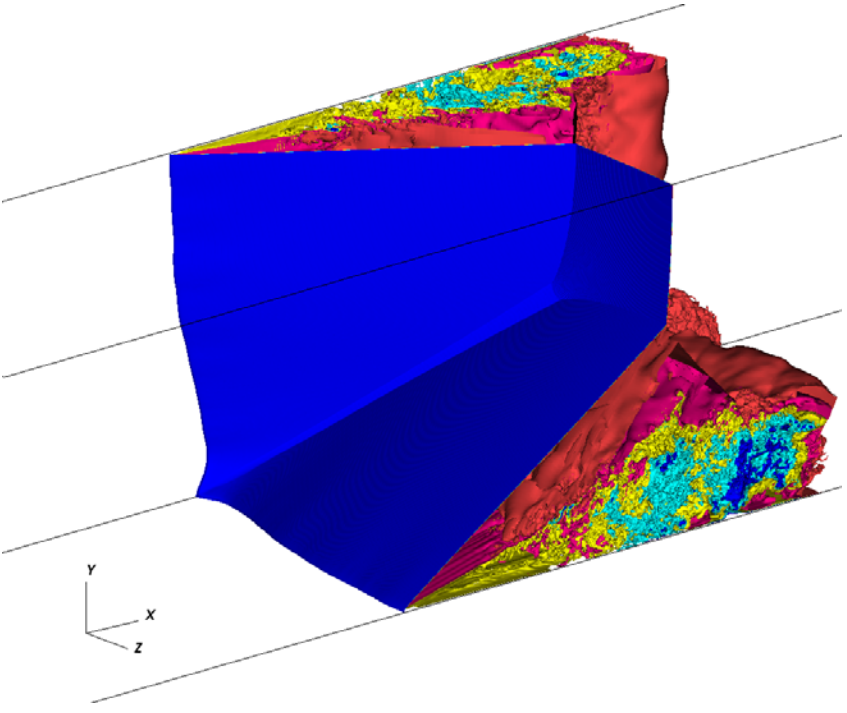

Fig. 1 Reflected shock density contours. The shock surface is blue. Incident shock $M_s = 3.0$.

hydrogen-oxygen combustion. The code is based on the fully threaded tree (FTT) dynamic adaptive mesh refinement, Godunov-type fluid-dynamic solver for Euler terms and second-order central differencing for viscous terms [9, 10, 11]. In the simulations presented in this paper the mesh is refined around shocks, discontinuities and in regions containing large gradients of physical variables such as density, temperature, and shear. The computational domain is a 2.5×2.5 cm square channel of 10 cm length with a closed end wall representing a quarter of the crossection of a square tube. Maximum resolution is 25 μm. Non-slip adiabatic boundary conditions are imposed on the side and end walls, symmetry conditions on center-planes, and zero-gradient conditions on the inflow boundary.

Simulations were carried out for three incident shock Mach numbers: $M_s = 1.5$, 2.0, and 3.0 in a (non-reactive) $2H_2$-O_2 mixture initially at 0.1 atm and 300 K. A sample three-dimensional plot of the reflected wave structure ($M_s = 3.0$) is shown in Figure 1 when the main shock is at 45 mm from the end wall. An oblique shock developed near the side walls, the boundary layer separated from the wall, and a growing low pressure recirculation bubble formed, with a turbulent jet moving along the side walls towards the oblique shock. The simulation reveals a narrow three-dimensional Mach stem structure due to interaction of the two systems of bifurcated shocks, one for each wall. The growth of the boundary layer behind the incident and

reflected shocks is resolved, and the development of a highly non-equilibrium and non-isotropic turbulence in the recirculated region is revealed.

Figure 2 shows schlieren images for all three M_s when the reflected wave is at 45 mm distance from the end wall. The color palette of the images has been adjusted to reveal features for all cases. The reflected shock structure at a given location exhibits significant sensitivity to M_s. The weakest case, M_s=1.5, does not show a distinct triple point kink. The three-shock bifurcated structure is formed in M_s=2.0 and 3.0 cases.

Mark's theory predicts transition from normal to bifurcated reflection regimes (from his Region 1 to Region 2, respectively) with increasing M_s when the post-shock static pressure behind the reflected shock, P_{4m}, becomes greater than the stagnation pressure, $P_{stag,bl}$ in the incoming boundary layer (we use here Mark's nomenclature). We cannot directly use Mark's formulae for the critical M_s separating the two regions as the present wall boundary condition is adiabatic, rather than isothermal. To address this, we first recover the universal scaling of the velocity profile in the boundary layer and calculate the mean velocity and the sound speed in the boundary layer. The boundary layer stagnation pressures are then calulated using these parameters.

P_{4m} and $P_{stag,bl}$ obtained for each of the three cases are listed in Table 1 for the channel center-planes. Results of our simulations are consistent with Mark's prediction for the onset of reflected shock bifurcation when $P_{4m}/P_{stag,bl}$ exceeds one, with our $M_s = 1.5$ case corresponding to conditions of Region 1 where bifurcation is not expected. For the Region 2 cases in which bifurcation occured, the shock and shear layer angles in the present study were measured. Near the channel center-planes the measured angles are within $\simeq 20\%$ of the Mark's theory, with the shock angles systematically underestimated (Table 2). The latter might be partially related with using adiabatic as opposed to isothermal boundary conditions (see [12]). The simulations reveal much more complex additional features of the flow, Figure 3. In the streamwise plane, the interaction of the reflected shock with the shear layer is evident with a significant increase in the shear layer instability and the formation of a colder region in the expansion wave created at the interaction. In the strongest incident shock case, significant instability is observed in the shear layer even upstream of the interaction point with fluctuations generating acoustic waves behind the oblique shock. The turbulent fluctuations in this case are on the order of the sound speed. These large velocity fluctuations are accompanied by a $\simeq 30-40\%$ decrease in pressure in the recirculation region. In the corner regions, the spanwise cross-sections reveal significant distortion of the boundary layer. This is consistent with the experimental observation of separation region deformation and retardation in square channels, with the length of the deformed region being of the order of the bifurcation foot height ([1, 7]). Whether this phenomenon can be interpreted within the existing theory is not clear. At the corners, the velocity in the incoming boundary layer is noticeably less then near the centerline. Based on Mark's transition criterion, we would thus expect the onset of bifurcation in the corners first but the present results do not reflect this. On the other hand, using Mark's argument that the shear layer angle is determined by the rate of the mass inflow through the

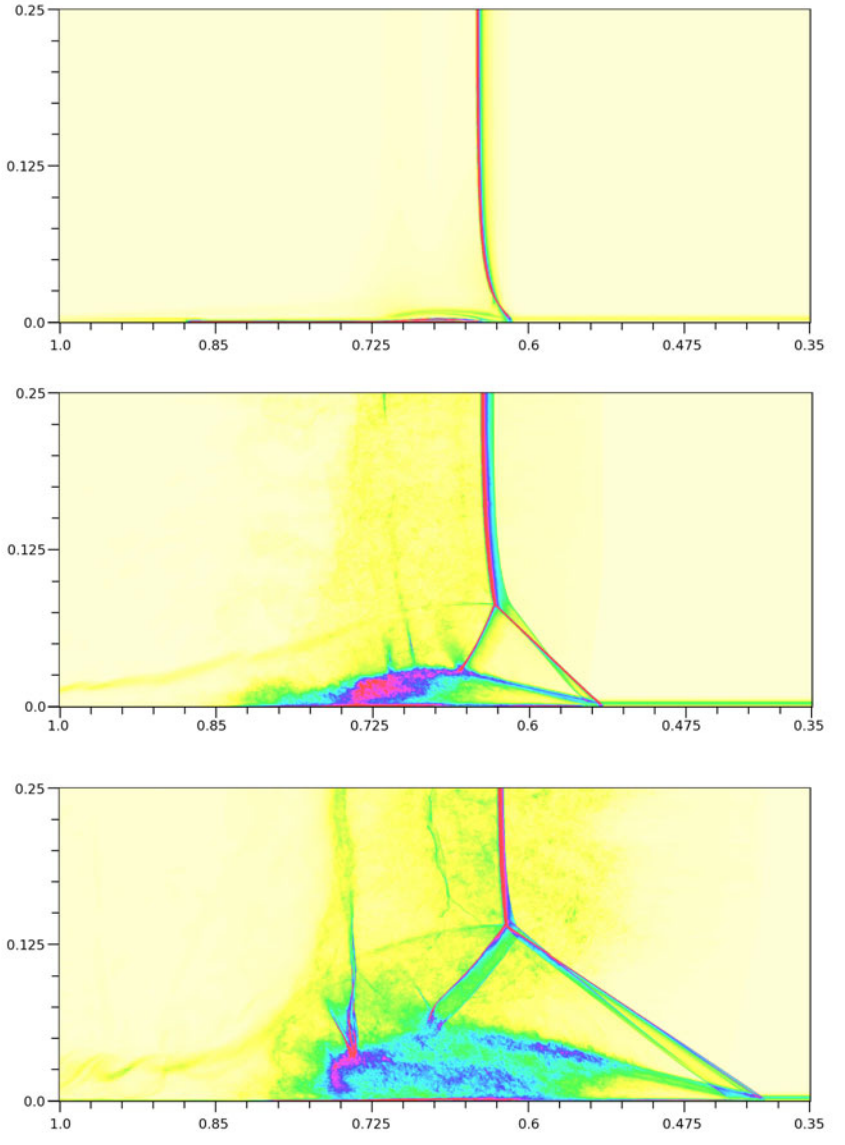

Fig. 2 Numerical schlieren images of the reflected wave for M_s = 1.5 (top), 2.0 (center), and 3.0 (bottom). Coordinates are scaled to the tube length.

boundary layer would lead us to the conclusion that, all else being equal, the shear layer angle in the corners should be less than on the centerline. The latter seems to be qualitatively consistent with the simulations. The difficulty should not be surprising. In a rectangular tube, the bifurcated shock structure and the recirculation

Table 1 Post-shock pressure P_{4m} and stagnation pressure in the incoming boundary layer $P_{stag,bl}$ normalized by the inflow static pressure P_2 along the channel centerline.

	M_s=1.5	M_s=2.0	M_s=3.0
P_{4m}	2.2	3.3	5.0
$P_{stag,bl}$	2.4	3.0	3.7

Table 2 Oblique shock and shear layer angles (degrees) from the present study compared with theory [1].

	M_s=2.0 Present	M_s=2.0 Theory	M_s=3.0 Present	M_s=3.0 Theory
Shock angle	43.5	50.2	34.1	46.5
Shear layer angle	14.2	12.8	14.1	17.4

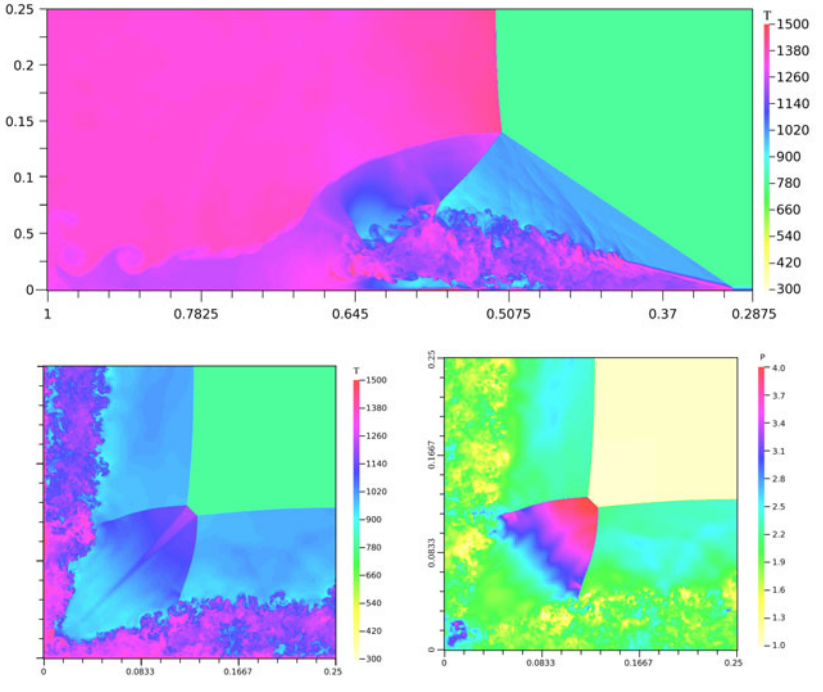

Fig. 3 Temperature field for M_s = 3.0. Top - centerline streamwise (XZ) plane, bottom - spanwise (YZ) plane at $x = 0.45$; left - T in Kelvin, right - P in atm. Coordinates are scaled to the tube length.

flow must simultaneously adjust to the varied mass inflow field in the corners and on the center-planes which cannot be considered in isolation. That this adjustment is indeed happening is evidenced, in particular, by the pressure buildup in the corners as compared to center-planes (see Fig. 3). A self-consistent three-dimensional treatment of the process would require a modification of the theory.

3 Conclusions

We carry out Navier-Stokes DNS to examine reflected shock bifurcation, a flow field known to be sensitive to three-dimensional effects, in a square channnel. The flowfield structure and the transition between regular and bifurcated shock reflection as a function of incident shock Mach number was found to be consistent with the existing theory of Mark. A reasonable agreement with predicted shock and shear layer angles was obtained near the channel center-planes. The simulations indicate that Mark's theory may not be adequate for the bifurcation structure in the corner regions. The simulations also reveal very large fluctuation velocities and a corresponding pressure loss in the recirculating region that are not included in the theory. The latter effect may be increasingly important at high Mach numbers.

The authors gratefully acknowledge the joint funding provided by the ASCR and the BES divisions of the DOE Office of Science DE-SC0002594 with managers Dr Mark Pederson, Dr Randall Laviolette (current), Dr Lali Chatterjee (former), and the resources of the Argonne Leadership Computing Facility under DE-AC02-06CH11357. AK acknowledges partial NSF support under AST-0709181 and TG-AST090074 grants.

References

1. Mark, H.: NACA TM 1418 (1958)
2. Strehlow, R., Cohen, A.: J. Chem. Phys. 30, 257–265 (1959)
3. Byron, S.R., Rott, N.: Proc. Heat Trans. & Fluid Mechs. Inst., vol. 38 (1961)
4. Matsuo, K., Shigetoshi, K., Kazuyuki, K.: Bull. JSME 17(110), 1039–1046 (1974)
5. Fokeev, V., Gvozdeva, L.: 17th Int. Symp. Shock Waves & Shock Tubes (1990)
6. Petersen, E.L., Hanson, R.K.: Shock Waves 15, 333–340 (2006)
7. Brossard, J., Charpentier, N., Bazhenova, T.V., Fokeev, V.P., Kalachev, A.A., Kharitonov, A.I.: 15th Int. Symp. Shock Waves & Shock Tubes, vol. 163 (1984)
8. Gamezo, V.N., Oran, E.S., Khokhlov, A.M.: Proc. Combust. Inst., pp. 1841–1847 (2005)
9. Khokhlov, A.M.: J. Comp. Phys. 143, 519 (1998)
10. Khokhlov, A.M., Chtchelkanova, A.Y.: 9th SIAM Conf. Parallel Proc. Scientific Computing (1999)
11. Khokhlov, A., Bacon, C., Austin, J.M., Aithal, S., Riley, K.: 31st Ann. Combust. Res. Meeting, Varrenton, VA (2010)
12. Weber, Y.S., Oran, E.S., Boris, J.P., Anderson, J.D.: Phys. Fluids 7, 2475–2488 (1995)

Experimental and Numerical Investigation of Shock Wave Interaction with Rigid Obstacles

E. Glazer, O. Sadot, A. Hadjadj, and A. Chaudhuri

1 Introduction

Shock wave interaction with obstacles of various geometric shapes has always attracted attention in a large number of experimental and numerical studies. During the interaction of a shock wave with an obstacle a very complex wave pattern is formed which affects the shock-wave induced flow. The interaction reduces the shock-wave strength and generates rotational flow behind the obstacle. The interaction of shock waves with rigid obstacles is of significant importance in aerodynamic science and other engineering applications. Whitham [1] formulated an approximate theory for the dynamics of two- and three-dimensional shock waves and applied this theory to the description of shock diffraction by wedges and corners. Bryson & Gross [2] broadened Whitham's theory and applied it to two- and three-dimensional bodies such as cylinders and spheres. They carried out theoretical and experimental work to assess the analytical computations that were made by Whitham. One dominant direction in investigation of shock-cylinder interaction is finding the RR→MR transition criterion. When the shock wave strikes a cylinder, it is reflected as an RR and then transforms to a Mach reflection MR. Major RR→MR transition criteria were summarized and discussed in a scientific monograph by Ben-Dor [3]. Since 1970, due to progress in numerical techniques, very accurate simulations of shock wave propagation over obstacles have been achieved. In most of studies efforts to validate the Euler scheme were undertaken. In the numerical study of Drikakis et al. [4] viscous effects were examined at various Mach numbers during of shock-cylinder interaction by comparing the inviscid and viscous calculations. It was found that the flow field in the downstream half of the cylinder is influenced by viscosity. The main objective of the present study is to better understand the physical elements governing the flow induced by the shock wave and

E. Glazer · O. Sadot
Shock Tube Laboratory, Protective Technologies R&D Center, Department of Mechanical Engineering, Ben-Gurion University of the Negev, Beer-Sheva, Israel

A. Hadjadj · A. Chaudhuri
National Institute of Applied Sciences, INSA & CORIA UMR 6614 CNRS, Rouen, France

the elements affecting the shock wave strength after passing the obstacle. To carry out the overall research plan two different approaches have been utilized - experimental and numerical. In the present study we focused on the investigation of the reflected shock wave from a single cylinder for low Mach numbers ($M_S \sim 1 - 1.4$) in order to characterize the physical factors affecting its propagation. The first part of a broad investigation of the shock wave interaction with complex geometries is presented.

2 Experimental System

Figure 1 presents a schematic diagram of the test section placed in the shock tube. The shock tube consists of a 2.3m long driver section of 80mm diameter and a 2.5m long driven section of 80mm×80mm square cross section. The driver and driven section are separated by a 0.1-0.25mm thick plastic membrane. The driver section is pressurized to the required initial pressure. The shock wave is formed by penetration of a plastic membrane by means of a striking pin. The shock wave interacts with a single cylinder placed in the test section. The research is carried out on a 10mm, 15mm and 20mm diameter and 80mm long circular PVC cylinder. Two transparent PMMA windows are mounted on the test section permitting a field of view of 115mm×56mm in order to visualize the shock-cylinder interaction. The cylinder is supported between these observation windows. Two pressure transducers are placed 0.5m apart in the driven section and another pressure transducer is placed on the lower side wall of the test section, 80mm from the center of the cylinder. The shock wave propagation and the induced flow are monitored by a high speed PHANTOM v12.1 digital camera capable of capturing images at a rate of 20,000 frames per second and a schlieren based optical system. The light source for this setup is a doubled frequency Nd:YAG pulsed laser at the appropriate rate of 20,000 pulses per second. The time interval between consecutive images is about $50\mu s$. The

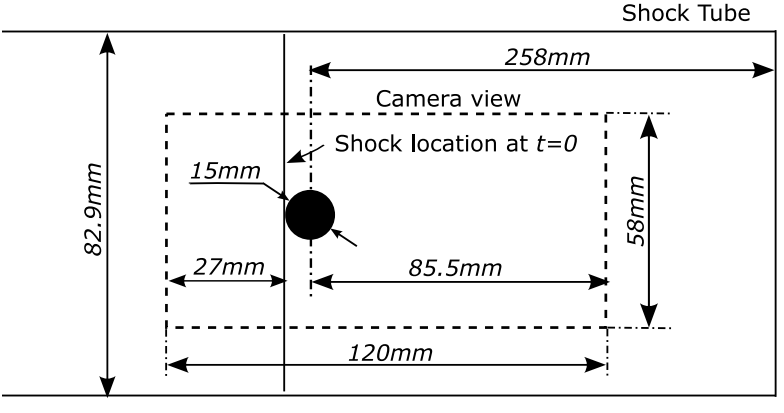

Fig. 1 A schematic diagram of the test section.

passage of the shock wave past the first pressure transducers on the driven section triggers the camera. The laser pulses pass through the test section and are recorded by the camera; each laser pulse produces a schlieren image, which is stored in the memory of the high-speed camera.

3 Numerical Approaches

In this study, a high-order shock-capturing scheme based on a weighted essentially non-oscillatory (WENO) approach is used [5]. This class of modern scheme is very attractive for simulating shocks, contact discontinuities, and fine-scale flow structures. The WENO schemes use an adaptive 'smoothest' sub-stencil chosen within a larger, fixed stencil to construct a high-order approximation of the solution, avoiding the interpolation across discontinuities and preserving a uniformly high order of accuracy at all points where the solution is smooth. The main concept is to use a superposition of several sub-stencils with adaptive coefficients to increase the order of approximations even further. In this paper, we adopt the finite difference, flux-based, fifth-order WENO scheme [6] with Roe splitting for calculating the numerical fluxes at cell interfaces. A robust and stable immersed boundary method (IBM) is also developed to deal with complex geometries on Cartesian grids.

4 Results

4.1 Comparison with the Numerical Results

Figure 2 presents a set of Schlieren images of the shock-wave (Ms=1.16) interaction with a single 15mm-diameter cylinder. The experimental images are presented in Figures 2(a, c, e, g, i, k) and the equivalent simulation images are shown in Figures 2(b, d, f, h, j, l). The time indicated on each picture corresponds to the time after the arrival of the incident shock wave at the tip of the cylinder. The time intervals between consecutive images are $55.56\mu s$. The laser non-uniformity and other spots on the images were removed by subtracting a background image from each original image; this leads to a very clean and uniform background and enhances the observed features. Since the system is symmetric, a horizontal symmetry plane is formed through the center of the cylinder. After the initial collision of the shock wave with the cylinder, part of it is reflected and a regular shock reflection occurs (not shown) which is followed by a Mach-reflection configuration, which consists of the incident shock, the reflected shock, the Mach stem and the slip line. The point of intersection of these features is named the triple point. Later, the two Mach stems collide downstream of the cylinder and as a result, a second Mach-reflection configuration is formed on either side of the symmetry plane. As can be seen, the experiment and simulation are in excellent agreement for the flow features such as triple-point trajectories and diffraction patterns of shock waves. Thus, these features have not been affected by viscosity, which is not accounted for by the Euler scheme used. From $t = 212\mu s$ more complex wave structures begin to appear, while

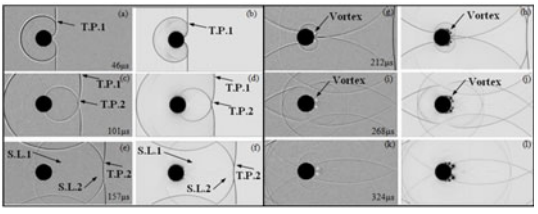

Fig. 2 Comparison of series of Schlieren pictures with the numerical simulation (Euler calculations) of shock wave propagation over a 15mm diameter cylinder, $M_S = 1.16$.

experimental and numerical features continue to agree in terms of wave locations. However, at the rear side of the cylinder, during the boundary layer separation, discrepancies arise in the loci of vortex positions. This can be explained by the fact that the Euler scheme does not account for viscosity. Half of the symmetrical triple-point trajectories are shown in Figure 3, in which the triple point position was measured from the images obtained from the experiment and the numerical simulation.

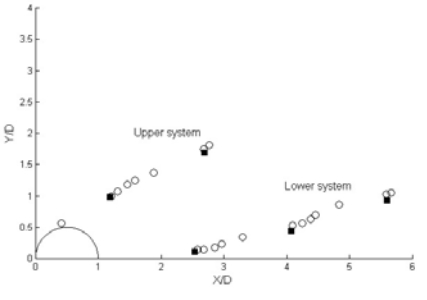

Fig. 3 Experimental results for upper- and lower-triple point trajectories at $M_S = 1.16$ and comparison with numerical simulation. (circles) Experiment; (squares) Simulation

4.2 Investigation of the Reflected Shock Wave from the Cylinder

In this section, a parametric study of the reflected shock-wave trajectories is presented. In order to examine parameters affecting the velocity of the reflected shock wave, a series of the experiments for different initial conditions (different shock-wave strengths, different diameter cylinders and different gases) and numerical simulations were performed. The time evolution of the reflected shock wave location on the symmetry plane was measured from numerical and experimental sequences based on schlieren images. This parameter was obtained up to the time when the reflected shock wave from the sidewalls enters the camera field of view. Based on the measurement results, it was observed that the absolute velocity of the reflected shock decreases due to the increased velocity of the induced flow behind the incident

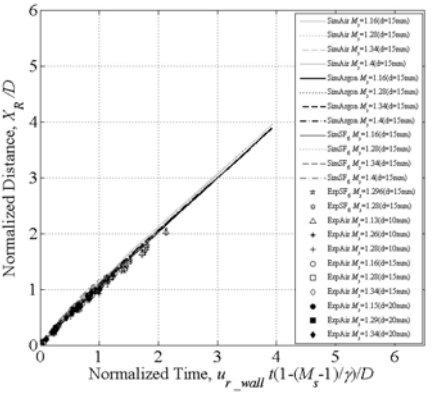

Fig. 4 The reflected wave location vs. time from experiments and simulations for different gases.

shock. The effect of the cylinder diameter on the reflected shock trajectory is minor. Using the appropriate non-dimensional coordinates, the data from various experiments with different initial conditions collapse into a single curve and the relevant parameters affecting the behavior of the reflected shock wave can be found. From the data analysis, the following linear relationship between the velocity ratio (the reflected shock velocity from the cylinder divided by the reflected shock velocity from a planar end-wall) and the Mach number is found:

$$1 - \frac{u_{r-cyl}}{u_{r-wall}} = f(\gamma)(M_S - 1) \tag{1}$$

The scaling function $f(\gamma)$,including the parameter γ, has been tested by the experiments and numerical simulations with different gases (air, SF_6). It is found that the value of the function equals $f(\gamma) = 1/\gamma$. Inserting this expression into Eq. (1) and performing appropriate mathematical operations gives the following time scaling:

$$\tilde{t} = \frac{u_{r-wall}t}{D}[1 - (M_S - 1)/\gamma] \tag{2}$$

In order to examine dimensionless time, the normalized reflected shock location along the line of symmetry as a function of $\tilde{t}$ is presented (Figure 4) for 15 different parameter combinations, such as type of working gas (air, Ar and SF_6), Mach number and cylinder diameter. As can be seen, all data collapse closely in a single curve, indicating that the approximate relation presented in Eq. 2 replicates very well the reflected shock trajectory on the symmetry plane from a rigid cylinder for different incident-shock Mach numbers, different cylinder diameters and different gases. However, there are still minor discrepancies between different data, probably due to the parameters that were not included in the approximate relation. Moreover, numerical simulations were carried out for longer times than the experiments, and

it appears that with time the computed lines approach each other, strengthening our confidence in the time scaling factor for the range of Mach numbers $M_S = 1.1 - 1.4$.

5 Conclusion

In the present study the interaction of a shock wave with a cylinder is investigated experimentally and numerically. The experimental investigation was carried out in a horizontal shock tube with a schlieren-based optical system. The computation scheme was based on the Euler equations, which ignore viscosity effects. The behavior of the reflected curved shock wave from the cylinder in the upstream direction for range Mach numbers $M_S = 1.1 - 1.4$ was emphasized. It was found that reflected shock wave trajectory from the cylinder can be approximated by a universal relation, which relates the reflected-shock velocity from a planar wall reduced by a universal factor that depends on the incident shock-wave Mach number and the heat capacity ratio. The approximated relation is limited to the range of Mach numbers $M_S < 1.4$ and valid in the range of 0.5-5D from the cylinder, but not closer than 0.1D.

Acknowledgements. This research is supported by The ISRAEL SCIENCE FOUNDATION (grant No. 139/10). Computations are performed using HPC resources from GENCI [CCRT/CINES/IDRIS] (Grant 2010-0211640), France.

References

1. Whitham, G.: A new approach to problems of shock dynamics: Part I: Two-dimensional problems. J. Fluid Mech. 2, 145 (1957)
2. Bryson, A.E., Gross, R.W.: Diffraction of strong shocks by cones, cylinders, and spheres. J. Fluid Mech. 10, 1–16 (1961)
3. Ben-Dor, G.: Shock Wave Reflection Phenomena. Springer, New York (1992)
4. Drikakis, D., Ofengeim, D., Timofeev, E., Voionovich, P.: Computation of non-stationary shock-wave/cylinder interaction using adaptive-grid methods. J. Fluids and Structures 11, 665 (1997)
5. Jiang, G., Shu, C.W.: Efficient implementation of Weighted ENO schemes. Journal of Computational Physics 126, 202–228 (1996)
6. Taylor, E.M., Wu, M., Martin, P.: Optimization of nonlinear error for weighted-essentially non-oscillatory methods in direct numerical simulations of compressible turbulence. J. Comput. Phys. 223, 384–397 (2007)

Computational Study of the Interaction of a Planar Shock Wave with a Cylinder/Sphere: The Reflected Wave Velocity

Y. Kivity, J. Falcovitz, A. Hadjadj, A. Chaudhuri, O. Sadot,
E. Glazer, A. Britan, and G. Ben-Dor

1 Introduction

The interaction of shock waves with rigid obstacles is of significant interest in aerodynamic science and other engineering applications. During the interaction of a shock wave with an obstacle, a very complex wave pattern which affects the shock-wave induced flow is formed. The interaction process depends on a variety of physical parameters such as the shape of the obstacle, the shock wave strength and the type of gas in which the interaction occurs. In the present paper, the interaction of a planar shock wave with a cylinder and a sphere is investigated. Our investigation follows closely the recent work of Sadot *et al.* [1] which dealt with shock tube experiments with low Mach number shocks, in the range 1.1 to 1.4. An empirical relation was proposed for the trajectory of the reflected wave. This relation was expressed in terms of non-dimensional distance and time and was shown to be applicable for the investigated range of Mach numbers, cylinder diameters and a general ideal gas. The purpose of the present work is to focus on the backward reflected wave, and in particular, on its velocity change as it progresses away from the leading edge of the cylinder/sphere. It is expected that the reflected wave initially propagates at the velocity of shock reflection from a rigid wall, and asymptotically decelerates to the velocity corresponding to that of a sonic wave in the shocked region. This theoretical behavior is born out by fine mesh hydro-code computations of the interaction problem. The paper is organized as follows: in Section 2 a theoretical background for the limiting velocities of the reflected shock is given, followed by a brief description of the numerical codes and the problem setup (Section 3). The results of simulations for various cases by different CFD codes are given in Section 4. We conclude (Section 5) with a summary and suggestion of future work.

Y. Kivity · O. Sadot · E. Glazer · A. Britan · G. Ben-Dor
Faculty of Engineering Sciences, Ben-Gurion University of the Negev, Be'er-Sheva, Israel

J. Falcovitz
Institute of Mathematics, The Hebrew University of Jerusalem, Israel

A. Hadjadj · A. Chaudhuri
National Institute of Applied Sciences, INSA, CORIA UMR 6614 CNRS, Rouen, France

2 Analytical Background

To get the sonic wave velocity of the backward traveling wave in the laboratory coordinates we must subtract the material velocity in the shocked region. Thus we may write for the sonic wave speed W_R (in a coordinate frame attached to the stationary cylinder):

$$W_R/a_0 = a_1/a_0 - u_1/a_0 \tag{1}$$

Here a is the speed of sound and u is the material velocity. The subscript "o" denotes values at the quiescent region ahead of the shock ($u_0 = 0$), and the subscript "1" denotes values in the shocked region. From the shock relations for a normal shock we have (Shapiro [2], p. 118, Eq. 5.19):

$$a_1/a_0 = \frac{1}{M_s}\left[\left(1+\frac{\gamma-1}{\gamma+1}\beta\right)\left(1+\frac{2\gamma}{\gamma+1}\beta\right)\right]^{1/2} \quad , \quad \beta = M_s^2 - 1 \tag{2}$$

Here M_s is the incident shock Mach number (in the laboratory coordinate system). For the material velocity u_1, we employ eq. 75.05 (Courant & Friedrichs [3]):

$$u_1/a_0 = \frac{2}{\gamma+1}\frac{M_s^2-1}{M_s} = \frac{2}{\gamma+1}\frac{\beta}{M_s} \tag{3}$$

Combining (2) and (3) according to (1), we get:

$$W_R/a_0 = \frac{1}{M_s}\left\{\left[\left(1+\frac{\gamma-1}{\gamma+1}\beta\right)\left(1+\frac{2\gamma}{\gamma+1}\beta\right)\right]^{1/2} - \frac{2}{\gamma+1}\beta\right\} \tag{4}$$

For the reflected wave speed from a rigid wall, U_{RW}, we use relation (70.02), (Courant & Friedrichs, p.153):

$$M_+ M_- = 1 \tag{5}$$

This gives:

$$M_+ = (M_s\, a_0 - u_1)/a_1$$

$$M_- = (u_1 + U_{RW})/a_1 \tag{6}$$

$$(u_1 + U_{RW})/a_1 = a_1/(M_s\, a_0 - u_1) \tag{7}$$

Let us get an expression for the reflected Mach Number, M_R, in a coordinate system attached to the incoming flow:

$$M_R = (u_1 + U_{RW})/a_1 = a_1/(U - u_1) = \frac{1}{M_s - \frac{2}{\gamma+1}\frac{\beta}{M_s}}\left(\frac{a_1}{a_0}\right) \tag{8}$$

Substituting u_1 from (3) and after some arrangements, we get:

$$M_R = \frac{\gamma+1}{2}\frac{M_s}{1+\frac{\gamma-1}{2}M_s^2}\left(\frac{a_1}{a_0}\right) = \frac{M_s}{1+\frac{\gamma-1}{\gamma+1}\beta}\left(\frac{a_1}{a_0}\right) \tag{9}$$

Expression (9) has the advantage that M_R can be calculated explicitly. Consequently, U_{RW} can be calculated from (8) as:

$$U_{RW}/a_0 = M_R\left(\frac{a_1}{a_0}\right) - u_1/a_0 \tag{10}$$

Using Eqs. (9), (2) and (3), we get a surprisingly simple expression:

$$U_{RW}/a_0 = \frac{1}{M_s}\left(1+2\frac{\gamma-1}{\gamma+1}\beta\right) \tag{11}$$

3 Numerical Simulations and Flow Parameters

In this study, three different codes are used: (1) a code based on the GRP method with cut-cells boundary [4]; (2) the MSC/Dytran code, using a second-order Roe solver [5]; and (3) an in-house compressible code using a fifth-order WENO scheme with an immersed boundary method [6]. The computational flow field consists of a rectangle having a 2:1 length to height ratio. Three sides of the computational rectangle have "non-reflecting" boundary conditions, which simulate an extension of the mesh designed to eliminate wave reflections from the boundaries, thereby approximating an unbounded flow domain. The bottom surface is a symmetry plane, representing either the wall of a shock tube or a symmetry plane between two mirror-image cylinders. The computations are carried out in a Cartesian mesh with the cylinder/sphere at its center, and the incident shock front placed just ahead of the cylinder. Flow variables behind the incident shock are initialized by the values obtained from the plane shock relations.

4 Results

The reflected wave velocity for a shock Mach number of 1.28 interacting with a cylinder in an unbounded domain is shown in Fig. 1. The results are given for the three numerical codes mentioned above. Determination of the reflected wave velocity requires special attention. A direct differentiation of the numerical trajectory of the shock front produces a very noisy curve, due to errors associated with the finite resolution of the numerical trajectory. For the Dytran results, we determined visually the position at which the pressure rise was half way through the shock, and then employed a smoothing algorithm found in the DPLOT graphic package. For the GRP results a more sophisticated algorithm was employed, based on constructing a parabolic fit to the pressure gradient in the vicinity of the shock front, and choosing the maximum of this local parabola. This algorithm produced a much smoother curve, as can be seen in Fig. 1. Two additional algorithms, one based on the

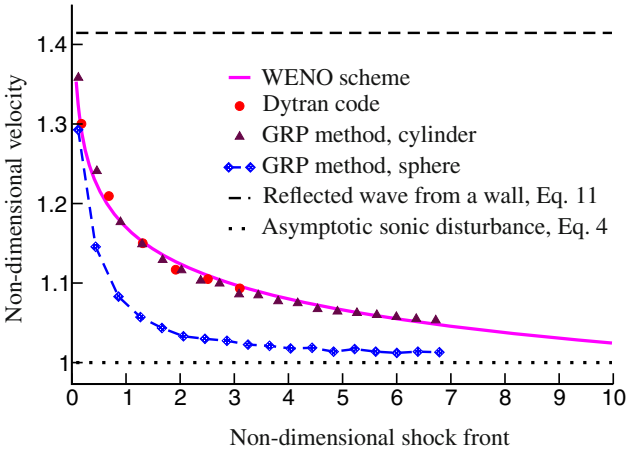

Fig. 1 The velocity of the reflected wave vs. distance for $M_s = 1.28$. Cylinder and sphere in an unbounded domain. The velocity is normalized by the asymptotic sonic wave, W_R. The distance is normalized by the diameter D. Lower curve shows the velocity for the case of a sphere.

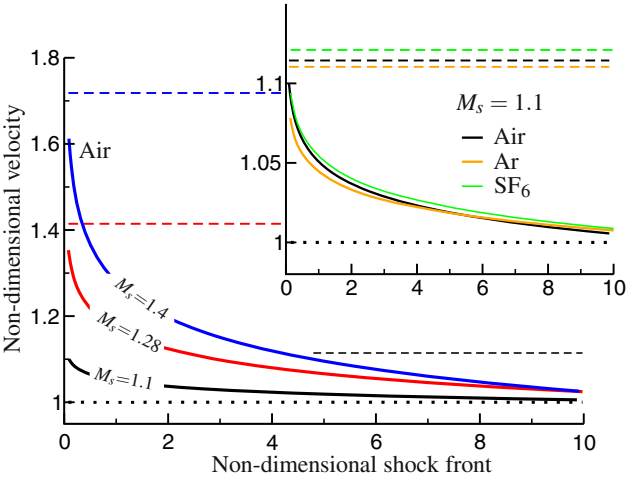

Fig. 2 The velocity of the reflected wave vs. distance as function of M_s and the gas constant γ (for definition of the normalized quantities see Fig. 1).

variation of the Riemann invariant across the shock (in GRP) and another based on the fifth-order WENO scheme, resulted in almost the same curve. The analytically evaluated limit velocities corresponding to rigid wall reflection (dash line) and sonic disturbance (dot line) are also shown in this figure. To bring out the effect of the

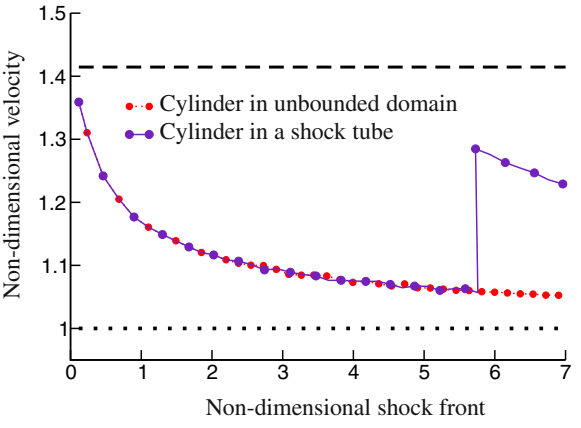

Fig. 3 The velocity of the reflected wave vs. distance for $M_s = 1.28$. Results for a cylinder in an unbounded domain and a cylinder in a shock tube with finite lateral extent (GRP code).

obstacle surface curvature, an additional GRP run is carried out for a sphere, having the same diameter as the cylinder. In this case, the code operated as 2D axisymmetric. A comparison between the cylinder and the sphere cases is shown in Fig. 1. It is obvious that the radial expansion of the reflected wave from a sphere gives rise to a higher rate of attenuation, approaching the sonic wave limit much faster than in the cylinder case. Further results are provided in Fig. 2 using the WENO scheme, with various working gases (Air, Ar and SF_6) and a range of M_s. The obtained results confirm the shock velocity tendency.

These calculations are performed in a computational domain large enough in both dimensions to ensure that no disturbances reach the main flow so that the condition of an unbounded domain is well approximated. In shock tube research, however, this condition is not easily met. To get some insight for the case where the cylinder occupies a significant fraction of the shock tube lateral dimension, we carried out similar runs with the top surface as a rigid boundary. As an example, Fig. 3 compares two reflected-wave velocity curves for $M_s = 1.28$: one curve pertains to the unbounded cylinder considered previously, and the other corresponds to the case of a cylinder in a shock tube of finite lateral dimensions, with a cylinder occupying one quarter of the shock tube cross-section. The area constriction effect is evident at a distance of $\sim 5.7D$, where transverse reverberations have overtaken the reflected wave, abruptly changing its velocity. This indicates a (large-time) transition of the shock-cylinder flow to a transmitted/reflected pattern obtained for shock-cylinder interaction in a very long duct.

5 Summary and Conclusion

The shock wave system arising from the interaction of a planar shock wave with a cylinder or a sphere were calculated using CFD- and hydro-codes. We focused

on the changing velocity of the backward reflected wave. Initially, the reflected shock propagates at the velocity corresponding to reflection from a rigid wall. Subsequently the velocity gradually decreases, approaching that of a sonic wave. The rate of attenuation is significantly higher for the sphere. Explicit expressions are developed for the two limiting velocities as function of the incident Mach Number and the ideal gas γ. Our calculations with various codes demonstrated the above trend of the reflected wave. Moreover, we showed that the reflected wave from a sphere decreases much faster than the corresponding one from a cylinder. Finally, we showed that when the obstacle is placed in a bounded domain, such as a shock tube with finite lateral extent, the shock wave velocity abruptly changes at some distance due to transverse wave reverberations. This change seems to indicate a switch of the wave pattern to that of transmitted/reflected waves in a long duct with an area constriction. Future work will address the interaction of a shock wave with an array of cylinders (or other objects). Such arrays were proposed [7] as passive shock deflectors for protecting openings in shelters.

References

1. Sadot, O., Glazer, E., Ben-Dor, G., Britan, A., Chaudhuri, A., Hadjadj, A.: Study on the Shock-Cylinder Interaction. In: ISIS19, Moscow, Russia, August 31-September 3 (2010)
2. Shapiro, A.H.: The Dynamics and Thermodynamics of Compressible Fluid Flow. The Ronald Press company, New York (1953)
3. Courant, R., Friedrichs, K.O.: Supersonic Flow and Shock Waves. Inter-Science Publishers, New York (1948)
4. Ben-Artzi, M., Falcovitz, J.: Generalized Riemann Problems in Computational Fluid Dynamics. Cambridge University Press, London (2003)
5. MSC.Dytran Theory Manual, MSC. Software Corporation, Santa Ana, US, pp. 6.1–6.8
6. Chaudhuri, A., Hadjadj, A., Chinnayya, A.: On the use of immersed boundary methods for shock/obstacle interactions. J. Comp. Physics 230, 1731–1748 (2011)
7. Baum, J.D., Lohner, R.: Numerical Simulation of Passive Shock Deflector Using an Adaptive Finite Element Scheme on Unstructured Grids, AIAA-92-0448 (1992)

Determination of the Sonic Point in Unsteady Shock Reflections Using Various Techniques Based on Numerical Flowfield Analysis

A. Hakkaki-Fard and E. Timofeev

1 Introduction

When a moving shock wave encounters a convex cylinder, reflects from it regularly, and propagates further, at one particular shock position corresponding to the so-called *sonic point* the flow on the cylinder's surface, just behind the reflected shock becomes sonic with respect to the moving reflection point. The sonic point is prominent in the theory of regular-to-Mach reflection transition as one of its possible criteria [1]. When the flow behind the reflected shock wave becomes sonic, downstream perturbations can reach the reflection point and, supposedly, may cause the regular-to-Mach reflection transition.

In a recent experiment Skews and Kleine [2] generated weak perturbations on the surface of circular cylinders (with minute grooves) and tracked them using time-resolved optical imaging [3]. In this way, they were able to identify the time moment and the point on the cylinder's surface when and where the disturbances for the first time catch up with the reflection point. The relationship between this experimentally determined *catch-up point* and the sonic point is not immediately obvious. It was found that the catch-up point is reached at a higher wall angle (a lower polar angle) as compared to the wall angle corresponding to the sonic point predicted by the steady-state two-shock theory applied to the unsteady flow.

In this study we attempt to shed some light on these matters by applying various techniques to determine the location of the sonic and catch-up points from flowfields obtained by numerical modeling of the shock wave reflection from a circular cylinder. Two-dimensional computations are performed using a locally adaptive unstructured unsteady Euler/Navier-Stokes code [4], which is based on a second order in space and time TVD Godunov-type finite-volume solver. In case of viscous computations the grid was sufficiently refined to resolve the physical thickness of shock waves and the boundary layer growth on the cylinder's surface, according to our methodological study in [5].

A. Hakkaki-Fard · E. Timofeev
Department of Mechanical Engineering, McGill University,
Montreal, Quebec H3A2K6, Canada

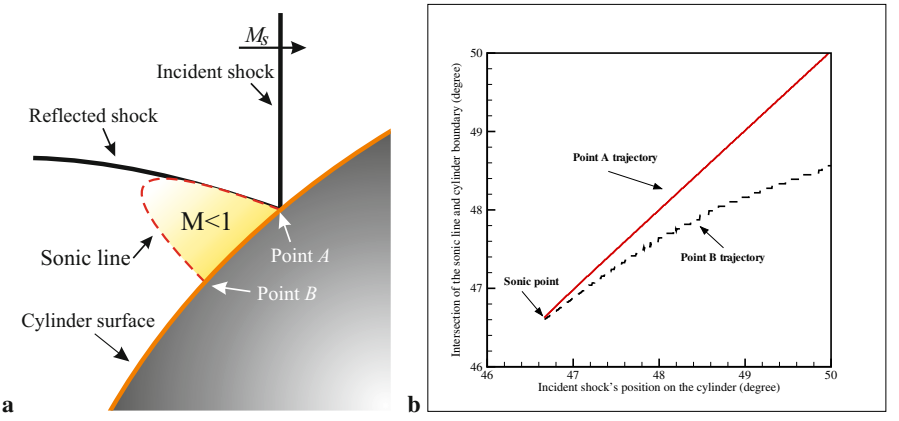

Fig. 1 Illustration of the Mach number based technique: (**a**) Developed sonic line and subsonic region when the incident shock has passed the sonic point (in the frame of reference attached to the reflection point); (**b**) Locations of points *A* and *B* (see Fig. 1a) vs. the incident shock position (all given in terms of polar angle)

2 Sonic/Catch-Up Point Determination Techniques

In order to obtain the theoretical sonic point for unsteady problems, the Navier-Stokes equations for viscous flows or the Euler equations for the inviscid case should be solved analytically. As stated in [6], "due to the complexity of the governing equations of unsteady shock reflections, simple transition criteria, such as those presented earlier for steady and pseudo-steady flows, can not be established." Ben-Dor and Takayama [7] suggested to divide the unsteady flow into a sequence of momentarily pseudo-steady states. Under this assumption, the sonic point can be predicted using the classical steady-state two-shock theory. However, it is not immediately obvious that the predictions are valid for the unsteady case under consideration, especially in view of the experiments [2]. Three different techniques are used in this paper to determine the sonic and/or catch-up points from numerical simulations for the problem of unsteady shock reflection from a convex cylinder: the Mach number based technique, the characteristic based technique, and the perturbation technique. Their principles are outlined in the following subsections.

2.1 Mach Number Based Technique

The Mach number based technique [8] implies direct application of the sonic point definition. Figure 1a shows the incident and reflected shock waves, the sonic line and the subsonic region developed behind the reflected shock wave, when the shock has *already passed* the sonic point. Points *A* and *B* are the intersections of the sonic line with the cylinder's surface. Their locations at each time moment can be determined from the Mach number distribution on the cylinder's surface in the frame of reference attached to the reflection point. Then the trajectories of points *A* and *B* can

be plotted together, as shown in Fig. 1b. Their intersection would give the location of the sonic point, where the flow right behind the reflection point would become sonic with respect to the reflection point for the first time.

2.2 Characteristic Based Technique

The characteristic based technique also analyzes flow parameters on the cylinder's surface only. Small perturbations propagate along the surface with the velocity $u_\tau + c$, where u_τ is the local tangential flow velocity and c is the local speed of sound. The reflection point moves along the cylinder's surface with velocity D, which is related to the incident shock Mach number M_s and the polar angle θ corresponding to the current shock position through $D = M_s/\sin\theta$. At the sonic point, downstream disturbances are capable, for the first time, of reaching the reflection point. This is possible only if $u_\tau + c \geq D$, which becomes the criterion for finding the sonic point. In other words, on an x-t diagram drawn for the cylinder's surface the inversed slope of $C+$ characteristic should become greater than the inversed slope corresponding to the trajectory of the incident shock along the surface. That is why this technique is termed as the characteristic based technique. The sonic point location would correspond to the time moment (shock location) when the condition $u_\tau + c \geq D$ is for the first time satisfied downstream of the reflection point.

2.3 Perturbation Technique

The perturbation technique is generally based on tracking of very weak (not altering essentially the flow under study) waves generated by sources on the boundary of the flow domain in order to interrogate how the domain geometry influences the flow. In case of shock wave reflection/difraction the shock wave itself may produce weak perturbation signals when passing over small geometrical features on the wall (e.g. minute bumps or grooves). These perturbations propagate outward in all directions with the signal speed, which is the local sound speed plus the local flow velocity. By tracking this perturbation signals, valuable information on the flowfield gasdynamics can be obtained. In particular, this approach represents another way to find the catch-up/sonic point, as the downstream perturbations can communicate to the reflection point only if the sonic point has been reached. Locks and Dewey [9] were one of the earliest researchers who applied an experimental diagnostics technique using weak waves in order to evaluate the sonic criterion for rigid inclined surfaces. Skews and Kleine [3] expanded the diagnostics technique based on the tracking of weak perturbations, in combination with high speed time-resolved imaging, to a wide variety of shock wave flows.

In order to simulate this technique numerically, it is required to generate perturbation signals. One way is to use small perturbation sources, such as small bumps/grooves on the boundary of the flow domain, similarly to the experimental perturbation sources. It may be considered as direct numerical modeling of the perturbation technique introduced by Skews and Kleine [2]. However, this method

would be very challenging and expensive computationally because in order to capture the evolution of such weak waves a very fine mesh is required. In the present paper we implement tracking of *imaginary, infinitesimally weak* perturbations as a postprocessing procedure performed after each time step of CFD simulation. Prior to commencing a simulation, the number and location of perturbation sources are decided. The obvious advantage of our approach is that any desired number of perturbation sources can be used. Each perturbation source is considered to be initiated when the incident shock wave reaches its position. From that time moment, the wave front of each initiated perturbation propagates in the flow field. Being only imaginary and by definition infinitesimally weak, these waves do not have any effect whatsoever on the flow field. This constitute another advantage over physical experiments in which the disturbances should be of some finite intensity to be visible and hence the degree of their influence on the flow field is a matter of concern.

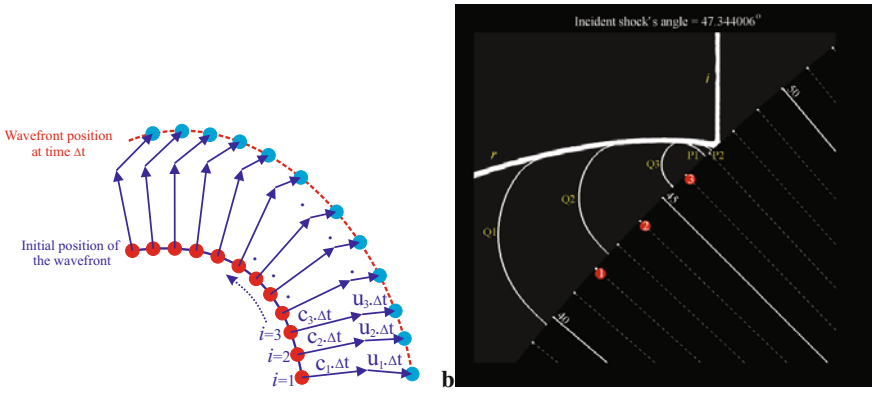

Fig. 2 Illustration of the perturbation technique: (**a**) Schematics of disturbance wave front advancement in the flow field by time step Δt; (**b**) A frame of the CFD movie demonstrating the evolution of the incident and reflected shocks as well as three disturbance fronts (their initiation points on the cylinder's surface are indicated as circles)

The perturbations propagate with the local speed of sound relatively to the fluid while the fluid itself moves with the local flow velocity relatively to the laboratory frame of reference. In order to track the weak perturbation wavefront the Huygens–Fresnel principle [10] is applied. According to this principle each point at a wavefront can be considered as a new perturbation source point. The propagated disturbance front would represent the envelope of all these perturbations. A schematic illustration of how a disturbance front represented by a set of points (which are not related to grid nodes in any way) is advanced by time step Δt is shown in Fig. 2a.

Figure 2b, which is similar to Fig. 4 of Ref. [2], shows a typical frame of the movie generated from CFD simulation of the unsteady shock reflection from a convex cylinder with three perturbation sources along the cylinder's surface, for an inviscid case. It is seen that the wave front of the third disturbance has already

reached the reflection point (zone). Therefore, the incident shock has already passed the sonic point.

3 Results

Due to lack of space, only a brief summary of results is given here. Detailed reporting with quantitative data will be done elesewhere. Numerical simulations are carried out for three different flow models. The first one is based on the Euler (inviscid, non-heat-conducting) equations and an ideal reflecting surface (the impermeable wall boundary condition). The results of inviscid numerical simulations of the problem with different grid resolutions show that the sonic points obtained with the Mach number- and characteristic-based techniques, coincide with the catch-up point obtained by the perturbation technique, even when using a finite number of perturbation sources. The obtained sonic point converges to the theoretical sonic point given by the two-shock steady-state theory as the grid is refined. At the same time, it is shown that the finite thickness of shock and perturbation fronts (unavoidable in experimental movies) may lead to the detection of the catch-up point at a higher wall angle as compared to its actual location.

The other two models are intended to investigate the influence of viscosity on the sonic/catch-up point. They are both based on the Navier-Stokes equations. At first, the ideal reflected surface is considered: the slip boundary condition is imposed on the wall, i.e., the boundary layer is not modeled but the finite physical thickness of shock waves is faithfully reproduced. The obtained results show that with finite shock thickness the sonic point is reached later, at lower wedge angles, as compared to the fully inviscid case. The last model employs the non-slip boundary condition on the wall, thus accounting for the presence of a boundary layer on the cylinder wall behind the incident shock wave. Since in this model the flow velocity at the wall is zero, in the frame of reference moving with the velocity of the reflection point (zone) the flow velocity is supersonic at the wall and within a portion of the boundary layer adjacent to the wall. Therefore, the sonic point cannot be obtained on the reflection surface for this case (neither with the Mach number based technique nor with the characteristic based technique). The perturbation technique still can be applied. It shows that the disturbance front may reach the reflection zone (the zone of intersection of the incident and reflected shocks which have a finite physical thickness determined by viscosity), however, this happens at some distance from the cylinder's surface. This may be considered as the generalization of the catch-up point concept for the fully viscous case. The catch-up point obtained in this way is reached even later, at lower wedge angles, as compared to the fully inviscid case and the viscous case with the slip boundary condition.

4 Conclusion

The determination of the sonic point in an unsteady flow is an important aspect in the field of shock reflections. A new experimental attempt in this area [2] led us

to conclusion that, in general, it is necessary to distinguish the sonic point and the catch-up point. In this paper, three techniques for determination of the sonic/catch-up point in unsteady shock reflection based on numerical flowfield analysis are introduced. Our results with these techniques regarding the sonic/catch-up point location are not in agreement with the experimental results [2], according to which the catch-up point is reached earlier (at higher wall angles) as compared to the two-shock theory predictions. From our study, for the inviscid case the sonic point and the catch-up point are actually the same points, which converge to the theoretical sonic point with grid refinement. For viscous simulations with the slip boundary condition the sonic and catch-up points are again the same points, but the viscous effects (finite shock thickness) cause the sonic/catch-up point to be delayed (happened at lower wall angles) as compared to the two-shock theory. Even larger delay for the catch-up point is obtained for the viscous case with the non-slip boundary condition (in the presence of boundary layer). The causes of the disagreement between the experiments and numerics are to be subjected to further studies. One possible reason is that the shock thickness on experimental images exceeds the shock physical thickness by a few orders of magnitude. Our attempts to imitate such images numerically indicate that this may lead to the detection of the catch-up point at higher wall angles.

Acknowledgments. The present study is supported in part by the NSERC Discovery grant RGPIN/298232-2009 and the FQRNT Team grant PR-126114.

References

1. Ben-Dor, G.: Shock wave reflection phenomena, 2nd edn. Springer (2007)
2. Skews, B.W., Kleine, H.: J. of Fluid Mech. 654, 195–205 (2010)
3. Skews, B.W., Kleine, H.: Experiments in Fluids 46(1), 65–76 (2009)
4. Drikakis, D., Ofengeim, D., Timofeev, E., Voionovich, P.: J. of Fluids and Structures 11(6), 665–691 (1997)
5. Hakkaki-Fard, A., Yu Su, Y., Timofeev, E.: Numerical modeling of shock wave front structure using the Navier-Stokes equations and adaptive unstructured grids. In: Proc. 17th Annual Conf. of CFD Society of Canada, Ottawa, May 3-5, 6 p (2009)
6. Ben-Dor, G., Takayama, K.: Shock Waves 2(4), 211–223 (1992)
7. Ben-Dor, G., Takayama, K.: AIAA Journal 24(4), 682–684 (1986)
8. Hakkaki-Fard, A., Timofeev, E.: High resolution determination of sonic and detachment angles at shock wave reflection from a circular cylinder. In: Proc. 17th Annual Conf. of CFD Society of Canada, Ottawa, May 3-5, 6 p (2009)
9. Lock, G.D., Dewey, J.M.: Experiments in Fluids 7, 289–292 (1989)
10. Longhurst, R.S.: Geometrical and physical optics, 2nd edn. Longmans, London (1968)

Part XIX
Shock Vortex Interaction

Shock Wave in Turbulent Flow Field

M. Tsukamoto and A. Sakurai

1 Introduction

We consider here the problem of a plane shock wave propagating in a turbulent flow field for the general purpose of investigating phenomenon of shock-turbulence interaction [1]. We compute this using a molecular kinetic model theory approach with the Boltzmann equation and the BGK approximation [2]. In practice, we first prepare an advancing plane shock wave in uniform gas made by shock-tube-flow computation as shown in the pressure distribution in Fig. 1 (right) and then run this into a prefabricated isotropic turbulent field in a square region from one end (Fig. 2). Particular attention is paid to the increasing shock front thickness compared to the shock in a non-turbulent field (see Fig. 3). This thickness is compared with the shock thickness given by mixing-length theory [3] and observational data of a shock-tube-wind-tunnel experiment [4].

2 BOLTZMANN—BGK Equation in Integral Form

We use the following kinetic model of the Boltzmann−BGK equation in integral form [2]

$$f(\xi,\mathbf{x},t+\Delta t) = f(\xi,\mathbf{x}-\xi\Delta t,t) + \Delta t\cdot\nu(\mathbf{x},t)\{f_0(\xi,\mathbf{x},t) - f(\xi,\mathbf{x},t)\}$$

where $f = f(\xi,\mathbf{x},t)$ is the molecular distribution function, $\xi = (\xi_x,\xi_y,\xi_z\xi)$ is the molecular velocity, $\mathbf{x} = (x,y,z)$ is the spatial coordinate, $\nu = \nu(\mathbf{x},t)$ is the collision frequency, and $f_0 = f_0(\xi,\mathbf{x},t)$ is the local Maxwellian. We consider here a two-dimensional (2D) flow and use the reduced distribution functions $g,h(\xi_x,\xi_y,x,y,t)$ given by

M. Tsukamoto · A. Sakurai
Tokyo Denki University
2-2 Kanda-Nishiki-cho, Chiyoda-ku, 101-8457 Tokyo, Japan

$$g = \int f d\xi_z, \qquad h = \int \xi_z^2 f d\xi_z$$

and their local Maxwellians g_0, h_0 given by

$$g_0 = (N/\pi T) exp\{-(C_x^2 + C_y^2)/T\}, \qquad h_0 = T g_0/2$$

derived from the local Maxwellian,

$$f_0 = (N/\pi T) exp\{-C_x^2/T\}, \qquad \mathbf{C} = \xi - \mathbf{u}$$

with density N , temperature T , and flow velocity $\mathbf{u}$ which are expressed in non-dimensional form based on representative density, temperature, and length L. Furthermore, we assume the Maxwell molecular model to have

$$\nu = k_0 N/K_n, \qquad K_n = l_0/L, \qquad , k_0 = 8/5\sqrt{\pi}$$

where K_n, l_0 represent the Knudsen number and the mean free path.

3 Plane Shock Wave in Shock−Tube Computation

We first produce a plane shock wave in a uniform gas by a shock-tube-flow computation. For this, we postulate the shock-tube configuration in Fig. 1(left), where two sections separated by a membrane are filled with gases of different pressures p_1, p_2. Computations are performed by applying the kinetic model equation above to the shock tube experiment. One of the results is presented in Fig. 1(right) in a pressure distribution at different times with $p_1/p_2 = 5$.

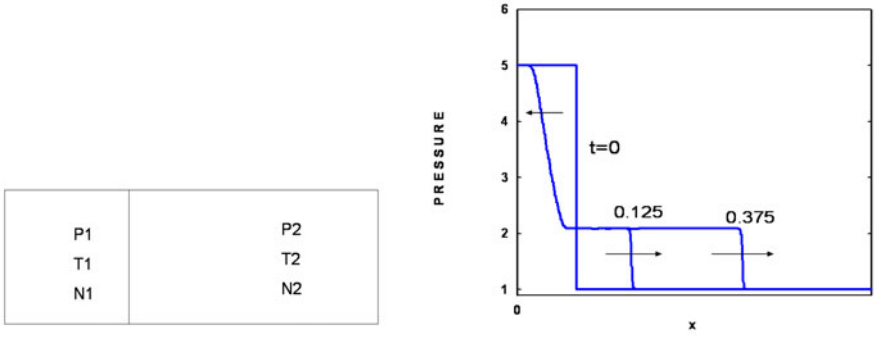

Fig. 1 (left) Shock tube type configuration. ; (right) Plane shock wave Profile propagating in shock tube type computation

4 Isotropic Turbulent Flow Field

We consider 2D developed isotropic turbulence [2] that is space periodic in a square region. This turbulence is produced from a random initial condition set at time $t = 0$ in a local Maxwellian f_{00};

$$f_{00} = \frac{N_{00}}{\pi T_{00}} exp\{-C^2/T_{00}\}, \qquad \mathbf{C} = \xi - \mathbf{u}_{00}$$

with a random velocity field given by

$$\mathbf{u} = \mathbf{u}_{00} = (u_{00}, v_{00}) = \sum_{\mathbf{n}} \mathbf{a}(n_1, n_2) \sin 2\pi\{n_1 x + n_2 y + \varepsilon_{\mathbf{n}}(\mathbf{n})\} + (U, V), n_{1,2} = 0, \pm 1, - - - \pm 4.$$

where

$$a = |\mathbf{a}| = \sqrt{E}, \quad E = \alpha^2 k^2 e^{-(k/k_0)^2},$$
$$\mathbf{k} = 2\pi\mathbf{n}, k = |\mathbf{k}| = 2\pi|\mathbf{n}| = 2\pi\sqrt{n_1^2 + n_2^2}, \qquad \alpha, k_0 \textit{ are constants}$$

$\varepsilon_{\mathbf{n}}(\mathbf{n})$ represents random numbers in [0,1], U and V represent (x, y)-components of the mean velocity, number density $N_{00} = 1$, and temperature $T_{00} = 1$.

One example of results for $U = V = 0$ is depicted in Fig. 2 in the density contours.

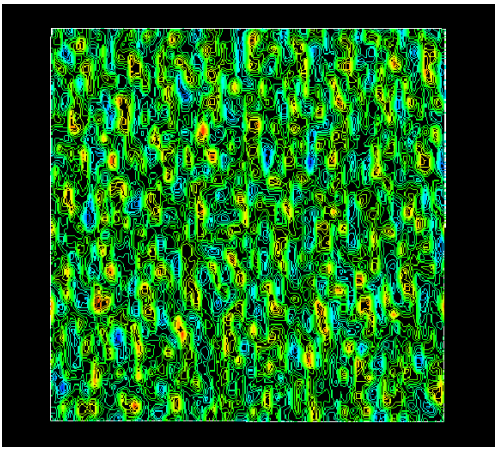

Fig. 2 Density contours for the turbulent flow field at t=0.0012 obtained by square region.

5 Shock Wave in Turbulent Flow Field

We considered two cases: (i) $U = 0.05, V = 0$ and (ii) $U = 0, V = 0.05$, where the number 0.05 represents 17m/sec on a real scale.

Computations are performed for $Kn = 0.01$, time step $\Delta t = 0.0001, 100 \times 100$ divisions for $\mathbf{x}$ and $\Delta\xi_x = \Delta\xi_y = 0.5$ for $-5 < \xi_x, \xi_y < 5$, and $p_1/p_2 = 3.5$. The computation starts from Reynolds number $R_e = 6700$ with $M = 4.5$ from the maximum initial velocity $U = 3.7\xi_0$, where $\xi_0 = \sqrt{2RT_{00}}$.

Example pressure distributions for both cases are presented in Fig.3 ; (left) for case (i) and (right) for case (ii). There the increasing shock front thickness due to the interaction with the turbulent flow is seen in TH, which is about 0.2 on a dimensionless scale for both cases.

The increase in shock thickness due to turbulence is expected to be caused by Reynolds stress, and it is naturally related to the scale of the mixing length in the turbulent flow field. The thickness derived from mixing length theory [3] is given as

$$TH = \frac{k}{C_0}\frac{M}{M^2-1}2\log_e 9, \qquad k = -\overline{u'^2}/\overline{\frac{du}{dx}}$$

where C_0 represents the velocity of sound, k represents eddy kinematic viscosity, M represents the Mach number of a shock wave, and u' and $\bar{u}$ represent respectively the fluctuation and the time average of the velocity. The shock thickness given by the formulae for the present case (0.22) is comparable to the shock thickness given above (0.2).

The result is also compared with data from an experiment [4] in which the interaction between a shock wave produced in a shock tube with grid-generated turbulence in a low-speed wind tunnel is examined. Its pressure data at a point in the tunnel is reproduced in Fig. 4, where we can see pressure data scattering in the turbulent flow of a comparable size as with the flow above.

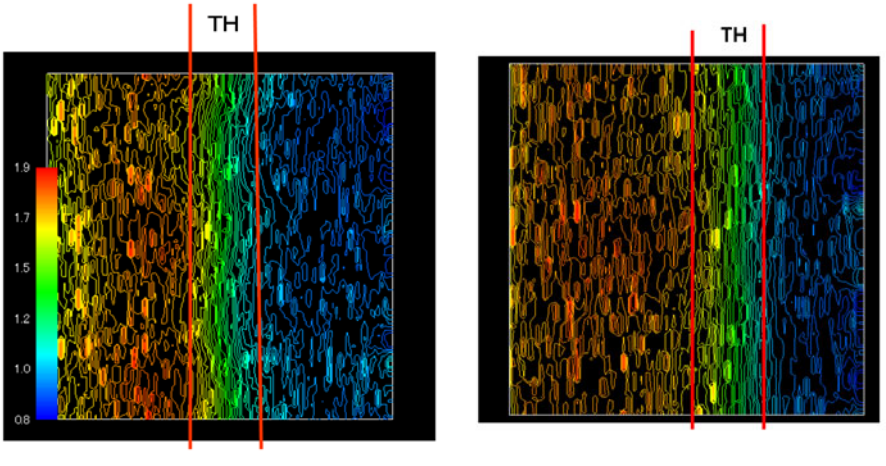

Fig. 3 (left) Plane shock wave in 2D isotropic turbulent flow field whose mean velocity is perpendicular to shock plane surface.; (right) Plane shock wave in 2D isotropic turbulent flow field whose mean velocity is parallel to the shock plane surface. TH:shock thickness

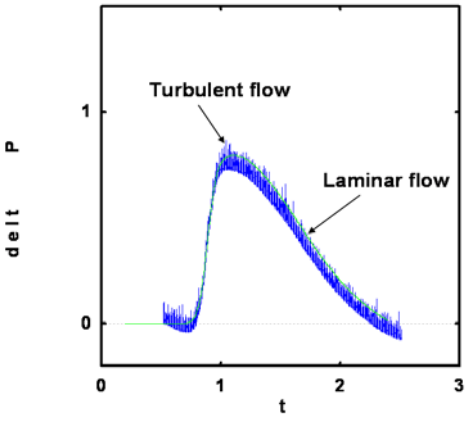

Fig. 4 Pressure vs time change at x=0.75, y=0.5

6 Conclusion

Use of the Boltzmann-BGK equation for the numerical simulation of shock/turbulence interaction is found to be workable, where productions of a plane shock wave by shock-tube type computation as well as a two-dimensional turbulent flow field and their interaction are performed. Widening of the shock front thickness due to turbulence is comparable in size with the ones by a mixing length theory and shock-tube/wind- tunnel experiment.

References

1. Hadjadi, A.: High-fidelity Numerical Simulation of Shock/Turbulence and Shock/Vortex Interaction. In: Proc. Int. Shock Wave Symp., vol. 27, pp. 881–885 (2008)
2. Sakurai, A., Takayama, F.: Molecular Kinetic Approach to the Problem of Compressible Turbulence. Phys. Fluids 15(5), 1282–1294 (2003)
3. Sakurai, A.: On the Thickness of Plane Shock Waves in a Gas in Turbulent Motion. J. Phys. Soc. Japan 5(2), 114–117 (1950)
4. Takagi, D., Matsuda, A., Sasoh, A., Ito, S., Nagata, K., Sakai, Y.: Pressure Modulation of Weak Shock Wave Through Turbulent Flow. AIAA paper, AIAA-2010-4472 (2010)

Vortex Induced Mach Waves in Supersonic Jets

H. Oertel Sen, F. Seiler, and J. Srulijes

1 Introduction

A supersonic jet is known as a source of remarkable noise which can become intolerable in the neighbourhood of jet engines, cutting torches and other supersonic jet producing devices. The most dangerous part of the noise is emitted in form of Mach waves. They appear inside as well as outside of the jet and are quite regular. The practically ideally expanded supersonic free jet in Figure 1 left hand side shows outside Mach waves visualized by Oertel sen. [1] using a differential interferometer. The Mach waves inside can best be detected by immobilisation records on moving film as shown in Figure 1 on the right hand photo with the w'-Mach waves outside, the w-Mach waves inside and outside and the w"-Mach waves inside.

In the past, the origin of the noise produced by Mach waves was attributed to a multitude of different phenomena. They have been assumed to originate inside of the jet's boundary layer from turbulence [2] as well as from coherent structures of different nature, e.g. [3] [4]. This is why various investigations were conducted by Oertel sen. [5] [6] at ISL. The kinetics of the Mach waves was investigated extensively using a large variety of interferometric visualization techniques with complementary double exposures or immobilizations on a film moving at the Mach wave speed using a drum camera.

The experiments were performed with the ISL high energy shock tubes using different methods [7] for jet formation (Figure 2). The jets were produced by blowing the jet gas into a vessel in order to control the pressure and temperature of the ambient gas. Cylindrical as well as slit jets have been studied with e.g. exit diameters between 1.9 mm and 20 mm and equality of exit and ambient pressures. On images as in Figure 1, two strong different Mach waves (w and w') can be seen to exist outside the jet as well as two different inside (w and w"). They were found to be produced by "jet boundary layer structures" propagating downstream at the three

H. Oertel Sen · F. Seiler
Karlsruhe Institute of Technology, 5 rue du Général Cassagnou,
D-76131 Karlsruhe, Germany

J. Srulijes
French-German Research Institute of Saint-Louis (ISL), F-68301 Saint-Louis, France

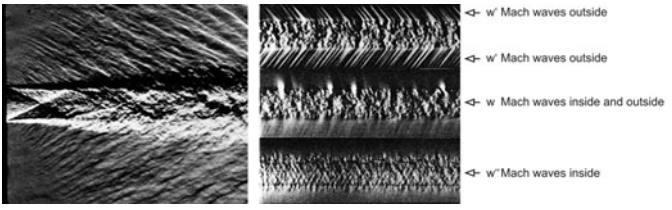

Fig. 1 Mach waves of supersonic Mach 2.1 free jets.

Fig. 2 Jet production: reflected mode left, non reflected mode right.

mentioned speeds. The Mach angles α (w-Mach wave inside and outside), α' (w'-Mach wave outside) and α" (w"-Mach wave inside) were measured and the Mach numbers were calculated by

$$sin\ \alpha = \frac{a_a}{w} = \frac{a_i}{u_i - w},\ sin\ \alpha' = \frac{a_a}{w'},\ sin\ \alpha'' = \frac{a_i}{u_i - w''} \tag{1}$$

The experimental data points in Figure 3 were empirically fitted to the Mach number equations (2 - 4), expressed with u_i the jet speed, and with the jet Mach number $M_i = u_i/a_i$. a_i and a_a are the speeds of sound in the jet's inner resp. in the gas outside.

$$\frac{u_i - w}{a_i} = \frac{w}{a_a} \text{ and } \frac{w}{a_a} = \frac{M_i}{1 + a_a/a_i} \tag{2}$$

$$\frac{u_i - w'}{a_i} = \frac{w'}{a_a} - 1 \text{ and } \frac{w'}{a_a} = \frac{M_i + 1}{1 + a_a/a_i} \tag{3}$$

$$\frac{u_i - w''}{a_i} = \frac{w''}{a_a} + 1 \text{ and } \frac{w''}{a_a} = \frac{M_i - 1}{1 + a_a/a_i} \tag{4}$$

2 Hints for Vortices in the Mixing Layer

Many different attempts of explaining the simple empiric formulae (2-4) theoretically by gasdynamic considerations had failed for a long time. A hint for the processes present in the mixing layer gave the experiments of Poldervaart and Wijands [8] demonstrating that vortex pairs might be the origin of the Mach waves. They took shadowgramms of a much bigger, colder and longer blowing supersonic jet, where they could use periodic spark shock waves for creating successive vortex pairs at the jet exit. Figure 4 shows a picture sequence from [8] with the supersonic jet and

the downstream moving vortices initiated by the spark's shock wave. In Figure 4 the middle of the vortex pair is displaced with speed w. But the other speeds did not correspond to the formulae for w' and w" of Oertel sen. [5] [6].

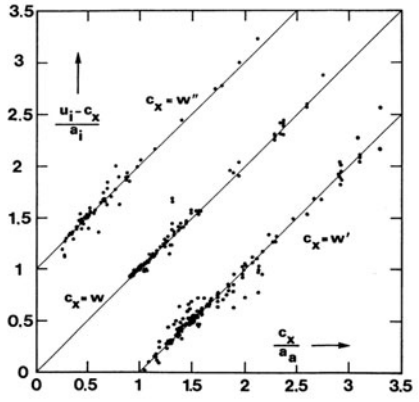

Fig. 3 Experimental Results

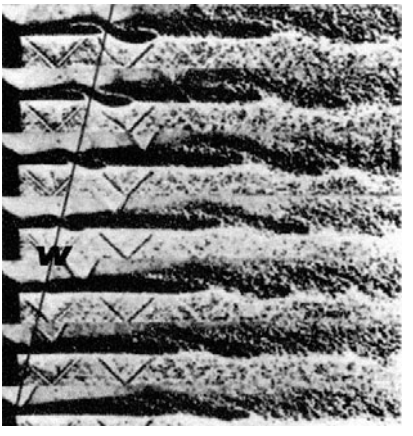

Fig. 4 Picture arrangement from [8]

Shock tube experiments with a jet produced with the reflected shock tube mode (see Figure 2) at a jet Mach number 2 visualized the behaviour of smoke particles in the jet's mixing layer. A thin light sheet illuminates the smoke tracers seeded. The scattered light observed shows clearly the mixing layer well established in Figure 5. The smoke is seeded inside and outside the jet.

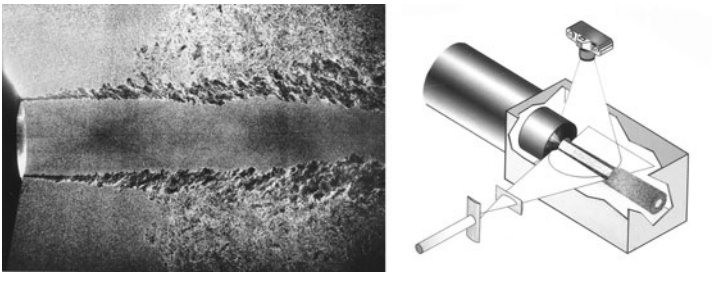

Fig. 5 Smoke particle visualization

An interesting feature is that "black holes" are repeatedly arranged downstream inside of the mixing layer, obviously seen by no light scattering dots. One explanation for that particle behaviour is that the particles are centrifuged out of the vortices and therefore no light is observed from the vortex centres. The "black holes" seen might be a further proof for the formation of vortices inside of the mixing layer.

3 Vortex Pair Formation

In some experiments of Oertel sen. [5] [6] a very thin jet boundary layer developed for a short distance after the jet's exit which could be considered as a shear layer deformation as shown in Figure 6. The deformation forms a convex bulge and a concave indentation and displaces with the constant speed w. At subsonic Mach numbers equal under pressures act on the bulges and over pressures in the indentations. Point symmetric deformations will then last for a long time. In a reference frame moving with speed w at equal Mach numbers at both sides of the deformation, the formula (2) is deduced as:

$$\frac{u_i - w}{a_i} = \frac{w}{a_a} \text{ and } \frac{\mathrm{w}}{\mathrm{a_a}} = \frac{\mathrm{M_i}}{1 + \mathrm{a_a}/\mathrm{a_i}} \tag{5}$$

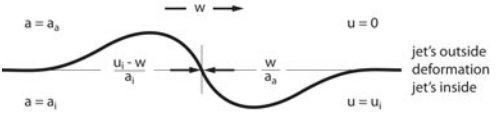

Fig. 6 Deformation of the shear layer

In the case of laminar exit boundary layer vortex pairs arise somewhat downstream by flow instabilities, called Kelvin-Helmholtz-Instability, of the layer deformations. When the boundary layer is already turbulent the vortex pairs are generated immediately at the exit. As mentioned above the source for the Mach waves may be by vortex pairs moving downstream inside of the jet's mixing layer as sketched schematically in Figure 7. The centre of the front vortex moves with speed w' within the inner zone and produces a weak shockwave called w'-Mach wave outside the jet. The centre of the rear vortex moves downstream with speed w'' within the outer zone and produces a weak shockwave called w''-Mach wave inside the jet. The plane with

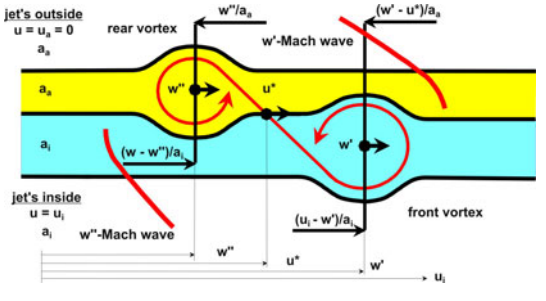

Fig. 7 Vortex pair formed inside the mixing layer

the mean flow velocity u^* separates the two zones. Writing the equilibrium conditions for the two vortices within two frames moving at their quite different speeds w' and w", in the w'-system the opposite subsonic flows over the front vortex and in the w"-system over the rear vortex produce equal under pressures at the following equal Mach numbers

$$\frac{u_i - w'}{a_i} = \frac{w' - u^*}{a_a} \text{ and } \frac{\mathrm{u}^* - \mathrm{w}''}{\mathrm{a_i}} = \frac{\mathrm{w}''}{\mathrm{a_a}} \tag{6}$$

An up till now neglected effect would come into play, called the "dredging effect" of the vortices. The two vortices continuously entrain fresh jet gas into the inner zone and fresh ambient gas into the outer zone. The smoke image in Figure 5 shows obviously the entrainment of inner and outer smoke particles into the mixing layer. Details on the vortex pair postulation are given in [9] [10]. As a result of this gas transport into the mixing layer the sound speeds a_a and a_i in the two zones each are practically constant.

The determination of u* can be done by the following claim:

$$\frac{u_i - w''}{a_i} = \frac{w'}{a_a} \text{ at } \mathrm{a_a} = \mathrm{a_i} \tag{7}$$

Together with the three equations (6) and (7) we find that

$$\frac{u^*}{a_a} = \frac{w}{a_a} = \frac{M_i}{1 + a_a/a_i} \tag{8}$$

Finally with w the following relations come out:

$$\frac{u_i - w'}{a_i} = \frac{w' - w}{a_a} \text{ and } \frac{\mathrm{w}'}{\mathrm{a_a}} = \frac{\mathrm{M_i} + \mathrm{w}/\mathrm{a_a}}{1 + \mathrm{a_a}/\mathrm{a_i}} \tag{9}$$

$$\frac{u_i - w''}{a_i} = \frac{w''}{a_a} \text{ and } \frac{\mathrm{w}''}{\mathrm{a_a}} = \frac{\mathrm{M_i} - \mathrm{w}/\mathrm{a_a}}{1 + \mathrm{a_a}/\mathrm{a_i}} \tag{10}$$

In the special case $w/a_a = 1$ at which the experimental studies have been undertaken, the theoretical relations (5, 9, 10) correspond exactly to the empirical ones (2, 3, 4).

4 Limitations and Remarks

The domain of validity of the formulae is limited by some Mach number considerations. The w'- and the w"-Mach waves can only exist at the following conditions:

$$w' > a_a \quad \text{at} \quad \mathrm{M_i} > \frac{(1 + \mathrm{a_a}/\mathrm{a_i})^2}{2 + \mathrm{a_a}/\mathrm{a_i}} \quad \text{and} \quad \mathrm{u_i} - \mathrm{w}'' > \mathrm{a_i} \quad \text{at} \quad \mathrm{M_i} > \frac{(1 + \mathrm{a_a}/\mathrm{a_i})^2}{(1 + 2\mathrm{a_a}/\mathrm{a_i})} \tag{11}$$

Both Mach waves may disappear when one of the two vortices has supersonic relative Mach numbers and at least the regularity can only exist for:

$$w'' < a_a \quad \text{at} \quad M_i < \frac{a_i}{a_a}(1 + a_a/a_i)^2 \quad \text{and} \quad u_i - w' < a_i \quad \text{at} \quad M_i < (1 + a_a/a_i)^2 \quad (12)$$

Only in the yellow domain of Figure 8 the conditions for regular w'-Mach waves are fulfilled. The boundaries (11) are very strong ones as proofed by Oertel [11].

Testing the limitations (12) experiments show a weak transition in suppressing the Mach wave production by putting more energy into the jet. This limitation lets the vortex pairs vanish by supersonic overpressures on the bulges. With growing distance from the jet exit the front vortex overtakes the rear vortex of the preceding one for forming one big vortex moving with velocity w. Bigger jets having much longer mixing layers must finally lead to create long chains of jet surrounding vortices travelling at this speed w. This might be the domain of considerations like those of Tam [12] and others. Their calculations of waves without beginning and end are certainly not able to describe the phenomena near the jet exit. Tam deals with the final phase far away from the exit.

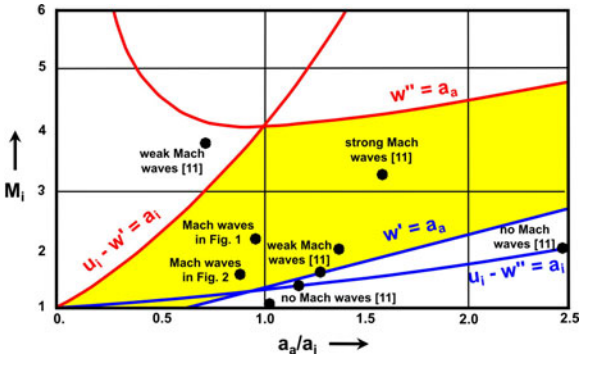

Fig. 8 Range of validity

References

1. Oertel, H.: Coherent structures producing Mach waves inside and outside of the supersonic jet. ISL report CO 82/218 (1982)
2. Ffowcs Williams, J.E., Maidanik, G.: The Mach wave field radiated by supersonic turbulent shear flows. J. Fluid Mech. 21(4), 641–657 (1965)
3. Tam, C.K.W.: Directional acoustic radiation from a supersonic jet generated by shear layer instability. J. Fluid Mech. 46(4), 757–768 (1971)
4. Michalke, H.: A note on the spatial jet-instability of the compressible cylindrical vortex sheet. DLR report, DLR-FB-70-51 (1970)
5. Oertel, H.: Jet noise research by means of shock tubes. In: 10th Int. Shock Tube Symposium, Japan, Kamimoto (1975)

6. Oertel, H.: Mach wave radiation of hot supersonic jets investigated by means of a shock tube and new optical techniques. In: 12th Int. Symp. on Shock-Tubes and Waves, Jerusalem (1980)
7. Oertel, H.: Stossrohre. Springer, Wien (1966)
8. Poldervaart, L.P., Wijands, A.P.J.: Sound pulse-boundary layer interaction studies. Technische Hogeschool Eindhoven, Netherlands (1974)
9. Sen, H.O., Seiler, F., Srulijes, J.: New Explanation of Noise Production by Supersonic Jets with Gas Dredging. In: Dillmann, A., Heller, G., Klaas, M., Kreplin, H.-P., Nitsche, W., Schröder, W. (eds.) New Results in Numerical and Experimental Fluid Mechanics VII. NNFM, vol. 112, pp. 389–397. Springer, Heidelberg (2010)
10. Sen, O.H., Seiler, F., Srulijes, J.: New explanation of noise production by supersonic jets. ISL-report PU 695/2010 (2008)
11. Oertel, H.: Kinematik der Machwellen von Überschallstrahlen. ISL-report R 112/78 (1987)
12. Tam, C.K.W., Fang, Q.H.U.: On the three families if instability waves of high-speed jets. J. Fluid Mech. 201, 447–484 (1989)

Post-shock Pressure Modulation through Grid Turbulence

D. Takagi, S. Ito, K. Takeya, A. Sasoh, K. Nagata, and Y. Sakai

1 Introduction

Interaction between a shock wave and turbulence gives challenging research problems. Interactions between a shock wave and a vortex or a flow element of the same kind have been studied in various manner.[1-8] Impacts of a shock wave to turbulence intensity is investigated by Honkan et al.[1] and Barre et al.[2]. On the other hand, the impact of isotropic turbulence on a shock wave has been studied mainly numerically[8]. Experimental data of shock wave and isotropic turbulence are currently insufficient. The purpose of this study is to obtain experimental data on the relationship between a post-shock overpressure and characteristics of isotropic turbulence.

2 Apparatus

In this study, turbulent flow is generated in a low-turbulence wind tunnel with a square grid. The length and the cross section of the wind tunnel were 4 m and 0.994 m $\times$ 0.46 m, respectively. A square grid was set at the entrance, and the test section of shock wave-turbulence interaction was 1.5 m downstream (Fig. 1.) In Region A in Fig. 1, the distribution of U_∞ (time-averaged flow speed) was set either to 10.0 m/s or to 17.5 with a spatial variation of better than $\pm$0.6 % on a basis; the turbulent intensity without a grid was 0.6 $\pm$ 0.05 %.

Two kind of square grids were used. Grid-A, made of steel, had a circular cross-section of 5mm in diameter, separation distance of 25 mm. Grid-B (Fig. 2), made of aluminum, had a square cross section of 20 mm $\times$ 20 mm, separation distance of 100 mm. The turbulent intensity with Grid-A in Region A was 1.9 $\pm$ 0.1 % with a length scale of 17.5mm; with Grid-B 5.8 $\pm$ 0.4 % with length scale of 59.5mm. In the range

D. Takagi · S. Ito · K. Takeya · A. Sasoh · K. Nagata · Y. Sakai
Graduate School of Engineering, Nagoya University, Furo-cho, Chikusa-ku,
Nagoya 464-8603, Japan

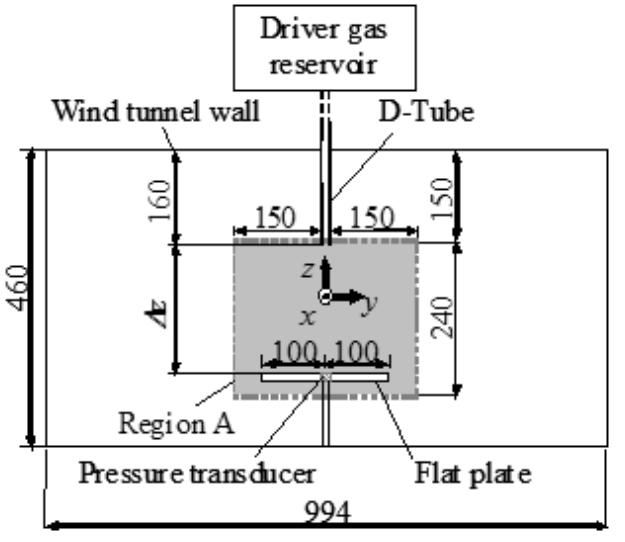

Fig. 1 Schematic illustration of test section, flow direction towards the reader (length unit in mm)

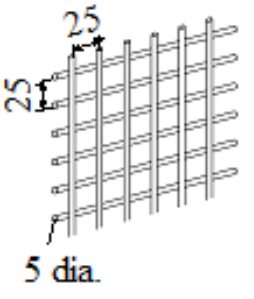

Fig. 2 Square grids (length unit in mm)

of $y = 0$ mm, -70 mm $\leq$ z $\leq$ 90 mm (see Fig. 1), turbulent intensities measured using an X-type anemometer were 5.9 $\pm$ 0.2 % in the longitudinal direction and 5.2 $\pm$ 0.8 % in a transverse (y), respectively. In the test section (Fig. 1), a shock wave was ejected from a 5.4-mm-inner-dia., 3.55-m-long tube, which hereafter will be referred to as eD-tube,f which was connected to a diaphragm-less shock tube using a quick piston valve (Oguchi piston, Oguchi et al.[9], Fig. 3). In order to prevent freezing, the air inside of the driver gas reservoir (p_s = 1.0 MPa) and the sub-chamber were purged to introduce dry air from a cylinder. Along D-tube, three pressure transducers (PCB Corp., H113A21, 3.6 mV/kPa, 500 kHz) were set to measure a shock Mach

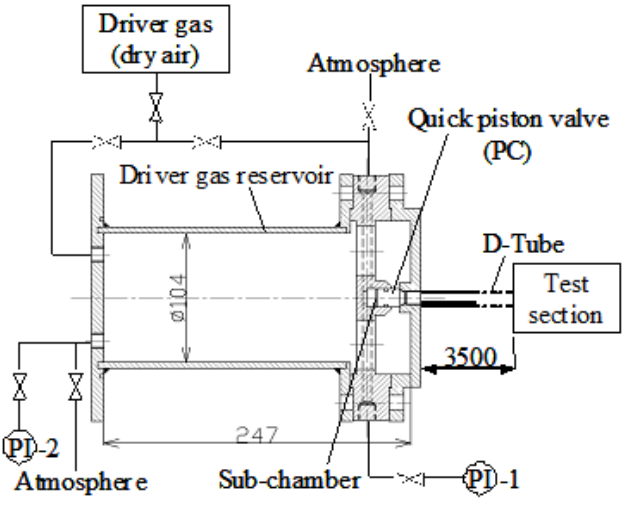

Fig. 3 Schematic illustration of shock wave generator (length unit in mm).

number. with a resolution in shock Mach number of 0.025. The average value and standard deviation of shock Mach number was 1.15 $\pm$ 0.00 (0.1 %) at 1.55m from the exit of D-tube.

The shock wave ejected from the open-end of D-tube propagated across the grid turbulence through a vertical distance, normal to the flow, which was ranged from 100mm to 200mm in Region A of Fig. 1. Vertical to the shock-wave propagation, that is parallel to the negative z-direction, an aluminum flat plate, 200 mm $\times$ 200 mm $\times$ 8.8 mm (thickness), was set. The pressure transducer (PCB Corp., M102B18, 14.9 mV/kPa, 500 kHz) was flush-mounted on the aluminum plate to measure the time-variation of overpressure ΔP, its peak value being denoted by ΔP_{peak}. To measure the time histories of ΔP, pressure transducer which had shortest rise time (1μs) and high sensitivity (14.9 mV/kPa) in the market was chosen. But in this experiments, the signal from the pressure transducer was overshot due to the mechanical resonance of the pressure transducer itself, because ΔP_{peak} was of the order of 1 kPa, that is as small as 1/700 of the full range of the overpressure. In order to take these effects into consideration, overshot ratio of 1.48 was measured a priori through shock-tube measurements. In the following experimental data, the peak value in the overpressure value will be corrected using this number.

3 Results and Discussion

Under each experimental condition presented hereafter, either thirty or one hundred measurements were conducted. The separation distance between the exit of the D-tube and the flat plate was set to 200 mm. The root mean square in the flow velocity

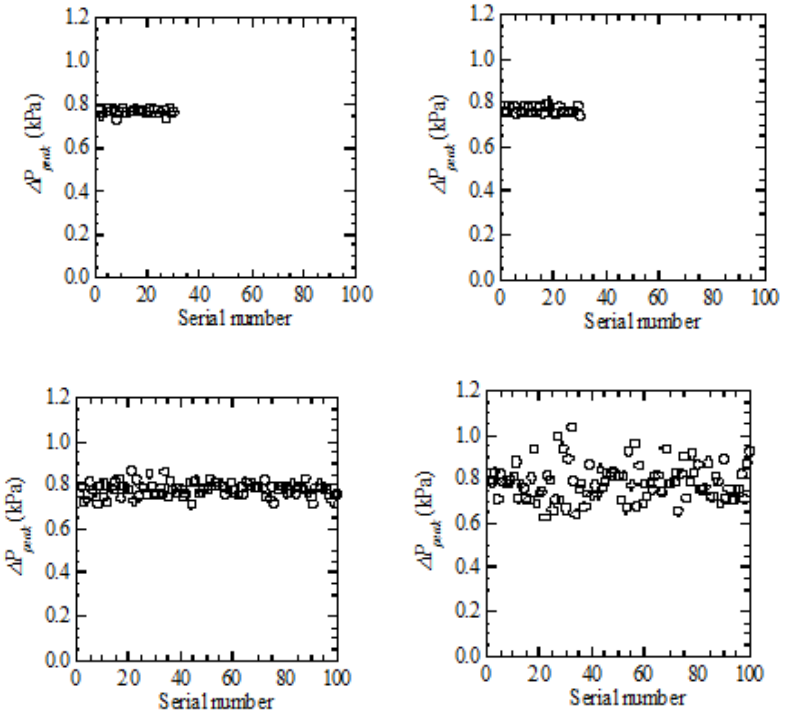

Fig. 4 Scatter in peak over pressure, (**a**) $U_\infty = 0$m/s without grid, (**a**) $U_\infty = 17.5$m/s without grid, (**c**) $U_\infty = 17.5$m/s with Grid-A, (**c**) $U_\infty = 17.5$m/s with Grid-B,

was varied by two methods, by varying the flow speed or using different grids. with U_∞ = 17.5 m/s and without grid (Fig. 4(b)), $\Delta P_{\text{peak}} = 0.772 \pm 0.015$ kPa. The standard deviation with the flow and Grid-A (Fig. 4(c), $\Delta P_{\text{peak}} = 0.784 \pm 0.032$ kPa) become twice; with Grid-B 5 times (Figs. 4(d) $\Delta P_{\text{peak}} = 0.788 \pm 0.081$ kPa). However, differences in average value among those conditions were 0.016kPa at most, which is only 24 % of the difference in standard deviations.

The turbulence intensity was varied also by varying the flow speed. With Grid-B, the peak over pressure was $\Delta P_{\text{peak}} = 0.777 \pm 0.048$ (6.2%) at U_∞ = 10 m/s (Fig. 6(a)). Yet with U_∞ = 17.5 m/s (Fig. 4(d)), the standard deviation became 1.69 times larger ($\Delta P_{\text{peak}} = 0.788 \pm 0.081$ kPa). The standard deviation characteristics in the post-shock overpressure which are presented in the previous two paragraphs can be generalized using U_{rms} as a control parameter, see Fig. 6.

ΔP_{peak} was modulated 1.9 % even in case without flow caused by uncertainty came from characteristics of experimental devices and hot wire anemometers had electrical noise which modulated 0.1 % of U_{rms}.

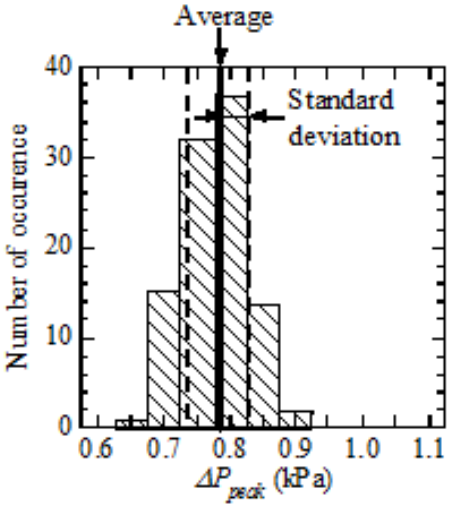

Fig. 5 Histograms, $U_\infty = 17.5$m/s, Grid-A

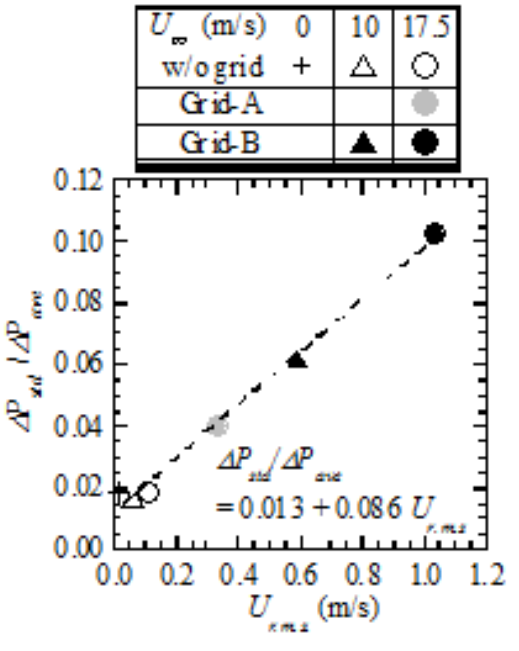

Fig. 6 Peak over pressure modulation vs. U_{rms}

The relative intensity (value of standard deviation divided by average) between U_{rmd} and ΔP_{peak} can be fit to a linear equation of $\Delta P_{\mathrm{peak}}/\Delta P_{\mathrm{peak}} = 0.013 + 0.086\ U_{\mathrm{rms}}$ in the range of experimental condition, see Fig. 6.

4 Conclusion

The standard deviation in ΔP_{peak} increases linearly with ΔP_{peak}.

Acknowledgements. The authors would like to express our gratitude to Mr. Kumazawa and Mr. Sumi, Technical Division, Graduate School of Engineering, Nagoya University for their valuable technical assistances. This research was supported by Japan Aerospace Exploration Agency project as No. 27-J-J6711, and by Japan Society for Promotion of Science as Grant-in-Aid for Scientific Research (S), No. 22226014.

References

1. Honkan, A., Andreopoulos, J.: Phys. Fluids 4, 11 (1992)
2. Barre, S., Alem, D., Bonnet, J.P.: AIAA J. 34, 968 (1996)
3. Ribner, H.S.: AIAA J. 36, 494 (1998)
4. Barre, S., Alem, D., Bonnet, J.P.: AIAA J. 36, 495 (1998)
5. Ribner, H.S., Morris, P.J., Chu, W.H.: J. Acoust. Soc. Am. 53, 926 (1971)
6. Lipkens, B., Blackstock, D.T.: J. Acoust. Soc. Am. 103, 148 (1998)
7. Kim, J.H., Sasoh, A., Matsuda, A.: Shock Waves 20, 339 (2010)
8. Hasegawa, T., Noguchi, S.: Int. J. Comput. Fluid Dynamics, 63 (1997)
9. Oguchi, H., Funabiki, K., Sato, S., Hatakeyama, M.: 1, 233 (1991)

Aerodynamic Vibrations Caused by a Vortex Ahead of Hemisphere in Supersonic Flow

Takafumi Kawamura and Toshiharu Mizukaki

1 Introduction

Parachutes are often used for planetary-entry and re-entry. Most of cases, parachutes are deployed at supersonic speed. Therefore, it is necessary to obtain aerodynamic characteristics at supersonic speed. However parachutes have wrinkles and seams. They make it difficult to study aerodynamic characteristics of the parachute shape. Therefore, experimental studies using solid models have been conducted from the 1960s re-entry program of the US [1]. In particular, Helmut G. Heinrich et al. visualized shockwaves, and shockwave vibrations in Mach number 3 [2]. These shockwave vibrations make the flow unstable, and the unstable flow gives model vibrations. They are risks of break.Therefore, Helmut G. Heinrich suggested an improved model.

Re-entry and planetary entry have also been conducted recently in Japan, so parachute shape characteristics have gained attention. Hiraki et al. conducted experiments using solid Hemisflo models, for the general shape of a supersonic parachute [3]. They attached pressure sensors on the model, and gained pressure distribution on the model. These experiments conducted at Mach number 1.5 to 4.0. The result of these experiments indicated that the cycle of shockwave vibrations is 1.2 ms. Takakura et al. conducted Computer Fluid Dynamics (CFD) for the purpose of investigating the cause of shockwave vibrations by using a High-resolutional WENO scheme. The results indicated pressure waves occurred near the model edge and spread toward the shockwave when Mach number was increased from 4.0 to 4.2. The spreading pressure waves interfere with the detached shockwave and caused shockwave vibrations.

Takafumi Kawamura
Graduate School of Engineering, Tokai University 4-1-1 Kitakaname,
Hiratsuka-shi, Kanagawa-ken, Japan

Toshiharu Mizukaki
School of Engineering, Tokai University, 4-1-1 Kitakaname,
Hiratsuka-shi, Kanagawa-ken, Japan

The final target of this study is to suggest a shockwave vibrations removed model. At the first step in this target, we attached a test model in a supersonic wind tunnel, and visualized pressure waves and shockwave vibrations by using Schlieren system with high speed camera. This paper shows the result of these experiments.

2 Experimental Method

Figure 1 shows a test model that mimicked a parachute deployed shape.

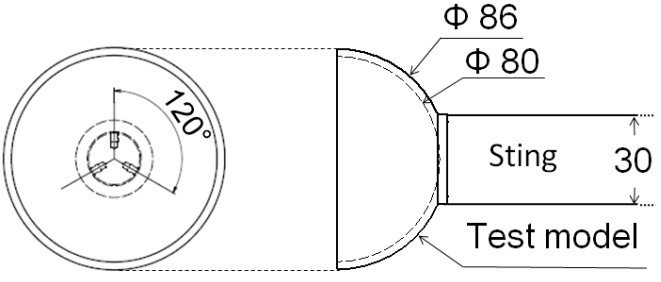

Fig. 1 Schematic of test model

The test model was a hemispheric bowl model with no porosity, 80 mm inner diameter and 86 mm outer diameter (Fig. 1). The test model was made by of 3 mm stainless steel. The test model has tap holes every 120 degrees at the top of the bowl shape to attach a wind tunnel with bolts. The hollow side faced windward. This hemispheric bowl model mimicked a Hemisflo shape, which is one of the supersonic parachute shape. Hemisflo has high drag over Mach number 1.5 to 2.5 and high stability. The sting diameter was 25 mm and the blockage area was 1.6 percent toward the test section, and the effect to the flow was quite small.

Table 1 shows specifications of supersonic wind tunnel.

Table 1 Specifications of wind tunnel

Type	Open Circuit Variable Pressure Type (Using Ejector near Mach Number 4.0)
Optical Window	0.6 m diameter
Test Section	0.6 m square
Mach number	1.5 - 4.0
Operating time	more than 30 s

Experiments were conducted by using the supersonic wind tunnel located at the Sagamihara Campus of Japan Aerospace Exploration Agency (JAXA). This wind tunnel uses an ejector at a high Mach number, around 4.0. Mach number and static pressure at a screen tube (P_0) can be selected for experiments.

Figure 2 shows Schlieren system using a high speed camera for the purpose of visualization.

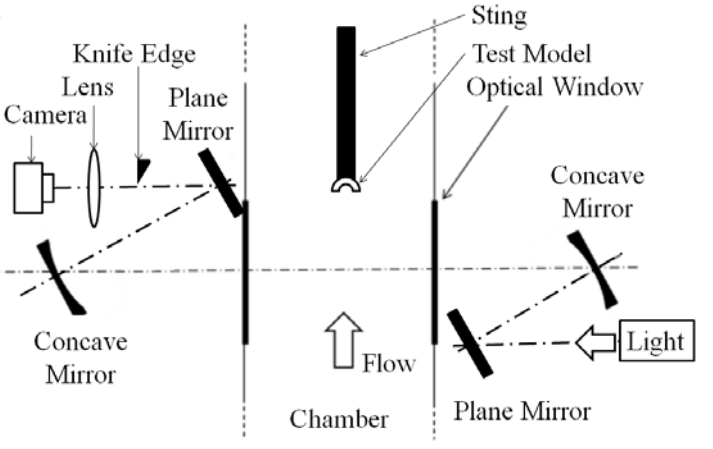

Fig. 2 Schematic of Schlieren system using high speed video camera

A high pressure Xenon lamp (500W, Ushio co., XB10201AAA) was used for a light source. The light was become collimated light by a 0.6 m diameter concave mirror via a 0.3 m diameter plane mirror. The light thorough the test section, and receive disturbance. The light was converged by the concave mirror, and changed direction toward the high speed camera. A knife edge was inserted at a third focused light point, the light projected on a recording surface of the high speed camera. The high speed camera (Vision Research co., Phantom V7.1) was used for the purpose of record photograph. Resolution was 256 by 256, interval was 200 μs, exposure was 10 μs. Because it is known from Hiraki et al.s research that the shockwave vibrations cycle is 1.2 ms [3].

Table 3 shows experimental conditions. It is known from Hiraki [3] and Takakura [4] reported that shockwave vibrations in front of the shape exist over Mach number 3. The experimental conditions are shown in Table 2. These pressure conditions were selected for the purpose of long time run.

Table 2 Experimental condition

Mach Number	P_0 (kPa)	Ejector (kPa)	Angle of attack
2.0	210	non	0
3.0	440	non	0
3.5	406	392	0
4.0	510	490	0
4.0	593	392	0

3 Results and Discussion

Figure 3 shows the representative example of an experiment at Mach number 2.0. Only stable detached shockwave was visualized at Mach number 2.0.

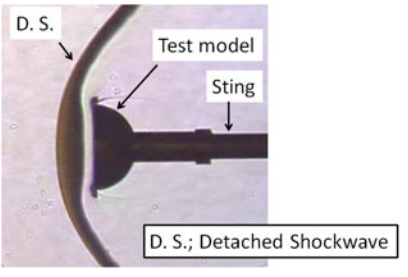

Fig. 3 Representative Example of an experiment at Mach number 2.0

Shockwave vibrations were detected at Mach number 3.0, 3.5, and 4.0. Figure 4 shows representative example of an experiment at Mach number 4.0.

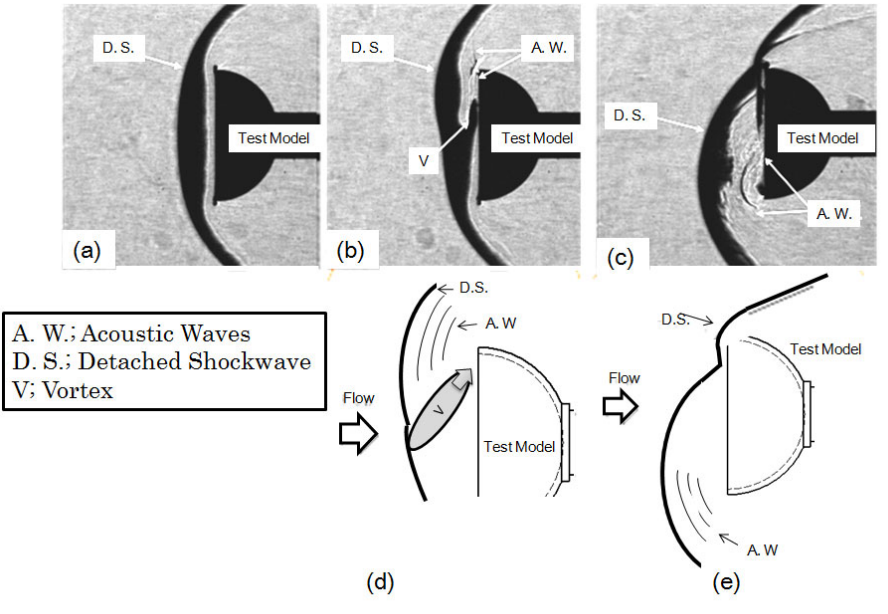

Fig. 4 Representative example of an experiment at Mach number 4.0

This paper explains on the supposition that the phenomena taken by the high speed camera were two-dimension phenomena. The detached shockwave in front of the test model was observed when the mean flow was statically determined (Fig. 4 (a)). The vortex occurred near the center of the detached shockwave 6.2 s after the mean flow, however, was statically determined. The vortex spread and moved to the edge of the model. It is agreed with CFD results [4]. A simplify phenomena shows at Fig. 4 (d). The vortex reached the edge of the model 1.2 ms after it occurred. After that, it spilled from the model and compression waves spread to the windward. In this paper, this side, vortex reached the edge at 1.2 ms after it occurred, called the right side compared with a center axis thorough the sting and test model. Compression waves interfered with the detached shockwave. The detached shockwave was moved to the right side of windward. At this time, the detached shockwave was located in front of the stable detached shockwave at Fig. 4 (a) (Fig. 4 (b)). After 600 μs, the spill from the model and compression waves were stopped, and the detached shockwave moved leeward. At the same time, the leeward of the detached shockwave went to the inside of the model. After 200 μs, compression waves occurred from the right side of the model edge. The compression waves pressed the detached shockwave to the right side of windward again. These sequences of vibration were successively observed.

At the time when 6.4 seconds after the mean flow statically determined, the top of the vibrated detached shockwave was moved to the left side (Fig. 4 (c)), simplify phenomena was shown in Fig. 4 (e).

The top of the shockwave vibrations gradually moved to the left side. It is because the phenomena rotated clockwise or anticlockwise around the center axis of the test model [3].

4 Summary

The solid hemispheric model attached in the supersonic wind tunnel, and experiments conducted at Mach number 2.0, 3.0, 3.5, and 4.0. Schlieren system with high speed camera was used for the purpose of visualization. The results indicate below.

- Shockwave vibrations were observed at Mach number 3.0, 3.5, 4.0.
- Shockwave vibrations were not observed at Mach number 2.0.

The cause of the shockwave vibrations was visualized. The results indicate below.

- The vortex occurred near the top of the detached
- The vortex moved the edge of the model, and turned out compression waves.
- Compression waves push the detached shockwaves to the right side of the windward.

Continuous shockwave vibrations were observed. The results indicate below.

- Compression waves that occurred previous shockwave vibrations push the detached shockwave to the right side of the windward
- Compression waves were disappeared 600 μs after the detached shockwave moved toward the right side of the windward.

- The detached shockwave moved leeward as a result of disappearance of compression waves. The leeward side of the detached shockwave intrude into the left side of the test model simultaneously.
- Compression waves appear again 200 μs after the previous item, and push the detached shockwaves toward the right side of the windward again.

References

1. Charczenko, N.: Wind tunnel investigation of conventional types of parachute canopies in supersonic flow. NASA TMX-991 (1964)
2. Heinrich, H.G.: Aerodynamics of the supersonic guide surface parachute. J. Aircraft 3(2), 105–111 (1966)
3. Kojyu, H.: Experimental study of aerodynamics about hemisphere model in supersonic flow, Tokyo university, Japan (2006)
4. Takakura, Y., Hiraki, H., Arai, N.: On the Flow Fields around a Concave Body in Supersonic Flow. In: Proceedings of Symposium on Shock Waves in JAPAN, vol. 18-C-1-3, pp. 259–262 (2008)

Numerical Investigation of 2D/3D Blade-Vortex Interactions

E. Yildirim and R. Hillier

1 Introduction

Vortex interaction with a rotating blade is fundamentally important in understanding the unsteady aerodynamics and aeroacoustics problems arising in a helicopter flight. The blade-vortex interaction (BVI) can occur when the main- and/or tail-rotor blades interact with tip vortices previously shed by preceding high speed blades of the main rotor. Most numerical studies have focused on limiting cases where an idealised vortex interacts with a single, non-rotating blade. Despite the significant differences between a real case scenario of BVIs involving more complex characteristics of blade tip vortices and rotating blades, numerical and computational studies nevertheless provide great insight into the deeper understanding of the fluid mechanics that are relevant to the problem. Our computational modelling approaches this problem in several steps. Firstly the 'impulsive' instantaneous blocking of the column vortex by a flat plate. This was studied theoretically for incompressible motion by Marshall [1], who produced an elegant model for 'area change' waves in the vortex core. Our Computational Fluid Dynamics (CFD) study essentially models this, together with the true compressible pressure wave formation that also arises. In the second step we extend this to the gradual cutting of the vortex by a sharp flat plate that moves, at a finite speed, through the vortex. Finally, we extend this to the gradual cutting of the vortex by a blunt leading edge aerofoil that moves, at a finite speed, through the vortex, which incorporates both the 'blocking' and also stretching and distortion of the vortex lines. In this paper, we present only the 3D numerical computations of a single columnar vortex instantaneously 'blocked' by a flat plate.

E. Yildirim · R. Hillier
Department of Aeronautics, Imperial College London
South Kensington Campus, SW7 2AZ London (UK)

2 Numerical Computation

In this study compressible, inviscid computations are performed based on a finite volume, Godunov type solver, which is second order in space and time. We start the computation with an initialised vortex cross-section profile, and although there is no single accepted distribution, the most commonly used swirl velocity profiles in terms of vortex core radius are represented by the following general expression

$$V_\theta = \frac{\Gamma}{2\pi r_c} \frac{\tilde{r}}{(1+\tilde{r}^{2n})^{\frac{1}{n}}} \tag{1}$$

Here we adopt the $n = 1$ vortex model, also referred to as Sculley's velocity profile.

Marshall [1] defines the axial flow parameter, $I_N = 2\pi r_c w_0/\Gamma$, where w_0 is the vortex core axial velocity and r_c is a measure of the core radius. According to Marshall, for $I_N > 1/\sqrt{2}$ the flow is termed *supercritical* and no area shock is possible on the compression side, where the vortex axial flow is directed towards the solid surface. If $I_N < 1/\sqrt{2}$, the flow is *subcritical* and formation of area shock are visible on both sides of the cutting surface. Marshall also predicts the change in the vortex core radius for both sides of the cutting blade as a function of I_N:

$$\frac{r_{comp}}{r_c} = \frac{1}{I_N}[((r_{comp}/r_c)^2 - 1)\ \ln(r_{comp}/r_c)]^{1/2} \tag{2a}$$

$$\frac{r_{exp}}{r_c} = [1 + I_N\sqrt{2}/2] \tag{2b}$$

Marshall & Krishnamoorthy [2] performed incompressible flow in their computational simulations of impulsive cutting of a vortex in supercritical and subcritical regimes, assuming axisymmetric inviscid vortex with non-zero axial flow. For the subcritical cases, an increase in vortex core radius on the compression side and a decrease on the expansion side were reported. Marshall & Krishnamoorthy [2] also carried out an experimental study in the subcritical regime and the measurements were reported to be consistent with their computations. On the other hand, as predicted, in the supercritical case the vortex flow acted in a similar manner to a non-rotating fluid jet impacting on a wall, no area shock was observed. This was also reported by Lee et al [3].

In the current study, we investigate the compressibility effects in the interaction. The analytical investigations of Marshall are based on an incompressible fluid. Accordingly we choose flow Mach numbers less than 0.3, which nonetheless will still produce significant compressibility effects for the transient waves. The computations are performed on a uniform Cartesian grid of 40 core radii in all three dimensions. The vortex is initialised at the grid centre, distance of $20r_c$ from the vortex centre line to the far field boundaries. The observation time range is chosen such that any numerical reflections at the far field boundaries do not have sufficient time to return to affect the area of interest. The axial velocity initialisation follows a Gaussian distribution, varying radially $exp(-r^2/r_c^2)$. At $t = 0$, the vortex is 'cut' along $x = 0$. The illustration of the vortex initialisation is shown in Figure 1.

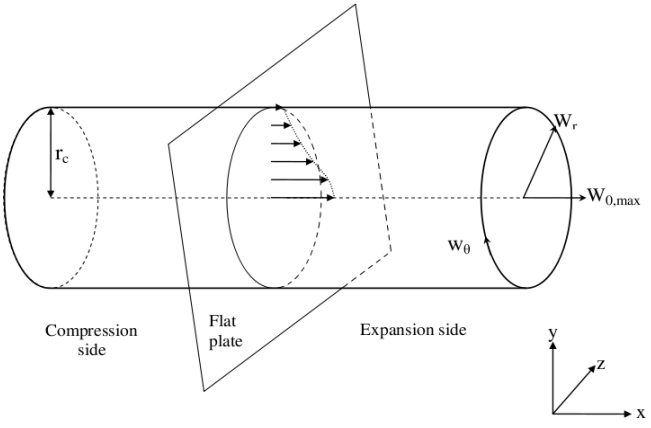

Fig. 1 Schematic illustration of a simplified model of instantaneous, 3-D vortex chopping case by a flat plate.

The chosen test cases are shown in Table 1. Following Marshall's definition, cases C1 and C2 fall in the subcritical regime, C3 is a supercritical case and C4 is analogous to a pure-jet impacting a solid wall. Figure 2 shows a detailed view of density (as solid lines) and vorticity contours for case C1 on the x-y plane through the 3D grid. The figure shows a typical density distribution at one instant, where the as-yet undisturbed part of the column vortex (A) can be seen, a compressive wave (B) is propagating outwards from the plate as a consequence of the blocking mechanism of the solid surface on the core flow and (C) is the region processed by the compressive wave.

Table 1 Investigated orthogonal BVI cases by the authors.

Case	w_0/a_∞	I_N	r_{comp}/r_c	r_{exp}/r_c
C1	0.1	0.21	1.86	0.80
C2	0.2	0.50	3.13	0.60
C3	0.2	0.71		
C4	0.2	∞		

In Figure 2, from the vorticity contours, we observe an anti-clockwise rotating vortex ring (D) followed by, an alternate sign, clockwise rotating second vortex ring (E). Vortex ring formations are also visible on the expansion side of the interaction. Sheikh and Hillier [4] demonstrated that it is the distortion of axial vortex filaments that give rise to the formation of alternate sign vortex rings. In time, more but progressively weaker alternate-sign vortex rings form, which causes the vortex core radius to reduce on the compression side after the initial rise of the core area. This can be seen from the swirl velocity distribution shown in Figure 3, which shows a time series of the variation of swirl on the cutting surface. On the compression

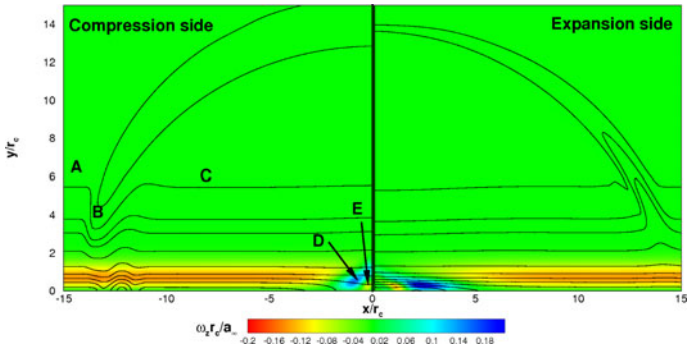

Fig. 2 Detailed view of the vorticity and density (solid lines) contours along the symmetry axis of case C1 at $t\overline{w}_0/r_c = 1.3$ on the x-y plane.

side, the swirl initially decreases with increasing radius, and the swirl profile shows a convergence pattern at later times until at about $t = 1.8$, when a second peak with smaller radius is visible due to strengthening of the second vortex ring on the cutting surface (represented by the letter E in Figure 2). From the swirl velocity distribution (Figure 3) we are able to deduce that the first vortex ring peaks at $r_{comp}/r_c \simeq 1.86$ on the compression side and the core radius converges to $r_{exp}/r_c \simeq 0.8$, a decrease on the expansion side. Marshall's prediction of the area changing shockwave for C1 are 1.17 and 0.87 for the compression and expansion sides, respectively. There is a good agreement between our computation and the theoretical value for the expansion side. However, the underestimation of the theory for r_{comp}/r_c suggests that compressibility has significant effect on the interaction. To further investigate, a computation with zero swirl velocity component, $w_\theta = 0$ analogous to a pure-jet impacting a solid wall is performed.

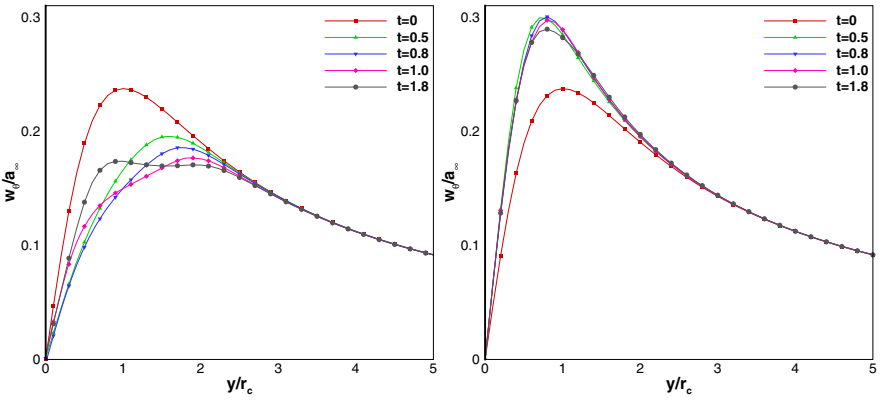

Fig. 3 A time-evolution swirl velocity profile of case C1 along the cutting surface, on the y-plane. Time is non-dimensionalised by $t\overline{w}_0/r_c$; left: Compression side, right: Expansion side.

This is shown in Figure 4 at an instant of the interaction. From the contour plot, it is clear that a region of high pressure (P) close to the flat plate on the compression side has formed, caused by the upstream propagating pressure (acoustic) wave at early times when the leading compression wave is at its strongest. The higher pressure region near the cutting surface would act to reduce the swirl and cause the vortex core area to increase more than the theory predicts. On the other hand, on the expansion side we observe a weaker expansion wave propagating away from the cutting surface and there is no significant distortion near the plate surface.

The computed core radius for case C2 are shown in Table 1. The analytical core radius predictions for $I_N = 0.5$ are 1.54 on the compression side and 0.74 on the expansion side. It is inferred that with increasing impact parameter, the propagating compression and expansion waves away from the cutting surface are also stronger, therefore the magnitude of disruptions to the core flow near the cutting surface are higher, as explained above. Furthermore, the computation show that with increasing impact parameter there is a longer delay in the formation of vortex rings on the compression side.

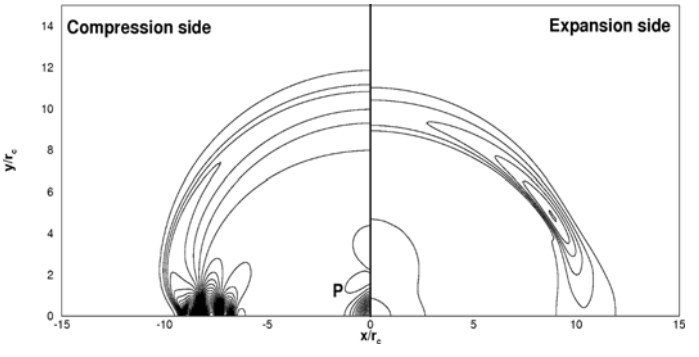

Fig. 4 Detailed view of the pressure contours, p/p_∞ along the symmetry axis of case C4 at $ta_\infty/r_c = 10$ on the x-y plane. Increment between contours is 0.005.

On the expansion side of case C2, although the computed core radius yields a reasonable agreement, the overestimation by the theory is more for case C2 than for C1.

Case C3 classifies as a supercritical flow, where it is stated that the core axial velocity, w_0 is expected to be higher than the phase speed of the azimuthal vorticity waves on the core. Therefore upstream-propagating waves should not be observed. However, in our CFD study we identify a delayed formation of upstream-propagating vortex ring (VR) on the compression side as shown in Figure 5, which indicates that the higher pressure region near the cutting surface also reduces the core axial flow, which by definition reduces the local impact parameter I_N. As a result, the flow does not behave as a supercritical motion.

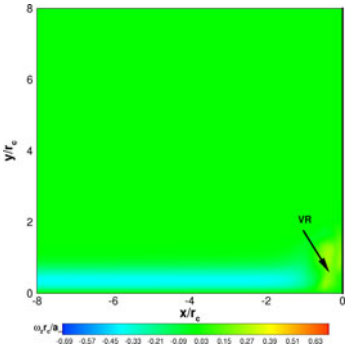

Fig. 5 Detailed view of the vorticity contours along the symmetry axis of case C3 at $t\overline{w}_0/r_c = 5.0$ on the x-y plane.

3 Conclusion

Present CFD study models the instantaneous cutting of the column vortex by a flat plate, which is the first step in our study to investigate the 3D BVI problem. Marshall [1] studied this theoretically for incompressible motion. Our investigation shows that the vortex response to cutting is highly dependent on the impact parameter, I_N. Computations predict that Marshall's analytical theory underestimates the increase of vortex core area on the compression side of the interaction due to not accounting the compressible effects. Higher pressure region created by the compression wave propagating away from the surface decreases the vortex swirl on the cutting surface, further increasing the core area. Furthermore, in a *supercritical* regime, our computations show that area shock is created on the compression side of the interaction. This is due to the fact that the higher pressure region on the blade surface reduces the local axial flow, and the axial flow effectively becomes lower than the phase speed of the azimuthal vorticity waves on the core. On the other hand, computed area shock on the expansion side for all the test cases yield a good agreement with Marshall's theory, as there is no significant disruption caused by the propagating expansion wave on this side of the interaction.

References

1. Marshall, J.S.: Vortex Cutting by a Blade, Part 1: General Theory and a Simple Solution. AIAA J. 32(6), 1145–1150 (1994)
2. Marshall, J.S., Krishnamoorthy, S.: On the Instantaneous Cutting of a Columnar Vortex with Non-Zero Axial Flow. J. of Fluid Mechanics 351, 41–74 (1997)
3. Lee, J., Xiao, Z., Burggraf, O., Conlisk, A., Komerath, N.: An Inviscid Analysis of Vortex-Surface Collisions. AIAA 1995-2237 (1995)
4. Sheikh, A.H., Hillier, R.: The Compressible Perpendicular Interaction of a Columnar Vortex-jet with a Flat Plate. AIAA 2001-2846 (2001)

Complex Conservative Difference Schemes in Modeling of Instabilities and Contact Structures

O.A. Azarova

1 Introduction

The family of the difference schemes on a minimal stencil is under consideration. Construction of the difference schemes on a minimal stencil is based on the scheme approximation order increasing procedure [1]. This method makes it principally possible to develop the schemes of arbitrary approximation order without extension of the scheme stencil by the use of differential consequences of the initial system of equations. Two-dimensional schemes of similar type for plane and cylinder flow symmetry were presented in [2] - [4]. The schemes on the flow oriented grids for plane, cylinder and spherical flow symmetry supplemented by shock-tracking procedures were presented in [5]. Validation and comparison of calculations with the use of the minimal stencil difference schemes and the other ones was conducted in [5] - [7].

In this paper the complex conservative modifications of 2D minimum-stencil difference schemes of the second approximation order for inviscid and viscous gas flows of plane and cylinder symmetry are presented. The Euler equations and the Navier-Stokes equations for an ideal gas are considered. The schemes are conservative not only over the divergent variables, but also over the divergent variables for space derivatives (in the cylinder case, too). The results of numerical modeling of primary and secondary instabilities accompanied by generation of contact structures in the problems of a heat layer/supersonic shock layer interaction obtained with the use of the presented schemes are discussed. This research was initiated by the investigations on flow/flight control via microwave energy deposition into a supersonic flow [8]. All calculations have been implemented without introduction of any artificial dissipative terms.

O.A. Azarova
Dorodnicyn Computing Centre of RAS Vavilova St. 40, 119333 Moscow, Russia

2 Difference Schemes Derivation

The schemes construction is presented for the Euler equations for an ideal gas:

$$\frac{\partial \mathbf{U} r^{\omega}}{\partial t} + \frac{\partial \mathbf{F} r^{\omega}}{\partial x} + \frac{\partial \mathbf{G} r^{\omega}}{\partial r} = \mathbf{H} \tag{1}$$

where

$$\mathbf{U} = \begin{pmatrix} \rho \\ \rho u \\ \rho v \\ E \end{pmatrix}, \mathbf{F} = \begin{pmatrix} \rho u \\ p + \rho u^2 \\ \rho uv \\ u(E+p) \end{pmatrix}, \mathbf{G} = \begin{pmatrix} \rho v \\ \rho uv \\ p + \rho v^2 \\ v(E+p) \end{pmatrix}, \mathbf{H} = \begin{pmatrix} 0 \\ 0 \\ \omega r^{\omega-1} p \\ 0 \end{pmatrix}, \tag{2}$$

$\omega = 0/1$ for plane/cylindrical symmetry, ρ, p are the density and pressure of the gas, u, v are the x-, r- components of the gas velocity, $E = \rho(\varepsilon + 0.5(u^2 + v^2))$ is the total energy per unit volume, ε is the specific internal energy and the specific heat ratio $\gamma = 1.4$. For the second approximation order assurance the systems of the differential consequences of (1) over x and r are used:

$$\frac{\partial \mathbf{U}_x}{\partial t} + \frac{\partial (\mathbf{F}_x + \omega(\mathbf{G} - \mathbf{H})/r)}{\partial x} + \frac{\partial \mathbf{G}_x}{\partial r} = \mathbf{0}, \tag{3}$$

$$\frac{\partial \mathbf{U}_r}{\partial t} + \frac{\partial \mathbf{F}_r}{\partial x} + \frac{\partial (\mathbf{G}_r + \omega(\mathbf{G} - \mathbf{H})/r)}{\partial r} = \mathbf{0}. \tag{4}$$

The systems (3), (4) have the divergent form providing realization of the conservation laws for the divergent variables for the space derivatives. Thus the conservative variables are

$$\rho, \rho u, \rho v, E, \rho_x, (\rho u)_x, (\rho v)_x, E_x, \rho_r, (\rho u)_r, (\rho v)_r, E_r, \tag{5}$$

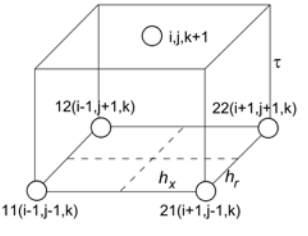

Fig. 1 Difference cell, grid points and accepted notation.

not taking into account the action of the volume forces at the right part of the third equation in (1). In the case of plane flow symmetry ($\omega = 0$) this property is fulfilled in the scheme described in [2] and here the same approach to scheme construction is applied.

At every time step the difference solution is supposed to be of piecewise-linear form over x and r in the neighborhood of the grid points, the difference solutions for x- and r-derivatives are applied to be piecewise-constant. The flux functions are supposed to have the piecewise-linear form in time. The systems (1) are integrated over the grid cell (Fig.1) guided by the Gauss-Ostrogradsky theorem:

$$\begin{array}{c}
\int\limits_S \mathbf{U} r^\omega dxdr + \int\limits_S \mathbf{F} r^\omega dtdr + \int\limits_S \mathbf{G} r^\omega dtdx = \\
= \int\limits_V \left(\frac{\partial \mathbf{U} r^\omega}{\partial t} + \frac{\partial \mathbf{F} r^\omega}{\partial x} + \frac{\partial \mathbf{G} r^\omega}{\partial r} \right) dV = \int\limits_V \mathbf{H} dV \\
\int\limits_S \mathbf{U}_x dxdr + \int\limits_S (\mathbf{F}_x + \omega(\mathbf{G}-\mathbf{H})/r) dtdr + \int\limits_S \mathbf{G}_x dtdx = \\
= \int\limits_V \left(\frac{\partial \mathbf{U}_x}{\partial t} + \frac{\partial (\mathbf{F}_x + \omega(\mathbf{G}-\mathbf{H})/r)}{\partial x} + \frac{\partial \mathbf{G}_x}{\partial r} \right) dV = \mathbf{0} \\
\int\limits_S \mathbf{U}_r dxdr + \int\limits_S \mathbf{F}_r dtdx + \int\limits_S (\mathbf{G}_r + \omega(\mathbf{G}-\mathbf{H})/r) dtdr = \\
= \int\limits_V \left(\frac{\partial \mathbf{U}_r}{\partial t} + \frac{\partial \mathbf{F}_r}{\partial x} + \frac{\partial (\mathbf{G}_r + \omega(\mathbf{G}-\mathbf{H})/r)}{\partial r} \right) dV = \mathbf{0}
\end{array} \tag{6}$$

Summarizing the relations (6) for $\mathbf{U}, \mathbf{U}_x$ and $\mathbf{U}_r$ over all grid cells defines the conservation laws for the conservative variables (5) in the computational domain. Note that shock containing solutions are not included into the differential expressions (1), (3), (4) but they are included into the integral representations (6). For obtaining the second approximation order scheme for (1) the schemes of the first approximation order are sufficient to employ for the solutions of (3), (4):

$$\begin{array}{l}
\mathbf{U}_{x\,i,j}^{k+1} = 0.25(\mathbf{X}_n - \mathbf{X}_{2122} + \mathbf{X}_{1112} - \mathbf{X}_{1222} + \mathbf{X}_{1121})/(h_x h_r), \\
\mathbf{U}_{r\,i,j}^{k+1} = 0.25(\mathbf{Y}_n - \mathbf{Y}_{2122} + \mathbf{Y}_{1112} - \mathbf{Y}_{1222} + \mathbf{Y}_{1121})/(h_x h_r),
\end{array}$$

$\mathbf{X_n}, \mathbf{X_{2122}}, \mathbf{X_{1112}}, \mathbf{X_{1222}}, \mathbf{X_{2121}}, \mathbf{Y_n}, \mathbf{Y_{2122}}, \mathbf{Y_{1112}}, \mathbf{Y_{1222}}, \mathbf{Y_{2121}}$ are the integrals over the cell sides from the piecewise-constant form of the difference solution for the space derivatives with the flux functions defined by (3), (4). All approximations are based on the values in according grid points (see details in [4]). The calculation formula for the difference solution of (1) in the grid point at the next time level is:

$$\begin{array}{c}
\mathbf{U}_{i,j}^{k+1} = 0.25(\mathbf{S}_h + 4\omega\tau h_x h_r \mathbf{H}_m)/(h_x h_r r_j^\omega) - \omega \mathbf{U}_{\mathbf{r}\,i,j}^{k+1} h_r^2/(3r_j), \\
\mathbf{S}_h = \mathbf{S}_n - \mathbf{S}_{2122} + \mathbf{S}_{1112} - \mathbf{S}_{1222} + \mathbf{S}_{1121},
\end{array} \tag{7}$$

$\mathbf{S_n}, \mathbf{S_{2122}}, \mathbf{S_{1112}}, \mathbf{S_{1222}}, \mathbf{S_{1121}}$ are the integrals from the piecewise-linear difference solution over the cell sides defined by the values in according grid points, all integrals over the grid sides in (7) being approximated without any averaging [4]. $\mathbf{H_m}$ is the cell volume averaged value of the right part of (1). Note that in these constructions the right part of (1), $\mathbf{H}$, may have an arbitrary form. Necessary t-derivatives of the divergent variables are expressed via x- and r-derivatives with the help of non-divergent form of the system (1). Approximation of the terms connected with viscosity and heat conduction for the full Navier-Stokes equations is found with the use of the space derivatives of the flow velocity components, these terms being included into the schemes via the flux functions. Details of schemes testing see in [4] - [7]. These schemes were used in the analyses of microwave impulse effect on the supersonic streamlining an aerodynamic body [6] - [9]. In addition, these schemes were used in DNS modeling of turbulent flows with shock waves [10], [11] and might be useful in the turbulence models, from RANS to LES models.

3 Results

The conservation laws for the space derivatives following from (3), (4) provide correct computational contact structures and vortexes representation via the minimization of computational noise in the areas of shear deformations and vortexes. Actually the realization of the conservation laws for the divergent variables of the space derivatives provides the absence of the parasitic numerical fluxes across the cell sides. Therefore it provides the correct computations of the phenomena described by the physical laws based on the relationships containing the first derivatives, i.e. the shear deformations and the viscous stresses.

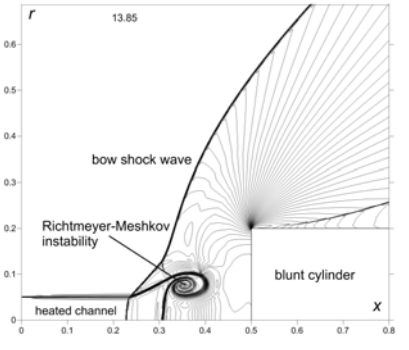

Fig. 2 Infinite heated rarefied channel/cylinder shock layer interaction, $\alpha_\rho = 0.5$

Consider the flows generated by the interaction of an energy release regarded as thin infinite heated rarefied channel and supersonic shock layer over blunt cylinder (the statement of the problem is analogous to [12]). Examples of the use of the presented difference schemes in modeling of instabilities of contact discontinuities inside the front separation area will be presented (in (1) ω=1). The Mach number of the oncoming flow was 1.89. Nondimensional undisturbed flow parameters corresponding to the normal conditions are $\rho_0 = 1, p_0 = 0.2, u_0 = 1, v_0 = 0$. Inside the channel the density ρ_i is lower than in the surrounding gas, $\rho_i = \alpha_\rho \rho_0, (\alpha_\rho$ is the degree of gas rarefaction in the channel), and the static pressure and velocity are equal to those of the undisturbed flow. Thus, the channel is regarded as a heated layer. Slip conditions are utilized on the bodies surfaces. On the entrance boundary the parameters of the oncoming flow are used. No-reflection conditions (in the direction normal to the boundary) are applied on the exit boundaries.

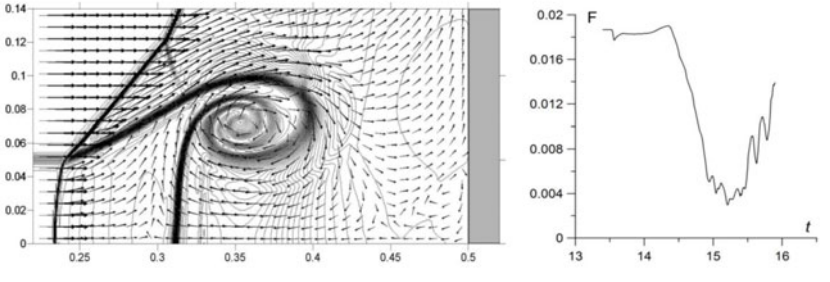

Fig. 3 Left: toroidal vortex contact structure generated as the result of Richtmeyer-Meshkov instability (density, isochores, and velocity; gray color - body); right: face drag reduction via the vortex effect

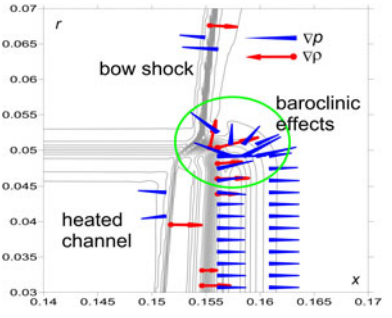

Fig. 4 Vorticity production via baroclinic effects during the Richtmeyer-Meshkov instability generation

At the first stage of the interaction the Richtmeyer-Meshkov instability [13], [14] is generated by the impulse effect of the bow shock wave upon the contact discontinuities (horizontal and vertical) representing the boundaries of the rarefied channel [4], [15]. This instability is generated for both contact discontinuities (boundaries of the heated channel) which are rolling together forming the density (and temperature) stratified vortex structure (Fig. 2). In this vortex the circulation flow area is larger than the density stratified area (Fig. 3, left). This vortex riches the body and becomes a reason of face drag force reduction [16] (Fig. 3, right). Fig. 4 shows that the reason of this instability generation is the baroclinic effects arising in the area of contact discontinuities immediately after the passage of the bow shock wave. These effects cause the vorticity production on the contact discontinuities. Similar baroclinic instabilities accompanying shock wave-gas bubble interaction were analyzed in [17].

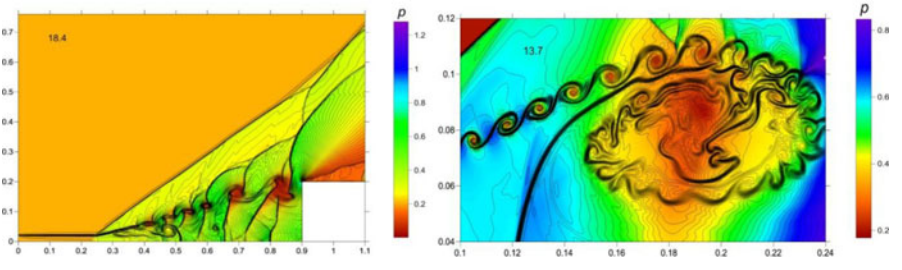

Fig. 5 Fields of density (isochores) and pressure; left: line-organized vortexes resulting from Kelvin-Helmholtz instabilities generation, $\alpha_\rho = 0.3$; right: secondary Kelvin-Helmholtz instability, $\alpha_\rho = 0.4$ (density, isochores, and pressure)

Another type of instability inherent to the flows under the interest is the shear layer instability of Kelvin-Helmholtz type [4], [15]. This instability causes the lines of density stratified vortexes (Fig. 5, left). A number of phenomena inside the front separation area is connected with the presence of these vortexes: stochastic flow mode; cumulating phenomena near the axis of symmetry; formation of the areas of turbulent-like fluctuations. On more fine grids the presented method allows obtaining the secondary Kelvin-Helmholtz instability generated on the shear layers accompanying the Richtmeyer-Meshkov instability (Fig. 5, right). Here the Kelvin-Helmholtz instabilities are the baroclinic ones. The baroclinic nature of Kelvin-Helmholtz instabilities of two-dimensional shear layers was established in [18].

Acknowledgements. The author is acknowledged to Doyle Knight for the previous mutual work and the European Office of Aerospace Research and Development (EOARD) for the partial support of the research presented.

References

1. Grudnitsky, V.G., Prohorchuk, Y.A.: One Approach to Constructing Difference Schemes with Arbitrary Order of Approximation of Differential Equations in Partial Derivatives. Dokl. AN SSSR 234(6), 1249–1252 (1977)
2. Belotserkovsky, O.M., Grudnitsky, V.G., Prohorchuk, Y.A.: Difference Scheme of the Second Order of Precision on a Minimal Stencil for Hyperbolic Equations. J of Comp. Math. and Math. Phys. 23(1), 119–126 (1983)
3. Grudnitsky, V.G., Podobrjaev, V.N.: On the Interaction of a Shock Wave with a Cylinder Resonator. J. of Comp. Math. and Math. Phys. 23(4), 1008–1011 (1983)
4. Azarova, O.A.: A Minimum-Stencil Difference Scheme for Computing Two-Dimensional Axisymmetric Gas Flows: Examples of Pulsating Flows with Instabilities. J. of Comp. Math. and Math. Phys. 49(4), 734–753 (2009)
5. Azarova, O.A.: Difference Scheme with Shock Tracking for Calculation of Explosion Flows in Liquids and Gases. Acoustics of Non-uniform Media. Dynamics of Fluid Medium 105, 8–14 (1992)
6. Farzan, F., Knight, D., Azarova, O., Kolesnichenko, Y.: Interaction of Microwave Filament and Blunt Body in Supersonic Flow. Paper AIAA-2008-1356, 1–24 (2008)
7. Azarova, O., Knight, D., Kolesnichenko, Y.: Pulsating Stochastic Flows Accompanying Microwave Filament/Supersonic Shock Layer Interaction. Shock Waves (in publishing, 2011)
8. Knight, D.: Survey of Aerodynamic Drag Reduction at High Speed by Energy Deposition. J. of Propulsion and Power 24(6), 1153–1167 (2008)
9. Azarova, O., Knight, D., Kolesnichenko, Y.: Instabilities, Vortices and Structures Characteristics During Interaction of Microwave Filaments with Body in Supersonic Flow. Paper AIAA-2010-1004, 1–16 (2010)
10. Azarova, O.A., Shtemenko, L.S., Shugaev, F.V.: Numerical Modeling of Shock Propagation Through a Turbulent Flow. Computational Fluid Dynamics J. 12(2), 41–45 (2003) (Special Issue) ISSN 0918-6654
11. Azarova, O.A.: Direct Numerical Simulation of One Type of Compressible Turbulence Interacting with a Shock Wave. J. of Comp. Math. and Math. Phys. 47(11), 1856–1866 (2007)
12. Artemev, V.I., Bergelson, V.I., Nemchinov, I.V., et al.: Changing the Regime of Supersonic Streamlining Obstacle via Arising the Thin Channel of Low Density. Mechanics of Liquids and Gases 89(5), 146–151 (1989)
13. Richtmyer, R.D.: Taylor Instability in Shock Acceleration of Compressible Fluids. Commun. Pure Appl. Math. 13, 297 (1960)
14. Meshkov, E.E.: Instability of the Interface of Two Gases Accelerated by a Shock Wave. Fluid Dyn. 4, 101 (1969); Izv. Akad. Nauk SSSR Mekh. Zhidk. Gaza 5, 151–158
15. Azarova, O., Kolesnichenko, Y.: On Details of Flow Structure During the Interaction of an Infinite Rarefied Channel with a Cylinder Shock Layer. In: Proc. 7th Int. Workshop on Magnetoplasma Aerodynamics, Moscow, Institute of High Temperatures, pp. 101–113 (2007)

16. Kolesnichenko, Y.F., Brovkin, V.G., Azarova, O.A., Grudnitsky, V.G., et al.: Microwave Energy Release Regimes for Drag Reduction in Supersonic Flows. Paper AIAA-2002-0353, 1–13 (2002)
17. Giordano, J., Burtschell, Y.: Richtmyer-Meshkov Instability Induced by Shock-Bubble Interaction: Numerical and Analytical Studies with Experimental Validation. Phys. Fluids 18, 036102:1–036102:10 (2006)
18. Reinaud, J., Joly, L., Chassaing, P.: The Baroclinic Secondary Instability of the Two-Dimensional Shear Layer. Phys. Fluids. 12(10), 2489–2505 (2000)

Bluntness Effects in Hypersonic Flow over Slender Cones and Wedges

Sebastian Karl, Klaus Hannemann, and Hans G. Hornung

1 Introduction

In hypersonic flow over slender bodies an important concern is the influence of nose bluntness on the viscous boundary layer behavior. This is particularly important in the consideration of boundary layer instability and transition. There exist numerous treatments, both theoretical and experimental on this subject. Representative excellent examples are [1] and [2] In this study we use the deviation from sharp–body theory of the heat flux distribution as obtained from computations of viscous perfect–gas flow over blunted slender bodies at zero incidence to estimate the point where the body has forgotten that it is blunt.

2 Theory

On a sharp cone or wedge, the boundary layer thickness at large x is given by

$$\frac{\delta_b}{x} = \frac{A}{\sqrt{Re_x}},$$

where Re_x is the Reynolds number based on free–stream conditions and distance x from the tip or leading edge. A is a dimensionless constant that depends on free–stream Mach number, gas properties and wedge or cone angle. The entropy layer thickness on a slender blunted cone or wedge is the region within which the effect of nose bluntness is not negligible. For a cone, the entropy layer thickness at large x is given by

$$\frac{\delta_e}{r} = B_c \frac{r}{x},$$

Sebastian Karl · Klaus Hannemann
DLR–AS/RF, 37073 Göttingen, Bunsenstr. 10, Germany

Hans G. Hornung
GALCIT, Caltech, 1200 E. California Blvd, Pasadena, CA91125, USA

where r is the nose radius and B_c is a dimensionless constant that depends on Mach number and gas properties. The x–dependence arises because the stream–surface defining the entropy layer edge approaches the cone surface in this manner in order to conserve mass flux as the cone circumference grows linearly with x.

For a wedge, the entropy layer thickness takes a constant value $\delta_w/r = B_w$, say. It is now a simple matter to obtain expressions for the distance x_s from the nose of a blunt cone or blunt wedge, at which the viscous boundary layer and the entropy layer have the same thickness. For the slender blunted cone, it is

$$\frac{x_s}{r} = \left(\frac{B_c}{A_c}\right)^{2/3} Re_r^{1/3},$$

where Re_r is the Reynolds number based on nose radius. For the wedge it is

$$\frac{x_s}{r} = \left(\frac{B_w}{A_w}\right)^{2} Re_r.$$

The remarkable feature of [1] is that, for the cone, it gives the detailed dependence of the coefficient in the expression for x_s/r on Mach number, specific heat ratio and cone angle.

3 Computational Method

The numerical computations were performed with the hybrid structured/unstructured DLR-Navier-Stokes solver TAU which has been validated for a wide range of steady and unsteady sub- trans- and hypersonic flow cases, see Schwamborn et al. [3] . TAU is a second order finite-volume flow solver for the compressible Euler and Navier-Stokes equations in the integral form.

For the present investigation the gas is considered to be calorically perfect with a ratio of specific heats $\gamma = 1.4$. Viscosity is modeled using Sutherland's law for air, and heat conductivity is calculated assuming a constant Prandtl number of 0.72. The wall boundary was modeled using a no–slip condition at a constant temperature of 300K. The free–stream Mach number and temperature were 8 and 200 K, respectively. The free–stream density was varied from 5.86E-4 kg/m^3 to 0.0176 kg/m^3 corresponding to Reynolds numbers of $Re_r = 1000$ to 30000.

An AUSMDV flux vector splitting scheme was applied together with MUSCL-type gradient reconstruction to achieve second order spatial accuracy. A structured grid topology was chosen and the grid was shaped to follow the bow shock. As an example, Fig. 1 (left) shows the grid used for the 35deg wedge case. Grid convergence was checked for all configurations as shown for the case of the 35 deg wedge in Fig. 1 (right).

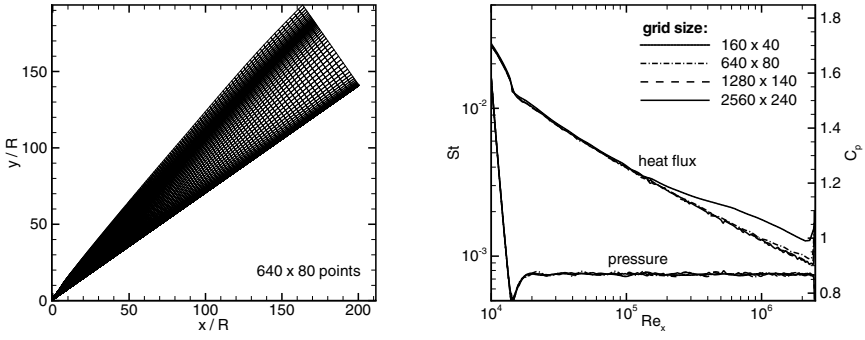

Fig. 1 LEFT: Example of the coarse grid used for the 35° wedge. RIGHT: Example of grid convergence test (35° wedge). Stanton number and pressure coefficient distributions are shown for different grid resolutions ranging from 160 to 2560 points in tangential and 40 to 240 points in wall–normal direction. The surface data used throughout the further analysis are taken from results obtained with the finest grid.

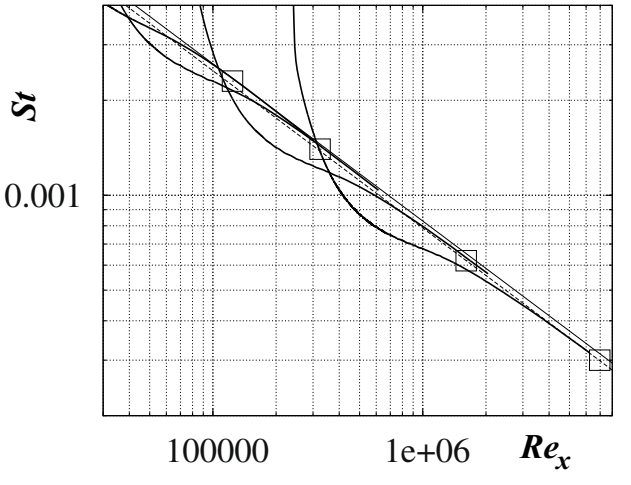

Fig. 2 Plots of St *vs.* Re_x for spherically blunted cones for Re_r=1460, 3000, 10000, and 30000. Thick full line: blunted cone, thin full line: sharp cone theory, thin dotted line: 0.95 times sharp cone theory. The four points are placed at the values of Re_x given by Rotta [1]

4 Blunted Cone

A half–angle of 7° was chosen for the cone computations, with a free–stream Mach number $M_\infty = 8$ and a specific heat ratio $\gamma = 1.4$. For this condition [1] gives $x_s/r = 7.5\,Re_r^{1/3}$. Four values of Re_r were chosen: 1460, 3000, 10000, and 30000. The results of the heat flux distribution are converted to Stanton number and Reynolds number according to

$$St = \frac{q}{0.5\rho_\infty U_\infty^3} \qquad \text{and} \qquad Re_x = \frac{\rho_\infty U_\infty x}{\mu_\infty},$$

where q is the surface heat flux, x is the distance measured along the surface from the virtual tip of the sharp cone, and the free–stream variables are defined as usual. The resulting plot is shown in Fig. 2.

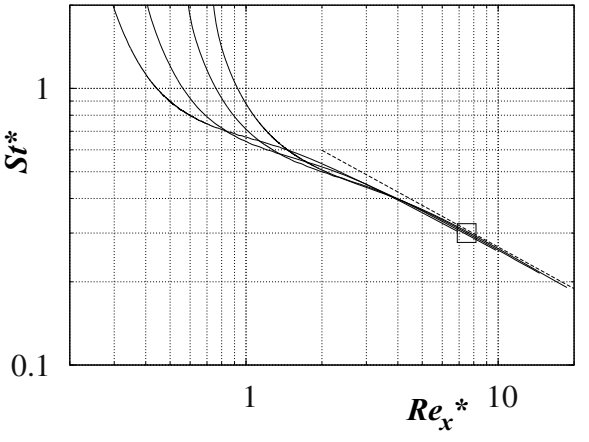

Fig. 3 If the coordinates are scaled, following [1], according to $St^* = St\, Re_r^{2/3}$ *vs.* $Re^* = Re_x/Re_r^{4/3}$ all the blunt–cone curves fall nearly on the same curve at the high–Re_x end. The point is placed at the value of Re_x^* given by Rotta [1].

By plotting these in the scaled variables of Fig. 3 the heat flux curves should all collapse at the high–Re_x end of the range according to the theory. While this is seen to be approximately true, and the point from [1] indicates reasonable confirmation, it has to be said that scaling with powers as different from 4/3 as 1.25 does not cause the comparison to be much different.

It is also interesting to plot the pressure coefficient $C_p = 2p/(\rho_\infty U_\infty^2)$ against Re_x. This plot is presented in Fig. 4.

5 Blunted Wedge

In the case of a blunted wedge, the entropy layer thickness is independent of x. For small wedge angles it is also quite large, so that one has to compute a huge domain in order to reach the point where the boundary layer thickness reaches the thickness of the entropy layer. In an initial attempt with a 20° wedge to reach the point where the entropy layer is swallowed, this point was not reached, and the Stanton number followed the blunt–body scaling

$$St\sqrt{Re_r} = f(x/r),$$

where f is a function of x/r. This is shown with surprising accuracy in Fig. 5.

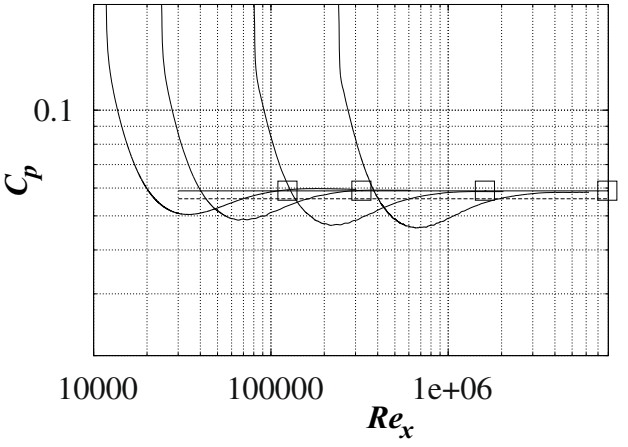

Fig. 4 Plots of C_p *vs.* Re_x for spherically blunted cones for Re_r=1460, 3000, 10000, and 30000. Thick full line: blunted cone, thin full line: sharp cone theory, thin dotted line: 0.95 times sharp cone theory. The four points are placed at the values of Re_x given by Rotta [1]

.

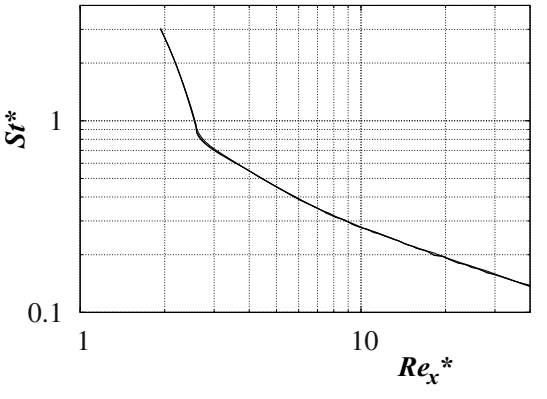

Fig. 5 Blunted 20° wedges. If the coordinates are scaled according to $St^* = St\sqrt{Re_r}$ *vs.* $Re^* = Re_x/Re_r$, which follows blunt–nosed body behavior, all three of the blunt–wedge curves (for Re_r=1000, 3000, and 10000) fall precisely on the same curve for the whole Re_x^* range. This is the expected behavior for blunt body flows. Clearly, the point where entropy and boundary layer thicknesses are comparable has not been reached in these computations.

To avoid this problem, we chose a wedge angle of 35°, for which the entropy layer thickness is smaller than one nose radius. The values of Re_r chosen for this body were 1000, 3000, and 10000. The results, plotted in scaled Reynolds and Stanton numbers according to the wedge theory are shown in Fig. 6. As may be seen, the theory agrees very well with the computation.

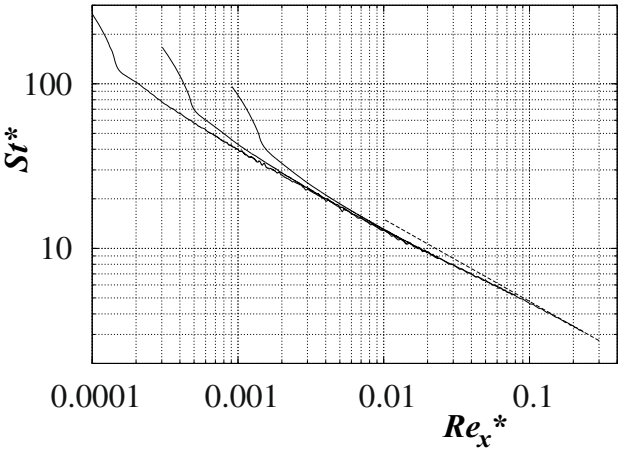

Fig. 6 Blunted 35° wedges. Scaling Stanton and Reynolds numbers according to the wedge theory for entropy layer swallowing, *i. e.*, $St^* = St\,Re_r$ *vs.* $Re^* = Re_x/Re_r^2$, causes the three curves to collapse very nicely at the high–Re_x end. The dashed line shows the sharp–wedge theory. From this result the swallowing distance for a 35° wedge is $x_s/r = 0.1\,Re_r$.

6 Conclusions

Theoretical arguments to determine the entropy layer swallowing distance as first presented by Rotta [1] for blunted cones were extended for blunted wedges. A new way of testing the theories uses the deviation of the heat flux and pressure distributions from the sharp–body behavior to determine the downstream point where the flow has forgotten that the body is blunt. Numerical computations support the theoretical arguments for both blunted cones and blunted wedges. This method is a useful tool for determining bluntness effects, for example, in the design of experiments for boundary layer transition.

References

1. Rotta, N.R.: Effects of nose bluntness on the boundary layer characteristics of conical bodies at hypersonic speeds. New York University Report NYU–AA-66-66 (1966)
2. Stetson, K.F.: Nosetip bluntness effects on cone frustum boundary layer transition in hypersonic flow. AIAA-83-1763 (1983)
3. Schwamborn, D., Gerhold, T., Heinrich, R.: The DLR TAU Code: Recent Applications in Research and Industry. In: Proceedings of the European Conference on Computational Fluid Dynamics ECCOMAS CFD 2006 (2006), http://tau.dlr.de

Hypersonic Interaction of a Vortex Wake with a Bow Shock Wave

A. Shevchenko, A. Shmakov, I. Kavun, M. Golubev, Ya. Ignatenko,
A. Kharitonov, A. Pavlov, and V. Zapryagaev

1 Introduction

Shock/Vortex Interaction is one of the fundamental problems of aerogasdynamics, which has been adequately studied neither theoretically nor experimentally [1, 2].

One of the main features of the vortex-shock interaction is its severe unsteadiness. It is experimentally observed in fluctuations of gas-dynamic parameters of the flow and changes in the flow structure and the size of the interaction region. Experimental data with quantitative estimates of manifestations of unsteadiness are rather limited. The absence of numerical and experimental data for hypersonic velocities should be specially noted. Obtaining results for this range of velocities is extremely important for the development of promising flying vehicles (avoiding of catastrophic operation regimes of a hypersonic inlet and improvement of mixing in the combustor).

Earlier studies [3] were found principal differences in unsteady regimes during the interaction at Mach numbers of 2–4 and at $M = 6$. Therefore two sets of experiments were performed. The first one was directed to conduct an experimental study of a free vortex wake behind a wing at Mach number of 6. An investigation of an unsteady nature of a wing wake / bow shock wave interaction was the goal of the second set of the experiments.

2 Experimental Set-Up and Techniques

Experiments were conducted in the hypersonic wind tunnel T-326 of the Khristianovich Institute of Theoretical and Applied Mechanics of the Russian Academy of Sciences. It is an intermittent blowdown facility with the gas flow through a

A. Shevchenko · A. Shmakov · I. Kavun · M. Golubev · Ya. Ignatenko ·
A. Kharitonov · A. Pavlov · V. Zapryagaev
Khristianovich Institute of Theoretical and Applied Mechanics,
Institutskaya 4/1, Novosivirsk, 630090, Russia

nozzle into the Eiffel chamber. The wind tunnel is capable of producing a Mach number range from 6 to 14. Figure 1 illustrates the schematic representation of the experimental setup of the free vortex wake experiments. A vortex wake is generated by an unswept semispan slender wing. The wing was mounted on the Eiffel chamber floor at the nozzle centreline.

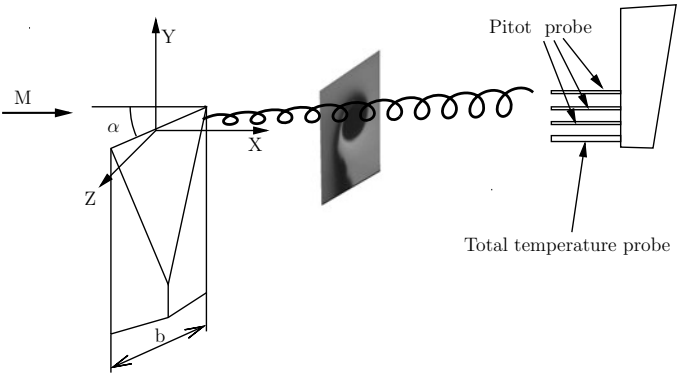

Fig. 1 Sketch of free vortex wake experiment

Flow visualization techniques included a multiple spark shadow photograph of 5 μs spark duration and a laser light sheet imaging technique.

Three Pitot probes with a diameter of 0.6 mm and one probe for stagnation temperature measurement with a diameter of 2.3 mm were used to measure local Pitot pressure and recovery temperature. The probes were mounted vertically into the traversing device at the distance of 10 mm from each other. Quantitative flowfield measurements and laser sheet visualization were performed at cross-sections at the distance from 5 mm to 155 mm downstream from the wing trailing edge. The experiments were performed at the Mach number of 6 and angles of attack of the wing up to 20 deg.

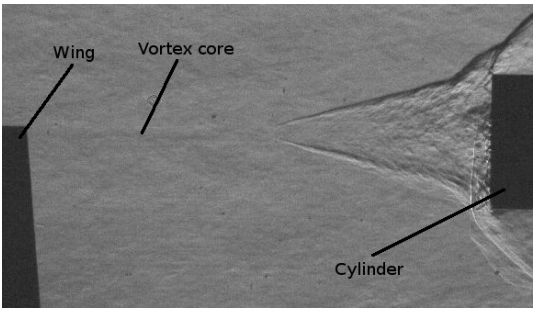

Fig. 2 Vortex wake / bow shock wave interaction

In the second set of experiments the vortex wake produced by the wing described above interact with a bow shock wave (see Fig. 2). The bow shock wave was generated by a cylinder with a flat end face and the diameter of 42 mm. The cylinder is placed 100 and 155 mm downstream of the trailing edge of the wing.

The shadowgraph images were carried out using a spark light source with 2 μs exposure times. The Phantom v12.1 high-speed video camera was used. The images were recorded at a rate of 10 kHz; the length of the sample was 4543 frames. The pressure fluctuations on the cylinder were measured by the fast-response Kulite XCE-062 sensors. Two sensors were mounted on the face of the cylinder: one at the center of the cylinder, and the other on the periphery, at a distance of 11.5 mm from the center. The amplified output from the transducer was digitized using an AD converter at a rate of 312.5 kHz and a sample size of 2^{17} per test case. The data acquisition system ensured synchronization of the sensors signals and video images obtained by the Phantom v12.1 high-speed video camera. Time-averaged pressure distribution on the cylinder butt was measured as well. Experimental data were obtained for wing angles of attack up to 20 deg.

3 Results

3.1 Free Wake

Figures 3–6 show flow patterns in the free vortex wake for near wake ($X/b = 0.625$) and far wake ($X/b = 3.875$). Video images were obtained, which make it possible to estimate the size and location of the vortex core in the wake flow behind the vortex generator, to refine the wake flow structure, to estimate the influence of the angle of attack on the wake flow structure, and to trace the development of the vortex wake with distance from the vortex generator. Flow instability on the vortex wake boundaries was observed at the near wake ($X/b = 0.625$).

In the free vortex wake experiments both sufficiently high Pitot pressure loss and total temperature loss was detected. As can be seen from Fig. 5 the wake flow is characterized by a decrease in the Pitot pressure approximately 10 times at $X/b = 3.875$ and 100 times at $X/b = 0.625$. A non-uniformity of the stagnation temperature (its decrease at the center of the vortex core and a small increase at the periphery) was detected.

At the angle of attack of 16 deg both laser sheet images and Pitot pressure measurements revealed the growth of the vortex core and of Pitot pressure as well as the stagnation temperature (Fig. 6). It can be caused the beginning of the vortex breakdown.

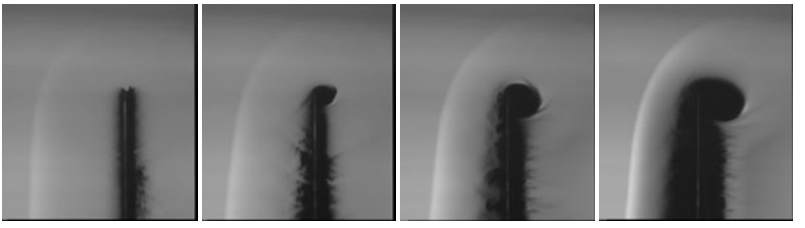

Fig. 3 Laser sheet images at $\alpha = 0, 4, 8, 12$ deg and $X/b = 0.625$

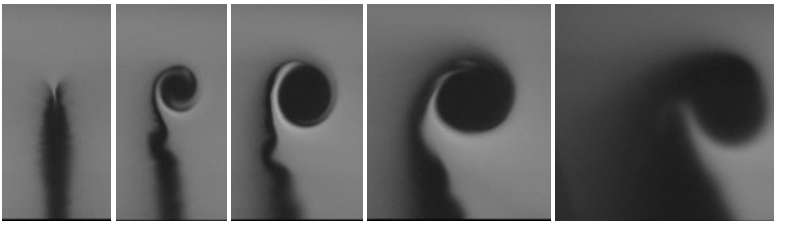

Fig. 4 Laser sheet images at $\alpha = 0, 4, 8, 12, 16$ deg and $X/b = 3.875$

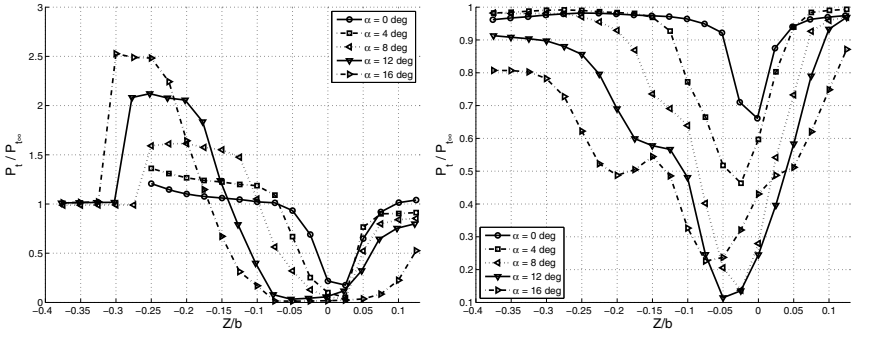

Fig. 5 Pitot pressure distribution across the vortex core

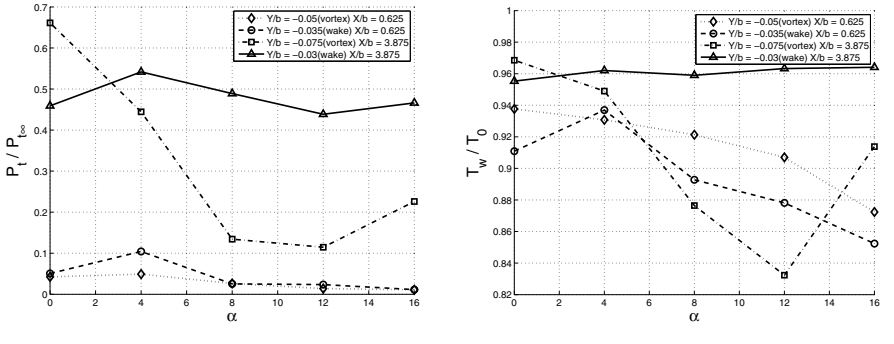

Fig. 6 Minimum values of Pitot pressure (left) and total temperature (right) vs angle of attack

3.2 *Vortex Wake / Bow Shock Interaction*

The experiments revealed different types of highly unsteady processes during the interactions. At low wing angles of attack ($\alpha < 6$ deg) an interaction process with a pulsing bow shock wave has detected (Fig. 7). The shape of the bow shock wave and the size of the interaction region change during one test. However the spectral analysis has not revealed discrete harmonic of pressure pulsations signals (Fig. 9). At moderate angles of attack ($\alpha = 6 \div 14$ deg) the self-oscillatory process with salient fundamental was observed (Fig. 8 and 9). A further increase in the angle of attack leads to vanishing of self-oscillations and to recovery of the mode with a pulsed shock wave. The reason of this vanishing of self-oscillations is, apparently, vortex breakdown at the high angels of attack that is accompanied by growth of total pressure. It should be noted that unlike the interactions at $M = 2 - 4$ [2, 3], it is not observed interaction regimes with conical shock wave at Mach number of 6. All types of the interactions are characterized by a high level of fluctuations.

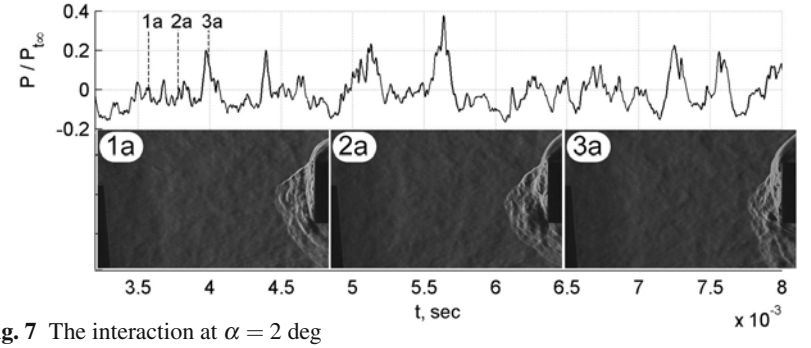

Fig. 7 The interaction at $\alpha = 2$ deg

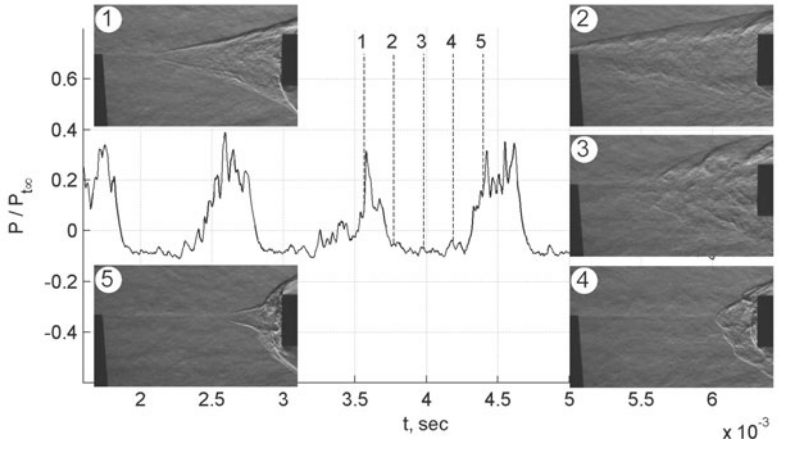

Fig. 8 The interaction at $\alpha = 10$ deg

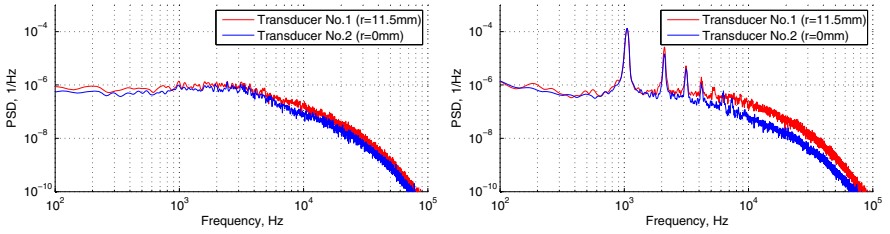

Fig. 9 Power spectra density distribution of pressure fluctuations at the face of the cylinder: $\alpha = 2$ deg (left); $\alpha = 12$ deg (right)

4 Conclusions

Comprehensive experimental study of the vortex wake behind of the wing and its interaction with a bow shock wave was performed at Mach number of 6. In the free vortex wake experiments both sufficiently high Pitot pressure loss and total temperature loss was detected. Vortex wake / bow shock wave experiments revealed two different modes of the interactions: the pulsing mode at low angles of attack and the self–oscillation mode at moderate angles of attack.

Acknowledgements. The work was supported by the International Science and Technology Center (ISTC), Moscow, (Project No 3872).

References

1. Delery, J.M.: Aspects of vortex breakdown. Prog. in Aerospace Sciences 30, 1–59 (1994)
2. Kalkhoran, I., Smart, M.: Aspects of shock wave-induced vortex breakdown. Prog. in Aerospace Sciences 36, 63–95 (2000)
3. Shevchenko, A.M., Shmakov, A.S.: Experimental techniques and results of investigations of an unsteady flowfield in wing wakes / bow shock wave interactions. In: Proc. at XIV Int. Conference for Aerospace Sci., Novosibirsk, June 30-July 6, Section 4, 10 p (2008), ISBN 978-5-98901-040-0

Part XX
Shockwave Phenomena and Applications

Density Field Measurements of a Micro–explosion Using BOS

P. Suriyanarayanan, N. Karthikeyan, L. Venkatakrishnan, Obed Samuelraj, R. Sriram, and G. Jagadeesh

1 Introduction

The flow field dynamics associated with blast waves can be better understood by generating controlled micro-explosions in the laboratory. In recent years microexplosions have also found interesting trans-disciplinary applications like food preservation, wood science, drug delivery, gene therapy and bio-medical applications [1], [2]. The blast waves produced by sudden release of energy are normally characterized by a supersonic shock front followed by an exponential type decay of its physical properties. Unlike shock waves that attenuate as they expand spherically, the shock wave from an internal blast can change its propagation properties depending on the physical barriers. The micro-blast provides a challenging case for application of novel flow diagnostic techniques in measuring flow properties. This learning can be scaled up to large scale explosions [3]. One such property is the density field, which although highly informative, is quite difficult to capture. The Background Oriented Schlieren (BOS) technique provides the capability of capturing the three dimensional density fields [4], [5]. This is an attempt to quantify the density flow field of a micro-explosion for the first time using BOS. In this study, a micro-explosion is generated using NONEL tube and the detonating device. The spatio-temporally evolving density field is captured at several instants by means of a precise triggering circuit used to control the illumination and imaging. The density field so obtained can be used for understanding both basic physics associated with explosive driven shock wave propagation as well as validation data attempts to model explosive driven shock wave propagation.

P. Suriyanarayanan · N. Karthikeyan · L. Venkatakrishnan
Council of Scientific and Industrial Research
National Aerospace Laboratories, Bangalore, India

Obed Samuelraj · R. Sriram · G. Jagadeesh
Department of Aerospace Engineering, Indian Institute of Science, Bangalore, 560 012, India

2 Experimental Description

2.1 Micro-explosion Generator

The micro-explosion is generated at the open end of a non-electrical (NONEL) tube (M/s Dyno Nobel, Sweden), an explosive transfer system (ETS). The system consists of a plastic tube of approximately 1.3mm inner diameter and 3 mm outer diameter with a thin layer of explosive material coating (HMX with traces of aluminum, at 18mg per unit length of the polymer tube) deposited on its inner wall of the tube. The ignition of the shock tube was done using NONEL Dynostart, an electronic blasting machine. It consists of an energy source (battery), a voltage converter, a capacitor for energy accumulation (2500V approx.), an electrode and push buttons to effect initiation. The electrical energy is converted to a powerful spark, (detonates at a velocity of $6,500m/s$) which the electrode in turn emits into the inner surface of the NONEL tube to initiate the ignition.

The ignition of the reactive material coated on the inner surface of the shock tube propagates a low energy signal along the length of the tubing with minimal disturbance outside of the tube, resulting in the formation of a shock front. The shock front also heats up the gases in the tube. The dispersed energetic material is heated and then combusted to release energy which supports the shock front at a typical rate of $2000m/s$. The detonation is confined to the plastic tube along its length and when the products of combustion are allowed to escape from the open end of the tube, it generates a micro-blast wave which escapes into the open domain.

2.2 Background Oriented Schlieren (BOS) Methodology

The principle of the technique is the refractive index variation due to density gradients in the flow. The determination of the density field using BOS thus involves the following steps: (a) calculation of displacements in the background which is imaged through the flow of interest (This is done through a PIV-type cross-correlation algorithm. These displacements are the vectors of density gradient at each point); (b) calculation of the line-of- sight integrated density field by solution of the Poisson equation, which is the gradient of the above displacement, and; (c) use of optical tomography (filtered back-projection) to determine the density field in the actual plane of interest. The reader is referred to Venkatakrishnan and Meier [4] for a derivation of the reconstruction function. The reconstruction of the entire field is achieved by inverse tomography [5]

2.3 Experimental Setup

A Sharpvision 1500EX camera is used to image the flow. Nikon 400mm lens is used as the imaging optics. A dynamic Schlieren light source (PAL Flash 501) which produces 750ns of pulse width is used for illumination. The dot pattern used for the study has resolution of 3000 dpi. The area of imaging is 120 x 90mm. IDT

proVISION® software is used to acquire and also to post–process the image to get the density gradient field. The image is acquired with a time delay (measured from the initiation of the ignition) is generated using a Stanford DG 535 signal generator. The nonel tube is cut to a length of 230*mm* and inserted into a Stainless steel (SS) tube of inner diameter 3*mm* as shown in the Figure 1. The tube is kept at a distance of 3.6*m* from the camera and 150*mm* from the background to get maximum sensitivity. The experimental set up is on an optical table to allow precise alignment of the components. The room was kept well ventilated to reduce the noise generated from the density gradients in the ambient.

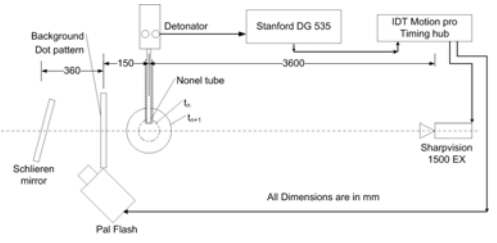

Fig. 1 Schematic of the experimental setup

2.4 Timing Circuit

Depressing the Dynostart firing button initiates the ignition as well as sends a trigger pulse to the DG 535 which triggers the IDT motion pro timing hub after a preset delay which controls the camera and the PAL flash. The evolution of the blast wave is captured at different time delays in the DG 535. A minimum delay of 250μs was required for the appearance of the flow at the tip of the SS tube and was incremented in steps of 10μs to capture the evolution of the flow. Calibration of the imaging area was carried out as in a PIV method to obtain data in real world dimensions.

The PAL flash has a 750*ns* width and creates an uncertainty of 1μs. The repeatability of the experiments was found to be 1μs of jitter.

3 Results and Discussion

3.1 Schlieren Measurements

The figure 2 reproduces images from a time resolved Schlieren imaging (500kHz) carried out at University of Manchester [6]. Figure 2 shows the growth of the high intensity region prior to the formation of the shock wave–the flash before the bang. The shock wave formed grows and evolves with distance having a highly turbulent core which contains the products of combustion.

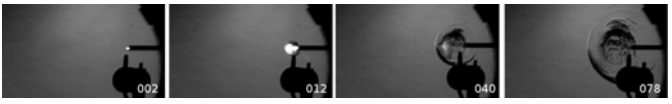

Fig. 2 Schlieren images at different time instants (time in microseconds) [6]

3.2 BOS Measurements

The figures 3(a) and 3(b) show the image of the background at no-flow condition and after the initiation of the detonation. In addition to the displacement of the blur, there is still a remnant of the flash of explosion.

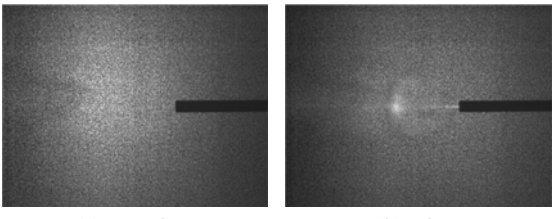

(a) No Flow (b) Flow

Fig. 3 Images taken before (a) and after (b) the flow

Figure 4 shows the gradients of the mean line-of-sight integrated density field obtained by correlation of no-flow and flow images which was obtained from a realization of the background (with flow). The vectors point in the direction of lower density and are color-coded to show the varying magnitude of the gradients that correspond to bi-directional Schlieren. The flash at the core of the blast prevents correlation in that region.

Figures 5(a)-5(d) show the density gradient field at four instances as captured by BOS. As in the continuous Schlieren presented earlier, the growth and evolution of the blast wave is well captured. This data can now be used as the input to calculate the density field which is then sliced using tomography to obtain the required sectional density field. Figure 6 presents the reconstructed three dimensional density field of the flow for a time delay of $44\mu s$. The normalized density field shows the across the shock as well as the density in turbulent vortex core.

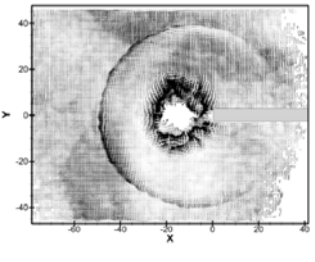

Fig. 4 Density gradients in vector plot

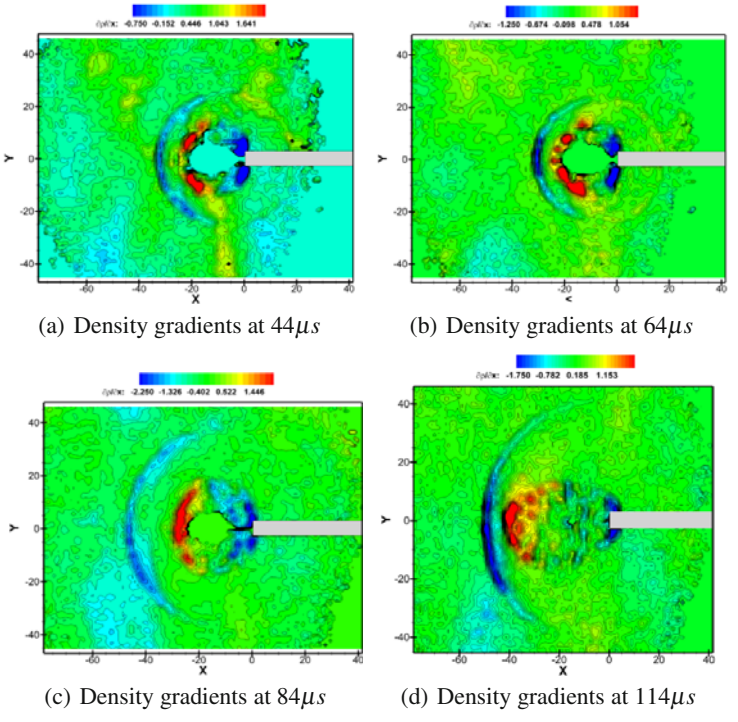

(a) Density gradients at $44\mu s$ (b) Density gradients at $64\mu s$

(c) Density gradients at $84\mu s$ (d) Density gradients at $114\mu s$

Fig. 5 Density gradients at various time instants

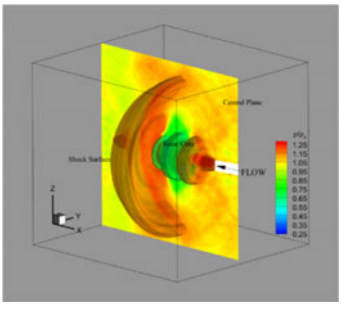

Fig. 6 Tomographic reconstructed density field

4 Conclusion

BOS measurements were carried at a micro-explosion to capture the density field. Using the axisymmetry of the flow density field was successfully reconstructed. The study shows enormous potential of BOS data for both density as well as validation of CFD models.

Acknowledgements. The authors acknowledge the support provided by Mr K. Prasada Rao in making the timing circuit work during the initial stages of the experiments. The help provided by the technical and support staff of $0.55m$ Low Speed Laboratory is acknowledged.

References

1. Jagadeesh, G.: From micro-explosions to drug delivery: Emerging paradigms of shock wave research. In: Proceedings of the 27th International Symposium on Shock Waves, St. Petersburg, Russia, July 19-24 (2009)
2. Jagadeesh, G.: US Patent applications 12/480,514 and 12/480,508 (2010)
3. Hutchens, G.J.: Approximate near-field blast theory: A generalized approach. J. Applied Physics 88(6), 3654–3658 (2000)
4. Venkatakrishnan, L., Meier, G.E.A.: Density measurements using background oriented Schlieren technique. Exp. Fluids 37(2), 237–247 (2004)
5. Venkatakrishnan, L., Suriyanarayanan, P.: Density field of supersonic separated flow past an afterbody nozzle using tomographic reconstruction of BOS data. Exp. Fluids 47(3), 463–473 (2009)
6. Obed, S.I., Jagadeesh, G., Kontis, K.: Micro-Blast Waves Using Detonation Transmission Tubing (manuscript submitted); 28th International Symposium on Shock Waves, Manchester, UK (in press)

High Speed Opening Operation of Diaphragmless Shock Wave Generator

A. Miyachi, K. Sugahara, and A. Abe

1 Introduction

The environmental destruction of marine ecosystem caused by micro-organism included in ship ballast water has been a global problem. The International Maritime Organization (IMO) adopted strict standard rule for control and management of ship ballast water in 2004 [1], after that, many ballast water treatment systems have been proposed and developed all over the world. However, a lot of practical problems have been remaining yet for development of energy-saving and space-saving systems. In general systems, shipping companies have to charge and manage chemicals on board to kill marine bacteria in the ballast water. Therefore, if troubles should happen in the ballast water treatment process, leaking chemicals from the system might contaminate the sea. In order to realize more secure and environmental friendly treatment method, the authors have proposed a new sterilization technique of ship ballast water using underwater shock waves. In the previous research, the result showed that a marine *Vibrio* sp. was completely inactivated when the excess pressure in cell solution contained in a small aluminum container was over 200 MPa in impact experiments by a gas gun [2]. In general, electric discharge, explosive or high-speed collision of a projectile is used as a power source to produce underwater shock waves and has been applied to engineering and medical fields. However, those power sources are unsuitable for practical use on board from a point of view on energy cost and safety. From the above-mentioned, the authors thought of killing marine bacteria in a large amount of ballast water by exposing to strong pressure pulses and free radicals created from collapse of microbubbles [3-6]. In this idea, the excess pressure of underwater shock waves plays only a role of leading to collapse of microbubbles, so that it does not necessarily need to release an extreme high-energy in water. Therefore, the method of hitting water surface with shock waves produced in gas would be an effective one of underwater shock wave

A. Miyachi · K. Sugahara · A. Abe
Graduate School of Maritime Sciences, Kobe University
5-1-1 Fukaeminami-machi, Higashinada-ku, Kobe, 658-0022, Japan

generation on board. In addition, it needs to develop the shock wave generator that can produce shock waves periodically by low driving cost for practical use.

This paper reports on high-speed opening operation of a diaphragmless shock wave generators. Two kinds of the diaphragmless shock wave generators have been designed to open the piston-valve quickly, and their driving performance was investigated. Those generators are equipped with a single piston as a high-speed valve. One of the generators has been designed to increase the opening rate of the piston-valve by using five neodymium magnets. The other is a slide-open type device. The moving direction of piston-valve is set up perpendicular to the center axis of the shock tube, and there is an approach for pre-acceleration of the piston-valve before the shock tube inlet. The performance of those generators was examined by experimental measurement of shock wave speed, pressure ratio and opening velocity.

2 Experiment

2.1 Shock Wave Generators

Figure 1 shows the schematic diagram of diaphragmless shock wave generator assisted by magnetic force (Type 1). Four columnar neodymium magnets which dimensions are 24 mm in diameter $\times$ 20 mm in height were placed around the shock tube inlet, and a fifth magnet which dimensions are 50 mm in diameter $\times$ 20 mm in height was put in the back side of the piston-valve. Attraction forces of those magnets were measured by tension test and consequently 394 N and 1770 N were obtained. The piston-valve was made of polycarbonate, and thin iron plates were embedded in the front face of the piston-valve. The diameter of the piston-valve was 80 mm and the weight was 84 g including iron plates. In the case of a diaphragmless shock tube in which a piston-valve moves parallel to the axis of shock tube, the opening rate is decided by the pressure change behind the piston-valve, i.e., decreasing rate of pressure behind the piston-valve is important. Type 1 makes the pressure difference between the front and the back of the valve increase by closing the shock tube inlet with magnetic force in order that the initial acceleration of the piston-valve may become high. Once the piston-valve starts to move, the magnetic forces rapidly decrease in proportion to square of the distance between the magnet at the shock tube inlet and the piston-valve, after that, attraction force of the fifth magnet at the back side of the piston-valve is going to increase.

Figure 2 shows the schematic diagram of the slide-open type diaphragmless shock wave generator (Type 2). The piston-valve was designed to move perpendicular to the axis of the shock tube. The shock tube is completely opened when the pre-accelerated piston-valve goes by the inlet of the shock tube. The piston-valve was made of ABS resin. The dimensions are 60 mm in diameter $\times$ 75 mm in length, and the weight was 97 g. The piston-valve closes the high-pressure chamber when high-pressure gas is supplied behind the piston-valve as shown in Fig.2 (a).

The high-pressure gas is filled in the high-pressure chamber through a small slot produced at the front part of the piston-valve. When pressure behind the piston-valve releases to atmosphere, the piston-valve starts to accelerate and the shock tube inlet is immediately opened (Fig.2 (b)).

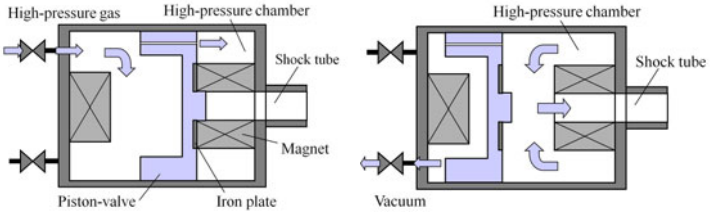

(a) Close shock tube (b) Open shock tube

Fig. 1 Schematic diagram of diaphragmless shock wave generator assisted by magnetic force

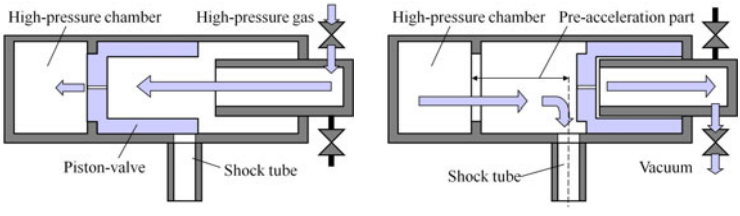

(a) Close shock tube (b) Open shock tube

Fig. 2 Schematic diagram slide-open type diaphragmless shock wave generator

2.2 Piston-Valve Opening Time and Pressure Measurement

The piston-valve opening time of Type 2 was measured by a velocity measurement system shown in Fig.3. The measurement system consisted of a laser diode (LDP2-6505, NEOARK Co.), its detector, two pairs of pin-sensors, and an oscilloscope (DS-4264M, Lecroy Co.). The pin-sensors were made from 0.3 mm dia. copper wire. The two pairs of pin-sensors were placed in a 10 mm dia. slot prepared for the pin-sensors. As shown in Fig.3 (a), the first signal of the laser detector is recorded at the start time of shock tube opening. The first pair of pin-sensors shown in Fig.3 (b) measure the complete time of shock tube opening. When the end-face of the piston-valve touches those pin-sensors, output signals are recorded instantaneously. In consequence, the time for the shock tube opening and its average rate are estimated by the interval time between the output signals from the laser detector and the first pin-sensor, and the terminal speed of the piston-valve is obtained by the output signals from two pairs of pin-sensors.

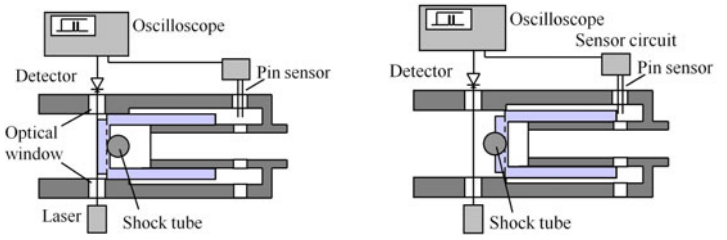

(a) Start of shock tube opening (b) Finish of shock tube opening

Fig. 3 Piston-valve velocity measurement system

Pressure variations in the shock tube were measured with pressure transducers (112A21, PCB Piezotronics Inc.). The transducers were placed at 50 and 100 mm from the exit of a shock tube that has 10 mm in diameter and 200 or 1100 mm in length.

3 Results and Discussion

Pressure measurement of Type 1 with 200 mm length shock tube was carried out under the initial pressure condition of 0.8 MPa air in the high-pressure chamber, and shock waves were discharged to the atmosphere. In this case, theoretical estimation of the excess pressure ratio at a shock wave front is about 2.60, but the experimental result was only 0.5, and we could not obtain pressure profile like a shock wave. Furthermore, there was not clear difference of pressure profile with or without magnetic forces. These results suggest that the opening time of the piston-valve is too long to generate shock waves and the volume of the high-pressure chamber is not enough. Therefore it is necessary to review the weight and the shape of piston-valve, the structure of high-pressure chamber and so on.

Figure 4 shows the relation between the piston-valve velocity and the initial high-pressure in the case of Type 2. In this figure, open circles indicate average velocities of the piston-valve opening and solid circles are the terminal velocities of the piston-valve for each initial condition. Those data trend upward with increasing of the initial pressure, and the maximum opening velocity is about 16.5 m/s at eight of the initial pressure ratio.

The effective opening time for shock wave generation is empirically known that it should be less than 1 ms. Figure 5 shows the relation between the opening time of the piston-valve and the initial pressure in the case of Type 2. The abscissa is the initial pressure ratio in the high-pressure chamber, and the ordinate is the opening time. It was found that the results approximately satisfy the effective opening time condition even when the initial pressure ratio is only two.

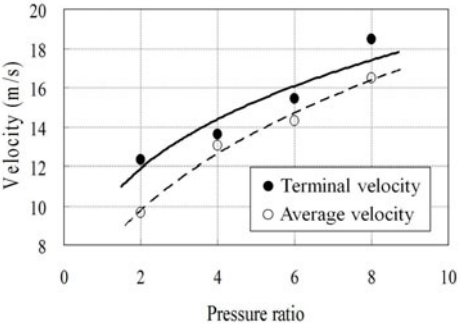

Fig. 4 Piston-valve velocity vs. initial pressure ratio in high-pressure chamber

Figure 6 shows a pressure profile of Type 2, and this profile was recorded at 100 mm from the exit of 1100 mm length shock tube. The initial pressure ratio in high-pressure chamber was eight. Shock Mach number 1.65 was obtained, and the excess pressure ratio of a shock wave was 2.65. Those values were approximately consistent with theoretical estimation of a shock wave generated by adiabatic compressed air in the high-pressure chamber. However, pressure change at the shock wave front was not discontinuous rising to the maximum value. We consider that interaction with an expansion wave generated at the shock tube exit and turbulence caused by slide-open of the piston-valve had an influence on the shape of shock wave front.

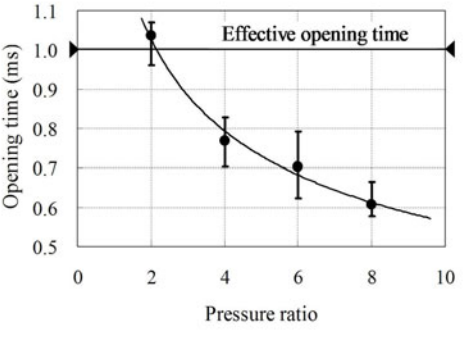

Fig. 5 Opening time of the piston-valve vs. initial pressure ratio in high-pressure chamber

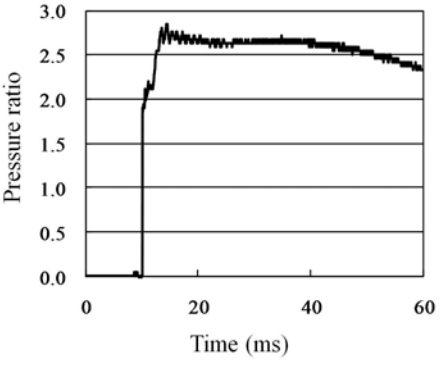

Fig. 6 Pressure variation at 100 mm from the exit of 1100 mm length shock tube

4 Conclusion

In this paper, a magnetic force assist type and a slide-open type diaphragmless shock wave generators were produced by way of trial, and the performance of piston-valve opening was examined. In the method using magnetic force, shock waves were not observed at all, and also there is no effect of magnetic force. In order to increase the opening velocity of the valve, improvements of the piston-valve weight, shape and the structure of the high-pressure chamber were required. On the other hand, in the slide-opening type generator, it was shown that the pre-acceleration of the piston-valve worked efficiently, and shock wave generation of Mach number 1.65 could be observed. We would improve those shock wave generators to apply to the shock sterilization technique in ship ballast water treatment.

Acknowledgements. The present work was supported by Grant-in-Aid for Scientific Research (B) (22360367). We would like to thank for the financial support offered by JSPS.

References

1. International Convention for the Control and Management of Ships Ballast Water and Sediments, BWM/CONF/36, February 16 (2004)
2. Abe, A., Mimura, H., Ishida, H., Yoshida, K.: The effect of shock pressures on the inactivation of a marine Vibrio sp. Shock Waves 17(1-2), 143–151 (2007)
3. Mimura, H., Abe, A., Yoshida, K., Ishida, H.: Changes in the Number of Colony-Forming Marine Vibrio sp. Cells After Exposure to Shock Pressures in the Presence of Sodium Ascorbate. Bull. Soc. Sea Water Sci. 61(2), 132–133 (2007)

4. Abe, A., Ohtani, K., Takayama, K., Nishio, S., Mimura, H., Takeda, M.: Pressure Generation from Micro-Bubble Collapse at Shock Wave Loading. Journal of Fluid Science and Technology 5(2), 235–246 (2010)
5. Takahashi, M., Chiba, K., Li, P.: Free-Radical Generation from Collapsing Microbubbles in the Absence of a Dynamic Stimulus. J. Phys. Chem. B 111(6), 1343–1347 (2007)
6. Takahashi, M., Chiba, K., Li, P.: Formation of Hydroxyl Radicals by Collapsing Ozone Microbubbles under Strongly Acidic Conditions. J. Phys. Chem. B 111(39), 11443–11446 (2007)

Numerical Analysis of Interaction between Moving Shock Wave and Solid Particle Layer

K. Doi and Y. Nakamura

1 Introduction

When a shock wave propagates over many small solid particles on a horizontal wall, some particles near the surface of the layer are lifted and dispersed into the shock-induced flow. These dispersed particles is called the dust cloud. This phenomenon is actually seen in galleries of coal mines or in pipelines for neumatic transportation of powder, and mixing dispersed flammable dust particles with high-temprature and high-pressure gas behind the shock wave sometimes causes the dust explosion. And this phenomenon includes some interesting factors, such as the shock structures interacted with the dust layer, interactions between gas and solid particle, and interactions between solid particles.

This phenomenon has been investigated by many researchers. Dawes[1] reproduced the dust cloud by the shock-tube experiment, and examined the characteristics. Gerrard[2] and Fletcher[3] conducted similar shock-tube experiments to examine the initial stage of the dust cloud formation, but the dyanmical mechanism was not able to be shown clearly. Bracht[4] searched for the transitional regime to turbulent flow in the dust cloud by the observation of more time. Suzuki et al.[5] examined the translational and rotational motions of dust particles in detail. On the other hand, Khul et al.[6] conducted the numerical simulation based on the mixture model, and showed appearance of a vortex generated from the interaction between the shock wave and dust layer by baloclinic effect. Jiang[7] and Thevand[8] also conducted the numerical simulation based on the two fluid model. However, they has not shown the dynamic structure of the dust cloud formation clearly.

In the present study, it aims to pay attention at the initial stage of the dust cloud formation process, and to clarify the dynamic mechanism by the numerical simulation. A discrete model is applied to the solid particles whereas a continuum model is applied to the gas in this simulation. As a result, the dynamic status of an individual

K. Doi · Y. Nakamura
Department of Aerospace Engineering, Nagoya University
Furo-cho, Chikusa-ku, Nagoya, 464-8603 Japan

particle that composes the dust cloud can be clearly shown, and the particle-particle interaction can be considered easily in addition.

2 Computational Model

Governing equations for gas phase are as follows.

$$\frac{\partial}{\partial t}(m_f) + \nabla \cdot (m_f \mathbf{u}_f) = 0 \tag{1}$$

$$\frac{\partial}{\partial t}(m_f \mathbf{u}_f) + \nabla \cdot (m_f \mathbf{u}_f \mathbf{u}_f) = -\alpha_f \nabla p + \alpha_f \nabla \cdot \mathbf{T} - \mathbf{F}_i \tag{2}$$

$$\begin{aligned} \frac{\partial}{\partial t}(m_f E_f) + \nabla \cdot (m_f H_f \mathbf{u}_f) \\ = \nabla \cdot (\alpha_f \mathbf{T} \cdot \mathbf{u}_f) - \nabla \cdot (\alpha_f \mathbf{q}) - Q_i \end{aligned} \tag{3}$$

$$p = \rho_f R T_f \tag{4}$$

$\rho_f, p, \mathbf{u}_f, T_f, E_f, H_f$ is gas density, pressure, velocity vector, temperature, total energy, and total entalpy, respectively. α_f is void fraction, and $m_f = \alpha_f \rho_f$. R is gas constant. $\mathbf{T}$ is gas viscous tensor, and $\mathbf{q}$ is gas heat conduction. $\mathbf{F}_i$ and Q_i are interactions of momentum and energy between gas and solid particles.

Governing equations for each solid particle are as follows.

$$\frac{d}{dt}(\mathbf{r}_p) = \mathbf{u}_p \tag{5}$$

$$\frac{d}{dt}(m_p \mathbf{u}_p) = \mathbf{f}_i + \mathbf{f}_c + m_p \mathbf{g} \tag{6}$$

$$\frac{d}{dt}(I_p \omega_p) = \mathbf{M}_i + \mathbf{M}_c \tag{7}$$

$$\frac{d}{dt}(C_p T_p) = q_i + q_c \tag{8}$$

$\mathbf{r}_p, \mathbf{u}_p, \omega_p, T_p$ is position, translational velocity, rotational velocity, and temperature of the particle, respectively. m_p, I_p, C_p is mass, moment of inertia, and heat capacity of the particle, respectively. $\mathbf{f}_i$,$\mathbf{M}_i$, and q_i are interactions of momentum, angular momentum, and energy between gas and each particle. $\mathbf{f}_c$, $\mathbf{M}_c$, and q_c are particle-particle and particle-wall interactions.

The gas-particles interactions, $\mathbf{f}_i$, $\mathbf{M}_i$, and q_i, are assumed to be composed of drag force, $\mathbf{f}_{iD}$, Saffman force, $\mathbf{f}_{iS}$, Magnus force, $\mathbf{f}_{iM}$, macroscopic pressure gradient, $\mathbf{f}_{iP}$, drag torque $\mathbf{M}_{iD}$, and heat transfer q_{iT}. They are estimated by some results of experimental measurements and numerical simulations for a sphere.

The particle-particle and particle-wall interactions, $\mathbf{f}_c$ and $\mathbf{M}_c$, are estimated by the discrete element model (DEM), where elastic collisions are modeled by springs, dampers, and sliders.

3 Computational Method and Conditions

The governing equations for gas phase are discretised in space by the finite volume method. The solution vectors at the cell-boundary are evaluated by the 3rd order MUSCL method with Van Albada's limiting function, and then the invicid flux is estimated by the approximated Riemann solver. And, spatial gradients of solution vector is estimated by the least square method. On the time integrations, LU-SGS method is used for the gas-phase and the two-stages Runge-Kutta method for solid particles, and they are coupled weakly.

The gas phase is air, and the viscous coefficient is estimated by the Sutherland's equation. The shock wave Mach number is $M_S = 1.44$. The shock-induced flow velocity is $U_O = 211[m/s]$ and the particle Reynolds number is $Re_D = 2100$ in this condition. Each solid particle is a sphere, the diameter is $D = 0.1[mm]$Cthe density is $\rho_p = 980[kg/m^3]$, and the heat capacity is $c_p = 1200[J/kgK]$. As parameters of the DEM, the spring coefficient is $k = 2.05 \times 10^4[N/m]$, the damper coefficient is $c = 7.33 \times 10^{-4}[Ns/m]$Cand the Coulomb's friction coefficient is $\mu = 0.3$, the restitutive coefficient at the collision is $e = 0.7$ and the contacting period is $T_c = 0.5[\mu s]$ in these conditions.

The computational domain is three-dimensional, $0 \leq x \leq 400[mm]$, $0 \leq y \leq 0.3[mm]$, $0 \leq z \leq 100[mm]$. And a trough with depth of $2[mm]$ on the wall of $100 \leq x \leq 400[mm]$ is set to accumurate the solid particles. The conditions of the solid particle layer are shown in Table 1.

Table 1 Conditions of particle size and initial distributions of solid particle layer.

	DL1	DL2	DL3
Basic diameter D [mm]	0.10	0.10	0.10
Contact diameter D_c [mm]	0.10	0.14	0.10
Number of particles N_p	202,000	104,000	101,000
Mean volume fraction $\overline{\alpha_p}$	0.59	0.30	0.29
Particle contact condition	Contact	Contact	Dispersed

4 Results and Discussions

Distribution of solid volume fraction and gas pressure at $t = 0.8[ms]$ in the case of DL1 are shown in Figure 1(a), Figure 1(b), respectively. The shock wave propagated from left to right, the shock is at the position of 290[mm] from a leading edge of the dust layer. The dust cloud is formed behind the shock, where the pressure is disturbed.

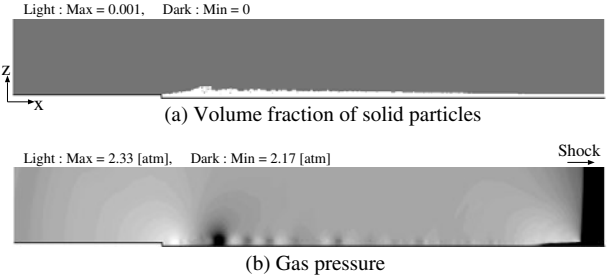

(a) Volume fraction of solid particles

(b) Gas pressure

Fig. 1 Shock wave propagating on the solid particle layer in the case of DL1.

The distributions of solid particles composing the dust cloud at $t = 0.8[ms]$ is shown in Figure 2. The horizontal axis is the distance from the shock, X, and the vertical axis is the height from the surface of the dust layer, h. Comparing the height of computational result with the experimental result, they are almost corresponding. And, it can validate the computational results in this study.

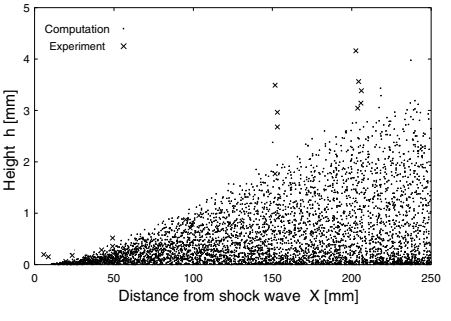

Fig. 2 Distribution of solid particles composing the dust cloud in the case of DL1, The "computation" means the height of each particle in the computational result of this study, the "experiments" means the maximum height of particles in the experimental results conducted by Suzuki et al.[5].

Outer shapes of the dust clouds in each cases of initial solid particle layer, DL1, DL2, and DL3 are shown in Figure 3. And, one in the case of DL1 without Saffman and Magnus forces are also shown in the same figure. It is shown in this figure

that the initial condition of the solid particle layer, contacted (DL1,DL2) or dispersed(DL3), is more dependent on the height of the dust cloud than the fluid lift forces. This result means that dust cloud formation is mainly caused by particle-particle direct interactons, that is contacts and collision between solid particles at the initial stage of the dust cloud formation.

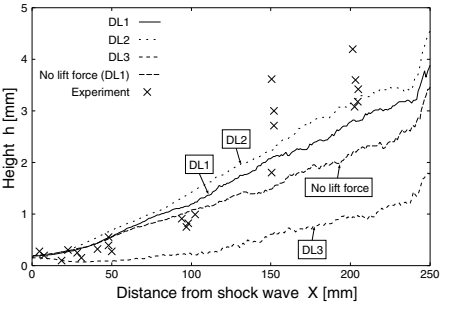

Fig. 3 Outer shapes of dust clouds; effects of initial condition of the solid particle layer and fluid lift force

Pressure distribution where the shock wave interacts with the solid particle layer in the case of DL1 and DL2 are shown in Figure 4. It is shown that the shock wave on the surface of the solid particle layer is curved by the interaction, and it raises the pressure on the surface behind the shock. And, the interaction in the case of DL2, higher void fraction, is stronger than that in the case of DL1, lower void fraction.

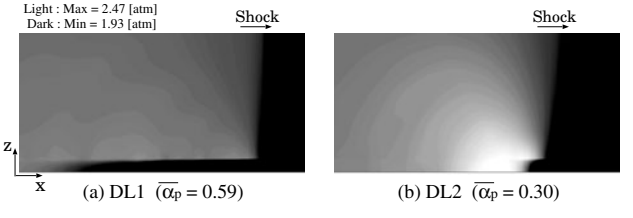

Fig. 4 Gas pressure distributions in shock structures interacting with dust layer; effect of the void fraction of the solid particle layer

Distributions of gas pressure and particle-contacting pressure on the bottom wall of the solid particle layer are shown in Figure 5. The gas pressure in this figure is a difference from that in front of the shock wave, and the particle-contacting pressure is averaged over 1[mm]. Furthermore, both of pressure values are nondimensionalized by the difference between the pressure behind the shock and that in front of the shock. The curvature of the shock generates the downward flow behind the shock, and then the downward flow pressed the solid particles to the bottom wall and raises the gas pressure in the solid particle layer behind the shock.

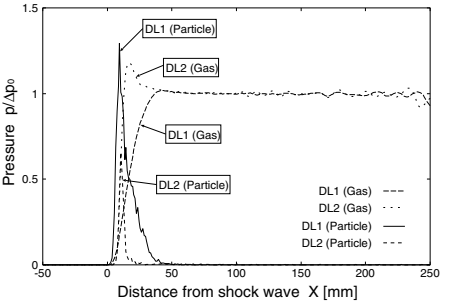

Fig. 5 Gas and solid particles pressure distributions on wall in overpressure behind shock

5 Conclusion

In the present study, the initial process of forming the dust cloud was numerically simulated to examine its dynamic mechanism. The simulated dust cloud was close to experimental results. It was found by comparing several types of dust layers that the upward velocity of lifted particles was more produced by particle-particle interactions than by fluid lift forces such as the Saffman force and the Magnus force. Moreover, it was confirmed that a relatively strong downward flow was induced just behind the foot of the shock by its curved shape, which promotes the interactions and causes an overpressure on the wall.

References

1. Dawes, J.G.: Safety in Mines Research Establishment. Ministry of Fuel and Power 36, 1–69 (1952)
2. Gerrard, J.H.: Brit. J. Appl. Phys. 14, 186–192 (1963)
3. Fletcher, B.: J. Phys. D: Appl. Phys. 9, 197–202 (1976)
4. Bracht, K., Merzkirch, W.: Int. J. Multiphase Flow 5, 301–312 (1979)
5. Suzuki, T., Adachi, T.: JSME Journal B 52(483), 3742–3746 (1986)
6. Khul, A.L., Ferguson, R.E., Chien, K.Y., Collins, P.: Progress in Astronautics and Aeronautics, vol. 154, pp. 491–515. AIAA, Wash., D.C. (1993)
7. Jiang, J.P.: Ph. D. Dissertation of Ben-Gurion University of the Negev (1996)
8. Thevand, N., Daniel, E.: Shock Wave 11, 279–288 (2002)

Hybrid Finite Element/Molecular Dynamics Simulations of Shock-Induced Particle/Wall Collisions

Michael M. Micci and Mark W. Crofton

1 Introduction

Contaminant metal particles of the order of 100-500 microns in diameter in the liquid propellant feed systems of rocket engines are a significant hazard and safety concern. These particles may originate from within the propellant tanks, valves, feed lines, pumps, or the propellant itself. Ignition and combustion of the particles when located within a supercritical oxygen-rich environment, such as would be found in an oxidizer-rich rocket engine system, could release a significant amount of energy. In addition, particle impacts with the walls of the propellant feed systems could sufficiently heat the particles to ignite them or to fracture them into smaller particles that are easier to subsequently ignite. Experiments are currently underway at The Aerospace Corporation to improve the knowledge base for particle-impact ignition. Oxygen pressure, particle size and kinetic energy, and the occurrence of fragmentation upon impact are among the parameters to be studied where impacting particle velocity is induced by the passing of a shock wave [1]. A simulation capability, validated by the experiments, would be of value to predict the risk of possible particle contamination.

An atomistic-based simulation such as Molecular Dynamics (MD) would be ideal for such a capability. Using MD, particle fracture is reproduced in the normal course of the simulation without the need to explicitly track surface boundaries during fracture [2]. Particle heating is tracked simply by the increase in an averaged atomic kinetic energy. The limitation to MD is that since the positions and velocities of individual atoms are being computed, current available computational capabilities still restrict system sizes to submicron sizes. The finite element method (FEM) can be utilized to simulate the compression and fracture of full size particles ($\sim$100 μm) but does not include the physics of what is happening at the contact point between the particle and the wall, which is controlled by atom-to-atom interactions. An ideal

Michael M. Micci
Pennsylvania State University, University Park, PA, USA

Mark W. Crofton
The Aerospace Corporation, El Segundo, CA, USA

simulation would combine MD to capture the physics occurring at the collision point with FEM to take into account the entire aluminum particle.

Finite elements and molecular dynamics have been combined previously by other investigators. Smirnova et al. modeled laser ablation generated pressure wave propagation through a two-dimensional solid, where MD was utilized in the region of laser impingement and wave generation and FEM for the surrounding region to examine the wave propagation [3]. Rudd and Broughton developed a three-dimensional hybrid MD/FEM model of a micro-resonator [4]. Here MD was used for the resonating microstructure and FEM for the attachment structure at the two opposing ends. Broughton et al. simulated fracture in a macroscopic sample [5]. All the groups used the same method to interface the MD and FEM regions, although they use different names for it (handshaking versus transition region). The MD and FEM regions are overlapped at the interface, with the MD results providing boundary conditions for the FEM simulation and the FEM simulation providing boundary conditions for the MD simulation. All the groups used classical techniques for the FEM region.

2 Simulation

MD simulations were constructed for an atomistic aluminum lattice to be located on the surface of the aluminum particle at the collision contact point, an atomistic nickel lattice to simulate the impacted wall, and the gaseous oxygen molecules initially between the two as well as any aluminum-oxygen reactions that may occur. MD simply solves the equation of motion, $F = ma$, for each atom where the force comes from the negative of the gradient of the interatomic potential. Thus knowledge of accurate interatomic potentials is key to obtaining realistic results. The ReaxFF interatomic potentials for Al-Al [6], Ni-Ni [7], Al-Ni [8], O-O [9], and Al-O [10] were used. ReaxFF is a relatively new potential that has the capability to simulate chemical bonding and reactions and potentials are now available for a wide number of elements. The interatomic potential parameters within ReaxFF are obtained by comparison to quantum mechanical calculations made using density functional theory (DFT).

The Velocity Verlet algorithm was used to compute the positions and velocities of each atom and neighbor lists were used to reduce the computation time. Both the aluminum and nickel lattices were initialized in a FCC lattice configuration with initial atomic velocities sampled from a velocity Maxwellian distribution corresponding to the desired initial temperature. Both the aluminum and nickel lattices were approximately 13 nm square and 1 nm thick. The aluminum lattice consisted of 16,384 atoms while the nickel lattice consisted of 17,328 atoms. The larger number of nickel atoms is a result of the interatomic lattice spacing for nickel being smaller than that for aluminum. The initial separation between the aluminum and nickel lattices was 1.7 nm, which is large enough that the aluminum and nickel atoms are not initially interacting.

Gaseous oxygen molecules were initialized between the lattices at random positions at a density corresponding to the desired gas pressure and temperature. Initial

velocities for the oxygen molecules were also sampled from a velocity Maxwellian distribution corresponding to the desired temperature.

For the FEM portion of the simulation the FORTRAN 95 source code of Smith and Griffiths was used [11]. This code is available in both serial and MPI-based parallel versions. A three-dimensional mesh was generated using cubes to construct a spherical aluminum particle, with each cube then decomposed into six tetrahedral elements. At the interface region between the aluminum atomistic and finite element regions, the atomistic forces calculated by the MD simulation are transferred to the finite element nodes at the interface. The finite element algorithm then solves for the displacements of the nodes (along with all the other nodes within the sphere) due to the atomistic forces and the nodal displacements are then transferred back to the aluminum atoms in the interface region to repeat the MD simulation. Due to the small size of the MD time step (2.5 fs) a number of MD time steps, equivalent to the time it takes for an acoustic wave to propagate across one aluminum finite element, are computed in between each transfer of forces and displacements.

Figure 1 shows the initial finite element meshed aluminum sphere with the atomistic aluminum (red) surface. It can be seen that the atomistic region spans several finite elements. The finite element mesh for the 0.19 m diameter aluminum sphere shown in Fig. 1 consists of 85,968 tetrahedral elements and 16,567 nodal points. Figure 2 shows a close-up of the collision portion of the mesh and the initial aluminum (red) and nickel (blue) lattices with molecular oxygen (green) between them at a gaseous pressure and temperature of 560 psia and 910 K respectively, which are typical test conditions [1, 12].

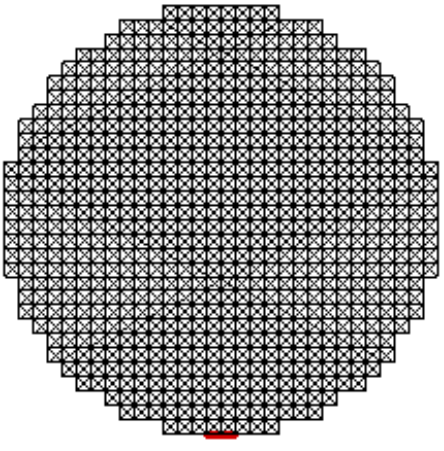

Fig. 1 Finite element mesh for a 0.19 μm aluminum sphere with attached (red) atomistic aluminum lattice at collision contact point.

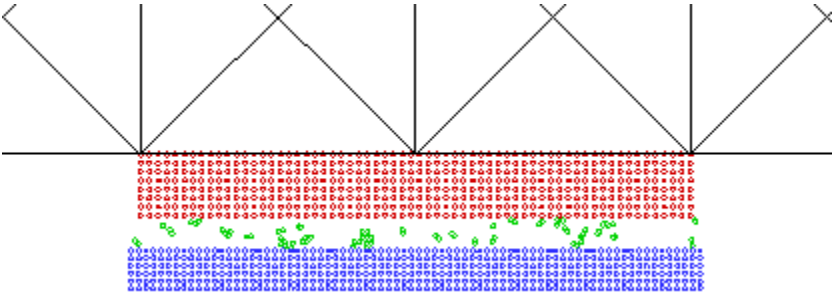

Fig. 2 Initialized aluminum (red) and nickel (blue) atomic lattices with gaseous oxygen (green) between them at start of simulation.

3 Results

The atomistic aluminum and nickel lattices were each initially equilibrated within the MD algorithm only until they were able to maintain a constant temperature of 300 K without any external forcing. To simulate a particle/wall collision, the side of the sphere opposite the collision contact point (top) was constrained against translation and rotation. The nickel lattice was then given a velocity of 500 m/s toward the aluminum lattice (up). The temperatures of the aluminum and nickel atoms and the oxygen molecules during the collision process were tracked by monitoring their respective kinetic energies.

Figure 3 shows the collision of the aluminum and nickel lattices shortly after impact. The compression and deformation of the lattices can be clearly seen. It can also be seen that the top layer of aluminum atoms are anchored to the FEM mesh.

Figure 4 plots the temperature rise of the aluminum and nickel lattices due to the collision. Both lattices start at an initial temperature of 300 K. The fluctuations in the temperatures are a result of the statistical variation in the temperatures since the plotted temperatures are at discrete time steps and not averaged over time. The temperature rise of the aluminum lattice is higher because its motion is constrained

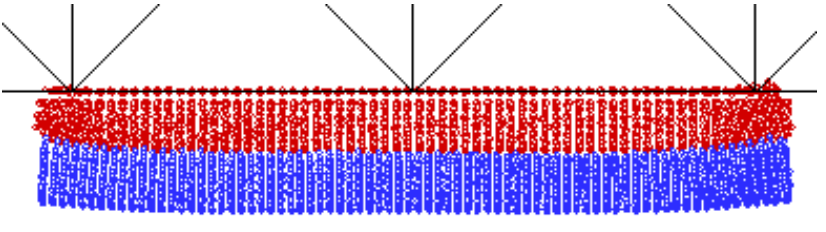

Fig. 3 Collision of a nickel (blue) lattice moving at 500 m/s with an aluminum (red) lattice connected to the finite element mesh of the larger aluminum sphere.

by the much heavier mass of the attached aluminum sphere while the nickel lattice is unconstrained. The temporary halt in the rise of the aluminum lattice temperature at approximately 1.2 ps is due to a fracturing effect that is temporarily absorbing the impact energy.

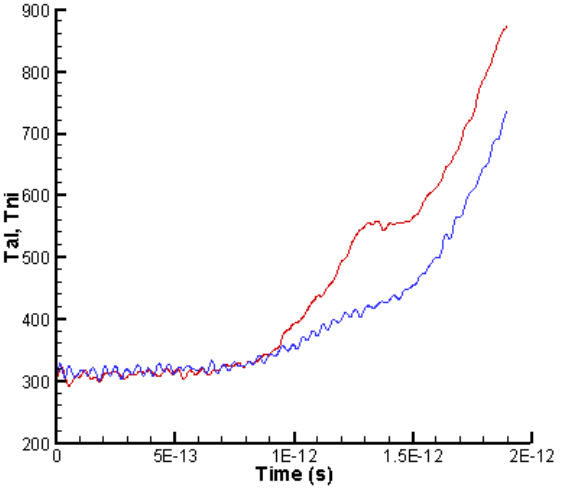

Fig. 4 Temperature of aluminum (red) and nickel (blue) atomistic lattices colliding with a velocity of 500 m/s.

4 Conclusions

A hybrid FEM/MD simulation has been constructed to model the impact of shock-induced macroscopic size aluminum particle collisions with a nickel wall in a high temperature and pressure gaseous oxygen environment. The region of the collision contact is simulated using MD on the atomistic level to accurately capture the oxygen-aluminum chemical reaction and aluminum fracture dynamics. A macroscopic size aluminum particle is able to be simulated by coupling the atomistic aluminum lattice at the contact point to a much larger (0.19 μm) FEM modeled spherical particle. Simulation results show the rise in temperatures of the two lattices due to the high velocity impact energy and the effect of fracturing on the temperature rise. Future work will further examine the effects of impact velocity and gaseous oxygen environment temperature and pressure. In addition different wall materials such as Inconel, Monel and Haynes alloys will be substituted for the nickel and their effects on the collision process and aluminum ignition investigated.

Acknowledgments. The work was supported under The Aerospace Corporation′s Independent Research and Development Program. The project manager is Dr. Jeff Emdee.

References

1. Crofton, M.W., Petersen, E.L.: Particle-Impact Ignition in High Pressure Oxygen: Initial Results. AIAA Paper 2010-7134 (2010)
2. Abraham, F.F., Brodbeck, D., Rafey, R.A., Rudge, W.E.: Physical Review Letters 73, 272–275 (1994)
3. Smirnova, J.A., Zhigilei, L.V., Garrison, B.J.: Computer Physics Communications 118, 11–16 (1999)
4. Rudd, R.E., Broughton, J.Q.: Phys. Stat. Sol (b) 217, 251–291 (2000)
5. Broughton, J.Q., Abraham, F.F., Bernstein, N., Kaxiras, E.: Physical Review B 60, 2391–2403 (1999)
6. Ojwang, J.G.O., van Santen, R., Kramer, G.J., van Duin, A.C.T., Goddard III, W.A.: J. Chem. Phys. 129, 244–506 (2008)
7. Mueller, J.E., van Duin, A.C.T., Goddard III, W.A.: J. Phys. Chem. C 114, 4939–4949 (2010)
8. van Duin, A.C.T.: Personal communication (2011)
9. Valentini, P., Schwartzentruber, T.E., Cozmuta, I.: J. Chem. Phys. 133, 084703:1–084703:9 (2010)
10. Zhang, Q., Cagin, T., van Duin, A., Goddard III, W.A., Qi, Y., Hector Jr., L.G.: Physical Review B 69, 045423-1–045423-11 (2004)
11. Smith, I.M., Griffiths, D.V.: Programming the Finite Element Method, 4th edn. John Wiley and Sons (2004)
12. Crofton, M.W., Stout, P.T., Albright, T.V., Worshum, M.D., Emdee, J.L., Petersen, E.L.: Development and Characterization of a Particle-Impact Ignition Facility. AIAA Paper 2010-7133 (2010)

Starting Flow through Planar Wedged Nozzle: Effect of Nozzle Asymmetry

Y. Shahack, O. Sadot, A. Britan, G. Ben-Dor, A. Hadjadj, and A. Chaudhuri

1 Introduction

The starting process of supersonic planar nozzles has been the subject of great number of the shock tube researches in the past. Initially this was motivated by the need to clearly separate the unsteady and quasi-steady parts of the expansion flow and thus specify the so-called ”test time” period of shock tube tunnels. Among other, the best known images illustrating the starting process were published by Amann [1]. It was clearly shown that the starting flow initiated by the primary shock wave (PS) includes the contact surface (CS) and the secondary shock (SS). Smith [2] was the first to show that the unsteady expansion wave (UEW) which follows the SS can also affect the total duration of the starting flow. Actually, the SS initiates flow separation and transient structure of the separation points (SP). Next, complex phenomenon which requires fundamental knowledge on the parameters of the external flow and the condition inside the boundary layer was discussed by Dussauge & Piponniau [3]. Flow separation may also cause significant effects on the trajectory of the SS and increase the total duration of the starting flow pattern. The renewed interest in nozzle starting phenomena appears due to wide application of the transient nozzle flow in different devices. The effect of separation, for example, becomes important inside the nozzles of rockets, missiles and/or supersonic aircrafts where it is usually undesirable since it may cause a dangerous lateral force which can damage the nozzle [4]. On the other hand, flow separation and the resulting instability of the exit plume could have positive effect when used in high speed mixing devices (Jonson & Papamoschou [5]). Despite a plentiful history and significant progress in the numerical as well as in the experimental investigations, many features of the nozzle starting, flow separation and its asymmetry are still open. Even a brief summary of the involved process clearly shows that the nozzle geometry, the viscous effects and

Y. Shahack · O. Sadot · A. Britan · G. Ben-Dor
Shock Tube Laboratory, Protective Technologies R&D Center, Department of Mechanical Engineering, Ben-Gurion University of the Negev, Beer-Sheva, Israel

A. Hadjadj · A. Chaudhuri
National Institute of Applied Sciences, INSA & CORIA UMR 6614 CNRS, Rouen, France

the flow conditions at the entrance and exit are important parameters that must be examined [6]. The current investigation was conducted to evaluate how the nozzle starting process depends on the initial conditions and on the asymmetry of the nozzle installation. In order to assess the role of these factors the incident shock wave Mach number was varied between $M_s = 1.2$ and $M_s = 1.9$ and the nozzle asymmetry was introduced by the relative shifting of half of the nozzle.

2 Experimental Part

The experimental set up includes a vertical shock tube apparatus, a set of pressure transducers and a schlieren visualization system. The cylindrical, $1.9m$ long driver section of the shock tube is separated from a $3.75m$ long square cross section channel ($80 \times 80mm^2$) by a $0.25 - 0.75mm$ thick plastic membrane. The driver is pressurized by air to the required pressure and the shock wave is generated by the rupture of the plastic membrane by a striking pin. The design of the wedged plane nozzle used in these experiments is shown in Fig. 1a. The nozzle, which was placed in the square test section of the shock tube channel, has a rounded inlet of radius $R = 10 \pm 0.01mm$, length $L = 142.87 \pm 0.01mm$, throat width $h_c = 9.5 \pm 0.01mm$ and angle $\alpha = 15^\circ \pm 0.01^\circ$. For the right half-nozzle (see Fig. 1a) a movable installation is used. The special linear translation stage (model MT1 - Thorlabs Co. USA) allows controllable ($\Delta = 0 \div 3.5mm$) movement along the horizontal axis. The resulting asymmetry in the nozzle installation can be controlled with an accuracy of about $\pm 1\mu m$. To prevent the movement of the fixed half-nozzle along the axis during the shock wave impact, all construction is provided by additional screws to fix the half-nozzle to the shock tube side wall. To measure the incident shock wave velocity two Endevco pressure transducers are flush mounted to the channel side wall at a known distance, as shown in Fig. 1. The sidewalls of the test section consist of large PMMA windows providing visualization of the internal flow field of $146 \times 75mm^2$. The standard optical schlieren system is shown in Fig. 1b. As a stroboscopic light source a 20 kHz doubled frequency Nd:YAG laser is used. A high speed PHANTOM v12.1 digital camera captures the pictures at a frame rate of 20,000 frames per second with a resolution of 352×680 pixels.

3 Results

3.1 Symmetrical Nozzle

To illustrate the starting phenomenon of a planer symmetrical nozzle the first series of tests was conducted using the so-called "minimal" shift of the half-nozzle $\Delta < 0.05mm$. Notice that an uncertainty of about $0.05mm$ corresponds to the standard accuracy of the Vernier caliper which is generally used for installation control in the laboratory tests. Typical flow images of this series are shown in Fig. 2 for three different times after the incident shock impinges the nozzle face. At the arrival of the incident shock wave, both lateral parts of the incident shock wave are

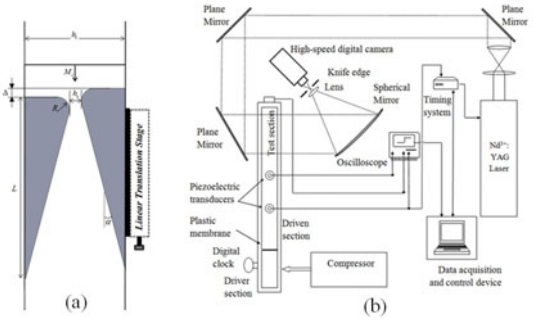

Fig. 1 (a) A schematic diagram of the test section. (b) The shock tube and optical apparatus.

reflected at the nozzle entrance and propagate backward as RS. The central part of the incident shock wave enters the nozzle throat and forms PS propagating into the gas occupying the nozzle, which is initially at rest. This generates the transverse flow to the main shocks that propagate towards the plane of symmetry where they collide and interact with each other with formation of the Mach configuration (MR). Two slip lines (SL) are clearly seen in the pictures of Fig. 2b. The symmetry of the input flow pattern demonstrates the symmetry of the expended flow inside the nozzle. A large difference in the tangential velocities at the CS separating the gases which originally occupies the nozzle from the upstream flow generates a series of small vortices that are also seen in Fig. 2b. The series of transverse shock waves behind the PS demonstrates repeated reflections between the nozzle walls. Soon a SS appears which is facing upstream because of the pressure gradient created in the nozzle. However, it is pushed downstream by the flow expanding from the nozzle throat. Due to interactions with the boundary layers, the SS is bifurcated at the wall, creating the flow separation. Two separation points (SPs) and the resulting bubbles of turbulent boundary layer fluid are clearly visible in Fig. 2b. The separation effect

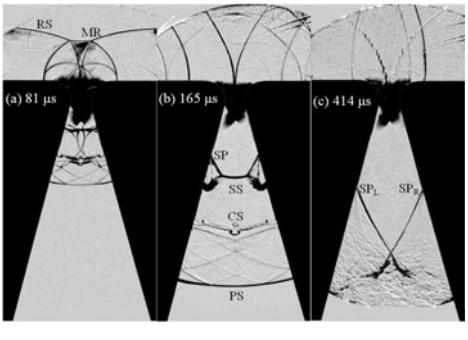

Fig. 2 Schlieren pictures of the starting flow (weak asymmetry) $M_s = 1.86$, $R = 10mm$, $\Delta = 0.05$

finally gives rise to two oblique shock-waves which move downstream and then intersect with each other. Interestingly, despite the negligibly small asymmetry of the nozzle setup, the positions of the left (SP)L and the right (SP)R separation points in Fig. 2c do not coincide. The visible asymmetry in the final flow pattern leads us to test this effect in more details.

3.2 Asymmetrical Nozzle

Small Shift: 0.05 $\leq \Delta \leq$ **0.23**. The observed asymmetry flow which is caused by a small inaccuracy in the nozzle setup has not been discussed so far in the related literature [4]. Among the nozzle characteristics which can initiate an asymmetrical starting flow, Bourgoing and Reijasse [6] focused on the wall roughness. They investigated the unsteady aspects of shock- induced separation patterns inside a planer nozzle. Asymmetry flow was derived by coating the nozzle throat with a rough surface in order to modify the state of the incoming boundary layers. Clearly, both strips modified the upstream boundary layer conditions in a similar manner, giving rise to the symmetric shock structure. In contrast, when applying a strip only on one side, an asymmetrical configuration was induced. This example ensures that asymmetry in the separated flow is a direct consequence of asymmetry in the upstream flow conditions. As a continuation of this approach in our study, a controllable shift of one side of the nozzle is used in order to initiate asymmetry in the nozzle flow. To obtain reliable results this method requires a high repeatability of the initial conditions. The error in the repeatability in the incident shock Mach number M_s is about 0.3%. The high accuracy of the data processing gives reliable results that enable measuring the asymmetry in high accuracy. With these data in hand the results shown in Fig. 3 allow us to conclude that the small shift, which could be also referred to as accuracy of the nozzle setup, has a minor effect on the trajectories of both starting shocks. A peak difference (about 3%) in the SS positions is seen when comparing the data registered for $\Delta = 0.05mm$ and $\Delta = 0.16mm$. The error bars in Fig. 3 are smaller than the marks which appear in the figure.

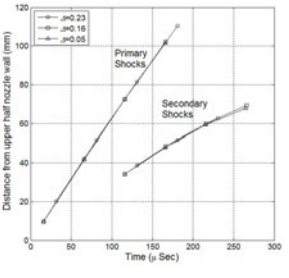

Fig. 3 Shock waves trajectories for small shift, $0.05 \leq \Delta \leq 0.23$, $M_s = 1.86$.

Large Shift: $0.05 \leq \Delta \leq 3.11$mm. Experiments were conducted for two different values of the incident shock Mach number, $M_s = 1.68$ and $M_s = 1.86$. Similarly to the previous case, the resulting data (shown in Fig. 4) demonstrate that the PS trajectory is insensitive to the shifting of the half-nozzle. As Δ increases, SS appears closer to the nozzle throat; however, its velocity weakly depends on Δ. Comparing the SS position inside the nozzle at some specific time one finds that as Δ increases the SS moves downstream. The shifting of the half-nozzle evidently changes the following: (a) the flow pattern at the nozzle entrance and (b) the flow width distribution along the nozzle axis. Comparing the trajectories of the SS presented in Fig. 5 one can see that when using the Flow-Width (FW) as a parameter, the transient dynamic of the SS becomes insensitive to the value of Δ. From that one can conclude that the role of the factor (a) is small - the SS propagation over the asymmetric nozzle is weakly dependent on the modified initial conditions, as seen in Fig. 6. In contrast, the role of the factor (b) is crucial - SS history is largely governed by actual distribution of the FW along the nozzle axis. As Δ increases, the flow pattern becomes more asymmetrical. The formation of the SS for a shifted nozzle was examined. The SS first appears near the right half-nozzle, Fig. 6a. Thereafter it approaches the left half-nozzle while an asymmetry lambda shock configuration is established, Fig. 6b. That can be attributed to the inclined inflow near the throat. This in turn causes strong lateral gradients affecting the pressure field and leads to asymmetry of the flow separation. In Fig. 6c the relative position of the SPs is inversed (SPR become lower then SPL) and remains asymmetric in Fig. 6d when the discharged flow becomes quasi-steady.

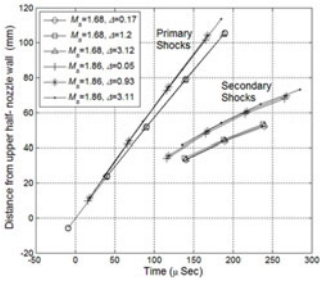

Fig. 4 Shock waves trajectories for large shift, Δ and two different Mach numbers, M_s

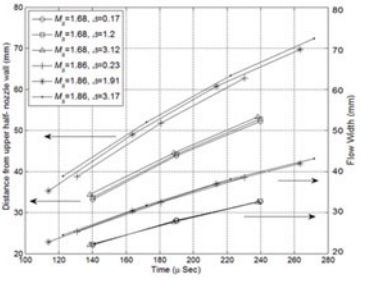

Fig. 5 Comparison between the Time-Distance and the Time-Flow-Width presentation of the SS trajectories

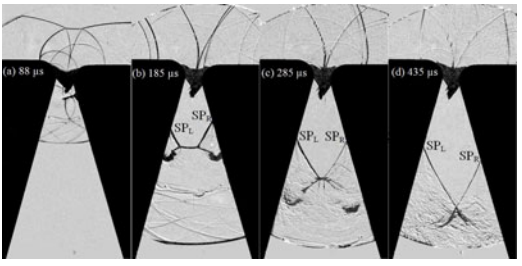

Fig. 6 Schlieren pictures of asymmetric starting flow, (strong asymmetry) $\Delta = 3.11mm$. $M_s = 1.86$.

4 Conclusion

The flow inside a planar nozzle induced by shock wave has been quantitatively investigated using the high speed schlieren photography. In order to initiate asymmetry in the flow pattern the new method of controllable shift of one half-nozzle was used. In the present paper, we focused on investigating the trajectories of the PS, SS and the resulted asymmetry obtained. It was found that even a negligible shift, or very small asymmetry, may result in asymmetry of the flow. While the PS shows weak dependence on the shift, the SS trajectory is strongly governed by the shift-modified distribution of the FW along the nozzle.

Acknowledgements. This research is supported by The ISRAEL SCIENCE FOUNDATION (grant No. 139/10).

References

1. Amann, H.O.: Experimental Study of the Starting Process in a Reflection Nozzle. Physics of Fluids Supplement 12, 150–153 (1967)
2. Smith, C.E.: The Starting Process in a Hypersonic Nozzle. Journal of Fluid Mechanics 24, 625–640 (1966)
3. Dussauge, J.P., Piponniau, S.: Shock/ boundary Layer interactions: Possible source of unsteadiness. Journal of Fluids and Structures 24, 1166–1175 (2008)
4. Abdellah, H., Marcello, O.: Nozzle Flow Separation. Shock Waves 14, 251–258 (2005)
5. Johnson, A.D., Paoamoschou, D.: Instability of shock-induced nozzle separation. Physics of Fluids 22, 016102 (2010)
6. Bourgoing, A., Reijasse, P.: Experimental analysis of unsteady separated flows in a supersonic planar nozzle. Shock Waves 14(4), 251–258 (2005)

Magnetic Configuration Effect on the Interaction between the Weakly Ionized Flow and the Applied Magnetic Field

M. Kawamura, H. Katsurayama, H. Otsu, K. Yamada, and T. Abe

1 Introduction

Since the pioneering work by Ziemer et al.[1], the interaction of the weakly ionized flow with a magnetized body has been investigated both experimentally[3, 4, 5, 6, 7, 2, 8] and numerically[9, 10, 11, 12]. This interaction has become a topic of interest as it has attractive applications to the mitigation of aerodynamic heating in hypersonic flight vehicles, which was numerically demonstrated by Poggie[9] and known as the electrodynamic heat-shield. Thus far, except for limited reports[13, 8], mitigation of aerodynamic heating has not been experimentally demonstrated. One such recent report was made by G*ü*lhan, but its result is still debatable[14]. Alongside the experimental efforts, numerical investigations have been conducted intensively[10, 11, 12]. It has come to our attention that, unlike the simple flow model assumed by Poggie[9], the interaction may be influenced by a variety of effects such as the Hall effect [10].

Thus far, research has been focused only on a specific magnetic field configuration against the flow; in this configuration, one of the magnetic poles is set normal to the incoming flow. The study of the interaction in case of other magnetic configurations is expected to provide an insight into the mitigation phenomenon of aerodynamic heating.

M. Kawamura
University of Tokyo, 7-3-1, Hongo, Bunkyouku, Tokyo 113-8656 Japan

H. Katsurayama
Yamaguchi University, Ube, Yamaguchi 755-8611, Japan

H. Otsu
Ryukoku University, Otsu, Shiga 520-2149, Japan

K. Yamada · T. Abe
Institute of Space and Astronautical Science/JAXA, 3-1-1, Yoshinodai, Sagamihara, Kanagawa 252-5210, Japan

In this paper, we aim to experimentally clarify the mitigation phenomenon of aerodynamic heating expected from the interaction and to investigate the influence of the magnetic field configuration on the mitigation phenomenon of aerodynamic heating.

2 Experiment

To generate a weakly ionized supersonic flow, an arc-jet wind tunnel is employed[5]. The specifications for typical flow conditions at the location where the model is inserted are summarized in Table 1. The model is equipped with a shutter at its front end to protect it from the flow before testing. Once the shutter is opened, the flow hits the model and a steady flow sets in around the model instantly.

Table 1 Test flow condition.[5]

Test gas	Argon	
Mach number, M^{∞}	1.7	
Flow speed, v_{∞}	1600	[m/sec]
Heavy particle temperature, T^{∞}	2000	[K]
Electron temperature, T_e^{∞}	≈ 10000	[K]
Electron number density, n_e^{∞}	$\approx 1\times10^{19}$	[m^{-3}]
Ionization degree, α^{∞}	≈ 0.005	
Static pressure, p^{∞}	34	[Pa]
Interaction parameter, $\hat{Q}(=Q/\mid B\mid^2)$	242	[T^{-2}]
Electric conductivity, σ^{∞}	1400	[S/m]
Hall parameter $\hat{C}_{H,\infty}$ ($=C_{H,\infty}/\mid B\mid$)	833	[T^{-1}]

In the present experiment, we used a spherically blunted cylindrical model (diameter: 22 mm), as shown in Fig. 1. The head of the model is made of ceramic shell (Marcor) to resist the high-temperature plasma flow and to prevent heating up of the inner part of the model. The thickness of the shell is 1 mm. The permanent magnet, spherical (diameter: 15 mm) and composed of neodymium, is installed inside the ceramic shell by means of a supporting structure made of brass. To prevent the heating up of the permanent magnetic, a gap of 1 mm is made behind the back surface

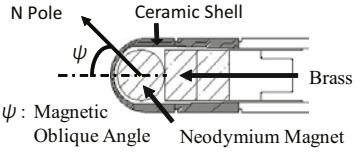

Fig. 1 Model configuration.

of the ceramic shell. As illustrated in the right panel of Fig. 2, the magnetic field around the magnet is symmetric around the magnet center except in the direction of the magnetic flux vector. In the left panel of Fig. 2, the distribution of the magnetic flux intensity around the magnet is shown. Here, the value is measured at a location 2 mm above the surface of the magnet.

To examine the effect of the magnetic field configuration around the model, the central axis of the permanent magnet is intentionally canted against the model central axis. Hereafter, we refer to such an angle defining the magnetic field configuration as the magnetic oblique angle. It should be noted that the case of 0° magnetic oblique angle is identical to the cases of the 180° magnetic oblique angle, except in the direction of the magnetic flux vector. Note that the magnetic field intensity appearing for a specific latitude in Fig. 2 appears at the stagnation point of the model surface for the corresponding magnetic oblique angle since the gap between the stagnation point and the sphericaly magnet is separated by 2 mm.

In the present experiment, a permanent magnet installed inside the model is employed to generate a strong magnetic field at the head of the model. In previous experiments[1, 8], however, this purpose was served by the electromagnet, which needs not only a large electric current but also a cooling system for the heated coil. Therefore, unlike the previous experiments[1, 8], we can investigate genuinely the magnetic field effect and easily modify the magnetic field configuration by changing the magnetic oblique angle of the permanent magnet inside the model.

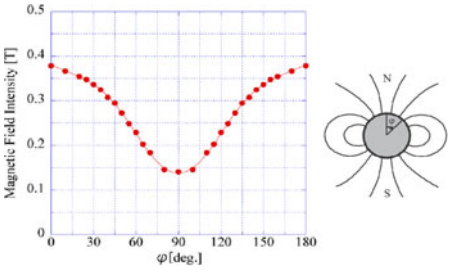

Fig. 2 Sketch of the magnetic field configuration (right) and surface distribution of the magnetic field intensity (left) of the spherical permanent magnet installed inside the model.

To measure the heat flux distribution over the model surface, we measure the temperature rising history of the model surface after the shutter is opened. For this purpose, we employ an infrared camera (TH9100PWV, NEC, Avio Infrared Technologies Co., Ltd., Japan). Typical images are shown in Fig. 3. From these views, we can obtain the image of any location of the model; this image can then be converted to the temperature distribution over the model surface using a properly calibrated local emission coefficient.

Since the model surface temperature starts to increase once the shutter is opened, the local heat flux causing this temperature increase was determined by assuming

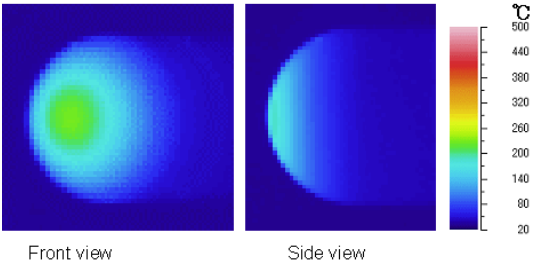

Fig. 3 Typical IR images from two different perspectives after 1 second.

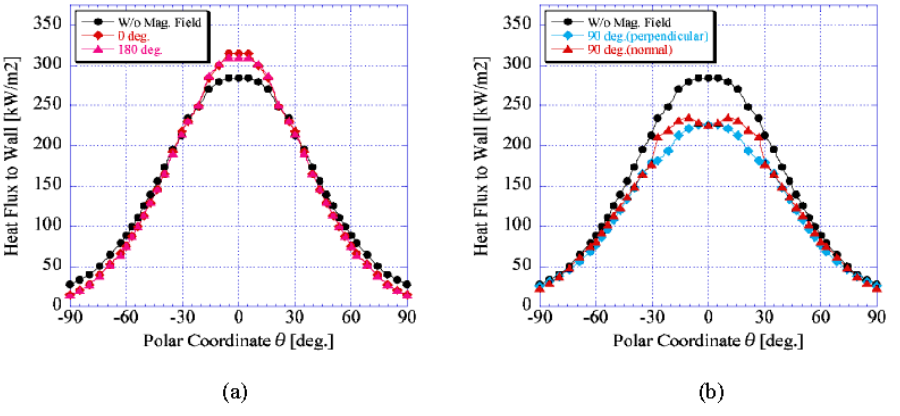

(a) (b)

Fig. 4 Heat flux surface distribution in the spherical part of the model with 0° and 180° magnetic oblique angles in (a) and with a 90° magnetic oblique angle,along the normal and perpendicular surface lines in (b). For reference, the result for the case without the magnetic field is also shown.

simple one-dimensional heat conduction and matching the heat conduction simulation result to the measured temperature history.

3 Result

The heat flux distribution on the magnetized model is depicted in Fig. 4(a) for the cases of 0° and 180° magnetic oblique angles. Here the horizontal axis belongs to the polar coordinate system of the spherical part of the model over the surface line; this surface line is defined as the intersection of the model surface with the plane that includes the central axis of the model. The stagnation point has a zero polar coordinate. The measurement was conducted 5 times under the same condition and the measured values were averaged; the averaged value is shown in the figure. The size of the error bar is reasonably small and within the size of the symbol. The result

in case of no magnetic field is shown for reference. To realize the situation of no magnetic field, the permanent magnet was intentionally demagnetized. According to the previous numerical simulation of the flow neglecting the Hall effect, the heat flux to the model surface with the magnetic field is smaller than that without the magnetic field. This is because the expulsion force generated by the magnetic field widens the shock layer, thereby relaxing the temperature gradient at the model surface[9]. Contrary to such an expectation, the heat flux in the case of the magnetic field is larger than that in the case of no magnetic field for the surface range between -30° to 30° of the polar coordinate but smaller for other regions. Unlike the assumption in the previous numerical simulation, the Hall effect in the present experiment is large as shown in Table 1, especially near the head of the model. At the region with large Hall effect, we should expect large Joule heating. Because of the Joule heating, the temperature inside the shock layer can be increased, which in turn may cause an increase in the heat flux[12]. Since the results for the cases of 0° and 180° of magnetic oblique angle are in good agreement, we can conclude that the effect of magnetic polarity change does not exist.

In the case of the 90° magnetic oblique angle, the flow behavior cannot be circumferentially axisymmetric around the body center axis. Therefore, it is necessary to investigate the heat flux distribution along both the surface lines. The heat flux distributions along the normal and perpendicular surface lines are depicted in Fig. 4(b). Both these distributions are symmetric at the stagnation point. The heat flux distribution along the perpendicular surface line has a peak at the stagnation point and is considerably more reduced as compared to that without the magnetic field. The reduction at the peak becomes as large as approximately 20%. On the contrary, the heat flux distribution along the normal surface line has peak values at around $\pm 10°$, which is slightly larger than that at the stagnation point. At the larger polar coordinates, the heat flux decreases and the difference between the heat flux with and without the magnetic field becomes smaller. In summary, the heat flux in the case of 90° magnetic oblique angle is much more reduced than that without the magnetic field especially in the region where the heat flux becomes significant; i.e., in the region within the -30° and 30° polar coordinates. This reduction is much larger than that in the case of a 45° magnetic oblique angle.

The heat flux increase caused by the Hall effect does not occur only in the case of 0° magnetic oblique angle. Since the Hall effect appears in proportional to the Hall parameter and the Hall parameter is proportional to the intensity of the magnetic field, the Hall effect should appear at the polar region the most significantly. In the case of 0° magnetic oblique angle, the polar region resides at the stagnation region where the increase of the heat flux is observed. In the case of 45° magnetic oblique angle, the slight increase of the heat flux appears near the polar region; i.e., between the stagnation point and the polar location. In the case of 90° magnetic oblique angle, both the poles reside in the locations where the heat flux is originally weak. Therefore, the slight increase of the heat flux caused by the Hall effect at the polar regions is barely visible.

4 Conclusion

According to the theory, the interaction of the magnetized body with the weakly ionized flow could cause the modification of the thermal boundary layer around the body and induce the modification of the aerodynamic heating distribution around the body. The present experimental investigation verifies such an expectation by means of the arc-jet wind tunnel and a blunted model with a spherical permanent magnet inside. It is found that, despite the theoretical expectation, the heat flux at the area of the stagnation point of the body increases compared with the one for the non-magnetized body, when the magnetic field configuration is set so that the axis penetrating both the poles of the magnet is parallel to the flow direction, while at the area other than the stagnation region, the aerodynamic heating is reduced as expected from the theory. It is also verified that such an interaction is strongly influenced by the magnetic field configuration around the body. Especially when the axis penetrating both the poles of the magnet is perpendicular to the flow direction, the aerodynamic heating is reduced at the whole area of the model surface compared with the one for the unmagnetized body.

References

1. Ziemer, R., Bush, W.: Magnetic Field Effects on Bow Shock Stand-Off Distance. Physical Review Letters 1(2), 58–59 (1958)
2. Bityurin, V., Bocharov, A., Lineberry, J.: MHD Flow Control in Hypersonic Flight. AIAA Paper 2005-3225 (2005)
3. Takizawa, Y., Matsuda, A., Sato, S., Abe, T., Konigorski, D.: Physics of Fluids 18, 117105–117110 (2006)
4. Matsuda, A., Otsu, H., Kawamura, M., Konigorski, D., Takizawa, Y., Sato, S., Abe, T.: Physics of Fluids 20, 027102 (2008)
5. Matsuda, A., Otsu, H., Kawamura, M., Konigorski, D., Takizawa, Y., Abe, T.: Physics of Fluids 20, 127103 (2008)
6. Tanifuji, T., Wasai, K., Makino, H., Otsu, H., Furudate, M., Yamasakik, H., Konigorski, D., Abe, T.: AIAA Paper 2008-3789 (2008)
7. Kawamura, M., Matsuda, A., Katsurayama, H., Otsu, H., Konigorski, D., Sato, S., Abe, T.: Journal of Spacecraft and Rockets 46(6) (November-December 2009)
8. Gülhan, A., Esser, B., Koch, U., Siebe, F., Riehmer, J., Giordano, D., Konigorski, D.: Journal of Spacecraft and Rockets 46(2) (March-April 2009)
9. Poggie, J., Gaitonde, D.V.: Physics of Fluids 14, 1720–1731 (2002)
10. Otsu, H.: AIAA J. 48(10), 2177–2186 (2010)
11. Katsurayama, H., Kawamura, M., Matsuda, A., Abe, T.: Journal of Spacecraft and Rockets 45(2), 248–254 (2008)
12. Katsurayama, H., Abe, T., Otsu, H., Konigorski, D.: AIAA Paper 2007-4529 (2007)
13. Nowak, R., Yuen, M.: AIAA Journal 11(11), 1463–1464 (1973)
14. Bityurin, V.A., Bocharov, A.N., Popov, N.: AIAA Paper 2010-4485 (2010)

Features of the Impact of a Solar Wind Shock Wave on the Earth's Bow Shock in a Strong Interplanetary Magnetic Field

E.A. Pushkar

1 Introduction

At present, there are several groups of spacecraft (THEMIS, Cluster, Double Star) rotating around the Earth on orbits whose elements are located in the outer magnetosphere, magnetosheath, and in the neighborhood of the Earth's bow shock S_b at distances of $10 \div 25$ Earth's radii R_E. Other spacecraft (Wind, SOHO, ACE) are located in the free solar wind in the neighborhood of the Lagrange point L_1 at $\sim 250\ R_E$ from the Earth. The data on the solar wind, the interplanetary magnetic field (IMF) and the magnetosheath parameters are continuously transferred to the Earth and actively analyzed. The measurement results are used to identify sharp changes in the solar wind associated with shock waves and other discontinuities and their manifestations in near space [1–4]. These investigations are due to the need for forecasting the cosmic weather which manifests itself on the Earth in the form of sudden storm commencements, magnetic substorms, and sudden impulses.

As a rule, the measurements are analyzed using the results of the one-dimensional analytic investigation [5] in which the structure of flow generated under the impact of a solar wind shock perturbation corresponds to the subsolar point and the propagation of the perturbation along the Sun-Earth radius [6, 7]. The fact that the wave flow pattern depends on the latitude and longitude of an element on the bow shock with which the perturbation interacts [8] and varies qualitatively (may be, discontinuously) as the perturbation propagates is ignored. However, the perturbations penetrating in the magnetosheath are subjected to significant quantitative variations due to different effects of the IMF in the subsolar zone, on the "dawn-dusk" flanks in the neighborhood of the plane of ecliptic [9], near the midday meridian and in polar zones [8]. In analyzing the events, the results of numerical MHD simulations are also used but their spatial resolution is frequently insufficient to identify close MHD waves which are merged with one another and can hardly be discerned [10, 11].

E.A. Pushkar
General and Applied Mathematics Department,
Moscow State Industrial University, Avtozavodskaya 16, Moscow, 115280, Russia

In order to interpret adequately spacecraft's measurements we need for exact solutions of the problem of interaction between a solar wind shock wave and the Earth's bow shock in which the wave flow pattern is a function of the latitude and longitude of a point on the bow shock. These solutions can serve as the boundary conditions for calculating the flow generated in the magnetosheath and the successive impact on the magnetopause and Earth's magnetosphere.

2 Formulation of the Problem and Method of Solution

We will consider propagation of the plane front of an interplanetary shock S_f along the Earth's bow shock S_b with a velocity $\mathbf{V}_{Sf}$ in the solar wind stream that flows past the Earth's magnetosphere and S_b at a velocity $\mathbf{V}_{sw}$ (Fig. 1). We will assume that the IMF $\mathbf{B}_{sw}$ is inclined to $\mathbf{V}_{sw}$ at an angle ψ_B and, to be specific, lies in the plane of the ecliptic. The normal $\mathbf{n}_{Sf}$ to the front S_f is aligned with $\mathbf{V}_{sw}$ and $\mathbf{V}_{Sf}$ ($\mathbf{V}_{Sf} \| \mathbf{V}_{sw}$). In the Cartesian coordinate system moving with the Earth (the X axis is directed to the Sun, the Y axis lies in the plane of the ecliptic, and the Z axis is perpendicular to the XY plane) the bow shock is assumed to be steady-state (Fig. 1). The position of each element of S_b approximated by the tangential plane with the normal $\mathbf{n}_{Sb}$ can be given by two angular coordinates, namely, the angle α of inclination of this element to the X axis and the angle τ of inclination of $\mathbf{n}_{Sb}$ to the XY plane (Fig. 1).

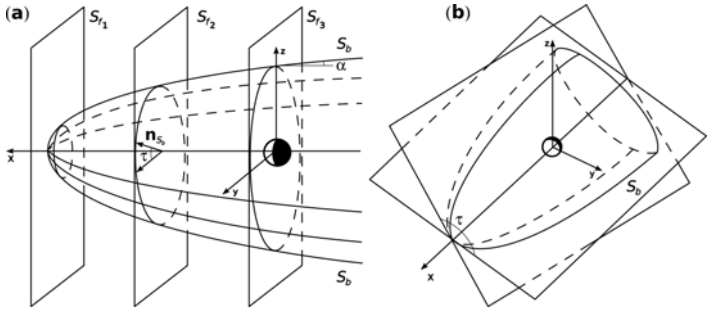

Fig. 1 Positions of the solar wind shock wave S_{fi}, $(i = 1,2,3)$ and the curve L_{SfSb} of intersection of S_f and S_b when S_f moves (**a**); cross-section of the surface of S_b by a half-plane $\tau = \text{const}$ (**b**)

If the density ρ_{sw}, the pressure p_{sw}, the velocity $\mathbf{V}_{sw}$, and $\mathbf{B}_{sw}$ are known in the undisturbed solar wind stream ahead of S_b, then all the parameters behind S_f are also known and the parameters behind S_b can be found as functions of the angles α and τ from the relations on the oblique non-plane-polarized fast MHD shock wave [12] after going over to a coordinate system moving with the curve L_{SfSb} of intersections of the S_f and S_b fronts. On L_{SfSb} each of the fronts is approximated by a plane.

After coming in contact of S_f and S_b at the subsolar point ($\alpha = 90^\circ$), the shock wave S_f moves along the S_b front so that $\alpha = \text{const}$ on the curve L_{SfSb} (Fig. 1);

thus, the time dependence for S_f is transformed into a parametric dependence on α and τ. In fact, when $\alpha = \text{const}$ the dependences of all quantities on τ give them in the neighborhood of L_{SfSb} at a certain instant of time. When $\tau = \text{const}$ the dependences on α represent the time dependences of the quantities along the curve of intersection of a half-plane $\tau = \text{const}$ with the surface of S_b when the front S_f moves (Fig. 1*b*). The motion is supersonic and the process of collision of S_f and S_b can be considered locally assuming that the establishment of flow takes place in a fairly short time negligibly small compared with the characteristic time of motion. Thus, a discontinuity between the states behind S_b and S_f arises at each point on L_{SfSb}. In order to solve the Riemann problem of breakdown of the discontinuity it is necessary to go over in a local coordinate system moving with a point on L_{SfSb} and use a Riemann MHD solver [12]. In the solution thus obtained all the discontinuities and rarefaction waves composing the flow are explicitly distinguished, i.e., the exact solution of the Riemann problem can be found numerically using a computer.

A regular solution includes two combinations of self-similar stationary flows consisting of a fast MHD wave (shock S^+ or centered rarefaction wave R^+), a non-plane-polarized Alfvén discontinuity A, and a slow MHD wave (S^- or R^-) divergent from L_{SfSb} and conjugated on a contact discontinuity C [12]. Six independent boundary conditions, namely, the no-flow condition and the conditions of continuity of the velocity, pressure, and magnetic field, must be satisfied on C. The originality of the Riemann solver proposed in [12] consists in overcoming the difficulty of description of the entire flow developed as a result of the interaction. For this description we must have all possible sets of systems specifying individual elements in accordance with the wave flow pattern to satisfy the boundary conditions on C. Since the wave flow pattern is not known in advance, such a system cannot be written a priori. However, an exact solution can be found using a special iteration method [12] in which the wave flow pattern can change when searching the solution.

3 Results of Numerical Simulation: Analysis of the Solution

On the Earth's orbit the solar wind represents a supersonic stream with the velocity of 400–450 km/s, the temperature of $(1.0 \div 1.2) \cdot 10^5$ °K, the particle concentration 10 cm^{-3}, the IMF strength $|\mathbf{B}|_{sw} \approx 6.2$ nT, and $\psi_B \approx 45°$ [13]. In the quiescent state the mean dimensionless solar wind parameters are as follows: the gasdynamic Mach number $\mathrm{M}_{sw} \approx 8$ and the beta-parameter $\beta = 8\pi p/B_{sw}^2 \approx 1$. However, considerable deviations from these values are observed. For example, the magnetic field can be significantly stronger in a magnetic cloud and the solar wind can be a slow plasma stream. We will study the interaction between S_f and S_b for a slow solar wind stream with the strong magnetic field when $\mathrm{M}_{sw} = 4.5$, the Alfvén number $\mathrm{N} = a_A/a_0 = (|\mathbf{B}|_{sw}/\sqrt{4\pi\rho_{sw}})/\sqrt{\gamma p_{sw}/\rho_{sw}} = 2.0$ ($\beta = 0.3$), $\psi_B = 45°$, and $\gamma = 5/3$. For these values of M_{sw}, N, and ψ_B there is a point ($\alpha = 45°$, $\tau = 180°$) on the dawn flank of S_b at which $\mathbf{B}_{sw}$ is collinear to $\mathbf{n}_{Sb}$ (S_b is quasi-parallel [14] on the dawn flank) and the conditions of existence of a switch-on shock S_b^* are satisfied:

$$1 < \mathrm{N}^2 < \mathrm{M}_{Sb}^2 < ((\gamma+1)\mathrm{N}^2 - 2)/(\gamma-1), \tag{1}$$

where $\mathrm{M}_{Sb} = \mathrm{M}_{sw} \sin\alpha$ is the Mach number of this element of the S_b front ($\alpha = 45°$).

The calculations were carried out for $\mathrm{M}_{Sf} = 3$ and 4.5. The first case corresponds to a relatively weak S_f in which ρ_{sw} and $|\mathbf{B}|_{sw}$ increase by factors of 1.55 and 1.48, while in the second case S_f has an intermediate intensity with increase in ρ_{sw} and $|\mathbf{B}|_{sw}$ by 2.4 and 2.1 times, respectively. From the mathematical point of view it is important to clarify how does the presence of the switch-on shock S_b^* affect the process of interaction between S_f and S_b since in S_b^* the electric current is reversed and this is accompanied by jumps in the velocity and the magnetic field.

The asymmetry of interaction between S_f and S_b on the dawn-dusk flanks is associated with different orientation of $\mathbf{B}_{sw}$ with respect to S_b and the reference-frame velocity $\mathbf{V}_{st}$ of L_{SfSb}: on the dawn flank ($\tau \approx 180°$) the angle ψ between $\mathbf{V}_{st}$ and $\mathbf{B}_{sw}$ is $\sim 90°$, the Alfvénic and magnetosonic characteristics can merge and, as a result, catastrophic global and local flow restructurings occur, the medium is strongly accelerated by the IMF and the density and gas-kinetic pressure grow more appreciably as compared with the opposite flank. On the dusk flank ($\tau \approx 0°$) ψ is close to zero, but, as compared with the situation for $\mathrm{M}_{sw} = 8$ and $\mathrm{N} = 1.1$ considered in [8], for $\mathrm{M}_{sw} = 4.5$ and $\mathrm{N} = 2$ the conditions of appearance of the tangential discontinuity catastrophe [8, 15] are not fulfilled and the flow varies smoothly and continuously.

When S_f propagates along S_b, the main features of the interaction are as follows. The maximum density and pressure are reached in the transmitted shock wave S_f' on the dawn flank ($\tau = 180°$, $\alpha' = 180° - \alpha$): $p_{Sf'}/p_{sw} \approx 19$ and 40 at $\alpha' = 110$ and 120° for $\mathrm{M}_{Sf} = 3$ (Fig. 2) and 4.5, respectively. At $\alpha' = 135°$ the pressure in S_f' increases suddenly by $\sim 1.5 p_{sw}$ for $\mathrm{M}_{Sf} = 3$ (by $\sim (3 \div 4) p_{sw}$ for $\mathrm{M}_{Sf} = 4.5$) in the global catastrophe K_G (see jumps in p in Fig. 2, variation in p in slow waves R_f^- and S_f^- corresponds to the difference between the ordinates of curves for C and S_f'). The maximum pressure is reached in S_f' on the dusk flank and in S_b^- on the dawn flank (when $\alpha' > 135°$), at $\alpha' = 135°$ the slow rarefaction waves R_f^- being transformed into the slow shock waves S_f^- ($\mathrm{M}_{Sf} = 3$, Fig. 2) The density and pressure decrease smoothly and monotonically in all the waves with decrease in α on the dusk flank, while on the dawn flank the pressure (Fig. 2) and other parameters change jumpwise due to redistribution of the electric currents in S_b^* (catastrophe K_G, $\alpha' = 135°$).

As α decreases, the profiles $p(\tau)$, very flattened at $\alpha \sim 85°$, become more and more steep due to smooth decrease in the pressure in S_b and all other flow components on the dusk flank and increase in the pressure on the dawn flank. Thus, the relative pressure difference between the flanks becomes twofold at $\alpha = 60°$ and even threefold at $\alpha = 45°$, the greater pressure difference between the flanks being characteristic of $\mathrm{M}_{Sf} = 3$. As a result of K_G, the pressure decreases sharply in S_b but remains a continuous function of α (Fig. 2). However, the pressure drops jumpwise in S_b' due to changes in the magnetic field and velocity in S_f and a narrow zone of width $\pm 10°$ in τ is formed in the neighborhood of $\tau = 180°$ in which the pressure behind S_b' is less than the pressure for $|\tau - 180°| > 10°$ by $(3 \div 4) p_{sw}$. As α decreases, this zone extends to $\tau = 180° \pm 20°$ and, as a result of the strong pressure

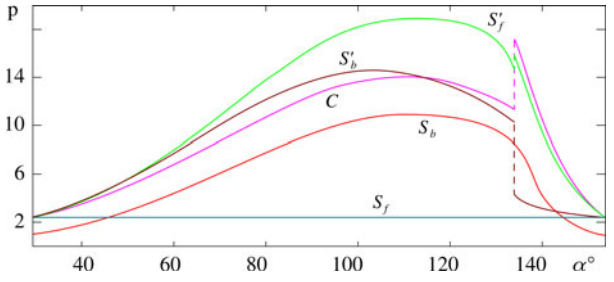

Fig. 2 Dimensionless pressure p/p_{sw} as a function of the latitude α for $\tau = 0^\circ$ ($\alpha < 90^\circ$) and $\tau = 180^\circ$ (plotted values of $\alpha > 90^\circ$ correspond to $\alpha' = 180^\circ - \alpha$ on S_b), $M_{Sf} = 3$

drop, for $M_{Sf} = 4.5$ the refracted bow shock S'_b is transformed into a rarefaction wave R_b^+ at $\alpha \approx 35^\circ$. Thus, in the strong IMF the flow past the dawn flank of the Earth's magnetosphere can occur in the neighborhood of the plane of ecliptic in the form of a fast rarefaction wave R_b^+ and a subsequent strong slow shock wave S_b^-.

The crucial influence of the IMF on the flow and the difference between the dawn and dusk flanks can be illustrated by the behavior of the magnetic field in the neighborhood of $\alpha = 45^\circ$ (Fig. 3). Almost on the entire dusk flank when $\tau < 80^\circ$ or $\tau > 280^\circ$ the physical quantities either do not vary or vary only slightly, while on the dawn flank the variations in all the quantities as functions of τ are fairly large and sharp due to the different influence of the IMF for $\alpha > 45^\circ$ and $\alpha < 45^\circ$.

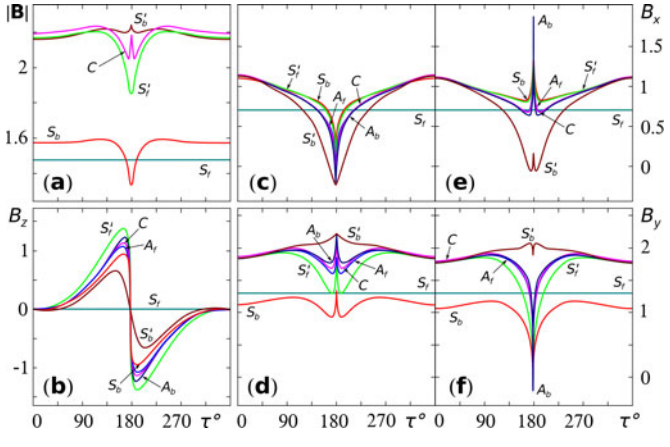

Fig. 3 Magnetic field strength $|\mathbf{B}|$ (**a**) and its components B_z (**b**), B_x (**c**), (**e**), and B_y (**d**), (**f**) as functions of the longitude τ for $M_{Sf} = 3$, $\alpha = 46^\circ$ (**a**) – (**d**) and $\alpha = 44^\circ$ (**e**), (**f**)

A narrow zone is formed on S_b near $\tau = 180^\circ$, where the magnetic field components change sharply and heavy electric currents are generated (Fig. 3). This occurs due to vanishing of the currents in the Alfvén discontinuities A_f and A_b at $\tau = 180^\circ$

since there are no A_f and A_b in the plane-polarized flow [16] and the electric currents in A_f and A_b have to be redistributed over other waves as $\tau \to 180^\circ$. In particular, as $\alpha \to 45^\circ$ the slow waves change abruptly and R_f^- are transformed into S_f^- (Fig. 2).

As S_f propagates further along S_b, at $\alpha = 45^\circ$ the entire flow is suddenly restructured due to the presence of a switch-on non-plane-polarized shock S_b^* for $\tau = 180^\circ$ (Fig. 3). Jumpwise reversion of the electric current leads to jumpwise change in the velocity and magnetic field components behind S_b and, consequently, in the neighborhood of $\tau = 180^\circ$ when $\alpha = 45^\circ - 0$ the S_f front interacts already with another state of the medium and another magnetic field. When the electric current in S_b is reversed, the discontinuity between the states behind S_f and S_b changes jumpwise when crossing $\alpha = 45^\circ$ and, as a result, the global catastrophe K_G takes place.

An important feature of the interaction at $\alpha = 45^\circ$, $\tau = 180^\circ$ is the jumpwise change in $B_z(\tau)$ in all the waves except for S_b' (Fig. 3*b*). In this case only for S_b' the initial state of the plasma is such that the velocity and IMF vectors lie in the plane of ecliptic since the interplanetary shock wave S_f is plane-polarized in accordance with its propagation along the solar wind. Therefore, as $\tau \to 180^\circ$ the refracted bow shock S_b' should tend to a plane-polarized shock so that the magnetic field component $B_z \to 0$ downstream of S_b' as $\tau \to 180^\circ$. However, already the reflected A_b in the wake of S_b' need not be plane-polarized and the electric currents flowing along its front and changes in the magnetic field in A_b are determined by the conditions of existence of the solution of the whole Riemann problem of breakdown of an arbitrary discontinuity formed by the states behind S_b^* and S_f. Since the S_b^* is non-plane-polarized and $B_z \neq 0$ downstream of it, then all the other waves, except for S_b' which necessarily be plane-polarized in accordance with the formulation of the problem when $\tau = 180^\circ$, are also non-plane-polarized and jumps in B_z are generated.

4 Conclusions

The propagation of an interplanetary shock wave S_f along the Earth's bow shock S_b and their interaction are considered in the 3D formulation within the framework of a magnetohydrodynamic model. The global 3D pattern of the interaction is constructed as a mosaic of exact solutions of the problem of breakdown of an MHD discontinuity developed at various points on the surface of S_b during collision of S_f with S_b. The investigation is carried out for relatively slow solar wind streams when the magnetic pressure is twice or more as higher than the gaskinetic one. It is found that the dawn-flank flow is catastrophically restructured at a point, where the interplanetary magnetic field is parallel to the normal to S_b. This is accompanied by jumps in the velocity and magnetic field, while the electric currents are reversed and strong rotational discontinuities and slow waves are generated. As a result, a narrow zone of width $\sim 20^\circ$ with abrupt variations in the plasma and magnetic field parameters is formed on the dawn flank. An intense interplanetary shock (e.g., with $M_{Sf} = 4.5$) can transform the bow shock into a fast rarefaction wave R_b^+ so that the

shock-perturbed flow past the dawn flank of the Earth's magnetosphere consists of an R_b^+ and strong rotational discontinuity and slow MHD shock.

Acknowledgements. The work was carried out with support from the Russian Foundation for Basic Research (project No. 11-01-00235) and a Russian Federation President's Grant for Leading Science Schools (project No. NSh-4810-2010.1).

References

1. Přech, L., Němeček, Z., Šafránková, J.: Geophys. Res. Lett. 35, L17S02 (2008)
2. Maynard, N.C., Farrugia, C.J., Ober, D.M., et al.: J. Geophys. Res. 113, A10212 (2008)
3. Keika, K., Nakamura, R., Baumjohann, W., et al.: J. Geophys. Res. 114, A00C26 (2009)
4. Pallocchia, G., Samsonov, A.A., et al.: Ann. Geophys. 28, 5 (2010)
5. Grib, S.A., Brunelli, B.E., Dryer, M., Shen, W.W.: J. Geophys 84, A10 (1979)
6. Zhuang, H.C., Russell, C.T., Smith, E.J., Gosling, J.T.: J. Geophys. Res. 86, A7 (1981)
7. Grib, S.A.: Space Sci. Rev. 32, 1–2 (1982)
8. Pushkar, E.A.: Fluid Dynamics 44, 6 (2009)
9. Grib, S.A., Pushkar, E.A.: Geomegnetizm i Aeronomiya 46, 4 (2006)
10. Samsonov, A.A., Němeček, Z., Šafránková, J.: J. Geophys. Res. 111, A08210 (2006)
11. Samsonov, A.A., Sibeck, D.G., Imber, J.: J. Geophys. Res. 112, A12220 (2007)
12. Pushkar, E.A.: Fluid Dynamics 34, 4 (1999)
13. Hundhausen, A.J.: Coronal Expansion and Solar Wind. Springer, New York (1972)
14. Anderson, K.A.: Nuovo Cimento 2C, 747–771 (1979)
15. Grib, S.A., Pushkar, E.A.: Planetary and Space Science 58, 14–15 (2010)
16. Barmin, A.A., Pushkar, E.A.: Fluid Dynamics 27, 4 (1992)

Shock Wave–Boundary Layer Interaction from Reflecting Detonations

J. Damazo, J. Ziegler, J. Karnesky, and J.E. Shepherd

1 Introduction

The present work is concerned with the differences in how shock and detonation waves inside pipes or ducts reflect from closed ends. One of the motivations for the present study is that the large pressure rise associated with a detonation poses a hazard to pipes that contain flammable mixtures [1]. A detonation impinging normally on a planar wall creates a reflected shock wave to bring the flow at the wall to rest [2] and produces pressures 2.4 times that of an incident Chapman-Jouguet (CJ) detonation [3]. In examining the material deformation produced by reflected detonation loading [4] an inconsistency was discovered between the measured pressure jump across the reflected shock wave and the measured speed of the shock, with the measured pressure being as much as 25% below that predicted by the shock jump relations for the given shock speed. This was theorized to be due to bifurcation of the reflected shock wave associated with shock-wave boundary layer interaction.

Previous researchers have observed shock wave bifurcation in experiments pertaining to shock tube performance [5, 6, 7, 8, 9]. Shock bifurcation is the splitting of a reflected shock near the wall into an oblique and a normal wave due to interaction with the fluid in the boundary layer created by the incident shock. This results in a foot extending from the wall to the primary reflected shock as sketched in Fig. 1. Mark [5] developed a theory describing reflected shock wave bifurcation and created a model for predicting the conditions under which bifurcation will occur. However, the differences between shock and detonation waves prevent this theory from being directly applied to the reflected detonation case. Previous computational work [10] has suggested reflected detonations do bifurcate, but these simulations did not consider the three-dimensional flow behind a detonation nor heat loss to the wall, both of which may affect bifurcation behavior. The goal of the present study is to experimentally investigate the influence of the boundary layer in detonation reflection.

J. Damazo · J. Ziegler · J.E. Shepherd
Graduate Aerospace Laboratories, California Institute of Technology, Pasadena, CA, USA

J. Karnesky
Propulsion Directorate, Wright-Patterson Air Force Base, Dayton, OH, USA

2 Theory

A sketch illustrating archetypical shock wave bifurcation is shown in Fig. 1 with velocities given in the shock-fixed frame. A reflected shock wave of speed U_R is passing into fluid set in motion by the incident wave to speed u and has developed a boundary layer at the bottom wall due to the no-slip condition. The fluid velocity will be a function of space and time due to the boundary layer and the presence of the Taylor wave behind a detonation [11]. The primary reflected shock wave propagates into the fluid outside the boundary layer in a one-dimensional fashion and determines the shock speed. In the boundary layer the combination of low-speed fluid and the prescribed pressure rise across the shock wave may cause the fluid to detach and form a separated bubble that, due to insufficient static pressure [5], will travel with the reflected shock wave and cause the bifurcated region to grow.

A simple theory has been developed by Mark [5] and refined by Davies and Wilson [7] to predict if bifurcation will occur for a given mixture and Mach number. This theory uses a simplified flow field where the fluid inside the boundary layer has zero velocity and is at the initial temperature and the fluid outside the boundary layer is unaffected by the wall. Bifurcation, Mark argues, will then occur if the stagnation pressure of the fluid inside the boundary layer relative to a frame stationary with respect to the reflected shock is less than the pressure behind the reflected shock wave. In the detonation case the assumption of a cold boundary layer is questionable due to the large temperature variations within the boundary layer. Furthermore, the flow field behind the detonation is three-dimensional with transverse waves and shear layers complicating theoretical predictions. The absence of an applicable theory for the reflected detonation case has led us to pursue experimental work examining reflecting detonation waves and how they compare to reflecting shock waves of similar molecular composition and initial pressure.

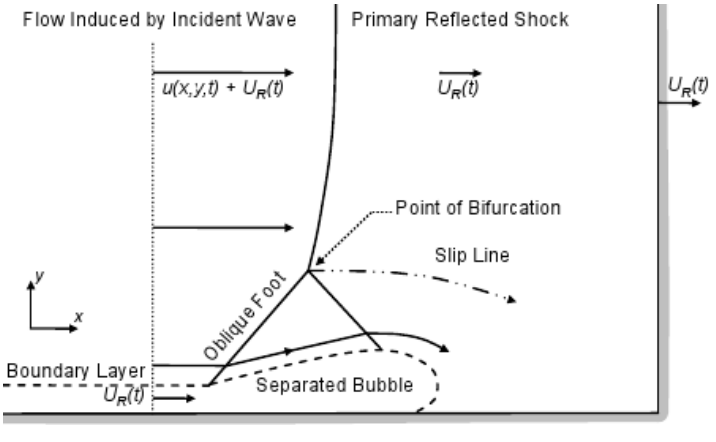

Fig. 1 Sketch of reflected shock wave bifurcation with velocities shown in the shock-fixed frame

3 Experimental Setup

All experiments were performed in the GALCIT Detonation Tube (GDT). (For a description of the facility, see [12].) The GDT is a 7.6 m long detonation tube of inner diameter 280 mm equipped with a test section of 150 mm wide square cross section and two quartz windows to provide optical access. The tube is initially evacuated and then filled via the method of partial pressures to the desired composition; a circulation pump is then employed to ensure proper mixing. After the mixing period, a sequence of events is initiated that begins the experiment: 1) A mixture of acetylene and oxygen is injected into the ignition end of the GDT for a duration of 4.5 s. 2) The mixture is allowed to settle for a period of 1 s. 3) A 2 μF capacitor charged to 9 kV is discharged through an 80 μm diameter 30 mm long copper wire located in the ignition end of the GDT. This discharge vaporizes the copper wire and detonates the acetylene-oxygen buffer. The strong shock wave generated from this detonation then propagates into the test mixture. This shock wave will either detonate the test mixture or, in the case of a non-reacting test mixture, begin to decay. In the results presented herein the test mixture is either air, pure nitrous oxide, or a mixture of nitrous oxide and hydrogen as given in Table 1. Nitrous oxide is chosen for the ease with which it has been observed to bifurcate in reflected shock wave experiments [6]. Four PCB 113B26 pressure transducers mounted in the GDT and test section are used to monitor the wave speeds. Table 1 shows large deviations from the theoretical CJ speed with the pure nitrous oxide mixture implying a detonation is only observed in the hydrogen-nitrous oxide mixture as expected from previous tests [13].

After the ignition sequence occurs, there will either be a decaying shock wave or a detonation wave entering the test section shown in Fig. 2. Two aluminum plates are mounted so that the boundary layer behavior may be seen through the windows. A Z-type schlieren setup consisting of a 400 ns duration spark light source, two 1600 mm focusing mirrors, and a Nikon D200 CCD camera is used to visualize the fluid mechanics. The camera is operated with an open shutter and the timing is controlled via the spark light source. This setup is not capable of obtaining multiple images of a single experiment. In cases where multiple images of the same mixture are shown (as in Fig. 3), the experiment is repeated and the spark timing is altered to create a sequence of events.

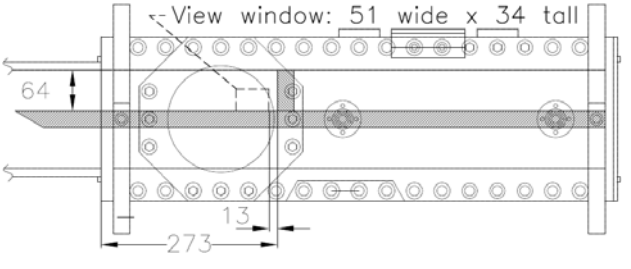

Fig. 2 Detail view of the test section for the GDT; dimensions in mm

Table 1 Run conditions with incident shock speed U_I, theoretical CJ detonation speed U_{CJ}, incident shock Mach number M_I, reflected shock Mach number M_R, temperature behind the incident wave T_2, and ratio of specific heats γ behind the incident wave

Mixture	Initial Pressure (kPa)	U_I [a] (m/s)	U_{CJ} [b] (m/s)	M_I [a]	M_R [a]	T_2 [b] (K)	γ [b]
79% N_2, 21% O_2	25	770	N/A	2.2	1.6	557	1.4
100% N_2O	15	730	1690	2.7	1.6	578	1.28
90% N_2O, 10% H_2	15	1670	1804	5.9	1.6	2827	1.27

[a] Calculated using the shock jump relations with the pressure rise across the shock as measured by the pressure transducer located in the test section.
[b] Computed using Cantera 1.8 and the Shock and Detonation Toolbox [3].

4 Discussion

The case of a shock wave propagating in air is shown in Fig. 3. Fig. 3a shows the incident shock propagating to the right of the figure. Fig. 3b is taken 200 μs later than 3a and shows the reflected shock propagating to the left. Visible at the wall is the bifurcated foot propagating ahead of the primary shock wave and a turbulent boundary layer behind the reflected shock. This test serves as a point of comparison as we examine the nitrous oxide mixtures.

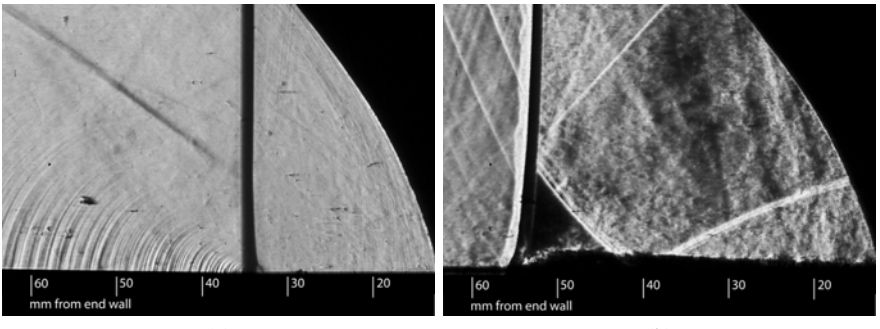

(a) (b)

Fig. 3 (**a**) Incident shock wave of Mach number 2.2 in 25 kPa initial pressure air propagating to the right. (**b**) Reflected shock wave in the same mixture propagating to the left and interacting with the boundary layer created by the incident wave

Fig. 4a shows the reflected shock wave in the pure nitrous oxide mixture. Complicating the image is the boundary layer interaction and bifurcation on the side wall formed by the windows, but it is readily observed that the bifurcated region is substantially larger than that observed in the higher pressure air mixture and qualitatively similar to the images obtained in carbon dioxide by Taylor and Hornung [8]. This enhanced effect is due [6] to the lower ratio of specific heats, γ, in nitrous

oxide (see Table 1). Comparing Fig. 4a to the reflected detonation shown in Fig. 4b reveals that, although bifurcation is still present, the height of the bifurcated foot at similar distance from the end-wall is substantially reduced by the detonation despite a similar computed specific heat ratio. The observed reduction in bifurcation height is explained by considering the bifurcation theory developed by Mark [5]. As given in Table 1, the temperature behind the incident shock wave is 578 K for the pure N_2O mixture and 2827 K for the N_2O–H_2 detonation. If, like Mark, we assume that the temperature of the fluid in the boundary layer behind the incident wave equals the initial wall temperature then the Mach number of the reflected shock traveling in the boundary layer will be affected much more by the cold boundary layer in the case of an incident detonation than an incident shock wave. Specifically, the reduction in sound speed due to the cold boundary layer will result in a substantially larger Mach number than would be computed using the sound speed in the center of the vessel. This has the effect of hindering bifurcation by increasing the stagnation pressure in the boundary layer. In other words, although the Mach numbers in the free stream are comparable, the reflected shock Mach number in the boundary layer is much higher for an incident detonation than an incident shock wave and thus the potential rise in the boundary layer stagnation pressure is larger in the detonation case. Further investigation is required to better understand the behavior of the boundary layer behind detonations and properly interpret these results.

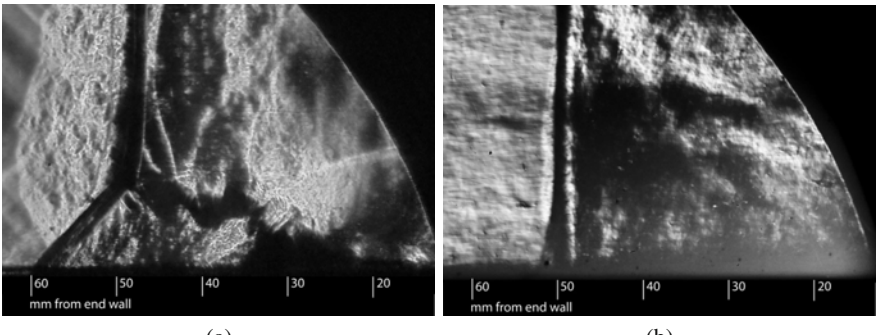

(a) (b)

Fig. 4 (**a**) Reflected shock wave in pure N_2O and (**b**) reflected detonation wave in 90% N_2O, 10% H_2. Both tests had initial pressure 15 kPa and the waves are propagating to the left

5 Conclusion

Bifurcation of a reflecting shock wave is readily observed in a pure nitrous oxide mixture of initial pressure 15 kPa. However, adding a small amount of hydrogen to the mixture thereby creating a detonation wave drastically reduces the degree of bifurcation observed. The present work is preliminary and further study is in progress to generalize this to other mixtures and obtain a clear explanation for this effect.

Acknowledgements. This research is sponsored by the DHS through the University of Rhode Island, Center of Excellence for Explosives Detection. J. Damazo is supported by a DOD NDSEG Fellowship and J. Zeigler is supported by a DOE CSGF Fellowship. The authors would also like to thank Bahram Valiferdowsi, Jeff Odell, and Rémy Mevel for their skill, help, and advice.

References

1. Shepherd, J.E.: Structural Response of Piping to Internal Gas Detonation. Journal of Pressure Vessel Technology 131 (2009)
2. Shepherd, J.E., Teodorcyzk, A., Knystautas, R., Lee, J.H.S.: Shock Waves Produced by Reflected Detonations. Progress in Astronautics and Aeronautics 134 (1991)
3. Browne, S., Ziegler, J., Shepherd, J.E.: Numerical Solution Methods for Shock and Detonation Jump Conditions. Tech. Rep. FM2006-006, GALCIT (2006)
4. Karnesky, J., Damazo, J., Shepherd, J.E., Rusinek, A.: Plastic Response of Thin-Walled Tubes to Detonation. In: Proceedings of the ASME 2010 Pressure Vessels and Piping Conference, Bellevue, USA, July 18-22 (2010)
5. Mark, H.: The Interaction of a Reflected Shock Wave with the Boundary Layer in a Shock Tube. NACA TM14818 (1958)
6. Strehlow, R.A., Cohen, A.: Limitations of the Reflected Shock Technique for Studying Fast Chemical Reactions and Its Application to the Observation of Relaxation in Nitrogen and Oxygen. Journal of Chemical Physics 30, 1 (1959)
7. Davies, L., Wilson, J.L.: Influence of Reflected Shock and Boundary-Layer Interaction on Shock-Tube Flows. In: Shock Tube Symposium
8. Taylor, J.R., Hornung, H.G.: Real Gas and Wall Roughness Effects on the Bifurcation of the Shock Reflected from the End Wall of a Tube. In: Proceedings of the 13th International Symposium on Shock Tubes and Waves, Niagara Falls, USA, July 6-9 (1981)
9. Petersen, E.L., Hanson, R.K.: Measurement of Reflected-Shock Bifurcation Over a Wide Range of Gas Composition and Pressure. Shock Waves 15, 333–340 (2006)
10. Damazo, J., Ziegler, J., Karnesky, J., Shepherd, J.E.: Investigating Shock Wave–Boundary Layer Interaction Caused by Reflecting Detonations. In: Proceedings of the 8th ISPHMIE Conference, Yokohama, Japan, September 5-10 (2010)
11. Lee, J.H.S.: The Detonation Phenomenon. Cambridge University Press (2008)
12. Akbar, R.: Mach Reflection of Gaseous Detonations. PhD Thesis, Rensselaer Polytechnic Institute, Troy, New York, USA (1997)
13. Pfahl, U., Schultz, E., Shepherd, J.E.: Detonation Cell Width Measurements for H_2–N_2O–N_2–O_2–CH_4–NH_3 Mixtures. Tech. Rep. FM98-5, GALCIT (1998)

Shock Dynamics for Cylindrical/Spherical Converging Shocks in Elastic-Plastic Solids

A. López Ortega, M. Lombardini, D.J. Hill, D.I. Pullin, and D.I. Meiron

1 Introduction

The study of cylindrical and spherical converging shock waves propagating in solid materials is relevant to the production of high temperatures and pressures in condensed matter with applications to inertial confinement fusion [1]. However, experimental studies conducted in the area are prone to complications derived from the measurement techniques available and the difficulty of producing a quasi-radially symmetric flow.

The origin of analytical studies of converging shocks waves began with Guderley [2], who showed that for an initially strong shock wave in an inviscid ideal gas, there exist similarity solutions in which the radial location $R(t)$ of the shock follows a power law of the time measured from the instant the shock reaches $r = 0$. This problem was later addressed using Whitham's Shock Dynamics (WSD) theory [3], which gives a good approximation to the values predicted by the similarity solutions. Through the years, WSD has proved itself as a powerful tool for the study of shock evolution in other non-planar problems such as shock diffraction by a wedge and shock stability [5]. WSD was also extended to initially infinitesimally weak imploding shocks [4].

A direct application of WSD to spherically converging shocks in metals was used by Yadav and Singh [6], using a Mie-Gruneisen equation of state for pressure, which did not account for shear stresses and possible plasticity. Their solution for the post-shock pressure approaches an inverse power of R, the exponent varying with the effective specific heat ratio of the material. A similar equation of state was used by Hiroe et al. [7] in combination with a random choice method. Their simulation of a cylindrically imploding shock shows that the flow only exhibits the self-similar regime typical of gases in close proximity to the axis.

A. López Ortega · M. Lombardini · D.J. Hill · D.I. Pullin · D.I. Meiron
California Institute of Technology, Graduate Aerospace Laboratories
1200 E. California Blvd. Pasadena, CA 91125 (USA)

This article is structured as follows: we first introduce in Section 2 an Eulerian description of the conservation laws governing the finite-deformation evolution of a hyper-elastic material under radially symmetric conditions. The WSD analytical solution is subsequently constructed and compared against high-resolution numerical simulations. Section 3 extends the study to finite-deformation plasticity.

2 Elastic Motion

2.1 Governing Equations for Radially Symmetric Motion

We introduce in this section an Eulerian description of the radially symmetric motion of an elastic medium induced by cylindrical and spherical imploding shock waves. We account for conservation of mass, momentum and energy. In addition, as stresses in solids are proportional to deformations, we evolve the inverse deformation tensor $f_{ij} = \partial X_i/\partial x_j$ which represents the gradient of the mapping that transforms Eulerian coordinates $\mathbf{x}$ to Lagrangian (material) coordinates $\mathbf{X}$. In a cylindrical/spherical frame of reference, this tensor is diagonal and the density constraint $\rho/\rho_0 = \det(\mathbf{f})$ reduces the extra equations needed to close the system to the one for the radial component f_{rr}. The equations of motion are then

$$\frac{\partial \rho}{\partial t} + u\frac{\partial \rho}{\partial r} + \rho\frac{\partial u}{\partial r} = -(s-1)\frac{\rho u}{r}, \tag{1a}$$

$$\frac{\partial u}{\partial t} + u\frac{\partial u}{\partial r} - \frac{1}{\rho}\frac{\partial \sigma_{rr}}{\partial r} = (s-1)\frac{\sigma_{rr} - \sigma_{\theta\theta}}{\rho r}, \tag{1b}$$

$$\frac{\partial e}{\partial t} + u\frac{\partial e}{\partial r} - \frac{\sigma_{rr}}{\rho}\frac{\partial u}{\partial r} = (s-1)\frac{u\sigma_{\theta\theta}}{\rho r}, \tag{1c}$$

$$\frac{\partial f_{rr}}{\partial t} + f_{rr}\frac{\partial u}{\partial r} + u\frac{\partial f_{rr}}{\partial r} = 0, \tag{1d}$$

where r is the distance to the axis/origin, ρ the density field, u the radial component of velocity vector, e the internal energy and s the space index, with $s = 1, 2, 3$ for the planar, cylindrical and spherical problem respectively. The material is homogeneous isotropic and hyper-elastic, where e only depends on the three invariants (I_1, I_2, I_3) of the right Cauchy-Green tensor $\mathbf{C} = \boldsymbol{f}^{-T}\boldsymbol{f}^{-1}$ and on the specific entropy ς. From e, we deduce $\sigma = -\rho \boldsymbol{f}^T \partial e/\partial \boldsymbol{f}$.

The equations of motion (1) are rewritten in a conservative form and numerically solved using a shock-capturing method implemented within an adaptive mesh refinement framework for comparison with WSD results.

2.2 Whitham's Shock Dynamics

The WSD approach is based on the idea that the shock is minimally influenced by the flow behind it when it is adjusting to changes in geometry. To apply WSD, the system of PDEs (1) is first decoupled into the set of 'characteristic' equations.

The motion of the shock is then approximated by integrating the equation along the characteristics $u+a$, a being the sound speed. This means that the shock is assumed to follow the same spatial motion as the set of characteristics immediately behind it and that, as a consequence, any influence of the processed flow is ignored. As the shock progresses, the errors produced by this assumption might accumulate but they are neglected in the WSD theory. Finally, the characteristic equation is further simplified by using the Rankine–Hugoniot (RH) jump conditions across the moving shock, which gives the primitive variables immediately behind the shock in terms of the shock Mach number M.

2.3 Constitutive Laws

Two constitutive laws are presented here. The first is the fairly general Blatz and Ko [8] isothermal, (i.e. e independent of ς), constitutive law:

$$e(\boldsymbol{f}) = \frac{\mu}{2\rho_0}(I_1 - 3I_3^{1/3}) + \int_{\rho_0}^{\rho} \frac{p(\rho')}{\rho'^2}\, d\rho', \quad \text{with the density constraint } I_3 = J^2 = \left(\frac{\rho_0}{\rho}\right)^2, \tag{2}$$

where μ is the shear modulus and the pressure p is assumed to not depend on the specific entropy. Two models for p are:

$$p\left(\frac{\rho_0}{J}\right) = \sum_{\alpha=1}^{3} c_\alpha \left(\frac{1}{J} - 1\right)^\alpha, \tag{3}$$

$$p\left(\frac{\rho_0}{J}\right) = p_0 \left(\frac{\text{Arctanh}\,(J_\infty/J)}{\text{Arctanh}\,(J_\infty)}\right)^\beta. \tag{4}$$

The first, proposed by Miller and Colella in [9] for the Wilkins' flying aluminum plate problem, has the drawback of leading to unbounded densities. Equation (4) corrects for this behavior, with $J \to J_\infty$ as $p \to \infty$.

The second constitutive law is non-isothermal:

$$e(\boldsymbol{f}, \varsigma) = \frac{\mu}{2\rho_0} I_1 + c_v T_0 J^{1-\gamma} \exp\left(\frac{\varsigma - \varsigma_0}{c_v}\right), \tag{5}$$

where ρ_0, T_0 and ς_0 refer to the unshocked density, temperature and specific entropy respectively, and c_v and γ are the specific heat at constant volume and specific heat ratio. The first part of this constitutive law accounts for the elastic shear deformation of the material, while the second part simply represents the internal energy of an ideal gas.

The complete evolution of the converging shock is obtained by numerically solving the ODE given by WSD. As an example, the expression for the isothermal case is presented:

$$\frac{\mathrm{d}R}{R} = -\frac{1}{s-1}\frac{a\left[a+a_0(1-J)M\right]\left[-a/J+a_0(1-J)\frac{\mathrm{d}M(J)}{\mathrm{d}J}-a_0M\right]}{(1-J)\left[a_0\left(a^2-2a_\mu^2J^2\right)M+a_\mu^2a(1+J)\right]}\mathrm{d}J, \quad (6a)$$

$$M(J) = \frac{1}{a_0}\sqrt{\frac{1}{1-J}\left[\frac{p(\rho_0/J)}{\rho_0}-a_\mu^2\left(J-J^{-1/3}\right)\right]}, \quad (6b)$$

$$a(J) = \sqrt{a_\mu^2\left(J^2+\frac{1}{3}J^{2/3}\right)-\frac{J^2}{\rho_0}\frac{\mathrm{d}p}{\mathrm{d}J}}, \quad \text{with } a_\mu \equiv \sqrt{\mu/\rho_0}. \quad (6c)$$

Results for the non-isothermal constitutive law compared to numerical simulations are shown in Fig. 1. In the strong shock limit ($M \to \infty$) analytical expressions can be obtained for the evolution of the Mach number with the distance to the center/axis. These expressions show that the behavior close to the axis/origin $r = 0$ depends on the constitutive law used. For the polynomial pressure law, where ρ is unbounded at $r = 0$, the shock strength increases at a logarithmic rate, $M \propto \log(1/R)^\alpha$, which is lower than for the two other constitutive laws investigated and depends only on the order of the polynomial. The maximum compression ratio at $r = 0$ does not affect the Arctanh strong-shock limit, $M \propto R^{-(s-1)}$, which only depends on the geometry, but it appears indirectly in the non-isothermal ideal gas-like material rate, $M \propto R^{-(s-1)/n}$, where $n = n(\gamma)$ and the maximum compression ratio at $r = 0$ is a function of γ through $J_\infty = (\gamma-1)/(\gamma+1)$.

3 Plastic Motion

The plastic regime is observed in most materials when undergoing sufficiently high stresses. It is defined by the presence of large deformations with small stress increments, and by the residual deformations that remain even when the stresses are removed. The transition between the elastic and the plastic state is given by a yield criterion and a limit stress (yield stress), which is considered a material property. The results shown in the previous section correspond to a material with an infinitely large yield stress. In this section, as the converging shock processes the solid with an increasing strength, the shocked material is expected to ultimately reach its yield stress.

Finite-deformation plasticity is introduced as a complement to the elastic theory developed earlier. The inverse deformation tensor is factored as a product of elastic and plastic parts: $\boldsymbol{f} = \boldsymbol{f}^p\boldsymbol{f}^e$. By the particular geometry of the problem, only the diagonal components of these tensors are nonzero once transformed to curvilinear coordinates. From the compressibility constraints, $J = 1/\det\boldsymbol{f}$ and $J^p = 1/\det\boldsymbol{f}^p = 1$ (i.e. no change in volume for plastic deformation). Because the internal energy accounts for the energy that is stored in the solid and that can be released by means of elastic deformation, the internal energy is now $e = e(\boldsymbol{f}^e, s)$, and stresses are computed by $\sigma = -\rho\boldsymbol{f}^{e^T}\partial e/\partial\boldsymbol{f}^e$.

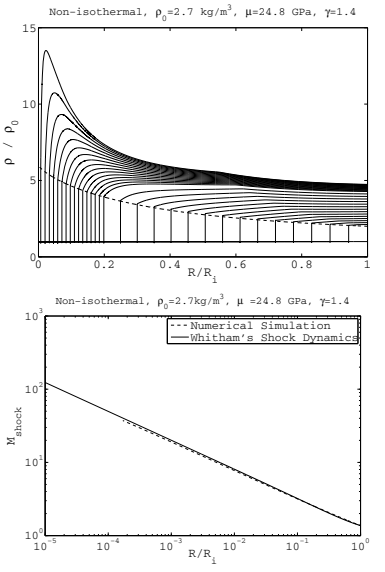

Fig. 1 **(a)** Density radial profiles computed with numerical simulation at different times t, the dashed line shows the density immediately behind the shock evaluated from WSD at the corresponding shock locations; **(b)** Logarithmic plot for the Mach number as a function of the distance to the origin. The converging shock is spherically symmetric ($s = 3$) and was initially started at $r = R_i$ with $J_i = 0.9$ ($M_i \approx 1.14$)

For simplicity, we consider here an elastic–perfectly plastic material. In uniaxial stress, this means that plasticity occurs at a constant stress equal to the yield stress σ_Y (i.e. no incremental stress is needed to achieve large deformations). This concept is easily extended to a yield criterion of the form $\sigma_Y = \sigma_{eff}$, where σ_{eff} is an effective stress function. Yield criteria have been usually developed from empirical observations and rely on the deviatoric part of the stress tensor. We use the von Mises constraint, which is written as

$$\sigma_{eff} = \sqrt{\frac{3}{2}\mathrm{tr}\left(\Sigma'^{T}\Sigma'\right)} = \sigma_Y, \tag{7}$$

where Σ' is the deviatoric part of the Mandel stress tensor $\Sigma' = -(\rho_0/\rho)\boldsymbol{f}^{e^{-T}}\boldsymbol{\sigma}\boldsymbol{f}^{e^{T}}$ [10]. Substituting the stresses as functions of the elastic deformations gives the expression relating f^e_{rr} to the yield stress and J that closes the system needed to solve the WSD ODE for a converging shock that is started in the plastic shock regime.

3.1 Elastic–Plastic Transition

WSD theory has limitations when trying to predict the behavior of complex wave structures. This is the case of the elastic-plastic transition. While WSD can be applied to the pure elastic and pure plastic regimes, numerical simulations were needed to describe the transition between the two. As shown in Fig. 2, an elastic shock is initially generated. This first regime can be approximated by WSD. As this shock converges, a plastic region, where the yield stress has been reached, is formed behind and WSD is not applicable. As the two structures converge towards the center, the plastic region becomes steeper and narrower while the elastic precursor keeps a constant strength. When approaching the center further, the elastic precursor disappears and a quasi-discontinuous plastic region remains. The motion after this event can be described by WSD again.

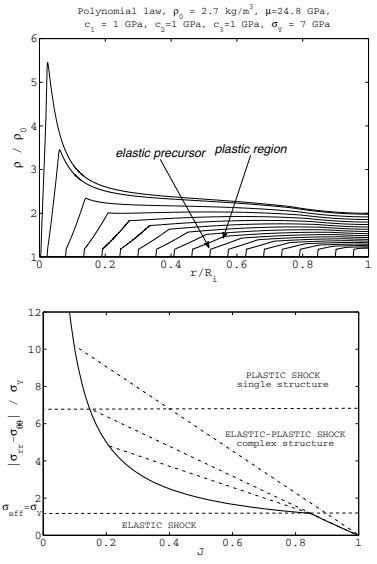

Fig. 2 **(a)** Density radial profiles computed from numerical simulation at different times t. Elastic-plastic motion. The values of the parameters were chosen to notice the elastic-plastic transition better. The converging shock is spherically symmetric ($s = 3$) and was initially started at $r = R_i$ with $J_i = 0.9$ ($M_i \approx 1.00$). **(b)** Hugoniot curve for the material, which provides a physical explanation of the existence of the elastic precursor and the plastic region

4 Conclusion

We have shown that Whitham's shock dynamics approach is a rather accurate tool for studying converging shocks, even when shear deformations are considered in addition to the usual hydrostatic pressure terms. Purely plastic shocks can also be described using this approximate theory.

Analysis of the strong-shock limit revealed that the behavior of an elastic–plastic material close to the axis/origin $r = 0$ is highly dependent on the pressure equation that is used. For a polynomial pressure law, the shock strength increases at a logarithmic rate which is lower than the power law obtained for the two other examples investigated.

The transition from an elastic to a plastic shock was described by a complex structure of two compression waves moving at different velocities that falls beyond the capabilities of Whitham's shock dynamics. Numerical simulations showed that the converging geometry modifies the elastic precursor-plastic shock structure usually observed in planar symmetry, making the converging plastic shock travel faster than the elastic precursor as the compression ratio increases.

Future work could include the extension of the analysis to more general constitutive laws, i.e. including a non-constant shear modulus which depends on thermodynamic variables, and the possible application of WSD to help with the description of complex problems, such as the analysis of the Richtmyer–Meshkov flow in converging geometries for different material interfaces (e.g. solid–solid or solid–gas). See [11, 12] for previous work in these areas.

This Material is based upon work supported by the Department of Energy National Nuclear Security Administration under Award Number DE-FC52-08NA28613.

References

1. Lindl, J.D.: Inertial confinement fusion: The quest for ignition and energy gain using indirect drive. Springer (1998)
2. Guderley, G.: Starke Kugelige und zylindrische Verdichtungsstösse in der Nähe des Kugelmittelpunktes bzw der Zylinderachse. Luftfahrtforschung 19, 302–312 (1942)
3. Whitham, G.B.: Linear and Nonlinear Waves. John Wiley and Sons (1974)
4. Hornung, H.G., Pullin, D.I., Ponchaut, N.: On the question of universality of imploding shock waves. Acta Mechanica 201(1), 31–35 (2008)
5. Whitham, G.B.: A new approach to problems of shock dynamics Part I Two-dimensional problems. Journal of Fluid Mechanics 2, 145–171 (1957)
6. Yadav, H.S., Singh, V.P.: Converging shock waves in metals. Pramana 18(4), 331–338 (1982)
7. Hiroe, T., Matsu, H., Fujiwara, K.: Numerical simulation of cylindrical converging shocks in solids. Journal of Applied Physics 72(7), 2605–2611 (1992)
8. Blatz, P.J., Ko, W.L.: Application of finite elastic theory to the deformation of rubbery materials. Trans. Soc. Rheology 6(1), 223–252 (1962)
9. Miller, G.H., Colella, P.: A High-Order Eulerian Godunov Method for Elastic–Plastic Flow in Solids. Journal of Computational Physics 167, 131–176 (2001)
10. Cleja-Tigoiu, S., Maugin, G.: Eshelby's stress tensors in finite elastoplasticity. Acta Mechanica 139(1), 231–249 (2000)
11. López Ortega, A., Hill, D.J., Pullin, D.I., Meiron, D.I.: Linearized Richtmyer–Meshkov flow analysis for impulsively accelerated incompressible solids. Phys. Rev. E 81(6), 066305 (2010)
12. Lombardini, M., Pullin, D.I.: Small-amplitude perturbations in the three-dimensional cylindrical Richtmyer–Meshkov instability. Physics of Fluids 21(11), 114103 (2009)

Study of the Stability of $Na_{0.7}CoO_2$ Thermoelectric Materials under Shock Dynamic Loading in a Shock Tube

V. Jayaram, C. Shivakumara, M. Satyanarayana, and K.P.J. Reddy

1 Introduction

The thermoelectric material is a material that shows large thermo power, low resistivity and low thermal conductivity. Recently, layered cobalt oxides have been extensively investigated as a promising candidate as thermoelectric material. Important feature of sodium cobalt oxides is that, the sodium ions (Na^+) randomly occupy the regular site by 50% and the sodium content can go up to 70% changes[1]. In this sense layered cobalt oxides, NaCo_2O_4 should be written as Na_xCoO_2 (x = 0.5) and the compound is quite promising for thermoelectric power generation. Terasaki et al. found that a single crystal $NaCo_2O_4$ exhibits good thermoelectric property[2]. These layered oxides consist of two layers: CoO_2 layer and Na ion layer. CoO_2 layers acting as an electron reservoir which are responsible for the electrical conductivity and large thermoelectric power. Na ions layer sandwiched between two neighboring CoO_2 layers adjust the concentration of electron in CoO_2 layers and decrease the thermal conductivity along the stacking direction c[3]. Since the discovery of moderately large thermoelectric power (Seebeck coefficient) together with high electrical conductivity in Na_xCoO_2(x is 0.70), experiments were done to find new phases for thermoelectric conversion applications[4]. A single-crystal X-ray diffraction study confirmed that Na_xCoO_2 (x = 0.74) adopted the hexagonal $P6_3/mmc$ space group[5]. Neutron diffraction and electron diffraction study shows that the crystal structure of the oxides is strongly dependent on sodium content. The crystal structure of $Na_{0.75}CoO_2$ was studied at ambient and low temperatures down to 10 K at pressures up to 40 GPa using a diamond cell shows an increase in Co-O bond length and decrease in Na-O bond length[6]. Here we present the experimental results on the interaction of shock heated test gases with Na_xCoO_2 at high temperature and moderate reflected shock pressure.

V. Jayaram · C. Shivakumara · M. Satyanarayana
Solid State and Structural Chemistry Unit,
Indian Institute of Science, Bangalore-560012, India

K.P.J. Reddy
Department of Aerospace Engineering, Indian Institute of Science, Bangalore-560012, India

2 Experimental Description

2.1 *Synthesis of* $Na_{0.7}CoO_2$

The thermoelectric compound $Na_{0.7}CoO_2$ was synthesized by nitrate-citrate gel combustion method. Stoichiometry amount of Na_2CO_3 (1.6322 g, 10% excess) was dissolved in 10 ml of 8 M HNO_3 and $Co(NO_3)_3.6H_2O$ (11.6416 g) was dissolved in 20 ml deionized water. Citric acid (20 g) was dissolved in 100 ml of distilled water and added to the nitrate solution. The clear solution was evaporated on hot plate $\sim$ 353 K, to form a thick viscous gel. The resulting gel was heated on hot plate until it turned into a black porous mass, on further heating, slowly burned to yield black powder. The resulting powder was X-ray amorphous in nature. To obtain crystalline black powder it was calcined at 1073 K for 2 h. The calcined sample was characterized by powder X-ray diffraction (XRD). Pellets are prepared with pellet pressing unit by applying 75 kN load before exposing to shock heated test gases.

2.2 *Experimental Facilities and Test Gas Condition*

A simple shock tube consists of two major sections, the driver and driven sections and is separated by a metal diaphragm. Recently established shock tube is a stainless steel tube of 117 mm outer and 80 mm inner diameter with driver and driven sections of 2.12 m and 5 m long. Schematic diagram of a shock tube with necessary measuring system is shown in figure 1. Driver section is equipped with an arrangement to feed the high-pressure gas from cylinders by using appropriate high-pressure regulators. Driven section has provision for evacuating the tube and a gas handling system to fill desired ultra high pure (UHP) test gas. In the driven section two ports are separated by 0.5 m apart were used to mount pressure sensors for measuring the shock speed. To measure reflected shock pressure another port is used at the end of the driven section of the shock tube. Experiments were conducted with different test gas (O_2 or N_2) by mounting thermoelectric $Na_{0.7}CoO_2$ compound on the end flange of the shock tube. Aluminum diaphragm of 3mm thick is placed in between the driver and driven section the shock tube. The driven section of the shock tube is initially evacuated using vacuum pump and ultra high pure (UHP) test gas (O_2 or N_2) is purged for number of times and then filled with required pressure. High pressure helium gas is filled in the driver section until it bursts the Al diaphragm. This produces a strong primary shock wave, traveling into the driven section of a shock tube, which is reflected finally at the end of the shock tube. The reflected shock wave produces high pressure and temperature test gas, which interacts with $Na_{0.7}CoO_2$ compound. The temperature behind the reflected shock wave calculated using 1-D normal shock theory[7]. Experiments were performed using shock heated O_2 ($\sim$3000 K) and N_2 ($\sim$2700 K) at elevated pressure of about 15 bar for 1-2 ms duration.

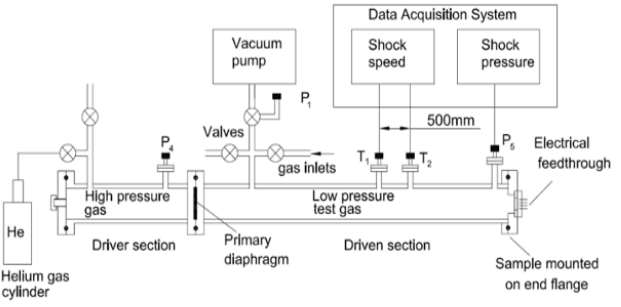

Fig. 1 Schematic diagram of shock tube with electronic control

2.3 Characterizations

The characterization of $Na_{0.7}CoO_2$ was carried out before and after the interaction of shock heated test gases using different experimental methods. Powder X-ray diffraction (XRD) of the compound was recorded in a Phillips X-Pert diffractometer using Cu $K\alpha$ ($\lambda = 1.5418\mathring{A}$) radiation at scan rate of $0.25^0 min^{-1}$ with 0.01^0 step size in the 2θ range between 10^0 to 70^0. Electronic structure of the compounds were characterized by X-ray Photo-electron spectroscopy (XPS) using Al Kα radiation (1486.6 eV), C(1s) at 284.5 eV was taken as reference and binding energy (BE) reported here are in the accuracy of $\pm 0.1eV$ (MultiLab 2000, ThermoFisher Scientific). SEM (Philips SIRION) was used to study surface morphology of $Na_{0.7}CoO_2$ before and after shock treatment

3 Results and Discussion

Figure 2 shows the SEM micrographs of thermoelectric $Na_{0.7}CoO_2$ compound before and after exposure to shock heated test gases. Micrographs of $Na_{0.7}CoO_2$ pallet before exposure to shock heated gas is shown in figure. 2(a). After exposure to shock heated O_2 the surface of the compound reacted with high temperature O_2 gas and there is a change in the surface morphology 10000x (figure. 2(b)) and 50,000x magnification (figure. 2(c)) we can observe the layers of $Na_{0.7}CoO_2$ compound. On exposure to shock heated N_2 gas, similar morphological change was observed as shown in figure. 2(d).

XPS has been widely used in the characterization of materials. XPS of Co (2p) region of as prepared $Na_{0.7}CoO_2$ sample before exposure to shock is shown in figure 3(left (a)). Co ($2p_{3/2}$) peak at 779.1 eV alongwith Co ($2p_{1/2}$) peaks at 794.3 eV are characteristic of Co^{3+} in $Na_{0.7}CoO_2$[8, 9]. In the shock exposed $Na_{0.7}CoO_2$, the XPS of Co ($2p_{3/2}$) shift to higher binding energy indicates Co^{3+} changed to Co^{4+} state as shown in figure 3(left (b,c)). XPS of Na (1s) peak at 1071.4 eV due to sodium metal ion (Na^+) as shown in figure 3(right(a)). Shock treated $Na_{0.7}CoO_2$ shows two peaks for Na(1s) due to Na^+ ion and sodium oxide on the surface. XPS spectra

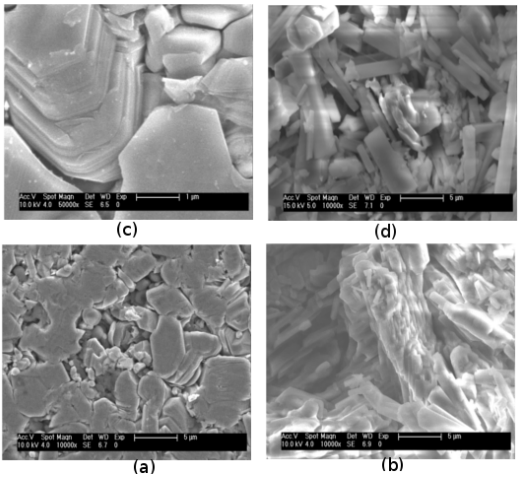

Fig. 2 SEM micrographs of $Na_{0.7}CoO_2$ material (a) before shock at 10000 x and (b) after shock treatment in presence of O_2 at 10000x and (c) 50000x and (d) after shock treatment in presence of N_2 at 10000 x

of Na(1s) peaks at 1071.4 eV and 1075.5 eV are attributed to Na^+ ion present in $Na_{0.7}CoO_2$ and more oxidised sodium rich phase (Na_2O) present on the surface of the compound as shown in figure. 3(right(b)) and figure. 3(right(c)). Interaction of shock heated gas ($O_2 or N_2$) with the compound shows decrease in intensity of Na^+ ion on the surface of $Na_{0.7}CoO_2$. Decrease in Na^+ ion concentration after shock treatment can alter the thermoelectric property of $Na_{0.7}CoO_2$.

Powder XRD pattern of the thermoelectric $Na_{0.7}CoO_2$ compound before and after exposure to shock heated test gases are shown in figure4. All the peaks indexed in reference with JCPDS: 87-0274 results to hexagonal structure and no impurity peaks were detected in $Na_{0.7}CoO_2$ compound as shown in Fig 4. Thus the compound explicitly crystallizes to desired hexagonal gamma phase (space group: $P6_3/mmc$, lattice parameter a = 2.836 (2) Å, c = 10.910(2) Å). Figure 4(b) shows XRD of $Na_{0.7}CoO_2$ compound remains hexagonal phase after exposure to shock heated O_2, in addition to this few diffraction lines corresponds to cubic Co_3O_4 are observed due to shock heated O_2 gas which matches with reported literature[8, 9]. Additional diffraction lines observed are due to the formation of CoO and Co_3O_4 on the surface when shock heated O_2 gas interacted with $Na_{0.7}CoO_2$. If the powder is heated to high temperature then the Co_3O_4 can partially convert to a CoO impurity phase. With the shock heated N_2 gas, XRD of $Na_{0.7}CoO_2$ shows additional diffraction lines may be due to formation of different compounds like CoO, Co_3O_4 and Cobalt oxynitride on the surface as shown in Fig. 4(c).

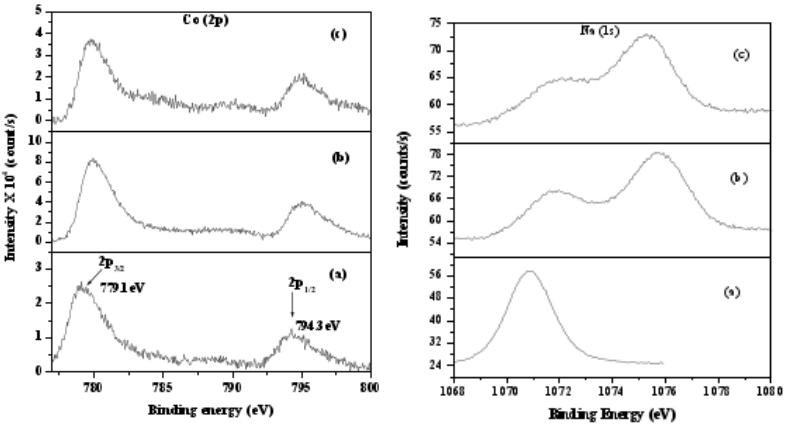

Fig. 3 Left:XPS spectra of Co(2p) peak (a) as prepared sample (b) after exposure to O_2 shock (c) after exposure to N_2 gas , Right: XPS spectra of Na (1s) peak in $Na_{0.7}CoO_2$ (a) as prepared sample (b) after exposure to O_2 gas (c) after exposure to N_2 gas .

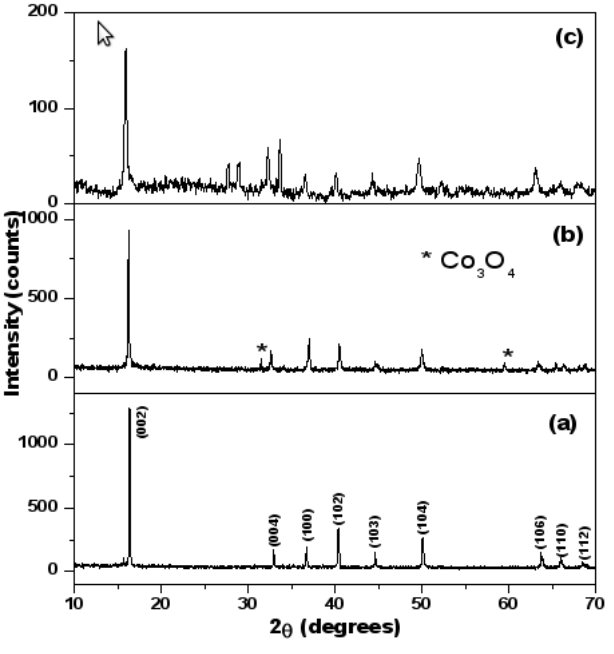

Fig. 4 XRD spectra of $Na_{0.7}CoO_2$ (a) as prepared sample (b) after exposure to O_2 gas (c) after exposure to N_2 gas

4 Conclusion

We have demonstrated the possibility of formation of Co_3O_4 on the surface of $Na_{0.7}CoO_2$ with shock heated O_2 and N_2 test gas. When compound exposed to shock heated N_2 gas, the Co_3O_4 can partially convert to a CoO impurity phase. Shock interaction study shows the formation of impurity compounds at elevated temperature, this may leads to degradation of thermoelectric property of $Na_{0.7}CoO_2$. It is required to measure the thermoelectric property (Seebeck coefficient) of $Na_{0.7}CoO_2$ after shock treatment. Intensive experimental and theoretical study is required to understand the thermoelectric property and stability of Na_xCoO_2 under shock dynamic loading.

Acknowledgement. Financial support for establishing shock tube facility from the ISRO-IISc Space Technology Cell, Government of India, is gratefully acknowledged.

References

1. Yoshiya, M., Okabayashi, T., Tada, M., Fisher, C.A.J.: A first-principles study of the role of Na vacancies in the thermoelectricity of Na_xCoO_2. Journal of Electronic Materials 39(9), 1681–1686 (2010)
2. Terasaki, I., Sasago, Y., Uchinokura, K.: Large thermoelectric power in $NaCo_2O_4$ single crystals. Phys. Rev. B. 56, R12685 (1997)
3. Nakatsugawa, H., Nagasawa, K.: Evidence for the two-dimensional hybridization in $Na_{0.79}CoO_2$ and $Na_{0.84}CoO_2$. J. Solid State Chem. 177, 1137 (2004)
4. Liu, P., Chen, G., Cui, Y., Zhang, H., Xiao, F., Wang, L., Nakano, H.: High temperature electrical conductivity and thermoelectric power of Na_xCoO_2. Solid State Ionics 179, 2308–2312 (2008)
5. Takahashi, Y., Akimoto, J., Kijima, N., Gotoh, Y.: Structure and electron density analysis of $Na_{0.74}CoO_2$ by single-crystal X-ray diffraction. Solid State Ionics 172, 505 (2004)
6. Kumara, R.S., Rekhi, S., Prabhakaran, D., Somayazulud, M., Kima, E., Jeremy, D., Cooke, Stemmlere, T., Boothroyd, A.T., Chance, M.R., Cornelius, A.L.: Structural studies on $Na_{0.75}CoO_2$ thermoelectric material at high pressures. Solid State Communications 149, 1712–1716 (2009)
7. Gaydon, A.G., Hurle, I.R.: The shock tube in high temperature chemical physics, pp. 23–28. The Reinhold Publishing Corporation, New York (1963)
8. Wang, X., Chen, X., Gao, L., Zheng, H., Zhang, Z., Qian, Y.: One-Dimensional Arrays of Co_3O_4 Nanoparticles: Synthesis, Characterization, and Optical and Electrochemical Properties. J. Phys. Chem. B 108, 16401–16404 (2004)
9. Kim, M.H.: Surface Chemical Structures of CoO_x/TiO_2 Catalysts for Continuous Wet Trichloroethylene Oxidation. Korean J. Chem. Eng. 22(6), 839–843 (2005)

Structure of Shock Waves in Dense Media

Z.A. Walenta and A. Slowicka

1 Introduction

The behaviour of shock waves propagating in a gas has been studied for more than a century, experimentally, theoretically and numerically. It was established, in particular, that the thickness of a shock wave (the layer, in which parameters of the medium vary rapidly in space) is of the order of several mean free paths of the gas molecules, provided that the shock is of moderate intensity. Distributions of the parameters of the medium inside the shock resemble the hyperbolic tangent function. The necessary condition for the above to be fulfilled is that the gas is dilute, which means that its molecules interact (collide) with only one neighbour at a time, and between collisions they move with constant speed along straight lines (concept of a mean free path – the average distance travelled this way). Duration of a single collision is negligibly short as compared to the time of free flight (mean free time). In dilute gas the mean free path of the molecules is much larger than the diameter of the molecule and larger than their average separation distance (Figure 1 – left).

Shock waves may also be generated in dense media: dense gases, liquids and solids. Under ”dense medium” we understand medium consisting of molecules so closely packed, that the average distance between the closest neighbours is of the same order of magnitude as the distance characteristic for the intermolecular forces. A simplified model of a dense medium consists of hard sphere molecules of finite size, interacting with each other during collisions only. The gaps between neighbouring molecules in such medium are smaller, or at most equal to the diameter of a molecule (Figure 1 – right).

In such simplified, dense medium the mean free path can be defined too, however the molecules may collide with the closest neighbours only. The speed of transfer of momentum and energy in such a medium is, in average, approximately equal to the ratio of the sum of the mean free path and the diameter of the molecule

Z.A. Walenta · A. Slowicka
Institute of Fundamental Technological Research
Pawinskiego 5b 02-106 Warszawa, Poland

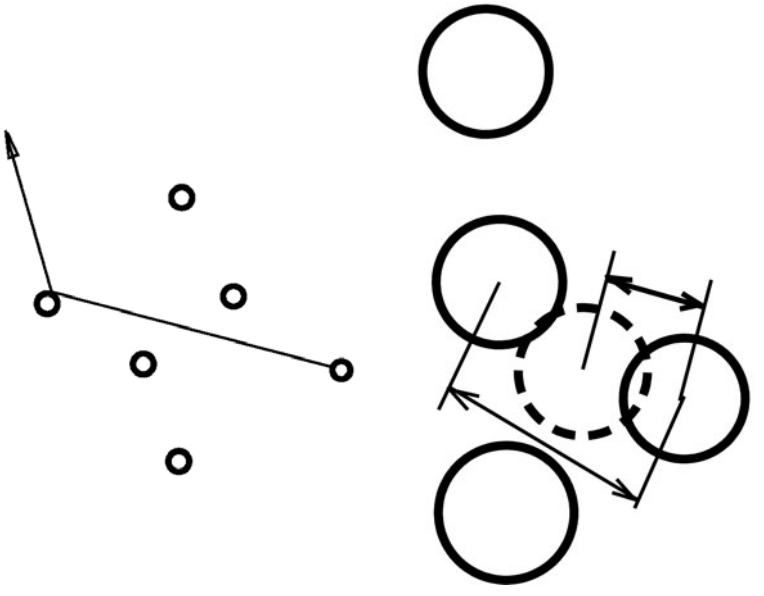

Fig. 1 Left: dilute gas – mean free path larger than average distance between molecules. Right: dense medium – gaps between neighbouring molecules (hard spheres) smaller than diameter of a molecule – collisions occur between closest neighbours only.

to the mean time between collisions. In fact, the same applies to dilute gases too, however the diameter of the molecule is there negligibly small as compared to the mean free path. The sum of the mean free path and the molecular diameter may therefore be considered as the length scale characteristic for the momentum and energy transfer. As can be seen in Figure 1 – right, in dense medium this sum is very close to the average distance between the centres of the neighbouring molecules (the ”mean molecular distance”). This, in turn, is close to the inverse of the cubic root of the number density of the molecules of the medium. The parameter defined in this way was introduced for the first time by Bridgman in 1923 [1] The last definition is particularly useful if more realistic molecular models are employed (e.g. molecules interacting with Lennard-Jones potential). The molecules of a dense medium are then in permanent contact through the long-range forces and no mean free path can be defined. It will be demonstrated, that the thickness of the shock wave in dense gas (Argon), related to the cubic root of the number density is of the same order of magnitude as that in dilute gas related to mean free path and that this thickness gradually decreases with increasing density. This is contrary to the results of the earlier investigators (Montanero et al. 1999 [2], Schlamp et al. 2007 [3]), who related the shock thickness to the mean free path in the whole range of densities.

2 Flow Arrangement – Details of Simulation and Experiment

2.1 Molecular Dynamics – General Description of the Procedure

All Molecular Dynamics computations reported here were performed with the program MOLDY [4]. This program has originally been designed for stationary configurations of the molecules, however it is easy to supplement with additional procedures for calculating the behaviour of the flowing medium. To produce the flow we place the molecules regularly in space, give them random velocities according to the Maxwellian distribution for the required temperature and wait until the system equilibrates. During the equilibration period we perform velocity scaling in order to suppress the unwanted temperature rise (which would occur because the molecules had initially higher potential energy than in equilibrium). When the system is in equilibrium we make the medium move adding the macroscopic velocity V to the x – component of the thermal velocity of each molecule. At the same time we insert into the flow the impermeable, reflecting planes, which generate the shock and rarefaction waves. The number of Argon atoms taken for each simulation run was equal to 125000. The time step was assumed equal to 0.001 of a picosecond, the equilibration period was 10000 time steps long (10 picoseconds). The subsequent actual simulation of the flow was stopped when the produced shock and rarefaction waves met disturbing each other.

2.2 Physical Conditions for the Simulated Flow

In the present research the flow of Argon at initial temperature T = 300 K and initial velocities: V = 404.8 m/s, 607.2 m/s and 809.6 m/s is simulated. For the case of dense medium three values of the initial density ρ have been taken as specified below. The corresponding values of the mean molecular distance λ are also given:
1) $\rho = 1000 kg/m^3$, $\lambda = 4.048$Å;
2) $\rho = 307.09 kg/m^3$, $\lambda = 6.0$Å;
3) $\rho = 125.55 kg/m^3$, $\lambda = 8.0$Å.
Argon atoms have no electric charge and interact with each other only with the Lennard-Jones interaction potential.

2.3 Direct Simulation Monte-Carlo

The flow configuration used for DSMC calculations was identical with that of Molecular Dynamics. Here it was not necessary to go through equilibration process before the actual simulation. The program used was a modification of that by Bird [5] and the sampling procedure for collisions was due to Yanitskiy [6]. The computation domain was split into cells of linear dimension equal to 0.25 of the mean free path in the region in front of the shock. The total number of molecules in the computation domain was 24 million.

2.4 Experiment

The measurements of the shock wave structure (density) were performed in the low density shock tube at the Institute of Fundamental Technological Research in Warsaw. The tube, was 250 mm in diameter, which made it possible to make experiments at initial densities corresponding to mean free paths up to a couple of millimeters. The initial pressure of the test gas (Argon) in the experiments was about 7.5 Pa, the initial temperature about 300 K, which corresponded to mean free paths about 0.95 mm and the shock thicknesses about 4 mm. Under such conditions it was possible to measure the gas density in the shock with the standard electron beam attenuation technique [7].

3 Results

3.1 Plane, Perpendicular Shock Wave in Argon

In Figure 2 – left the diagrams of density distributions inside the shock wave, calculated for the three initial gas densities and the initial velocity V = 404.8 m/s are shown superimposed upon one another.

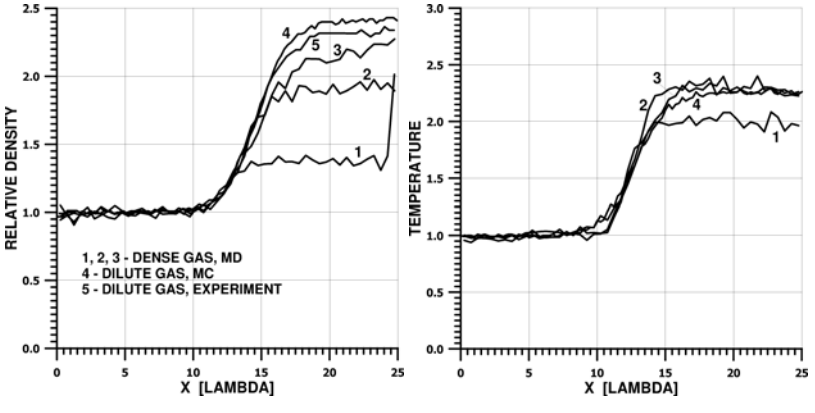

Fig. 2 Left: density distributions, right: temperature distributions inside the shock wave for the initial velocity V = 404.8 m/s

The density distributions inside the shock in a dilute gas, taken from DSMC calculations and from experiment, are shown there too. The unit length on the X – axis of this figure is equal to the ”mean molecular distance” (as defined above) for the dense gas and to the mean free path for the dilute gas. From these diagrams it is evident, that the ”mean molecular distance” plays really the same role for dense gases as the mean free path for dilute. It is also worth noting, that the front parts

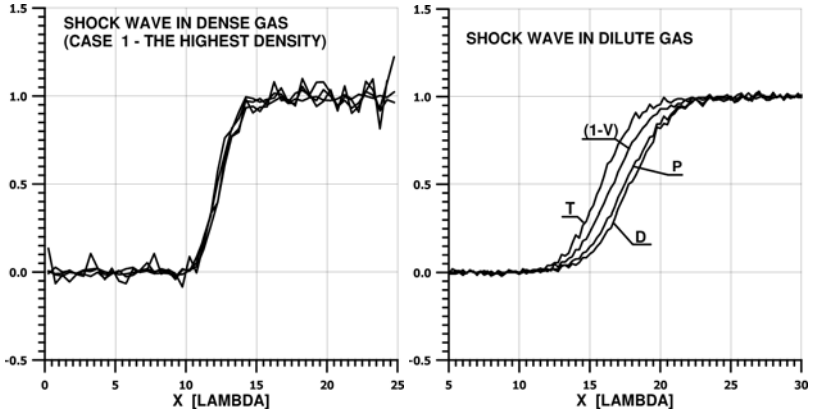

Fig. 3 Left: normalized diagrams of density, pressure, macroscopic velocity and temperature for the highest density. Right: normalized diagrams of density, pressure, macroscopic velocity and temperature for the dilute gas.

of all presented diagrams are practically identical. The differences can be seen in the rear parts: the higher the initial density, the lower the density ratio across the shock. As a result – in more dense gas the shock wave is relatively thinner. Figure 2 – right shows in a similar fashion the temperature distributions. The temperature jumps (temperature ratios) are equally high for all considered cases (including DSMC result for a dilute gas) with the exception of the highest gas density. In this case the temperature jump is lower, which is probably due to the fact, that relatively large part of the internal energy is stored in the mutual interactions of the molecules. Figure 3 – left presents normalized diagrams of density, pressure, macroscopic velocity and temperature inside the shock wave for the highest density considered. The four curves can hardly be distinguished, which is different from the case of a dilute gas, where the curves are distinctly shifted with respect to each other, as shown in Figure 3 – right.

4 Conclusion

The presented results for Argon seem to support the validity of the ”mean molecular distance” as the proper length scale for the structure of the shock wave in dense media. The shock thickness under rarefied conditions related to mean free path and for dense medium related to the ”mean molecular distance” are close to each other. Moreover – the relative thickness of the shock wave defined above decreeses smoothly when density increases from low to high values.

References

1. Bridgman, P.W.: The termal Conductivity of Liquids under Pressure. Proc. Amer. Acad. Arts and Scie. 59, 141–169 (1923)
2. Montanero, J.M., Lopez de Haro, M., Santos, A., Garzo, V.: Simple and accurate theory for strong shock waves in a dense hard-sphere fluid. Phys. Rev. E 60, 7592 (1999)
3. Schlamp, S., Hathorn, B.C.: Incomplete molecular chaos within dense-fluid shock waves. Phys. Rev. E 76, 026314 (2007)
4. Refson, K.: Moldy: a portable molecular dynamics simulation program for serial and parallel computers. Comput. Phys. Commun. 126(3), 309–328 (2000)
5. Bird, G.A.: Molecular Gas Dynamics. Clarendon Press, Oxford (1976)
6. Yanitskiy, V.E., Belotserkovskiy, O.M.: The statistical method of particles in cells for the solution of problems of the dynamics of a rarefied gas. Part I, Zh. Vychisl. Mat. Mat. Fiz. 15, 1195–1208; Part II, Zh. Vychisl. Mat. Mat. Fiz. 15, 1553–1567 (1975)
7. Ballard, H.S., Venable, D.: Shock front thickness measurements by an electron beam technique. Phys. Fluids 1(3), 225–229 (1958)

Structure of the Plume Emitted during Laser Ablation of Materials

A. Slowicka, Z.A. Walentam, and Z. Szymanski

1 Introduction

Laser ablation is a frequently used method of removing material from a solid surface by irradiating it with a powerful laser beam. It may be applied to machining materials, cleaning contaminated surfaces, deposition of thin coatings on surfaces etc. High energy, short duration laser pulse, focused on a small area of the target surface heats and evaporates it, forming eventually a plume which moves outwards from the target with high speed. The behaviour of the plume may influence the quality of the deposited layer, which is important if deposition is the goal of the process. This is particularly the case if the deposited material consists of disparate mass components. The light components move faster than the heavy ones and tend to spread on larger area of the substrate. In consequence the stoichiometry of the deposited material is not preserved. To improve the situation, the deposition process may be performed in the atmosphere of an ambient gas, which decelerates both the motion of the plume as a whole and its expansion. Deceleration is stronger for light components of the plume, which makes the expanding plume more uniform.

2 Model of Expansion of the Plume into Ambient Gas

When the plume moves through the ambient gas with supersonic speed, the bow shock (”external shock”) is formed in front of it. The increased pressure behind this shock acts on the front side of the plume decelerating it and generating a backwards oriented compression wave inside the plume. This compression eventually transforms into a backward facing shock wave (”internal shock”). The gas from the rear part of the plume, moving faster than the front, passes through the internal shock, is

A. Slowicka · Z.A. Walentam · Z. Szymanski
Institute of Fundamental Technological Research
Pawinskiego 5b 02-106 Warszawa, Poland

compressed and decelerated. The internal shock moves backward with respect to the centre of the plume and may disappear after reaching its rear border. This happens if the speed of the plume is high enough to produce vacuum behind it. No wave reflection from vacuum takes place. The model of the plume expansion with the external and internal shocks has been adopted from the spherically symmetric solution of the point explosion of Zeldovich [1] modified by Arnold et al [2]. Arnold et al [2] assumed that particles leave the surface with a velocity $v_0 = (8kT/(\pi m))^{0.5}$ corresponding to the surface temperature T. However, contrary to slow effusion-like evaporation assumed there, a strong evaporation – ablation, described by the Knudsen layer theory is present in our case. The particles released from the target have half-maxwellian velocity distribution – they can move only forward. The full maxwellian distribution is reached after some collisions in the Knudsen layer [3] a few mean free paths thick. At the outer border of the Knudsen layer the particles have the macroscopic velocity $v_0 = a$ perpendicular to the target surface (a – local speed of sound), therefore the velocity distribution of particles is "shifted maxwellian". The ablated medium absorbs more energy from the laser beam (by photoionization and inverse Bremsstrahlung) and its temperature and pressure grow further. The thickness of the ablated layer is small compared to its other dimensions, therefore the large pressure gradient inside the major part of this layer is nearly perpendicular to the surface and accelerates the plasma to high velocity ($1 \div 5 \cdot 10^4 m \cdot s^{-1}$) perpendicular to the target. This eventually results in formation of a nearly spherical plume moving outwards from the target.

3 DSMC Simulation

Expansion of a plume of carbon atoms into an ambient atmosphere of nitrogen was simulated with the standard DSMC technique (Bird [4]). The pairs of molecules for collisions were selected according to the "ballot box" algorithm of Yanitskiy [5]. The collision cross-sections for all considered molecules were taken from [6], [7], [8], [9]. The plume consisted of 10^{16} carbon atoms at initial temperature of 8000 K. Its initial shape was spherical, 3 mm radius, and it moved perpendicularly to the target with macroscopic velocity 20 km/sec. The ambient nitrogen gas had temperature of 300 K and pressures 10 Pa, 20 Pa and 40Pa (at this highest ambient pressure the plume radius was 1.5 mm). Dissociation of nitrogen molecules after collisions with fast moving atoms of the plume was taken into account. Here we present the results for ambient nitrogen pressure 20 Pa only.

4 Results

In Figure 1 we show contour maps of the number density of carbon (top), the temperature (middle) and the diagram of density and temperature distributions along the axis of symmetry of the plume (bottom), 247 nanoseconds after beginning of the simulation. In Figs. 2 and 3 we show similar diagrams for molecular and atomic nitrogen, respectively. In Fig. 1 the internal shock, directed towards the target, is

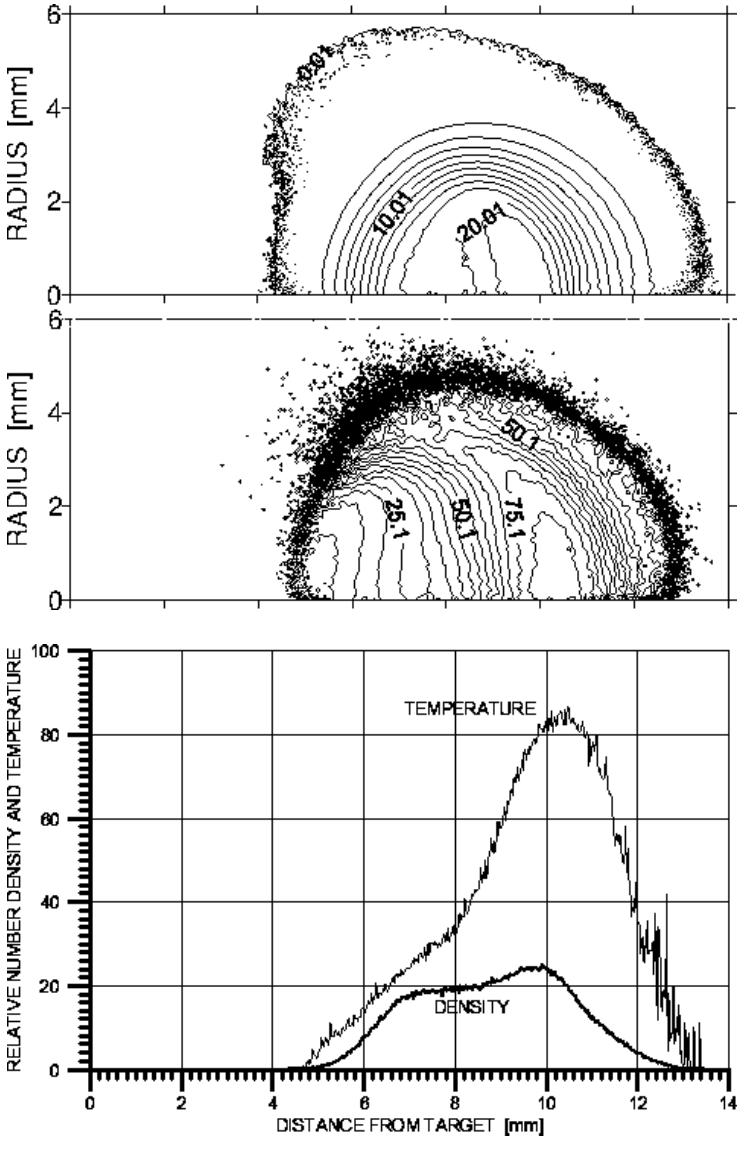

Fig. 1 Contour maps of relative number density of carbon (top), temperature (middle), density and temperature distributions along axis of symmetry (bottom). Reference number density: $0.473 \cdot 10^{16} cm^{-3}$, reference temperature: 300 K.

clearly visible. As estimated from the earlier pictures (not shown here) its velocity relative to the plume is more than 3 times higher than the respective speed of sound. The corresponding density increase is much too low for such a shock speed, which indicates, that the shock is not fully developed. The temperature of carbon

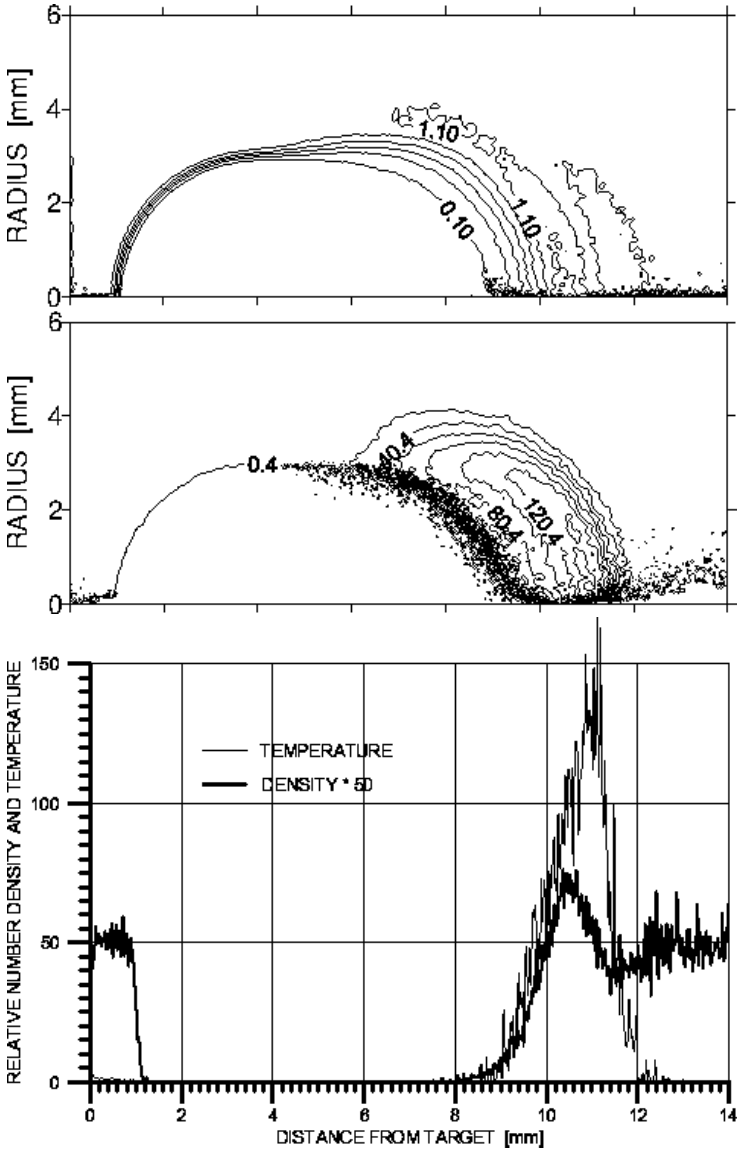

Fig. 2 The same as Figure 1 for molecular nitrogen

begins increasing above the initial level inside this internal shock, however the main temperature increase takes place at larger distance from the target, in the ”contact layer”, where the highly energetic carbon atoms and ambient nitrogen molecules diffuse. In Figure 2 the external shock in ambient nitrogen, directed from the target, can be seen. Similarly to the internal shock, this is not fully developed either. The density ratio across the shock moving in nitrogen at the speed of 20 km/sec would

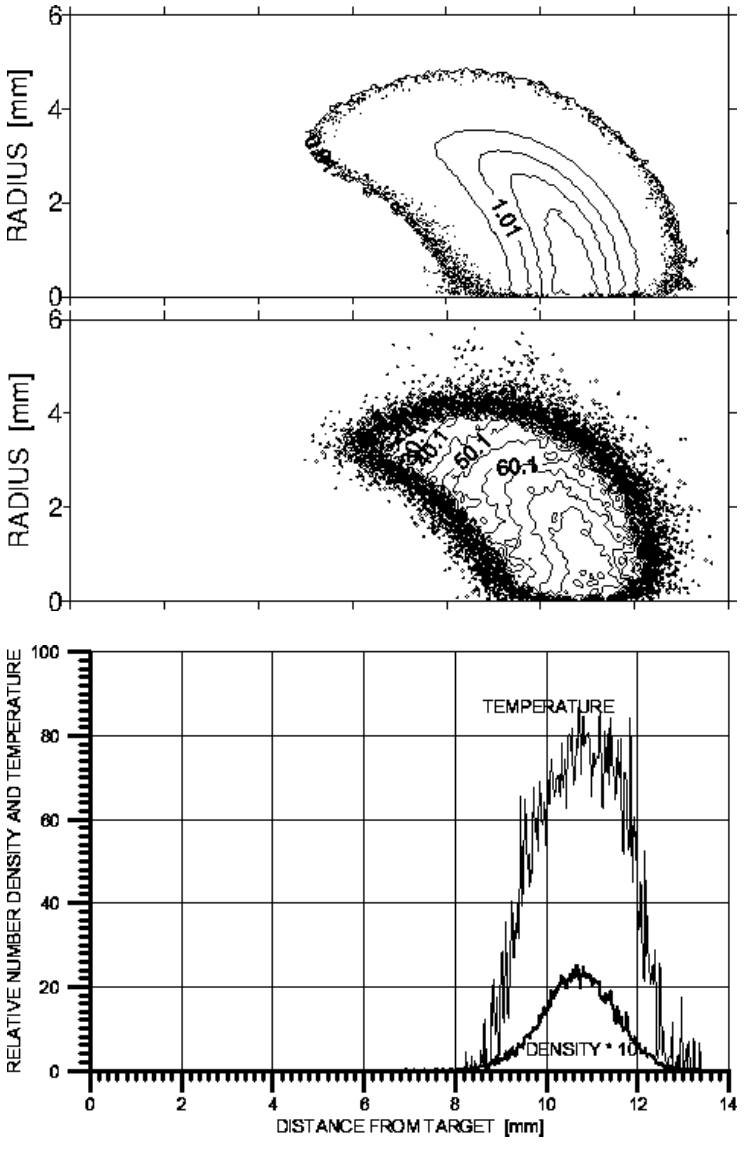

Fig. 3 The same as Figure 1 for atomic nitrogen

be close to 6, while here it is less than 2. The small decrease of density of nitrogen in front of the external shock is due to dissociation; without dissociation this decrease is not present. Figure 3 shows, that the atomic nitrogen is produced as a result of dissociation in the area where the energetic carbon atoms are scattered by ambient nitrogen molecules and attain high temperature at the cost of the former kinetic energy. When comparing the figures one can see that the temperatures of carbon and

atomic nitrogen begin increasing farther ahead of the plume than that of molecular nitrogen. This may be because the majority of collisions of the carbon atoms (very fast in this area) with nitrogen molecules lead to dissociation. Hot atomic nitrogen is produced and the temperature of the remaining molecular nitrogen stays unchanged.

5 Conclusion

Expansion of a plume generated during laser ablation of materials was studied with the Direct Simulation Monte Carlo method. The plume consisting of carbon atoms expanded into atmosphere of molecular nitrogen. Dissociation of nitrogen molecules was taken into account. Two shocks were found: the external shock moving forward in ambient gas in front of the plume and the internal shock moving backwards inside the plume. This is in qualitative agreement with the model of spherical explosion, also predicting the existence of the same two shocks. However in the model of spherical explosion the internal shock could reflect from the centre of explosion and then move forward, while here if the plume moved with sufficient speed (which usually is the case) and vacuum was generated behind it, no reflection from the rear edge of the plume could occur.

References

1. Zeldovich Ya, B., Raizer Yu, P.: Physics of Shock Waves and High-Temperature Hydrodynamic Phenomena. Academic, New York (1966)
2. Arnold, N., Gruber, J., Heitz, J.: Spherical expansion of the vapor plume into ambient gas: an analytical model. Appl. Phys. A 69(suppl.), S87 (1999)
3. Knight, C.J.: Theoretical modelling of rapid surface vaporization with back pressure. AIAA Journal 17, 519 (1979)
4. Bird, G.A.: Molecular Gas Dynamics. Clarendon Press, Oxford (1976)
5. Yanitskiy, V.E., Belotserkovskiy, O.M.: Yanitskiy VE, Belotserkovskiy OM (1975) The statistical method of particles in cells for the solution of problems of the dynamics of a rarefied gas. Part I, Zh. Vychisl. Mat. Mat. Fiz. 15, 1195–1208; Part II, Zh. Vychisl. Mat. Mat. Fiz. 15, 1553–1567 (1975)
6. Stallcop, J.R., Partridge, H., Pradhan, A., Levin, E.: Potential Energies and Collision Integrals for Interactions of Carbon and Nitrogen Atoms. Journal of Thermophysics and Heat Transfer 14, 480 (2000)
7. Levin, E., Partridge, H., Stallcop, J.R.: Collision Integrals and High Temperature Transport Properties for N–N, O–O, and N–O. Journal of Thermophysics and Heat Transfer 4, 469 (1990)
8. Stallcop, J.R., Partridge, H., Levin, E.: Effective potential energies and transport cross sections for interactions of hydrogen and nitrogen. Phys. Rev. A 62, 062709 (2000)
9. Stallcop, J.R., Partridge, H., Levin, E.: Effective potential energies and transport cross sections for atom-molecule interactions of nitrogen and oxygen. Phys. Rev. A 64, 042722 (2001)

Laser Driven Burning and Detonation Waves in SilicaBased Optical Fibers

V.P. Efremov, V.E. Fortov, A.A. Frolov, E.M. Dianov, and I.A. Bufetov

1 Introduction

Laser energy focused in bulk of transparent dielectric creates heated and elevated pressure zone producing nonreversible media destruction. Physical nature of this effect is steady in focus of modern physical studies since laser invention. Silica is quite attractive object for this due to its numerous physical and technical applications. Silica-based optical fibers provided new unique possibility for laser damaged zone study. Single mode optical fiber has constant laser radiation distribution in any transverse cross-section along the full length. This property makes available to observe propagation of energy deposition zone under steady-state conditions as opposed to laser focused into unknown initial volume of transparent dielectric target, particularly for long laser pulses ($\tau_p > 1ns$). The damage zone in optical fiber can expands to any distance to laser direction. Such laser driven wave (LDW) destroys the core and sometimes cladding too. Temperature in fiber optic core can achieve up to $\sim 10^4 K$ and silica goes to hot plasma with solid density.

In present work we have represented the recent results of experimental investigation of two types of self-maintaining destructions processes in silica-based optical fiber under intense laser beam action [1, 2, 3]. Propagation velocities of slow process (burning) are $\sim$ some meters per second. Velocity of fast process (detonation like mode) is $\sim 10^3$ times more. These velocities in optical fiber core are strongly depended on carried (pumped) laser intensity. Both investigated modes are accompanied by generation of hot plasma, pressure wave and decomposition core material. In a both cases we have transition of laser energy to thermal one. But temperatures gradients in fronts are rather different. Heated decomposition products are described as black body [4]. We are connecting the propagation of slow process with heating wave and the propagation of fast one with pressure wave.

V.P. Efremov · V.E. Fortov
Joint Institute for High Temperatures of RAS, Izhorskaya st.,
13, Bd. 2, 125412, Moscow, Russia

A.A. Frolov · E.M. Dianov · I.A. Bufetov
Fiber Optics Research Center RAS Russia, 119991, Moscow, Vavilova 38

2 Silica-Based Optical Fibers

We have mainly used silica-based optical fibers with GeO_2-doped core. Parameters of the tested types of fibers are given in the Table 1, where δn core-cladding refractive index difference, d_{core} - core diameter, λ_C cut wavelength of second mode, MFD mode field diameter and I_{th} support threshold for laser burning $\lambda = 1,06\mu m$.

Table 1 Parameters of the tested types of fibers.

	δn	$d_{core}, \mu m$	MFD, μm	$I_{th}, MW/cm^2 (P_{th}, W)$	$\lambda_C, \mu m$
A (SMF28)	0.006	8.8	8.9	1.45 (0.90)	1.3
B	0.026	4.5	4.0	3.8 (0.48)	1.12
C	0.013	8.0	6.13	2.65 (0.78)	1.6

Percent mole concentrations of GeO_2 in tested fibers were 4 (A), 20 (B) and around 15 (C). All claddings consisted of pure silica and had diameters $125\mu m$. Optical fiber densities were $2.2g/cm^3$. Samples for experiments were prepared specially. Before experiments tested part of optical fiber was striped from polymer cover and optical fiber was immersed in glycerol with density $1.26g/cm^3$ between two thin glass plates. Refractive index of glycerol is close to silica one. It allowed see processes in the core distinctly. Microscopic observation of LDW is necessary because of a fiber core diameter is rather small $(4.5-8.8\mu m)$. Images were obtained by using 300x magnification optical microscope and CCD camera with resolution 1388x1038pxl at 250ns exposure time. Fast frame camera Nanoscan^{TM} was used.

3 Burning Mode

Laser driven burning is not definitely the same that usual burning when heat wave is supported by energy release of chemical reactions. At chemical burning the thermolization zone is equal to chemical reaction zone. In laser driven burning wave (LDBW) the thermolization zone is equal to absorption zone. In absorption zone the transparent core comes to absolute black body [4]. During this threshold silica had dissociated. LDBW propagation in silica fibers under low and middle laser intensities is determinated by temperature dependence of optical absorption. In silica-based fibers absorption coefficient is rapidly increased above $1.05x10^3$ [5]. Burning initiation is simple touching of fiber output end by any absorption surface. This surface absorbed the laser radiation and heats of the fiber core what results in to plasma appearance and LDBW begins to propagate inside the core towards the laser. For backlighting we have used argon laser irradiation with wavelength 488nm. Interference band-pass filter at 480nm (25nm FWHM) was used to block the majority of a bright Planck radiation generated by plasma. The wave was supported by Yb^{3+} fiber laser radiation ($1,085\mu m$, CW). Tested fiber with 2m length was spliced to output of a Yb^{3+} single mode fiber laser. At this only first mode propagated through the fiber.

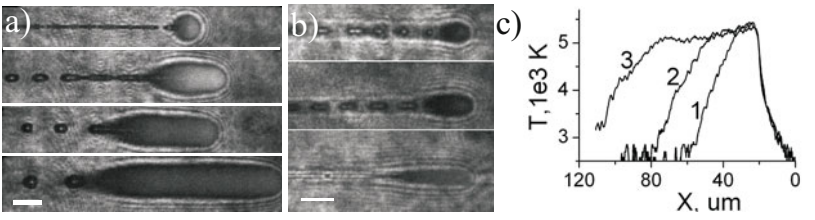

Fig. 1 Bright-field micrograph of LDBW: in fiber A, top-down, at P=1.15, 2, 3, 5W (a) and fiber B at P=0.58, 0.75, 1.5W (b). Distribution of temperature along axe of LDBW (c): in fiber A at P=2W (1), 3W (2) and 5W (3). LDBW has moved from left to right. White linear segment is $10\mu m$.

Obtained photos of burning wave are shown in Fig. 1a and Fig. 1b. Luminous region has a clear boundary. Transverse cross-section size coincides with mode one at $1/e^2$ level of laser radiation (MFD) for all tested fibers. Temperature distribution along axis LDBW in fiber A at P=2W (1), 3W (2) and 5W (3) are shown in Fig. 1c. Temperature was obtained from darkness treatment by methods developed in early work [2].

Micrographs have presented significant details: gas filled cavities, boundary layer between a luminous LDBW and cladding. In the layer one can see absorption and refraction of backlighting. Around patterns have been visualized by the backlighting interference. With increasing laser power two different shape of damage track have taken place. In fiber (A) regular sequence of bubbles is formed. Fiber B has the damage track like a capillary. Inflation of tail part of LDBW is observed in fiber A. In fiber B the wave is drop-shaped. Gas jet forms bubbles in inflation zone (Fig. 1a). The front temperature almost has not changed for 10m core at range of laser power 2-5W. Only the plateau length has been increased (Fig. 1c).

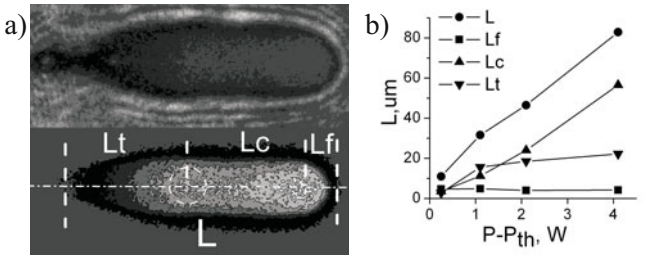

Fig. 2 LDBW structure: front, channel, tail. Bright-field image and plasma irradiation of LDBW in fiber A at P=3W (a). Lengths of LDBW parts vs laser power (b).

Burning wave structure (in fiber A) is easy sectionalized into three parts (Fig. 2a). In front part the glass becomes a supercritical fluid absorbing most of laser radiation.

A front curvature is determined by the laser energy distribution in the core and practically unchanged in the investigated power range (Fig. 2a Fig. 2b). A conical shape of opposite part (tail) is determinated by cooling to cladding. At stationary condition its possible to evaluate conical angle (α): $tg(\alpha/2) = MFD/2H_C = \sqrt{\chi t}/(V_W t) = \sqrt{\chi/V_W H_C}$ $H_C = L_{tail} - R_{in} = L_{tail} - 0.5MFD$ where α - the cone angel, H_C - the height of the cone, R_{in} the inflation radius, V_W the LDBW velocity, χ - temperature conductivity.

Establishment of bubble generation caused by a hydrodynamic instability [6] in a steady-state oscillation mode correlates with tail elongation. In a middle part of LDBW the supercritical fluid would has time to be separated into gas and liquid. It has called a channel part. The cannel part ends a local inflation: In X_{infl} position cross-section diameter of LDBW is slightly increased. The channel has a constant cross-section diameter and length linearly increased with laser power (Fig. 2b).

4 Detonation Mode

Very first results of fast destruction mode detecting have been reported in our previous work [1]. In the present work we have continued investigation of detonation-like regimes. Laser driven detonation wave (LDDW) had been investigated in A and C fibers (see Table 1). Driving laser pulses were supplied by Nd^{3+}: YAG laser ($\lambda = 1.064\mu m$) in Q-switched mode with 5 kHz repetition frequency. Time profile was near-Gaussian shape (250ns FWHM) with peak intensity $4 - 4.5GW/cm^2$ (in fiber). The laser radiation was input into fiber by means of microscope objective (8x magnification). For recording the plasma and destruction zone propagation we have used streak camera and optoelectronic camera with exposure time 2ns (Nanogate-3n, NPP Nanoscan). Second laser harmonic has been used for backlighting and obtaining micrographs in bright field mode. For magnification we have used microscope objective (10x magnification).

After initiation LDDW propagated in self-supported mode during a part of laser pulse. When the laser intensity exceeded the threshold value ($I_{th} = 2GW/cm^2$) the process starts. Velocity establishing takes places at distance not more than $\sim 1-2$ core diameters only. Later on plasma and destruction zone was moving with near constant velocity of 3 km/s more than ~ 110 own diameters. In approximation of complete transfer of laser radiation energy to thermal one the average deposited specific energy was $\sim 4.5kJ/g$. For comparison the specific energy of cast TNT detonation is $\sim 4.2kJ/g$. This high-speed movement of LDW was terminated at $I = 1.5GW/cm^2$. Note that between start point and stop one the plasma zone moves with steady velocity $\sim 3km/s$. (Fig. 3a, fiber C) nevertheless laser intensity is changed 2 times at the same time.

Distance between stop point and start one of a next laser pulse is near 10m (Fig.3b) and the corresponding time is $\tau = 200\mu s$. In our opinion it is explained by movement of absorption front with heat wave velocity. Heat wave front displacement is determined by $l = \sqrt{\chi\tau} = 12\mu m$. Where χ is temperature conductivity ($0.7x10^{-2}cm^2/s$ for fused quartz). Obtained value gives good agreement with

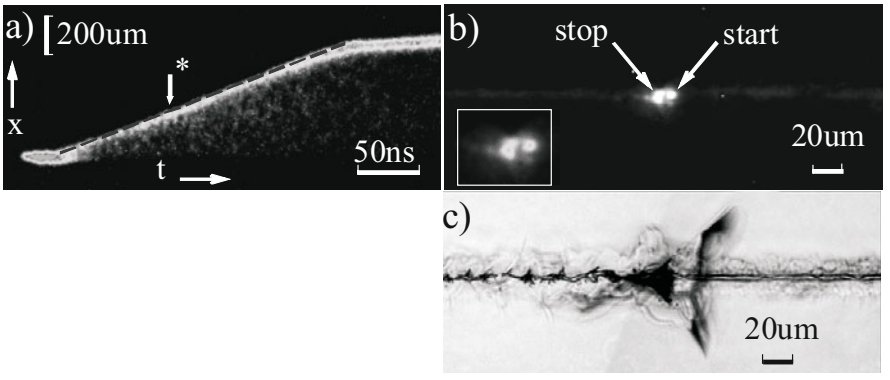

Fig. 3 LDDW in silica-based optical fiber: a the streak-camera image of plasma front movement through the fiber core, direct dotted line passes through local maximums, * - a time position of the laser pulse maximum; b and c - optical micrographs of a stop-start domain obtained with digital photo camera (LDDW moved from left to right): b - total fluorescence of the plasma track, the camera exposure time $\sim$ 1 sec, c - a damage morphology in the domain.

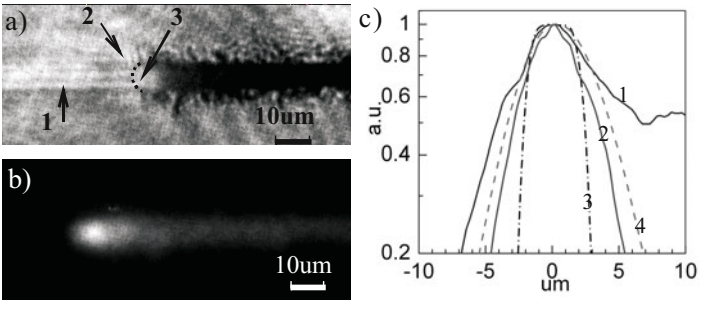

Fig. 4 2ns exposure micrographs of LDDW moved from left to right (fiber A). a - a bright-field micrograph: 1 - the core-cladding interface, 2 separated radial cracks in the silica cladding, 3 the plasma, the dotted line is a boundary of high optical disturbance in the core. b irradiation plasma micrograph of LDDW moving with 2.8km/s. c intensity profiles of plasma irradiation on Fig. 4b along the core axe (1) and crosswise direction (2); 3 the instrumental function, 4 the convolution of 2 and 3.

experiment. Note that in the start point a plasma shape looks like sphere (Fig.3b). It means a continuity of material in this region is not strongly disturbed by micro cracks from the previous stop point and an induced absorption is still sufficient for emergence of plasma. Optical fiber with enough a large diameter ($600\mu m$, without polymer jacket) can localize plasma pressure. Such fiber (with glycerol immersion) was not completely fractured what let us obtain high quality optical micrographs (Fig. 3c). Stop point has a long conical crack with a diameter around 120m. After LDDW termination the plasma (product of SiO_2 dissociation) continues to absorb a

remainder of the laser pulse and expands into the crack (Fig.3c). Later on condensation forms opaque layer (a dark apex of the crack cone on Fig.3c) hiding next start place on photos of damaged fibers. There is a dramatic change of a silica cladding damage during the laser pulse. Start of motion is characterized by uniform crushability but ending one demonstrates some intermediate attempts to stop (Fig.3c). New micrographs of LDDW (with 2ns exposure) demonstrate a formation of separated radial cracks in silica cladding (Fig.4a). The cracks arise in a cross-section ahead of a plasma front. Crack appearance indicates an availability quite strong local pressure in core. The plasma irradiation is shown in Fig.4b and one can see that high temperature domain has a rather small size. Different treatments of image brightness are presented in Fig.4c. Intensity along the fiber core axe ((1), Fig.4c) let us estimate heating rate in front as $Kt \sim 0.54 * 10^{12} K/s$. For comparison, heating rate in burning front is about $Kt \sim 0.45 * 10^{9} K/s$ at propagation velocity V=0.82m/s. Instrumental function (3) (Fig. 4c) takes into account displacement of LDDW during exposure time (2ns). The convolution (4) of crosswise direction brightness (2) and the instrumental function (3) is represented as dashed line (4) in Fig.4c. The convolution (4) has good coincidence with (1) in the hottest part (Fig.4c). Therefore the high temperature domain is closed to spherical-shaped with the radius around $3\mu m$. This high-speed LDW we have designated LDDW that to underscore pressure role in inducing of absorption in the fiber core glass. But of course laser driven detonation of optical fibers is not completely classical detonation. Processes in front of LDDW demand additional studies.

5 Conclusions

For the first time the high resolution micrographs of LDBW have been obtained in bright-field techniques. Significant details has been obtained in the micrographs: gas filled cavities, boundary layer between a luminous LDBW and host glass. Detonation-like regimes of plasma propagation ($\sim 3km/s$) under intensive laser beams were investigated in different silica-based optical fibers. For the first time the structure of failure and plasma of LDDW were recorded by frame camera with 2ns exposure in core of silica-based fiber. Process model is briefly discussed.

References

1. Dianov, E.M., Fortov, V.E., Bufetov, I.A., et al.: J. Exp. Theo. Phys. Lett. 83(2), 75 (2006)
2. Dianov, E.M., Fortov, V.E., Bufetov, I.A., et al.: IEEE Photon. Technol. Lett. 18(6), 752 (2006)
3. Efremov, V.P., Fortov, V.E., Dianov, E.M., et al.: 18th International Symposium on Heavy Ion Inertial Fusion, HIF 2010, Darmstadt, Germany, August 30-September 3 (2010)
4. Carr, C.W., Radousky, H.B., Rubenchik, A.M., et al.: Phys. Rev. Lett. 92, 087401 (2004)
5. Kashyap, R.: Conf. Lasers 1987, Lake Tahoe, Nevada, December 7-11, p. 859 (1987)
6. Ganan-Calvo, A.M., Gordilo, J.M.: Phys. Rev. Lett. 87(27), 274501 (2001)

3D MHD Description and Animation of the Process of Collision of a Solar Wind Shock with the Earth's Bow Shock

E.A. Pushkar and A.S. Korolev

At present, several groups of spacecraft in the vicinity of the Earth's bow shock S_b, magnetosheath, and outer magnetosphere and spacecraft located in the free solar wind stream near the Lagrange point L_1 are measuring the magnetosphere and solar wind parameters and the interplanetary magnetic field (IMF). The data obtained on the Earth are analyzed to forecast the cosmic weather, in particular, to identify sharp changes in the solar wind associated with shock waves [1, 2]. For interpreting adequately spacecraft's measurements it is necessary to have exact solutions of the problem of interaction between a solar wind discontinuity and the bow shock in which the wave flow pattern is known as a function of coordinates of a point on S_b.

1 Formulation of the Problem and Method of Solution

We will consider the process of collision of a fast shock wave S_f propagating from the Sun with a velocity $\mathbf{V}_{Sf}$ with the Earth's bow shock S_b developed as a result of supersonic solar wind flow past the Earth's magnetosphere (blunt obstacle of radius $10 \div 13R_E$) (Fig. 1). The IMF $\mathbf{B}_{sw}$ is assumed to be frozen in the solar wind and inclined to its velocity $\mathbf{V}_{sw}$ at an angle $\psi_{sw} = 45^\circ$ and, to be specific, lies in the plane of ecliptic. The normal $\mathbf{n}_{Sf}$ is aligned with $\mathbf{V}_{sw}$ ($\mathbf{V}_{Sf} \| \mathbf{V}_{sw}$). In the Cartesian coordinate system moving with the Earth (the X axis is directed to the Sun, the Y axis lies in the plane of ecliptic, and the Z axis is perpendicular to the XY plane) the bow shock is assumed to be steady-state (Fig. 1). The position of each element of S_b approximated by the tangential plane with the normal $\mathbf{n}_{Sb}$ can be given by two angular coordinates, namely, the latitude α (angle of inclination of this element to the X axis) and the longitude τ (angle of inclination of $\mathbf{n}_{Sb}$ to the XY plane) (Fig. 1).

The global interaction pattern is constructed by solving the MHD Riemann problem of breakdown of a discontinuity between the states behind S_f and S_b on their

E.A. Pushkar · A.S. Korolev
General and Applied Mathematics Department, Moscow State Industrial University, Avtozavodskaya 16, Moscow, 115280, Russia

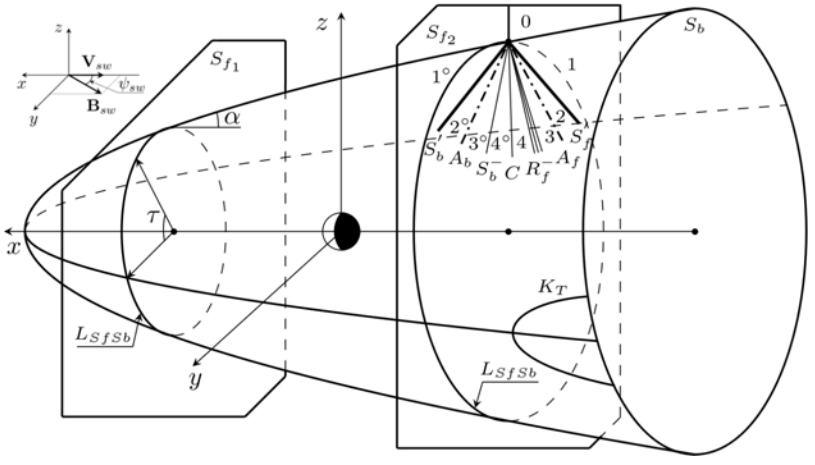

Fig. 1 Positions of solar wind shock wave S_{fi}, $(i = 1,2)$ and curve L_{SfSb} and a regular solution

curve of intersection L_{SfSb} as a function of α and τ (Fig. 1) using an original numerical-analytic method [3]. Each of the waves appearing in the interaction is distinguished individually and calculated with a given accuracy by means of relations on a strong MHD discontinuity (fast and slow shock waves $S^{\pm}$ and Alfvén discontinuities A) or differential equations (rarefaction waves $R^{\pm}$). The state behind S_f is fixed and the state behind S_b depends on the latitude α and the longitude τ so that the time dependence can be transformed into a parametric dependence on α and τ. The curve L_{SfSb} moves with a supersonic velocity; therefore, the collision can be considered locally. The establishment of flow is assumed to occur in a fairly short time negligible as compared with the characteristic propagation time. Together with the wave flow pattern, the physical parameters of the waves generated in the interaction at each point on S_b, namely, those propagating forward in the magnetosheath between S_b and the magnetopause and acting upon the Earth's magnetosphere (refracted on S_b and denoted by subscript f) and those propagating backward in the disturbed solar wind toward the Sun (denoted by subscript b), are also calculated.

A regular solution (Fig. 1) includes two combinations of self-similar flows consisting of a fast MHD wave (shock S^+ or centered rarefaction wave R^+), a nonplane-polarized Alfvén discontinuity A, and a slow MHD wave (S^- or R^-) divergent from L_{SfSb} and conjugated on a contact discontinuity C [3]. Six independent boundary conditions, namely, the no-flow condition and the conditions of continuity of the velocity, pressure, and magnetic field must be satisfied on C. The originality of the Riemann solver proposed in [3] consists in overcoming the difficulty of description of the entire flow developed as a result of the interaction in which the wave flow pattern is unknown in advance and depends on α and τ. Nevertheless, exact solutions can be found at each point on S_b using a special iteration method [3], the wave flow pattern being changed in searching the solution.

2 Results and Analysis of the Solution

On the Earth's orbit the solar wind represents a supersonic stream with the velocity of 400–450 km/s, the temperature of $(1.0 \div 1.2) \cdot 10^5$ °K, the particle concentration 10 cm^{-3}, the IMF strength $|\mathbf{B}|_{sw} \approx 6.2$ nT, and $\psi_{sw} \approx 45°$ [4]. In the quiescent state the mean dimensionless solar wind parameters are as follows: the gasdynamic Mach number $M_{sw} \approx 8$ and the beta-parameter $\beta = 8\pi p/B_{sw}^2 \approx 1$. We will investigate the interaction between S_f and S_b for the quiescent state of the solar wind assuming that $M_{sw} = 8$ and the Alfvén number $N = a_A/a_0 = (|\mathbf{B}|_{sw}/\sqrt{4\pi\rho_{sw}})/\sqrt{\gamma p_{sw}/\rho_{sw}} = 1.1$ ($\beta \approx 1$), and $\gamma = 5/3$.

We will consider the propagation of the front S_f along the Sun-Earth radius at various velocities (gasdynamic Mach numbers $M_{Sf} = 2,\ 3,\ 5$, and 8) which are important for the following reasons. The shock wave S_f has a fixed intensity, while S_b has a variable intensity dependent on the latitude α and the longitude τ since the inclination of $\mathbf{B}_{sw}$ to an element of S_b significantly affects its intensity and the local Mach number of this element $M_{Sb} = M_{sw} \sin\alpha$ depends on α. The nature of interaction between S_f and S_b depends on the angle $\theta = 90° - \alpha$ between their fronts, their intensities, and the orientation of the magnetic field with respect to the shock waves. When $\theta \in [0,\ 15°]$ the interaction is quasi-one-dimensional, the two-dimensional effects begin to manifest themselves at $\theta \geq 20°$ and strengthen significantly with increase in θ. As α and τ vary, S_b varies continuously along its surface from a strong shock wave when $90° \geq \alpha \geq 70°$ to weak when $20° \geq \alpha \geq 11°$. In this case the angle of inclination of $\mathbf{B}_{sw}$ to S_b also varies. Therefore, the global nature of the impact of a shock wave S_f of different intensity on S_b will be qualitatively different. For example, when $M_{Sf} = 2$ a weak shock wave (the density and magnetic field increase by factors of 1.6 and 1.5, respectively) interacts initially with a strong shock wave, then on the flanks ($\alpha \simeq 40 - 30°$) with a shock wave of intermediate intensity, and only when $\alpha \approx 15 - 20°$ do the intensities of S_f and S_b approach one another. It is important also to clarify how much the intensity of S_f affects the three-dimensional interaction pattern as compared with the two-dimensional pattern [5, 6] and to which quantitative and qualitative transformations a change in the intensity of S_f and the non-plane-polarized nature of the interaction can lead.

An important property of the interaction is the flow asymmetry resulting from the different inclination of the vector $\mathbf{B}_{sw}$ to the surface of S_b on its dawn ($\tau \approx 180°$) and dusk ($\tau \approx 0°$) flanks (Fig. 2). The density, the pressure, and the magnetic field strength also vary in different ways and there is symmetry only about the plane of the ecliptic ($z = 0$). In the two-dimensional formulation flow asymmetry was found on the dawn–dusk flanks in the plane of ecliptic [5, 6] and the asymmetry of the density variation [7] was confirmed by measurements on spacecraft [8].

The global wave flow pattern of the interaction depends significantly on M_{Sf} (Fig. 2). As the S_f front progresses (latitude α decreases), the wave flow pattern is subjected to continuous and jumpwise restructurings different along various meridians $\tau = \text{const}$. The direction of the reference-frame velocity $\mathbf{V}_{st}$ at which L_{SfSb} moves with respect to $\mathbf{B}_{sw}$ plays a determining role. On the dawn flank the angle ψ between $\mathbf{V}_{st}$ and $\mathbf{B}_{sw}$ is $\sim 90°$ and the "quasi-perpendicular" interaction takes

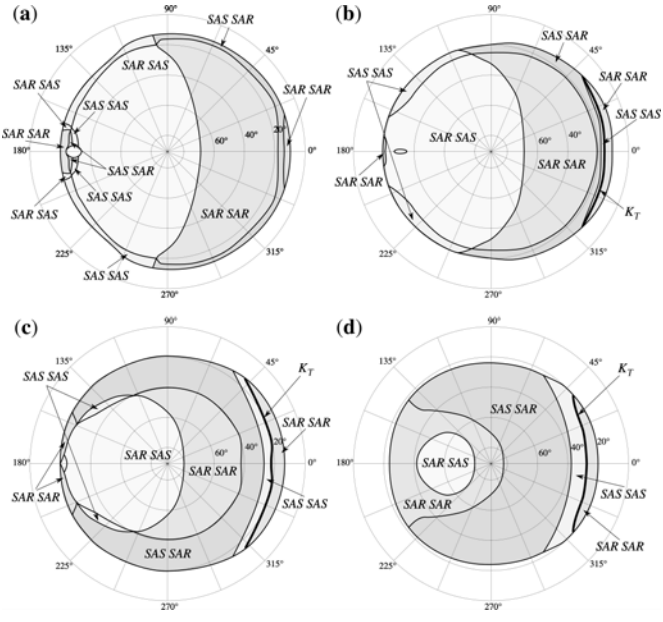

Fig. 2 Wave flow patterns of the interaction between S_f and S_b for $M_{Sf} = 2,\ 3,\ 5$, and 8 (**a**–**d**) as functions of α (circles $\alpha = \text{const}$, $\alpha = 90^\circ$ at the origin) and τ (polar angles). The waves in the magnetosheath corresponds to first three waves (refracted shock wave S'_f, Alfvén discontinuity A_f, and slow shock S_f^- or rarefaction wave R_f^-) and the reflected waves to the last three waves (refracted bow shock S'_b, Alfvén discontinuity A_b, and slow shock S_b^- or rarefaction wave R_b^-)

place [9]. It is characterized by a greater acceleration of the gas and a higher compression of the medium due to the influence of the magnetic field and by relatively weak change in the latter. In this case the Alfvénic and magnetosonic characteristics may coincide and catastrophic flow restructurings develop [9]. For example, when $M_{Sf} = 2$ the Alfvén and magnetosonic velocities are equal at $\alpha \approx 34^\circ$ and an Alfvén discontinuity A_b of finite intensity is split off from the slow switch-off shock wave S_b^{-*}. The wave flow pattern is restructured several times in a zone $|\tau - 180^\circ| < 15^\circ$, $\alpha < 34^\circ$ (Fig. 2*a*), the magnetic field changes suddenly, a local catastrophe K_{L-} and other catastrophes occur [5, 6]. When $M_{Sf} = 3$ the zone with the catastrophic flow restructurings on the dawn flank is displaced toward the lower latitudes and becomes narrower (Fig. 2*b*) and when $M_{Sf} = 5$ it is located on the boundary of existence of the regular solution $\alpha \approx 20^\circ$ (Fig. 2*c*). When $M_{Sf} = 8$ there are no flow restructurings on the dawn flank since the condition of coincidence of the Alfvén and magnetosonic velocities is nowhere fulfilled and the flow patterns are $S'_f A_f R_f^- C R_b^- A_b S'_b$ or $S'_f A_f R_f^- C S_b^- A_b S'_b$ around $\alpha = 60^\circ$, $\tau = 180^\circ$ (Fig. 2*d*).

The "quasi-parallel" interaction ($\psi \approx 0^\circ$) [9] takes place on the dusk flank. There exist critical values α^* and τ^* (dependent on M_{Sf}) lying on a curve K_T in the neighborhood of $\tau = 0^\circ$ (Fig. 1) on which the projections of $\mathbf{V}_{st}$ and $\mathbf{B}_{sw}$ to a plane

orthogonal to L_{SfSb} are collinear. On the curve K_T five characteristics, namely, two Alfvénic, two slow, and entropy characteristics, coincide simultaneously on both sides of C, i.e., the velocities of the corresponding waves become equal. As a result, the Alfvén discontinuities and slow waves draw together, merge with C and form a tangential discontinuity T, the vectors of the flow velocity and the magnetic field strength being parallel to the T front. The boundary conditions on T reduce to the no-flow condition and continuity of the total pressure $p + |\mathbf{B}|^2/8\pi$.

The plasma and magnetic field parameters on both sides of T are the limits of the parameters behind the fast shock waves S'_f and S'_b. They do not coincide with the parameters behind the slow waves which are different on both sides of T: slow shock waves S_f^- and S_b^- are transformed in rarefaction waves R_f^- and R_b^- and, accordingly, the Alfvén discontinuities A_f and A_b change jumpwise on the boundary of flows $S'_f A_f S_f^- C S_b^- A_b S'_b$ and $S'_f A_f R_f^- C R_b^- A_b S'_b$ (curve K_T in Figs. 2*b*-2*d* and Fig. 1). Thus, when S_f progresses colliding with S_b and α and τ pass through α^* and τ^*, the plasma and magnetic field parameters on C change abruptly (catastrophe K_T). As distinct from the catastrophe K_{L-} inherent to plane-polarized flows [6] and occurring at a point on the dawn flank, the catastrophe K_T has the non-plane-polarized nature and takes place on a certain curve K_T on the dusk flank of S_b. The K_T is accompanied by reversal of the electric currents, the ponderomotive forces, and the electric field $\mathbf{E} = -(\mathbf{V}/c) \times \mathbf{B}$ in the coordinate system traveling with the curve L_{SfSb}. The stronger the difference between S_f and S_b and the greater their intensities, the greater the jump in all the physical parameters on the curve K_T. For example, when $\mathrm{M}_{Sf} = 8$ increase in the magnetic field strength on the curve K_T is $\sim (2 \div 4)|\mathbf{B}|_{sw}$ and it is accompanied by decrease in the pressure ($\sim (30 \div 40) p_{sw}$) and the density ($\sim \rho_{sw}$).

The appearance of T and the location of curve K_T on S_b depend on M_{Sf} (Fig. 2) and the orientation of the S_f front in the solar wind. If the S_f front propagates along the solar wind velocity, the catastrophe K_T develops when $\mathrm{M}_{Sf} > 3$, the higher $\mathbf{M}_{Sf}$, the greater the latitudes of the curve K_T and the wider the domain inside this curve on the dusk flank. If the S_f front propagates at a certain angle to $\mathbf{V}_{sw}$ so that the angle between $\mathbf{n}_{Sf}$ and $\mathbf{B}_{sw}$ decreases (point of impingement of S_f is displaced toward the dawn flank) then the conditions of appearance of T are satisfied for greater α^* and

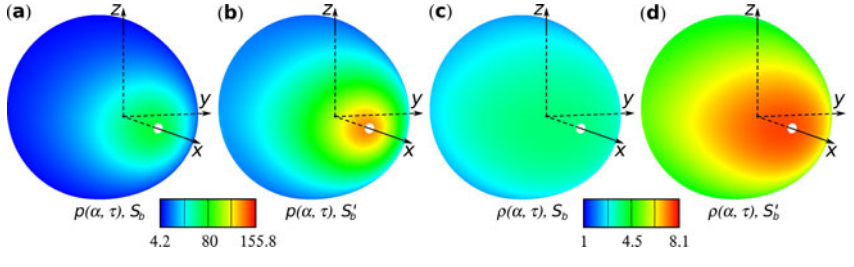

Fig. 3 Pressure (**a**, **b**) and density (**c**, **d**) distributions over the unperturbed (**a**, **c**) and perturbed (**b**, **d**) bow shocks S_b and S'_b for $\mathrm{M}_{sw} = 8$ and $\mathrm{M}_{Sf} = 3$

τ^* and the curve K_T is displaced toward the greater latitudes and widens over the flank, moreover, the tangential discontinuity can develop for the lower M_{Sf}.

An analysis of the complex interaction pattern in which six MHD waves of different types evolve as S_f progresses (Fig. 2) shows that usual graphic instruments that enable to plot the profiles of the quantities in various cross-sections in the neighborhood of the Earth's bow shock are not sufficient to represent clearly the interaction processes. A special software is developed for constructing 3D static and dynamic images illustrating the interaction. The software depicts the density, pressure, and velocity fields and the magnetic field strength in any combination of waves in the form of 3D dynamic animation patterns which can be stopped and magnified at any instant of propagation of S_f. This makes it possible to clarify the development of catastrophic flow restructurings. In Figs. 3 and 4 we have plotted screen-shots of the density, pressure and magnetic field strength distributions over the undisturbed and disturbed bow shock and behind the reflected A_b. In Fig. 4 the three-dimensional structure of the local catastrophe K_{L-} on the dawn flank of S_b can clearly be seen.

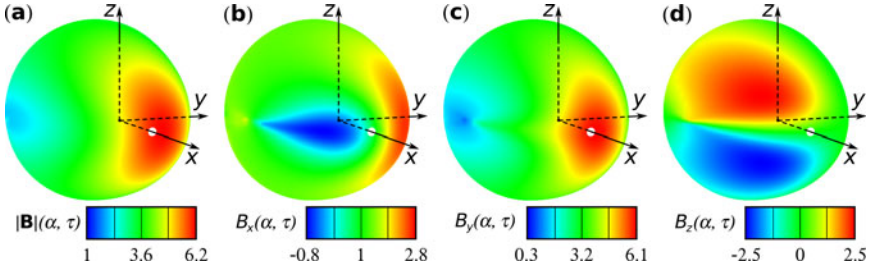

Fig. 4 Magnetic field strength and its components in the reflected Alfvén discontinuity A_b in the vicinity of S_b' for $M_{sw} = 8$ and $M_{Sf} = 3$: (**a**) $|\mathbf{B}|(\alpha, \tau)$; (**b**) $B_x(\alpha, \tau)$; (**c**) $B_y(\alpha, \tau)$; and (**d**) $B_z(\alpha, \tau)$

The solutions are necessary to interpret the data on the solar wind and IMF parameters measured by spacecraft located near the Lagrange point L_1 and orbited the Earth in the neighborhood of the bow shock and inside the Earth's magnetosheath.

3 Conclusions

The global 3D pattern of the interaction between an interplanetary shock wave S_f and the Earth's bow shock S_b is constructed within the framework of an MHD model as a mosaic of solutions of the Riemann MHD problem in the neighborhood of S_b for shock-wave Mach numbers M_{Sf} from 2 to 8 and typical solar wind and IMF parameters on the Earth's orbit. It is found that the wave flow pattern depends strongly on M_{Sf} and changes locally as the S_f front progresses. The dawn-dusk asymmetry due to the influence of the IMF found in the 2D model is confirmed in the 3D model. The difference between the impact of S_f propagating at the lower and the higher velocities consists in different flow restructurings on the dusk and dawn

flanks. When $M_{Sf} \leq 3$ the wave flow pattern changes qualitatively on the dawn flank, where Alfvén discontinuities of finite intensity appears suddenly at some point and the density, pressure, velocity and magnetic field changes abruptly in a 20° zone near the plane of ecliptic. When $M_{Sf} > 3$ there are no such restructurings on the dawn flank but a tangential discontinuity may appear on a curve on the dusk flank instead of a set of Alfvén discontinuities and slow waves.

A special software for constructing static and dynamic images illustrating the interaction is designed to represent the flow pattern in which six MHD waves of different types evolve as S_f propagates. The software depicts the density, pressure, and velocity fields and the magnetic field strength in any combination of the waves in the form of dynamic animation patterns. This makes it possible to clarify the causes of appearance and the development of catastrophic flow restructurings.

Acknowledgements. The work was carried out with support from the Russian Foundation for Basic Research (project No. 11-01-00235) and a Russian Federation President's Grant for Leading Scientific Schools (project No. NSh-4810-2010.1).

References

1. L. Přech, Z. Němeček, and J. Šafránková: Geophys. Res. Lett. **35**, L17S02 (2008)
2. K. Keika, R. Nakamura, W. Baumjohann et al.: J. Geophys. Res. **114**, A00C24 (2009)
3. E.A. Pushkar: Fluid Dynamics, **34**, 4, 567–579 (1999)
4. A.J. Hundhausen: *Coronal Expansion and Solar Wind*, Springer, New York (1972)
5. E.A. Pushkar, A.A. Barmin, and S.A. Grib: Geomegnetizm i Aeronomiya **31**, 3, 522–525 (1991)
6. A.A. Barmin and E.A. Pushkar: Fluid Dynamics **27**, 4, 560–572 (1992)
7. S.A. Grib and E.A. Pushkar: Geomegnetizm i Aeronomiya **46**, 4, 442–448 (2006)
8. K.I. Paularena, J.D. Richardson et al.: J. Geophys. Res. **106**, A11, 25377–25394 (2001)
9. A.A. Barmin and E.A. Pushkar: Fluid Dynamics **26**, 3, 428–437 (1991)

Interaction between Laser Induced Plasma and Boundary Layer over a Flat Plate in Hypersonic Flow

L. Yang, H. Zare-Behtash, E. Erdem, and K. Kontis

1 Introduction

Laser energy deposition has brought great interest to researchers due to its applications in drag reduction [1, 2], shock wave modification [3, 4], fuel ignition [5], and optical perturber for transition study [6, 7, 8]. Compared to the electric discharge flow control techniques, laser energy deposition can excite the flow non-intrusively with almost any pulse-width and repetition rate [9] with out any electrodes.

Yan et al. [10, 11] investigated the laser energy deposition effect in quiescent air and upstream of an intersecting shock in Mach 3.45 supersonic flow numerically and experimentally. The induced shock wave was clearly visualized using Rayleigh scattering in quiescent air at 101 kPa. The Mach stem height was found to reduce to 20% of the original height in the laser pulse duration. A similar approach was used for control of shock-shock interaction by Adelgren et al. [12] as well. These can be classified as volumetric laser energy deposition.

Kähler et al. [9] used the laser energy deposition technique as a boundary layer control method in low speed flow. The laser energy deposition was obtained using optics installed underneath a flat plate test model at a 10 m/s freestream velocity. The benefit of this setup is that it can avoid surface ablation when focusing the laser beam. It successfully demonstrated that artificial turbulent flow structure can be generated by laser energy deposition non-intrusively. This might have potential for preventing separation in low speed flow control. Besides the expected artificial disturbances obtained in a Mach 6 transition investigation experiment by Heitmann et al. [13], it is noticed that the boundary layer was significantly altered in the laser pulse duration. The generation of an induced shock wave forces the neighbourhood boundary layer to separate and cause local pressure variation. This experiment might bring an idea of using laser energy deposition as a boundary layer control technique in hypersonic flow. Since the mechanism and control effect of this technique is still

L. Yang · H. Zare-Behtash · E. Erdem · K. Kontis
The School of MACE, The University of Manchester
Sackville St., M60 1QD Manchester, UK

not fully understand, it is necessary to further investigate the potential of laser energy deposition used for boundary layer control in hypersonic flow.

2 Experimental Setup

The main facility used in the current research is an intermediate blow-down hypersonic tunnel using dry air as working fluid. The entire system mainly includes high pressure vessel, vacuum tank, electric heater, axisymmetric nozzle, working section and auxiliary pumping and pressure supply system. The experimental tunnel is identical to that of Erdem et al. [14].

Experimental conditions of total pressure and temperature are monitored using the stagnation pitot and thermocouple probe. The pitot probe is connected to a Kulite pressure transducer (XTE-190M, 0-100psi) and data is acquired by National Instruments (NI) system and operated using Labview.

A 150 mm long stainless steel flat plate was chosen as the test model with 60 mm width and 5 mm thickness. The flat plate was chamfered to generate a sharp leading edge. The top surface was polished and painted white to avoid any roughness disturbance to the flow. This paint can be removable and re-applied to keep a smooth surface at all times if any roughness caused during the experiment.

A high-speed Schlieren system is utilised for visualising the laser induced air breakdown. Schlieren images are recorded by a high speed camera (Photron SA-1) at 90 kfps frame rate and 1 μs exposure time. The light source of Schlieren is a Xenon lamp which gives a strong illumination, enough to capture images at 1 μs exposure time. The system was reported by Erdem [15] as well.

3 Laser Energy Deposition

A double-cavity Q-switched 532 nm Nd:YAG laser with peak power 200 mJ per pulse was focused on a concentrated volume on the flat plate. To achieve a higher perturbation of laser energy deposition, the laser system is run at the maximum power. The diameter of output laser beam is 6 mm as quoted by the manufacturer.

Laser energy deposition was obtained by focusing the laser beam using concave-convex lens system. A combination of three lens is adapted as suggested by Schmisseur et al. [7, 8]. The first 25.4 mm concave lens with focal length of f=-100 mm expands the laser beam and a following 50 mm diameter convex lens with 250 mm focal length then collimates or converges the beam expansion slightly. Finally, the laser beam is focused to the wind tunnel test section through the top Quartz window by a third convex lens. The set up of laser beam is inclined at a small angle respect to the normal direction of top window with aim of avoiding the risk of unexpected focusing from reflection of test section window. The benefit of using combination lens to focus is that laser beam can be focused into a smaller spot to obtain higher energy density even at the same laser beam energy level. The position of laser focusing spot is chosen at the centre spanwise and 40 mm from leading edge on the flat plate.

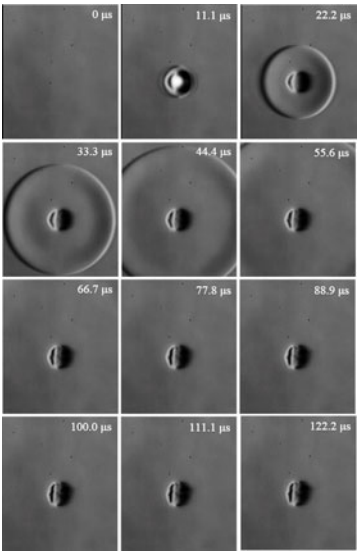

Fig. 1 Laser focusing in quiescent air at 100 kPa.

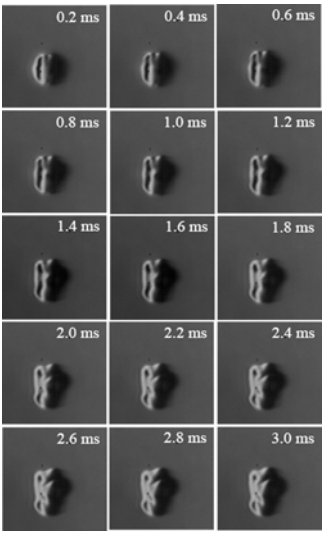

Fig. 2 Kernel development at later time.

4 Results and Discussion

4.1 Laser Energy Deposition in Quiescent Air at 100 kPa

To understand the fundamental structure of laser energy deposition, laser is focused in ambient quiescent air and visualized by high-speed Schlieren. In Fig. 1, sequence of Schlieren images shows temporal evaluation of induced structure after energy deposition. At 100 kPa pressure, the laser energy density is believed to be over the laser breakdown threshold with current lens setup and it is confirmed by the experimental findings [5, 16]. The centre of bright region in the second images indicates the focal point while the laser beam is coming from left. When the laser is focused to a concentrated volume of air, local air is heated and expanded. A laser caused air breakdown will occur when the laser energy density reach certain threshold level related to the local pressure. An induced shock wave follows with the breakdown and propagates to the surrounding region at a speed of approximately 400 m/s at beginning. The radius of spherical shock wave keeps increases while the shock wave speed and strength decrease with time.

A kernel structure can also be seen from the Schlieren images with a much less growth rate compared to the shock wave. The development of kernel structure in a longer time is shown in Fig. 2. As can be seen, the development of kernel mainly occurs in the vertical direction with a slow growing rate. The size does not change too much even at 3 ms after laser breakdown. At a later time, a toroidal seems to begin to slowly generate as explained by Bradley et al. [5].

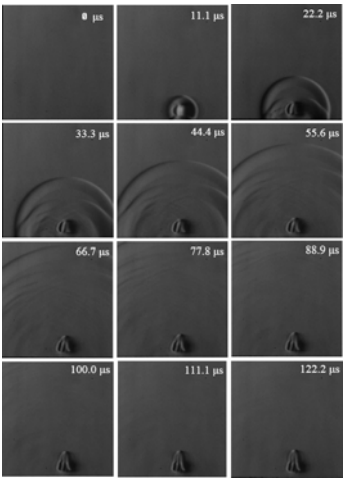

Fig. 3 Laser deposition at 2 mm above flat plate surface.

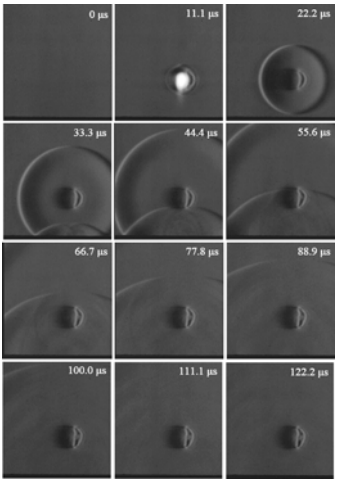

Fig. 4 Laser deposition at 10 mm above flat plate surface.

4.2 Laser Energy Deposition at Different Heights above the Flat Plate at 100 kPa

The laser energy deposition was also conducted at different height from the model surface in quiescent air. Location of focal point is chosen at 2, 5 and 10 mm height from flat plate model surface because the boundary layer thickness at 150 mm from leading edge of flat plate is estimated to be 5 mm from previous experience under the general freestream Reynolds number condition $13.5 \times 10^6 \mathrm{m}^{-1}$.

Schlieren images of laser energy deposition at height 2 mm and 10 mm from flat plate model surface is presented in Fig. 3 and 4. Generally, air breakdown is induced after breakdown following with the induced shock wave propagation. At certain time, this induced shock wave impinges the model surface and is reflected. The shape of the kernel is deformed by the reflected shock wave and shows distinct pattern at different height from model surface. Compared to 10 mm height, the induced shock wave contacts the flat plate surface earlier when focused at 2 mm height and kernel structure is deformed more significantly. That is reasonable since the distance between the focus spot is shorter and the strength of reflected shock wave is stronger than the other heights. As can be seen from Fig. 3, the major development of kernel occurs in vertical direction and the shape points to the reflected direction. Temporal evaluation of internal plasma kernel at different height from model surface in a longer time is presented from Fig. 5 and 6. As can be seen from the Schlieren images, the kernel is affected more significantly when focal point is closer to the model surface. It is clearly clarified that the development of kernel occurs in axis direction other than later direction. Especially at 2.4 ms from the air breakdown, the height of kernel structure shows most difference.

It can be concluded that stronger perturbation are generated when the focal point is closer to the model surface. To obtain sufficient disturbance to the freestream flow, laser beam is focused on the model surface in the following section.

4.3 Laser Energy Deposition in Hypersonic Flow

When the laser beam is focused on the model surface in hypersonic flow, the local air is heated and a shock wave is formed which is believed to be laser-ablation effect. It should be noted that the energy density for the current setup and laser system is below the air breakdown energy threshold at the freestream pressure. A sequence of high-speed Schlieren images of induced flow structure are presented in Fig. 7 and 8 in the presence of hypersonic flow. The energy deposition position was chosen at 20 mm and 40 mm from the leading edge of flat plate test model and centre in spanwise direction, respectively. The flow is believed to be laminar at the local Reynolds number and the boundary layer can be seen fully attached to the model surface. Flow is from left to right. Oblique shock wave visible on the top of the Schlieren image is the leading edge shock. In presence of the induced shock wave generated by energy deposition, a separation shock wave was formed due to the adverse pressure gradient in neighbouring downstream. This induced shock wave was carried by the flow downstream and lifts up from model surface. Although the laser pluse width is only 4 ns long, the entire interaction duration can last about 78 μs. The strength of shock wave decays as the induced structures moving away from model surface.

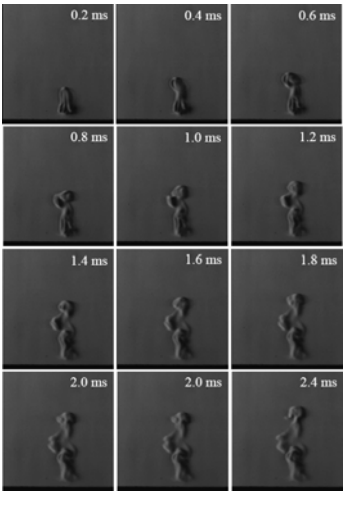

Fig. 5 Laser deposition at 2 mm above flat plate surface at later times.

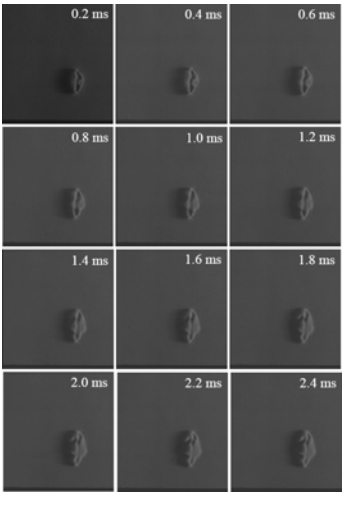

Fig. 6 Laser deposition at 10 mm above flat plate surface at later times.

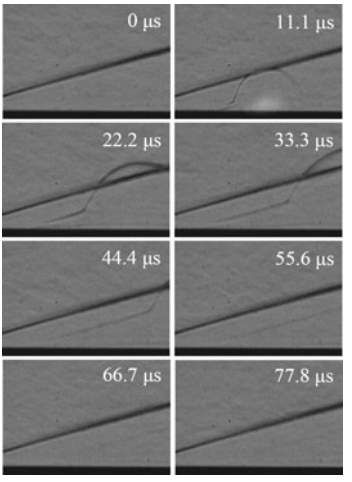

Fig. 7 Laser deposition on flat plate 20 mm from leading edge in Mach 5 flow.

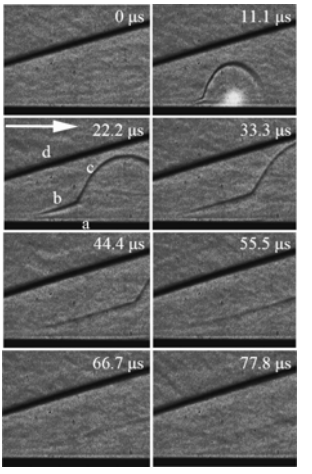

Fig. 8 Laser deposition on flat plate 40 mm from leading edge in Mach 5 flow.

5 Conclusions

Laser energy deposition was experimentally studied in quiescent air with varying pressures as well as in the presence of hypersonic flow. Air optical breakdown was achieved at 100 kPa with laser beam energy of 200 mJ per pulse using a concave-convex lens focusing system. A shock wave is created after the air optical breakdown. The velocity and strength of shock wave decays while propagating. The internal induced kernel structure is more stable and has a slow growth rate. At low pressure, the induced shock wave was obtained while laser beam was focused on the model surface mainly due to the laser-ablation effect. In presence of incoming Mach 5 flow, this induced shock wave causes the local boundary layer to separate and lifts up while moving to downstream. The entire induced structure is much similar to the flow pattern induced by pulse micro-jet. For further investigation, surface pressure measurement will be conducted to study its effect quantitatively.

It is noted that a burning mark left after the experiment. When the laser is focused at the local position, high temperature heated the surface will melt and vaporise the local material. Even this ablation is in a tiny scale and not touchable, whether it will cause serious melting during longer operation time is still unknown.

References

1. Minucci, M.A.S., Toro, P.G.P., Chanes Jr., J.B., Ramos, A.G., Pereira, A.L., Nagamatsu, H.T., Myrabo, L.N.: Investigation of a laser-supported directed-energy air spike in hypersonic flow. J. Spacecraft Rockets 40(1), 133–136 (2003)
2. Minucci, M.A.S., Toro, P.G.P., Oliveira, A.C., Ramos, A.G., Chanes Jr., J.B., Pereira, A.L., Nagamatsu, H.T., Myrabo, L.N.: Laser-supported directed-energy air spike in hypersonic flow. J. Spacecraft Rockets 42(1), 51–57 (2003)

3. Macheret, S.O., Shneider, M.N., Miles, R.B.: Scramjet inlet control by off-body energy addition: A virtual cowl. AIAA J. 42(11), 2294–2302 (2004)
4. Zaidi, S.H., Shneider, M.N., Miles, R.B.: Shock-Wave Mitigation Through Off-Body Pulsed Energy Deposition. AIAA J. 42(2), 326–331 (2004)
5. Bradley, D., Sheppard, C.G.W., Suardjaja, I.M., Woolley, R.: Fundamentals of high-energy spark ignition with lasers. Combust. Flame 138(1-2), 55–77 (2004)
6. Heitmann, D., Kähler, C., Radespiel, R.: Investigation of laser-generated flow perturbations in hypersonic flow over a flat plate. AIAA 2008-3737 (2008)
7. Schmisseur, J.D., Collicott, S.H., Schneider, S.P.: Laser-generated localized freestream perturbations in supersonic and hypersonic flows. AIAA J. 38(4), 666–671 (2000)
8. Schmisseur, J.D., Schneider, S.P., Collicott, S.H.: Supersonic boundary-layer response to optically generated freestream disturbances. Exp. in Fluids 33(2), 225–232 (2002)
9. Kähler, C.J., Dreye, M.: Dynamic 3D Stereoscopic PIV and Schlieren Investigation of Turbulent Flow Structures Generated by Laser Induced Plasma. In: 12th International Symposium on Applications of Laser Techniques to Fluid Mechanics (2004)
10. Yan, H., Adelgren, R., Elliott, G., Knight, D., Beutner, T., Ivanov, M.: Laser Energy Deposition in Intersecting Shocks. AIAA 2002-2729 (2002)
11. Yan, H., Adelgren, R., Boguszko, M., Elliott, G., Knight, D.: Laser Energy Deposition in Quiescent Air. AIAA 2003-1051 (2003)
12. Adelgren, R., Elliott, G., Knight, D., Zheltovodov, A.A., Beutner, T.: Energy Deposition in Supersonic Flows. AIAA 2001-0885 (2001)
13. Heitmann, D., Kähler, C., Radespiel, R.: Installation of a System for Laser-Generated Perturbations in Hypersonic Flow. In: 14th International Symposium on Applications of Laser Techniques to Fluid Mechanics, Portugal (2008)
14. Erdem, E., Yang, L., Kontis, K.: Drag reduction by energy deposition in hypersonic flows. AIAA 2009-7347 (2009)
15. Erdem, E., Yang, L., Kontis, K.: Drag Reduction Studies by Steady Energy Deposition at Mach 5. AIAA 2011-1027 (2011)
16. Sircar, A., Dwivedi, R.K., Thareja, R.K.: Laser induced breakdown of Ar, N2 and O2 gases using 1.064, 0.532, 0.355 and 0.266 um radiation. App. Phys. B-Lasers O. 63(6), 623–627 (1997)

Fracture Evaluation Using Shock-Induced Borehole Waves

Huajun Fan and D.M.J. Smeulders

1 Introduction

In the oil industry, acoustic techniques are commonly practiced to determine the position and the properties of the reservoir and the overburden. These techniques comprise the use of seismic surveys, cross-well tomography, and borehole logging. In the latter technique, acoustic sources and detectors are installed in a logging tool that is run in the borehole penetrating the potential hydrocarbon reservoir (i.e., a porous rock formation). The acoustic source generates a variety of borehole wave modes among which the Stoneley wave is most prominent [1]. In the field, the borehole is usually intersected by natural reservoir fractures and faults that may extend over several kilometers and dramatically affect the borehole acoustics [2]. Here we use a conventional vertical shock tube to generate and study wave propagation in a borehole intersected by a single horizontal permeable fracture.

2 Theoretical Formulation

We consider a single horizontal fracture, having a width h, intersecting the borehole (see Fig. 1). The fracture is of infinite

extent in the radial (r) direction. The borehole has radius R. The plane $z = 0$ is in the middle of the fracture. The z-coordinate is pointing downwards. We assume that the borehole fluid pressure is uniform across the borehole, which seems reasonable for not too high frequencies [4]. The borehole wave equation is

$$\frac{d^2\Phi}{dz^2} + \kappa^2\Phi = 0, \tag{1}$$

Huajun Fan · D.M.J. Smeulders
Delft University of Technology, Stevinweg 1, 2628 CN, Delft, Netherlands

D.M.J. Smeulders
Eindhoven University of Technology, PO Box 513, 5600 MB Eindhoven, Netherlands

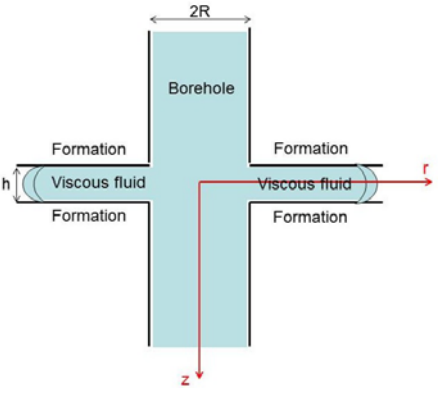

Fig. 1 Borehole intersected by a single horizontal gap representing the fracture

where Φ is the displacement potential, and κ is the wavenumber. The fluid pressure p and the axial fluid displacement U in the borehole are given by

$$p = \rho_f \omega^2 \Phi, \qquad U = \frac{d\Phi}{dz}, \tag{2}$$

where ρ_f is the fluid density, and ω is the angular frequency. Borehole wave propagation is described by

$$\Phi = A^+ e^{i\kappa_1 z} + A^- e^{-i\kappa_1 z} \quad \text{for } z < -h/2, \tag{3}$$
$$\Phi = B^+ e^{i\kappa_2 z} + B^- e^{-i\kappa_2 z} \quad \text{for } -h/2 < z < h/2, \tag{4}$$
$$\Phi = C^+ e^{i\kappa_1 z} \quad \text{for } z > h/2. \tag{5}$$

In the region $z < -h/2$, $A^+ e^{i\kappa_1 z}$ and $A^- e^{-i\kappa_1 z}$ represent the incident wave propagating in the positive z direction and the reflected wave propagating in the negative z direction, respectively. Note that κ_1 is the fluid wavenumber in the undisturbed borehole, and κ_2 is the fluid wavenumber where the borehole is intersected by the fracture. A^+ is the incident amplitude, and A^- is the reflected amplitude. In the region $-h/2 < z < h/2$, B^+ and B^- are the amplitudes of the waves propagating in the positive and negative z directions, respectively. C^+ is the amplitude of the transmitted wave in the region $z > h/2$. The fluid displacement and the pressure should be continuous at $z = h/2$ and $z = -h/2$. The coefficients A^-, B^+ ,$B^-$and C^+ can now be calculated as a function of the incident amplitude coefficient term A^+

$$A^-/A^+ = 2i(\kappa_2^2 - \kappa_1^2) sin(\kappa_2 h)/G, \tag{6}$$
$$B^+/A^+ = 2\kappa_1(\kappa_1 + \kappa_2) e^{-i\kappa_2 h}/G, \tag{7}$$
$$B^-/A^+ = 2\kappa_1(\kappa_2 - \kappa_1) e^{i\kappa_2 h}/G, \tag{8}$$
$$C^+/A^+ = 4\kappa_1 \kappa_2 e^{-i\kappa_1 h}/G, \tag{9}$$

where G is given by

$$G = (\kappa_1 + \kappa_2)^2 e^{-i\kappa_2 h} - (\kappa_1 - \kappa_2)^2 e^{i\kappa_2 h}. \tag{10}$$

The above equations were also found by Tang and Cheng [4]. Assuming a rigid formation, the Stoneley wave number in the upper and lower fracture regions is simply $\kappa_1 = \omega/c_f$, with c_f the acoustic velocity in the fluid. The wavenumber in the borehole region $\kappa_2 = \omega\sqrt{\rho_f/K_{eff}}$, with K_{eff} the effective fluid bulk modulus, allowing for the additional compliance of the borehole fluid due to the lateral fluid outflow into the fracture. Tang and Cheng [3] studied the dynamic viscous (dynamic viscosity η, kinematic viscosity ν) compressible fluid motion in the fracture, and found that

$$\frac{1}{K_{eff}} = \frac{1}{K_f}\left[1 - \frac{2}{\kappa R}\frac{H_1(\kappa R)}{H_0(\kappa R)}\right], \tag{11}$$

where H_0 and H_1 are Hankel functions of zeroth and first order, respectively, and the wavenumber in the fracture κ is found from the secular equation

$$\kappa^2 tan(\frac{h}{2}\bar{f}) + f\bar{f}tan(\frac{h}{2}f) = 0, \tag{12}$$

with the auxiliary wavenumbers f and $\bar{f}$ given by

$$f^2 = \frac{\omega^2}{c_f^2 - \frac{4}{3}i\omega\nu} - \kappa^2, \qquad \bar{f}^2 = \frac{i\omega}{\nu} - \kappa^2. \tag{13}$$

Another approach is to assume incompressible dynamic (Darcy) fluid motion in the fracture. Contrary to the Tang and Cheng approach, fluid shear wave diffusivity is now neglected. Applying straightforward mass and momentum balance equations we now find that [5]

$$\frac{1}{K_{eff}} = \frac{1}{K_f} + \frac{1}{6}\frac{h^2\mu}{i\omega\eta R}\frac{K_1(\mu R)}{K_0(\mu R)}, \tag{14}$$

with $\mu = i\omega/D_h$, and $D_h = h^2 K_f/(12\eta)$ the hydraulic diffusivity of the fracture. K_0 and K_1 are Kelvin functions of zeroth and first order, respectively. A comparison of both methods is given in Fig. 2 for three different fracture widths. We consider a water-filled 1.0 cm diameter borehole and three different water-filled fracture widths. The reflection coefficient A^-/A^+ and the transmission coefficient C^+/A^+ are plotted as a function of frequency. We notice that the theoretical predictions are in close agreement, for these (minute) fracture widths. It is clear that larger fractures will induce more reflectivity, as is intuitively expected.

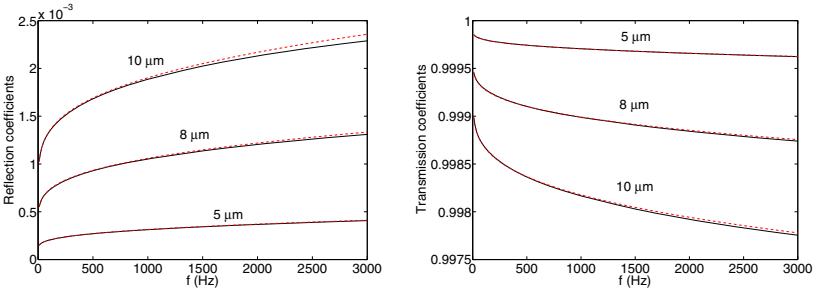

Fig. 2 Reflection and transmission coefficients for three different fracture widths. The solid lines represent Tang and Cheng's theory; the dashed lines represent White's approach.

3 Experiment

A schematic overview of the set-up is shown in Fig. 3. A 40 cm long Polyvinyl Chloride cylinder with a diameter of 7.7 cm is mounted in the driven section of the shock tube. The sample has a 1.0 cm diameter borehole drilled down the centre of the cylinder. An artificial fracture is cut in the middle of the sample (see Fig. 3). The fracture horizontal length is slightly less than the sample radius so that the fracture remains open. Both borehole and fracture are carefully filled with water. The water level is some 70 centimeters above the sample. The impact shock wave

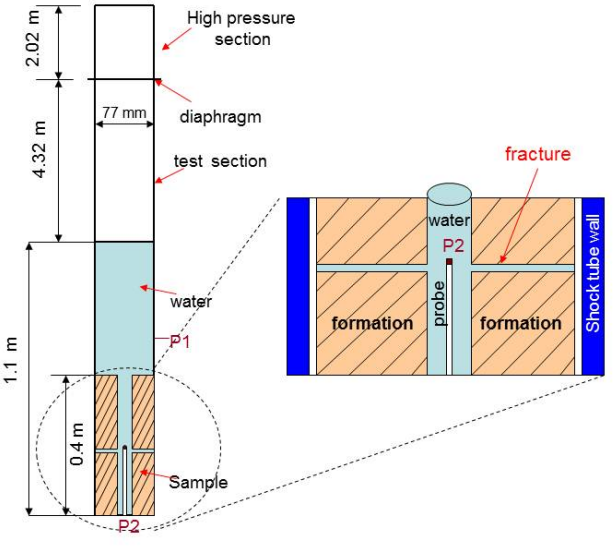

Fig. 3 Schematic of the Shock tube setup and the fractured sample cylinder

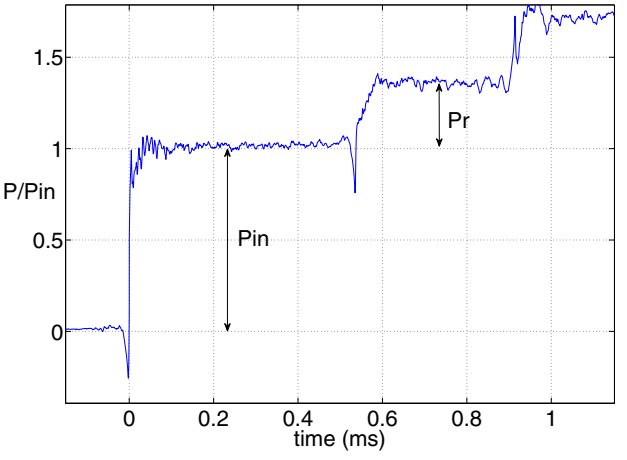

Fig. 4 Recorded pressure signal P1, which is used to trigger the data acquisition system

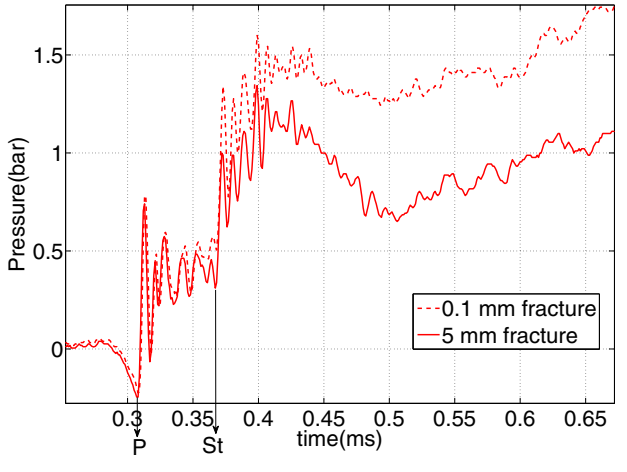

Fig. 5 Recorded pressure signal from the mobile probe P2 at 110 mm above the fracture. The fracture width are 0.1 mm and 5 mm. The fracture is at 200 mm from the sample top

hits the water layer on top of the sample and is partially reflected, and partially transmitted as a ramp-like pressure step wave. This pressure step wave subsequently arrives at the top of the borehole, where the Stoneley wave is generated. The pressure above the sample is measured by pressure gauge P1. Pressure hydrophone P2 is installed in a thin probe that can be run up and down the borehole, thus simulating the actual acoustic logging tool [1]. A typical relative pressure recording of the

trigger channel P1 is shown in Fig. 4. At time $t = 0$, the incident pressure wave arrives at P1, followed by the reflected wave from the sample top at $t = 0.535$ ms. At time $t = 0.899$, the reflection from the sample bottom is recorded. Next, the mobile probe is used to record the pressure inside the borehole 110 mm above the fracture center. At 0.308 ms, the P-wave arrives. At 0.368 ms, the Stoneley wave arrives. From 0.4 ms onwards, there is a decrease of the pressures for both cases, but the 5 mm fracture width recording decreases much more than the 0.1 mm fracture width recording (see Fig. 5). We thus notice that larger fractures cause steeper pressure declines caused by higher borehole fluid compliance.

4 Conclusion

Computations suggest that Stoneley wave propagation is strongly affected by fractures intersecting the borehole. Fluid wave regimes inside the fracture are taken into account to compute the attenuation and reflection at the fracture region of the Stoneley wave in the borehole. Full wave theory predict almost the same results as simplified dynamic Darcy flow, for small fracture widths. Our shock tube setup generates borehole Stoneley waves that are used for fracture characterization. Experiments on Polyvinyl Chloride samples with one single horizontal fracture show that varying fracture widths significantly alter the recorded Stoneley wave pressure signal at fixed depth. The technique is easily extensible to fractured porous samples for hydrocarbon reservoir applications.

References

1. Chao, G., Smeulders, D.M.J., van Dongen, M.E.H.: An experimental and theoretical study of shock-induced surface waves in porous boreholes. In: Shock Waves, Proc. 24th ISSW, Beijing, pp. 1043–1048 (2004)
2. Hornby, B.E., Johnson, D.L., Winkler, K.W., Plumb, R.A.: Fracture evaluation using reflected Stoneley-wave arrivals. Geophysics 54(10), 1274–1288 (1989)
3. Tang, X.M., Cheng, C.H.: A dynamic model for fluid flow in open borehole fractures. Journal of Geophysical Research 94(B6), 7567–7576 (1989)
4. Tang, X.M., Cheng, C.H.: Borehole Stoneley wave propagation across permeable structures. Geophysical Prospecting 41(2), 165–187 (1993)
5. White, J.E.: Underground sound, application of seismic waves. Elsevier Science Publishing Co. (1983)

Part XXI
Special Session Medical and Biological Applications

Improved Shock Wave-Assisted Bacteria Transformation

A.M. Loske, J. Campos-Guillén, M. de Icaza-Herrera,
F. Fernández, and E. Castaño-Tostado

1 Introduction

The research on shock-wave induced bio-effects is expanding rapidly where an emerging field is the so-called cell transformation, i.e., the uptake of deoxyribonucleic acid (DNA) from the surrounding. 'Competent bacteria' are those which are capable of being transformed. The standard method to identify transformed cells uses plasmids (DNA molecules that replicate independently of the chromosomal DNA) containing a gene that increases bacteria resistance to the antibiotic they are normally sensitive to. After plating the bacteria on a medium containing the antibiotic, only the transformed cells proliferate. Chilling the cells in $CaCl_2$, shocking them with an electric field to create holes in the membrane, and ultrasound are physical methods to increase bacteria competence [1]. Nevertheless, there is still a lack of efficient methods for DNA delivery. Cell transformation by ultrasound is based on cavitation-induced membrane permeability [2]. Shock wave-induced sonoporation has also been associated with cavitation, i.e. growth and collapse of microbubbles [3-5]. In most studies clinical shock wave generators have been adapted to apply up to several hundredths of shock waves to a vial containing cells in suspension. After passage of each shock wave, a cloud of bubbles forms inside the vial. These bubbles expand and collapse violently after approximately $250 - 500\ \mu$s, emitting high speed microjets that are supposed to be responsible for cell transformation [6]. Microjet emission can be intensified if a second shock wave (Fig. 1) arrives shortly before the bubbles start to collapse. This phenomenon has been used to improve

A.M. Loske · M. de Icaza-Herrera · F. Fernández
Centro de Física Aplicada y Tecnología Avanzada, Universidad Nacional Autónoma de México, Blvd. Juriquilla 3001, Juriquilla Querétaro, Qro., 76230, Mexico

J. Campos-Guillén
Facultad de Ciencias Naturales, Universidad Autónoma de Querétaro,
Avenida de las Ciencias s/n, Juriquilla Querétaro, Qro., 76230, Mexico

E. Castaño-Tostado
Facultad de Química, Universidad Autónoma de Querétaro, Apdo. 184 Querétaro,
Qro., 76010, Mexico

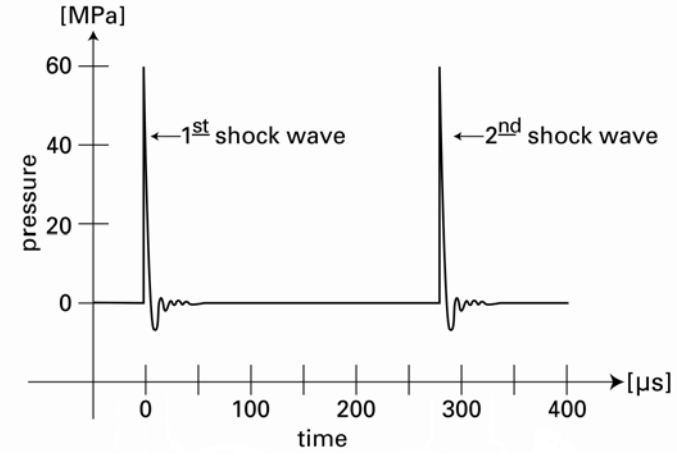

Fig. 1 Sketch of twin or tandem shock waves showing the first pressure pulse, followed 280 μs later by a second pressure pulse.

kidney stone fragmentation [7-8]. Temperature is another factor affecting cell transformation. Increased membrane permeability due to a temperature reduction has been reported [9]; however, if temperature reduction enhances microjet emission and thus contributes to cell transformation is unknown. To analyze this issue, the dynamics of a bubble immersed in water was simulated by using a well-known numerical model. The object of this study is to enhance shock wave-induced transfer of plasmids into *E. coli* using tandem shock waves and to analyze the influence of the temperature on bubble dynamics and cell transformation.

2 Materials and Methods

A Piezolith 2300 lithotripter (Richard Wolf GmbH, Knittlingen Germany) was used. The device produces shock waves by the abrupt expansion of about 3000 ceramic elements mounted on a bowl-shaped backing and excited by a high-voltage pulse. It generates a dynamic focus (volume in which the pressure equals to more than 50% of the maximum amplitude) in the shape of a cigar measuring about 17 x 3 mm. Water is used as a coupling media (Fig. 2). To produce twin shock waves, the discharge circuit, consisting of a capacitor charging system and a trigger unit was duplicated. A pulse generator triggers both systems with an adjustable delay between 50 and 950 μs [7]. Under a potential difference of 7.5 kV, the pressure profile at the focus F consists of a compression pulse with a pressure amplitude of about 38 MPa, and a decompression pulse with a tensile peak of 18 MPa. Single and tandem shock waves were generated at a frequency of 0.5 Hz. A special holder was designed to center the vial at F.

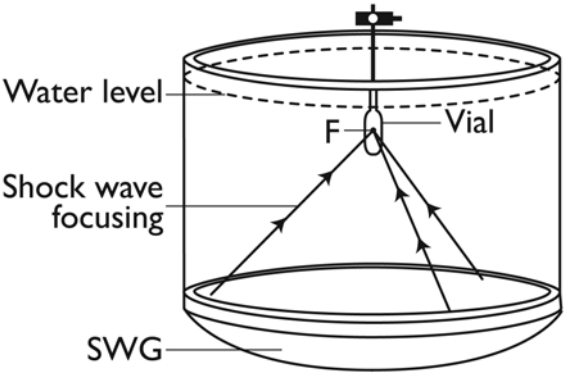

Fig. 2 Sketch of the piezoelectric shock wave generator (SWG) used to perform shock wave assisted bacteria transformation.

500 μl of *Escherichia coli* (*E. coli*) Top10 were inoculated in 20 ml broth. The culture was incubated until the suspension reached an optical density of about 0.45 OD_{600}, then the suspension was cooled and aliquots were centrifuged at 4 ^{o}C. The pellet was harvested in 1 ml of 100 mM $CaCl_2$ and cooled. The cells were centrifuged again at 4 ^{o}C and resuspended in 200 μl of 100 mM $CaCl_2$. 200 μl of competent cells and 1 ng/ml of plasmid were transferred to 4-ml polyethylene pipettes and heat-sealed [10]. A plasmid, which provided both ampicillin resistance and green fluorescent protein (GFP) expression, was used. Transformants were selected on plates containing ampicillin. Colonies with GFP expression were counted in an UV transilluminator. After shock wave treatment all cells were plated on broth with ampicillin and incubated. The transformation efficiency (TE), defined as the number of colony forming units (CFU) per μg of plasmid, was compared with the $CaCl_2$ method of transformation (control vials). A random two-factorial design was used. The varied factors were the delay and the temperature as follows: 45 vials containing bacterial suspension were divided into three temperature groups (0, 10 and 25 ^{o}C). In each group, three vials were exposed to 1000 single-pulse shock waves, and three vials to 500 tandem waves produced at delays of 250, 500 and 750 μs. Three sham vials were included per group. Analysis of variance, followed by a Tukey multiple comparison test was performed. The dynamics of a single spherical air bubble in water exposed to a shock wave was modeled by the Gilmore-Akulichev formulation [12] at 0 and 20 ^{o}C. The analytical description defined by Church (1989) was used for the single pressure pulse: $P_C(t) = 2P^+ \exp[-\alpha t][\cos(\omega t + \pi/3)]$, where P^+ is the peak positive pressure (101 MPa), $\alpha = 9.1 \times 10^5$ s^{-1} is the decay constant and

$\omega = 2\pi \times 83.3$ kHz is the angular frequency. The largest modulus of the negative pressure P^- is 16.4 MPa. The rise time t_r was chosen equal zero for simplicity, the duration of the positive pulse t^+ and the time t between the positive and the negative peak were fixed to be 0.338 μs and 1.998 μs, respectively.

3 Results

Each test vial contained $(7 \pm 1.9) \times 10^8$ bacteria. After 500 tandem shock waves $(1 \pm 0.9) \times 10^8$ viable bacteria were recovered. This number did not change significantly after exposure to tandem shock waves at the chosen delays. A significant interaction ($p < .0001$) between delay and temperature was observed. The only transformation efficiency that was different ($\alpha = .05$) from all other groups was the one obtained at 0 ^{o}C and a delay of 750 μs as shown in Fig. 3.

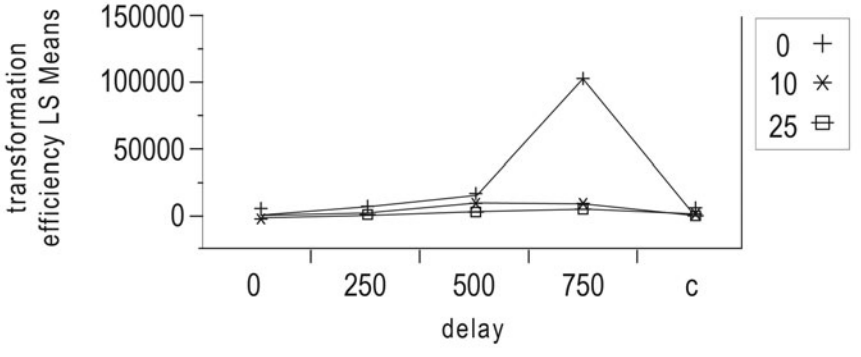

Fig. 3 Transformation efficiency in $CFU/\mu g$ of DNA vs shock wave mode at 0, 10 and 25 ^{o}C. (0 = single pulse shock waves; 250, 500 and 750 refers to the delay of tandem shock waves, c = control group)

As shown in Fig. 4, the radius of the bubble varies by several orders of magnitude in response to the shock wave in water at 20 ^{o}C. As the positive pulse reaches the bubble, it suffers a forced compression. Once the shock wave has passed, the bubble grows until its radius reaches a maximum after about 130 μs. The second minimum occurs 291 μs after arrival of the shock wave. Finally, the bubble keeps ringing for several hundred microseconds (not shown). The dynamics of the bubble at 0 ^{o}C is not shown because no difference can be observed at this scale. The difference between the graphs at both temperatures is plotted in Fig. 5. It is clear that the shift in time produced by reducing the temperature from 20 to 0 ^{o}C is extremely short. The bubble radius at the second collapse did not vary significantly due to the temperature reduction.

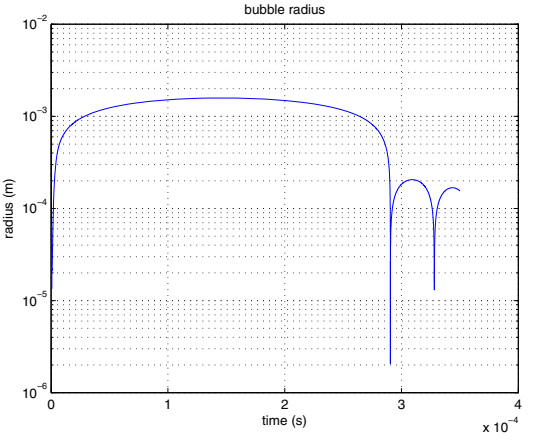

Fig. 4 Computer-simulated response of an air bubble in water to a single shock wave at 20 ^{o}C. The base 10 logarithm of the bubble radius normalized by the initial bubble radius R0 = 0.07 mm was plotted as a function of time.

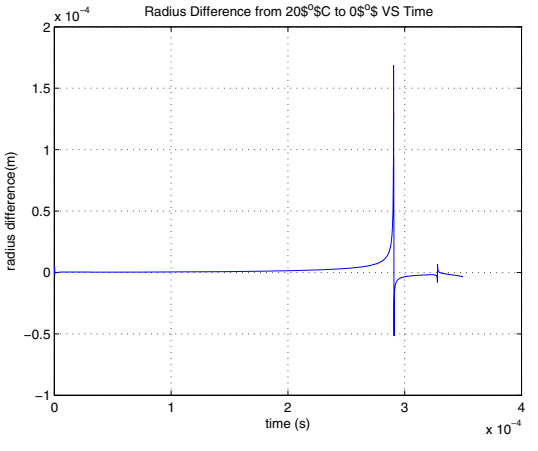

Fig. 5 Difference between the graph shown in Fig. 4 and the response of the same air bubble at 0 ^{o}C.

4 Discussion and Conclusions

Low temperature bacteria transformation by tandem shock waves may open up new opportunities for gene delivery into bacteria. Our results demonstrate that cavitation is responsible for cell transformation, because the TE increased as bubble collapse was enhanced. With the new methodology gene transfer to *E. coli* raised up to 50 times compared to the standard $CaCl_2$ method of transformation. The radius (R2) of the bubble at the second collapse gives a good measure of the capability of the

pressure field to increase collapse energy and consequently of microjet emission. Smaller R2 values indicate that the pressure field produced a stronger second collapse. Further oscillations only occur if the bubble maintains its spherical symmetry. Due to the small difference in R2 when running the simulation at 20 and 0 ^{o}C, we conclude that temperature reduction has a negligible effect on microjet enhanced TE. Further research will require determination of the influence of shock wave amplitude, pulse length, and the number of pulses on TE.

References

1. Chen, I., Christie, P.J., Dubnau, D.: The ins and outs of DNA transfer in bacteria. Science 310(5753), 1456–1460 (2005)
2. Newman, C.M.H., Bettinger, T.: Gene therapy progress and prospects: Ultrasound for gene transfer. Gene Ther. 14, 465–475 (2007)
3. Lauer, U., Bürgelt, E., Squire, Z., Messmer, K., Hofschneider, P.H., Gregor, M., Delius, M.: Shock wave permeabilization as a new gene transfer method. Gene Ther. 4, 710–715 (1997)
4. Jagadeesh, G., Nataraja, K.N., Udayakumar, M.: Shock waves can enhance bacterial transformation with plasmid DNA. Curr. Sci. India 87(6), 734–735 (2004)
5. Armenta, E., Varela, A., Martínez de la Escalera, G., Loske, A.M.: Transfección de células por medio de ondas de choque. Rev. Mex. Fis. 52(4), 352–358 (2006)
6. Ohl, C.D., Ikink, R.: Shock-wave-induced jetting of micron-size bubble. Phys. Rev. Lett. 90(21), 214502–214505 (2003)
7. Loske, A.M., Prieto, F.E., Fernández, F., van Cauwelaert: Tandem shock wave cavitation enhancement for extracorporeal lithotripsy. J. Phys. Med. Biol. 47(22), 3945–3957 (2002)
8. Fernández, F., Fernández, G., Loske, A.M.: Treatment time reduction using tandem shockwaves for lithotripsy: an in vivo study. J. Endourol. 23(8), 1247–1253 (2009)
9. Hanahan, D.: Studies on transformation of *Escherichia coli* with plasmids. J. Molecular Biol. 166(4), 557–580 (1983)
10. Chung, C.T., Niemela, S.L., Miller, R.H.: One-step preparation of competent *Escherichia coli*: Transformation and storage of bacterial cells in the same solution. P. Natl. Acad. Sci. USA 86, 2172–2175 (1989)
11. Church, C.C.: A theoretical study of cavitation generated by an extracorporeal shock wave lithotripter. J. Acoust. Soc. Am. 86, 215–227 (1989)

Light Syringes Based on the Laser Induced Shock Wave

T. Han, J. Hah, S. Kim, and Jack J. Yoh

1 Introduction

Drug Needle injectors have been the common means by which vaccines and protein therapeutics are transdermally delivered. However, the use of needle injectors have elicited painful reactions, and have also caused infection due to repeated use of needles particularly in under-developed countries [1]. Because of these disadvantages, researchers have endeavored to developing alternative methods for drug delivery. New methods incorporating liquid jet injections have been developed [2]; however, liquid jet has not succeeded in replacing needle based injectors yet. Despite the fact that jet injection can alleviate patients aversion to needles, it has not gained much popularity for the following reasons: i) it is still reported to be painful, ii) it is not stabilized in control, and iii) the risk of cross-contamination due to back splash is still prevalent [3, 4]. Therefore, in order to release the stronghold that needle injection has on the drug delivery domain, methods such as jet injection must make a major breakthrough.

Recently, investigations have been conducted on a method involving biological ballistic drug delivery, which uses a laser pulse that mechanically accelerates drug particles fast enough to penetrate soft human tissue. In our previous paper, we presented a bio-ballistic microparticle accelerator in which laser pulse energy is converted into the kinetic energy of micro drug particles [5]. As an extension of the development of a biological ballistic device for drug delivery, we have investigated a liquid microjet injector using a laser pulse as its energy source [6]. Microjet injection has been considered an alternative to the current state of jet injection for minimizing the jet diameter and injection volume, and the precise control of the penetration depth. A conventional drug jet may possess a volume in the range of 30 to 100 microliters, while the proposed microjet maintains a volume of a few

T. Han · J. Hah · S. Kim · Jack J. Yoh
School of Mechanical and Aerospace Engineering,
Seoul National University Seoul, Korea, 151-742
e-mail: jjyoh@snu.ac.kr

hundreds of microliter, preventing back splash of interstitial liquid and delivering the same amount of drug by concentration change or multiple injections. This back splash is mainly caused by a large injected jet volume and is responsible for cross-contamination. Furthermore, the small amount of liquid transdermally injected with a microjet enables precise targeting of the epidermis above the pain sensory, effectively avoiding nerves that spread under the epidermis. The deposited drug materials instantaneously diffuse into the target spot. In other words, the precise accumulation of micro drug jets at the epidermis (200 - 400 μm) will facilitate a painless and efficient transdermal drug delivery [6]. Additionally, multiple shots would allow a practitioner to locate a drug on the target tissue without pain and subsequently deliver the remaining dose at that target location. Our previous device demonstrated fast micro liquid jet injection for drug delivery [7]. Difficulties encountered during the initial investigations involved the damaging of the chamber seal and the melting of the elastic membrane, both of which were caused by the high pulse energy. However, our second generation injector successfully overcame these difficulties. The improved chamber design and the elastic silicon membrane endure the high pulse energy input without causing the elastic membrane to melt, and completely confines the driving fluid. This study presents experimental evidence substantiating that our new injector is an efficient device for drug delivery.

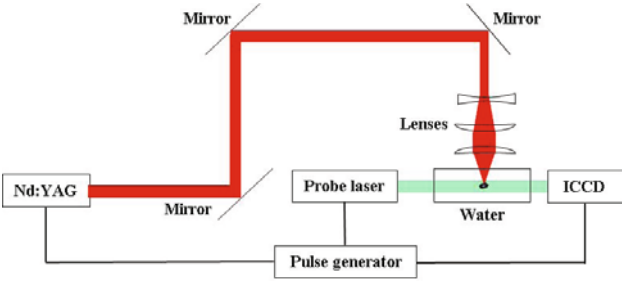

Fig. 1 The schematic of the experimental setup for generating a bubble in distilled water.

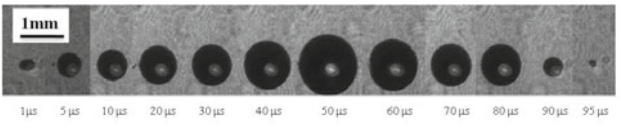

Fig. 2 The sequential images of a bubble induced by a laser pulse with 35 mJ. The bubble reached its maximum radius of about 0.5 mm at 50 μs, and it collapsed at 95 μs.

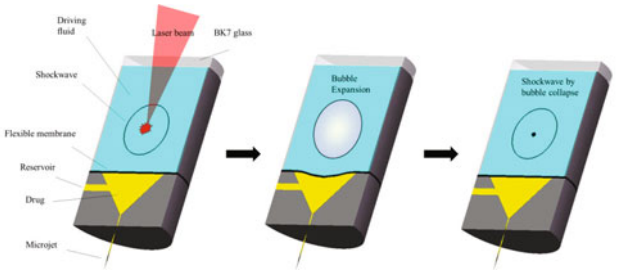

Fig. 3 Illustration of the sequential mechanisms of the laser based microjet generation.

2 Principle and Experiment

When a nanosecond laser pulse is focused in distilled water, a plasma with high temperature and pressure is created. The surrounding liquid is compressed and begins to flow radially outward. Thus, the first shock wave propagates through the liquid. Upon the breakdown of water, bubbles are generated and expanded during the isothermal expansion, followed by the secondary shock wave as the bubbles implode. As shown in Fig. 1, the Q-Switched Nd-YAG laser system (Powerlite Precision II Plus, 1064 nm wavelength) with 35 mJ and the pulse duration of 10 ns is used for the formation of a bubble, and it is focused into distilled water in the test chamber (diameter 114 mm, height 320 mm) by a set of three lenses; one bi-concave lens with by a set of three lenses; one bi-concave lens with f1 = -30 mm and D1 = 50 mm, and two planar convex lenses with f2 = f3 = 50 mm and D2 = D3 = 50 mm. The three lenses are mounted outside the chamber. The diameter of focused laser beam is around 0.25 mm. A probe laser (Minilite, 8-12 mJ/pulse, 3 ns pulse duration), which is aligned parallel to the sample target and perpendicular to the main beam, is irradiated at several nanoseconds following the main laser. The beam is forced to expand and collimate through a bi-concave lens and a planar-convex lens in order to cover the entire test section. The experiment is conducted under normal room temperature (293 K) and pressure (10^2 kPa). Figure 2 shows a sequence of growth and collapse of a laser induced bubble.

We have adopted these shockwaves and explosive bubble expansion induced by laser irradiation as power sources of creating microjets. Figure 3 illustrates the mechanism of microjets generation by this method. A laser pulse focuses on the driving fluid within a chamber through a transparent confining material. The pulse then induces various energy releasing processes. Firstly, a laser ablation induced shockwave propagates toward the nozzle exit, driving the liquid drug inside of the nozzle to flow out in the form of a microjet. Secondly, an explosive growth of bubbles caused by an optical breakdown in the driving fluid produces a considerable volume change within the chamber, thus deforming the thin elastic membrane. The elastic membrane acts as a piston and pushes the drug contents inside the nozzle to flow out again while it minimizes drug damage by heat transfer from the focal spot,

due to its low heat conductivity. Afterwards, the propagation of the second shock-wave, which is induced by a collapse of the bubbles, generates another microjet.

In the experiment, the irradiance of the 1064 nm beam was directed to concentrate on the center of the cylindrical chamber (Stainless steel, 10 mm of diameter, and 10 mm of height) through the same optical setup as above. We used a BK7 glass (5 mm of thickness) as the confining transparent material. The nozzle was fabricated from tungsten carbide with 15 mm of outer diameter, 5 mm of inner diameter, 39 ° of inner taper angle, 4 mm of height, and 0.98 mm of exit hole. The small nozzle diameter facilitated an effect in which the surface tension and the interactive force between the liquid and the nozzle surface material trapped the liquid inside the nozzle when there was no external pressure. In addition, the nozzle was connected to a reservoir that fed the liquid drug to the system and recharged the nozzle after each shot. After an injection was completed, the elongated elastic membrane, which was fabricated from a silicon rubber (0.2 mm of thickness, 1.15 of specific gravity, 50 of hardness shore, 93 kgf/cm^2 of tensile strength, 489 % of elongation, and 30 kgf/cm tear strength), recovered its original planar shape as the bubbles collapsed.

In order to visualize evolution of microjet, we took time-resolved images of microjet generation and evolution of water using a high speed camera (Ultima APX-RS, maximum 250,000 fps) as shown in figure 3. We filled 5 % weight ratio of salt-water solution in the chamber, because a number of ions could help to enhance the efficiency of plasma production. Distilled water was filled in the nozzle.

To prove its practicality as a drug delivery device, we prepared a gelatin-water solution with 5 % weight ratio as the target replicating a soft biological tissue, and penetrated it with 0.1 % HA(Hyaluronic acid dermal) filler solution which is typically used for wrinkle therapy.; The gelatin-water solution was chosen because it possesses a similar Youngs modulus as tissue [8, 9], and the HA filler solution has a 1 - 10 times higher viscosity than pure water. Also, commercially available fatty pork tissue was taken as the target where we injected water-based black ink at room temperature. After the injections were made, the treated pork fat was frozen at -20 °C for 30 minutes and sliced for cross-sectional observation.

3 Results and Discussion

Figure 4 shows evolution of microjet driven by 314 mJ of a laser pulse energy. From the pictures of the early stage (40 μs), we could investigate a slow microjet (25 m/s) forming from the nozzle exit. Before its leading edge reaches 1 mm from the nozzle end, the very fast second microjet, of which averaged velocity before it broke up was about 230 m/s, overlapped the first one (80 μs). The first slow microjet was caused by the propagation of the first shock wave due to the optical breakdown of water in the chamber, but it was soon overtaken by the second one due to rapid bubble expansion in the chamber. After about 200 μs when the second microjet appeared, the third microjet started to emerge from the nozzle end. Its velocity was about 25 m/s, which was similar value to that of the first one, so we deduce that it was driven by the second shock wave due to the bubble collapse. Afterwards,

it took about 1.8 ms that the system was stabilized as such the system was ready to send another pulse. Figure 5 shows the deposited water-based black ink inside the pork fat using pulse energy of 3 J. The diameter of the penetrated hole was measured to be about 150 μm, and the penetrated depth and width were about 100 μm and 750 μm, respectively. The penetration depth was over the objective range of the epidermis at 200 - 400 μm; and, the penetration width was satisfactorily narrow, within 100 μm. These are promising results substantiating our claim that the microjet injector can be used as a successful drug delivery system, regardless of the differences existing between the target pork tissue and living tissue. Figure 6 shows two deposited 0.1 % HA filler solution inside a 3 % weight ratio of gelatin-water solution. The penetration depth and width were about 600 μm and 0.5 μm, respectively.

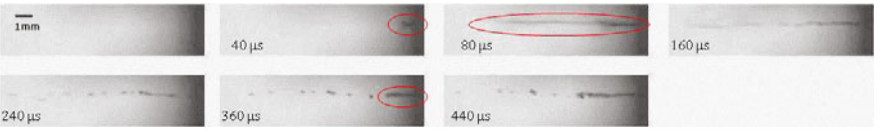

Fig. 4 The images of microjet creation with a 314 mJ of infrared laser pulse. Numbers on the left indicates the time elapsed after the first image. The black region on the right is the nozzle surface, and microjets are emerged from the nozzle exit at the center.

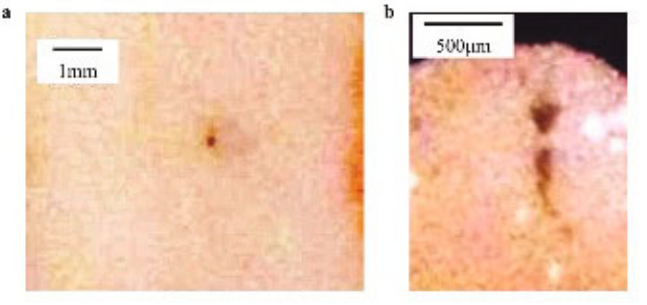

Fig. 5 Penetrated pork fat. Water-based black ink was injected into the pork fat tissue with 3 J of pulse energy. a, top view of the penetrated target; the hole diameter was about 150 μm. b, cross sectional view of the target; the penetrated depth and width were about 100 μm and 750 μm, respectively.

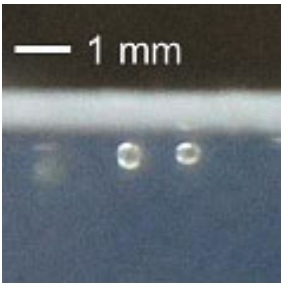

Fig. 6 Two deposited 0.1 % HA filler solution inside a 3 % weight ratio of gelatin-water solution.

4 Conclusion

High energy of nanosecond infrared laser beam generates shock waves and explosively expanding bubbles inside the chamber. The resulting pressure distribution induces three microjets. Among them, the second microjet due to the bubble growth is faster and much elongated than others, such that majority of penetration and drug delivery is done through this jet. This strong jet has also helped the following one to be delivered with ease by forming a pre-drilled hole for easier delivery of drugs. A new and improved microjet drug delivery scheme has been verified through visualization of the microjet generation with a high-speed camera, deposition of distilled water into pork fat tissue, and deposition of HA filler solution into a 3 % gelatin-water target. The experimental results show good agreement with the claim on the mechanism of microjet generation. On-going integrating effort is aimed at minimizing the laser energy while maintaining precise depth control of the drug dose into the dermal layer.

Acknowledgements. This work has been supported by the Korean National Research Foundation (KOSEF-2009-0076557, KOSEF-2009-0059432, NRF-0498-20100023) through IAAT at Seoul National University.

References

1. Nir, Y., Paz, A., Potasman, I.: Fear of injections in young adults: prevalence and associations. Am. J. Trop. Med. Hyg. 68(3), 341–344 (2003)
2. Mitragotri, S.: Current status and future potential of transdermal drug delivery. Nat. Rev. Drug Discov. 3, 115–124 (2004)
3. Theintz, G.E., Sizonenko, P.C.: Risks of jet injection of insulin in children. Eur. J. Pediatr. 150(8), 554–556 (1991)
4. Hoffman, P.N., Abuknesha, R.A., Andrews, N.J., Samuel, D., Lloyd, J.S.: A model to assess the infection potential of jet injectors used in mass immunization. Vaccine 19(28), 4020–4027 (2001)

5. Han, T., Gojani, A.B., Yoh, J.J.: Biolistic injection of micro particles with high power Nd:YAG laser. Appl. Opt. 49(16), 3035–3041 (2010)
6. Han, T., Yoh, J.J.: A laser based reusable microjet injector for transdermal drug delivery. J. Applied Physics 107, 103–110 (2010)
7. Stachowiak, J.C., Li, T.H., Arora, A., Mitragotri, S., Fletcher, D.A.: Dynamic control of needle-free jet injection. J. of Cont. Release 135(2), 104–112 (2009)
8. Shangguan, H., Casperson, L.W., Shearin, A., Gregory, K.W., Prahl, S.A.: Drug delivery with microsecond laser pulses into gelatin. Appl. Opt. 35(19), 3347–3357 (1996)
9. Rosenschein, U., Frimerman, A., Laniado, S., Miller, H.I.: Study of the mechanism of ultrasound angioplasty from human thrombi and bovine aorta. Am. J. Cardiol. 74(12), 1263–1266 (1994)

Shock Wave Generation through Constructive Wave Amplification

S. Dion, L.-P. Riel, and M. Brouillette

1 Introduction

As new biomedical and industrial applications of shock waves emerge, the need to accurately and economically generate shocks is becoming more critical. Since a very large potential resides in biology and medicine areas for diagnostic and therapeutic uses, shock waves need to be efficiently produced in cells, tissues and organs. In the past, there have been a number of methods used to produce shock waves in liquids, all characterized by a large and rapid energy deposition, either through the detonation of an explosive, the irradiation of a target with a pulse of laser energy, the dumping of electricity through a spark gap, or the sudden acceleration of a piston, either by electromagnetic or piezoelectric means. There are well known shortcomings associated with each of these methods, such as the requirement for high-voltage electronics, the manipulation of explosives and/or the lack of control over the shock properties [1]. This paper presents a new method to generate high-amplitude pressure pulses in liquids exploiting the advantages of low amplitude piezoelectric generators.

We developed an innovative acoustic pulse amplifier that allows for the controlled generation of high pressure shock waves from the constructive interference of a large number of low amplitude acoustic waves [2]. The main advantage of this method, compared to other means of generating high amplitude shocks in liquids, is that it does not requires high voltage equipment, thus considerably reducing cost and electromagnetic noise issues. Also, such a device allows for tailoring the shape of the shock wave through software control, which is not possible with discharge-type devices. Finally, it can easily be scaled depending on the application.

S. Dion · L.-P. Riel · M. Brouillette
Department of Mechanical Engineering,
Université de Sherbrooke, Sherbrooke, Canada J1K 2R1

2 Principle

Here we exploit the fact that, contrary to wave propagation in a fluid, waves in a solid do not all propagate at the same velocity. Indeed, different modes of propagation are possible, and they propagate at different velocities which depend on their frequency. This phenomenon is generally known as wave dispersion.

This can be studied by considering the equation of motion for the 2-D displacement, as a function of axial and radial position and time, of material elements for a long rod of diameter $d = 2a$ having an elastic modulus E and a density ρ. When the wavelength λ of the signal is greater than the rod diameter, wave propagation remains non-dispersive and all waves propagate either at the longitudinal wave velocity c_0, the shear wave velocity c_S or the Rayleigh surface wave velocity c_R depending on the mode of propagation [3].

When the wavelength becomes comparable or smaller than the rod diameter, dispersion takes place and the velocity of propagation of a given wave depends on its wavelength and mode. Pochhammer (1876) and Chree (1889) have solved the wave equation in cylindrical coordinates assuming a free surface boundary condition, to yield the dispersion relation for the wave velocity as a function of wavelength (or frequency). For longitudinal propagation modes this relation is given by [4]:

$$\frac{2p}{a}(q^2+k^2)J_1(pa)J_1(qa)-(q^2-k^2)J_0(pa)J_1(qa)-4k^2pqJ_1(pa)J_0(qa)=0 \quad (1)$$

with $p^2=(\omega^2/c_L^2)-k^2$, $q^2=(\omega^2/c_S^2)-k^2$, J_0 and J_1 Bessel functions and $k=2\pi/\lambda$ the wavenumber. This equation can then be solved numerically to yield dispersion curves, as shown in Figure 1 for the first three longitudinal modes of a material with a Poisson ratio of 0.29.

It can be seen from Figure 1 that, for long wavelengths, only the first mode is possible and it propagates at the wave velocity c_0, in accordance with the one-dimensional wave equation in an elastic solid. Around a diameter-to-wavelength ratios around 0.8, the velocity of the first mode decreases by almost half. Above a certain critical wavelength, other modes of propagation are possible and these are dispersive as well. For example, for diameter-to-wavelength ratios around 2, three modes of propagation are possible, with the second and third modes highly dispersive.

Therefore, to produce a single short amplitude high pressure pulse at the exit of a solid waveguide, we generate many low amplitude pulses at the entrance of the same waveguide such that, as these waves propagate at different velocities, they reach the exit simultaneously, leading to constructive amplification. The required input signal can be theoretically or experimentally determined from the dispersion characteristics of the waveguide, which depend on its diameter, length and composition.

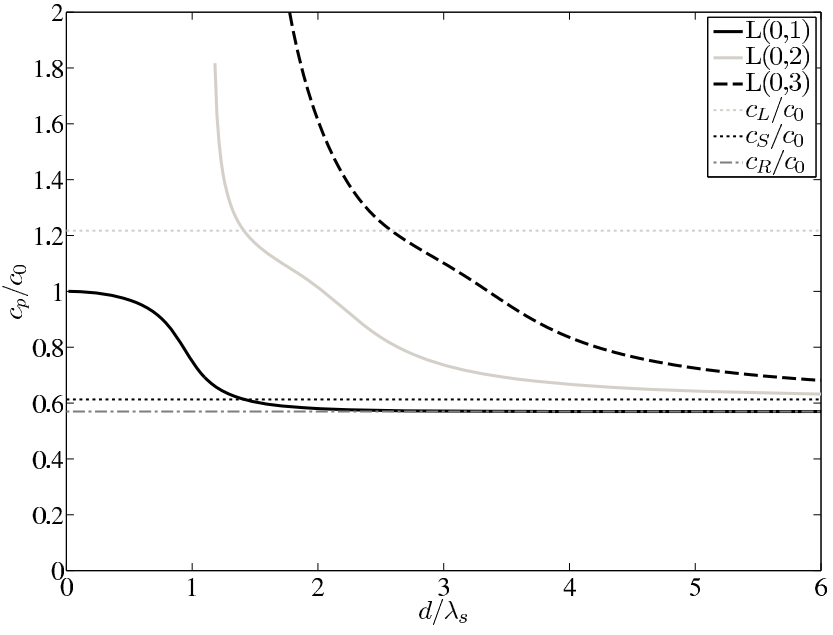

Fig. 1 Normalized dispersion curves expressed as a function of phase velocity $c_p = \omega/k$ for the first three longitudinal modes L(0, 1), L(0, 2) et L(0, 3) in a solid elastic waveguide with a Poisson ratio of 0.29. c_L is the longitudinal wave propagation velocity, c_S the shear wave propagation velocity and c_R the Rayleigh wave propagation velocity; $c_0 = \sqrt{E/\rho}$ and λ_s is the wavelength based on the shear velocity c_S.

3 Experimental Validation

The generator concept comprises a long solid cylindrical waveguide with a piezoelectric pressure generator attached at the input end. The output end is in contact with water, our target medium. From the dispersion curves seen above it is observed that the first longitudinal mode is most dispersive at a diameter-to-wavelength ratio around 0.8, while higher longitudinal modes are dispersive at smaller wavelengths. The first longitudinal mode is also the easiest and most accurate to excite with a cylindrical piezoelectric transducer. Also, diffraction takes place at the exit end of the waveguide in the target medium, which can be exploited to focus a nominally plane wave; this also depends on the diameter-to-wavelength ratio. Furthermore, the signal wavelength directly determines the shock formation distance into the target medium. As well, a longer waveguide produces a greater temporal spread of the signal between fast and slow waves, potentially allowing for more amplification. However, this has to be balanced against higher intrinsic attenuation of the signal as the waveguide length is increased. Finally, to reduce the acoustic impedance mismatch between the waveguide and medium into which we want to produce the shock wave, an acoustic coupler can be attached to the exit end of the waveguide.

These considerations guide the design of the shock wave generator. For example, consider a 2.5 cm diameter, 59 cm long aluminum waveguide, shown in Figure 2.

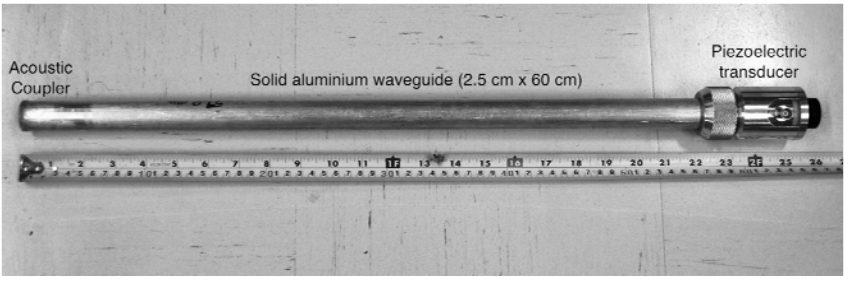

Fig. 2 Photograph of prototype generator.

To excite this, we use a gas-matrix piezoelectric transducer manufactured by The Ultran Group, which has a diameter of 2.8 cm and a central frequency of 600 kHz for the present application. This transducer can produce, by itself, pressure pulses of a maximum amplitude of about 5 bars in water with the available signal processing equipment. To match the acoustic impedance of the aluminum waveguide to the water target medium, a two-layer epoxy-glass acoustic coupler is used.

The required input signal can be obtained theoretically, numerically or experimentally by properly characterizing the dispersion characteristics of the waveguide. For example, this can be achieved experimentally using inverse filter techniques: First, the piezoelectric generator is excited using a known input signal and the output of the dispersive waveguide is measured using a calibrated pressure transducer. The input and output signals are used to compute the frequency response function (FRF) of the entire system, which can subsequently be used to calculate the required input for a given output. This input can be further treated using various signal processing methods, to improve pulse shape and/or further increase amplification.

Figure 3 shows an example of input signal used to produce a short Gaussian pressure pulse. The many input pulses it contains are spread over a 75 μs time interval and have a complex frequency and temporal signature. Figure 4 shows the output signal measured with a needle hydrophone (Precision Acoustics Ltd.) in degassed water at a distance 69 mm from the exit of the waveguide, using the input of Figure 3. Amplitudes exceeding 100 bars are produced using a piezoelectric generator which by itself can only generate 5 bars, an amplification factor of 20. It can also be seen that the signal of Figure 3 has temporally been compressed to below 1 μs duration for the main pressure peak. The two secondary pulses around the main pressure peak are characteristic of these signal processing methods and can be minimized by further input treatment. The amplitudes produced are comparable to those obtained with other current medical devices [5].

Figure 5 shows a comparison between the maximum output signal of the piezoelectric transducer by itself and that of the generator prototype at its output end, both

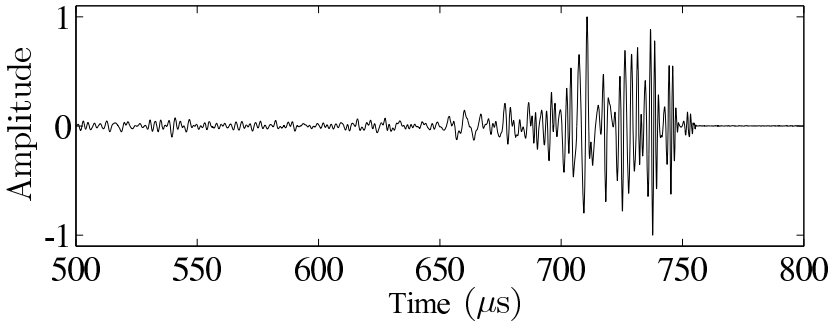

Fig. 3 Example of input wavetrain into 2.5 cm diameter, 59 cm long aluminum waveguide.

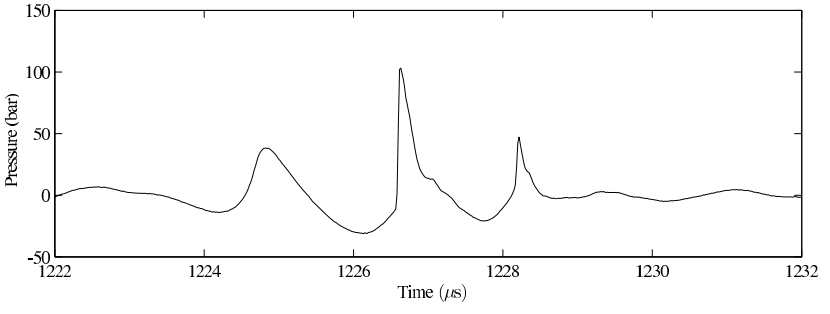

Fig. 4 Example of waveguide output for the wavetrain of figure 3, measured in water with a needle hydrophone 69 mm from the exit of the waveguide.

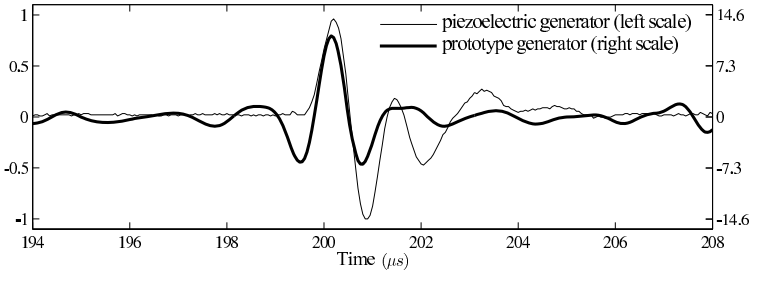

Fig. 5 Comparison between the maximum output signal of the piezoelectric transducer and the output of the generator prototype, both measured with a contact transducer. Left scale for piezoelectric generator (light line), right scale for prototype generator (dark line), same arbitrary units.

measured by a contact transducer. It is seen that the dispersive waveguide can produce similar pulse shapes and durations as compared to the piezoelectric generator alone, but with an amplification factor of around 15 afforded by the careful exploitation of the dispersion characteristics of the solid waveguide. Steepening of the pressure pulse in the water target medium due to non-linear effects further increases the pulse amplitude and shorten pulse duration, leading to an overall amplification factor of 20, as shown in Figure 4.

4 Conclusions

We have devised a new method to generate high-amplitude short-duration shock waves in liquids which profits from the constructive interference of a large number of low amplitude pressure pulses in a solid dispersive waveguide. This method was validated experimentally and amplification ratios of around 20 using a 2.5 cm aluminum waveguide were demonstrated. This principle can be applied to other configuration as well, for example using a smaller diameter waveguide where space limitations are important or a combination of multiple waveguides when high-amplitude three-dimensional pulses are required. By using different input signals and processing routines, a wide array of generated pressure pulses are also feasible. Absolute control over the features of the pressure pulse is thus possible with this new method, which opens the door to real-time modification of the shock wave features as required by each particular application.

References

1. Dion, S., Hebert, C., Brouillette, M.: Comparison of methods for generating shock waves in liquids. In: Hannemann, K., Seiler, F. (eds.) Shock Waves, pp. 851–856. Springer, Heidelberg (2009)
2. Brouillette, M., Dion, S., Riel, L.-P.: Mechanical wave generator and method thereof, U.S. Provisional Patent Application No. 61/377,519 (August 27, 2010)
3. Puckett, A.D., Peterson, M.: A semi-analytical model for predicting multiple propagating axially symmetric modes in cylindrical waveguides. Ultrasonics 43, 197–207 (2005)
4. Kolsky, H.: Stress waves in solids. Dover (1963)
5. Buizza, A., dell'Aquila, T., Giribona, P., Spagno, C.: The performance of different pressure pulse generators for extracorporeal lithotripsy: A comparison based on commercial lithotripters for kidney stones. Ultrasound in Medicine & Biology 21, 259–272 (1995)

Applications of Underwater Shock Wave Research to Therapeutic Device Developments

Kazuyoshi Takayama

Invited Presentation

Shock wave applications to medicine conducted in the Interdisciplinary Shock Wave Laboratory of the Institute of Fluid Science, Tohoku University were based on accumulation of underwater shock wave research and bubble dynamic study, and initiated with the development of micro-explosion assisted Extracorporeal Shock Wave Lithotripsy (ESWL). The Ministry of Health Japan approved in 1987 our ESWL system as clinical device. The result was then continued to therapeutic devices in orthopedic surgery, gastro surgery, neurosurgery, drug delivery and recently cardio vascular treatments. In these projects, we have been working with colleagues in the School of Medicine, Tohoku University, and always target to develop therapeutic devices as a fruit of our shock wave dynamics and bubble dynamic studies. Our methodology is primarily based on the control and use of shock waves and high-speed flows generated. We at first worked with micro-electric discharges in water and soon found difficulties in controlling electrical noises. Then we adopted laser focusing and micro-explosions intensively backed up with flow visualization methods and numerical simulations. We learned to optimize the characteristics of underwater shock waves and high-speed liquid flows and gradually directed our shock wave research to following medical applications.

0.1 Soft Tissue Dissection Device

As we understood shock/bubble interaction was a major mechanism of tissue damages occurring inevitably during ESWL treatments, we started to apply micro-jets developed to penetrate soft tissues in a controlled fashion. The first target was to

Kazuyoshi Takayama
Interdisciplinary Shock Wave Research Laboratory of the Institute of Fluid Science,
Tohoku University

the revascularization cerebral thrombosis. Then we developed a laser induced liquid jet (LILJ) device, in which pulsed Ho:YAG laser beams were intermittently irradiated at 3 Hz in a Y-tube and induced relatively high-speed water jets from a flexible nozzle of 0.2 mm in diameter. We confirmed that this catheter based on this structure successfully penetrated mechanically cerebral thrombosis in vivo tests. We then converted it to dissect soft tissue and now successfully remove brain glioma minimizing blood vessel damages. We then developed an actuator driven water jet generator, which had 0.1 mm nozzle diameter and operated at 1 kHz is now finalized for its clinical tests.

0.2 Shock Interaction with Cells

To investigate temporal disorders in cells at shock wave exposures at various intensity levels, we designed a device precisely focusing shock wave onto a mouse brain by introducing a 20 mm exit diameter of a half truncated ellipsoidal reflector, whose major to minor radii ratio is 1.41 and detonating 10 mg silver azide placed at the focal point inside the reflector. Extending this result, we transmitted Q-switched Ho:YAG laser beams through 0.6 mm diameter optical fiber, generated a micro-shock wave at a focal point of a 3.6 mm diameter half truncated ellipsoidal reflector, and successfully created high pressure of well over 40 MPa at 300 ns duration, which was effective enough to damage mouse's myodium. Encourages by this result, we put the whole system in a 4 mm diameter catheter, and are developing a safe and reliable system for treating arrhythmia by shock wave focusing.

0.3 Shock Interaction with Cells

When a pulse laser beam is exposed onto a metal foil, its surface is ablated driving a shock wave inside it. Reflected shock waves from the other side of the foil instantaneously bulge the metal foil. Such a sudden acceleration of metal foil surface can project solid particles at high speed. We used this mechanism to deliver drug particles into living tissue, drug delivery system (DDS). We developed laser ablation assisted DDS, which would be comparable one to the DuPont's Biolistic devices and also the Powderject.

High Repetitive Pulsed Streamer Discharges in Water, Their Induced Shock Waves and Medical Applications

S.H.R. Hosseini and H. Akiyama

Invited Presentation

Medical, industrial, and environmental applications of pulsed power technology have been developing rapidly in many fields including bioelectrics for cancer treatment and induction of apoptosis; treatment of exhaust gases; sterilization of microorganism; removal of biological wastes; fragmentation of rocks; recycling of concrete and electrical appliances; and surface treatments of material[1]. The application of electric fields with a short pulse width allows direct interaction with biological cells substructure without heating the tissue[2], which suggests interesting comparison and/or combination with shock waves for medical applications. The breakdown phenomena in liquids have been studied for a long time, in particular for its relation to electrical insulation. Large volume streamer discharges can be produced in liquids using the recent development in pulsed power technology. The characteristics and the propagation mechanism of streamer discharges in liquids are different from those of gas discharges, which remain to be clarified. The streamer discharges in liquids are accompanied by several physical events such as the generation of extremely intense electric fields, high energy electrons, ultraviolet rays, chemically active species, and shock waves. To better understand streamer generation and propagation, individual investigation of each of these events are of high interest. A few studies of ultraviolet radiation and the generation of free radical species have been reported. The paper reports quantitative studies performed to investigate the shock waves induced by underwater streamer discharge. Underwater shock waves were generated by nanosecond pulse electric discharges. Magnetic pulse compression circuits were used as energy source. Input voltage and current were measured by using an oscilloscope, a high voltage probe, and a current monitor. The water was degassed to reduce losses of shock wave propagation and to prevent cavitation.

S.H.R. Hosseini · H. Akiyama
Bioelectrics Research Center
New Frontier Sciences, Graduate School of Science and Technology,
Kumamoto University, Kumamoto 860-8555, Japan

Generated spherical underwater shock waves were reflected from generators to produce shock wave focusing or uniform shock waves. The whole sequences of the shock wave generation, propagation, and focusing were observed by time-resolved high speed shadowgraph visualization method[3]. Pressure histories were measured at different stand-off distances by using a fiber optic probe hydrophone and PVDF needle hydrophones pressure transducers. A wide range of pressure values from 5 to 200 MPa with variety of energy flux density at the exit of the generators was obtained. The pressure of shock waves were increased with the applied pulse voltage and its variation was clarified. The characteristics of compact shock wave generators for application in precise and sensitive medical procedures were determined. The shock waves exposure effects on the embryonic development of the medaka (Oryzias latipes) are compared with the application of 50 to 300 nanosecond pulsed electric field. The goal of the current study was to find and compare the effects of short nanosecond pulsed electric field and shock waves in-vivo during embryo development for controlling the embryonic cell differentiation and proliferation with application in regenerative medicine.

References

1. Akiyama, H.: IEEE Trans. Dielectr. Electr. Insul. 7 (2000)
2. Schoenbach, K.H., Beebe, S.J., Buescher, E.S.: Intracellular effect of ultrashort electrical pulses. Bioelectromagnetics 22 (2001)
3. Hosseini, S.H.R., Menezes, V., Moosavi-Nejad, S., Ohki, T., Nakagawa, A., Tominaga, T., Takayama, K.: Minim. Invasive Ther. 15 (2006)

Development of Medical and Biological Applications by Shock Waves and Bubbles

M. Tamagawa and N. Ishimatsu

1 Invited Presentation

In this presentation, development of medical and biological applications by shock waves and bubbles, especially drug delivery systems, regenerative therapy (angiogenesis) and water treatment, is explained. We have developed the drug delivery systems using shock waves from fundamental investigations. In this system, microcapsules including gas bubbles are flown in the blood vessel, and broken by shock induced microjet, and then drug is reached to the affected part in the body. For developing the microcapsules including gas bubbles, the penetration force of microjet should be controlled by shock wave, rise time of pressure history, and capsule geometry and material properties. To optimise the design of the microcapsules, the fundamental results about these parameters were obtained. Many prototypes of microcapsule (30-50 μm) including gas bubbles by polymer were made, and the relations between the probability of disintegration of membrane and the parameters (gas/liquid ratio, membrane thickness, kind of gas) were obtained. It is concluded that the deformation process of a bubble in a microcapsule has specific patterns with changing the parameters. As for the regenerative therapy (angiogenesis) by shock wave, effects of plane shock waves on endothelial cells have been investigated. In the experiments, the plane shock waves using diaphragmless shock tube apparatus are applied to the endothelial cells. The initial growth rate of the shock-worked cells was higher than that of non worked ones, and the effects of rise time on it were obtained. In the computations, the effects of rise time on the pressure and stress distribution in the cells, fluid and structure were analyzed by FEM. These preliminary results are applied to fundamental investigations about shock wave stimulus on stem cells and iPs cells. In other approach, we applied the interaction between shock waves and bubbles to water treatment process. In this system, the cavitation bubbles are generated in the special nozzle pipe, and they are broken by shock wave

M. Tamagawa · N. Ishimatsu
Graduate School of Life Science and Systems Engineering,
Kyushu Institute of Technology, Japan

with discharge. By optimizing the parameters such as bubble diameter, number of bubbles and distance from generation of shock waves, the efficiency of the water treatment was increased. In conclusion, key points to apply shock wave technology to other advanced research field are explained by using above examples.

Focused Tandem Shock Waves in Water and Their Potential Application in Cancer Treatment

P. Lukes, P. Sunka, P. Hoffer, V. Stelmashuk, J. Benes, P. Pouckova, M. Zadinova, J. Zeman, L. Dibdiak, H. Kolarova, K. Tomankova, and S. Binder

1 Introduction

Extracorporeal shock wave lithotripsy (ESWL) has been successful for more than 30 years in non-invasive treating patients with stone deceases (mostly kidney stones). ESWL devices (lithotripters) generate shock waves outside the patient's body and concentrate them on the kidney stone. Over 40 models of lithotripter (electrohydraulic, piezoelectric and electromagnetic) are commercially available worldwide [1],[2]. At the end of 1980's one of modified versions of electrohydraulic type of lithotriptor was developed also in the Institute of Plasma Physics AS CR [3]-[5]. Such generators serve up to now as a therapeutic unit in the lithotripters Medilit (produced by the company MEDIPO, Brno, Czech Republic) at about 20 hospitals in the Czech and Slovak Republic [6]. So far more than 120 thousands patients have been successfully treated by these devices.

The great success of the ESWL stimulated research on applications of focused shock waves in other branches of medicine. Most attention has been paid to the role of cavitation in ESWL induced biological effects on soft tissues and possible treatment of some types of cancers. It was initially studied to identify possible side effects of the lithotripsy therapy on kidney wall [1]. There is evidence that collapsing cavitations create strong secondary shock waves of nanosecond duration (tens of micrometers scale) that can interact with cell scale structures [2]. New lithotripters and protocols are being designed to modify the cavitation field and to control

P. Lukes · P. Sunka · P. Hoffer · V. Stelmashuk
Institute of Plasma Physics, Academy of Sciences of the Czech Republic, Za Slovankou 3, Prague 8, 182 00, Czech Republic

J. Benes · P. Pouckova · M. Zadinova · J. Zeman · L. Dibdiak
First Faculty of Medicine, Charles University, Katerinska 32, Prague 2, 121 08, Czech Republic

H. Kolarova · K. Tomankova · S. Binder
Faculty of Medicine and Dentistry, Palacky University, Hnevotinska 3, Olomouc, 775 15, Czech Republic

cavitation in an attempt to accelerate stone comminution or enhance tissue damage [7]-[12]. A promising approach to control bubble growth and collapse has been the use of the so-called tandem shock waves, which intensify the collapse of cavitation bubbles by means of a second shock wave impacting before the compression produced by the first one [13]-[15]. Most of these experimental studies demonstrated a significant effect on stone comminution and/or tissue injury, attributed in large part to the modified cavitation field. However, the optimal shock wave profile and pulse combination have yet to be established. In general, it is assumed that intensity of the secondary shock wave and the velocity of the microjet depend on the initial bubble radius. The larger the bubbles grow, the more violent their collapse is, which may be more suitable for stone or tissue damage [9].

To enhance cavitations and interaction of shock waves with soft tissues we have during recent years developed a novel type of generator of focused shock wave in water (FSW) [16]-[18]. A cylindrical pressure wave is produced by underwater multichannel electrical discharge at composite cylindrical metallic electrode covered with a thin porous ceramic layer deposited on the electrode surface by the technology of plasma spraying. The primary pressure wave is focused by a metallic parabolic reflector to a common focal point and only close to focus is transformed into a strong shock wave. In highly conducting water (15-20 mS/cm) it has been demonstrated that amplitude of the pressure wave generated by this FSW generator reaches up to 100 MPa at the focus with the rarefaction wave typically down to -25 MPa. In our recent experiments, the composite electrode was divided into two parts, which are energized from separate pulse power supplies. This way, we were able to generate either one shock wave, or two successive shocks focused to a common focal point (i.e., focused tandem shock waves, FTSW) with adjustable delay between the waves in order of microseconds [19]. We have found that at time interval of 10-15 μs between the two shocks the second, originally pressure wave, is strongly attenuated at the focal region and reaches the focus as a rarefaction wave. Amplitude of the pressure wave is up to 100 MPa, while the amplitude of the rarefaction wave falls down up to -80 MPa, producing thus at the focus a large number of cavitation. In this work parameters of modified FTSW generator and the results on biological effects of focused tandem shock waves are presented.

2 Physical Effects of FTSW

Fig. 1 shows scheme of generator of focused two successive (tandem) shock waves in water. The generator is divided by acoustically transparent membrane into two parts. The first part, which is filled with highly conducting saline solution (18 mS/cm), consists of two metallic cylindrical high-voltage electrodes of different diameter d and length h (A1: d=90 mm, h=17 mm; A2: d=60 mm, h=55 mm) covered by a thin porous ceramic layer (composite anode) placed along the axis of the outer metallic parabolic reflector (cathode). The role of the ceramic layer is to redistribute and enhance electric field on the electrode during the pre-discharge phase by the differences in conductivity and permittivity between water and the ceramic layer. This electric field enhancement results in the initiation of large number of

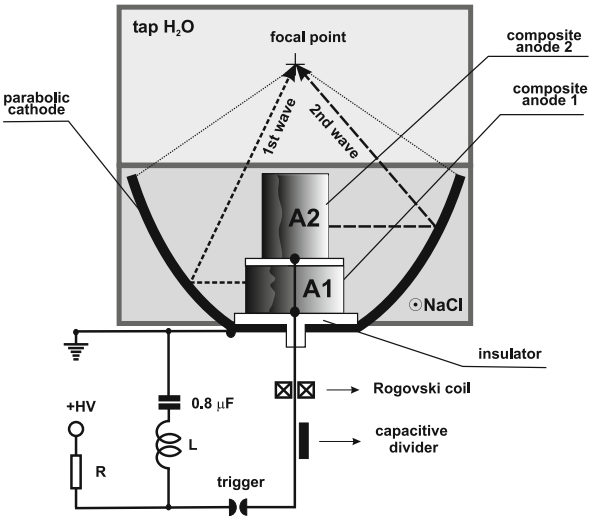

Fig. 1 Scheme of generator of focused tandem shock waves in water.

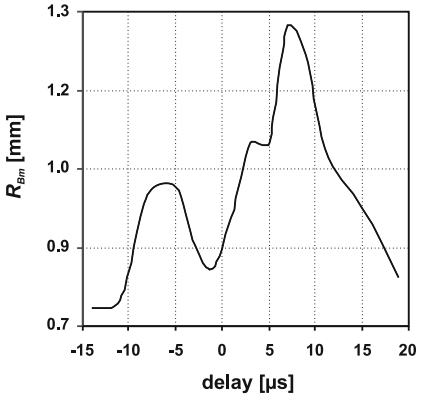

Fig. 2 Dependence of the bubble radius R_{Bm} on the time delay between the first and second shock waves.

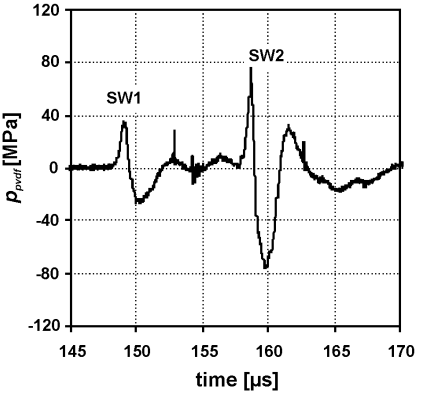

Fig. 3 The pressure waveform of focused tandem shock wave. Peaks SW1 and SW2 correspond to shock waves from anodes A1 and A2.

filamentary discharge channels distributed almost homogeneously along the whole surface of the composite electrode at a moderate applied voltage (20-30 kV) [20].

A positive polarity pulsed high voltage of 30 kV is simultaneously applied to both composite electrodes using one pulse power supply that consists of high voltage DC source, 0.8 μF capacitor and trigerred spark gap. The focal point of the reflector is situated in the second part of the generator, which is filled with a tap water. Each

discharge channel creates a semi-spherical pressure wave, and by superposition of all of the waves a cylindrical pressure wave propagating from the anode is formed. The primary pressure wave is focused by the reflector and near the focus it is transformed into a strong shock wave with focus dimension ⌀ 2.5 mm×32 mm (FWHM).

Time delay between the first and the second shockwave at the focus was set to 10 μs by focal parameter of parabolic reflector and difference in diameter of electrodes A1 and A2, which determine distance of propagation of cylindrical pressure wave formed at each composite electrode to the focus. This time delay was chosen based on previous analysis of pressure field and cavitation dynamics at the focus in dependence on delay between the first and the second shock wave, which showed very complex pressure field [19] and formation of large cavitation bubbles ($>$ 2 mm) at the focus with maximum for delay in the range of 5-10 μs (Fig. 2).

Fig. 3 shows a typical pressure waveform generated by modified FTSW generator at applied voltage of 30 kV. Pressure waveforms of the shock waves at the focus were measured by PVDF shock gauge sensors (S25_04, Piezotech SA, France). Two strong pressure peaks are apparent. The first peak corresponds to the compression caused by the shock wave arriving from anode A1, and the second peak, delayed by 10 μs, corresponds to the shock wave arriving from anode A2. The peak amplitude of the second positive pressure wave is 80 MPa with phase duration of 0.7 μs, which is similar to shock wave formed by the FSW generator with one composite electrode [17]. The amplitude of the following rarefaction wave falls down up to -80 MPa with a wave duration of 2 μs, producing thus at the focus a large number of cavitation.

3 Biological Effects of FTSW

Biological effects of FTSW has been demonstrated *in vitro* on hemolysis of erythrocytes and cell viability of acute lymphoblastic leukemia CEM cells. Freshly drawn human blood was treated with anticoagulant heparin and diluted to 50% hematocrit in saline solution. The blood samples (1.5 ml) were exposed in sealed PE tubing.

PE tubing was positioned to the SW focal region horizontally along the system axis. After the shock wave exposure degree of hemolysis of red blood cells was determined by absorption spectroscopy (λ= 576 nm). Similarly, viability of leukemia cells (5×10^5) exposed to FTSW in PP eppendorf vials (0.4 ml) was determined using the MTT colorimetric assay. Figs. 4 and 5 show that both types of cells were damaged efficiently with increasing number of applied shocks.

Consequently, *ex vivo* experiments were performed with melanoma B16 cell line. After exposure to FTSW, melanoma cells (6×10^6) were subcutaneously transplanted to syngeneic inbred female C57B1/6 mice. The tumor growth was monitored by measuring the volume of the growing melanoma three times weekly using vernier calipers and compared with the control (non exposed) group (6 animals in each group). Fig. 6 shows that in comparison with the intact controls the latency period in the experimental group was extended by 13 days and tumor growth was

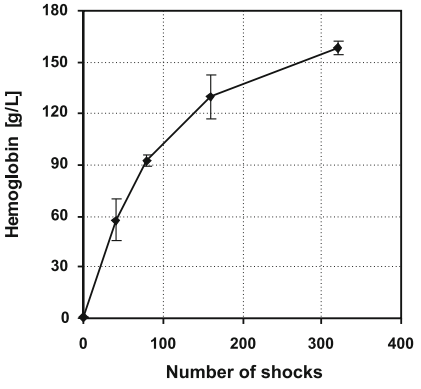

Fig. 4 Hemolysis of human blood cells in dependence on the number of applied focused tandem shock waves.

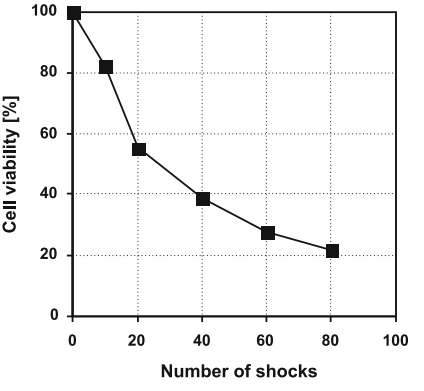

Fig. 5 Cell viability of human acute lymphoblastic leukemia CEM cells in dependence on the number of applied FTSW.

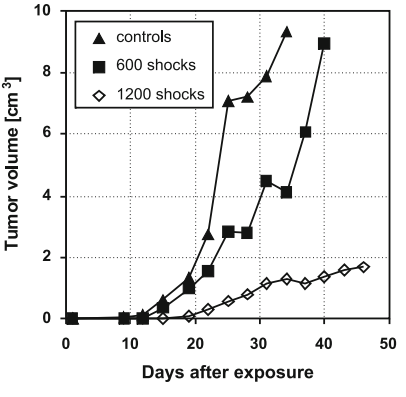

Fig. 6 Growth of the melanoma B16 tumor in inbred C57B1/6 mice growing from melanoma B16 cells applied after exposure to FTSW.

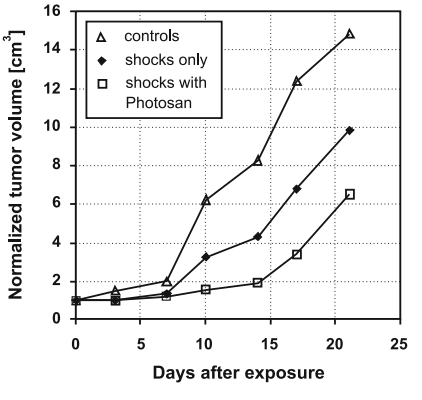

Fig. 7 Growth of the B-lymphoma tumor in outbred rats SD/CUB after *in vivo* exposure to FTSW w/w applied Photosan (dose 2.5 mg/kg).

significantly delayed. More pronounced effect was observed for exposure of the cells to 1200 shocks than for 600 shocks.

Fig. 7 shows *in vivo* effect of FTSW on growth of tumor B-lymphoma inoculated subcutaneously into the left flanks of outbred rats SD/CUB with/without application of Photosan (dose 2.5 mg/kg applied 48 hours before FTSW exposure). The tumors were treated 20 days after B-lymphoma cells transplantation (1×10^6) when the tumor became detectable by palpation. Exposure of tumors was made by 600

shocks with anesthetized animals placed in water bath of FTSW generator. Photosan, a porphyrin-based photosensitizer, is used worldwide for photodynamic therapy of cancer. More recently porphyrins have been also used as sonosensitizers in ultrasound-induced reactions. In contrast to anti-cancer drugs, porphyrins are nontoxic in the absence of ultrasound and their synergistic effect is thought to be associated with cavitation which generates sonoluminescence that might cause electronic excitation of porphyrins and initiate a photochemical process resulting in the formation of the cytotoxic singlet oxygen [21]. Therefore, we suppose that enhanced effect of FTSW on tumor growth delay with applied Photosan might be due to sonodynamic effect of cavitation induced by FTSW. Further evaluation of these effects and research on possible application of FTSW with cytotoxic drugs is in progress.

4 Conclusions

Physical principles of novel type of generator of focused tandem shock waves with time delay between the first and second shock waves of 10 μs have been presented. Generator produces at the focus strong shock wave with peak positive pressure up to 80 MPa followed by tensile wave with peak negative pressure down up to -80 MPa, generating thus at the focus a large number of cavitation. Biological effects of FTSW were demonstrated *in vitro* on hemolysis of erythrocytes and cell viability of acute lymphoblastic leukemia cells, and on tumor growth delay experiments *ex vivo* and *in vivo*. Synergetic cytotoxicity of FTSW with Photosan on tumor growth was observed, possibly due to cavitation induced sonodynamic effect of FTSW.

Acknowledgment. Work is supported by Czech Science Foundation (202/09/1151) and Czech Ministry of Education, Youth and Sports (MSM 0021620808).

References

1. Coleman, A.J., Saunders, J.E.: Ultrasonics 31, 75 (1993)
2. Bailey, M.R., Khokhlova, V.A., Sapoznikov, O.A., Kargl, S.G., Crum, L.A.: Acoust. Phys. 49, 369 (2003)
3. Benes, J., Sunka, P., Kordac, V., Barta, Z., Stuka, C., Figura, Z., Jirsa, M.: Apparatus for clinical performance of extracorporeal lithotripsy. UK Patent GB2199249 (1988)
4. Sunka, P., Babicky, V., Barta, Z., Benes, J., Kolacek, K., Kordac, V., Stuka, C.: Method and apparatus for adjusting the spark gap of a non-invasive lithotriptor. EU Patent EP0349915 (1990)
5. Stuka, C., Sunka, P., Benes, J.: New discharge circuit for efficient shock wave generation. In: Brun, R., Dumitrescu, L.Z. (eds.) Shock Waves@Marseille III, p. 455. Springer (1995)
6. MEDIPO-ZT, s.r.o. (Ltd.), http://www.medipo.cz/litotryptor.htm
7. Bailey, M.R., Blackstock, D.T., Cleveland, R.O., Crum, L.A.: J. Acoust. Soc. Am. 104, 2517 (1998)
8. Bailey, M.R., Blackstock, D.T., Cleveland, R.O., Crum, L.A.: J. Acoust. Soc. Am. 106, 1149 (1999)
9. Zhong, P., Lin, H., Xi, X., Zhu, S., Bhogte, E.S.: J. Acoust. Soc. Am. 105, 1997 (1999)

10. Sokolov, D.L., Bailey, M.R., Crum, L.A.: J. Acoust. Soc. Am. 110, 1685 (2001)
11. Sokolov, D.L., Bailey, M.R., Crum, L.A.: Ultrasound Med. Biol. 29, 1045 (2003)
12. Huber, P., Debus, J., Jochle, K., Simiantonakis, I., Jenne, J., Rastert, R., Spoo, J., Lorenz, W.J., Wannenmacher, M.: Phys. Med. Biol. 44, 1427 (1999)
13. Prieto, F.E., Loske, A.M.: J. Endourol. 13, 65 (1999)
14. Loske, A.M., Prieto, F.E., Fernandez, F., van Cauwelaert, J.: Phys. Med. Biol. 47, 3945 (2002)
15. Alvarez, U.M., Ramirez, A., Fernandez, F., Mendez, Loske, A.M.: Shock Waves 17, 441 (2008)
16. Sunka, P.: Phys. Plasmas 8, 2587 (2001)
17. Sunka, P., Babicky, V., Clupek, M., Benes, J., Pouckova, P.: IEEE Trans. Plasma Sci. 32, 1609 (2004)
18. Sunka, P., Babicky, V., Clupek, M., Fuciman, M., Lukes, P., Simek, M., Benes, J., Majcherova, Z., Locke, B.R.: Acta Phys. Slovaca 54, 135 (2004)
19. Sunka, P., Stelmashuk, V., Babicky, V., Clupek, M., Benes, J., Pouckova, P., Kaspar, J., Bodnar, M.: IEEE Trans. Plasma Sci. 34, 1382 (2006)
20. Lukes, P., Clupek, M., Babicky, V., Sunka, P.: IEEE Trans. Plasma Sci. 36, 1146 (2008)
21. Rosenthal, I., Sostaric, J.Z., Riesz, P.: Ultrason Sonochem 11, 349 (2004)

Part XXII
Special Session Shockwave Moderation

Improvement of Supersonic Aerodynamic Performance Using Repetitive Laser Energy Depositions

J.-H. Kim, K. Yamashita, T. Sakai, and A. Sasoh

1 Introduction

Repetitive-laser pulse energy depositions are contributed to reduce the wave drag of supersonic flight in this study. The intensive laser-heated gas generated by laser beam focusing is useful to control the supersonic flow field. When the laser energy is deposited into the air, blast waves and spherical laser heated gas interacts with bow shock wave in front of supersonic flight. Thereafter, laser-heated gas is transmitted to shock wave, and vortex is generated by baroclinic effects.

Tret'yakov et al. [1] conducted steady-state drag measurement in Mach-2 argon flow by irradiating CO2 laser pulses at a repetition frequency of up to 100 kHz. A significant drag reduction of up to 45 % of the baseline drag was obtained. However, operation data with the efficiency of energy deposition being larger than unity was not presented. [2] characterizes the energy deposition scheme by using a deposited energy, pulse duration and pulse interval in respective dimensionless forms. If the pulse interval is long enough, flow after a pulse energy deposition is independent from previous pulses.

Sasoh et al. [3] successfully measured the time-averaged drag reduction modulated with repetitive laser pulse energy depositions up to 10kHz. They used a load cell controlled by back pressure to estimate the drag reduction performance, and obtained drag reduction of 3% with energy deposition efficiency of 10. However, since laser pulses were irradiated from head of model, refraction problem of laser beam was occurred. Therefore, the disturbed shock layer degrades the effective laser power transmission performance at a high repetition frequency of around 10 kHz.

The main objective of this study is experimentally to investigate the drag reduction characteristics due to the energy deposition with high-repetitive laser pulses up to 80kHz. Amount of drag reduction is verified by force balance system and associated the power gain of energy deposition is estimated. In high repetitive laser

J.-H. Kim · K. Yamashita · T. Sakai · A. Sasoh
Department of Aerospace Engineering, Graduate School of Engineering,
Nagoya University, Furo-cho, Chikusa-ku, Nagoya, 464-8603, Japan

energy depositions, virtual spike which is featured as low density regime caused by baroclinic effects is presented remarkably.

2 Experimental Methods

Figure 1 shows a schematic diagram of experimental system with laser beam path. In-draft wind tunnel of Mach number=1.94 is connected to vacuum chamber of inner volume = $11.5m^3$. In supersonic wind tunnel, size of test section is $80mm \times 80mm$ square cross section. A highly-repetitive, Nd:YLF (Neodymium: Yttrium Lithium Fluoride) laser (wavelength; 1047nm, pulse duration; 10ns, repetition frequency; 10 kHz max., average power; 85 W max.) is used for energy depositions with a repetition frequency of up to 10kHz. The output laser beam with a $5mm \times 5mm$ square cross-section is reflected against three 45-degree reflection mirrors for 1m wavelength light before the wind tunnel. Another laser of a higher repetition frequency yet with a smaller pulse energy, Nd:YVO_4 laser (wavelength; 1064nm, pulse duration; 10ns, repetition frequency; 100 kHz max., average power; 400 W max.) was also used to a repetition frequency of up to 80 kHz. A laser beam is focused by a convex lens with a focal length of 60 mm which is installed right before a wind tunnel window. The window is made of BK-7, has a diameter, thickness and transmittance of 90mm, 15mm and over 99%, respectively.

In this study, a 20-mm-dia. cylinder model is used to evaluate the drag on its forehead. The model is made of brass and is held in the 35mm-outer-dia. brass housing. The clearance between the cylinder model and the housing with two O-rings is set to the order of 500m. The aft-head of the cylinder model is set in a room, which is pneumatically isolated from the wind tunnel test section and connected to a sub-chamber (inner volume; $0.018m^3$) outside of the wind tunnel. The cylinder model is also backed by a load cell (MR-50N-0418, Showa Measurement Instrument co., maximum load 50 N) in the room to measure the force balance over it. For further details of the force balance in the drag measurement, reader should refer to reference[2].

The stagnation pressure, which in this paper implies a pressure on the forehead of the cylinder model on the centerline, is measured by a flush-mounted piezoelectric pressure transducer (PCB Piezoelectronics, Inc. Model-H112A21, rise time of 1m , natural frequency of 250 kHz). A diameter of sensing part is 5.56 mm. The signal sampling rate is 10Ms. The output signals of the load cell, the pressure in the sub-chamber and stagnation pressure are recorded in a digital storage scope (DL750Yokogawa co.) with a sampling rate of 20ks.

Framing Schlieren visualization is done using a high-speed framing camera (HPV-1, Shimadzu Co., 312×260 pixcels, 106 frame/s max., 100 frames). A xenon flush lamp (SA-200FNissin Electronic co., duration; 2ms)) is used as the light source. A pair of 300-mm-dia. concave mirrors (focal lengths; 1 m and 2 m) are used to obtain and image a collimated beam in the Schlieren setup.

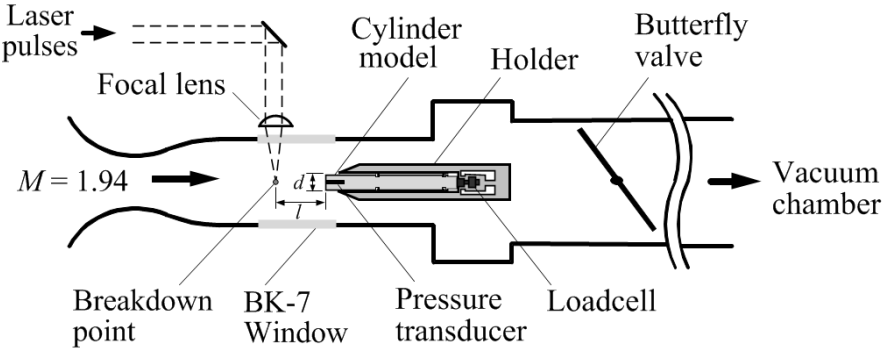

Fig. 1 Experimental apparatus and laser path, side view

3 Results and Discussion

Schlieren images for a cylinder model corresponding to repetitive laser frequency are shown in Fig. 2. In the steady-state supersonic flow without energy depositions, a standing bow shock wave is formed over the cylindrical model with a stand-off distance of about 0.45 d. Apex angle of distorted shock shape due to the interaction with laser-heated gases becomes smaller with frequency increasing. As seen in Fig. 2(a), When laser pulses of f=25kHz is irradiated, three vortex rings can be found obviously between bow shock wave and blunt body model, and vortex ring moves downstream axisymmetrically. With f=50kHz, clear vortex ring due to the effect of baroclinic could not be observed because vortex rings are broken rapidly, since vortices leads to the flow instability in front of the model. However, the bow shock layer which is composed of several vortices has cone shape like a virtual spike, and its effective apex angle decreases with increasing frequency.

The histories of $p_{st}/p_{st,0}$ with various values of f are shown in Fig. 3. Even though the pressure modulation is repeated in an almost independent manner, with higher f, the baseline value does not go back to unity for high repetitive laser pulses. As seen in Fig. 2(a), pressure fluctuations caused by laser pulses interaction is significantly affects to pressure history with f=25kHz,. In this case, vortex ring generated by another pulse influence the pressure field in front of the model before former vortex ring induced pressure disturbance is not perfectly recovered. These pressure characteristics make new steady flow field after laser irradiation and time-averaged stagnation pressure is decreased by around $p_{st}/p_{st,0} = 0.85$ with standard deviation, σ, of about 10 %. Time-averaged stagnation pressure is more significantly decreased as repetitive frequency becomes higher. It can be observed that the stagnation pressure ratio has 0.7 for f=50kHz. With high-repetitive laser pulse, next vortex is arrived to the distorted shock before shock shape is restored to the original form. Therefore, apex angle of shock layer becomes smaller with time, and transition of shock layer is maintained during short time.

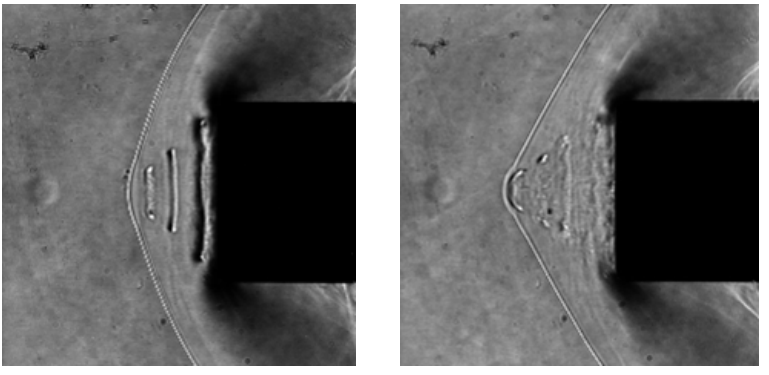

(a) f = 25kHz (b) f = 50kHz

Fig. 2 Still Schlieren image induced by high-repetitive laser pulses, E=6.2mJ/pulse

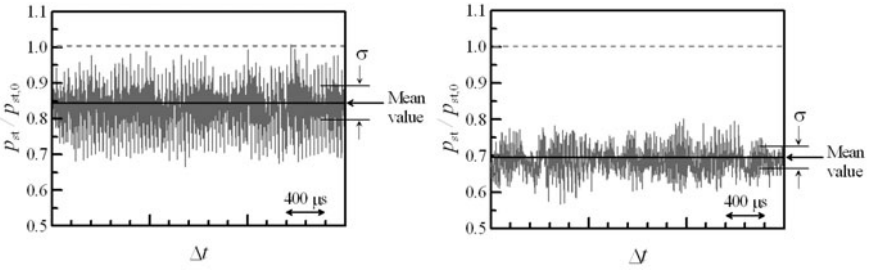

Fig. 3 Stagnation pressure histories, E=6.2mJ/pulse

Figure 4 presents the drag reduction characteristics with varying f. With a constant value of E, $\Delta D/D_0$ almost linearly increases with f. The coefficient in the linearity is slightly larger with the Nd:YVO_4 laser presumably due to better beam quality. If same laser energy per pulse is irradiated into the flow field, laser induced laser-heated gas of same size and strength has influence on the drag reduction. Consequently, it is indicated that increase of repetitive frequency might affect linearly to drag reduction, and amount of drag reduction can be predicted if pulse energy is known. With the cylinder model, drag reduction is realized by about 21% at f=50kHz and E=6.2mJ. The power gain of energy deposition, η, is defined as the ratio of a saved propulsion power to a deposited laser power(fE) by,

$$\eta = \mathrm{U}\Delta D\,/fE, \tag{1}$$

where U is freestream velocity. As seen in Fig. 4, the power gain, η, depends primarily on the value of E. With the E=6.2-6.6mJ, η has a nearly constant value of around 7.

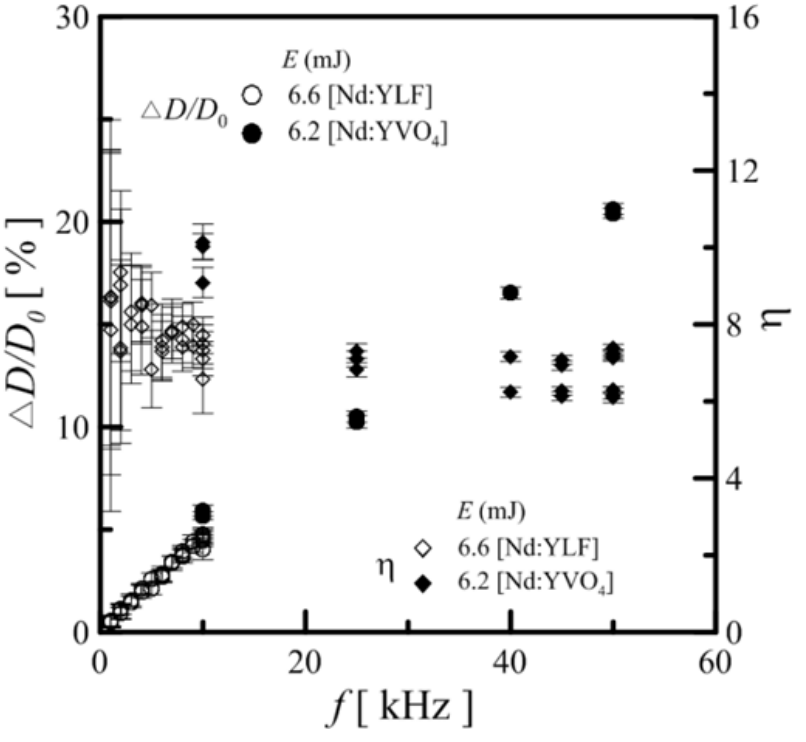

Fig. 4 Drag reduction performance vs laser frequency

4 Conclusion

Experimental study had been performed to investigate the drag reduction performance due to laser induced energy deposition. It has been experimentally demonstrated time-averaged drag reduction performance. Pulse-to-pulse interaction in stagnation pressure history becomes significant with increasing the laser pulse repetition frequency, yet the drag reduction scales almost linearly with the laser frequency. The power gain is a function of only laser pulse energy, and the power gain of energy deposition of 7 is obtained at the value of around E=6.2-6.6 mJ.

References

1. Tret'yakov, P.K., Garanin, A.F., Grachev, G.N., Krainev, V.L., Ponomarenko, A.G., Tishchenko, V.N., Yakovlev, V.I.: Control of Supersonic Flow around Bodies by Means of High-Power Recurrent Optical Breakdown. Physics-Doklady 41(11), 566–567 (1996)
2. Knight, D.: Survey of Aerodynamic Drag Reduction at High Speed By Energy Deposition. Journal of Propulsion and Power 24(6), 1153–1167 (2008)
3. Sasoh, A., Sekiya, Y., Sakai, T., Kim, J.-H., Matsuda, A.: Wave Drag Reduction over a Blunt Nose with Repetitive Laser Energy Depositions. AIAA J. 48(12), 2811–2817 (2010)

The Control of Supersonic Flow Past Bodies by Upstream Energy Deposition in Toroidal-Type Regions

P. Georgievskiy and V. Levin

Introduction

The idea to use the energy deposition, localized in supersonic flow upstream of a body, for the improvement of aerodynamic characteristics was proposed in Russia more than 20 years ago. Theoretically the effects of wave drag reduction and flow reorganization were observed for supersonic flow past sphere by Georgievskiy and Levin [1]. Experimentally the wave drag reduction of blunt and streamlined bodies was confirmed when the optical laser spark was realized in upstream supersonic flow in single pulse mode by Yuriev et al. [2] and in pulse-periodic quasi-stationary mode by Tretiyakov et al. [3]. The recent survey of flow control and aerodynamic drag reduction by the energy deposition was presented by Knight [4].

According to [5] the interaction of thin high temperature wake downstream of small-size energy deposition region with shock layer ahead of a body is the reason for front separation zone formation and effective wave drag reduction. The existence of isobaric front separation zones is acceptable from classic gasdynamic point of view for "wake-type" upstream flow inhomogeneity of any nature [6]. In particular for thin high temperature wakes the efficiency of the wave drag reduction theoretically is infinitely high because static pressure inside the front separation zone is determined by dynamic pressure inside the temperature wake but not by the temperature wake thickness [7]. However the serious possible problem was pulsing and shift instabilities of front separation zones, which had been noticed during numerical simulations for small energy deposition regions [8].

In the present paper the comparative numerical investigation of supersonic flow past blunt bodies in the presence of steady and pulsing toroidal-type upstream

P. Georgievskiy
Institute for Mechanics, Moscow State University,
1 Michurinskiy prosp., Moscow 119192, Russia

V. Levin
Institute for Automation and Control Processes RAS, 5 Radio st.,
Vladivostok 690041, Russia

energy deposition was carried out. The stability of gasdynamic structures and the wave drag reduction efficiency were analyzed. The conditions for equivalence of steady and pulse-periodic modes of the energy deposition were determined.

1 Formulation of the Problem

The Euler equations were used for numerical simulation of unsteady inviscid flows in the presence of localized energy deposition. Only axially symmetrical flows were examined. The equations for spherical coordinates (θ, R) are:

$$\frac{\partial}{\partial t}\sin\theta\begin{pmatrix}\rho\\ \rho u\\ \rho v\\ e\end{pmatrix}+\frac{\partial}{\partial\theta}\frac{\sin\theta}{R}\begin{pmatrix}\rho u\\ p+\rho u^2\\ \rho uv\\ (e+p)u\end{pmatrix}+\frac{\partial}{\partial R}\sin\theta\begin{pmatrix}\rho v\\ \rho uv\\ p+\rho v^2\\ (e+p)v\end{pmatrix}=$$

$$=\frac{\sin\theta}{R}\begin{pmatrix}-2\rho v\\ p\operatorname{ctg}\theta-3\rho uv\\ \rho(u^2-2v^2)\\ -2(e+p)v\end{pmatrix}+\sin\theta\begin{pmatrix}0\\ 0\\ 0\\ \rho\dot{Q}\end{pmatrix};$$

Here p is pressure, ρ is density, u, v are velocity component along θ, R coordinates, e is the total energy of volume unit. For the ideal gas with constant specific gas ratio: $e = p/(\gamma-1)+\rho(u^2+v^2)/2$.

The energy deposition was assumed to be predetermined function of coordinates and time (the "energy source" mathematical model was used). The power input per mass unit $\dot{Q}$ was preset for cylindrical coordinates (r, z) by the formula:

$$\dot{Q} = Q_0 f(t)\exp\left(-\left(\frac{r-r_0}{\Delta r}\right)^2-\left(\frac{z-z_0}{\Delta z}\right)^2\right),\ r = R\sin\theta,\ z = -R\cos\theta; \quad (1)$$

The wave drag coefficient c_x was determined as integral of extra pressure over the body surface with respect to the normal vector direction. The efficiency coefficient η was defined as ratio of the saved power to the total power input W (S_B – the body midsection):

$$c_x = \frac{4\pi}{\gamma M_\infty^2 S_B}\int(p-1)\,r\,dr dz,\ W = 2\pi\iint\rho\dot{Q}r\,dr dz,\ \eta = \frac{\gamma^{3/2}M_\infty^3 S_B\Delta c_x}{2W} \quad (2)$$

The explicit MacCormack scheme [9] of the second order accuracy with coordinates and time was used for numerical simulation. Special procedures were applied to ensure the slipping conditions on the body surface and the condition of free outlet – on the outgoing surface. On the incoming surface the flow was uniform:

$$p = 1,\ \rho = 1,\ u = \sqrt{\gamma}M_\infty\sin\theta,\ v = -\sqrt{\gamma}M_\infty\cos\theta;$$

Typical parameters for the upstream flow were $\gamma = 1.4, M_\infty = 2$. The time marching procedure was used to establish steady solutions or to examine unsteady processes. The Courant-Friedrich-Levy stability condition was used to determine the time step.

2 Supersonic Flow Past Sphere in the Presence of Steady Toroidal-Type Energy Deposition

The supersonic flow past sphere (initial wave drag coefficient $c_x^0 = 0.78$) in the presence of upstream toroidal-type energy deposition was examined. The primary idea was to use the direct effect of density and dynamic pressure decreasing inside the tube-type temperature wake downstream of the energy deposition region for decreasing of static pressure on the periphery of the body surface (to improve the effect of the wave drag reduction of axisymmetrical body). Depending on the parameters of the toroidal energy deposition regions different regimes of flow were realized (Fig. 1, 2).

For the situation when the toroid radius was large enough ($r_0 = 0.5$) the Mach reflection of the shock, generated by the energy input, was observed (Fig. 1 – left). This regime can be identified as "double effect regime" because two factors are essential for the wave drag reduction. The first one is static pressure decreasing on the periphery of the body because of direct interaction with the tube-type temperature wake. The second one is the reorganization of the flow (the front separation zone formation) because of the Mach reflection effect (total pressure decreasing near the symmetry axes downstream of the Mach stem). The wave drag reduction was considerable and the efficiency was sufficient ($\Delta c_x = 44\%,\ \eta = 1.9$). The flow structure was stable and in addition the body surface was isolated from the tube-type high temperature wake by the high enthalpy cold stream.

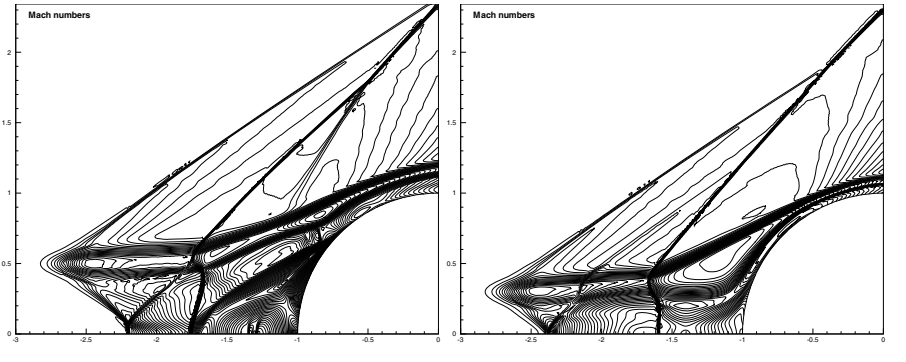

Fig. 1 Stable regimes of supersonic flow past sphere in the presence of steady toroidal-type energy deposition $Q_0 = 50,\ \Delta z = 0.2,\ \Delta r = 0.05,\ z_0 = -2.5$: left – $r_0 = 0.5,\ \Delta c_x = 44\%,\ \eta = 1.9$ – Mach reflection and formation of front separation zone; right – $r_0 = 0.3,\ \Delta c_x = 37\%,\ \eta = 2.7$ – "wake explosion".

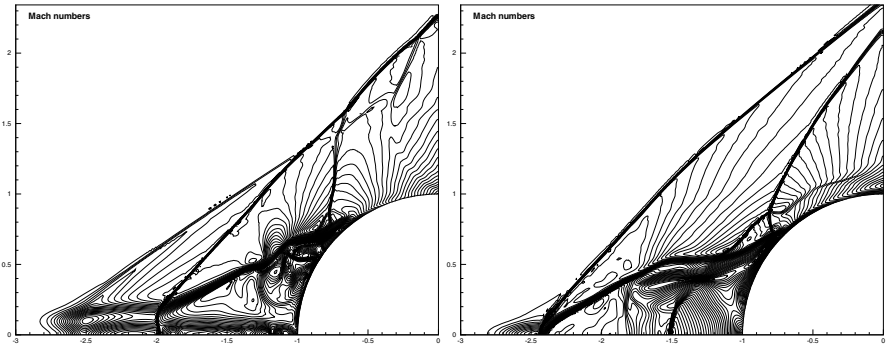

Fig. 2 Pulsing regimes of supersonic flow past sphere in the presence of steady toroidal-type energy deposition $Q_0 = 50,\ \Delta z = 0.2,\ \Delta r = 0.05,\ z_0 = -2.5$: left – $r_0 = 0.1,\ \Delta c_x = 37\%,\ \eta = 8$ – pulsing front separation zone with central high enthalpy stream; right – $r_0 = 0.0,\ \Delta c_x = 34\%,\ \eta = 48$ – pulsing front separation zone.

For smaller toroid radius value ($r_0 = 0.3$) when the Mach stem near the symmetry axes was very short, the appearance of the front separation zone wasn't fixed. In this case sudden enlargement of the high temperature wake during the interaction with the bow shock ahead of the sphere was observed (Fig. 1 – right). Similar effect of "vortex explosion" was analyzed in [10] for the related problem of vortex - shock wave interaction. The regime of "wake explosion" was very stable, surface of the body was isolated from the high temperature wake, the wave drag reduction was considerable and the efficiency was acceptable ($\Delta c_x = 37\%,\ \eta = 2.7$).

For small toroid radius ($r_0 = 0.1$) the front separation zone of specific type with central high enthalpy stream appeared (Fig. 2 – left). The shift layer instability was observed and the flow was unstable. Nevertheless the wave drag reduction was considerable and the efficiency coefficient was high ($\Delta c_x = 37\%,\ \eta = 8$). The configuration (Fig. 2 – right) when the energy deposition region was located on the symmetry axes ($r_0 = 0.0$) was even more effective for wave drag reduction ($\Delta c_x = 34\%,\ \eta = 48$). However in this case the front separation zone was very unstable. Some methods for flow stabilization and instability dumping were proposed in [8]. Another problem for these two regimes was high temperature inside the front separation zones and especially – near the stagnation points on the body surface.

3 Supersonic Flow Past Sphere in the Presence of Pulse-Periodic Toroidal-Type Energy Deposition

The numerical investigation of supersonic flow past sphere in the presence of steady and pulse-periodic toroidal-type upstream energy deposition was carried out. Pulse-periodic unsteady regimes with rectangular pulses of the period duration T and the pulse duration τ were examined (typically $\tau = T/2$). The time-modulating function $f(t)$ in the equation (1) was:

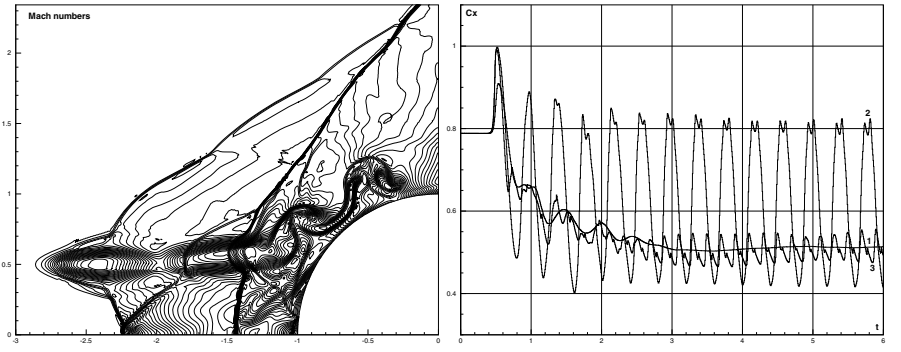

Fig. 3 Supersonic flow past sphere in the presence of pulse-periodic toroidal-type energy deposition $Q_0 = 50,\ \Delta z = 0.2,\ \Delta r = 0.05,\ z_0 = -2.5,\ r_0 = 0.5$: left – $T = 0.4,\ \tau = 0.2$ – essentially pulsing regime; right – dynamics of wave drag reduction with time for steady $T = \tau$ (1), essentially pulsing $T = 0.4,\ \tau = 0.2$ (2) and quasi-stationary regimes $T = 0.2,\ \tau = 0.1$ (3).

$$f(t) = \begin{cases} T/\tau, & 0 \le \mathrm{mod}(t,T) < \tau \\ 0, & \tau \le \mathrm{mod}(t,T) < T \end{cases}$$

The sufficient condition for the quasi-stationary regime realization is the continuity of the temperature wake downstream of the energy deposition region. So the simplest estimation for the critical period duration T^* could be delivered. The drift of the temperature cloud by the ambient flow during time between pulses should be less than the length of the energy deposition region:

$$\sqrt{\gamma} M_\infty (T^* - \tau) < 2\Delta z.$$

Flow structures for the essentially unsteady mode (Fig. 3 – left) were different from the steady analogs (Fig. 1 – left) – large scale vortexes were generated inside the shock layer by every pulse. Flow structures for the quasi-stationary mode were similar to the steady ones.

The dynamics of the wave drag coefficient c_x with time t for steady, essentially unsteady and quasi-stationary time modes was analyzed (Fig. 3 – right). The quasi-stationary mode curve (3) and steady mode curve (1) were the same within some small oscillations. So the transitional dynamics during the numerical time-marching process for quasi-stationary and steady regimes were equivalent. The amplitude pulsations for the essentially unsteady mode (2) were large and pick values were even higher than the initial wave drag level.

So the equivalence of steady and pulse-periodic regimes of the energy deposition is the necessary condition for the effective wave drag reduction. The pulse period duration should be shorter than critical value to secure quasi-stationary regime of the energy deposition. The critical period duration is proportional to the elongation of the energy deposition region. For the period duration longer than critical one essentially unsteady mode was realized, vortex generation in the shock layer was observed and pulsations of wave drag were inadmissibly large.

Conclusions

The comparative numerical investigation of supersonic flow past blunt bodies in the presence of steady and pulsing toroidal-type upstream energy deposition was carried out. Depending on the geometry of the energy deposition region, different regimes were noticed. The wave drag reduction was considerable and effective for blunt bodies. The flow structure was stable and the body surface was isolated from the tube-type high temperature wake by the high enthalpy cold stream. The conditions for equivalence of steady and pulse-periodic modes of the energy deposition were determined. For realization of quasi-stationary regimes the period duration should be less than critical value, which is proportional to elongation of the energy deposition region. The realization of quasi-stationary regimes of the energy deposition is the important condition for the effective wave drag reduction.

Acknowledgments. These investigations were supported financially by Russian Foundation for Basic Researches (grant 11-01-00052), Ministry of Education and Sciences of Russian Federation (grant NSh-8424.2010.1) and Russian Academy of Sciences (as Part of Special Program for Supporting of Fundamental Researches).

References

1. Georgievsky, P.Y., Levin, V.A.: Supersonic Flow over Bodies in Presence of External Heat Supply Sources. Letters Journal of Technical Physics 14(8), 684–687 (1988)
2. Borzov, V.Y., Mikhailov, V.M., Rybka, I.V., Savishenko, N.P., Yuriev, A.S.: Experimental Research of Supersonic Flow over the Obstacle at the Energy Supply into the Undisturbed Flow. Inzh.-Phyz. Zhurn. 66(5), 515–520 (1994)
3. Tretiyakov, P., Garanin, A., Grachev, G., Krainev, V., Ponomarenko, A., Ivanchenko, A., Yakovlev, V.: Control of a Supersonic Flow over Bodies by Powerful Optical Pulsing Discharge. Doklady Adademii Nauk 351(3), 339–340 (1996)
4. Knight, D.: Survey of Aerodynamic Drag Reduction at High Speed by Energy Deposition. Journal of Propulsion and Power 24(6), 1153–1167 (2008)
5. Georgievskii, P.Y., Levin, V.A.: Control of the Flow past Bodies Using Localized Energy Addition to the Supersonic Oncoming Flow. Fluid Dynamics 38(5), 154–167 (2003)
6. Guvernyuk, S.V., Savinov, K.G.: Isobaric Separation Structures in Supersonic Flows with a Localized Inhomogeneity. Doklady Physics 52(3), 151–155 (2007)
7. Georgievskiy, P.Y., Levin, V.A.: Front Separation Regions for Blunt and Streamlined Bodies Initiated by Temperature Wake - Bow Shock Wave Interaction. In: Hannemann, K., Seiler, F. (eds.) Shock Waves. 26-th International Symposium on Shock Waves, vol. 2, pp. 1273–1278. Springer, Heidelberg (2009)
8. Georgievsky, P.Y., Levin, V.A., Sutyrin, O.G.: Front Separation Regions Initiated by Upstream Energy Deposition. AIAA Paper 2008-1355 (2008)
9. MacCormack, R.W.: The Effect of Viscosity in Hypervelocity Impact Cratering. AIAA Paper 1969-354 (1969)
10. Zheltovodov, A.A., Pimonov, E.A., Knight, D.D.: Numerical Modeling of Vortex-Shock Wave Interaction and its Transformation by Localized Energy Deposition. Shock Waves 17(4), 273–290 (2007)

Experimental Studies on Micro-ramps at Mach 5

R. Saad, E. Erdem, L. Yang, and K. Kontis

1 Introduction

The performance of hypersonic propulsion can be critically affected by shock wave/boundary layer interactions (SBLIs), whose severe adverse pressure gradients can cause boundary layer separation. This phenomenon is very undesirable in engine intakes leading to total pressure loss and flow distortion which can cause engine unstart. Hence, it is essential to apply flow control method to the flow, either at the beginning or during the interaction phenomenon to prevent the shock-induced separation [1].

Recent developments of a novel flow control device called micro-ramps, a part of the micro-vortex generators (VGs) family revealed its potential in solving the problem. The theory behind the operation of the micro-ramp is to produce streamwise vortices that help to suppress the SBLIs and improve the boundary layer health. Due to their small size, micro-ramps are embedded in the boundary layer which minimises the drag compared to the traditional vortex generators. They are also cost-effective, physically robust and do not require a power source.

Babinsky et al. [2] conducted experimental investigation at Mach 2.5 applying the optimum geometries of the micro-ramp suggested by the numerical studies of Anderson et al. [3] and revealed the ability of the micro-ramps in delaying and breaking up the separation region. A complex structure of counter-rotating vortices travelling downstream were observed from the micro-ramp trailing edges. The vortices act to entrain the high momentum fluid from the outer region into the near wall surface and at the same time displacing the low momentum fluid at the surface outside the boundary layer. Further downstream the vortices were believed to dissappear after lifting off from the surface.

On the other hand Lu et al. [4] added more explanation on the flow structure downstream the micro-ramp. The primary trailing vortices were observed to

R. Saad · E. Erdem · L. Yang · K. Kontis
The School of Mechanical Aerospace & Civil Engineering, The University of Manchester
Sackville St., M60 1QD Manchester (UK)

breakdown due to Kelvin-Helmhotz instability and formed hair-pin or ring-like structures. These structures travel further downstream and interact with the shock-wave hence reducing its intensity. This detailed the lift-off theory proposed by Babinsky et al. [2] earlier.

The purpose of this experimental study is to investigate the behaviour of the flow over and downstream the micro-ramp and its potential effect in suppressing turbulent boundary layer separation at Mach 5 flow conditions. Most of the previous studies were done in supersonic conditions. Therefore it is essential to conduct studies on how hypersonic flow behaves when it is being controlled by micro-ramps and how the micro-ramps are able to manipulate the hypersonic flow and consequently improve the separated boundary layer caused by the incident shock.

2 Experimental Setup

The experiments are conducted at Mach 5 flow with a unit Reynolds number of 13.2×10^6 m^{-1} in the hypersonic blow-down wind tunnel in the Aero-Physics Laboratory, University of Manchester. Stagnation temperature of the wind-tunnel was set at 375K ($\pm$5 K) and stagnation pressure of 6.50 bar ($\pm$0.05 bar). Due to the fluctuations of the stagnation temperature and pressure of the tunnel, the freestream Reynolds number fluctuates at values no more than 3.7%, which is sufficiently small and the results can be assumed not affected.

In this investigation, two micro-ramps of different sizes (MR-1 and MR-2) were tested. Both micro-ramps are designed based on the computational studies by Anderson et al. [3] and are shown in Figure 1 together with the baseline model. Each micro-ramp is machined on top of a metal strip and fixed to a 360 mm-long flat plate. The characteristics of each micro-ramp model is listed in Table 2. The overall configuration including the location of pressure tappings is illustrated in Figure 2.

Quantitative measurements of the surface pressure are being carried out using Kulite XTE 190M pressure transducers. The visualisation of the flow directions are done using oil-dot technique. The oil used for the experiment is a mixture of titanium

Fig. 1 Micro-ramp models of different sizes. MR-1 (left), MR-2 (middle) and baseline model (right).

Table 1 Dimensions of micro-ramp models

Dimensions (mm)	MR-1	MR-2
Height	4.64	3.48
Chord Length	33.4	25.1
Width	27.2	20.4

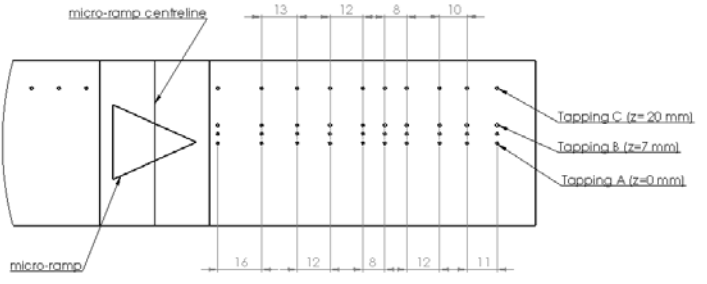

Fig. 2 Overall experiment configuration: location of micro-ramp and pressure tappings.

dioxide, silicone oil, linseed oil, oleic acid and Ruthenium. Grids were drawn on the matte-black painted plate and oil-dots of approximately 1-mm diameter were applied as shown in Figure 3. The Toepler's z-type Schlieren technique was also employed in this experiment.

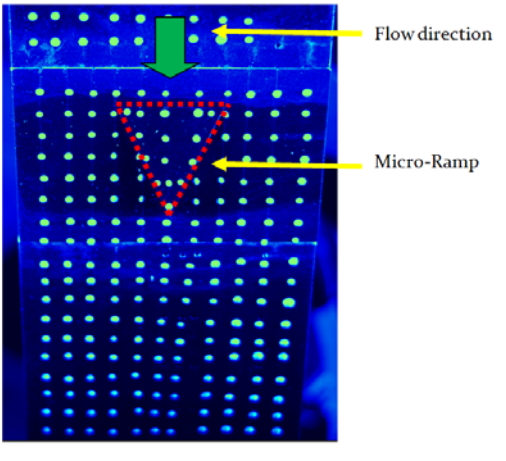

Fig. 3 View from top of oil-dots applied on the grids inside the wind tunnel test section.

3 Results

Figure 4 shows the Schlieren images of the micro-ramp models. The boundary layer thickness of the plate at the micro-ramp leading edge is approximately 6 mm. This is estimated from the baseline Schlieren images. An oblique shock wave can be identified emanating from the leading edge of the micro-ramps. The baseline model schlieren shows well-developed turbulent boundary layer without the presence of the micro-ramp. MR-1 and MR-2 were submerged 80% and 60% respectively inside the boundary-layer hence satisfying the criteria of micro-vortex generator.

The wake area of the micro-ramps are complicated and were not adequately visualised by the Schlieren images due to low spatial resolution. It can only be observed from Figure 4 that the boundary layer continues to ”fly-off” after leaving the apex of the micro-ramp. However from Schlieren technique, the anticipated presence of downstream vortices from the micro-ramp was not clear. Therefore spanwise pressure measurements in the downstream region were taken and compared. Tapping A (centreline) alligns with the apex of the micro-ramp while Tapping B (z = 7mm) is downstream the micro-ramp foot. For comparison, Tapping C (z = 20mm) measures the undisturbed region of the flow. These are clearly shown in Figure 2.

From Figure 5, the most affected region of the flow due to the micro-ramp presence was at the centreline. A pressure reduction of approximately 40% is achieved using the micro-ramp compared to the baseline case which indicates the strength of the two counter-rotating vortices that were present. These vortices are predicted to decrease the upstream interaction length due to the shock-impingement [1]. On the other hand, the pressure reduction at location z = 7mm was approximately 20%, indicating the presence of smaller vortices downstream the micro-ramp foot which are termed secondary vortices or also known as horseshoe vortices [2]. This vortex originates from the corner separation at the leading edge of the micro-ramp. Figure 6 gives a clear representation of the flow structure.

Oil-dots downstream the slant edges of the micro-ramps moved towards the apex centreline as can be seen from Figure 7. This verifies the existence of the

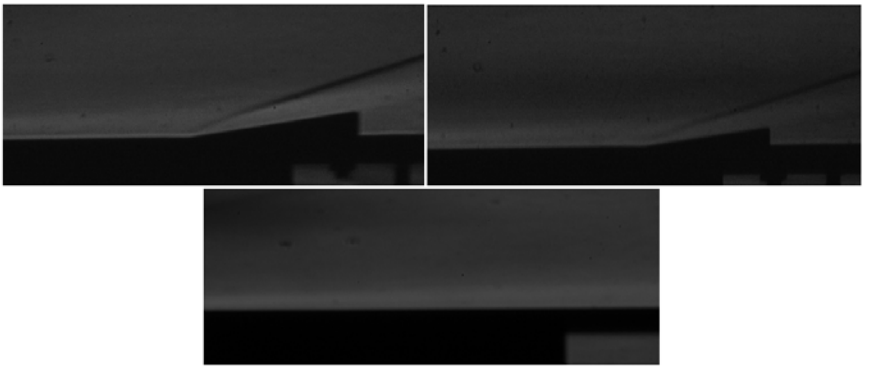

Fig. 4 Schlieren image of MR-1 (left), MR-2 (right) and baseline (bottom).

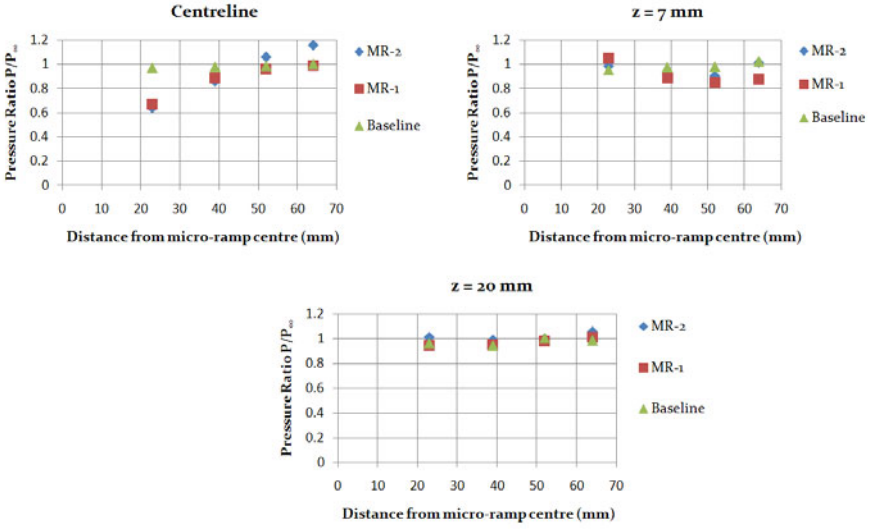

Fig. 5 Pressure measurements downstream micro-ramp at different spanwise locations.

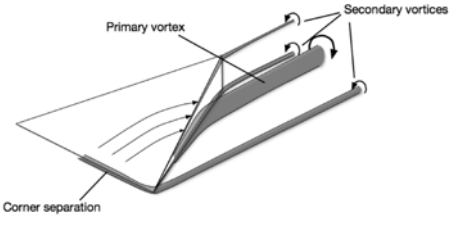

Fig. 6 Representation of the micro-ramp flow structures by [2].

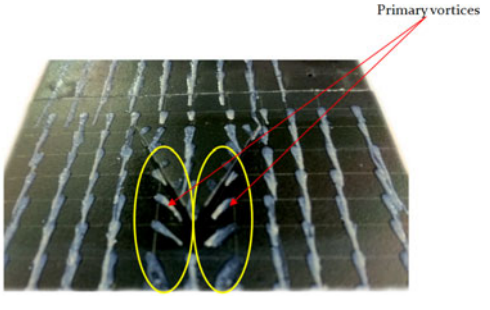

Fig. 7 Oil-dot visualization revealing presence of vortices.

counter-rotating vortices that pull the flow inwards. The direction of the vortices can also be deduced. Since the oil dots moved inwards, the primary vortices must be spiralling outwards from the centreline as shown in Figure 6.

Comparing the micro-ramp sizes, both display similar effects especially when referring to the pressure readings of Figure 5. There are no significant differences to the flow structure between MR-1 and MR-2 either upstream or downstream the micro-ramp as observed from the Schlieren images. Both sizes also manage to create downstream vortices as visible in the oil-dot results.

4 Conclusion

The structure of flow over micro-ramps in hypersonic flow has been characterised in this studies. The information obtained proved that the role of micro-ramps in controlling hypersonic flow does not differ from supersonic cases. Two primary counter-rotating vortices downstream the micro-ramp slant edges were observed while weaker secondary vortices from the micro-ramp foot were also detected. The existence of these multiple pairs of vortices are identified as the keyplayer in suppressing the boundary layer separation caused by the shock-wave/boundary layer interactions.

References

1. Delery, J.M.: Shock-wave/Turbulent Boundary Layer Interaction and its Control. Progr. Aerosp. Sci. 22, 209–280 (1985)
2. Babinsky, H., Li, Y., Pitt Ford, C.W.: Micro-ramp Control of Supersonic Oblique Shock-Wave/Boundary Layer Interactions. AIAA J. 47(3) (2009)
3. Anderson, B., Tinapple, J., Surber, L.: Optimal Control of Shock-Wave Turbulent Boundary Layer Interactions using Micro-Array Actuations. AIAA Paper 2006-3197 (2006)
4. Lu, F.K., Pierce, A.J., Shih, Y.: Experimental Study of Near Wake of Micro Vortex Generators in Supersonic Flow. AIAA Paper 2010-4623 (2010)

Effect of Dielectric Barrier Discharge Plasma in Supersonic Flow

Suparna Pal, R. Sriram, M.V. Srisha Rao, and G. Jagadeesh

1 Introduction

In the recent past, there is a growing interest in using the Dielectric Barrier Discharge (DBD) based plasma actuators for active control of the boundary layer in different speed regimes. The plasma actuators are attractive flow control devices because of their simplicity of construction and their very short response time. The plasma actuation relies on one or more of the three basic mechanisms viz., volumetric joule heating, electrohydrodynamic (EHD) forcing and magnetohydrodynamic (MHD) forcing. DBD actuation has been widely accepted as due to EHD force it generates. Beouf et.al[1] have discussed the basic mechanisms responsible for EHD force exerted by DBD. The EHD forces on the fluid generates a flow in the vicinity of the DBD. A planar configuration of DBD in flush with surface generates a wall jet as reported by Moreau[2]. The planar configuration has been extensively explored for aerodynamic flow control at subsonic speed. Roth et.al [3] have used DBD based plasma actuators for stabilization of boundary layers on a flat plate configuration at subsonic speed. Jukes et.al.[4] have used surface plasma for drag reduction by controlling the turbulent boundary layer. While the use of DBD for low speed flow control is fairly known, its use in high speed flows is still debated. The typical wall jet velocities of DBD are very small compared to the typical velocities of supersonic or hypersonic flows. But even for such high speed flows the velocities close to the surface are small and the DBD can be a significant perturbation to the boundary layer, especially when pulsed at specific frequencies. It is with this backdrop that investigations are initiated in Laboratory for Hypersonic and Shockwave Research at IISc to study the interaction of DBD with high speed flows. This paper explores the flow generated by surface DBD, the suitability of popular models for theoretical study of interactions of DBD with high speed flow, and presents some preliminary results on the study of effect of surface mounted DBD on a Mach 1.6 wall jet.

Suparna Pal · R. Sriram · M.V. Srisha Rao · G. Jagadeesh
Department of Aerospace Engineering, Indian Institute of Science, Bangalore

Suparna Pal
Defence Research and Development Laboratory, Hyderabad

2 Characterization of DBD Flow Field

Figure 1(a) shows the typical planar configuration of electrodes used for creating surface DBD. The DBD plasma actuator consists of two electrodes made of copper that are separated by a dielectric layer of Kapton. The upper electrode is exposed to the air and the lower one is encapsulated in the dielectric material. The electrodes and the dielectric are so thin as to have the entire set up almost in flush with the surface. The distance of overlap between the electrodes on the plane of surface is the span of the DBD as indicated in Figure 1(a).

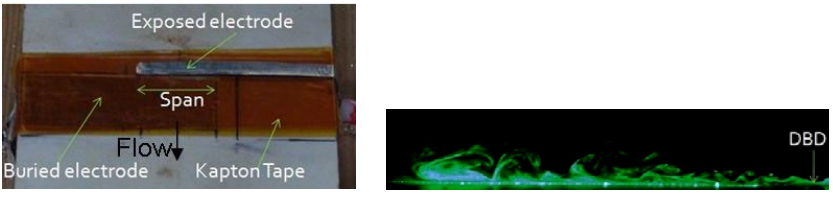

(a) Photograph of DBD setup

(b) smoke visualization of wall jet induced by DBD (continuous operation)

Fig. 1 DBD and induced wall jet

When high AC voltage is applied, the surrounding air is ionized. Charged particles moving with electric field in the partially ionized gas collide with neutral atoms and molecules transferring momentum that causes convective motion of the gas. With the typical planar configuration, the electric field is directed from the line edge of exposed electrode to the buried electrode. Thus the DBD creates a wall jet on the surface perpendicular to the span (in longitudinal direction). Figure 1(b) shows the smoke visualization of the typical wall jet in the longitudinal direction along the spanwise centre line generated by continuous operation of DBD with AC frequency of 2 kHz for 50mm span DBD.

The smoke flow visualizations are carried out using a laser source to illuminate the flow seeded with smoke and a high speed camera. The high speed camera, Phantom V7.2, was used to capture images at a frame rate 2000 frames/sec with a resolution of 800 X 600 pixels. This image resolution and frame rate was found suitable to resolve the temporal evolution of the flow. The starting of the DBD flow and the time evolution of the flow is shown in Figure 2(a). At the start of the DBD flow, when the vortex is not formed the maximum velocity of the smoke front is found to be 5 m/s from the initial frames. This could be taken as the characteristic wall jet velocity. Subsequently after the vortex is formed, the vortex velocity (velocity of the centre of the vortex) is obtained and is found to be typically of the order of 0.2 m/s. The velocity of the starting vortex thus obtained can be used to characterize the wall jet as a function of various parameters of DBD, viz. AC frequency, span, pulsing frequency and duty cycle.Planes in spanwise direction were also visualized. Spanwise motion is monitored by letting the smoke settle and then visualizing the DBD flow sweeping away the smoke. It was found that with the decrease in the span

of DBD the 3-dimensionality of the flow becomes evident. Figure 2(b) shows the spanwise plane at 10 mm from the exposed electrode, for a DBD with span of 2 mm. It can be seen from the figure that the smoke is swept away in both spanwise directions. With longer spans (25 mm and 50 mm) most of the settled smoke was swept streamwise thus letting less smoke available to visualize the spanwise motion. By comparing the spanwise and streamwise flows it is evident that with shorter span the 3-dimensional effects become prominent. Along with the wall jet, the spanwise motion induced by such shorter span DBD can play a crucial role in flow control. Further details of the parametric study are beyond the scope of the paper and are not presented.

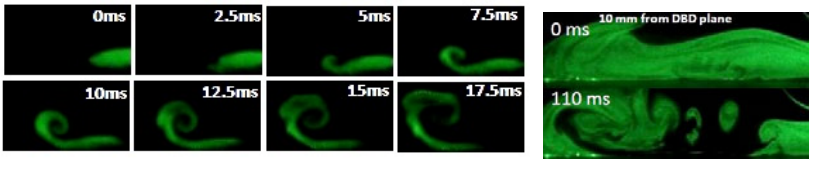

(a) Time evolution of the flow induced by DBD in quiescent air

(b) Flow in the spanwise direction at 10 mm from exposed electrode

Fig. 2 Streamwise and Spanwise flow induced by DBD in quiescent air

3 Numerical Modeling

Numerical simulation of the DBD flow in quiescent air is attempted and compared with the experiments, so as to validate a DBD flow model that can be used to theoretically investigate the interaction of DBD with high speed flows. The flow due to DBD can be simulated if the EHD force due to DBD is modeled and is used as a source term in flow computations. There are simple phenomenological models based on empiricism that suggests adding locally, a body force to the fluid, as a function of DBD parameters. For the present study the phenomenological proposed by Shyy et.al. [5] is used. The body force computed using this phenomenological model acts as a source term in the momentum equation of the Navier Stokes equations. The coupled pressure-velocity SIMPLE scheme of commercial software FLUENT is used to solve the two/three dimensional flow. The 2-dimensional numerical computations were in good agreement with the schlieren flow visualization for the case of 50 mm span and 2 kHz AC frequency as shown in Figure 3.

The agreement of the simulation with the schlieren implies that the numerically computed wall jet velocities can be used to characterize the wall jet, admitting that the velocity profiles need not have a match. The typical velocity from the computation is 6 m/s. It can be noted that this velocity is comparable with the velocity calculated from the smoke visualizations during the initial frames before the vortex is formed.

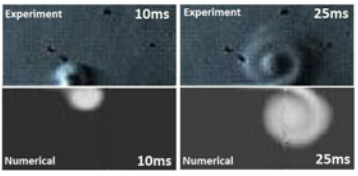

Fig. 3 Comparison of experimental results (schlieren) and numerical computation

While the phenomenological model shows good agreement for the specific case, it must be admitted based on observations that the model will not hold good for frequencies far off from 2 kHz (for the specific device used for the experiments). According to the model the body force increases linearly with the AC frequency. It implies that the wall jet velocity and thus the velocity of the starting vortex should increase with AC frequency. But experimental observations do not indicate this behaviour. Figure 3 shows the observed average velocity of the starting vortex as a function of AC frequency. It can be seen that there is (non linear) increase in vortex velocity upto 2 kHz and then there is a decrease in velocity, falling to zero velocity at a frequency of 10000Hz.

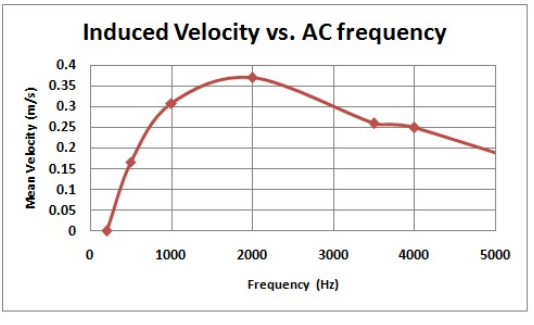

Fig. 4 Mean velocity of the starting vortex vs. frequency

The maximum velocity is observed at 2 kHz, and thus 2 kHz is the frequency with which most other studies are done. Although it is only coincidental that the model works at 2 kHz, considering that further studies on application of DBD for high speed flows are done at the specific frequency regime, the model can be used faithfully to simulate the EHD forcing on flow fields.

4 Investigations on the Effect of DBD on Mach 1.6 Wall Jet

Experiments are initiated to investigate the effect of DBD on a supersonic wall jet of Mach 1.6. Figure 5(b) is a schematic of the flow facility where compressed air

stored at 12 bar in the reservoir is blown down. The solenoid valve is used to operate the facility while the pressure in the stagnation chamber can be regulated by the pressure regulator.Air with stagnation pressure of 4.5 bar is allowed to expand to Mach 1.6 through a 2-D convergent-divergent contoured nozzle of exit area 80 mm x 15 mm. The Mach 1.6 flow at the exit of the nozzle is allowed to expand over a flat plate of 80 mm width, aligned with the bottom wall of the nozzle. The other side of the jet is exposed to the atmosphere. Figure 5(a) shows a schematic of the flat plate (top view). The flat plate is made of HYLEM for electrical insulation. The DBD is placed at 30 mm from the exit of the nozzle on the flat plate. The flat plate is equipped with PCB pressure sensors to measure the surface pressure of the wall jet. A typical run lasts for 3-4 seconds.

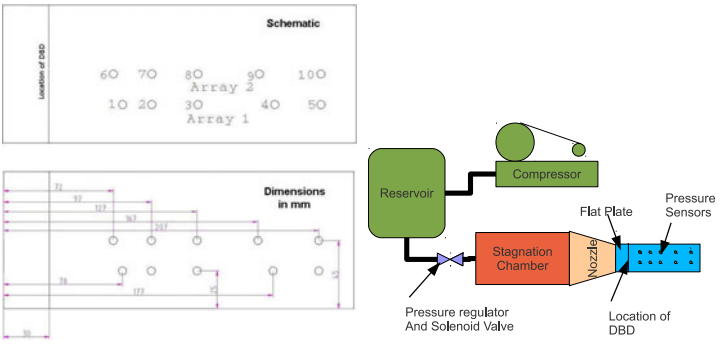

(a) Schematic of the flat plate (top view)

(b) Schematic of the supersonic wall jet facility

Fig. 5 Schematic of flat plate and the flow facility

The surface pressures are measured along the centre line (Array 2) and along a line 20 mm from the centre (Array 1), with and without DBD. Figure 4 shows the consolidated results of the pressure measurements. It can be seen that the surface pressure with and without DBD does not show significant differences. At the last sensor in Array 2 (centre line), slightly higher pressure can be seen with DBD, but the difference is still within the error bar. The momentum flux induced by DBD (through the body force) estimated using phenomenological model is found to be only $2.8x10^{-3}$ times the momentum flux of the supersonic flow at the exit of the nozzle. Because the DBD induced velocities are very small in comparison with supersonic speeds, they may not bring significant changes to the outer flow, but can be a significant perturbation to the boundary layer. Efforts are underway to investigate the evolution of DBD induced disturbances close to the wall.

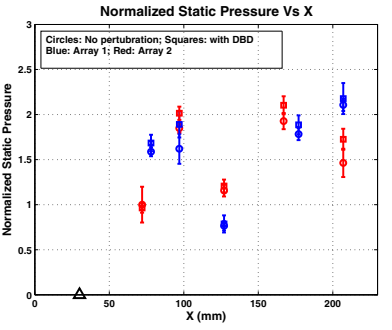

Fig. 6 Consolidated results of the pressure measurements

5 Conclusions

Investigations are initiated to study the interaction of Dielectric Barrier Discharge (DBD) with high speed flows. To begin with, the flow field generated by DBD in quiescent air is examined. It is seen that the DBD generates a wall jet on the surface with a maximum velocity of 5 m/s. Characterization of the DBD induced flow for different DBD parameters are examined. It is observed that maximum flow velocity is observed at AC frequency of 2 kHz, and thus it is with this frequency that further studies are done. At 2 kHz frequency the numerical computations using the phenomenological model by Shyy et.al.[5] shows good agreement with schlieren visualization of the DBD flow, thus validating the model for use in planned supersonic flow simulations with DBD. It is also observed that the 3-D effects become prominent when the DBD span is reduced. Preliminary experimental results on interaction of DBD with supersonic wall jet show no changes in surface pressures in the presence of DBD. Further experimental and numerical investigations are underway to study the evolution of DBD induced disturbances close to the wall.

References

1. Boeuf, J.P., et al.: Journal of Phys. 40, 652–662 (2007)
2. Moreau, E.: Journal of Phys. D: Appl. Phys. 40, 605–636 (2007)
3. Roth, J.R., Sherman, D.M.: Boundary Layer Flow Control with a One Atmosphere Uniform Glow Discharge Surface Plasma 36th AIAA Aerospace Sciences Meeting and Exhibit, Reno (1998)
4. Jukes, T.N., Choi, K.S., Johnson, G.A., et al.: Turbulent boundary layer control for drag reduction using surface plasma. Technical Report, AIAA Paper 2004-2216 (2004)
5. Shyy, W., Jayaraman, B., Anderson, A.: Journal of Appl. Phys. 92, 6434–6443 (2002)

Two Modes of Shock Interaction with Zone of Pulse Volume Discharges in the Channel

J. Jin, D. Koroteev, I. Mursenkova, N. Sysoev, and I. Znamenskaya

1 Introduction

A great number of researches in the recent years deal with the problem of non-equilibriums plasma flow control in aerodynamics [1]. Different approaches are used for efficient flow moderation with energy deposition in a boundary layer, compression wave area, duct inlets and others [1, 2, 3]. Energy input using pulse discharge plasmas appeared to be rather promising. Pulse and pulse-periodic energy supply is the most effective way to improve high-speed flow characteristics; shock waves arising from local pulse energy input area may influence high speed flow with shock configurations.

The paper deals with the problem of pulse volume energy input influence on the plane shock wave moving in the channel. Transversal pulse volume discharge was used for pulse volume energy input in front of shock wave. Special type of combined discharge was used: pulse discharge with ultraviolet preionization by radiation from the sliding surface discharges, which form plasma electrodes. Discharge plasma was very homogeneous due to gas preionization [3, 4, 5, 6], electric current time is 200ns. Discharge chamber was mounted in a shock tube channel (cross section 24mm$\times$48mm) as a special section. Two sidewalls of the test chamber are the quarts windows. Another two walls are plasma electrodes (plasma sheet discharges, sliding on dielectric surfaces).

Big part of discharge electric energy is converted directly to translational degrees of freedom [6]. High current pulse discharge can be used for a rapid heating of gas area. Quick heating time is 10^{-7}s and the impact area can be localized in front of shock wave. These features allowed realizing the diaphragmless discontinuity breakdown conditions on shock wave front experimentally [3, 4, 7].

Discharge area length was 100 mm. The initial pressure was 70-75 Torr, initial plane shock waves Mach numbers were 2.2-2.5.

J. Jin · D. Koroteev · I. Mursenkova · N. Sysoev · I. Znamenskaya
Moscow State University, Faculty of Physics, Russia,
119991, Moscow, GSP-1, 1-2 Leninskie Gory

Two different modes of the shock wave interaction with the nanosecond volume discharge area were shown to be possible. First mode is: discharge is initiated before initial shock wave S_0 reaches the discharge area. Second mode is: the discharge is initiated at the moment when the shock wave S_0 is passing through the inter-electrode area. Discontinuity breakdown may occur in the second case in discharge section, it was analyzed experimentally and compared to CFD using gas dynamic model of instant energy release in the previous works [3, 4]. This paper presents the investigation of the flow resulting after realization of the first configuration and its comparison to the second pattern.

2 Description of the Experiment

The high voltage pulse between the two plasma sheets on the top and bottom walls initiates a volume discharge in the whole discharge section. When the voltage is higher than the breakdown, a system of surface discharge channels is formed along the surfaces of dielectric walls (plasma sheets), it pre-ionizes the gas, and volume discharge is switched. Energy about 0.5J is deposited into the discharge gap within 200 nanoseconds. Two shock waves spread from the plasma sheets transversal to the shock tube channel. In 40-50 μs they decay.

The flow visualization system (Fig. 1) includes shadow method and background oriented schlieren (BOS). Two methods record the flow images in the discharge section at the same moment of time. The angle between the lines of observation of the two methods is about 10 degrees. The source of light for both methods was pulse Nd:YAG laser, exposure time was 6ns. The plasma emission was filtered with a color filter. Shadow images were recorded by digital photo camera with a 6.1 million pixels matrix. It was shown [5], that about 20-50 percent of high current nanosecond discharge's energy is converted directly to the gas heating. VT relaxation time for the other part of discharge's energy is quite long (more than 10^{-4}s), so under the conditions of described experimental setup we may consider only instant part of energy release.

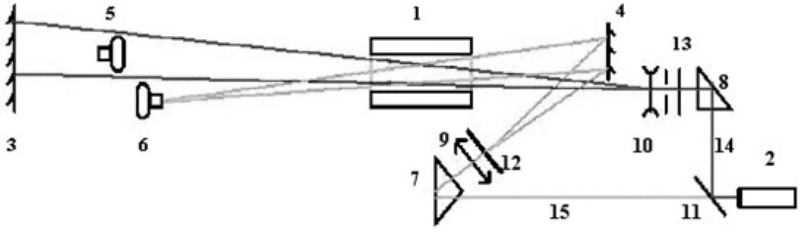

Fig. 1 Optical scheme: 1-discharge chamber (cross section), 2-laser, 3-schlieren screen, 4-BOS background, 5, 6-digital cameras, 7, 8-rotary prism, 9, 10-lens, 11-divider plate, 12, 13-filters 14(black line)-the path of schlieren method, 15(gray line)-the path of BOS.

3 First Mode of Interaction of Shock Wave with Volume Discharge Area

The experiment scheme in the first mode was the following:

Pulse volume discharge was switched on before shock reaches the discharge area. Fig. 2a, shows the shadow image of the initial shock S_0 and Fig. 2b shows the combined volume discharge in the discharge section. Shock wave entered the discharge gap after delay time t. A synchronizing module was used to initiate the laser pulse at the required time of gas dynamics flow after the discharge pulse. The position of the initial plane shock wave at the moment of discharge x, $x=x_0$. Delay time of the shock wave entering the discharge gap was: -100 +100μs.

As a result of interaction with the discharge area, velocity of the shock wave was changed. Its form is no longer plane (Fig. 2c). The shock wave front moderation is due to non-uniform energy deposition - plasma sheets zones are the zones of high energy input, also discharge volume was spoiled by weak transversal disturbances. Flow close to the walls behind shock wave is turbulent. Density fields (at the same moments of time), were obtained using BOS method [8, 9].

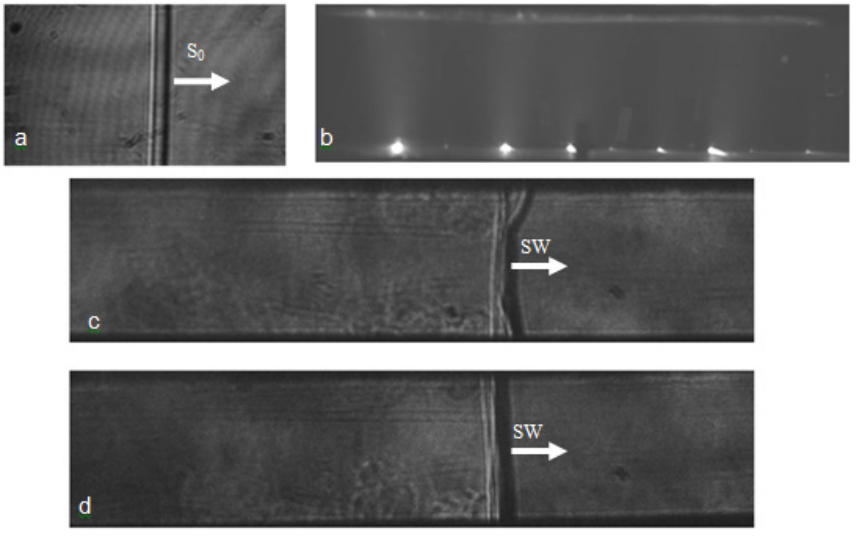

Fig. 2 Plane shock wave interacts with volume discharge zone. Shadow image of the initial shock S_0 (a). Volume discharge (b). Original Mach number S_0= 2.4, x_0=-10mm t=140μs (c). Original Mach number S_0= 2.3, x_0=-105mm t=286μs (d).

After some time the shock front is straightened (Fig. 2d, t=286μs) - the plasma sheet zone has the same parameters as the volume gas. Flow behind shock wave is still turbulent. The volume discharge effect on the shock wave is negligible if the shock wave is far (over 100mm) from the zone of discharge.

4 Second Mode of Interaction; Discontinuity Breakdown

The experiment scheme in the second mode was the following:

Pulse volume discharge was switched at the moment when the shock was in the interelectrode area. Fig. 3a, shows the shadow image of the initial shock S_0 and the discharge, boarded by S_0. The phenomenon of discharge "self localization" in front of shock wave is seen (Fig. 3b) [3, 4, 5].

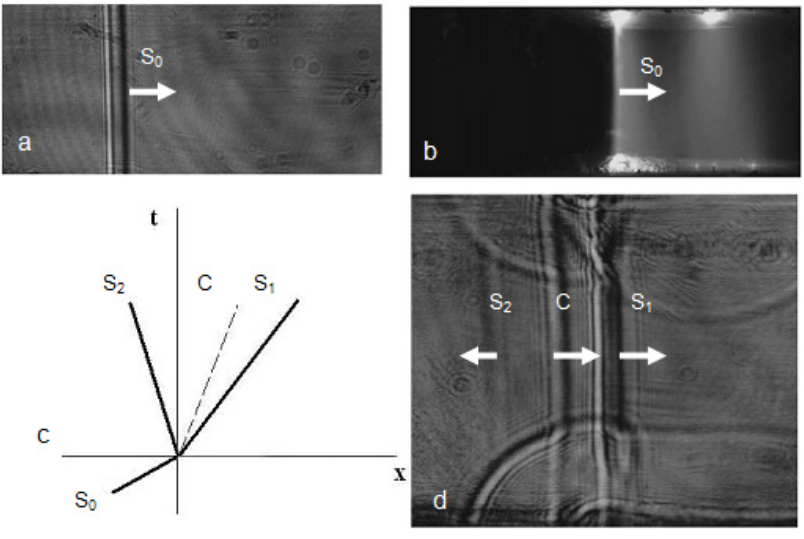

Fig. 3 Plane shock wave interacts with volume discharge zone. Original shock (a,b). Scheme of discontinuity breakdown (c). Original Mach number S_0=1.7, x_0=+20.1mm t=8.8μs (d)

Laser flash was at the required time of gas dynamics flow after the discharge pulse. All instant energy release was self-localized in spatial area, boarded by shock. Discontinuity breakdown occurs in this case in discharge section, and the original shock wave separates into two shock fronts and contact discontinuity (Fig. 3c: S_1 S_2 C). Shadow images demonstrate that after the discharge self-localization effect, the flow is close to two dimensional. Two shock fronts and contact discontinuity (resulting from discontinuity breakdown) are clearly seen: S_1 S_2, C. They are interacting with transversal shock waves from plasma sheets.

Fig. 4a presents shadow image of flow 240μs after the discharge; the distance between discontinuities is 2-3 cm; transversal shocks became weak. The BOS results of density field are on Fig. 4b. X-t diagram of shock wave S_1 and contact C_1 movement in the pulse volume discharge zone is on Fig. 5. Two series of experiments with different x_0 (x_0=20mm, x_0=60mm,) were analyzed. The volume discharge influence on the velocity of the shock wave is governed by energy deposition value and initial shock wave S_0 velocity. The velocity of S_1 after interaction is close to constant.

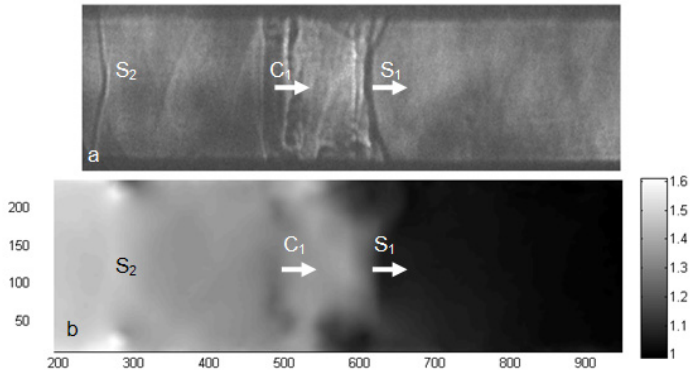

Fig. 4 Plane shock wave interacts with volume discharge zone. Original Mach number S_0= 2.2, x_0=+60mm t=48μs. Shadow image (a), BOS image of density (b).

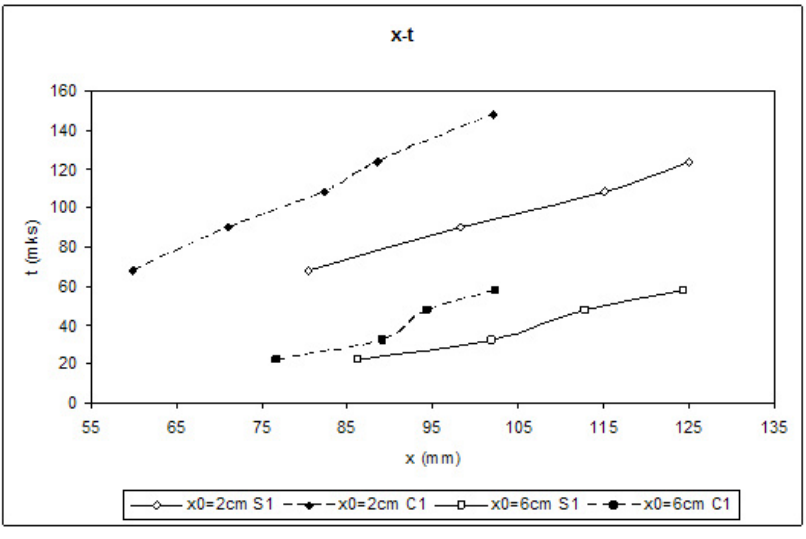

Fig. 5 Schematic diagram of shock wave after interaction with volume pulse discharge zone ($0<x_0<+100$mm). Solid lines represent the front with higher speed S_1 and dotted lines represent the front with lower speed C_1.

5 Conclusion

Two modes of shock wave interaction with pulse volume discharge were investigated. Shadow and BOS analysis show the shock wave and flow moderation after pulse energy deposition in 2D configuration.

In the first mode shock entering discharge area becomes disturbed. After some time the shock front is straightened. Flow behind shock wave becomes turbulent. The volume discharge effect on the shock wave is negligible if the shock wave is over 100mm from the zone of discharge. Discontinuity breakdown mode changes the flow dramatically.

Acknowledgment. This work was supported by the grant RFBR 11-08-00297.

References

1. Bletzinger, P., Ganguly, B.N., Van Wie, D., Garscadden, A.: Plasmas in high speed aerodynamics. Phys. D: Appl. Phys. 38(4), R33–R57 (2005)
2. Sasoh, A., Ohtani, T., Mori, K.: Pressure effect in a shock-wave-plasma interaction induced by a focused laser pulse. Phys. Rev. Lett. 97(20), 205004-1–205004-4 (2006)
3. Znamenskaya, I.A., Koroteev, D.A., Lutsky, A.E.: Discontinuity breakdown on shock wave interaction with nanosecond discharge. Physics of Fluids 20, 056101 (2008)
4. Znamenskaya, I.A., Koroteev, D.A., Lutsky, A.E.: Realization of Riemann Problem at Gas-Plasma Boundary Formed by Shock Wave 27th International Symposium on Shock Waves, St. Petersburg, Russia, Book of Proceedings, p. 194 (2009)
5. Znamenskaya, I.A., Koroteev, D.A., Popov, N.A.: Teplofiz. Vys. Temp. 4, 820 (2005)
6. Karlov, N.V., Kuz'min, G.A., Prokhorov, A.M.: Izv Akad. Nauk SSSR, Ser. Fiz. 48, 1430 (1984)
7. Guluzade, T.A., Mursenkova, I.V., Znamenskaya, I.A.: Proceedings of the 22nd International Symposium on Shock Waves, London, pp. 489–491 (1999)
8. Jin, J., Lutsky, A.E., Mursenkova, I.V., Vinnichenko, N.A., Znamenskaya, I.A.: Application of BOS method for analysis of the flow after surface discharge. In: The 21th International Symposium on Transport Phenomena (2010)
9. Popova, E.M., Kompenhans, J., Skornyakova, N.M.: Investigation of the Accuracy of the Background Oriented Schlieren Method. In: ISFV13 - 13th International Symposium on Flow Visualization. FLUVISU12 - 12th French Congress in Visualization in Fluid Mechanics, Nice, France, July 1-4 (2008)

Steady Energy Deposition at Mach 5 for Drag Reduction

E. Erdem, L. Yang, K. Kontis, and A. Nigam

1 Introduction

Historically the potential of energy-assisted shaping of high-speed flows with modest on board power requirements has been the subject of a number of earlier investigations. The possibility of obtaining drag reduction using energy sources upstream of blunt bodies has been pioneered by Georgievskii and Levin [1] and Myrabo and Raizer [2] in theoretical studies. In their studies the magnitude of the drag reduction was found to be insensitive to the location of energy deposition at a sufficiently large distance from the body. This was followed up by various computational studies; Levin and Terenteva [3] and Riggins et al. [4] showed power savings over cones and blunt bodies using two dimensional Euler/laminar computations. Kolesnichenko et al. [5] conducted unsteady/quasi steady Euler computations over a rectangular body. They observed that quasi-steady energy deposition was more efficient than unsteady energy deposition in reducing the time integrated frontal drag. The strongest effect on drag reduction was the magnitude of the density gradient around the localised thermal spot. Girgis et.al [6] suggested that there was an optimum energy source distance for drag reduction for a given power for a cone in supersonic flow, and energy distribution was assumed to have a Gaussian profile. The study yielded promising results with drag reduction of up to 35%. Zheltovodov et al. [7] explains the physical phenomenon as follows. The energy input results a high temperature plasma, which creates a localised blast wave, which penetrates the bow shock and reflects off the surface. The thermally heated region that is created interacts with the bow shock which becomes distorted. This is known as Len's effect. The area of intersection between the bow shock and the blast wave is a region of recirculation, which induces streamwise vortical systems to be formed. This alters overall surface pressure distribution, leading to a reduction in drag. The stagnation pressure reduction is directly related to the circulation production, which varies with the length of the thermal spot and the density in the heated zone. It is noted by Kolesnichenko [8] that the

E. Erdem · L. Yang · K. Kontis · A. Nigam
AeroPhysics Lab, School of MACE, University of Manchester, Manchester, M13 9PL, UK

lateral extent of the filament does not impact the circulation production, and so the most efficient energy addition processes will be the ones with very thin channels.

Electric input is an attractive but intrusive way of depositing energy in front of a blunt body due to the support to hold electrodes to create an arc. Myrabo et al. [9] recently used thin rods of a tungsten-zirconium alloy electrodes to deliver the arc discharge upstream of a disc shaped body at Mach 10 in a hypersonic shock tunnel. The arc was supplied by a number of lead acid car batteries at low voltage but very high current levels. The arc created its own shock wave and the drag level was decreased several orders of magnitude and a significant gain was obtained in the total consumption of energy. Furthermore, Satheesh and Jagadeesh [10] also carried out experiments in a hypersonic shock tunnel at various Mach numbers, freestream densities with two test gases (air and argon) using an electric arc discharge upstream of a blunt cone model. Their results suggested that low density test conditions resulted in an ineffective interaction and argon was found to be more receptive to energy deposition than air due to lower number of degrees of freedom. The energy spot was not found to be strong enough to produce its own shock, and the shock structure observed was a result of the heated channel formed behind the energy source interacted with the blunt body shock that causes flow alteration. A maximum drag reduction of about 50% and 84% reduction in stagnation point heating rate was observed momentarily as a result of energy addition only in argon environment.

Current investigation aims at the investigation of flowfield due to electric discharge occurring between two electrodes in front of the blunt models. And the effect of discharge is evaluated in comparison to no discharge case with the electrodes. The effect of the truncation, the distance between the electrodes and the model are examined.

2 Experimental Setup and Models

All of the experiments are conducted in the High SuperSonic Tunnel (HSST) of the University of Manchester. The tunnel is of the intermediate blowdown (pressure-vacuum) type which uses dry air as working fluid. The details of the facility together with standard instrumentation for stagnation pressure and temperature mesurements as well as high speed schlieren photography setup can be found in Ref. [12]. The layout of the optical setup and the data acquisition architecture with measurement chain is shown in Fig. 1. Lift, drag and pitching moment measurements are collected by a 3-component Aerotech© force balance. The details of the force balance can be found in Ref. [13].

High voltage is generated inside an earthed Faraday cage that is positioned just underneath the test section. The details of the components and connections can be found in Ref. [13]. The high voltage output is routed inside the test section with insulating wires and connected to one of the two electrode holders. A schematic diagram of the electrode arrangement that shows reasonable flow interference with enough structural stability is shown in Fig. 1. In this arrangement, the electrodes are at an angle of 63° with the flow direction and with their tips at distances of

$l/d_t = 1.5, 1.3 and 0.9$ from the model, where d_t is diameter of the truncated face encountering the flow. The distance over which the arc is created is kept around 2mm as it has been suggested by Knight [11] and Kolesnichenko [8] as the most efficient energy addition processes with very thin channels. The voltage output is monitored using a LeCroy PPE-20kV high voltage probe and the current is monitored using a Tectronix current probe. These output signals are connected to a Picoscope 3201 250MHz oscilloscope.

Test models for the drag reduction studies are an axisymmetric cone-cylinder model with two blunt faced truncated cone-cylinder models, as shown in Fig. 1. It has to be noted that the dimensions are in mm.

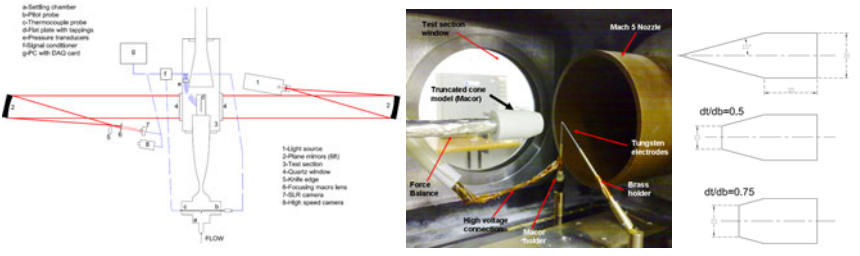

Fig. 1 Left: Schematic setup of Schlieren visualisation with DAQ architecture by Erdem et al. [12]. Middle: Electrodes arrangement inside test section. Right: axisymmetric cone-cylinder models.

3 Results

The freestream flow conditions are tabulated in Table 1 for all the tests.

Table 1 Free stream conditions at Mach 5.

M_∞	p_0 $(mbar)$	T_0 (^0K)	Re/m $(\cdot 10^6 1/m)$	p_{dyn} $(mbar)$	p_∞ $(mbar)$	u_∞ (m/s)
5.0 $\pm$0.2%	6495 $\pm$0.6%	372.3 $\pm$2.3%	13.2 $\pm$3.9%	215 $\pm$1.4%	12.28 $\pm$1.3%	790$\pm$1.2%

The efficiency of energy deposition on drag reduction is the ratio of the propulsive power savings due to flowfield modification divided by the energy required to modify the flow and defined as $Eff = \int V_\infty (D_0 - D) dt / \sum Q$. Large values are desirable for effective drag reduction.

3.1 Visual Observations and High Speed Schlieren Photography

Tests without and with discharge are conducted to examine the effects of the presence of electrodes and the energy deposition. The flow interference and stability of the electrodes are investigated. The truncated cone-cylinder with $d_t/d_b = 0.75$ is chosen for that purpose due to its greater frontal area compared to electrode diameters and the size of the arc as the efficiency is proportional to the ratio of the cross section of the aerodynamic body to the cross section of energy deposition, depicted by Knight [11]. The distance between the electrodes and the truncated face is set to 1.5 times the truncation diameter. At the start of the run the electrodes move downstream due to aerodynamic force and then stabilise for the rest of the run. The main effect of the electrodes is the destruction of the strong bow shock in front of the model and the formation of relatively weak axisymmetric oblique shocks instead, sitting on top of the wake. This wake is causing low frequency oscillatory behaviour of the oblique shocks.

For the tests with discharge measured voltage history during a tests is shown in Fig. 2 with subfigures showing the physical phenomenon. Before the test vacuum conditions are present with $p_{vac} = 1mbar$, hence a region of certain size in the earthed electrode is glowing. The voltage is around 0.6kV at that duration of time. When the test gas arrives glow discharge transforms into an arc that sustain steadily and convects downstream about $5.0mm$. This distance is named as the relaxation distance by Satheesh and Jagadeesh [10]. The voltage level is around 0.6kV during the steady period. The current in this period is about 0.011A making the consumed power around 7W; thus considering the flow energy is around 370kW for the flow condition specified in Table 1, the input electrical energy is merely 0.02% of the flow energy.

The discharge-on case is compared to discharge-off case in terms of schlieren images recorded at 20000 fps with 3.25μ sec exposure. The statistical analysis from schlieren images is conducted based on 1000 images during the period when the electrodes are stabilised. In order to quantify the shock wave positions, a number of image processing algorithms were developed to extract the required information from the images. Firstly the sharpening and edge-detection filtering are applied and then averaged and root mean square images are obtained as shown below in Fig. 2. The difference is barely distinguishable from the discharge-off case for truncation cone-cylinder with $d_t/d_b = 0.75$. The reasons for that might be the strong dominant wake of the electrode resulting unsteady behaviour at the nose of the model as well as the low energy input. Thus the influence of arc becomes small, yet in both case the bow shock in front of the model is killed and upstream flow structure is altered. As a consequence the reduction in drag force on the frontal area is accomplished. For the discharge-on case the compression wave structure has further moved about 1mm downstream with discharge, resulting a longer wake. This is believed as the cause of reduced stagnation pressure on the frontal area by the authors as the stagnation pressure reduction varies with the length of the thermal spot and the density in the heated zone.

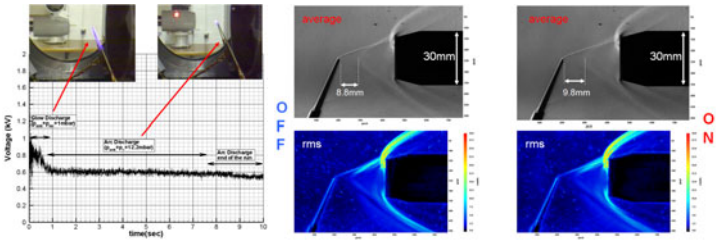

Fig. 2 Left: Voltage history during a test run with discharge over a truncated cone-cylinder with $d_t/d_b = 0.75$. Right: Comparison of discharge-on case with discharge-off case in terms of averaged and rms Schlieren images over a truncated cone-cylinder with $d_t/d_b = 0.75$ and $l/d_t = 1.5$.

3.2 Drag Force Measurements

Fig. 3 shows measured drag force signals for the truncated models. The images show the drag histories for the truncated cone-cylinder models with $d_t/d_b = 0.75$, $d_t/d_b = 0.5$ and varying distances between the electrodes and the truncated face. There are three repeats conducted for each case without and with discharge. The repeatability of the tests without discharge is very good; however the tests with discharge show test to test variations and fluctuations owing to the unsteady interaction with the heated channel and the compression waves. In addition the drag force history in all cases exhibits a steady decrease during the test runs, which is found to be around $\pm 4\%$ throughout the run. It can be easily observed that drag level reduces considerably just by the presence of the electrodes (from 14.75N to 6.5N level for model with higher truncation) due to the significant modification of the bow shock mentioned above, a passive effect namely. At the nearest distance, i.e $l/d_t = 0.9$ the drag levels have the highest value around 10N, however the drag reduction is very clear between the discharge off and on. As the distance increases the drag levels become smaller so does the drag reduction up to $l/d_t = 1.5$. For the other truncated cone-cylinder model with $d_t/d_b = 0.75$; the arc discharge is efficiently reducing drag at the shortest distance yet the repeatability for the ON case from run to run is slightly degraded. As the distance is increased drag reduction vanishes and energy deposition becomes ineffective. This might be due to the fact that the area of the energy spot becomes comparable with frontal face area.

The following table summarises the measured drag force values for truncated models without and with discharge.

The real contribution of the discharge is varying from 0 to 0.64N, in terms of efficiency (Eff) the maximum reduction results a value of around 72 (not percent) at a speed of 790m/s. This clearly shows that the use of small amount of onboard energy to create a local focused thermal spot in front of a vehicle is an efficient way of reducing drag. Following figure further shows the effectiveness of arc discharge on truncated cone-cylinder models with increasing distance between the electrodes and the frontal area. As a general trend the effectiveness is diminishing as the distance

Table 2 Drag force comparison of the truncated cone-cylinder models without and with discharge. All the values are in N.

Model Name	OFF l/dt=0.9	ON l/dt=0.9	OFF l/dt=1.3	ON l/dt=1.3	OFF l/dt=1.5	ON l/dt=1.5
Truncated Cone-cylinder ($d_t/d_b = 0.75$)	10.06±0.8%	9.42±1.1%	7.91±0.7%	7.61±1.6%	8.78±0.7%	8.42±2.4%
Truncated Cone-cylinder ($d_t/d_b = 0.5$)	5.83±0.6%	5.26±3.3%	5.24±0.5%	5.23±0.8%	5.14±0.7%	5.17±0.2%
Cone-cylinder	2.78±0.2%	without	electrodes			

is increased for both models. It might be due distance stabilisation phenomenon mentioned by Georgievskii and Levin [1]. In case of the model with higher truncation the decreasing trend is milder than the model with $d_t/d_b = 0.5$. Considering the electrodes and the energy spot have a certain size adding up to 3mm, as the frontal

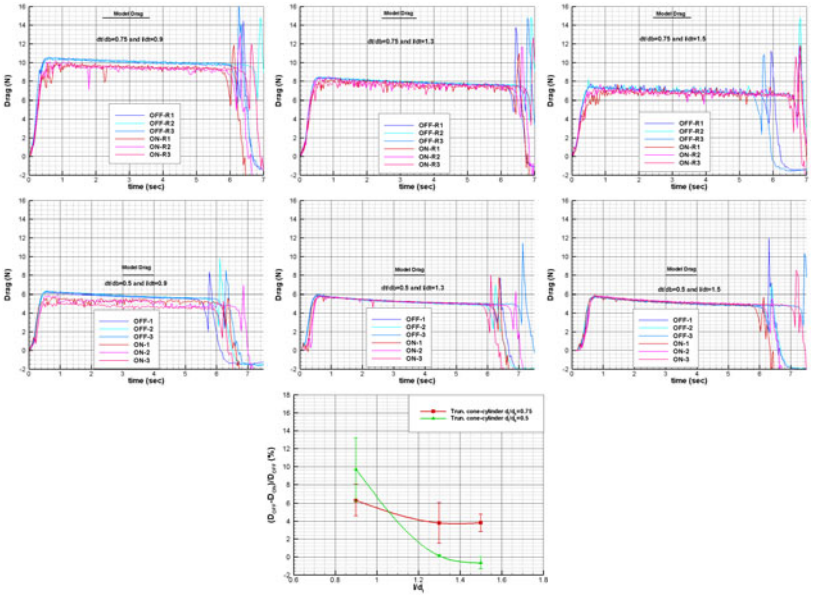

Fig. 3 Comparison of discharge-on case with discharge-off case in terms of drag force histories over truncated models; top left: $d_t/d_b = 0.75$ and $l/d_t = 0.9$, top centre: $d_t/d_b = 0.75$ and $l/d_t = 1.3$, top right: $d_t/d_b = 0.75$ and $l/d_t = 1.5$, middle left: $d_t/d_b = 0.5$ and $l/d_t = 0.9$, middle centre: $d_t/d_b = 0.5$ and $l/d_t = 1.3$, middle right: $d_t/d_b = 0.5$ and $l/d_t = 1.5$, bottom centre: the effectiveness of arc discharge on truncated models against distance between the electrodes and the frontal area.

area is increased the effectiveness increases from 0 to 9% for smaller truncation and from 4 to 6.7% for higher truncation. Shorter distances and bigger energy deposition area to frontal area ratios are favourable for effective drag reduction.

4 Conclusion

Experiments addressing the effect of energy deposition via an electric arc discharge on 15° half angle truncated cone-cylinder configurations at Mach 5 flow were carried out. Discharge-on tests were compared to discharge-off tests to evaluate the net effect of energy deposition. Visual observations revealed that there is a certain size of the relaxation distance as the test gas sweeps the energy spot downstream forming a heated wake. The compression waves occur on top of the wake of the heated channel and are oscillatory in nature. The deposited energy of 7W has its repeatable influence on drag force for all the models. The effectiveness of energy deposition was found to be increasing with increasing truncation or the frontal area up to a point and then started to decrease. One important thing to note is that energy deposition at shorter distances might result higher stagnation point heating rates which are detrimental. As a final conclusion the test campaign clearly renders that the use of small amount of onboard energy to create a local focused thermal spot in front of a vehicle is an efficient way of reducing drag.

References

1. Georgievskii, P., Levin, V.: Supersonic Flow over a Body with Heat Supply Ahead of it. In: Proceedings of the Steklov Inst. of Mathematics, Steklov Inst. of Mathematics, pp. 229–234. American Mathematical Society, Providence (1991)
2. Myrabo, L.N., Raizer, Y.P.: Laser Induced Air Spikes for Advance Trans. Atmospheric Vehicles. AIAA 1994-2451
3. Levin, V.A., Terent'eva, L.V.: Effect of a Local Energy Supply Region on 3-D Flow Around a Cone. Fluid Dynamics 31(3), 388–394 (1999)
4. Riggins, D., Nelson, H.F., Johnson, E.: Blunt-Body Wave Drag Reduction using Focused Energy Deposition. AIAA Journal 37(4), 460–467 (1999)
5. Kolesnichenko, Y., Brovkin, V., Azarova, O., Grudnitsky, V., Lashkov, V., Mashek, I.: Microwave Energy Release Regimes for Drag Reduction in Supersonic Flows. AIAA 2002-0353
6. Girgis, I.G., Shneider, M.N., Macheret, S.O., Brown, G.L., Miles, R.B.: Creation of Steering Moments in Supersonic Flow by Off-Axis Plasma Heat Addition. AIAA 2002-0129
7. Zheltovodov, A.A., Pimonov, E.A., Knight, D.: Energy Deposition Influence on Supersonic Flow over Axisymmetric Bodies. AIAA 2007-1230
8. Kolesnichenko, Y.F., Brovkin, V.G., Khmara, D.V., Lashkov, V.A., Mashek, I.C., Ryvkin, M.I.: 2004 4th Int. Workshop on Thermochemical and Plasma Processes in Aerodynamics (2004)
9. Myrabo, L.N., Raizer, Y.P., Shneider, M.N., Bracken, R.: Reduction of Drag and Energy Consumption during Energy Release Preceding a Blunt Body in Supersonic Flow. Heat and Mass Transfer and Gasdynamics, High Temperature 42(6), 901–910 (2004)

10. Satheesh, K., Jagadeesh, G.: Experimental Investigations on the Effect of Energy Deposition in Hypersonic Blunt Body Flow Field. Journal of Shock Waves 18, 53–70 (2008)
11. Knight, D.: Survey of Aerodynamic Drag Reduction at High Speed by Energy Deposition. Journal of Propulsion and Power 24(6), 1153–1167 (2008)
12. Erdem, E., Yang, L., Kontis, K.: Drag Reduction by Energy Deposition in Hypersonic Flows. AIAA 2009-7347
13. Erdem, E., Yang, L., Kontis, K.: Drag Reduction Studies by Steady Energy Deposition at Mach 5. AIAA 2011-1027

Interaction of a Shock Wave with a Contact Discontinuity for Local Heat Release in a Flow

P. Tretyakov, A. Tupikin, and V. Zudov

1 Introduction

It is known [1] that the interaction between shock waves and a discontinuity surface is poorly studied, in particular, in the presence of a local unsteady heat release in the flow. Increased interest in the propagation of shock waves in a moving medium is caused by the problems arising when studying supersonic burning in gas and optical discharges and the generation of control efforts on a flowed around surface with the organization of a heat release zone above it. An unsteady contact surface can exist, for example, in the wake of a pulse-periodic optical discharge. It is possible to single out the line recently developed and related to the possibility of attenuating a shock wave after the passage of the thermal layer formed by a pulse-periodic energy source [2, 3, 4, 5]. When the incident shock wave interacts with a contact discontinuity surface, transmitted and reflected disturbances arise.

In second part we will considers a jet trace in a supersonic flow, which represents a narrow but rather extended region with gasdynamic parameters (temperature, density) sharply different from those in the oncoming flow. We considered unsteady interaction of a shock wave with a heated layer (jet trace) and analyzes how a reduced density and lower Mach number in this layer as compared to those in the main flow influence the regimes of its interaction with the incident shock wave.

2 Numerical Computation of the Flow with Energy Supply over a Flat Plate

We considered the unsteady problem on shock wave diffraction in the wake from the pulse-periodic energy source. In a supersonic steady flow with Mach number

P. Tretyakov · A. Tupikin · V. Zudov
Institute of Theoretical and Applied Mechanics, Siberian Branch
Russian Academy of Sciences, Novosibirsk, 630090 Russia

M = 2, the pulse-periodic energy source with the ratio of 4 : 1 between the longitudinal and transverse sizes is arranged above the surface. The energy release time is 10^{-6} s. The pulse repetition rate is 100 kHz. The calculations were carried out in the range E = 1÷15 J of the energy supplied in one pulse to the selected mass. From the problem formulation, it follows that the wake is formed behind the energy source, and then, the shock wave reflected from the surface falls on it. The problem is considered within the framework of the Euler twodimensional unsteady equations with a constant adiabatic exponent. For solving the Euler equations, we used the Godunov method. In the calculations, an unsteady shock wave generated in front of the pulse-periodic energy source was obtained; the wave fell on the surface and reflected also as the shock wave. Depending on the energy source intensity, a supersonic, transonic, or subsonic quasi steady wake [2] can be generated behind it. The calculations show that the velocity in the wake from the energy source is very high and exceeds 10÷15 times that outside the wake for the energy range E = 8÷15 J. For these energies, the density in the wake is several tens times lower than that in the region outside the wake. For high energy supply frequencies (f≥50 kHz), the moving gasdynamic regions (packages), which either follow one after another or move with partial superposition against each other [2], are formed in the flow. The velocity in packages can be both subsonic and supersonic. The length of these packages is commensurable with the length of the energy supply region. The packages moving downstream are decelerated by the external flow, the longitudinal velocity of which, as was already noted, is much lower than the longitudinal velocity inside the wake. At low supplied energies, it can result in a global transition of the flow in the wake through the speed of sound in a certain downstream cross section, i.e., further behind the sound line, the flow in the wake is completely subsonic. Nevertheless, this subsonic velocity is much higher (approximately 5 times) than the longitudinal velocity outside the wake. At the place of transition of velocity through the speed of sound, an expansion of the transverse cross section of the wake takes place. Therefore, the shock wave is formed at this place on the external side of the wake. It has an unsteady character, which is expressed in its vibrations with respect to a certain middle position. The variation of the supplied energy within E = 1, 8, 15 J results in a considerable modification of the flow structure in the wake. At the energy E = 1 J, the wake behind the energy source becomes almost completely supersonic. It occurs before the interaction between the shock wave and the wake. The velocity in the wake exceeds that outside the wake approximately 1.5 times. The incident shock wave passes through the wake and propagates under a certain angle in the upper region outside the wake (Fig. 1). The disturbance reflected from the contact surface is very weak. At E = 8 J, it is possible to note the following features: at the initial portion, the wake becomes transonic, and then, the transition through the speed of sound takes place in the wake, and the shock waves are formed at its lower and upper boundaries (Fig. 1).

The shock waves have an unsteady character. It manifests itself in their vibrations with respect to a certain middle position. The amplitude of the shock wave vibrations can be significant. For example, the spatial vibration amplitude $\Delta x \approx 8$ (the length of the energy supply region is 4) at the energy E = 12 J. If we

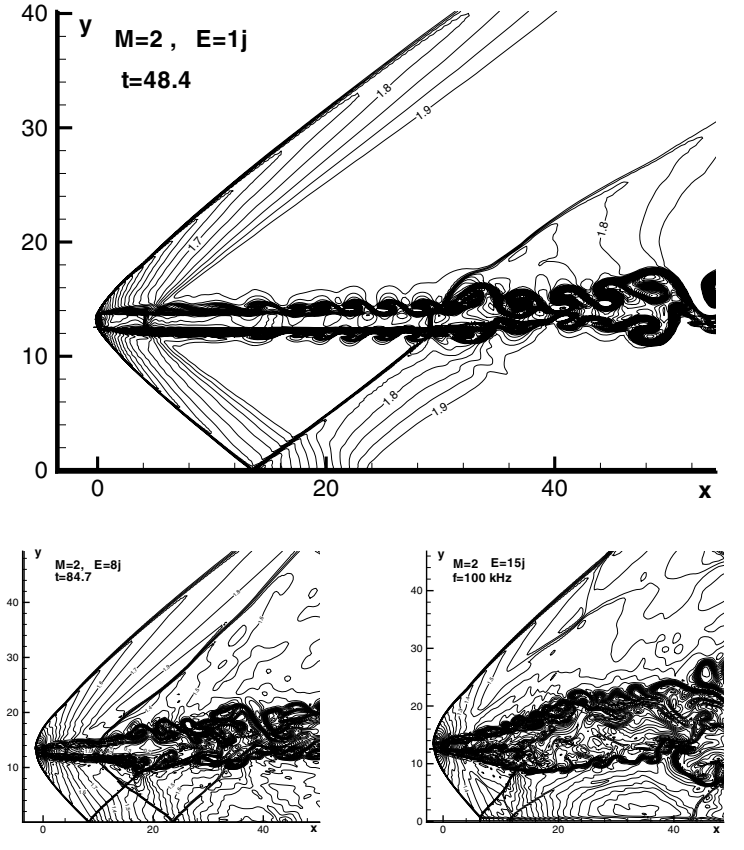

Fig. 1 Mach number isolines. E = 1 (top), 8(left), 15 J(right); M = 2,f = 100 kHz.

compare it to the sizes of the energy source, the amplitude of spatial vibrations was either comparable to the energy source length or exceeded it approximately twice depending on the supplied energy. The estimations of frequency of the shock wave vibrations show that it was about several hertz. The quasi steady head shock wave generated in front of the energy source falls on the surface and is reflected from it as the quasi steady shock wave. The reflected shock wave falls now on the subsonic portion of the wake and is reflected from it as a rarefaction fan (Fig. 1). At E = 15 J, the flow in the wake is completely subsonic , which results in the disappearance of shock waves on its external side (Fig. 1(right)). The shock wave reflected from the wall falls on the subsonic wake and is reflected from it as a rarefaction fan.

This part of our work we considers unsteady interaction of a shock wave with a heated layer (jet trace) and analyzes how a reduced density and lower Mach number in this layer as compared to those in the main flow influence the regimes of its interaction with the incident shock wave. Let a gas jet of limited height to occur in a supersonic flow of an ideal gas. The parameters of this jet can be either super or subsonic. The jet symmetry axis is parallel to the velocity vector on the oncoming flow. Let a wedge shaped body to be suddenly introduced into the supersonic flow so as to generate a shock wave that begins to interact with the jet trace. A jet trace with a height of 1 cm occurred in a supersonic flow with a Mach number of M = 2. All calculations were performed for air at a flow velocity corresponding to M = 2.0, a total pressure of P_0 = 0.25 MPa, and a retardation temperature of T_0 = 288 K. The shock wave was generated by a wedge with an angle of 20. The main flow velocity was always supersonic, whereas the jet velocity was varied from sub to supersonic. The main flow was characterized by the Mach number, total pressure, and temperature; the jet was characterized by the Mach number] and the pressure that was equal to that in the main flow. In addition, the ratio of densities in the main flow and in the jet was also specified. Calculations were performed for the jet efflux with M_j = 0.7, 1.05, and 2.0 and the jet density being half that in the main flow. Let us consider changes in the flow structure depending on the Mach number in the jet trance. Figure 1 shows the results of calculations for M_j = M = 2. Since the pressure in the jet is the same as in the main flow, while the densities differ by a factor of 2, the equation of state suggests that the temperature in the jet will be twice that in the main flow. Note the following features in the flow structure. The jet remains supersonic behind the;point of interaction of the incident shock wave and the jet trace. The. shock wave produces the following changes in the jet trace structure. The shock wave passes through the jet trace and then propagates at a certain angle relative to it. The transmitted shock wave retains a significant intensity. The differential head (i.e., the ratio of pressures behind and in front of the shock wave) is 2.8 in the incident shock wave and 2.41 in the transmitted shock wave, which implies that the shock wave attenuation is small. Inside the jet trace (in the interaction region), the jet velocity does not exceed the velocity of sound. The flow structure pattern shows that the jet trace rather weakly changes its height (Fig. 1). Now let us consider the second regime of flow, which corresponds to M_j = 1.05 (Fig. 2). In contrast to the case considered above, the jet trace exhibits a new effect, whereby a transonic transition takes place and shock waves are formed at the corresponding sites on the lower and upper boundaries of the jet. The transonic transition takes place inside the jet, at the forward shock, which continues outside the jet in the form of oblique shock waves. The forward head occurs on the left of the point of intersection of the incident shock wave and the jet boundary (initially, the forward head exhibits nonstationary propagation upstream the flow and then occupies a certain stationary position).

The transmitted shock wave is inclined at a smaller angle than the incident shock wave. The intensity of the transmitted wave is still significant. Indeed, the differential head changed from 2.8 in the incident shock wave to 1.97 in the transmitted shock wave, so that the attenuation is still not large. The jet exhibits an extended

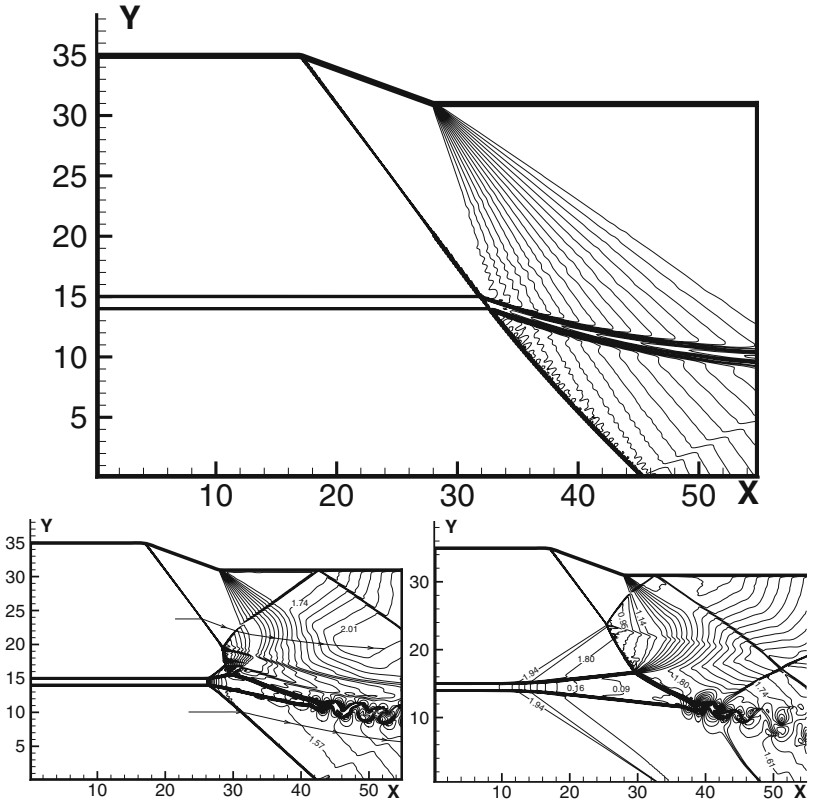

Fig. 2 top – Pattern of Mach number isolines for M = M_j = 2; left–M = 2, M_j = 1.05; right–M = 2, M_j = 0.7.

subsonic region immediately behind the forward head. The transverse section in this region significantly exceeds the initial jet height. Subsequently, the subsonic jet becomes supersonic. The point of arrival of the incident shock wave is the break point of the jet boundary. Thus, an expansion corner appears in which the incident shock wave coexists with a fan of rarefaction. Note also the presence of a reflected shock wave in the region above the jet trace boundary (Fig. 2).

Finally, consider the third regime of flow with $M_j = 0.7$ (Fig. 2). First, note that a decrease in the M_j value leads to a significant increase in the region where the jet trace is affected by the incident shock wave. The perturbation goes farther upstream the flow from the point of interaction of the shock wave with the jet trace. In contrast to the case of M_j = 1.05, the third regime is characterized by a smooth expansion of the jet boundary. Instead of a cone shaped head, there appears a region of compression, in which the slope of the Mach number (or density) isolines relative to the jet axis is small. The maximum increase in the transverse section of the jet is observed at the point of arrival of the incident shock wave on the jet boundary (Fig. 2). The jet

also becomes supersonic at a certain distance downstream the flow from, the interaction region. In contrast to the regimes considered above, waves of compression are formed on the outer (upper and lower) boundaries. Previously, a transmitted shock wave was observed and a fan of rarefaction was formed at the point of interaction of the incident shock wave with the boundary of the subsonic jet. The differential head in the transmitted shock wave dropped to 1.4. Thus, a decrease in the Mach umber of the heated layer is accompanied by decreasing differential head in the transmitted shock wave. A minimum value is observed for the heated subsonic jet trace. Therefore the intensity of the incident shock wave can be significantly attenuated by interaction with a heated subsonic jet trace.

3 Conclusion

Thus, the obtained results indicate the fact that three modes of interaction are possible depending on the released energy.

The results of numerical calculations revealed three possible regimes of the interaction of incident shock waves with a heated layer of finite thickness. A significant decrease in intensity of the incident shock waves takes place during its interaction with a heated subsonic jet trace.

References

1. Cherny, G.G.: Gas Dynamics. Nauka, Moscow (1988) (in Russian)
2. Zudov, V., Tretyakov, P., Tupikin, A., Yakovlev, V.: Supersonic Flow Past a Thermal Source. Fluid Dynamics 38(5), 782–793 (2003)
3. Tretyakov, P., Grachev, G., Ivanchenko, A., et al.: Dokl. Akad. Nauk 336(4), 466–467 (1994) (in Russian)
4. Zudov, V.: Influence of a Periodic Pulsed Energy Source on the Regime of Supersonic Flow past a Body. J. Technical Physics Letters 35(4), 315–317 (2009)
5. Zudov, V., Tretyakov, P., Tupikin, A.: Unsteadiness Effects at a Pulsed-Periodic Energy Supply. AIAA Paper No. 2009-3586, San Antonio, TX (2009)

Part XXIII
Student Competition

Head on Collisions of Compressible Vortex Loops on a Solid Wall Effects of Wall Distance Variation

R. Mariani and K. Kontis

1 Introduction

Since the dawn of time, human kind have felt the presence of shock waves in nature through thunders and vulcano eruptions and, unable to understand them, have associated their often destructive might to divinities such as Zeus and Jupiter in the Greek and Roman mythology, the Norse divinity of Thor, and the elusive Thunderbird in the Native North American culture. Through history, albeit unknowingly, humans have been able to generate shock waves via the cracking of a whip or the explosion of fireworks. It was the invention of the atomic bomb that brought back fear and respect towards the might of this natural phenomena [1]. For research purposes, shock waves can be easily generated in a laboratory environment using shock-tubes where a high-to-low pressure discontinuity is initially present. The disruption of this discontinuity initiates a series of waves that coalesce into a single compression wave travelling downstream [2]. Upon exiting the shock tube into the surrounding atmosphere, the moving shock wave transitions attenuating from a planar to a spherical shock wave. In the presence of confining walls, it reflects from the surrounding surfaces producing high levels of blasts and reflections [3]. The flow contained in the shock tube also exits forming a contact surface with the external fluid. This contact surface is carried away from the tube exit and starts rolling to form a vortex loop [4]. The interaction of this vortex loop with a wall and the reflected shock wave is still a topic of extensive research.

Significant work has been conducted on the topic of supersonic jets impinging on stationary flat surfaces. An initial comprehensive study was carried out by Ladenburg et al. [5] who summarised the work by Mach and Prandtl stating that the oblique shock system present in the jet is reflected by the jet boundary with a change in phase and that the resulting Mach reflection (MR) configuration is stationary rather than a transient non-stationary phenomenon. With the space race in

R. Mariani · K. Kontis
The School of MACE, The University of Manchester
Sackville St., M60 1QD Manchester (UK)

full swing in the 1960s and the goal of landing on the moon and safely returning to Earth by the end of the decade, studies were completed by NASA on the effects of jet impingement on a flat surface in vacuum conditions with a high Mach number jet [6]. Three shock formations were found to exist based on the surface distance and pressure ratio. At close plate distances, a stand-off shock wave is formed close to the surface. With an increase in plate distance, the stand-off shock behaves similarly to a Mach disk and moves closer to the nozzle exit transitioning, at very large distances, to an oblique shock system in the jet with a normal shock at the plate surface. Further studies were completed by Lamont and Hunt [7] who characterised the flow into a highly complex mixture of subsonic and supersonic regions with interacting shocks and expansions regions in the jet. They also described the presence of a stagnation bubble with recirculation and separation of the boundary layer over the plate. This work was expanded by Henderson et al. [8, 9] by studyng the effects that the impingement has on the sound production. The interaction amongst stationary objects, shock waves, and compressible vortex loops has been studied at the University of Manchester by Kontis et al. [3, 10]. The shockwave is reflected from the plate impinging on the approaching vortex ring. The central part of the reflected shock wave is captured by the vortex ring and is intensified by the opposing high speed flow, while the outher section is diffracted by the vortex core. Upon impingement the vortical flow rapidly expands radially developing a boundary layer on the surface which slows down the flow and increases the pressure distribution on the plate. After some time the boundary layer separates from the plate generating a series of secondary wall vortices. The combination of the shock/vortex and wall/vortex interactions is of great interest for future applications such as space vehicle return lift-off or non-destructive weapons and it is the aim of the present study to enhance the knowledge in the field of shock wave and compressible vortex loops interaction with a stationary flat surface.

2 Experimental Set-Up

Experiments have been carried out in a 30mm inner diameter constant cross section shock tube. Air was used as both the driver and driven gas with a diaphragm pressure ratio P_4/P_1 of 12, producing a Mach number of 1.61. The shock wave Mach number M_1 was used to calculate the critical length of the driver section needed to eliminate the disturbances caused by rarefaction waves reflected by the end wall of the driver section[2]. High speed schlieren photography was employed to visualize the flow. The schlieren set up was the same as previously used at the University of Manchester[11]. A Shimadzu HPV-1 hypervision camera was used to capture the flow features of the travelling vortex rings. A range of acquisition times was used which produced a set of 100 pictures per run. The image acquisition speed was 1600μs to 3200μs from the triggering moment. The repeatability of the Schliren experiment is determined by setting the same driver pressure, having the same time delay output, and acquisition speed. The repeatability error is found to be approximately 3%.

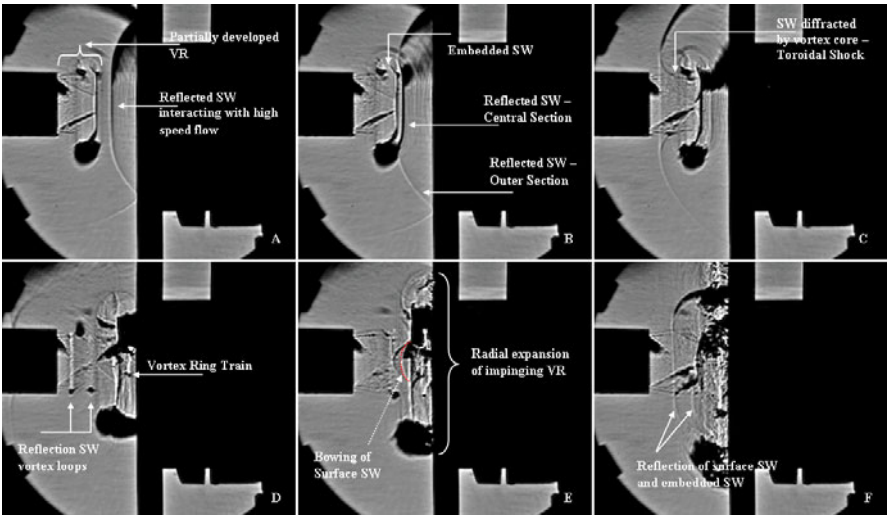

Fig. 1 Flow impingement process with a plate distance of $1.66d_i$.

3 Results and Discussion

An experiment has been conducted on the effects of the variation of distance on the head-on collision of compressible vortex loops on a stationary smooth flat wall. A standard pressure ratio P_4/P_1 of 12 generating a Mach number inside the shock tube of 1.61 was used. The surface was placed at a distance of $1.66d_i, 3.33d_i$, and $5.00d_i$ from the shock tube exit. The three distances correspond to a developing vortex loops ($1.66d_i$), a loop just after the full development threshold ($3.33d_i$), and a fully developed vortex loop ($5.00d_i$).

The configuration with the plate at $1.66d_i$ is shown in Fig. 1. The close proximity of the plate to the nozzle exit reduces the attenuation of the moving shock wave leading to a strong reflection process (A). The shock wave rapidly collides with the approaching vortex loop (B) and is deformed: the central part interacts and merges with the embedded rearward facing shock wave, which in a free vortex ring prior to impingement moves at the same speed as the vortex ring and where the pressure is higher upstream of the shock rather than downstream, while the outer section is refracted by the vortex core (C) generating a toroidal shock wave [12] which sides converge on the central axis at the back of the vortex loop [13]. The focusing process may affect the shape of the oblique shock system present in the vortex ring trailing jet. The reflected toroidal shock wave travels towards the shock tube exit and it is diffracted again generating a second set of vortex rings (D) which move towards the wall. The variation in the jet Mach number and pressure distribution along the plate varies the velocity profile across the jet leading to the formation of a dome shock between the oblique shock system and the impinging embedded

rearward facing shock (E). The dome shock transitions to a flat surface shock wave which is reflected along with the embdedded rearward facing shock (F)by the central section of the shear layer. During the impingement process the main vortex ring and the developing vortex rings train expand radially forming a shear layer on the wall ([14]) and continuously varying the pressure distribution on the plate.

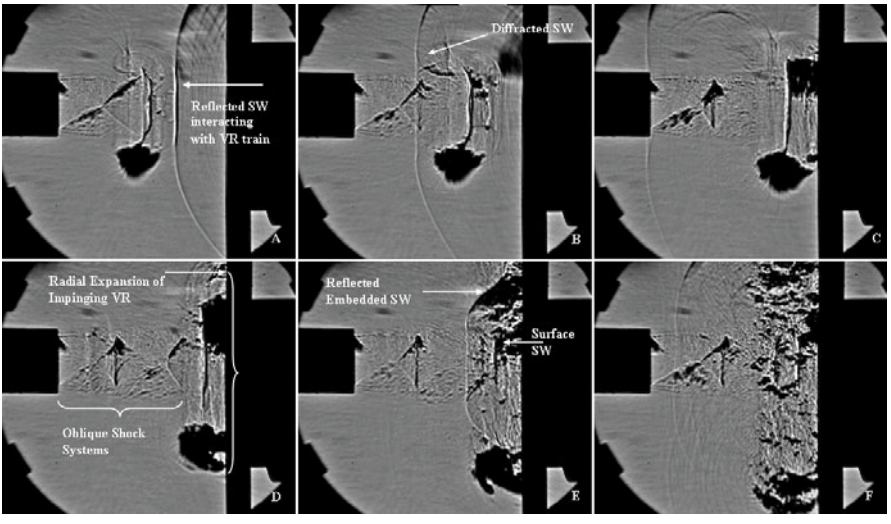

Fig. 2 Flow impingement process with a plate distance of $3.33d_i$.

An increase in surface distance affects the impingement process of both the incidence shock wave and vortex loop. With the plate at a distance of $3.00d_i$ as shown in Fig. 2, the incidence shock undergoes a larger attentuation prior to being reflected by the wall. The larger distance between the shock tube exit and the surface allows the vortex ring to fully develop. In this instance the reflected shock wave interacts first with the vortex rings train (A) causing an intensification of the vortex system. The centre section of the reflected shock again interacts and merges with the embedded rearward facing shock while its outer section is diffracted by the vortex core (B) ([12]). Results suggest that the diffraction is weaker since the focusing of the resulting toroidal shock wave does not appear to affect the flow structure of the oblique shock system in the trailing jet. The vortex ring then impinges on the surface with the embedded rearward facing shock undergoing a straightening process. The vortex rings train impinges and begins to expand radially (C) generating an area of strongly compressed flow between the wall and the embedded shock wave (D) which effectively reflects the embedded reardaward facing shock (D). At this stage a surface shock wave is formed (E), which is still visible during the formation of the secondary vortex rings linked to the development of a boundary layer on the surface, which changes the pressure distribution along the wall [3, 10].

At a plate distance of 5.00_{di} the vortex loop is fully developed (Fig. 3). The reflected wave interacts first with an almost fully developed vortex ring train (A),

where at least a set of counter rotating rings have completed the move around the periphery of the main ring, and subsequently with the main vortex loop. The shock/vortex interaction is similar to previously explained cases with the reflected shockwave inner section interacting with the embedded rearward facing shock in the vortex ring and the outer section being diffracted by the vortex core (B). The main vortex loop now impinges on the surface after the vortex ring train has moved around its periphery (C and D) reducing the visible turbulence in the flow along the wall surface (D) and reducing the reflection strength of the embedded rearward facing shock (E). The surface shock and the most downstream oblique shock system are visibly oscillating (E and F).

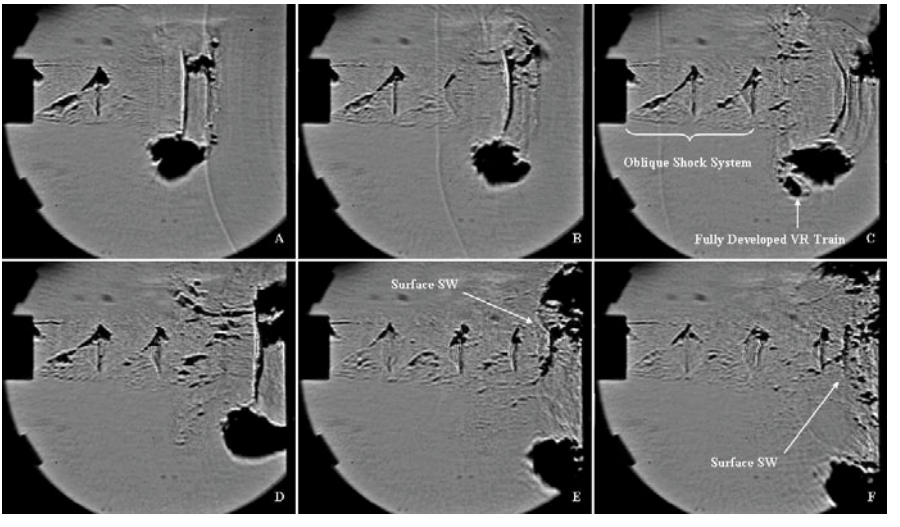

Fig. 3 Flow impingement process with a plate distance of $5.00d_i$.

4 Conclusions

An experiment has been conducted on the effects of the variation of distance on the head-on collision of compressible vortex loops on a stationary smooth flat wall. Qualitative results showed that there is a correlation between the shock/vortex interaction process and the nozzle exit-to-surface distance primarily linked to the development stage of the vortex loop. The most significant flow features are visible with the plate close to the nozzle exit resulting in a strong reflected shock wave interacting with the approaching vortex loop. As the surface distance is increased, the incidence and reflected shocks are increasingly more attenuated reducing the strength of the shock/vortex interaction. The increase in nozzle exit-to-surface distance results in a decrease in vortical flow generated on the wall due to a gradual decrease in strength of the moving vortex loop. The location and shape of the surfce shock are also affected.

Acknowledgements. The authors wish to acknowledge the financial support of the EPSRC and the technical staff at the University of Manchester for the manufacturing of the required experimental parts.

References

1. Glass, I.I.: Shock Waves and Man, pp. 1–7. The Toronoto University Press (1974)
2. Gaydon, A.G., Hurle, I.R.: The Shock Tube in High-Temperature Chemical Physics, pp. 1–107. Chapman and Hall (1963)
3. Kontis, K., An, R., Zare-Behtash, H., Koundais, D.: Physics of Fluids 20 (2008)
4. Broadbent, E.G., Moore, D.W.: Proc. Royal Soc. London Series A Mathematical and Physical Sciences 709 (1987)
5. Ladenburg, R., Van Voorhis, C.C., Winckler, J.: Physical Review 76 (1949)
6. Vick, A., Andrews Jr., E.H., Winckler, J.: NASA Technical Note D-3269 (1966)
7. Lamont, P.J., Hunt, B.L.: J. Fluid Mech. 100, 3 (1979)
8. Henderson, B.: J. Acoust. Soc. Am. 111, 2 (2001)
9. Henderson, B., Bridges, J., Wernet, M.: J. Fluid Mech. 542 (2005)
10. Kontis, K., An, R., Edwards, J.A.: AIAA Journal 44, 12 (2006)
11. Mariani, R., Kontis, K.: 47th AIAA Aerospace Science Meeting, Orlando AIAA2009-410, January 5-8 (2009)
12. Liang, S.-M., Ching, W.-T., Chen, H.: AIAA Journal 43, 2 (2005)
13. Tokugawa, N., Ishii, Y., Sugano, K., Takayama, F., Kambe, T.: Fluid Dynamics Research 21 (1997)
14. Minota, T., Nishida, M., Lee, M.G.: Fluid Dynamics Research 21 (1997)

Hypersonic Flow Past Spiked Bodies

R.G. Fernandes and J.L. Stollery

1 Introduction

The drag and heat transfer are very important parameters to be taken into account in the design of hypersonic vehicles. Under certain conditions, spikes can substantially reduce the drag of axisymmetric blunt bodies at supersonic and hypersonic speeds with the deliberate use of flow separation. This happens mainly due to the induced formation of a conical shock in opposition to a normal one.

The major parameter that controls drag reduction in spiked bodies is the spike length to model diameter ratio, l/d. Additionally, there are other parameters that have an impact in the drag reduction of the model such as the angle-of-attack, the spike tip geometry, the free stream Reynolds number or Mach number. Fig 1 shows the main features and terminology of the flow past spiked bodies.

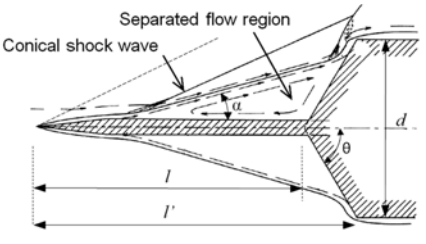

Fig. 1 Main features and terminology of flow past spiked bodies [1]

Nevertheless, a number of seemingly adverse factors have tended to discourage consideration of spiked blunt bodies for engineering applications. One of those is that, under certain conditions, unsteady separation regions may occur causing drag and heat transfer rates to fluctuate. However, probably the most discouraging reason

R.G. Fernandes · J.L. Stollery
Department of Aerospace Sciences, School of Engineering,
Cranfield University, Cranfield, UK

is the lack of a theory explaining the behavior of separated regions promoted by spikes. The ultimate objective of this study is to make an attempt to contribute to further knowledge in this area.

It is well known from the studies of [2] and later [1] that the shoulder geometry of the body is extremely important to the shock wave stability. However, to what extent the general shape of the nose of the cylinder is important to the overall characteristics of the flow is still not well understood. Therefore, the main aim of the present study is to analyse, through experiments, the consequences of having different nose geometries in terms of the flow pattern, drag reduction and shock unsteadiness.

2 Experimental Programme

Two cone-cylinder models with different cone semi vertex angles θ (see Fig. 1) were designed and tested at hypersonic speeds. Furthermore, additional data from [3], who tested an Apollo re-entry shape at the same conditions as the present study, were analysed together with the results gathered from the present experiments. The models can be seen in Fig. 2.

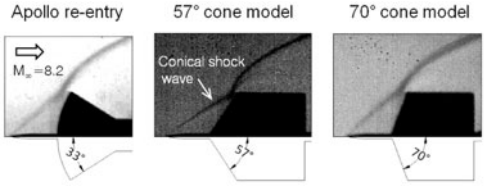

Fig. 2 Schlieren pictures of the different nose geometries analysed

The 57° cone model has the same shoulder angle as the Apollo re-entry capsule model. The objective of this model is to study the influence of the nose shape in the flow pattern and drag reduction. The 70° cone model was designed based on [1] and [4] results in order to have unstable shock waves for a limited range of spike lengths. The objective of this model is to study the shock unsteadiness as well as the drag reduction and flow pattern. Both models were equipped with a cylindrical steel spike of variable length, radius of $d/40$ and a conical spike tip angle of 7°. The angle-of-attack remained zero for the whole range of tests analysed in this study.

The models were tested in the Cranfield University gun tunnel (for details see ref. [5]) at a free stream Mach number (M_∞) of 8.2±0.05 and Reynolds number, based on body diameter, (Re_d) of $0.36 \times 10^6 \pm 7.6\%$. Schlieren images were recorded with a high speed digital camera operating at about 4000 frames per second. Drag force was measured with a force balance (for details see ref. [6]) for several spike lengths ranging from l/d equal to 0 to 2.75.

3 Results and Discussion

3.1 Flow Pattern

The separation angle α (see Fig. 1) is an important parameter that influences, among other things, the amount of drag that a spiked body experiences and the shape of the effective body. In Fig. 3 it is possible to see a compilation of data, gathered from the experimental results, that shows the behavior of this parameter with the spike length.

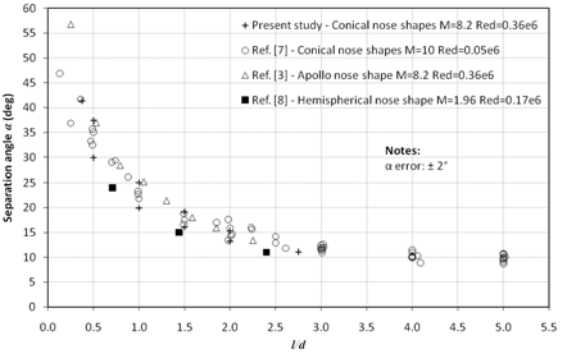

Fig. 3 Separation angle versus l/d

It was shown by many authors, such as [1] and [2], that the flow reattachment at the shoulder is of paramount importance. This suggests that a different length, l' (horizontal distance measured from the tip of the spike to the shoulder of the cylinder, see Fig. 1) might be relevant. Hence α is plotted against l'/d in Fig. 4.

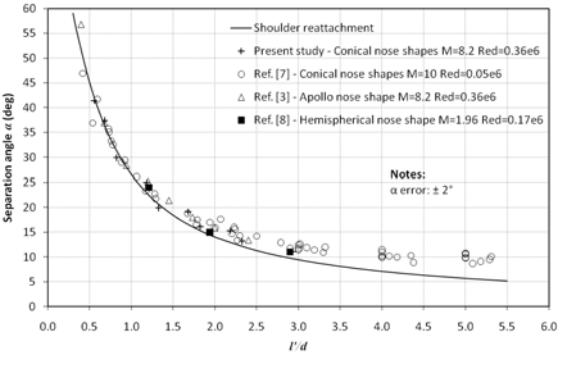

Fig. 4 Separation angle versus l'/d

In addition, the behavior of the separation angle if the separation had begun at the tip of the spike and if the flow had reattached at the shoulder of the cylindrical

body (named "shoulder reattachment"), which is based purely on geometrical considerations, is also shown in Fig. 4.

The experimental data follows the shoulder reattachment line very well until $l'/d \approx 1.5$. This fact might indicate that, for $l'/d > 1.5$, the separation point moves slightly downstream. In Fig. 5 this suggestion is confirmed through Schlieren pictures from [8] where it is shown the separation point moving downstream when l'/d is increased from 1.21 to 1.94.

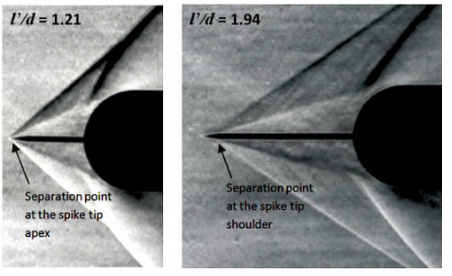

Fig. 5 Displacement of the separation point with increase of l'/d [8]

According to [9], the separation angle has low sensitivity to the variation of the Reynolds number until transition occurs in the shear layer. Furthermore, the data presented in Fig. 4 features three different M_∞: 1.96 for [8], 10.0 for [1] and 8.2 for the other references. This might be an indication that the separation angle has low sensitivity to the free stream Mach number too. If the separation angle behaves in this way, this trend may be a useful information for the development of a drag model for spiked bodies.

3.2 Drag Reduction

In Fig. 6 a comparison between the ratio of the drag coefficient (C_D) and the drag coefficient for the no-spike configuration (C_{D0}) for the different nose-shaped cylindrical bodies is made. The drag coefficients are based on the free stream parameters and on the frontal area of the cylinders.

There are important differences between the data from the three models that cannot be explained by experimental errors. It is noticeable that the spike is more efficient when it is applied to the 70° cone whereas there is not much difference between the drag reduction for the other two models. The reason for this behavior might be explained by the data in Fig. 7.

Fig. 7 shows that the C_{D0} for the 70° cone model is larger than the 57° cone model and the Apollo shape capped model. On the other hand, the C_D for the bodies with several spike lengths is almost the same for the three models compared.

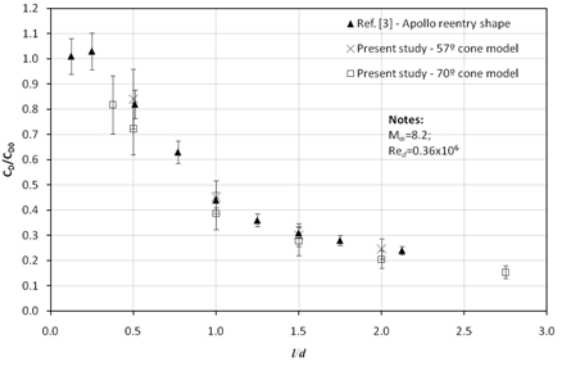

Fig. 6 Effect of the nose shape on drag reduction. Drag coefficient ratio versus l/d

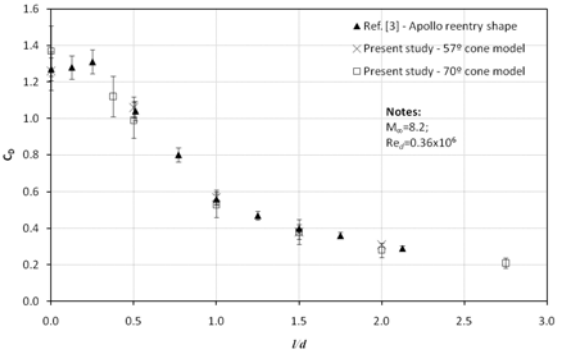

Fig. 7 Effect of the nose shape on drag reduction. Drag coefficient versus l/d

This fact explains the difference found in Fig. 6 where the spike was more efficient for the 70° cone model. This model has the greatest C_{D0} and, as the C_D is similar for the three models tested, it is logical that the ratio C_D/C_{D0} for the several spike lengths is smaller than the rest of the models.

The fact that C_D is similar for the three models tested means that when a spike is protruded in front of a body it alters the effective shape of that body in a way that is almost independent of its initial nose shape. Therefore, if one body is blunter than another, a spike protruded in front of it will be more effective in reducing drag.

3.3 Shock Unsteadiness

The 70° cone model was specially designed to have unstable flow for certain spike lengths. According to the results of [1] and [4] it is likely that for l/d between the shock stand-off distance and one the pulsation mode of instability is present (see Fig. 8b).

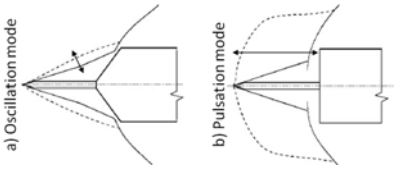

Fig. 8 Schematic of the instability modes [10]

However, for the experimental conditions of the present study the pulsation mode was not found for any spike lengths. The Schlieren pictures only showed the concave-convex lateral oscillation known as the oscillation mode of instability (see schematic in Fig. 8a and an example shown in Fig. 9 from the present study). This oscillation mode persisted within a limited range of spike lengths but with different intensities.

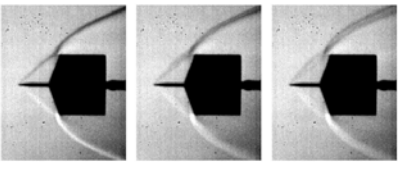

Fig. 9 Schlieren pictures of the oscillations around the 70° cone model with $l/d = 0.5$

In [11] the authors stated that their experiments showed that with increasing M_∞ the minimal cone vertex semi angle θ (see Fig. 1) at which pulsations occur increases too. Thus, there is a possibility that, for $M_\infty = 8.2$, the minimum θ at which pulsations occur is such that is greater than 70°. In relation to the results of [1] and [4], some important experimental conditions could have accounted for the non existence of the pulsation mode. Namely the M_∞ which was 8.2 in the present study and 10.0 in the aforementioned references and the fact that they used conical nozzles in the gun tunnel as opposed to the use of a contoured one.

4 Conclusions

It is an interesting fact that the separation angle follows l'/d while the drag coefficient follows l/d. One way of interpreting this behavior is that for the same l/d it was seen in Fig. 7 that the drag coefficients of the three different forebody shapes with spikes are similar. Conversely, each of those forebody shapes, for the same l/d, have different l'/d values associated with them and, hence, different separation angles (see Fig. 4). If they have different separation angles but similar drag coefficients, this means that the conical flow (whose pressure coefficient is highly dependent on the separation angle) is not the whole story. The overall drag of the body also depends critically on the pressures in and around the reattachment region.

In terms of the flow unsteadiness, the capture of sharp conical shock wave images (as shown in Fig. 9) as opposed to blurred ones due to the violent longitudinal oscillation (pulsation mode) is an indication of the absence of this flow instability. This fact should be further investigated in order to understand how this phenomenon behaves with the free stream parameters and general spiked body geometry.

References

1. Wood, C.J.: Journal of Fluid Mechanics 12, 4 (1962)
2. Maul, D.J.: Journal of Fluid Mechanics 8, 4 (1960)
3. D'Humières, G., Stollery, J.L.: Aeronautical Journal 114, 1152 (2010)
4. Holden, M.S.: AIAA Journal 4, 4 (1966)
5. Lanson, F., Stollery, J.L.: Aeronautical Journal 110, 1105 (2006)
6. Opatowski, T.: A three component gun tunnel balance designed for testing thin delta wings, R/M-3664 (ARC (1969)
7. Wood, C.J.: A study of hypersonic separated flows. PhD thesis, Imperial College London, UK (1961)
8. Mair, W.: Philosophical Magazine 43, 342 (1952)
9. Crawford, D.H.: Investigation of the flow over a spiked-nose hemisphere-cylinder at a Mach number of 6.8, TN-D-118, NASA (1959)
10. Feszty, D., Badcock, K.J., Richards, B.E.: AIAA Journal 42, 1 (2004)
11. Antonov, A.N., Shalaev, S.P.: Fluid Dynamics 14, 1 (1979)

Analytical Estimation of Microbubble Motion Exposed to Discontinuous Pressure Change

Shinya Fukuda, Biyu Wan, and Akihisa Abe

1 Introduction

The authors have proposed a new method for ship ballast water treatment using shock pressure generated by collapse of microbubbles. Our previous study showed that the marine *Vibrio* sp. in an aluminum container was killed by exposing to the excess pressure higher than 200 MPa directly generated in the suspending medium by the impact of a projectile accelerated with high-pressure gas [1]. Applying the shock pressure sterilization to a huge volume of ballast water, the projectile impact method is not a practical way to generate shock waves successively in liquids. For the practical use, we have suggested the use of microbubbles for one of the alternative methods as a micro-generator of impulsive pressures. When microbubbles collapse, they generate shock pressures and free radicals that can oxidize something around them [2, 3]. However, it has been not well known about the inactivation effects of shock pressure produced from collapse of microbubbles on the marine bacteria. In order to find the effective conditions on the shock wave sterilization, it is important to investigate the motion of microbubbles exited by shock waves experimentally and analytically.

The purpose of this study is to examine analytically the potential for generation of high impulsive pressure by spherical collapse of a microbubble exposed to shock waves. To confirm that, analysis combined with the experimental pressure records of shock waves is carried out. The basic bubble equation used in the analysis is Herring's bubble motion equation [4] for a single spherical bubble in compressible liquids. The experimental pressure record is obtained from the pressure measurement of underwater shock waves generated by high voltage electric discharge in a water tank. We investigated the condition of generating high impulsive pressure of over 200 MPa that probably inactivates marine bacteria.

Shinya Fukuda · Biyu Wan · Akihisa Abe
Graduate School of Maritime Sciences, Kobe University
5-1-1 Fukaeminami-machi, Higashinada-ku, Kobe 658-0022, Japan

2 Experimental Pressure Measurement of Underwater Shock Wave

Due to record of the incident shock pressure profile, the experiment was carried out using electric discharge in a water tank. Underwater shock wave was generated by means of high voltage electric discharge of an electric power supply (HPS18K-A, TAMAOKI ELECTRONICS Co-Ltd.). Figure 1 shows schematic diagram of the experimental setup. The electrodes were made of stainless steel, and polishing sharpened their tips up. In addition, the electrodes are covered by rubber paint for insulation except their tips, and the distance between the electrodes was about 8 mm. Pressure was measured by a fiber optic probe hydrophone (FOPH2000, RP acoustics). Its detective element of measuring pressure is the 100 μm diam. tip of optical fiber. The pressure is measured by the change of light reflection at the interface between fiber and water caused by the pressure/density influence on the refractive index of water. Therefore it is possible to measure short time high pressure with high spatial and temporal resolution by FOPH2000. In Fig.1, the dimensions of the tank were 180 mm $\times$ 250 mm $\times$ 180 mm, and the distance between discharge position and the tip of pressure sensor was approximately 60 mm.

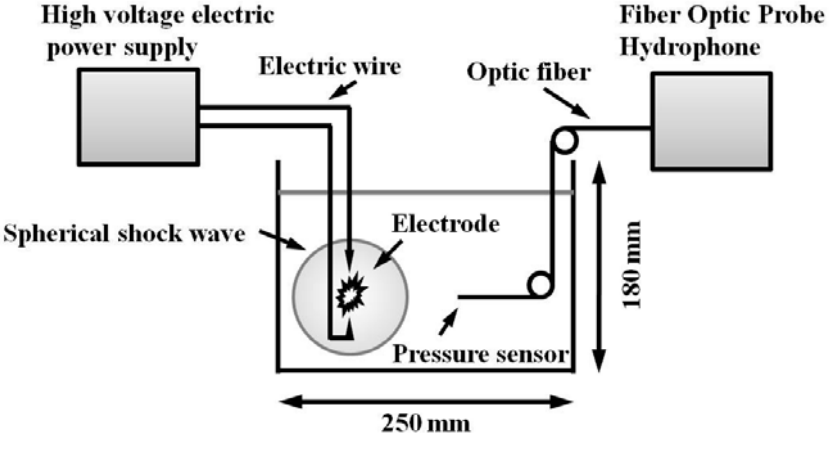

Fig. 1 Schematic diagram of the experimental apparatus

3 Analysis of Microbubble Motion

To estimate impulsive pressure generated by a spherical microbubble exposed to experimental shock wave pressure, Herring's bubble dynamics equation [4] is solved with one-dimensional spherical bubble model shown in Fig. 2. The gas in a bubble is considered as non-condensable and the initial pressure is equal to atmospheric pressure. Wolfrum,et al. have compared their experimental results of microbubble

motion induced by underwater shock wave with the prediction results of a simple one-dimensional model for spherical bubbles using the experimental shock pressure profile, and consequently they obtained good agreement about the first contraction and expansion [5].Though one-dimensional spherical bubble model calculated in the present analysis is also classical, the prediction of microbubble dynamics would bring useful information. Herring's bubble dynamics equation that takes compressibility of liquids into account is written in the following form;

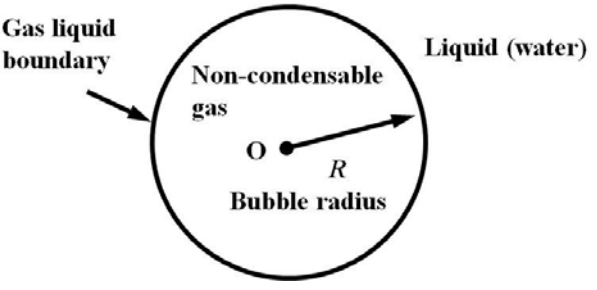

Fig. 2 One-dimensional spherical symmetry single bubble model

$$\left[R\left(1-\frac{2\dot{R}}{C}\right)+\frac{4\mu}{\rho C}\right]\ddot{R}+\frac{3}{2}\left(1-\frac{4\dot{R}}{3C}\right)\dot{R}^2 - \frac{1}{\rho}\left[P_{b0}\left(\frac{R_0}{R}\right)^{3\gamma}\left(1-\frac{3\gamma\dot{R}}{C}\right)+\frac{2\sigma+4\mu\dot{R}}{R}\left(\frac{\dot{R}}{C}-1\right)-P\right]=0, \quad (1)$$

where, R is the bubble radius, R_0 the initial bubble radius, ρ = 999.7 kg/m^3 the density of water, μ=1.307$\times$10^{-3} Pa·s the viscous modulus, σ = 74$\times$10^{-3} N/m the surface tension, γ =1.4 the specific heat of bubble gas, P the external pressure induced by the shock wave, and P_{b0} the initial bubble internal pressure. C is the speed of sound in the liquid given by the following relation;

$$C=\sqrt{\frac{n(P+B)}{\rho}}, \quad (2)$$

here, constant values are n = 7.15 and B = 304.7 MPa. Bubble internal pressure P_b is assumed to be $P_b = P_{b0}(R_0/R)^{3\gamma}$. Eq.(1) is solved numerically by the fourth order Runge-Kutta-Gill method.

4 Results and Discussion

Figure 3 shows the excess pressure of a spherical shock wave measured at 60 mm from the discharge position in the water tank shown in Fig. 3. In this figure, abscissa is time and it is indicated just from when the output signals recovered from the

singular noise caused by the influence on the flash of electric discharge. The excess pressure at the shock wave front is about 6 MPa.

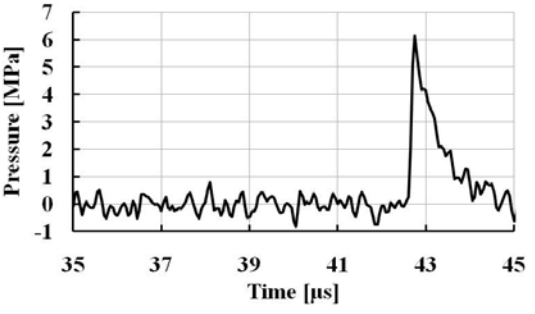

Fig. 3 Experimental pressure record in the water tank detected at 60 mm from the discharge position by FOPH2000 pressure transducer.

Using the experimental pressure record shown in Fig. 3, Eq. (1) was solved numerically for 5, 15, and 25 μm in the initial bubble radius. The analytical results, radius time curves and time changes of pressure in a bubble, are depicted in Fig. 4. The time of abscissa is transformed to the time taken from just after the first shock wave passed through the bubble. Figure 4 (a) shows that the first rebound occurs at approximately 110 ns, and the pressure inside bubble simultaneously increases up to about 430 MPa. Similarly, Fig. 4 (b) shows approximately 700 MPa at 250 ns, Fig. 4 (c) shows approximately 560 MPa at 390 ns. From the above, it comes out that time for shrink and rebound takes short with decreasing of bubble radius. On the other hand, peak pressure in a bubble indicates the highest value when bubble radius is 15 μm.

Furthermore, the analysis for the initial bubble radii from 5 μ to 25 μm is done and the result is depicted in Fig. 5. The vertical axis shows maximum pressure generated in a bubble, and the horizontal axis shows initial radius of bubble. Figure 5 shows the maximum pressure value of approximately 720 MPa at the initial radius of 12 μm. As a comparison, in case of analysis with a step-like external pressure of 5 MPa, we have obtained the peak pressure of approximately 800 MPa that is higher than that in Fig.5, however, the change of maximum pressures are indicated approximately almost constant.

In the previous work [6], it was predicted that the generation of the rebound pressure higher than 200MPa, that is probably the effective pressure of inactivation of marine bacteria, required the incident shock pressure of higher than 3MPa. From above-mentioned, it has been come out that the relation between bubble size and pressure profile of incident shock wave is also important. As a result of the analysis using the pressure profile shown in Fig. 3, the optimum initial radius of bubbles that can produce the highest rebound pressure is presumed to be about 12 μm. In other words, the bubble of R_0<12 μm already finishes converging before it is exposed to the maximum pressure of shock wave, while the bubble of R_0>12 μm cannot

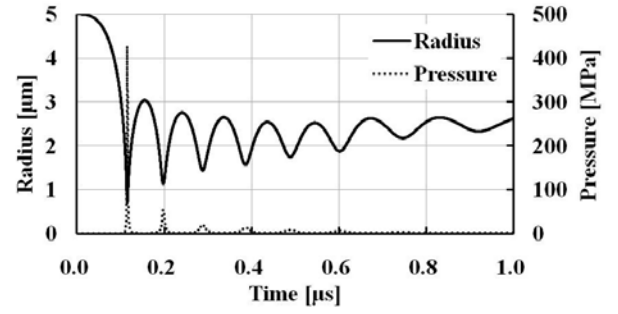

(a) R_0=5 μm

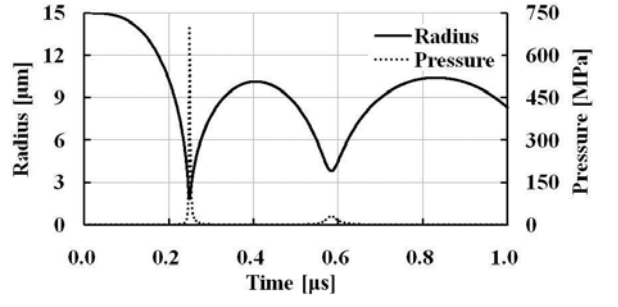

(b) R_0=15 μm

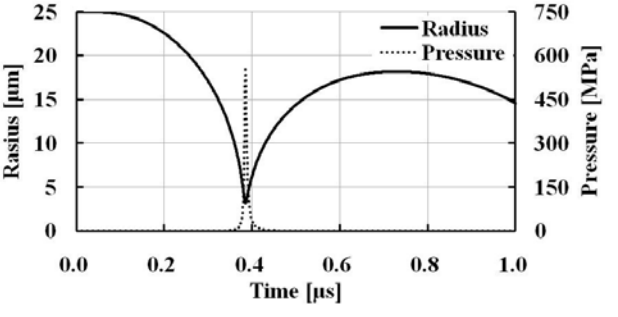

(c) R_0=25 μm

Fig. 4 Results of numerical analysis combined with the experimental pressure record shown in Fig. 3

converge enough because the pressure behind the shock wave starts decreasing in process of bubble shrinking. Therefore, the strong pressure generation by rebound of bubbles relates closely with the initial bubble radius, values of the peak pressure of the incident shock wave and its pressure gradient. For the application to practical inactivation treatments of the marine bacteria, it is important to find the optimum conditions of them and carry on the study with respect to the control of the bubble sizes and the incident shock wave profiles.

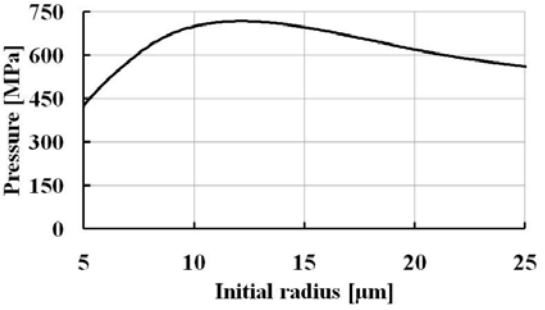

Fig. 5 Relation between generated peak pressure and initial bubble radius calculated using pressure record of Fig.3.

5 Conclusions

The numerical analysis of the bubble motion equation combined with the experimental shock pressure profiles estimated the behavior of a 5, 15, and 25 μm radius bubble applied by the incident shock wave. The analytical results showed that the pressure inside a microbubble at the first rebound could reach 200 MPa that will be the inactivate pressure of the marine bacteria, and it has been found that the peak pressure value relates closely with the initial bubble radius and the pressure profile of the incident shock wave. In order to provide the optimum condition for good performance of shock wave sterilization by collapsing bubbles, it will be necessary to clarify the details of the dynamics of a microbubble interacted with shock pressures.

Acknowledgements. The authors wish to acknowledge that this research is assisted from the advanced research grants for the research project entitled "the creation of an international marine transportation system integrating three-principles of transportation" offered by MEXT, and also from Grants-in-Aid for Scientific Research (B) (No.22360367) offered by JSPS.

References

1. Abe, A., Mimura, H., Ishida, H., Yoshida, K.: Shock Waves 17, 1–2 (2007)
2. Takahashi, M., Chiba, K., Li, P.: J. Phys. Chem. B 111, 6 (2007)
3. Takahashi, M., Chiba, K., Li, P.: J. Phys. Chem. B 111, 39 (2007)
4. Herring, C.: OSRD Rep. 236 (1941)
5. Wolfrum, B., Kurz, T., Mettin, R., Lauterborn, W.: Physics of Fluids 15, 10 (2003)
6. Abe, A., Ohtani, K., Takayama, K., Nishio, S., Mimura, H., Takeda, M.: Journal of Fluid Science and Technology 5, 2 (2010)

Experimental Study on Inactivation of Marine Bacteria Using Electrodischarge Shock Waves

Nobuhito Tsujii, Biyu Wan, Haruo Mimura, and Akihisa Abe

1 Introduction

The trans-boundary movement of the microorganism included in the ship ballast water causes the destruction of an marine ecosystem globally. The restrictions concerning the ballast water managements provided by International Maritime Organization (IMO) probably take effect for all new ships in the near future, so that enterprises and research institutions in the world have developed many kinds of ballast water treatment systems to obtain the IMO approval. In most of all systems, chemical treatment is used to kill marine bacteria such as cholera and colon bacillus. For marine environment convention, safe and economic and eco-friendly ballast water treatment systems are desired.

Concerning the ship ballast water problem, the authors have proposed a new treatment method for marine bacteria using the impulsive pressure generated by collapse of microbubbles. In the previous study, they investigated the characteristics of a marine microbe, *Vibrio* sp., to shock pressures by impact of a bullet accelerated with a gas gun. As a result, it was found that the marine *Vibrio* sp. is inactivated by exposing to shock pressures larger than 200 MPa [1]. However, it is difficult to apply this impact method to a large amount of ship ballast water, so that the authors thought a use of micro-scale shock waves generated by collapsing of microbubbles instead of the above method. They confirmed that the interaction between microbubbles and a shock wave produced by a micro explosive, 10 mg of AgN_3, generates impulsive pressures larger than 150 MPa [2, 3]. There have been a lot of works on sterilization of direct use of underwater shock waves, such as by Teshima, et al. [5] or Loske, et al. [6, 7].

In this study, shock sterilization of marine bacteria using electric discharge is examined for development of ship ballast water treatment. In order to obtain high excess pressure by the shock-focusing phenomenon, a two-dimensional ellipsoidal

Nobuhito Tsujii · Biyu Wan · Haruo Mimura · Akihisa Abe
Graduate School of Maritime Sciences, Kobe University
5-1-1 Fukaeminami-machi, Higashinada-ku, Kobe 658-0022, Japan

chamber was used. The optimum condition to get high-pressure was investigated by the observation with a high-speed video camera and pressure measurements with a fiber optic probe hydrophone. In addition, the sterilization effects for the marine *Vibrio* sp. by flash with the electrical discharge were also evaluated.

2 Experiment

2.1 Experimental Setup

Fig. 1 shows the schematic diagram of the experimental setup. It consists of a discharge chamber, a container, a high-voltage power supply (HPS18K-A, Tamaoki Electronic Industry Ltd), two electrodes and a fiber optic probe hydrophone (FOPH2000, RP acoustics). Shape of the discharge chamber is ellipse, and its dimensions were 100 mm in major axis by 60 mm in minor axis by 15 mm in depth, and the distance between first and second focal points was 80 mm. Both the discharge chamber and the lower container were made of acrylic material for the observation of shock wave propagation. The maximum output of this power supply is 20 kV. The electrodes are sharpened stainless wires and coated with nonconducting material except their tip. The distance between the electrodes is 8 mm and they were set up in perpendicular to the windows.

FOPH2000 is the optical pressure transducer and its sensitive part is fiber tip of only 0.1 mm in diameter. It is possible to measure pressures in the flow field with any electric current and magnetic noise with high spatial and temporal accuracy. To confirm the state of wave reflection on the reflector and converging wave, shock wave propagation was observed by the shadowgraph method with a high-speed video camera (FASTCAM SA5, Photron Co.). When cell experiments were carried out, the cell suspension in the lower container was separated by a thin silicone film to prevent inflow from the discharge chamber.

2.2 Cell Preparation

In order to investigate the sterilization effects of ultraviolet (UV) light included in flash light generated by electric discharge and shock pressures, the cell experiment was carried out. The solution of marine *Vibrio* sp. was used as an experimental specimen. The marine *Vibrio* sp. generally exists in seawater and it belongs to the same genetic group as cholera bacteria restricted severely by convention of ship ballast water management provided by IMO. The marine *Vibrio* sp. was isolated from seawater and cultivated. After the shock event, the solution was diluted several times and cultivated for 24 hours, and then the number of colonies were counted for estimation of active cell number.

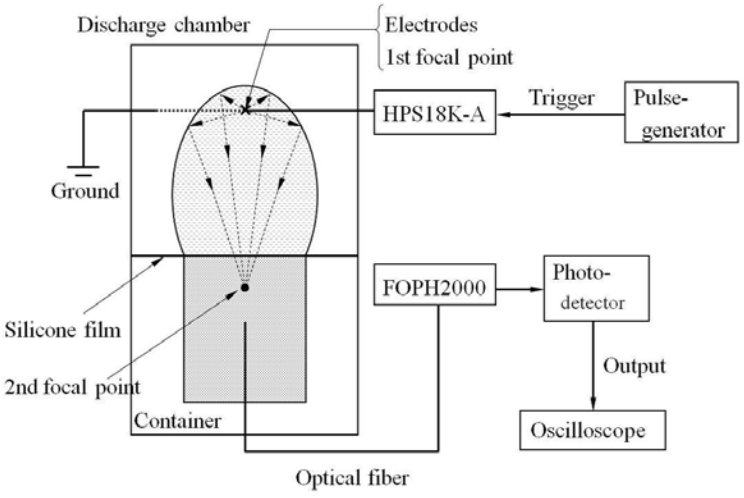

Fig. 1 Schematic diagram of experimental setup

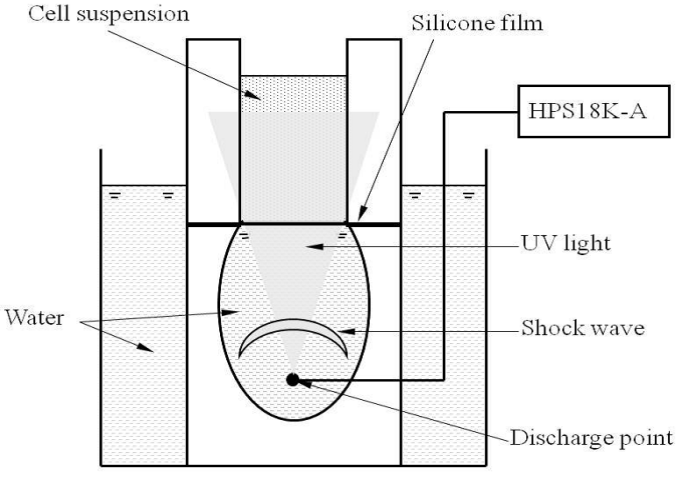

Fig. 2 Experimental setup using cell suspension

2.3 Influence of UV Light on Cell Solution

To evaluate the inactivation effect of only microbubbles on the marine *Vibrio* sp., it is necessary to know the influence of UV light and induced electrodischarge shock waves. The experimental setup is shown in Fig. 2. The dimensions of the shock generation chamber were 50 mm in major axis by 30 mm in minor axis by 10 mm in depth, and the distance between first and second focal points was 40 mm. The upper

container was filled with the cell suspension, while the lower discharge chamber was filled with water. A silicone rubber film (about 0.5 mm in thickness) was set up between the cell suspension container and the discharge chamber to prevent from blending of upper and lower liquids. In addition, to get rid of the influence of the water temperature rising caused by frequent electric discharge on the marine *Vibrio* sp. the discharge chamber was put in an external water tank filled with water. In the case of the experiment for the effect of flash light on the cells, 5 mm-width air gap was laid on between the discharge chamber and the cell suspension container to prevent shock waves from propagating into the cell solution.

In this experiment, electric discharge was carried out every four seconds, and cell solutions were picked up at every hundred shots. The cell viability was estimated by using the plate counting method [6]. Briefly, the cell suspension exposed to the flashlight emitted from the electrodes was diluted serially, and then spread onto agar plates. The plates were incubated at 37 degrees Celsius for 24 hours, and after that, colonies on the plate were counted. The total number of colony forming cells in 1 ml of the cell suspension after the event were evaluated based on the dilution ratio of the cell suspension and the number of colonies on the plate.

3 Results and Discussion

3.1 Generation and Focusing of Underwater Shock Wave

Figure 3 shows the sequential images of shock wave generation. In Fig. 3, the resolution is 128 $\times$ 104 pixels, the framing speed is 300 kfps, and the exposure time is 370 ns. The discharge energy is explosively released with a strong flash and the generation of a cylindrical shock wave around the electrode is observed in Fig. 3(b). It seems that the shape of shock wave is formed as an ideal concentric circle. This first shock wave propagates directly downward (indicated by a solid arrow), and after that, shock waves reflected on the inner wall surface of the chamber form a contour converging to the second focal point (indicated by a dashed arrow). The first shock waves enter the lower container at about 54 μs and it can be observed that the converging reflected shock waves are focused at the second focal point in Fig. 3(f).

Figure 4 shows the pressure record measured at the second focal point. The arrival times at the second focal point of the first shock wave front and the converged one are estimated respectively 53 μs and 67 μs under the assumption that the propagation velocity of the underwater shock wave is a constant value of 1,500 m/s. In Fig. 4, peak pressure values are observed at 56 μs and 70 μs, so that those pressure risings correspond with that of the first shock wave and the second converged one. The peak pressure value of the first shock wave is about 2.7 MPa, while that of the second converged shock wave is about 4.5 MPa, i.e., the focused pressure reaches about 1.7 times of the first shock wave pressure. However, we think that it is possible to improve more the value of focusing pressure by adjustment of reflection condition on the discharge chamber.

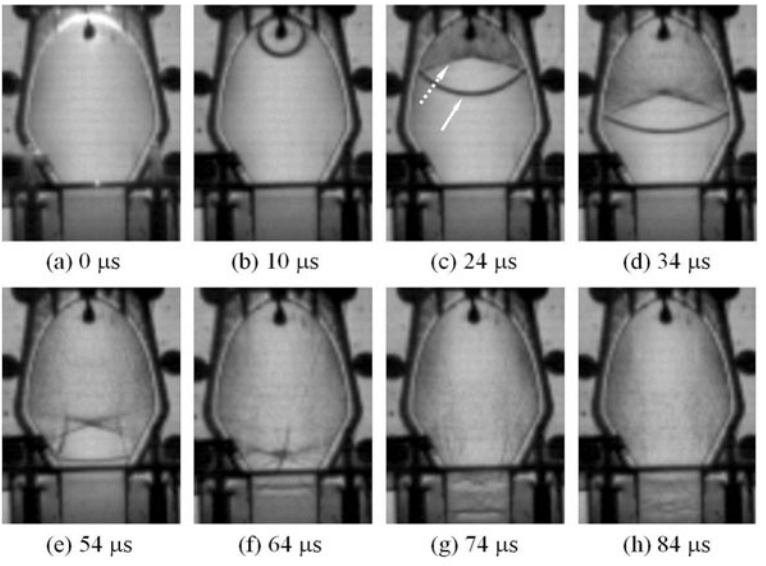

Fig. 3 Sequential observation of generation and propagation process of underwater shock wave in the discharge chamber

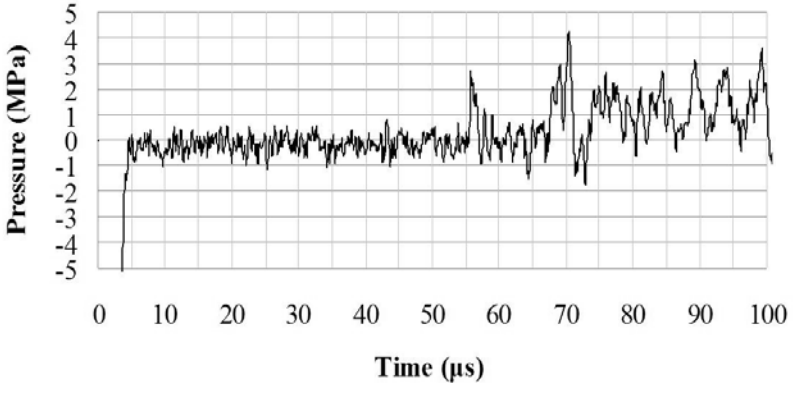

Fig. 4 Pressure fluctuation measured at the second focal point

3.2 *Inactivation Effects of UV Light and Shock Pressure on the Marine Vibrio sp.*

Table 1 shows the living number of the marine *Vibrio* sp. in two-hundred sequential shots under the different two experimental conditions, one is exposure of only the flash light by electric discharge and another is exposure of both flash light and shock pressure. Those results were obtained from the colony counting method of samples picked up at 0 (control), 100 and 200 shots. In the case of applying only flash light of discharge to the cell solution, decreasing of the colony number of the cell indicate only about 30% from 100 to 200 shots. On the other hand, in the case of applying both flash light and shock pressures, decreasing of the colony number indicates 98%. From above-mentioned, it is obvious that shock pressure contributes explicitly to cell inactivation. The peak pressure value of shock wave generated in the present experiment was relatively low, so that the inactivation effect would be better if we can generate higher shock pressure.

Table 1 Living number of the marine *Vibrio* sp. (unit is cfu/ml)*

	Control	100 shots	200 shots
Only flash light	$O(10^6)$	2.4×10^6	1.6×10^6
Flash light and shock pressures	1.8×10^6	5.8×10^5	1.0×10^4

* cfu, colony forming unit, is the number of colonies formed by cells.

4 Conclusions

In order to investigate the shock sterilization effect on the marine *Vibrio* sp., the experimental device that can produce periodically strong underwater shock waves has been designed using a two-dimensional ellipsoidal chamber, and its performance testing and the cell experiment were carried out. Underwater shock generation was successful, however the peak pressure at the focal point was relatively low and room for improvement remained. In the cell experiment using the marine *Vibrio* sp., the sterilization effect of flash light emitted by electric discharge and shock pressures have been examined. The number of cells decreased about 30% by only flash light radiation. On the other hand, the application of flash light and shock pressures made the viability number of the cells decrease about 98%. Those results showed that shock pressure contributes obviously to cell inactivation. However, the present sterilization effect was not enough to apply to ship ballast water treatment. We consider improvement of generating higher pressure and introduce of microbubbles in order to achieve larger sterilization effect.

Acknowledgements. A part of the present study has been supported by JSPS under Grant-in-Aid for Scientific Research (B), No.22360367. The authors would like to express their thanks to Mr. K. Takayama of Photron for his corporation on providing a high-speed video camera.

References

1. Abe, A., Mimura, H., Ishida, H., Yoshida, K.: The effect of shock pressures on the inactivation of a marine Vibrio sp. Shock Waves 17(1-2), 143–151 (2007)
2. Abe, A., et al.: Pressure Generation from Micro-Bubble Collapse at Shock Wave Loading. Transactions of the Japan Society of Mechanical Engineers(B) 75(752), 668–675 (2009)
3. Abe, A., et al.: Application of Shock Pressures Generated by Collapsing Microbubbles to Inactivation Treatment of Marine Bacteria in Ship Ballast Water. International Symposium on Marine Engineering, DT-1(16) (2009)
4. Teshima, K., et al.: Biomechanical effects of shock waves on Escherichia coil and λphage DNA. Shock Waves (4), 293–297 (1995)
5. Loske, A.M., et al.: Repeated application of shock waves as a possible method for food preservation. Shock Waves (9), 49–55 (1999)
6. Loske, A.M., et al.: Tandem shock wave cavitations enhancement for extracorporeal lithotripsy. Phys. Med. Biol. (47), 3945–3957 (2002)
7. Mimura, H., Katakura, R., Ishida, H.: Changes of microbial populations in a ship's ballast water and sediments on a voyage from Japan to Qatar. Marine Pollution Bulletin (50), 751–757 (2005)

Numerical Simulation of a Shock-Accelerated Multiphase Fluid Interface

Michael Anderson, Peter Vorobieff, Sanjay Kumar, Joseph Conroy, Ross White, Charles Needham, and C. Randall Truman

1 Introduction

A Richtmyer-Meshkov Instability (RMI) [1, 2] is generated when an interface between two different fluids is impulsively accelerated. The instability develops due to misalignment of the density and pressure interfaces. This misalignment results in the deposition of vorticity, causing the formation of an instability that grows nonlinearly with time and eventually may transition to fully turbulent flow. It has been recently shown that a similar class of instability can evolve in a multi-phase flow [3], where the density gradient is caused by a second, non-fluid phase.

The experiments modeled here involve a shock wave impulsively accelerating a column of gas at a density higher than ambient air. This column is referred to as the initial conditions (IC). Experiments were performed using two different IC types. The first was a column of sulfur hexafluoride, which has a density of approximately five times that of air. Sulfur hexafluoride has been used successfully past RMI studies [4, 5] and thus employed in these experiments to establish a baseline. The second type of initial conditions studied was a column of air seeded with micron-sized dipropylene glycol droplets. These initial conditions are unique in that there is no difference in the density of the fluid phases of the column or the surrounding ambient atmosphere; however, due to the presence of the glycol droplets,

Michael Anderson · Charles Needham
Applied Research Associates, Inc., Albuquerque, New Mexico 87110

Michael Anderson · Peter Vorobieff · Joseph Conroy · Ross White · C. Randall Truman
Department of Mechanical Engineering, University of New Mexico,
Albuquerque, New Mexico 87131

Sanjay Kumar
Department of Engineering, University of Texas - Brownsville, Texas 78520

the effective density of the initial conditions is higher than the surrounding air and in turn generates an RMI-like instability when impulsively accelerated.

1.1 Test Setup

The experiments were conducted at the University of New Mexico (UNM) shock tube originally built with DTRA funding in 2007-2009. The facility is used to study planar and oblique shock wave interaction with gaseous density interfaces and multiphase flows. The shock tube with an optically transparent polycarbonate test section is securely mounted to the wall of the facility to ensure that it does not move during the experiment. The shock tube is mounted on an adjustable pivot, which allows the shock tube to be placed at various angles with respect to the horizontal to study oblique shock waves.

Before an experimental run, a plastic diaphragm is inserted between the flanges of the driver and the driven section, which makes it possible to pressurize the driver section with helium. The diaphragm is ruptured by an electrically driven four-blade puncture device located inside of the driver section, releasing a planar shock wave into the driven section. The driven section is instrumented with two Omega pressure transducers to record the pressure traces. The pressure signal from the second transducer is used to trigger the imaging system. This system consists of two Stanford Research DG-535 digital delay generators, a DRS Imaging IMACON-200 high framing rate intensified camera, and two New Wave Gemini double-pulsed Nd:YAG lasers used to produce horizontal laser sheets illuminating the camera field of view. The laser pulses are emitted at 532 nm, have a duration of about 5 ns, and an optical energy about 0.2 J per pulse.

1.2 Modeling Setup

The Eulerian hydrocode SHAMRC (Second-order Hydrodynamic Automatic Mesh Refinement Code) [7] was used to perform all of the numerical simulations. SHAMRC is a government owned fluid dynamics code under high technology export control. ARA (Applied Research Associates, Inc.) maintains and upgrades the code, monitors distribution, and is one of the major users of the code. It is used to solve a variety of airblast related problems which include high explosive (HE) detonations, nuclear explosive (NE) detonations, structure loading, thermal effects on airblast, cloud rise, conventional munitions blast and fragmentation, shock tube phenomenology, dust and debris dispersion and atmospheric shock propagation. SHAMRC has been used in the past to successfully model RMI [6].

A 2D Cartesian mesh was used with dx and dy of roughly 0.005 cm. These dx and dy were chosen so that there would be exactly 128 zones across the diameter of the IC column which was set to the inner diameter of the injection tube, 0.635 cm. The validity of this choice was verified by examining images taken of the initial conditions during experiments. The mesh extended to the shock tube wall in the y direction, a distance of 7.62 cm. The x extent was set to 51 cm so that approximately

2 ms of instability growth could be modeled before it is swept from the grid. Additionally, a half plane of symmetry was used to reduce the total number of zones required to approximately 9 million.

The experimental initial conditions consist of air seeded with glycol droplets. To model the initial conditions in SHAMRC, the air-glycol mixture is approximated by a perfect gas with the same average density as the air-glycol mixture. The perfect gas equations of state are defined as $P = (\gamma - 1)\rho I$, $T = (PM)/(R\rho)$.In these equations, P is the pressure, ρ is the density, γ is the ratio of specific heats, I in the specific internal energy, T is the temperature, W_M is the molecular weight, and R is the universal gas constant. To determine this density of the pseudo-glycol fluid, a container with a known volume of the air-glycol mixture was weighed with a high accuracy scale. The result is a difference between the densities of air and the air-glycol mixture, found to be 0.06 ± 0.01 kg/m^3. The local elevation results in a reduction to 85% of the standard air density of 1.225 kg/m^3, yielding an Atwood number $A = (\rho_2 - \rho_1)/(\rho_2 + \rho_1)$ of approximately 0.03 for the initial conditions, where subscripts 1 and 2 correspond to air and heavier gas respectively. To match actual laboratory conditions, the simulations run at an ambient density of 1.051 kg/m^3 and the density of the pseudo-glycol fluid 1.116 kg/m^3. The ambient energy and atomic weight were chosen to maintain pressure and temperature equilibrium at ambient conditions. Simulations were run at several A to examine the instability evolution as a function of density.

To look at the effects of Mach number, experiments and numerical simulations were performed at M ranging from 1.2 to 2. The normal shock relations were used to determine the conditions fed into the mesh at the left boundary.

2 Results and Discussion

In the experiments at M=1.67, the column of glycol droplets and the surrounding unseeded air is accelerated by a planar shock moving at an average velocity of 570 m/s. The shock passage accelerates the air behind it to a piston velocity of about 300 m/s. The glycol droplets, which have a much higher density than that of the surrounding air, are accelerated by drag forces and lag behind the embedding air. Fig. 1 shows side-by-side comparisons of images taken during several experiments and images from a SHAMRC calculation run with $A = 0.03$ and $M = 1.67$. The images from the calculation display the density of the pseudo-glycol fluid and have all been scaled to the same size. The scaling factor was chosen so that the images of the initial conditions are the same size for the test data and numerical results. This scaling allows the direct comparison of the sizes of the instabilities observed in experiments and those generated in the numerical simulation. The timings of the exposures are displayed to the right of the corresponding images. The time $t = 0$ corresponds to the time at which the shock wave reaches the center of the initial conditions. From this image, it is clear that the instability created in the numerical calculation is a good approximation of what is observed in experiments. To quantify these results, measurements were taken from each image to determine the width

of the instability as a function of time. The width is defined as the extent of the instability in the direction of the shock.

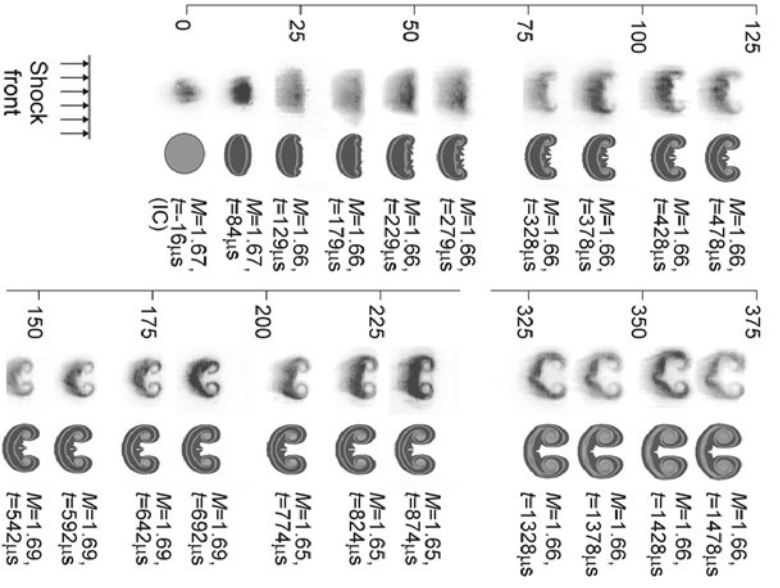

Fig. 1 Instability Evolution. Grayscale images - experiment (planar laser visualization), color images - numerics. Scale above images indicates downstream distance in mm, labels below – timings and Mach numbers of experimental images.

While the timings displayed in Fig. 1 are the same for both the numerical and experimental data, the downstream positions are not. While the two data sets have the same slope, denoting that they are moving at the same velocity, there is a small offset between the experimental and numerical data, with the experiment lagging behind the numerics, which can be explained by the delay in acceleration of the particles.

The comparisons above demonstrate that SHAMRC can be used with the current assumptions to model the first order effects of the glycol-air initial conditions and the resulting instabilities that are formed. SHAMRC was used to perform a small Atwood number variation study by changing the density of the pseudo-glycol fluid. Experimentally, this is equivalent to changing the mass of droplets present in the initial conditions. This would be done by either changing the density (type) of the embedded droplets or changing the seeding density of the particles. Fig. 2, left shows selected images from these calculations at different times. It is clear that by increasing the Atwood number of the initial conditions, the growth rate of the instability has been increased. Fig. 3, left shows a compilation of measured instability widths in the streamwise direction.

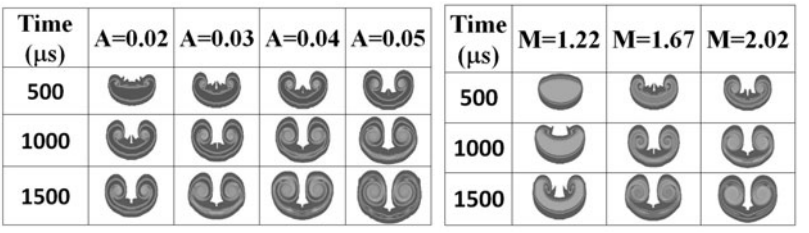

Fig. 2 Instability size comparison for multiple Atwood numbers at $M = 1.67$ (left) and for multiple Mach numbers at $A = 0.03$ (right).

For RMI, it has been reported that the instability amplitude growth curves produced from the same initial conditions at different Mach numbers can be collapsed by plotting them in appropriate dimensionless coordinates [8, 9]. The dimensionless temporal coordinate $\tau = 2kA\Delta V(t - t_0)$ relates to time after shock acceleration. Here k is the wave number associated with the primary perturbation wavelength of the initial conditions (in this case, the wavelength would be the seeded column diameter), V is the difference in the pre-shock and post-shock average velocity of the medium, and t_0 is the time at which the shock wave arrives at the initial conditions. In addition, the instability width can be non-dimensionalized by dividing by the minimum instability width, which occurs during the compression of the initial conditions during shock acceleration. This scaling causes the growth curves to collapse for different Mach numbers at the same initial conditions and Atwood numbers. Fig. 3, right shows how the SHAMRC results collapse to a single curve.

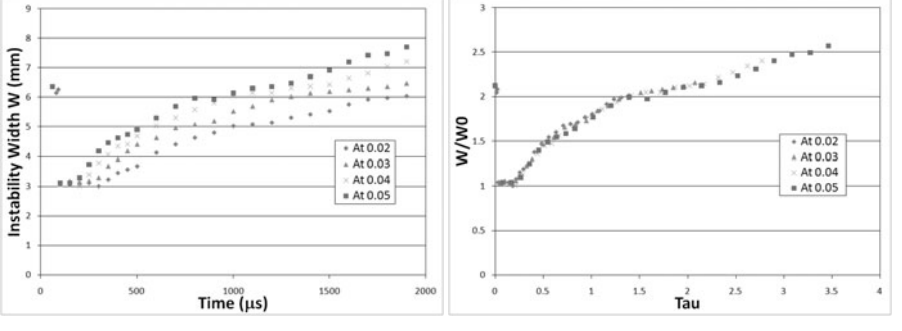

Fig. 3 Growth Rate for Various Atwood Numbers - unscaled (left) and scaled (right)

In addition to the Atwood number variation, an experimental study was done on variation of the shock wave Mach number. These results were reproduced in SHAMRC. Fig. 2, right shows the instabilities at three different times for three different Mach numbers. All images are plotted on the same density scale. Note the increased compression with increasing Mach number in the initial conditions denoted by the successively darker densities for higher Mach numbers. Fig. 4, left

shows all the test data collected along with the SHAMRC data for Mach numbers of 1.22 (squares), 1.67 (diamonds), and 2.02 (triangles) for an initial condition Atwood number of 0.03. The test data are shown as open symbols, while the SHAMRC data points are closed. The instability size increases with M in a non-linear fashion. For each Mach number, the spread in the test data is primarily due to differences in the shape of the initial conditions resulting in non-uniform vortex formation. The SHAMRC data was generated in calculation with a perfectly formed initial condition and as such does not display this spread. The numerical results form a lower bound for the experimental data with a slope that matches the experimental data, indicating a similar growth rate. The main difference between the two data sets is the larger size of the measured experimental instability sizes, which is nearly constant over time. This is due to the assumption made to model the initial conditions as a continuous fluid instead of discrete particles. In the experiments, the larger particles get accelerated to the piston velocity more slowly than their smaller counterparts. This lag causes a spread in the initial conditions which can be seen clearly in the early images of Fig. 1.

Varying M results in a different amount of compression of the initial conditions, however, this value does not appear to be sufficient to collapse these results to a single curve. A similar result was already observed [9], where the difference between the instability widths was shown to be constant for two differing Mach numbers. This difference could not be reconciled by dividing the instability widths by the compression factor w_0. As the instability size also appears to be a function of Mach number, a scaling factor $w^*$is proposed: $w^* = M^a w/w_0$, where a is a constant to be determined. Fig. 4, right shows this scaling function if a is set to -0.5. This method appears to be reasonable, although the physics behind the scaling are not understood at this time. More experimental and numerical work will be required to prove that this is an accurate scaling method and to fully understand the physics behind this relationship.

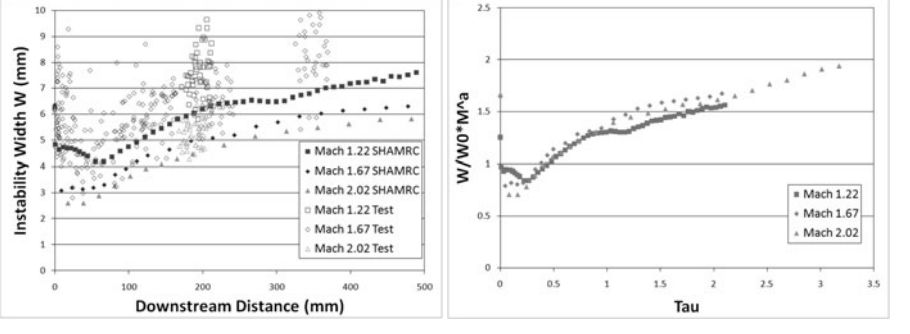

Fig. 4 Left – instability size comparison for different Mach numbers (experiment and numerics), right – collapse of numerical growth curves with new proposed scaling method.

3 Summary

A multiphase analogue to RMI has been shown to exist in laboratory testing. This instability is unique in that it is generated not by the deposition of vorticity due to a misalignment of the density and pressure gradients, as is the case with traditional RMI, but instead by a transfer of momentum between a continuous fluid phase and a discrete particle phase. This generalized RMI has been show to exhibit the same non-linear growth parameters as traditional RMI in both experiments and numerical simulation. SHAMRC has been used to successfully recreate the first order phenomena of the generalized RMI by approximating the discrete phase as a fluid with an average density. Favorable comparison between the test and SHARMC data allows for a more detailed analysis of the instabilities growth rate dependence on the Atwood number and Mach number of the flow. These calculations also provide a means to validate scaling methods used to collapse growth rate data for different Atwood and Mach numbers into a single expression. SHAMRC results were successfully scaled using current scaling laws for Atwood number and a new scaling method for instability size based on Mach number was proposed.

Acknowledgments. We thank Professor S. "Bala" Balachandar (U. of Florida) for providing the suggestions that led to the experiments described here. This research is funded by the US National Nuclear Security Agency (NNSA) under the Stewardship Science Academic Alliances program through DOE Grant DE-PS52-08NA28920 and by the US Defense Threat Reduction Agency (DTRA) under awards HDTRA1-07-1-0036 and HDTRA1-08-1-0053.

References

1. Richtmyer, R.D.: Taylor instability in shock acceleration of compressible fluids. Comm. Pure App. Math. 13, 297–319 (1960)
2. Meshkov, E.E.: Instability of the interface of two gases accelerated by a shockwave. Izv. AN SSSR, Mekh. Zhidk. Gaza 4, 151–157 (1969)
3. Vorobieff, P., et al.: Shock-driven hydrodynamic instability induced by particle seeding. Procedings of the National Academy of Sciences (under consideration)(2010)
4. Jacobs, J.W.: The dynamics of shock accelerated light and heavy gas cylinders. Phys. Fluids A 5, 2239 (1993), doi:10.1063/1.858562
5. Tomkins, C., et al.: Flow morphologies of two shock-accelerated unstable gas cylinders. Journal of Visualization 5(3), 273–283 (2002), doi:10.1007/BF03182335
6. Carney, T., Needham, C.E.: Instabilities and Turblence in Intermediate Altitude Fireballs, September 3 (1991) (UNCLASSIFIED)
7. Crepeau, J., Hikida, S., Needham, C.E.: Second Order Hydrodynamic Automatic Mesh Refinement Code (SHAMRC): Methodology, vol.1, May 16 (2001) (UNCLASSIFIED)
8. Rightley, P.M., Vorobieff, P., Benjamin, R.F.: Evolution of a shock-accelerated thin fluid layer. Phys. Fluids 9, 1770–1782 (1997)
9. Orlicz, G.C., et al.: A Mach number study of the Richtmyer-Meshkov instability in a varicose, heavy-gas curtain. Phys. Fluids 21, 064102

Numerical Simulation of Shock Wave Entry and Propagation in a Microchannel

G.V. Shoev, Ye.A. Bondar, D.V. Khotyanovsky, A.N. Kudryavtsev, G. Mirshekari, M. Brouillette, and M.S. Ivanov

1 Introduction

The effects of viscosity and heat conduction, heat losses due to the wall heat transfer, as well as nonequilibrium phenomena can play an important role in microflows. Recent numerical investigations [1] of shock wave propagation in a microchannel with allowance for viscosity and rarefaction effects revealed significant differences from the inviscid theory, which ensures a correct description of the majority of specific features of macroflows. In that work, the shock wave was generated by breakdown of a diaphragm separating high-pressure and low-pressure domains. At the moment, however, such an experiment is not feasible inside a microchannel, as was noted in [2]. Nevertheless, an alternative variant of shock wave generation in a microchannel was proposed in [3]. The idea was to generate the shock wave in a conventional shock tube and then make it move from the low-pressure chamber to the microchannel. The numerical studies [3] based on Navier-Stokes (NS) computations demonstrated the attenuation of the shock wave in the microchannel. The necessity of further research with allowance for rarefaction effects was noted in that paper. A recent experimental study of the shock wave entry and propagation in a contracting channel [4] showed attenuation of the shock inside the microchannel. Nevertheless, full understanding of this process is still unavailable.

The basic goal of our research is numerical simulations of the shock wave entry and propagation in a microchannel with allowance for viscosity and rarefaction effects. In this paper, we use two different simulation approaches: the kinetic approach (DSMC method) and the continuum approach (Euler and NS equations). Euler computations are necessary for comparisons with viscous simulations to reveal effects

G.V. Shoev · Ye.A. Bondar · D.V. Khotyanovsky · A.N. Kudryavtsev · M.S. Ivanov
Khristianovich Institute of Theoretical and Applied Mechanics, Institutskaya 4/1, Novosibirsk, Russia, 630090

G. Mirshekari · M. Brouillette
Department of Mechanical Engineering, Universite de Sherbrooke, Sherbrooke, Canada J1K 2R1

of viscosity. In NS computations, the rarefaction effects are taken into account by imposing the velocity slip and temperature jump boundary conditions on walls. As the Knudsen number in this research is approximately $Kn \sim 8 \cdot 10^{-3}$, the applicability of NS equations cannot be taken for granted. The DSMC [5] computations are additionally performed for verification of numerical results.

2 Numerical Techniques and Boundary Conditions

The Euler/NS code is a time-explicit shock-capturing code based on 5^{th} order WENO reconstruction [6] of convective fluxes. Central 4^{th} order approximation of dissipation terms was used in NS computations. The numerical solution is advanced in time with the third-order Runge-Kutta scheme until the transmitted shock (hereinafter, the transmitted shock wave is understood as the shock passed in the microchannel) reaches the right wall. As the main task of the present work was modeling the shock wave entry and propagation in a microchannel, the inviscid wall conditions (denoted by E in Fig. 1) are imposed on the upper boundary of the conventional shock tube and on the right boundary of the microchannel. The right boundary of the conventional shock tube is subjected to the isothermal no-slip boundary condition (denoted by W in Fig. 1). The present study includes two series of computations with different boundary conditions on the upper wall of the microchannel: isothermal no-slip and isothermal slip boundary conditions (denoted by W/S in Fig. 1). In Euler computations inviscid walls are used for all boundaries of channels. To model shock wave propagation, conditions corresponding to the Rankine-Hugoniot conditions behind the normal shock wave with the corresponding shock wave Mach number M_{is} are imposed on the left boundary of the computational domain.

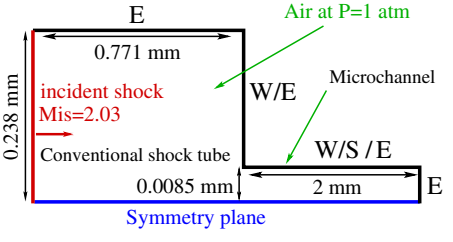

Fig. 1 Computational domain and boundary conditions.

The DSMC computations are performed by the SMILE software system [7]. The computational domain is similar to the domain used in the NS computations (see Fig. 1). The walls with specular reflection conditions are denoted by E in Fig. 1. The walls with diffuse reflection model with complete energy accommodation are denoted by W in Fig. 1.

A diatomic gas (N_2) with the ratio of specific heats $\gamma = 1.4$ and a power-law dependence of the dynamic viscosity coefficient μ on the temperature T with the

exponent $\omega = 0.74$ is used in the computations. The variable hard sphere (VHS) model [5] was used in the DSMC computations with the VHS-parameter chosen to provide the same viscosity-temperature dependence as in the NS computations. The initial data were chosen to be the same as in [4]: $P_0 = 1$ atm, $T_0 = 293^o$ K, $M_{is} = 2.03$, $L = 8.5\ \mu m$ and $w_c = 2\ mm$ where P_0, T_0 are the pressure and temperature of the quiescent gas, M_{is} is the incident shock wave Mach number (hereinafter, the incident shock wave is understood as the shock wave propagating in the conventional shock tube), L is microchannel half-height, w_c is microchannel length. An experiment [4] provided pressure histories from transducers mounted on the microchannel wall. In this study the results of Euler and NS computations are compared with the measurements: the pressure values on the wall at points corresponding to each transducer location were calculated at various time moments.

3 Results and Discussion

Figure 2 shows the Mach number fields at various time moments where $t = 0$ corresponds to the instant when the incident shock wave enters the microchannel. The incident shock wave is shown in Fig. 2a. After the incident wave enters the microchannel, an expansion fan is formed on the microchannel corner (see Fig. 2b), in which the gas velocity increases and the flow becomes supersonic. After that (see Fig 2c-f), the boundary layer is formed on the upper wall of the microchannel and Mach reflection of shock waves is formed on the symmetry plane in the conventional shock tube. Shock reflections also appear inside the microchannel. Thus, the

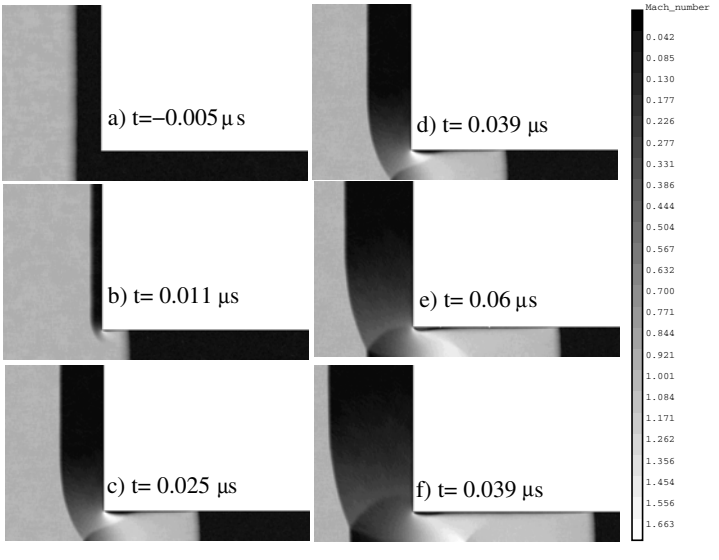

Fig. 2 Mach number at different time instants. DSMC computations.

flow behind the shock wave that entered the microchannel is far from being uniform, which may lead to shock wave amplification.

The NS computation with the slip condition and the DSMC computation are compared in Fig. 3. Figure 3 shows the density fields (normalized to the quiescent gas density), which are in good agreement. Some difference is observed for the thickness of the transmitted shock, but the thicknesses of the other shock waves are commensurable. Figure 3b shows the density profiles at Y=L where L is the microchannel half-height and Y=0 corresponds to the symmetry plane. The value corresponding to the density behind the incident shock wave is shown by the dashed curve. The segment AB in Fig. 3b corresponds to the transmitted shock; the segment CD is the expansion fan formed on the corner. The segment FE refers to the shock wave reflected from the right wall of the conventional shock tube. It is seen that the density in the microchannel differs substantially from the values corresponding to the Rankine-Hugoniot conditions.

Results (see Fig. 4) of numerical simulations of shock wave propagation in the microchannel are presented in the form (M_s,t) and (x_s,t), where M_s and x_s are the Mach number and the coordinate of the shock wave propagating in the microchannel, and t is the time. The coordinate system is chosen so that the point

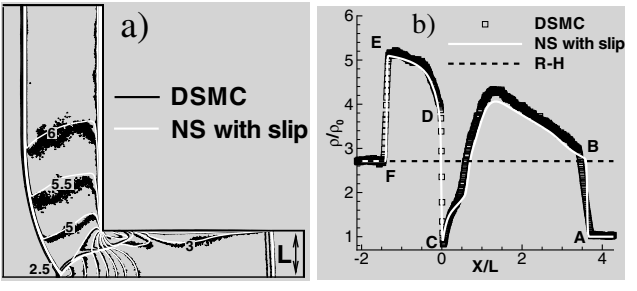

Fig. 3 Comparison of DSMC and NS with slip computations. a) Density contours. b) Density profiles near the top wall of the microchannel.

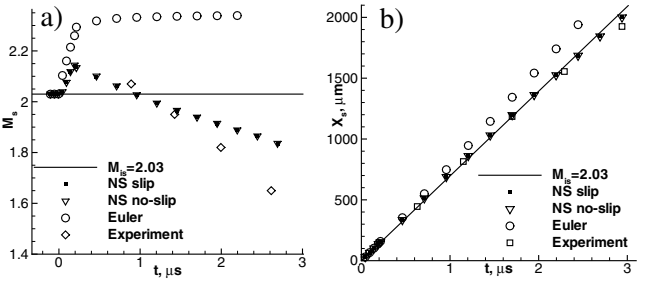

Fig. 4 Shock wave propagation diagram inside the microchannel. a) (M_s,t) diagram. b) (x_s,t) diagram

(0,0) in the plane (x_s, t) corresponds to the time instant when the incident shock wave reaches the microchannel. It is seen from Fig. 4a that the shock wave Mach number increases after the wave enters the microchannel and reaches a maximum value at the point $t \sim 0.2\mu s$. After that, the shock wave starts to attenuate in the viscous computation owing to its interaction with the wall of the microchannel, whereas the shock wave in the inviscid case propagates with a constant velocity. As it is seen from the figures (Fig. 4a and Fig. 4b), the numerical solutions of the NS equations with different boundary conditions (isothermal no-slip and isothermal slip boundary condition) on the upper wall of the microchannel are indistinguishable. The numerical results of the viscous computation on the (x_s, t) diagram practically do not differ from a line (see Fig. 4b) corresponding to shock wave propagation with a constant velocity equal to the incident wave velocity. It is worth noting that in the viscous case it looks like effects of viscosity, heat conduction compensate for shock wave amplification after entry inside the microchannel, and the average shock velocity is close to the incident shock velocity. Figure 4 also shows the experimental data [4].

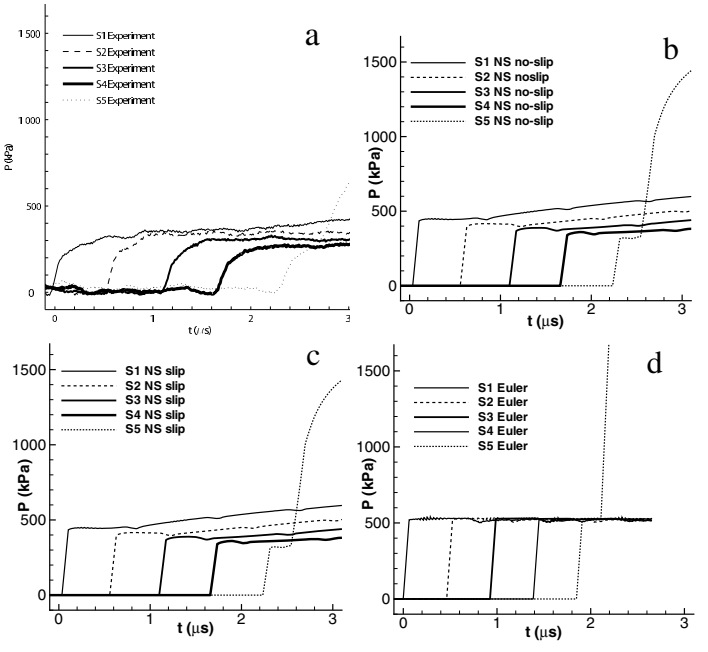

Fig. 5 Pressure histories inside the microchannel. a) Experiment, b) NS computations with no-slip boundary conditions, c) NS computations with slip boundary conditions, d) Euler computation.

These results allow us to conclude that numerical simulations with allowance for viscosity effects qualitatively agree with the experimental data: the shock wave is amplified immediately behind the microchannel entrance and then attenuates.

The pressure histories obtained in numerical simulations and experiments [4] are compared in Fig. 5. The coordinate system is chosen the same as in experiment [4]. Figures 5b-d show the pressure histories obtained by the numerical solution of Euler and NS equations. The difference ($\sim$60 kPa) between the experimental and numerical data in those areas where the shock wave has already passed over the pressure transducers is clearly visible. A possible reason for this difference is three-dimensional effects, which were ignored in numerical simulations. It is also clearly seen that inviscid numerical simulation differs substantially from the viscous simulations and experiment - pressure on each transducer is constant and greater than in NS computations and experiment. As a whole, we can state that reasonable agreement for a first simulation was obtained.

4 Conclusion

The shock wave entry into a microchannel and its propagation in the microchannel at $M_{is} = 2.03$ is studied numerically with the use of the continuum and kinetic approaches. A significant difference between the inviscid and viscous numerical computations is demonstrated. The numerical data obtained show that the shock wave is amplified after it enters the microchannel. After that, the inviscid computation predicts shock wave propagation with a constant velocity, whereas the shock wave in the viscous case starts to attenuate. The results of viscous computations are in qualitative agreement with the experimental data [4], which show shock amplification after it enters the microchannel and its further attenuation.

Acknowledgements The research performed at ITAM was supported by the IFS Collaborative Research Project "Numerical studies of the reacting rarefied flows in tubes", Program No. 11 of the RAS Presidium, Lavrentyev Youth Grant "High-altitude aerothermodynamics of advanced spacecraft taking into account non-equilibrium chemical reactions" and the Russian Foundation for Basic Research (Grant no. 10-08-01203-a). The computations were performed at the Siberian Supercomputer Center, Novosibirsk, and at the Joint Supercomputer Center, Moscow. This support is gratefully acknowledged.

References

1. Zeitoun, D.E., Burtschell, Y., Graur, I.A., Ivanov, M.S., Kudryavtsev, A.N., Bondar, Y.A.: Numerical simulation of shock wave propagation in microchannels using continuum and kinetic approaches. Shock Waves 19, 307–316 (2009)
2. Mirshekari, G., Brouillette, M.: One-dimensional model for microscale shock tube flow. Shock Waves 19, 25–38 (2009)
3. Parisse, J.D., Giordano, J., Perrier, P., Burtschell, Y., Graur, I.A.: Numerical investigation of micro shock waves generation. Microfluid Nanofluid 6, 699–709 (2008)

4. Mirshekari, G., Brouillette, M.: Experimental study of the shock propagation in a micron-scale channel. In: Proceedings of the 27th ISSW, vol. 260 (2009)
5. Bird, G.: Molecular gas dynamics and the direct simulation of gas flows. Oxford Press (1994)
6. Jiang, G., Shu, C.: Efficient Implementation of Weighted ENO Schemes. J. Comput. Phys. 126, 202–228 (1996)
7. Ivanov, M., Markelov, G., Gimelshein, S.: Statistical simulation of reactive rarefied flows: numerical approach and applications, AIAA Paper, 98-2669 (1998)

Characteristics of Shock Wave Propagating over Particulate Foam

M. Liverts, A. Britan, and G. Ben-Dor

1 Introduction

For many applications where solid and heavy protections against blast are inoperative, the mitigation of the blast wave loading in a cost-effective manner could be achieved using aqueous foam. The protective behavior of aqueous foam is mainly ascribed to high compressibility of the gas bubbles, which is generally accomplished with energy losses due to side wall friction, viscous losses, evaporation, foam shattering and acceleration of the resulted droplets [1, 2, 3]. As transient processes, these factors introduce uncertainty into the predicted behavior of the foam based protection [4]. Recently it has been established that solid additives slow down the foam decay due to the increase in the liquid viscosity [5, 6] as well as enhance the mitigation performance of the foam barriers [7]. A diversity of physical mechanisms responsible for the final effect complicates the issue, and to obtain reliable data, one has to use specially designed tests. Since the main purpose of this study was the particle related effect on the characteristics of the transmitted shock wave, we concerned only with:

- Step-wise shock waves of constant duration (about $5ms$). This excludes the "beneficial" mitigation specific to the pressure pulses of short duration [7];
- Homogeneous, freshly prepared samples of wet foam of constant initial liquid fraction, $\varepsilon_0 = 0.2$. This excludes the role of liquid gradient caused by the foam decay [8].

The observed phenomena of the shock wave propagation over the conventional (no particles) wet foam were systematically compared with those registered inside the particulate foam sample. As the main parameter controlling the problem, the shock wave Mach number, M_S was used as the variable.

M. Liverts · A. Britan · G. Ben-Dor
Shock Tube Laboratory, Protective Technologies R&D Center, Department of Mechanical Engineering, Faculty of Engineering Sciences, Ben Gurion University of the Negev, Beer-Sheva 84105, Israel

2 Experimental Setup

The construction and instrumentation of a vertically positioned shock tube, and the foam preparation, were described in detail by [4]. The samples of particulate foam were prepared by whipping the foaming liquid with added powder of coal fly ash. Weighted fraction of additives was $n = 0.20 \pm 0.01$, here $n = m_p/(m_l + m_p)$, where m_p is the mass of the powder and m_l is the mass of the foaming liquid, and a liquid fraction of the foam sample was $\varepsilon_0 = 0.20 \pm 0.02$. The repeatability of the impact conditions in our tests ensured a thin diaphragm of mylar, separating the driver and the channel, which was force ruptured by a home-made cross-knife. Using the variable driver pressure $0.5 < P_4 < 11$ bars, the incident shock wave Mach number was in the range $1.02 < M_S < 1.5$. The freshly prepared foam sample was poured into the test section of the shock tube, which was already set for a new run. As a result the time elapsed between the foam preparation and the diaphragm rupture usually did not exceed $2min$. To control over the possible changes in the foam structure that could appear during this time duration, optical observation and conductivity measurements were used (for details see [4]).

3 Results and Conclusions

3.1 Foam Homogeneity and Repeatability of the Results

The flow velocity in each cross section of the sample during the foam decay reflects the balance between the input and the output flows of the foaming liquid [9]. Fig. 1a demonstrates that while the wet foam generally starts to drain once prepared, the local liquid fraction initially remains constant. This shows that the liquid flux through the cross-section here is not changed yet. Thereafter, once the foaming liquid supply from the upper layers is terminated, the local liquid fraction reduces, while the front of the decaying foam moves downstream. Once reaching the lower cross-sections, the resulted gradient of the liquid fraction appears. It increases in time and finally occupies the whole sample. The propagating trajectory of the liquid

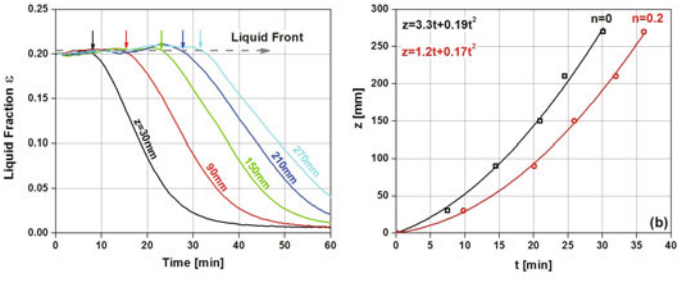

Fig. 1 (a) Liquid fraction dynamics along the foam's column, (b) trajectory of liquid front in conventional ($n = 0$) and particulate ($n = 0.2$) foams.

front along the foam column which is based on the conductivity measurements, is shown in Fig. 1b. The points in this figure were deduced assuming that the gradual decrease in liquid fraction starts upon the arrival of the liquid front at the measuring point. These time instants are shown by arrows in each curve $\varepsilon(t,z)$ of Fig. 1a. The resulted trajectories of the liquid front, shown in Fig. 1b, fit well the parabolic law that ensures that the initial velocity, u_{1f}, and further acceleration of the liquid front are both slower inside the particulate foam. There are at least three mechanisms which can explain this effect. The particles enter the Plateau channels and the resulted blockage increases their resistance to the liquid flow; the particles attached to the bubble surface prevent the foam coarsening; and finally, the particles presence increases viscosity of the slurry [5, 6]. Using the results of Fig. 1b, e.g. the peak value of the registered velocity, $u_{1f} = 3.3mm/min$, it could be easily seen, that during the first $5min$ the volume occupied by the variable liquid fraction is about $16.5mm$-high, which for the $220mm$ foam sample (foam height used in shock tube tests) is still small to be important. Comparing the data shown in Fig. 2a and Fig. 2b one can observe how the added particles modify the bubble growth during the same time period, $\Delta t = 5min$, at the cross sections positioned $8cm$, $20cm$ and $32cm$ from the top of the foam sample. Notice that all points for both, conventional (a) and particulate (b) foams, as seen to correlate well with each other and any sensitivity is observed to the measurement position. However, the added particles make the distribution function narrower and shift the peak diameter closer to the limiting value, about $D \approx 100\mu m$. Accounting for the possible scattering in the initial foam structure, the data in Figs. 1 and 2 enable the conclusion that during the shock wave loading the foam samples remain homogeneous over the full height. To assure that further results of the shock tube tests with this foam are duplicated, we compared the pressures traces registered in a course of three subsequent tests. Beside the small, about 6-8% fluctuation of the signals, which are a direct response to the random variations of the foam structure, the reproducibility of the results was high enough.

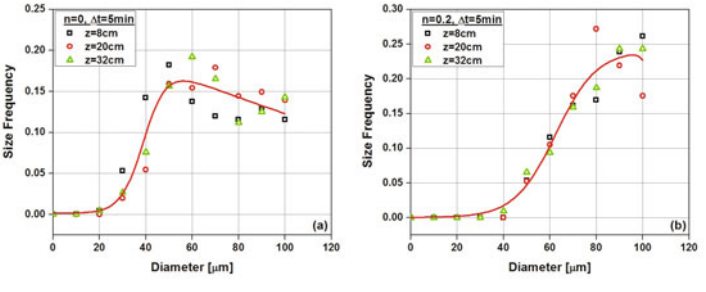

Fig. 2 Bubble size distribution along the column of (a) conventional ($n = 0$) and (b) particulate ($n = 0.2$) foam, $\Delta t = 5min$.

3.2 Shock Wave Refraction

Assuming that foam is homogeneous and neglecting any internal dissipation, the system of hydrodynamic conservation equations has a well-known analytical, quasi-steady solution [10]. The shock wave transmitted inside the foam, $\mathtt{Tr}$, specifies the Mach number $M_{\mathtt{Tr}} = V_{\mathtt{Tr}}/c_{1\mathtt{f}}$, where $V_{\mathtt{Tr}}$ is the transmitted shock wave velocity. The sound velocity in foam $c_{1\mathtt{f}}$; the pressure behind the transmitted shock wave front, $P_{2\mathtt{f}}$; and the velocity of the foam face, $u_{2\mathtt{f}}$ are:

$$c_{1\mathtt{f}} = \sqrt{\frac{\Gamma P_{1\mathtt{f}}}{\rho_{1\mathtt{f}}\varepsilon_a}}, \quad P_{2\mathtt{f}} = P_{1\mathtt{f}}\frac{2\Gamma M_{\mathtt{Tr}}^2 - (\Gamma-1)}{\Gamma+1}, \quad u_{2\mathtt{f}} = \frac{2V_{\mathtt{Tr}}}{\Gamma+1}\left(1-\frac{1}{M_{\mathtt{Tr}}^2}\right) \tag{1}$$

where Γ is the ratio of the specific heats of the foam, $\rho_{1\mathtt{f}}$ and $P_{1\mathtt{f}}$ are the density and pressure of the undisturbed foam, ε_a is the air (compressible phase) void fraction. Correspondingly, for the local parameters behind the incident shock wave within the air domain 2:

$$P_2 = P_1\frac{2\gamma M_{\mathtt{S}}^2 - (\gamma-1)}{\gamma+1}, \quad u_2 = \frac{2V_{\mathtt{S}}}{\gamma+1}\left(1-\frac{1}{M_{\mathtt{S}}^2}\right) \tag{2}$$

where $M_{\mathtt{S}} = V_{\mathtt{S}}/c_1$, is the incident shock wave Mach number, $V_{\mathtt{S}}$ is the shock velocity, c_1 is the sound velocity in undisturbed air, γ is the air specific heats ratio. Since the Mach number of the reflected shock wave, $\mathtt{Rf}$, is $M_{\mathtt{Rf}} = V_{\mathtt{Rf}}/c_2$, the pressure and the gas velocity within domain 5 are:

$$P_5 = P_2\frac{2\gamma M_{\mathtt{Rf}}^2 - (\gamma-1)}{\gamma+1}, \quad u_5 = u_2 - \frac{2V_{\mathtt{Rf}}}{\gamma+1}\left(1-\frac{1}{M_{\mathtt{Rf}}^2}\right) \tag{3}$$

For a fixed value of the Mach number, $M_{\mathtt{S}}$, the gas flow parameters ρ_2, P_2, c_2 and u_2 are known in advance while the matching conditions across the foam face: $u_{2\mathtt{f}} = u_5$ and $P_{2\mathtt{f}} = P_5$ give the lacking values of $V_{\mathtt{Tr}}$ and $V_{\mathtt{Rf}}$. Notice that this approach neglects the cellular structure of the foam, internal dissipation, surface tension and inter-phase heat transfer. As a result, the predicted flow pattern resulted by shock wave/foam interaction has to depend only on the acoustic impedance mismatch at the foam face, $\chi = (\rho c)_{1\mathtt{f}}/(\rho c)_2$ where ρ is the material density. It also suggests that:

- The transient effects on both sides of the air/foam boundary, $\mathtt{FF}$, are small or quickly subside;
- The foam obeys the equation of state of a perfect pseudo-gas used for this modeling.

In Fig. 3 we compare the predicted and the recorded values of the transmitted shock wave velocity and pressure versus the impedance ratio, χ. Notice that under the tested conditions the added particles do not affect the specific heats ratio, Γ, which for both conventional and particulate foams was calculated to be [10]:

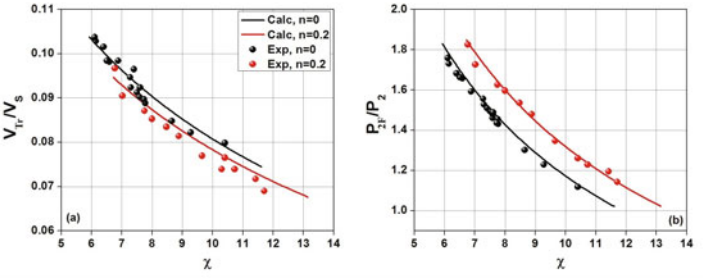

Fig. 3 Experimental and calculated values of dimensionless velocity (a) and pressure (b) in the foam, as functions of acoustic impedance mismatch, χ.

$$\Gamma = 1 + \frac{\rho_a \varepsilon_a R}{\sum_i \rho_i \varepsilon_i C_i} = 1.0003 \tag{4}$$

where R is the specific gas (air) constant, ε is the void fraction, ρ is the density, C is the heat capacity and the indexes $i = a, l, p$ stand for air, liquid and particles, respectively. However, the density of the particulate foam increases to about $\rho_{\mathrm{pf}} = 228 kg/m^3$ (in the conventional foam it is $\rho_{\mathrm{cf}} = 183 kg/m^3$). Notice that the acoustic impedance ratio, χ, increases as the incident shock wave intensity reduces and/or as the foam becomes wetter. Note that the acoustic impedance ratio, χ, increases as the incident shock wave intensity reduces and/or as the foam becomes wetter. However, in both cases the transmitted shock wave velocity and the pressure enhancement in the foam reduce. Interestingly, the simulated curves in these graphs agree with the measured data and resolve well the gap between the points obtained for the regular and the particulate foams. Beside the shock wave velocity, V_{Tr} and the peak pressure, $P_{2\mathrm{f}}$ the last while not least important characteristic, which could not be described by the simple models in their present form, is the rise time of the pressure pulse, t_{rise}. In this study it was agreed that it is a time required for the side wall pressure traces, shown in Fig. 4a, to change from their initial, zero value seen before the shock wave arrival, to a peak, quasi-steady amplitude in the post shock wave

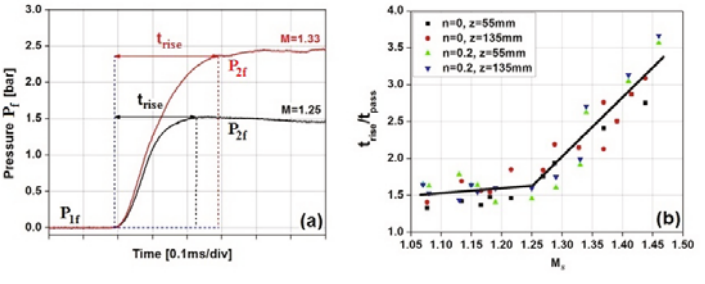

Fig. 4 (a) Typical examples of the pressure traces and (b) registered values of the rise-time in conventional ($n = 0$) and particulate ($n = 0.2$) foams.

flow. However, even for the ideal step-wise pressure pulse generated in air, at least three main factors affect the accuracy of such measurements: The first is the high frequency response of the amplifier and the acquisition system. In our case, the role of this factor is negligible since it is well above $100kHz$; The second is the sensor diameter, d, which is about $0.5cm$; The third is the shock wave velocity, V_{Tr}, whose contribution to the registered value, t_{rise}, was accounted using scaling of the data in Fig. 4b with the "pass" time, $t_{\mathrm{pass}} = d/V_{\mathrm{Tr}}$. Of particular note is that $t_{\mathrm{rise}}/t_{\mathrm{pass}} > 1$ tends to increase solely due to the increasing Mach number, M_{S}. Since all points for both, conventional ($n = 0$) and particulate ($n = 0.2$) foams scale well and do not show any dependence on the measurement cross section, this ensures that the intensity of the impact is a single parameter responsible for this behavior. Note that the inflection point between the two linear approximations in Fig. 4b responds to the Mach number $M_{\mathrm{S}} \approx 1.25$. This is rather close to critical impact conditions, which may cause foam shattering [1]. A better insight into the observed finding can give an optical control of the post shock wave conditions. These experiments as well as a new series of more comprehensive numerical simulations are now underway.

References

1. Raspet, R., Griffiths, S.K.: The reduction of blast noise with aqueous foam. J. Acoust. Soc. Am. 74(6), 1757–1763 (1983)
2. Vakhnenko, V.A., Kudiniv, V.M., Palamarchuk, B.I.: Effect of thermal relaxation of attenuation of shock waves in two-phase medium. Prikladnaya Mekh 18(12), 91–97 (1982) (in Russian)
3. Gelfand, B.E., Silnikov, M.V.: Explosions and blast control. St. Petersburg, Asterion (2004)
4. Britan, A., Liverts, M., Ben-Dor, G., Koehler, S.A., Bennani, N.: The effect of fine particles on the drainage and coarsening of foam. Colloids and Surfaces A: Physicochem. Eng. Aspects 344(1-3), 15–23 (2009)
5. Moxon, N.T., Torrance, A.C., Richardson, S.B.: The attenuation of acoustic signals by aqueous and particulate foams. Appl. Acoust. 24(3), 193–209 (1988)
6. Senapati, P.K., Mishra, B.K., Parida, A.: Modeling of viscosity for power plant ash slurry at higher concentrations: Effect of solids volume fraction, particle size and hydrodynamic interactions. Powder Tech. 197(1-2), 1–8 (2010)
7. Britan, A., Liverts, M., Ben-Dor, G.: Blast wave mitigation by particulate foams. In: The 4th Euro. Conf. Computational Mech., Solid Structure and Coupled Problems in Eng., Paris, France, May 16-21 (2010)
8. Britan, A., Ben-Dor, G., Shapiro, H., Liverts, M., Shreiber, I.: Drainage effects on shock wave propagating through aqueous foams. Colloids and Surfaces A: Physicochem. Eng. Aspects 309(1-3), 137–150 (2007)
9. Koehler, S.A., Hilgenfeldt, S., Stone, H.A.: Liquid flow through aqueous foams: The node-dominated foam drainage equation. Phys. Rev. Lett. 82(21), 4232–4235 (1999)
10. Rudinger, G.: Some effects of finite particle volume of the dynamics of gas-particle mixture. AIAA J. 3, 1217–1222 (1965)

Triple–Shock–Wave Configurations: Comparison of Different Thermodynamic Models for Diatomic Gases

P.S. Mostovykh and V.N. Uskov

1 Introduction

Triple–shock–wave configurations (TC) were experimentally reported by E. Mach in 1878 [1]. The first detailed experimental and theoretical investigation of the TC was fulfilled by J. von Neumann in 1943 [2]. In the theoretical description of the TC in the von Neumann article [2] (known as the three–shock theory) gas was supposed thermally and calorically perfect. The three–shock theory is based on the Euler equations in the integral form, and expresses all non–dimensional TC parameters through the two basic ones: the initial flow Mach number M and either the incident shock intensity J_1 or its inclination angle σ_{e1} [3]. In [4] the problem of a moving shock wave reflection from a plane wedge with a TC formation in real gases (nitrogen, air and oxygen) was considered.

In this paper gas is supposed thermally perfect, but calorically imperfect, i.e. the dependence of its specific heats on the gas temperature is taken into account. Steady flows are considered. The aim of the present paper is to estimate the influence of this factor on the gas flows parameters behind the reflected and the bow shocks at different initial flow Mach number and the incident shock wave inclination angle values. The TC calculation was fulfilled using the caloric equations of gas state corresponding to oxygen O_2, nitrogen N_2, carbon monoxide CO, hydrogen H_2, fluorine F_2 and chlorine Cl_2.

The gas behind a shock wave of high intensity is in a nonequilibrium state, i.e. the average energies per different molecular degrees of freedom (translational, rotational, vibrational) are different. The relaxation with respect to nonequilibriums takes place in some layer behind the shock, so the equilibrium thermodynamics relations between the gas pressure, density, temperature and enthalpy are valid only behind this layer. In this paper the relaxation layer thickness is neglected with respect to the flow characteristic lengths scale, what means that the equilibrium thermodynamic relations are used for the flows behind all three shocks. Chemical reactions

P.S. Mostovykh · V.N. Uskov
Aerospace Dept., Baltic State Technical University, St. Petersburg, Russia

in the gas, including dissociation, are supposed frozen. The mathematical model of the TC based on these assumptions has the form of the algebraic, not the differential relations.

2 The Mathematical Model

The scheme of the TC is presented on Fig. 1: 1 is the incident, 2 is the reflected and 3 is the bow shock, τ is the slipline. Shock waves are described by the dynamic compatibility conditions (DCC) on them, which follow from the integral forms of the conservation of mass, momentum and energy and the entropy growth for non-viscous nonheatconductive gas. The DCC on the shocks and the formulae for the flows deflection angles β_i on them are given in Table 1. The gas parameters (pressure p, density ρ, temperature T, velocity magnitude V) without index and with indices 1, 2, 3 refer to the initial flow, the flows behind the incident, the reflected and the bow shocks, respectively. The angles β_i, as well as the shock inclination angles σ_i and the tangential to the shocks velocity components v_i have the indices of the corresponding shocks. The normal to the shocks velocity components u_{ij} have the indices shown on Fig. 1. The DCC on the slipline (dividing the flows with indices 2 and 3) are confined to the equality of the gas static pressures and collinearity of the velocity vectors of the gas flows on the sides of the slipline:

$$p_2 = p_3, \qquad \beta_1 + \psi_2\beta_2 = \psi_3\beta_3.$$

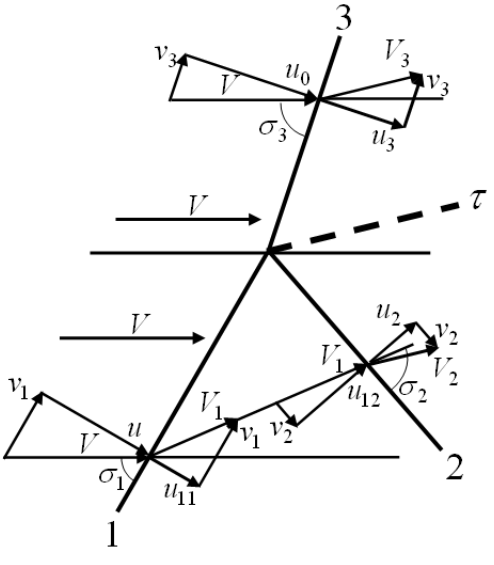

Fig. 1 The scheme of TC.

Table 1 The DCC on the shock waves

the incident shock	the reflected shock	the bow shock
$\rho u = \rho_1 u_{11}$	$\rho_1 u_{12} = \rho_2 u_2$	$\rho u_0 = \rho_3 u_3$
$p + \rho u^2 = p_1 + \rho_1 u_{11}^2$	$p_1 + \rho_1 u_{12}^2 = p_2 + \rho_2 u_2^2$	$p + \rho u_0^2 = p_3 + \rho_3 u_3^2$
$h(T) + \frac{u^2}{2} = h(T_1) + \frac{u_{11}^2}{2}$	$h(T_1) + \frac{u_{12}^2}{2} = h(T_2) + \frac{u_2^2}{2}$	$h(T) + \frac{u_0^2}{2} = h(T_3) + \frac{u_3^2}{2}$
$s(T,\rho) \le s(T_1,\rho_1)$	$s(T_1,\rho_1) \le s(T_2,\rho_2)$	$s(T,\rho) \le s(T_3,\rho_3)$
$\beta_1 = \arctan\left(\frac{(u-u_{11})v_1}{v_1^2 + u u_{11}}\right)$	$\beta_2 = \arctan\left(\frac{(u_{12}-u_2)v_2}{v_2^2 + u_{12}u_2}\right)$	$\beta_3 = \arctan\left(\frac{(u_0-u_3)v_3}{v_3^2 + u_0 u_3}\right)$

Here ψ_i are the flow deflection indices, $\psi_i = \pm 1$. For example, on the scheme, shown on Fig. 1, $\psi_2 = -1$, $\psi_3 = +1$.

The Clapeyron equation $p_i = \rho_i R T_i$ was used as a thermal equation of gas state and the polynomial interpolation of the specific heat at constant pressure as a function of temperature $c_p = c_p(T)$ for different temperature T intervals was used as a calorical equation of state [5, 6]:

$$c_p(T) = R\left(\frac{A_1}{T^2} + \frac{A_2}{T} + A_3 + A_4 T + A_5 T^2 + A_6 T^3 + A_7 T^4 + A_8 T^5\right).$$

Here R is the gas constant, measured in $J/(kg \cdot \mathrm{K})$. The coefficients $R, A_1, \ldots, A_8$ for different gases and their mixtures are cited in the tables [6, 7]. For a thermally perfect gas the specific heat at constant volume is given by the Robert Mayer formula $c_v(T) = c_p(T) - R$. The gas enthalpy $h(T)$ and the gas entropy $s(T,\rho)$ are cited in [6]:

$$h(T) = R\left(-\frac{A_1}{T} + A_2 \ln T + A_3 T + \frac{A_4}{2}T^2 + \frac{A_5}{3}T^3 + \frac{A_6}{4}T^4 + \frac{A_7}{5}T^5 + \frac{A_8}{6}T^6 + B_1\right);$$

$$s(T,\rho) = R\left(-\frac{A_1}{2T^2} - \frac{A_2}{T} + (A_3 - 1)\ln T + A_4 T + \right.$$
$$\left. + \frac{A_5}{2}T^2 + \frac{A_6}{3}T^3 + \frac{A_7}{4}T^4 + \frac{A_8}{5}T^5 + B_2 - \ln\rho\right).$$

The coefficients B_1, B_2 for different gases are also cited in the tables [6, 7]. The constant B_1 is determined from the condition $h(298.15\,\mathrm{K}) = 0$. The problem of the flow parameters behind the incident shock determination leads to solving the equation

$$h(T)+\frac{u^2}{2}\left(1-\frac{\rho^2}{\rho_1^2}\right)-h\left(\frac{p+\rho u^2-\rho^2u^2/\rho_1}{\rho_1 R}\right)=0.$$

The density and the temperature behind the reflected shock meet the relation

$$RT_2\rho_2^2+(2\rho_1(h(T_1)-h(T_2))+RT_2\rho_1-p_1)\rho_2-p_1\rho_1=0.$$

After solving it with respect to density, other parameters behind the reflected shock can also be found as a function of temperature T_2. The pressure behind the bow shock and the flow deflection angle on it are expressed through parameters behind the reflected shock using the DCC on the slipline. Its inclination angle is given by the formula:

$$\tan\sigma_{e3}=\frac{p_2-p}{(p+\rho V^2-p_2)\tan|\beta_1+\psi_2\beta_2|}.$$

The parameters u_0, v_3, u_3, ρ_3, T_3 are expressed through the mentioned named above. As a result, all components in the energy equation for the bow shock are expressed through T_2, and it can be solved with respect to this unknown.

3 The Results Analysis

The TC calculation problem can have several solutions. The solution with the maximal pressure behind the reflected shock p_2 value is called the main one; other solutions are called the alternative ones and are numbered in the value p_2 descending order [3, 8, 9].

In this work the following TC parameters were found: the flows deflection angles β_i on the three shocks, the shock inclination angles σ_i, as well as the gas pressures p_i, temperatures T_i, enthalpies $h(T_i)$, Mach numbers M_i behind the three shocks. The calculation was fulfilled at the following input quantities values: the thermodynamical parameters of the initial flow are normal room conditions: $p=10^5$ Pa and $T=300$ K; the initial flow Mach number $M=5$ and the incident shock inclination angle $\sigma_{e1}=0.9344$. This σ_{e1} value leads to the reflected discontinuity in the alternative solution being weak (with the intensity equal to unity) for the perfect gas. At these M and σ_{e1} values the main solution with $\psi_2=-1$, $\psi_3=+1$ and one alternative solution with $\psi_2=\psi_3=+1$ exist.

The tables 2 and 3 give the obtained temperature values behind all three shocks for the considered gases, as well as the flow parameters (pressure, Mach number, specific heat at constant pressure divided by the gas constant and enthalpy divided by the gas constant) behind the bow shock and the flow deflection angle on it. The table 2 data refers to the main solution, the table 3 data refers to the alternative solution, respectively.

The results from tables 2 and 3 show that the influence of the gas imperfection on the TC parameters is significant. For both solutions the flow behind the bow shock Mach number decreases and the flow deflection angle on the shock increases. The thermodynamic parameters for the two solutions change differently. In case of the main solution the incident and the reflected shocks turn the flow into the opposite

Table 2 The TC parameters. The main solution ($\psi_2 = -1$; $\psi_3 = +1$). $p = 10^5$ Pa; $T = 300$ K; $M = 5$; $\sigma_{e1} = 0.9344$.

	T_1, K	T_2, K	T_3, K	p_3, MPa	M_3	C_{p3}/R	h_3/R, K	β_3
Perfect gas	1224	1381	1706	2.83	0.524	3.500	4927	0.501
Hydrogen	1210	1357	1657	2.88	0.516	3.965	4981	0.499
Nitrogen	1170	1302	1588	2.91	0.504	4.221	4989	0.504
Carbon monoxide	1161	1291	1576	2.92	0.502	4.259	4995	0.505
Oxygen	1125	1246	1525	2.93	0.494	4.404	4995	0.513
Fluorine	1052	1159	1428	2.90	0.483	4.578	4897	0.526
Chlorine	1008	1110	1374	2.83	0.481	4.557	4768	0.532

Table 3 The TC parameters. The alternative solution ($\psi_2 = \psi_3 = +1$). $p = 10^5$ Pa; $T = 300$ K; $M = 5$; $\sigma_{e1} = 0.9344$.

	T_1, K	T_2, K	T_3, K	p_3, MPa	M_3	C_{p3}/R	h_3/R, K	β_3
Perfect gas	1224	1224	1224	1.87	1.533	3.500	3240	0.647
Hydrogen	1210	1234	1278	2.03	1.422	3.767	3515	0.680
Nitrogen	1170	1215	1301	2.21	1.304	4.107	3793	0.720
Carbon monoxide	1161	1209	1302	2.24	1.285	4.159	3841	0.723
Oxygen	1125	1179	1294	2.34	1.219	4.328	3986	0.751
Fluorine	1052	1111	1247	2.41	1.140	4.533	4073	0.780
Chlorine	1008	1067	1206	2.38	1.118	4.529	4004	0.788

directions, the temperatures behind the shocks drop noticeably and the densities increase. In case of the alternative solution the mentioned shocks turn the flow into the same direction, the real gas pressure is significantly higher than the perfect gas one.

As an example the dependence of the flow deflection angle on the bow shock β_3 on the value characterizing the gas calorical imperfection — its specific heat at constant pressure calculated for the temperature behind the bow shock $c_p(T_3)$ (i.e. at the maximal temperature in the TC in the considered model) — for the main and the alternative solutions is shown on Fig. 2.

Shock polars for different real gases and the perfect gas were compared. Fig. 3 shows the shock polars where the flow inclination angle is plotted on the ordinates axis. The incident shock inclination angles are given by the polars intersection points with the line $\sigma_{e1} = 0.9344$. The dots on Fig. 3 show the flow deflection and the shock inclination angles β_3 and σ_{e3} values, corresponding to the bow shock for the main (closed points) and the alternative (open points) solutions.

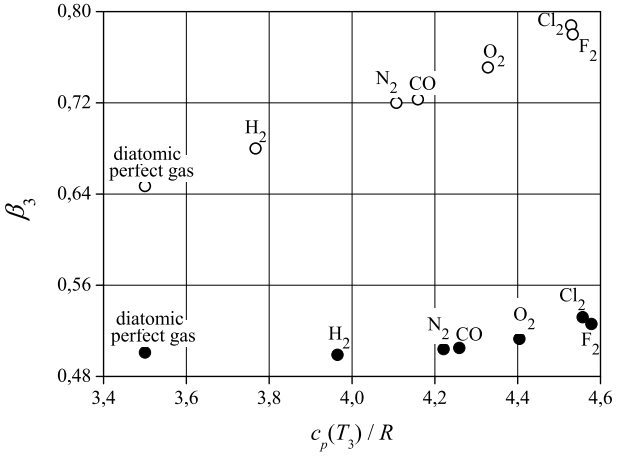

Fig. 2 Dependence of the flow deflection angle on the bow shock β_3 on the specific heat at constant pressure $c_p(T_3)$ for the main (closed points) and the alternative (open points) solutions.

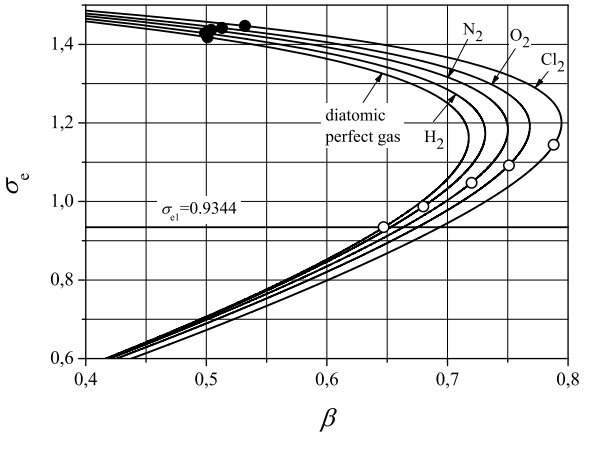

Fig. 3 Shock polars for perfect and imperfect gases; the dots show the values, corresponding to the bow shock for the main (closed points) and the alternative (open points) solutions.

4 Conclusion

Taking the gas calorical imperfection into account significantly changes the flow picture in the TC. The specific heat increase leads to the flow behind the bow shock Mach number decrease and the flow deflection angle on the shock increase. The

thermodynamic parameters for the two solutions change differently. In case of the main solution the temperatures behind the shocks drop noticeably and the densities increase. In case of the alternative solution the real gas pressure is significantly higher than the perfect gas one. Shock polars for different real gases and the perfect gas were compared. Further research should include the comparison of these results with the experiment.

References

1. Mach, E.: Uber den verlauf von funkenwellen in der ebene und im raume. Sitzungsbr. Akad. Wiss. Wien 78, 819–838 (1878)
2. von Neumann, J.: Oblique reflection of shocks. In: Collected Works, 6th edn., pp. 239–299. Pergamon (1943, 1963)
3. Henderson, L.F.: On the confluence of the three shock waves in a perfect gas. Aeronautical Quarterly XV, 181–197 (1964)
4. Ben–Dor, G., Glass, I.I.: Domains and boundaries of non–stationary oblique shock–wave reflexions. Diatomic gas. J. Fluid Mech. 92, pt. 3, 459–496 (1979)
5. Tatum, K.E.: Computation of thermally perfect oblique shock wave properties, pp. 1–1, AIAA Paper 97–0868 (1997)
6. McBride, B.J., Gordon, S., Reno, M.A.: Thermodynamic data for fifty reference elements. NASA TP–3287 (1993)
7. McBride, B.J., Heimel, S., Ehlers, J.G., Gordon, S.: Thermodynamic properties to 6000^0K for 210 substances involving the first 18 elements. NASA SP–3001 (1963)
8. Kalghatgi, G.T., Hunt, B.L.: The three–shock confluence problem for normally impinging overexpanded jets. The Aeronautical Quarterly XXVI, 117–132 (1975)
9. Uskov, V.N., Chernyshov, M.V.: Special and extreme triple–shock–waves configurations. J Appl. Mech. Tech. Phys. 47(4), 492–504 (2006)

Numerical Study on the Evolution of Shock-Accelerated Interface: Influence of the Interfacial Shape

M. Fan, Z. Zhai, T. Si, X. Luo, J. Yang, J. Tang, and X. Liu

1 Introduction

The Richtmyer-Meshkov (RM) instability [1, 2] occurs on a perturbed interface separating two fluids with different densities when impulsively accelerated, which has received much attention because of its academical significance in the field of vortex dynamics and turbulent mixing, and having important applications in inertial confinement fusion, supersonic combustion, and supernova collapse. In the past decades, scientists have performed many experimental, numerical and theoretical researches on RM instability. Numerically, the research work is usually carried out based on the experiment in order to further understand the instability phenomenon. Meyer and Blewett [3] employed a Lagrange algorithm to simulate the process of the RM instability. Later, the front tracking, high order WENO shock-capturing method and LES have also been developed to study the corresponding problems. However, the previous study mainly focused on the circle or single-mode interfaces. Recently, the shock interaction with a rectangular block was studied by Bates *et al.* [4]. Bai *et al.* [5] performed the experimental and numerical investigation on the shock-accelerated elliptic SF_6 gas cylinder. For other shapes of interfaces, they have been seldom investigated until now. Normally, two kinds of mechanisms are used to interpret the occurrence of RM instability. One is the baroclinic mechanism which comes from the misalignment between pressure and density gradients, the other one is the pressure disturbance mechanism which includes the shock refraction, reflection, and focusing[6]. The initial shape/perturbation of the interface affect the vorticity production and wave system during the interaction, which leads to different evolution modes [7]. In order to further understand the effect of interface shape on

M. Fan · Z. Zhai · T. Si · X. Luo · J. Yang
Department of Modern Mechanics, University of Science and Technology of China, Hefei 230026, P.R. China

J. Tang · X. Liu
The 3rd Research Academy of CASIC, Beijing 100074, P.R. China

interface instability, three two-dimensional interfaces with different initial shapes, i.e. rectangle, triangle and ellipse, are investigated in the present work.

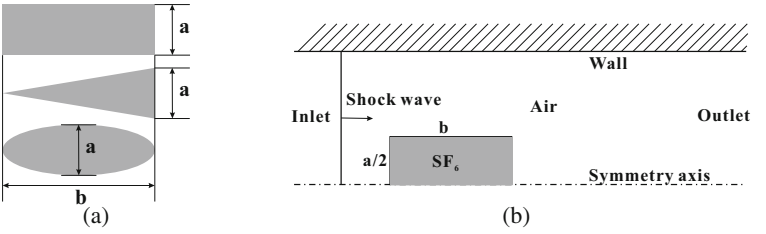

Fig. 1 The initial shapes of three interfaces (a) and the sketch of the computational domain for the case of rectangular interface (b).

2 Numerical Method

The numerical algorithm of VAS2D (2D & Axisymmetric Vectorized Adaptive Solver) developed by Sun and Takayama [8] is adopted in the present simulation, which solves the Euler equations discretized by the finite-volume method and has the second order accuracy both in space and time based on the MUSCL-Hancock scheme. The three initial interfaces are shown in Fig. 1(a). The height and width of interfaces on the three shapes are 20 mm and 60 mm, respectively. Fig. 1(b) shows the initial condition of simulation. The total computational domain is 250 mm $\times$ 80 mm and only one half of the area is simulated because of the symmetry of the three interface shapes. The incident shock wave of Ma = 1.2 moves from left to right. The internal gas of the rectangular interface is SF_6 surrounded by ambient air.

3 Results and Discussions

3.1 Rectangle

The numerical schlieren (upper) and vorticity (lower) contours of the shock-rectangle interaction are shown in Fig. 2. The moment when the incident shock collides with the rectangular interface is defined as $t = 0$ μs.Fig. 2(a) shows the situation at 3 μs after shock impact. Fig. 2(b) reveals the wave pattern including the incident,reflected and transmitted shock waves. The transmitted shock (inside the interface) is slower than the incident shock wave because the speed of sound in SF_6 is slower than that in air. Additionally, four triple points and two Mach stems appear, which are very similar to the numerical and experimental results obtained by Bates *et al.* [4]. Meanwhile, due to the baroclinic mechanism, vorticity is generated on the up- and down-left corner of the interface. As the incident and transmitted shocks move forward, the incident wave circumvents the interface and reaches the center

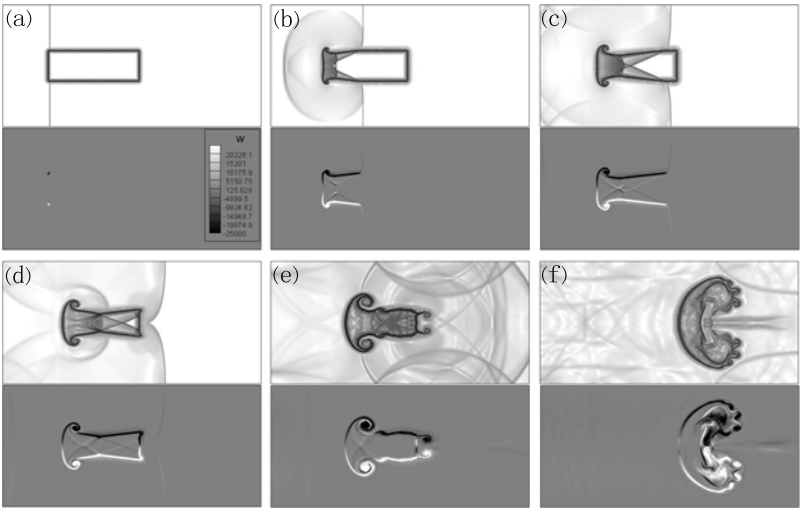

Fig. 2 The schlieren images (upper) and vorticity contours (lower) on the interaction of a shock wave of Ma=1.2 with a rectangular interface at $t = 3, 73, 133, 183, 363, 1003$ μs after shock impact.

of the downstream interface, which also produces vorticity on the downstream (see Figs. 2(c) and (d)).

From Fig. 2(e), we can note that the vorticity mainly distributes on the upstream. Induced by the vortex-pair on the upstream, the speed of the upstream interface is larger than that of the downstream, and the former will catch up with the latter, as shown in Fig. 2(f). In the late stage, the flow field becomes more complex due to small vortices generated at the edge of the interface when the Kelvin-Helmhotz instability occurs.

3.2 Triangle

Fig. 3 illustrates the schlieren sequences (upper) and the corresponding vorticity contours (lower) of the shock interaction with triangle. Fig. 3(a) shows the situation 3μs after the shock impact, where the shock contacts with the leftmost cusp first. When the incident shock wave moves forward, the transmitted, reflected shocks and internally reflected rarefaction shock are formed and very little vorticity appears on the cusp, see Fig. 3(b). A 'bud' is formed resulting from the interface compressed by the refracted shocks and the transmitted shock. As the refracted and transmitted shocks moving forward, this 'bud' will also move towards downstream as shown in Fig. 3(c)-(e). For this shape of interface, most of the vorticity distributes on the three cusps on the triangular interface and the vorticitices on the upstream and downstream are in the same order, so the distance between the upstream and the

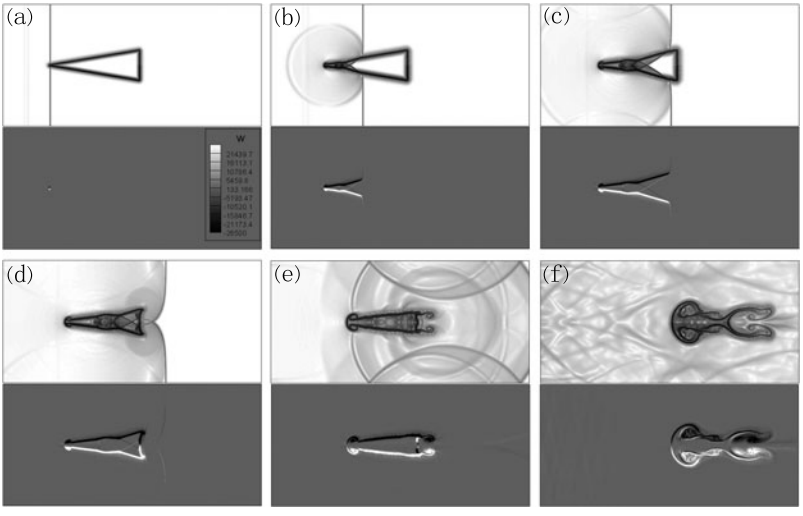

Fig. 3 The schlieren images (upper) and vorticity contours (lower) on the interaction of a shock wave of Ma=1.2 with a triangular interface at $t = 3$, 73, 133, 183, 363, 1003 μs after shock impact.

downstream keeps a constant. Therefore, the conclusion of catching up in the rectangular case won't occur here.

3.3 Ellipse

Fig. 4 presents the numerical schlieren (upper) and vorticity

The shape of transmitted shock is a concave arc in the early state and that will separated into two arcs as time goes by and transmitted through the side interface on the downstream. Besides, the vorticity on the elliptical interface mainly accumulates on the upstream edge as well as the highest and lowest point in the y-direction. Thus, the upstream interface will also catch up with the downstream interface just like the rectangular interface. From the numerical vorticity contours, we can find that the vortex begins to form at about 283 μs for ellipse, 133 μs for triangle and only 73 μs for rectangle. Therefore, the shape of interface has an important effect on the generation of the vortex, which results in different development of interface and occurrence of RM instability.

3.4 The Evolution of Interface

As discussed above, differences are found in the evolution of the three interfaces with the same initial condition. Fig. 5 provides the definitions for several parameters to describe the interfacial evolution, i.e. X_{left}, X_{right} and Y_{top} and L. The characteristic length L_0 and height A_0 are the initial width and height of the interface

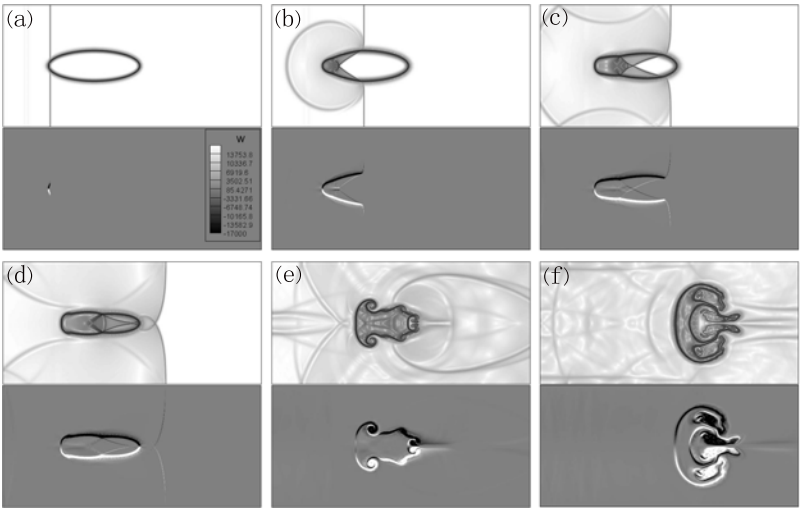

Fig. 4 The schlieren images (upper) and vorticity contours (lower) on the interaction of a shock wave of Ma=1.2 with a elliptical interface at t = 3, 73, 133, 183, 483, 1003 μs after shock impact.

Fig. 5 The definitions of an interface evolution: X_{left}, X_{right} and Y_{top}.

respectively (L_0=60 mm and A_0=20 mm), and the characteristic time t_0 is defined as $t_0 = L_0/U_{flow}$ with U_{flow} the flow velocity behind the incident shock (in the present study, $U_{flow} = 107.55$ m/s, which results in $t_0 = 0.56 \times 10^{-3}$ s). Fig. 6(a) describes the evolution of the relative displacement ($X_{left} - U_{flow}t$) of the left point of the interface between the interface and the post-shock air flow versus a normalized time t/t_0. It can be found that the relative displacement grows approximately linearly. Due to the less amount of vorticity generated in the upstream for the triangular interface, the upstream interface X_{left} moves slower than that of the other two shapes while the opposite situation is found for the downstream interface. The downstream of the triangular interface X_{right} moves faster than that of the other two interfaces because of more vorticity accumulated on the downstream for the triangular interface, as shown in Fig. 6(b). Fig. 6(c) indicates that the variation of Y_{top} of the rectangular interface is larger than that of the other two interfaces, which is also related to the vorticity on the upstream interface. In addition, Y_{top} decreases at the early time because of the compression after the incident shock impact. The variations of the length of the three shapes are shown in Fig. 6(d).

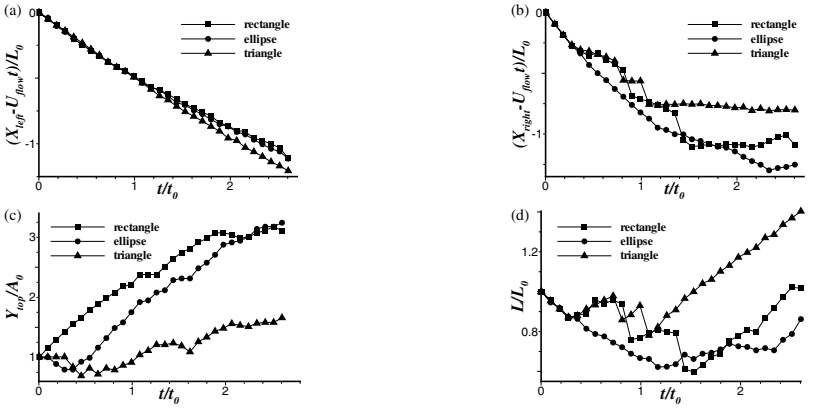

Fig. 6 The evolution of X_{left} (a), X_{right} (b), Y_{top} (c) and L (d) for three different interfaces.

4 Conclusion

Through the analysis above, we can conclude that the development of the RM instability is closely related to the interfacial shape. The influence of the interface shape behaves on the shape of refracted shock wave, generation or distribution of the vorticity, the evolution of interface. In future work, we will investigate more cases with different density ratios and simulate more shapes of interfaces. At the same time we will conduct some experiments so that the influence of the interface shape on the evolution of the RM instability can be evaluated completely.

References

1. Richtmyer, R.D.: Taylor instability in shock acceleration of compressible fluids. Commun. Pure Appl. Math. 13, 297–319 (1960)
2. Meshkov, E.E.: Instability of the interface of two gases accelerated by a shock wave. Fluid Dyn. 4, 101–104 (1969)
3. Meyer, K.A., Blewett, P.J.: Numerical investigation of the stability of a shock accelerated interface between two fluids. Phys. Fluids 15(5), 753–759 (1972)
4. Bates, K.R., Nikiforakis, N., Holder, D.: Richtmyer-Meshkov instability induced by the interaction of a shock wave with a rectangular block of SF_6. Phys. Fluids 19, 036101 (2007)
5. Bai, J., Zou, L., Wang, T., Liu, K., Huang, W., Liu, J., Li, P., Tan, D., Liu, C.: Experimental and numerical study of shock-accelerated elliptic heavy gas cylinders. Phys. Rev. E 82, 056318 (2010)
6. Haas, J.F., Sturtevant, B.: Interaction of weak shock waves with cylindrical and spherical gas inhomogeneities. J. Fluid Mech. 181, 41–76 (1987)
7. Brouillette, M.: The Richtmyer-Meshkov instability. Annu. Rev. Fluid Mech. 34, 445–468 (2002)
8. Sun, M., Takayama, K.: Conservative smoothing on an adaptive quadrilateral grid. J. Comput. Phys. 150(1), 143–180 (1999)

Imploding Conical Shock Waves

R.T. Paton, B.W. Skews, S. Rubidge, and J. Snow

1 Introduction

Following the original numerical work by Hornung, [1], an experimental study of the behaviour of imploding conical shock waves was undertaken by Skews et al [2] in which good correlation was exhibited with the patterns of reflection for waves of various strengths. This study extends that study to various incident wave strengths.

2 Apparatus

The shock tube used to generate the conical waves to be studied is vertically oriented with a cylindrical driver of 300mm internal diameter and 750mm length. The driver is capable of testing at pressures up to 15 bar, supported by circular diaphragms burst using a pneumatically actuated pin. Immediately below this there is a 550mm long initial driven section fitted directly above a perforated plate. This plate is 36mm thick with 49 evenly spaced holes 30mm in diameter and is designed to smooth irregularities in the incident shock wave resulting from uneven bursting of the diaphragm. This plate also supports a 70mm diameter sting which hangs down into the lower driven section, which is 710mm in length. Steel cones of various angles can be fitted at the base of this sting. Above these cones there is a shaped wooden contraction designed to smoothly focus the incident plane shock wave into the annular gap between the central steel cone and an external steel plate with a conical hole forming a converging conical gap. A schematic of the shock tube is given in figure 1. The conical shock wave thus produced emerges at the apex of the inner cone and the focusing behaviour there is visualised using a z-configuration shadowgraph system. The light source used is a collimated Hamamatsu Xenon arc flash lamp and images are taken using a standard DSLR camera.

R.T. Paton · B.W. Skews · S. Rubidge · J. Snow
Flow Research Unit, School of Mechanical, Industrial, and Aeronautical Engineering, University of the Witwatersrand, Johannesburg, PO WITS 2050, South Africa

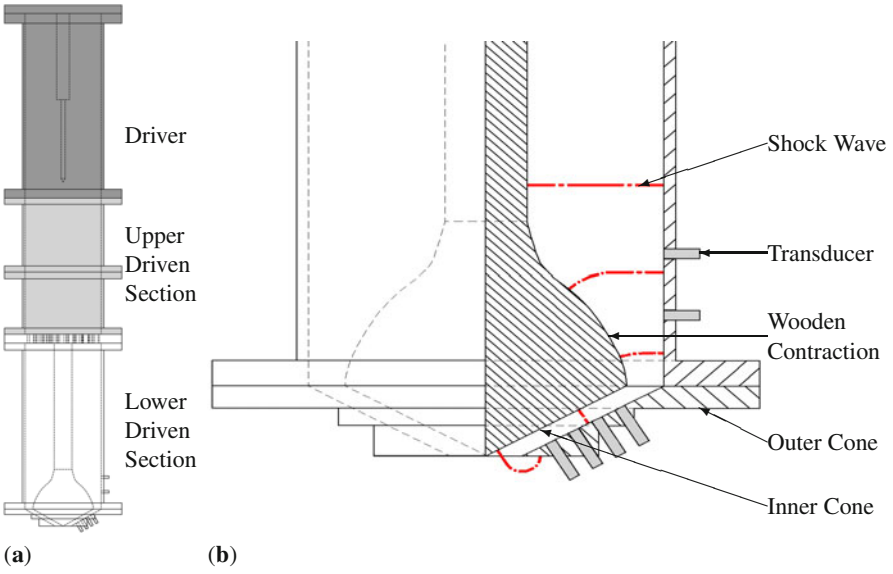

Fig. 1 Schematic of shock tube used (**a**) in the installed position and (**b**) showing detail of the simplified shock wave focusing around the wodden contraction into the conical gap between the inner and outer cones

3 Reflection Behaviour

Tests were conducted for driver gauge pressures of 2, 4, 6 and 8 bar. Time evolutions of the shock behaviour are given in figures 2a and b for pressures of 2 and 8 bar respectively. In all of these there is a vortex induced by the diffraction of the imploding shock wave over the lip of the outer cone, not to be confused with the vortex present in the V-type reflection [1]. At early times this diffracted shock wave and induced vortex obscure the focusing behaviour of the section of the shock wave in contact with the inner cone or reflecting at the axis of the system.

In figure 2a, at early times the reflection pattern may be of type S as identified in [1] but from the second frame the curvature of the Mach disc is quite evident. The Mach disc grows in radius as the wave expands outwards until eventually the wave front resembles a single hemispherical wave. The vortex behind the Mach disc is evident in these frames, making this a V-type reflection. In the last frames the shear layer emerging from the triple point of the Mach reflection is entrained in this vortex.

Initially the curved reflected wave is smooth but undergoes a typical shock-vortex interaction with the diffraction vortex although, atypically, the portion between the exit plane and core of the diffraction vortex appears to steepen initially.

The case of the much stronger wave driven by the 8 bar pressure in figure 2b is very similar. However, preceding the interaction of the reflected wave with the diffraction vortex, a shocklet develops on the inner upstream side of the vortex due

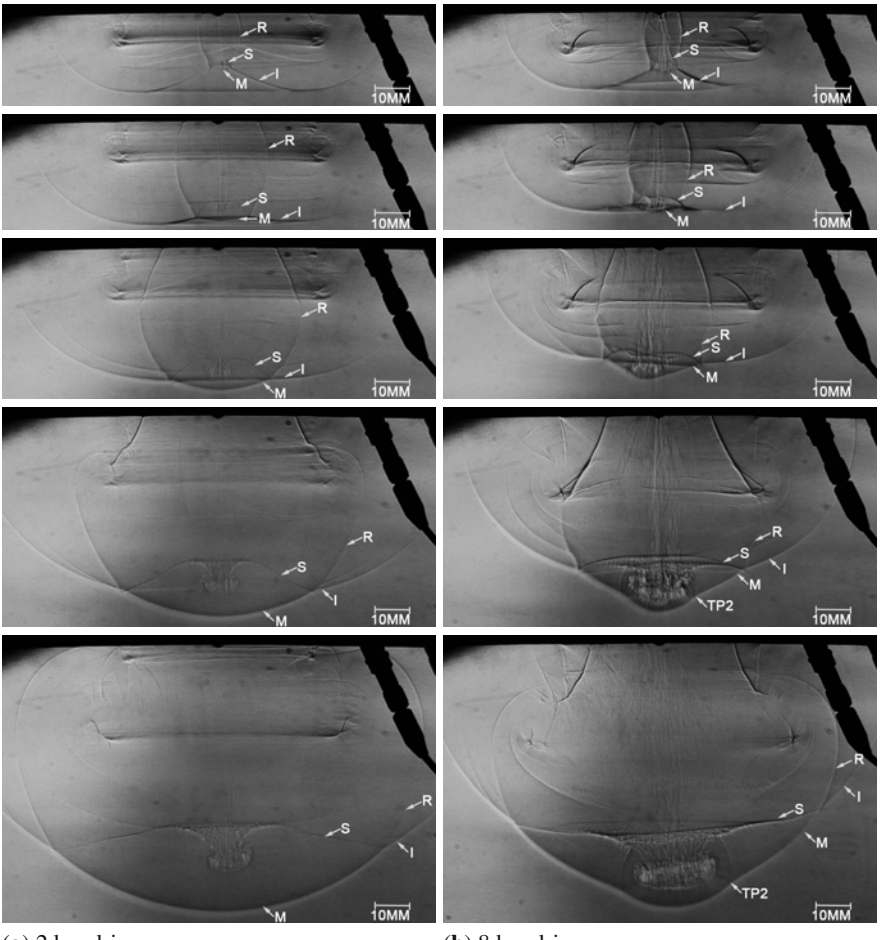

(**a**) 2 bar driver pressure (**b**) 8 bar driver pressure

Fig. 2 Evolution of the flow from a conical gap with a 60° half apex angle (*I - incident wave, R - reflected wave, M - Mach disc, S - primary shear layer, TP2 - second triple point*)

the very high induced velocities here caused by the vortex flow and the jetting of the flow along the axis caused by the Mach reflection there. This shocklet is evident from the first frame in this series and merges with the steepened reflected wave so that only one wave is evident in the final frame.

The Mach disc appears curved from the first frame in this series suggesting that, if it does occur, the S-type reflection does not persist for strong driver pressures. The induced vortex behind the curved Mach disc is clearly visible, as is the entrained shear layer from the primary triple point. In the final frame the second bulge of the Mach disc caused by the induced flow through the centre of the vortex is clearly visible. The second triple point of the DS-type reflection can be clearly distinguished though the reflected wave can only be clearly identified at the left of the vortex and

the resulting shear layer is indistinguishable from the boundary of the vortex plume, although part may be seen to the right of the vortex in the final image.

Also of note is that the Mach disc vortex is closer to the Mach disc itself for higher driver pressures than for lower ones. For example, the vortex is approximately one vortex diameter upstream of the Mach disc in the final frame of figure 2a for the 2 bar driver pressure while the vortex for the 8 bar driver pressure in figure 2b is less than half of the vortex diameter upstream of the Mach disc.

4 Computational Fluid Dynamics

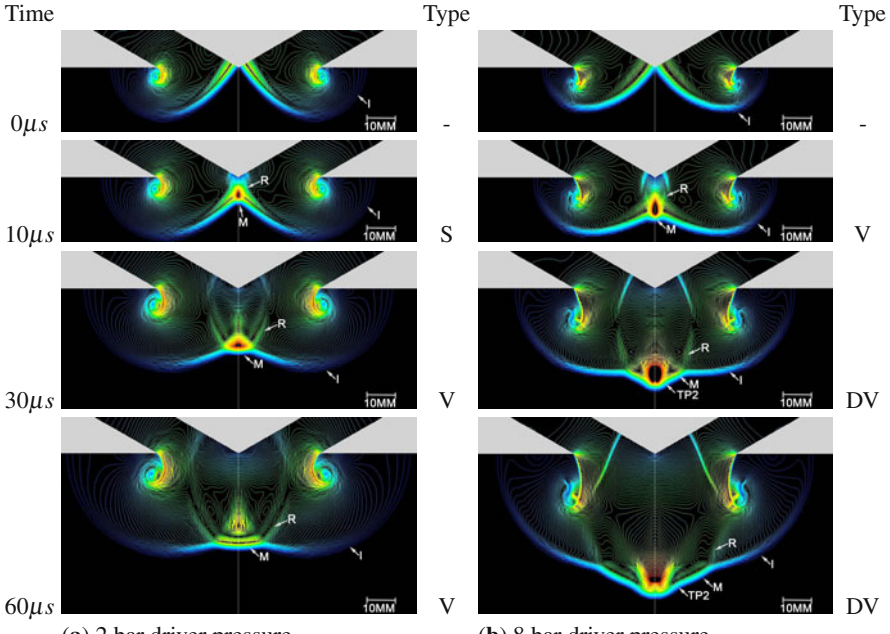

(**a**) 2 bar driver pressure
$V \in [0,500] m.s^{-1}$

(**b**) 8 bar driver pressure
$V \in [0,1000] m.s^{-1}$

Fig. 3 Velocity contours showing the diffraction of the emerging shock, and the development of the triple points on the primary wave (*I - incident wave, R - reflected wave, M - Mach disc, TP2 - second triple point*)

The experimental apparatus was modelled using the commercial code Fluent 12.0 using a truncated axisymmetric domain, where the inlet was located halfway between the perforated plate and exit plane. An Euler solver was used for a mesh divided into several blocks meshed with uniform quadrilateral cells ranging in size from 3mm in the inlet region to 1mm at the exit. The model additionally used dynamic mesh refinement to locally refine the mesh based on normalised gradients of

density and Mach number. The series presented in figure 3 show the evolution of the wave from the computational model from the initial incidence of the converging wave on the axis taken as time = $0\mu s$. All images have been reflected about the axis of symmetry, indicated by a white line down the centre of each image, to be directly comparable with the experimental data.

The curvature of the outer portion of the wave and vortex produced by the diffraction over the outer lip are clearly evident in the first frame of each series. While the Mach disc in the second frame of figure 3a appears quite flat and is hence possibly an S-type reflection, the Mach disc in the second frame of figure 3b is clearly curved. This suggests that the S-type reflection may occur for lower driver pressures but is obscured by the diffraction vortex and that for higher driver pressures S-type reflection may occur but quickly transitions into a V-type reflection.

While for the 2 bar driver pressure the Mach disc remains smooth and the V-type reflection persists, for the 8 bar driver pressure V-type reflection quickly develops and then becomes DV-type reflection. The greater strength of the jetting from the intial reflection and of the Mach disc vortex resulting from the higher driver pressure induce much higher velocities behind the primary front than the 2 bar case resulting in the second Mach disc forming in the primary wave. As with the experimental images, the reflected wave is only vaguely distinguishable here and the shear layer of the second triple point is indistinguishable from the vortex plume.

5 Other Flow Features

In some tests at lower driver pressure it was noted that the shear layer emerging from the primary triple point shows signs of instability as shown in figure 4a. This instability shows the patterned lighter and darker regions which typically indicate the presence of the Kelvin-Helmholtz instability. The smaller scale and three-dimensional shape of this shear layer mean that it is difficult to resolve this instability better than shown and it is suspected that further computational work may reveal more detail of this behaviour though it was not very repeatable experimentally.

In some tests at higher driver pressure the trajectory of the Mach disc was not directly along the axis of symmetry of the system. This was attributed to uneven bursting of the diaphragms and to a slight eccentricity of the location of the inner cone. In such cases it was noted, as shown in figure 4b, that the Mach disc vortex followed a curved trajectory and that secondary vortices emerged from the plume trailing the main vortex. Visually these plumes show some resemblance to the Richtmeyer-Meshkov instability with the formation of a mushroom-shaped instability at the vortex plume boundary. However, it could also be that this secondary vortex is as a result of the strong axial jetting caused by the stronger incident shock. If the curved trajectory of the primary vortex and Mach disc is as a result of eccentricity of the flow at the exit, this would also result in one side of the axial jet being slightly stronger than the other which may account for the emergence of the secondary vortex almost normal to the primary vortex plume and unaligned with the

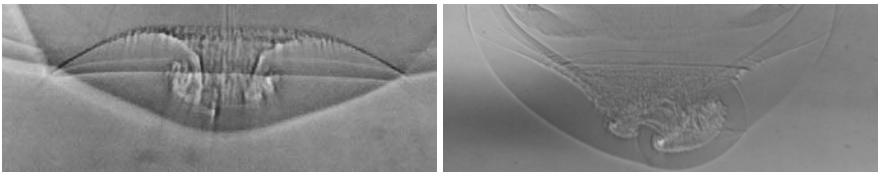

(**a**) (**b**)

Fig. 4 (**a**) Possible Kelvin-Helmholtz instability of the primary shear layer for 60° cone at 2 bar driver pressure and (**b**) instability of the Mach disc vortex plume for 50° cone at 8 bar driver pressure

axis of the system. Further work, both experimental and computational, would be required to confirm this.

6 Conclusion

Experimental and computational studies of the behaviour of imploding conical shock waves confirmed the existence of V- and DV-type reflections identifed by Hornung [1] but the S-type reflection was not clearly identified. It does seem to occur for lower driver pressures but would appear to be highly transient for higher incident shock strength, if it occurs at all. The possibility of the Kelvin-Hemholtz instability of the shear layer disc emerging from the primary triple point was noted and secondary vortices resembling the Richtmeyer-Meshkov instability were noted for instances of non-axial Mach disc propagation. Further experimentation and computational work are recommended.

References

1. Hornung, H.G.: J. Fluid Mechanics 409, 1–12 (2000)
2. Skews, B.W., Menon, N., Bredin, M., Timofeev, E.V.: Shock Waves 11, 323–326 (2002)

Experimental Studies on Mixing in Supersonic Ejector

M.V. Srisha Rao and G. Jagadeesh

1 Introduction

A supersonic ejector uses a primary flow expanded from high pressure to supersonic speeds to entrain a secondary flow and pump it to higher pressures. Figure 1 shows the schematic of the flow through an ejector that has complex interactions between shock, shear layers, boundary layers within a varying area duct. The understanding of mixing between a supersonic stream and its coflow within a duct is crucial in design of a supersonic ejector. The length of the duct required for complete mixing of the streams followed by shock trains is specified by rule of thumb methods. Hence most of the literature deals with designing ejector for various applications and there is scarcity of experimental data on mixing phenomena in ejector, an essential requirement for optimal design considerations[3]. This motivated setting up a 2D supersonic ejector facility at the Laboratory for Hypersonic and Shock Wave Research, IISc, Bangalore, for experimentation on flow mechanics and mixing studies within the ejector. Static pressure measurements along the wall and shadowgraphs obtained at different operating conditions and their interpretations towards the objectives are described in this paper.

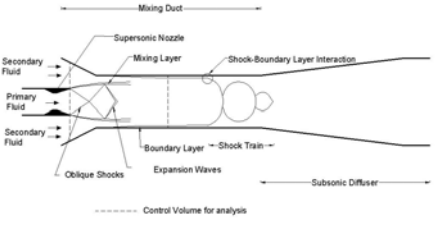

Fig. 1 Schematic of flow within a supersonic ejector

M.V. Srisha Rao · G. Jagadeesh
Department of Aerospace Engineering, Indian Institute of Science, Bengaluru, India, 560012

It has been found that compressibility impedes growth of shear layers [1]. Any possibility of improving mixing between the streams is a bonus for shorter and efficient ejector. Various active and passive methods have been tried for enhancing mixing [2]. Two techniques a passive and an active method to enhance mixing are proposed in this paper. A novel passive technique for enhancing mixing, that uses a flexible oscillating flap, excited by the flow to disturb the shear layer is brought out in the paper. The active method uses a Dielectric Discharge Barrier(DBD) actuator placed at appropriate location, that acts like a source of momentum perturbation to the shear layer.

2 Supersonic Ejector Experimental Setup

Extensive control volume calculations followed by numerical computations were carried out before arriving at the final ejector geometry[3, 4]. The 2D supersonic ejector has a supersonic nozzle of Mach numer 2.5 and glass windows on the side for flow visualization.

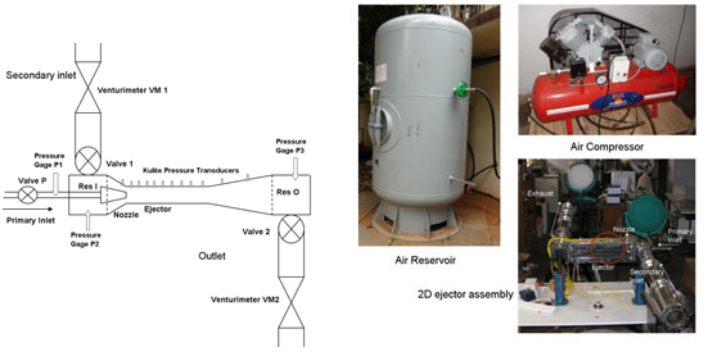

(a) Schematic of the ejector setup (b) Photographs of the ejector facility

Fig. 2 The 2D supersonic ejector facility

Figure 2(a) is a schematic of the entire setup and Figure2(b) shows the photographs of the established facility.The primary flow is fed by an air reservoir, controlled by valve P.The mass flow rate of the secondary flow and the exhaust are measured using venturimeters and can be conrolled by means of valves. The suction of the secondary flow and the compression achieved are measure at reservoirs Res1 & Res2 respectively; so in effect the ejector operates between these pressures. The top wall has 12 Kulite pressure transducers mounted to obtain the static pressure profile through the ejector.The pressure signals are acquired by DEWETRON data acquisition system. The shadowgraphs are taken using Phantom V7.2 high speed

camera at 2000 fps, to capture any unsteadiness in the flow.Typically a run lasts for 3 seconds.

3 Results and Discussions

Results of three different cases of operation are presented here. The data for every case is an average of 5 runs with a maximum variation of about 6% from the mean.The stagnation pressure of the primary flow is maintained at 5.6 bar and the secondary valve V1 is adjusted to achieve the different operating conditions, which are given in Table 1 where m_p is the primary mass flow rate, m_s is the secondary mass flow rate, $P02$ is the secondary stagnation pressure, $P03$ is the outlet stagnation pressure and $P01$ is the inlet stagnation pressure.

Table 1 Mass flowrates and Stagnation Pressures of the Flows

Case	m_p(kg/s)	m_s (kg/s)	$P02$(bar)	$P03$(bar)	$P01$(bar)
1	0.192	0.169	0.85	1.14	5.6
2	0.192	0.131	0.75	1.09	5.6
3	0.192	0.085	0.60	1.04	5.6

The primary flow being choked at the throat of the supersonic nozzle and the stagnation pressure being maintained constant; has a mean mass flow rate of 0.192 Kg/s among all the runs. The operating and performance parameters of the ejector are usually given in non-dimensional terms, which for the three cases are tabulated below(Table 2) where $P02/P01$ is the stagnation pressure ratio, $m_p/m_s(\omega)$ is the entrainment ratio and $P03/P02(CR)$ is the compression ratio.

Table 2 Non-Dimensional operating parameters

Case	$P02/P01$	$m_p/m_s(\omega)$	$P03/P02(CR)$
1	0.15	0.91	2.40
2	0.13	0.68	2.67
3	0.11	0.43	3.24

3.1 Static Pressure Measurements

Figure 3 shows the plot of the static pressure along the top wall for all the three cases. The square markers are the pressure gages at the reservoirs. The pressures are extracted from that portion of the signal that excludes by a good margin the effects of starting and stopping of the ejector and in an average sense is flat.

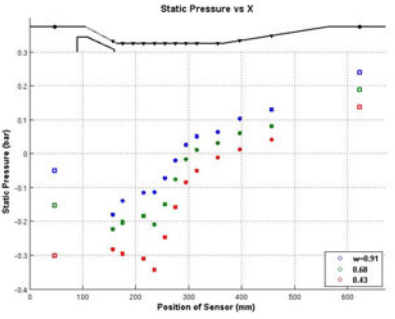

Fig. 3 Static pressure plot and shadowgraph picture

The plot brings out the trend of suction and pressure recovery within the ejector clearly. Right close to the exit of the nozzle there is a strong suction in all the three cases. In case 1 where ω is maximum the suction is followed by two consecutive sensors measuring nearly the same mean static pressure. This points to a region of constant pressure mixing. In case 3 with the least ω the pressure continues to drop since the jet remains distinct for a longer distance. The pressure recovery process has two distinct regions, a sharp rise followed by a relatively gradual rise. This indicates the presence of shock trains in the region of steep pressure recovery. This picture becomes more clear with the help of shadowgraph pictures.

3.2 Shadowgraphy

The supersonic jet issuing out of the nozzle with a shock diamond structure is sharply visible in Figure 4. The edge of the jet separating the two streams is also faintly seen. This is followed by a region of vague structures and then by a series of criss-cross shock train. The flow towards the end of the constant area section is smooth and devoid of any waves implying a subsonic flow. From the picture it

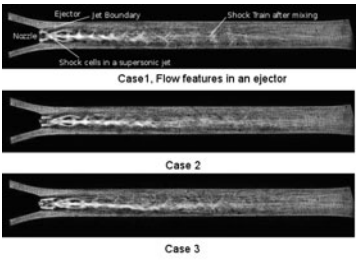

Fig. 4 Comparison of shadowgraph pictures for the three different cases

is clear that the mixing and shock train sections are over well before the end of the constant area portion, which conventionally is taken to be a length about 10-15 times the diameter of the duct. This points out the need to have a precise knowledge of mixing within a supersonic ejector. A comparison of all the three cases is shown in Figure 4.

The jet penetration is maximum in case three which has the least mass flow rate and high compression ratio. The jet is relatively short in case 1, with maximum mass flow rate and lower compression ratio. The locations and shapes of jet structures, shock trains is strongly influenced by the mass flow rate and the compression ratio, however in all the three cases the total mixing region is well within the length designed. Thus improving mixing would involve direct interaction with the shear layer, an active and a passive method are explored in this paper.

4 Preliminary Experiments on Mixing Enhancement

Before actual runs mounted inside the ejector, the techniques for mixing enhancement are tried out on a rectangular convergent nozzle open to ambient. Schlieren pictures of the sonic jet and the effect due to actuators are given.

4.1 A Passive Method-Flow Excited Oscillating Flap

The proposal is to use a series of thin flexible strips with cylinders attached to their ends as shown in Figure 5(a), which lie completely within the shear layer in the near field of the jet. The unsteady forcing of the cylinder due to the combined action of non-uniformity of shear layer and the cantilever's restoring force in effect would improve mixing.

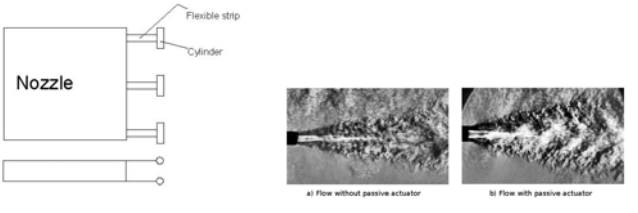

(a) Schematic of the oscillating flap actuator for mixing enhancements

(b) Comparison of Flow with and without the actuator

Fig. 5 A passive method to enhance mixing

Figure 5(b) shows the jet coming out into the ambient from a rectangular nozzle. Figure 5(b)a, is the flow without the actuator. The actuator is visible in Figure 5(b)b, their oscillations were observed of which only a snapshot is presented here. Qualitatively the flow with the actuator has a more corrugated appearance, than the one without the actuator. A shortening of the core region at the near field can be observed, hence an improvement in mixing can be inferred.

4.2 An Active Actuator-Dielectric Barrier Discharge Actuator

The Dielectric Barrier Discharge(DBD) Actuator consists of a ground and line electrode separated by a dielectric(Figure 6(a)) mounted on the surface. When charged with a high voltage high frequency AC, producing a plasma that induces a wall-jet kind of flow and acts as a momentum source to the flow [5]. Research efforts have met with a degree of success in application of these devices for flow control in low speeds. Here their use for disturbing the compressible shear layer is being investigated Figure 6(b) shows the placement of DBD on the rectangular nozzle and the schlieren of the flow with the actuator. However the flow was disturbed completely by hanging wires. Better arrangement and careful experiments are in progress.

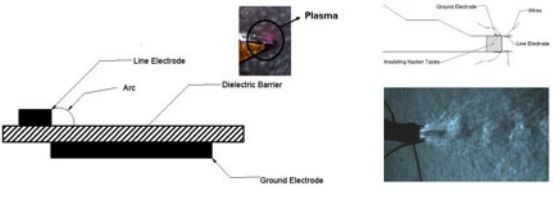

(a) Schematic of a Dielectric Barrier Discharge actuator

(b) DBD mounted on the rectangular nozzle and the flow with the actuator

Fig. 6 An active method to enhance mixing

5 Future Work

A more precise picture of mixing within the ejector needs to be obtained by use of optical diagnostics like laser sheet visualization of seeded flows, with a quantitative assessment using PIV technique. Detailed experiments have to be carried out to understand the suitability as well as the capability of both kinds of actuators; ultimately use it inside the ejector.

References

1. Papamoschou, D., Roshko, A.: Journal of Fluid Mechanics 197, 453–477 (1988)
2. Gutmark, E.J., et al.: Annual Reviews of Fluid Mechanics 27, 375–417 (1995)
3. Srisha Rao, M.V., Jagadeesh, G.: Journal of Fuel Cell Science and Technology. Journal of Fuel Cell Science and Technology 7 (2010)
4. Srisha Rao, M.V., Jagadeesh, G.: ISSW-27 St.Petersburg, Russia (2009)
5. Corke, T.C., et al.: Annual Reviews of Fluid Mechanics 42, 505–529 (2010)

On the Evolution of Spherical Gas Interface Accelerated by Planar Shock Wave

Z. Zhai, T. Si, X. Luo, J. Yang, D. Li, J. Liu, and J. Tang

1 Introduction

When a shock wave passes an interface between two fluids with different densities, the initial perturbation on the interface will grow with time, which is known as the Richtmyer-Meshkov (RM)instability [1, 2]. Due to the academic significance in interface stability, vortex dynamics and the formation mechanism of turbulence and many applications such as inertial confinement fusion and supernova explosions, much attention has been paid to the RM instability and turbulent mixing in recent decades. Many groups in different countries, such as America, France, Japan and Israel, have carried out researches respectively and obtained original achievements. Experiments with air-SF_6 and air-helium were conducted in shock tube by Benjamin *et al.* [3]. The investigation on the interaction of a shock wave with a spherical or cylindrical gas interface (helium and R22) was undertaken and the velocities of shock waves and interface were analyzed by Hass and Sturtevant [4] while the accuracy and reliability of the results were limited because only one frame was obtained per run. Plenty of efforts have been made by Layes *et al.* [5, 6, 7, 8] in this field, including the development of wave patterns and interface and also quantitative analyses of interface distortion with different shock Mach numbers. It should be noted that, in the work of Layes *et al.* [5, 6, 7, 8], the time interval between two frames is 70 μs and the Atwood number, which is defined as $A = (\rho_b - \rho_a)/(\rho_b + \rho_a)$ with ρ_b the gas density inside the bubble and ρ_a the gas density outside the bubble, studied is smaller than 0.5.

In this study, a higher frame rate as well as a larger Atwood number is used (SF_6 to air), which is realized by a high-speed schlieren system to visualize the interaction of a planar shock wave with a soap film bubble. Due to the complexity of the

Z. Zhai · T. Si · X. Luo · J. Yang
University of Science and Technology of China, Hefei 230026, P.R. China

D. Li · J. Tang · J. Liu
The 3rd Research Academy of CASIC, Beijing 100074, P.R. China

shock-bubble interaction process, a numerical simulation is performed as well for detailed analysis.

2 Experimental and Numerical Methods

Experiments are conducted in a shock tube with a driver section of 1.7 m and a driven section of 3.9 m. The cross section is 70 mm$\times$40 mm and the length of test section is 250 mm. The soap film is used to create the initial interface and a high-speed schlieren system is employed to visualize the flow field. Different bubble configurations, i.e. a 'heavy bubble' (SF_6, A=0.669) and a 'light bubble' (helium, A=-0.757), are considered. In present experiments, an incident shock Mach number of 1.23, a bubble radius of 15 mm and a frame rate of 35000 fps are adopted. Additionally, the numerical method VAS2D (2-Dimensional & axi-symmetric Vectorized Adaptive Solver) [9] is adopted, which solves the two-dimensional or axi-symmetric Euler equations and has been well-validated in simulating compressible flows. The finite volume method combining with unstructured mesh adaption refines local complex areas and could capture wave patterns such as shocks and interfaces.

3 Results and Discussion

3.1 Heavy Bubble: SF_6

Figure 1 illustrates the process of a planar shock interacting with a spherical SF_6 bubble. The refracted shock inside the bubble propagates slower than the incident shock outside (frames 1 to 2) and appears convergent. Immediately after the intersection of the diffracted shock outside the downstream interface, a higher pressure zone is formed while the initial pressure of 1 atm remains in the vicinity of the downstream inside the bubble at this moment. As a consequence, the phenomenon that the downstream interface moves upwards is observed from both numerical and experimental results (frame 5) while a similar phenomenon has not been observed for krypton[5, 6, 7, 8]. The emergence of this phenomenon is directly related to the movement of the shock waves, which is mainly depended on the sound speeds of the bubble interior and exterior. It should be noted that this phenomenon only lasts for a very short period ($\leq 50\mu$s), which may not be captured in a relatively lower frame rate as used by Layes *et al.*[5, 6, 7, 8]. Subsequently, the refracted shock converges to a very small zone (inside the bubble close to the downstream interface) with high pressures and densities. Driven by the high pressures, an outward jet is formed (frame 6) while an inward jet is formed for krypton bubble. As time proceeds, the interface deforms greatly as the jet length increases, and a vortex ring appears and develops in the downstream interface(frames 13 to 19). In the late stage, the downstream interface breaks up and lots of small scale vortical structures are generated (frames 25 to 37). Eventually, the jet as well as the interface diffuses and the turbulent mixing takes place.

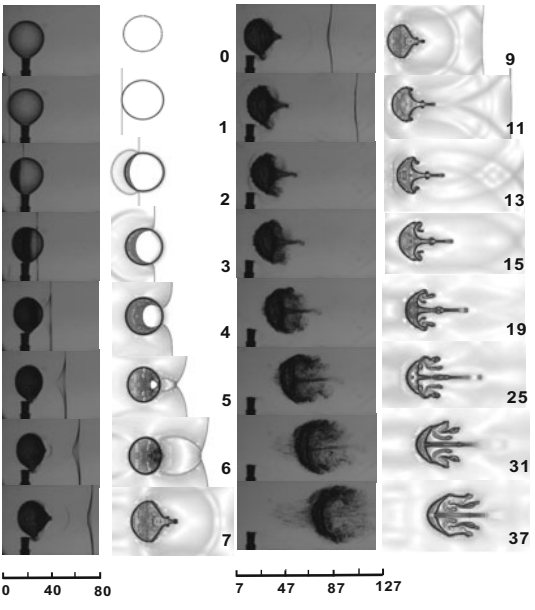

Fig. 1 Schlieren frames of a shock ($M_s = 1.23$, moving from left to right) interacting with a SF_6 bubble. The time interval between two consecutive frames is 28.6 μs.

Quantitatively, the variations of some interface structures are measured and compared with numerical results. The initial diameter of the gas bubble D_0 is used as the characteristic length, and the characteristic time is defined as $t_c = D_0/U_f$ with U_f the flow velocity behind the incident shock.

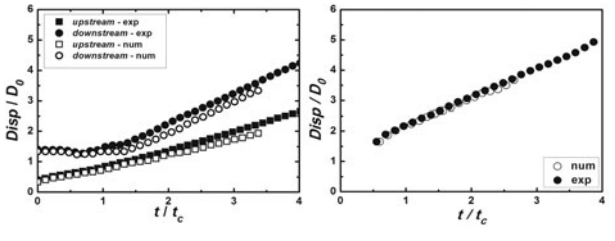

Fig. 2 Evolution of SF_6 interfaces: displacements of upstream interface and downstream interface (left), and displacement of jet head (right).

In the early stage, the downstream interface does not move until the incident shock passes through the bubble. Then the velocity of the downstream interface is larger than that of the upstream one due to the accumulated vorticity. Figure 2 reflects the variation of the interface displacement with time. There is a vortical structure in the jet head resulting from the shear velocity induced by the vorticity.

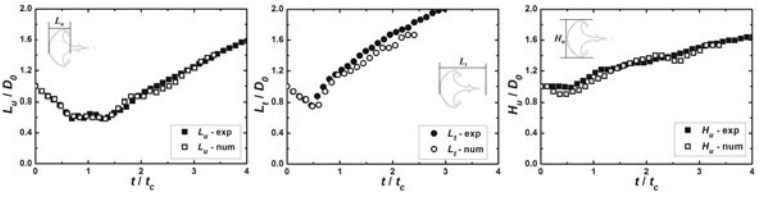

Fig. 3 Dimensionless time evolution of SF_6 interface structures: length of the upstream interface L_u (a), total length including jet L_t (b) and height of the upstream interface H_u (c).

The interface length initially begins to diminish because of the shock compression while the height increases as shown in Figure 3. The upstream interface length L_u and the total length of interface L_t show the same behaviors before the jet is formed. When the jet and the vortex ring are generated, both the length and the total length increase due to the velocity increase. With the bubble evolution, the jet becomes longer and the vortical structure of the head increases, and so does the vortex ring of the downstream which can be ascribed to the spinning effect of the vortices. The instability is then intensified further.

3.2 Light Bubble: Helium

As shown in Figure 4, when the incident shock impinges on the helium bubble, the refracted shock moves faster inside the bubble. As the incident and refracted shocks propagate downwards, the diffracted and transmitted shocks are generated, inducing the whole structure as a twin Mach reflection (frame 3). The air around the bubble begins to enter the bubble and then a re-entrant jet appears. The jet moves downwards within the bubble and eventually encounters the downstream interface (frames 4 to 7). In the downstream interface, a vortex ring is generated and the bubble length as well as the scale of the vortex ring increases, whereas the connection between upstream and downstream interfaces becomes slender and breaks off at last (frames 9 to 35).

Figure 5 shows the variation tendency of upstream and downstream interfaces. After the downstream vortex is formed, the velocity of downstream is larger than that of the upstream. In Figure 6, the changes of L_t and H_u are analogical with those of SF_6 initially (Figure 6(a-b)). As the jet transfers gradually to the downstream, an amount of vorticity around is involved in the vortex ring and the scale of vortex ring increases. Along with the separation of the upstream and the downstream interfaces, H_u decreases slightly and then tends to stable (Figure 6(b)). In the process after the downstream vortex is generated, both H_d and D_v change a little because of the stability of vortex ring scale (Figure 6(c-d)).

Good agreement is found between the experimental and numerical results. Discrepancy, however, also exists, especially in the late stage. The existence of soap film and the bubble support as well as the imperfection of numerical method and the imprecise measurement may all have effects on the bubble deformation. Besides, a

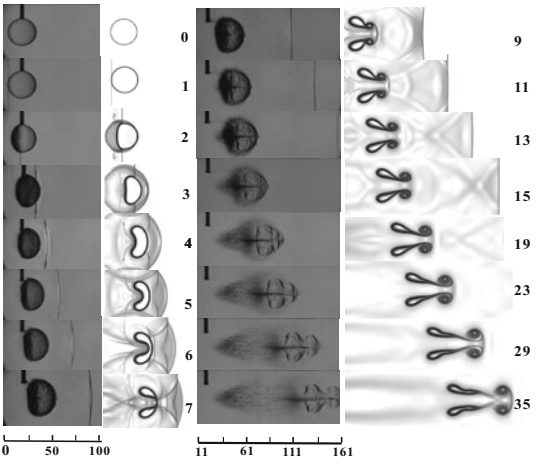

Fig. 4 Schlieren frames of a shock ($M_s = 1.23$, moving from left to right) interacting with a SF_6 bubble. The time interval between two consecutive frames is 28.6 μs.

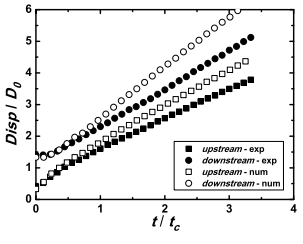

Fig. 5 Dimensionless time evolution of displacements of upstream and downstream interfaces (helium bubble).

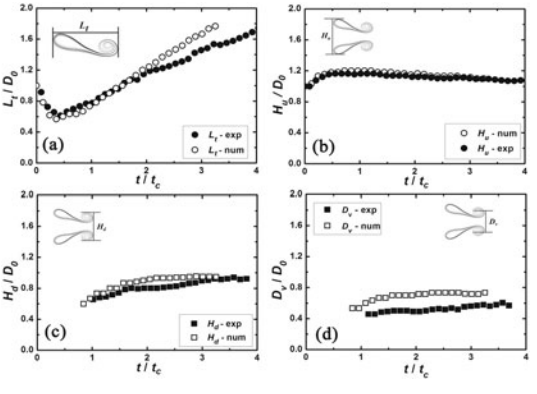

Fig. 6 Dimensionless time evolution of helium interface structures: total length of interface L_t (a), height of upstream H_u (b), height of downstream H_d (c) and vortex distance D_v (d).

better agreement can be found in the experiments of air-SF_6 than that of air-helium, which can be ascribed to the lower density and stronger penetration of helium. The purity of helium in the bubble changes and leads to some additional errors.

4 Conclusion

Experiments of RM instability on the interaction of a shock wave with spherical gas bubbles, including SF_6 and helium, were conducted using the high-speed schlieren system in this study. For comparison, numerical simulation was carried out as well. Distinct images and quantitative data of the interface deformation visualize the physical patterns and reveal the mechanism of evolution and development of spherical gas bubble. From the discussion above, we can find the coincidence between experimental and numerical results. For future work, some quantitative techniques such as PIV and PLIF will be introduced to gain more effective data for better understanding the physical patterns of RM instability.

Acknowledgment. This research was carried out with the support of the National Natural Science Foundation of China under grants NSAF10776031 and 10972214. The authors would like to thank Meiru Fan and Minghu Wang for their valuable assistances.

References

1. Richtmyer, R.D.: Taylor instability in shock acceleration of compressible fluids. Commun. Pure Appl. Math 13, 297–319 (1960)
2. Meshkov, E.E.: Instability of the interface of two gases accelerated by a shock wave. Fluid Dyn. 4, 101–104 (1969)
3. Benjamin, B., Besnard, D., Haas, J.: Shock and reshock of an unstable fluid interface. LA2UR 9221185 (1993)
4. Haas, J.F., Sturtevant, B.: Interaction of weak shock waves with cylindrical and spherical gas inhomogeneities. J. Fluid Mech. 181, 41–76 (1987)
5. Layes, G., Jourdan, G., Houas, L.: Distortion of a spherical gaseous interface accelerated by a plane shock wave. Phys. Rev. Lett. 91, 174502 (2003)
6. Layes, G., Jourdan, G., Houas, L.: Experimental investigation of the shock wave interaction with a spherical gas inhomogeneity. Phys. Fluids 17, 028103 (2005)
7. Layes, G., Le, M.O.: Quantitative numerical and experimental studies of the shock accelerated heterogeneous bubbles motion. Phys. Fluids 19, 042105 (2007)
8. Layes, G., Jourdan, G., Houas, L.: Experimental study on a plane shock wave accelerating a gas bubble. Phys. Fluids 21, 074102 (2009)
9. Sun, M., Takayama, K.: Conservative smoothing on an adaptive quadrilateral grid. J. Comp. Phys. 150, 143–180 (1999)

Experimental Investigations on the Effect of Dielectric Barrier Discharge on the Hypersonic Flow Around a Flat Plate

R. Sriram, G. Jagadeesh, and K.P.J. Reddy

1 Introduction

Surface dielectric barrier discharges (DBD) are known to offer potential flow control techniques for low speed flows. A well known application of DBD in low speed flows is separation control as illustrated by Little et al. [1]. For high speed flows (supersonic and hypersonic flows) there is a need for deeper understanding of their nature of interaction and applicability. Literature on low speed flows suggests the body force field created by DBD, as the reason for flow alteration (Boeuf and Pitchford [2]). High speed flows, hypersonic flows in particular, are characterized by high flow kinetic energy, and thus one cannot ignore the possible energy interactions the flow can have with the regions of high temperature in the field (as may be the case with discharge). There are a number of works reported in the literature that discuss the energetic interactions of high speed flows. Satheesh and Jagadeesh [3] reported significant reduction of drag on a blunt body in hypersonic flow by the upstream deposition of energy. Numerical investigations by Yan and Gaitonde [4] on the effect of steady and pulsed thermal disturbances on a flat plate at supersonic speed have shown that a finite span thermal disturbance leads to the formation of stream-wise vorticity which can grow downstream, affecting the stability of the flow. It is premature to tell the way the DBD can affect the high speed flows. The fact that the high speed airflow has a significant influence on plasma characteristics of DBD (Pavon et al. [5]) adds further complexities. Not many experimental evidences are there in literature even on the gross effects of DBD on any specific high speed flow. It is with this backdrop that experiments are initiated to observe the effect of DBD on certain high speed flows, and to understand the phenomenon. The case of hypersonic flow over a flat plate is taken for the present investigation.

R. Sriram · G. Jagadeesh · K.P.J. Reddy
Department of Aerospace Engineering, Indian Institute of Science
Bangalore (India)

2 Shock Tunnel Experiments

The experiments are carried out in the IISc hypersonic shock tunnel HST5. Before the experiments with the flat plate model a calibration of the tunnel was done with a pitot rake measurement. A rake of 12 pitot probes spanning the diameter of the nozzle (300 mm) was placed facing the freestream. The pitot pressures were measured by means of kulite transducers which are less noisy. Apart from this, the shock tube pressures were measured at 2 locations, one near the end of the driven section and another one, a little ahead in the shock tube (separated by 205 mm), so as to measure the flow stagnation pressure as well as the shock speed inside the shock tube. The repeatability of the experiments is ensured by monitoring the repeatability in the diaphragm rupture pressure. Air and Argon were the test gasses used. The freestream conditions are estimated by means of isentropic and normal shock relations from the measured reservoir pressure p_0 (stagnation pressure in the shock tube before expanding through nozzle), pitot pressure (pressure behind normal shock) averaged over the core region and shock Mach number in the shock tube. The typical freestream conditions are tabulated in Table 1.

Table 1 Typical freestream conditions of experiments

Test Gas	M_∞ ±1.5%	P_0 (bar) ±7%	T_0 (K) ±6.5%	P_∞ (Pa) ±11%	T_∞ (K) ±9.5%	ρ_∞ (kg/m^3) ±13%	$Re_\infty * 10^6$(/m) ±16%
Air	6.25	29.1	1474.2	1450.8	167.3	0.0302	4.30
Argon	9.07	26.26	2228.4	625.7	78.03	0.0386	9.86

A flat plate model with sharp leading edge is used for the experiments. The model is made of Bakelite hylem material to ensure complete insulation. The test model has a flat surface of length 20 cm and span 12 cm, and is exposed to the freestream at 9^0 45'. The model is of 5 cm thickness to accommodate the sensors. The model is equipped with 2 rows of PCB pressure sensors, one along the centre line, and the other along a line, 3 cm spanwise from the centre line as shown in Figure 1. The centre row of pressure sensors is labeled as Array A, and the side on as Array B. Each row has 5 sensors, each spaced 2 cm from each other, with the first sensor at a distance of 9 cm from leading edge. The model is also equipped with 2 rows of platinum thin film sensors painted on a Macor substrate. The measured heat transfer rate values were very low for the selected enthalpy and the angle of attack of the flat plate, and were subject to electromagnetic interference with plasma despite shielding the cables. The data is thus less reliable and is not reported here.

Surface dielectric barrier discharge is created at a distance of 5 mm from the leading edge (at spanwise centre). DBD needs a high voltage alternating current source (for the present case, 25 kV peak, 50 mA). Figure 2(a) shows the block diagram of the plasma generation and control unit. The plasma is controlled from a PC through a NI interface. While DBD can be made in any configuration, for the

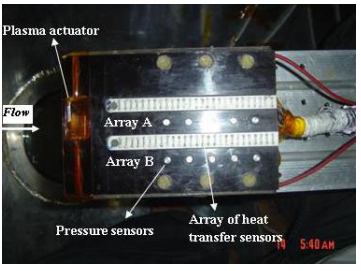

Fig. 1 A photograph of the flat plate model

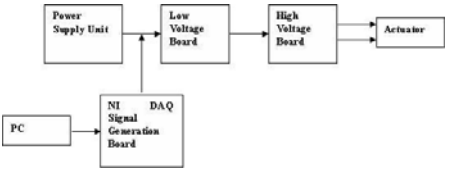

(a) Block diagram of the pulsed plasma generation and control unit

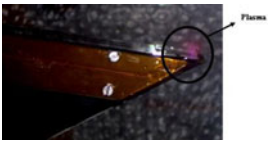

(b) A photograph of the plasma generated by the DBD device near leading edge

Fig. 2 The DBD actuator

present experiments a typical planar configuration wherein two parallel plates of electrodes are placed on the surface with a dielectric barrier (kapton tapes) between them. The electrodes and the dielectric layers are so thin that the entire setup is almost level with the surface as can be seen in Figure 2(b), which shows the plasma generated on the model surface near the leading edge. The effect of plasma actuator length is investigated by having actuators of lengths 15 mm and 5 mm. The effect of plasma pulsing frequency is also investigated.

3 Surface Pressure Measurements

The surface pressures over the flat plate are measured using PCB pressure sensors. Measurements are made for the base case without plasma and for the case with plasma. Two different lengths of the plasma actuator are experimented, one with 15 mm and other with 5 mm. Also the effect of plasma pulsing frequency was investigated by operating the 15 mm actuator at 2 different frequencies, 8 kHz and 19 kHz. The 5 mm actuator was operated at 6 kHz, which was the resonant frequency of the device. Figure 3 shows a comparison of the pressure signals measured by the 3rd sensor in Array A, with and without plasma, for actuator length of 15 mm with air as test gas. Clearly the pressure signals are not affected by electromagnetic interference. It can also be seen that there has been a considerable change in the measured

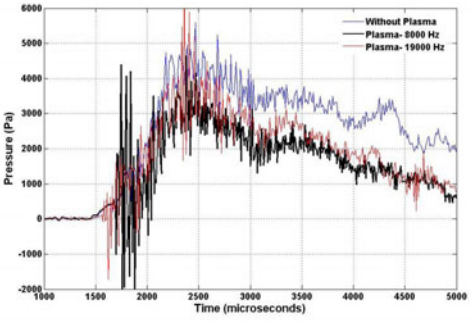

Fig. 3 Surface Pressure signals in sensor 3 in the centre array with and without plasma, with actuator of 1.5 mm length, with air as test gas

signal by the presence of plasma, and also that the plasma pulsing frequency has a role to play. The trends will be discussed in subsequent section.

4 Results and Discussions

The effect of plasma frequency (with 15 mm actuator) can be seen in Figure 4 with air as test gas and in Figure 5 with argon as test gas. The effect of the length of the actuator is investigated by comparing the pressures for the cases with actuators of length 5 mm and 15 mm, each of which is operated at their resonant frequencies. Figure 6 shows the comparison for the case with air as test gas, and Figure 7 with argon. Note: The surface pressures in the figures are normalized by freestream pressures of the corresponding run and the distances are normalized by span length.

It can be seen from the above figures that the presence of DBD does alter the surface pressure distribution. At many locations there is a significant deviation from the base pressure values with the DBD. The effect is best seen at the last 2 sensors in Array B (near the side, 3 cm away from centre line) with argon as test gas and with a plasma pulsing frequency of 8 kHz, when the surface pressure drops there drastically to values that are lower than the measurable range of the sensors. This could possibly indicate a local separation at the location for the specific condition. At most of the locations there is a drop in surface pressure with the plasma, although there are some places where an increase is seen. There is also a considerable difference observed between the cases of different actuator lengths. It was initially expected that the smaller the length of the actuator, more could the plasma intensity be. But the drastic differences observed downstream with 15 mm actuator with argon as test gas was not seen with 5 mm actuator. It is thus not possible to make further conclusions with the observed trend and the intuitions may be misleading. Further investigations have to be done to understand the observations. Investigations are underway to understand the nature of disturbance DBD offers. This can be started by comparing

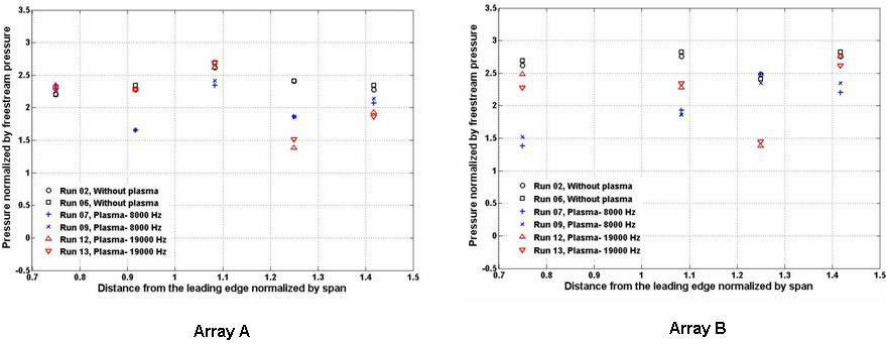

Fig. 4 Effect of plasma pulsing frequency on surface pressure distribution with air as test gas (15mm actuator)

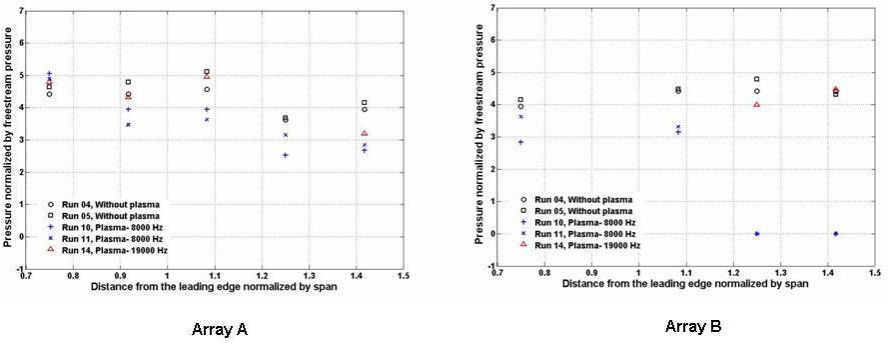

Fig. 5 Effect of plasma pulsing frequency on surface pressure distribution with argon as test gas (15mm actuator)

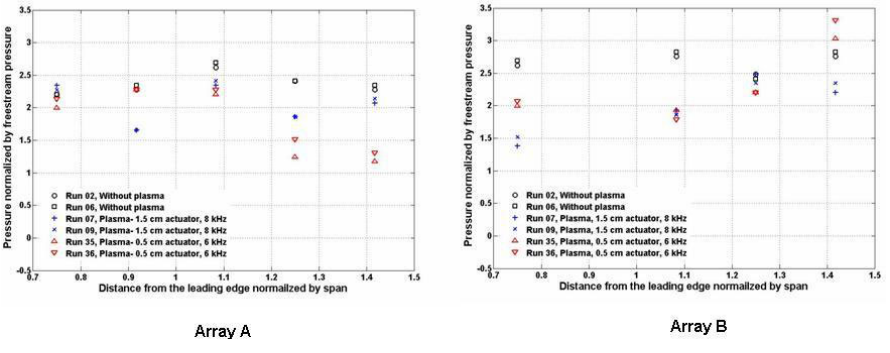

Fig. 6 Effect of plasma actuator length on surface pressure distribution with air as test gas

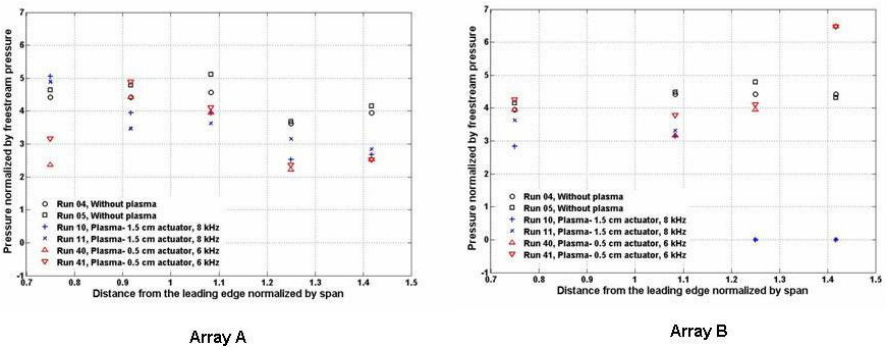

Fig. 7 Effect of plasma actuator length on surface pressure distribution with argon as test gas

the flow field with DBD, with that of purely mechanical and thermal disturbances. Experiments with a surface mounted heating element (commercially available glow plug) close to leading edge as a source of thermal disturbance and micro ramps at corresponding location as source of mechanical disturbance are planned for near future.

5 Conclusions

Experiments are carried out with the aim of understanding the effect of dielectric barrier discharge in the hypersonic flow field over a flat plate. Surface pressures on the flat plate are measured with and without DBD with air and argon as test gas. With the obtained measurements it is not possible to give any conclusive remarks about the general trends and phenomenology involved. But the measurements show considerable differences in surface pressure with the presence of DBD. It is also observed that the pulsing frequency of plasma and the length of the plasma actuator play a role in affecting the flow dynamics. At the same time making a general conclusion at this stage would only be speculative and thus the document only reports the measurements. A proper characterization of the plasma should also be done to make better statements about the parameters affecting the overall flow dynamics. Efforts are underway to have a better understanding of the phenomenon by improving the heat transfer rate measurements and by implementing of flow visualization techniques.

References

1. Little, J., Nishihara, M., Adamovich, I., Samimy, M.: High-lift airfoil trailing edge separation control using a single dielectric barrier discharge plasma actuator. Exp. Fluids 48, 521–537 (2010)

2. Boeuf, J.P., Pitchford, L.C.: Electro-hydrodynamic force and aerodynamic flow acceleration in surface dielectric barrier discharge. Journal of Applied Physics 97(103307), 1–10 (2005)
3. Satheesh, K., Jagadeesh, G.: Effect of concentrated energy deposition on the aerodynamic drag of a blunt body in hypersonic stream. Physics of Fluids 19(031701), 1–4 (2007)
4. Yan, H., Gaitonde, D.: Effect of thermally induced perturbation in supersonic boundary layers. Physics of Fluids 22(064101), 1–16 (2010)
5. Pavon, S., Dorier, J.-L., Hollenstein, C., Ott, P., Leyland, P.: Effects of high-speed airflows on a surface dielectric barrier discharge. J. Phys. D: Appl. Phys. 40, 1733–1741 (2007)

Free-Piston Driver Optimisation for Simulation of High Mach Number Scramjet Flow Conditions

D.E. Gildfind, R.G. Morgan, M. McGilvray, P.A. Jacobs,
R.J. Stalker, and T.N. Eichmann

1 Introduction

Scramjet-powered access to space is expected to entail flight between Mach 10 and 15, along a dynamic pressure ascent trajectory of up to 100 kPa [1]. These flow conditions are characterised by total pressures of the order of gigapascals. Expansion tubes such as X2 and X3 at The University of Queensland (UQ), which add total enthalpy and total pressure to the test gas through an unsteady expansion, are the only current facilities which have the potential to achieve these very high total pressures.

The free-piston driver is the technique preferred by UQ to achieve high performance drivers for its impulse facilities. Since the driver gas is compressively heated, it can achieve both the high pressures and the high sound speeds required to generate strong shock waves. However, operating the free-piston driver presents two main challenges: firstly, preventing damage to the piston, to the buffer, and to the compression tube; secondly, achieving constant driver pressure for a sufficient duration.

In order to achieve a high driver gas temperature, large compression ratios are used, therefore the driver gas volume at diaphragm rupture is relatively small [2]. If the piston is moving with low velocity at this point, the driver gas slug has approximately constant volume, therefore the unsteady expansion will lead to a rapid pressure drop [2]. A reflected $u+a$ wave is then transmitted downstream, potentially interfering with downstream flow processes before, or during, the test time.

Initial attempts to produce a Mach 13 high total pressure flow condition in X2 did not achieve expected results. The existing 35 kg piston is relatively heavy for the compression tube length and therefore is operated at slow speeds; as a result the driver gas only maintains its pressure for a relatively short duration. For the high speed flow conditions for which X2 is typically used (such as planetary entry

D.E. Gildfind · R.G. Morgan · P.A. Jacobs · R.J. Stalker · T.N. Eichmann
University of Queensland, St. Lucia, QLD, 4067, Australia

M. McGilvray
University of Oxford, Oxford, OX1 2JD, United Kingdom

between 6 and 10 km/s), critical flow processes occur in the test section before the reflected $u + a$ wave arrives at the test section. However, for high total pressure conditions, slow shocks in the dense test gas take more time to traverse the tube. Early driver gas pressure loss manifests itself in shocks which rapidly weaken before critical flow processes reach the test section. Table 1 summarises the Mach 13 flow condition; Figure 1 shows shock speeds measured at different tunnel locations and compares these to target speeds based on analytical and 1-D CFD calculations.

Table 1 Mach 13 calculated flow condition for X2.

Symbol	Value	Units	Description		Symbol	Value	Units	Description
$p_{A,0}$	1.1	MPa	Reservoir fill pressure, air.		p_{shk}	330	kPa	Shock tube fill pressure, air.
$p_{D,0}$	30.0	kPa	Driver fill pressure, 100% helium.		p_{acc}	254	Pa	Acceleration tube fill pressure, air.
p_{rupt}	15.5	MPa	Primary diaphragm rupture pressure.		M_e	13.4	-	Predicted Mach number at nozzle exit.
λ	42.5	[-]	Driver compression ratio.		u_e	3.950	km/s	Predicted flow velocity at nozzle exit.
m_p	35.0	kg	Piston mass.		$p_{e,0}$	1,450	MPa	Predicted total pressure at nozzle exit.
p_{sec}	150	kPa	Secondary driver fill pressure, helium.					

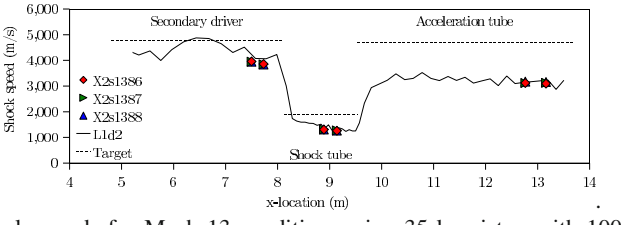

Fig. 1 X2 shock speeds for Mach 13 condition, using 35 kg piston with 100% He driver. 'X2s...' indicates experimentally measured shock speeds. Maximum experimental uncertainty of $\pm 3\%$.

`L1d2` is a 1-D Lagrangian flow solver developed by Jacobs [3] to analyse unsteady flow processes in impulse facilities such as X2. `L1d2` predicted shock speeds in Figure 1 demonstrate good agreement with the experimental results. Detailed analysis with `L1d2`, which includes full piston dynamics, indicated that shock attenuation was due to rapid expansion of the driver gas following diaphragm rupture. This expansion can be weakened by operating the piston sufficiently fast after rupture that its displacement temporarily substitutes for vented gas, maintaining or even increasing driver pressure. This is referred to as tuned operation [4], and has been implemented with X2 to prevent the shock attenuation observed in Figure 1.

2 Tuned Free-Piston Driver Operation

Tuned free-piston driver operation, originally proposed by Stalker [2], can increase the duration over which driver gas is held at a useful pressure. Ignoring wave processes, after diaphragm rupture occurs there is a reference piston speed, U_{ref}, which will compensate for driver gas loss to the driven tube, resulting in approximately constant driver pressure. Itoh et al. [7] later non-dimensionalised the *actual* piston speed at the moment of rupture, u_{rupt}, by U_{ref}, producing the piston over-drive parameter, $\beta = u_{rupt}/U_{ref}$. Stalker [2] essentially proposed the idea of configuring the

driver such that $\beta > 1$, thereby "over-driving" the piston. For $\beta > 1$, the piston will continue to increase the driver pressure following diaphragm rupture, before it slows and the pressure begins to fall. The duration over which this variation in driver pressure is within acceptable limits (typically around 10% of the target pressure [2, 7]), can correspond to a significantly extended period of useful supply time.

3 Soft Landing with a New Lightweight Piston

Over-driving the piston results in it having a relatively high velocity (typically 100 – 300 m/s) when the diaphragm ruptures. However, the piston must also be prevented from hitting the end of the tube. Itoh et al. [7] identified the types of motion possible, after diaphragm rupture, as the piston approaches the end of the compression tube, as being either 'piston rebound', 'soft landing', or 'direct impact'. Itoh et al. [7] proposed targeting the soft landing condition and sizing the buffer to catch the piston when its velocity and acceleration are simultaneously zero.

An analysis following the arguments of Stalker [2] indicated the need to develop a new piston of minimum mass. A tuned driver requires a lightweight piston for two reasons. Firstly, for X2's relatively short 4.5 m compression tube, the piston must be light enough to accelerate to the necessary high speeds over this short distance, or else reservoir pressures must be prohibitively high. Secondly, for large compression ratios, the piston is only a short distance from the end of the compression tube at the point of diaphragm rupture; for a given driver gas pressure at rupture, the piston needs to be very light to decelerate to rest over this short distance. It was considered impractical to incorporate brakes in the piston (which help prevent rebound motion), and designing for survival of direct impact at high speed is not feasible. A soft landing condition was thus targeted for the new X2 free-piston driver.

Strength and facility interface requirements (i.e. the ability to use the piston with the existing compression tube and launcher arrangement) placed restrictions on how light the piston could be made. However, the final mass of 10.5 kg was determined to be sufficiently low to achieve a tuned driver condition which would have sufficient performance to achieve the target flow conditions. The piston, described in [8], is machined from 7075-T6 Aluminium alloy and was designed for maximum driver and reservoir pressure operational loads of 40 MPa and 10 MPa respectively.

4 Calculation of New Free-Piston Driver Conditions

Several variables remained available for driver condition design: Reservoir fill pressure (<8 MPa); driver fill pressure (<1 MPa) and composition (%He/%Ar); diaphragm thickness and material (1.2, 2.0 and 2.5 mm thick, cold-rolled steel sheet pre-scored to 0.2mm depth); buffer length. The process used to develop new driver conditions is outlined in Figure 2. The first step was to develop a rapidly solved 0-D perfect gas analytical model of the free-piston compression process based on piston equations of motion by Hornung [9], which was then used to manually identify a range of potential tuned driver solutions.

The 0-D model proved capable of modelling the driver compression process fairly effectively but could not make accurate predictions of the required reservoir fill pressure. The reservoir gas was assumed to undergo an ideal unsteady expansion, however the actual gas must pass through an area change and slotted launcher. This convoluted flow path throttles the flow, significantly reducing the reservoir pressure force acting on the piston. Further, the unsteady expansion through the reservoir eventually reflects from the upstream end causing a further pressure drop. Both of these factors necessitate a much better predictive tool for the reservoir gas flow.

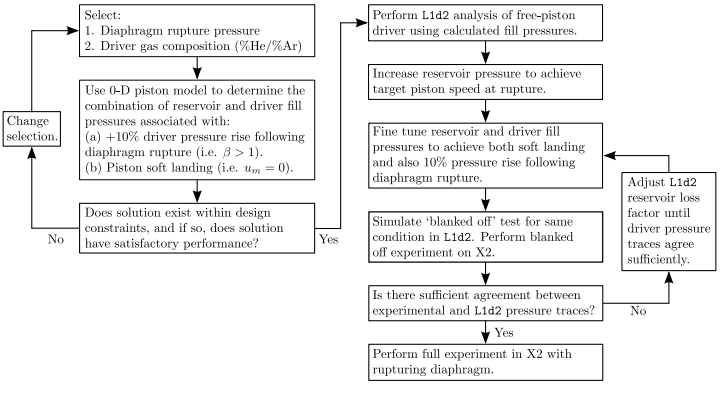

Fig. 2 X2 free-piston driver condition development process.

`L1d2` was used to fine tune the driver configuration prior to experimental testing. The code is capable of capturing the longitudinal unsteady wave processes which occur during piston operation and includes piston friction, flow chemistry, and pipe-flow viscous effects along the tube walls. Gradual area changes can be handled by the code, however 2-D and 3-D physical processes, such as flow through the launcher, cannot be directly modelled. To simulate the effect of these complex flow paths, a loss factor is applied over a finite length of the tube where the area contraction etc. is present. Representative loss factors can only be determined from experimental data, therefore their development must occur in conjunction with experimental testing. Experience indicates that the modelling tool is quite effective once tuned for a given test condition.

5 Blanked Off Driver Tests

Given the combination of high piston speed and short stopping distance, the risk of facility damage due to analysis uncertainty is significant, therefore predictive tools must be as accurate as possible. To achieve this accuracy with `L1d2`, a series of blanked off tests was performed, which involves replacing the diaphragm with a piece of thick steel plate with a PCB transducer located in it. During the test the piston bounces back and forth until it comes to rest. So long as the driver pressure

does not exceed the facility pressure limit, no damage will be done. A corresponding analysis is performed with an `L1d2` model, which is then tuned until an acceptable level of correlation is obtained between the experimental and numerical pressure traces. This methodology allows full correlation of the driver pressure right up until diaphragm rupture; good agreement increases confidence that the post-diaphragm rupture piston dynamics will also be predicted with good accuracy.

A broad analysis of different driver conditions using the 0-D analytical model, followed by detailed analysis with `L1d2`, eventually led to the three new driver configurations detailed in Table 2. Blanked-off tests were performed for each condition prior to conducting diaphragm rupturing experiments. Figure 3 compares pressure traces between `L1d2` and experiment for driver case X2-LWP-2.0mm-0, showing close correlation between *average* pressure magnitudes. There is some difference in the unsteady behaviour; `L1d2` has difficulty predicting the detailed unsteady driver pressure behaviour through the sharp area change to the primary diaphragm.

Table 2 X2 lightweight piston finalised driver conditions.

Driver Case ID [-]	Diaphragm thickness [mm]	Rupture pressure [MPa]	Reservoir fill pressure [MPa]	Driver fill pressure [kPa]	Buffer length [mm]
X2-LWP-1.2mm-0	1.2	15.5	4.94	110.3 (80% He / 20% Ar)	100
X2-LWP-2.0mm-0	2.0	27.9	6.85	92.8 (80% He / 20% Ar)	45
X2-LWP-2.5mm-0	2.5	35.7	6.08	77.2 (80% He / 20% Ar)	45

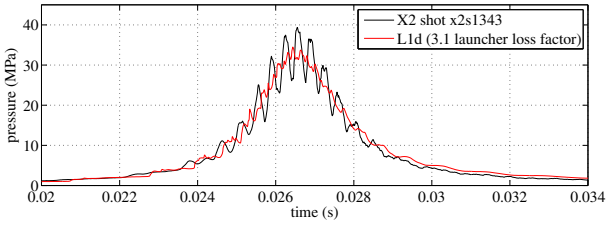

Fig. 3 Comparison of experimental and numerical driver pressures for driver condition X2-LWP-2.0mm-0. Experimental trace has been time shifted. Note: driver fill pressure was increased by 1.62× to ensure peak pressure did not exceed the facility 40 MPa limit.

6 Performance of the New Tuned Driver

Figure 4 shows averaged experimental shock speeds for each of the three driver conditions described in Table 2. The secondary driver shock speed is lower than the 0-D analytical prediction due to the primary diaphragm being offset from the area change in the driven tube, which delays the shock reaching its full strength. It can be seen that there is no longer the characteristic shock attenuation observed with the previous driver. With the 2.0mm and 2.5mm thick diaphragm conditions, target shock speeds are approached, thus achieving the original goals of the study. None of these new driver conditions caused any damage to the facility, indicating that

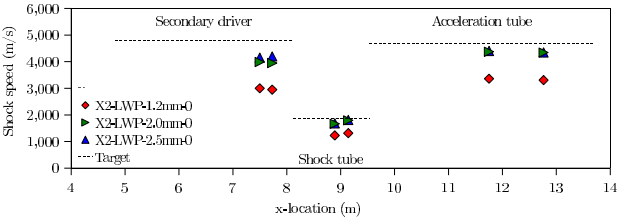

Fig. 4 Comparison of experimental and analytical shock speeds for new X2 tuned driver conditions (refer Table 2). Experimentally determined shock speeds shown are averaged speeds for three shots at each condition. Maximum experimental uncertainty of $\pm 2\%$.

the combined analytical/numerical/experimental development process managed to safely determine tuned, workable, driver conditions.

7 Conclusion

UQ is currently using its X2 and X3 expansion tube facilities to develop Mach 10-15 high total pressure scramjet flow conditions to simulate scramjet access to space flight. Fundamental to this objective is the development of new free-piston driver conditions optimised to produce long duration driver gas supply. This requires much lighter pistons to be operated at much higher speeds. An initial driver study undertaken in X2 resulted in the development of a new 10.5 kg aluminium piston. A combination of analytical modelling, numerical analysis with `L1d2`, and blanked-off driver experiments, has produced three new tuned driver conditions. These conditions run the piston sufficiently fast to maintain driver pressure at high levels for a long duration *after* diaphragm rupture, ensure that the piston comes to rest at the buffer without significant impact speed, and achieve similar shock strengths to the existing 35 kg piston driver.

Acknowledgements. The authors wish to thank: Mr B. Loughrey and Mr F. De Beurs for X2 technical support; The Australian Research Council and The Queensland Smart State Research Facilities Fund 2005 for support and funding.

References

1. Hunt, J.L., Martin, J.G.: Rudiments and Methodology for Design and Analysis of Hypersonic Air-Breathing Vehicles. In: Curran, E.T., Murthy, S.N.B. (eds.) Scramjet Propulsion, vol. 189, pp. 939–978. AIAA (2000)
2. Stalker, R.J.: A Study of the Free-Piston Shock Tunnel. AIAA Journal 5, 2160–2165 (1967)
3. Jacobs, P.A.: L1d: A computer program for the simulation of transient-flow facilities. Report 1/99, Department of Mechanical Engineering, University of Queensland, Australia (1999)

4. Hornung, H.G., Belanger, J.: Role and Techniques of Ground Testing for Simulation of Flows up to Orbital Speed. AIAA 90-1377 (1990)
5. Morgan, R.G.: Free-Piston Driven Expansion Tubes. In: Handbook of Shock Waves, vol. 1, pp. 603–622 (2001)
6. Paull, A., Stalker, R.J.: Test flow disturbances in an expansion tube. Journal of Fluid Mechanics 245, 493–521 (1992)
7. Itoh, K., Ueda, S., Komuro, T., Sato, K., Takahashi, M., Myajima, H., Tanno, H., Muramoto, H.: Improvement of a free piston driver for a high-enthalpy shock tunnel. Shock Waves 8, 215–233 (1998)
8. Gildfind, D.: Stress Analysis of a New Lightweight Piston for X2. Report 2009/16, Department of Mechanical Engineering, The University of Queensland, Australia (2009)
9. Hornung, H.G.: The Piston Motion in a Free-Piston Driver for Shock Tubes and Tunnels. GALCIT Report FM 88-1, Graduate Aeronautical Laboratories, CALTECH (1988)

Reflection Transition of Converging Cylindrical Shock Wave Segments

B.J. Gray and B.W. Skews

1 Introduction

An investigation was carried out into the transition between various types of reflection of converging cylindrical shock wave segments over various wedges, and the effect of the wave incidence angle and the Mach number of the incident wave on the reflection type. Such a reflection differs significantly from those of planar waves, as both the Mach number and the incident angle of the shock wave are time dependant. The transition conditions were examined in terms of transition criteria that have been suggested for planar waves in the literature.

In general, current research on the behaviour of curved waves is limited to cylindrical and spherical waves. In particular, the only previous work that related to reflection of curved waves that could be found were those relating to the reflection of blast waves generated by explosions at a certain height above the ground. This included the work of Takayama and Sekiguchi [1], Hu and Glass [2], and Liang et al.[3, 4]. However, there is no research to be found in the literature on the reflection of a free curved shock segment that encounters an inclined surface, despite the possible significance such research may have in a number of fields.

2 Review of Transition Criteria for Planar Waves

When an oblique shock wave encounters a solid boundary, reflection needs to occur in order for the flow to meet boundary conditions. For a plane wave reflecting off an inclined surface, reflection in steady conditions will be either a Mach reflection (MR) or regular reflection (RR), and the reflection pattern that occurs is a function of the wave incident angle and Mach number [5]. For a given Mach number, there is a critical incident angle (known as the maximum-deflection angle) above which

B.J. Gray · B.W. Skews
Flow Research Unit, School of Mechanical, Industrial and Aeronautical Engineering, University of the Witwatersrand, Johannesburg, 2050, South Africa

no reflected wave exists that is capable of deflecting the flow so that it runs parallel to the boundary. If the incident angle of the shock wave exceeds the maximum deflection angle, Mach reflection must occur according to the maximum-deflection condition.

The sonic condition infers that in order for a Mach reflection to occur, some form of length scale needs to be transmitted to the reflection point in order for the Mach stem to form [6]. This is not possible if the flow behind the reflected wave is supersonic relative to the reflection point. Thus the sonic condition states that transition from regular reflection to Mach reflection will occur when the flow behind the reflected wave becomes sonic relative to the reflection point. The transition angles predicted by the maximum-deflection and sonic criteria typically vary by fractions of a degree, and it is difficult to experimentally distinguish the difference between the two criteria.

In unsteady flows, the above mentioned criteria require a discontinuous pressure change in the region behind the reflected shock wave. Such a discontinuous change would cause unsteady pressure waves to form in the system in order to maintain mechanical equilibrium. Consequently, a new transition criterion was proposed by Henderson and Lozzi [7], which stated that the transition would occur at a critical angle at which the pressure behind the reflected shock can vary continuously as the reflection transition takes place, which would occur when the flows predicted by two- and three-shock theories coincide. For a Mach reflection at this particular incident angle, the flow behind the reflected shock is parallel to the reflection surface. This represents the limit at which direct Mach reflection (DiMR) can occur. Below this angle, any Mach reflection that occurs must be an inverse Mach reflection (IMR), which is an unstable reflection in which the triple point moves towards the reflection surface, eventually terminating in transitioned regular reflection (TRR). Below a Mach number of 2.23, the mechanical equilibrium criterion coincides with the maximum deflection criterion.

Ben-Dor [5] describes some analytical models for predicting the transition from MR to TRR for a planar wave impinging on a concave cylindrical surface. The basis of these models is that the Mach stem in a TRR represents the limit which corner signals carrying information about the length scale of the system can reach. However, they are independent of the radius of curvature of the wall, yet experimental observations have shown that the radius does play a role in determining the transition angle. Ben-Dor states that a model taking the radius into account [8] is still incomplete.

3 Numerical Computation of Cylindrical Shock Waves over Inclined Surfaces

Numerical simulations were carried out in FLUENT® using an inviscid, second order implicit density based solver. The flow was modelled using a third order MUSCL scheme with Roe's Flux-Difference Splitting scheme, with least squares, cell-based spatial discretisation. The domain consisted of a curved pressure inlet,

two converging walls, and an inclined wedge, which was meshed using a mapped quadrilateral meshing scheme. The pressure at the inlet was set such that a cylindrical shock wave would be generated so as to have a specific Mach number at the wedge apex. Initially, simulations were run using three different mesh densities, these being 100, 150, and 200 cells across the inlet. In addition, the mesh was adaptively refined up to 6 times in regions where the density gradient exceeded 2% of the maximum density gradient in the domain. The general behaviour of the shock wave for all three meshes was found to be similar, but for further investigation, the mesh density of 200 cells across the inlet was used as this offered better resolution of flow features which formed during the reflection transition.

Computations were carried out for shock waves with a radius of 100 mm, and Mach numbers at the wedge apex of 1.29, 1.43, 1.57 and 1.70 impinging on wedges of angles of 20°, 25°, 30°, 35°, 40°, 45° and 50°to the original flow direction. Initially, the reflection pattern that resulted was a direct Mach reflection (DiMR), with the shear layer starting at the the triple point and sloping towards the surface, and with the triple point trajectory directed away from the surface. This transitioned into an inverse Mach reflection (IMR) in which the triple point trajectory turns back toward the reflection surface, and the shear layer slopes from the triple point away from the surface. The Mach reflection eventually terminates in a transitioned regular reflection (TRR), which is characterised by a Mach stem which follows the reflection point up the wedge, but at a slower velocity. An example of the evolution of the reflection structure is shown in Figure 1.

4 Discussion

The sequence of reflection patterns of DiMR→StMR→IMR→TRR is similar to the sequence that takes place in the analogous case of a planar shock impinging on a curved wall, and that of the reflection of an oblique shock in a wind tunnel with continuously varying upstream geometry. However, the cases investigated differ from those situations in that the Mach number of the shock wave and the conditions behind the shock vary continuously.

In Figures 1(**d**) to (**f**), a Kelvin-Helmholtz instability is seen to form in the shear layer. Such instabilities are typically greatly exaggerated in high resolution solutions to the Euler equations (such as the one carried out here), and are usually much smaller or not present at all in experimental results or solutions to the full Navier-Stokes equations, as discussed by Sun and Takayama [9]. However, the instabilities only form after the transition to TRR, and thus do not affect the validity of the results. Furthermore, the Kelvin-Helmholtz instability is not expected to have a significant effect on the shape of the shock structure.

For planar shock waves in pseudosteady flows (such as those which occur in shock tubes), the criterion which is considered to come closest to predicting transition is the sonic condition. Figure 2 shows a plot of the transition angle for a planar wave predicted by the sonic condition against Mach number. Cases that lie above the transition curve would be expected to show a Mach reflection, while cases below the

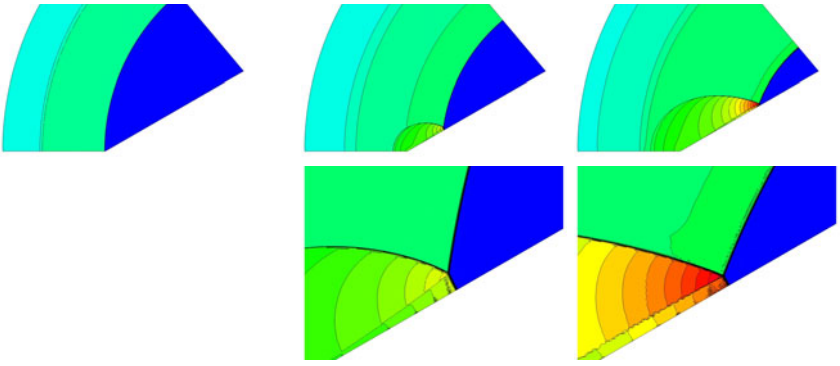

(**a**) Shock immediately before encountering the wedge at t=0μs

(**b**) Direct Mach reflection (DiMR) at t=34μs

(**c**) Stationary Mach reflection (StMR) at t=68μs

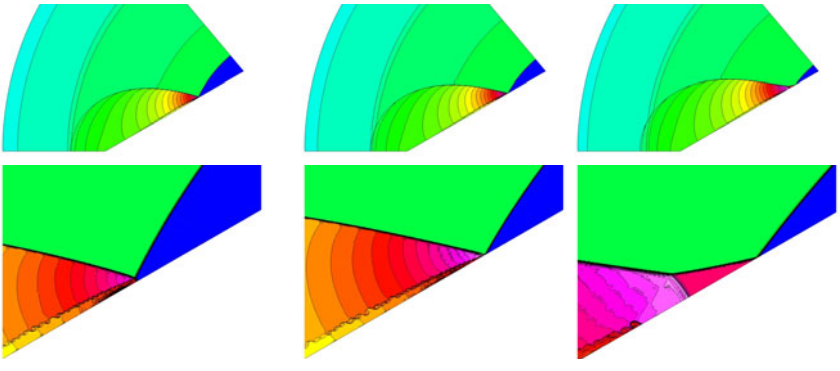

(**d**) Inverse Mach reflection (IMR) at t=77μs

(**e**) Triple point colliding with the reflection surface at t=82μs

(**f**) Transitioned regular reflection (TRR) at t=89μs

Fig. 1 Evolution of the shock reflection structure for a shock reflecting off a 30° wedge with a Mach number of 1.43 and shock radius of 100 mm at the wedge apex, showing contours of constant density. A 6x zoomed image of the reflection is shown below each image

curve would be expected to show regular reflection. On the same axes, the reflection type obtained in this study immediately after the shock encounters the wedge apex are plotted.

A Mach stem and shear layer was evident in 22 of the 28 cases tested, allowing those reflection patterns to be identified as Mach reflections. The remaining 6 cases showed no visible Mach stem or shear layer, and were classified as regular reflections. Comparing the results to the transition line predicted by the sonic criterion, it is apparent that 5 cases which demonstrated a Mach reflection after the wedge apex should have shown a regular reflection. The fact that Mach reflection could occur below the theoretical transition line implies that the transition criteria are different

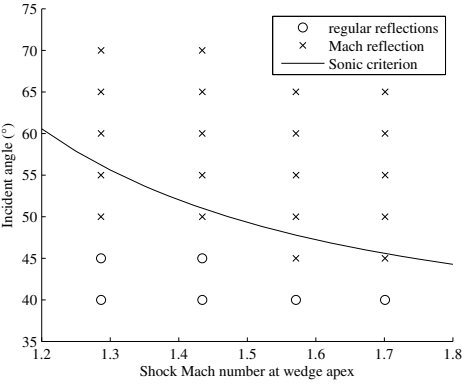

Fig. 2 Initial reflection patterns obtained immediately behind the wedge apex, including the transition line predicted by the sonic transition criterion

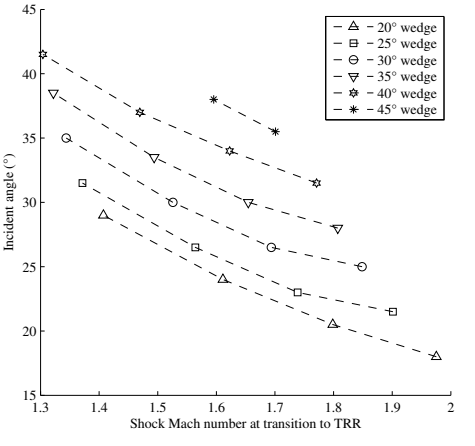

Fig. 3 Variation of shock incident angle at the point of transition to TRR

for curved waves, although whether this is due to the radius of curvature of the shock wave or the rate of amplification of the Mach number is unclear.

Figure 3 shows the points at which transition to TRR occurred. These points cannot be directly compared to the first three of the transition criteria described in section 2, as these criteria were developed for application to the RR→MR transition of a planar shock with a constant Mach number. Ben-Dor's models for predicting TRR transition make a number of assumptions which make a direct comparison invalid in this case — he assumes that the incident shock is planar and propagates at a constant velocity; the reflected shock has negligible strength compared to the incident shock; the conditions behind the shock are uniform; and that information

about the length scale needs to be transmitted to the reflection point along the wedge. The results show that the first three of these assumptions do not hold. In addition, the length scale need not be carried to the reflection point by corner generated signals, as information about a length scale is inherently carried to the transition point in the Mach stem of the IMR (although this information is lost at the transition point).

5 Conclusion

MR was found to occur when the shock encountered the wedge in most cases, even in some cases where the sonic condition predicts RR for planar waves at the same incident angle and Mach number. Thus, shock wave curvature has some impact on which reflection pattern occurs. When the transition from MR to TRR is considered, there is significant disagreement between the transition points predicted by the results of the numerical simulations of converging cylindrical waves, and those predicted by the transition criteria for planar waves. A more accurate transition criterion would have to take into account the radius of the shock wave and the time taken for the triple point to return to the surface once IMR occurs. A unique facility is currently being constructed to validate the above findings experimentally.

References

1. Takayama, K., Sekiguchi, H.: Triple-point trajectory of a strong spherical shock wave. AIAA Journal 19, 815–817 (1981)
2. Hu, T., Glass, I.: Blast wave reflection trajectories from a height of burst. AIAA Journal 24, 607–610 (1986)
3. Liang, S.M., Hsu, J.L., Wang, J.S.: Numerical study of cylindrical blast-wave propagation and reflection. AIAA Journal 39(6), 1152–1158 (2001)
4. Liang, S.M., Wang, J.S., Chen, H.: Numerical study of spherical blast-wave propagation and reflection. Shock Waves 12(1), 59–68 (2002)
5. Ben-Dor, G.: Shock wave reflection phenomena, 2nd edn. Springer, Heidelberg (2007)
6. Hornung, H.: Regular and Mach Reflection of Shock Waves. Annual Review of Fluid Mechanics 18(1), 33–58 (1986)
7. Henderson, L.F., Lozzi, A.: Experiments on transition of Mach reflexion. Journal of Fluid Mechanics 68, part 1, 139–155 (1975)
8. Ben-Dor, G., Takayama, K.: The dynamics of the transition from Mach to regular reflection over concave cylinders. Israel Journal of Technology 23, 71–74 (1986/1987)
9. Sun, M., Takayama, K.: A note on numerical simulation of vortical structures in shock diffraction. Shock Waves 13, 25–32 (2003)

Development of Blast-Wave Mediated Vaccine Delivery Device

G. Divya Prakash, S.G. Rakesh*, Dipshikha Chakravortty,
K. Kontis, and G. Jagadeesh

1 Introduction

Shockwaves are essentially non-linear waves that propagate at supersonic speeds. Such disturbances occur in steady transonic or supersonic flows, during explosions, earthquakes, hydraulic jumps and lightning. Rapid movement of piston in a tube filled with gas generates a shock wave. Any sudden release of energy (within few μs) will invariably result in the formation of shock waves since they are one of the efficient mechanisms of energy dissipation observed in nature. The dissipation of mechanical, nuclear, chemical, and electrical energy in a limited space will usually result in the formation of a shock wave. Because of the dissipative nature of shock waves they invariably need a medium both for generation as well as for propagation.

It is possible to generate spherical shock waves with typical radius of few mm, both in ambient air as well as in water, expending energies of the order of few joules [1]. Micro-shock waves can be generated in ambient air by focusing the energy [2] from a pulsed laser beam into small spherical volumes. There have been several attempts [3, 4] in the past to experimentally re-create a large scale explosion in the laboratory using negligible amounts of primary explosives.

Considering the various difficulties involved with the known methods of generating controlled micro-blast waves in the laboratory, a new method to generate

G. Divya Prakash · G. Jagadeesh
Department of Aerospace Engineering, Indian Institute of Science, Bangalore-560012, India

G. Divya Prakash · S.G. Rakesh · Dipshikha Chakravortty
Department of Microbiology and Cell Biology, Indian Institute of Science, Bangalore-560012, India

K. Kontis
School of Mechanical, Aerospace and Civil Engineering, The University of Manchester, Manchester, M13 9PL, UK

* Department of Mechanical Engineering, Amrita School of Engineering, Amrita Vishwa Vidyapeetham, Bangalore-560035, India.

spherical micro-blast waves has been proposed. In this study, a new method to generate controlled micro-blast waves in the laboratory from the open end of a plastic tube has been proposed. Small amounts (18mg/m length) of micro explosive (High Melt Explosive (HMX) and traces of Aluminium) is uniformly coated on the inner wall of a polymer tube (1mm inner diameter; wall thickness 1mm, M/s Dyna Nobel, Switzerland) of arbitrary length. When the micro explosive is electrically triggered from one end of the polymer tube, a detonation wave is generated inside the tube. When this detonation front is allowed to escape from the open end of the polymer tube, a micro-blast wave is generated. Since the amount of energy expended in the generation of the blast wave from the open end of the polymer tube is very small (8.7 Joules; TNT equivalent 1.63 mg) they are referred here as micro-blast waves. Thin metal foils placed at the open end of the polymer tube along with appropriate mechanical fixtures is used to transfer the impulse-momentum generated by micro-blast wave to appropriate medium. Utilizing the inherent kinetic energy associated with propagating micro-blast wave, a new fluid delivery system has been designed [5].

2 Experimental Description

The needle-less drug/vaccine delivery device comprises of a drug chamber, metal foil and a polymer tube coated with explosive (Figure 1). When the polymer tube is ignited micro-shock waves are produced in the other end of the polymer tube and it deflects the metal foil placed in that end. The micro-shock waves can propagate through the liquid. The pressure profile in the drug chamber was measured using PCB Piezotronics pressure transducers with a sensitivity of 4.989 mV/psi.

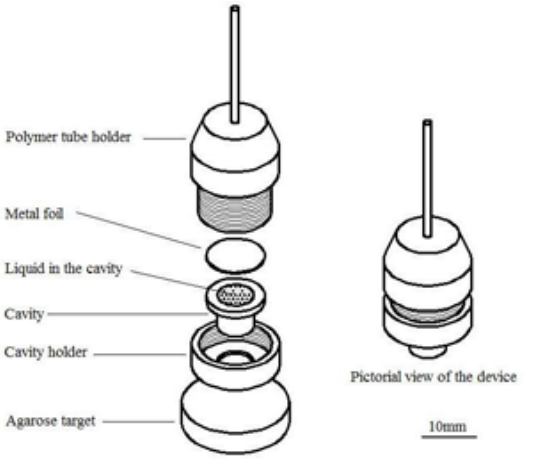

Fig. 1 A diagram showing the exploded and assembled pictorial views of the fluid jet delivery system

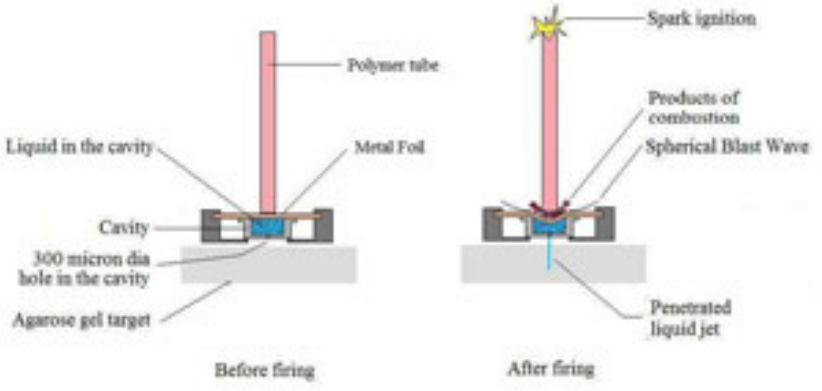

Fig. 2 Schematic diagram of liquid jet delivery system

This increase in pressure leads to the production of liquid jet through a small hole in the drug chamber (Figure 2).

The overpressure behind the micro-blast wave and the subsequent impulse that can be generated when any inelastic material is subjected to blast wave loading is an attractive proposition for designing a fluid delivery system. If an appropriate mechanical fixture arrangement can be designed that can block all the by-products of the micro-explosion and transfer only the energy when subjected to blast wave loading, then this method can be used to propel the fluid to the desired biological targets. This mechanism must be capable of transferring the momentum of the micro-blast wave to the fluid with minimum energy loss.

The idea is to produce a liquid jet by subjecting the foil to micro-blast wave loading from one side, so that the metal foil deforms instantaneously transferring the momentum to the liquid. The use of metal foil can serve two purposes: (1) transferring the momentum to the liquid so that it gets ejected at very high velocities and (2) obstructing the flow of combustion products (debris cloud) and hence avoiding mixing of combustion products with the liquid. The device was used for vaccination in murine salmonellosis model to check its efficiency. A vaccine is a biological preparation that improves immunity to a particular disease. A vaccine typically contains an agent that resembles a disease-causing microorganism, and is often made from weakened or killed forms of the microbe or its toxins. The agent stimulates the body's immune system to recognize the agent as foreign, destroy it, and remember it, so that the immune system can more easily recognize and destroy any of these microorganisms that it later encounters. Vaccination will be very efficient when the vaccine is delivered in the epidermal layer of the skin. There are no efficient delivery systems which can deliver vaccine in the skin. Salmonella is a bacterial pathogen which causes typhoid in human. A typhoid vaccine developed in Indian Institute of Science [6] was delivered using the device and the efficiency of the device for vaccination was checked. The device was placed in the abdominal position of mice and vaccine was administered (Figure 3). Salmonella typhimurium vaccine strain

Fig. 3 Vaccination of mouse using the device

(DV-STM-07) was delivered to mice using the device and then infected with virulent Salmonella. The survival assay of mice after the infection was performed.

3 Results

From the visualisation studies it is confirmed that the micro-blast waves can be generated using polymer tubes coated with small amounts of explosives. It appears from the schlieren images that the micro-blast waves which are generated are spherical in nature and they can produce the liquid jet from the drug loading chamber (Figure 4). From the high speed image visualization, the liquid jet produced by the micro-shock waves propagates in a velocity of 100 m/s. The velocity of the jet coming out of the discharge hole depends on the pressure acting on the liquid column inside the cavity. The pressure acting on the liquid inside the cavity is found using a needle

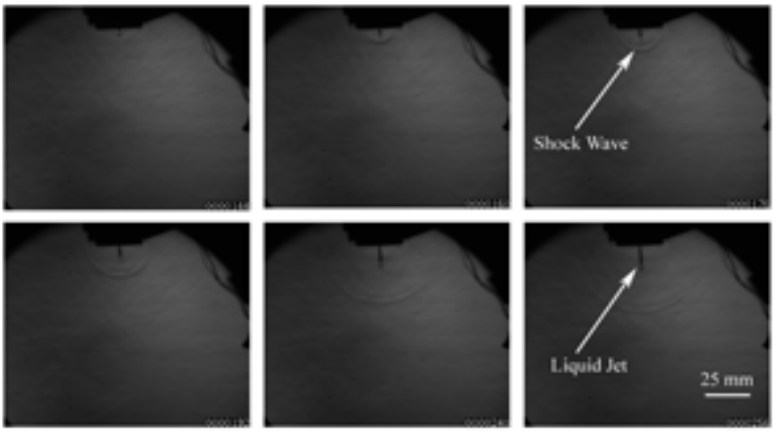

Fig. 4 Sequential images of the micro-blast wave and liquid jet ejecting from the micro discharge hole

gauge (Dr. Muller Instruments, Oberursel, Germany). The pressure signals picked up by the needle gauge is recorded in the oscilloscope (Yokogawa Electric Corporation, Japan). The over pressure was observed between 50-100 bar (Figure 5). This pressure can produce the liquid jet in high velocity. The penetration of liquid jet into agorose gel shows the effectiveness of the device for delivering drugs (Figure 6).

Mice vaccinated (DV-STM-07) through device and through intra-peritoneal (I.P) route showed 100 % survival upon challenge with virulent Salmonella, whereas all the unvaccinated mice died within 8 days after the challenge (Figure 7). These results clearly demonstrate that the vaccination through the new micro-shock wave assisted device measures up to the traditional vaccination strategies in this efficacy of protection even at the reduced dosage. The mice were comfortable while vaccination by our device whereas they were uncomfortable when needle injection was

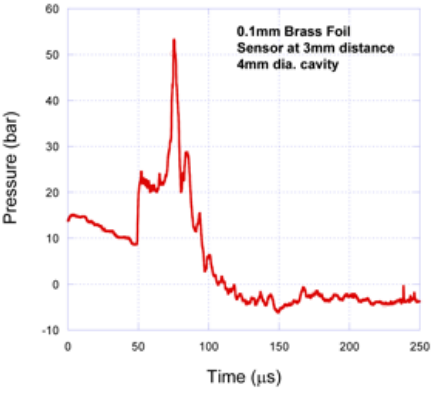

Fig. 5 Graph showing variation of overpressure value with respect to time inside medium cavity

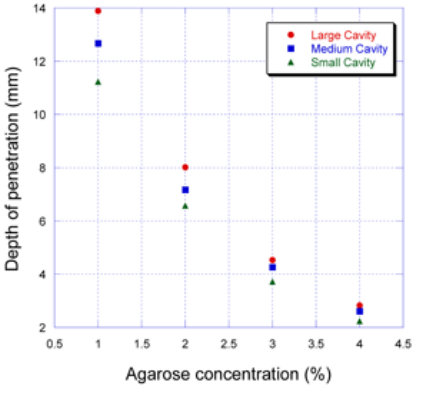

Fig. 6 Experimentally observed penetration depth with the three cavities as a function of agarose concentration

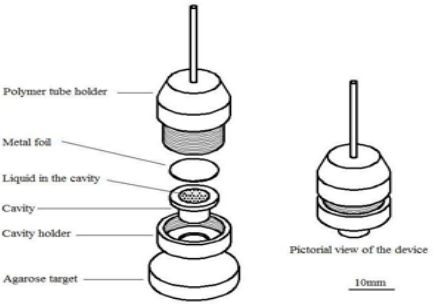

Fig. 7 Survival assay of mice

used for vaccination. So the needle-less delivery device can be used for efficient vaccination without pain.

4 Conclusion

Polymer tubes have been used to generate micro-blast waves in a repeatable fashion. Time resolved flow visualizations study indicate almost spherical blast waves emerge from the open end of the polymer tube. The enargy transfer mechanism effectively produced the liquid jet which panetrate the target to deliver the drug.

Studies show that intradermal vaccination offers better protection than the other routes of immunization [7]. The delivery of vaccines to the epidermal layer of the skin is a big challenge while using needle injections. Vaccination to the epidermal layer of skin can be done with high efficiency using our device. Delivering vaccines in close proximity to the epidermal layer may facilitate the antigen-recognition and uptake process by Langerhans cells[8]. Since intra-dermal injection of hepatitis B and rabies vaccines required only 10% of an intramuscular dose to elicit an equivalent antibody response and seroconversion rate [9], the dosage of vaccine can be reduced by using our device. The cost of our needle-less device will be 200$ and cost per shot will be 10 cents. As sensitive nerve endings are not present in the epidermal layer of skin, delivery of vaccine using our device will be safer than intradermal needle injection. Given that most of the vaccines commercially available are in liquid formulations, our device can be used to deliver those vaccines regardless of their particle size and chemical nature.

References

1. Jagadeesh, G., Takayama, K.: Novel applications of micro-shock waves in biological sciences. J. Indian Inst. Sci. 82, 49–57 (2002)
2. Jiang, Z., Takayama, K., Moosad, K.P.B., Onodera, O., Sun, M.: Numerical and experimental study of a micro-blast wave generated by pulsed-laser beam focusing. Shockwaves J. 8, 337–349 (1998)

3. Kleine, H., Timofeev, E., Takayama, K.: Laboratory-scale blast wave phenomena optical diagnostics and applications. Shockwaves J. 14(5/6), 343–357 (2005)
4. Hargather, M.J., Settles, G.S.: Optical measurement and scaling of blasts from gram-range explosive charges. Shockwaves J. 17, 215–223 (2007)
5. Jagadeesh, G.: Apparatus and method for delivering biologically-active substances or micro-medical devices to a target. US Patent App. No. 12480514 (under consideration) (2009)
6. Chakravortty, D., Negi, V.D.: Mutated Salmonella Typhi Strain and use thereof in a vaccine. Int. Patent App. No. PCT/IN2008/000524 (2008)
7. Hunsaker, B.D., Perino, L.J.: Efficacy of intradermal vaccination. Vet Immunol Immunopathol 79, 1–13 (2001)
8. Merad, M., Ginhoux, F., Collin, M.: Origin, homeostasis and function of Langerhans cells and other langerin-expressing dendritic cells. Nat. Rev. Immunol. 8, 935–947 (2008)
9. Fadda, G., Maida, A., Masia, C., Obino, G., Romano, G., Spano, E.: Efficacy of hepatitis B immunization with reduced intradermal doses. Eur. J. Epidemiol. 3, 176–180 (1987)

Micro-shock Wave Assisted Bacterial Transformation

G. Divya Prakash, S.G. Rakesh*, Dipshikha Chakravortty,
Nataraja Karaba, and G. Jagadeesh

1 Introduction

A gene is a unit of heredity in a living organism. It normally resides on a stretch of DNA that codes for a type of protein or for an RNA chain that has a function in the organism. All living things depend on genes, as they specify all proteins and functional RNA chains. Genes hold the information to build and maintain an organism's cells and pass genetic traits to offspring. The gene has to be transferred to bacteria or eukaryotic cells for basic and applied molecular biology studies. Bacteria can uptake exogenous genetic material by three ways: conjugation, transduction and transformation. Genetic material is naturally transferred to bacteria in case of conjugation and transferred through bacteriophage in transduction. Transformation is the acquisition of exogenous genetic material through cell wall. The ability of bacteria of being transformed is called competency and those bacteria which have competency are competent cells. Divalent Calcium ions can make the bacteria competent and a heat shock can cause the bacteria to uptake DNA. But the heat shock method cannot be used for all the bacteria. In electroporation, a brief electric shock with an electric field of 10-20kV/cmmakes pores in the cell wall, facilitates the DNA to enter into the bacteria. Microprecipitates, microinjection, liposomes, and biological vectors are also used to transfer polar molecules like DNA into host cells.

G. Divya Prakash · S.G. Rakesh · G. Jagadeesh
Department of Aerospace Engineering, Indian Institute of Science, Bangalore-560012, India

G. Divya Prakash · Dipshikha Chakravortty
Department of Microbiology and Cell Biology, Indian Institute of Science, Bangalore-560012, India

Nataraja Karaba
Department of Crop Physiology, University of Agricultural Sciences, Bangalore-560012, India

* Department of Mechanical Engineering, Amrita School of Engineering, Amrita Vishwa Vidyapeetham, Bangalore-560035, India.

In molecular biology, the process of electroporation is often used for the transformation of bacteria,yeast, and plant protoplasts. Electroporation can cause cell damage and it requires ion free medium for transformation. It can lead to non-specific transformation also. Electroporation is expensive and transgene expression is not homogenously distributed in the treated tissue. While creating random libraries, procedures based on standard CaCl2 wash method result in substantial decrease in transformation efficiency. Therefore a method for obtaining high transformation rates need attention. With the arrival of Human genome project and revolution in recombinant DNA technology we found it mandatory to develop a rapid and efficient transformation protocol.

2 Experimental Description

Although shock waves can be used to deliver DNA and macro molecules into eukaryotic cells ([2];[3];[4]), there are no reports stating bacterial transformation using shock waves. Shock waves, which are energy dissipation mechanism, produced by an explosion can be channeled to perform bacterial transformation. Kidney and gallstone disease are being treated by using pressure pulses generated by lithotripter shock waves. Shock waves have been used in orthopaedics and traumatology to treat insertion tendinitis, avascular necrosis of the head of femur and other necrotic bone alterations. In a specially designed transformation device, the bacterial culture is exposed to a sudden release of micro-shock waves ([1]). The energy released is equivalent to 0.168 mg trinitrotoluene containing chemical energy. The shock wave mediated transformation device arrangement contain a polymer (coated inside with high melt explosive and trace of Aluminium) which ends up to a metal foil and the other side of the tube is connected to an igniter, which produce the spark. The spark discharge causes the combustion throughout the polymer tube, which produces the spherical micro-shock wave which is passed on to the transformation chamber beneath the metal foil. Enough safety precautions by way of miniature rubber gaskets have been incorporated in the device to ensure that the gaseous products of combustion do not leak into the transformation chamber. A schematic diagram of the experimental device is shown in Figure 1. The maximum pressure observed by the bacterial culture inside the cavity was 40 to 100 bar (Figure 2).

There are two types of cells namely; (1) Prokaryotic cells and (2) Eukaryotic cells. The prokaryote cell is simpler than a eukaryote cell, lacking anucleus and most of the otherorganellesof eukaryotes. Eukaryoticcells are about 10 times the size of a typical prokaryote. The major difference between prokaryotes and eukaryotes is that eukaryotic cells contain membrane-bound compartments in which specific metabolic activities take place. Eukaryotic cells have a true nucleus, bound by a double membrane. Prokaryotic cells have no nucleus. There are few well established methods for transformation of bacterial cell. Two such conventional methods with which the results of the present study are compared with are (1) Freeze-Thaw method and (2) KCM method. A schematic diagram of preparation of cell suspension for treatment using micro-blast waves is shown in Figure 3.

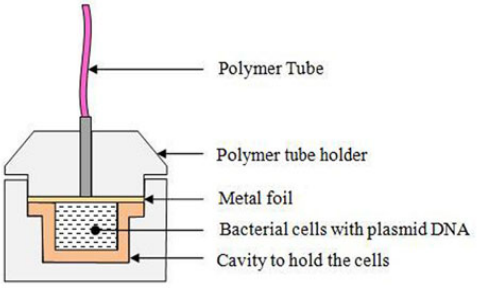

Fig. 1 Schematic sketch of the experimental setup to carry out bacterial cell transformation experiments

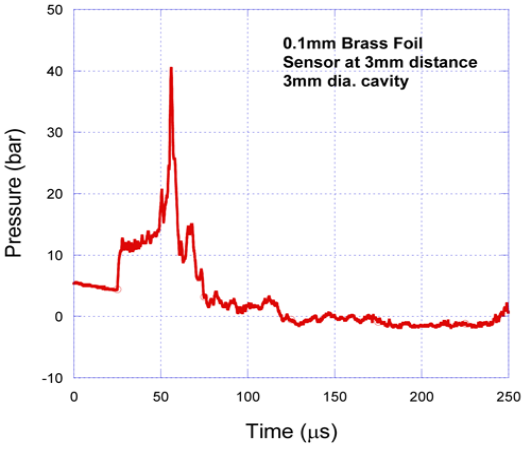

Fig. 2 A graph showing variation of overpressure value with respect to time inside medium cavity

Prokaryotic cells E.coli and Agrobacterium are grown to log phase (37oC for E.coli and 28oC for Agrobacterium) and then mixed with isolated plasmid DNA. Prokaryotic cells mixed with plasmid DNA is taken in the cavity and covered with a metal foil. This metal foil is subjected to the micro-blast wave loading from the open end of the polymer tube. The metal foil deforms instantaneously, and subsequently a strong compression wave travels through cell suspension underneath. Because of the disturbance created in the cell suspension, the prokaryotic cells are induced to uptake DNA and this is confirmed by the growth of cells in plates containing antibiotic Kanamycin. The isolated colonies are counted to express the transformation efficiency.

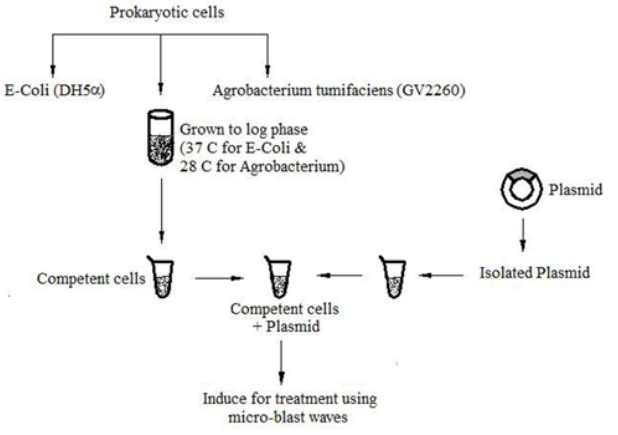

Fig. 3 A schematic diagram of preparation of cell suspension for treatment using micro-blast waves

The transformation efficiency (TE) is calculated using the following equation

$$TE = \left\{ A \left(\frac{B}{C} \right) \right\} \times \frac{1}{D} \quad \text{CFU}/\mu\text{g of DNA} \tag{1}$$

where, A - No. of colonies
B - Total volume
C - Volume plated
D - Micro gram of DNA used
CFU - Colony Forming Units

Transformation efficiency of the device was also compared with electroporation for *E.coli* bacterial transformation. Plasmid DNA coding for cherry red protein was transferred to *E.coli* by electroporation and by micro-shock wave device. The transformed bacteria will express red colour cherry red protein which can be visualized under fluorescent microscope.

3 Results

The cavitation produced by the shock wave is neither lethal to the bacteria like *E. coli*, *Pseudomonas aeruginosa* and *Salmonella typhimurium* nor cause the loosening of plasmid integrity, even after five consecutive shots. *E.coli* and *Agrobacterium* are transformed using our transformation device. The results obtained from polymerase chain reactions clearly demonstrate that shock wave assisted cell transformation can be successfully used to transform prokaryotic cells with plasmid DNA. The transformation efficiencies obtained (Figure 4) are comparable with those of conventional methods. The transformation efficiency compared with electroporation method showed that the micro-shock wave assisted bacterial transformation is

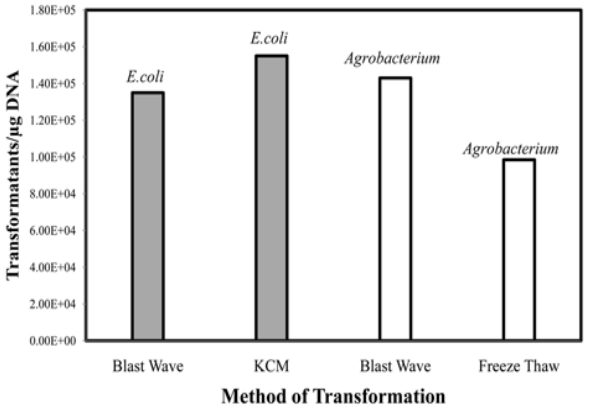

Fig. 4 Transformation efficiency with the device and by other methods

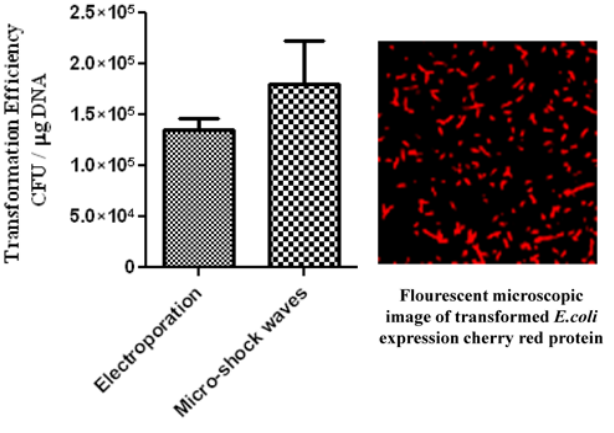

Fig. 5 Comparison of micro-shock wave device and electroporator mediated transformation

as efficient as electroporation (Figure 5). The micro-shock waves produce the acoustic cavity in the liquid inside the chamber and that leads to the temporary change in the membrane permeability. Simultaneously the propagating shock wave pushes the plasmid inside the cell for certain microsecond and then reversal of cell to normal stage happens, leaving the cell viability unaffected. Electroporation can lead to irreversible change in the membrane permeability leading to the loss of bacterial viability, unlike the shock wave. Moreover, the transformation efficiency of shock wave mediated bacterial transformation remains unaltered even though there may be a delay in nutrient media addition, whereas, electroporated culture has to be added with media immediately. The technique evolved in this study can be efficiently used

with suitable modification for introduction of macromolecules including DNA into different cell types.

4 Conclusions

The new device developed is simple, cheaper and efficient for bacterial transformations. Following are the reasons which can make this device commercially very robust in the near future 1) There is no need to prepare competent cells which involves numerous washing steps with ultrapure water followed by glycerol 2) Salt-free DNA is not required unlike in existing electroporator machine, where the presence of salt will lead to spark and abortive transformation 3) There is no hurry to add the nutrient media immediately after transformation unlike with the existing electroporator 4) All the parts are reusable and autoclavable and the use of expensive cuvettes can be minimized.

This device can be a potential future instrument for bacterial transformation in laboratories with excellent transformation efficiency, low cost and without the fear of losing the viability of bacteria.

References

1. Jagadeesh, G.: Apparatus and method for delivering biologically-active substances or micro-medical devices to a target. US Patent Application No. 12480514 (under consideration) (2009)
2. Kodama, T., Doukas, A.G., et al.: Shock wave-mediated molecular delivery into cells. Biochim. Biophys. Acta 1542(1-3), 186–194 (2002)
3. Lauer, U., Burgelt, E., et al.: Shock wave permeabilization as a new gene transfer method. Gene Ther. 4(7), 710–715 (1997)
4. Tschoep, K., Hartmann, G., et al.: Shock waves: a novel method for cytoplasmic delivery of antisense oligonucleotides. J. Mol. Med. 79(5-6), 306–313 (2001)

Starting Characteristics of Hypersonic Inlets in Shock Tunnel

Z. Li, B. Huang, J. Yang, Y. Wei, X. Liu, and J. Liu

1 Introduction

The starting-characteristic of inlet is one of the key factors that govern the performance of hypersonic airbreathing propulsion system. For efficient operation, the inlets must operate in a started mode. Inlet starting has been extensively studied,[1] [2] however, it is difficult to accurately predict whether the inlet is started or unstarted. Therefore, it will be useful to find an easy way that is capable of testing various behaviors of the inlet starting process. Pulse facilities could play an important role in these ground tests. But it has been shown that the inlet could be started with larger internal contraction ratio (ICR) in pulse facilities,[1] such as a shock tunnel, because of the unsteady effects in flow establishment of the facility[3] which have strong capability of helping inlet to start. So, there is a large discrepancy compared with conventional facilities. However, every coin has two sides. Whether the strong help-to-start capability of pulse facility can be switched 'on' and 'off'? The present paper reports our recent progress related to the above ideas.

The inlet leading edges of forebody, cowl and sidewalls must be blunted due to aerothermal heating of the hypersonic vehicle. The leading edge bluntness not only affect the external flow patterns, such as the shock wave shape, but also affect the internal inlet performance,[4] such as the inlet starting characteristics. The latter may be worse. A reliable inlet should successfully survive in severe aerothermal environment and simultaneity retain the inlet performance at an acceptable level.[2] As such, the knowledge of the leading edge bluntness influence on the inlet performance is of vital significance in the practical design of a hypersonic inlet.

In the present study, the starting characteristics of hypersonic inlets with different ICR and leading edge bluntness were tested in a shock tunnel. Various behaviors of the inlet starting process were reported.

Z. Li · B. Huang · J. Yang
University of Science and Technology of China, Hefei 230027, Anhui, P. R. China

Y. Wei · X. Liu · J. Liu
The 3rd Research Academy of CASIC, Beijing 100074, P. R. China

2 Experimental Facility and Test Model

The experiments were conducted in the shock tunnel JB430 of the University of Science and Technology of China (USTC). For a detail description of the facility, refer to Ref. [5]. This shock tunnel can operate in a reflected mode with a Mach number 5.5 by changing the throat portion of the nozzle and able to provide flow enthalpy about 1 MJ/kg for a test time about 15 ms. The freestream flow conditions used for the present study were Mach number M_∞=5.5, total pressure $p_0 = 0.78$MPa, total temperature T_0= 712K, static pressure p_∞= 834Pa, static temperature T_∞= 101K and unit Reynolds number $Re_\infty = 4.5 \times 10^6$/m.

The basic inlet model for present study is a generic two-dimensional planar mixed external and internal compression system as shown in Fig.1. It consists of two compression ramps forebody, a horizontal cowl and a constant area isolator. Two sidewalls (non-compression) are adopted to ensure the inlet flow is quasi-two-dimensional. To make sure that the shock structure can be visualized, part of the each sidewall is replaced by glass for optical access. Figure1(a) shows a photograph of the inlet model with one sidewall removed. The basic model has a constant inner width of 54 mm and overall length 450 mm. The first ramp has an angle of 9 degree and length of 126 mm. The second ramp provides additional 5 degree compression with a length of 120 mm. The location of the cowl can be adjusted 10 mm by 10 mm horizontally and vertically by varying the assembly bolted position in the forebody and the sidewall. The inner side of the 50 mm height forebody of the basic model can also be inserted thin plate with a ramp like leading edge. As a result, the inlet internal entrance height h_i and the throat height h_t at the entrance of the isolator are changeable. Various ICR of different inlet configurations are archived as may be required in the experiments. During the present study the leading edges of the forebody and the cowl can be blunted by attaching variable radius parts to evaluate the influence of leading edge bluntness on flow patterns and starting characteristics of the inlet. Figure1(b) shows the schematics and dimension of the model.

To visualize the flow field of the inlet model, the JB430 shock tunnel is equipped with a high-speed schlieren system. For the present set of experiments the high-speed camera (Photron FASTCAM SA5 1000K-M2, Japan) is operated at a framing rate of 20 kHz with a resolution of 1024×320 pixels and exposure time of 1μs. The camera is focused on near the cowl, the region of interest, to detect the inlet starting/unstarting process.

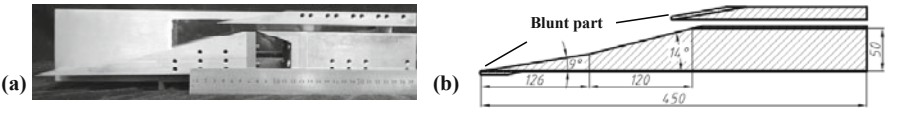

Fig. 1 Basic inlet model.

3 Results and Discussions

As mentioned above, the shock tunnel has strong capability of helping inlet to start. A shutter-like obstacle, placed at the rear part of the inlet channel, is used to switch 'off' the strong help-to-start capability. The obstacle will generate 'choking' effect to force the inlet unstarting at the initial operation of the shock tunnel, and then quickly open the channel once the steady flow is set up. So the inlet could be 'pre-set' in either started or unstarted mode, prior to the steady test flow. Then what happens next is catched by the high-speed schlieren system. It is important that the 'choking' time must be long enough to suppress the strong help-to-start capability of the shock tunnel, but short enough as compared with the total test time of the facility. With the help of a shutter-like obstacle, the action of it demonstrated next, various behaviors of the inlet starting process can be achieved.

3.1 Shutter-Like Obstacle Action

Figure 2 shows a series of schlieren photographs in run 281, that is, the shutter-like obstacle action in an inlet model has an ICR of 1.53. As discussed in the previous paragraphs, the 'choking' time of the obstacle is important. The location and weight of the obstacle determines the 'choking' time. The obstacle located at the rear part of the inlet channel is beyond the visualization region. But a little mark attached to the obstacle by a cotton thread make it possible to detect the inlet open time, that is, when the the obstacle is blown out. In Fig. 2 t = 0ms, the flow is near to come, the cotton thread is slack. At t = 0.70ms the flow inner the inlet is established. But the channel is choked at the rear part of the inlet because of the obstacle and the cotton thread is becoming tight. The generated separation shock begins to move upstream. At the moment t = 1.60ms the expelled separation shock stands at the internal entry section and still moves upstream. The inlet is unstarted. The large displacement of the mark indicates that the obstacle is near to be blown out. When t = 2.55ms the channel has already open and the 'choking' effect is finished. The separation shock stands at the farthest upstream and begins to move back. The steady test flow is also coming, the inlet inner flow will be reestablished. At t = 3.05ms the separation shock stands at the internal entry section again. After t = 4.35ms the separation shock has already swallowed, the inlet is restarted and retain started mode till the test flow

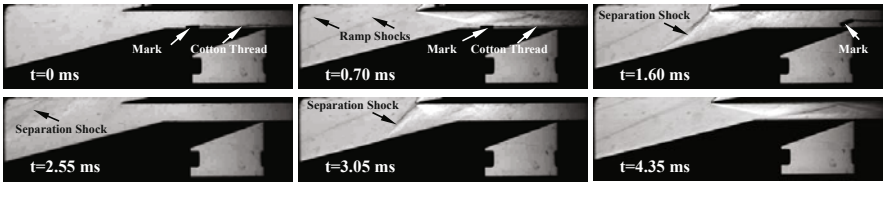

Fig. 2 Schlieren images of the self-starting process in run 281.

break-up. It was found that nice shutter-like obstacle action can be obtained when the 'choking' time to be an order of 1 ms.

3.2 Sharp Leading Edge Inlet Starting Characteristics

Preliminary estimate of the inlet starting characteristics can be obtained by comparing the inlet ICR with the Kantrowitz limit and isentropic limit.[1] The average Mach number at the inlet internal entry section M_i is used for the calculation. The Kantrowitz limit is for self-starting and is calculated by assuming a normal shock at the internal entry and calculating a quasi-one-dimensional, quasi-steady isentropic internal area ratio that will produce sonic flow at the throat. The isentropic limit is calculated for un-starting. An inlet with an ICR less than the Kantrowitz limit will have self-starting ability. An inlet will not be started with an ICR greater than the isentropic limit. But for efficiency a reliable inlet operates at neither isentropic nor normal shock at the internal entry. Furthermore a sonic flow at the inlet throat is not always satisfied. This means that an ICR greater than the Kantrowitz limit can also be tolerated and the reliable inlet operates at an ICR between the Kantrowitz limit and the isentropic limit. It is difficult to accurately predict the inlet starting characteristics, because of the isentropic limit is far beyond the Kantrowitz limit. Mölder [6] introduced a start-ability index S for this challenge. $S = 0$ for an ICR corresponding to the isentropic limit, $S = 1$ for the Kantrowitz limit. While S varies from 0 to 1 large gap between the two classic limits can be covered.

As described previously, a shutter-like obstacle can force the inlet to be unstarted. So with the help of the obstacle the inlet could be 'pre-set' in the state of unstarted mode at the initial stage of the shock tunnel operation. After the obstacle is blown out, if an inlet is restarted thus the inlet of this configuration has a self-starting ability. If the inlet can not be restarted, it is an unself-starting configuration. While without the obstacle the inlet could be 'pre-set' in started mode. If an inlet can not be started with the help of shock tunnel initial operation, this configuration inlet is unstarting. We did find that the shock tunnel has strong capability of helping inlet to start, and it was found that even though the ICR is far beyond the Kantrowitz limit, the inlet still can be pulse started during nozzle set-up process if the vacuum tank is highly evacuated before the shot, although the shock waves will be expelled out of the inlet very soon because the inlet is unstart in the reality. On the other hand, if the ICR is low enough, the inlet will undergo self-starting process even if a strong shutter action is 'pre-set' at the beginning. It is also easy to perform the experiments related to 'dual-solution area' [7] with present method. For a certain range of ICR, the inlet with the same configuration, can maintain either started mode or unstarted mode based on the 'pre-set' mode. This means that an unself-starting inlet may be started without the 'pre-set' obstacle. Various behaviors of the sharp leading edge inlet starting process were tested with different ICR in JB430.

Therefore, it is now possible to compare the results obtained in shock tunnel with that of conventional wind tunnel. Present test results (ICR vs. M_i) are compared with the data from Van Wie [1], Sun and Zhang[8], Wang and Cheng[9], Wang

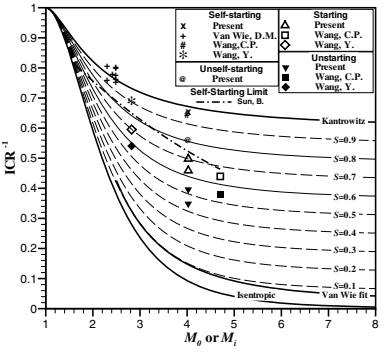

Fig. 3 The internal contraction ratio (ICR) vs. Mach number (subscript 0 for freestream, *i* for internal contraction section) diagram, wherein *S* is the start-ability index.

and Fan[10]. As shown in Fig. 3 fairly good agreement was obtained. In this figure the data are plotted in terms of the inverse of ICR. From Fig. 3 the ICR for self-starting limit could be estimated at about $S = 0.8$ and the un-starting limit at about $S = 0.6$.

3.3 Blunt Leading Edge Inlet Starting Characteristics

Furthermore, some preliminary experiments on the effect of inlet leading edge bluntness were tested, in which the concentration was also focused on the starting behaviors. It was found that the leading edge bluntness play quite important roles during the starting process as shown in Fig. 4. The inlet flow may deviate from started mode (Fig. 2) to un-started mode when the cowl leading edge is blunted (Fig. 4 a). On the other hand, with the same bluntness at the cowl leading edge, the inlet flow may also deviate from started mode (Fig. 4 b) to unstarted mode when the leading edge of the forebody is blunted(Fig. 4 c). When the cowl lip leading edge is blunted the stagnation point at the cowl is changed outward and forward, the amount of flow go through the throat may be increased. The choked inner flow result in unstart finally. When the forebody leading edge is blunted the shock shape is changed and the generated entropy layer developed along the forebody ramps surface may

Fig. 4 Leading edge bluntness effect on the inlet starting characteristics. Cowl lip and forebody leading edge radius are r_c, r_f, respectively. Throat height h_t. (a) h_t =10mm, (b) and (c)r_c=2mm, h_t=20mm. (a)Run 309 un-starting inlet with r_c=2mm blunted; (b)Run 355 self-starting inlet; (c)Run 366 unself-starting inlet with r_f=3mm blunted.

interact with the boundary layer. The complex flow may not be swallowed by the throat of the inlet, also result in un-starting. More detailed study will be presented in the future.

4 Conclusions

The starting characteristics of hypersonic inlets with different ICR and leading edge bluntness were tested in shock tunnel. A high speed schlieren system was used to detect the various behaviors of the inlet starting process. The 'choking' effect of a shutter-like obstacle can be used to 'switch off' the help-to-start effects in shock tunnel initial operation and to 'pre-set' the inlet in un-started mode. The inlet self-starting process was investigated with the help of such a shutter-like obstacle. Inlet starting characteristics were also tested without such an obstacle. Based on the inlets tested in present study, the ICR for inlet self-starting limit and un-starting limit could be estimated at about $S = 0.8$, $S = 0.6$, respectively. The effect of leading edge bluntness on the inlet starting behaviors were also tested. It was found that the inlet self-starting ability level is poorer when the leading edge is blunted.

References

1. Van Wie, D.M., Kwok, F.T., et al.: Starting characteristics of supersonic inlets. AIAA Paper 1996-2914 (1996)
2. Starukhin, V.P., Chevagin, A.P.: Leading-Edge Bluntness effect on Performance of Hypersonic Two-Dimensional Air Intakes. In: Curran, E.T., Murthy, S.N.B. (eds.) Scramjet Propulsion, pp. 353–367. AIAA (2001)
3. Smith, C.E.: Journal of Fluid Mechanics 24, 4 (1966)
4. Van Wie, D.M.: Scramjet Inlets. In: Curran, E.T., Murthy, S.N.B. (eds.) Scramjet Propulsion, pp. 447–511. AIAA (2001)
5. Huang, B., Li, Z.-F., et al.: An Experimental Observation Of 3-D Scramjet Inlet Flow In Shock Tunnel. In: 10th International Conference on Fluid Control, Measurements, and Visualization (FLUCOME), Moscow (2009)
6. Mölder, S., Timofeev, E.V., et al.: Flow starting in high compression hypersonic air inlets by mass spillage. AIAA Paper 2004-4130 (2004)
7. Veillard, X., Tahir, R., et al.: Journal of Propulsion and Power 24, 5 (2008)
8. Sun, B., Zhang, K.Y.: Journal of Propulsion and Power 26, 4 (2010)
9. Wang, C.-P., Cheng, K.-M.: Journal of Aerospace Power 23, 6 (2008) (in Chinese)
10. Wang, Y., Fan, X., et al.: Acta Aeronautica Et Astronautica Sinica 31, 2 (2010) (in Chinese)

2D Phenomena of Shock Wave Propagation along a Non-equilibrium Thermal Zone Formed by Surface Discharge

E.Yu. Koroteeva, I.E. Ivanov, D.M. Orlov, and I.A. Znamenskaya

1 Introduction

Shock waves have traditionally been studied and characterized by their movement through media. And alternatively, the parameters of a medium have been successfully diagnosed by its influence on a shock-waves motion. The propagation of shock waves through media with various types of inhomogeneity has always been of particular interest for a wide range of application in different fields of physics, like astrophysics, laser physics, aerodynamics and many others. There are lots of experimental, theoretical and numerical studies concerning interactions of shock waves with turbulence [1], vortices [2], near-wall fine particle or dust layers [3], preshock inhomogeneities induced by non-uniform energy deposition [4], isolated bubbles [5], thermal layers [6, 7], plasma formations [8, 9], etc. These interactions are apparently mutual - not only are the dynamics and the structure of waves altered but also the properties of the medium are changed in a post shock flow. The present work studies the structure of the gas-dynamic flow resulting from the propagation of a plain shock wave along a near-wall expanding layer of the gas excited by a high-current sliding surface discharge ("plasma sheet").

The plasma sheet, which is initiated on the bottom wall of a shock tube channel, represents a special type of a pulse surface discharge. It is composed of a continuous system of parallel streamers sliding over the dielectric surface and has a rectangular configuration of $100mm \times 30mm$. The discharge electric current pulse duration does not exceed 200 *ns*, providing localized and rapid energy deposition into a thin (about 0.5 *mm*) near-wall layer of gas, without heating the wall itself. This pulsed energy is sufficient to alter a supersonic flowfield and it may be used to obtain controlled changes in flow structures.

The ignition of a surface plasma discharge in quiescent air (Fig. 1a) involves complicated phenomena: plasma kinetics, gasdynamics, transport phenomena. In the experiments a plane shock wave enters the discharge gap at various (but more

E.Yu. Koroteeva · I.E. Ivanov · D.M. Orlov · I.A. Znamenskaya
Lomonosov Moscow State University (Russia)

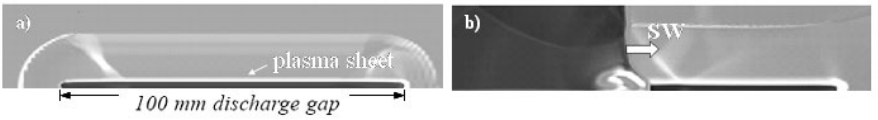

Fig. 1 Schematic profile of a discharge chamber 10-20 μs (a) and the shock wave movement in it approximately 100 μs (b) after the discharge initiation.

than 40–50 μs) delay times after the plasma sheet initiation. By this time multiple shocks produced by rapid energy release into a confined volume ([10]) decay, and a non-equilibrium thermal layer of excited gas is formed in the vicinity of the surface. Shadow images of shock waves propagating in the discharge chamber reveal (Fig. 1 b):

- the shock front distortion and the formation of a thermal precursor shock wave;
- the expansion of vortical structures behind the shock.

Shadow images may serve as a diagnostic tool for a plasma-induced thermal layer analysis. Numerical simulations in the models of uniform and non-uniform energy deposition from the plasma sheet were also performed. They help to explain experimental results and to solve the inverse problem of discharge energy allocation.

2 Experimental Setup and Procedure

The experimental part of the present research was conducted in a shock tube facility schematically shown in Fig 2. Its principal part consists of a discharge chamber

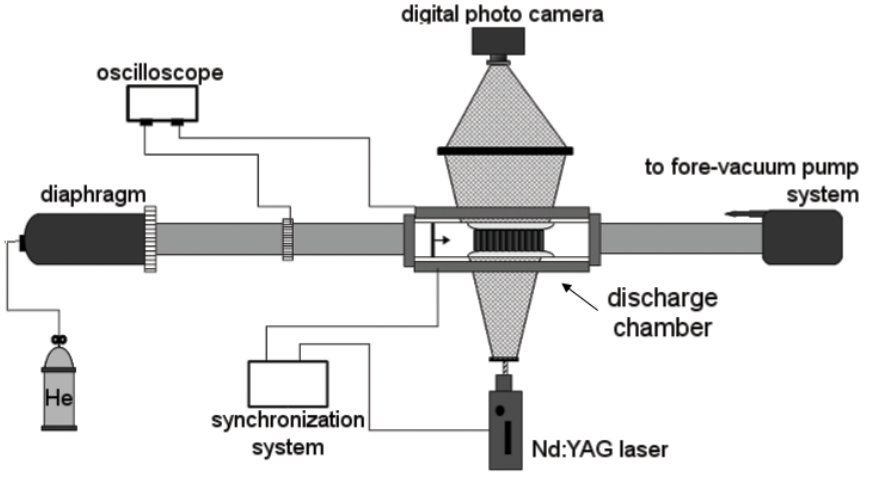

Fig. 2 Experimental setup.

mounted within a low-pressure section of a single-diaphragm shock tube. The tube and the chamber both have a rectangular cross-section of 48 *mm* (width) x 24 *mm* (height). The driven gas in the low-pressure section is air, and the driver gas is helium. Two sidewalls of the discharge test chamber are partially replaced with 17 *cm* panes of quartz glass to provide optical access.

On the bottom wall of the discharge chamber there are two parallel electrodes of 100 *mm* length, immersed flush on the surface and separated by 30 *mm*. When a high voltage pulse with a peak of 25–30 *kV* is applied to this system, a pulsed sliding surface discharge (plasma sheet) is formed transversely to the flow in the shock tube. Instantaneous energy deposition into the near-wall air is provided. The discharge images show that when the initial air pressure is less than 20–40 Torr the discharge glow mostly exhibits a homogeneous structure while for pressure values greater than 60–70 Torr spatially non-uniform plasma glow is observed more often (see Fig. 4a, 5a).

A synchronization system allows an incident shock to enter the 100 *mm* discharge gap at any specified delay time (t_{delay}) after the plasma sheet initiation (40–300 μs). Nd:YAG laser with 532 *nm* wavelength is a source of single-pulse coherent light with a pulse duration of 5 *ns* for the shadowgraph technique.

3 Numerical Simulation

Because the flow in the shock tube by virtue of the experimental geometry is close to two-dimensional, the CFD simulations of the problem can be performed in 2D. As long as complex plasma relaxation processes do not have any significant impact on the essential behavior of the flow at relatively large delay times after the plasma sheet switch-off, the equations of gasdynamics were used. The calculations were based on a high-order Godunov-type scheme solving the system of 2D Raynolds-averaged Navier-Stokes equations for a compressible flow. The turbulence model was k-epsilon. The system was closed by the ideal gas equation of state (air with $\gamma = 1.4$) together with the Sutherland viscosity law.

A rectangular domain of $16.8cm \times 2.4cm$ with a stretched grid with up to 1400 x 400 cells represented a part of the discharge chamber (Fig. 1). The initial conditions differed depending on the energy deposition model. The first model assumed that energy with uniform density $\triangle$E was added to a thin area near the plasma sheet location, which led to the gas pressure increase by $\triangle p=(\gamma\text{-}1)\ \triangle E$. At t=0, discontinuity breakdown at the boundary occurred and by t_{delay} the thermal layer was formed near the discharge gap in the computational domain. In the second approach the propagation of a plain shock wave along a layer with already assigned non-uniform spatial temperature distribution ($T(x,y) = T_0 + \triangle T(x,y)$) was considered. The choice of $\triangle T(x,y)$ and the geometry of the non-uniform thermal zone were based on the analysis of the corresponding discharge glow and the shadow image for each experimental shot.

4 Results and Discussion

The formation of a precursor with an intensive vortex flow and its unbounded development were observed in the experiments for all considered values of initial pressure (P_0=20–80 Torr), wave Mach numbers (M=1.5–3.0) and delay times till approximately 150–200 μs. The appearance of a toe wave moving faster than the main shock (Fig. 3a) is apparently explained by the "thermal layer" (TL) effect - an interaction of a shock wave with a thin layer of reduced density ([6, 7]).

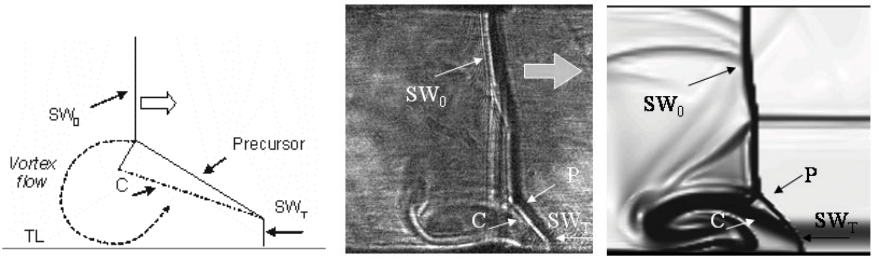

Fig. 3 (Left) Sketch of SW-TL interaction: TL - thermal layer, C - contact surface, SW_T - toe wave, SW_0 - main shock; (Middle) shadow image and (Right) CFD visualization of density gradient calculated in the model of uniform energy deposition for P_0=25 Torr, M=2.5 and t_{delay}=60 μs.

The characteristic features of a flow with a precursor shock were reproduced in CFD simulations with the model of instantaneous uniform energy deposition from the surface discharge, which showed a good agreement with corresponding shadow images (Fig. 3b-c).

However, as mentioned above, the discharge energy allocation at pressure values (P_0=60–100 Torr) is less homogeneous. As a consequence, the flow with a shock wave in the discharge chamber is more complicated than that on Fig. 3a, and can not be properly simulated in the model of uniform energy deposition.

Fig. 4b shows the flow in the discharge chamber approximately 150 μs after the plasma-sheet initiation (t_{delay}=50 μs). The shadowgram demonstrates the "classical" thermal layer effect but with an essentially perturbed vortex flow behind the shock front. Association of the shadow image with the corresponding initial plasma glow shows that the shock wave has just passed an area of bright set of streamers. A similar flow pattern was obtained in the numerical simulation (Fig. 4c), in which a plane shock had interacted with non-homogeneous gas zone: sinusoidal-shaped spatial temperature distribution was tested with an average temperature of $3T_0$.

The isolated bright streamers in the uniform plasma glow apparently provide more intensive heating to the neighboring gas. Some time after the discharge initiation (in the order of 10^2 μs) these "hot points" evolve into mushroom-shape structures visible in the thermal layer in front of the shock wave (marked by black dash-lines on Fig. 4, Fig. 5).

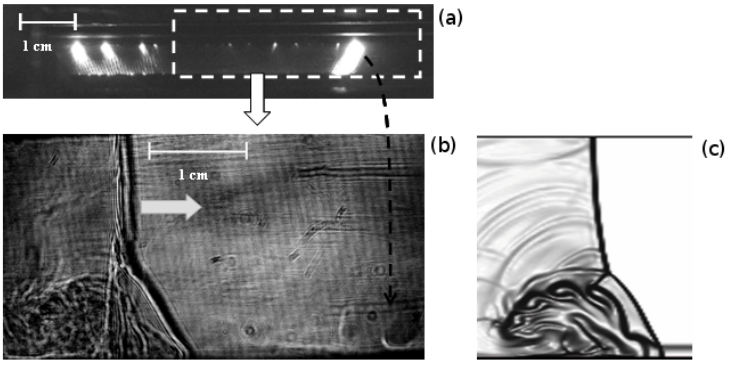

Fig. 4 Plasma glow (a), shadow image (b) and CFD visualization of density gradient (c) for P_0=75 Torr, M=2.5 and t_{delay}=50 μs. The white dash-line indicates the space recorded on the shadow image.

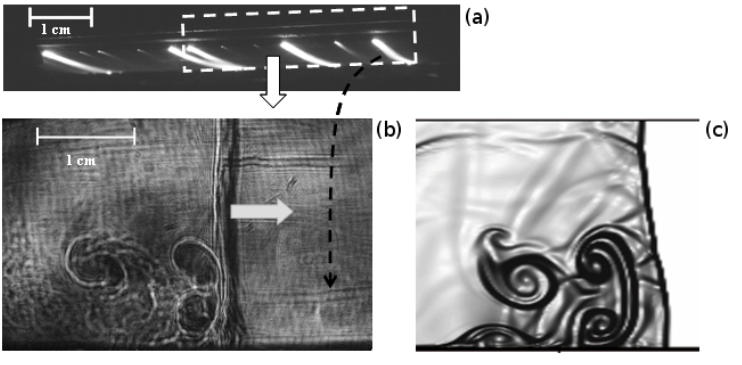

Fig. 5 Plasma glow (a), shadow image (b) and visualization of density gradient in calculated flow (c) for P_0=75 Torr, M=2.5 and t_{delay}=200 μs. The white dash-line indicates the space recorded on the shadow image.

Fig. 5 shows the flow in the discharge chamber approximately 300 μs after plasma sheet initiation for the initial experimental conditions of P_0=75 Torr, M=2.5 and t_{delay}=200 μs. By this time the thermal layer had cooled to room temperature: there is virtually no precursor shock wave on the shadow images. However, localized zones of hotter air are still present and this inhomogeneity is enhanced by the impingement of an incident shock. Fig. (5c) shows the numerical simulation of a plain shock wave interaction with warm air 2D "bubbles" placed slightly above the bottom wall.

5 Conclusion

The nanosecond discharge produced thin heated near-wall zone without heating the wall itself. The shock wave interaction with a thin relaxing plasma zone was studied. It was shown that the initiation of a sliding pulse surface discharge 40–300 μs before a plane shock wave enters the discharge zone affects both the structure of the wave front and the flow behind it. Due to the presence of a plasma-induced thermal layer in the vicinity of the surface a precursor-shock phenomenon was observed; non-uniformities in the plasma energy deposition gave rise to the turbulization and the formation of vortices in the post-shock flow. The distribution of discharge energy depending on experimental conditions was reconstructed by comparison between the shadow images and CFD simulation results.

Acknowledgements. This work was supported by the RFBR grant 08-08-00903-a.

References

1. Andreopoulos, Y., Agui, J.H., Briassulis, G.: Shock wave-turbulence interactions. Annu. Rev. Fluid Mech. 32, 309–345 (2000)
2. Henneke, M.R., Ellzey, J.L.: The effect of a shock on vortex interactions. In: Proceedings of the 19th International Symposium on Shock Waves, Marseilles, France (1993)
3. Gerrard, J.H.: An experimental investigation of the initial stages of the dispersion of dust by shock waves. Brit. J. Appl. Phys. 14, 186–192 (1963)
4. Baymirov, B.M., Grudnitski, V.G.: Numerical investigation of interactions between shock waves and thermal inhomogeneities after "multipoint" energy emission. Shock Waves 4, 193–198 (1995)
5. Bagabir, A., Drikakis, D.: Mach number effects on shock-bubble interaction. Shock Waves 11, 209–218 (2001)
6. Nemchinov, I.V., Artem'ev, V.I., Bergelson, V.I., Khazins, V.M., Orlova, T.I., Rybakov, V.A.: Rearrangement of the bow shock shape using a "hot spike". Shock Waves 4, 35–40 (1994)
7. Gion, E.J.: Plane shock interacting with thermal layer. The Physics of Fluids 20(4), 700–702 (1977)
8. Sasoh, A., Ohtani, T., Mori, K.: Pressure effect in a shock-wave–plasma interaction induced by a focused laser pulse. Phys. Rev. Lett. 97, 205004 (2006)
9. Moreau, E.: Airflow control by non-thermal plasma actuators. Journal of Physics D: Applied Physics 40, 605–636 (2007)
10. Latfullin, D.F., Mursenkova, I.V., Znamenskaya, I.A., Bazhenova, T.V., Lutsky, A.E.: Shock Waves Dynamics Investigations for Surface Discharge Energy Analysis. In: Proceedings of 26th International Symposium on Shock Waves, Gottingen, Germany (2007)

Three-Dimensional Simulation of Bow-Shock Instability Using Discontinuous Galerkin Method

Y. Sato, Y. Suzuki, K. Yasue, and N. Ohnishi

1 Introduction

Many experiments and numerical simulations for a bow shock that forms over a blunt body have been conducted. In general, the bow shock formed in a uniform flow is stable, and a steady bow shock can be easily obtained. However, instability of the bow shock was observed in front of nearly flat bodies in a difluorodichloromethane atmosphere, using a ballistic range 30 years ago [1]. Baryshnikov et al. classified the features of this bow-shock instability into three types: small deformation (Fig. 1(a)), large deformation (Figs. 1(b) and (c)), and complete disruption of shock wave (Fig. 1(d)). From experiments under various conditions, it was concluded that bow-shock instability occurs depending on not only the Mach number and atmospheric pressure, but also the roundness of the edge and the curvature of the body surface. They suggested two candidates for the main mechanism of this phenomenon. One is dynamical nonequilibrium behind the shock wave due to a low specific heat ratio γ of the difluorodichloromethane; the other is chemical nonequilibrium with a quick increase in temperature at the shock front. Since direct experimental analysis of these mechanisms is difficult, numerical analysis using a sophisticated computational fluid dynamics (CFD) technique is expected to identify the mechanism that has not yet been revealed.

For a relatively strong shock parallel to computational grids, however, most conventional shock-capturing schemes are numerically unstable; this instability is called the carbuncle phenomenon or carbuncle instability [2]. Unfortunately, since the carbuncle phenomenon depends on various factors such as flow condition (Mach number, Reynolds number, and specific heat ratio), computational grids (grid size

Y. Sato · Y. Suzuki · N. Ohnishi
Department of Aerospace Engineering, Tohoku University
6-6-01 Aramaki-Aza-Aoba, Aoba-ku, Sendai 980-8579, Japan

K. Yasue
Aerospace Research and Development Directorate, Japan Aerospace Exploration Agency
7-44-1 Jindaiji-Higashi, Chofu, Tokyo 182-8522, Japan

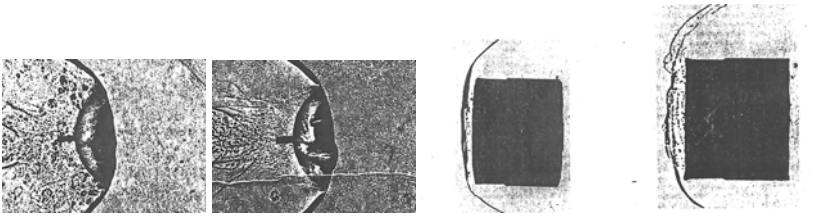

(a) Freon12, $\gamma \sim 1.14$, $M = 4.3$, $p = 0.38$ atm

(b) Freon12, $\gamma \sim 1.14$, $M = 3.9$, $p = 0.38$ atm

(c) Freon14, $\gamma \sim 1.16$, $M = 8.4$, $p = 0.2$ atm

(d) Freon14, $\gamma \sim 1.16$, $M = 9.9$, $p = 0.2$ atm

Fig. 1 Experimental observation of bow-shock instability [1].

and aspect ratio), and computational scheme (numerical flux and high-order reconstruction), it is difficult to prepare an appropriate numerical condition assuring a robust computation. Two matters are known about the computational grid, while an unstable phenomenon is likely to originate from discretization models [3]. (1) Unstable phenomena tend to occur when the shock is aligned with any coordinate axis or with planes formed by two coordinate axes. (2) The scale of unstable phenomena depends on the scale of the computational grid, not on the scale of the physical phenomenon.

In the present study, we developed a three-dimensional CFD code with unstructured grids for resolving non-axisymmetric perturbation growth in a shock layer ahead of a supersonic blunt body, based on the discontinuous Galerkin (DG) method, which can be extended to high-order numerical accuracy. We examined numerical stability with three different flux functions to find the appropriate one for simulating bow-shock instability because the carbuncle phenomenon tends to occur due to large gradient of pressure and density across the shock wave in a low-γ ($\sim$1) flow. It is difficult to distinguish an unstable phenomenon appearing in a numerical simulation as physical instability or numerical instability. Therefore, using the most favorable flux function, we measured perturbation growth in shock-surface deformation with spectral decomposition in an ideal gas without any chemistry.

2 Computational Methods and Conditions

As previously mentioned, it is necessary to suppress the carbuncle phenomenon even with a low-γ flow. Dependency of this phenomenon on the computational grid is usually crucial, but the flexibility representing the blunt body surface may enable us to avoid some difficulties associated with numerical implementation. The unstructured grid is suitable for our simulation, but it is generally difficult to achieve high accuracy with finite-difference or finite-volume representation. Thus, the DG method [4], which is a kind of finite-element method and can achieve high accuracy even with an unstructured grid, is employed in our code.

Physical quantities inside each cell are described by basis functions in the DG method. Namely, solutions of each cell are approximated by a linear combination of the products of the basis functions and their degrees of freedom. Numerical accuracy is determined by how many basis functions we use and does not depend on the number of stencils. In the present study, four basis functions are used so that the solution is obtained in second-order accuracy in the smooth region. This accuracy may not be sufficient but is necessary to represent acoustic waves in the shock wave, which play an important role in the development of the instability.

The DG method employs the Riemann flux function at the cell interface at which solutions can have two distinct values defined by the neighboring cells. Since the carbuncle phenomenon also depends on this flux, we examined three flux functions: AUSM-DV [6], HLLC [7], and SLAU [8]. These functions are relatively robust against numerical instability. For the time integration, the two-stage TVD Runge-Kutta method [9] is used for accurately capturing the unsteady nature of the instability. However, we do not consider any chemistry behind the bow shock, in order to focus on the effect of mechanical nonequilibrium in the bow-shock instability.

Bow-shock formations over a hemi-ellipsoid whose aspect ratio of major axis to minor axis is 1–10 have been computed by our code. A flatter body has a higher aspect ratio, as indicated in Fig. 2(a), which represents computational grids over the hemi-ellipsoid with an aspect ratio of 5. We employed prism unstructured cells. The total number of cells is 99,600, and there are 1,992 surface triangular interfaces.

The mainstream Mach number is 3.9, and the angle of attack is 0, following the conditions of the experiments by Baryshnikov et al. [1]. We set the specific heat ratio γ to be 1.01 in the present study, while the actual γ for difluorodichloromethane exceeds 1.1, so that the shock instability can be found easily. The computations were performed in an explicit manner with a CFL number of 0.5.

3 Results and Discussions

3.1 Numerical Flux Dependence

The numerical flux function severely characterizes the flow property induced by numerical instabilities. As depicted in Figs. 2(b) and (c), inherent perturbations are stimulated in the shock layer, and the shock surfaces are deformed for computations with AUSM-DV and HLLC. Since the wavelength of the perturbation for AUSM-DV and HLLC is as short as the grid size, these two fluxes are responsible for the carbuncle phenomenon. However, with SLAU, the flowfield is maintained in steady state without any perturbation growth in the shock layer. The SLAU flux function seems to be robust for bow-shock formation under this condition.

Although the flowfield obtained with SLAU is steady and stable, the stagnation point was observed to stretch along the direction of the grid lines. This feature highly depends on the grid conditions. Finding an appropriate grid condition may be another important issue for the computation of bow-shock instability.

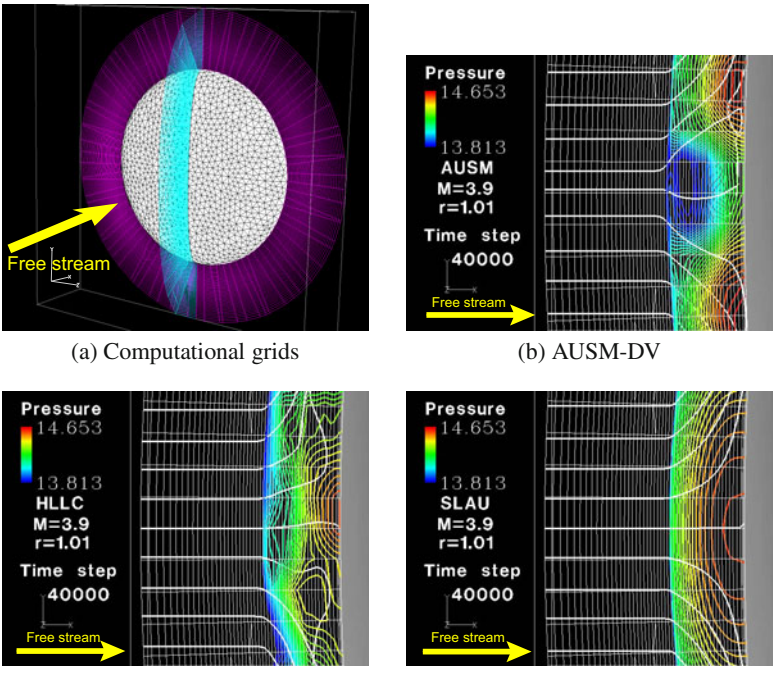

(a) Computational grids (b) AUSM-DV

(c) HLLC (d) SLAU

Fig. 2 (a) Example of computational grids over a hemi-ellipsoid and pressure contours and streamlines at 40,000 step with (b) AUSM-DV, (c) HLLC, and (d) SLAU for an ellipsoid aspect ratio of 5.

3.2 Computational Grid Dependence

Hereafter, we discuss the computational results using SLAU only because it is expected that less numerical instability occurs with SLAU than with the other schemes. No bow-shock instability was observed in the computations using SLAU with an ellipsoid aspect ratio of 1–5. Experimental results suggest that the instability tends to occur with flatter bodies [1]. We therefore examined the computations for a flatter body with an ellipsoid aspect ratio of 10. We used three different computational grids. Each grid is defined as follows.

(A) Computational grid whose number of surface interfaces is 3,984, total number of cells is 199,200, and resolution near the body is relatively high.
(B) Computational grid whose number of surface interfaces is 12,810, total number of cells is 677,690, and resolution near the body is relatively high.
(C) Computational grid whose number of surface interfaces is 3,984, total number of cells is 199,200, and stream-ward resolution is uniform.

Figure 3 depicts the shock location (iso-density line) from the body surface calculated by linear interpolation on the equatorial plane as a function of the surface

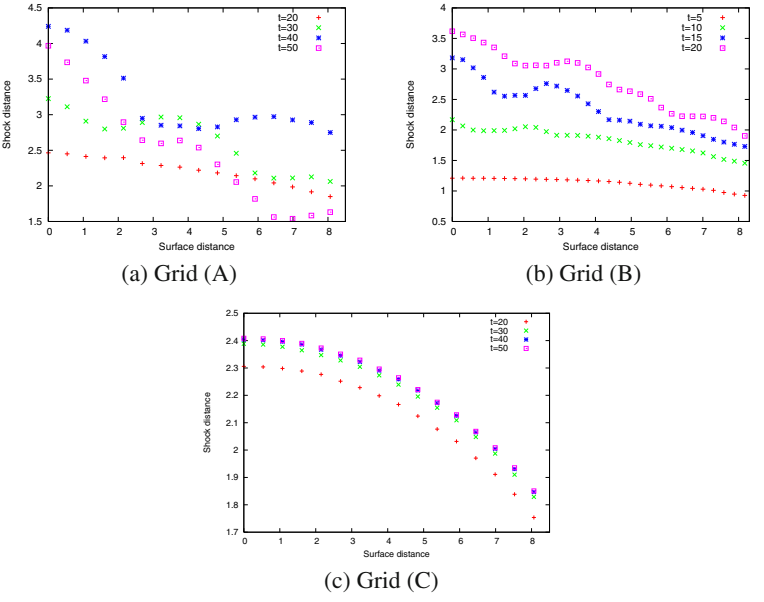

(a) Grid (A) (b) Grid (B)

(c) Grid (C)

Fig. 3 Shock location from the body surface for ellipsoid aspect ratio of 10 with SLAU.

distance from the stagnation point. The shock surface is detected by searching for the point where the density reaches 6 from the upstream side along the streamlines. Figs. 3(a) and (b) indicate that with grids (A) and (B), shock surfaces deform and unstable. However, with grid (C), steady shock surface is obtained. Therefore, the stream-ward grid resolution should be sufficient for the entire shock layer not only near the body surface.

3.3 Spectral Analysis of Shock Surface Deformation

In hydrodynamic instability, the growth of a particular wave component may characterize development of the instability. If the most growing component depends on the computational grids, numerical instability is predominant in the computed flowfield. In contrast, physical instability must be identified with the wave component growing independently of the computational grids since it depends on the fundamental flow characteristics.

Shock locations obtained in the previous section were Fourier-transformed to find features of wave components. Figure 4 depicts time evolution of normalized amplitude of wave components with each computational grid. As shown in Figs. 4(a) and (b), arising wavelengths and their growth rates are different depending on the number of the surface interfaces. Moreover, specific wave components that identify instability are not observed. This fact indicates that the instability is induced by the numerical origin. And the timing when the unstable phenomenon appears is earlier

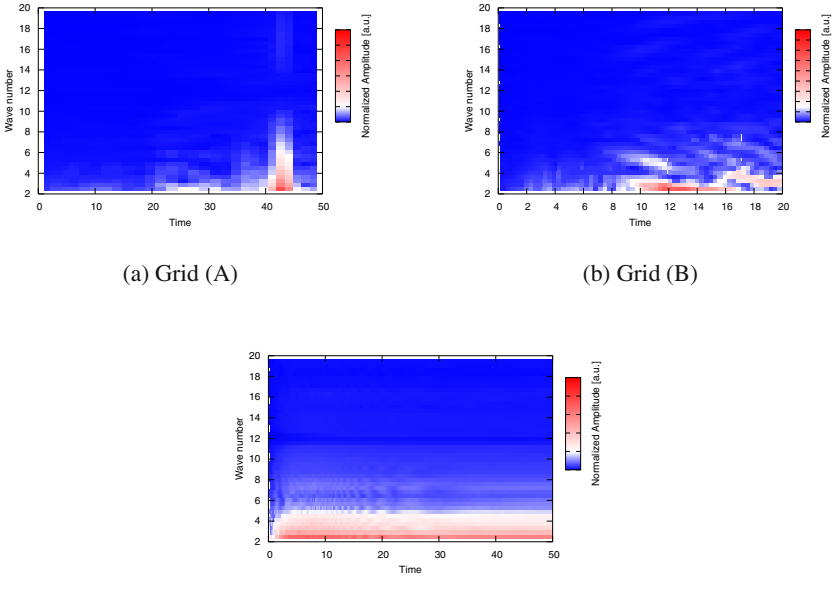

(a) Grid (A)

(b) Grid (B)

(c) Grid (C)

Fig. 4 Fourier-decomposed perturbation growth for the shock-surface deformation.

with grid (B) than with grid (A). Since the stream-ward resolutions of grid (A) and (B) are identical, numerical disturbance, which is generated at near the shock surface or behind it and is parallel to the shock surface, must be resolved better with grid (B). However, the bow shock obtained with grid (C) is steady rather than grid (B) as shown in Fig. 4(c). In grid (C), the stream-ward resolution is relatively high over the shock layer, so that moving shock surface is resolved precisely. On the other hand, although the shock surface is highly resolved near the body in the cases of grid (A) and (B), it will be smeared after leaving the body. The coarser grid around the shock surface may result in the numerical instability.

4 Conclusion

Three-dimensional numerical simulations were performed to examine the mechanism of bow-shock instability using the DG finite-element method. The bow shock wave ahead of a nearly flat body may be unstable at Mach 3.9 and low-γ flow according to the experimental observation while the carbuncle phenomenon also easily occurs under this condition. Comparing the numerical stability among three flux functions (AUSM-DV, HLLC, and SLAU), SLAU seems most suitable for simulating bow-shock instability. Computational grid dependence of the instability was

examined with SLAU. The result indicates that for analysis of bow-shock instability, stream-ward resolution is more important than the resolution near the body. In order to find the condition with which the physical instability can be observed, elaborate surveys (body shape dependence and/or effect of chemical reactions) should be pursued based on the consequences obtained in the present paper.

References

1. Baryshnikov, A.S., Bedin, A.P., Maslennikov, V.G., Mishin, G.I.: Stability of a bow shock. Soviet Technical Physics Letters 5, 113–114 (1979)
2. Quirk, J.: A contribution to the great Riemann solver debate. International Journal for Numerical Methods in Fluids 18, 555–574 (1994)
3. Aiso, H., Abouziarov, M., Takahashi, T.: Carbuncle instability, which does not come from the original continuous model, pp. 148–153, JAXA-SP-03-002 (2003) (in Japanese)
4. Cockburn, B., Shu, C.-W.: The Runge-Kutta discontinuous Galerkin method for conservation laws V: Multidimensional systems. Journal of Computational Physics 141, 199–224 (1998)
5. Sherwin, J.: Hierarchical hp finite elements in hybrid domains. Finite Elements in Analysis and Design 27, 109–119 (1997)
6. Wada, Y., Liou, M.S.: A Flux Splitting Scheme with High-Resolution and Robustness for Discontinuities. AIAA Paper 94-0083 (1994)
7. Toro, E.F., Spruce, M., Speares, W.: Restoration of the contact surface in the HLL-Riemann solver. Shock Waves 4, 25–34 (1994)
8. Shima, E., Kitamura, K.: On New Simple Low-Dissipation Scheme of AUSM-Family for All Speeds. AIAA paper 2009-136 (2009)
9. Gottlieb, S., Shu, C.-W.: Total Variation Diminishing Runge-Kutta Schemes. Mathematics of Computation 67, 73–85 (1998)

Micro-blast Waves Using Detonation Transmission Tubing

S.I. Obed, G. Jagadeesh, and K. Kontis

1 Introduction

Experiments with blast waves at a reduced scale can be of much use to acquire a qualitative understanding of the highly complex, large scale flow phenomenon, provided appropriate scaling laws can be developed. This being the motivation, micro-blast waves have been generated in the laboratory using several means in the recent past. Jiang [1] had used laser to deposit energy within a small region (point source of energy), Kleine [2] and Settles [3] reported generation of micro-blast waves by ignition/detonation of gram sized explosive charges. Interestingly, the work of Kleine [2], using milligram sized silver azide charges, had shown the validity of the popular cubic root scaling laws, hitherto used with the large scale blast waves, for the milligram charges too. This paves the way for the use of micro blast waves as an experimental tool for a qualitative study of the large scale blast waves, within the laboratory, which is impossible with the large scale blast waves.

However, with the above methods of producing micro-blast waves, there exist several drawbacks, such as the lack of sphericity of the blast waves, difficulty in ensuring repeatability and most importantly, handling/safety issues. In view of these, the use of the Detonation Transmission tubing (DTT) as a means for producing micro blast waves inside the laboratory in a safe and repeatable manner was proposed by C. Oommen et al [4].

To this end, the blast waves which are formed on the rapid exit of high pressure combustion gases from the Detonation Transmission Tubing have been studied from an experimental standpoint, ably supported by simple 1D Numerical Modeling of the detonation process inside the DTT. Thus the primary aim of this investigation is to come up with suitable scaling laws for the blast waves produced by the DTT and

S.I. Obed · G. Jagadeesh
Department of Aerospace Engineering, Indian Institute of Science, Bangalore, 560 012, India

K. Kontis
The School of MACE, University of Manchester, Manchester, M60 1QD, UK

also to estimate the energy levels in these kind of micro blast waves as a function of time.

1.1 Detonation Transmission Tubing (DTT)

NONEL shock tube (M/s Orica Mining Services, formerly M/s DynoNobel, Sweden), also called Detonation Transmission Tubing (DTT) is a three layered polymer tube (ID 1.3mm OD 3mm) coated on the inner side with a thin layer of explosive mixture(HMX 16mg/m and Al 2mg/m). The detonation process inside the tube is initiated by using an electrical spark, obtained by suitable means, to ignite the explosive mixture at one end of the tube. The resulting detonation wave traverses down the tube reaching a constant Velocity of Detonation (VOD) of about 2000m/s. The products of combustion so formed, that are in a state of high pressure and temperature, if allowed to expand into ambient air from the open end of the tube result in the formation of the blast wave.

1.2 Scaling Laws for Blast Waves

The scaling laws, based on the well established theory of dimensional analysis are used to report blast wave experimentation data such as the overpressure level at a particular distance from the blast, the arrival time at that point and the impulse at that location [5]. Hopkinson's rule and Sachs' scaling law are two such commonly used laws. Hopkinson's rule and Sachs' scaling law are two such commonly used laws. Sachs' scaling, which is an extension of the Hopkinson's scaling law, attempts to take into account the variations in the reported values due to differences in the ambient conditions at the experimentation site. The other more popular scaling rule, due to Hopkinson, has been chosen in this work for its simplicity. It relates the charge mass(or energy), W and the distance to the measurement station from the centre of the charge, R by means of a simple cube-root relationship as $WR^3 = Const$.

The implications of this are that, if a property of the blast wave at a particular point is known, it can be related to the distance at which the same property value would be produced by a standard explosive, say TNT. The experiments being well documented for TNT explosions, this would give us an exact measure of the destructive power of the blast at that point. Further, because the other properties for TNT at that corresponding distance are well known, the values for those properties at that location for the given blast can be very accurately stated. However, if the material or the detonation mechanism for the second explosive is different from that of TNT, this law ceases to be accurate (Kleine et al [2]).

2 Experiments and Data Obtained

The experiments performed with the DTT were reported by C.Oommen et al [4]. For the sake of completeness, a few results which are used in this investigation are

Fig. 1 Evolution of the Blast Wave : Schlieren clippings are 20 microseconds apart

summarized here. Blast waves from the DTT were allowed to expand freely into the open domain, and the resulting evolution of the blast wave was captured using a high speed digital camera(Shimadzu Hyper-Vision Camera), running at a frame rate of $0.5MHz$ (Figure 1). Side-on overpressure measurement was also done in a similar set-up. It was noticed that irrespective of the length of the DTT(ranging from $0.5m$ to $3m$), the measured overpressure levels were fairly constant, implying that a constant amount of energy was responsible for the formation of the blast wave. Further, with experiments inside a confined chamber, the minimum length of the DTT required for such a repeatable blast wave was found to be $225mm$.

2.1 Photogrammetric Measurements

The Schlieren clippings, recorded using the high speed camera were digitally analyzed to get the location of the blast wave at different instants of time. The radius of the blast wave was extracted using the edge detections tool available in MATLAB. These data were curve fitted by method of least squares in the exponential form ($R = R_0 t^n$; $R_0 = 102.35$ and $n = 0.807$).

Further, to ensure that the variations in the explosive coating thickness inside DTT do not interfere with the repeatability of the blast wave, the radii were measured for two other inclinations (45^0 and 90^0) of the DTT, and they were found to correlate quite well with the above values measured for horizontal position of DTT.

3 Energy Analysis

Accurate estimation of the amount of energy expended in the formation of the micro-blast wave from the open end of the tube is a very important parameter. In order to get reasonable estimates for this variation of energy rate at the tip of the tube(DTT), a simple numerical model was used.

Tsang [6] had developed a simple numerical model to analyse the DTT. The tube expansion effect and the heat loss by conduction from the tube wall were also considered. Quasi 1-D euler equations were solved for both combustion gases and the aluminium particles inside the tube. The kinetics of the reaction between HMX–Al

mixture and the air inside the tube were modeled by assuming a single stage, temperature independent kinetic equation as $HMX + 1.372Al + 0.704N_2 + 0.155O_2 \rightarrow 0.583Al_2O_3 + 4CO + 2.251H_2O + 1.749H_2 + 4.704N_2$. The flow variables and their other associated values were found to reach constant values in about 225*mm* from the start of the detonation. This in a way validates the code as it confirms the earlier experimental finding of energy remaining constant beyond 225*mm*.

Using this numerical tool, the rate at which energy leaves the tube as the gas expands into open air was found. From this, the net energy released into the open domain as a function of time was obtained as shown in Figure 2. The average energy is about 3.5*J* (considered for a time of about 200 microseconds). The particles contribute about 10% to the total energy. Their role in pushing the ambient air along with the combustion gases being unclear, the solid particles' effect has been ignored in further analysis. This brings the TNT equivalent to 0.83*mg*. Earlier, Oommen et al [4] had arrived at a TNT equivalent value of 1.6*mg*.

As a further step, the energy obtained from the above numerical code was given as input to the self-similar laws for both cylindrical and spherical blast wave theory, following the approximate near–field blast theory given by Hutchens [7]. This theory takes into account the effect of source mass, which was assumed to be a very small value in this case. The radii are plotted against time in Figure 3.

The radius of the blast wave from the DTT seems to follow the cylindrical blast wave theory for about 50 microseconds from the exit of the combustion gases(error being in the range of -20% and 0%). Later on, it deviates considerably(upto to a maximum of about 30%). This deviation may be due to the low overpressure levels (about 2 atmospheres at that time), at which it is no longer a strong blast, and thus the theory no longer holds.

Spherical blast wave theory seems to deviate completely. This may be due to the initial directionality in the jet from the DTT, and so, the cylindrical blast wave may be used to predict the radius of blast waves from DTT, at least for the initial stages.

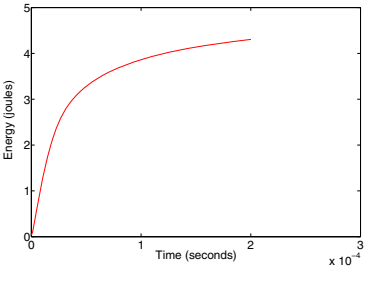

Fig. 2 Energy in open domain as a function of time

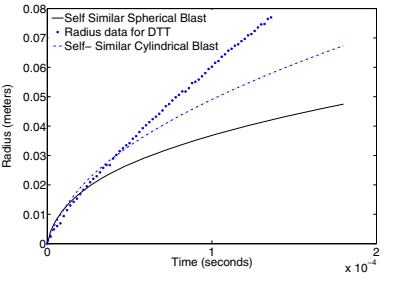

Fig. 3 Radius of the blast wave from DTT compared with the equivalent Self-Similar Cylindrical and Spherical Blast Wave theory

4 TNT Equivalence of DTT

TNT equivalence will be different at various locations if the explosive mechanism is not similar. Since use of DTT is an entirely different method of generating controlled micro blast waves, we choose to calculate the TNT equivalence as a function of overpressure, following the work of Kleine [2].

The radius of the blast wave and the time were scaled by using the energy, E obtained from the numerical model. The scaling was done to $1mg$ of TNT using the scaling factor S; where $S = \left(\frac{E}{4.184}\right)^{1/3}$, $R_s = \frac{R}{S}$ and $T_s = \frac{T}{S}$. Here 4.184 refers to the energy (in joules) contained in $1mg$ of TNT. The scaled radius and the scaled time are shown in Figure 4. They were fitted into an exponential curve of the form $R = R_{0s}t^{ns}$; $R_{0s} = 0.9609$ and $ns = 1.3764$. Further, the overpressure(in atmospheres) at different locations were estimated from the variation of blast wave radius with time using the gas dynamic relation between shock Mach number (M_S) and pressure (P_S). The data so obtained were fit into a curve of the form $ln(R_s) = E + F(lnP) + G(lnP)^2 + H(lnP)^3$; where $E = 4.0373$, $F = -0.7724$, $G = -0.2004$ and $H = 0.0177$. Proceeding along similar lines, the overpressures were plotted against scaled distance for TNT, using data from Kleine's work [2]. The values so obtained and the curve–fit are plotted against scaled distance are shown in Figure 5.

The equivalence ratio η_{DTT} is the ratio by which a unit mass of TNT is to be scaled to produce the same blastwave properties at that location. This can be put as

$$\eta_{DTT} = \left(\frac{R_s}{R_{TNT}}\right)^3 = \left(\frac{W_s}{W_{TNT}}\right) \tag{1}$$

where R_{TNT} is the corresponding scaled radius. As overpressure is the most important parameter in blast waves, we choose to describe η_{DTT} in terms of overpressure.

It was found to vary between 1.68 for an overpressure of 3 atmospheres to 11.92 for 0.5 atmospheres, in an exponential fashion. The average TNT equivalent was determined to be 1.8.

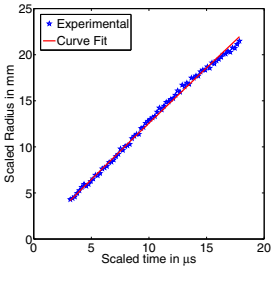

Fig. 4 Plot of Scaled Radius R_s against Scaled Time T_s

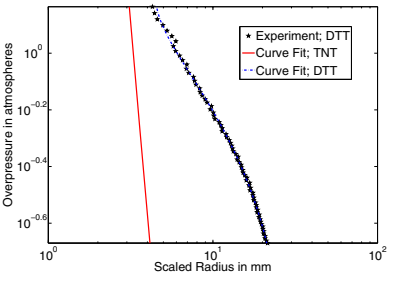

Fig. 5 Plot of Overpressure against Scaled Radius for DTT and TNT

5 Conclusion

Present investigation aimed to obtain the scaling laws and energy for the blast waves from DTT and to understand the reason behind the constancy of the energy beyond a particular legth of DTT . The average energy was found to be about $3.5J$. Based on this, the average TNT equivalent was found to be $1.8mg$. In terms of overpressures, it was found to vary between $1.68mg$ for about 3 atmospheres overpressure to $11.9mg$ for 0.5 atmospheres. Further, the micro blast waves from DTT appear to closely follow the self-similar cylindrical blast wave theory, thus enabling us to use this an alternate way of looking at micro blast waves.

References

1. Jiang, Z., Takayama, K., Moosad, K.P.B., Onodera, O., Sun, M.: Numerical and experimental study of a micro-blast wave generated by pulsed-laser beam focusing. Shock Waves 8, 337–349 (1998)
2. Kleine, H., Dewey, J.M., Ohashi, K., Mizukaki, T., Takayama, K.: Studies of the TNT equivalence of silver azide charges. Shock Waves 13, 123–138 (2003)
3. Hargather, M.J., Settles, G.S.: Optical measurement and scaling of blasts from gram-range explosive charges. Shock Waves 17, 215–223 (2007)
4. Oommen, C., Jagadeesh, G., Raghunandan, B.N.: Studies on micro explosive driven blast wave propagation in confined domains using NONEL tubes. In: Hannemann, K., Seiler, F. (eds.) Proceedings of the 26th International Symposium on Shock Waves, Gottingen, Germany, July 15-20 (2007)
5. Baker, W.E.: Explosions in Air. University of Texas Press, Austin (1973)
6. Tsang, D.K.L.: A numerical study of a detonation wave in detonation transmission tubing. Mathematical and Computer Modeling 44, 717 (2006)
7. Hutchens, G.J.: Approximate near-field blast theory: A generalized approach. J. Applied Physics 88(6), 3654–3658 (2000)

Supersonic Combustion Flow Visualization at Hypersonic Flow

T.V.C. Marcos, D. Romanelli Pinto, G.S. Moura, A.C. Oliveira, J.B. Chanes Jr., P.G.P. Toro, and M.A.S. Minucci

1 Introduction

Currently, a new generation of scientific aerospace vehicles, using advanced hypersonic airbreathing propulsion based on supersonic combustion technology, is in development at several research centers [1].

The 14-X Brazilian Hypersonic Aerospace Vehicle, Figure 1, designed by Rolim et al. [2], at the Prof. Henry T. Nagamatsu Laboratory of Aerothermodynamics and Hypersonics, Figure 2, at the Institute for Advanced Studies (IEAv), is part of the continuing effort of the Department of Aerospace Science and Technology (DCTA), to develop a technological demonstrator using: i) "waverider" technology to provide lift to the aerospace vehicle, and ii) "scramjet" technology to provide hypersonic airbreathing propulsion system based on supersonic combustion.

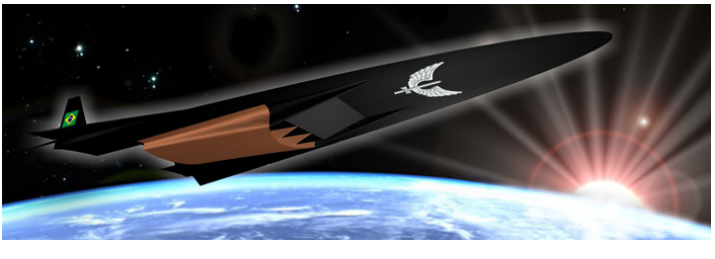

Fig. 1 14-X Hypersonic Aerospace Vehicle.

T.V.C. Marcos · D. Romanelli Pinto · G.S. Moura · A.C. Oliveira · J.B. Chanes Jr. · P.G.P. Toro · M.A.S. Minucci
Prof. Henry T. Nagamatsu Laboratory of Aerothermodynamics and Hypersonics
Institute for Advanced Studies
Rodovia dos Tamoios km 5,5 12228-001 São José dos Campos, SP(BR)

Fig. 2 T2 Hypersonic Shock Tunnel, visible at the left of the T3 Hypersonic Shock Tunnel.

Aerospace vehicle using ”waverider” technology obtains lift using the shock wave, formed during supersonic/hypersonic flight throught the Earths atmosphere, which originates at the edge and it is attached to the bottom surface of the vehicle, generating a region of high pressure, resulting in high lift and low drag [3]. Atmospheric air, pre-compressed by the shock wave, which lies between the shock wave and the leading edge of the vehicle may be used in hypersonic propulsion system based on ”scramjet” technology.

Hypersonic airbreathing propulsion, that uses supersonic combustion ramjet (scramjet) technology [4], offers substantial advantages to improve performance of aerospace vehicle that flies at hypersonic speeds through the Earth’s atmosphere, by reducing on-board fuel. Basically, scramjet is a fully integrated airbreathing aeronautical engine that uses the oblique/conical shock waves generated during the hypersonic flight, to promote compression and deceleration of freestream atmospheric air at the inlet of the scramjet. Fuel, at least sonic speed, may be injected into the supersonic airflow just downstream of the inlet. Right after, both oxygen from the atmosphere and on-board fuel are mixing. The combination of the high energies of the fuel and of the oncoming supersonic airflow the combustion at supersonic speed starts. Finally, the divergent exhaust nozzle at the afterbody vehicle accelerates the exhaust gases, creating thrust.

2 IEAv T2 Hypersonic Shock Tunnel

The development of such airbreathing propulsion system requires experiments, those may be done in Hypersonic Shock Tunnel (pulsed hypersonic wind tunnel) [4], which reproduces the flight conditions encountered in a scramjet engine in flight.

The IEAv T2 Hypersonic Shock Tunnel [5], Figure 2, used for the present investigation, is capable of generating high to low enthalpy hypersonic flow conditions.

In the high and medium enthalpy runs, helium is used as the driver gas and the tunnel operates in the equilibrium interface condition to produce a useful test time of roughly 500 s to 1.5 ms, reservoir conditions of 5,000 K to 1685 K and 120 bar to 173 bar, respectively. In the low enthalpy case, air is used as the driver gas to produce a useful test time of about 1.5 ms and reservoir conditions of 950 K and 25 bar. The test section airflow Mach number is 6.2 and 7.3 in the high and medium enthalpy tests, respectively, and 7.8 in the low enthalpy ones.

In the present investigation dry air was used as a test gas. Conical nozzle, 15 degree half angle and adequate throat to obtain airflow Mach number 7 in the test section. The different Mach numbers achieved in the test section are the result of the different reservoir conditions and real gas effects present in the tests. The test conditions did not vary more than 5% from run to run.

3 Supersonic Combustion Model

The conceptual design of the supersonic combustion model, Figure 3, was based on the configuration of existing compression ramp at the inlet of scramjet of the 14-X Hypersonic Aerospace Vehicle, Figure 1. The 15 degree compression ramp was made of stainless steel. A piezoelectric Pressure Transducer, as a pitot pressure, was installed right above of the ramp. Therefore, the detached normal shock established ahead of the pitot pressure will have no influence in the oblique shock wave established at the edge of the supersonic combustion model.

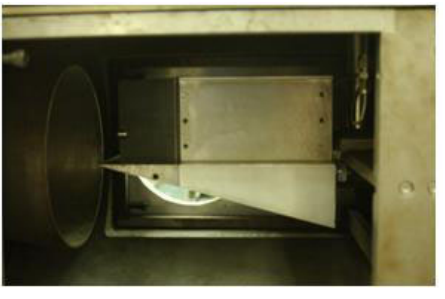

Fig. 3 Supersonic combustion model installed at the T2 Hypersonic Shock Tunnel test section.

4 Supersonic Combustion Flow Visualization Results

The supersonic combustion model (2D wedge) allows flow visualization of the combustion phenomenon through the non intrusive schlieren technique. The fuel tank volume was adequate to produce equivalence factor of 1.6.

The conventional schlieren arrangement was adopted and conceived to illuminate most of the test-section optical windows. The test section has two 8-in. diameter

quartz windows with a 190-mm. effective vision area. Because of the positions of the optical tables in the laboratory, an auxiliary optical mounting was necessary to redirect the collimated lamp beam to/from the test section and to make it possible to fix the source light at the parabolic-mirror focus. The schlieren visualization system is composed of a xenon flash lamp, two parabolic mirrors (8-in. diameter and 64-in. focal length), a knife edge (razor blade), an ultrahigh speed camera (Cordin 550) used to record the events, and an objective lens. The camera has 32 CCDs and can capture at a maximum rate of 2,000,000 frames per second. In the present work, the camera was set to operate at 100,000 frames per second.

For tightness and to qualify the device used to inject on-board Hydrogen gas fuel into Mach number 7 airflow, Helium gas was inject in the quiescent gas at 80 mbar (test section in vacuum), Figure 4, and no hypersonic airflow.

The sequence of schlieren photographs of the Mach number 7 airflow over supersonic combustion model, Figure 5, shows the oblique shock wave attached to the leading edge of the model as expected. Observe that there is no gas injection in the Mach number 7 airflow. Also, oblique shock angle of 22 degree agrees with the theoretical calculation by oblique shock theory for freestream Mach number 7 airflow.

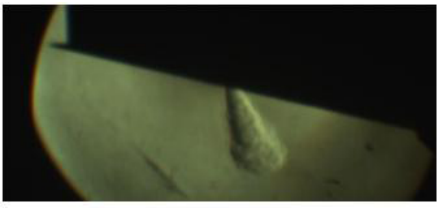

Fig. 4 Helium gas injection in vacuum and no hypersonic airflow.

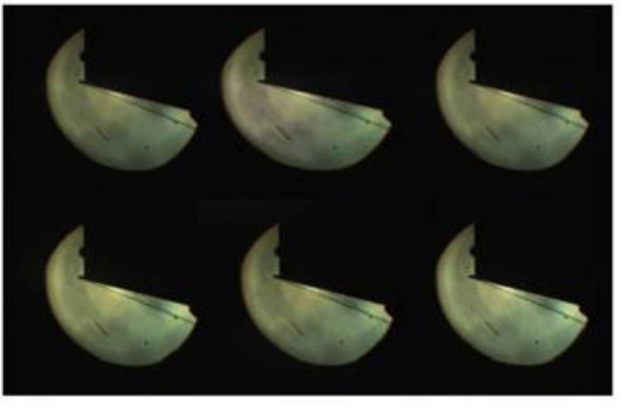

Fig. 5 Sequence of schlieren photographs of the Mach number 7 airflow over supersonic combustion model and no on-board Hydrogen gas injection.

Fig. 6 Schlieren photography of on-board Hydrogen gas injected into Mach number 7 airflow over supersonic combustion model.

The schlieren photography of the on-board Hydrogen gas injection into Mach number 7 airflow shows a small increase in the slope of the shock wave after the region of Hydrogen gas injection, Figure 6, which may be the result of heat release, resulting in a decrease of Mach number in the region.

However, since the schlieren photographs obtained during the test with on-board Hydrogen gas injection were quite similar to the schlieren photographs of the Mach number 7 airflow over supersonic combustion model without gas injection, an obstacle was added in the supersonic combustion model to create a high temperature stagnant region to increase the probability to start the combustion.

Again, the sequence of schlieren photographs of the Mach number 7 airflow over supersonic combustion model, Figure 7, shows not only the 22 degree oblique shock angle attached to the leading edge of the model, but also the interaction of the compressed supersonic airflow, by the oblique shock wave, and the obstacle (located downstream of the Hydrogen gas injection).

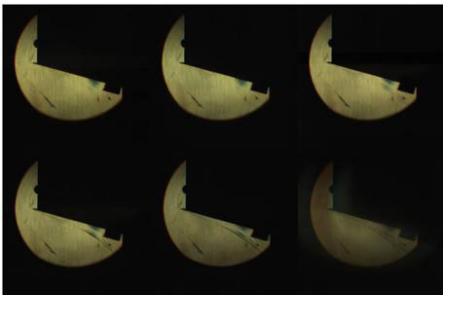

Fig. 7 Sequence of schlieren photographs of the Mach number 7 airflow over supersonic combustion model, with no gas injection.

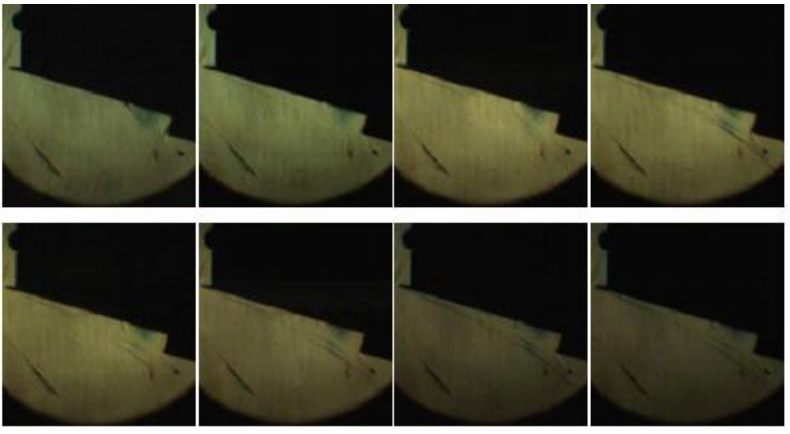

Fig. 8 Sequence of schlieren photographs of the Mach number 7 airflow over supersonic combustion model and the injection of the on-board Hydrogen gas.

As expected, after place the barrier (obstacle) in front of the supersonic airflow, resulting in a stagnation point and in a significant rise in temperature. The exact moment when the on-board Hydrogen gas injected into airflow the schlieren photographs, Figure 8, show the rapid expansion of mixed gas. Also, this sequence of schlieren photographs shows the time when the shock wave is formed and it is destroyed by the combustion, of the mixed Hydrogen gas and the Oxygen from the supersonic airflow.

5 Conclusion

Supersonic combustion using a 2D model (wedge), based on the compression ramp of the 14-X Brazilian Hypersonic Aerospace Vehicle, has been experimentally investigated at the T2 Hypersonic Shock Tunnel, at the Prof. Henry T. Nagamatsu Laboratory Aerothermodynamics and Hypersonics, at the Institute for Advanced Studies. Schlieren photographs, of the combustion of the mixed Oxygen from the supersonic airflow and the on-board Hydrogen gas, show the destruction of the oblique shock wave right at the time when the on-board Hydrogen gas injected meets Oxygen from the supersonic airflow.

References

1. Curran, E.T.: Scramjet Engines: The First Forty Years. Journal of Propulsion and Power 17(6) (November-December 2001)
2. Rolim, T.C., Minucci, M.A.S., Toro, P.G.P., Soviero, P.A.O.: Experimental Results of a Mach 10 Conical-Flow Derived Waverider. In: 16th AIAA/DLR/DGLR International Space Planes and Hypersonic Systems and Technologies Conference, AIAA 2009-7433 (2009)

3. Wang, Y., Zhang, D., Deng, X.: Design of Waverider Configuration with High Lift-Drag Ratio. Journal of Aircraft 44(1), 144–148 (2007)
4. Heiser, W.H., Pratt, D.T., Daley, D.H., Mehta, U.B.: Hypersonic Airbreathing Propulsion. AIAA Education Series, 594 p. AIAA (1994)
5. Nagamatsu, H.T.: Shock Tube Technology and Design. In: Ferri, A. (ed.) Fundamental Data Obtained from Shock Tube Experiments, ch. III. Pergamon Press (1961)
6. Nascimento, M.A.C.: Gaseous Piston Effect in Shock Tube/Tunnel When Operating in the Equilibrium Interface Condition. Doctoral Thesis. Instituto Tecnológico de Aeronáutica - ITA, São José dos Campos, SP, Brazil (October 1997) (in English)

Supersonic Combustion Experimental Investigation at T2 Hypersonic Shock Tunnel

D. Romanelli Pinto, T.V.C. Marcos, R.L.M. Alcaide, A.C. Oliveira, J.B. Chanes Jr., P.G.P. Toro, and M.A.S. Minucci

1 Introduction

The aerospace technological products have grown that one cannot conceive of putting payloads (satellites) into Earth orbit or beyond using technologies in operation (rockets carry out solid or liquid fuel). The knowledge required to keep the current launching vehicles is already so high that if the countries do not have a technological support for their own industry, they will depend on of the supplier countries and not have independent capacity sustained. Aerospace vehicle limitations for launching payloads into orbit or beyond require a continuous reduction in size, weight and power consumption of launch vehicles. Some solutions to these challenges require paradigm shifts, new production methods, and new technologies of strategic nature. The requirements of platformslaunched satellites, high performance and reliability, as well as the strict limitations of fuel (reduction of size, weight and power consumption) for launching payloads into orbit or beyond provide the development of hypersonic aircraft using hypersonic airbreathing propulsion based on supersonic combustion.

The recent intensification of international efforts to develop hypersonic propulsion system based on supersonic combustion, signals that this is the way of effective access to space in a not too distant future. Therefore, the field of Hypersonic Airbreathing Propulsion basd on Supersonic Combustion, will be essential in the near future for the aerospace industry, and allow the man to build hypersonic planes, to reach other continents in hours and achieve low orbits around Earth.

Experimental investigation of the supersonic combustion is being carried out using the T2 Hypersonic Shock Tunnel at the Prof. Henry T. Nagamatsu Laboratory of

D. Romanelli Pinto · T.V.C. Marcos · R.L.M. Alcaide · A.C. Oliveira · J.B. Chanes Jr. · P.G.P. Toro · M.A.S. Minucci
Prof. Henry T. Nagamatsu Laboratory of Aerothermodynamics and Hypersonics
Institute for Advanced Studies
Rodovia dos Tamoios km 5,5 12228-001 São José dos Campos, SP(BR)

Fig. 1 Prof. Henry T. Nagamatsu Laboratory of Aerothermodynamics and Hypersonics. T2 Hypersonic Shock Tunnel, visible at the left of the T3 Hypersonic Shock Tunnel.

Aerothermodynamics and Hypersonics, Figure 1, which is capable of providing total temperature flows and speed (Mach number) enough to duplicate the environment of high enthalpy and thermochemical characteristics close to those encountered during flight vehicles at high speeds in the Earth atmosphere.

The scramjet is the only airbreathing propulsion system to be able to provide the thrust needed efficiently in hypersonic flight [1]. In addition, it has the advantage over rocket engines not lead to oxidizing substance, reducing vehicle weight. To get an idea of structural weight savings this fact, one should bear in mind that the first stage of the Saturn-1, a rocket widely used by NASA, must carry 285ton of liquid oxygen to burn 125ton of RP-1 (a type of highly refined kerosene for rocket). Aerospace vehicles using scramjet have no moving parts, and the scramjet works as follows: slows the flow into the air intake through oblique shock waves until the inlet air reaches the velocity and pressure necessary to ensure that there is combustion. Thus, the gases produced in combustor with its high enthalpy and pressure are expanded in the nozzle. This cycle is then responsible for the thrust generated by the engine. Normally, the fuel chosen for the scramjet is Hydrogen, due to the fast time of ignition and high specific impulse.

2 IEAv T2 Hypersonic Shock Tunnel

Ground based test facilities, such as shock tube and hypersonic shock tunnels are the only laboratory devices able to provide total temperature and Mach number sufficient to duplicate the environment of high enthalpy and thermochemical

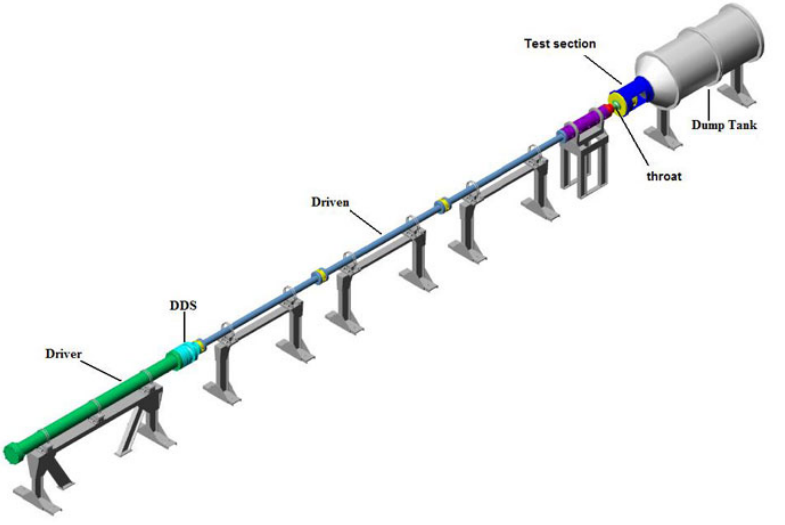

Fig. 2 T2 Hypersonic Shock Tunnel.

characteristics close to those encountered during flight vehicles at high speeds in the Earth atmosphere [2].

The T2 Hypersonic shock tunnel [3], Figures 1 and 2, consists of a shock tube (two reservoirs kept at different pressures, separated by a set of two diaphragms, DDS), where a convergent-divergent nozzle is coupled at the end of the low-pressure shock tube. The compressed and heated gas (dry air to simulate flight in the Earths atmosphere) behind the incident shock wave (in the shock tube) is expanded to high speeds and high temperatures (in the divergent nozzle section) to produce hypersonic flow in the test section.

The T2 Hypersonic Shock Tunnel used for the present experimental investigation is capable of generating high to low enthalpy hypersonic flow conditions. In the high and medium enthalpy runs, helium is used as the driver gas and the tunnel operates in the equilibrium interface condition to produce a useful test time of roughly 500 s to 1.5 ms, reservoir conditions of 5,000 K to 1685 K and 120 bar to 173 bar, respectively. In the low enthalpy case, air is used as the driver gas to produce a useful test time of about 1.5 ms and reservoir conditions of 950 K and 25 bar. The test section airflow Mach number is 6.2 and 7.3 in the high and medium enthalpy tests, respectively, and 7.8 in the low enthalpy ones.

In the present investigation dry air was used as a test gas. Conical nozzle, 15 degree half angle, with adequate throat diameter is used to obtain airflow Mach 7 number in the test section. The different Mach numbers achieved in the

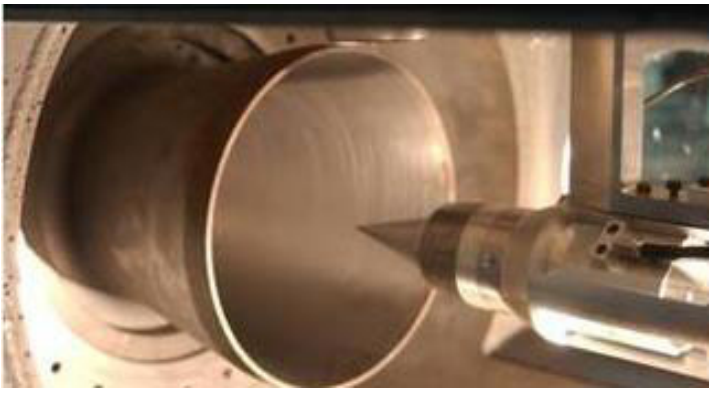

Fig. 3 Supersonic combustion model installed at the T2 Hypersonic Shock Tunnel test section.

test section are the result of the different reservoir conditions and real gas effects present in the tests. The test conditions did not vary more than 5% from run to run.

3 Supersonic Combustion Model

Basically, supersonic combustion ramjet (scramjet), Figure 3, is an aeronautical engine that has no moving parts and uses shock waves generated during hypersonic flight, to promote compression and deceleration of atmospheric air. This atmospheric air at supersonic speed, is mixed and burned with a on-board fuel suitable for the production of thrust. Therefore, the combustion process occurs in supersonic regime. When the combustion process occurs in subsonic regime, it is called subsonic combustion or ramjet, the predecessor of the scramjet, which already finds many applications. The total pressure loss that occurs through normal shock wave (which slows the flow in ramjets) makes use of these engines impractical at hypersonic speeds.

An important feature of the scramjet is a highly integrated system, where engine and vehicle are indistinguishable. This tight integration is caused by the fact that the front section of the vehicle contributes to the compression of atmospheric air, while the rear contributes to the generation of thrust. The net thrust produced by the scramjet is the difference between the thrust (force that propels the vehicle) generated by the expansion of exhaust gases from the rear of the engine and the total drag (force that resists the movement of the vehicle). These forces may produce thrust to the flight of the vehicle or not depending on the balance of these forces in engine design in question.

Thus, aerospace vehicles propelled by scramjets carry only the fuel, usually Hydrogen, using atmospheric air as an oxidant itself by acquiring most of the kinetic energy required to reach Earth orbit during atmospheric flight.

As a result of self-propulsive nature of the reactors, they are unable to produce thrust while standing still. The static thrust is zero. Accordingly, they must be accelerated to a speed such that the shock waves produced by the air intake are able to compress the atmospheric air. This velocity is approximately four times the speed of sound, Mach 4, considering scramjet.

The conceptual design of the supersonic combustion model, Figure 3, consists by a conical region following by cylindrical section, where, internally, there is the fuel tank. The cylindrical part is tightly integrated with the front and rear in order to reduce drag and weight at hypersonic speeds. At the rear has a cone shape, where the products of combustion are exhausted.

The schlieren system was assembled for the evaluation of flow established on the model, as well as for checking the on-board Hydrogen gas fuel injection, during the tests.

4 Supersonic Combustion Results

Experimental investigation of supersonic combustion at the T2 Hypersonic Shock Tunnel were performed in medium enthalpy (3000 psi on the driver and 3 atm at driven, respectively), operating in equilibrium interface mode.

Schlieren visualization system using high speed camera, Cordin 550-32C, was used to observe the injection of fuel (on-board Hydrogen gas) during the test time of

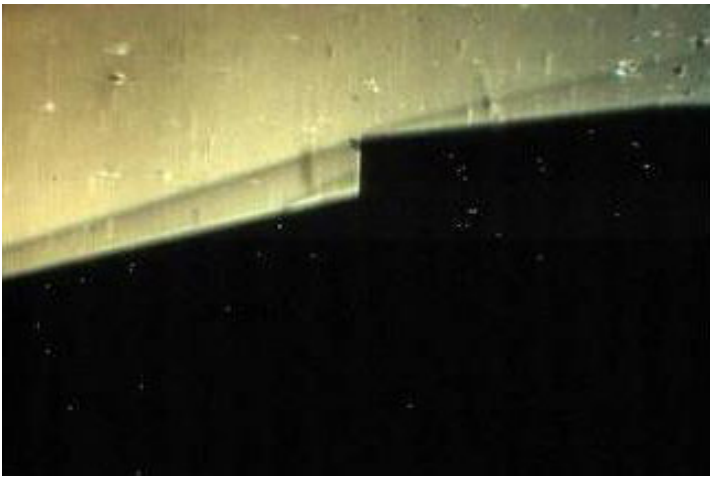

Fig. 4 On-board Hydrogen gas injection in supersonic airflow.

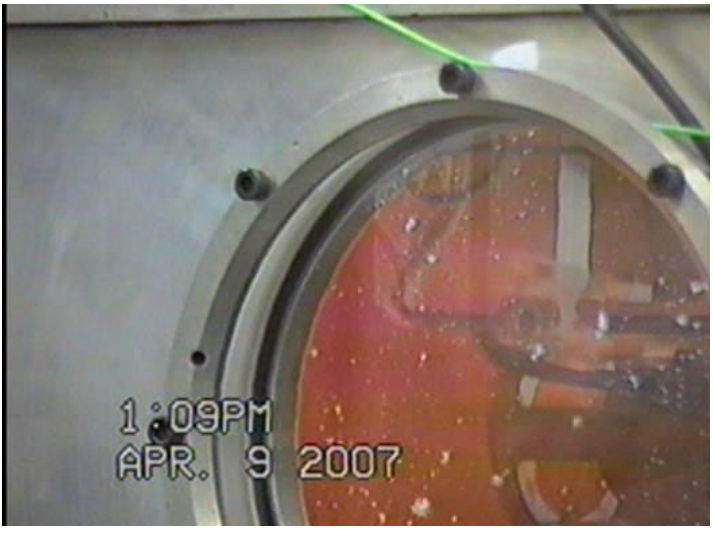

Fig. 5 Time-lapse photography of the combustion produts.

the T2 Hpersonic Shock Tunnel, Figure 4. One may observe that the conical attached shock wave at the leading edge of the scramjet model reach the cowl of the inlet. The on-board Hydrogen gas fuel is injected into the atmospheric supersonic airflow. Due to the geometry of the scramjet (axissymetrical) is not possible to visualize the combustion.

A time-lapse photography obtained through the integrated camera Nikkon D-1, Figure 5, shows the exhaustion of combustion products during the test of supersonic combustion.

No intrusive absorption technique by Diode Laser will be applied in the supersonic combustion experimental investigation. This technique allows to measure the water vapor concentration and temperature of the combustion products.

5 Conclusion

Supersonic combustion using an axissymetrical model (conical section following by cylindrical section, where, internally, there is the fuel tank and, at the rear section is a cone shape), has been experimentally investigated at the T2 Hypersonic Shock Tunnel, at the Prof. Henry T. Nagamatsu Laboratory Aerothermodynamics and Hypersonic, at the Institute for Advanced Studies. Schlieren photography, of the injection of on-board Hydrogen gas, and time-lapse photography, of the combustion produts in the exhaust section are presented.

References

1. Curran, E.T.: Scramjet Engines: The First Forty Years. Journal of Propulsion and Power 17(6) (November-December 2001)
2. Nagamatsu, H.T.: Shock Tube Technology and Design. In: Ferri, A. (ed.) Fundamental Data Obtained from Shock Tube Experiments, ch. III. Pergamon Press (1961)
3. Nascimento, M.A.C.: Gaseous Piston Effect in Shock Tube/Tunnel When Operating in the Equilibrium Interface Condition. Doctoral Thesis. Instituto Tecnológico de Aeronáutica - ITA, São José dos Campos, SP, Brazil (October 1997) (in English)

OH Emission Diagnostics Applied to Study Ignition of the Supersonic Combustion

R.G.S. Vilela, C.S.T. Marques, L.G. Barreta, A.M. Santos,
P.G.P. Toro, and M.A.S. Minucci

1 Introduction

Experimental investigations conducted in ground-based test facilities are essential for the successful development of hypersonic airbreathing propulsion based on supersonic combustion [1].

Fuel injection, mixing and ignition of the oxygen from the atmosphere and onboard fuel, flame holding and spreading are technical challenges to develop scramjet engines for hypersonic vehicles [2].

Ignition delay is an important issue to concern in the scramjet design, since it is a result of fuel injection, mixing and ignition source [3]. Also, it permits an evaluation of engine efficiency. Furthermore, in low hypersonic range (M less or eqaul to 8) it could be difficult to achieve sufficiently fast and stable ignition [4].

OH* chemiluminescence in the (0,0) band of the $A^2\Sigma \rightarrow X^2\Pi$ electronic transition at 306.4 nm has been much used to establish both qualitative and quantitative time histories of the excited states in combustion processes [4-9]. At ignition, there are a collection of species actives, although OH* radicals are in minor concentration, the fast formation and short lifetime make them an excellent marker for the ignition event [7, 9]. Images of the OH* chemiluminescence have also been obtained to investigate ignition, and combustion propagation and efficiency [10, 11].

The hydrogen ignition experiments were carried out using the 0.3-m. nozzle exit diameter Hypersonic Shock Tunnel at the Professor Henry T. Nagamatsu Laboratory of Aerothermodynamics and Hypersonics, Figure 1.

R.G.S. Vilela · C.S.T. Marques · L.G. Barreta · A.M. Santos · P.G.P. Toro · M.A.S. Minucci
Prof. Henry T. Nagamatsu Laboratory of Aerothermodynamics and Hypersonics
Institute for Advanced Studies
Rodovia dos Tamoios km 5,5 12228-001 São José dos Campos, SP(BR)

Fig. 1 Prof. Henry T. Nagamatsu Laboratory of Aerothermodynamics and Hypersonics. T2 Hypersonic Shock Tunnel, visible at the left of the T3 Hypersonic Shock Tunnel.

2 Experimental Setup

The T2 Hypersonic Shock Tunnel, Figure 2, which is capable to produce high to low enthalpy hypersonic flow conditions is used in this present work and medium enthalpy flight conditions was achieved using 20.7 MPa of Helium gas and 100-101.3 kPa of dry air in the high and low pressure reservoirs. A 0.30-m nozzle exit diameter coupled a 19.58-mm throat diameter makes possible to obtain Mach number 7 in the test section of the Hypersonic Shock Tunnel.

Two windows installed symmetrically on the sides of the test section is used as flow visualization windows and to install several different diagnostics techniques as the present OH Emission Diagnostics, Figure 2.

A wedge ramp scramjet engine model, Figure 3, was used in the present experimental investigations.

The OH* emission, Figure 4, was collected by using an UV plane-convex lens (f = 300 mm, f/5.9) and was analyzed and detected by applying a 0.5-m spectrometer set to 306.4 nm with a measured spectral resolution of 0.155 nm. The narrowband emission detection was applied to remove the light emission from interferences as aluminum from diaphragm, O-atoms ($\left({}^4P_{5/2} - {}^4D^0_{7/2}, {}^4P_{3/2} - {}^4D^0_{5/2}\right)$) and slightly 0_2 molecules from air ($B^3\Sigma_u^- - x^3\Sigma_g^-$). An oscilloscope (Yokogawa, DL 750) was used to register the time-resolved OH* emission signals.

Fig. 2 T2 Hypersonic Shock Tunnel.

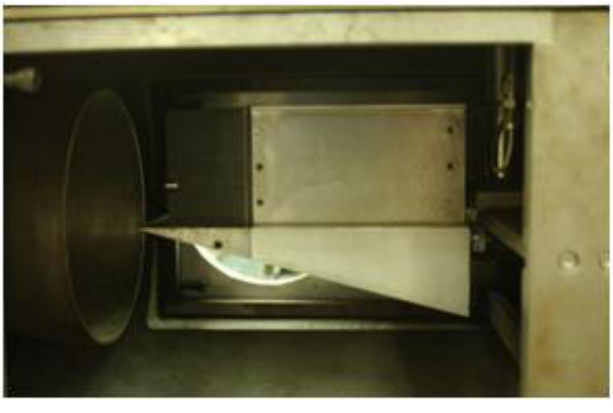

Fig. 3 Ramp Scramjet model used for supersonic combustion experiments.

3 Results

The emission system was carefully aligned by using a He-Ne laser at bottom of obstacle edge. The obstacle was placed on model to promote ignition through rapid temperature increase.

Also, emission images were acquired by applying a home-made interference filter coupled to a color filter (UG11) for IR emission blockage and suitable detection of OH* radicals next to the characteristic times for ignition.

Fig. 4 Photography of experimental setup for time-resolved OH* emission measurements.

Combustion in the scramjet engine model, used in this work, was demonstrated earlier through other optical techniques by our research group [12, 13], although there was no observable pressure increase at the time of ignition due to the pressure transducer position or diluted mixture conditions. As the other optical techniques, time-resolved emission is able to notice ignition in more dilute experiments [9].

Figure 5 displays an example of medium enthalpy run of the T2 Hypersonic Shock Tunnel, using the scramjet engine model and with on-board Hydrogen gas injection into the supersonic airflow.

The useful test time begins at 500 μs after trigger given by pressure transducer P5 (0 μs) to measure the stagnation pressure at the low pressure reservoir. Without hydrogen injection there was no emission within the test time. Only our reference background emission (narrow peak with higher intensity) was detected. Hence, OH* emission from 500 μs to 2750 μs is recognizable, Figure 3. From time-resolved OH* emission measurements, the characteristic times for hydrogen ignition in the scramjet engine model were established, Figure 6, for the ignition delay and peak times for the scramjet model used under Mach number 7.

The characteristic times for ignition were determined from shock wave arrival measured by Pitot probe located immediately in front of the model, Figure 3.

For operational scramjet engines in low hypersonic range (Mach number less than 8), the time scale of ignition delays should be $10^{-}4$ s [2, 14]. Ignition delay times for detonations are within 10-100 μ s, above these values high speed deflagrations occurs. For engine operation with supersonic combustion it should be in acceptable times of 300 μ s [2]. From ignition delay times experimentally determined, the scramjet engine under experimental condition investigated can properly operate. In addition, high speed deflagrations were observed, which explain undetectable pressure change at the time of ignition.

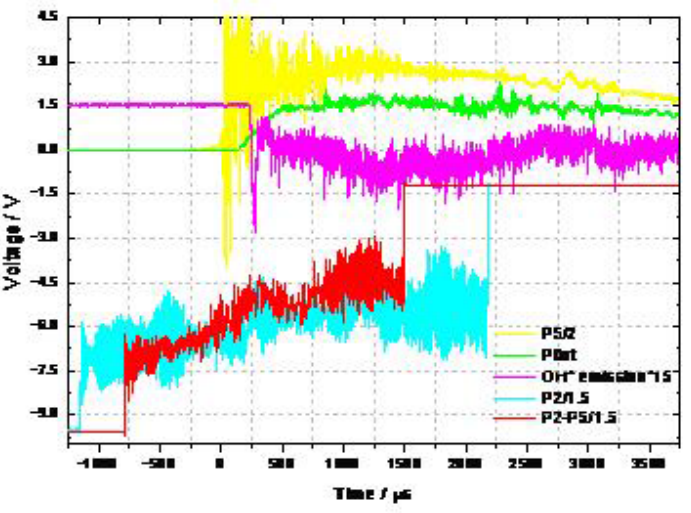

Fig. 5 Oscilloscope registers of pressure transducers and OH* emission intensities. Measured time profiles: yellow line - stagnation pressure, green line - Pitot pressure and magenta - OH* emission. Cyan and red lines - pressure transducers for the shock wave time measurement.

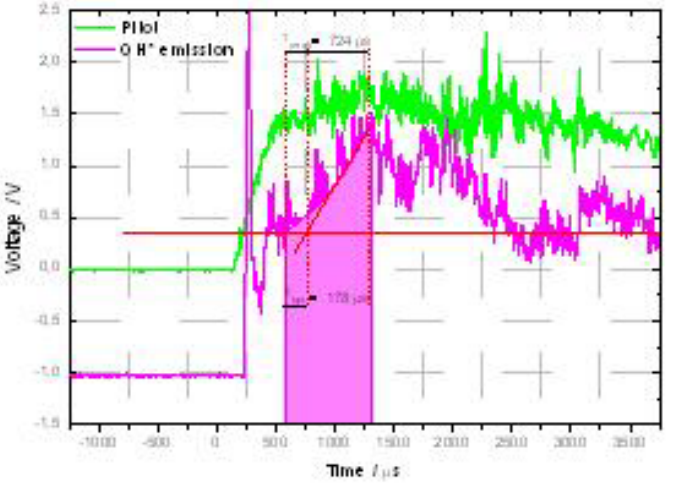

Fig. 6 Determination of characteristic times for ignition in a scramjet engine model. Experimental time profiles of Pitot pressure and OH* emission.

4 Conclusion

Supersonic combustion using a 2D model (wedge) has been experimentally investigated at the T2 Hypersonic Shock Tunnel, at the Prof. Henry T. Nagamatsu Laboratory Aerothermodynamics and Hypersonic, at the Institute for Advanced Studies. Time-resolved OH* chemiluminescence in the (0,0) band of the $A^2\Sigma \rightarrow X^2\Pi$ electronic transition, collected by an UV plano-convex lens, detected and analyzed by applying a 0.5-m spectrometer set to 306.4 nm with a measured spectral resolution of 0.155 nm was used to measure the Hydrogen ignition of the supersonic combustion investigation.

References

1. McIntyre, T.J., Houwing, F.P., Palma, P.C., Rabbath, P.A.B., Fox, J.A.: Optical and Pressure Measurements in Shock Tunnel Testing of a Model Scramjet Combustor. J. Prop. Power 13, 388–394 (1997)
2. Macheret, S.O., Shneider, M.N., Miles, R.B.: Energy-Efficiency of Plasma-Assisted Combustion in Ram/Scramjet Engines. In: 36th AIAA Plasmadynamics and Lasers Conference, Toronto, Ontario, AIAA Paper 2005-5371, June 6-9 (2005)
3. Hall, J.M., Rickard, M.J.A., Petersen, E.L.: Comparison of Characteristic Time Diagnostics for Ignition and Oxidation of Fuel/Oxidizer Mixtures Behind Reflected Shock Waves. Combust. Sci. and Tech. 177, 455–483 (2005)
4. Riva, G., Daminelli, G., Reggiori, A.: Hydrogen Autoignition and Combustion in Supersonic Flow at Low Equivalence Ratio. J. Prop. Power 13, 532–537 (1997)
5. Bertran, C.A., Marques, C.S.T., Benvenutti, L.H.: Mapping of Luminescent Species in a Front Flame. Combust. Science and Tech. 139, 1–13 (1998)
6. Hall, J.M., Petersen, E.L.: An Optimized Kinetics Model for OH Chemiluminescence at High Temperatures and Atmospheric Pressure. Int. J. Chem. Kinet. 38, 714–724 (2006)
7. Marques, C.S.T., Benvenutti, L.H., Bertran, C.A.: Kinetic Modeling for Chemiluminescent Radicals in Acetylene Combustion. J. Braz. Chem. Soc. 17, 302–315 (2006)
8. Petersen, E.L., Hall, J.M., Smith, S.D., de Vries, J., Amadio, A.R., Crofton, M.W.: Ignition of Lean Methane-Based Fuel Blends at Gas Turbine Pressures. J. Eng. Gas Turb. Power 29, 937–944 (2007)
9. Petersen, E.L.: Interpreting Endwall and Sidewall Measurements in Shock-Tube Ignition Studies. Combust. Sci. and Tech. 181, 1123–1144 (2009)
10. Hönig, R., Theisen, D., Fink, R., Lachner, R., Kappler, G., Rist, D., Andresen, P.: Experimental Investigation of a Scramjet Model Combustor with Injection through a Swept Ramp using Laser-Induced Fluorescence with Tunable Excimer Lasers. Proc. Combust. Inst. 26, 2949–2956 (1996)
11. Do, H., Mungal, M., Capelli, M.A.: Jet Flame Ignition in a Supersonic Crossflow using a Pulsed Nonequilibrium Plasma Discharge. IEEE Trans. Plasma Sci. 36, 2918–2923 (2008)
12. Santos, A.M.: FINEP Report (2009)
13. Moura, G.S., Lacava, P.T., Toro, P.G.P., Minucci, M.A.S.: Proc. CREEM (2009)
14. Gruenig, C., Mayinger, F.: Supersonic Combustion of Kerosene/H2-Mixtures in a Model Scramjet Combustor. Combust. Sci. and Tech. 146, 1–22 (1999)

Polygonal Shock Waves: Comparison between Experiments and Geometrical Shock Dynamics

M. Kjellander, N. Apazidis, and N. Tillmark

1 Introduction

The propagation of converging polygonal shocks was studied theoretically and numerically by Schwendeman and Whitham (1987)[1]. Using the approximate theory of geometrical shock dynamics (GSD), they found solutions of the behaviour of cylindrical polygonal shock waves. They showed that an initial polygonal shape repeats at different intervals during the converging process. We have conducted experiments creating similarly shaped shock waves and compared with their work.

Polygonal shocks have been studied previously at the department of Mechanics, [2], [3], [4], [5] using different measured to control the shape of the shock. The method to shape the shocks in the present work was used in spectrometric investigations [6]. The measurements required good repeatability and the polygonal shocks proved to be more stable from run to run. However, we found the peculiar behaviour of the re-orienting polygons interesting enough in itself to warrant some additional study. The purpose with this paper is to present results on the dynamics of the shocks and how they stand a comparison with GSD.

2 Theory

This section is a short summary of [1], which is recommended for further reading. In the strong shock approximation, the area-Mach number relation becomes:

$$A = f(M) \propto M^{-n}, \tag{1}$$

where $n = 5.074$ for $\gamma = 1.4$. The predicted behaviour of a converging shock wave is displayed in Fig. 1(a). The initial shock wave consists of a number of plane fronts

M. Kjellander · N. Apazidis · N. Tillmark
Department of Mechanics, Royal Institute of Technology
Stockholm, Sweden

of strength M_0 making up a polygon, here a hexagon. At each corner the plane sides reflect against each other, with Mach stems appearing at the intersections. These will move with a stronger Mach number M_1 and eventually form a new polygon rotated with the angle $\angle$BON whereupon the process starts over. The converging process is equivalent for other polygons where Mach reflections occur in the corners. A triangular shock experiences regular reflection; this has been subjected to studies by [7], [5]. Reflected shocks also appear, but for the sake of brevity they will be ignored for the length of this work.

The increase in Mach number at each repeated interval P was shown to be, with $P = 0$ being the initial polygon:

$$\frac{r_P}{r_0} = \left(\frac{M_P}{M_0}\right)^{nP} \tag{2}$$

The radii r_P are measured from the centre to the side mid-points, and not to the vertices. Further, the Mach number ratios can be expressed as:

$$\frac{M_P}{M_0} = \mu^P, \tag{3}$$

where the constant μ is dependent on the number of sides in the polygon. Values for μ obtained by Schwendeman & Whitham are tabulated in Table 1 at the end of the paper.

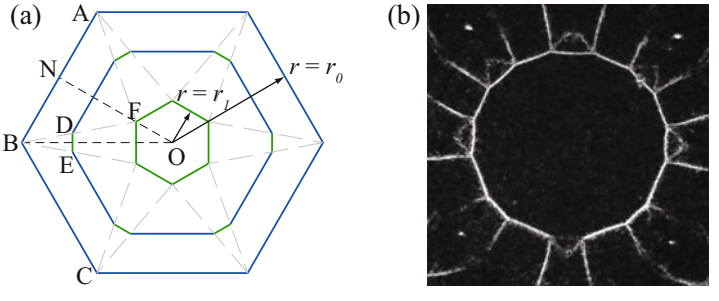

Fig. 1 (a) Converging process of hexagonal shock wave, after Schwendeman & Whitham (1987). The plane shocks AB and BC of Mach number M_0 reflect against one another, forming the Mach stem DE. DE propagates at a higher Mach number M_1, overtaking the adjoining shocks and eventually forming the side FG in a new hexagon, P=1. Image (b) Shows a schlieren image of the middle step illustrated in (a), of an octagonal shock (detail from [6]).

3 Experiment

The experiments were performed in the same shock tube facility as the previously conducted studies at KTH Mechanics cited above. The experimental setup is illustrated in Fig. 2. The tube is a plane-annular-cylindrical construction akin to that of

[8], designed to create cylindrically converging shocks. A co-axially aligned inner body transforms the incoming plane shock wave into an annular shape. The annular channel ends into a chamber with a sharp 90° bend. The test section consists of the central part of the chamber which is framed on both sides by glass windows.

A conventional parallel-light schlieren system was used for visualisation. Light is provided with either an Nd:YAG pulse laser or a continuous HeNe laser. A metal sphere with a diameter of 0.67 mm is used as a schlieren stop and photographs taken with a SensiCam PCO CCD camera or a Nikon D80 system camera. The SensiCam allows images to be taken with several individual exposures. The continuous HeNe laser is comparatively weak, resulting in relatively long individual exposures, around 0.2 μs. The shock Mach number was measured in the annular channel by two platinum film temperature sensors. These are inserted flush with the outer wall of the channel, separated by 25 cm.

To form the shock wave into the desired polygonal forms, the test section has been divided into separate radial channels. Shaped as circular segments, 50 mm long, flow dividers were inserted with their centre lines aligned radially. The outer edges are touching the annular channel entering the test section, and the inner edges ends 20 mm from the centre. Through reflections and change of curvature due to the wing-shaped dividers, the initially curved shock is divided into straight segments at the exit of the radial channels. This method was used in [6], where more details may be found. A drawing of the layout of the test section with an octagonal configuration of flow dividers is provided in Fig. 2(b).

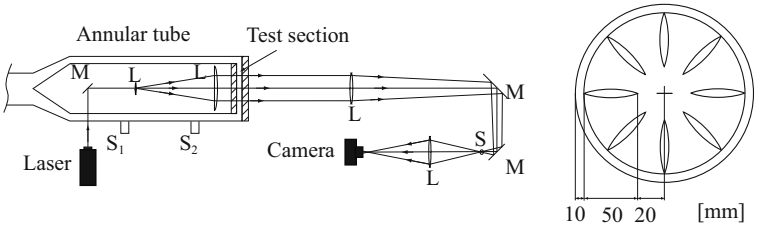

Fig. 2 Experimental setup: (a) sketch of the end of the shock tube and the schlieren setup. L, lens, M, mirror and S, the schlieren stop. S_1 and S_2 are the shock sensors. Image (b) shows a sketch of the test section from the front with an octagonal channel configuration.

4 Results and Discussion

Symmetric polygonal shock waves with six, eight and twelve sides were generated. Test gas was air and the initial low pressure was p_1=13.3 kPa. Shock strength was M=2.4 in the annular channel. As the shocks waves reached the trailing edges of the flow dividers in the test section, they had accelerated to M=3.0. A series of stronger

shocks were made with the twelve-sided configuration, with M=3.0 in the annular section and M=4.9 at the trailing edges. The Mach number at the edges becomes the initial Mach number of the sides making up the first, starter polygon. Single and multiple exposure schlieren photographs were taken to study the dynamics.

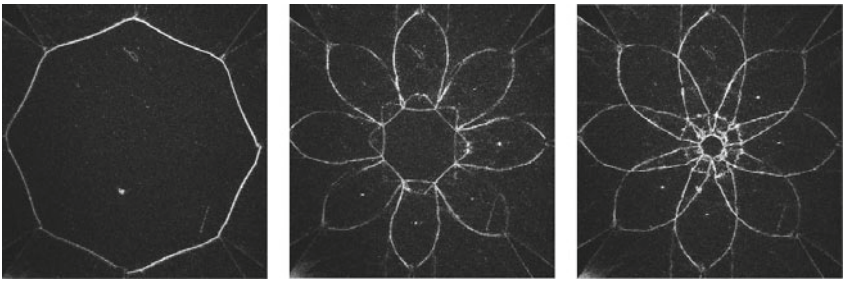

(a) $p = 0,\ t = 0$ μs (b) $p = 1,\ t \approx 11.5$ μs (c) $p = 2,\ t \approx 14.5$ μs

Fig. 3 Schlieren photographs of octagonal shocks.

Figure 3 shows three polygonal shock waves at different times with a configuration of eight wings. In image (a) the shock wave has just passed the trailing edges and each side started reflecting against the adjoining sides. This corresponds roughly to the first iteration of the octagon, P=0. The Mach number of the incident shock is M_0=3. In the second image the appearing Mach stems have overtaken the incident shocks and the front retaken an octagonal shape, rotated by 22.5°. New small Mach stems have already appeared. The process is repeated and a third octagon, interval $P = 2$, appears, now reoriented with the vertices in the same positions as the original. The shape of the shock is not entirely symmetric, which is most visible in the perturbed front in (b). The photograph in Fig. 1(b) is an intermediate step between Fig. 3(a) and (b).

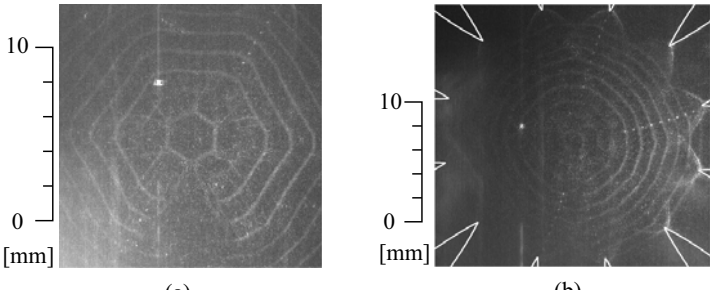

(a) (b)

Fig. 4 Multiply exposed schlieren images of hexagonal (a) and dodecagonal (b) shock waves. The wings have been outlines in (b), while they are off the picture in (a). For the two cases, the time between each exposure was 1.8 μs and 1.4 μs, respectively, while each exposure was 0.3 μs, in both cases.

Figure 4 shows multiple-exposure photos of initially six- (a) and twelve-sided (b) shocks. The radius and Mach-number variation with radius were deduced from photographs exposed at ten different intervals 0.8-1.8 μs apart, with each exposure being 0.1-0.3 μs long. Figure 5(a) shows the radius of two dodecagonal shock waves of different initial Mach numbers. The radii were measured along two diagonals, one between the focal point and an initial vertex and another between the centre and an initial side midpoint (corresponding to lines ON and OB in Fig. 1), thereby showing the propagation of the initia.l and new sides corresponding to AB and DE. Different symbols have been used in the figure to clarify when reflections occur: each symbol is used for one side from its creation until it is completely overtaken by the adjoining shocks. The fronts had almost constant velocity until reflection. For example, the circles represent the position of original incoming shock front AB propagating from N to F, again referring to Fig. 1.

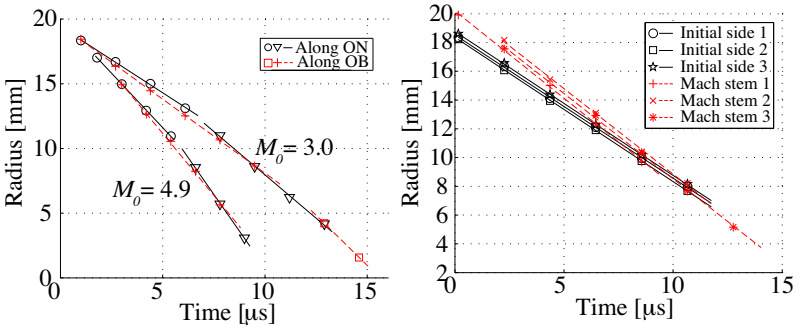

Fig. 5 (a) Position of converging dodecagonal shock waves of two different initial Mach numbers, M_0 =3.0 and M_0 =4.9. The radial position along two diagonals, ON and OB, are plotted, see Fig. 1. (b) Radius of different segments of the same octagonal shock wave. Full lines: initial sides, dashed lines: new sides appearing through the Mach reflections. The lines are best fits to the different segments.

As the individual parts of the shock were not accelerating, the acceleration of the overall shock took part through reflections where faster shocks appeared. This is a slight simplification, as the supposedly straight shocks always have a small curvature and not entirely constant velocity. As this effect was visibly small, linear fits were made to determine M_0, M_1, M_2 and M_3, the Mach numbers of each successive iteration. The twelve-sided shape experienced more recognisable iterations than the other configurations. In the octagonal case, Mach numbers up to M_2 could be measured. Table 1 shows the obtained values compared to the theoretical. The experimental values are averaged over all available ratios M_{p+1}/M_p, several runs and along three sides for each run. Figure 5(b) demonstrates the variation in one single run. The hexagonal case was problematic: the shock fronts were far from straight when arriving in the test section. The flow dividers were too short for straight shocks

Table 1 Table over values of $\mu = M_{P+1}/M_P$ for polygons with number of sides N. No meaningful experimental value for $N = 6$ could be obtained.

N	GSD[1]	This paper
6	1.289	-
8	1.201	1.21 ± 0.03 $M_0 = 3.0$
12	1.126	1.14 ± 0.04 $M_0 = 3.0$ 1.15 ± 0.04 $M_0 = 4.9$

to form. This means that a quantitative comparison with the idealised case is not reasonable and no computation of the ratios were performed.

The degree symmetry of the shock waves was highly sensitive to the inner body alignment. This initial asymmetry may be seen in Figs. 3(a) and 4(b), where vortices created during the shear at the trailing edge are seen. Care was taken to align the body to produce as symmetric shock shapes as possible. During the presented experiments, the initial relative deviation from the radius, measured as $(r_{i,max} - r_{i,min})/\overline{r_i}$, where r_i is the radius of the sides i making up the polygon, was about 3%. We believe it is possible to gain better symmetry, but this was deemed adequate for our purposes. It is also possible to use the flow dividers as a test of symmetry, also when circular shock waves are to be studied. In any case, to avoid effect of asymmetry, the quantitative results of the radius and Mach number ratios were only taken from sections where adjacent shocks arrived in the open section at virtually the same instant.

5 Conclusions

Converging polygonal shock waves were studied using schlieren optics. The octagonal and dodecagonal shapes showed the predicted alternating pattern, but the hexagonal shape was not achieved due to how the flow dividers were constructed. The dynamic process of the alternating polygons were observed and the Mach number increase measured and compared with geometrical shock dynamics, showing reasonable agreement. Slightly higher values for μ was found experimentally than theoretically, but the error of margin is too large to draw any conclusions. Increasing the Mach number showed no significant change.

References

1. Schwendeman, D.W., Whitham, G.B.: Proc. R. Soc. Lon. A 413, 297 (1987)
2. Apazidis, N., Lesser, M.: J. Fluid Mech. 309, 301 (1996)
3. Apazidis, N., Lesser, M., Tillmark, N., Johansson, B.: Shock waves 12, 39 (2002)
4. Eliasson, V., Apazidis, N., Tillmark, N.: Shock Waves 17, 29 (2007)
5. Eliasson, V., Kjellander, M., Apazidis, N.: Shock Waves 17, 43 (2007)
6. Kjellander, M., Tillmark, N., Apazidis, N.: Phys. Fluids 22, 046102 (2010)
7. Betelu, S., Aronson, D.: Phys. Rev. Letters 87, 3058 (2001)
8. Takayama, K., Kleine, H., Grönig, H.: Exps. Fluids 5, 315 (1987)

Radiative Heat Transfer Measurements in a Nonreflected Shock Tube at Low Pressures

C.M. Jacobs, R.G. Morgan, T.N. Eichmann, and T.J. McIntyre

1 Introduction

At high flight speeds, radiation becomes an important component of aerodynamic heat transfer, and its coupling with the flow field can significantly change the macroscopic features of the flow. As radiating flight conditions are typically encountered in re-entry trajectories, the associated flight regimes range from rarefied to continuum, and may have many levels of thermal, chemical and electronic nonequilibrium. Accurate estimates of the nonequilibrium radiation involved in high speed operations such as reentry are essential in order to more efficiently design thermal protection systems.

2 Experimental Facility

The X2 facility at the University of Queensland is predominantly used as an expansion tube facility for testing of scaled hypervelocity vehicle models. Ground testing facilities such as hypersonic expansion tunnel X2 take advantage of binary scaling to test small scale models of flight vehicles, which matches many of the most important parameters in high speed flight. Binary scaling requires that the product of density and the characteristic length of the vehicle must be the same in flight and experiment in order to reproduce aerodynamic similarity. However, it has been shown [3] that radiative heat transfer does not follow this same scaling factor, and true similarity with flight is not achieved for flows where the radiative and heat transfer is high and strongly coupled with the flow field. This can result in significant

C.M. Jacobs · R.G. Morgan
The Centre for Hypersonics, School of Mechanical and Mining Engineering,
The University of Queensland, Brisbane 4072, Australia

T.N. Eichmann · T.J. McIntyre
The Centre for Hypersonics, School of Mathematics and Physics,
The University of Queensland, Brisbane 4072, Australia

errors in the associated flow properties and the estimation of the heat transfer due to radiation.

To allow for experimental investigation into radiative heat transfer, the X2 facility was modified by Brandis to function as a nonreflected shock tube [2]. Nonreflected shock tube operation allows experiments to be conducted at true flight densities, avoiding the introduction of any scaling issues due to the incorrect coupling of radiation in scaled flows. In this mode, similarity with flight could only be achieved by using full size flight models. Therefore, it is not possible to reproduce the full aerodynamics of flight around a capsule this way, and experiments must be focussed on the small region of nonequilibrium post-shock flow which dominates the radiation.

This modification permitted experiments to be conducted for conditions with freestream pressures as low as 9 Pa for Titan reentry conditions (altitude 322 km [4]). Further modifications were made in order to extend the facility's range to low density conditions.

Unfortunately, the achievable conditions are limited by the boundary layer entrainment experienced as the shock propagates down the shock tube. This has been modelled by the analysis of Mirels [5], and the effect of the process is to cause the interface between the test gas and the driver gas to be reduced over the length of the tube, lowering the test time available for radiation measurements.

As the length of usable test gas has been shown to scale with the square of diameter of the tube for laminar flows, the standard shock tube in the X2 facility (bore 85 mm) was replaced with a section of larger diameter. This second modification allowed for measurements to be taken at pressures as low as 1 Pa, however contamination of the test gas restricted this to 4 Pa for gas mixtures other than pure air (altitude 359 km for Titan simulated atmospheres [4]). The modification theoretically increases the amount of available test gas by a factor of 3.3.

Figure 1 provides a schematic of the modified X2 facility and a space-time diagram of the flow. The facility uses a single-stage, free piston driver. The bore diameter in the aluminium shock tube section is 155 mm and the tube extends 5.018 m downstream of the secondary diaphragm station.

Spectral imaging was achieved using an intensified CCD camera (Princeton Instruments PI-MAX) coupled to an imaging spectrograph (Acton Research Spectra Pro SP2300 series). The system used for these experiments was capable of imaging over the wavelength range of 200-600 nm, with an optimal range of 280-500 nm. A region approximately 80 mm long by 1 mm high was imaged onto the entrance slit of the spectrometer, and a magnification factor of 0.059 was measured for these experiments.

Figure 2 provides a schematic of the optical setup using a spherical curved mirror to focus the beam onto the spectrometer slit. Two aluminium mirrors affixed to the optical table, on which the spectrometer rests, were used as a combined beam rotator and periscope to turn the image of the horizontal flow so that it fell onto an f=100 UV fused silica spherical mirror and then to the vertical spectrometer entrance slit via a straightening mirror. The iris aperture was 15 mm.

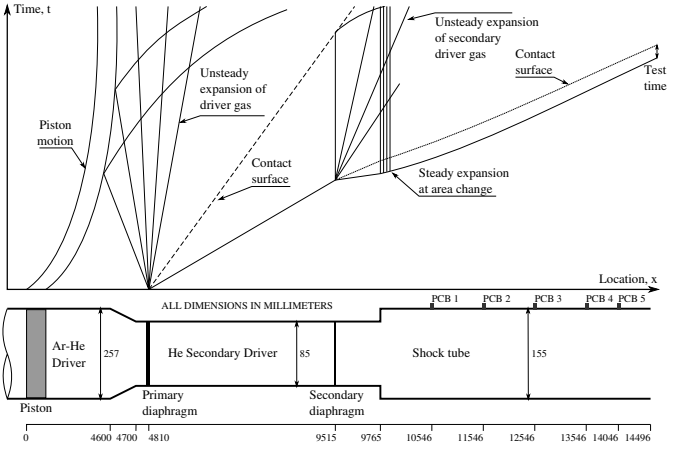

Fig. 1 Nonreflected shock tube mode schematic and space-time diagram. (NOT TO SCALE)

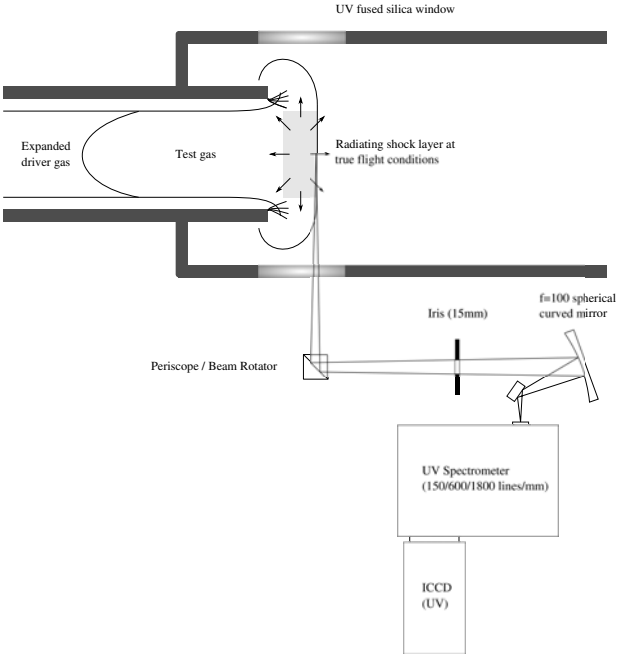

Fig. 2 Schematic of the final optical layout used in the experiments.

3 Results

Three Titan conditions (98 % N_2, 2 % CH_4) were examined. Measurements were made in the region immediately behind the shock along the centreline of the core

flow, where the shock remained planar. Test flow was achieved at pressures as low as 4 Pa in a Titan atmospheric mixture - approximately one third of the pressure previously marking the lower limit of the facility [2].

The first condition, with a freestream pressure of 13 Pa, was designed to allow a comparison between the nonreflected shock tube setup of the X2 facility and the work of Brandis [2]. In order to demonstrate the ability of the modified X2 facility to provide emission spectroscopy data for Titan reentry conditions at very low freestream pressures, two further conditions - with freestream pressures of 8 Pa and 4 Pa - were also investigated.

For the three conditions, the average shock speed over all experiments was 6.4, 6.2, and 9.0 km/s (13, 8, and 4 Pa conditions respectively). There was a significant spread in the shock speeds calculated in different experiments - 0.5, 0.5, and 1.2 km/s (13, 8, and 4 Pa respectively). This was due to air contamination in the two driver tubes and dump tank.

Results from three experiments are presented here. Experiments in the modified facility are refered to as 'NRST-Al' experiments, while comparisons to results from the older facility are refered to as 'NRST'. All measurements shown were taken with a 600 lines/mm grating, 100 μm spectrometer slit width, and 100 ns exposure time.

Figure 3(a) presents a comparison of the power density measured in the modified facility at a freestream pressure of 13 Pa with an experiment completed by Brandis [2] in the unmodified X2 facility. The power density results were integrated over the wavelength range of 310-450 nm. The NRST-Al experiment at 13 Pa had a shock speed of 6.58$\pm$0.12 km/s, while the NRST experiment had a shock speed of 7.4 km/s. It can be seen that the peak power density level matches quite well between the two facilities, although there is a decrease in the decay rate behind the shock front in the modified facility when compared to the older results. Unfortunately, in the single comparable experiment of Brandis, the front of the shock has been cut off in the spectral image, and therefore the rise time cannot be compared between the two experiments. Indicated in the figure is the length of useful gas achieved in the experiment. There is a significant improvement in both the length of measurable test gas in the NRST-Al experiment and in the signal-to-noise ratio of the results produced when compared to the NRST results. Figure 3(b) shows the spectral power density and its cumulative integration for the NRST-Al experiment.

Similar results are presented in Figure 4 for a freestream pressure of 8 Pa and a shock speed of 5.81$\pm$0.10 km/s for the NRST-Al facility. Unfortunately, no condition at 8 Pa freestream pressure in the older facility configuration is available for comparison. Therefore, the measurements have been compared with a NRST condition at a freestream pressure of 9 Pa and a shock speed of 5.7 km/s, also completed by Brandis [2]. Again, it can be seen that the modification of the facility to NRST-Al mode produced a longer length of useful test gas and greatly improved the signal-to-noise ratio.

Figure 5 presents the results of one experiment completed at a freestream pressure of 4 Pa in the modified facility, with a measured shock speed of 9.09$\pm$0.22 km/s. No measurements exist at a comparable condition in the older X2 facility, so a

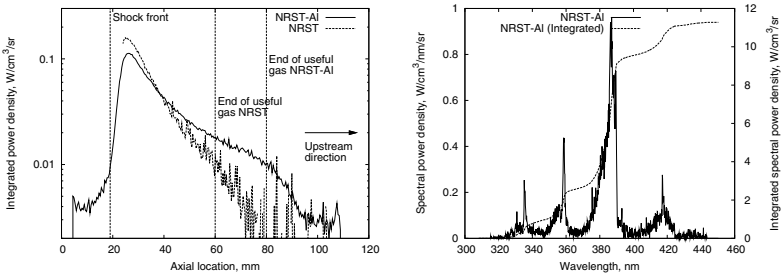

Fig. 3 (**a**) An axial profile of the power density at shock tube exit, integrated from 310-450 nm. (**b**) Spectral power density and its cumulative integration at the axial location of the peak in (**a**). The NRST-Al data was taken in the modified facility, while the NRST data were taken by Brandis [2] in the old facility. The freestream pressure was 13 Pa.

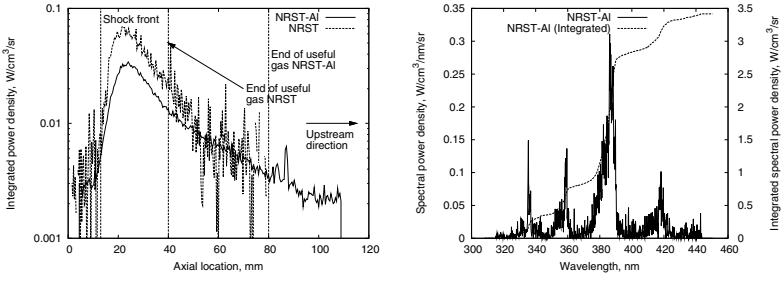

Fig. 4 (**a**) An axial profile of the power density at shock tube exit, integrated from 310-450 nm. (**b**) Spectral power density and its cumulative integration at the axial location of the peak in (**a**). The NRST-Al data was taken in the modified facility, while the NRST data were taken by Brandis [2] in the old facility. The freestream pressures for NRST-Al and NRST were 8 and 9 Pa respectively.

comparison of experimental results is not possible. The results show that the facility modifications were successful in creating usable test flow at much lower pressures than previously possible.

No noise removal has been completed for these results, however, the observed signal-to-noise ratio has been improved markedly over previous experiments in the modified facility. This is due to a combination of improved optical components and the larger length of test gas in the transverse direction. From the results presented, it can be seen that, as well as producing usable flow at lower pressure, the reduction in the signal noise and the increased distance between the shock front and the driver gas indicates that more test gas is available in the modified facility at similar pressures.

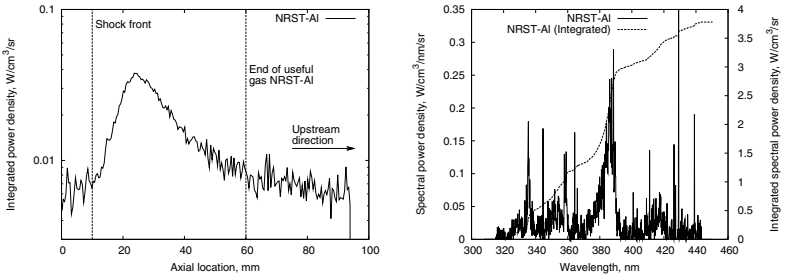

(a) (b)

Fig. 5 (**a**) An axial profile of the power density at shock tube exit, integrated from 310-450 nm. (**b**) Spectral power density and its cumulative integration for the NRST-Al condition at the axial location of the peak in (**a**). The freestream pressure was 4 Pa.

4 Conclusions

The X2 facility at the University of Queensland was modified in order to conduct emission spectroscopy measurements behind a shock wave at lower pressures than were previously possible. These measurements were successful, and calibrated data has been presented for conditions at freestream pressures as low as 4 Pa.

Acknowledgements. This work was supported by an Australian Research Council grant and the Queensland Smart State Research Facilities Fund.

References

1. Bose, D., et al.: Modeling and experimental validation of CN radiation behind a strong shock wave. In: 43rd AIAA Aerospace Sciences Meeting and Exhibit, Reno, Nevada (2005)
2. Brandis, A.: Experimental study and modelling of non-equilibrium radiation during Titan and Martian entry. PhD thesis, Mechanical Engineering, The University of Queensland (2009)
3. Capra, B.R.: Aerothermodynamic simulation of subscale models of the FIRE II and Titan Explorer vehicles in expansion tubes. PhD thesis, Mechanical Engineering, The University of Queensland (2007)
4. Justus, C.G., et al.: Engineering-level model atmospheres for Titan and Neptune. In: 39th AIAA/ASME/SAE/ASEE Joint Propulsion Conference and Exhibit, Huntsville, Alabama (2003)
5. Mirels, H.: Physics of Fluids 6, 9 (1963)

Model Experiment of Munroe Jet Formation Using Gelatin Driven by a Moderate-Speed Impactor

K. Suzuki, A. Sasoh, K. Shimizu, A. Matsuda, and M. Katayama

1 Introduction

The cylinder of explosive with hollow cavity in one side and detonator at opposite side is called as hollow charge [1]. Chemical energy generated by initiation of explosive is focused on the center of hollow cavity. And this concentrated force generates a jet with high penetration power. This phenomenon is well known as Munroe effect, and the generated jet is called as Munroe jet. When the hollow cavity is lined thin layer of metals and various materials, the liner form jet with higher penetration power than hollow charge. This is called as shaped charge which utilizes Neumann effect. Because many studies about hollow charge and shaped charge [2] are focused on property of penetration which is one of the most important factors of these phenomena, explosive and various metals have been used in experiments. In this study, simulation experiments of Munroe jet were conducted by replacing detonator and explosive in hollow charge by impactor with a velocity up to 800 m/s against shaped gelatin [3].

2 Experimental Apparatus

Phenomena of the interest are generated in a 1.0-m-dia., 2.5-m-long, stainless-steel vacuum chamber that is connected with a 25 mm $\times$ 25 mm square-bore ballistic

K. Suzuki · A. Sasoh · K. Shimizu
Department of Aerospace Engineering, Nagoya University, Furo-cho, Chikusa, Nagoya, Aichi 464-8603, Japan

A. Matsuda
Department of Mechanical Engineering, Meijo University, Shiogamaguchi, Tenpak, Nagoya, Aichi, 464-8502, Japan

M. Katayama
ITOCHU Techno-Solutions Corporation, 2-5, Kasumigaseki 3-chome, Chiyoda-ku, Tokyo 100-6080, Japan

range [4], and its ambient pressure in experiment was 1 kPa. An impactor made of polycarbonate launched from its muzzle free-flies by 100 mm before impinging a layer of gelatin target, see Fig. 2. The impactor has a 24.9 mm × 24.9 mm square flat head with 1-mm-wide side corners, that is the effective flat area of 22.9 mm × 22.9 mm square. The thickness of the impactor behind the flat surface is 10 mm (Fig. 3 (a)). The muzzle speed is measured by the method of time of flight using two combinations of a diode laser and a photo diode. The gelatin target is set with its flat surface parallel with the impactor head. Two kinds of gelatin target are examined; one with a flat surface also on the other side (Fig. 3 (b)), the other with a saw-tooth shape (Fig. 3 (c)). Composition of gelatin is 78 % water, 21 % protein and 1 % others. Its density and sound speed are 0.95 g/cm^3 and about 1520 m/s [5]. Events occurring after the impingement are visualized with a back-light arrangement, and recorded on to a high-speed framing camera (HPV-1, Shimadzu co.).

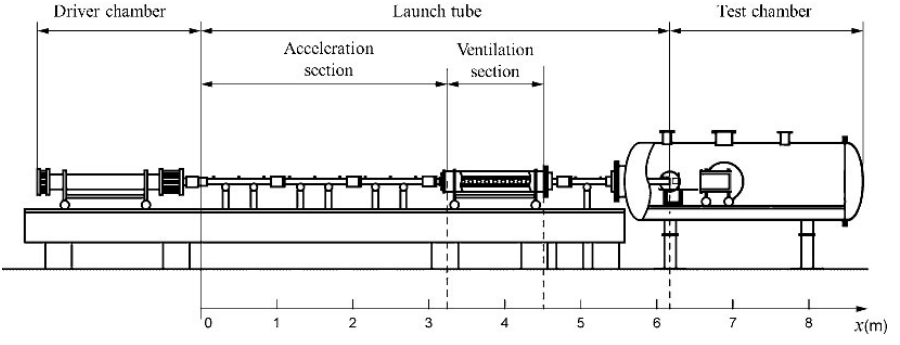

Fig. 1 Overall view of ballistic range

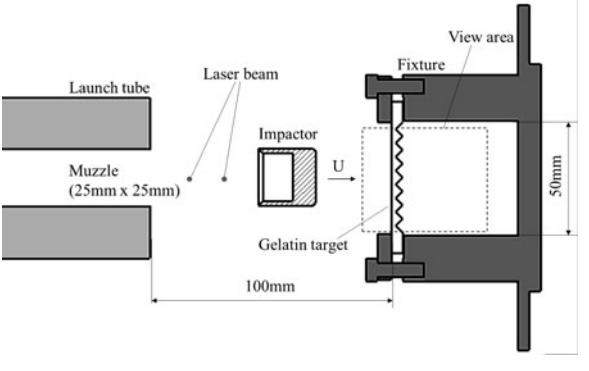

Fig. 2 Regime of visualization.

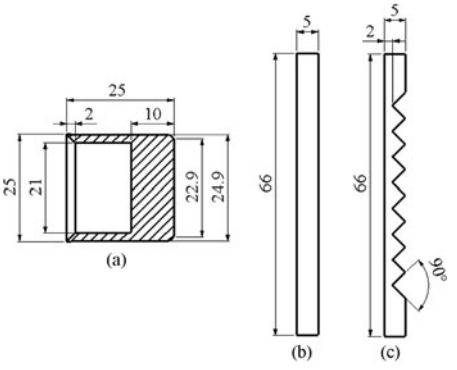

Fig. 3 Cross-sectional view of impactor and target, (a) impactor, (b) target with rear flat surface, (c) target with saw-tooth surface

3 Numerical Simulation

Numerical simulation was conducted to investigate the velocity field in the gelatin target and was performed with a hydrocode, Autodyn-2D [6]. In the numerical simulation, water was assumed to simulate gelatin.

4 Impact against Flat Target

First, experiment against the target with rear flat surface (Fig. 3 (b)) was conducted. Backlight images and corresponding numerical simulation of impact event to flat target is shown in Fig. 4. It can confirm that the rear flat surface of gelatin target projects uniformly near the center axis. In this area, flat wave reaches to rear flat surface without being contaminated by rarefaction wave generated from the edge of square flat head of impactor at collision. The side length of this area obtained from numerical simulation is about 13 mm. Next, the trajectory and speed of projection (Fig. 5) of gelatin target on the center axis in experiment was obtained from backlight images. The trajectory in the experiment agrees almost with the that of numerical simulation. The speed of projection was compared with theoretical value $2u_f$. Although speed of projection in experiment has fluctuation, the average of speed from 5 μs to 10 μs is about 851 m/s, and is nearly numerical simulation and $2u_f$.

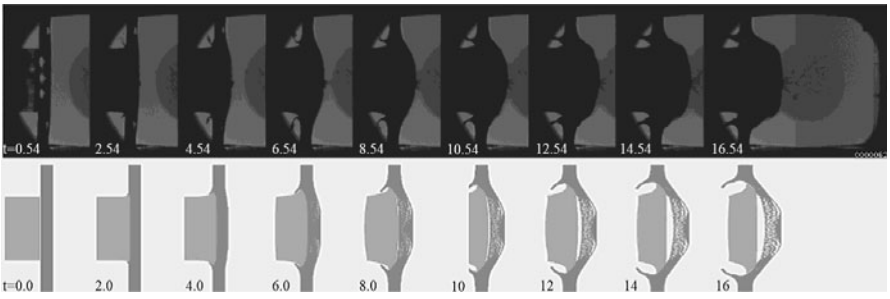

Fig. 4 Backlight projection images and corresponding numerical simulation, flat target; impact velocity is 696m/s and time interval is 2μs

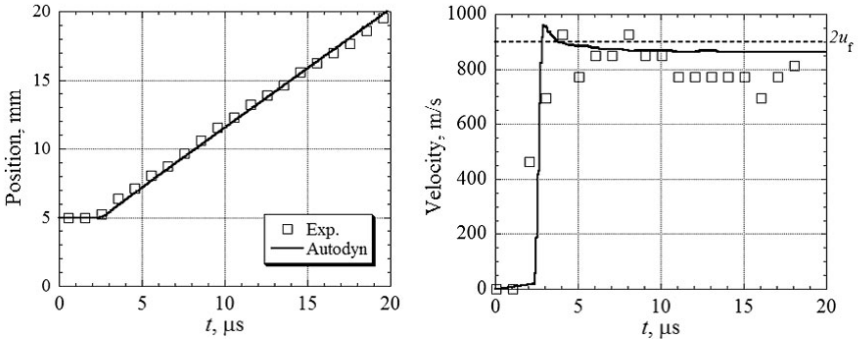

Fig. 5 Leading edge trajectory and its velocity, flat target

5 Impact against Target with Saw-Tooth Surface

Munroe jet formation was realized by using gelatin target with saw-tooth shape. It is shown by images (Fig.6) that the jets generated from hollow points of saw-tooth shape. Two lines of jet that is near center are located in effective area confirmed by experiment against flat target. Trajectories and speeds of point A and B that are shown in Fig.6 were analyzed from backlight images, and it is plotted in Fig.7. Points of A and B correspond to jet and thickest point of former shape, respectively. The speed of point A reaches to 1500 m/s in 5μs from impact event. On the other hand speed of point B is lower than $2u_f$ so that energy of impact concentrated on hollow point. The relationship between jet speed and impact speed in Fig.8 was investigated by experiments of various impact speeds. Jet speed in the range of impact speed up to 800 m/s is higher than $2u_f$.

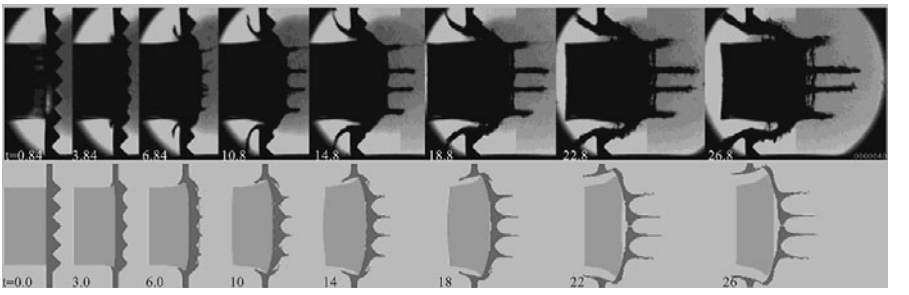

Fig. 6 Backlight projection images and corresponding numerical simulation, target with saw-tooth surface; impact velocity is 741 m/s

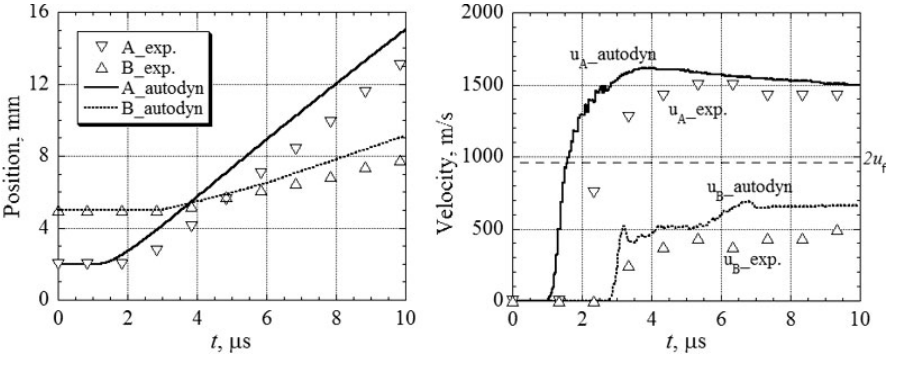

Fig. 7 Leading edge trajectory and its velocity, target with saw-toothed surface

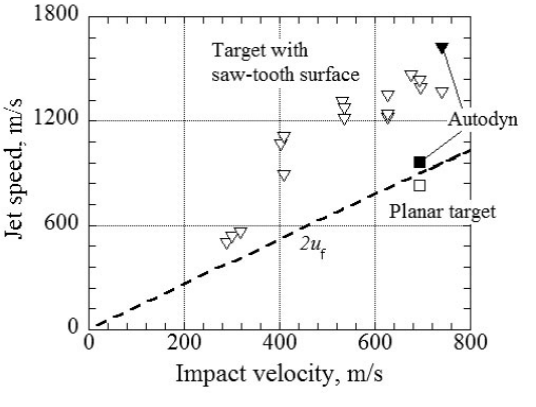

Fig. 8 Leading edge speed vs. impact speed

6 Conclusion

We have conducted model experiments to simulate Munroe jet formation by impingement of target and impactor with a velocity below 800 m/s. First, backlight images of impact events were obtained, and leading edge trajectory and its velocity were analyzed based on those images. Second, trajectories and velocities obtained on the experiment and numerical simulation were approximately similar against target with flat surface and saw-tooth surface. Finally, in every experiment against target with saw-tooth surface, jet was generated and its speed is higher than the spallation velocity, $2u_f$.

Acknowledgments. We would like to thank Mr. Koji Yamamoto who is chief technical staff in the technical center of Nagoya University.

References

1. Kinelovskii, S.A., Trishin, Y.A.: Physical Aspects of the Hollow-Charge Effect. Combustion, Explosion, and Shock Waves 16(5), 504–515 (1980)
2. Chou, P.C., Carleone, J., Karpp, R.R.: Criteria for Jet Formation from Impinging Shells and Plate. Journal of Applied Physics 47(7), 2975–2981 (1976)
3. Matthujak, A., Hosseini, S.H.R., Takayama, K., Sun, M., Voinovich, P.: High Speed Jet Formation by Impact Acceleration Method. Shock Waves 16, 405–419 (2007)
4. Sasoh, A., Kikuchi, K., Shimizu, K., Matsuda, A.: Aluminum-extrusion, Square-Bore, Aero-Ballistic Range for Launching Three-Dimensional Projectiles. International Journal of Aerospace Innovations 2(3), 147–156 (2010)
5. Bush, N.L., Hill, C.R.: Gelatine-Alginate Complex Gel: A New Acoustically Tissue-Equivalent Material. Ultrasound in Med. and Biol. 9(5), 479–484 (1983)
6. Birnbaum, N.K., Cowler, M.S., Itoh, M., Katayama, M., Obata, H.: AUTPDYN - An Interactive Non-Linear Dynamic Analysis Program for Microcomputer through Supercomputers. Transactions of 9th Structural Mechanics in Reactor Technology B, 401–406 (1987)

Benchmarking a New, Open-Source Direct Simulation Monte Carlo (DSMC) Code for Hypersonic Flows

Abdul O. Ahmad, Thomas J. Scanlon, and Jason M. Reese

1 Nomenclature

k	Boltzmann constant
L	Length scale
m	Atomic mass
Ma	Mach number
N_2	Nitrogen gas
p	Pressure
q	Heating rate
R	Gas constant
S	Distance along surface from nose radius tip
T	Temperature
z	Distance from cone tip (bi-conic case)
β	Constant
λ	Mean free path
μ	Gas dynamic viscosity
ρ	Gas density
ϕ	Diameter of circle
ω	Temperature coefficient of viscosity

Subscripts

$_W$	Wall quantity
$_\infty$	Free-stream conditions
$_0$	Stagnation conditions

2 Introduction

This paper describes the application of a new DSMC code, called *dsmcFoam*, which has been written within the framework of the open-source computational fluid dynamics (CFD) toolbox OpenFOAM [1]. The main features of *dsmcFoam* are its C++ modularity, its unlimited parallel processing capability and its ability to easily handle arbitrary, complex 3D geometries. Results of initial benchmark trials [2] have shown excellent agreement with both analytical solutions and other conventional DSMC codes.

In order to extend the range of applications of *dsmcFoam*, two hypersonic test cases are considered in the present paper:

1. Ma 15.6 flow over a 25°/ 55° bi-conic cylindrical object,
2. Ma 20.2 flow over a planetary probe geometry.

Abdul O. Ahmad · Thomas J. Scanlon · Jason M. Reese
Department of Mechanical Engineering, University of Strathclyde, Glasgow G1 1XJ, UK

Both cases represent a significant challenge to numerical codes as they must capture flow physics including weak and diffuse shocks, boundary layer separation, flow recirculation, rapid expansion and re-compression, and shear layers with steep gradients of velocity, temperature and density. Furthermore, numerical codes for high speed, rarefied gas flows should also have the ability to capture shock-boundary layer and shock-shock interactions.

3 *dsmcFoam* Characteristics

Hypersonic vehicles which operate in rarefied gas environments may encounter non-equilibrium and non-continuum flow conditions that can have a significant influence on aerodynamic performance and vehicle surface heat flux. Numerical techniques which fail to incorporate such behaviour miss an essential part of the flow physics surrounding the vehicle. Under such conditions, a particle-based method best captures the dilute flow environment.

The DSMC technique, originated by Bird [3] in the 1970s, allows particles to move and collide using kinetic-theory considerations that treat the non-equilibrium gas behaviour accurately. DSMC considers molecular collisions using stochastic rather than deterministic procedures and each DSMC particle represents a large number of real gas molecules. The decoupling of particle ballistic motion and particle collisions improves the computational efficiency of DSMC greatly in comparison with other particle methods such as molecular dynamics (MD). As a result, the DSMC technique is the dominant numerical method for applications involving rarefied gas flow.

The DSMC code *dsmcFoam* is available in the latest version of OpenFOAM, which is freely obtainable and open source under the GNU general public licence. *dsmcFoam* originated from the core characteristics of a MD code implemented by some of the present authors in the OpenFOAM toolbox. The core characteristics of *dsmcFoam* include particle initialisation in arbitrary geometries and particle tracking in unstructured, arbitrary, polyhedral meshes.

Molecular collisions in *dsmcFoam* are simulated using the variable hard sphere (VHS) model [4], with the Larsen-Borgnakke phenomenological model [3] controlling the energy exchange between kinetic and internal modes; for the present paper, energy is exchanged between translational and rotational modes only, and non-reacting gas models are used. The gas dynamic viscosity, μ, and the VHS mean free path, λ_{VHS}, are determined through:

$$\mu = \beta T^{\omega}, \tag{1}$$

$$\lambda_{\mathrm{VHS}} = (2\mu/15\rho)(5-2\omega)(7-2\omega)(2\pi RT)^{-1/2}. \tag{2}$$

For symbol meanings, please refer to section 1, Nomenclature. The temperature coefficient of viscosity, ω, of N_2 is 0.74 [3].

4 Simulation Methodology

This section details the geometries and flow conditions of the two hypersonic test cases listed in section 2, along with the numerical conditions used by *dsmcFoam*.

Experimental investigations, to obtain surface heating rates and pressure measurements, were performed by Holden *et al.* [5][6] for Ma 15.6 flow of N_2 over a 25°/ 55° bi-conic cylindrical object. The bi-conic configuration is illustrated in figure 1 and the free-stream experimental conditions are shown in table 1. Numerical input parameters are given in tables 2 and 3.

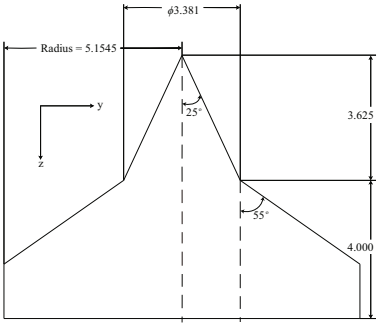

Fig. 1 25°/ 55° bi-conic cylindrical object configuration. Dimensions are in inches.

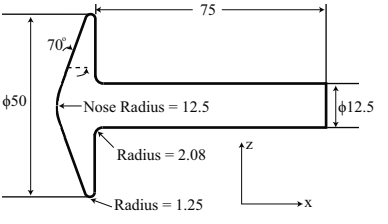

Fig. 2 Planetary probe configuration. Dimensions are in millimetres.

Table 1 Free-stream flow conditions for the two test cases.

Condition	Ma_∞	T_0 [K]	p_0 [bar]	ρ_∞ [g/m^3]	Species	λ_{VHS} [m]	Length scale [m]	Knudsen number
Bi-conic case	15.6	2089.6	20.9	0.1757	N_2	$\approx 2.19\times10^{-4}$	0.043	0.005
Planetary probe case	20.2	1100	3.5	0.0173	N_2	$\approx 1.7\times10^{-3}$	0.025	0.067

The planetary probe, considered as a test case model by AGARD[1], is a 70° spherically-blunted cone mounted on a cylindrical sting as illustrated in figure 2. The forebody configuration is identical to that of the Mars Pathfinder probe. Allègre *et al.* [7, 8, 9] conducted experiments to obtain density flowfields, drag coefficients and surface heat transfer in the SR3 low-density wind tunnel of the Centre National de la Recherche Scientifique, for Ma 20.2 flow of N_2 over the planetary probe. The flow conditions, along with numerical parameters used in the *dsmcFoam* simulation, are shown in tables 1, 2 and 3. Three numerical simulations were run for the planetary probe as a different surface temperature was required for each investigation, as

[1] Advisory Group for Aerospace Research and Development (AGARD) Fluid Dynamics Panel and its Working Group 18.

listed in table 3. The length scales presented in table 1 are the radius of the 25° section of the bi-conic cylindrical object, and the radius of the forebody configuration of the planetary probe.

Table 2 Set-up parameters for the numerical investigations.

Case	Time step (s)	No. mesh cells	No. particles	One particle represents	Processors used	Time taken to reach steady state
Bi-conic case	$\approx 5.89\times10^{-8}$	$\approx 3\times10^{6}$	$\approx 91.8\times10^{6}$	$\approx 3.3\times10^{11}$ molecules	64	28 hours
Planetary probe case	$\approx 1.3\times10^{-7}$	$\approx 7.7\times10^{6}$	$\approx 79.9\times10^{6}$	$\approx 1.3\times10^{10}$ molecules	64	2.8 hours

Both cases were modelled as three-dimensional quarter-section models, with symmetry boundary conditions, as *dsmcFoam* does not currently have an axisymmetric capability. With the use of the meshing utilities *blockMesh* and *snappyHexMesh*, available within the OpenFOAM toolbox [1], the two cases with complex geometries were meshed with ease. For good DSMC practice the mesh size is smaller than λ_{VHS}, and the numerical time-step is smaller than the mean-free-time. When the simulation has reached steady state, time-averaging is started for a period roughly equal to 5 times the duration to steady state. The bi-conic case takes longer to resolve due to the complex nature of the flow physics, involving a shock-shock interaction, in this instance compared with the planetary probe. Numerical calculations were performed on Strathclyde University's Engineering Faculty High Performance Computer (1088 cores, 100TB disk storage, 13 TeraFlops peak performance).

Table 3 Surface temperatures of the different cases.

Investigation	T_W [K]
Bi-conic case	297.2
Planetary probe case [7]: density flowfield	290
Planetary probe case [8]: drag coefficient	350
Planetary probe case [9]: heat transfer	300

5 Results and Discussion

5.1 Bi-conic Test Case

Experimental [5][6] measurements of surface heating rates and pressure measurements on the bi-conic cylindrical object are compared with the data obtained from

dsmcFoam in figures 3 and 4. The *dsmcFoam* pressure data shows a reasonable concurrence with the experimental data. The agreement is less evident for the heat flux in the 25° section of the bi-conic cylindrical object but improves in the 55° section.

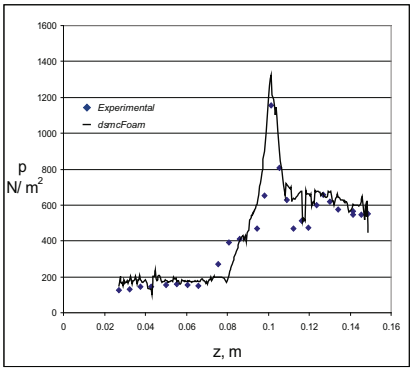

Fig. 3 Bi-conic case: comparison of experimental data and *dsmcFoam* calculations of surface pressure.

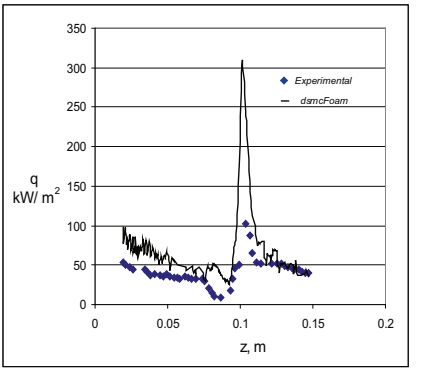

Fig. 4 Bi-conic case: comparison of experimental data and *dsmcFoam* calculations of surface heat transfer.

Within the shock-shock interaction, which occurs at z≈0.1 m, a higher surface heating rate has been observed from *dsmcFoam* in comparison to the experiment. To adequately resolve the surface heating rate in the shock-shock interaction a refined mesh is required in this region. Further DSMC studies will reduce the noise in the surface heating rate and pressure values by using more simulated particles.

5.2 *Planetary Probe Test Case*

Dimensionless density flowfields from the experimental observations of Allègre *et al.* [7], and *dsmcFoam* results are presented in figure 5. The contour plots show a very good agreement between experiment and *dsmcFoam*. The maximum density occurs in the stagnation region directly in front of the object, with a maximum relative density of approximately 16. The bow shock structure upstream of the forebody has been particularly well captured. The largest area of discrepancy appears in the wake region immediately downstream of the forebody, adjacent to the sting. This zone has highly rarefied flow so, in order to adequately resolve the flow-field in this area, a coarser mesh is required. Further DSMC studies will assess the mesh sensitivity in this area.

Comparisons of surface heat transfer between experiment [9] and *dsmcFoam* are shown in figure 6. Very good agreement is observed at the different thermocouple locations, illustrated in figure 6. Some discrepancies appear in the highly-rarefied region (at thermocouple locations 5 and 6). However, Allègre *et al.* [9] state that there is a degree of experimental uncertainty in this region due to the difficulty in

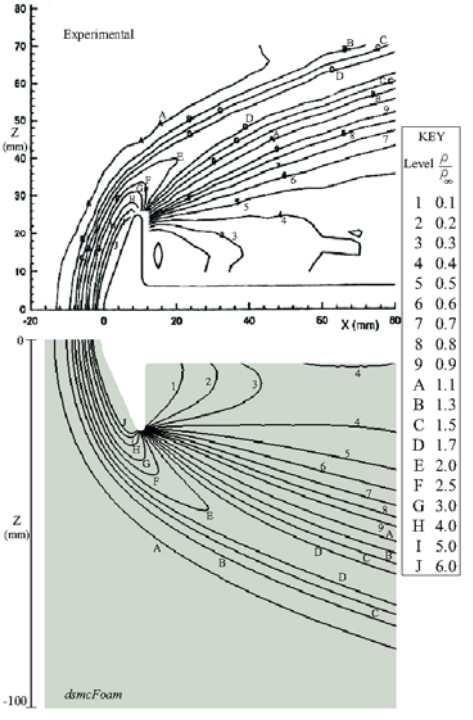

Fig. 5 Planetary probe case: comparison of experimental data (top half) and *dsmcFoam* calculations (bottom half) of dimensionless density profiles.

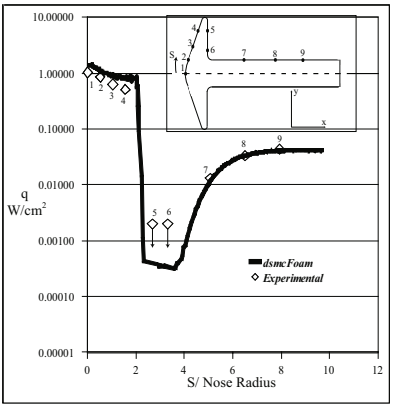

Fig. 6 Planetary probe case: comparison of experimental data and *dsmcFoam* calculations of surface heat transfer.

accurately measuring such low heat fluxes. This makes it difficult to ascertain the level of numerical-experimental agreement in this area.

The experimental [8] drag coefficient, for zero degree angle of attack, is 1.657. In comparison, *dsmcFoam* has predicted 1.89. Although this is a reasonable agreement, further grid, time-step and particle number sensitivity analyses are required to optimise the DSMC results. Furthermore, the results presented in this paper are based on particle collisions involving energy exchange between the translational and rotational modes only. However, the maximum overall temperatures encountered in the planetary probe and bi-conic cases were 1011 K and 2389 K, respectively. Under such conditions the excitation of the vibrational energy mode requires to be included in order to capture the correct flow physics. This is currently being incorporated into *dsmcFoam*.

6 Conclusions

We have presented benchmark trials of a new, open-source DSMC code called *dsmcFoam*. The code has been written within the framework of the open-source numerical analysis toolbox OpenFOAM. The principal features of *dsmcFoam* are its C++ modularity, its unlimited parallel processing capability and its ability to easily handle arbitrary, complex 3D geometries.

Results for initial benchmark trials [2] showed good agreement with analytical solutions and other conventional DSMC codes. The two hypersonic cases considered in the present paper have also shown good agreement with experimental data, however further work is required to consider permutations of different numerical parameters (e.g. altering the cell size, time step and molecules per particle). Future work on *dsmcFoam* includes the implementation of the vibrational energy mode and the inclusion of thermo-chemistry models.

References

1. OpenFOAM: The open source CFD toolbox, user guide, version 1.6 (2009), http://www.openfoam.com
2. Scanlon, T.J., Roohi, E., White, C., Darbandi, M., Reese, J.M.: An open source, parallel DSMC code for rarefied gas flows in arbitrary geometries. Computers and Fluids 39(10), 2078–2089 (2010)
3. Bird, G.A.: Molecular Gas Dynamics and the Direct Simulation of Gas Flows. Clarendon, Oxford (2009)
4. Bird, G.A.: Definition of mean free path in real gases. Physics of Fluids 26(11), 3222–3223 (1983)
5. Holden, M.S., Wadhams, T.P., Candler, G.V., Harvey, J.K.: Measurements in regions of low density laminar shock wave/ boundary layer interaction in hypervelocity flows and comparison with Navier-Stokes predictions. AIAA Paper 2003-1131 (2003)
6. Moss, J.N., Bird, G.A., Markelov, G.N.: DSMC simulations of hypersonic flows and comparison with experiments. In: AIP Conference Proceedings, vol. 762, pp. 547–552 (2004)
7. Allègre, J., Bisch, D., Lengrand, J.C.: Experimental rarefied density flowfields at hypersonic conditions over 70-degree blunted cone. Journal of Spacecraft and Rockets 34(6), 714–718 (1997)
8. Allègre, J., Bisch, D., Lengrand, J.C.: Experimental rarefied aerodynamic forces at hypersonic conditions over 70-degree blunted cone. Journal of Spacecraft and Rockets 34(6), 719–723 (1997)
9. Allègre, J., Bisch, D., Lengrand, J.C.: Experimental rarefied heat transfer at hypersonic conditions over 70-degree blunted cone. Journal of Spacecraft and Rockets 34(6), 724–728 (1997)

Author Index